

NASA



IEEE

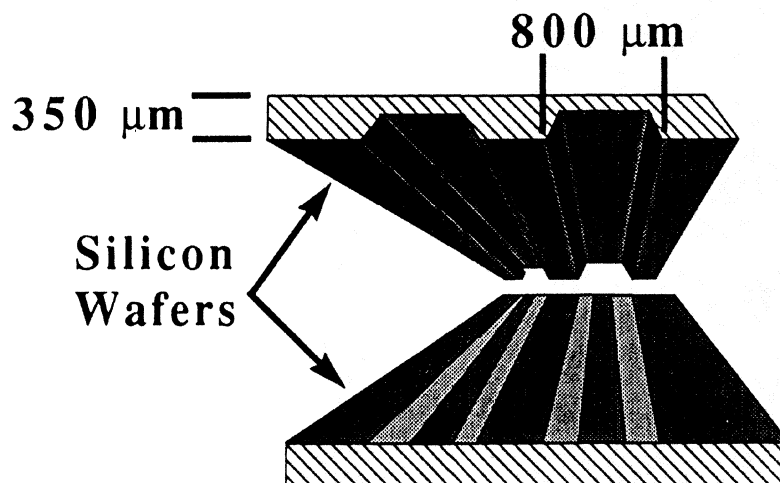
**FIFTH INTERNATIONAL SYMPOSIUM ON
SPACE TERAHERTZ TECHNOLOGY**

JPL



**The University
of Michigan**

SYMPOSIUM PROCEEDINGS



Shielded Transmission Lines

May 10-12, 1994

Iacocca Auditorium, Herbert H. Dow Building
University of Michigan, Ann Arbor, Michigan

Sponsored by:

NASA Office of Advanced Concepts and Technology, University Space Engineering Research Centers Program, and cosponsored by the Microwave Theory and Techniques Society of IEEE.

Organized Jointly by:

The University of Michigan's NASA Center for Space Terahertz Technology and JPL's Center for Space Microelectronics Technology.

Proceedings of the
FIFTH INTERNATIONAL SYMPOSIUM ON
SPACE TERAHERTZ TECHNOLOGY

May 10-12, 1994

University of Michigan
Ann Arbor, Michigan

Symposium Co-chairs:	Fawwaz T. Ulaby, University of Michigan Carl Kukkonen, Jet Propulsion Laboratory
Technical Chair:	Gabriel M. Rebeiz, University of Michigan
Local Arrangements:	Janice Rosan, University of Michigan Sue Duncan, University of Michigan
Symposium Proceedings:	Janice Rosan, University of Michigan

Preface

The Fifth International Symposium on Space Terahertz Technology was held at the University of Michigan in Ann Arbor, Michigan, on May 10-12, 1994. The Symposium, which was attended by approximately 125 scientists and engineers from the U.S., Europe, and Japan, featured papers relevant to the generation, detection, and use of the terahertz spectral region for space astronomy and remote sensing of the Earth's upper atmosphere. The program included twelve sessions covering a wide variety of topics including solid-state oscillators, power-combining techniques, mixers, harmonic multipliers, antennas and antenna arrays, submillimeter receivers, and measurement techniques.

The Symposium was sponsored by the University Space Engineering Research Centers Program of NASA's Office of Advanced Concepts and Technology (OACT), and organized jointly by the University of Michigan's NASA Center for Space Terahertz Technology and JPL's Center for Space Microelectronics Technology. The Microwave Theory and Techniques Society of IEEE served as a cooperative sponsor of the Symposium, as well as a medium for publication of some of the papers that were presented at the Symposium in the form of a mini-special issue (1995) of the *IEEE-MTT Transactions*.

The Sixth International Symposium on Space Terahertz Technology will be held at the California Institute of Technology, Pasadena, California on March 21-23, 1995.

Fawwaz T. Ulaby
Carl Kukkonen

Table of Contents

Opening Session

Chair: Fawwaz Ulaby

Welcoming Remarks
Carl Kukkonen

Novel Devices for Terahertz Generation and Radiation.....
E. Brown

Terahertz-Research at the Erlangen University Laboratories for
High Frequency Technology - A 5-Year Review.....1
H.H. Brand, J. Brune, A.J. Harth, R.H. Janker, M.G.März,
S.L. Martius, D.P Steup, B.G. Stöckel

Session 1: SIS Receivers

Chair: Margaret Frerking

A Wideband Fixed-Tuned SIS Receiver for 200 GHz Operation.....27
R. Blundell, C-Y.E. Tong, D.C. Papa, R.L. Leombruno, X. Zhang,
S. Paine, J.A. Stern, H.G. LeDuc, B. Bumble

180-425 GHz Low Noise SIS Waveguide Receivers Employing Tuned
Nb/AlO_x/Nb Tunnel Junctions.....38
J.W. Kooi, M. Chan, B. Bumble, H.G. LeDuc, P.L. Schaffer,
T.G. Phillips

SIS Receivers with Large Instantaneous Bandwidth for Radio
Astronomy60
K. Jacobs, U. Müller, U. Schwenk, D. Diehl, C.E. Honingh, S. Haas

Millimeter and Submillimeter SIS Mixers with the Noise Temperature
Close to the Quantum Limit73
A. Karpov, J. Blondel, B. Lazareff, K.-H. Gundlach

A 100 GHz Band Planar Type SIS Mixer84
M. Hieda, K. Kojima, T. Takami, T. Kashiwa, A. Iida, T. Imatani,
J. Inatani

Session 1 (Cont.): SIS Receivers

Chair: Bob McGrath

FANATIC: An SIS Radiometer for Radio Astronomy in the
660-690 GHz Band91
A.I. Harris, K.-F. Schuster, K.-H. Gundlach, B. Plathner

High Frequency Effects and Performance of a 600 GHz-635 GHz SIS Receiver Using Nb/AlO _x /Nb Junctions.....	109
M. Salez, P. Febvre, W.R. McGrath, B. Bumble, H.G. LeDuc	
Quasi-Optical SIS Mixer with a Silicon Lens for Submillimeter Astronomy	125
N.G. Ugras, J. Zmuidzinas, H.G. LeDuc	
A Low Noise 565-735 GHz SIS Waveguide Receiver.....	126
J.W. Kooi, C.K. Walker, H.G. LeDuc, P.L. Schaffer, T.G. Phillips	
An Airborne SIS-Receiver for Atmospheric Measurements at 625 to 720 GHz	142
J. Mees, S. Crewell, H. Nett, G. de Lange, H. van de Stadt, J.J. Kuipers, R.A. Panhuyzen	

**Session 2: Hot-Electron Mixers &
Superconducting Detectors**

Chair: Erich Grossman

A Superconducting Hot Electron Bolometer Mixer for 530 GHz.....	157
A. Skalare, W.R. McGrath, B. Bumble, H.G. LeDuc, P.J. Burke, A.A. Verheijen, D.E. Prober	
Investigation of a Superconducting Hot Electron Mixer	169
H. Ekström, B. Karasik, E. Kollberg, K.S. Yngvesson	
Cyclotron Resonance Detectors for THz Frequencies	189
D. Dai, C.R. Lutz, Jr., C.M. Musante, K.S. Yngvesson, K.M. Lau, E.S. Jacobs, E.R. Mueller, J. Waldman, M.A. Tischler	
Slot-Line Tapered Antenna with NbN Hot Electron Mixer for 300-360 GHz Operation	209
G. Gol'tsman, S. Jacobsson, H. Ekström, B. Karasik, E. Kollberg, E. Gershenzon	
NbN Hot Electron Waveguide Mixer for 100 GHz Operation.....	214
O. Okunev, A. Dzardanov, H. Ekström, S. Jacobsson, E. Kollberg, G. Gol'tsman, E. Gershenzon	
Noise Temperature of a Superconducting Hot-Electron Mixer	225
A.I. Elantev, B.S. Karasik	

Session 3: Josephson Effect Devices**Chair: Jonas Zmuidzinas**

Radiation from a Quasioptical Josephson Junction Array	226
M.J. Wengler, B. Guan, E.K. Track	
Characterization of the Emission from 2D Array Josephson Oscillators	234
P.A.A. Booij, S.P. Benz	
Heterodyne Mixing and Direct Detection with High Temperature Josephson Junctions.....	244
E.N. Grossman, L.R. Vale	
Measurements of Noise in Josephson-Effect Mixers	264
R.J. Schoelkopf, J. Zmuidzinas, T.G. Phillips	

**Session 4: Nonlinear Transmission Lines
& Transistors****Chair: Michael Wengler**

High Power Impulse Generation Using Lateral Stacked Nonlinear Transmission Lines.....	285
H. Shi, C.W. Domier, N.C. Luhmann, Jr.	
Millimeter-Wave On-Wafer Waveform and Network Measurements Using Active Probes	290
R. Yu, M. Reddy, J. Puhl, S. Allen, M. Case, M. Rodwell	
Cryogenic Performance of Monolithic Amplifiers for 85-115 GHz.....	309
N.R. Erickson, S. Weinreb, B.C. Kane	
Monolithic 155 GHz & 213 GHz Quasi-Optical Transistor Oscillators....	316
B.K. Kormanyos, S.E. Rosenbaum, L.P. Katehi, G.M. Rebeiz	
Monolithic Nonlinear Transmission Line Using Multi-Barrier Devices	324
W-M. Zhang, X-H. Qin, J.Y. Liao, R.P. Hsia, W.R. Geck, F. Jiang, Y. Li, C.W. Domier, N.C. Luhmann, Jr.	
Monolithic Millimeter Wave Beam Control Grid.....	332
X. Qin, W-M. Zhang, J.Y. Liao, R.P. Hsia, W.R. Geck, C.W. Domier, N.C. Luhmann, Jr., W. Bert, S. Duncan, D.W. Tu	

Session 5: Terahertz Schottky Diodes & Receivers**Chair: Peter Siegel**

A Novel Biased Anti-Parallel Schottky Diode Structure for Subharmonic Mixing.....	342
T-H. Lee, C-Y. Chi, J.R. East, G.M. Rebeiz, G.I. Haddad	
GaAs Schottky Diodes for Atmospheric Measurements at 2.5 THz	355
P.A.D. Wood, D.W. Porterfield, W.L. Bishop, T.W. Crowe	
A Monolithic Double-Slot Schottky-Diode Receiver.....	369
S.S. Gearhart, G.M. Rebeiz	
Effect of Parasitic Capacitance on the Performance of Planar Subharmonically Pumped Schottky Diode Mixers	379
I. Mehdi, P.H. Siegel	
Design Optimization of Schottky Barrier Diodes at THz Frequencies.....	394
A. Grüb, V. Krozer, A. Simon, H.L. Hartnagel	
Novel Chip Geometries for THz Schottky Diodes	404
W.M. Kelly, S. MacKenzie, P. Maaskant	

Session 6: Multipliers & Varactor Devices I**Chair: Andrew Harris**

A Balanced Doubler Using a Planar Diode Array for 270 GHz	409
N.R. Erickson, J. Tuovinen, B.J. Rizzi, T.W. Crowe	
Planar Balanced Doubler Chip to 320 GHz.....	414
B.J. Rizzi, T.W. Crowe	
On the Modelling of the Millimeter Wave Schottky Varactor	426
J.T. Louhi, A.V. Räisänen	
Verification of the Finite Element Analysis and Study of Losses of a Planar Diode Doubler.....	437
J. Tuovinen, N.R. Erickson	
Solid-State Local Oscillator Sources for 600-900 GHz.....	448
P.A. Jaminet	
Novel Varactor Diode Structures for Improved Power Performance.....	460
F.T. Brauchler, J.R. East, G.I. Haddad	

Session 7: Multipliers & Varactor Devices, II**Chair: Neil Erickson**

A Tripler to 220 GHz Using a Back-To-Back Barrier-N-N ⁺ Varactor Diode.....	475
D. Choudhury, P.H. Siegel, A.V. Räisänen, S.C. Martin, R.P. Smith	
Experiments with Single Barrier Varactor Tripler and Quintupler at Millimeter Wavelengths.....	486
T.J. Tolmunen, A.V. Räisänen, E. Brown, H. Grönqvist, S. Nielsen	
GaAs/InGaAs/AlGaAs Heterostructure Barrier Varactors for Frequency Tripling.....	497
J.R. Jones, S.H. Jones, G.B. Tait	
Planar Varactor and Mixer Diodes Fabricated Using InP-Based Materials.....	514
P. Marsh, D. Pavlidis, K. Hong	
Frequency Conversion to 368 GHz Using Resonant Tunneling Diodes.....	524
O. Tanguy, D. Lippens, J. Bruston, J.C. Pernot, G. Beaudin, J. Nagel, B. Vinter	
Quasioptical Multiplier Array with Separate Waveguide Feed.....	531
D. Steup, A. Weber	

Session 8: SIS Mixer Theory**Chair: Ray Blundell**

Theoretical and Practical Limits on the RF Bandwidth of SIS Mixers.....	548
A.R. Kerr	
Josephson Noise in SIS Receivers.....	558
B. Leridon	
Signal and Image Port Output Power in the Quantum Theory of Mixing.....	569
Q. Ke, M.J. Feldman	
Analytical Description of the Influence of the Quantum Susceptance of the Performance of SIS Mixers.....	580
P. Febvre	

Cancellation of Josephson Current in Superconducting Junction Arrays	599
R. Maoli, B. Leridon	

Session 9: Negative Resistance Devices I

Chair: Thomas Crowe

Design and Realization of GaAs D-Band IMPATT Oscillators	611
M. Tschernitz, J. Freyer	
Performance of GaAs TUNNETT Diodes as Local Oscillator Sources	622
H. Eisele, C-C. Chen, R. Mains, G.I. Haddad	
Second Harmonic 210 GHz InP Millimeter Wave Transferred Electron Oscillators.....	629
M.F. Zybura, S.H. Jones, G.B. Tait	
High-Efficiency InP IMPATT Diodes for High-Frequency Power Generation.....	648
C-C. Chen, R.K. Mains, G.I. Haddad, H. Eisele	
A Quasi-Optical Power Combiner with a Metallic Grating	659
K. Mizuno, J. Bae, Y. Aburakawa, T. Fujii	

Session 10: Passive Components and Quasi-Optics 1

Chair: Koji Mizuno

Near-Field Characterization of 2-D Beam Patterns of Submillimeter Superconducting Receivers.....	660
C-Y.E. Tong, S. Paine, R. Blundell	
A Submillimeter Wave Platelet Horn Array: Fabrication and Performance.....	674
R.W. Haas, S. Raman, G.M. Rebeiz, W.R. McGrath, G. Chin, H. Dave	
Quasi-Optical Optimization and Modal Analysis of Cornercube Schottky-Diode Mixers.....	682
J. Brune, P. Bierschneider	
Terahertz-Bandwidth Transmission Lines on Low-Permittivity Substrates.....	698
H. Cheng, J.F. Whitaker, T.M. Weller, L.P.B. Katehi	

Finite Difference Time Domain Analysis of Coplanar Transmission Line Circuits and a Post-Gap Waveguide Mounting Structure.....	700
J.E. Oswald, P.H. Siegel, S.M. Ali	
Time-Domain Characterization of Diode Mounting Structures.....	720
E. Tentzeris, N. Dib, L. Katehi, J. Oswald, P. Siegel	

Session 11: Negative Resistance Devices II

Chair: Gerard Beaudin

Large Signal Impedance of Resonant Tunneling Diodes.....	728
J.R. Lampin, O. Vanbésien, O. Tanguy, D. Lippens	
Excitation of an Oscillator with Several Resonant Tunneling Devices Integrated in Series Using RF Source.....	735
O. Boric-Lubecke, R. Sun, D-S. Pan, T. Itoh	
An Heterojunction Schottky Barrier Diode with RTD Emitter.....	742
X.J. Lu, T.E. Kosica, B.S. Perlman	
Demonstration of Power Combining at W-Band From GaAs/AlAs Resonant Tunnelling Diodes	756
D.P. Steenson, R.E. Miles, R.D. Pollard, J.M. Chamberlain, M. Henini	

Session 12: Passive Components & Quasi Optics II

Chair: Andreas Grüb

An Electro-Optic Attenuator for Terahertz Frequencies.....	768
G.F. Delgado, S. Jacobsson, J.F. Johansson	
Off-Axis Imaging Properties of Substrate Lens Antennas.....	778
D. Filipovic, G.V. Eleftheriades, G.M. Rebeiz	
230 GHz Beam Pattern Measurements of a Dipole Array-Fed Dielectric Filled Parabola.....	788
S. Raman, D.F. Filipovic, P. Stimson, R.J. Dengler, P. Siegel, G.M. Rebeiz	
Micromachined Detector Mounts for Millimeter Wave Applications.....	796
R.F. Drayton, C. Kidner, J. East, L.P.B. Katehi	
Millimeter and Submillimeter Wave Microshield Line Components.....	802
T. Weller, S. Robertson, L.P. Katehi, G.M. Rebeiz	

Beam Waveguide and Receiver Optics for the SMA.....	811
S. Paine, D.C. Papa, R.L. Leombruno, X. Zhang, R. Blundell	
Alignment for the PRONAOS Submillimeter Segmented Telescope.....	824
I. Ristorcelli, G. Recouvreur, M. Giard, B. Leriche, M. Gheudin, G. Beaudin, P. Encrenaz, F. Buisson, J. M. Lamarre, G. Serra	
Towards the Realisation of Space Borne Terahertz Waveguide Devices	842
C.M. Mann, B.J. Maddison, D.N. Matheson, M.L. Oldfield, B.N. Ellison	
Corrugated Feedhorns at Terahertz Frequencies - Preliminary Results.....	851
B.N. Ellison, M.L. Oldfield, D.N. Matheson, B.J. Maddison, C.M. Mann, A.F. Smith	

**TERAHERTZ-RESEARCH
AT ERLANGEN UNIVERSITY LABORATORIES
FOR HIGH FREQUENCY TECHNOLOGY**

- A 5-YEARS REVIEW -

by

H.H. Brand, J. Brune, A.J. Harth, R.H. Janker
M.G. März, S.L. Martius, D.P. Steup, B.G. Stöckel

Laboratories for High Frequency Technology
Friedrich-Alexander-Universität Erlangen-Nürnberg
D-91058 Erlangen, Cauerstr. 9, Germany

Abstract

Research activities in the 0.1 to 2.5 Terahertz-range at Erlangen University Laboratories for High Frequency Technology follow two main directions: establishing measurement systems and developing components following engineering design rules, that means minimizing weight and power consumption and optimizing performance and reliability whenever possible.

The paper describes fundamental research on submillimeter wave measurement systems and the development and manufacturing of the associated components. One special aspect is the multi-diode multiplier array as a stable source for different frequencies. On the mixer side, improvements can be reported by using broadband if-path design of the whisker/diode-connections and by real noise matching of the embedded HEMT if-amplifier.

Some application examples are demonstrated in detail: a broadband dual polarization scatterometer of about 600 GHz, a 4-diodes harmonic generator network, a vector doppler radar at 280 GHz in a dielectric line integrated module and a quasi-optical submillimeter wave interferometer system near 300 GHz for measurement of complex dielectric permittivity with improved accuracy. The paper is closed with an outlook to possible THz-applications in the future including the frequency range 1 THz and above. The short range radiometric imaging of a living object is demonstrated as an example.

1 Introduction: THz-Activities in Germany

Terahertz research at Erlangen University Laboratories for High Frequency Technology (ERU-LHFT) is embedded in the corresponding research activities of other German and international institutions.

In Germany, research in the Terahertz region, which will broad-mindedly include the 0.1 to 10 THz frequency range, is performed at present in 12 university laboratories and in 10 non-university research establishments, such as the Max-Planck-Institutes (MPI) or the Institutes of the Deutsche Forschungsanstalt für Luft- und Raumfahrt e.V. (DLR). In addition, there are activities in industrial laboratories, but they are not included in this survey. In Fig. 1a, universities and these research establishments are listed alphabetically with the names of their locations.

What are the fields of interest in these different types of institutions? Here we must differentiate between the natural science objectives, such as studies of star formation in molecular clouds in astrophysics or the ozone layer depletion in the earth's stratosphere, and the engineering goals to produce devices and instrumentation which enable one to make the observation of the earth's atmosphere or of the sky behind it.

As can be seen in Fig. 1b, there are the three fields of interest such as astrophysics, earth's atmosphere or plasma interaction, where high performance Terahertz-instrumentation can well be used, but it does not matter whether this high performance is best achieved by a GaAs-diode or a Niobium based SIS contact: the main scientific goal is the observation of a CO-transition in the Orion nebula or of the ClO-increase in the earth polar stratosphere or of the temperature distribution in a fusion-plasma, respectively. On the other hand there are some laboratories, where the fabrication of good semiconductor and superconductor devices or of measurement systems for THz-frequencies lies in the center of interest, independent of the field of application. In reality, there are many cross correlations of interest in the same laboratory and between the various institutions. However, this is only one aspect of a fair competition as well as of a fruitful cooperation in the Terahertz community.

2 Experimental Facilities and Research Goals at the ERU-LHFT

The research activities at the ERU-LHFT will first be reported in a survey and related to the actual facilities in the different fields. A more detailed description of some examples will follow afterwards.

The historical background of our submillimeter wave activities were some millimeter wave radar experiments in the mid seventies. To improve lateral resolution, we decided to shorten the wavelength and this was the beginning of our research on optically pumped far infrared lasers in 1979. In the meantime we could extend our source facilities by some backward wave oscillators which have the advantage of tunability but suffer in most cases from a bulky power supply. This was the reason

why we started to develop very recently a new type of lightweight and highly-stabilized power supply for microwave tubes as noted in Fig. 2.

On the other hand one can see in the next row of this list, that the interest in higher frequencies, which can be generated very easily with the optically-pumped far infrared (OPFIR) molecular gas lasers, led to some investigations in this field ([A1] - [A13]) associated with the interest in improvements for the necessary pump lasers ([B1] - [B7]).

Without going into too much detail, we should only like to mention the real improvements in amplitude and frequency stability that we achieved with the principle of the ring-type-system ([A1], [A11]) and the reduction of weight and complexity by using the rf-gas-excitation with low frequencies (around 100 kHz) for the CO₂-pump laser [B2]. A further improvement in efficiency can be expected from the sandwich type OPFIRL ([A8], [A9], [A12], [A13]) and a real reduction in costs has been achieved by using microwave excitation and diffusion cooling for the CO₂-laser [B6].

It may still be an open question, whether a gaseous OPFIR-laser system can be regarded as being able one day to become space qualified - on the grounds, there is no question, that this type of Terahertz source is a very versatile, flexible and not too expensive system for new experiments in an university laboratory.

However, we are also interested in harmonic generators using semiconductor diodes, especially in the multidiode version ([C1] - [C4]). This theme is extended in the next chapter as one of our examples for a new circuit design concept.

In the next Fig. 3, our facilities are summarized to use or to fabricate passive components and networks for the THz frequency range. Up to a frequency of about 300 GHz we try to use hollow metal waveguides and we intend to be able to fabricate nearly all passive components in our own workshop. We have re-activated the claw flange system suggested by DE RONDE in the sixties because it allows a lower total network attenuation caused by the shorter lengths one needs for each component.

Most of our measurement systems are operated in quasi optics by using either a lens-guiding or a mirror-guiding system. The different categories of the principle of invariance [E1] allow one to design beam-wave-guide networks, where the beam waist diameter or their location does not vary with frequency and that means that the transmission characteristics can be very broadband, apart from special filter functions that are required. In addition we intend to construct the "mental substrate" for the quasi-optics networks in such a way so that it can be used very flexibly by changing special components (e.g. beamsplitters or polarizers) without any new adjustment [E4]. For three years, we have been able to fabricate wire grids with a specially designed machine. Another example from our workshop is the all-metal freestanding mesh (with differently polarized and unpolarized windows) as a beam splitter for directional low-loss coupling [D2]. MARTIN-PUPLETT-diplexers can be tuned by micro-processors and pre-set to an operation frequency within a tolerance of 2 μm .

A new field of investigation is how to fabricate and how to design Dielectric Integrated Networks, that can be operated in the THz-region [D3]. This theme will also be described in more detail in the next chapter.

In Fig. 4 our situation in submillimeter wave detection and sensing is summarized. We are not primarily interested in an extremely low-noise temperature behaviour but more in good calibration facilities for power detectors and in broadband matching to the rf- and to the if-side of Schottky diode mixers [F4]. Another point of interest is the reduction of losses between the if-output of any mixing element and the input of the following if-transistor amplifier by avoiding unnecessary transformations and by utilizing direct noise matching [F5]. Further studies are going on in analyzing Gaussian beam mode mixtures in quasioptical networks [F6].

3 Examples of Measurement Systems and New Circuit Design & Technology

3.1 Dual-Polarization Scatterometry around 600 GHz

This is a 4-years project supported by the German National Science Foundation (DFG-Br 522/14) where we try to investigate how the scattering in different directions of a Gaussian beam from the surfaces of several natural and technical samples can be measured [E3]. In the frequency range from 0.1 to 10 THz, there is the situation that the wavelengths of the electromagnetic waves are of the same order of magnitude as the roughness of many body-surfaces. Therefore we cannot expect the pure diffusive scattering as is seen with visual light (Lambert's law), nor can we expect mirror-like reflection as we find at longer wavelengths. In many cases the polarization direction is also rotated by scattering so that we need two channels for measuring the co- and cross polarizations of the exact back-reflection and in addition two channels for the two polarizations at any angle of observation. In Fig. 5 the schematic of the measurement equipment is to be seen. As a signal generator, we use a wideband Russian BWO-tube, that can be tuned from 510 GHz to 700 GHz. In order to have a high dynamic range or a high sensitivity (necessary especially for the cross-polarization low level sidelobes) the heterodyn principle is utilized in all channels, where another BWO-tube or an OPFIR-laser may deliver the local oscillator power. Because of the fixed OPFIR-frequencies a tunable if-microwave amplifier in the 2 to 20 GHz range is needed together with a broadband mixer design [F4].

By rotating the sample (device under test = DUT in Fig. 5) the angle of incidence θ_i can be changed. In addition the angle of observation θ_{ob} can be changed independently. In Fig. 6, we can see how the transmitted beam hits the DUT at its waist. Assuming that the receiver optics selects again a Gaussian beam (of the lowest order) we can describe the scattered power in any direction from the scattered waves (and in the co- or cross-polarization) as is indicated in the upper part of Fig. 6. The lower part of Fig. 6 shows as one example the co-polarized power scattering versus the angle of observation for a slab of slate from a Norwegian rock (from the Porsanger Fjord). It should be remarked that in this case we found nearly no reflection peak at the angle $2\theta_i = \theta_{ob}$, (45°) which is for $\theta_i = 22.5^\circ$ the glancing angle of reflection from a smooth plane mirror. In Fig. 7 you can see the very different scattering behaviour from three surfaces with different roughness of the same artificial stone "concrete". In the case (a) of the smooth surface we observe a high reflection peak at $\theta_{ob} = 2\theta_i$ as

is expected from a plane mirror.

In the case (c) a very rough surface of the concrete block scatters the incoming wave over a wide range of angles. Obviously the different sides of an "object of observation" can be recognized by the scattering angle spectrum provided the sides differ in roughness. These investigations, which we presently carry on for many frequencies and some objects of observation, may be important for future imaging applications, either in the active radar or in the passive radiometry mode [E5].

3.2 SubMM-Wave Permittivity Measurement

In many cases of designing a lens, a beam splitter or a dielectric waveguide for example, you need the exact value of the complex dielectric permittivity (ϵ_r and $\tan\delta$) at the actual operation frequency required for an application. There are many methods known in the literature for this problem. STÖCKEL [E7] improved one of the quasi-optical methods of interferometry by investigating the errors that arise, as we know today, mainly by the mismatch of the feed horn (of the source) and the mismatch of the detector.

In Fig. 8a, this measurement system is shown schematically in the upper part, followed by an "Interferogram" which is the voltage of the pyroelectric power detector versus the shifted way of the movable (rooftop) mirror. One should expect a sinusoidal function as an interferogram, but in reality there are a lot of distortions; that can best be recognized in the Fourier-transformed spectrum of the interferogram. This can be seen in the lower part of Fig. 8a where the interferogram distortions now are clearly observed as wavenumber-harmonics. In [E7] it is described in detail how this information can be used to minimize the errors, especially for the determination of the loss factor. Results of these measurements near 300 GHz at several dielectric materials are given in Fig. 8b.

3.3 Multi-Diodes Harmonic Generator

Varactor diode harmonic generators, pumped by a compact solid state fundamental source, are today the preferred local oscillators for space or airborne application. The problem is the decrease in harmonic power P_n with increasing harmonic number n and the decrease of the conversion efficiency η_n with increasing pump power P_1 beyond a maximum value. In any case, for a given diode, a given pump frequency and a desired harmonic number, there is a maximum harmonic power that cannot be increased further even when more pump power is available - the ultimate limit being the breakdown of the diode by the pump.

This problem can be solved by using more than one diode, sharing the pump power among many diodes, driving them in the maximum efficiency-point and combining thereafter coherently (!) the harmonic power wanted for the application. This principle has been proposed several years ago but could only recently be implemented in a

reasonable approach.

In Fig. 9 the block diagram of the harmonic generation network is shown schematically. The one-diode network is seen in the upper part for comparison. If the efficiency η_n for the conversion from the fundamental pump power P_1 to the n -th-harmonic power P_n includes the linear losses of the fundamental low-pass filter F_1 and the losses of the harmonic bandpass-filter F_n , then we could write

$$P_n = \eta_n P_1 \quad (1)$$

However we should have in mind, that η_n depends on the pump power P_1 itself.

In the lower part of Fig. 9 here for example in the 4-diodes-network the efficiency η_n has the same meaning, and in addition we assume that its value is the same for each channel a, b, c and d. Then we take into account the lossy transmission through the dividing part of the network and the phase shifters for the fundamental frequency by a scattering coefficient $|^u s_1|^2$ for each channel.

In a similar way on the output side, but now at one specific harmonic number n , the transmission through the combining network is described by the scattering coefficient $|^u s_n|^2$. Here we define the transmission paths for the dividing and the combining part, respectively, according to

$$\text{Maximum of } |^u s_1|^2 = 1/M \quad (2a), \quad \text{Maximum of } |^u s_n|^2 = 1/M \quad (2b)$$

in the limit of a loss-free network and with M the number of the similar channels.

In a very simple model, neglecting linear and nonlinear interaction at the other unwanted harmonics, we can calculate the power of the n -th harmonic at the output of the combining network (and only with proper tuning of the phase in each channel) by summing up the n -th harmonic power of each channel. In the case of proper phase matching this can be for the "Multi-Diodes-Generator"

$$^M P_n = ^M P_1 \cdot \eta_n \cdot M \sum |^u s_n|^2 \cdot |^u s_1|^2 \quad (3)$$

When the fundamental power $^M P_1$ is significantly larger than the optimum value P_1 for maximum efficiency η_n , and when the losses by the dividing and combining processes are significantly low, that means, Eqn. (2) is valid, we then can expect more harmonic power at the n -th harmonic than in the "One-Diode-Generator".

In a separate paper [C4] at this conference STEUP and WEBER will describe in more detail an experimental quadrupler system for 580 GHz output frequency following these principles.

3.4 Dielectric Integrated Networks

In contrast to continuous waveguiding for example by hollow metal pipes or metal strip conductors, the waveguiding in a beam waveguide happens discontinuously by a set of lenses or mirrors. The propagation of the em-wave between two lenses or mirrors can only be in a straight forward line, not curved as in a hollow pipe.

Discontinuous waveguiding is a form of weak-guiding, but with the advantage that the beam diameter even at the fundamental mode can be somewhat larger than the wavelength. We indeed often design a beam waveguide according to $3\lambda < w_0$, where w_0 is the half diameter of the smallest part, the waist, of a Gaussian beam. This leads to the consequence that the lateral and longitudinal dimension are in an acceptable range of millimeters even when the wavelength is in the submillimeter range. In contrast to this, the lateral size of hollow pipes or strip waveguides have to be smaller than the wavelength, which means that we have difficulties in handling, fabricating or mounting at dimensions below 100 μm .

Another point are losses of the em-waves, which increase with decreasing lateral dimensions. Hence the success of quasi optics can be well understood for these above-mentioned reasons. However, concerning mass production, there is one disadvantage of beam waveguide networks: they cannot easily be produced in an integrated form. A new approach to this problem has been proposed in our laboratory by B. STÖCKEL and will be presented at the coming IEEE-MTT International Microwave Symposium [D3].

In Fig. 10a the new concept of low-loss weak waveguiding at THz-frequencies by a dielectric core inserted in a dielectric substrate is compared with the waveguiding in a beam waveguide. The new idea is to use a very small difference in the diffraction index of the core strip (n_c) and the embedding substrate (n_s). In both dielectric materials the loss factor has to be as small as possible of course, but the gain of this concept is an increase of lateral size and that means a reduction of fabrication difficulties and hence of production costs. In Fig. 10b an experimental "Vector Doppler Radar" is shown which was fabricated in our laboratory using this principle. This network was selected as a candidate because it needs directional couplers as well as normal transmission lines and of course bends for a change of propagation directions. In addition, even antennas can be easily made by this concept which is currently investigated in more details in our laboratory.

As can be seen from the photograph of Fig.11 the plastic substrate (TPX) can be fabricated by milling as in our workshop, or by casting into a special matrix. The core material, in our case paraffin, is cast into the channels at a temperature of about 80 °centigrade.

Vector doppler radars need a frequency-shifted local oscillator, which is provisionally done in our experiment by an external mechanical modulator, as is indicated in Fig. 10b. The advantage of this principle is, of course, to be able to differentiate between positive and negative velocities of a moved target.

4 Possible Future Terahertz Applications

The very center of interest of this conference lies on space-qualified devices and systems operating in the THz region, as is clearly indicated in the conference's name. This technology is highly sophisticated, used in only a few missions and is therefore very expensive. Before this technology has spin-offs into a low-cost mass application beyond space missions, the market for these mass applications has to be found. Hence, it might be of interest, even for the Space Terahertz community, to look back to the earth for new applications beyond astrophysics and earth's observation from space.

In the next Fig. 12 we have listed four fields of applications which have the potential of mass applications, when they are needed or wanted from a market in the future. We know very well that all the titles in the list are more speculative than shown to be a requirement. But nevertheless, we believe we should think about the future.

On the other hand people have today the desire to be protected better against illness, or environmental poisoning or criminal attacks. In the field of medical diagnostics it would be very helpful if the individual state of health could be recognized by a pure non-invasive measurement from the skin or with an expiration from the lungs. Can anyone answer the question whether THz-spectroscopy of man's expiration could work as an early warning system, e.g. for lungs cancer, before we have investigated it? There is no question that security services would welcome any system that could detect reliably concealed plastic bombs or drugs. Another interesting field of application could be that of personal identification.

In the field of bio-chemical research many questions concerning real application of THz-frequencies are still open today. Possibly, the close range observation of gas products, from waste tips or the emission from plants may yield indications of imminent danger. Experimentally, however, we have demonstrated that radiometric imaging of plant-elements like blossoms or leaves is possible at 600 GHz [E5], [E6]). In the next Fig. 13 the black-and-white copy of a false-coloured picture taken with a lateral resolution of 2 mm (3600 pixels) of a maple leaf is presented. The different colours indicate different temperatures or different emissivities along the leaf. The biological or chemical background of this emission variation is not yet understood. However, we have seen for the first time through a new window with 600 GHz-eyes into the very manifold life around us.

5 Conclusions

We have tried to report briefly on a 5-years-Terahertz-research periode at Erlangen University Laboratories for High Frequency Technology by scanning the experimental facilities and scientific goals in the three fields: sources, passive components/networks and detecting/sensing. These investigations and results are documented in 41 publications, which are cited as references. Four topics are discussed in more detail to illustrate our spectrum. The authors would like to thank 53 students for their efforts during their diploma-thesis and pre-diploma-thesis-work, concerning THz-research, our staff members G. Bauer, H. Bergmann, H. Ertl, H. Frisch, L. Höpfel, M. Kühn, F. Krug, A. Oswald and J. Popp for their very appreciated support in manufacturing, organization and preparation, the national German Science Foundation DFG for financial support in 4 Submillimeter Wave projects and many friends in industry, research establishments and other universities for experimental support and advice.

6. References

A. Optically Pumped FIR-Laser Sources

- [A 1] JANKER R., MÄRZ M., VOIGT Ch., BRAND H.: Compact Submillimeter Wave Ring Laser System for Field Experiments. 14th Int. Conf. on Infrared and Millimeter Waves. Würzburg, Oct. 2 - 6, 1989, Conf. Digest pp. 290-291
- [A 2] HARTH A.: Pump Beam Propagation in Circular Waveguides of Optically Pumped Far-Infrared Lasers. International Journal of Infrared and Millimeter Waves, Vol. 12, No. 3, 1991, 221 - 237
- [A 3] HARTH A.: Flächenresonatoren für Laser. Archiv für Elektrotechnik 74 (1991), 253 - 260
- [A 4] HARTH A., JANKER R.: Small-Signal Gain in CW Optically Pumped Far-Infrared Lasers. 16th Int. Conf. on Infrared and Millimeter Waves. Lausanne, Aug. 26-30, 1991, SPIE Vol. 1576 Conf. Digest. 110 - 111
- [A 5] JANKER R.: Matching The Pump Beam in Optically Pumped Far-Infrared Ring Lasers. 16th Int. Conf. on Infrared and Millimeter Waves, Lausanne, Aug. 26-30, 1991, SPIE Vol. 1576 Conf. Digest, pp. 114 - 115
- [A 6] JANKER R., KRÜGER A.: A Variable Output Coupler for Far-Infrared Ring Lasers. 16th Int. Conf. on Infrared and Millimeter Waves, Lausanne, Aug. 26-30, 1991, SPIE Vol. 1576 Conf. Digest, pp. 321 - 322
- [A 7] HARTH A.: Thermal Pump Saturation in CW Optically Pumped Far Infrared Lasers. Infrared Physics. Vol. 33, No. 6, 1992, pp. 523-529
- [A 8] HARTH A., BRAND H.: Transversely Pumped CW Submillimeterwave-Laser with Sandwich Resonator. IQEC '92, 18th International Quantum Electronics Conference, June 14-19, 1992, Vienna, Austria, PTu110
- [A 9] HARTH A.: Optically Pumped Far-Infrared Laser with Sandwich Resonator. Optical and Quantum Electronics 24 (1992) pp. 1339-1341
- [A10] JANKER R.: Diffusion of Excited State Molecules in FIR- and CO₂-Lasers. Int. Journal of Infrared and Millimeter Waves, Vol. 14, No. 7, 1993, pp. 1389 -1406
- [A11] HARTH A., JANKER R.: Optisch gepumpter Ferninfrarot-Laser mit gestreckten und Ring-Resonatoren - Ein Vergleich. Archiv für Elektrotechnik, Vol. 77, No 1, Nov. 1993, S. 41-44
- [A12] HARTH A., VOLKHOLZ P.: Gain of a CW Optically Pumped Far Infrared Laser with Sandwich Resonator. Int. Journal of Infrared and MM-Waves, Vol. 15, No. 2, pp. 4 - 39
- [A13] HARTH A.: New Results about the Efficiency Problem of CW Optically Pumped Far-Infrared Lasers. 1994 CIRP 6: Topical Meeting on Infrared Lasers, Ascona, Switzerland, May 19 - June 3, 1994, Conference-Proceedings (to be published)

B. CO₂-Pumped Laser Sources

- [B 1] RENZ W.: CO₂-Laseranregung durch eine Mikrowellengasentladung in einer nicht resonanten Entladungsstruktur. ITG-Fachtagung Vakuumelektronik und Displays, 8.- 0. Mai 1989, Garmisch-Partenkirchen, Tagungsband S. 341-345
- [B 2] HELLER F.J., JIRMANN J., BRAND H.: Low-Frequency RF-Excitation of CO₂-Laser. 14th Int. Conf. on Infrared and Millimeter Waves. Würzburg, Oct. 2 - 6, 1989, Conf. Digest pp. 292-293
- [B 3] BRAND H.: Hochfrequenzanregung von Gas Lasern. OPTO-Elektronik Magazin Vol. 5, 1989, S. 525 - 530
- [B 4] HAIDNER., KIPFER P. SHERIDAN J.T., SCHWIDER J., STREIBL N., COLLISCHON M., HUTFLESS J., MÄRZ M.: Diffraction Grating with Rectangular Grooves Exceeding 80 % Diffraction Efficiency. Infrared Physics, Vol. 34, No. 5, 1993, pp. 467-475
- [B 5] GRUDSZUS S., MÄRZ M.: Influence of Gas Dissociation and Xenon Addition on Steady-State Microwave-Excited CO₂ Laser Discharges. Journal of Physics D: Applied Physics 26 (1993) pp. 1980-1986
- [B 6] MÄRZ M., OESTREICHER W.: Microwave Excitation of a Diffusion-Cooled CO₂ Laser. Journal of Physics D Applied Physics, Vol. 27, No. 3 pp. 470-474
- [B 7] MÄRZ M., OESTREICHER W.: A versatile microwave plasma source and its application for a CO₂ laser. Review of Scientific Instruments (to be published)

C. Microwave Pumped Harmonic Generators

- [C 1] HENKE G.: Higher-Order Harmonic Generation by a Multi-Diode Phased Array. 14th Int. Conf. on Infrared and Millimeter Waves. Würzburg, Oct. 2 - 6, 1989, Conf. Digest pp. 353-354
- [C 2] STEUP D.: Submillimeterwellen-Frequenzvervielfacher mit quasioptischer Auskopplung. Archiv für Elektrotechnik, Vol. 77, No 1, Nov. 1993, S. 29-34
- [C 3] STEUP D.: Whisker-Contacted Diode-Multipliers as Quasioptical SMMW-Arrays. Int. Journal of Infrared and MM-Waves, Vol. 14, No. 12, 1993, pp. 2519-2531
- [C 4] STEUP D., WEBER A.: Quasioptical Multiplier Array with Separate Waveguides Feed. 5th International Symposium on Space Terahertz Technology, 1994, May 10 - 12, Ann Arbor, MI, USA. Conference Proceedings

D. MM- and SubMM-Wave Passive Components

- [D 1] STÖCKEL B.: A 300 GHz Hybrid Form Rotary Attenuator.
21st European Microwave Conference, 9 - 12 September 1991, Stuttgart,
Conference Proc. Vol. 1, pp. 812 - 817
- [D 2] STEUP D.: A Tunable 600 GHz Bandpass-Filter with large Free- Spectral-
Range. International Journal of Infrared and Millimeter Waves,
Vol. 13, No. 12, December 1992, pp. 1767-1779
- [D 3] STÖCKEL B.: Integrated Optics for the Terahertz-Region.
1994 IEEE MTT-S International Microwave Symposium, May 23-27, 1994,
San Diego, CA. Conference-Proceedings

E. MM- and SubMM-Wave Networks

- [E 1] STÖCKEL B.: Derivation of Invariant Quasi-Optical-Systems and Their
Applications - Especially at a mm-Wave-Fourier-Transform-Spectrometer.
AEÜ Band 44 (1990), Heft 4, S. 306 - 312
- [E 2] STÖCKEL B.: A MM-Wave Network Analyzer System with Fundamental
Frequency Conversion. 16th Intern. Conf. on Infrared and Millimeter
Waves. Lausanne, Aug. 26-30, 1991, SPIE Vol. 1576 Conf. Digest
p. 350-351
- [E 3] BRUNE J.: Polarimetric Submillimeterwave Reflectometry using a
Real-Time Quasi-Optical System. Intern. Microwave Symposium 1992,
Albuquerque. Symposium Digest IEEE-MTT-S, Session IF1-M7,
p. 357-360
- [E 4] BRUNE J.: A Flexible Quasi-Optical System for Polarimetric Submillimeter-
Wave Reflectometry. IEEE T-MTT, Vol. 40, No. 12, Dec. 1992,
pp. 2321-2324
- [E 5] BRAND H., BRUNE J.: Reflektivität und Abbildung von natürlichen und
technischen Objekten bei Submillimeterwellen. DGON 8.Radarsymposium,
Neubiberg, 14.-16.9.93, Tagungsband S. 51 - 58
- [E 6] BRUNE J.: Aktive und passive Terahertz-Meßtechnik mit einem flexiblen
quasioptischen Meßsystem bei 600 GHz. Archiv für Elektrotechnik, Vol. 77,
No. 1, Nov. 1993, S. 71-77
- [E 7] STÖCKEL B.: Quasi-Optical Measurement of Complex Dielectric Constant
at 300 GHz. Int. Journal of Infrared and Millimeter Waves, Vol. 14, No. 10,
1993, pp. 2131-2148
- [E 8] STÖCKEL B.: Planar Dielectric Waveguides with Small Index Difference
for Integrated Terahertz-Circuits. IEEE-MTT Vol. 42, 1994
(to be published)

F. MM- and SubMM-Wave Detection

- [F 1] BRAND H., STÖCKEL B.: Fibre-Ended Photoacoustic Millimeter-Wave Detector. 14th Int. Conf. on Infrared and Millimeter Waves. Würzburg, Oct. 2 - 6, 1989, Conf. Digest pp. 514-515
- [F 2] STÖCKEL B.: A Modular 300 GHz Waveguide Mixer with Ultra-Broad Bandwidth. 16th Intern. Conf. on Infrared and Millimeter Waves. Lausanne, Aug.26-30 1991, SPIE, Vol. 1576 Conf. Digest pp. 144 - 145
- [F 3] STÖCKEL B.: A Broad-Band Harmonic 300 GHz Mixer with Flexible LO-Feed. 16th Intern. Conf. on Infrared and Millimeter Waves. Lausanne, Aug.26-30,1991, SPIE Vol. 1576 Conf. Digest pp. 208 - 209
- [F 4] BRUNE J.: An Open Structure 600 GHz Mixer with Broadband IF Output Coupling. 21st European Microwave Conference, 9 - 12 September 1991, Stuttgart, Conference Proc. Vol. 1, pp. 247 - 252
- [F 5] MARTIUS S., WUNNER S.: Rauschoptimierte Zusammenschaltung THz-Mischer-HEMT- ZF-Verstärker. Archiv für Elektrotechnik, Vol. 77, No 1, Nov. 1993, S. 65-70
- [F 6] BRUNE J., BIERSCHEIDER P.: Quasi-Optical Optimization and Modal Analysis of Cornercube Schottky-Diode Mixers. 5th International Symposium on Space Terahertz Technology, 1994, May 10 - 12, Ann Arbor, MI, USA. Conference-Proceedings

ASTROPHYSICS	6, 13, 18, 19
EARTH'S ATMOSPHERE	2, 13, 14, 15, 21
PLASMA INTERACTION	12, 17, 20
FUNDAMENTAL PHYSICS and CALIBRATION	1, 10 22
SEMICONDUCTOR DEVICES	3, 7, 9
SUPERCONDUCTOR DEVICES	6, 10, 16
MEASUREMENT SYSTEMS	4, 5, 8, 11

(b) Research Topics

<u>Universities</u> 1 TU Braunschweig 2 U Bremen 3 TH Darmstadt 4 U Erlangen 5 U Karlsruhe 6 U Köln 7 TU München 8 TU München 9 TU München 10 U Regensburg 11 U Siegen 12 U Stuttgart	<u>Laboratories for</u> Semiconductors + Optics Remote Sensing High Frequency Electronics High Frequency Technology High Frequency Technology Physics Applied Electronics High Frequency Technology Walter-Schottky-Institute Physics High Frequency Technology Plasma Research
<u>Research Establishments</u> 13 DLR Berlin 14 DLR Wessling 15 DLR Wessling 16 KFA Jülich 17 KFA Karlsruhe 18 MPI Bonn 19 MPI Garching 20 MPI Garching 21 MPI Lindau 22 PTB Braunschweig	<u>Institutes for</u> Space Sensor Technology High Frequency Technology Optoelectronics Solid State Physics Technical Physics Radio Astronomy Extraterrestrial Physics Plasma Physics Atmospheric Research Frequency Measurement

(a) Locations and Institutions

Fig. 1: Terahertz-Research Activities in Germany

MILLIMETER- and SUBMILLIMETER-WAVE SOURCES																					
Facilities	Goals																				
BWO-TUBES <table> <tr> <th></th><th>f/GHz</th></tr> <tr> <td>RWO S 50 Siemens</td><td>33 - 51</td></tr> <tr> <td>RWO S 60 Siemens</td><td>40 - 60</td></tr> <tr> <td>RWO S 80 Siemens</td><td>60 - 90</td></tr> <tr> <td>RWO S 110 Siemens</td><td>75 - 110</td></tr> <tr> <td>RWO S 170 Siemens</td><td>110 - 170</td></tr> <tr> <td>2PA T 56 E-Dynam</td><td>140 - 149</td></tr> <tr> <td>TH 4219 Thomson</td><td>280 - 305</td></tr> <tr> <td>TH 42 XX Thomson</td><td>550 - 610</td></tr> <tr> <td>OB 74 Moscow U.</td><td>520 - 705</td></tr> </table>		f/GHz	RWO S 50 Siemens	33 - 51	RWO S 60 Siemens	40 - 60	RWO S 80 Siemens	60 - 90	RWO S 110 Siemens	75 - 110	RWO S 170 Siemens	110 - 170	2PA T 56 E-Dynam	140 - 149	TH 4219 Thomson	280 - 305	TH 42 XX Thomson	550 - 610	OB 74 Moscow U.	520 - 705	<ul style="list-style-type: none"> • Highly Stable Power Supply
	f/GHz																				
RWO S 50 Siemens	33 - 51																				
RWO S 60 Siemens	40 - 60																				
RWO S 80 Siemens	60 - 90																				
RWO S 110 Siemens	75 - 110																				
RWO S 170 Siemens	110 - 170																				
2PA T 56 E-Dynam	140 - 149																				
TH 4219 Thomson	280 - 305																				
TH 42 XX Thomson	550 - 610																				
OB 74 Moscow U.	520 - 705																				
GASEOUS LASERS <table> <tr> <td>SMMW: Different Lines from OPFIR-Lasers with CH₃OH, HCOOH, CH₃F</td><td> <ul style="list-style-type: none"> • Stabilized • Ring-Type • Sandwich-Type </td></tr> <tr> <td>Pump-Lasers with CO₂</td><td> <ul style="list-style-type: none"> • Compact • RF-Excited </td></tr> </table>	SMMW: Different Lines from OPFIR-Lasers with CH ₃ OH, HCOOH, CH ₃ F	<ul style="list-style-type: none"> • Stabilized • Ring-Type • Sandwich-Type 	Pump-Lasers with CO ₂	<ul style="list-style-type: none"> • Compact • RF-Excited 																	
SMMW: Different Lines from OPFIR-Lasers with CH ₃ OH, HCOOH, CH ₃ F	<ul style="list-style-type: none"> • Stabilized • Ring-Type • Sandwich-Type 																				
Pump-Lasers with CO ₂	<ul style="list-style-type: none"> • Compact • RF-Excited 																				
HARMONIC GENERATORS <table> <tr> <td>Experimental Test Chains</td><td> <ul style="list-style-type: none"> • Multi-Diode </td></tr> <tr> <td>37.5 75 150 GHz</td><td> <ul style="list-style-type: none"> • Coherent Harmonic Combining </td></tr> <tr> <td>150 300 600 GHz</td><td> <ul style="list-style-type: none"> • Open Structure </td></tr> </table>	Experimental Test Chains	<ul style="list-style-type: none"> • Multi-Diode 	37.5 75 150 GHz	<ul style="list-style-type: none"> • Coherent Harmonic Combining 	150 300 600 GHz	<ul style="list-style-type: none"> • Open Structure 															
Experimental Test Chains	<ul style="list-style-type: none"> • Multi-Diode 																				
37.5 75 150 GHz	<ul style="list-style-type: none"> • Coherent Harmonic Combining 																				
150 300 600 GHz	<ul style="list-style-type: none"> • Open Structure 																				

Fig. 2: MM- and SubMM-Wave-Sources:
Facilities and Goals at ERU-LHFT

TERAHERTZ-NETWORKS and PASSIVE COMPONENTS	
Facilities	Goals
HOLLOW METAL WAVEGUIDING	up to 300 GHz "Claw Flange"
Passive Components	
BEAM WAVEGUIDING	<ul style="list-style-type: none"> • Modular • Broadband • Flexible Systems
with Lenses (PE, TPX, PTFE) or Mirrors (plan, elliptical)	
Beam Splitter	
Wire Grids MP-Diplexer Pol-Rot., Phase S., Attenuator	<ul style="list-style-type: none"> • Unpolarized Metal Mesh 25 μm \varnothing • Pre-settable • Available
Integrated THZ-OPTICS	at 300 GHz
Dielectric Lines Directional Couplers Antennas	
	<ul style="list-style-type: none"> • Low Loss • Single Mode • Low Sidelobes

Fig. 3: Terahertz Networks and Passive Components
Facilities and Goals at ERU-LHFT

SUBMILLIMETER WAVE DETECTION and SENSING	
Facilities	Goals
THERMAL SENSORS	
Golay Cell Pyroelectric Detectors Large Aperture Sensors	
SCHOTTKY-DIODES	
Waveguide Mixers Open Structure Mixers IF-HEMT-Amplifier Spectral Analyser-Frontends 90 - 140 GHz 140 - 220 GHz 220 - 300 GHz 400 - 460 GHz 560 - 600 GHz	Fundamental and Subharmonic Mode • Broadband Design • Noise Matching
BEAM DIAGNOSTICS	• Mode Mixture Analysis
Near Field Sensing	

Fig. 4: SubMM-Wave Detection and Sensing
Facilities and Goals at ERU-LHFT

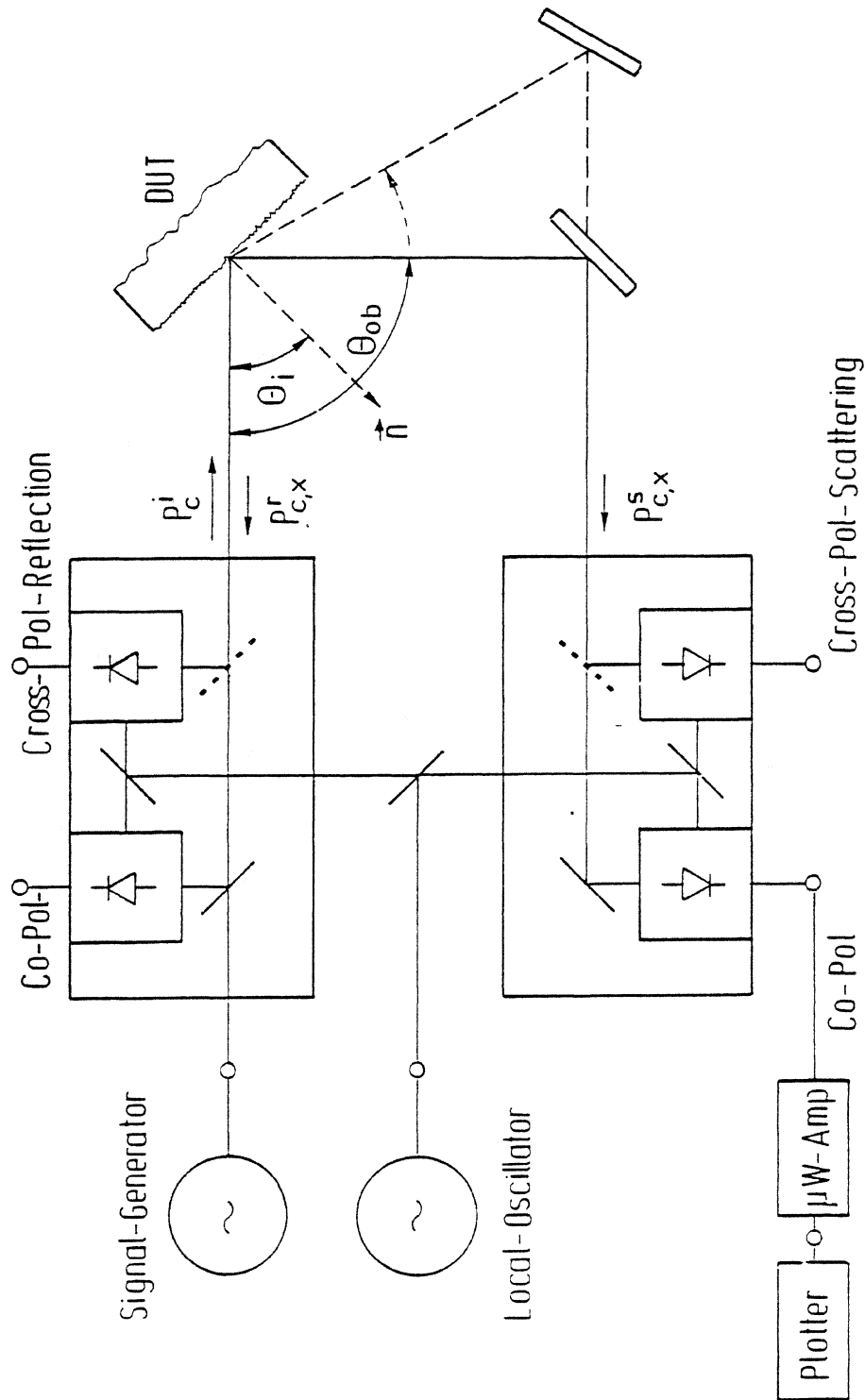


Fig. 5: Two-Polarization Multi-Angle SubMM-Wave Scatterometer

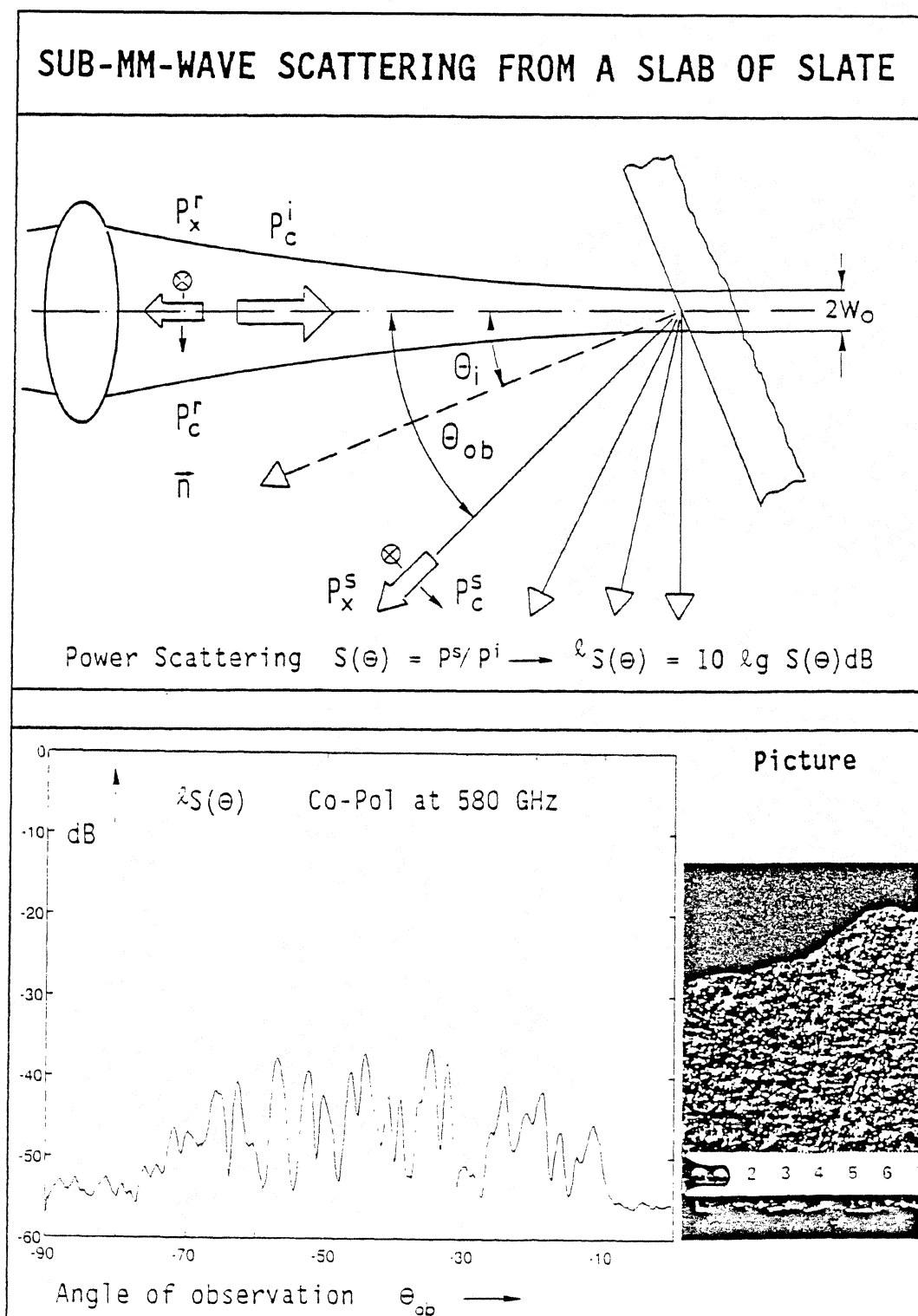


Fig. 6: SubMM-Wave Scattering from a Slab of Slate

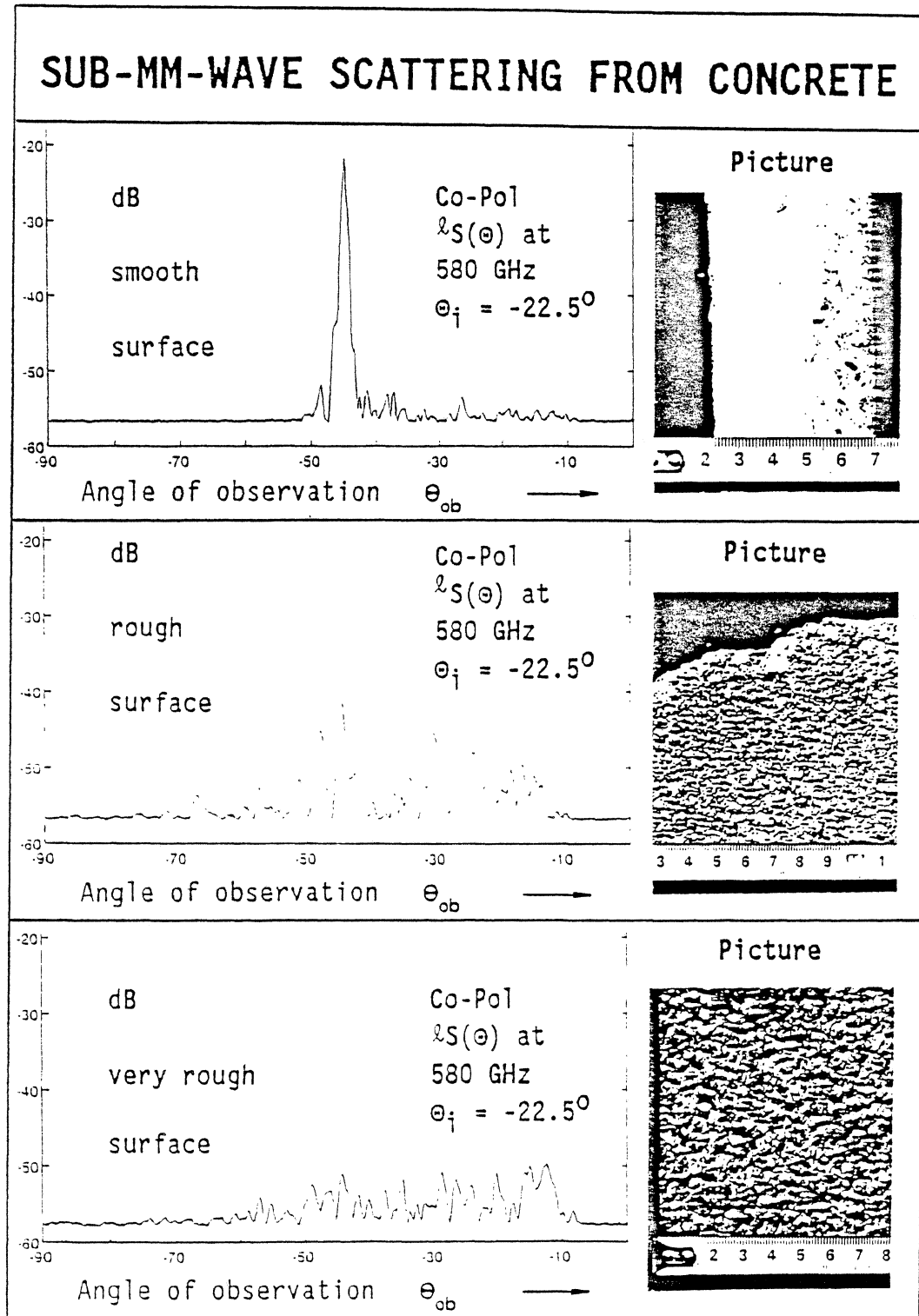


Fig. 7: Sub-MM-Wave Scattering from Concrete

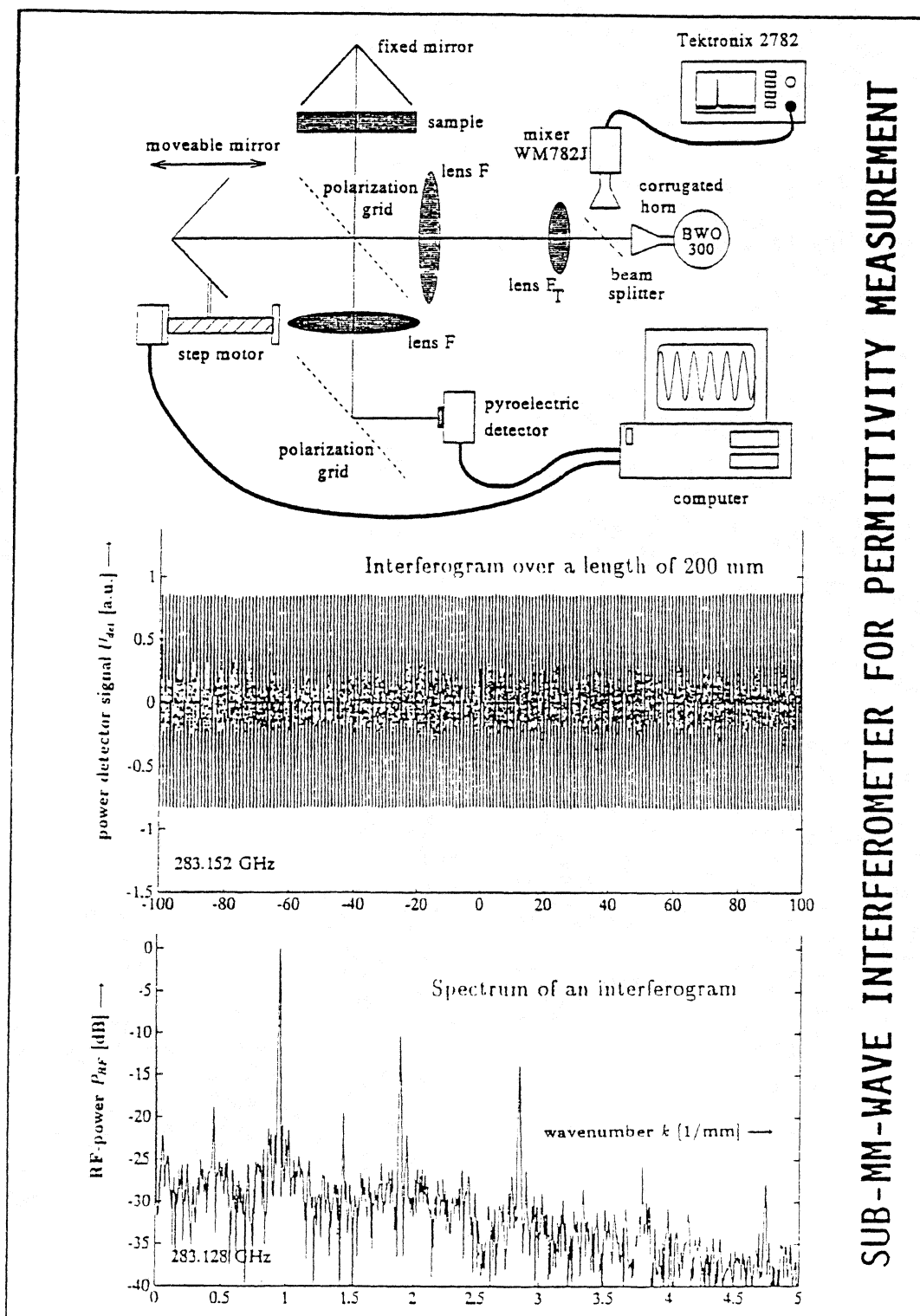


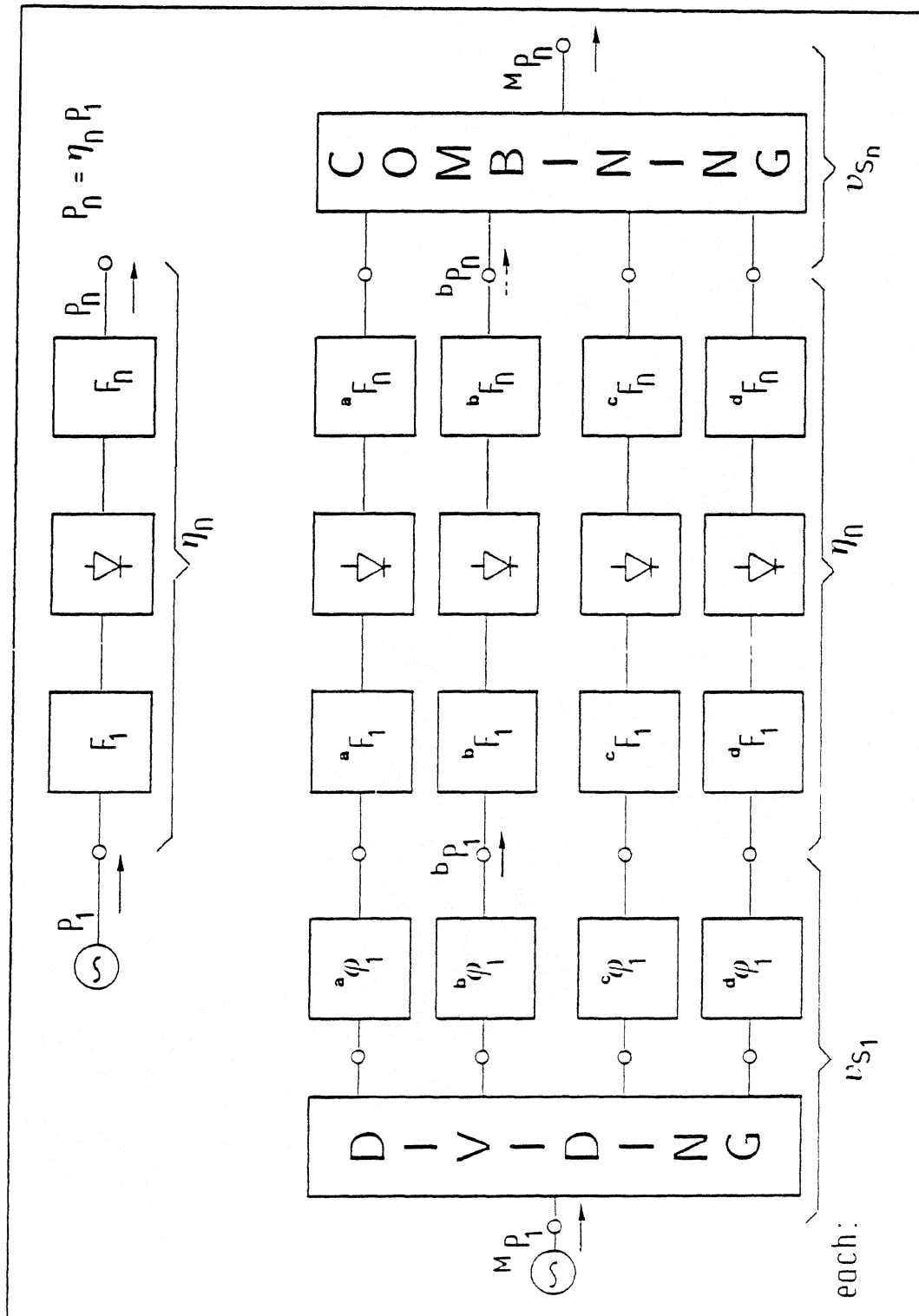
Fig. 8: SubMM-Wave Interferometer for Permittivity Measurement
(a) Block Diagram, Interferogram and Spectrum

Experimental results				
Material	Thickness [mm]	Frequency [GHz]	ϵ_r	$\tan \delta$ $\times 10^3$
Paraffin 48°C	4.87	283.388	2.264	2.0
Paraffin 48°C	4.87	294.425	2.260	8.2
Paraffin 48°C	7.92	283.387	2.260	0.6
Paraffin 48°C	7.92	294.424	2.265	2.6
Paraffin 72°C	4.63	283.389	2.272	6.0
Paraffin 72°C	4.63	294.426	2.260	10.5
Paraffin 72°C	7.41	283.388	2.268	8.2
Paraffin 72°C	7.41	294.427	2.260	7.0
TPX no. 1	5.07	283.386	2.122	1.0
TPX no. 1	5.07	294.424	2.114	1.6
TPX no. 2	5.07	283.387	2.133	2.5
TPX no. 2	5.07	294.423	2.114	0.32
Spectralon	5.45	279.723	1.724	22.5
Spectralon	5.45	292.816	1.710	22.5
Spectralon	5.45	301.539	1.728	19
Teflon	9.06	295.760	2.046	0.6
Teflon	9.06	301.548	2.038	1.1

B. STÖCKEL: Quasi-Optical Measurement of Complex Dielectric Constant at 300 GHz.
Int. Journal of Infrared and Millimeter Waves,
Vol. 14, No. 10, 1993, 2131 - 2148

SUB-MM-WAVE INTERFEROMETER FOR PERMITTIVITY MEASUREMENT

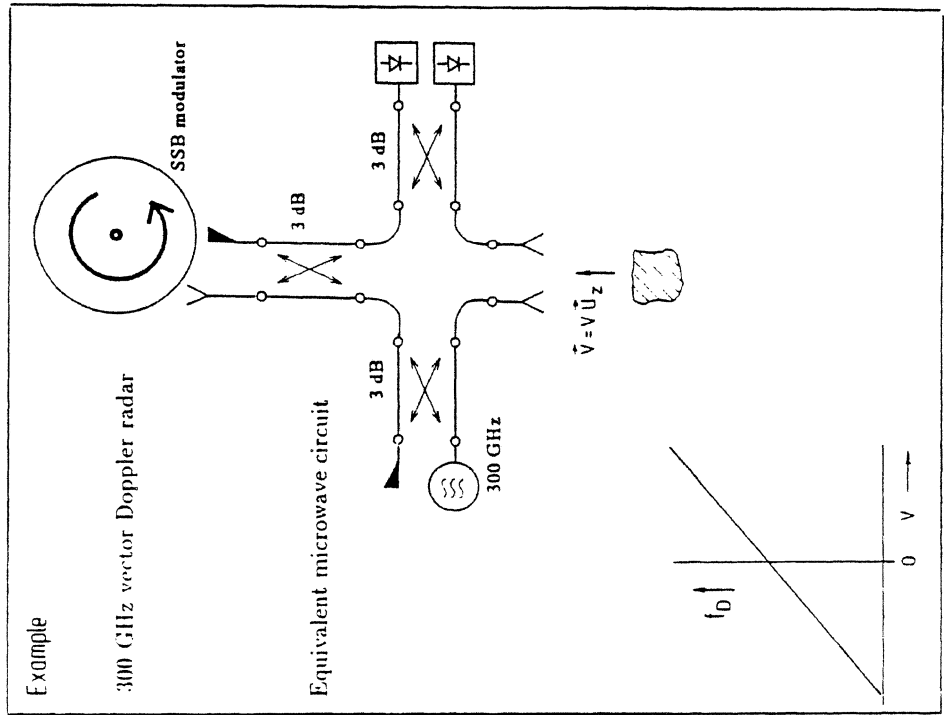
Fig. 8: SubMM-Wave Interferometer for Permittivity Measurement
(b) Experimental Results near 300 GHz



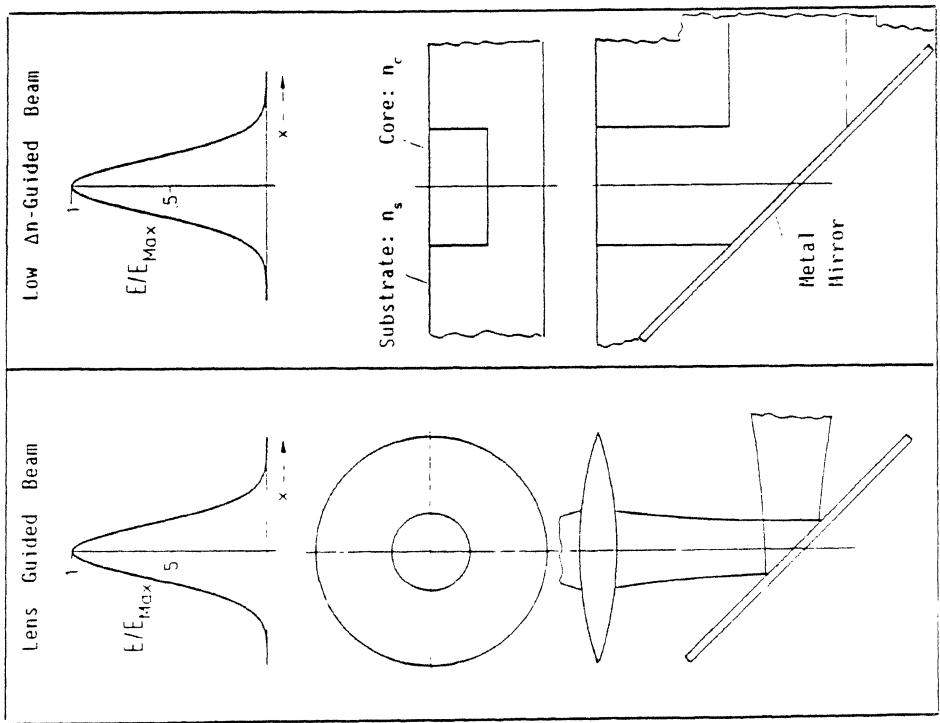
(a) One Diode System

(b) Four Diodes System

Fig. 9: Sub-MM Schottky Diode Harmonic Generator



(b) Realization Example: Vector Doppler Radar



(a) Beam Guiding Facilities

Fig. 10: Dielectric Integrated Network

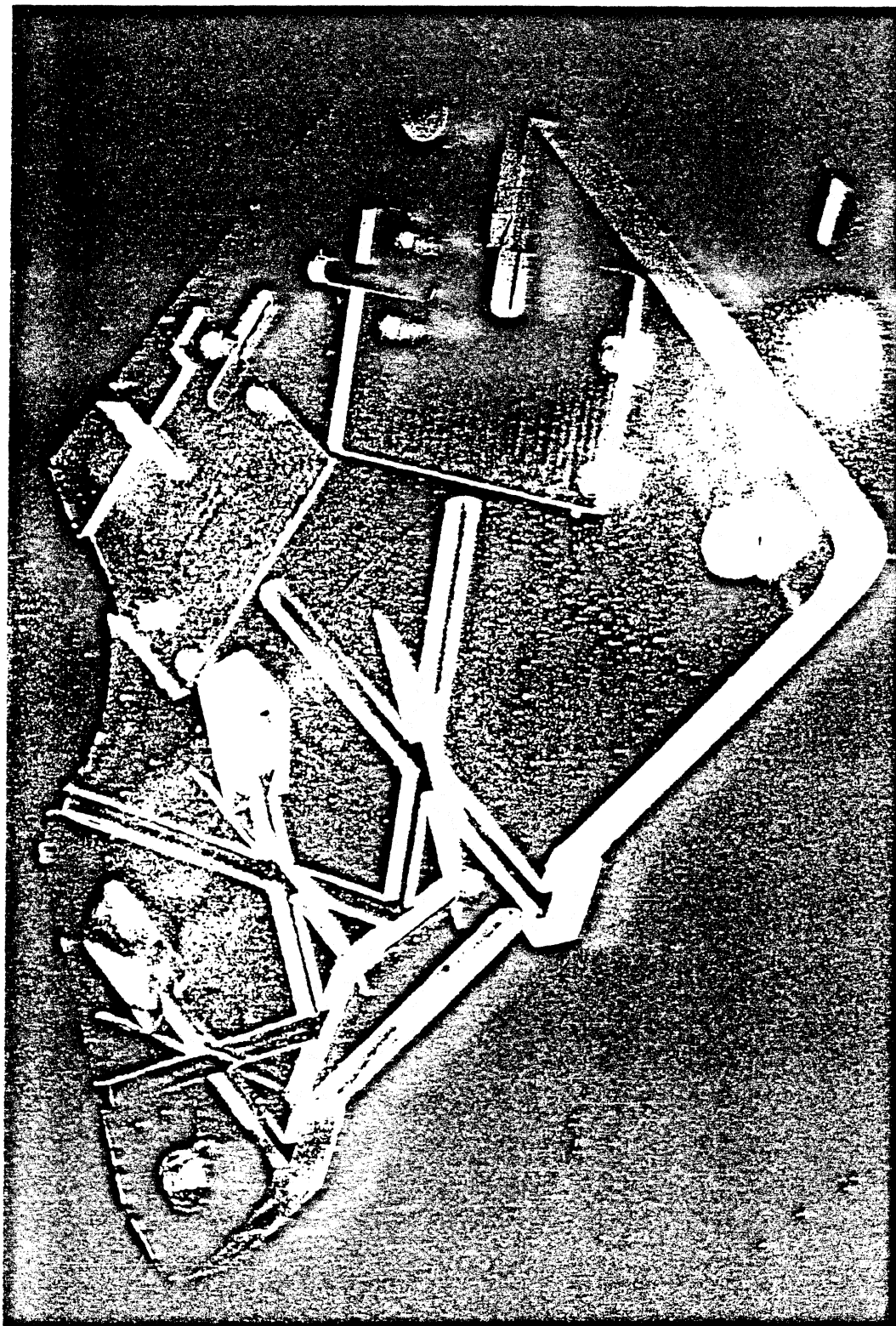


Fig. 11: Picture of the Substrate for the 300 GHz-
Dielectric Integrated Vector Doppler Radar

FUTURE TERAHERTZ APPLICATIONS
beyond Astrophysical, Atmospheric & Plasma Research

*** MEDICAL DIAGNOSTICS**

Multifrequency Reflection from Skin
Multifrequency Emission from Tissue
Spectroscopy of Expiration

*** BIO-CHEMICAL RESEARCH**

Spectroscopy of Gas-Products
Radiometry of Plants
Environmental Early Warning Systems

*** SECURITY CHECK-UP**

Detection of Concealed Drugs
Detection of Concealed Bombs
Biometrics: Identity Verification

*** SHORT RANGE INFORMATION**

Use of Attenuation Screening

Fig. 12: List of Possible Future THz-Applications

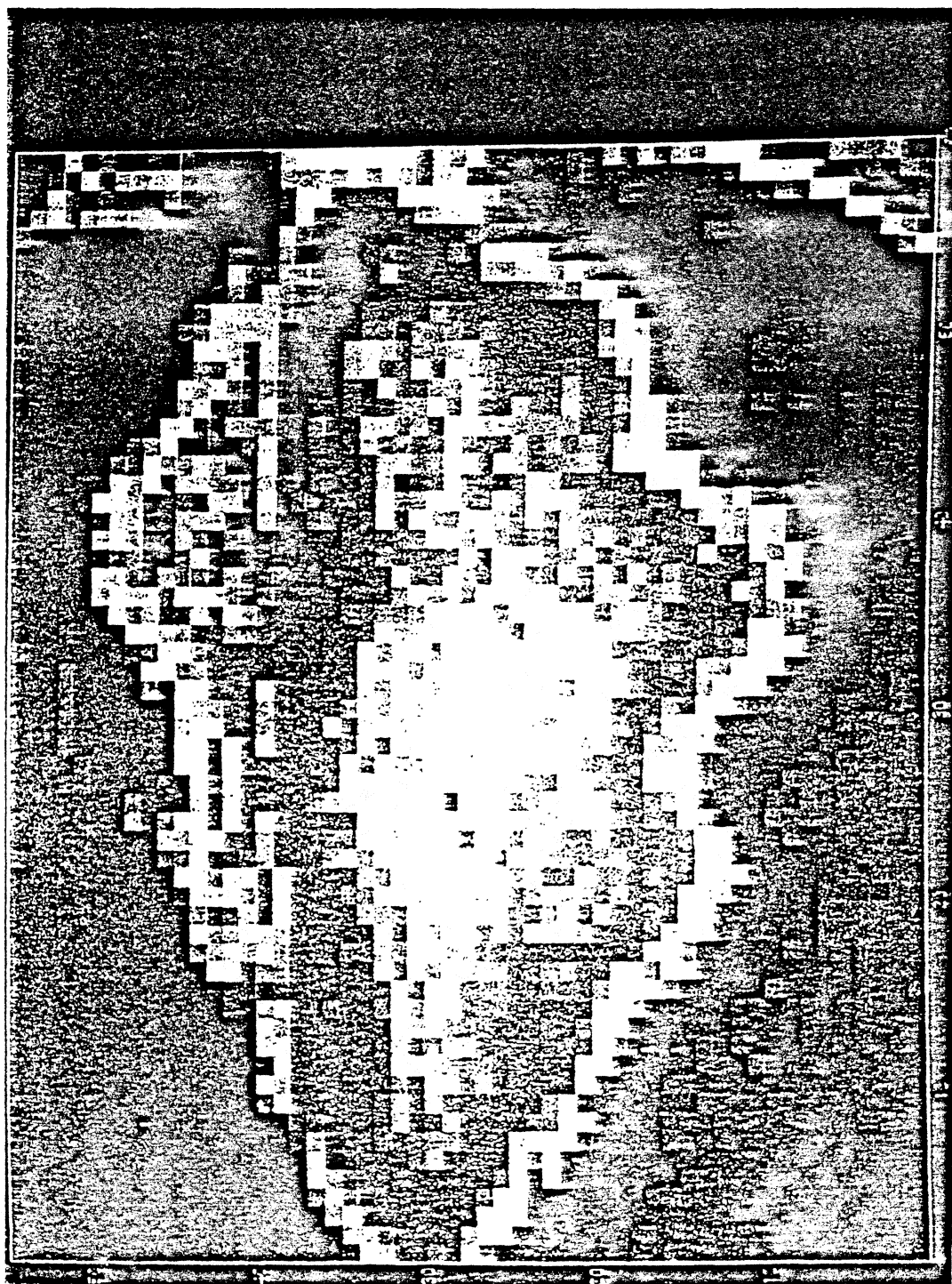


Fig. 13: Short Range Radiometric Image of a Maple Leaf at 585 GHz

A Wideband Fixed-Tuned SIS Receiver For 200 GHz Operation

**R. Blundell, C.-Y. E. Tong, D. C. Papa, R. L. Leombruno,
X. Zhang, and S. Paine.**

Harvard-Smithsonian Center for Astrophysics
60 Garden Street, Cambridge, MA 02138, USA

J. A. Stern, H. G. LeDuc, and B. Bumble.

Center for Space Microelectronics Technology,
Jet Propulsion Laboratory,
California Institute of Technology,
Pasadena, CA 91109, USA

Abstract

We report on the design and development of a heterodyne receiver, designed to cover the frequency range 176 GHz to 256 GHz. This receiver incorporates a niobium superconductor-insulator-superconductor (SIS) tunnel junction mixer, which, chiefly for reasons of reliability and ease of operation, is a fixed-tuned waveguide design. On-chip tuning is provided to resonate out the junction's parasitic capacitance and produce a good match to the waveguide circuit.

Laboratory measurements on the first test receiver indicate that the required input bandwidth (40%) is achieved with an average receiver noise temperature of below 40 K. Mixer conversion gain is observed at some frequencies, and the lowest measured receiver noise is less than 30 K. Furthermore, the SIS mixer used in this receiver is of simple construction, is easy to assemble and is therefore a good candidate for duplication.

I. Introduction

The first radio astronomy observations of the millimeter-wave molecular transitions of CO and CN were made in 1970 [1,2]. Since that time, millimeter-wave radio astronomy has evolved considerably: numerous millimeter-wave observatories are now in routine operation and receiver technology has reached a high degree of maturity [3]. At submillimeter wavelengths this is not the case. There are only two specially designed ground based submillimeter-wave observatories in routine operation: the Caltech Submillimeter Observatory and the James Clerk Maxwell Telescope. A number of other submillimeter-wave observatories are being developed (e.g., the Submillimeter Telescope, a joint project between the University of Arizona and the Max Planck Institut für Radio-astronomie), or are under construction (e.g., the Antarctic Submillimeter Telescope Remote Observatory).

The Submillimeter Array (SMA), currently under construction at the Smithsonian Astrophysical Observatory, will be the first submillimeter-wave synthesis telescope. Consisting of six 6-meter antennas, each to be equipped with eight SIS receivers designed to operate throughout the major atmospheric windows from below 200 GHz to above 900 GHz, the SMA will benefit from the rapid evolution of Nb SIS mixer technology.

II. Mixer Design

Given that many SIS receivers currently operate in the 1.3 mm atmospheric window [3], the lowest frequency unit appears to be the easiest of the SMA receivers to design. However, a number of factors render its design more difficult. For example, operating at its lowest frequency, with an intermediate frequency (IF) of 5 GHz, the signal to IF ratio is only a factor of 30, compared to about 100, typical of most working SIS receivers. Extra care is therefore required in the design of on-chip mixer tuning so as not to inadvertently short out part of the IF signal. Also, since the interferometer will operate at a remote high altitude site, where mechanical tuning of the mixer circuit is excluded, a fixed-tuned design with an instantaneous input bandwidth of about 40% is required.

Current technology dictates the choice of a waveguide based mixer with corrugated feed for high efficiency operation. The large instantaneous signal bandwidth is most readily achieved using an inductively compensated SIS junction. The mixer mount is therefore chosen to present a real impedance at the junction feed point across the signal input band. Furthermore, since the mixer

output is reasonably coupled to the 50 Ω IF amplifier network by using a junction with normal state resistance of about 20 Ω , a low mount impedance is required. A low mount impedance is also required to ease the design constraints of the thin-film tuner. Following standard design procedures and using experience gained with SIS mixers operating at similar wavelengths, a scale model mixer mount was made in reduced height waveguide. The dimensions of the waveguide and suspended substrate filter design were selected so as to produce a 35 Ω real impedance at the junction feed point, located at the center of the symmetrical low-pass filter structure. This impedance is transformed via an integrated thin-film microstrip circuit fabricated with the SIS junction to achieve the required signal coupling at the junction.

A block diagram of the mixer circuit is given in Figure 1a. The substrate carrying the junction and filtering structure is sandwiched between the corrugated waveguide horn feed and a back-section containing a short length of waveguide. The low-pass filter design is shown in Figure 1b; the substrate is suspended with the metalization facing the corrugated horn feed. The length of the mixer back-section and the dimensions of the first element of the filter that deliver the desired impedance at the feed point have been determined from the scale model measurements. The measured feed point impedance is shown in Figure 1b. Measurements were made over the frequency range 4.4 GHz - 6.4 GHz, and indicate that an instantaneous signal bandwidth of about 40% is possible with this design.

III. Junction Tuning and Fabrication

In order to achieve wideband operation an ωCR product of 2.3 (at 200 GHz) was chosen. For a reasonable match to the IF port, a normal state resistance of 17 Ω was used as a design goal. This implies the use of trilayer material with a current density of 7500 A.cm⁻² for a nominal junction area of 1.5 μm^2 . The corresponding optimum source conductance was deduced from an empirical formula [4].

An integrated series inductive line and a two section impedance transformer, similar to that previously described [5], were used to match the optimum source conductance in parallel with the junction geometrical capacitance to the 35 Ω feed point impedance provided by the waveguide mount. The design of the matching network was performed with the help of Touchstone, taking the kinetic inductance of the superconducting strips into account, and is shown schematically in Figure 2. Also shown in the Figure is the calculated return loss for this arrangement as a function of signal frequency. Clearly, a reasonably good match, better than 10 dB, is possible over the

required signal input bandwidth of 80 GHz.

The SIS junctions used in this receiver were made using optical lithographic techniques similar to those described in the literature [6]. In order to allow for some parameter variation during fabrication, three junction sizes were made, each with the same on-chip tuning circuit.

IV. Receiver Performance

The SMA receiver package will consist of eight receivers, housed in a common cryostat and cooled using a closed-cycle helium refrigerator. For receiver noise measurements in the laboratory, however, it is more convenient to use a small liquid helium filled test dewar. Receiver noise measurements are made using the Y-factor method with room-temperature (295 K) and liquid nitrogen (77 K) cooled loads. Since the mixer has a wide signal input bandwidth, all receiver noise data should be considered double-side-band and are obtained with the mixer at 4.2 K. A beamsplitter, presenting low-loss in the signal path, is used to combine signal and LO input to the mixer. The signals then pass through a laminated plastic vacuum window [7], a cooled porous Teflon window [8], and a Teflon lens, cooled to 4.2 K, before entering the mixer feed horn. We should note that no corrections are made to our data for losses in front of the receiver.

The measured receiver noise as a function of local oscillator (LO) frequency for a number of different mixers is displayed in Figure 3. For all these measurements, the IF amplifier network has a center frequency of 1.5 GHz, an instantaneous bandwidth of 500 MHz and a noise temperature of about 5 K. From the Figure, the mixer incorporating the SIS junction with an area of $1.3 \mu\text{m}^2$ and a normal resistance of 22.5Ω , i.e. that closest to the nominal design ($1.5 \mu\text{m}^2$ and 17Ω respectively), offers excellent low-noise performance over a band that is centered slightly lower than the design frequency, by about 3%. In an effort to push the operating band upwards, the same type of junction was used in a mixer whose back-section was shorter than that determined by scale model measurements, by about 60 μm . In this case, the center frequency of the receiving band was increased by about 3%, i.e. to the desired value, with little change in average receiver noise. A junction with area $1.1 \mu\text{m}^2$ and normal resistance 27.5Ω was then tested in the original mixer. In this case, the receiver noise floor increased by about 5 K and the receiving band center remained unchanged. Clearly, any of the configurations tested offer performance, both in bandwidth and in noise, that will enable the SMA to start operations with state-of-the-art receivers. Furthermore, testing of a number of similar mixers indicates that the performance shown is readily achievable.

Standard measurement techniques [9,10,11] have been used to separate the receiver noise into three components: noise due to input losses, mixer noise, and multiplied IF noise. Figure 4 shows the breakdown of noise for the receiver incorporating the small area SIS junction mixer. With mixer noise close to the quantum limit at these frequencies, a total receiver noise of about 30 K should be considered as a good design goal, with about equal noise arising from input losses, mixer noise and multiplied IF noise. From the Figure we observe that, while the individual sources of noise contribute about equally at some frequencies, there is room for some improvement at low frequencies through the use of lower-loss input optics. We also note that the mixer noise is relatively high at the center of the receiving band, and that some small reduction in noise may be possible as lower noise IF amplifiers become available.

In Figure 5 we present current-voltage characteristics and IF output power curves for four different LO frequencies. The Figure indicates that excellent mixer conversion is obtained at 230 GHz, good conversion at 180 GHz and 205 GHz and poorer conversion at 255 GHz. We should note that only the LO frequency and drive level were changed between the different receiver noise measurements, all other parameters were fixed. In particular, the mixer bias and magnetic field were held constant. This demonstrates that good receiver performance is readily achievable. Optimization of receiver noise at all frequencies may require fine adjustment of all parameters. However, since only a few K reduction in receiver noise is achieved, it is thought that further optimization may not be justified.

Finally, in Figure 6, we show the receiver noise performance as a function of LO frequency for different IF amplifier networks. Two sets of data are presented in the Figure, one for an IF 500 MHz wide, centered at 1.5 GHz, the other for an IF 2.5 GHz wide, centered at 5 GHz — the IF of the SMA. Since the mixer gain is close to unity over a large part of the receiver's operating frequency, the difference in receiver noise is approximately equal to that of the difference in IF amplifier noise, i.e. about 7 K. The lowest measured receiver noise is about 25 K for the 1.5 GHz IF and 30 K for the 5 GHz IF. From the Figure, the receiver noise averaged over an 80 GHz input bandwidth is about 30 K for the 1.5 GHz IF and below 40 K for the 5 GHz IF.

V. Conclusion

We have developed a wideband, fixed-tuned SIS receiver for 200 GHz operation. The receiver noise is below 40 K across the majority of the observing band, about 80 GHz wide. Although some improvement may be possible through the use of lower-loss input optics and IF

amplifiers offering superior noise performance to those currently available, it is thought that the current receiver design, which is particularly well adapted to duplication, will prevail and offer state-of-the-art performance when the SMA begins operations in 1997.

Acknowledgement

We should like to thank M.J. Smith for his superior technical assistance in developing the mixer used in this work.

References

- [1] R.W. Wilson, K.B. Jefferts, and A.A. Penzias, "Carbon monoxide in the Orion nebula," *Astrophys. J.*, vol. 161, pp. L43-L44, July 1970.
- [2] K.B. Jefferts, A.A. Penzias, and R.W. Wilson, "Observation of the CN radical in the Orion nebula and in W51," *Astrophys. J.*, vol. 161, pp. L87-L89, Aug. 1970.
- [3] R. Blundell and C.-Y.E. Tong, "Submillimeter receivers for radioastronomy," *Proc. I.E.E.E.*, vol. 80, pp. 1702-1720, Nov. 1992.
- [4] Q. Ke and M.J. Feldman, "Optimum source conductance for high frequency superconducting quasiparticle receivers," *IEEE Trans. on Microwave Theory and Techniques*, vol. MTT-41, pp. 600-604, 1993.
- [5] T.H. Büttgenbach, H.G. LeDuc, P.D. Maker, and T.G. Phillips, "A fixed tuned broadband matching network for submillimeter SIS receivers," *IEEE Trans. Applied Superconductivity*, vol. AS-2, pp. 165-175, 1992.
- [6] H.G. LeDuc, J.A. Stern, S. Thakoor, and S. Khanna, "All refractory NbN/MgO/NbN SIS tunnel junctions," *IEEE Trans. Maggetics*, vol. MAG-23, pp. 863-865, 1987.
- [7] Hercules HR500/2S, a product of Hercules Inc., Wilmington DE, USA.
- [8] Zitex A, a product of Norton Performance Plastics, Wayne NJ, USA.
- [9] D.P. Woody, R.E. Miller, and M.J. Wengler, "85-115 GHz receivers for radio astronomy," *IEEE trans. on Microwave Theory and Techniques*, vol. MTT-33, pp. 90-95, 1985.
- [10] R. Blundell, R.E. Miller, and K.H. Gundlach, "Understanding noise in SIS receivers," *Int. J. IR & MM Waves*, vol. 13, pp. 3-14, 1992.
- [11] Q. Ke and M.J. Feldman, "A technique for accurate noise temperature measurements for the superconducting quasiparticle receiver," in *Proc. Fourth Int. Symp. on Space Terahertz Technology*, Los Angeles, pp. 33-40, 1993.

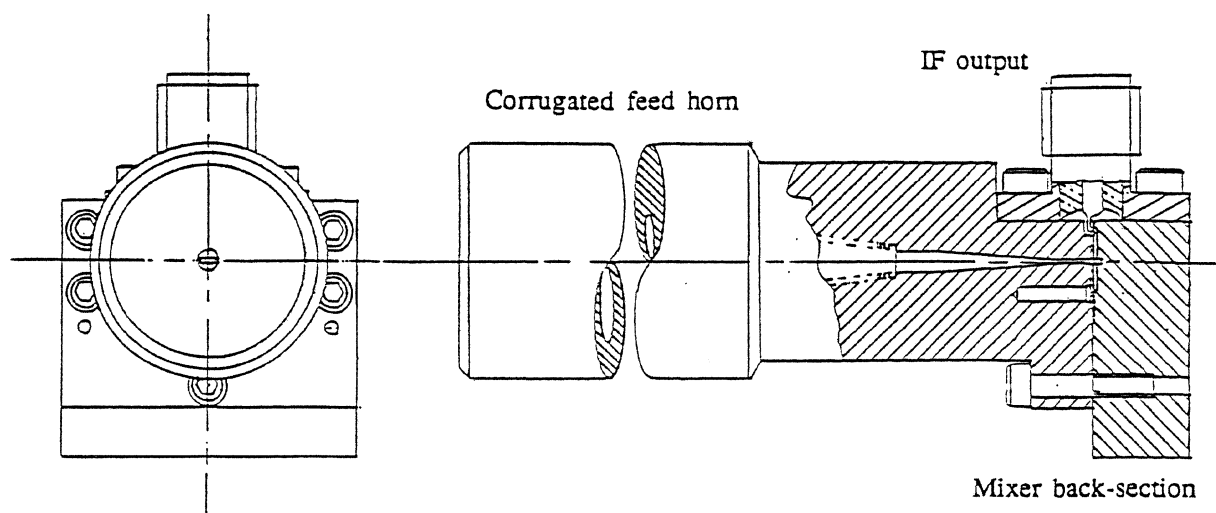


Figure 1a. Mixer mount detail showing the corrugated horn feed and mixer back-section.

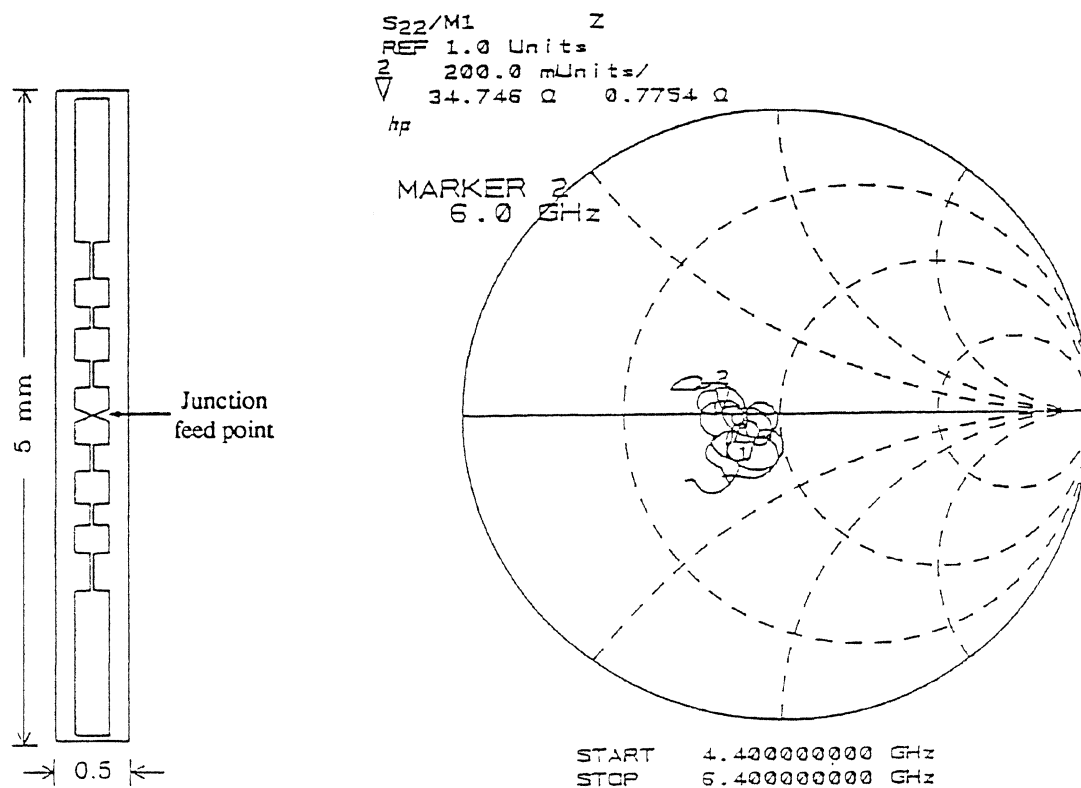


Figure 1b. Suspended substrate filter layout, and the locus of the junction feed point impedance.

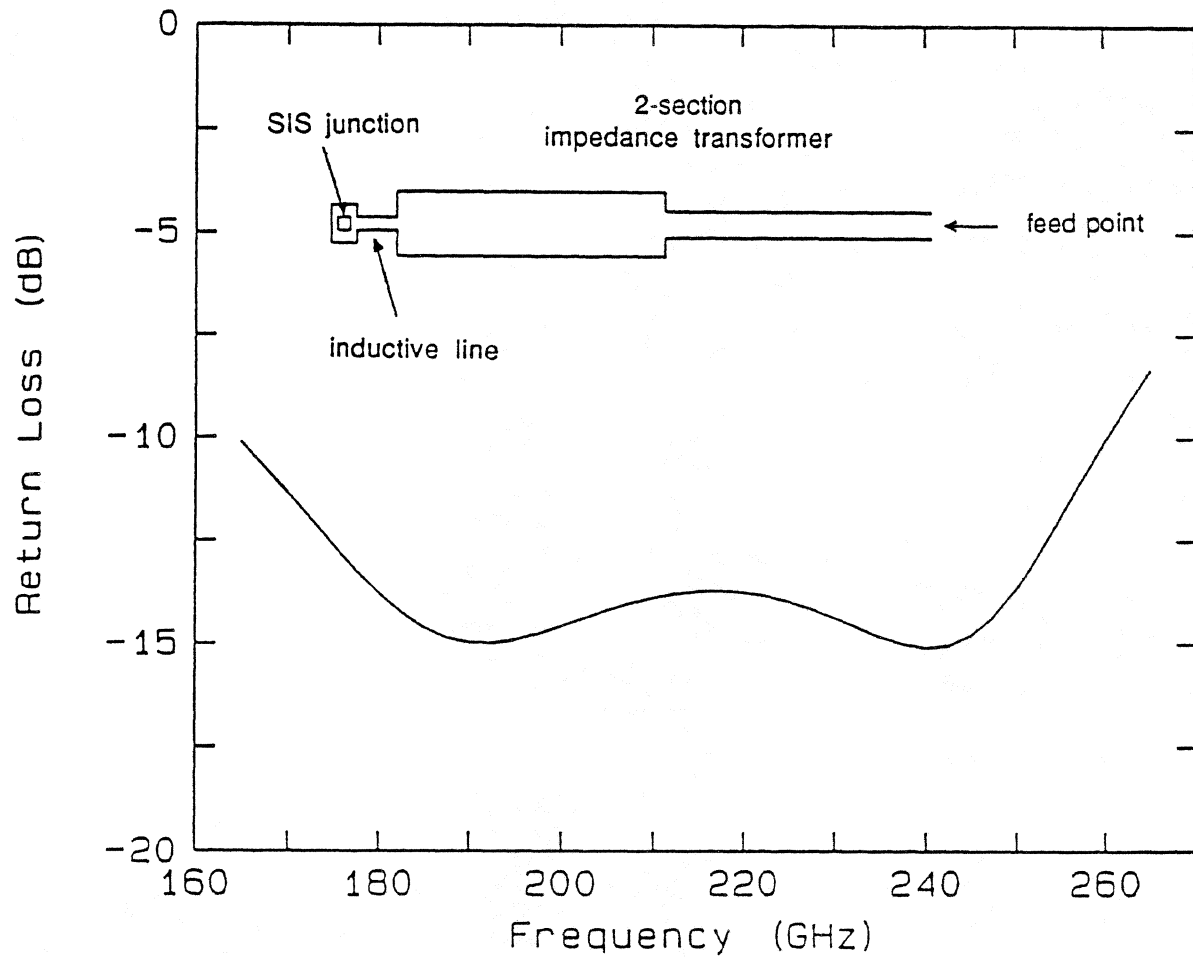


Figure 2. Layout of the integrated microstripline tuning structure showing the SIS junction, the inductive line and the two step impedance transformer. Also shown is the calculated return loss across the signal frequency band.

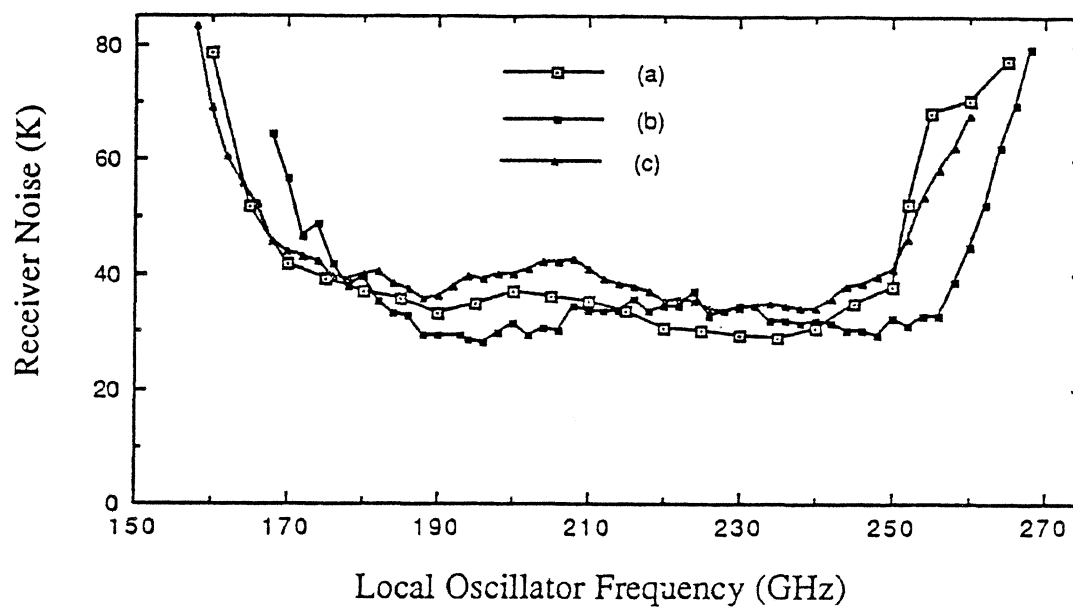


Figure 3. The receiver noise is plotted as a function of LO frequency for three mixer configurations:

- (a) 1.3 square micron junction in a mixer with the standard length back-section,
- (b) 1.3 square micron junction in a mixer with reduced length back-section,
- (c) 1.1 square micron junction in a mixer with the standard length back-section.

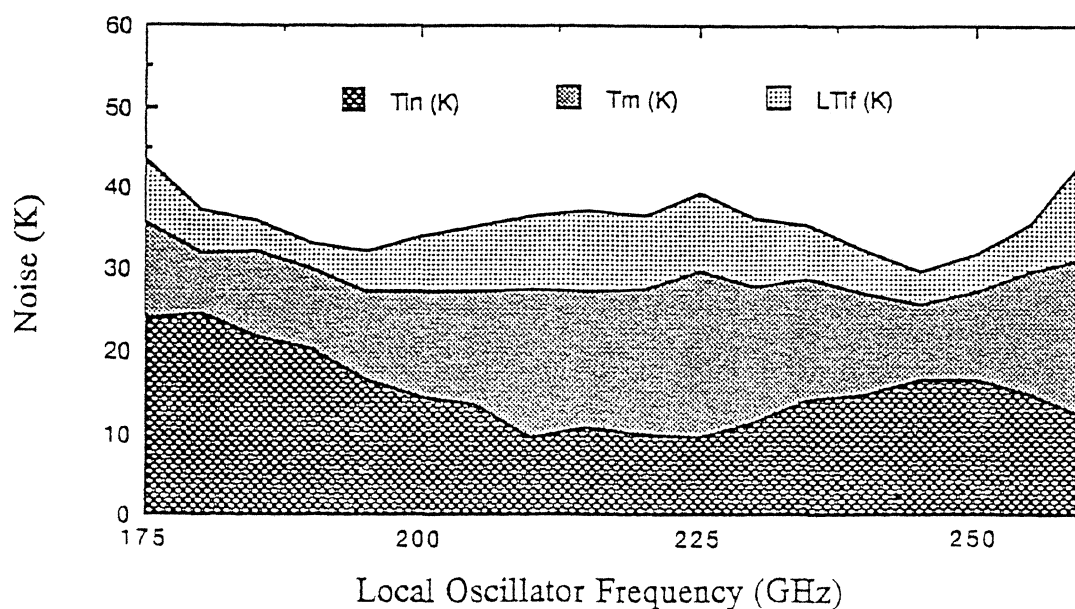


Figure 4. A breakdown of receiver noise into its three components: input loss noise, T_{in} (K), mixer noise, T_m (K), and multiplied IF noise, LT_{if} (K) is plotted as a function of LO frequency.

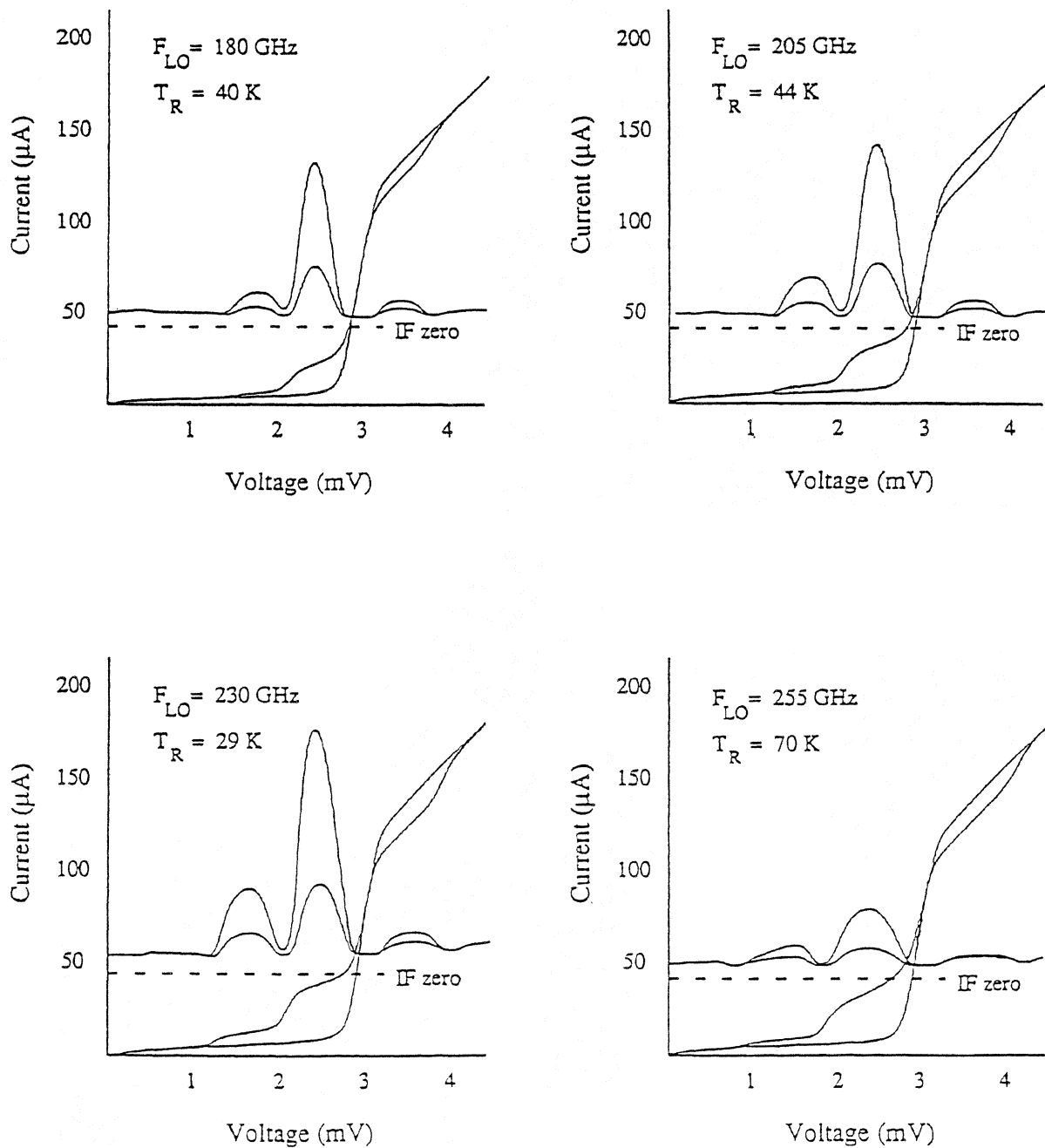


Figure 5. Current-voltage characteristics, pumped and unpumped, are given for four different LO frequencies. Also shown is the receiver output in response to hot (295 K) and cold (77 K) input loads.

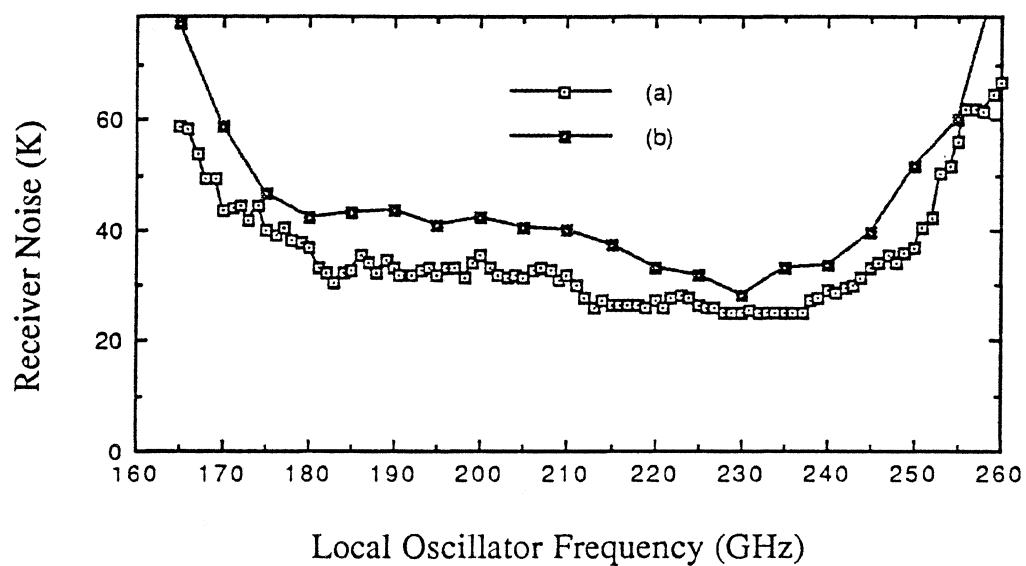


Figure 6. The receiver noise is plotted as a function of LO frequency for two different IFs:
(a) 1.5 GHz center frequency, 0.5 GHz bandwidth.
(b) 5 GHz center frequency, 2.5 GHz bandwidth

180-425 GHz LOW NOISE SIS WAVEGUIDE RECEIVERS EMPLOYING TUNED Nb/AlO_x/Nb TUNNEL JUNCTIONS

*J. W. Kooi¹, M. Chan¹, B. Bumble²,
H. G. LeDuc², P. L. Schaffer¹, and T.G. Phillips¹*

1- Caltech Submillimeter Observatory

Division of Physics, Mathematics and Astronomy
California Institute of Technology, Pasadena, California 91125

2- Center for Space Microelectronics Technology, Jet Propulsion Laboratory

Abstract

We report recent results on a 20% reduced height 270-425 GHz SIS waveguide receiver employing a $0.49\mu\text{m}^2$ Nb/AlO_x/Nb tunnel junction. A 50% operating bandwidth is achieved by using a RF compensated junction mounted in a two-tuner reduced height waveguide mixer block. The junction uses an "end-loaded" tuning stub with two quarter-wave transformer sections. We demonstrate that the receiver can be tuned to give 0-2 dB of conversion gain and 50-80% quantum efficiency over parts of its operating range. The measured instantaneous bandwidth of the receiver is ≈ 25 GHz which ensures virtually perfect double sideband mixer response. Best noise temperatures are typically obtained with a mixer conversion loss of 0.5 to 1.5 dB giving uncorrected receiver and mixer noise temperatures of 50K and 42K respectively at 300 and 400 GHz. The measured double sideband receiver noise temperature is less than 100K from 270 GHz to 425 GHz with a best value of 48K at 376 GHz, within a factor of five of the quantum limit. Preliminary tests of a similar junction design in a full height 230 GHz mixer block indicate large conversion gain and receiver noise temperatures below 50K DSB from 200-300 GHz. Best operation is again achieved with the mixer tuned for 0.5-1.5 dB conversion loss which at 258 GHz resulted in a receiver and mixer noise temperature of 34K and 27K respectively.

Introduction

A 20% reduced height waveguide superconductor-insulator-superconductor (SIS) heterodyne receiver with a center frequency of 345 GHz has been designed and installed at the Caltech Submillimeter Observatory (CSO) on Mauna Kea in Hawaii. The low noise results discussed here were achieved by employing a $0.49\mu\text{m}^2$ Nb/AlO_x/Nb tunnel junction with a lithographically produced "end-loaded" stub matching network to tune out the junction capacitance.

To improve the bandwidth and performance of the receiver over the suc-

cessful Ellison design [2, 3], a 20% reduced waveguide mixer block with a tuned Nb/AlO_x/Nb tunnel junction was used. The mixer block incorporates magnetic field concentrators [4] and an octave wide bandwidth IF matching network [5]. A variety of inductive tuning stubs have been introduced [6, 7, 8, 9, 10, 11] to improve the junction match to the embedding impedance. In recent years quasi-optical techniques with lithographically produced matching structures have been successfully used to build sensitive submillimeter receivers [12, 13, 14]. A review of the conventional tuning circuits has been given by Zmuidzinas *et al.* [12]. The series tuned "end-loaded" stub as discussed by Büttgenbach *et al.* [13] has been used in the junction designs because it has several advantages over the conventional open and short circuit shunted stubs.

RF Matching Network

For an SIS tunnel junction the geometric capacitance of the two niobium films separated by a very thin insulator dielectric, ($\approx 12 \text{ \AA}$), is in parallel with the quantum of the tunnel barrier. For bias voltages on the first quasiparticle step the imaginary part of the junction's RF admittance is nearly zero, and the junction susceptance is dominated by the geometric capacitance, C_j . The RF conductance for a junction is described by Tucker's quantum theory.

$$G_j = \frac{e}{2\hbar\omega} \sum J_n^2(\alpha) \left[I_{dc} \left(V_o + \frac{(n+1)\hbar\omega}{e} \right) - I_{dc} \left(V_o + \frac{(n-1)\hbar\omega}{e} \right) \right] \quad (1)$$

In the low LO power limit where $\alpha \equiv eV_{lo}/\hbar\omega < 1$, G_j is given by the slope of the line joining points on the pumped IV curve one photon step above and below the dc bias point [1, 15]. R_j (G_j^{-1}) ranges from $R_n/3$ in the lower part of the sub-millimeter band to R_n for frequencies $\geq 500 \text{ GHz}$. R_n is the above gap normal state resistance of the SIS tunnel junction. The admittance of the junction can thus be described as

$$Y_j = (G_j + i\omega C_j) \quad (2)$$

Where C_j is the junction capacitance, $\approx 65\text{-}85 \text{ fF}/\mu\text{m}^2$. The RF conductance varies slowly with frequency and for our design purposes is assumed to be constant. The coupling efficiency between two admittances has the form

$$\eta = \frac{4G_j G_p}{|Y_j + Y_p|^2} \quad (3)$$

Y_p is the admittance presented to the junction by the bow-tie antenna probe that is positioned in the center of the waveguide. This includes the reduced height waveguide impedance, $\approx 390 \text{ } \Omega$, which is transformed by means of a series

inductance (E-plane tuner) and shunt susceptance (backshort tuner). The probe admittance is a function of frequency but in the ideal case can be held constant by adjusting the E-plane and backshort tuners. For our design purpose we have taken Y_p to be constant. It is however possible to carefully model $Y_p(\omega)$ and use it to design tunerless mixers. This technique has not been attempted here, but could conceivably yield good results for imaging arrays. To obtain an optimum coupling efficiency it is required that $Y_p = Y_j^*$. The simplest way to achieve this condition is to tune out the junction susceptance with an open ended stub.

The admittance of a transmission line with a characteristic admittance $Y_o = Z_o^{-1}$ is given by

$$Y_s = Y_o \frac{Y_l + iY_o \tan(\beta l)}{Y_o + iY_l \tan(\beta l)} \quad (4)$$

β is the propagation constant $= 2\pi/\lambda$, Y_l the load impedance and βl the electrical length. For $Y_l = 0$ (open circuit) the input susceptance becomes

$$B_s = iY_o \tan(\beta l) \quad (5)$$

The shunt susceptance of the open ended stub cancels the junction susceptance for $Y_o = \omega C_j$ and $l = 3/8 \lambda$ giving perfect coupling efficiency provided that the probe admittance is real and equals the RF conductance of the junction G_j . Similar results can be obtained with a shorted $1/8 \lambda$ transmission line or an ideal inductor. The latter requires a series capacitance to allow the junction to be dc biased and as such is not physically realizable at submillimeter wavelength's. For a $1/8 \lambda$ shorted stub we get

$$B_s = -iY_o \cot(\beta l) \quad (6)$$

The shorted stub provides a larger frequency range over which a match to the junction can be achieved. This can be observed by comparing the derivatives of (5) and (6). It can be shown that the open-circuited stub has a theoretical fractional bandwidth of $\approx 0.35 K^{-1}$ while the short-circuited stub has a bandwidth of $\approx 0.93 K^{-1}$, where $K \equiv \omega R_j C_j$. The main disadvantages of the open ended stub is the small bandwidth over which a good match can be achieved and the critical dependence of the match on the effective electrical length of the stub. The short-circuited stub has a nearly three times larger bandwidth than the open-circuit stub. Unfortunately the overall performance is still critically dependent on the actual stub length. In practice it is difficult to design a tuning stub that resonates at the design frequency. This is largely due to uncertainties in the manufacturing process and properties of niobium at 4K.

These problems can to some extent be overcome by the use of an "end-loaded" tuning circuit as discussed by several authors [13, 16]. The "end-loaded" stub puts a small section transmission line in series with the junction. This results

in the transformation of the complex junction admittance, Y_j to the real axis of the Smith Chart.

Consider a transmission line with a characteristic admittance $Y_o = \omega C_j$ and a load $Y_l = (G_j + i\omega C_j)$. Using (2) and (4) we calculate the electrical length of the "end-loaded" stub (βl_s) for which the imaginary part of Y_s equals zero.

$$\tan(\beta l_s) = \frac{Z_o^2}{2} \left(\sqrt{G_j^4 + 4Y_o^4} - G_j^2 \right) \quad (7)$$

Where Z_o is the characteristic impedance, Y_o^{-1} . We can simplify (7) for $G_j < Y_o$.

$$\tan(\beta l_s) \simeq 1 - \frac{1}{2K^2}, \quad K > 1.2 \quad (8)$$

Combining (8) and (4) we can solve for the real part of the transformed junction admittance.

$$G_s \simeq Y_o \left(\frac{K(2K^2 - 1)}{2K^4 - 2K^3\sqrt{K^2 - 1} - 1} \right), \quad l = l_s \quad (9)$$

For $\omega R_j C_j \gg 1$ equation (9) simplifies to

$$R_s \approx \frac{R_j}{2K^2} \quad (10)$$

This is similar to an expression derived by Büttgenbach *et al.* [13] for $R_j \rightarrow R_n$. R_s is the transformed resistance of a junction connected to an "end-loaded" stub of electrical length βl_s (Fig. 5b). Expressing (9) in terms of the electrical length of the series transmission line we get

$$R_s \approx R_j \cos(2\beta l_s) \quad (11)$$

As the frequency increases we see from (8) that the stub length l_s approaches $\pi/4$, which reduces R_s to very small values (11). This is a serious drawback of the "end-loaded" stub. For frequencies above 500 GHz it gets more and more difficult to transform R_s to match the probe impedance over a reasonable bandwidth (Fig. 1).

To transform R_s to Z_p^* , we used a two section equal-ripple Chebyshev transformer [17]. This type of transformer gives the maximum bandwidth while allowing a tolerable pass band ripple. If we define ρ_m as the maximum allowed voltage reflection coefficient of the passband ripple (Fig. 3), we can derive the impedances for the two quarter-wave sections that give the widest possible fractional bandwidth.

$$Z_1^2 = R_p \sqrt{R_s R_p} \sqrt{\frac{1 - \rho_m}{1 + \rho_m}} \quad (12)$$

$$Z_2^2 = R_s^2 \sqrt{\frac{R_p}{R_s}} \sqrt{\frac{1 + \rho_m}{1 - \rho_m}} \quad (13)$$

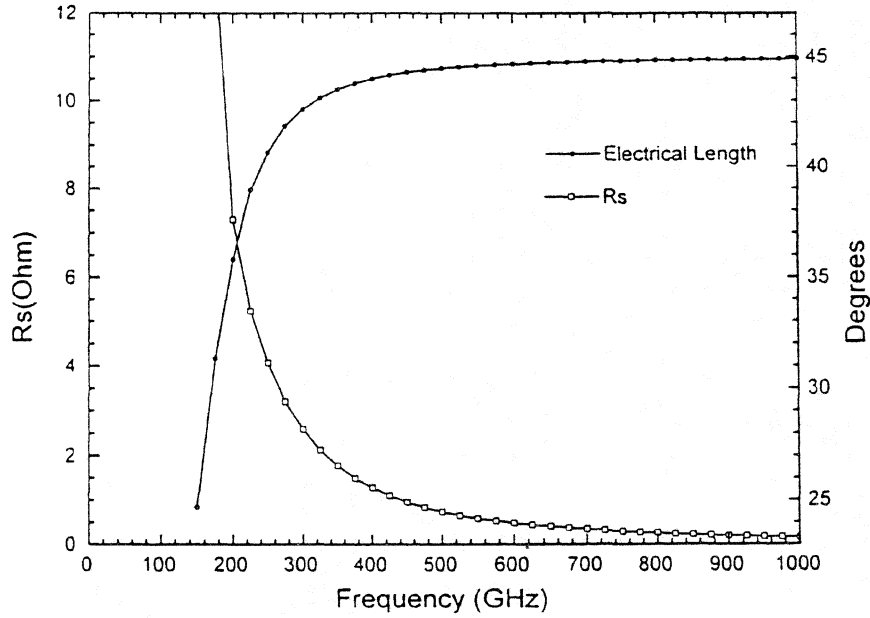


Fig. 1. The real part of the transformed junction impedance (9) and electrical length of the "end-loaded" stub (7) as a function of frequency. The junction's RF conductance is obtained from Tucker's theory. The calculations assume a $0.5 \mu\text{m}^2$, 8000 A/cm^2 tunnel junction with a geometric capacitance of 40 fF .

Z_1 is the high impedance section which connects to the probe and Z_2 is the low impedance section connected to the "end-loaded" stub (Fig. 5). Using (10) we can express Z_1 and Z_2 in terms of K and the RF resistance of the junction, R_j .

$$Z_1^2 \approx \frac{R_p}{K} \sqrt{\frac{R_j R_p}{2}} \sqrt{\frac{1 - \rho_m}{1 + \rho_m}}, \quad K \gg 1 \quad (14)$$

$$Z_2^2 \approx \frac{R_j}{4K^3} \sqrt{2R_j R_p} \sqrt{\frac{1 + \rho_m}{1 - \rho_m}}, \quad K \gg 1 \quad (15)$$

Equations (14) and (15) show that $Z_1 \propto K^{-0.5}$ and $Z_2 \propto K^{-1.5}$. For frequencies in the upper half of the submillimeter band Z_2 becomes very small

for junctions with current densities less than 10kA/cm^2 . In practice it is difficult to realize a very low impedance superconducting microstrip transmission line because its aspect ratio, (length/width), becomes rather small. Connecting the high impedance "end-loaded" stub to a low impedance transmission line results in a large discontinuity which increases the effective electrical length of the "end-loaded" stub. This is an especially serious effect at frequencies above 500 GHz considering that the center frequency of the RF matching network is critically dependent on the "end-loaded" stub's electrical length (Fig. 1). Figure 2 shows the calculated impedances of a two section quarter-wave transformer in the submillimeter band for a worst case in-band reflection coefficient, ρ_m , of -9 dB.

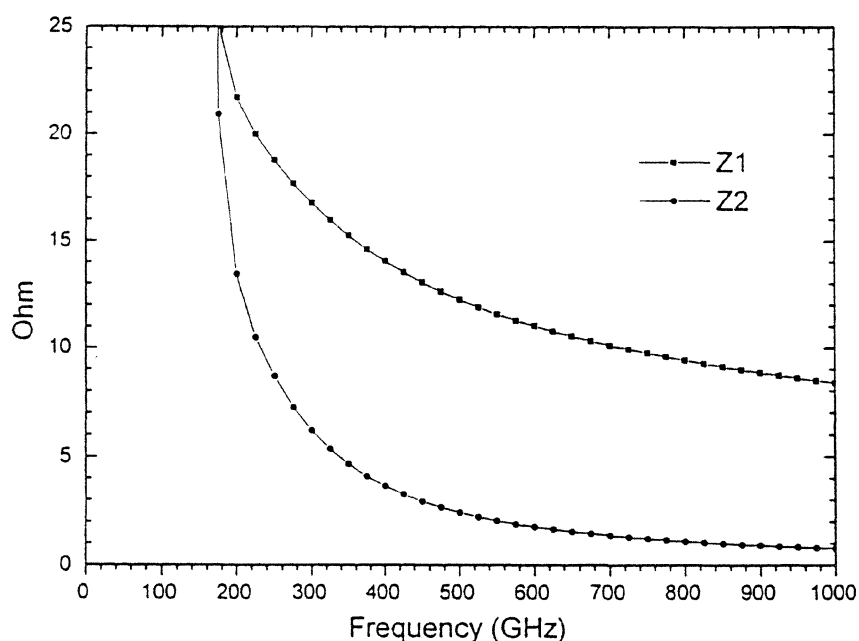


Fig. 2. Characteristic impedances of an equal-ripple two-section Chebyshev quarter-wave transformer needed to transform R_s (Fig. 1.) to a $40\ \Omega$ probe impedance. For frequencies exceeding 500 GHz $Z_2 < 2\ \Omega$, which makes implementation difficult.

Radially shorted inductive stubs [11] and two junction type tuning circuits as described by Zmuidzinis *et al.* [12] are good candidates for the upper half of the submillimeter band.

Junction Design

The waveguide of the 345 GHz mixer supports single, TE_{10} , mode operation from 222–444 GHz. The 270–420 GHz frequency band was chosen to be within these limits and to provide adequate overlap between the 230 and 492 GHz SIS receivers [4, 5]. These along with the newly installed 665 GHz receiver [18] provide complete coverage for the 180–730 GHz CSO submillimeter astronomy band. To achieve a good match over the desired 270–420 GHz frequency band it is imperative that a probe impedance, $Z_p(\omega)$, is selected that can easily be tuned to over the entire frequency range [19]. Räsänen *et al.* [20] have made scale model measurements on full and reduced-height waveguide embedding impedances. Their data indicates that the embedding impedance of a probe, with 45 degree lead shapes, at the center frequency of the mixer is slightly inductive and has a real part less than 50Ω . This result has recently been confirmed Honingh *et al.* [21]. For our "end-loaded" stub design we assumed the probe impedance equal to $40 + 10i\Omega$.

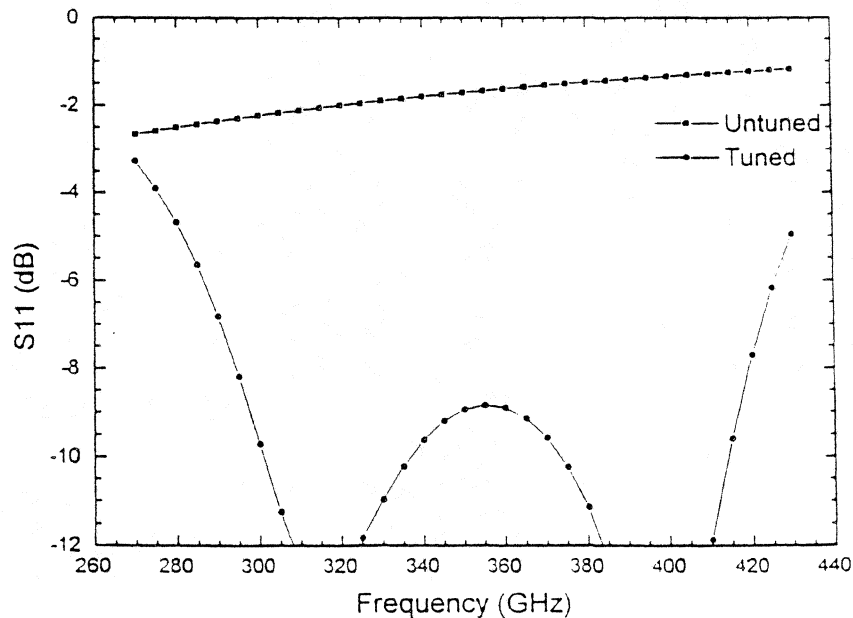


Fig. 3. Input reflection coefficient (dB) of a tuned and untuned 50Ω $0.49\ \mu\text{m}^2$ Nb/AlO_x/Nb tunnel junction. The designed inband reflection coefficient is -9 dB, which was a trade off between maximum RF bandwidth and optimum impedance match.

By adjusting the non-contacting tuners we keep $Z_p(\omega)$ approximately constant over the entire frequency range [16]. To keep the $\omega R_j C_j$ product (K) as small as possible, allow good coupling to an IF impedance of 160Ω [5], and maintain high quality junctions we decided to use 50Ω $0.49\mu\text{m}^2$ Nb/ AlO_x /Nb SIS tunnel junctions with current densities of ≈ 8000 A/cm². Using (1) the RF resistance of the pumped IV curve for small values of alpha is approximately $.67R_n$ at 345 GHz and $0.55R_n$ at 230 GHz.

In Fig. 4 we plot the junction impedance of an "end-loaded" stub tuned junction and untuned junction.

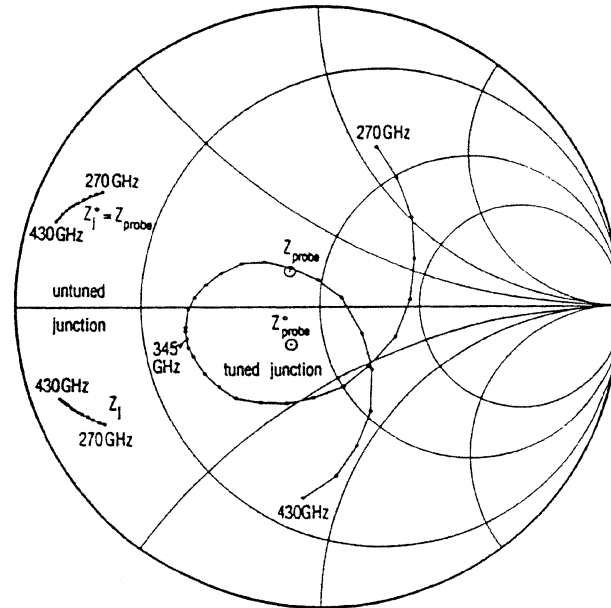


Fig. 4. Tuned and untuned junction impedance plot. The tuned junction is matched to Z_p . For untuned junctions very high quality (Q) tuners are needed to tune the probe impedance to Z_j^* .

The "end-loaded" stub length and transformer impedance sections Z_1 and Z_2 were initially calculated using a 40Ω probe impedance. We then ran Touchstone [22] to optimize the transformer for a probe impedance $Z_p = 40 + 10i \Omega$. The width's and length's of the optimized normal metal microstrip were used to calculate the characteristic impedance and electrical length of the individual sections using Linecalc [22].

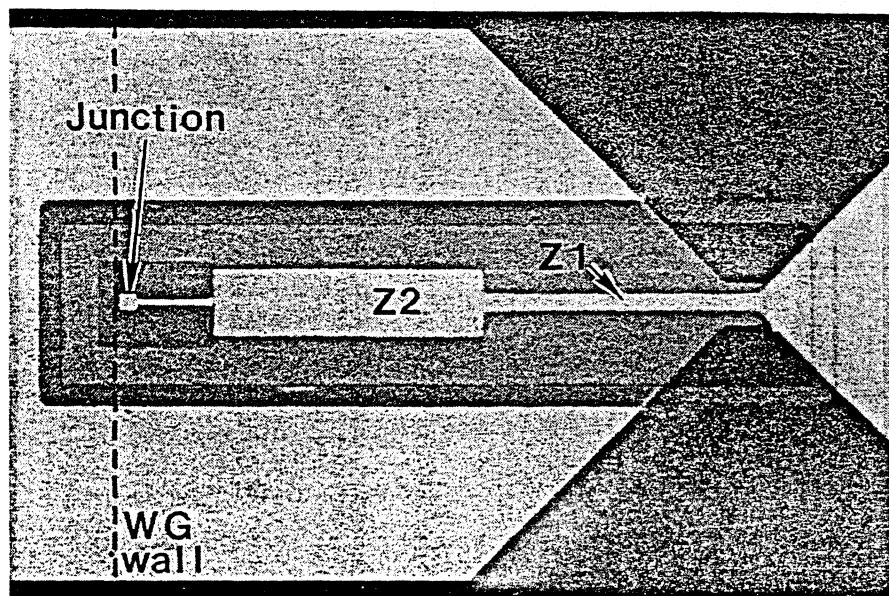


Fig. 5. (a) Physical layout of a 230/345 GHz tuned junction. The junction and "end-loaded" stub are fabricated on 150nm SiO while the two section transformer is fabricated on 450nm SiO. The junction is deposited inside a $5 \times 5 \mu\text{m}^2$ pad whose effect has been taken into account in the computer simulations. At 345 GHz the width and electrical length of the "end-loaded" stub are $2\mu\text{m}$ and 39.8 degrees respectively.

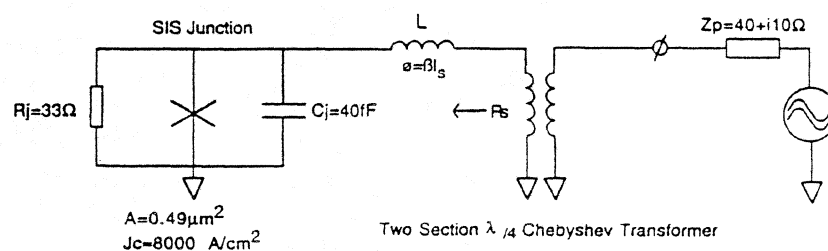


Fig. 5. (b) Electrical diagram of the RF matching network at 345 GHz. The probe impedance is defined as the impedance seen by the bowtie antenna placed in the center of the waveguide.

Using a program developed by Zmuidzinis *et al.* [23], which is based on work by Whitaker, Kautz, Hammerstad and Jensen, we proceeded to calculate the required superconducting microstrip width, length and effective dielectric constant of the different line sections. This procedure was iterative because the junction mask was layed out using integer length and width dimensions for different superconducting microstrip transmission line sections. The numerical results of the superconducting transmission line sections are summarized below.

Table 1

230 GHz and 345 GHz Tuned Junction Parameters.

	230 Theory	230 Optimized Results	345 Theory	345 Optimized Results
$Z_p^*(\Omega)$	$40 + 0i$	$40 - 10i$	$40 + 0i$	$40 - 10i$
ρ_m	0.2512	0.2445	0.3548	0.3631
$\beta l_s(^{\circ})$	38.3	40.2	43.2	39.8
$Y_o (\Omega^{-1})$	0.0578	0.0702	0.0867	0.0692
$R_s(\Omega)$	5.28	4.01	1.95	1.87
$Z_1(\Omega)$	20.86	16.41	15.62	13.64
$Z_2(\Omega)$	9.48	6.22	4.95	4.06

Nb/AlO_x/Nb Junction Fabrication

Fabrication of the Nb/AlO_x/Nb tunnel junction is accomplished using a standard trilayer deposition technique [24]. The trilayer is patterned on a 200 μm thick, 25mm diameter fused quartz substrate by a lift-off process employing image reversal of AZ5206 photoresist. Magnetron sputter deposition and room temperature oxide growth are done in-situ in an ultra-high vacuum system with a base pressure of 5×10^{-9} Torr. One side of the antenna/filter structure is formed by the trilayer with 160nm Nb base, 6nm Al, and a 90nm Nb counter-electrode. A junction mesa of $0.49 \mu\text{m}^2$ area is defined by direct write electron beam lithography in a 100nm thick PMMA stencil. Chromium is deposited through the PMMA stencil and serves as an etch mask over 500nm of polyimide. Contact regions of the trilayer are then protected with a photoresist stencil. The combined chromium+photoresist/polyimide structure is etched using an oxygen reactive ion etch (RIE) process step. Polyimide remaining defines an isolation window and junction mesa for subsequent Nb RIE. To achieve Nb etch directly

we utilize a gas mixture of $62\% \text{CCl}_2\text{F}_2 + 31\% \text{CF}_4 + 7\% \text{O}_2$. Electrical isolation of the base electrode from the wire layer is provided by thermal evaporation of 150nm of SiO. Samples are rotated at a slight tilt angle during SiO deposition to assure both good isolation and self-aligned lift-off with the polyimide. After this lift-off step, another photoresist pattern is used to produce SiO thickness of 450nm on both transformer sections. The second half of the antenna/filter is formed by a blanket deposition of 300nm Nb capped with 30nm gold for contacts. Processing is completed by RIE etching and subsequent dicing of the wafer with a diamond saw [25]. Tunnel junctions with areas down to $0.25 \mu\text{m}^2$ have been fabricated using this technique.

Receiver Description

Optics

The block diagram of the 345 GHz receiver is similar to that of the 665 GHz receiver [18]. The optics was designed to give a 14 dB edgetaper on the secondary mirror of the telescope. Local oscillator (LO) injection is accomplished with a $13 \mu\text{m}$ mylar beam splitter mounted at 45° to the LO path. The local oscillator's electric field is perpendicular to the plane of incidence and about 1.8% of the radiation couples into the cryostat, the remainder is absorbed by a sheet of Eccosorb. The vacuum window is made out of $19 \mu\text{m}$ HR500/2S material manufactured for food packaging by Hercules Inc. [26]. It has a dielectric constant of ≈ 2.6 and is a laminate of biaxially oriented polypropylene with $2.5 \mu\text{m}$ layers of polyvinylidene chloride on both sides. Laboratory experiments have shown that the material has adequate strength to function as a vacuum window for apertures diameters $\leq 25 \text{ mm}$. Experiments indicate that this Hercules material is considerably more opaque to He^4 than $25 \mu\text{m}$ mylar. The material is also expected to have a low permeability to water and atmospheric gasses. The infrared blocking filter on the 12K window consists of a half wavelength thick fluorogold disk. The mixer lens is made out of low density polyethylene, with an approximate dielectric constant of 2.41 at 4.2K ambient temperature. To better understand the nature of the optical losses we measured the transmission losses of selected materials. With the receiver tuned to 345 GHz we obtained the hot (293K) and cold (80K) IF power response with and without an optically thick 'lossy' slab of material inserted in the beam [18, 27]. The measured transmission losses for mylar and fluorogold at 345 GHz are shown in Table 2.

Table 2**345 GHz Measured Absorption Losses**

Material	Dielectric Constant (ϵ')	α (np/mm)	$\tan(\delta)$
Fluorogold	2.56-2.64	.0266	4.5×10^{-3}
Mylar	3.0	.288	3.8×10^{-2}

The optics are designed to give a frequency independent illumination of the secondary (Goldsmith [28]). The low loss polyethylene lens is placed in the near field of the scalar feedhorn. Antenna pattern measurements give reasonably close agreement to the theoretically expected response.

345 GHz Mixer Block Construction

The 20% reduced waveguide mixer block is based on the full-height 230 GHz waveguide design by Ellison *et al.* [2] and uses magnetic field concentrators as discussed by Walker *et al.* [4]. The mixer block utilizes a double tuning structure and is composed of four sections. The front section constitutes the corrugated feedhorn with a beam waist of 1.44 mm. The second section holds the circular to rectangular waveguide transformer and E-plane tuner. Six quarter-guide wavelength transitions were used to transform the circular TE_{11} mode to the reduced height TE_{10} mode over the specified frequency range. The E-plane tuner is situated $1/2\lambda_g$ in front of the junction. The third section is the junction block with the built in IF matching network, while the last section holds the non-contacting rectangular backshort tuner. A 200 μm by 200 μm groove cut across the face of the waveguide and parallel to the E-field holds the junction. The fused quartz substrate dimensions are 175 μm in width and 100 μm in height. Care has been taken to center the bowtie antenna in the waveguide. Silver paint has been used to make contact with both ground and IF side of the RF choke. The IF side of the junction contacts a 25 μm Au wire which is soldered to a 1-2 GHz wide IF matching network situated in the junction block [4, 5]. The matching network is designed to transform a 160 Ohm IF impedance to 50 Ohms and to provide a short to out of band signals up to \approx 22 GHz. The latter is needed to avoid saturating the junction with unwanted out of band signals. The output of the mixer block is directly connected to a 1-2 GHz 5K balanced HEMT amplifier, which is based on work by Padin *et al.* [29]. Any impedance mismatch between the matching network and low noise amplifier is absorbed by the amplifier's input Lange coupler. The RF choke structure is a 4 section Chebyshev bandpass filter designed to give maximum rejection ($S_{11} \leq -23$ dB) at 345 GHz. Rectangular non-contacting tuners are

used in the mixer block for both the backshort and E-plane tuners as described by Brewer and Räisänen [30]. Both tuners have three low and high impedance sections. Circular non-contacting tuners [18, 31] give higher VSWR ratios (more ideal) and are excellent candidates for use with uncompensated junctions.

Results and Discussion

The 376 GHz pumped/unpumped I-V curves and hot(295K)/cold (80K) total power response are shown in Figure 6. The Josephson oscillations were carefully suppressed by adjusting the magnetic field.

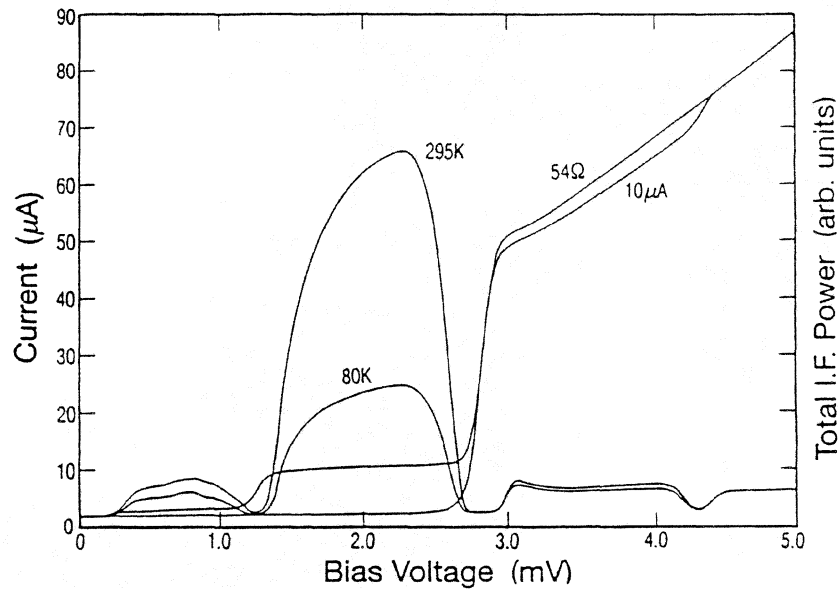


Fig. 6. I-V/Total power response. The optimum receiver noise temperature at 376 GHz was 48K DSB with an uncorrected mixer noise temperature of ≈ 40 K and 0.5dB of mixer conversion loss. The junction has a sub-gap leakage of $1.25 \mu\text{A}$.

The pumped I-V curve is nearly flat below the gap which is an indication that the junction is well matched to the probe impedance. With a $10\text{k}\Omega$ current bias circuit it was impossible to hold the junction voltage stable for very large or negative sub-gap impedances. To provide a stable voltage bias to the junction

we put a 100Ω resistor in parallel with the junction and a 20Ω current sense resistor in series with the junction [32, 33].

Best receiver noise temperatures were typically obtained with the receiver tuned for a mixer conversion loss of 0.5-1.5 dB. In this case the slope of the sub-gap pumped I-V curve is still slightly positive providing some reasonable IF impedance to the matching network. For large conversion gains the slope of the pumped sub-gap I-V curve is negative giving reflection gain. With the Josephson effect suppressed reflection gain can be readily observed from instabilities in the IF power response. Pumped I-V curves with negative slopes were easily detected with the $10k\Omega$ current bias by monitoring the voltage across the junction on an oscilloscope. By de-tuning the mixer backshort we could stabilize the junction bias which nearly always resulted in a slight conversion loss and optimum receiver sensitivity. The voltage bias circuit solves bias instability problems but does not provide a convenient feedback to detect possible mixer conversion gain. As the sub-gap IF impedance approaches infinity, ideally a transresistance amplifier is needed since the junction now acts as a current source. With the existing IF matching scheme, a cooled isolator or balanced IF amplifier is needed to absorb the large reflections between the junction and low noise amplifier.

For SIS mixers operating with a mixer conversion loss > 3 dB it is common to tune for maximum IF power or pumped junction current. Tuning for maximum IF power under these conditions nearly always gives the lowest mixer conversion loss because the IF mismatch is very small and the receiver output noise power is almost completely determined by the mixer conversion loss. The conversion loss was derived from the shot noise method [34], and has been corrected for the IF mismatch between the junction and low noise amplifier. With conversion gains > -2 dB the IF junction impedance is $\gg R_n$, which increases the IF mismatch and limits the sensitivity of the receiver. The optimum trade-off between mixer conversion gain and IF coupling efficiency is typically found by first tuning the receiver for maximum IF power (or pumped SIS current) and then optimizing the Y-factor by adjusting the backshort tuner. The receiver response of Fig. 6 was optimized for lowest noise temperature (i.e. largest Y-factor) instead of maximum IF noise power.

To confirm the calculated mixer noise temperature we used a technique described by Blundell *et al.* [35, 36]. By plotting the total IF power as a function of input load temperature for different values of LO drive level we obtained a mixer noise temperature of 38 ± 2 K, in good agreement with the shot noise result (Fig. 6). At 376 GHz the calculated optics loss contributes ≈ 26 K to the mixer noise temperature. By taking into account the increase of mixer noise temperature (3.8 K) over the quantum limit due to the sub-gap leakage current [37], we calculate a SSB mixer response of $22 \text{ K} \pm 3 \text{ K}$ (≈ 1.2 times the quantum noise limit).

Fig. 7 depicts the uncorrected mixer, receiver noise temperatures and conversion gain at 376 GHz as a function of bias voltage with the receiver tuned for maximum IF power response. Although not clear from the graph the total power did have some instability. Note that even though the mixer exhibits conversion gain the receiver noise temperature does not decrease accordingly. The receiver sensitivity is limited to $\approx 50\text{K DSB}$ by the IF coupling efficiency and front-end loss generated noise ($\approx 26\text{K}$). It is possible to trade IF coupling efficiency for mixer conversion gain in certain parts of the frequency band. This has little or no effect on the receiver sensitivity but does degrade the stability of the receiver.

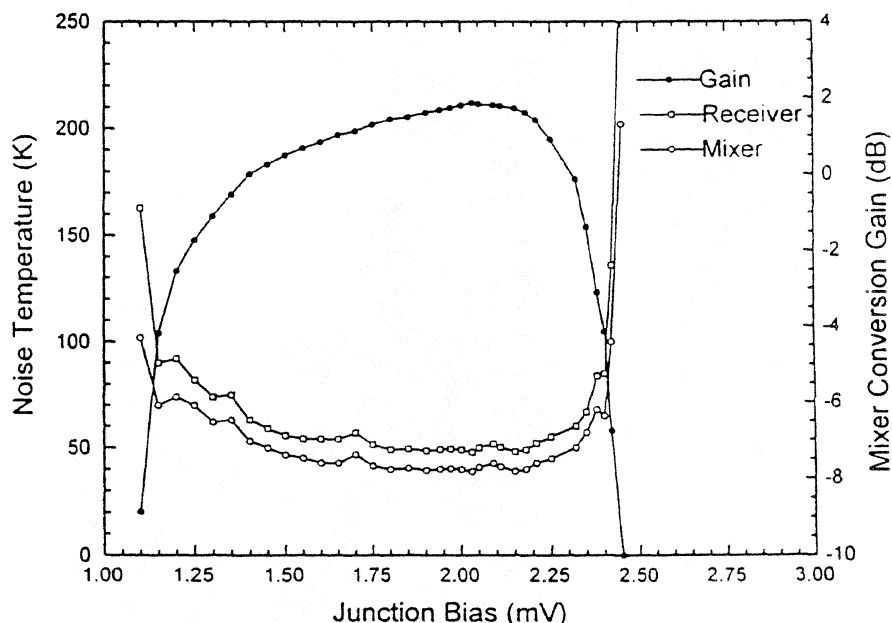


Fig. 7. Noise temperatures of the receiver and mixer, and conversion gain as a function of bias voltage at 376 GHz. The corrected SSB mixer noise temperature is $\approx 22\text{K}$ (80% quantum efficiency). The optimum bias voltage is between 2.0 and 2.2 mV which is similar to the 230, 492, and 665 GHz Nb/AlO_x/Nb SIS quasi-particle receivers currently in operation at the CSO.

Stable operation and optimum receiver sensitivity is typically obtained with a conversion gain of $-1 \pm 0.5\text{ dB}$, (Fig. 6).

The instantaneous bandwidth for the "end-loaded" stub tuned junctions is ≈ 25 GHz, which ensures true double sideband mixer performance.

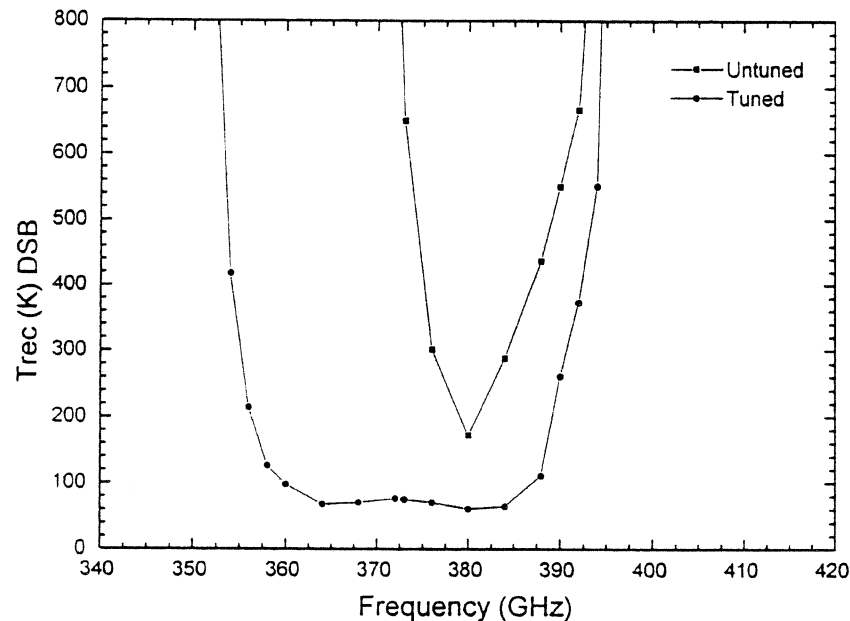


Fig. 8. Instantaneous bandwidth of both a tuned and untuned junction with the receiver centered at 380 GHz. The asymmetry of the tuned response is determined by the corner frequency of the RF matching network, ≈ 390 GHz. A similar result is seen at 300 GHz giving an effective tuned bandwidth of approximately 90 GHz (26%).

The measured DSB receiver noise temperature was less than 100K between 275-425 GHz. Fig. 9 depicts the frequency response of the receiver overlaid by the atmospheric transmission (1mm H₂O) on Mauna Kea, Hawaii. The receiver covers several atmospheric bands and fills the gap between the 230- and 492 GHz SIS receivers. The double tuned response of the equal-ripple transformer is evident from the receiver's frequency response (Fig. 3.). At 345 GHz the mixer conversion loss is ≈ 3 dB, which allows tuning for the maximum noise power as discussed in the text. Of course it is possible to trade bandwidth for sensitivity and to design an RF matching network which gives a better match in the center of the band.

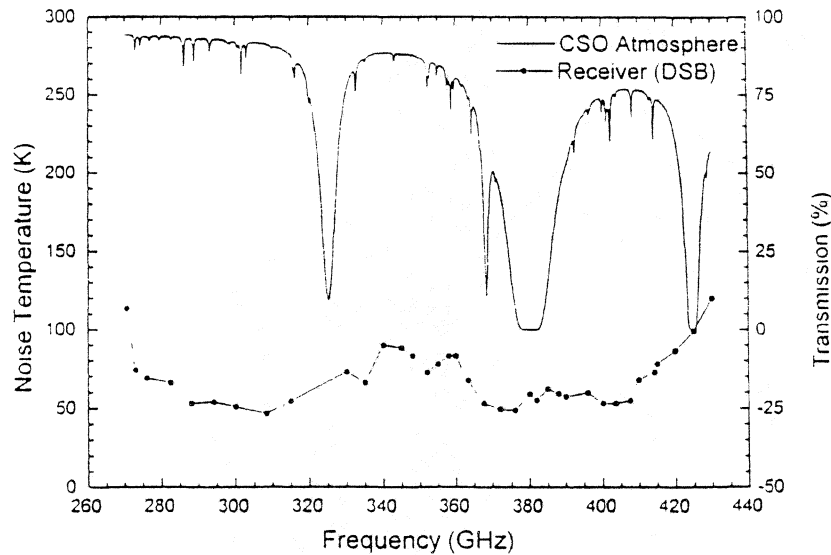


Fig. 9. Frequency response of the 345 GHz receiver from 270-430 GHz.

230 GHz Receiver Results

The 230 GHz "end-loaded" stub tuned junction was tested in a full height waveguide mixer block [2, 5]. Preliminary measured receiver noise temperatures vary from 30K-50K DSB across the 200-300 GHz band. Magnetic field concentrators to suppress Josephson oscillations were not incorporated in the mixer block [4]. For frequencies above 260 GHz we noticed small fluctuations in the total power response, which is attributed to our inability to suppress the Josephson effect. Conversion gain was encountered over much of the 200-300 GHz range, however best results were again obtained with the receiver tuned for 0.5-1.5 dB mixer conversion loss. The pumped/unpumped I-V curves and the hot(295K)/cold(80K) total power response are shown in Fig. 10.

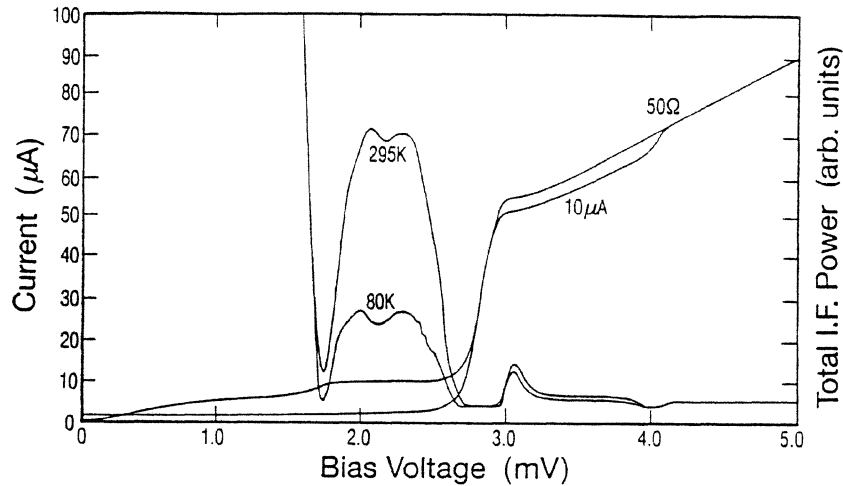


Fig. 10. Pumped and unpumped total power and I-V curves at 258 GHz. The measured receiver noise temperature at 2.05 mV bias was 34K DSB, ≈ 5.5 times the quantum noise limit. The mixer has an uncorrected noise temperature of $27\text{K} \pm 2\text{K}$, 0.5 dB of conversion loss and $\approx 70\%$ quantum efficiency. The junction has a current density of $\approx 8000 \text{ A/cm}^2$ and a sub-gap leakage of $1.25 \mu\text{A}$.

Conclusion

A SIS heterodyne quasi-particle mixer has been developed for the 270-430 GHz submillimeter band. The mixer employs a tuned $0.49 \mu\text{m}^2$ Nb/ AlO_x /Nb tunnel junction mounted in a 20% reduced height waveguide block. The RF matching network consists of an "end-loaded" stub with a two section equal-ripple transformer, which in combination with a two-tuner reduced height waveguide mixer block provides for 50% overall and 7% instantaneous bandwidth. The receiver has a double sideband noise temperature of $< 100\text{K}$ from 270-425 GHz and has been successfully installed at the Caltech Submillimeter Observatory in Hawaii. 1-3 dB of conversion gain and 50-80% quantum efficiency has been demonstrated over parts of the 180-430 GHz frequency band. As the junction capacitance is tuned out the junction behaves like a current source and has a receiver noise temperature that is limited by the front-end loss and the IF coupling

efficiency. Under the condition of near unity mixer conversion gain higher current density junctions should ideally be used to improve the IF match and retain the same RF bandwidth. The receivers can be tuned for either a slight conversion loss and good IF match, or conversion gain and poor IF match! The latter condition should be avoided. Best receiver sensitivity and stability is typically achieved with the mixer tuned for 0.5-1.5 dB conversion loss, which minimizes the IF noise contribution. For frequencies above 500 GHz the real part of the transformed junction impedance and the physical length of the transmission lines become very small. This reduces the bandwidth over which a good RF match can be achieved and at the same time dictates a very low impedance value for the second transformer section, with L/W ratio's near unity. In this case the junction becomes part of the "end-loaded" stub which introduces serious modeling and fabrication problems. For frequencies exceeding 500 GHz radially shorted tuning stubs and two junction matching techniques as described by Zmuidzinas *et al.* are good candidates for tuned junction designs. The "end-loaded" stub is a promising technology for the lower half of the submillimeter band. It enables development of tuned waveguide mixers with high quantum efficiency as well as fix-tuned receivers for use in imaging arrays.

Acknowledgments

We wish to thank Jonas Zmuidzinas, Thomas Büttgenbach, Chris Walker, Rob Schoelkopf, Todd Groesbeck, George Ugras, Dominic Benford, Dave Woody, Mei Bin, John Cortese and Tony Kerr for helpful discussions and John Carlstrom for supplying the 100-143 GHz wideband Gunn oscillators which were a tremendous aid in measuring the frequency response of the mixers. Work at Caltech is supported in part by NSF grant[#] AST-9015755 and NASA grant[#] NAGW-107.

References

- [1] J.R. Tucker and M.J. Feldman, "Quantum Detection at Millimeter Wavelength," *Rev. Mod. Phys.* 57, 1055-1113, 1985
- [2] B.N. Ellison and R.E. Miller, "A Low Noise 230 GHz SIS Receiver," *Int. J. IR and MM Waves*, Vol 8, 609-625, 1987
- [3] B.N. Ellison, P.L. Schaffer, W. Schaal, D. Vail, and R.E. Miller, "A 345GHz SIS Receiver for Radio Astronomy," *Int. J. IR and MM Waves*, Vol 10, No. 8, 1989
- [4] C.K. Walker, J.W. Kooi, M. Chan, H.G. Leduc, P.L. Schaffer, J.E. Carlstrom, and T.G. Phillips, "A Low-noise 492 GHz SIS waveguide receiver," *Int. J. IR and MM Waves*, Vol. 13, pp. 785-798, June 1992.
- [5] J.W. Kooi, M. Chan, T.G. Phillips, B. Bumble, and H.G. Leduc, "A low noise 230 GHz heterodyne receiver employing $0.25 \mu\text{m}^2$ area Nb/AlO_x/Nb tunnel junctions," *IEEE trans. Microwaves Theory and Techniques*, Vol. 40, pp. 812-815, May 1992.
- [6] L.R. D'addario, "An SIS Mixer for 90-120 GHz with Gain and Wide bandwidth," *Int. J. IR and MM Waves*, Vol 5, No. 11, pp. 1419-1433, 1984.
- [7] A.V. Räisänen, W.R. McGrath, P.L. Richards, and F.L. Lloyd, "Broad-band RF match to a Millimeter-Wave SIS Quasi-Particle Mixer," *IEEE Trans. Microwave Theory and Techniques*, Vol. MTT-33, No. 12, pp. 1495-1499, 1985.
- [8] A. R. Kerr, S.K. Pan, M.J. Feldman, "Integrated Tuning for SIS Mixers," *Int. J. IR and MM Waves*, Vol 9, No. 2, pp. 203-212, 1988.
- [9] C.E. Honingh, G. de Lange, M.M.T.M. Dierichs, H.H. Schaeffer, Th. de Graauw, and T.M. Klapwijk, "Performance of a Two-Junction Array SIS-Mixer Operating Around 345 GHz," *IEEE Trans. Microwave Theory and Techniques*, Vol. MTT-41, No. 4, pp. 616-623, 1993.
- [10] G. de Lange, C.E. Honingh, M.M.T.M. Dierichs, H.H.A. Schaeffer, H. Kuipers, R.A. Panhuyzen, T.M. Klapwijk, H. van de Stadt, M.W.M. de Graauw, and E. Armandillo, "Quantum limited responsivity of a Nb/Al₂O₃/Nb SIS waveguide mixer at 460 GHz", *Proc. 4th Int'l Symp. Space THz Technology*, Los Angeles, pp. 41-49, 1993
- [11] M. Salez, P. Febvre, W.R. McGrath, B. Bumble, H.G. LeDuc, "An SIS Waveguide Heterodyne Receiver for 600 GHz - 635 GHz," *Int. J. IR and MM Waves*, Vol 15, No. 2, Feb. 1994.
- [12] J. Zmuidzinas, H.G. Leduc, J.A. Stern, and S.R. Cypher, "Two-junction tuning circuits for submillimeter SIS mixers," *IEEE accepted*.

- [13] T.H. Büttgenbach, H.G. LeDuc, P.D. Maker, T.G. Phillips, "A Fixed Tuned Broadband Matching Structure for SIS Receivers," *IEEE Trans. Applied Supercond.*, Vol. 2, No. 3, pp. 165-175, 1992.
- [14] K.F. Schuster, A.I. Harris, K.H. Gundlach, "A 691 GHz SIS Receiver for Radio Astronomy," *Int. J. IR and MM Waves*, Vol 14, No. 10, Oct. 1993.
- [15] E.C. Sutton, "A Superconducting Tunnel Junction Receiver for 230 GHz," *IEEE Trans. Microwave Theory and Techniques*, Vol. MTT-31, No. 7, pp. 589-592, 1983.
- [16] K. Jacobs, U. Kotthaus, and B. Vowinkel, "Simulated Performance and Model Measurements of an SIS Waveguide Mixer using Integrated Tuning Structures," *Int. J. IR and MM Waves*, Vol 13, No. 1, pp. 15-26, 1992.
- [17] "Foundations for Microwave Engineering," McGraw-Hill Physical and Quantum Electronics Series. 1966.
- [18] J.W. Kooi, C.K. Walker, H.G. LeDuc, T.R. Hunter, D.J. Benford, and T.G. Phillips, "A Low Noise 665 GHz SIS Quasi-Particle Waveguide Receiver," submitted to *Int. J. IR and MM Waves*, December 1993.
- [19] T.H. Büttgenbach, T.D Groesbeck, and B.N. Ellison, "A Scale Mixer Model for SIS Waveguide Receivers," *Int. J. IR and MM Waves*, Vol 11, no 1, 1990.
- [20] A.V. Räisänen, W.R. McGrath, D.G. Crete, and P.L. Richards, "Scale Model Measurements of Embedding Impedances for SIS Waveguide Mixers," *Int. J. IR and MM Waves*, Vol 6, No. 12, pp. 1169-1189, 1985.
- [21] C.E. Honingh, "A Quantum Mixer at 350 GHz based on Superconducting-Insulator-Superconducting (SIS) Junctions," PhD Dissertation, Groningen, The Netherlands, June 1993.
- [22] HP/EESOF CAD, Westlake Village, Ca. 91362.
- [23] J. Zmuidzinas, and H.G. LeDuc, "Quasi-Optical Slot Antenna SIS Mixers," *IEEE Trans. Microwave Theory and Techniques*, Vol. MTT-40, No. 9, pp. 1797-1804, September 1992.
- [24] M. Gurivch, M.A. Washington, and H.A. Huggins, "High Quality Josephson Tunnel Junctions Utilizing Thin Aluminum Layers," *Appl. Phys. Lett.*, v.42, 472-474, 1983.
- [25] H.G. LeDuc, B. Bumble, S.R. Cypher, and J.A. Stern, *Second International Symposium on Space Terahertz technology*, Pasadena, Ca. Feb. 26-28 (1991).
- [26] A.R. Kerr, N.J. Bailey, D.E. Boyd and N. Horner, "A study of materials for a broadband millimeter-wave quasi-optical vacuum window," Electronics Division Internal Report No. 292, National Radio Astronomy Observatory, Charlottesville, VA 22903, August 1992.
- [27] J. W. Lamb, "Infrared filters for cryogenic receivers," Electronics Division Internal Report No. 290, National Radio Astronomy Observatory, Charlottesville, VA 22903, April 1992.

- [28] P.F. Goldsmith, "Quasi-Optical techniques at Millimeter and Submillimeter Wavelength," . *Infrared and Millimeter Waves*, Vol 6, pp. 277-343, 1982.
- [29] S. Padin, G. Ortiz, "A Cooled 1-2 GHz Balanced HEMT Amplifier," *IEEE, Microwave Theory and Techniques*, Vol 39, No 7, pp. 1239-1243, 1991.
- [30] M.K. Brewer, and A.V. Räisänen, *IEEE Trans. Microwave Theory and Techniques*, Vol. 30, pp. 708, 1982.
- [31] A.R. Kerr, "An Adjustable Short-Circuit for Millimeter Waveguides," Electronics Division Internal Report No. 280, National Radio Astronomy Observatory, Charlottesville, VA 22903, July 1988.
- [32] A.R. Kerr, S.-K. Pan, M.J. Feldman, and A. Davidson, "Infinite Available Gain in a 115 GHz SIS Mixer," *Physica B*, vol. 108, pp 1369-1370, Sept. 1981.
- [33] S.-K. Pan, M.J. Feldman, A.R. Kerr, E.S. Palmer, J.A. Grange, and P. Timbie, "Superconducting Tunnel Junction Receiver for 2.6 mm," Digest of 8th International Conference on Infrared and Millimeter Waves, pp. M6.2/1-2, Dec. 1983.
- [34] D.P. Woody, R.E. Miller and M.J. Wengler, "85-115 GHz Receivers for Radio Astronomy," *IEEE trans. Microwaves Theory and Techniques*, Vol. MTT-33, 1985, pp. 90-95
- [35] R.Blundell, R.E. Miller, and K.H. Gundlach, "Understanding Noise in SIS Receivers," *Int. J. IR and MM Waves*, Vol 13, No. 1, pp. 3-26, 1992.
- [36] Q. Ke, and M.J. Feldman, "A Technique for Accurate Noise Temperature measurements for the Superconducting Quasiparticle Receiver," *Fourth international Symposium on Space Terahertz technology*, UCLA, 1993.
- [37] M.J. Feldman, "An Analytical Investigation of the Superconductor Quasiparticle Mixer in the Low Power Limit," *IEEE Trans. Magnetics*, Vol. 27, No. 2, pp. 2646-2649.

SIS Receivers with Large Instantaneous Bandwidth for Radio Astronomy

K. Jacobs, U. Müller, U. Schwenk, D. Diehl, C.E. Honingh, S. Haas



KOSMA

*I. Physikalisches Institut der Universität zu Köln
Zùlpicher Str. 77
D-50937 Köln
Germany*

Introduction

The fast progress in developing low noise SIS receivers up to the 700GHz range is mainly due to the application of the niobium technology which enables the use of various types of low loss tuning structures to tune out the large geometrical capacitance of SIS junctions. This paper describes receivers in the 230GHz, 345GHz, and 490GHz bands that all use the "three step transformer" circuit presented in [1]. This wide band tuning structure is an excellent choice to develop fixed tuned mixers, which are convenient for the facility-type operation of the receivers intended at the KOSMA Gornergrat telescope. The mixers are used in polarization-split dual frequency receivers, one with channels at 230GHz and 345GHz for the summer months and 490GHz and 345GHz for the months with highest atmospheric transmission [2]. The second dual channel receiver will operate at 490GHz and 690GHz, with a possible exchange of one mixer for a 809GHz system. The waveguide mixer blocks, the Nb-Al₂O₃-Nb SIS junctions and the cooled IF amplifiers are fabricated at the University of Cologne. The local oscillator-sources are commercial components (Radiometer Physics, Millitech, Carlstrom).

230GHz receiver

The 230GHz mixerblock has a half height waveguide (0.275mmx1.1mm) and a single contacting backshort. The block is fabricated in split-block technology, including a diagonal horn [3]. The RF-filter and SIS junction are fabricated on a 100μm thick fused quartz substrate. The embedding impedance presented by the waveguide and the RF-filter section extending into the waveguide was analyzed and optimized using a frequency scaled model [1].

The junction used in this experiment has a nominal area of 2μm², a gap voltage of 2.75mV with ΔV_g=73μV, a normal resistance R_N=17Ω, a critical current of I_c=120μA (=0.7xΔI_{qp}) and a subgap current I_{sg}(2mV)=7.3μA. The tuning structure is shown schematically in Fig.1. Impedances and phase velocities of the superconducting microstrip lines were calculated from

$$L_l = \frac{\mu_0}{k \cdot w} \cdot \left[t_d + t_p \cdot \cosh\left(\frac{t_1}{t_p}\right) + t_p \cdot \cosh\left(\frac{t_2}{t_p}\right) \right]$$

$$C_l = \frac{k \cdot \epsilon_0 \cdot \epsilon_{r,eff} \cdot w}{t_d}$$

$$\epsilon_{r,eff} = \frac{\epsilon_r + 1}{2} + \frac{\epsilon_r - 1}{2} \cdot \frac{1}{\sqrt{1 + 12 \cdot \frac{w}{t_d}}} - \frac{\epsilon_r - 1}{4.6} \cdot \frac{t_2}{t_d \cdot \sqrt{\frac{w}{t_d}}}$$

$$v_{ph} = \frac{1}{\sqrt{L_l \cdot C_l}}$$

$$Z_0 = \sqrt{\frac{L_l}{C_l}}, \quad \text{with } \epsilon_r(\text{SiO})=5.5, t_d=200\text{nm}, t_1=100\text{nm}, t_2=350\text{nm}, t_p=75\text{nm}$$

L_l is the inductance per unit length, C_l the capacitance per unit length, and k is the fringing factor taken from [4]. ε_{r,eff} also takes the thickness of the strip conductor into account[5]. In the calculations leading to the design of the mask we did not include the step discontinuity effect, which is mainly an added inductance from line 2 to line 3. This will be discussed in more detail in the 345GHz part of the paper.

Fig. 2 shows the receiver noise temperatures where local oscillator power, backshort setting and mixer bias were all optimized. Fig.3 shows the DC-I/V curve with applied local oscillator power and the IF output power as a function of bias voltage for Hot and Cold input at 245GHz. The local oscillator (Gunn oscillator and frequency tripler) is coupled by a 50 μ m 1% mylar beamsplitter. The vacuum window and 80K IR window are made of teflon with a resonant thickness of 450 μ m. The cooled HEMT amplifier has a nominal noise temperature of 9K at 1.4GHz. All measurements were made in a 100MHz bandwidth centered at 1.4GHz. Fig.4 shows the receiver noise temperatures for a fixed backshort position tuned to optimum performance at 245GHz. At all other frequencies, only LO-power and bias voltage were optimized. The receiver noise temperature is below 100K from 225-255GHz. The resulting mixer noise and gain is shown in Fig.5. We used the "shot noise method" (see e.g. [8]) to determine gain and noise temperature of the IF chain. It turned out that the HEMT amplifier had a noise temperature of 20K instead of the previously measured 9K. Results will therefore slightly improve, especially at the higher frequencies where the gain is small, when this amplifier is replaced.

All data were taken with a computerized setup, giving digitized data which can be easily analyzed. We used MathCad Ver. 4.0 for most of the calculations. The embedding impedance of the SIS junction was determined from the measured pumped I/V curves by evaluating the large signal equations for the local oscillator equivalent circuit at selected points on the I/V curve [6]. The embedding impedance includes the geometrical capacitance of the junction and is shown in Fig. 6 for the fixed tuned case from 225-250GHz. The Smith chart in Fig.6 and all other Smith charts in this paper are normalized to 25 Ω . The discontinuity at the higher frequencies could be a resonance which is not resolved. The impedance is inductive at the low frequencies and has a real part somewhat higher than the junction normal resistance of 17 Ω . At 210GHz the junction had to be pumped at a very low level in order to avoid too much gain and subsequent instability. At the higher frequencies the impedance becomes more and more capacitive and the real part drops, leading to mixer loss and poorer performance. The influence of the integrated tuning structure on this behaviour will be discussed in the next part of the paper.

345GHz receiver

The mixer is a scaled version of the 230GHz mixer, except for the substrate thickness which was kept at 100 μ m for ease of fabrication and handling. The vacuum window and IR filter were made resonant at 350GHz. A 50 μ m Mylar beamsplitter was used. The IF chain includes a 6K noise temperature HEMT amplifier. The junction used in this experiment has a nominal area of 1.44 μ m² with a current density of $\cong 5.6$ kA/cm², $V_g=2.79$ mV, $I_c=83.3\mu$ A, $I_{sg}(2mV)=3.8\mu$ A, $R_N=22.4\Omega$. Again a three element tuning transformer has been used as integrated matching structure.

The receiver noise, the gain and the mixer noise for the fixed tuned case are shown in Fig.7 and 8, respectively, again using the shot noise method for the IF calibration. The embedding impedance was determined using the method described above and is shown in Fig.9. It is capacitive over the whole frequency range and ends in a very low real part at 360GHz. This, of course, leads to a strong mismatch and a corresponding loss of performance. Analysis of the mixer performance with the Quantum Theory of Mixing [7] using the three frequency, low IF approximation and the measured embedding impedances and the unpumped I/V-curve as input, resulted in the receiver noise temperatures given by the open squares in Fig. 8. The value of the LO-power was varied to fit the measured pumped I/V curve and was in the range of 20-50nW. The calculated values for the mixer gain are also indicated in Fig.8. The (DSB) gain values are quite accurately reproduced. The receiver noise follows the experimental data but is a factor of two or more lower, a result that was also seen by other authors [8].

This unexpected, rather poor impedance match lead to remodelling the structure in "Touchstone". An equivalent circuit for the simulation is shown in Fig.10. The waveguide and RF-filter impedance were modelled as a fixed real impedance in series with a frequency dependent reactive part (using an inductor in Touchstone), going from capacitive to inductive values with increasing frequency, approximating the scaled model measurements. We implemented the equations given above to calculate the superconducting microstrip lines. The three-step tuning transformer was more accurately described than in the initial calculations by including the inductive effect of the microstrip step discontinuities as a series inductance according to:

$$L_s = t_d \cdot \frac{\mu_0}{\pi} \cdot \ln \left(1 / \sin \left(\frac{\pi}{2} \cdot \frac{Z_{L1} \cdot \sqrt{\epsilon_{r,eff,L1}}}{Z_{L2} \cdot \sqrt{\epsilon_{r,eff,L2}}} \right) \right) \quad [9]$$

with $Z_{L1} < Z_{L2}$. This equation is valid for frequencies $f \ll f_{gHE2}$ with $f_{gHEm} = \frac{c_0 \cdot m}{2 \cdot k \cdot w \cdot \sqrt{\epsilon_{eff}}}$, which

is ≥ 4.5 THz for $k \cdot w \leq 30 \mu\text{m}$ and $m=2$.

The structure was designed for a junction capacitance of 105fF including the contact layer pad. From optical inspection during manufacturing of the device it was known that the size was close to $(1.3 \mu\text{m})^2$ instead of $(1.2 \mu\text{m})^2$ so that a higher capacitance was anticipated. A best fit to the data was obtained for a capacitance of 110fF and a waveguide impedance of $25-i33\Omega$ at 310GHz and $25+i9\Omega$ at 360GHz. Waveguide impedance and junction capacitance are relatively independent fit parameters, with the waveguide data being rather insensitive. The data indicate a specific junction capacitance of $65\text{fF}/\mu\text{m}^2$ at $5.6\text{kA}/\text{cm}^2$, which corresponds exactly to data measured at JPL [10]. A similar fit can be obtained neglecting the step inductance and taking $C_j=135\text{fF}$, which would lead to a specific capacitance of $78\text{fF}/\mu\text{m}^2$, which appears to be too high to be realistic.

It would seem that reducing the length of the inductive line to the junction to include the step inductance would give the optimum performance, because this would move the band of optimum coupling to the center of the receiver band. As shown in Fig.12 this results in a strongly inductive embedding impedance at the lower end of the band. As the QTM calculations show, this leads to a mixer gain of the order of 10dB which will cause severe stability problems that also have been observed by several authors [11,12]. This means that the step transformer has to be carefully designed to be of practical value in broadband fixed-tuned mixers. Shown in Fig. 14 is the effect of "shifting" the complete transformer structure so that the inductive line leading to the junction gets shorter. This procedure is possible by shifting the wiring layer mask level as shown in Fig.13. The embedding impedance stays moderately capacitive over the desired band from 310-360GHz. The (small) effects of the short line ending in the (former) contact pad and the longer first line are both taken into account. Fig. 15 shows the receiver noise temperatures and the mixer gain calculated from QTM using the embedding impedances of Fig. 14. The noise temperature and the mixer gain

is now more uniform over the receiver band. This means that there is a possibility of "fine tuning" the circuit during fabrication.

490GHz receiver

The 490GHz mixer is an exactly scaled version of the 230GHz mixer, using a half height waveguide of dimensions (0.135mmx0.54mm) and a single contacting backshort. The substrate thickness is now 50 μ m. The junction has an area of 1 μ m², critical current is $I_c=56.7\mu$ A, subgap current is $I_{sg}=2\mu$ A, $V_g=2.8$ mV, $\Delta V_g=90\mu$ V. It again uses a three element transformer. Fig.16 shows the first noise temperature measurements taken with this mixer, again with fixed backshort position. The vacuum window and IR filter are both resonant at 470GHz. The LO was coupled with a 1% beamsplitter. The full Planck law is applied to calculate the hot/cold load blackbody power. In this first measurement we were not able to suppress the Josephson currents completely, so only a small part of the photon step could be used for stable biasing, as shown in the example for 460GHz in Fig.17.

660GHz and 809GHz receivers

We are presently working on the development of mixers for 660-690 GHz and 809 GHz. At these frequencies, conservative limits on current density and area of the SIS junctions, which are presently $A=0.8\mu$ m² and $j_c=10$ kA/cm² for our fabrication laboratory, make an accurate design of the three step transformer more difficult. The impedance of the wide section (line 2 in Fig. 1) must be lower than at 490GHz, resulting in a linewidth exceeding the length. In addition, the inductive section (line 3 of Fig. 1) becomes very short, which makes treating the junction as a lumped element less accurate and makes the design sensitive to alignment inaccuracies.

At 660-690GHz, close to the gap frequency (700GHz) of niobium, the superconducting transmission lines also become dispersive. The equations for the superconducting microstrip

transmission lines given above do not hold anymore. The phase velocity can be calculated approximately using the Mattis-Bardeen theory in the extreme anomalous limit [13]. Uncertainty in the phase velocity has a more pronounced effect on the design accuracy of longer line tuning structures.

Because of its large bandwidth the transformer design will nevertheless be implemented. In Fig. 18 the resulting embedding impedance for a three step transformer is given, including fringing effects, step discontinuities and dispersion. Performance is partly sacrificed to keep the line dimensions within limits that still can be calculated with a lumped junction model and fabricated with the same accuracy as at the 490GHz design. It can be seen that a suitable embedding impedance can be reached over the frequency interval 650GHz-750GHz for a junction with parameters as mentioned above. The impedance of the waveguide mount is thereby taken at a fixed backshort position.

Another way to achieve a large instantaneous bandwidth is to use a 'shorted' stub as tuning element. The impedance of the parallel resonance of this stub/junction combination changes from inductive to capacitive as a function of frequency in a direction opposite to the frequency change of the waveguide impedance at fixed backshort position. This enables an approximate conjugate match over a wide frequency band. The embedding impedance achieved for an identical junction as used in the three step transformer using a stub 'shorted' by a large lumped capacitance [14] is also shown in Fig. 18. For both structures double side band (DSB) receiver noise temperatures below 200K are expected for frequencies up to 700GHz. The calculated noise temperatures still stay below 400K up to 750GHz. Calculated receiver noise temperatures, assuming an IF-amplifier noise temperature of 10 K at 5 GHz and 5% loss in the warm input optics, are given in Fig. 19 for both structures.

At 809GHz, above the gap frequency, the niobium tunnel junctions still function very well as mixing elements [15]. The performance of the tuning structure however is dominated by the loss in the niobium transmission lines. In Fig. 20 the calculated embedding impedances for a one step transformer (end-loaded stub) (A) and a shorted stub (B) for the frequency range 750-850GHz are shown. The waveguide mount is the same as used at 660-690GHz. The loss in the

superconducting transmission line is estimated by taking twice the value as calculated by the Mattis-Bardeen theory in the extreme anomalous limit [16]. In both cases the resulting optimum embedding impedance lies in the same, capacitive, region close to the edge of the Smith Chart, clearly showing that the geometrical capacitance is partly 'inaccessible' for tuning due to the loss in the tuning structure. The main optimization that can be made in this case is to keep the tuning structure short to minimize transmission loss and to provide a perfect match between the waveguide mount and the stub/junction combination. The use of a shorted stub in this lossy case has the advantage, being a parallel resonance, that an uncertainty in loss only causes a change in coupling efficiency, whereas for a series resonant circuit like the end loaded stub also a frequency shift of the resonance occurs.

Estimated receiver noise temperatures for these two tuning structures are given in Fig. 21. It has to be noted that if only the (non-optimal) embedding impedance is taken into account in the calculation, considerably lower noise temperatures are calculated than with the transmission loss included. This indicates that a reduction of the loss in the stripline is beneficial even for a not optimally tuned junction. To this purpose either a junction with a much smaller area without integrated tuning or a transmission line material with lower losses have to be used. We are presently developing electron beam direct writing using an appropriately equipped Scanning Electron Microscope [17] to fabricate junction areas $\leq 0.5\mu\text{m}^2$. A collaboration with IRAM (Grenoble) is set up to develop NbN layers with good RF-properties.

Acknowledgements

Finishing the setup of a fabrication lab in August 1990, fabricating the first Nb-AlO_x-Nb junction in March 1991 and getting results at 230, 345 and 490GHz in spring 1992, 1993, and 1994, respectively is the product of constant teamwork of all people involved in the project. We are very grateful to Gisbert Winnewisser for his strong support of the project from its beginnings, and to Jürgen Stutzki for his stimulating interest in the results. Ulrich Kotthaus did most of the RF design for the first 230GHz results and constructed the dewar setup for 230 and 345GHz. Special thanks go to Stephan Wulff for his assistance at various stages of junction fabrication. We wish to thank Bernd Vowinkel for developing the low noise HEMT amplifiers. This work is supported by the Deutsche Forschungsgemeinschaft, Sonderforschungsbereich 301 and the Bundesministerium für Forschung und Technologie, Verbundforschung Astronomie, grant 05-2KU134(6).

References

- [1] K. Jacobs, U. Kotthaus, B. Vowinkel, "Simulated performance and model measurements of a SIS waveguide mixer using integrated tuning structures", *Int. J. Infrared and Millimeter Waves*, Vol.13, 15-26, Jan. 1992
- [2] C. Kramer, J. Stutzki, "Atmospheric Transparency at Gornegrat", KOSMA Technical Memorandum No.5, 1990
- [3] J.F. Johansson, N.D. Whyborn, "The diagonal horn as a sub-millimeter wave antenna", *IEEE Trans. Microwave Theory Tech*, Vol. MTT-40, pp 795, May 1992 (equation for phase center position corrected)
- [4] J.W. Chang, "The inductance of a superconducting strip transmission line", *J.Appl.Phys.*, Vol 50, pp.8129-8134, 1979
- [5] R.C. Gupta, R. Garg, I.J. Bahl, "Microstrip lines and slotlines", Artech House, Massachusetts, 1979
- [6] A. Skalare, "Determining embedding circuit parameters from DC measurements on quasiparticle mixers", *Int. J. Infrared and Millimeter Waves*, Vol 10, pp. 1339 Oct. 1989
- [7] J.R. Tucker, M. Feldman, "Quantum detection at millimeter wavelengths", *Review of Modern Physics*, Vol. 57, No.4, pp 1055-1113, Oct. 1985
- [8] C.E. Honingh, G. deLange, M.M.T.M. Dierichs, H.H.A. Schaeffer, J. Wezelman, J.v.d.Kuur, Th. de Graauw, T.M. Klapwijk, "Comparison of measured and predicted performance of a SIS waveguide mixer at 345GHz", *Proceedings of the 3rd Int. Symposium on Space Terahertz Technology*, pp.251-265, Ann Arbor, MI, March 1992
- [9] R. K. Hoffmann, "Integrierte Mikrowellenschaltungen", Springer-Verlag, Berlin 1983
- [10] J. Stern, priv. comm. 1992
- [11] K. Jacobs, U. Kotthaus, "Performance of a 230GHz SIS receiver using broadband integrated matching structures", *Digest of the 17th Int. Conf. on Inf. an Millimeter Waves*, pp. 332-333, Caltech, Pasadena, 1992
- [12] P. Febvre, W.R.McGrath, P. Batelaan, B. Bumble, H.G. LeDuc, S. George, P. Feautrier, "A low noise SIS receiver measured from 480GHz to 650GHz using Nb junctions with integrated RF tuning circuits", to appear in *Int. J. Infrared and Millimeter Waves*, Vol. 15, No. 6, June 1994
- [13] R.L.Kautz, "Picosecond pulses on superconducting striplines", *J. Appl. Phys.* Vol. 49, 308, 1978
- [14] A.Karpov, M.Carter, B.Lazareff, M.Voss, D.Billon-Pierron, K.H.Gundlach, "Wide band fixed tuned and tunable SIS mixers for 230 GHz and 345 GHz receivers", *Proc. Fourth Int.. Symp. on Space Terahertz Technology*, 698 (1993)
- [15] G.de Lange, C.E.Honingh, M.M.T.M.Dierichs, H.H.A.Schaeffer, J.J.Kuipers, R.A.Panhuyzen, T.M.Klapwijk, H.v.d.Stadt, M.W.M.de Graauw, and E.Armandillo, "Quantum limited responsivity of a Nb/Al₂O₃/Nb SIS waveguide mixer at 460 GHz and first results at 750GHz and 840GHz", *Proc. Fourth Int. Symp. on Space Terahertz Technology*, 41 (1993)
- [16] R. Pöpel, "Surface impedance and reflectivity of superconductors", *J. Appl. Phys.*, Vol. 66, No. 12, pp. 5950-5957, 15 Dec. 1989
- [17] K.Fiegle, Dissertation, University of Cologne, in preparation

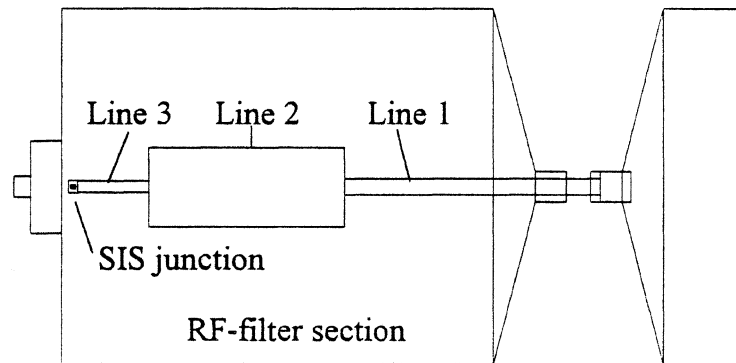


Fig. 1: Three step impedance transformer

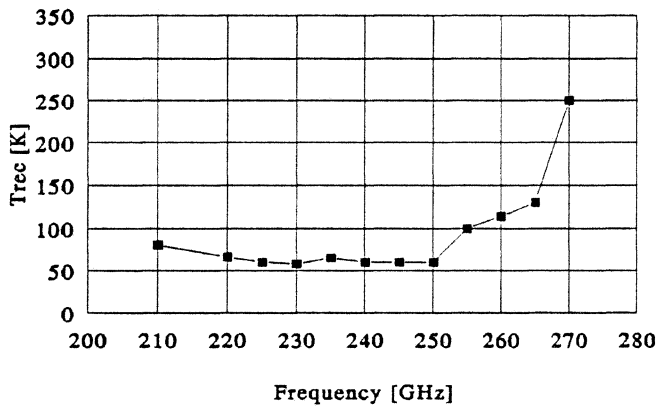


Fig. 2: Noise temperatures with optimized backshort

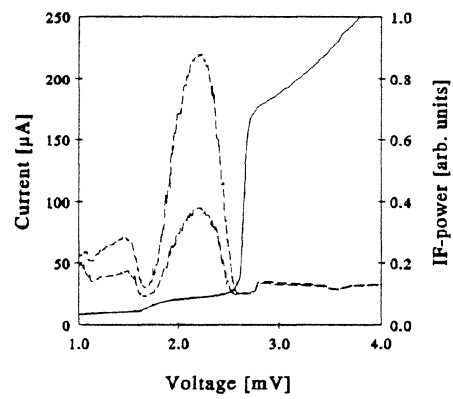


Fig. 3: Noise measurement at 245GHz

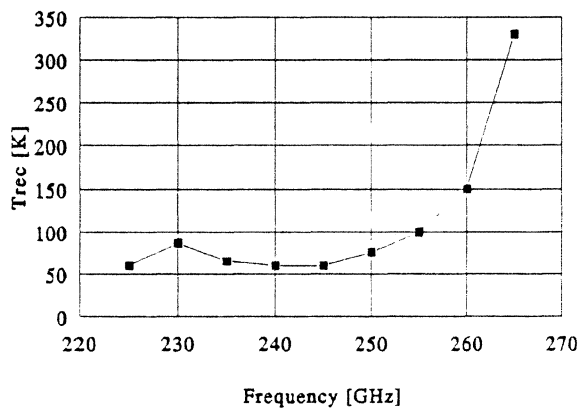


Fig. 4: Noise temperatures with fixed backshort

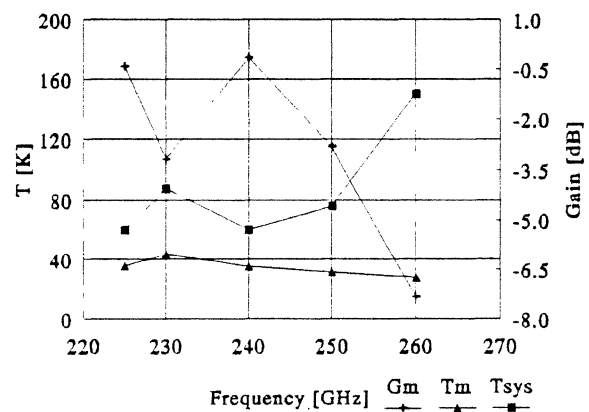


Fig. 5: Mixer noise and gain, fixed backshort

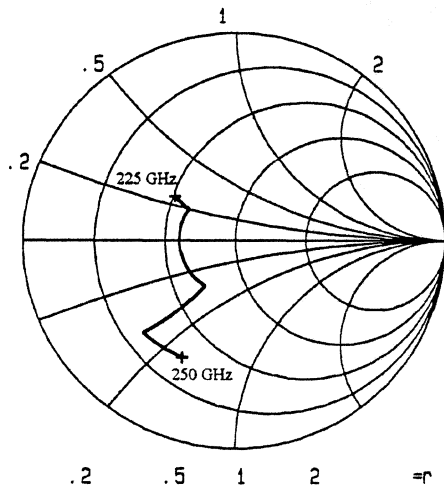


Fig. 6: Embedding impedance of junction for 230GHz mixer, fixed backshort

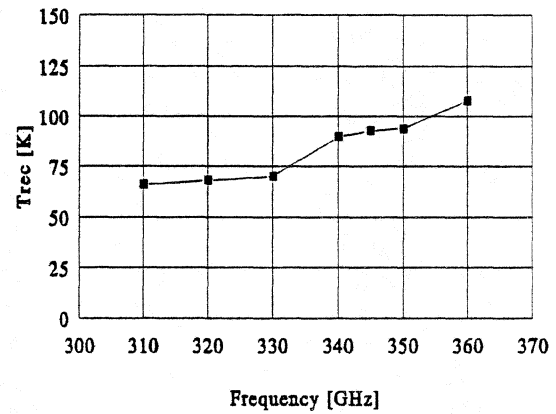


Fig. 7: Noise temperatures for fixed backshort, 345GHz receiver

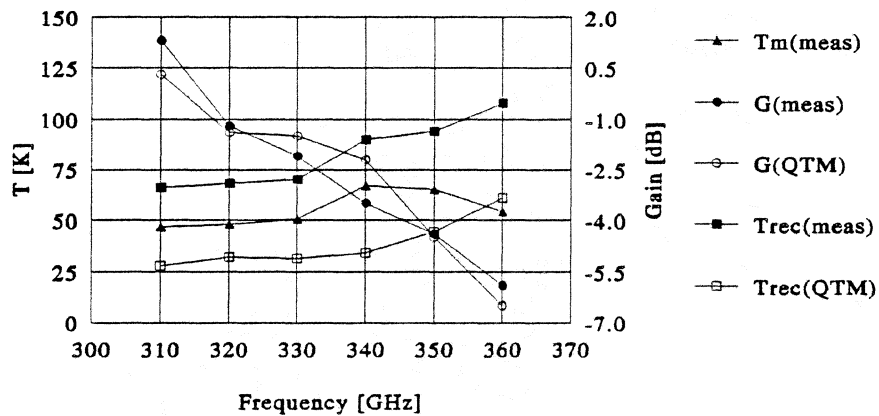


Fig. 8: Mixer noise and gain for 345GHz receiver

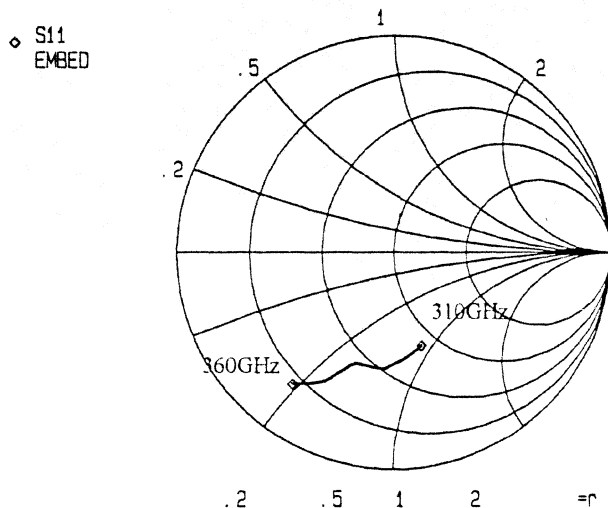


Fig. 9: Embedding impedance normalized to 25Ω

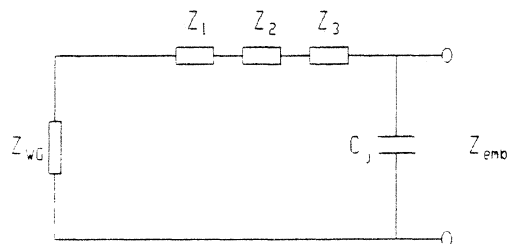


Fig. 10: Equivalent circuit for simulation

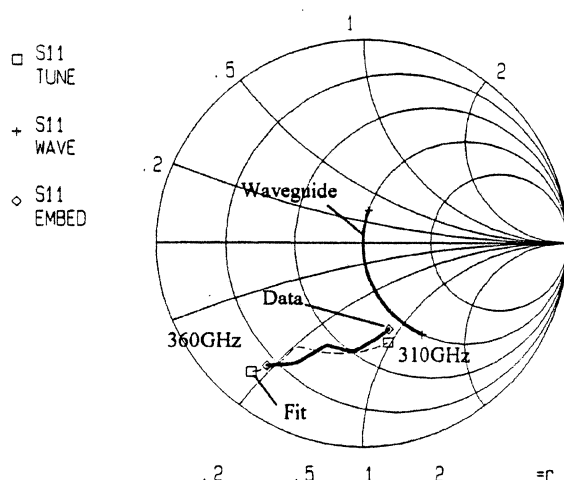


Fig. 11: Simulated and measured embedding impedance of 345GHz mixer

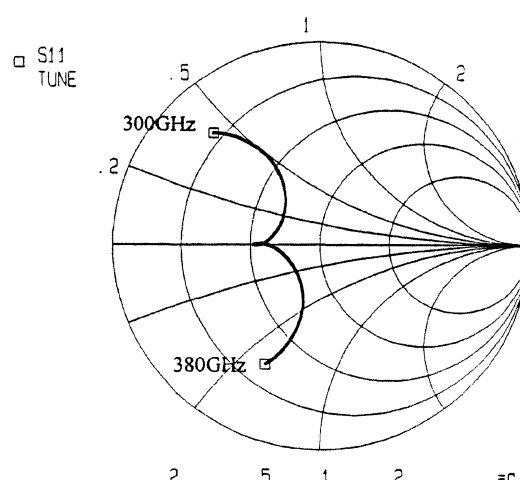


Fig. 12: Embedding impedance centered at 340 GHz

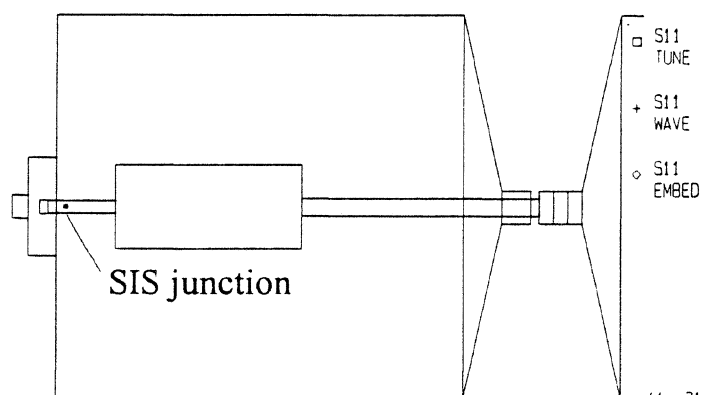


Fig. 13: Shifted tuning structure (8 μ m shift)

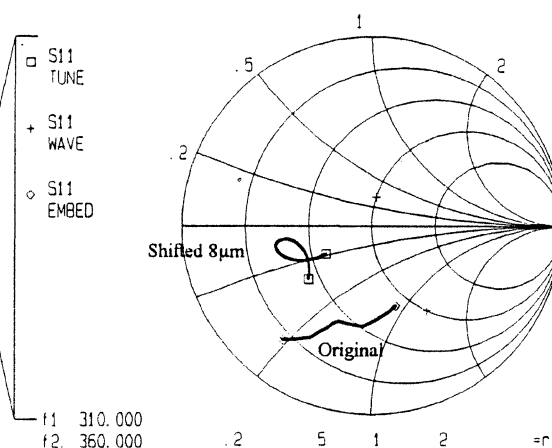


Fig. 14: Embedding impedance for shifted structure (310GHz-360GHz)

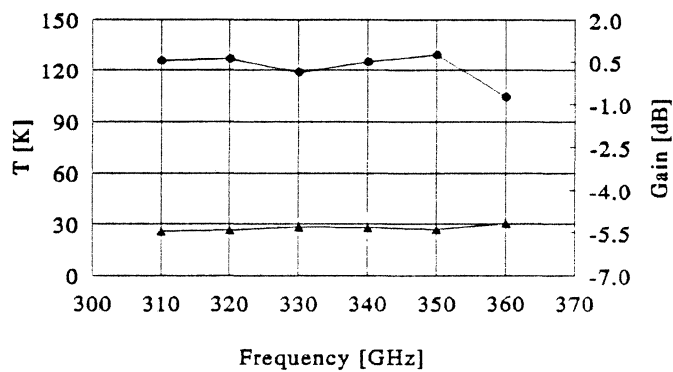


Fig. 15: Calculated receiver noise temperatures and gain for shifted structure

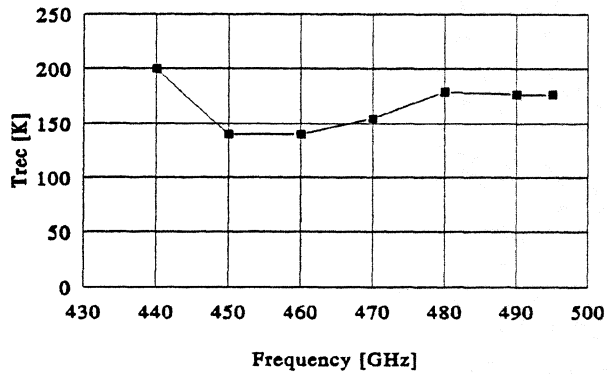


Fig. 16: Noise temperatures for 490 GHz receiver, fixed backshort

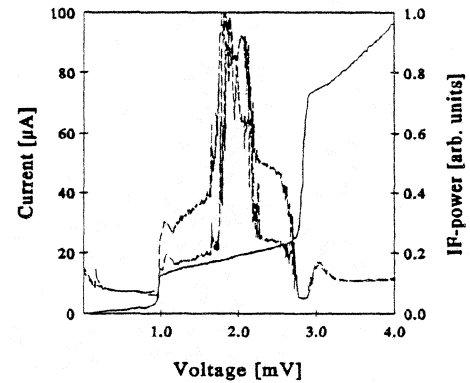


Fig. 17: Noise measurement at 460GHz

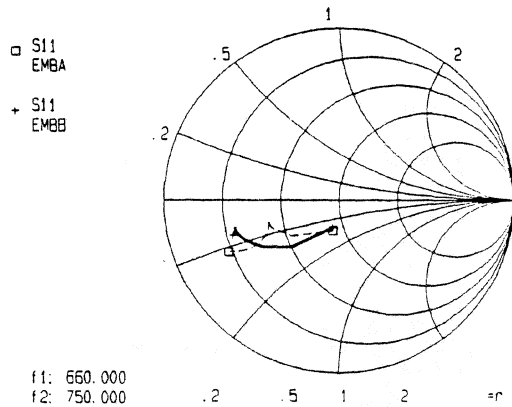


Fig. 18: Embedding impedance from 660-750GHz for 3-step-transformer(+) and shorted stub(□)

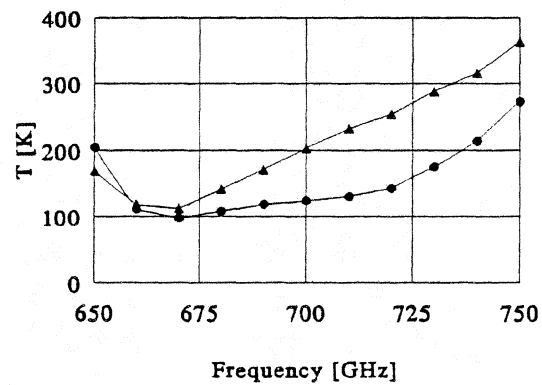


Fig. 19: Calculated DSB receiver noise for embedding impedance of Fig. 18

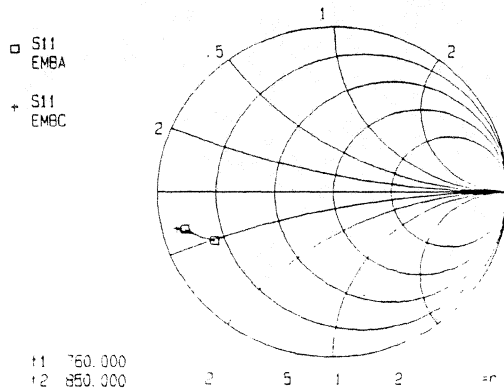


Fig. 20: Embedding impedance from 760-850 GHz for end loaded stub(+) and shorted stub(□)

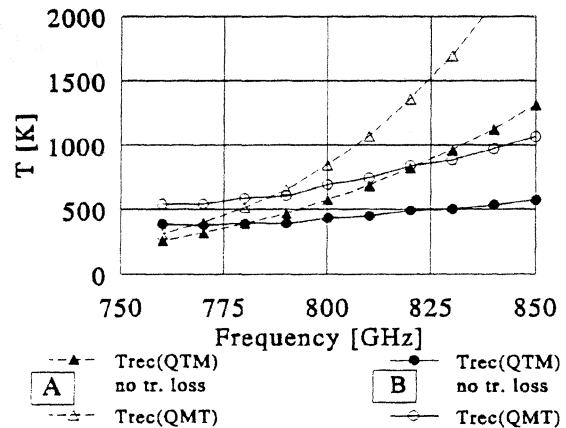


Fig. 21: Calculated DSB receiver noise temperatures for embedding impedance of Fig. 20

Millimeter and Submillimeter SIS Mixers with the Noise Temperature Close to the Quantum Limit

A. Karpov*, J. Blondel*, B. Lazareff*, K. H. Gundlach*

ABSTRACT

We report the ultra low noise SIS mixers built for the radio astronomy at millimeter wavelength (1.3 mm) and at submillimeter wavelength (0.8 mm). Mixers sensitivity is found to be close to one photon.

A mixer with the superconducting tunnel diode developed for 0.8 mm receiver is able to operate in 290-370 GHz band been fixed tuned. The receiver minimum DSB noise temperature of about 30 K corresponds to the $1.9h\nu/k$ level. Expressing this noise (or sensitivity) in photon number we get the four photons level. Measured mixer noise temperature in this receiver is about 10 K equal to $0.6h\nu/k$ level.

This receiver has been used for the observation in the winter 1994 period at 30 m IRAM radio telescope at Pico Veleta. Telescope system noise temperature of 500 K SSB has been achieved when the opacity was about 0.17.

In 1.3 mm band the minimum receiver noise is 32 K DSB ($2.9h\nu/k$ level). Measured mixer DSB noise temperature is about 5 K ($0.5h\nu/k$ level).

INTRODUCTION

The development of the ultra low noise receivers at submillimeter wave length is stimulated by the progress in radio astronomy instrumentation. In the present work we studied the possibility to reach quantum limited detection with the superconducting tunnel quasiparticle mixer

* A. Karpov, J. Blondel, B. Lazareff, and K. H. Gundlach are with INSTITUT DE RADIOASTRONOMIE MILLIMETRIQUE, 300, rue de la Piscine, 38406 St Martin d'Hères, France

receiver around 345 GHz and 230 GHz, the frequency of the CO 3-2 and CO 2-1 transitions often used for the observation in radio astronomy.

The quantum noise level ($h\nu/k$) or the number of photons $N=2T_{\text{rec DSB}}/(h\nu/k)$ may be used as a reference for comparison of the different receiver sensitivities at different frequencies. From the literature we know the DSB receiver results around $3h\nu/k$ ($N\approx 6$) at the lower frequencies. At 115 GHz the best published result is 17 K ($3.1 h\nu/k$) DSB receiver noise temperature [1]. Around 150 GHz the best result is 23 K DSB ($3 h\nu/k$) [2].

The aim of this work is to extent equivalent good quality of the receiver operation to higher frequencies.

345 GHz RECEIVER

RECEIVER DESIGN

The heterodyne receiver consist of the Superconducting Tunnel Diode mixer mounted with the first Intermediate Frequency amplifier at the 4 K stage of the liquid helium Infrared Laboratory cryostat, of the ambient temperature second IF amplifier and of the local oscillator. Local oscillator power is injected on the waveguide mixer input port through a cooled waveguide coupler. The mixer operates in all the receiver band without tuning and the only one tunable part of the receiver is the local oscillator.

SIS MIXER DESIGN

The goal of this mixer design was to get the fixed-tuned operation around 345 GHz (280-370 GHz band). It is a single backshort waveguide mixer. In the mixer block the waveguide height is reduced to the quarter of the standard size. In this mixer we use two 0.9 square micron seriesly connected Nb- Al oxide-Nb junctions with $R_0C\approx 6$. Critical current density is about 8 KA/cm². The individual inductive tuning elements are integrated with the junctions. A new version of a non contacting backshort is developed for the reduced waveguide height mixer block. Magnetic field has been applied to the junctions in order to suppress the Josephson current.

The mixer backshort once fixed in the mixer block remains in the optimal positions. For this backshort position the receiver exhibits a low noise operation across ~30% band. Estimation of the SIS junction mach calculated for the optimal backshort position is presented in Fig. 1. Mixer operation is in a good accord with the model prediction. The standard equivalent circuit of the mixer block has been used to optimize the mixer circuit without the scale-model experiments.

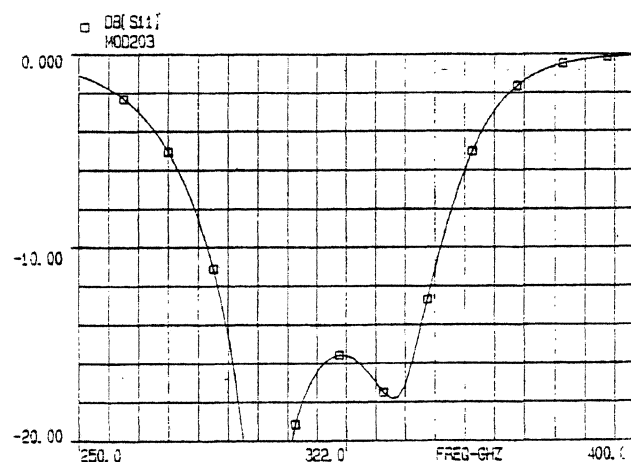


Fig. 1. Estimation of the SIS junction mach for the optimal backshort position in the fixed tuned mixer.

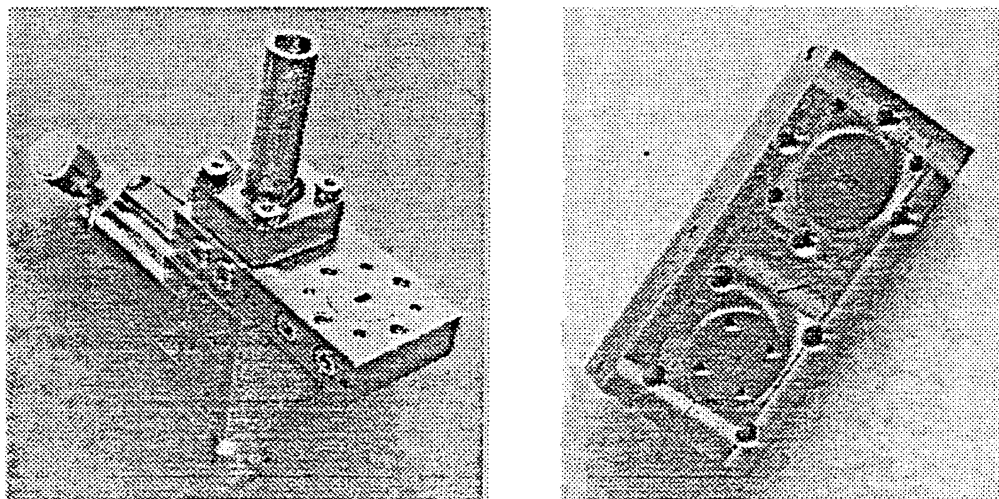


Fig 2. The 280-370 GHz mixer with the corrugated horn and the LO coupler (left) and the waveguide coupler prepared for the local oscillator power injection (right).

Mixer with the corrugated horn and the LO waveguide coupler is presented in Fig 2 (left). The waveguide 17 dB coupler for 260-380 GHz is presented in Fig 2 (right).

Measured mixer DSB noise temperature is 10 K (0.6hv/k level). According to this data mixer sensitivity may be estimated as one photon.

MIXER NOISE MEASUREMENT

In the mixer test we measured the receiver conversion gain G_R , using the calibration by the junction shot noise, and the receiver optics contribution to the receiver noise T_{FE} according to [3],[4]. Measured receiver noise temperature and conversion gain are presented in Fig. 3 as the function of the junction current. In this experiment the bias voltage is fixed and the current is tuned by the local oscillator power

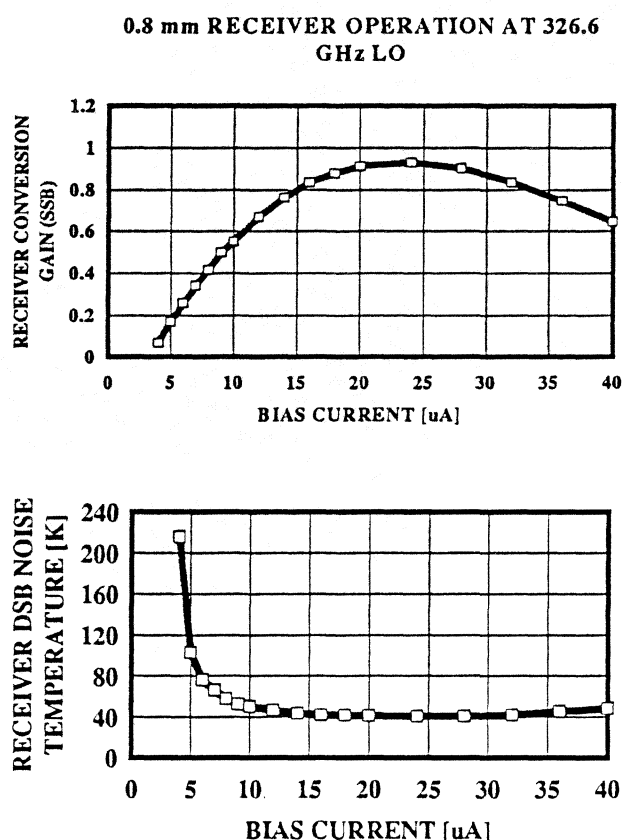


Fig. 3 Laboratory test of the receiver gain and noise(mixer at 4.8 K). Bias voltage is fixed and the current is tuned by the local oscillator power

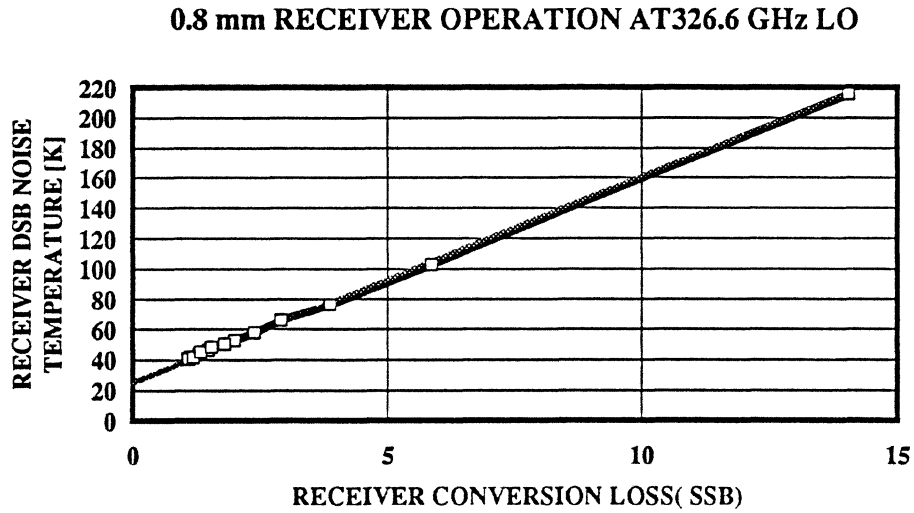


Fig. 4 Receiver noise versus receiver loss for the different local oscillator power levels. Bias voltage is fixed.

Relation between the receiver noise temperature and the receiver loss is nearly linear for all values of the junction current (Fig. 4). Receiver optics contribution to the noise according to this data is about $T_{FE}=27$ K [4]. The minimum receiver noise in this test is $T_R=39$ K (mixer at 4.8 K), receiver conversion gain is about $G=1$ and the IF chain noise is $T_{IF}=4$ K. Mixer noise is determined as usually:

$$T_M = T_R - T_{FE} - T_{IF}/2G$$

and $T_M=10$ K.

RECEIVER TEST

In the receiver test the equivalent noise temperature has been determined in the standard ambient load and nitrogen load experiments. At the telescope (Pico Veleta 2850 m) the cold load temperature drops with the nitrogen temperature, to 75 K. The best receiver sensitivity has been achieved at the telescope (2850 m altitude) where the mixer physical temperature was 4.2 K about 0.5 K lower than in laboratory at the sea level. Minimum receiver DSB noise

temperatures are presented in the Fig 5. In the Fig 6 the receiver sensitivity is given in the photons.

For the noise measurements, the output receiver power is integrated over the whole 500 MHz wide IF band. The best measured value of the Y factor in this experiment was about 3. It corresponds to the receiver DSB noise temperature 30 K (1.9hv/k level at 325 GHz). Expressing this noise (or sensitivity) in photon number we get the four photons level N=4.

The cold and hot load temperatures have to be corrected for the first order term coming from the Planck relation

$$\Delta T_{h,c} \approx -\frac{1}{2} \frac{h\nu}{k}.$$

It gives at 330 GHz correction in the receiver noise: $\Delta T_{R_n} = -\Delta T_{h,c} = +8K$

The reflections on the surface of the cold load give the opposite effect:

if Y=3 and reflection is of about -17 dB $\Delta T_c \approx +6K$ and $\Delta T_{R_c} \approx -9K$

The receiver noise corrections coming from the last two cold and ambient load temperature corrections seems to be nearly in balance in the conditions of our receiver test.

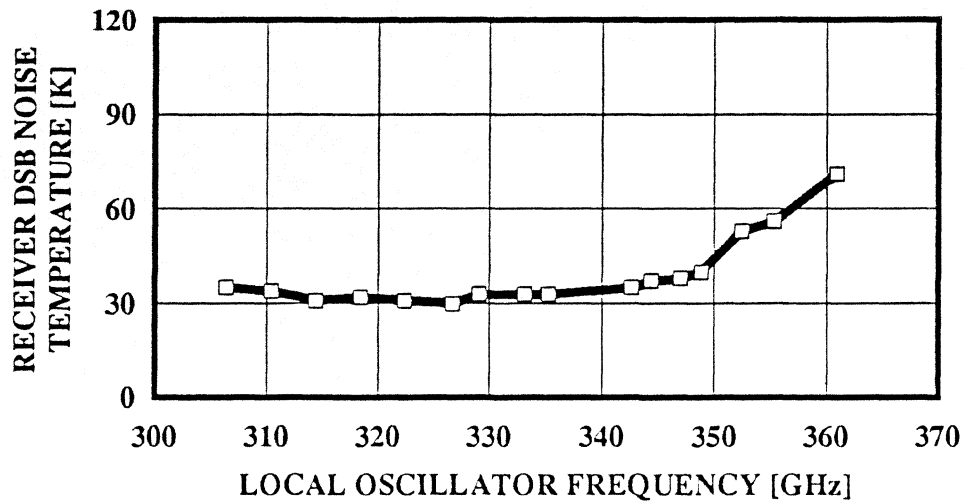


Fig 5. Fixed tuned receiver DSB noise temperature

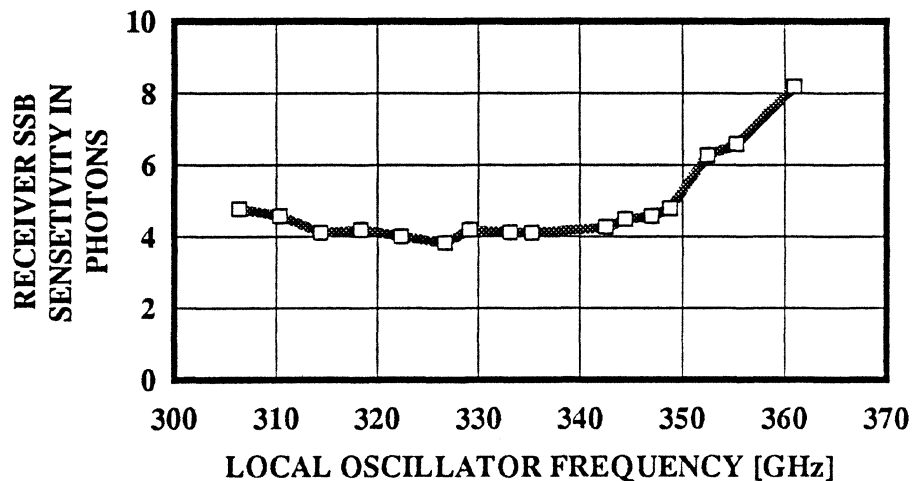


Fig 6. Fixed tuned receiver sensitivity in photons.

An example of the receiver DSB noise behavior in the intermediate frequency band 1250-1750 MHz is given in the Fig 7 for the 325 GHz LO. This curve is measured at the radio telescope with an autocorrelator. In the curve we can see a subdivision of the band to the regions with a small difference in noise level, specific imperfection in the autocorrelator measurements (so called "platforming"). In this measurement the middle DSB noise temperature is about 32 K. The receiver response in the 500 MHz IF band is rather constant (variation of about ± 1 K).

0.8 mm RECEIVER OPERATION ON THE 30 M RADIOTELESCOPE

Receiver has been used for the observation at IRAM 30 m radio telescope at Pico Veleta in the mountains of Sierra Nevada (Spain) in February 1994. The 30 m telescope is equipped with the multiplexing quasi-optical system for the parallel observation in 3 frequency bands. It was possible to operate in parallel in 0.8 mm, 1.3 mm and in 3 mm bands. The system noise temperature out of the atmosphere in 0.8 mm band is strongly dependent on the frequency, the weather and the telescope orientation. The best SSB system noise temperature during the observation period was 500 K at 330 GHz.

In Fig 8 is presented an example of the $^{13}\text{CO}(3-2)$ transition spectrum of the IC342 measured with the new receiver at the telescope (by courtesy of Andreas Schulz et al).

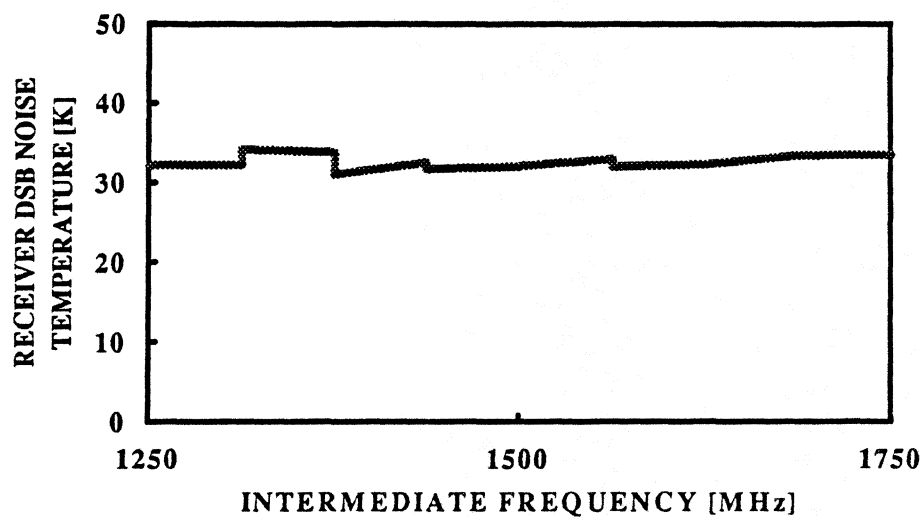


Fig 7. Receiver DSB noise temperature in the 500 MHz intermediate frequency band measured with an autocorrelator at the 30 m IRAM radiotelescope.

IC342 13CO(3-2) IRAM-30M 0: 6-FEB-1994
 Tau: 0.2566 Tsys: 663.0 Time: 12.00
 El: 40.85 F0: 330587.957

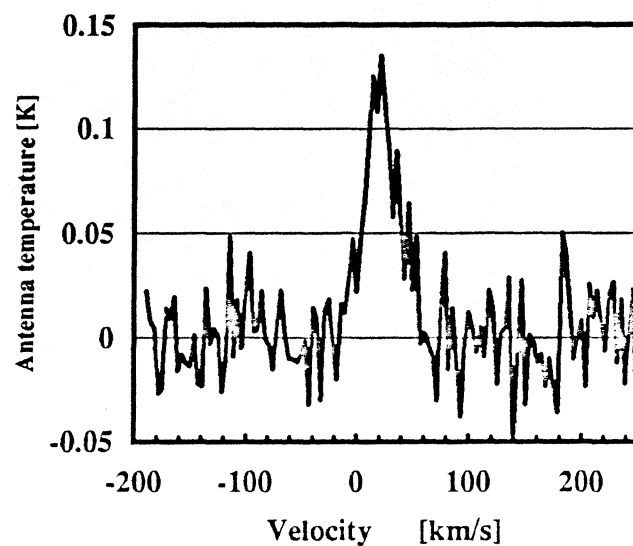


Fig 8. The 13CO(3-2) transition spectrum of the IC342 measured with the new receiver at the telescope (by courtesy of Andreas Schulz et al)

230 GHz RECEIVER

SIS MIXER AND RECEIVER DESIGN

The 1.3 mm mixer was tested in laboratory in the receiver similar to the 0.8 mm receiver. It is a receiver with the cooled optics, with the local oscillator injection through the cooled waveguide coupler, and with the 1.2-1.8 GHz IF 5 K amplifier.

The goal of this mixer design was to get the low noise operation in 205-250 GHz band. It is a single backshort waveguide mixer. In the mixer block the waveguide height is reduced to the quarter of the standard size. In this mixer we use two 2 square micron seriesly connected Nb-Al oxide-Nb junctions with $R\omega C \approx 6$. Critical current density is about 3.5 KA/cm². The individual inductive tuning elements are integrated with the junctions.

RECEIVER AND MIXER PERFORMANCE

1.3 mm receiver noise temperature is presented in the Fig. 9. The minimum receiver DSB noise temperature is 32 K at 230 GHz.

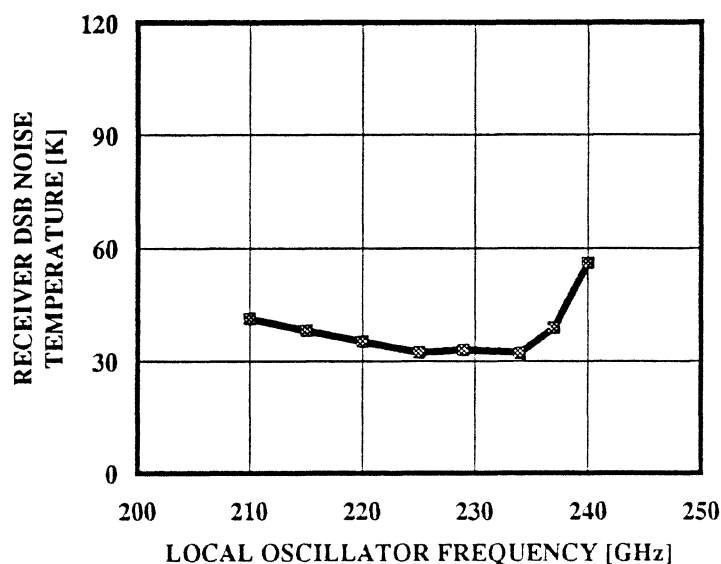


Fig. 9. Receiver DSB noise temperature in the 1.3 mm band. Cooled optics receiver with the IF amplifier noise temperature 5 K.

Mixer noise temperature was measured with the IF amplifier noise temperature 10 K. In this test at 230 GHz receiver noise is 36 K and IF chain contribution to receiver noise is 5 K. Receiver optics contribution at 230 GHz is found to be close to 27 K according [3,4] (Fig. 10). Mixer noise temperature is about 5 K

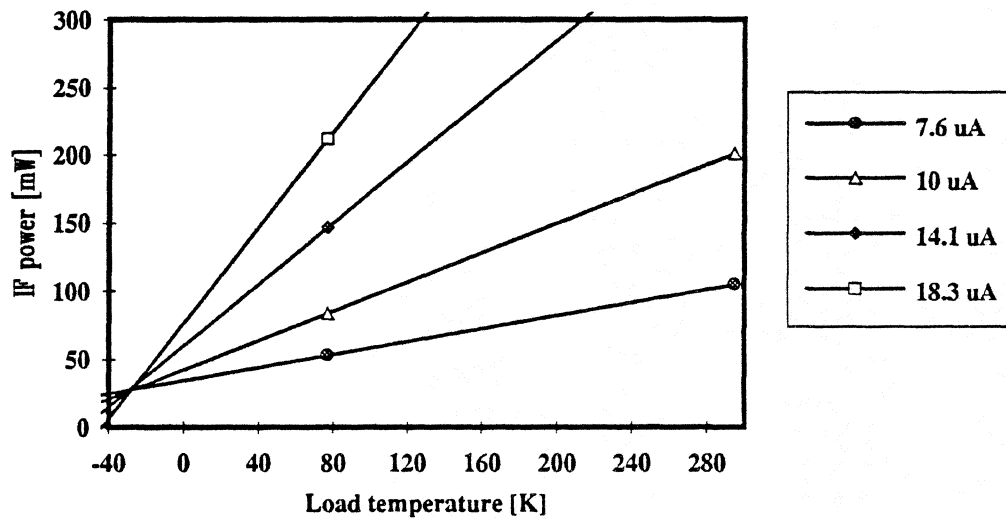


Fig 10. Receiver IF output power for the different junction currents and the different noise temperatures of the load before the receiver. According to [3,4] the intersection point gives the contribution of the optics to the receiver noise.

CONCLUSION

In this work the possibility to achieve the four photon receiver sensitivity at submillimeter wavelength has been shown. The minimum receiver DSB noise temperature is 30 K at 330 GHz

The mixers sensitivity about one photon was demonstrated around 230 GHz and 345 GHz.

The new version of the fixed tuned superconducting tunneling diode mixer covering the relative band of 30% around 345 GHz seems to be useful for the application in ground-based and airborne radioastronomy receivers.

REFERENCES

1. H. Ogawa, A. Mizuno, H. Hoko, H. Ishikawa, Y. Fukui, A 110 GHz SIS receiver for radio astronomy, *Int. J. IR and MM Waves*, vol. 11, pp. 717-726, June 1990.
2. A. R. Kerr, S. K. Pan, A. W. Lichtenberger, F. L. Lloyd, N. Horner, A new SIS mixer for the 2-mm band, in Proceedings of the *Fourth International Symposium on Space Terahertz Technology*, 1993, Los Angeles, US, pp 1-10
3. R. Blundell, R. E. Miller, and K. H. Gundlach, "Understanding noise in SIS receivers", *Int. J. IR and MM wavwes*, Vol13, No 1, pp 3-26, 1992.
4. Q. Ke, and M. Feldman, "A technique for accurate noise temperature measurements for the superconducting quasiparticle receiver", in Proceedings of the *Fourth International Symposium on Space Terahertz Technology*, 1993, Los Angeles, US, pp 33-40.

A 100 GHz BAND PLANAR TYPE SIS MIXER

M. Hieda*, K. Kojima*, T. Takami*,
T. Kashiwa*, A. Iida*, T. Imatani*, J. Inatani**

* Mitsubishi Electric Corporation
5-1-1 Ofuna, Kamakura, Kanagawa 247, JAPAN

** Nobeyama Radio Observatory, National Astronomical Observatory
Nobeyama, Saku-gun, Nagano 384-13, JAPAN

ABSTRACT

A planar type SIS (Superconductor-Insulator-Superconductor) mixer at 100 GHz band has been developed. From the viewpoint of both mechanical stability and reproductivity, a planar type mixer has advantages compared with waveguide type mixers. Experimental results show a minimum receiver noise temperature of 90 K (DSB) in the 100 GHz band.

INTRODUCTION

In recent years, the spectroscopy of the atmosphere from satellites in millimeter-wave and sub-millimeter-wave bands has been proposed. In the system for this spectroscopy, ultra low noise characteristics are required for the receiver. In order to obtain low noise characteristics, HEMT amplifiers are usually used up to 100 GHz, and SIS mixers are usually used above 100 GHz. Several SIS mixers were developed [1]-[4], and most of them were of waveguide type. For waveguide SIS mixer, great efforts are also required to sustain against mechanical and thermal shocks to achieve space qualifications. This paper describes a planar type SIS mixer consisting of microwave integrated

circuit elements. This mixer has advantages compared with waveguide type mixers as follows: (1) mechanical stability, (2) manufacturing precision, and (3) reproductivity. Experimental results of the fabricated SIS mixer at 100 GHz are presented.

2. CIRCUITS CONFIGURATION AND FABRICATION

Fig.1 and Fig.2 show the block diagram and the configuration of the mixer, respectively. RF and LO signals are supplied to the mixer through the space in order to isolate heat conduction from the outer circuits. These two signals are received by separate horn antennas, and then supplied to the mixer chip through waveguide-microstrip transitions individually. In order to supply DC bias to the SIS junction, a bias tee is connected to the IF output port of the mixer. The mixer chip consists of a 100 μ m thick sapphire substrate (R-cuts), and the metal of both strip and ground conductors is Nb. The other chips consist of alumina substrates, and the metal is Au. Both chips are fixed on Cu-W carrier plates. The mixer is mounted on a 4K stage, and an IF amplifier connected to the IF output port of the mixer is cooled down at 12K.

Fig.3 shows the configuration of the mixer chip. The chip size is 2 mm \times 3 mm. This chip contains (1) a directional coupler which combines RF and LO signals, (2) matching circuits [5], (3) 8 SIS (Nb/Al-AlO_x/Nb) junctions with normal resistance of 100 ohm, and (4) a band rejection filter (BRF) which rejects the RF and LO signals, and transmits the IF signal. The size of the unit

SIS junction is $1.5 \mu\text{m} \times 1.5 \mu\text{m}$. Fig.4 shows SEM photograph of the SIS junctions.

3. EXPERIMENTAL RESULTS

Fig.5 shows the unpumped and LO pumped I-V characteristics of the 8 SIS junctions. At the potential of the 2nd and 3rd photon assisted steps, hysteresis caused by negative resistance is observed.

The total receiver noise temperature is determined by Y-factor method using hot (295 K) and cold (77 K) load. The reference plane for these measurements is the input of the horn antenna. Fig.6 shows the measured receiver noise temperature in DSB. Bias voltage is fixed at the potential of the 2nd photon assisted step. LO frequency is 100 GHz. Minimum noise temperature of 90 K is obtained at 6.3 GHz IF frequency.

4. CONCLUSION

A planar type SIS mixer at 100 GHz band has been developed. The mixer has advantages compared with waveguide type mixers. Experimental results show the minimum receiver noise temperature of 90 K (DSB) at 100 GHz band. By combining two mixers of this type, single-side-band SIS mixer will be obtained in the near future.

REFERENCE

- [1] R. Blundell, M. Carter and K. H. Gundelach, "A LOW NOISE SIS RECEIVER COVERING

THE FREQUENCY RANGE 215-250GHz", International Journal of Infrared and Millimeter Waves, Vol.9, No.4, 1988

[2] J. Ibruegger, M. Carter and R. Blundell, "A LOW NOISE BROADBAND 125-175 GHz SIS RECEIVER FOR RADIOASTRONOMY OBSERVATIONS", International Journal of Infrared and Millimeter Waves, Vol.8, No.6, 1987

[3] P. Febvre, W. R. McGrath, P. Batelaan, H. G. LeDuc, B. Bumble, M. A. Frerking, J. Hernichel, "A 547 GHz SIS RECEIVER EMPLOYING A SUBMICRON Nb JUNCTION WITH AN INTEGRATED MATCHING CIRCUIT", IEEE MTT-S International Microwave Symposium Digest, Vol. 2, pp771-774, June 1993

[4] R. Kawabe, J. Inatani, T. Kasuga, M. Ishiguro, M. Yamamoto, K. Yamaji and K. Watasawa, "A Dual-Frequency 40/100 GHz SIS Receiver for the Nobeyama Millimeter-Wave Array", The 3rd Asia-Pacific Microwave Conference Proceedings, pp217-220, 1990

[5] S. C. Shi, J. Inatani, T. Noguchi, and K. Sunada, "ANALYTICAL PREDICTION FOR THE OPTIMUM OPERATING CONDITIONS OF SIS MIXERS", submitted to International Journal of Infrared and Millimeter Waves.

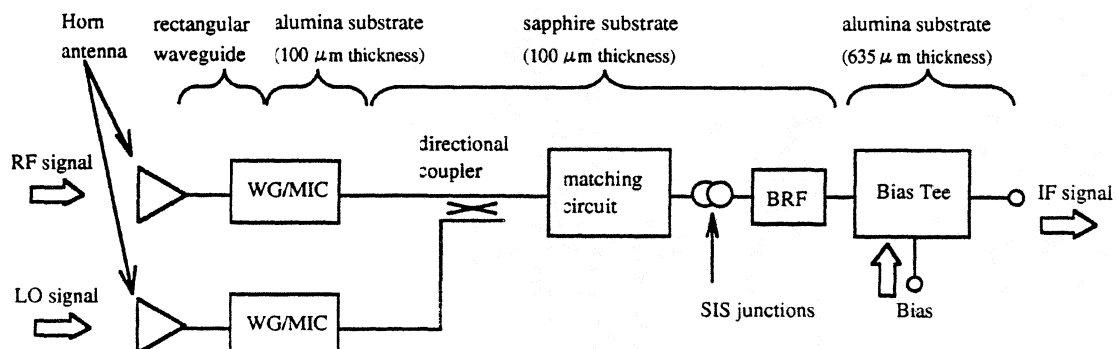


Fig.1 Block diagram of the mixer.

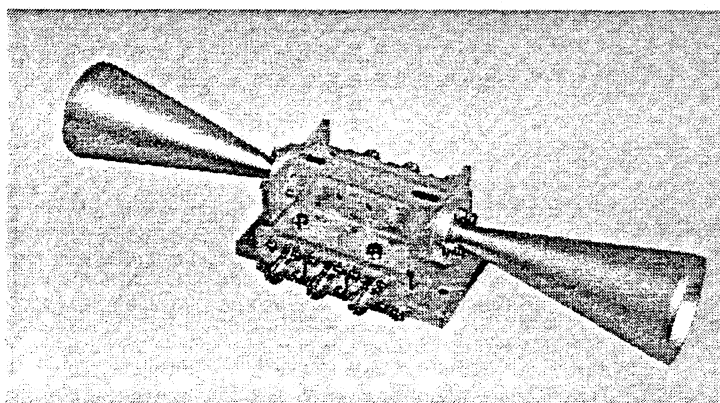


Fig.2 Configuration of the mixer.

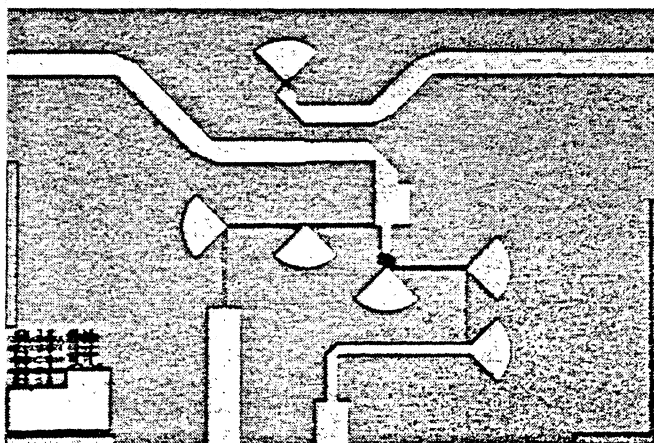


Fig.3 Configuration of the mixer chip.

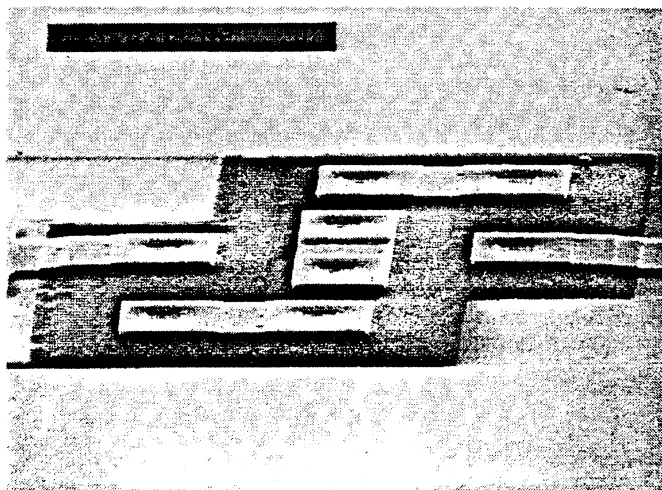


Fig.4 SEM photograph of the SIS junctions.

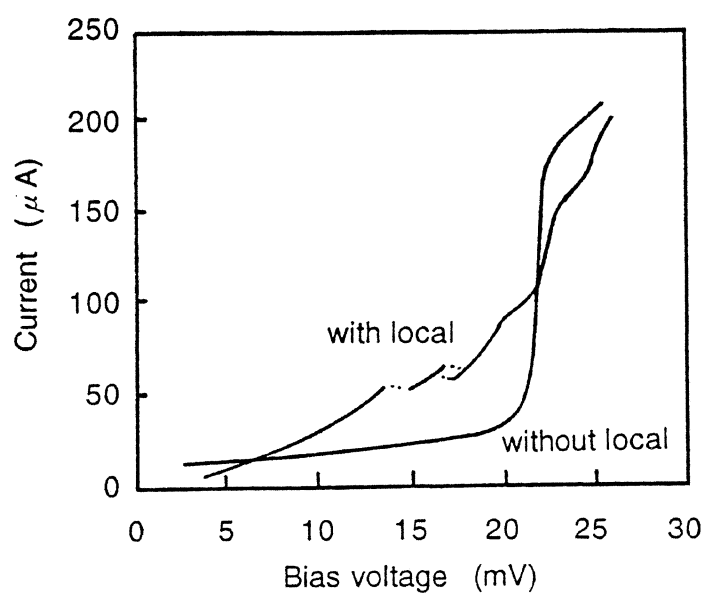


Fig.5 I-V characteristics of the 8 SIS junctions.

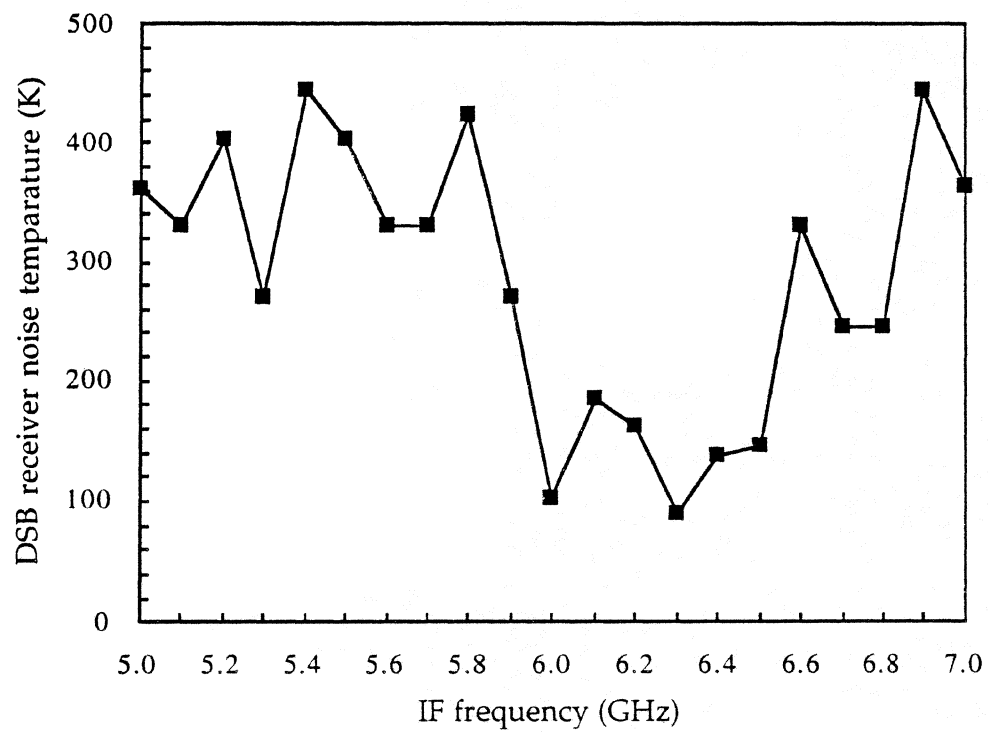


Fig.6 Noise performance of the receiver.

FANATIC: AN SIS RADIOMETER FOR RADIO ASTRONOMY IN THE
660–690 GHz BAND

A.I. Harris¹, K.-F. Schuster^{1,2}, K.-H. Gundlach², and B. Plathner²

¹Max Planck Institute for extraterrestrial Physics,
Postfach 1603, D-85740 Garching, Germany
harris@fcrao1.phast.umass.edu

²IRAM, 300 rue de la Piscine, Domaine Universitaire de Grenoble,
F-38406 St. Martin d'Heres Cedex, France
schuster@iram.grenet.fr

ABSTRACT

FANATIC is a compact radiometer optimized for radio astronomy from about 660 to 690 GHz ($\lambda\lambda$ 455 – 435 μm). We observed a large number of molecular and atomic spectral lines from galactic and extragalactic sources during *FANATIC*'s first run on the James Clerk Maxwell Telescope in early March 1994. Double sideband receiver temperatures during observations were about 800 K ($25\ h\nu/k$). The heart of the receiver is a two-junction Nb/AlO_x/Nb SIS array fed by a sandwiched V-Antenna. The junction array and antenna are fabricated together at IRAM's Grenoble SIS laboratory. Each junction has a normal resistance of $R_n \sim 10\ \Omega$, an area of $\sim 2\ \mu\text{m}^2$, an individual radial stub circuit to resonate the capacitance, and a $\lambda/4$ transformer to match to the antenna. The solid-state local oscillator is a mm-wave Gunn oscillator followed by a doubler and tripler. The LO diplexer is a Martin-Puplett interferometer, which insures that there is always abundant LO power for operation and speedy tuning. The receiver and telescope coupling optics, LO, dewar, and calibration system fit on an 0.6×0.8 m optical breadboard.

1 INTRODUCTION

Radio astronomy, with its constraints of limited observing time and very weak signals, has benefitted greatly from the decreases in noise temperatures provided by SIS mixers. SIS

(Superconductor-Insulator-Superconductor) tunnel junction mixers have replaced Schottky diode mixers for most radio astronomical applications at millimeter wavelengths, and they are now spreading rapidly on to telescopes at the high end of the submillimeter band [1–5].

We have constructed an SIS mixer receiver, named *FANATIC*, that has now replaced our Schottky diode mixer facility receiver at the James Clerk Maxwell Telescope in Hawaii [6]. *FANATIC* is a compact radiometer optimized for radio astronomy from about 660 to 690 GHz ($\lambda \lambda$ 455 – 435 μm). This frequency range lies within the second-highest atmospheric window at submillimeter wavelengths. This window includes many astrophysically important transitions, including lines from isotopomers of the CO molecule (C^{18}O , ^{13}CO , and CO $J = 6-5$) as well as the more density-sensitive CS $J = 14-13$ and H^{13}CN $J = 8-7$ lines.

2 RADIOMETER LAYOUT

2.1 Mixer and Cryostat

Design considerations for the mixer, its tuning structure, and the fabrication have been recently been described [1,7] so we give only a synopsis here. The mixer is a two-junction SIS tunnel junction array fed by a sandwiched V-Antenna. The junction array and antenna are fabricated together at IRAM's Grenoble SIS laboratory on a 0.4 mm thick piece of fused quartz that is sandwiched between 3 mm thick sub- and superstrates. Eckart et al. [8] found that air gaps within the sandwich bigger than $\lambda/300$ (1.4 μm at 690 GHz) generate surface waves that degrade the antenna performance, so all of the quartz pieces are optically flat and are clamped together without films of glues or oils. Beam profiles show no trace of fine structure that would indicate surface waves. While not the optimum antenna for a current new development, the V-antenna is in fact fairly reasonable (comparable to a smooth-wall conical horn), and it is certainly suitable for a developmental system.

Each of the Nb/ AlO_x /Nb junctions in the array has a normal resistance of $R_n \sim 10 \Omega$, areas of $\sim 2 \mu\text{m}^2$, a short length of transmission line terminated in a radial stub to resonate the capacitance, and a $\lambda/4$ transformer to match to the antenna (Fig. 1). The transformation is made for the optimum power match, as is appropriate at these frequencies [1,7,9].

One of the main concerns in the design was finding structures and parameters were as insensitive as possible to precise relative alignment, taking $1\text{ }\mu\text{m}$ as a reasonable alignment tolerance.

The mixer sandwich is clamped by a solid copper holder attached to a copper block soldered to the vacuum side of the cold plate in an Infrared Laboratories HD-10 dewar. The IF matching network and a superconducting magnet coil also attach to the copper holder. A high permeability Cryoperm structure with a loop in front of the V's mouth and a post behind the mixer concentrates the field along the axis of the "V."

The beam from the V-antenna is fast enough that some reimaging is necessary inside the cryostat to keep the mechanical sizes of optical elements and heat loads at a reasonable level. A single off-axis ellipse reimages the 0.45 mm beamwaist from the V-antenna to a 3.5 mm waist at the cryostat wall (Fig. 2). This ellipse's f/D ratio is small, so keeping the angle of incidence as small as mechanically practical (30°) substantially reduces distortion and cross-polarization losses [10]. The radiation load on the quartz is kept low by reflecting the submillimeter signal from a wire grid and through a hole in a copper shield that surrounds the block. The grid also transmits cross-polarized power from the mixer and elliptical mirror to terminate it inside the cryostat at low temperature. Sensitivity to only one polarization is important because only one polarization is transmitted by the external Martin-Puplett interferometer that combines the LO and signal beams. Drives from outside the cryostat can tilt the grid about two axes to peak up alignment of the internal cryostat optics. A crystalline quartz filter on the liquid nitrogen temperature radiation shield reduces the room temperature heat load on the helium bath. The room-temperature cryostat vacuum window is also crystalline quartz, in this case anti-reflection (AR) coated with TPX $\lambda/4$ foils held in place with a thin layer of silicone glue. The AR coatings have very low loss: the receiver noise temperature was not measurably changed by adding or removing an extra external AR-coated window, and the noise temperature definitely dropped at frequencies away from the uncoated window's resonance. Leak testing did indicate that helium could diffuse into the cryostat from the edge of the vacuum-side TPX layer, but this did not cause any noticeable problems.

Radio-frequency interference pickup is a potential hazard with an open structure mixer, which has poorly shielded input terminals at the front of the entire IF system. The optical entrance into the dewar accordingly includes of a long aluminium tube that is fixed to the outer wall. This tube is sized to yield more than 100 dB attenuation at the high end of the IF band. All electrical leads pass through standard bulkhead RF filters that are soldered to brass houses below each of the hermetic seals on the dewar top plate. The mixer DC bias preamplifier is in a small aluminium box permanently mounted on the dewar, and the control signals to and from the rest of the bias electronics are at volt levels. The dewar case is a very good electrostatic shield, and magnetic pickup is minimized by using a twisted pair of twisted-pair wires for the conventional four-point bias circuit. These precautions solve all pickup problems except occasional flux trapping in one or the other of the junctions when motors switch on near the receiver. Warming the junctions for about 15 seconds with a small heater inside the mixer block solves this problem, however.

The cryogen hold time is adequate for our needs: 16 hours with the first IF amplifier switched on and 36 hours with it switched off.

2.2 Optical and Mechanical

The optical train matches the 3.5 mm beamwaist at the cryostat wall to the 11.8 mm waist necessary to illuminate the telescope properly, provides the diplexer for the LO and signal, and matches the LO horn's 0.77 mm waist to cryostat's beamwaist. Insensitivity to exact beamwaist sizes — a fundamental Gaussian beam analysis is certainly only approximate for the V-antenna — and the small LO beamwaist are the main drivers for magnification in stages. The beam from the dewar is refocussed by a second off-axis elliptical mirror to make a 6 mm beamwaist near the mean center of the diplexer. A third off-axis mirror reimages this intermediate beamwaist to make the 11.8 mm beamwaist required to produce a ~ 13 dB telescope edge taper. The second and third mirrors are separated by approximately the sum of their focal lengths (nearly a Gaussian telescope) as this reduces the sensitivity of the output against small changes in beamwaist sizes, locations, and mirror positions. The 6 mm beamwaist in the diplexer is just big enough to keep the diplexer loss low, but is still reasonable in terms of matching the LO beam. Lowest possible loss in the LO arm

was not a design driver, and a moderate amount of mismatch due to frequency dependence or errors in the large magnification ratio between the horn and intermediate beamwaist is acceptable. The third mirror is pinned in place for accurate relocation. It can be removed easily to let the beam go straight from the diplexer through an ambient chopper wheel and into a liquid nitrogen load for tuning. When the third mirror is in place the beam from the diplexer reflects vertically to the fourth and final mirror, a flat at the height of the telescope's elevation bearing. This flat bends the beam horizontally through a hole in the bearing and has fine adjustments for tilt and height to precisely coalign the receiver's beam with the telescope's optical axis.

The Martin–Puplett interferometer diplexer that combines the LO and sky signals considerably simplifies receiver operation. Tuning is fast because the LO chain need not be tuned to optimum points with several interacting LO adjustments, but just close enough to produce sufficient power. With the high efficiency optics, tuning is limited by the Gunn diode's tuning limits. The main penalty is somewhat decreased optical transmission away from band center, with a power coupling efficiency of

$$\eta = \frac{1}{2} \left[1 + \cos \left(\frac{\Delta\nu}{\nu_{IF}} \pi \right) \right] \quad (1)$$

when the diplexer is set to the minimum distance that couples both sidebands and the LO ($\lambda/4$ one-way path difference). For our $\nu_{IF} = 1.5$ GHz IF center frequency, the maximum loss, at $\Delta\nu = \pm 500$ MHz from band center, is a factor of 1.33 (1.25 dB). In a practical sense we compensate for much of this loss by being able to work more efficiently when the weather is good at the telescope.

Although the V-antenna produces a mostly Gaussian beam, it is only approximately so, and some fraction of the power is in modes that might not couple properly to the calibration loads or telescope. We need to constrain and characterize the beam distributions at the calibration loads, telescope focus, and on the sky to insure that we properly calibrate our astronomical data. One of useful effects of the optics in this respect is that it serves as a kind of spatial filter to clean up the beam from the receiver, diffracting out higher modes that would not couple to the telescope before they reach the calibration system. Counting this spatial filtering effect, we measured the optical train's transmission efficiency by placing a 50% transmission beamsplitter directly in front of the dewar and measuring the total power

with a large cold load; and then by moving the same beamsplitter in front of the calibration load, readjusting the LO attenuator to give the same operating point, and measuring the new power level from the cold load. This method gave a coupling efficiency of 0.8, which includes mode mismatch, power lost to scattering from wide-angle sidelobes, and all other losses.

By the time the beam leaves the receiver, the power is consequently in a well defined Gaussian beam with some power still in a larger scale beam. We decomposed the beam power distribution into a few Gaussian components by measuring the peak power change from a family of liquid-nitrogen temperature disks with known diameters. The power coupling efficiency η of a Gaussian beam of power FWHM θ_b centered on a uniform temperature disk source of diameter D is

$$\eta = 1 - e^{-\ln 2 (D/\theta_b)^2}. \quad (2)$$

At the telescope it is unusual that a range of planets is available, so it is useful instead to vary the coupling by changing the center-to-center distance between the beam and a planet. When the beam and disk are not concentric the coupling efficiency is reduced by a weighting factor $w(s)$, normalized so $w(0) = 1$:

$$w(s) = \frac{2\alpha e^{-\alpha s^2} \int_0^R e^{-\alpha r^2} I_0(2\alpha s r) r dr}{1 - e^{-\alpha R^2}}, \quad (3)$$

where $\alpha = 4 \ln 2 / \theta_b^2$, R is the disk radius, and I_0 is a zero-order modified Bessel function of the first kind.

In the general case of a beam with i components of FWHM θ_i and peak power amplitude a_i (the integrated power in a given beam is $a_i \theta_i^2 / \sum_i a_i \theta_i^2$) the equation for coupling is:

$$\eta = \frac{\sum_i a_i \theta_i^2 \eta_i w_i}{\sum_i a_i \theta_i^2}. \quad (4)$$

Fitting the measured data with Eq. 4 produces good estimates for the beam FWHMs θ_b , and those can in turn be used to derive the beamwaists from

$$w_o^2 = \frac{1}{2} \left[w^2 \pm \sqrt{w^4 - \left(\frac{2\lambda z}{\pi} \right)^2} \right] \quad (5)$$

where

$$w = \frac{\theta_b}{\sqrt{2 \ln 2}}. \quad (6)$$

As a final step, we estimate the edge taper T_e (in dB) for a telescope with f -ratio f/D from the approximate expression

$$T_e = \left(4.63 w_o \frac{D}{f} \frac{1}{\lambda} \right)^2. \quad (7)$$

We centered disks with diameters up to 150 mm in the beam at distance $z = 3400$ mm in the laboratory to find that 70% of the power has the distribution that produces a 10.3 dB taper, with the remaining 30% in a very wide angle beam. Figure 3 is a plot of the data and theoretical curves. It is worth noting that it would be hard to find the large scale beam with a small load because η is small in this case; large loads are needed to find the large-scale beams. This is of course a scalar measurement, but the agreement with the design beamwaist size after passage through the optical train is a good sign that the phase fronts are well behaved.

The cryostat, optical, and LO subassemblies are attached to a 0.6 by 0.8 meter commercial optical breadboard table mounted at the right Naysmith focus port of the JCMT. A computer-controlled calibration system with a hot load and ambient chopper for calibrating receiver gain and atmospheric transmission is mounted in the beam just above the receiver. A half-height rack nearby contains bias and control electronics and an IF receiver for tuning.

2.3 Local Oscillator, Intermediate Frequency, and Backend Systems

The local oscillator itself is from Radiometer Physics in Meckenheim, and consists of a 115 GHz Gunn diode oscillator that drives a doubler and then tripler. The oscillator tunes from 659 to 695 GHz with tens of microwatts of power. The phase lock is a STS-800 module connected with a Pacific Millimeter Products model WM 115 GHz harmonic mixer and a HP-8671B frequency synthesizer that provides both the microwave signal for the harmonic mixer and a 100 MHz reference signal for the phase lock loop. A rotatable grid between the LO and diplexer is a variable attenuator for the mixer power level. Typical attenuation levels are around 10 dB. A more elegant solution would have been to vary the bias voltage on the tripler to change the LO chain's output power level electrically.

The IF signal is brought off the mixer contact pads with an unbalanced circuit: one side of the "V" is connected to the mixer block and the other is connected to a $\lambda/4$ IF

transformer. This is a historical holdover, and a balanced IF connection would certainly be better here [11]. Although the dimension of the antenna is small compared with an IF wavelength, the unbalanced connection makes the impedance match somewhat indeterminate by allowing currents to flow to the outside of the mixer block. This is analogous to attempting to make a short circuit by connecting the center conductor of a coax cable to the shield with a wire. No matter how short the wire, the open end of the cable allows currents to be excited on the electrically long outside of the shield. This allows changes far from the end to influence the current distribution, preventing the circuit from being an unambiguous good short.

A short length of coaxial cable brings the signal to a Berkshire Technology 40 dB HEMT amplifier on the helium cold plate. Berkshire provided an integral bias tee for the mixer in the amplifier. We do not use an isolator because it would limit the bandwidth, so the IF matching network in the mixer is the only component that sets the source impedance for the HEMT amplifier. The next amplifier is a low noise Miteq room temperature module with 37 dB gain on the outside of the dewar. A subsequent mix to 4.6 GHz permits us to use a 4–8 GHz IF receiver for tuning, minimizes RFI from other signals at the observatory, and separates the overall system gain in frequency. The signal is sent down a 50-foot long coaxial cable to another IF converter, which converts the band center to 2.2 GHz for the backend spectrometer. All IF components are on thick aluminium plates that are weakly thermally coupled to the external environment for temperature stabilization. The spectrometer is a University of Cologne 1.2 GHz-wide acousto-optical spectrometer with 1.6 MHz noise bandwidth per channel. We enclosed it in a case whose temperature is stabilized by circulated heated water for operation in the observatory dome.

3 PERFORMANCE AT THE TELESCOPE

3.1 Internal Measurements

The lower pair of curves on Figure 4 are plots of the mixer junction DC current vs. DC bias voltage with and without the optimum level of local oscillator power. The Josephson currents have been suppressed with a magnetic field, and the lack of structure shows clearly

that the photon energies are slightly larger than the gap energy. The upper pair of curves are the IF power vs. DC bias voltage for ambient and liquid nitrogen temperature black body loads. These curves are smooth and free of fine scale peaks that might indicate magnetic field effects.

The m-shaped curve at the top of Fig. 4 is the IF signal-to-noise ratio: the AC-detected signal divided by the averaged DC signal by an analog ratioing circuit in an Ithaco 391A lock-in amplifier. This curve is reasonably flat away from the Shapiro steps, showing that the exact DC bias voltage point is not very critical. The analog ratioing, the insensitivity to exact bias, and an abundance of LO power allows us to rapidly tune the receiver to optimum.

The noise temperature across the tuning band is shown in Figure 5. The curve is smooth and reproducible; these particular data are typical results from careful but not exceptional tunings made on the last night at the telescope. The noise temperature is about 800 K (DSB) at band center ($25 h\nu/k$), rolling smoothly up to both higher and lower frequencies but remaining below 1000 K over almost the entire 660–690 GHz band.

We made all of these measurements with a liquid nitrogen cold load of diameter 70 mm located 500 mm beyond the diplexer's nominally 6 mm beamwaist. We measured the ambient temperature (5° C) and corrected the liquid nitrogen temperature to 73 K because of the high altitude (the pressure at the telescope is about 0.6 that at sea level). The noise temperature is averaged over the central 500 MHz of the passband, band-limited and measured with a carefully linearized detector system in the 4–8 GHz tuning receiver.

Figure 6 shows the variation of noise temperature across the 1 GHz wide IF band, in this case measured with the acousto-optical spectrometer and the 80° C hot load in the computer-controlled calibration system used during observations. The noise increase at the ends of the superposed astronomical spectrum's baseline (light lines) shows that the effect of the noise rollup near the band edges is acceptable.

Following custom, these receiver temperatures are Rayleigh-Jeans limit temperatures and do not include higher terms. A second order expansion of the Planck equation gives a modified version of the standard Y-factor equation,

$$T_{rec} = \frac{T_H - Y T_C}{Y - 1} + \frac{h\nu}{2k}, \quad (8)$$

where T_H , T_C , and Y have their usual meanings of the physical temperatures of the hot and cold loads and the power detector's voltage ratio $Y = V(T_H)/V(T_C)$ for the two loads. At 690 GHz, $h\nu/2k = 16.6$ K, which is not a large correction.

Although it is difficult to be quantitative at present, the main limit on noise temperature for the present design seems to be some kind of instability noise. The receiver is certainly stable at the gross level, judging from total power strip-chart records and the system Allen variance time of about 30 sec, but this is shorter than the Schottky system's 100 sec and there are occasional steps in total power for no obvious reason. Some low-level instability may come from some interaction between the two not-quite-identical mixers in the array or a lack of simultaneous cancellation of Josephson effects in the two junctions. The IF noise power does depend on the magnetic field strength, but there is a large range of field that has a relatively weak effect on the IF S/N ratio measured with the ratioing circuit. It is also possible that the source impedance presented by the mixer and matching circuit is unfavorable for the first IF amplifier's stability.

Physical temperature effects on noise temperature are weak. Although the gap voltage increased slightly, the sub-gap current decreased, and the corner sharpened somewhat, the 690 GHz noise temperature changed by only 10–15% when the liquid helium bath temperature was reduced from 4.2 K to 1.6 K. The improvement was somewhat larger for the poorer junctions in the sample, but never brought them to the performance of the best junctions.

3.2 Characterizations with Astronomical Measurements

Spectral line observations of astronomical sources are the cleanest test of the overall system. We observed sources we had previously observed with the Schottky system to cross-check the intensity scales, and found agreement within 10%. This agreement in relative calibration shows that the system is either very well behaved or so fiendishly pathological that it imitated normal behavior on our test sources. For one, the agreement showed that "bolometric" effects are completely absent, as one would expect from the smooth IF power vs. DC bias curve. For another, the receiver must be double balanced at at least the 691.5 GHz line frequency. This was theoretically expected from the mixer tuning structure design and

is also suggested experimentally from the smooth tuning curve. Figure 7 shows a more direct measurement, the CO J=6-5 line from Orion observed with the LO both above and below the line. The excellent agreement in intensities (no baseline corrections have been made) with a calibration scheme that assumes equal sideband gains is a nearly positive indication that the receiver is very closely double sideband.

The beam distribution is somewhat better than the Schottky system's, and is still heavily influenced by telescope surface errors. We derived the beam distribution on the sky by observing Jupiter (which is a uniform temperature disk to good approximation) at a number of angular offset to vary its coupling to the beam, and then fitting the data to Eq. 4. Figure 8 is a plot of the measured data with the theoretical curve derived from Eqs. 3 and 4. This shows that 40% of the power in the 8" FWHM "diffraction" beam and the remaining 60% is in a 25" beam produced by mid-scale antenna surface errors.

4 CONCLUSION

There is no better conclusion for a paper about a radio astronomical radiometer than to present astronomical data, and Fig. 9 is just that: a map of the Orion outflow made during part of a night of moderate weather. The dramatically increased sensitivity with *FANATIC* made the March 1994 observing run one of the most astronomically fruitful runs we have had. There are obviously several avenues of improvement possible for *FANATIC*. Chief among these are improving the optical coupling. The V-antenna was certainly a good choice historically, but fabrication techniques at these frequencies are also maturing fast, and retrieving the efficiency and background factors of 0.8 in the optics and 0.7 in the beam distribution would drop the present receiver temperature from 800 K to 350 K. Further improvements in AR coating the cold transmission optics and IF matching would drop the receiver temperature well below $10 h\nu/k$. Now that the noise temperatures are dropping rapidly, and given the possibility of arraying mixers that need only little LO power, high frequency ground-based submillimeter line astronomy will certainly develop rapidly in the next few years.

5 ACKNOWLEDGEMENTS

We thank M. Carter and J. Lamb for their help with the AR coating on the dewar vacuum window, and are very grateful to U. Graf and the University of Cologne mechanical shop for fabricating the large off-axis mirrors. L.J. Tacconi and L. Avery worked very hard in preparations and at the telescope to make the March run a success. The assistance from P. Friberg and the JCMT day crews and staff was, as always, outstanding. This project would not have been possible without the support and encouragement of R. Genzel.

6 REFERENCES

- [1] K.-F. Schuster, A.I. Harris, and K.-H. Gundlach 1993, "An SIS Receiver at 690 GHz," *Internat. J. IR and mm Waves* **15**, 1867
- [2] J. Zmuidzinas, H.G. LeDuc, J.A. Stern, and S.R. Cypher 1994, "Two-junction Tuning Circuits for Submillimeter SIS Mixers," *IEEE Trans. Microwave Theory Tech.* **42**, no. 4
- [3] J.W. Kooi, C.K. Walker, H.G. LeDuc, P.L. Schaffer, T.R. Hunter, D.J. Benford, and T.J. Phillips 1994 "A Low Noise 665 GHz SIS Quasi-Particle Waveguide Receiver," *Internat. J. IR and mm Waves* **15**, 477
- [4] M. Salez, P. Febvre, W.R. McGrath, B. Bumble, and H.G. LeDuc 1994, "An SIS Waveguide Heterodyne Receiver for 660-635 GHz, *Internat. J. IR and mm Waves* **15**, 349
- [5] J. Mees, S. Crewell, H. Nett, G. de Lange, H. van de Stadt, J.J. Kuipers, R.A. Panhuyzen, "An Airborne SIS Receiver for Atmospheric Measurements at 630 to 720 GHz," these *Proceedings*
- [6] A.I. Harris, D.T. Jaffe, J. Stutzki, and R. Genzel 1987, "The UCB/MPE Submillimeter Heterodyne Spectrometer," *Internat. J. IR and mm Waves* **8**, 857
- [7] K.-F. Schuster 1993, "Submillimeterspektroskopie in der Umgebung junger Sterne und Entwicklung eines 690 GHz SIS-Empfängers," Ph.D. Thesis, Ludwig-Maximilians-Universität München

- [8] A. Eckart, A.I. Harris, and R. Wohlleben 1988, "Scaled Model Measurements of the Sandwiched V-Antenna," *Internat. J. IR and mm Waves* **9**, 505
- [9] A.R. Kerr and S.-K. Pan 1990, "Some Recent Developments in the Design of SIS Mixers," *Internat. J. IR and mm Waves* **11**, 1169
- [10] J.A. Murphy 1987, "Distortion of a Simple Gaussian Beam on Reflection from Off-Axis Ellipsoidal Mirrors," *Internat. J. IR and mm Waves* **8**, 1165
- [11] A.I. Harris, K.-F. Schuster, and L.J. Tacconi 1993, "Broadband IF Matching for Quasioptical Mixers," *Internat. J. IR and mm Waves* **14**, 715

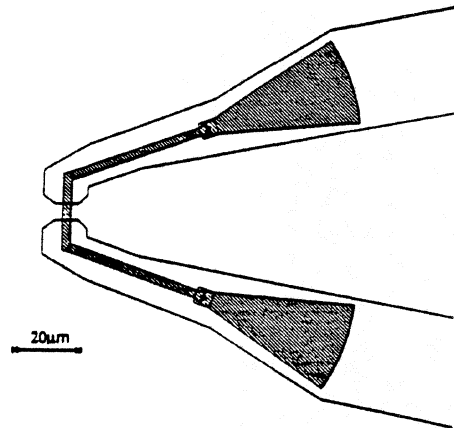


Figure 1: Footpoint of the V-Antenna showing the junctions (small squares), resonators, and transformers. From [1].

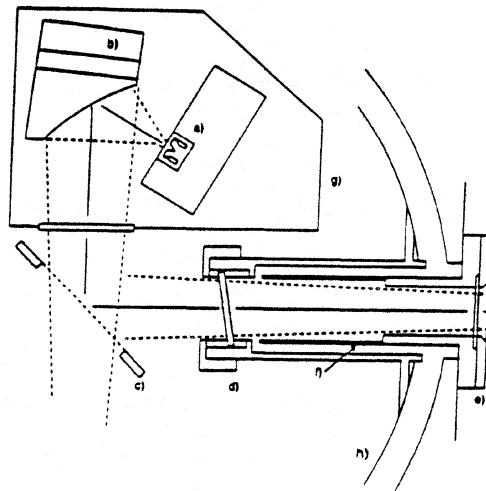


Figure 2: Cryostat internal layout, from [1]. *a*: Mixer; *b*: Off-axis Ellipse; *c*: Wire grid; *d*: Quartz IR filter at 77 K; *e*: AR-coated vacuum window; *f*: RFI suppression tube; *g*: Copper thermal radiation shield housing; *h*: 77 K shield.

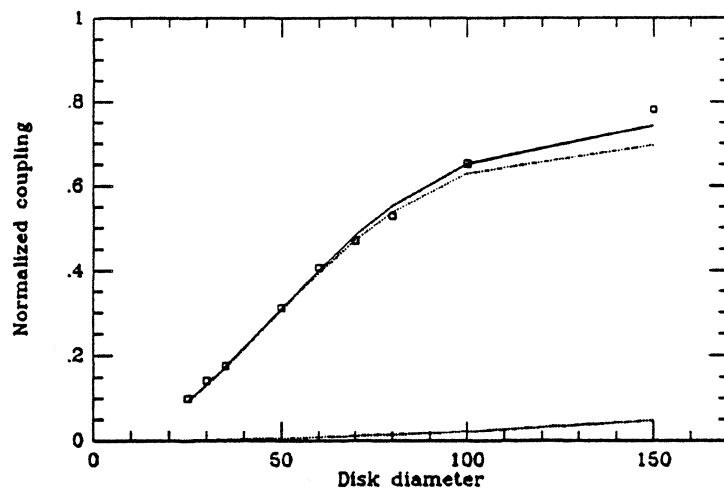


Figure 3: Coupling efficiency of receiver beam to disks of various sizes at $z = 3400$ mm (crosses), with best-fit theoretical coupling curve (solid lines: Eq. 4). The dotted lines are the individual components, showing the importance of measuring large-scale beams with large loads. 70% of the power is in the smaller beam that couples well to the telescope.

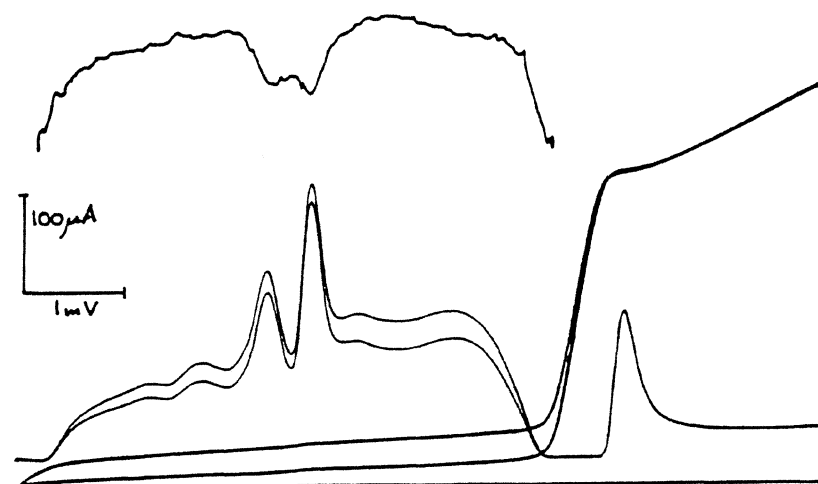


Figure 4: Conversion curves at 690 GHz. The m-shaped curve at the top is the IF signal-to-noise ratio vs. DC bias voltage.

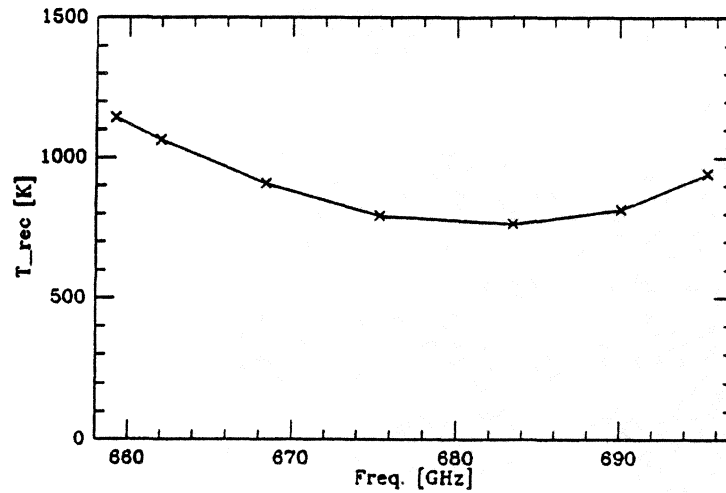


Figure 5: DSB receiver noise temperature vs. tuning frequency, averaged over a 500 MHz IF bandwidth.

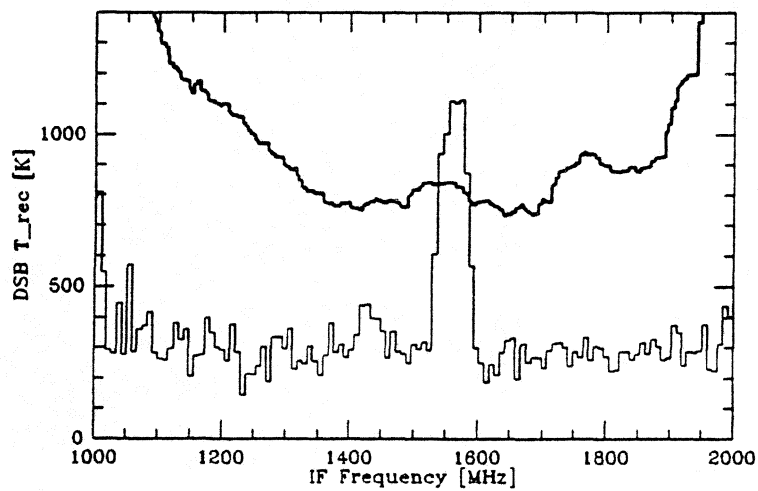


Figure 6: DSB receiver noise temperature vs. IF frequency (heavy lines). The light line spectrum of IRC+10216 shows the effect of increasing noise temperature on the spectral baselines. The baseline is DC shifted to fit in this plot but no tilts or structures have been removed.

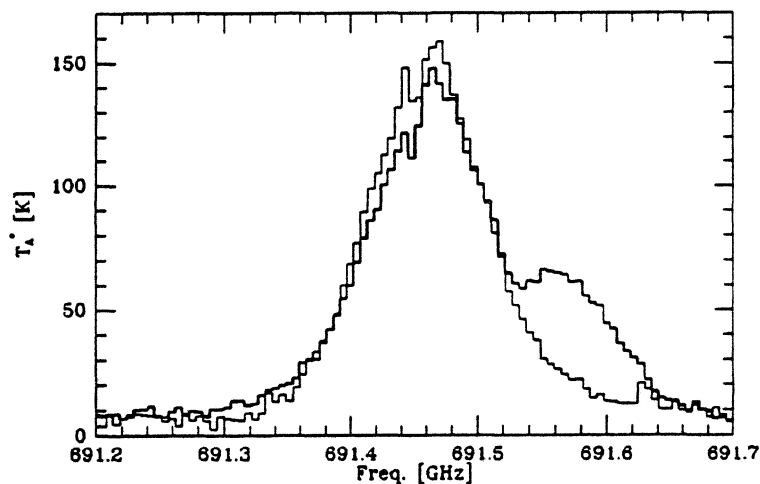


Figure 7: Spectra of the CO J=6-5 line from Orion in both sidebands. The heavy line is USB (and shows a strong line from the other sideband on its wing); the light line is LSB. No baseline corrections have been made, and there is a slight frequency shift due to Orion's 9 km/s LSR velocity. The agreement in peak intensity is within 10% and shows that the receiver is closely double-sideband.

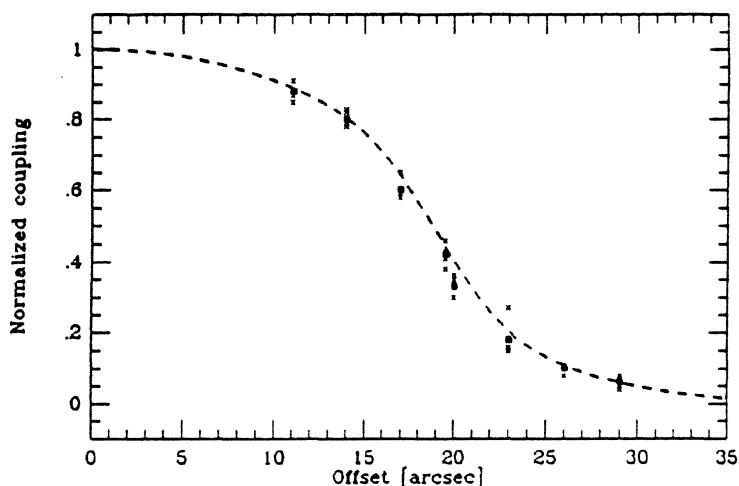


Figure 8: Coupling efficiency of telescope beam to Jupiter for different angular offsets, with best-fit theoretical coupling curve (dashed lines; Eq. 4). Crosses are individual measurements, boxes are the averages. 40% of the power in the 8" FWHM "diffraction" beam and the remaining 60% is in a 25" beam produced by mid-scale antenna surface errors.

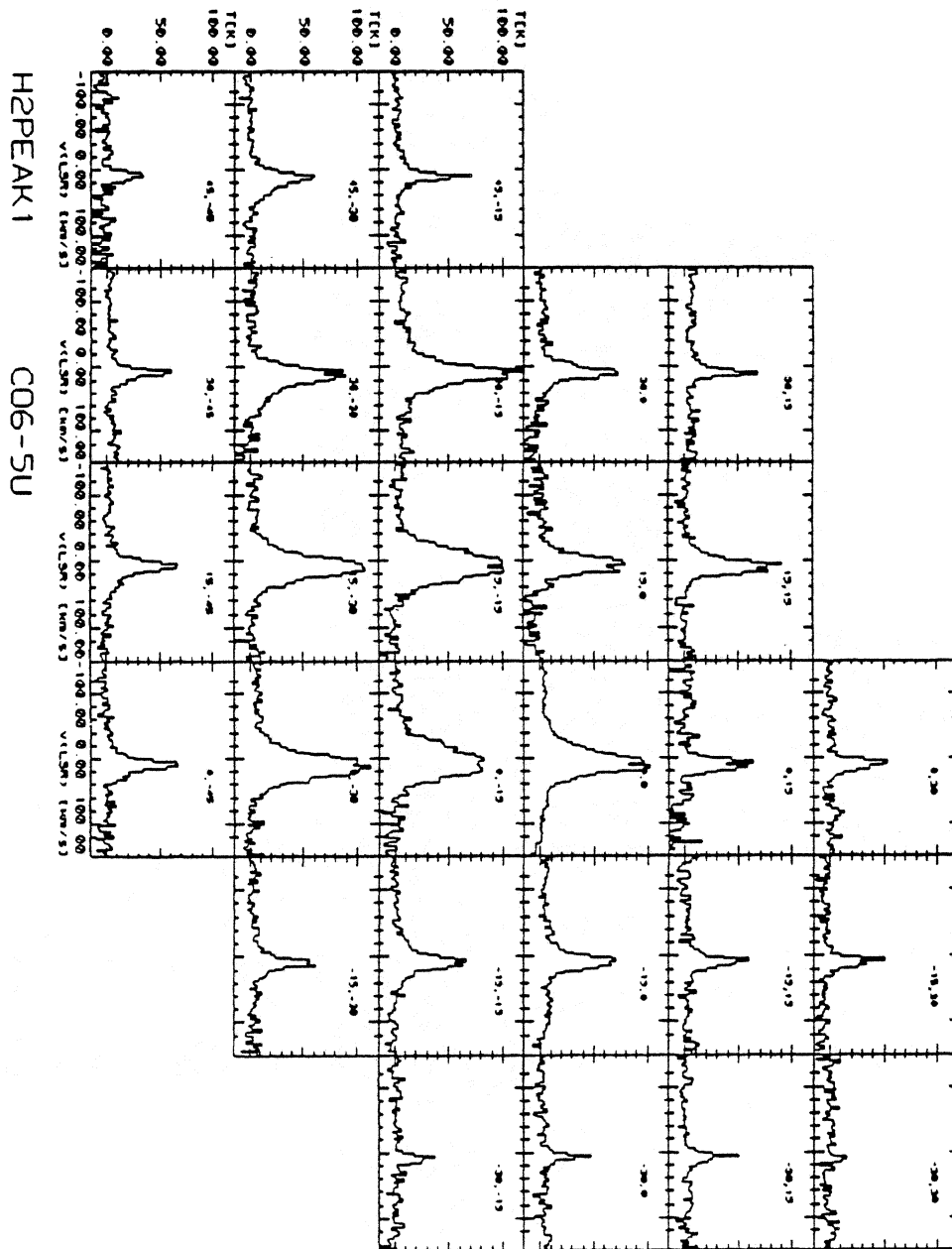


Figure 9: Map of the 691.5 GHz CO J=6-5 map in the Orion outflow. Integration time was 2 min. per point, and no baseline corrections have been made.

HIGH FREQUENCY EFFECTS AND PERFORMANCE OF A 600 GHz - 635 GHz SIS RECEIVER USING Nb/AlO_x/Nb JUNCTIONS

M. Salez, P. Febvre*, W. R. McGrath, B. Bumble, H. G. LeDuc

Jet Propulsion Laboratory, 4800 Oak Grove Drive, 91109 Pasadena

**DEMIRM -Observatoire de Paris-Meudon, 5 place Jules Janssen, 92195 Meudon, France*

ABSTRACT

A 600 GHz - 635 GHz waveguide SIS heterodyne receiver was built and used for astronomical observations at the Caltech Submillimeter Observatory (CSO) in Hawaii. The mixer employs a $0.25\text{-}\mu\text{m}^2$ Nb/AlO_x/Nb junction integrated with a Nb/SiO/Nb microstrip tuning circuit. The double sideband receiver noise temperature is 245 K - 310 K over the tunable bandwidth. At frequencies approaching the gap frequency of niobium (700 GHz), the optimization of the receiver is limited by the overlap of second-order and first-order photon steps of opposite signs. A noise increase of 10% - 40% is measured when the junction is biased in the region where the photon steps overlap, in agreement with the calculations using Tucker's theory. The bias range yielding the best performance is a small portion of the photon step in the vicinity of the second Shapiro step, which makes the cancellation of the AC Josephson effect with an external magnetic field critical.

1. INTRODUCTION

The importance for radioastronomy of molecular rotational lines at submillimeter wavelengths has led to the development of low-noise heterodyne receivers. The most sensitive spectrometers at millimeter and submillimeter wavelengths make use of quasiparticle SIS (Superconductor-Insulator-Superconductor) mixers [1 - 9], for which the quantum mixer theory predicts both high RF-to-IF conversion efficiency and quantum-limited noise [10]. SIS mixers

are expected to work well at frequencies up to the gap frequency of the superconductor used, and up to twice this frequency with a somewhat degraded performance [11-13]. While some preliminary measurements have been done on low energy gap superconductors, like aluminum [14], at millimeter wavelengths, few experimental studies have been performed at submillimeter wavelengths near the energy gap.

Almost all SIS receivers presently used on radiotelescopes use niobium junctions for their ruggedness and high quality I - V characteristics. Recently, a few niobium-based receivers have been operated on telescopes [1 - 5] and aboard airplanes [6, 7] at frequencies approaching 700 GHz, the gap frequency of niobium. Furthermore, the use of SIS mixers at still higher frequencies has been demonstrated in the laboratory [8]. The SIS receiver described here was designed to operate at frequencies around 625.9 GHz to allow for the detection of hydrochlorine in the interstellar medium and planetary atmospheres. This frequency range also provides a unique opportunity to investigate several consequences of operating an SIS receiver near the gap frequency. In particular, we find an increase of the receiver noise at bias voltages where the photon steps overlap, as predicted by theory.

2. RECEIVER DESCRIPTION

An extensive discussion of the receiver design has been given elsewhere [15]. The mixer uses a single Nb/AlO_x/Nb junction of area $0.5\text{ }\mu\text{m} \times 0.5\text{ }\mu\text{m}$. The junctions are fabricated from a DC-sputtered trilayer using electron-beam lithography, with a self-aligned insulator lift-off technique which has been described previously [16]. The junction critical current density is 11 kA/cm^2 and its normal resistance at 4.2 K is $R_N \approx 73\text{ }\Omega$. The capacitance per unit area is estimated to be $100\text{ fF}/\mu\text{m}^2$, and hence $C \approx 25\text{ fF}$. The value of $\omega R_N C$ is ~ 6.8 at 600 GHz, and thus the geometric capacitance significantly shunts the RF signal from the quasiparticle tunneling conductance.

In order to optimize the RF impedance match, a superconductive microstrip circuit is integrated with the junction which tunes out the capacitance C by providing a distributed inductance $\sim 1/\omega^2 C$ in parallel. Figure 1 shows the particular circuit which has yielded the best receiver noise results so far. It consists of a quarter-wavelength microstrip stub which provides a wide-band RF

short, used in combination with a 25- μm long, 5- μm wide section of transmission line which transforms this RF short into the appropriate inductance. This circuit design and its calculated performance are discussed elsewhere [15,17].

The fused-quartz substrate with the SIS junction and the integrated superconductive circuit is placed in a waveguide mount along the E-field direction across a 170 μm rectangular waveguide. The radiation is coupled into this waveguide via a dual-mode conical feedhorn [18].

A backshort and an E-plane tuner are used to match the junction RF complex impedance. Both tuners are of the contacting type. A symmetrical RF choke filter prevents the submillimeter-wave radiation from leaking out of the waveguide through the bias/IF leads.

The local oscillator (LO) consists of a 100 GHz - 106 GHz Gunn source followed by x2 x3 whisker-contacted Schottky varactor multipliers [19]. A harmonic mixer with an internal -10 dB coupler is inserted between the Gunn oscillator and the multipliers to provide a reference signal for a phase-lock system.

The low-noise IF amplifier is a 3-stage HEMT (High Electron Mobility Transistor) amplifier from Berkshire Technologies [20], cooled to 13 K. The amplifier gain and noise temperature, specified at 77 K, are 33 dB and 2-3 K over nearly 800 GHz of bandwidth centered at 1.4 GHz.

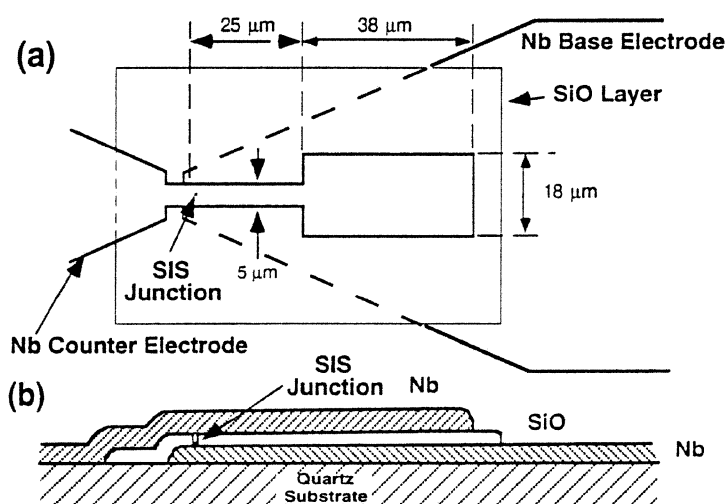


Fig. 1. Top (a) and cross-section (b) views of the microstrip Nb/SiO/Nb tuning circuit integrated with the junction (not to scale).

To average out the Josephson currents which are a source of noise in a quasiparticle mixer, a coil of superconducting NbTi wire produces a magnetic field of up to 1000 Gauss aligned with the plane of the junction. This is sufficient to apply at least three magnetic flux quanta within the junction since the magnetic field corresponding to one flux quantum (2×10^{-15} Wb) is about 300 Gauss.

The mixer and the optics are mounted on a 4-liter liquid helium tank, which cools the components to about 4.5 K by thermal conduction. In addition, a closed-cycle helium refrigerator cools two concentric jackets surrounding the helium tank down to 13 K and 80 K. Under typical operating conditions, the measured receiver hold time is about 5 days.

3. RECEIVER PERFORMANCE

In Fig. 2, the double-sideband (DSB) receiver noise power per unit bandwidth (expressed in temperature units using the Rayleigh-Jeans formula $P/B = kT$) is plotted versus LO frequency. The frequency range of the receiver is presently set by the local oscillator. For each point, the backshort and E-plane tuner positions, the LO power, the bias voltage and the magnetic field have been optimized. The best noise temperature is $245 \text{ K} \pm 15 \text{ K}$ at 610 GHz. The frequency response is relatively flat and the noise rises to $330 \text{ K} \pm 19 \text{ K}$ at 635 GHz. The variations of T_R across the IF bandwidth have also been measured, with a tunable 40-MHz bandpass filter. The receiver noise varies smoothly within the IF bandwidth of $\sim 600 \text{ MHz}$. T_R was derived using the 'Y-factor' method, i.e., from the relation

$$T_R = (T_h - Y T_c) / (Y - 1) \quad (3)$$

where Y is the ratio P_h/P_c of the IF output powers measured in response to a hot ($T_h = 295 \text{ K}$) and a cold ($T_c = 82 \text{ K}$) *Eccosorb* load placed at the receiver RF input. The IF bandwidth for the noise measurements was 500 MHz. The response of the receiver to the hot and cold loads can be seen in Fig. 3.

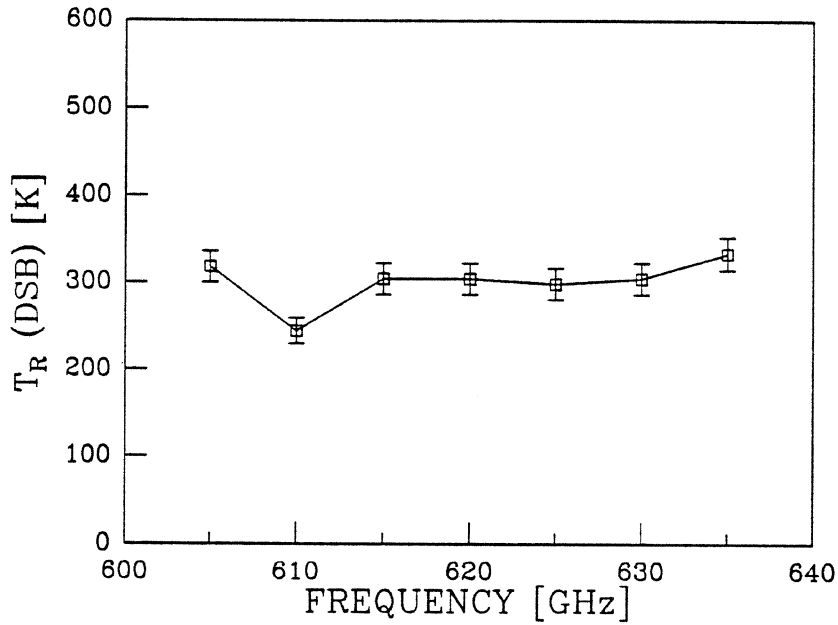


Fig. 2. Double-sideband receiver noise temperature versus LO frequency.

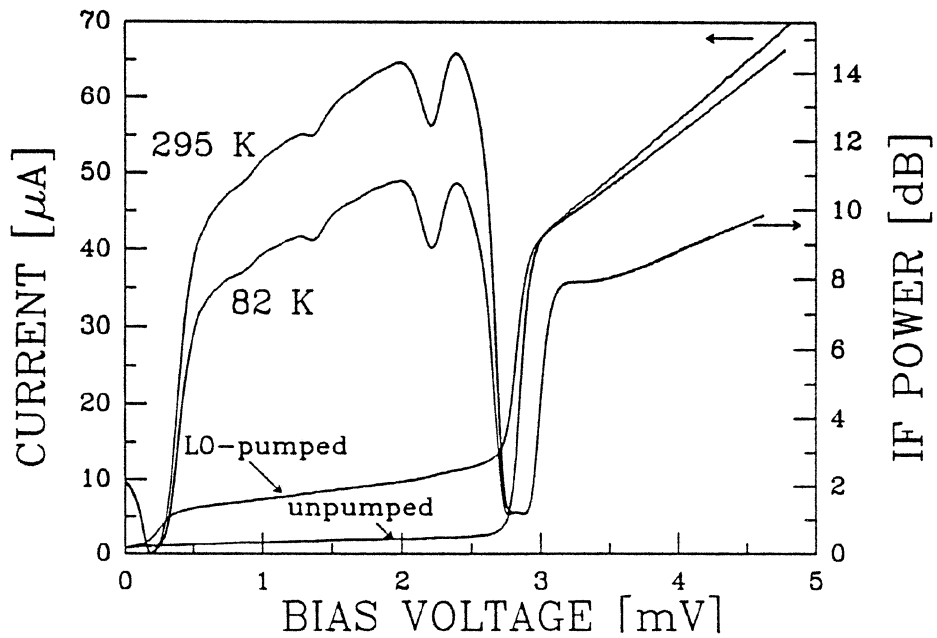


Fig. 3. Typical IF output power versus bias voltage, for a hot (295 K) and a cold (82 K) load presented to the receiver input. Superimposed are the unpumped and the corresponding LO-pumped I - V characteristics.

4. OVERLAP OF PHOTON STEPS

4.1. Experimental observations

Figure 3 shows the typical IF power response of the receiver for the hot (295 K) and cold (82 K) loads, as a function of the bias voltage. The LO-pumped and unpumped I - V characteristics are also shown. The magnetic field applied in the plane of the junction has completely zeroed the amplitude of the Shapiro steps and the corresponding flux is one flux quantum $\Phi_0 = h/2e$.

A minimum at 2.2 mV followed by a peak at 2.4 mV, is seen in the IF output power. This feature was seen in all IF power curves for all LO frequencies, although its exact voltage location in the upper part of the photon step varies directly with frequency. The peak is always close to where one expects the second Shapiro step, but its amplitude remains unchanged by a magnetic field applied to the junction. Furthermore, the 2nd Shapiro step could be seen as an *independent*, much narrower and noisier component, the amplitude of which could be strongly affected by the applied magnetic field.

The feature was seen for all LO powers above a certain level, and is enhanced with large LO powers. In Fig. 4, which shows experimental data for a large LO pumping level, one can easily detect an inflection point in the pumped current-voltage characteristic at the voltage where the narrow minimum in the IF output power (now sharper and deeper) occurs. The voltage at which inflection point and IF power-drop occur turns out to be identical.

4.2. Predicted photon step overlap

The inflection point in the pumped I - V curve and the sharp minimum in the IF power curve both result from the overlap of the $n = 1$ photon step of the positive voltage region with the $n = 2$ photon step from the negative voltage region (see Fig. 5). The latter decreases the pumped current in the region of overlap, hence causing an inflection point in the former. Part of the drop in the IF output power is due to a poorer coupling at the inflection point, where the IF impedance is smaller than on the rest of the photon step. In addition, the mixer conversion loss is proportional to the IF conductance, and hence exhibits a change at any voltage where the conductance varies sharply. This "photon-step-overlap" interpretation is a convenient way for describing the shape of an RF-

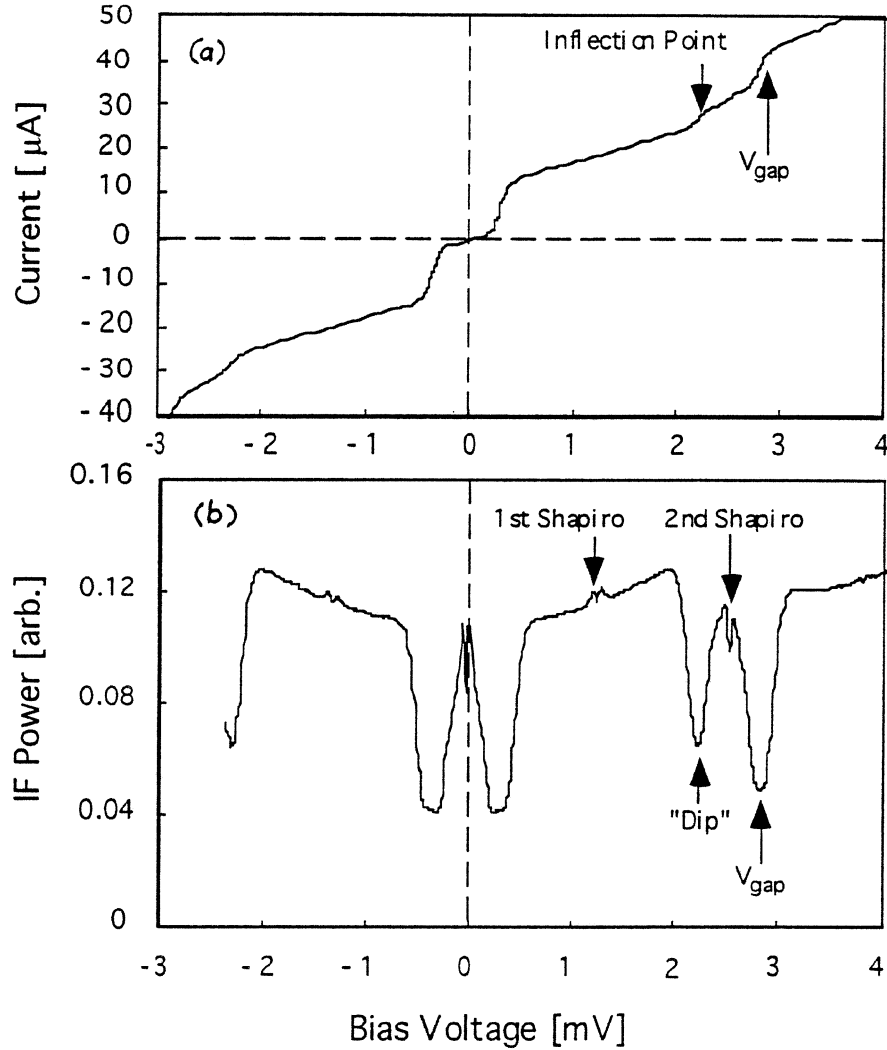


Fig. 4. (a) LO-pumped I - V curve and (b) receiver IF output power versus bias voltage with the hot load at the receiver input for $\Phi = \Phi_0$ and a large LO power, at $f = 635$ GHz.

pumped SIS I - V curve, which is antisymmetric about the origin.

The fact that high LO powers enhance the inflection point in the pumped I - V curves supports this interpretation. Furthermore, the inflection point voltage is directly correlated with the voltage expected for the overlap

$$V_{\text{overlap}} = 2 \hbar \omega / e - V_g \quad (4)$$

as the experimental points plotted in Fig. 6 demonstrate. In Eq. (4), V_{overlap} is defined as shown in Fig. 5, \hbar is Planck's constant, ω is the angular frequency, and V_g is the junction gap voltage. For comparison, the voltage corresponding to the

$n = 2$ Shapiro step has also been plotted and conforms to the Josephson voltage-frequency relation

$$V_{shapiro} = 2 (h\omega/2e) \quad (5)$$

For sufficiently high LO powers, a minimum in the coupled IF power could also be observed *above* the gap, involving the $n = 3$ negative photon step, at

$$V_{overlap}' = 3 h\omega/e - V_g \quad (6)$$

This effect is predicted by the Tucker theory and has been observed in Al-based junctions at 73 GHz [14]. It has not been mentioned in the literature so far at higher frequencies, possibly because its appearance in niobium mixers is limited to frequencies between 470 GHz and 690 GHz (see section 4.4) and only a few SIS receivers have been reported in this range. Also, the effect of the overlap is LO-power dependent, and not all SIS receivers require the same amount of LO power when optimized.

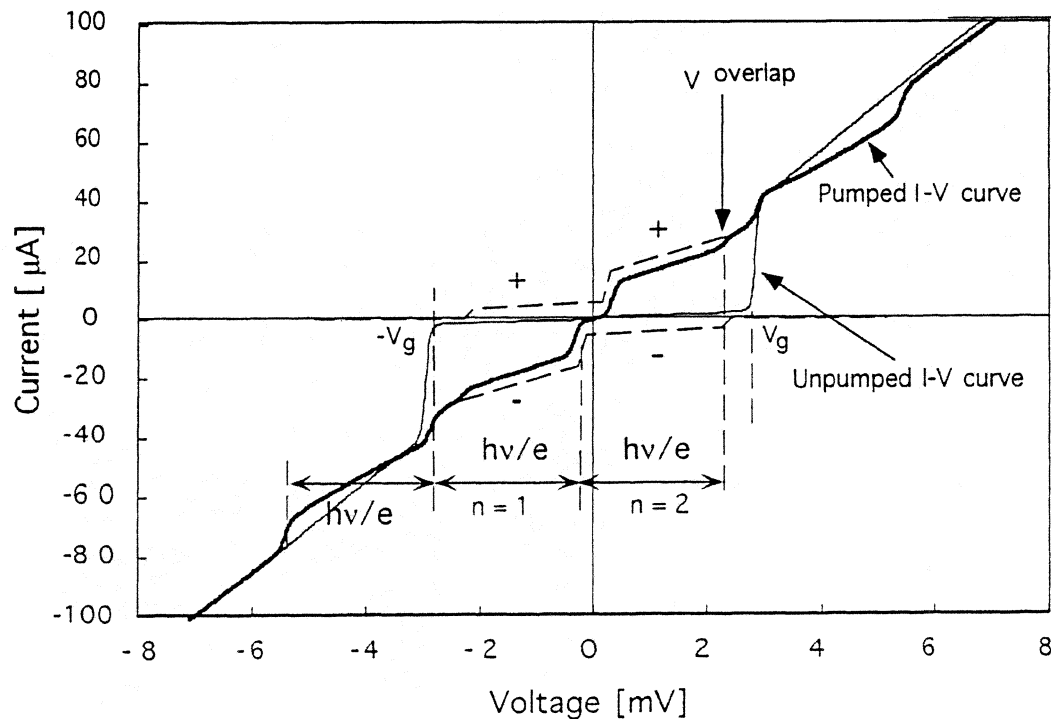


Fig. 5. Schematic reconstruction of an experimental pumped I - V curve displaying an inflection point (heavy line) using the photon step overlap argument. The dashed curves show the photon steps of width $h\nu/e$ from the positive and negative voltage regions "before" their effects are added.

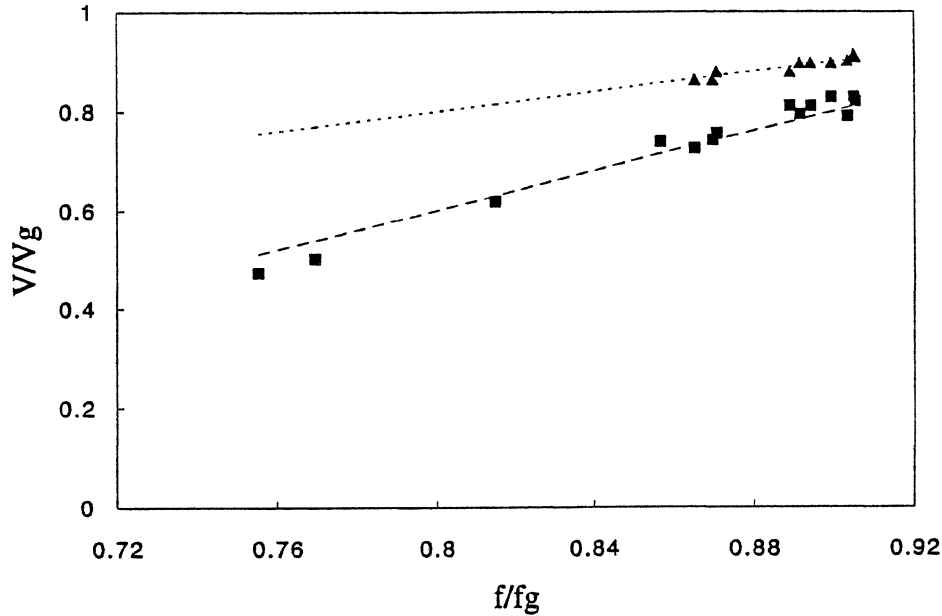


Fig. 6. Measured voltages for the inflection point (squares), normalized to the gap voltage hf_g/e , as a function of the normalized LO frequency f/f_g . The dashed line represents the predicted voltages for the photon step overlap. For comparison, the 2nd Shapiro steps (triangles) are also shown and compared to the prediction (dotted line).

We have experimentally and theoretically investigated how this overlap affects the performance of a submillimeter-wave receiver. We have systematically measured the increase in receiver noise in the overlap region for several frequencies between 600 GHz and 635 GHz and for various LO power levels. We find that when biased at voltages where the photon steps overlap, the receiver exhibits a noise typically higher by 10%-40%. Although not prohibitive for the use of an SIS receiver, this is a significant reduction in performance.

4.3. Theoretical fits

We have performed theoretical calculations using the Tucker theory to analyze the inflection point caused in the pumped I - V curves by the photon step overlap, and to investigate the predicted effect on the mixer noise temperature and gain. The numerical program fits pumped I - V curves and thus provides the LO power applied to the SIS junction and the embedding impedance of the mixer [12]. Calculated pumped I - V curves can then be generated for any LO pumping level, and the corresponding available mixer gain and mixer temperature can be calculated as a function of the bias voltage. In addition, the measured noise and gain of the IF system have been included in order to predict the increase in receiver noise and the receiver output IF power for the hot RF load.

Figure 7(a) shows a calculated pumped I - V curve fitting experimental data at 631.14 GHz. The corresponding LO power is $P_{LO} = 125.7$ nW. The embedding impedance $Z = 17.8 - j 42.7 \Omega$ used for the calculation has been derived first, by fitting the experimental pumped I - V characteristic. The experimental values of the receiver noise temperature and of the receiver IF output power for the RF hot load as a function of the bias voltage are shown in Fig. 7(b). The calculated IF output power for the hot load and the DSB receiver noise temperature are shown in Fig. 7(c) along with the available and coupled mixer gains.

The dip observed in the IF power output in Fig. 7(b) at the inflection point proves not only to be an effect of IF mismatch, but also to correspond to a sharp decrease of the *available* mixer gain at $V_{overlap}$, which is proportional to the mixer IF resistance. Qualitatively and quantitatively, the agreement between the calculated and measured receiver noise *variations* is good, despite the uncertainties intrinsic to this type of calculation. A noise increase of about 100% is predicted as one biases the mixer from $V > V_{overlap}$ to $V < V_{overlap}$. In the data, a receiver noise variation of nearly 40% is observed. This level of LO pump is close to the level required to optimize the receiver performance.

4.4. Consequences for SIS receiver operation

The photon step overlap described above has practical consequences for submillimeter wave receivers. Near the superconductor energy gap frequency, the voltage range where the best mixer performance can be obtained is restricted to only a small fraction of the photon step. The frequency for which an overlap starts 'eating away' the bias region on the first photon step can be simply expressed by:

$$f = \left(\frac{2}{n+1} \right) \cdot f_g \quad (7)$$

where n is the order of the photon step of opposite sign to be considered. From this equation, one sees that the $n = 3$ photon step plays a role at $f > f_g/2$, that is $f > 350$ GHz in the case of a niobium mixer. However, for the typical levels of LO power involved in receiver operation, the effect on the noise of this 3rd step is negligible.

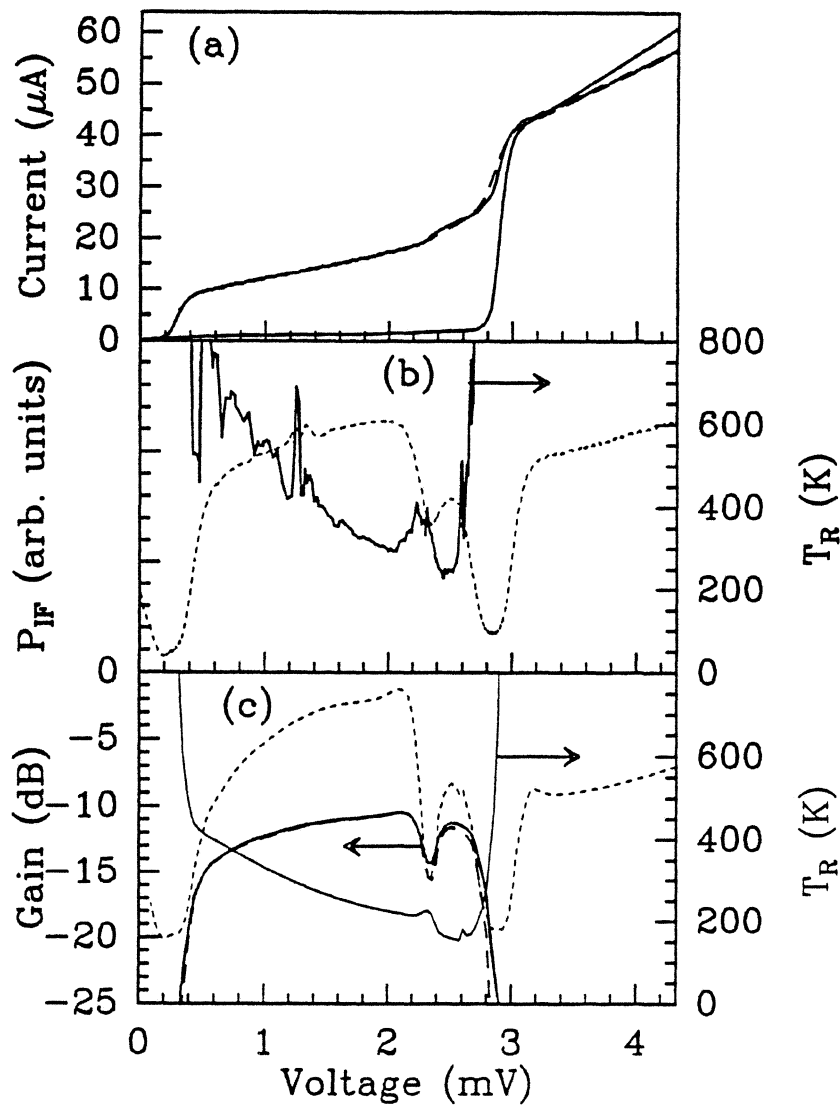


Fig. 7. (a) Un pumped I - V curve and measured (dashed) and calculated (solid) pumped I - V curves at 631 GHz for $P_{\text{LO}} = 125$ nW; (b) measured double-sideband T_{rec} and P_{IF} (295 K) versus bias voltage; (c) calculated T_{rec} and P_{IF} (295 K) versus bias voltage along with the available (solid) and coupled (dashed) mixer gains $G_{\text{mix}}^{\text{a}}$ and $G_{\text{mix}}^{\text{c}}$.

The case $n = 2$ occurs at frequencies higher than $2/3 f_g$, or 466 GHz. At 547 GHz, the overlap is observed [9] but is of little importance for receiver operation as a large part of the photon step can still be used to bias the junction with an optimum noise. However, this region shrinks as the frequency increases and ends up corresponding to a very narrow peak in the IF power curves. At 600 - 635 GHz, the change with frequency is big and this effect has a strong impact on biasing the junction to obtain the lowest noise possible. At frequencies around 660 - 690 GHz, this region is already vanishingly small, allowing no practical bias at $V > V_{overlap}$, and the effect discussed here would be unnoticed [4,5].

At frequencies above 700 GHz ($n = 1$), niobium-based SIS mixers can perform reasonably well [8] but the response degrades because the $n = 1$ and $n = 2$ photon steps completely overlap. In addition, the mixer can then only be operated at $V > h\omega/e - V_g$ because of the overlapping $n = 1$ photon step from the negative region. Nevertheless, this problem could be circumvented if the amount of LO power required to operate the mixer was lower, which is in theory possible with different mixer RF source impedances [22]. The final limit to the use of niobium SIS mixers is at 1400 GHz ($n = 0$), i.e. *twice* the gap frequency of niobium, when the $n = 1$ photon step from either side covers the entire $(-V_g, V_g)$ bias range.

At 600 - 635 GHz, the photon step overlap has another consequence on the biasing conditions. Coincidentally, the small portion of the photon step where one should bias to yield the best performance is *in the vicinity of the second Shapiro step*. It is obvious from Fig. 6 that as the frequency increases, the locations of the Shapiro step and of the discussed overlap *converge*, hence making biasing more restricted. This is not yet a problem at 547 GHz [9], but becomes of concern at 600 GHz and above. Therefore, the perfect cancellation with an external field of the AC Josephson effect is critical to avoid instabilities and additional noise.

The suppression of the Shapiro steps by the application of a suitable magnetic field is always possible in theory. However in practice, noise spikes often remain in the IF power at the Shapiro voltages although the I - V characteristics looks completely smoothed. It is not clear how well a flux quantum which averages out completely the DC Josephson current does in averaging out the AC counterpart which can mix down to the IF frequency.

The averaging process may be more efficient for a larger number of applied flux quanta, but then, the intense magnetic field may slightly *reduce* the gap of the junction, as shown in Fig. 8 for $\Phi \sim 3 \Phi_0$. Not only does the gap voltage decrease for a large magnetic field, but as a result $V_{overlap}$ given by eq. (4) also becomes higher. These two effects add up to further reduce the bias region of lowest noise. In the example of Fig. 8, one has $V_g^{reduced} \sim V_{overlap}$, meaning that the voltage region where there is no overlap has disappeared.

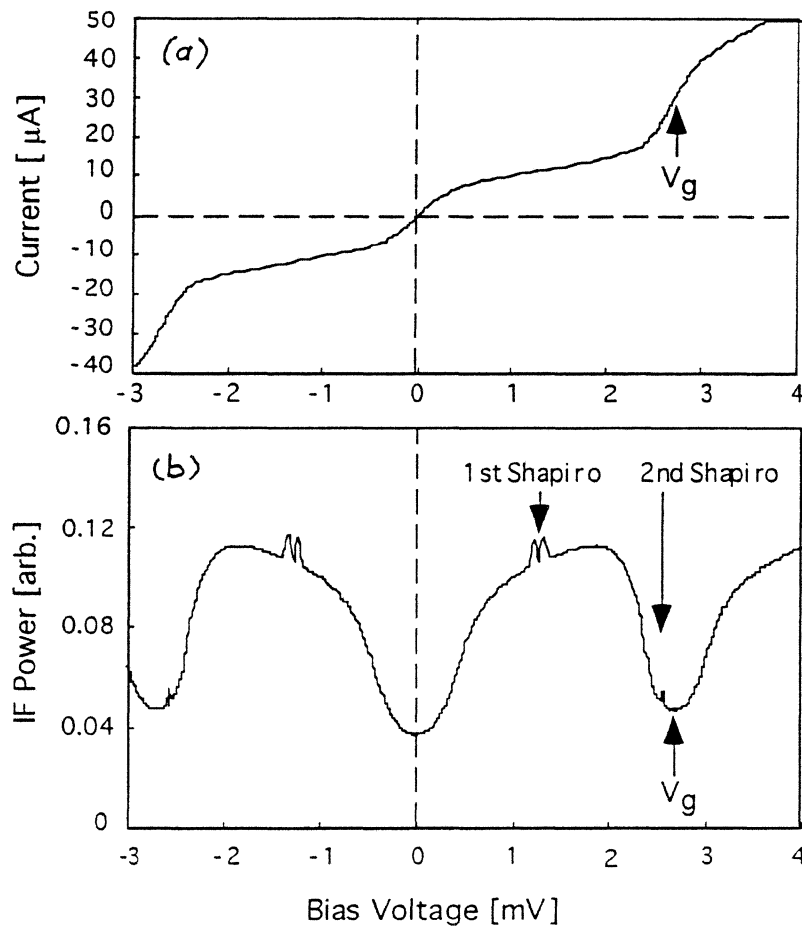


Fig. 8. Measured LO-pumped I - V characteristics (a) and P_{IF} (295 K) (b) for an applied magnetic flux of $\Phi = 3 \Phi_0$ at $f = 635$ GHz. The second Shapiro step and the overlap-induced inflection point are now located at the magnetically-reduced gap voltage.

V. OBSERVATIONS AT THE CSO

The receiver was installed at the Cassegrain focus of the 10.5-m CSO telescope, on Mauna Kea in Hawaii, in November 1993. The weather was exceptionally good, and for a DSB receiver noise temperature on site of 250 K - 350 K, the system noise temperature, which is dominated by the atmospheric attenuation, ranged from 2000 K to 8000 K DSB, varying with frequency, day, and zenith angle. The receiver was tuned at each frequency for the optimum Y-factor and biased on the best performance region discussed earlier. In terms of trapped flux and coupled LO power, the receiver was very stable throughout the night, as determined from frequent sweeps of the I - V curve for check-up. The externally applied flux was less than two flux quanta to avoid a gap reduction, and the $n = 2$ Shapiro step could always be completely quenched in the IF output power curve.

Both H^{35}Cl and H^{37}Cl isotopes were detected in emission in several molecular clouds, along with other molecules in the 600 GHz - 636 GHz range. Figure 9 shows the spectrum of a particular region of the molecular cloud OMC-1 in Orion, with the expected hyperfine structure of the H^{35}Cl ($J=1-0$) transition at 625.92 GHz.

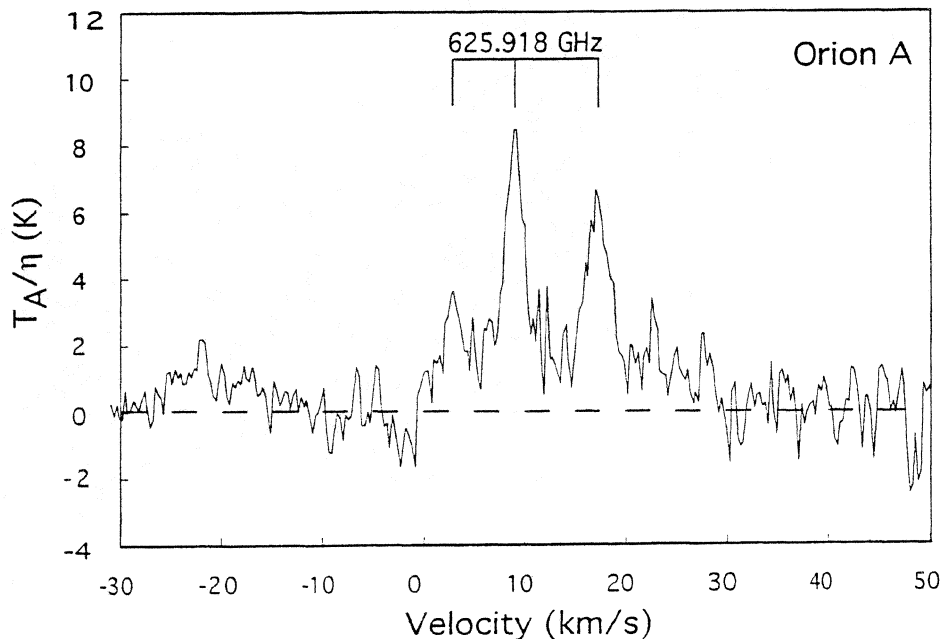


Fig. 9. Spectrum of the H^{35}Cl ($J=1-0$) line at 625.918 GHz, taken in a region of Orion A with an integration time of 30 minutes ($T_{\text{sys}} = 6550$ K). All three hyperfine lines are seen.

7. CONCLUSION

We have discussed the performance of a waveguide SIS heterodyne receiver using a submicron Nb/AlO_x/Nb junction and a niobium-based integrated tuning circuit, in the frequency range 600 GHz - 635 GHz, i.e. as high as 90% of the niobium gap frequency of 700 GHz. The lowest noise temperature of the receiver is 245 K DSB, and is close to 300 K DSB elsewhere in the LO frequency range. At these frequencies, the performance of the receiver is somewhat limited by the overlap of the second-order and first-order photon steps of opposite signs. In the bias region where the steps overlap we have measured a receiver noise increase of 10% - 50%, depending on the amount of LO power. This noise increase is qualitatively and quantitatively consistent with theoretical calculations using the Tucker theory. As the frequency of operation is increased, the fraction of the photon step where one expects the best performance is reduced to a small region, undesirable because of its proximity with the second Shapiro step, and shrinking to zero as the frequency approaches 700 GHz. Furthermore, an intense magnetic field applied to suppress the Josephson currents may further reduce the availability of this region. At frequencies higher than 700 GHz, this photon step overlap modifies the operating conditions of niobium-based SIS receivers and particular attention must be paid to optimize the LO level and source impedance. This receiver was successfully operated and used for astronomical observations at the CSO telescope, in Hawaii.

8. ACKNOWLEDGEMENTS

This research was performed by the Center for Space Microelectronics Technology, Jet Propulsion Laboratory, California Institute of Technology, and was jointly sponsored by the National Aeronautics and Space Administration / Office of Advanced Concepts and Technology and the Office of Space Science, and the Innovative Science and Technology Office of the Ballistic Missile Defense Organization. Morvan Salez and Pascal Febvre have been partly sponsored by Matra-Marconi Space, Toulouse, France, and DEMIRM, Observatoire de Meudon, France. Morvan Salez is currently sponsored by the Research Associateship Program of the National Research Council. We acknowledge, for their technical assistance at various stages of the receiver development: Dick Denning, Juergen Hernichel, Karl Jacobs, Mark Natzic, and in particular Joe Voeltz and Hardy Moham of JPL's Space Instruments Machine Shop, who fabricated most of the receiver components. We wish to thank M. Feldman, J. Kooi and J. Zmuidzinas for helpful comments, and also M. Frerking, S. Gulkis, and T. Spilker for contributing to the CSO observations, and T.G. Phillips for his continued support of this project.

IX. REFERENCES

- [1] A. Karpov, M. Carter, B. Lazareff, M. Voss, D. Billon-Pierron, K.H. Gundlach, *Proc. 4th Internat. Symp. on Space Terahertz Technology*, p. 11, UCLA, CA (1993).
- [2] C.K. Walker, J.W. Kooi, M. Chan, H.G. LeDuc, P.L. Schaffer, J.E. Carlstrom and T.G. Phillips, *Proc. 3rd Internat. Symp. on Space Terahertz Technology*, p. 266, University of Michigan, MI (1992).
- [3] B.N. Ellison, S.M.X. Claude, A. Jones, D.N. Matheson, L.T. Little and S.R. Davies, *Proc. 18th Internat. Conf. on Infrared and Millimeter Waves*, p. 106, Colchester, U.K. (1993).
- [4] J. Kooi, these proceedings.
- [5] K. Schuster, A.I. Harris, K.H. Gundlach, *Int. J. of Infrared and Millimeter Waves* **14**, (10) pp. 1867-1887 (1993).
- [6] J. Zmuidzinas, H.G. LeDuc, J.A. Stern, S.R. Cypher, *Proc. 4th Internat. Symp. on Space Terahertz Technology*, p. 72, UCLA, CA (1993).
- [7] J. Mees, these proceedings.
- [8] G. DeLange, C.E. Honingh, M.M.T.M. Dierichs, H.H.A. Schaeffer, H. Kuipers, *Proc. 4th Internat. Symp. on Space Terahertz Technology*, p. 41, UCLA, CA (1993).
- [9] P. Febvre, W.R. McGrath, P. Batelaan, H.G. LeDuc, B. Bumble, M.A. Frerking and J. Hernichel, *Digest of IEEE MTT-S Int. Microwave Symposium*, p. 771, Atlanta, GA (1993) ; *Proc. 18th Internat. Conf. on Infrared and Millimeter Waves*, p. 263, Colchester, U.K. (1993).
- [10] J.R. Tucker, *Appl. Phys. Lett.* **36**, 477 (1980).
- [11] M.J. Feldman, *Internat. J. of Infrared and Millimeter Waves* **8**, 1287 (1987).
- [12] W.C. Danchi and E.C. Sutton, *J. Appl. Phys.* **60**, 3967 (1986).
- [13] Tek-Ming Shen, *IEEE J. of Quant. Electronics* **QE-17**, 1151 (1981).
- [14] D. Winkler and T. Claeson, *J. Appl. Phys.* **62**, 4482 (1987).
- [15] M. Salez, P. Febvre, W.R. McGrath, B. Bumble, H.G. LeDuc, *Internat. J. of Infrared and Millimeter Waves* **15**, (6) 349 (1994).
- [16] H.G. LeDuc, B. Bumble, S.R. Cypher, A.J. Judas and J.A. Stern, *Proc. 3rd Internat. Symp. on Space Terahertz Technology*, p. 408, University of Michigan, MI (1992).
- [17] P. Febvre, W.R. McGrath, P. Batelaan, H.G. LeDuc, B. Bumble, to appear in *Internat. J. of Infrared and Millimeter Waves* **15**, (6) (June 1994).
- [18] H.M. Pickett, J.C. Hardy, J.C. and J. Farhoomand, *IEEE Trans. Microwave Theory and Techn.* **MTT-32**, 936 (1984).
- [19] Radiometer Physics, Bergerwisen Straß 15, 53340 Meckenheim, Germany.
- [20] Berkshire Technologies Inc., 5427 Telegraph Ave, Oakland, CA.
- [21] A. Skalare, *Int. J. Infrared and Millimeter Waves* **10** (11) (1989).
- [22] P. Febvre, these proceedings.

Quasi-Optical SIS Mixer with a Silicon Lens for Submillimeter Astronomy**N.G. Ugras*, J. Zmuidzinas*, H.G. LeDuc****

We have designed and tested a quasi-optical low-noise SIS receiver for the submillimeter band. The radiation is focused onto a twin slot antenna by a hyperhemispherical silicon lens. The forward coupling efficiency for silicon ($\epsilon_r=11.7$) is 91% compared to 70% in quartz ($\epsilon_r=4.5$). However the relatively high dielectric constant of silicon would cause a reflection loss of $\approx 30\%$ at the front surface of the lens compared to $\approx 15\%$ in quartz. We have eliminated this reflection loss by antireflection coating the lens with an alumina loaded epoxy ($\epsilon_r=4.0$). A uniform epoxy thickness of $68\mu\text{m}$ ($=\lambda/4$ at 550 GHz) over the hemispherical lens is obtained by diamond machining the surface. The twin slot antenna has good directivity and a low impedance which is well matched to the rf impedance of the SIS junctions. The mixer circuit consists of two SIS junctions separated by a superconducting microstripline acting as the tuning inductance. The area of the tunnel junctions ranges between $0.56\text{--}1.56\ \mu\text{m}^2$, with a current density of $10,000\text{A}/\text{cm}^2$, and $R_{sg}/R_n=15$. Preliminary results indicate typical receiver noise temperatures ranging from 130 K to 160 K in the 500 to 600 GHz band. The spectral response of the mixer agrees well with the direct detector response obtained by a Fourier transform spectrometer. The measured input beam pattern is well collimated and has a Gaussian distribution. This receiver is being used for radio-astronomical observations aboard NASA's Kuiper Airborne Observatory.

This work was supported by NASA/JPL and NASA grant NAWG-107.

*N.G. Ugras and J. Zmuidzinas are with the Downs Laboratory of Physics, 320-47, California Institute of Technology, Pasadena, CA 91125.

**H.G. LeDuc is with the Jet Propulsion Laboratory, 302-231, Pasadena, CA 91109.

A LOW NOISE 565-735 GHz SIS WAVEGUIDE RECEIVER

J. W. Kooi¹, C. K. Walker², H. G. LeDuc³, P. L. Schaffer¹, and T.G. Phillips¹

1- Caltech Submillimeter Observatory

Division of Physics, Mathematics and Astronomy

California Institute of Technology, Pasadena, California 91125

2- University of Arizona, Tuscon, Arizona

3- Center for Space Microelectronics Technology, Jet Propulsion Laboratory

Abstract

We report recent results on a 565-735 GHz SIS heterodyne receiver employing a $0.36\mu\text{m}^2$ Nb/AlO_x/Nb SIS tunnel junction with high quality circular non-contacting backshort and E-plane tuners in a full height waveguide mount. No resonant tuning structures have been incorporated in the junction design at this time, even though such structures are expected to help the performance of the receiver. The receiver operates to 735 GHz, well above the gap frequency of niobium, ≈ 680 GHz. Typical receiver noise temperatures from 565-690 GHz range from 160K to 230K with a best value of 185K DSB at 648 GHz. At 730 GHz the receiver noise temperature has gradually increased from 230K to 300K. The monotonic rise in noise temperature above 680 GHz is attributed to a combined effect of absorption loss in the niobium RF choke and antenna transmission lines and inability to tune out the large parasitic junction susceptance. With the mixer cooled from 4.3K to 2K the measured receiver noise temperatures decreased by approximately 15%, giving roughly 180K DSB from 660 to 680 GHz. The receiver has a full 1 GHz IF passband and has been successfully installed at the Caltech Submillimeter Observatory in Hawaii.

Introduction

A waveguide superconducting insulator superconducting (SIS) heterodyne receiver with a center frequency of 665 GHz has been designed to take advantage of 600 to 730 GHz atmospheric window. The results discussed here were achieved by using a $0.36\mu\text{m}^2$ Nb/AlO_x/Nb tunnel junction in a full height rectangular waveguide mixer [2] with two circular non-contacting tuning elements [3,4] and an integrated 1-2 GHz wide IF matching network.

It is clear that near quantum limited results [1] have been achieved by scaling SIS waveguide receivers to higher frequencies [5, 6]. Since a SIS junction is essentially a sandwich of two superconducting electrodes separated by a very thin insulating material, ($\approx 12\text{\AA}$), the geometric capacitance is appreciable, 75-85 fF/ (μm^2) . To achieve a good RF match to the embedding impedance it is important to tune out the geometric capacitance of the junction. This becomes

increasingly difficult as the operating frequency of the mixer is raised. For this purpose waveguide receivers typically employ high 'Q' non-contacting backshort and E-plane tuners.

Recently advances in niobium thin film processing have permitted RF matching on the chip itself, by means of lithographically produced tuning structures, to tune out the parasitic capacitance. This technique has been very effectively used in both open structure devices [7,8] and waveguide mixers [9-16].

Above the gap frequency, ($2\Delta/h \approx 680$ GHz), the photon energy is large enough to break Cooper-pairs in the superconductor causing large absorption losses in the material. Dierichs *et al.* [17] have measured intensities for loss-less resonant stubs and compared them against calculated intensities according to Mattis-Bardeen theory. These measurements did not indicate any resonances above the gap frequency of niobium. Calculations at 750 GHz show that the film losses of the niobium antenna mount and RF choke structure will increase fifteen fold compared to below the gap. The transmission line losses are therefore significant, ($\geq 40\%$ /wavelength) [18], making it difficult to design a superconducting matching network centered at 665 GHz with the required 20% bandwidth. To minimize the effect of the increased absorption losses near and above the gap frequency it was decided to improve the waveguide tuners and use untuned Nb/AlO_x/Nb tunnel junctions. This approach would ensure a broadband 600-730 GHz SIS receiver provided of course that high quality non-contacting backshorts were found that would meet our design objectives. The theory and performance of these waveguide tuners will be elaborated on by Walker *et al.* [4] in a separate paper. However the results of preliminary scale model testing will be presented in this paper.

Nb/AlO_x/Nb Junction Fabrication

The Nb/AlO_x/Nb tunnel junctions were fabricated using a standard self-aligned lift-off trilayer process. The Nb/AlO_x/Nb trilayer was deposited in-situ in a high vacuum deposition system with a base pressure of 4×10^{-9} Torr, through a photoresist lift-off stencil (AZ5214) onto 50 μ m thick quartz substrates. The trilayer remaining after lift-off formed the first half of the antenna/filter structure. The junction mesa was patterned using electron beam direct writing on a 120 nm thick PMMA followed by evaporation of ≈ 50 nm chromium metal and subsequent lift-off. Contact regions of the trilayer are then protected with a photoresist stencil and the combined chromium/photoresist mask was used to etch the junction in a parallel plate reactive ion etcher (RIE). The etch parameters were 62% CCl₂F₂ + 31% CF₄ + 7% O₂, 30 mTorr pressure, and .18 Watts/cm². The electrical isolation of the base electrode and subsequent wire layer are provided by thermal evaporation of 150 nm of SiO. The substrates were tilted and rotated during this operation. The chrome was lifted off using a commercial wet etch. The second half of the antenna was formed by a whole wafer deposition of Nb

in the same vacuum system used for trilayer deposition and was patterned using RIE. Tunnel junctions with areas down to $0.25\mu\text{m}^2$ were fabricated using this technique.

Receiver Description

Optics

Fig. 1 shows a block diagram of the 665 GHz receiver. The optics was designed to give a 14 dB edge taper on the secondary mirror of the telescope. A $13\mu\text{m}$ mylar beam splitter is mounted at 45° to the signal and local oscillator beams. The local oscillator's electric field is perpendicular to the plane of incidence and about 5.7% of the radiation couples into the cryostat, the remainder is absorbed by a sheet of Eccosorb. The vacuum window is made out of $19\mu\text{m}$

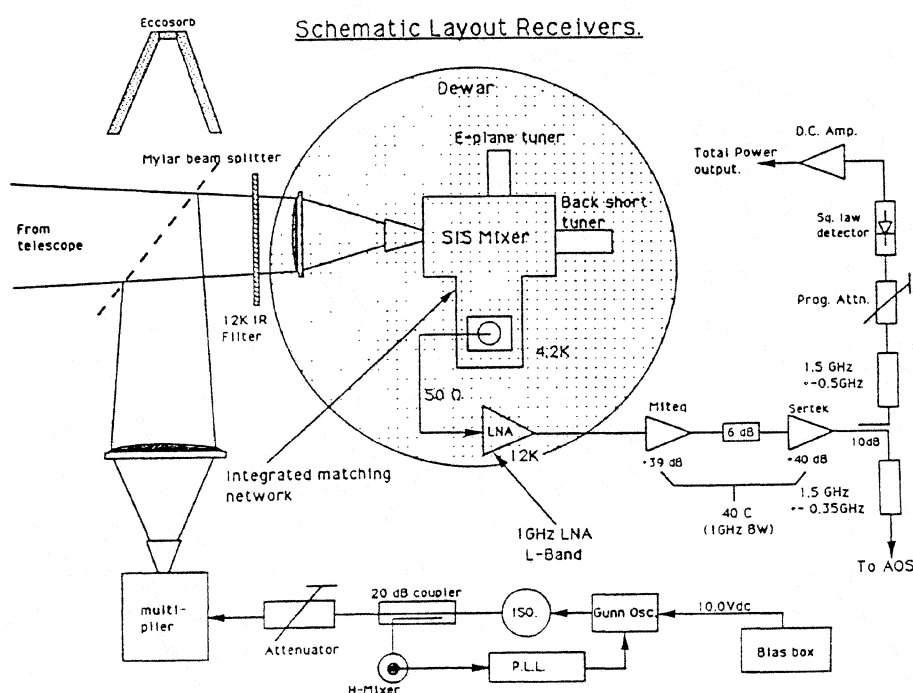


Fig. 1. Schematic layout of the receiver. Beam splitter, window reflection, and IR filter losses at 665 GHz contribute about 65 Kelvin to the receiver noise temperature. The matching network is mounted in the mixer block and is followed by a two stage balanced HEMT amplifier. The IF passband is 1.0 to 2.0 GHz.

HR500/2S material manufactured for food packaging by Hercules Inc. [19]. It has a dielectric constant of ≈ 2.6 and is a laminate of biaxially oriented polypropylene with $2.5 \mu\text{m}$ layers of polyvinylidene chloride on both sides. Laboratory experiments have shown that the material has adequate strength to function as a vacuum window for aperture diameters $\leq 25 \text{ mm}$. Experiments indicate that the Hercules material is considerably more opaque to He^4 than $25 \mu\text{m}$ mylar. The material is also expected to have a low permeability to water and atmospheric gasses. The infrared blocking filter on the 12 Kelvin window consists of a one wavelength thick fluorogold disk. The mixer lens is made out of low density polyethylene, with an approximate dielectric constant of 2.41 at 4.2K ambient temperature. The optics are designed to give a frequency independent illumination of the secondary (Goldsmith 1982). The low loss polyethylene lens is placed in the near field of the scalar feedhorn. Antenna pattern measurements give reasonably close agreement to the theoretically expected response.

Reflection and Absorption Losses

To better understand the noise contribution of the front-end optics of the receiver, losses of different slabs of selected materials were measured at 654 GHz. With the receiver tuned, the hot (293K) and cold (80K) IF power response was measured with or without a 'lossy' slab of material inserted in the beam. This procedure gave information on the effective 'cold' blackbody temperature from which the total insertion loss of the material was computed. L includes both the reflection and transmission losses of the sample.

$$T_{eff} = L(T_{hot}) + (1 - L)T_{cold} \quad (1)$$

Correcting for the reflection loss of the optically thick slab gives the transmission loss, α . Table 1 tabulates the dielectric constant and the loss tangent. The dielectric constant was obtained from the literature [20] and is assumed to be relatively constant with frequency.

$$\tan(\delta) = \left(\frac{\lambda_o \alpha}{\pi \sqrt{\epsilon'}} \right) \quad (2)$$

α = transmission loss per unit wavelength.
 ϵ' = the real part of the dielectric constant.

Table 1. 654 GHz Measured Absorption Losses

Material	Dielectric Constant (ϵ')	α (np/mm)	$\tan(\delta)$
Fluorogold	2.56-2.64	0.120	10.8×10^{-3}
Mylar	3.0	0.451	3.8×10^{-2}
Styrofoam packaging 1 lb/ft ³	1.1	$8.6-17.2 \times 10^{-4}$	$1.2-2.4 \times 10^{-4}$
Radvai Styrofoam 1.75lb/ft ³	1.1	0.0023	3.2×10^{-4}

Mixer Block Construction

The basic waveguide mixer block is scaled from the 230 GHz design of Ellison *et al.* [2] and utilizes a double stub tuning structure. The block is composed of two sections and uses magnetic field concentrators as discussed by Walker *et al.* [12]. The front section constitutes the corrugated feedhorn, circular to rectangular waveguide transformer and E-plane tuner. The back section holds the junction and backshort tuner. The corrugated feedhorn beamwidth was measured by Walker *et al.* on a scaled version at 115 GHz. It measures 10.5° at the ϵ^{-2} power contour in both E and H planes. The three section circular to full height rectangular waveguide transformer and E-plane tuner were constructed on the same mandrel as the corrugated feedhorn. This reduces number of waveguide discontinuities and minimizes ohmic loss in the guide. The E-plane is situated $1/2\lambda_g$ in front of the junction. The junction is mounted in a $90 \mu\text{m}$ by $100 \mu\text{m}$ groove which cuts across the face of the waveguide, parallel to the E-field. The junction is fabricated on a highly thermally conductive piece of single crystal quartz. The substrate dimension are $75 \mu\text{m}$ in width and $50 \mu\text{m}$ in height. The junction has been carefully centered in the waveguide [21] and is contacted with silver paint on both the ground and IF side. Fig. 2 shows the result of using Indium to try to contact the junction substrate on the ground side up to the waveguide wall. Using Indium on the ground side close to the waveguide wall introduces a shunt susceptance and loss. The danger of introducing a low Q resonant circuit by using indium so close to the waveguide wall far outweighs any thermal and mechanical benefits.

The thermal conductivity of the single crystal quartz is high enough to keep the junction cold with only silver paint on both IF and ground sides of the RF choke.

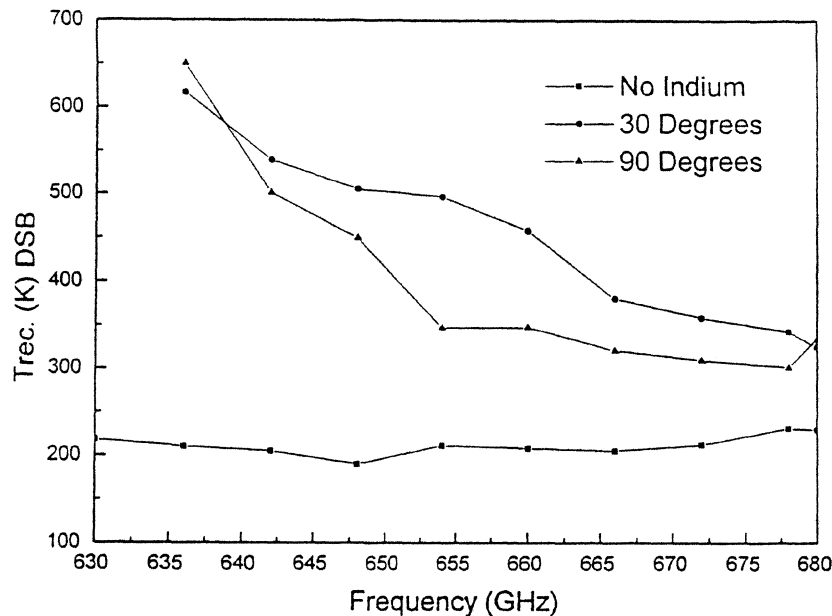


Fig. 2. Result of using indium close to the waveguide wall to provide both mechanical support and a thermal and electrical short circuit. Data is taken with the same junction.

On the IF side the junction is contacted with a $25\ \mu\text{m}$ Au wire soldered to a 1-2 GHz wide IF matching network [22] which is mounted in the mixer block. The matching network is designed to transform a 160 Ohm IF impedance to 50 Ohm and to provide a short to out of band signals up to ≈ 22 GHz. The latter is needed to avoid saturating the junction with unwanted out of band signals. The output of the mixer block is directly connected to a 1-2 GHz balanced HEMT amplifier based on work by Padin *et al.* [23]. Any impedance mismatch between the matching network and low noise amplifier is absorbed by the amplifier's input Lange coupler. The RF choke structure is a 5 section Chebyshev bandpass filter designed to give maximum rejection ($S_{11} \leq -25$ dB) at 665 GHz and presents a short circuit at the waveguide wall. Computer simulations of the RF choke at 750 GHz indicate that reflection (S_{11}) and transmission (S_{21}) characteristics are not severely effected above the gap frequency by the fifteen fold increase in niobium film loss (Fig. 7).

The 492 GHz receiver discussed by Walker *et al.* [12] has demonstrated 9 dB of conversion loss at 492 GHz with a receiver temperature of 178 K DSB using an untuned $0.16\mu\text{m}^2$ Nb/AlO_x/Nb SIS tunnel junction. This block uses rectangular non-contacting tuners for both the backshort and E-plane as described by Brewer and Räisänen [24]. In order to ensure similar results at 665 GHz, tuners with a higher VSWR are needed to tune out the increased junction susceptance. Kerr *et al.* [3] have further investigated the use of tuners for the millimeter band. They found that tuners with multiple circular non-contacting sections have lower loss, and more smoothly varying reflection (S11) and phase characteristics than rectangular tuners. Fig. 3 shows the result of scaled model measurements on both the circular and rectangular non-contacting tuner designs. Both tuners have four low and high impedance sections. The input reflection (S11) of the circular tuner is approximately -0.06dB (VSWR \approx 144). The VSWR of the rectangular non-contacting tuner with mylar tape is

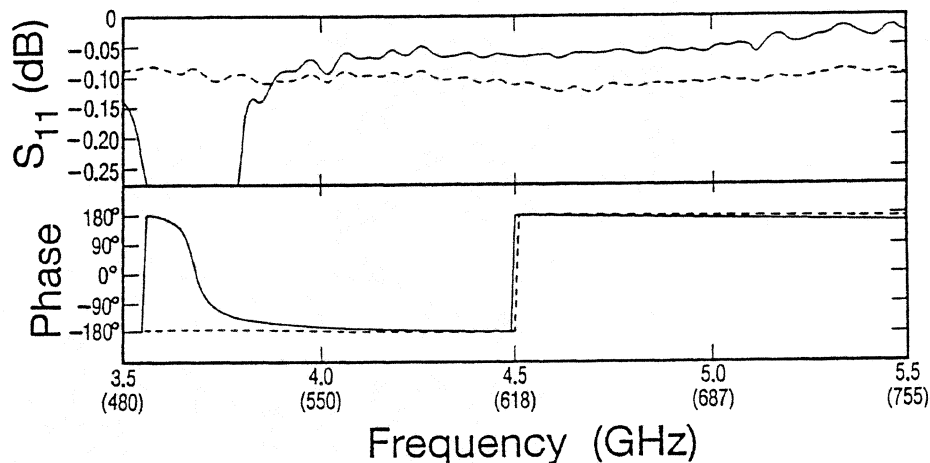


Fig. 3. Scale model tuner measurement on both the input reflection coefficient (S11) and phase response of the circular non-contacting tuner (solid line) and mylar covered rectangular tuner (dashed line). The resonance occurs when the combined length of one high-low impedance section approaches a quarter guide wavelength (Eq. 3). At 564 GHz this begins to show up in the frequency response of the receiver.

\approx 78. At 665 GHz the VSWR of the rectangular tuner will degrade significantly because of increased dielectric losses in the mylar tape, resulting in higher mixer conversion loss. The poor phase characteristic of the reflection coefficient shows up as irregular receiver sensitivity across the frequency band. These problems, in theory, can be minimized by employing tuned SIS tunnel junctions although,

as has been mentioned, the microstrip loss problem has to be avoided. Care has been taken in these model measurements to scale everything exactly to the dimensions in the actual mixer block. In the scale model the effective short circuit plane is located $\approx 10^\circ$ behind the first dumbbell section. The tuner response degrades catastrophically when the first high-low section combined length (l_t) approaches a quarter guide wavelength. The resonant cutoff frequency can be approximated by

$$f_{res} = k \sqrt{\left(\frac{c}{4l_t}\right)^2 + f_c^2} \quad (3)$$

f_c is the cutoff frequency of the TE₁₀ mode (431 GHz), k is (0.9-0.97) depending on the number of sections and c is the speed of light. Walker *et al.* will elaborate more on this in a separate paper [4].

The tuner itself consists of four beryllium copper concentric circular sections that extend from a rectangular shaft which is carefully fit in the waveguide. Scale model measurements have indicated that the position of the tuner in the waveguide is not critical as long as wall contact by the round sections is avoided. Fig. 4 shows a drawing of the backsort and E-plane tuners. The resonance occurs at ≈ 523 GHz which is starting to show up at 563 GHz (Fig. 7).

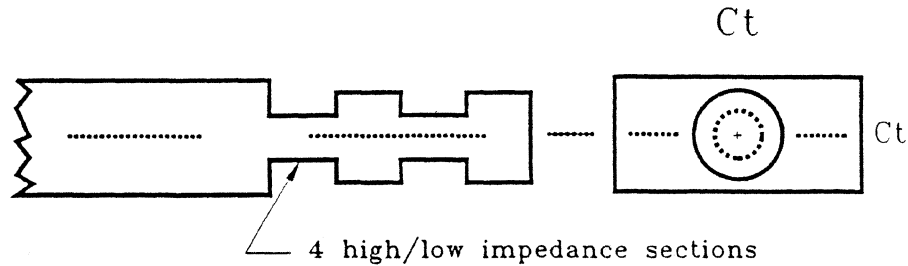


Fig. 4. Drawing of the 665 GHz circular non-contacting tuner. The tuner has 8 dumbbell sections, each being $\lambda_o/4$ long at the design frequency. The waveguide to tuner clearance is $4 \mu\text{m}$. To avoid electrical contact with the waveguide walls it is important to coat the tuners with an insulator such as aluminum oxide.

Results and Discussion

The mixer uses a high quality $0.36 \mu\text{m}^2$ Nb/AlO_x/Nb tunnel junction with a current density of $\approx 10 \text{ kA/cm}^2$, a sub-gap leakage current of $2.6 \mu\text{A}$ and a normal state resistance R_n of 50 Ohms. These characteristics allow the junction to be efficiently coupled to both the RF embedding impedance and IF impedance

(160 Ω), for which the matching network was designed. The junction has a $\omega R_n C_j$ product of approximately 5.9. C_j is the geometric junction capacitance and is ≈ 28 fF for this junction. Different junctions with either higher current density (larger sub-gap leakage) or smaller areas (larger normal state resistance) have been tested but did not perform quite as well as the 50 Ω 0.36 μm^2 tunnel junction. The junction is fabricated on a 50 μm thick single crystal quartz substrate.

Fig. 5 shows the pumped and unpumped I/V curves as well as the hot (295K) and cold (80K) total power response. The data was taken at 672 GHz with the mixer cooled to 4.2 K. At this particular frequency the DSB receiver noise temperature was 212 K. The mixer noise temperature is not sensitive to the magnetic field.

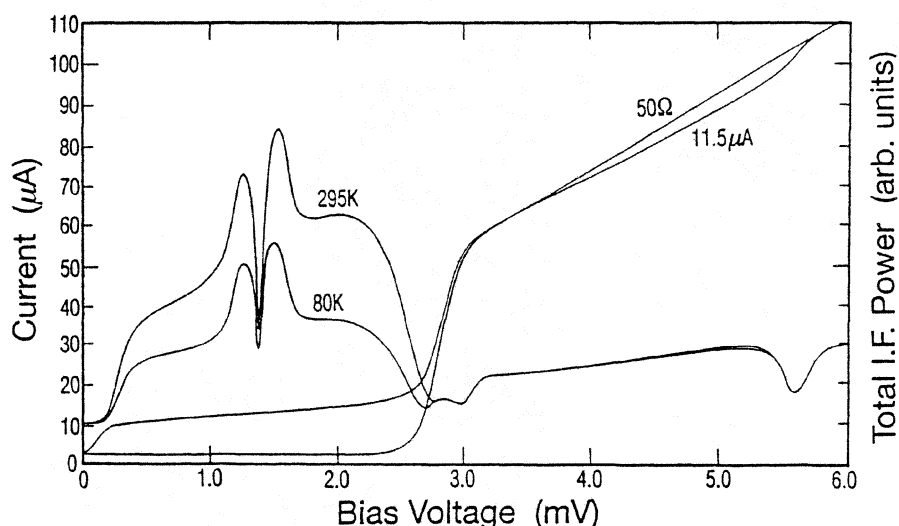


Fig. 5. Pumped and unpumped total power and I/V curves at 672 GHz. The uncorrected mixer noise temperature is 133K with 9.45 dB of mixer conversion loss. The best Y-factors were obtained at 2.1 mV and 11.5 μA of pumped current ($I_c/3$). The second Shapiro step is visible at 1.39 mV and can be nulled by adjusting the magnetic field

Using the Shot Noise method [25] the IF amplifier noise temperature is calculated to be 6 Kelvin, which is in good agreement with the actual measured noise temperature of the amplifier. The resulting mixer conversion loss is 9.45 dB with an uncorrected double sideband mixer temperature of 133 K. This mixer noise temperature is approximately 8.3 times the theoretical SSB quantum limit.

Cooling the mixer block to 2K improved the conversion loss by 1 dB and resulted in a receiver temperature of 180K and mixer noise temperature of 110K. The most likely cause of the improved mixer conversion loss and lower mixer noise temperature is the sharpening of the gap and reduction in the subgap leakage current. At 672 GHz the quasi-particle step width is 2.78 mV which is just below the band gap of niobium (≈ 2.85 mV). Just above the gap frequency of niobium, 690 GHz, the receiver noise temperature was ≈ 230 K and gradually increases to 300K at 730 GHz inspite of a factor of 16 higher absorption loss in the niobium film as compared to the loss below the gap frequency. The effect of dispersion loss in an untuned junction is relatively small because there are no high Q lossy niobium tuning structures with large current concentrations present. Another possible reason for the increase in mixer conversion loss above the gap is the inability to tune out the increasing parasitic junction susceptance. Adjusting the magnetic field on the junction had no significant effect on the receiver noise temperature.

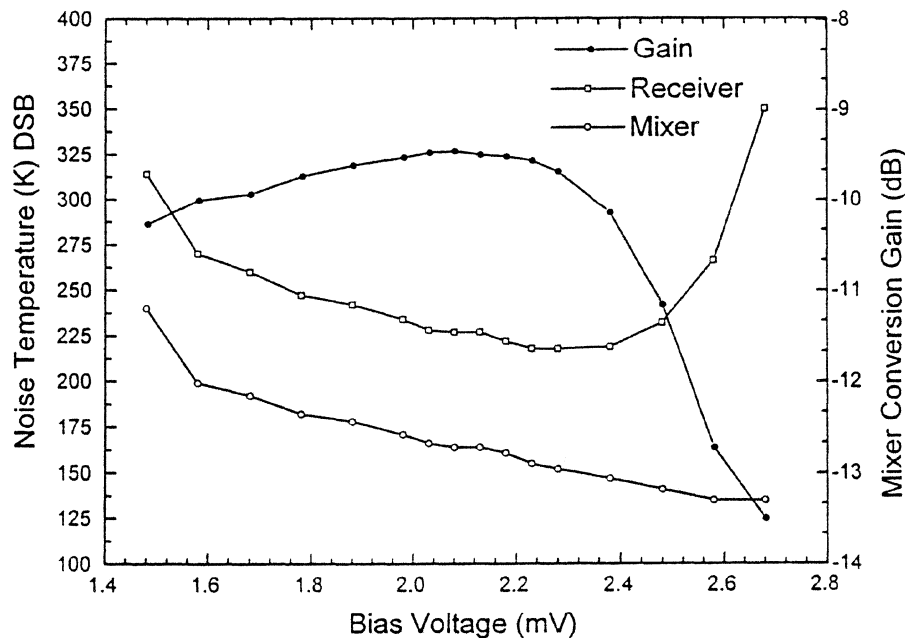


Fig. 6. Noise temperature and mixer conversion gain as a function of bias voltage at 654 GHz. The mixer temperature corrected for beamsplitter & window reflections is 89K.

Figure 6 shows the receiver noise temperature as a function of bias voltage. The best place to bias the mixer is between 2.1 and 2.25 mV. Similar results are observed with the 230-, 345-, and 492 Nb/AlO_x/Nb SIS quasi-particle mixers. The optimum LO drive is $I_c/3$, where I_c is the critical current of the junction, $\approx 35\mu\text{A}$. Figure 7 shows the frequency response of the receiver from 560 to 738 GHz. The quality of the circular non-contacting tuners is apparent from the well behaved frequency response of the mixer.

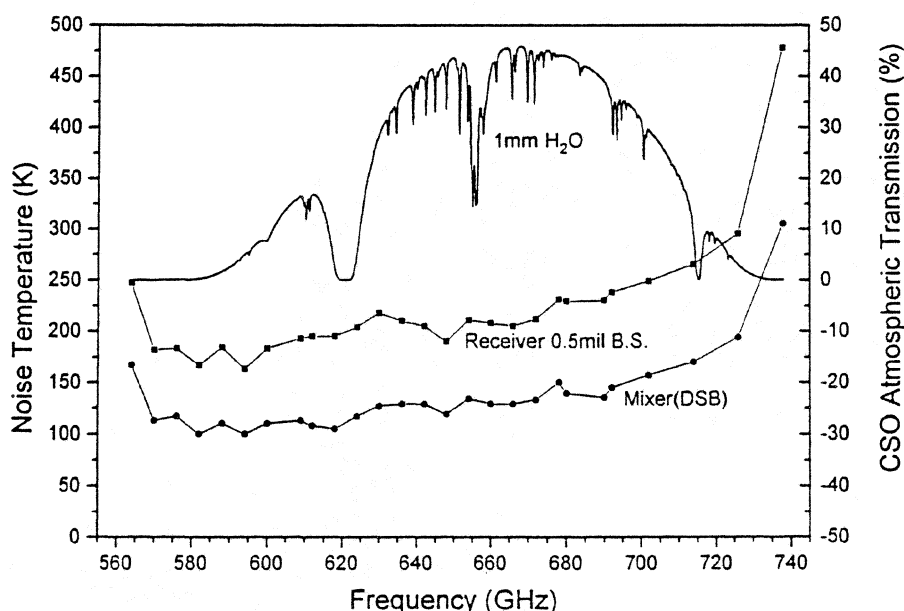


Fig. 7. Frequency response of the receiver from 560-738 GHz. The increase of noise temperature at 564 GHz is likely caused by the tuner resonance (Fig. 3). Cooling the mixer to 2K improved the receiver noise temperature by $\approx 15\%$

All measurements from 564-680 GHz were made with a $13\mu\text{m}$ beamsplitter. Data from 690-738 GHz were taken with a $20\mu\text{m}$ Hercules beamsplitter which has a reflection loss of $\approx 10.0\%$ at 700 GHz. The quoted 690-738 GHz noise temperatures are referred to a $13\mu\text{m}$ beamsplitter.

In figure 8 and 9 we present double sideband spectrum taken with a 500 MHz acousto-optical spectrometer at the Caltech Submillimeter Observatory toward Orion A and IRC+10216 respectively.

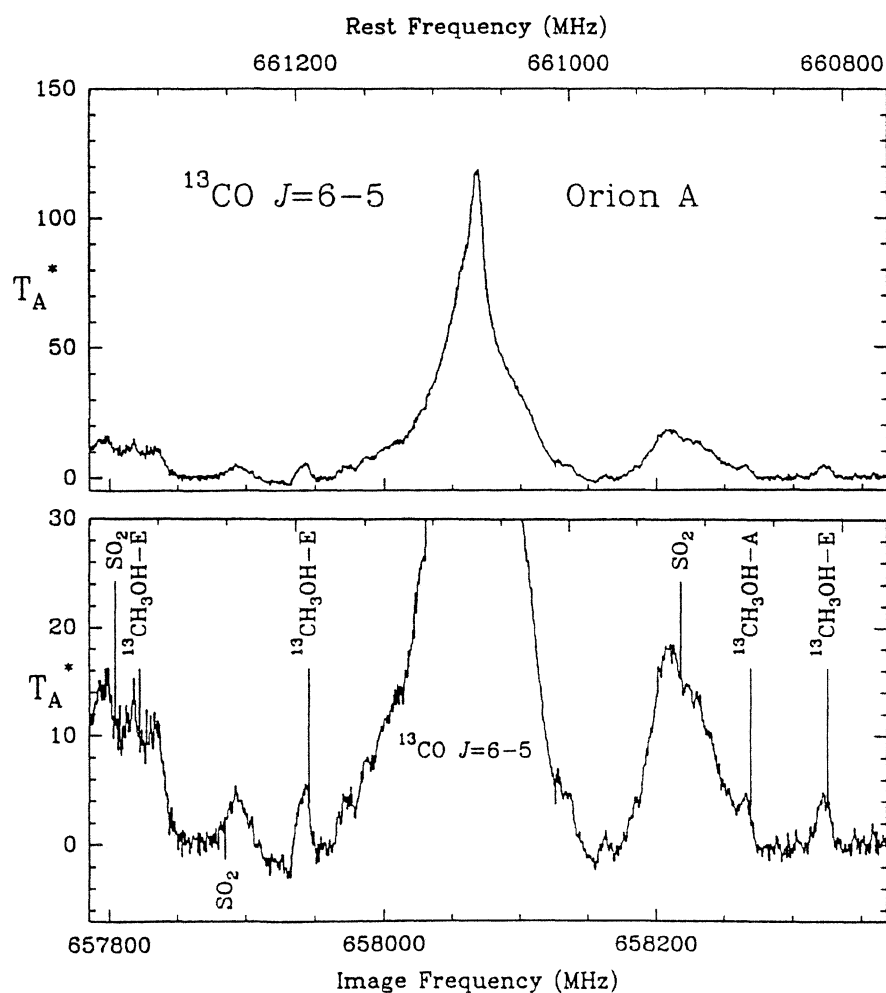


Fig. 8. $^{13}\text{CO } J=6-5$. The system temperature was 3900K with a $\tau_{225\text{GHz}} = 0.040$. Total integration time was 1.9 minutes at an airmass = 1.22

The measured main beam efficiency at these frequencies is 30%, but due to the small beam size (11 arcsec) and the extended nature of the source these spectra are corrected for the 60% coupling efficiency to the Moon. Some of the molecular transitions have been identified in both upper and lower sidebands as indicated by the label.

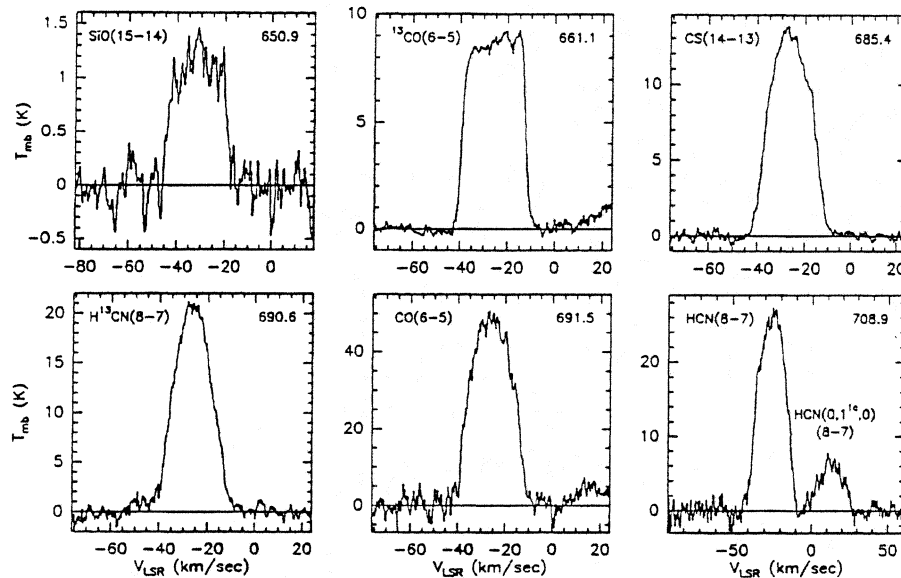


Figure 9. Spectral line survey of the most prominent molecular emission lines in IRC+10216 [26]. System noise temperatures varied from 5000-7000K with 1.0 - 1.5mm precipitable H₂O. Total integration time in all instances was less than 5 minutes.

Conclusion

A 665 GHz SIS heterodyne receiver has been developed to take advantage of the 600-730 GHz atmospheric window. The receiver has a full 1 GHz IF bandwidth and has been under test at the Caltech Submillimeter Observatory in Hawaii since August, 1993. The mixer employs an untuned $0.36\mu\text{m}^2$ Nb/AlO_x/Nb tunnel junction with a current density of $\approx 10 \text{ kA/cm}^2$. No adverse effect on the mixer conversion loss or noise temperature is seen up to the gap frequency of niobium (680 GHz). Above 680 GHz however the measured mixer conversion loss increases by $\approx 0.028\text{dB/GHz}$. This increase is most likely caused by a combination of niobium loss and inability to tune out the large parasitic junction susceptance. To minimize the dispersion loss effect of the niobium film above the gap no tuning structures were incorporated on the junction. It is expected that tuned junctions will improve the performance below the gap

frequency but will suffer from a much larger increase in conversion loss above the gap due to the high currents in the lossy tuning elements. The mixer block uses backshort and E-plane tuners with four circular non-contacting dumbbell sections. Scale model measurements of these tuners indicate an improved phase and VSWR over rectangular non-contacting tuners. Their superior performance is reflected in the flat frequency response of the mixer. Receiver noise temperatures are $205\text{K} \pm 20\text{K}$ DSB dipping to 185K at 648 GHz. The mixer conversion loss varies from 9-11 dB and is comparable to the 492 GHz waveguide receiver installed at the CSO in September 1991 [12]. When the mixer was cooled to 2K the measured receiver noise temperatures decreased by approximately 15% which is similar to the result obtained on a 230 GHz waveguide receiver [22]. Pumping on the mixer resulted in a measured DSB receiver noise temperature of approximately 180 Kelvin from 660 to 680 GHz.

Acknowledgments

We wish to thank Jonas Zmuidzinas, Rob Schoelkopf, Todd Groesbeck, Man Chan, Dominic Benford, Todd Hunter, Ken Young, and Tony Kerr for helpful discussions. We also like to thank John Carlstrom for supplying the high frequency Gunn Oscillators and Keith Horvath at Custom Microwave for his skill in machining the mixer block to tolerances of $< 2\mu\text{m}$. Work on high frequency receivers at Caltech is supported in part by NASA grant# NAGW-107 and NSF grant# AST-9015755.

References

- [1] J.R. Tucker and M.J. Feldman, "Quantum Detection at Millimeter Wavelength," *Rev. Mod. Phys.* 57, 1055-1113, 1985
- [2] B.N. Ellison and R.E. Miller, "A Low Noise 230 GHz SIS Receiver," *Int. J. IR and MM Waves* 8, 609-625, 1987
- [3] A. R. Kerr, "An Adjustable Short-Circuit for Millimeter Waveguides," Electronics Division Internal Report No. 280, National Radio Astronomy Observatory, Charlottesville, VA 22903, July 1988.
- [4] C. K. Walker, J. W. Kooi, in preparation.
- [5] R. Blundell and C. E. Tong, "Submillimeter Receivers for Radio Astronomy," *Proc. IEEE*, vol. 80, no. 11, pp. 1702-1720, Nov. 1992.
- [6] M. J. Wengler, "Submillimeter-wave detection with superconducting tunnel diodes," *Proc. IEEE*, vol. 80, no. 11, pp. 1810-1826, Nov. 1992.
- [7] J. Zmuidzinas, H.G. Leduc, J.A. Stern, and S.R. Cypher, "Two-junction tuning circuits for submillimeter SIS mixers," *IEEE accepted*.
- [8] T.H. Buttgenbach, H.G. LeDuc, P.D. Maker, T.G. Phillips, "A fixed tuned broadband matching structure for submillimeter receivers," *IEEE Trans. Applied Supercond.*, Vol. 2, No. 3, pp. 165-175, September 1992.

- [9] A.R. Kerr and S.K. Pan, "Integrated tuning elements for SIS mixers," *Int. J. IR and MM Waves*, vol. 9, No. 2, pp. 203-212, 1988.
- [10] A. Karpov, M. Carter, B. Lazereff, D. Billon-Peron and K.H. Gundlach, "Modelling and performance of Nb SIS mixers in the 1.3mm and 0.8mm bands," in *proc. Third Intl. Symp. Space Terahertz Technology*, pp. 244-250, March 1992.
- [11] J. W. Kooi, M. Chan, B. Bumble, T. G. Phillips, "A low noise 345 GHz waveguide receiver employing a tuned $0.50 \mu\text{m}^2$ Nb/AlO_x/Nb tunnel junction," in preparation.
- [12] C. K. Walker, J. W. Kooi, M. Chan, H. G. Leduc, P.L. Schaffer, J.E. Carlstrom, and T.G. Phillips, "A Low-noise 492 GHz SIS waveguide receiver," *Int. J. IR and MM Waves*, vol. 13, pp. 785-798, June 1992.
- [13] G. de Lange, C.E. Honingh, M.M.T.M. Dierichs, H.H.A. Schaeffer, J.J. Kuipers, R.A. Panhuyzen, T.M. Klapwijk, H. van de Stadt, M.W.M. de Graauw, E. Armandillo, "Quantum limited responsivity of a Nb/Al₂O₃/Nb SIS waveguide mixer at 460 GHz," in *proc. Fourth Intl. Symp. Space Terahertz Technology (UCLA)*, 1993.
- [14] G. de Lange, C.E. Honingh, J.J. Kuipers, H.H.A. Schaeffer, R.A. Panhuyzen, T.M. Klapwijk, H. van de Stadt, M.W.M. de Graauw, "Heterodyne mixing with Nb tunnel junctions at 720 and 840 GHz", *submitted to Applied Physics letters*.
- [15] M. Salez, P. Febre, W.R. McGrath, B. Bumble, H.G. LeDuc, "An SIS Waveguide Heterodyne Receiver for 600 GHz- 635GHz," *Intl. J. IR and MM Waves*, Vol 15, No.2, Feb. 1994.
- [16] K.F. Schuster, A.I. harris, K.H. Gundlach, "A 691 GHz SIS Receiver for Radio Astronomy," *Intl. J. IR and MM Waves*, Vol. 14, no. 10, Oct 1993.
- [17] M.M.T.M. Dierichs, C.E. Honigh, R.E. Honingh, R.A. Panhuyzen, B.J. Feenstra, A. Skalare, J.J. Wijnbergen, H. v.d. Stadt, and Th. de Graauw, "Evaluation of integrated tuning elements with SIS devices," *IEEE trans. Microwaves Theory and Techniques*, Vol. 41, No. 4, April 1993.
- [18] R.L. Kautz, *Journal of Applied Physics* 49, 308 (1978).
- [19] A.R. Kerr, N.J. Bailey, D.E. Boyd and N. Horner, "A study of materials for a broadband millimeter-wave quasi-optical vacuum window," Electronics Division Internal Report No. 292, National Radio Astronomy Observatory, Charlottesville, VA 22903, August 1992.
- [20] J. W. Lamb, "Infrared filters for cryogenic receivers," Electronics Division Internal Report No. 290, National Radio Astronomy Observatory, Charlottesville, VA 22903, April 1992.
- [21] T.H. Büttgenbach, T.D. Groesbeck, and B. Ellison, "A scale mixer model for SIS waveguide receivers," *Intl. J. Infrared and Millimeter Waves*, vol. 11, no. 1, 1990.

- [22] J. W. Kooi, M. Chan, T.G. Phillips, B. Bumble, and H. G. Leduc, "A low noise 230 GHz heterodyne receiver employing $0.25 \mu\text{m}^2$ area Nb/ AlO_x /Nb tunnel junctions," *IEEE trans. Microwaves Theory and Techniques*, Vol. 40, pp. 812-815, May 1992.
- [23] S. Padin, G. Ortiz. "A Cooled 1-2 GHz Balanced HEMT Amplifier," *IEEE, Microwave Theory and Techniques*, Vol 39, No 7, pp 1239-1243, 1991.
- [24] M.K. Brewer, and A.V. Räisänen, *IEEE Trans. Microwave Theory and Techniques*, Vol. 30, pp. 708, 1982.
- [25] D.P. Woody, R.E. Miller and M.J. Wengler, "85-115 GHz Receivers for Radio Astronomy," *IEEE trans. Microwaves Theory and Techniques*, Vol. MTT-33, 1985, pp. 90-95
- [26] K. Young, T.D. Groesbeck, A.E. Schinkel and G.R. Knapp, "*Astro-Physical Journal Letters*, in preparation.

AN AIRBORNE SIS-RECEIVER FOR ATMOSPHERIC MEASUREMENTS AT 625 TO 720 GHZ

J. Mees^a, S. Crewell^b, H. Nett^{b,c}, G. de Lange^d, H. van de Stadt^a,
J.J. Kuipers^d, and R.A. Panhuyzen^{a,d}

a) Space Research Organisation Netherlands (SRON), P.O. Box 800, 9700 AV Groningen, The Netherlands

b) Institute for Environmental Physics, University of Bremen, P.O. Box 330440, 28334 Bremen, Germany

c) presently at ESA/ESTEC, Mission Support, P.O. Box 299, 2200 AG Noordwijk, The Netherlands

d) Department of Applied Physics and Materials Science Centre, University of Groningen, Nijenborgh 4,
9747 AG Groningen, The Netherlands

Abstract

A heterodyne receiver using a SIS waveguide mixer with integrated horn and single backshort tuner has been built. It has been used for a series of airborne measurements of atmospheric trace gases, like HCl and ClO, above northern Europe during the winter of 1993/94. The receiver is suitable for measurements in the range of 625-720 GHz and shows stable performance in an airplane combined with high sensitivity. The best achieved noise temperature in the laboratory was $T_{DSB}=310$ K at 708 GHz and an all-over single sideband system noise temperature of $T_{SSB}=1500$ K at 625 GHz in the airplane.

Introduction

In a collaboration between the Laboratory for Space Research (SRON, Groningen) and the Institute of Environmental Physics (Bremen) the former submillimeter atmospheric sounder (SUMAS) [1,2,3,4] of the University of Bremen has been significantly improved by the use of a SIS junction as detection element instead of the conventional Schottky diode used before. First test flights of the new ASUR (Airborne Submillimeter SIS Radiometer) experiment onboard the German research aircraft FALCON were successfully performed in December 1993. Later, in February 1994 a flight campaign to northern Scandinavia was undertaken in order to measure atmospheric trace gases like ClO and HCl at the polar vortex. The system shows a significantly reduced overall noise temperature and good stability during flight. Due to this fact the emission lines of ClO and HCl could be measured with high temporal and spatial resolution.

Schottky diodes have been proven to be reliable heterodyne detectors for atmospheric and astronomical receivers over a wide range of frequencies up to several THz. However, Nb-tunnel junctions made out of a sandwich of superconductor-isolator-superconductor (SIS) offer today a significantly better sensitivity and wider bandwidth as non-linear mixing elements at frequencies up to 750 GHz than any other detector [5,6,7]. They were first used at lower frequencies only. Since then, the frequency range of SIS-mixer receivers could be highly increased - up to the superconducting gap frequency of Nb and above. This is due to great improvements in precision mechanical engineering, junction fabrication, and in the development of local oscillators for higher frequencies. This improvement in sensitivity is connected with the small disadvantage of lower operating temperatures (LHe₄) in comparison to Schottky diodes which can be operated at temperatures above 20 K. In this campaign it has been the first time that an airborne receiver with a SIS tunnel junction mixer has been used for atmospheric measurements of trace gases, like HCl and ClO, in the range of 625-720 GHz.

SIS-waveguide mixers are being developed at SRON for space applications like FIRST (far-infrared satellite telescope). Mixers have been made for 350 GHz [8], and in scaled versions [9] for 500 GHz and 750 GHz. A 1000 GHz mixer is under development. These mixers contain an integrated horn and a single backshort tuner and show besides a good beam pattern an excellent performance over the whole frequency band of the waveguide. Direct detection measurements with a Michelson spectrometer of Nb-junctions with integrated tuning elements demonstrate a broadband power incoupling. The bandwidth varies with the type of tuning network and can be as large as 170 GHz at 670 GHz. Heterodyne response has been obtained up to 840 GHz. Y-factor measurements in the laboratory show best double sideband noise temperatures of $T_{DSB}=310\text{K}$ (250K after correction for the beamsplitter transmission losses) at 708 GHz [10]. Single sideband noise temperatures of the complete receiver system can be as low as $T_{SSB}<1700\text{ K}$ in the range of 625-650 GHz measured during flight.

We will illustrate the sensitivity of our SIS-mixer around the gap-frequency and give an overview about the receiver design and its system performance. We will also show results of trace gas measurements during the flight campaigns.

Experiment description

Nb/Al₂O₃/Nb-tunnel junctions at SRON have an area of about 1 μm^2 and are fabricated with a Selective Niobium Over-Etch Process (SNOEP) [11]. Embedded in a matching and transforming network out of superconducting microstrips the junction impedance can be matched to the waveguide impedance at a broad range of frequencies. The mixer described here consists of a full-height wave guide measuring

300x150 μm^2 , with a single backshort and an integrated diagonal horn. The quartzchip with the junction lies across the waveguide and contains on-chip low-pass filter sections that prevent signal currents from leaking into the substrate channel.

We have successfully designed and fabricated several kinds of integrated tuning structures for different frequency regimes and bandwidths using SIS tunnel junctions as detectors. We studied the frequency response of waveguide mixers by means of a Fourier transform spectrometer (FTS) of the Michelson type. Video response could be obtained up to 750 GHz and quasiparticle heterodyne response was measured up to 850 GHz.

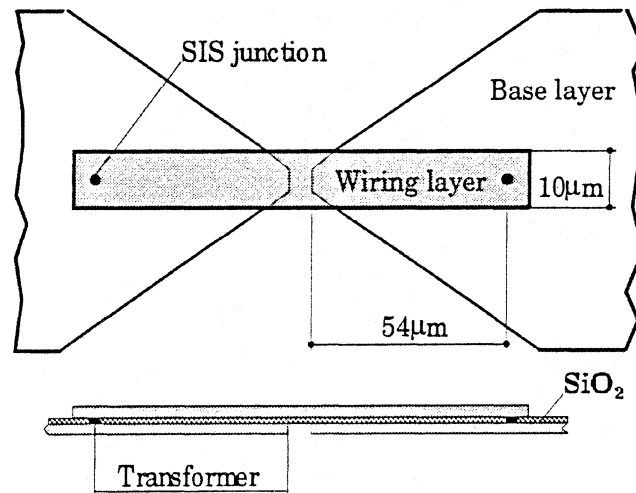


Fig. 1: Quartz chip with SIS-junction, tuning network and low-pass filter

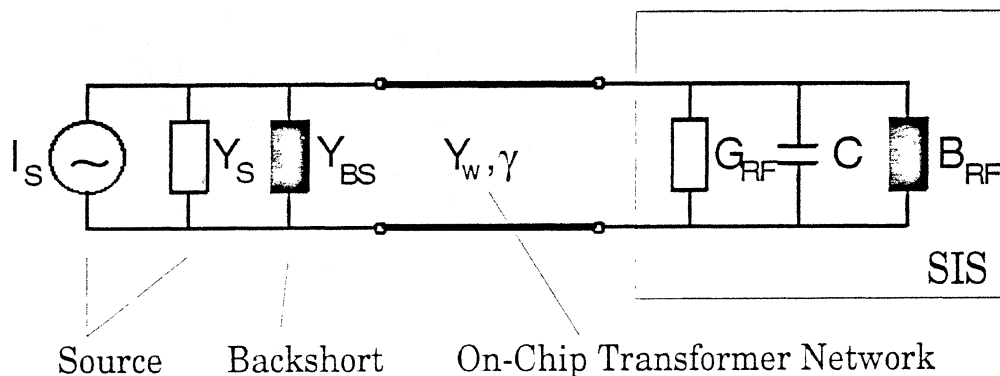


Fig. 2: Equivalent RF-circuit of the junction and environment.

Spectrometer measurements and tests in heterodyne experiments of various designs show that one-step transformers are most suitable for our purposes. This simple design, shown in Fig. 1, offers not only a broadband power incoupling to the junction but also a high sensitivity. It has been shown that transformer designs are most appropriate also for other detectors and environments. Two-step transformers offer up to 30% bandwidth in antenna-coupled designs. Complete on-chip filter structures with bandpass characteristics, e.g. Chebyshev filters, made out of superconducting striplines are possible [13].

Fig. 2 shows a simple equivalent electronic RF-circuit of a SIS junction and its surrounding waveguide. The junction is represented by the geometrical capacitance C , the non-linear admittance G_{RF} , and the susceptance B_{RF} . The latter are caused by internal quantum effects. The transformer network is represented by a lossy microstrip line with the characteristic admittance Y_w and wavenumber γ . The superconducting microstrip designs were calculated by means of the Mattis-Bardeen theory [12]. The admittance of the waveguide is assumed to be real and the influence of the backshort purely imaginary. Two FTS spectra show (Fig. 3) the video response due to the coupling of the SIS junction to an integrated tuning network. In both cases single-step transformers, $10\ \mu\text{m}$ wide and $54\ \mu\text{m}$ long, are used for coupling to the waveguide. The single element B6 shows a broad 3dB-bandwidth of about 125 GHz and sample B3 with two junctions in series with 90 GHz a somewhat smaller bandwidth. Both samples have the same resonance frequency of about 640 GHz.

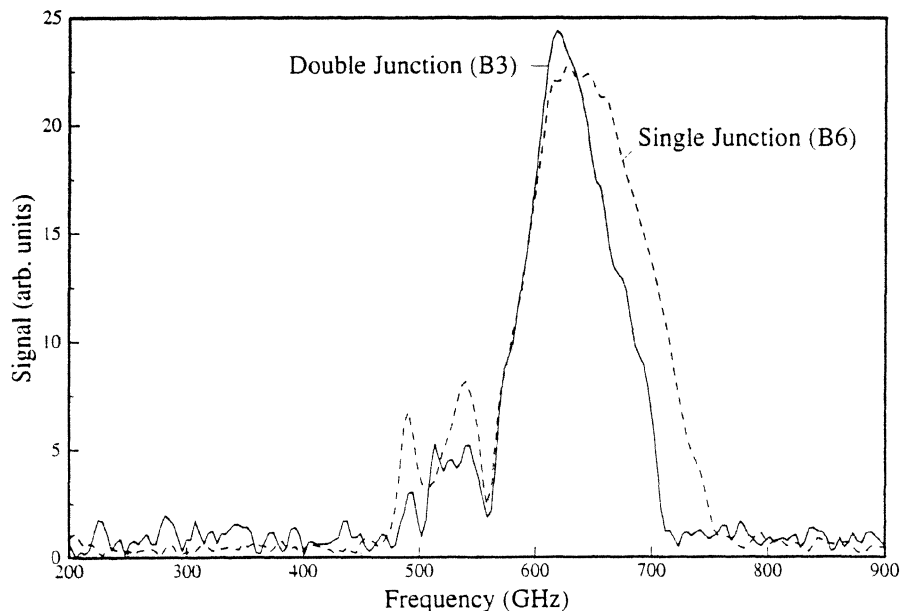


Fig. 3: FTS response of single junction B6 and double junction B3.

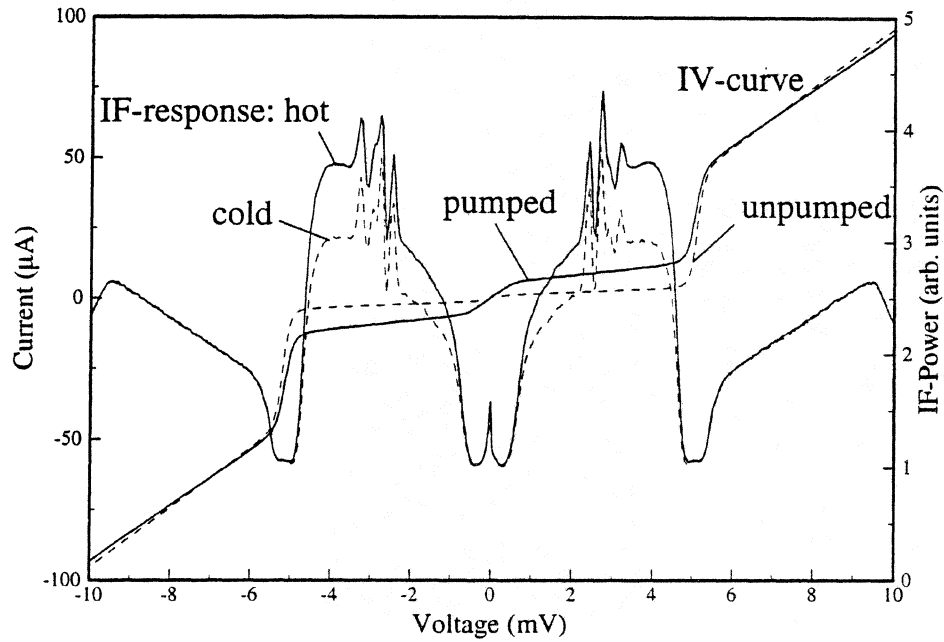


Fig. 4: Pumped and unpumped IV-curve of sample B3 with hot (300K) and cold (80K) IF-response at 680 GHz.

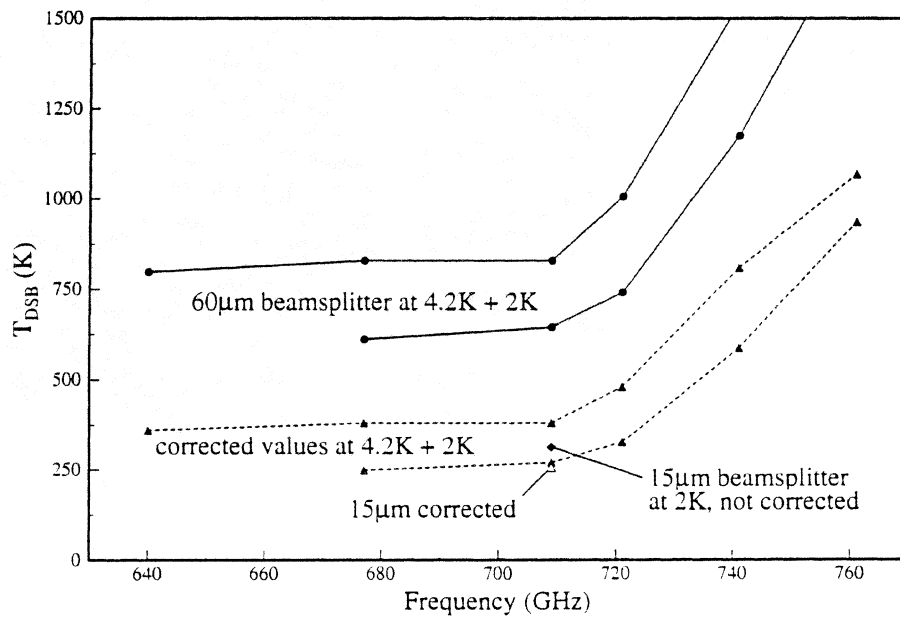


Fig. 5: Double sideband noise temperature T_{DSB} of sample B3 for different operating temperatures and frequencies from 640-750 GHz. The corrected values for T_{DSB} are also shown if the beamsplitter losses are taken into account.

Laboratory heterodyne tests showed a slightly better performance of the sample B3. Therefore sample B3 was used during all further laboratory tests and flight experiments. Fig. 4 shows its DCIV-curves, unpumped and pumped by the local oscillator at 680 GHz, together with the IF heterodyne response arising from a hot (300K) and cold (80K) load. The IF response shows also some remaining structures of the Josephson effect that could not be suppressed completely by the applied magnetic field.

Fig. 5 shows the laboratory heterodyne performance characterized by the double-sideband noise temperature T_{DSB} for different operating temperatures and frequencies from about 640 GHz up to 750 GHz. The two upper curves show measurements with a mylar beamsplitter of 60 μm thickness at 4.2 and 2 K He bath temperature. Curves that are corrected for the losses of the beamsplitter are shown below. To verify these corrections a measurement with a 15 μm thin beamsplitter was investigated. This measurement yields $T_{DSB}=310$ K at 708 GHz at 2 K physical temperature and is the lowest value above the gap frequency reported. The corrected value of this measurement is 250 K and lies within 5 K of that of the measurement with the 60 μm thick beamsplitter. Due to the lack of oscillator power more measurements with the 15 μm beamsplitter at other frequencies could not be performed. The tuned heterodyne bandwidth is rather wide (630-720 GHz), but could not be completely measured for the same reason.

Quasi-optics

The atmospheric signal was entering the airplane through a wedge-edged window especially designed for that frequency range to avoid standing wave problems. A rotating mirror was pointing in an alternating cycle to the window and to calibration loads at 300 and 80 K. A corner-cube wavelength modulator was used to eliminate the remaining standing wave problems. Two Martin-Puplett type interferometers were used as a single sideband filter (SSB) and as a diplexer in order to combine the atmospheric and the LO signal. A combination of an elliptical mirror and a cooled high-density polyethylene (HDP) lens in front of the mixer determined the optical system. The complete optical system was calculated with Gaussian beam optics to minimise losses in the optical system. The beam radius along the optical path was always smaller than 12.5 mm, since the aperture diameter of most optical components was 50 mm. The asymptotic angle of growth of the receiver beam radius is 0.7° .

The LO power requirement of a SIS junction is much smaller than that of a Schottky diode and the LO emits far more power than necessary for a SIS junction. We implemented therefore in the LO path a polarising wiregrid that can be rotated to attenuate the signal. The location of the grid in the LO path is just before the signal path entry. Fig. 6 shows a schematic layout of the optics.

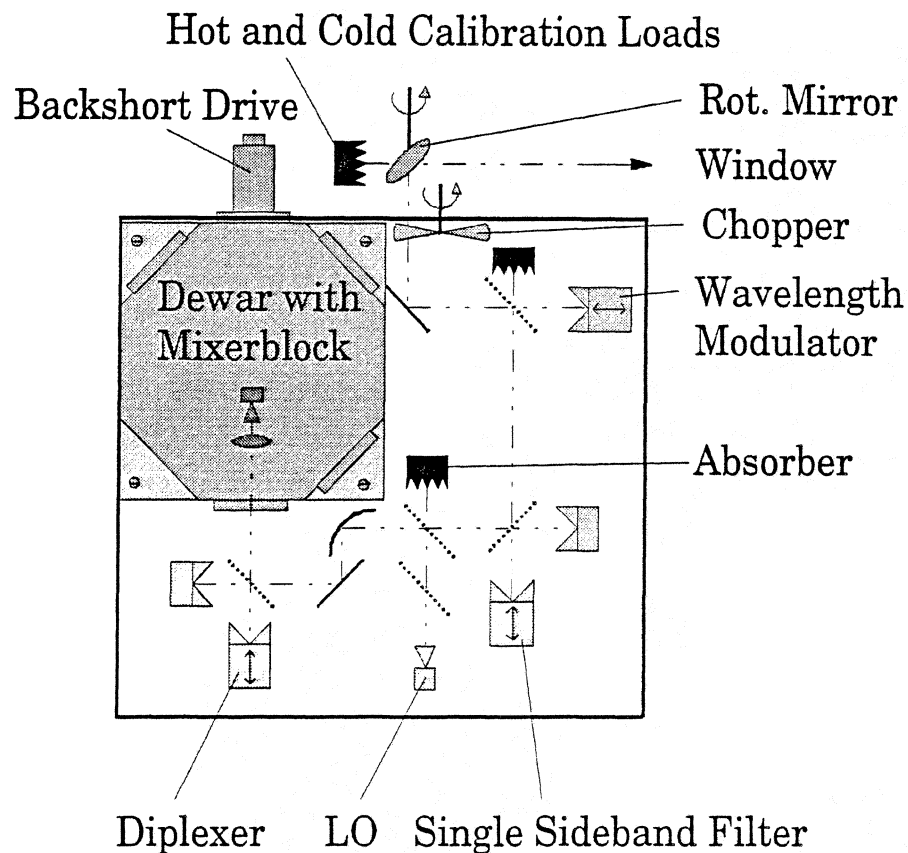


Fig. 6: Schematic layout of the quasi-optics.

Detector and IF-system

The electrical layout of the receiver system is shown in Fig. 7. Two solid state oscillators from Radiometer Physics served for the different frequency bands as local oscillator (1. LO) and were exchanged in various flights. One operated at 637-639 GHz to serve the lower frequency bands while the other radiated at 675 GHz for the higher frequency bands. The IF frequency was chosen to be 11.08 GHz, to cover with both sidebands interesting molecular lines. Switching between measurements of those lines can be done by adapting the single sideband filter (SSB).

The junction IF output was coupled over a commercial bias tee and an isolator directly to the first IF amplifier. As a first stage served a low-noise HEMT amplifier from Berkshire Technologies that was mounted inside the dewar at the 4K stage. The noise temperature of this amplifier is below 15 K for the

whole frequency band, from 10-12 GHz. The IF signal was amplified one more time and filtered before it was mixed down to 3.7 GHz by means of a second mixer.

The IF output towards the backend is centred at $f_{IF}=3.7$ GHz with a bandwidth of 1200 MHz. The power level varies between 0 and 10 dBm. The backend consists of an acousto-optical spectrometer (AOS), two filterbanks and a UNIX system for the data retrieval. The power is distributed via directional couplers to the different spectrometers and two sensors that register the power level. One fast detector, a RF Schottky diode, is used for bias sweeps made visible on an oscilloscope to optimise the SIS mixer. The slower sensor is a HP power meter whose measurements are taken permanently as housekeeping data by the computer system.

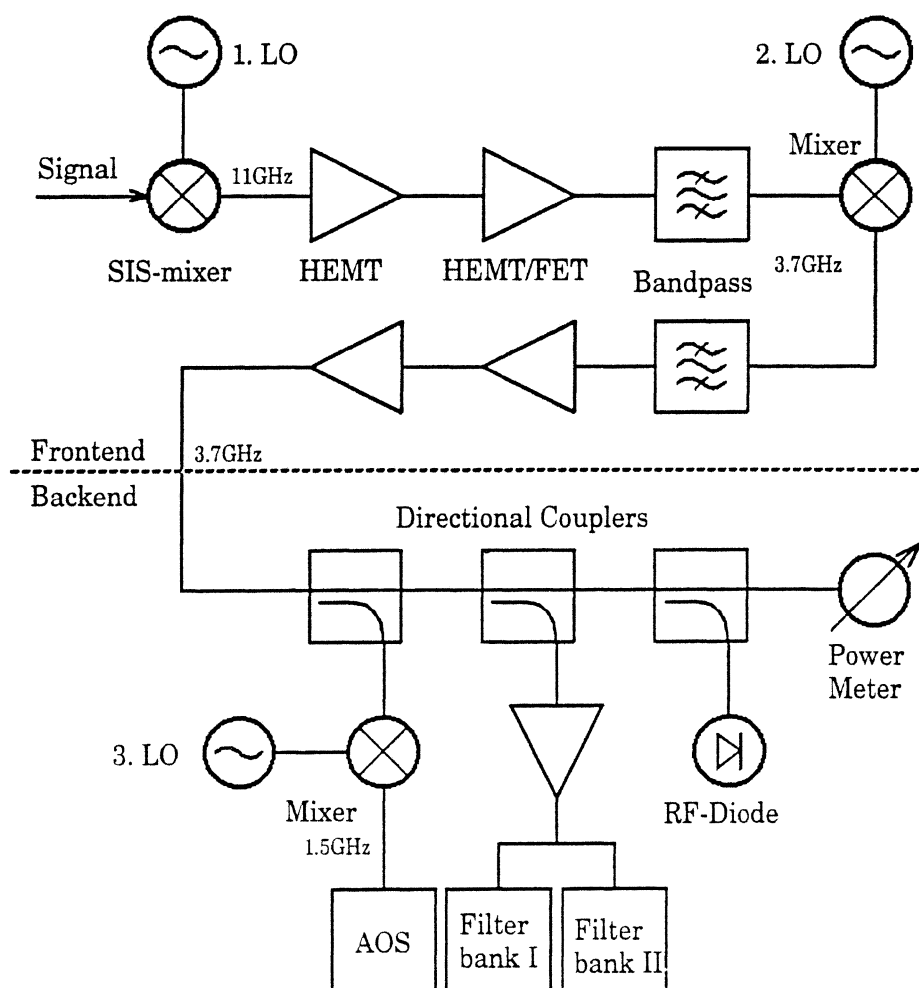


Fig. 7: IF-system

The resolution and the bandwidth of the AOS are described later in the chapter about the system performance. One of the filterbanks has been on loan from the Max-Planck-Institute for Aeronomy in Lindau/Katlenburg. The filterbanks have a central frequency of 3.7 GHz with 28 channels. The 8 channels in the centre have a bandwidth of 8 MHz each. On both sides of the centre are 4 channels with 40 MHz and 5 channels with 80 MHz bandwidth, respectively. This is done to cover a large bandwidth with a small number of channels, while simultaneously obtaining a high resolution in the centre.

The UNIX system is used to control important parts, e.g. the rotating mirror, of the experiment and to retrieve the data. It stores the data on tape together with housekeeping data from various sensors and gives an on-line quick-look of the obtained data and spectra.

Measurement campaign

The receiver system was built into a Falcon aircraft operated by the German space agency DLR in Oberpfaffenhofen. During the winter 1993/94 a total of 8 observation flights were made, five solely in an observation campaign to Kiruna in northern Sweden and above the polar sea. The flight campaign to Kiruna covered the time from February 7th to 18th, 1994. The typical flight time was about 2.5-3 h and covered a distance of about 2000 km. Measurements of 4 molecules were made at 6 different frequencies ranging from 625-686 GHz as listed in Table 1.

The flights were coordinated for comparison of the data with other experiments, like the balloon borne Submillimeter Limb Sounder (SLS) of the Jet Propulsion Laboratory, the MLS experiment on-board the UARS satellite² and a German research aircraft (Transall), which contained several instruments for trace gas measurements (O₃, ClONO₂, HNO₃, ...).

System Performance

During all flights the receiver frontend and the filterbank system showed an excellent performance. Only the acousto-optical spectrometer was not operational during the first flights due to electronic problems. However, the complete measurement program could be successfully completed as planned.

The overall system noise temperature (single sideband) were measured continuously by a powermeter during the flights and stored by the computer system on tape. These data compare well with the noise temperatures obtained from single channels of the AOS and the filterbanks. During a typical flight usually several molecules were measured. Switching from the upper into the lower sideband was done by tuning the SSB filter. The observation of ClO and HCl in one flight was of greatest interest and made it

² Microwave Limb Sounder on-board the Upper Atmospheric Research Satellite

also necessary to tune the LO to a new frequency. In either case optimisation of SIS bias voltage, back-short and diplexer position, and LO power level was necessary. In general, tuning to a new frequency band needed about 5-10 min.

The noise temperatures achieved for each molecule are shown in Table 1. Since the receiver has had to be tuned in a relatively short time the listed numbers may not represent the lowest reachable noise temperatures. The system noise temperature increased, as expected, towards higher frequencies. The over-all single sideband noise temperatures T_{SSB} given in Tab. 1 are somewhat higher than the laboratory measurements in Fig. 5. To compare both measurements the double sideband noise temperatures T_{DSB} have to be doubled and 300 K added for the warm sideband termination. Because the laboratory measurements have been performed using a simple set-up the residual differences can be explained by losses due to polarisation selection and in the optical system.

The AOS covers about 880 MHz containing 2000 channels with an effective resolution of 1.4 MHz. Fig. 8 shows the system noise temperature over the AOS bandwidth. For data analysis the bandwidth is restricted to 620 MHz where the noise temperature is relatively constant. In Fig. 8 four channels at a time are added to one data point to increase the signal to noise ratio. This results in an effective resolution of 2.8 MHz. The outer channels are not taken into account, because of their higher noise level.

Molecule	Frequency [GHz]	T_{sys} [K]
HCl	625.913±0.6	1.500
N ₂ O	627.286±0.6	1.500
O ₃	648.073±0.6	1.900
ClO	649.448±0.6	1.700
O ₃	664.300±0.6	1.950
ClO	686.460±0.6	2.300

Table 1: Mean system noise temperature (single sideband) for different molecules over the measured frequency band

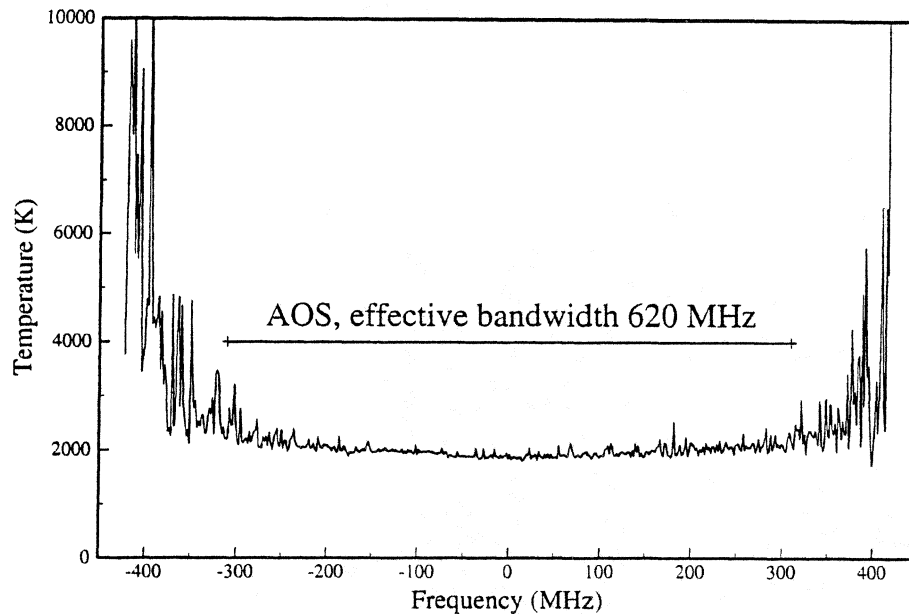


Fig. 8: System noise temperature over the AOS bandwidth. For data analysis the outer channels are not taken into account, because of the higher noise level there.

Measurements

To obtain the submillimeter emission spectra the raw data were calibrated with the measurements of the hot and cold calibration load. They were corrected for the window transmission and integrated to obtain sufficiently low signal to noise ratio. Only spectra above 30,000 feet with a roll angle lower than three degrees and a stable power level were used. Fig. 9 shows as an example the spectrum of HCl with an integration time of 630 sec together with a calculated spectrum at 625 GHz. Differences in the power levels of the measured and calculated spectra are due to different water vapour levels. The spectrum of ClO at 649 GHz was integrated during 562 sec and exhibits an amplitude of ~ 1.5 K (Fig. 10). There is also some indication for an additional, weak $^{18}\text{O}_3$ line in the vicinity of ClO.

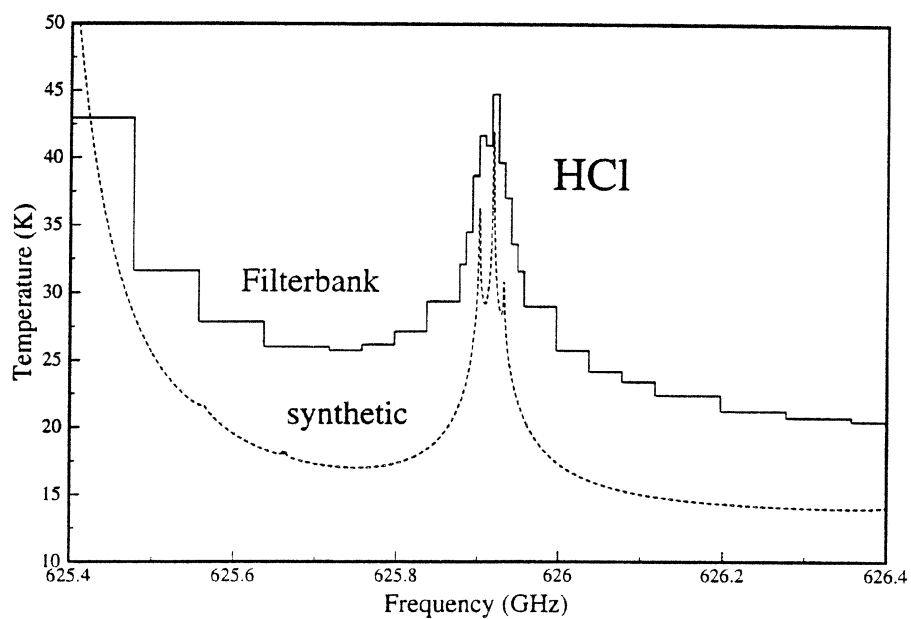


Fig. 9: Synthetic and measured spectra of HCl at $f=625.9168$ GHz measured on February 15, 1994. The integration time is 630 sec and the rms error 0.07 K.

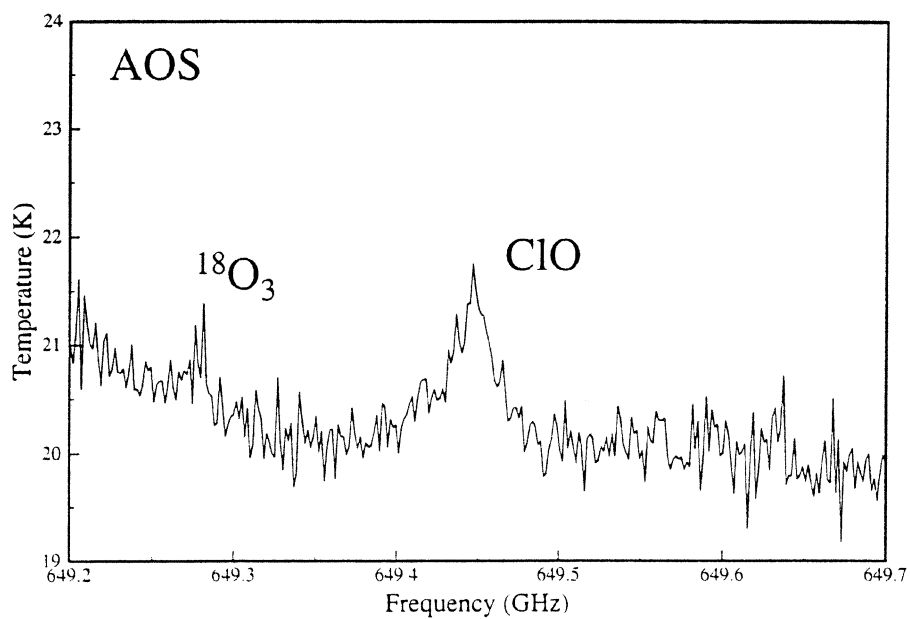


Fig. 10: AOS spectrum of ClO at $f=649.448$ GHz measured on February 15, 1994. The integration time is 562 sec and the rms error 0.1 K.

Conclusions

The application of a SIS tunnel junction mixer in airborne measurements in the frequency range from 625 to 720 GHz has been successfully demonstrated. The sensitivity compared to the former Schottky detector is about three times higher. The broadband response is due to the use of an integrated tuning network with a single-step microstrip transformer. During a series of eight flights in winter 1993/94 measurements of four different molecules at six different frequency bands could be performed with high spectral and spatial resolution. The lowest noise temperatures so far achieved are about $T_{\text{DSB}}=310$ K at 708 GHz in the laboratory and $T_{\text{SSB}}=1500$ K at 625 GHz for the complete receiver system in the airplane. This successful campaign has shown that airborne measurements using an appropriate extremely low-noise receiver is a convenient technique for fast and accurate investigation of trace gases in situations of disturbed atmospheric chemistry.

Acknowledgements

We acknowledge the help and support of H. Golstein, W. Horinga, G. Naeveke, D. Nguyen, H. Schaeffer, and B. Vahlenkamp, who designed and built electronic and mechanical components for the integration of the SIS mixer. U. Klein and J. Wezelman helped in the optical design and with the measurements. We thank J. Urban and H. Kuhlmann for support during the flight campaign and B. Franke, J. Wohlgemuth, T. Wehr, and J. Langen who participated in the data analysis and program developments. An important part of this work, the development of the SIS mixer, is based on the mixer work and filter design of C.E. Honingh. We thank P. Hartogh from the Max-Planck-Institute for Aeronomy in Lindau/Katlenburg for the loan of a filterbank. We acknowledge the continuous assistance of K. Künzi, T. de Graauw, and E. Armandillo. We are grateful for the help and support through the crew of the Falcon and, in general, through the DLR in München and Kiruna.

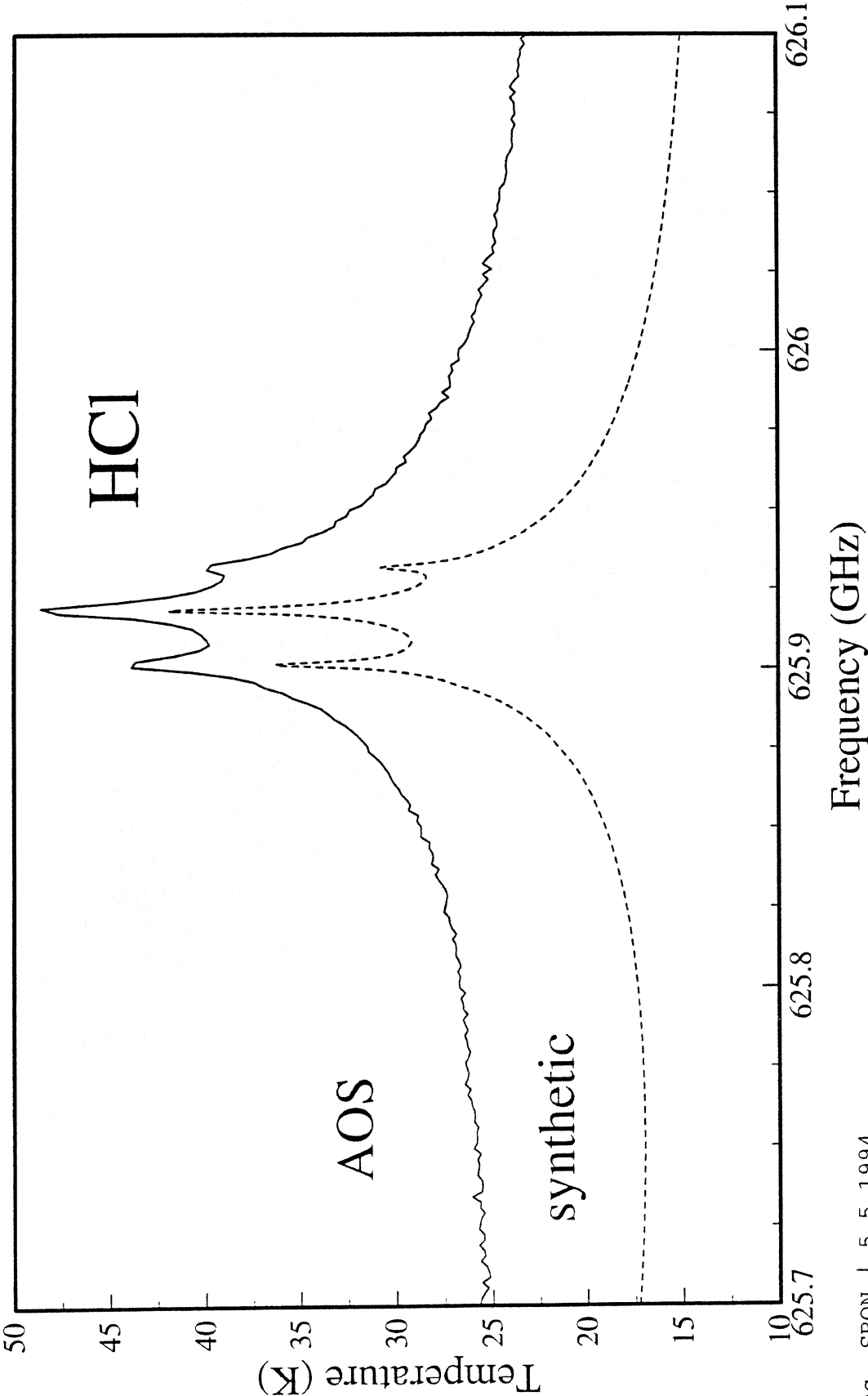
This work was supported by ESA under ESTEC contract No. 10655/93/NL/SF and by the German Ministry for Research and Technology under contract No. BMFT 01 LO 9320/0.

References

1. H. Nett, S. Crewell, U. Klein, and J. Langen, "Submillimeter-wave radiometry", European Polar Ozone Workshop, Schliersee, FRG, Oct. 1990, Air Pollution Research Report 34, ISBN 2-87263-060, pp. 81-84, 1990
2. H. Nett, S. Crewell, K. Künzi, "Heterodyne detection of stratospheric trace gases at submillimeter-wave frequencies", Int. Geoscience and Remote Sensing Symposium Helsinki, Finland, 1991, IEEE Cat. No. 91CH2971-0, Vol. 1, pp. 201-204, 1991
3. H. Nett, S. Crewell, K. Künzi, "A 625-650 GHz heterodyne receiver for airborne operation", 16th Int. Conf. on Infrared and Millimeter Waves, Symposium Digest Vol. 1576, pp. 470-461, 1992.

4. S. Crewell, P. Hartogh, K. Künzi, H. Nett, T. Wehr, "*Aircraft Measurements of ClO and HCl during EASOE 1991/92*" Geophys. Res. Letters, Special Issue on EASOE, (accepted).
5. J. Zmuidzinas, H.G. LeDuc, J.A. Stern, and S.R. Cypher, "*Two-junction tuning circuits for submillimeter SIS mixers*", IEEE Trans. Microwave Theory Tech., (accepted)
6. J.W. Kooi, C.K. Walker, H.G. LeDuc, T.R. Hunter, D.J. Benford, and T.G. Philips, "*A low noise 665 GHz SIS quasiparticle waveguide receiver*", submitted to IEEE Trans. Microwave Theory Tech.
7. M. Salez, P. Febvre, W.R. McGrath, B. Bumble, H.G. Leduc, "An SIS waveguide heterodyne receiver for 600-635 GHz", Intern. J. of Infrared and Millimeter Waves Vol. 15, No. 2, pp. 349-369, 1994
8. C.E. Honingh, G. de Lange, M.M.T.M. Dierichs, H.H.A. Schaeffer, Th. de Graauw, T.M. Klapwijk, "*Performance of a two-junction array SIS mixer operating around 345 GHz*", IEEE Trans. MTT. Vol. 41, No. 4, pp. 616-623, 1993
9. G. de Lange, C.E. Honingh, J.J. Kuipers, H.H.A. Schaeffer, R.A. Panhuyzen, T.M. Klapwijk, H. van de Stadt, and M.W.M. de Graauw, "*Heterodyne mixing with Nb tunnel junctions above the gap frequency*", to appear in Appl. Phys. Lett. Vol. 64 (22), May 1994
10. J. Mees, G. de Lange, A. Skalare, C.E. Honingh, S.V. Shitov, R.A. Panhuyzen, H. van de Stadt, Th. de Graauw, T.M. Klapwijk, "*SIS mixers around the gapfrequency*", SPIE International Conference on Millimeter and Submillimeter Waves and Applications, San Diego, 1994
11. M.M.T.M. Dierichs, R.A. Panhuyzen, C.E. Honingh, M.J. de Boer, T.M. Klapwijk, "*Submicron niobium junctions for submillimeter-wave mixers*", Appl. Phys. Lett. Vol. 62, pp. 774-776, 1993
12. R.L. Kautz, "*Picosecond pulses on superconducting striplines*", Journal of Applied Physics Vol. 49 (1), pp. 308-314, 1978
13. J. Mees, M. Nahum, and P.L. Richards, "*New Designs for antenna-coupled superconducting bolometers*", Appl. Phys. Lett. 59 (18), 1991

Emission spectrum of HCl at 625.917 GHz
ASUR campaign Feb. 1994, 630 sec. integration time



A SUPERCONDUCTING HOT ELECTRON BOLOMETER MIXER FOR 530 GHz

A. Skalare, W. R. McGrath, B. Bumble, H. G. LeDuc
*Jet Propulsion Laboratory, Center for Space Microelectronics Technology,
California Institute of Technology,
4800 Oak Grove Dr., Pasadena, CA 91109*

P. J. Burke, A. A. Verheijen, D. E. Prober
*Dept. of Applied Physics, Yale Univ., P.O. Box 208284,
New Haven, CT 06520-8284*

ABSTRACT

The paper describes a superconducting hot electron bolometer mixer that uses diffusion rather than interactions with phonons as a cooling mechanism for the hot electrons. The bolometer is a 0.14 μm wide niobium microbridge with a length less than 0.5 μm . The submicron length ensures rapid diffusion of the hot electrons into contacting gold films. This mechanism is believed to be fast enough to allow mixer operation with intermediate frequencies of several GHz. An electron cooling time of 55 ps is inferred from DC resistance versus temperature measurements, indicating a roll-off frequency close to 3 GHz. Initial receiver measurements using a two-tuner waveguide mixer confirm heterodyne mixing at 532 GHz with an intermediate frequency of 1.4 GHz.

INTRODUCTION

In recent years SIS devices have been used successfully for low noise astronomical receivers in the millimeter and submillimeter wave bands. There is a concern, however, that the superconducting energy gap will limit the performance of SIS mixers at frequencies above 1 THz. An alternative to SIS junctions above the gap frequency may be superconducting hot electron bolometer mixers, since the response of these should in principle be as good above the gap frequency as below. These bolometers do however have a limitation in the intermediate frequency (IF) bandwidth due to the finite time required to cool the heated electrons. This is a significant issue, since a bandwidth of at least 500-1000 MHz is required for astronomical observations. Other groups [1,2] have studied devices where the hot electrons are cooled by electron-phonon interaction, which for Nb films gives a cooling time of ~ 1 ns and an IF roll-off at around 160 MHz. A receiver using a NbN bolometer, however, has recently demonstrated mixing at an intermediate frequency of 1.4 GHz [3].

We are investigating a different approach, where the hot electrons are allowed to diffuse out at the ends of the bolometer into a contacting normal metal film. If the device is very short, less than 0.5 μm , the thermal conductance associated with the diffusion process can dominate by a factor of more than 10 over that due to the electron-phonon interaction, leading to predicted intermediate frequencies as high as 4 GHz.

One of the two objectives with the measurements presented here was to use the resistance versus temperature curve of a diffusion cooled bolometer to determine its thermal conductance, and to calculate from this value the highest usable intermediate frequency. The other objective was to adapt an existing 547 GHz SIS receiver for use with hot electron bolometers, and to attempt to make heterodyne measurements in this frequency regime.

BOLOMETER DESIGN AND FABRICATION

The bolometer consists of a niobium microbridge 0.14 μm wide and 10 nm thick. Different devices were fabricated with lengths ranging from 0.14 μm to 0.5 μm . The length was determined by varying the spacing of the gold pads that overlap the microbridge, see Fig.1. All bolometers were fabricated on 100 μm thick fused quartz wafers, which were lapped down to 50 μm after the device formation.

The first step in the device fabrication is the definition of the base wiring layer, which was patterned onto the quartz substrate using an optical lift-off process. The layer consists of 110 nm of magnetron sputtered Nb and 30 nm of evaporated Au. The device layer is then fabricated by a blanket deposition of 10 nm of Nb followed by 10 nm of Au. An etching mask of 30 nm of Cr is patterned using e-beam lithography with PMMA, which defines the bolometer. The microbridge is produced by Ar sputtering of the gold, followed by reactive ion etching of the Nb with a mixture of $\text{CCl}_2\text{F}_2 + \text{CF}_4 + \text{O}_2$. The chromium etch mask was subsequently stripped by a commercially available wet etch. The 100 nm thick gold leads were evaporation deposited using an e-beam defined PMMA lift-off mask. The 10 nm thick gold layer on top of the Nb bolometer was then removed by an Ar sputtering step. The finished devices were passivated by deposition of 40 nm of SiO in a lift-off process.

CALCULATED THERMAL RESPONSE TIME

The voltage responsivity of the bolometer can be written [4] :

$$S = I \cdot \frac{dR}{dT} \cdot \frac{1}{G \cdot (1 + \omega_{IF}^2 \tau^2)^{1/2}} \quad (\text{V/W}) \quad (\text{Eq. 1})$$

where I is the DC bias current, R is the microbridge resistance, T is the temperature, G is the thermal conductance between the hot electrons and the thermal bath, ω_{IF} is $2\pi \times$ the intermediate frequency, and τ is the thermal response time (cooling time) of the hot electrons. The response time is $\tau = C / G$, where C is the electronic specific heat of the bolometer.

From Eq.1 it is clear that the response rolls off at the frequency :

$$f_0 = \frac{1}{2\pi\tau} \quad (\text{Hz}) \quad (\text{Eq. 2})$$

The electronic specific heat of the bridge is given by:

$$C = \gamma \cdot T \cdot V \quad (\text{J/K}) \quad (\text{Eq. 3})$$

where V is the volume of the niobium microbridge and $\gamma \approx 700 \text{ J/K}^2\text{m}^3$ (experimental bulk value).

The Wiedemann-Franz law gives the ratio of the electronic thermal conductivity to the electrical conductivity. This predicts :

$$G_{WF} = \frac{\pi^2}{3} \left(\frac{k_B}{q_e} \right)^2 \cdot \frac{T}{R_{Eff}} \approx 2.44 \cdot 10^{-8} \cdot \frac{T}{R_{Eff}} \quad (\text{W/K}) \quad (\text{Eq. 4})$$

In our case $R_{Eff} = R/12$. This is an effective resistance that corrects for the distributed heat dissipation and for the two heat sinks at opposite ends of the microbridge [4]. The resulting value of the thermal response time is given below, and should be used in Eq. 1 if it is much smaller than the electron-phonon time.

$$\tau_{WF} = C / G_{WF} \quad (\text{s}) \quad (\text{Eq. 5})$$

MEASURED THERMAL RESPONSE TIME

The thermal conductivity G can be estimated from measuring the resistance versus substrate temperature characteristic for a bolometer at different DC bias currents. Figure 2 shows such a measurement for a $0.2 \mu\text{m}$ long microbridge. The power dissipated in the device by the DC current heats the electrons above the substrate temperature, thereby shifting the R - T curve. The shift in temperature for any given R is equal to the difference in dissipated power $(I_1^2 R - I_2^2 R)$ divided by G . The difference in dissipated power versus the shift in temperature for three pairs of currents (I_1, I_2) and several values of R is plotted in Fig.3. The slope of the fitted curve is the experimental value of G .

Table 1 compares the experimental value G_{Exp} to the Wiedemann-Franz limiting case G_{WF} for two bolometers of different lengths. It also lists the heat conductivity of the electron-phonon interaction $G_{el-ph} = 4 \cdot A \cdot T^3 V$, where $A \approx 1.1 \cdot 10^{10} \text{ W/K}^4 \text{m}^3$ [5]. As shown in the table, the experimental heat conduction is significantly better than that of the electron-phonon interaction, but it is less than that predicted by the Wiedemann-Franz law. The experimental values of the heat conduction together with the specific heat according to Eq. 3 above give estimated IF roll-off frequencies of close to 3 GHz for both bolometers.

Table 1 : Comparison of calculated and experimental values of thermal conductance, time constant and IF roll-off frequency. Two expressions used in creating the table are $\tau_{Exp} = C / G_{Exp}$ and $IF_{Max} = 1 / (2\pi \cdot \tau_{Exp})$. The device temperature is taken to be 5.2 K, and the width is $0.14 \mu\text{m}$.

Length [μm]	Resistance [Ω]	C [J/K]	G_{el-ph} [nW/K]	G_{WF} [nW/K]	G_{Exp} [nW/K]	τ_{Exp} [ps]	IF_{Max} [GHz]
0.14	12.1	$7.1 \cdot 10^{-19}$	1.2	127	12.5	57	2.8
0.2	18.3	$10.2 \cdot 10^{-19}$	1.7	83	18.5	55	2.9

MIXER MEASUREMENTS

Mixer measurements were carried out using a waveguide SIS receiver for 547 GHz [6]. The quartz chips with the bolometers were glued into a two-tuner mixer block, as shown in Fig. 4. The contacting sliding tuners were made from beryllium copper, and the DC and IF connections were made by wire bonding the device to the mixer block and to a matching circuit. The mixer block was mounted onto the 4 Kelvin cold surface of a vacuum cryostat, as shown in Fig. 5. A 1 k Ω metal film resistor in thermal contact with the mixer block was used as a heater to vary the temperature of the bolometer. The temperature of the block was monitored by a diode sensor. Because of temperature gradients in the mixer block, however, we found that the thermal noise power in the intermediate frequency band provided a more accurate way of measuring the device temperature. No feed-back loop was needed for the temperature control, as the diode sensor temperature versus heater voltage was reproducible to within 20 mK over a period of several hours. As shown in Fig.5 the beam from the signal source is focussed into the dual-mode conical feedhorn of the mixer block using off-axis elliptical mirrors. Two fluorogold infrared filters are placed in the beam path inside the cryostat, to reduce room temperature heat flux into the mixer.

The signal source was a $\times 2 \times 3$ multiplier that was pumped by two Gunn oscillators as shown in Fig.5. Gunn 1 in the figure was used to pump the multiplier at the frequency $f_{\text{Gunn 1}}$, thereby providing the local oscillator (LO) for the hot electron bolometer at $6 \times f_{\text{Gunn 1}}$. The second Gunn was used to inject a small amount of power at frequency $f_{\text{Gunn 2}}$ into the multiplier through a -20 dB coupler. This resulted in additional output power from the multiplier at a frequency $5 \times f_{\text{Gunn 1}} + f_{\text{Gunn 2}}$, thus providing a monochromatic signal. The reason that we used this source configuration was that only one multiplier was available for the experiments. The frequencies of the two Gunn oscillators could be independently measured with a frequency counter (Fig.5).

The 1.4 GHz intermediate frequency (IF) system is shown in Fig.6. The cooled amplifier had a nominal noise temperature of 5.6 K, but due to the other components in the system the total IF noise temperature was between 6.5 and 7.0 K, depending on the IF impedance of the device in the mixer block. Several configurations of the room temperature part of the IF system were used, giving total gain values from the mixer to the power meter ranging from 90 to 105 dB. Part of the IF output power was coupled to a spectrum analyzer, to verify the heterodyne response with the monochromatic signal source.

The bolometer used in the mixing experiments had a length of 0.2 μm , and a width of 0.14 μm . The normal resistance was 23.5 Ω . Fig. 7 shows two I-V curves. The first was measured on a dip-stick with the device immersed in liquid helium. The second was measured in the receiver cryostat, where the device was slightly warmer.

The receiver measurements were made at a local oscillator frequency of 532 GHz with the signal in the upper sideband. The temperature at the sensor on the outside of the mixer block was 4.6 K, but the actual temperature of the bolometer was a few tenths of a Kelvin lower. Figure 8 shows the IF spectrum for five different frequency settings of the signal Gunn oscillator. Shifting the monochromatic signal frequency causes a corresponding shift in the IF spectrum, which shows that the response is heterodyne. We also verified that the measured frequency of the IF signal equals the difference between the measured frequencies of the two Gunn oscillators. The mixer output shows a maximum at

a bias voltage of about 0.1 mV, as shown in Fig.9 . The figure shows the total output power in the intermediate frequency band with and without a signal. It also shows one pumped (with local oscillator power at 532 GHz) and one unpumped (no local oscillator power) I-V curve. In this measurement the total gain in the amplifier chain was ~94 dB, not including the mismatch between the device and the 105 Ω IF system.

When the mixer block was heated, the mixer output signal decreased. The data in Fig.10 was prepared by subtracting the output powers with and without signal at a few different temperatures. The local oscillator and signal power levels were held constant for the data points in the figure. As can be seen, the mixer output fell rapidly as the bolometer approached the critical temperature of the niobium film, which was 5 to 5.5 K. The temperatures in Fig.10 were inferred from measurements of the thermal noise in the intermediate frequency band from the device at zero bias current. Due to small uncertainties in the calibration of the intermediate frequency amplifier chain, we estimate the systematic error in the temperature readings to be approximately 0.4 K .

When the device is in the limit of small heating of the electrons above the bath temperature by the DC current, the temperature in the Wiedemann-Franz law may be approximated by the bath temperature T_b . This leads to a temperature increase for the hot electrons that is proportional to the DC power P_0 , so that $(T_h - T_b) \propto P_0 = R \cdot I_0^2$ where T_h is the hot electron temperature. The hot electron temperature increase should be proportional to I_0^2 . For large DC bias currents this approximation is incorrect, and instead the Wiedemann-Franz law leads to the dependence $(T_h^2 - T_b^2) \propto P_0 = R \cdot I_0^2$. This means that for large bias currents the hot electron temperature should increase in proportion to I_0 . This would cause the output thermal noise power from the device to increase in proportion to I_0 instead of I_0^2 . This linear dependence can be observed in Fig. 11 . It should be pointed out, that a linear dependence of output noise power with current can also be indicative of shot noise. This requires, however, that a tunneling barrier is present in the device. At this point we are not aware of any such barrier.

SUMMARY

The resistance versus temperature measurements of the 0.2 μm long electron diffusion cooled bolometer indicates that the thermal conductivity is approximately 18.5 nW/K. Together with an estimated electronic specific heat of $10.2 \cdot 10^{-19}$ J/K this gives a thermal response time of 55 ps, leading to an estimated highest intermediate frequency of 2.9 GHz. This would clearly be sufficient for heterodyne receivers for submillimeter astronomy. The shorter (0.14 μm) bolometer gave similar results, namely 57 ps and 2.8 GHz.

A quartz chip with a 0.2 μm long bolometer was mounted into an existing waveguide block SIS receiver. Measurements using a local oscillator and monochromatic source confirm that the bolometer shows heterodyne response at a local oscillator frequency of 532 GHz and an intermediate frequency of 1.4 GHz. The strongest mixing is seen at bias currents slightly above the non-linearity in the I-V curve. The IF signal output power decreases strongly with temperature, which suggests that the heterodyne response will be even stronger with the device cooled to lower temperatures than in our present measurements.

At high DC bias currents the output noise in the intermediate frequency band increases proportionally with the current, which is predicted by the Wiedemann-Franz law in the large heating limit. A proportional dependence of output power on bias current can also be expected from a shot noise source, but no such source in the device is known to us at this time.

ACKNOWLEDGEMENTS

We express our gratitude to Paul D. Maker and Richard E. Muller for their assistance in setting up the PMMA / Electron beam lithography.

This research was performed by the Jet Propulsion Laboratory, Center for Space Microelectronics Technology, California Institute of Technology and by Yale University and was jointly sponsored by the NASA Office of Advanced Concepts and Technology, the BMDO Innovative Science and Technology Office, and the National Science Foundation. Funding for P. J. Burke was provided by a NASA Graduate Student Fellowship as well as a Connecticut High Technology Fellowship.

REFERENCES

- [1] E. M. Gershenzon, G. N. Gol'tsman, I. G. Gogidze, Y. P. Gusev, A. I. Elant'ev, B. S. Karasik, A. D. Semenov, "Millimeter and Submillimeter Range Mixer Based on Electronic Heating of Superconducting Films in the Resistive State", *Superconductivity* 3 (10), pp.1582-1597 October 1990.
- [2] H. Ekström et al., These proceedings
- [3] O. Okunev et al., These proceedings
- [4] D. E. Prober, "Superconducting Terahertz Mixer using a Transition-Edge Microbolometer", *Appl. Phys. Lett.* 62(17), 26 April 1993
- [5] E. M. Gershenzon et al., *Superconductivity* 5 (6), pp. 1129, 1992
- [6] P. Febvre, W. R. McGrath, P. Batelaan, B. Bumble, H. G. LeDuc, S. George, P. Feautrier, "A Low-Noise SIS Receiver Measured from 480 GHz to 650 GHz using Nb Junctions with Integrated RF Tuning Circuits", To appear in *Int. J. Infrared & Millimeter Waves*, Vol. 15, No. 6, June 1994.

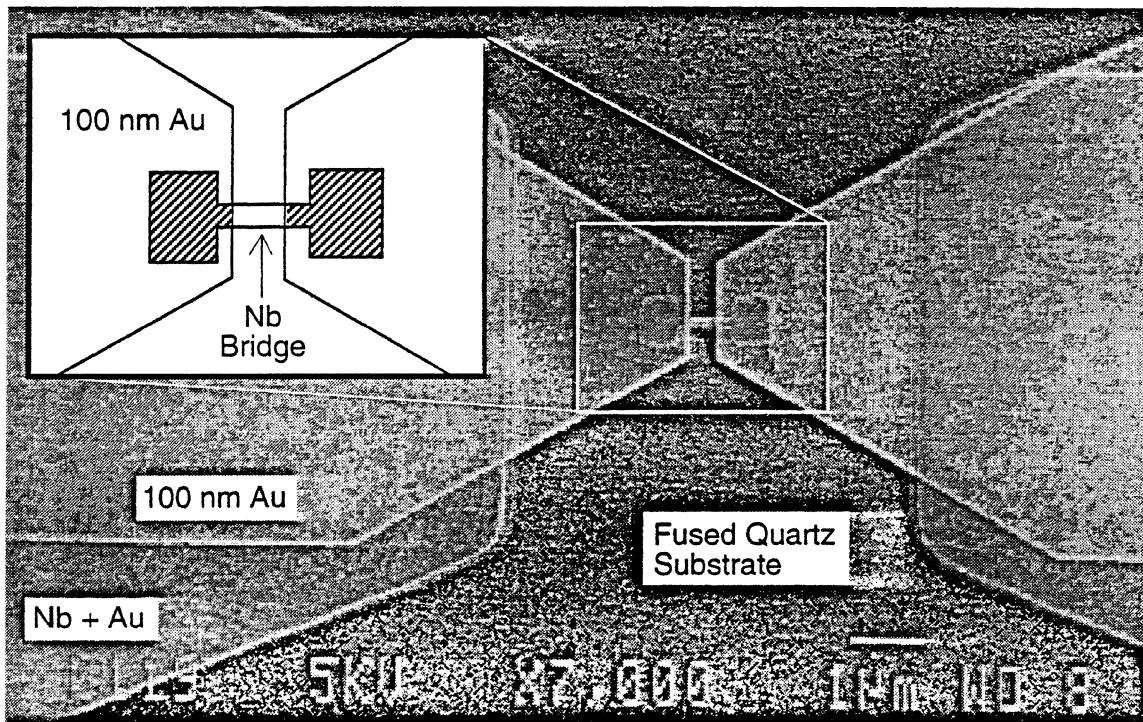


Fig. 1: SEM image of a hot electron bolometer. The crosshatched areas in the inset are 10 nm of Au on 10 nm of Nb; both layers are under the large 100 nm Au film.

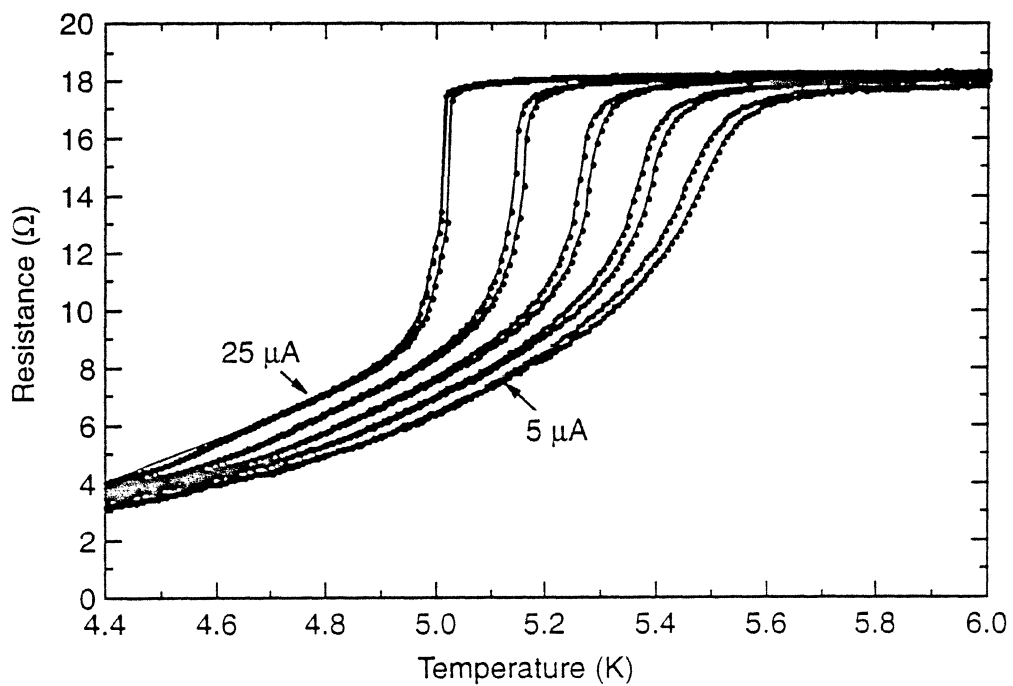


Fig. 2: R versus T for a $0.2\ \mu\text{m}$ long bolometer. The different curves were measured at 5, 10, 15, 20 and $25\ \mu\text{A}$.

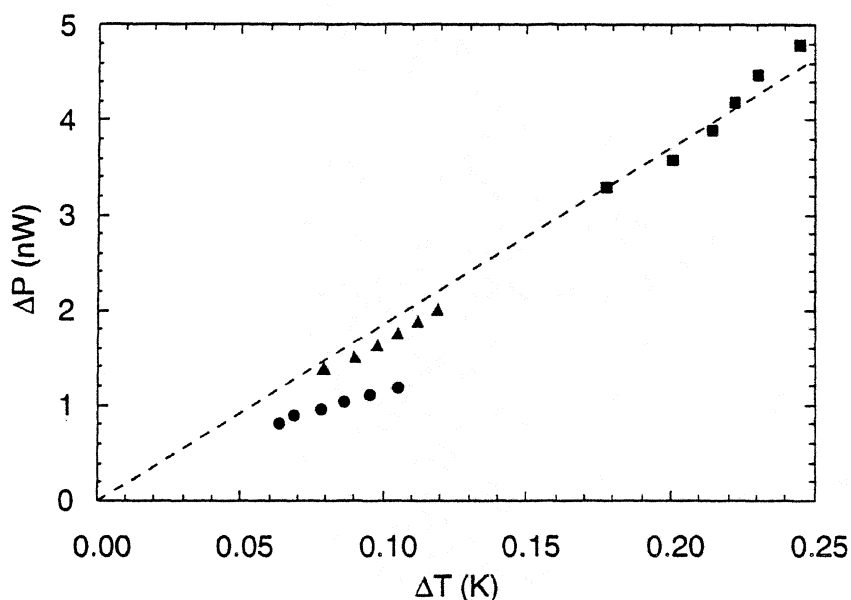


Fig.3: The difference in dissipated DC power ΔP plotted against the temperature shift ΔT , for three different pairs of R-T curves. Six points are plotted for each pair, corresponding to different resistance values. Ideally, all the points would fall on a straight line through the origin, the slope of which would be the thermal conductivity G . The dashed line in the figure gives $G_{Exp} = 18.5$ nW/K. The data is for an $0.2 \mu\text{m}$ long device. The three DC current pairs are: $I_1=5\text{mA}$ & $I_2=10\text{mA}$ (●); $I_1=10\text{mA}$ & $I_2=15\text{mA}$ (▲); $I_1=10\text{mA}$, $I_2=20\text{mA}$ (■).

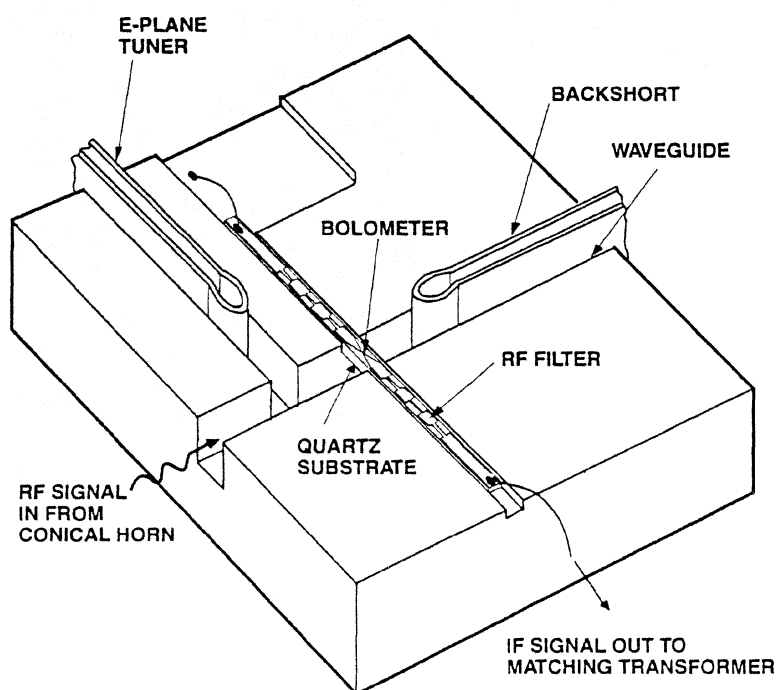


Fig. 4: Split view of the waveguide block showing the bolometer substrate.

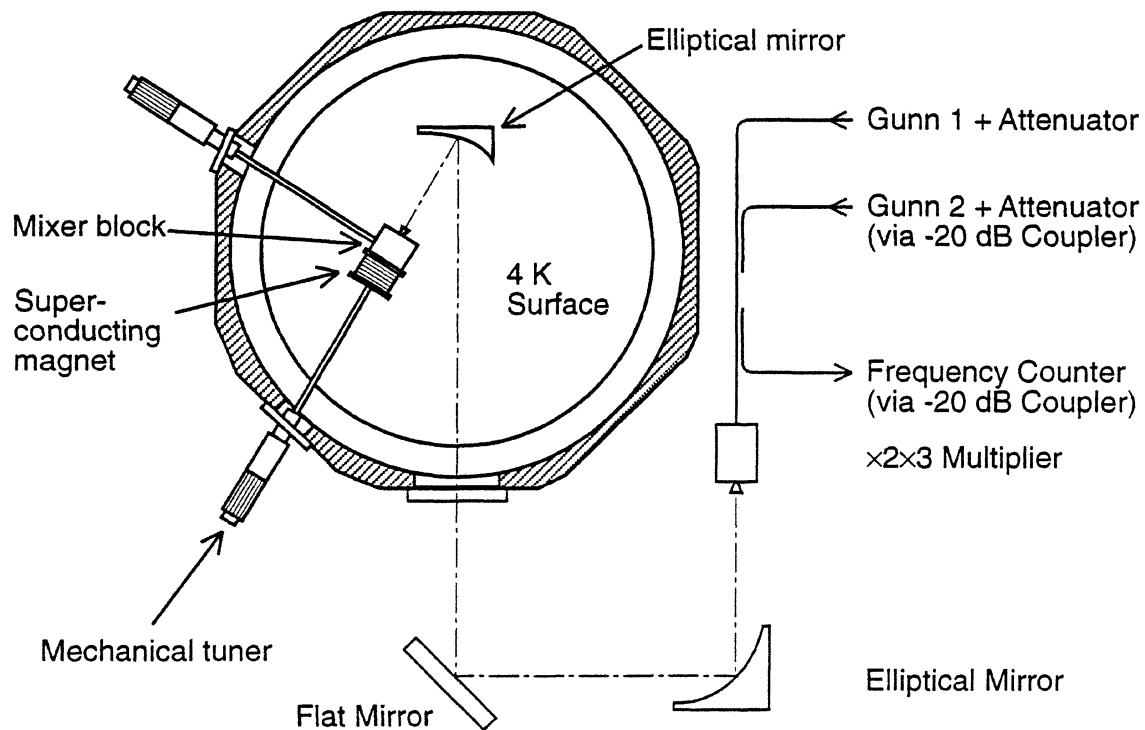


Fig. 5: Schematic view of the vacuum cryostat, the beam path and the multiplier source.

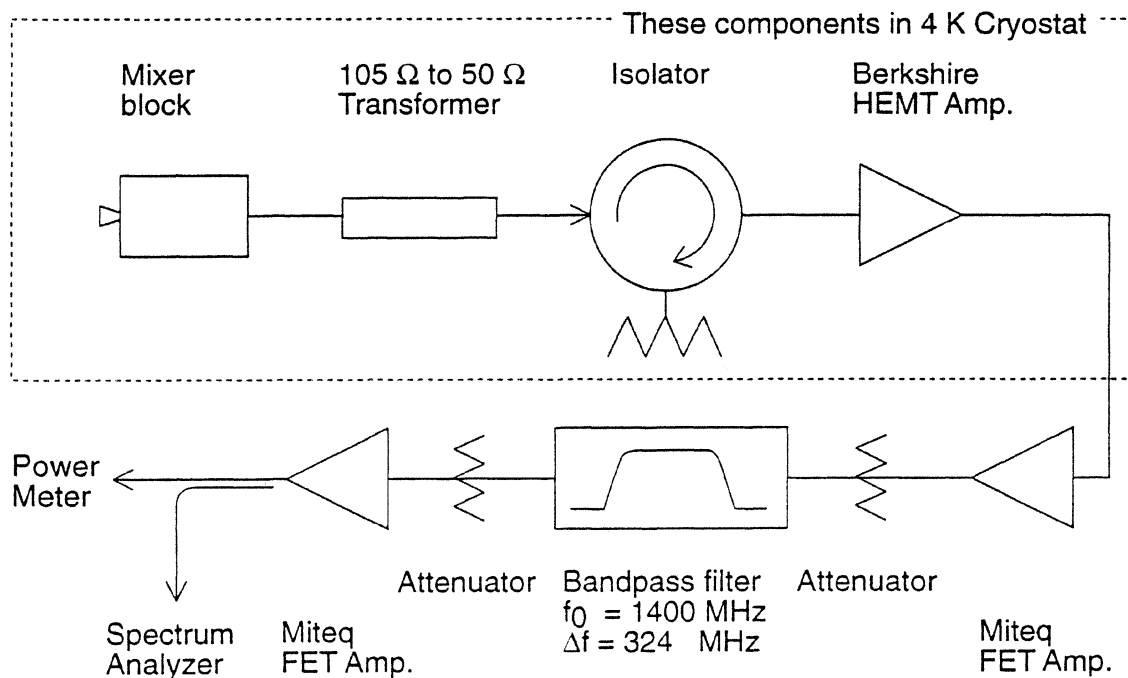


Fig. 6: The intermediate frequency (IF) chain.

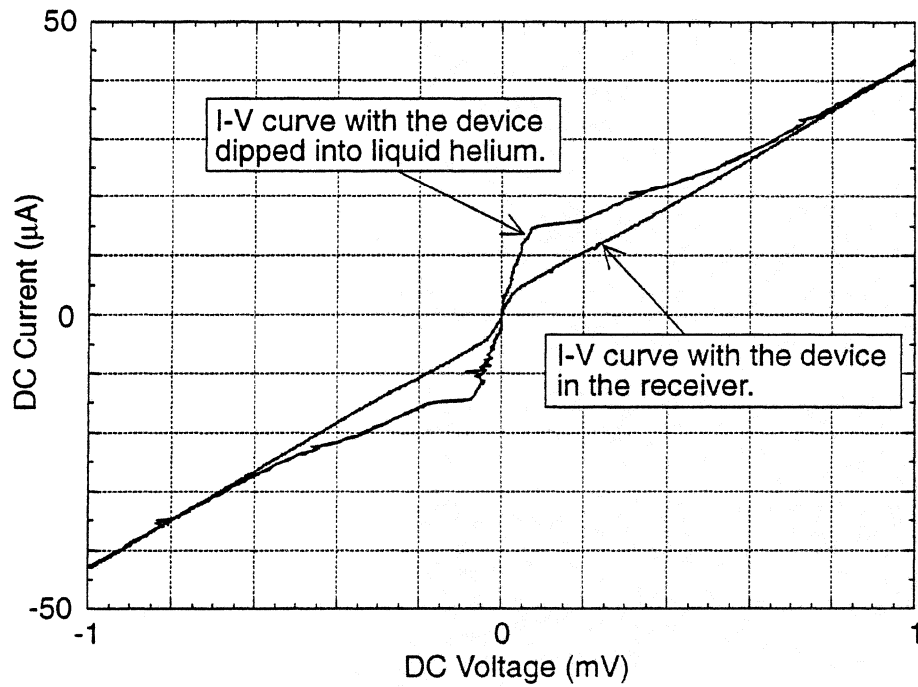


Fig. 7: Two DC I-V curves of the $0.2 \mu\text{m}$ device used in the mixer measurements. The difference between the I-V curves is due to the slightly warmer environment in the receiver.

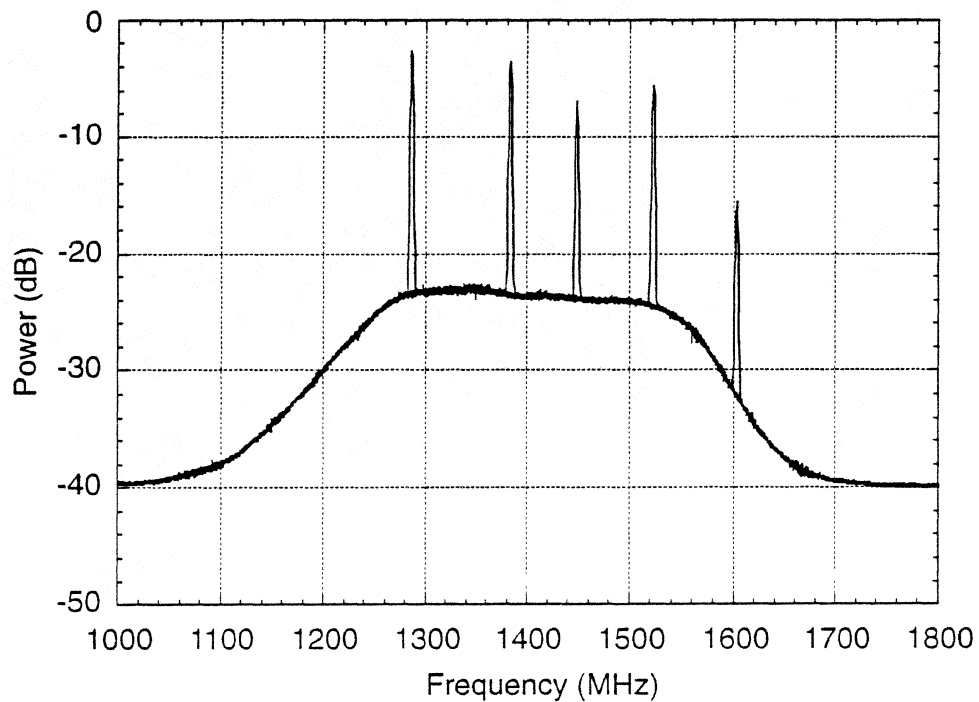


Fig. 8: The intermediate frequency spectrum for 5 different signal frequencies.

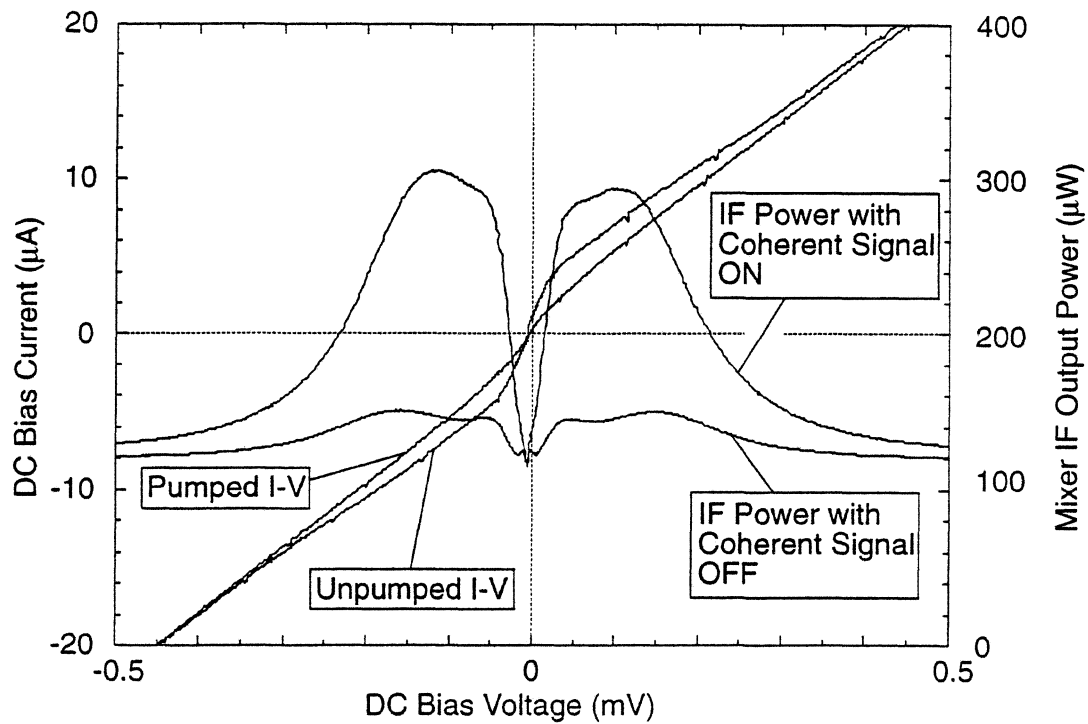


Fig. 9: Total output power in the intermediate frequency band as a function of DC bias voltage. The IF output power in this graph includes amplifier noise.

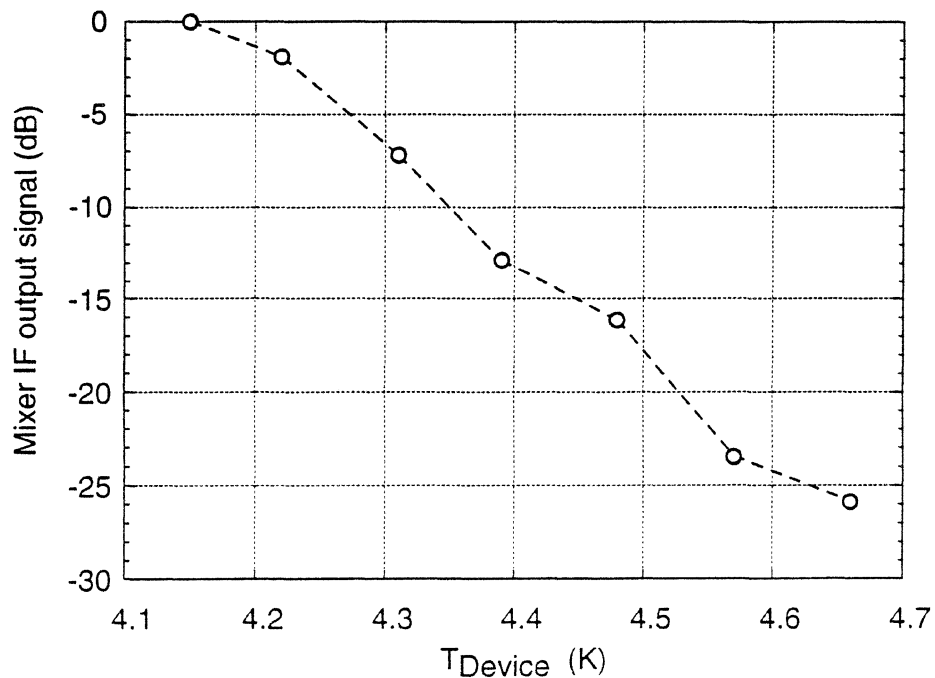


Fig. 10: The mixer output signal as a function of temperature.

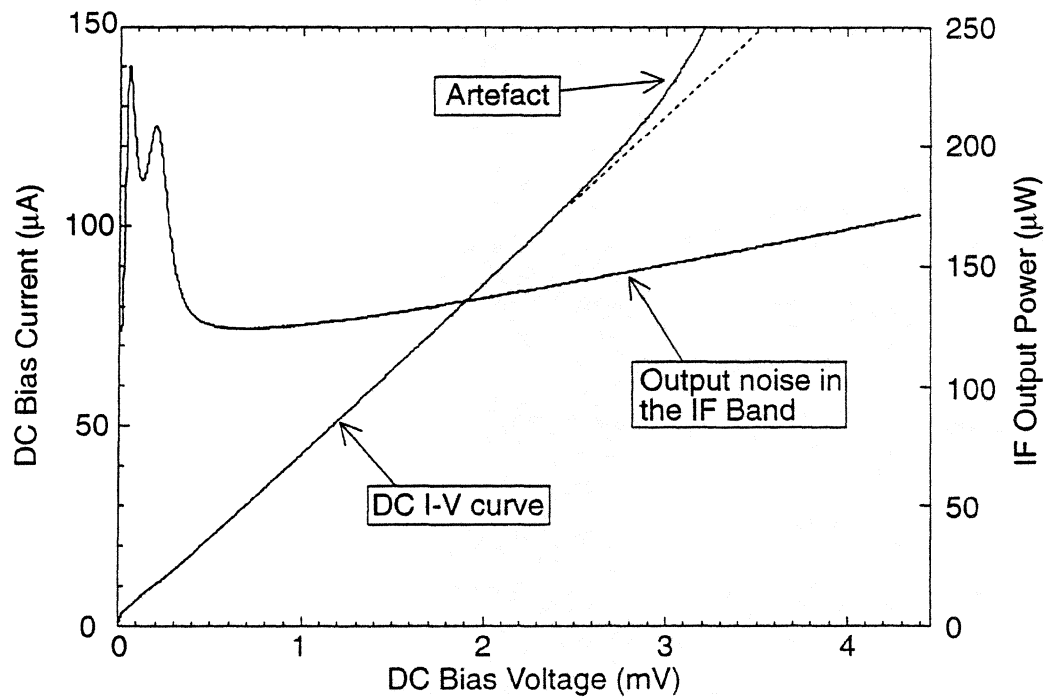


Fig.11: The I-V curve and output power in the intermediate frequency band. On this scale, the non-linear part of the I-V curve is barely visible at the lower left corner of the diagram. The bend upwards at high bias currents is an artefact caused by a current limiting diode in the bias circuit. The output noise power curve includes approximately 90 μW of amplifier noise.

INVESTIGATION OF A SUPERCONDUCTING HOT ELECTRON MIXER

by

H. Ekström, B. Karasik*, E. Kollberg, and K.S. Yngvesson#,

Chalmers University of Technology, S-412 96 Göteborg, Sweden,

*Moscow State Pedagogical University, Moscow 119435, Russia,

#University of Massachusetts, Amherst, MASS 01003, USA

ABSTRACT

Mixing at 20 GHz in niobium superconducting thin film strips in the resistive state is studied. Experiments give evidence that electron-heating is the main cause of the non linear phenomena. The requirements on the mode of operation and on the film parameters for small conversion loss and the possibility of conversion gain are discussed. Measurements indicate a minimum intrinsic conversion loss around 1 dB with a sharp drop for the lowest voltage bias-points, and a DSB mixer noise temperature between 100 and 450 K at 20 GHz. The device output noise temperature at the mixer operating point can be as low as 30-50 K. A simple theory is presented, which is based on the assumption that the small signal resistance is linearly dependent on power. This type of mixer is considered very promising for use in low-noise heterodyne receivers at THz frequencies.

1. INTRODUCTION

Recently proposed hot-electron bolometer (HEB) mixers utilising thin superconducting films in the resistive state [1-3], have a potential to be competitive with traditional mixers in heterodyne receivers at Terahertz frequencies for radio astronomy and remote sensing applications. These new types of mixers have the advantage of simplicity over SIS and Schottky mixers both from the circuit and the technological point of view. This is particularly obvious in comparison with SIS trilayer mixers, which show excellent performance below the bandgap frequency, approaching 650-700 GHz [4,5]. However, for frequencies above the gap frequency of the superconductors, the SIS mixers are not expected to perform as well. Schottky-diodes are known to work near and above 1 THz, but with lower sensitivity due to an increased noise temperature [4,6]. The well-known InSb hot electron mixers are sensitive enough in the range 0.5-1 THz but the bandwidth is too narrow for many interesting applications [7-9]. A more recent development where a 2D electron gas in heterostructures are used for hot electron mixing may possibly be competitive at THz frequencies [10,11]. Early experiments at 20 GHz with thin and narrow strips of non linear niobium elements, indicate good mixer performance, i.e. low conversion loss and noise temperature [3]. We anticipate that these results can be translated to the THz frequencies, based on the frequency insensitive nature of the electromagnetic interaction and non linearity of these devices.

The purpose of the effort presented in this paper has been to carefully measure and model conversion loss and noise properties of the HEB at a low millimeter wave frequency, in order to establish a firm basis for the design of future THz HEB mixers.

2. THE DEVICE

A superconducting Hot Electron Bolometer consists of one or several thin superconducting strips, deposited on a substrate of for example silicon, single crystalline quartz or sapphire. The strips are cooled to the superconducting state and then heated by DC and microwave power to the neighbourhood of the superconducting-normal transition temperature, T_c , the resistive state, where the superconductor will gradually become normal (Fig. 1)

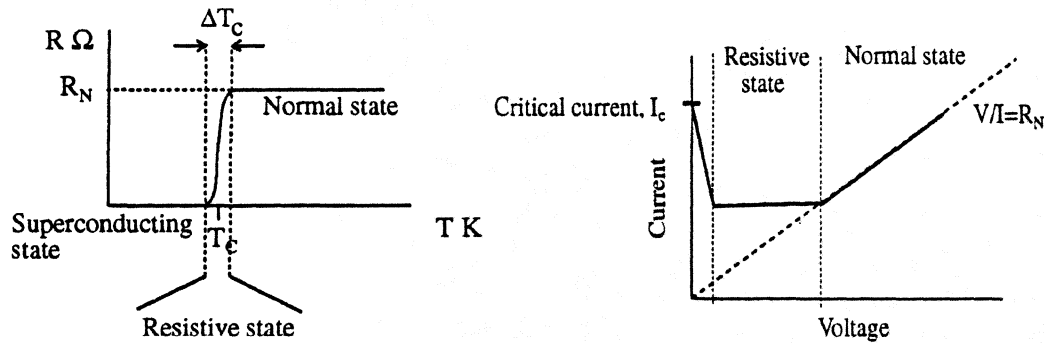


Fig. 1 The three states of the bolometer

The resistance of the device in the resistive state, may be explained by several possible physical phenomena, such as formation of normal domains, phase slip centers, and moving magnetic vortices. Let us adopt a simplistic model¹: assume one resistive region (or several that may be combined into one). This situation is illustrated in Fig. 2, where the electron temperature in the "resistive transition regions" is in the interval ΔT_c , marked in Fig. 1.

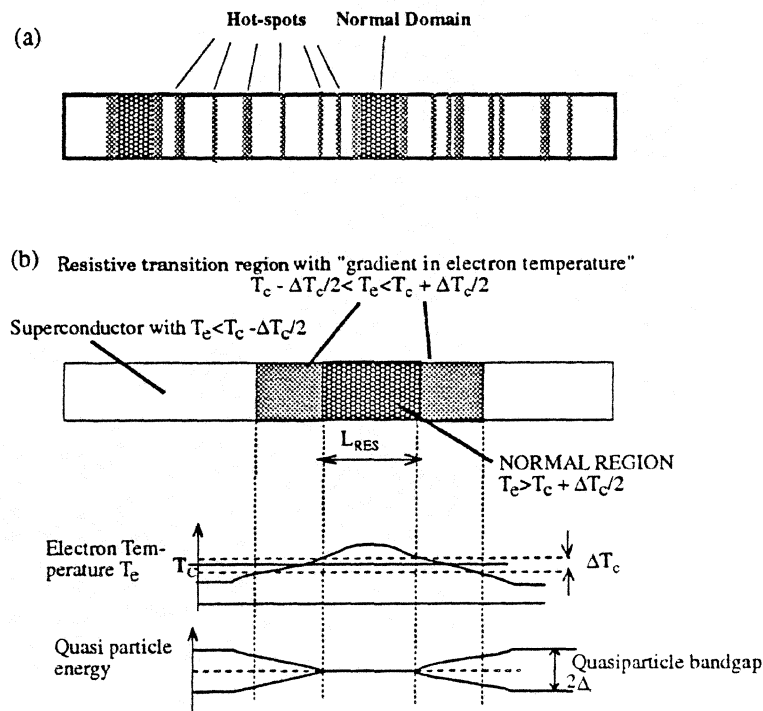


Fig. 2. Different possible regions in the bolometer strip.

The main power dependence of the resistance may be due to creation and annihilation of "hot spots" and heating of electrons in the resistive state. Here the gradient in the electron temperature is also steepest. The electron temperature as well as the lattice temperature of the superconductor outside these areas is close to T_c , but low enough to allow zero resistance.

¹Note that the validity of the circuit-based model which we will present in the next section does not depend on the details of the microscopic model, such as the one suggested here.

Note the quasi particle bandgap, 2Δ . If the signal and LO frequency are high so that $f_{LO}, f_s > 2\Delta/h$, the full length of the superconducting strip will be seen as a normal conductor strip. For $f_{LO}, f_s < 2\Delta/h$ the RF-resistance will depend on the bias point and the amount of normal regions in the strip. If the IF is such that $f_{IF} < 2\Delta/h$, it will only develop a voltage across the normal regions while the superconducting part is simply a short-circuit. These facts have important consequences on the functions of the mixer.

The response time of the device is related to a time constant τ_e , which determines the rate at which the excess energy absorbed by the electrons relaxes. Basically the maximum IF is determined by this energy relaxation or response time of the electrons, i. e. $f_{IF} < 1/(2\pi\tau_e)$. If the strips are made sufficiently thin, the time constant for phonons in the superconductor to escape to the substrate, τ_{ph-s} , may become shorter than the time constant for phonon electron collisions in the superconductor, τ_{ph-e} (for Nb τ_{ph-e} is shorter than τ_{e-ph}). If the strips are made narrow, then the back flow of phonons from substrate to the superconductor will be reduced, and thus τ_{s-ph} will be long. Consequently it is possible to heat the electrons *above* the temperature of the lattice and τ_e will be dominated by τ_{e-ph} , which is not the case for ordinary bolometers where the electrons and the lattice are heated to the same temperature. (compare Fig. 3).

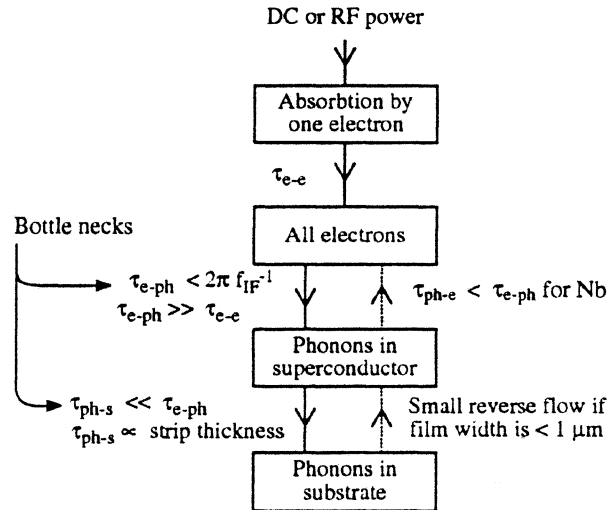


Fig. 3. Time constants for the hot electron bolometer.

In practice, to avoid lattice heating effects in the superconductor, the bolometer should be less than or about 100 \AA thick and about $1 \mu\text{m}$ wide. For Nb the resulting bandwidth corresponding to $(2\pi\tau_{e-ph})^{-1}$ is of the order 100-200 MHz, and for NbN several GHz [1,2]. With higher T_c , a higher operating temperature can be used, yielding shorter τ_{e-ph} . For Nb it may be possible to reach 500 MHz IF bandwidth.

The bolometer resistance may be adjusted by adding parallel strips and by changing the strip length. For $f_{LO}, f_s > 2\Delta/h$ the absorption of microwave power by the normal electrons in the HEB is essentially frequency independent. Therefore these mixers will operate to RF frequencies well into the THz range, i.e. much higher than the bandgap frequency of the superconductor. Previous work has in fact shown mixing at 1.5 THz [1].

3. MIXER THEORY

In Fig. 4 is shown an equivalent circuit of the mixer, where the device is biased by a constant DC current. The heating of the electrons by RF or DC power will increase the device resistance. The signal, when beating with the LO, will cause a modulation of the device resistance at the IF. An IF

voltage will appear across the device, causing a current through the IF load resistance. This current will go in the opposite direction to the DC bias current in the mixer device, and will create feed-back.

Note that the resistance of the device is time dependent only for the IF. For the signal the device impedance is assumed constant since these frequencies are higher than the inverse response time of the electrons. If this statement were not true, an image current would be created, and a more complicated theory will be necessary.

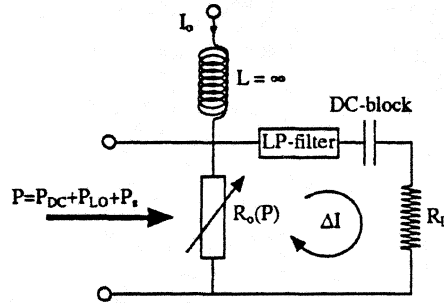


Fig. 4. Equivalent circuit of bolometer with load.

The same expression for the conversion gain has been derived for three different types of HEB mixers: (1) the superconducting HEB by employing an energy balance equation [1]; (2) the hot electron InSb [7] and (3) 2DEG mixers [10,11]. A basic assumption is that the DC and time-average RF power dependence of the bolometer resistance are equal. Assume that in the bias point of the device we have $V=V_0$ and $I=I_0$. Defining the device resistance as $R_0=V_0/I_0$, one obtains

$$G = \frac{P_{IF}}{P_s} = 2C_o^2 \frac{P_{LO} P_{DC}}{(R_L + R_o)^2} \frac{R_L}{R_o} \left(1 - C_o \frac{P_{DC}}{R_o} \frac{R_L - R_o}{R_L + R_o} \right)^{-2} \quad (1)$$

where $C_o = dR_o/dP_{device}$. R_L is the IF load resistance, P_{IF} , P_s , P_{LO} and P_{DC} , are the IF-, signal-, LO- and DC-power respectively.

For the types of IV-characteristics which apply to InSb and 2DEG mixers, an optimum conversion gain of -6 dB can be derived from (1), see [3]. The superconducting HEB has a different IV-characteristic, and a re-interpretation of (1) leads to a prediction that $G>0$ dB is possible, as shown in the next three sections. Conversion gain of >-6 dB for superconducting HEBs was originally derived in [1], but the present treatment is more extensive.

4. RELATING THE CONVERSION GAIN TO THE IV-CHARACTERISTIC

A basic assumption in our model is that the low frequency resistance of the device is dependent on electron temperature. Hence, if the temperature increases linearly with dissipated power, we have $\Delta R = C_o \cdot \Delta P$. This assumption has certain interesting implications: Consider a given IV-characteristic as shown in Fig. 5. For a given device resistance $R_0 = V_0/I_0$, the device temperature must be constant, i. e. the total power dissipated must be the same. When the device is pumped with a given LO-power, the IV will change, as shown in Fig. 5. The above argument indicates that in points A and a we have the same dissipated power; in A only DC power, and in a LO power plus DC power. If we increase either the LO power or the DC power, or both, the resistance will increase, and become $R_0 + \Delta R$.

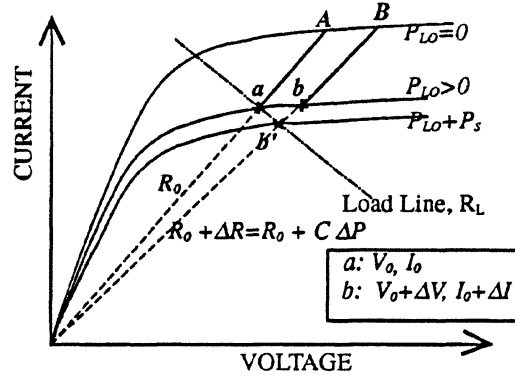


Fig. 5

We may now calculate ΔR and ΔP . Since it makes no difference whether ΔP is DC power or a combination of DC and LO power, we may use

$$\Delta R = \frac{V_o + \Delta V}{I_o + \Delta I} - \frac{V_o}{I_o} \approx \frac{V_o}{I_o} \frac{\Delta I}{I_o} \left(\frac{\Delta V}{\Delta I} \frac{I_o}{V_o} - 1 \right) \quad (2)$$

$$\Delta P = (V_o + \Delta V)(I_o + \Delta I) - V_o I_o \approx V_o \Delta I \left(\frac{\Delta V}{\Delta I} \frac{I_o}{V_o} + 1 \right) \quad (3)$$

From Eqs. (2) and (3) we get

$$C_o = \frac{dR}{dP} = \frac{1}{I_o^2} \frac{\frac{\Delta V}{\Delta I} \frac{I_o}{V_o} - 1}{\frac{\Delta V}{\Delta I} \frac{I_o}{V_o} + 1} = \frac{R_o}{P_{DC}} \frac{\left(\frac{dV}{dI} \right)_{DC} - R_o}{\left(\frac{dV}{dI} \right)_{DC} + R_o} \quad (4)$$

where $(dV/dI)_{DC}$ is the differential resistance of the pumped IV in the bias point determined by DC bias and LO power.

With Eq. (1) this leads to

$$G = \frac{1}{2} \frac{P_{LO}}{P_{DC}} \frac{R_L}{R_o} \left(1 - \frac{R_o}{(dV/dI)_{DC}} \right)^2 \left(1 + \frac{R_L}{(dV/dI)_{DC}} \right)^{-2} \quad (5)$$

There is still another relationship between the P_{LO} , P_{DC} and I_o that can be used to rewrite the expression for conversion gain. For constant $R_o = V_o/I_o$, the dissipated power in the device must be constant. This means that if we have a bias current I_{oo} for the unpumped IV, and I_o for the pumped IV, the following equality must be true:

$$R_o I_{oo}^2 = R_o I_o^2 + P_{LO} \quad (6)$$

Note that $P_{DC} = R_o I_o^2$. Moreover, since C_o is invariant for constant R_o , Eq. (4) yields

$$C_o = \frac{1}{I_o^2} \frac{\left(\frac{\Delta V}{\Delta I} \right)_{DC} - R_o}{\left(\frac{\Delta V}{\Delta I} \right)_{DC} + R_o} = \frac{1}{I_{oo}^2} \frac{\left(\frac{\Delta V}{\Delta I} \right)_{noLO} - R_o}{\left(\frac{\Delta V}{\Delta I} \right)_{noLO} + R_o} \quad (7)$$

With Eq. (1) (6) and (7) we get

$$G = 2 \left(C_o I_{oo}^2 \right)^2 \left(\frac{I_o^2}{I_{oo}^2} \right) \left(1 - \frac{I_o^2}{I_{oo}^2} \right) \frac{R_L}{R_o} \frac{1}{(R_L/R_o + 1)^2} \frac{1}{\left(1 - C_o I_{oo}^2 \frac{I_o^2}{I_{oo}^2} \frac{R_L/R_o - 1}{R_L/R_o + 1} \right)^2} \quad (8)$$

This equation can be rewritten as

$$G = 2 \left(1 - \frac{I_o^2}{I_{oo}^2} \right) \frac{(C_o I_o^2)^2}{(1 - C_o I_o^2)^2} \frac{R_o \cdot R_L}{\left(R_L + \left(\frac{dV}{dI} \right)_{DC} \right)^2} \quad (9)$$

from which it is seen that $R_L = (dV/dI)_{DC}$ yields maximum gain.

These equations for the conversion gain are valid for low intermediate frequencies, where the finite relaxation time of the device has no influence on the conversion gain.

5. MODELLING OF THE IV-CHARACTERISTICS

In Fig. 6 is shown the expected shapes of the IV under the assumptions of the model described above. (see Appendix). In this figure we have used a parameter, v , which defines a constant, normalised, LO power:

$$\frac{P_{LO}}{R_o I_{oo}^2} = \frac{v}{R_o I_{oo}} = \frac{v}{V_{oo}} \quad (10)$$

where V_{oo} is the voltage where R_o intersects $I_o = I_{oo}$. As a special case, we have chosen $dV/dI = \infty$ for $P_{LO} = 0$ (the horizontal curve, $I_{oo} = 1$ in Fig. 6). If the unpumped IV curve corresponds instead to e. g. the curve with $v=1$, we may treat this case as if an equivalent heating brings us from the $v=0$ curve to $v=1$ curve. Then the $v=2$ case corresponds to a normalised LO power of $v=1$. The same argument can be applied if the unpumped IV has a shape corresponding to $v=-1$. Consider e. g. the isotherm represented by R_{o1} and assume that the $v=-1$ curve represents the *unpumped* IV. The curve $v=+2$ then represents the pumped IV-characteristic for a normalised LO power of $(3/V_{oo}) \times (R_o I_{oo}^2)$.

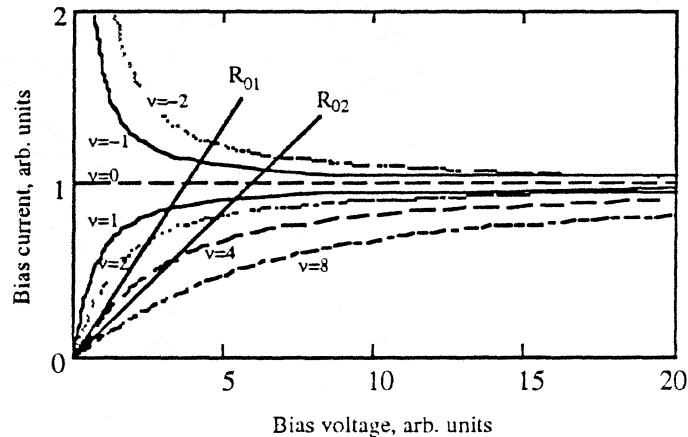


Fig 6. Calculated IV-curves assuming that for a particular isotherm V/I (e. g. $=R_{o1}$) dR/dP is constant. The parameter $v = P_{LO}/I_o$, where $I_o = 1$ in this diagram. The curves for $v < 0$ show negative resistance. See also the text.

The interesting observation in Fig. 6 is of course that *negative differential resistance* is allowed and included in the model. Hence, our conclusion is that the model as such allows for negative differential resistance, a feature which is necessary to achieve a conversion loss less than 6 dB, or even conversion gain.

To illustrate the negative resistance property further, let us calculate the differential resistance vs. current along an isotherm, i.e. for constant R_o . Let us assume that we have $(dV/dI)_{I=I_{oo}}$ for $I=I_{oo}$ and $(dV/dI)_{I=I_o}$ for $I=I_o$. Then

$$(dV/dI)_{I_{oo}} = R_o \frac{(I_o^2/I_{oo}^2)((dV/dI)_{I_o} + R_o) + ((dV/dI)_{I_o} - R_o)}{(I_o^2/I_{oo}^2)((dV/dI)_{I_o} + R_o) - ((dV/dI)_{I_o} - R_o)} \quad (11)$$

This equation is illustrated in Fig. 7.

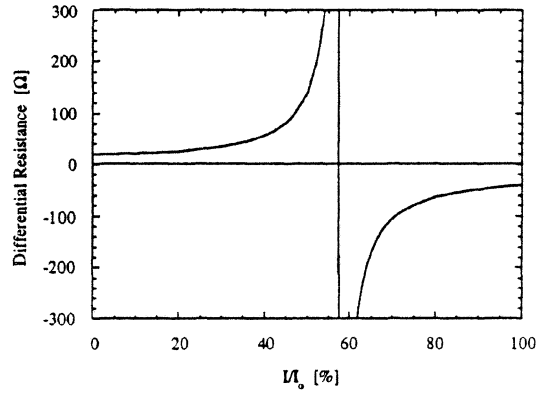


Fig. 7. Differential resistance of pumped IV-curve $(dV/dI)_{I=I_o}$ along an isotherm as function of bias current. $R_o = 20 \Omega$ and $(dV/dI)_{I=I_{oo}} = -40 \Omega$ are typical values from experiments.

6. PREDICTING THE CONVERSION GAIN

The negative resistance can be predicted if $C_o I_{oo}^2$ is known. From Eq. (7) the differential resistance can be expressed as:

$$\frac{dV}{dI} = R_o \cdot \frac{1 + C_o I_{oo}^2}{1 - C_o I_{oo}^2} \quad (12)$$

Hence a negative resistance corresponds to $C_o I_{oo}^2 > 1$. Using Eq. (8) we have calculated the conversion gain vs. $(I_o/I_{oo})^2 = P_{DC}/(P_{DC} + P_{LO})$.

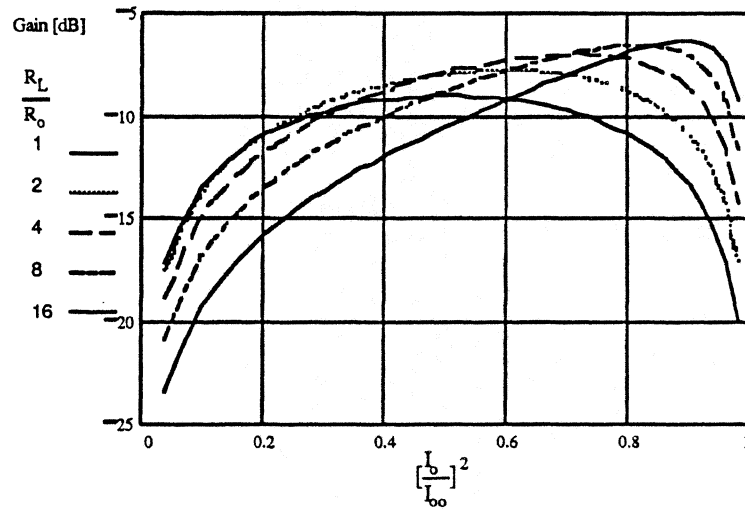


Fig. 8. Conversion Gain vs. $P_{DC}/(P_{DC}+P_{LO})$ for different IF load resistances. $R_L > R_0$. The differential resistance for the unpumped curve: $dV/dI=\infty$, or $C_0 \cdot I_{00}^2=1$.

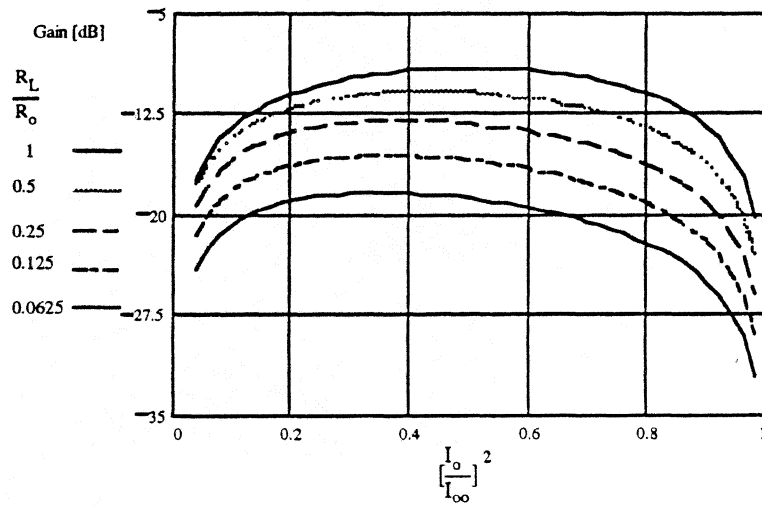


Fig. 9. Conversion Gain vs. $P_{DC}/(P_{DC}+P_{LO})$ for different IF load resistances. $R_L < R_0$. The differential resistance for the unpumped curve: $dV/dI=\infty$, or $C_0 \cdot I_{00}^2=1$.

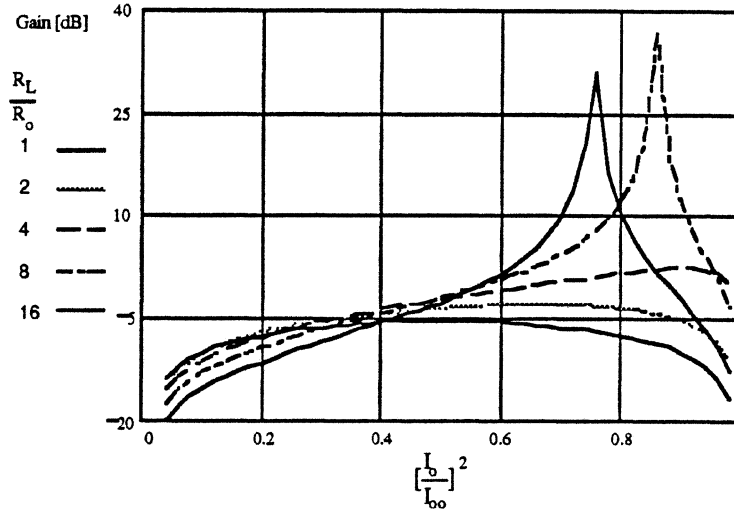


Fig. 10 Conversion Gain vs. $P_{DC}/(P_{DC}+P_{LO})$ for different IF load resistances. $R_L > R_0$. The differential resistance for the unpumped curve is negative: $dV/dI = -5 \cdot R_0$, or $C_0 \cdot I_{00}^2 = 1.5$.

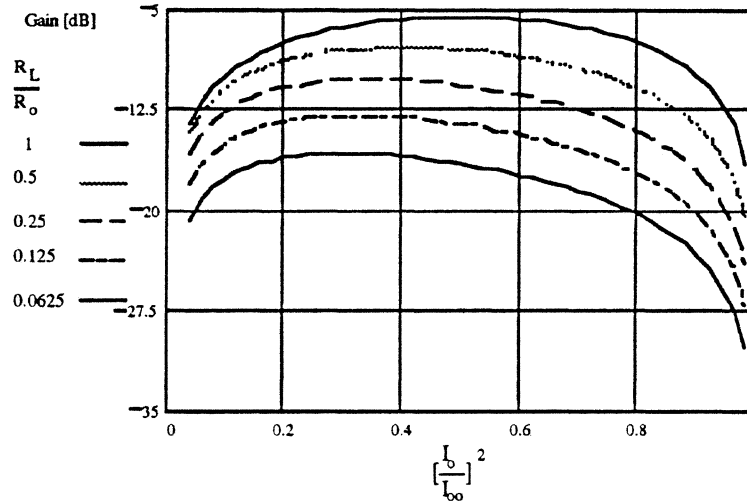


Fig. 11. Conversion Gain vs. $P_{DC}/(P_{DC}+P_{LO})$ for different IF load resistances. $R_L < R_0$. The differential resistance for the unpumped curve is negative: $dV/dI = -5 \cdot R_0$, or $C_0 \cdot I_{00}^2 = 1.5$.

The fundamental limit of -6 dB gain for InSb mixers [7] is obviously not valid for the superconducting HEB mixers since it is possible to achieve positive conversion gain with negative differential resistance of the unpumped IV-curve. From Fig. 8-11 obviously larger conversion gain is available for $R_L/R_0 > 1$ rather than $R_L/R_0 < 1$.

As mention above the load resistance for maximum gain is equal to the differential resistance of the IV-curve in the bias point of the pumped mixer. It is as well possible to find optimum LO power for a given R_L/R_0 or with R_L/R_0 equal to the differential resistance of the IV-curve in the bias point of the pumped mixer by determining $(I_0/I_{00})^2$ yielding maximum gain.

7. CONVERSION GAIN AND IF IMPEDANCE VS INTERMEDIATE FREQUENCY

The coefficient $C_o = dR/dP$ can be expressed as $C_o = [dR/dT] \cdot [dT/dP]$. Assuming that the factor dT/dP has a frequency dependence determined by the factor $1/(1+j\omega\tau_e)$, and that the term dR/dT is simply a constant, we may draw the conclusion that

$$C_o(\omega) = \frac{C_o(\omega = 0)}{1 + j\omega\tau_e} \quad (13)$$

Using this expression for C_o in the equations for G above, the IF dependence of the conversion gain of the mixer can be expressed as:

$$G = G(\omega = 0) \cdot \frac{1}{1 + (\omega\tau_{MIX})^2} \quad (14)$$

where

$$\tau_{MIX} = \frac{\tau_e}{1 - C_o I_o^2 \cdot \frac{R_L - R_o}{R_L + R_o}} \quad (15)$$

Evidently, it is possible to make the relaxation time shorter than τ_e (and the bandwidth wider), by making the factor $C_o I_o^2 \cdot (R_o - R_L)/(R_o + R_L)$ large ($R_o > R_L$). It is obviously possible to look for a compromise between IF bandwidth and conversion gain. We can also conclude that it is undesirable to attempt to utilise a large conversion gain, a feature which the HEB mixer shares with other negative resistance devices.

The frequency dependence of the IF impedance can be derived in the same way by using expression (13) and Eq. (4). We get

$$Z(\omega) = R_o \left(1 + \frac{2C_o I_o^2}{1 - C_o I_o^2} \frac{1}{1 + j\omega\tau_{imp}} \right) \quad (16)$$

where

$$\tau_{imp} = \frac{\tau_e}{1 - C_o I_o^2} \quad (17)$$

It is possible to rewrite the equation for conversion gain expressing the frequency dependence in terms of the electron energy relaxation time τ_e . Using a complex load impedance viz. $R_L \rightarrow Z_L = R_L + jX_L$ we obtain

$$G = \frac{2 \left(1 - \frac{I_o^2}{I_{oo}^2} \right) \frac{(C_o I_o^2)^2}{(1 - C_o I_o^2)^2} R_o \cdot R_L}{\left[R_L + (dV/dI)_{pumped} - \omega\tau_e \cdot \frac{X_L}{1 - C_o I_o^2} + j \left[X_L + \omega\tau_e \cdot \frac{R_o + R_L}{1 - C_o I_o^2} \right] \right]^2} \quad (18)$$

Hence it should be possible to improve the bandwidth somewhat by a proper design of the load circuit Z_L . Fig. 12.

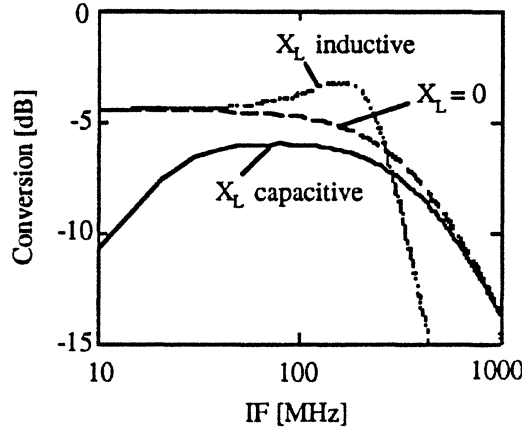


Fig. 12. IF Bandwidth for different load reactances.

8. THEORY OF NOISE IN HEBs

The main noise of concern for the superconducting HEB is that directly emitted by the device at the IF frequency. The noise theory does not need to take into account correlation of noise contributions at a number of frequencies, as is the case for the Schottky-barrier mixer, for example. The IF output noise is primarily of two types [12]: (1) Nyquist noise at the electron temperature, and (2) temperature fluctuation noise. The latter contribution is not usually important for microwave or millimeter wave mixers, but is likely to be the dominant one in superconducting HEB mixers. Temperature fluctuation noise is well-known from the theory of conventional (lattice) bolometers [13]. The electrons are assumed to form a subsystem in thermal equilibrium at the electron temperature, T_e , while conducting heat to the lattice heat reservoir at temperature T_L . The corresponding thermal conductance is G [W/K]. It is known from thermodynamics that the average temperature of the electron subsystem will show RMS fluctuations given by [13]:

$$\Delta T_e = \frac{4k_B T_e^2}{G} \quad (19)$$

The thermal conductance is

$$G = \frac{C_e V}{\tau_e} \quad (20)$$

where C_e is the electron specific heat and V the volume of the superconducting strip. Since the resistance of the HEB depends on T_e , and the device is biased with constant DC current, I_0 , there will be a noise voltage developed across the device. We can derive the equivalent device output noise temperature, $T_{d,t}$, by equating the noise power due to temperature fluctuations to that from a Nyquist source at $T_{d,t}$:

$$T_{d,t} = \frac{I_0^2 (dR/dT_e)^2 T_e^2}{R_0 G} \quad (21)$$

Here (dR/dT_e) must be evaluated for actual mixer operating conditions. The total device output noise temperature will be

$$T_d = T_e + T_{d,t}$$

This noise temperature can now be used in standard expressions for the mixer noise temperature, given the conversion loss, L .

If typical values are inserted in (21), one finds that this term is likely to dominate. Note that $T_{d,t}$ is proportional to the electron temperature squared. Further, T_e is expected to be close to T_c . HEBs based on superconductors with higher T_c then should have higher noise. The T_e -dependence may be

compensated by the appearance of G in the denominator, however. As a rule, higher T_c materials have shorter relaxation times, resulting in larger G (See Eq. 20). An optimum material in terms of device output noise temperature can therefore not be identified. One must also consider the conversion loss which can be achieved, in order to minimise the receiver noise temperature. These matters are under investigation, but have not yet been resolved in detail. Another noteworthy consequence of the dominance of $T_{d,t}$ is that the output noise temperature is predicted to fall with a time constant similar to τ_{mix} (See Eq. 14). If this can be verified, then one concludes that the bandwidth over which a given mixer noise temperature can be maintained is actually wider than $1/2\pi\tau_{mix}$, since the device output noise decreases at the same time that the mixer conversion gain decreases. Measurements of the output noise versus IF-frequency have so far given inconclusive results.

In conclusion, one can roughly estimate a device output noise temperature for Nb in the range 25-100 K. This is consistent with measurements, as described in a later section.

9. EXPERIMENT

HEB devices consisting of 2 parallel niobium strips, 100-150 Å thick, 1.5 µm wide and 7 µm long with normal resistance between 40 and 150 Ω have been manufactured on silicon substrates and measured at 20 GHz signal and 1-1000 MHz intermediate frequency. The HEB mixer is biased in the lower part of the resistive region (Fig. 13 and 16) for best conversion. The unstable part of the IV-curve between the pure superconductive state for zero bias and the resistive state indicates that a negative differential resistance region exists where conversion gain larger than one may be achieved. For no LO and low bias we have indeed observed a part of the resistive region with negative differential resistance. Compare Fig. 13 and 16 for no LO.

A) DETERMINATION OF RF COUPLING LOSS

The measured conversion loss was obtained by determining the RF coupling to the mixer from a set of IV-curves recorded for different LO power. It is again assumed that the response to time-average RF power is equal to the response to DC power taken as I-V from the IV-curve. The points on the IV-curves from which the DC powers are derived are along the isotherm which passes through the bias point A in Fig. 13.

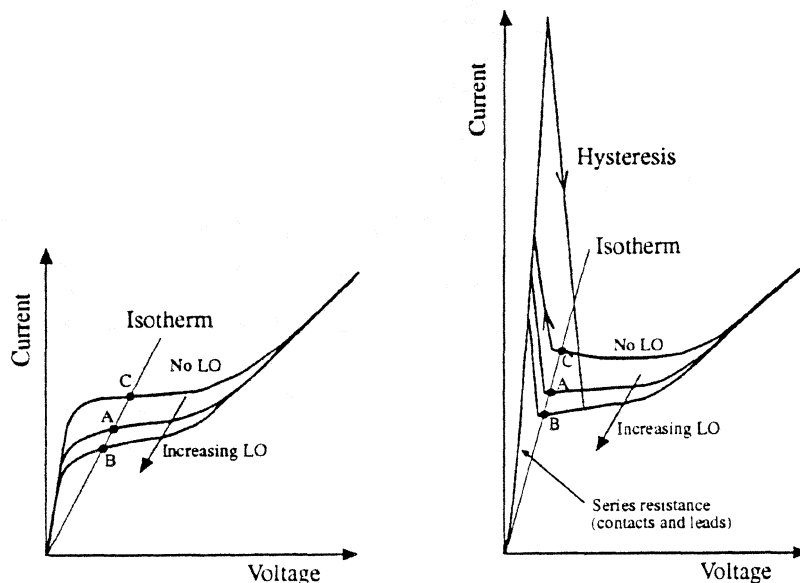


Fig. 13. IV curves for two different applied LO powers. To the left for temperatures very close to T_c , where there is no super-current, and to the right for temperatures less than about $0.9 T_c$, where there is also hysteresis.

We derive the RF Coupling Loss from:

$$L_c = \frac{P_{LO,B} - P_{LO,A}}{P_{DC,A} - P_{DC,B}} \quad (22)$$

where $P_{LO,A}$ and $P_{LO,B}$ are defined at the coaxial connector input to the liquid helium dewar. The coupling loss thus includes the attenuation in the input coaxial cable, and the microstrip circuit to which the device is connected. The sum of these contributions has been estimated to about 3 dB (see Fig. 20).

The incremental step in LO-power used in our experiments was typically between a half and one dB. Apart from the circuit losses of about 3 dB, we find that the coupling loss depends on the bias, as shown in Fig. 14. The bias-dependent coupling loss can be interpreted as the reflection loss of the device impedance with respect to the 50 ohm microstrip circuit. If we assume that the device impedance is R_0 , then we can calculate the reflection loss as shown in the full-drawn curve in Fig 14. At about 3 mV bias, R_0 , as defined above, is close to 50 ohm, and the reflection loss very small. The measured coupling loss shows a similar trend, but is about 1.5 dB higher at low bias voltages. The device resistance at 20 GHz thus is fairly close to R_0 . If the frequency of the RF radiation were higher than the bandgap frequency in the entire strip, then we would expect the resistance to be equal to R_N , and independent of the bias. This is likely to be the situation in THz versions of the HEB mixer, but is not the case in the 20 GHz prototype. The frequency and bias dependence of the device impedance thus requires further study, as we attempt to increase the frequency at which the HEB mixer operates.

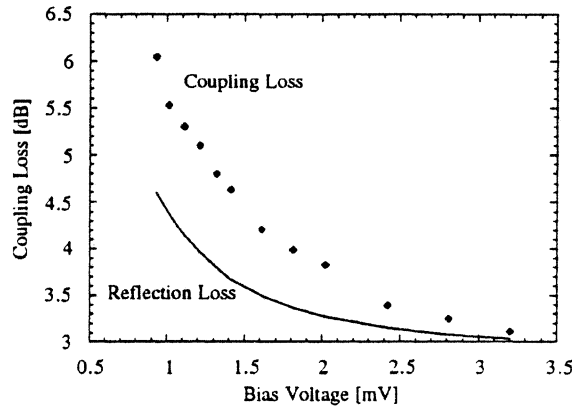


Fig. 14. Measured 20 GHz RF coupling loss (points) vs. bias voltage, and calculated reflection loss under the assumption that the bolometer microwave resistance is equal to its DC resistance. (sample #7)

B) CONVERSION LOSS

The lowest conversion loss of 7 investigated devices was around 1 dB at 20 MHz IF at an operating temperature of 2.1 K (sample #7). The IF of 20 MHz was chosen for the experiments since it is well below the cut-off frequency (Compare Fig. 17). In Fig. 15 one can see how the conversion loss depends on bias voltage (sample #7). The lowest conversion loss is found for the smallest bias, i.e. the lowest bolometer DC resistance. Comparing devices for equal bias, such as the points for samples 11.2 and 15.5 in Fig. 15, it is seen that sample #7 is not the best device, and it is reasonable to assume that samples 11.2 and 15.5 would attain lower conversion loss than sample #7, if measured at lower bias. Also of some importance for the mixer properties are R_N , ΔT_C , T_0 , and the number of strips. So far we have not carried out a complete investigation of the variation of conversion loss with these parameters. However in general terms we have found the following:

The best conversion gain is found for samples with the narrowest superconducting-normal transition ΔT_C , i.e. dR/dT is large.

The conversion gain improves for lower temperatures. Typically we observed one or two dB improvement per Kelvin for a mixer temperature of about 3K

More parallel strips yields a smoother IV-curve and a more stable output signal.

We have not observed any strong dependence on R_N .

In Fig. 15 the measured intrinsic conversion loss of sample #7, the most extensively investigated device, is compared with the theoretical conversion loss calculated from Eq. (1) and (8). In order to find the intrinsic conversion loss, we used the coupling loss, given by expression (22). The agreement is quite good despite the simplified model, which only takes into account uniform heating of the hot electrons, and for example does not consider the slight roughness of the IV-curve. The bias point and a set of DC IV-curves utilised for the RF coupling calculation are shown in Fig. 16. P_{LO} , R_0 , P_{DC} , I_0 , I_{00} and $(dV/dI)_{DC}$ were obtained from the DC IV-plot. The absorbed pump and signal powers, about -43 dBm and -72 dBm respectively, are typical values in our experiments.

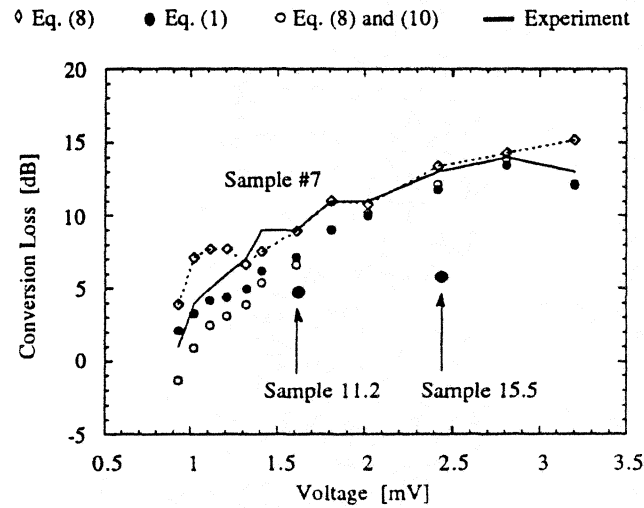


Fig. 15. Experimental and calculated conversion loss vs. bias voltage for sample #7 shown together with the conversion loss of two other samples. The LO power is optimised for the lowest bias and kept constant.

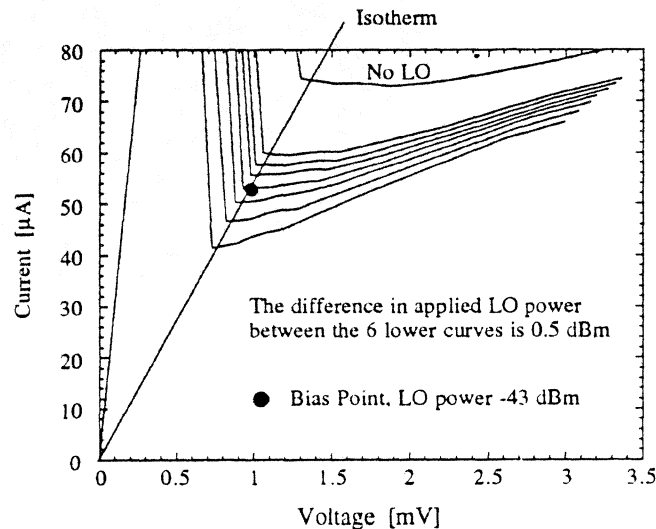


Fig. 16. IV curves for different pump-power. (sample #7)

Note in Fig. 16 that for low bias and no LO, a region with negative resistance is clearly observed. The differential resistance along the isotherm shown in Fig. 16 for different LO powers follows the prediction of Eq. (10). A probable explanation for the occurrence of the negative resistance is the following. When the bias is lowered, the heating is lowered and the temperature of the Nb lattice is lowered as well. This should lead to an increase in the maximum current density, and we consequently will see a negative differential resistance. The time constant for the combined heating phenomenon will be determined by τ_{e-ph} , since $\tau_{ph-s} \ll \tau_{e-ph}$.

C) IF BANDWIDTH

The conversion loss has dropped 3 dB at around 100 MHz IF, see Fig. 17. For larger bias there is a small increase in bandwidth, i.e. the mixer time constant will be slightly shorter. Assuming the relaxation time constant $\tau_e = 1.78$ ns, and calculating $C_0 I_0^2$ and R_0 from the DC IV-characteristic, we obtain theoretically from (Eq. 14) $\tau_{mix} = 2.6, 2.14$, and 1.83 ns, respectively, for the three bias voltages 1.1, 1.4 and 3.2 mV respectively, in excellent agreement with the experimental time constants. In Fig. 17 it can also be seen that there is an increased response at lower IF around 1-10 MHz. This is probably due to influence from slower processes, such as the relaxation of the normal domain size and back flow of phonons from the substrate.

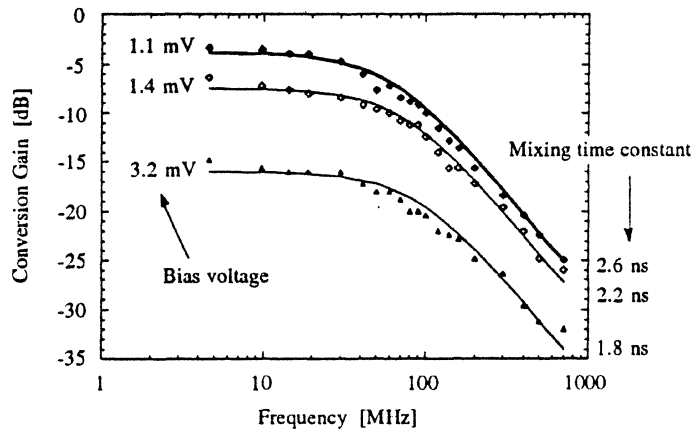


Fig. 17. Conversion Gain vs. frequency and bias, showing an increased mixing time constant for lower bias. (sample #7)

It should be possible to achieve a more uniform absorption of RF power in the strips by: (1) Application of a magnetic field, which reduces the superconducting energy-gap below $f_{RF} \cdot h$, allowing absorption also in the superconducting regions, (2) Use of higher LO and signal frequencies, comparable to or above the gap frequency of the superconductor at the actual temperature, (3) reduction of the superconducting energy-gap by increasing the lattice temperature to a value closer to T_c . It is noteworthy that a higher-frequency HEB mixer is expected to have more ideal performance than the low frequency prototype we have investigated.

D) IF IMPEDANCE

The device IF-impedance has been measured between 1 and 500 MHz (see Fig. 18). There is a transition of the impedance in the range 10 to 100 MHz from 90Ω , which is close to the DC differential resistance (108Ω) in the bias point, to 26Ω , which is the DC resistance in the bias point. The impedance could not be measured for lower biases due to influence from the network analyser.

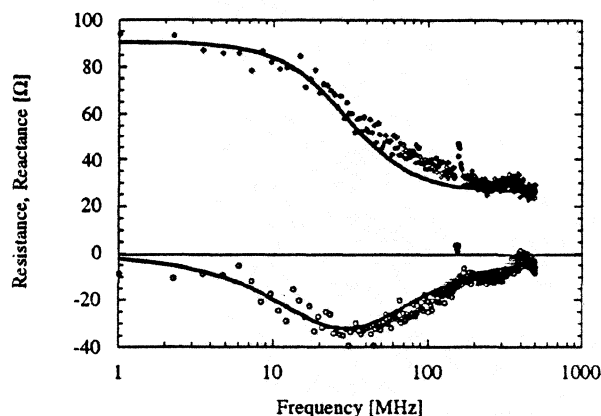


Fig. 18. The measured bolometer impedance for sample #7 (dots). The solid lines show the real and imaginary part of the circuit in Fig. 19. R_0 is $26\ \Omega$ and $(dV/dI)_{DC} = 108\ \Omega$. Optimum LO power is applied.

In Fig. 19 is shown the equivalent circuit of the device, which satisfies Eq. (16), as well as the measured data in Fig. 18. The time constant $\tau = R_2 C$ is 5.37 ns. Using the value for $C_0 I_0^2$ in the bias point and Eq. (17) we find a value for $\tau_e = 1.89$ ns, very close to the number obtained from the conversion loss measurement ($\tau_e = 1.78$ ns).

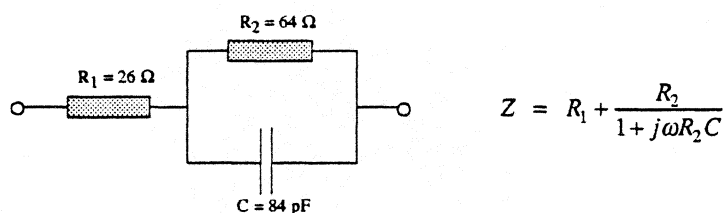


Fig. 19. Equivalent circuit for the bolometer. The values for R_1 , R_2 and C apply to sample #7 and were derived from the measured bolometer impedance data in Fig. 18.

E) NOISE

The receiver and device output noise temperatures, respectively, of the pumped bolometer were measured using the measurement set-ups shown in Figs. 20 and 21.

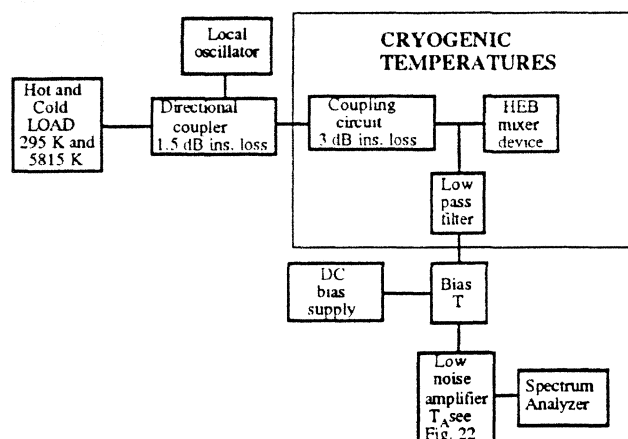


Fig. 20. Set-up for mixer noise measurement.

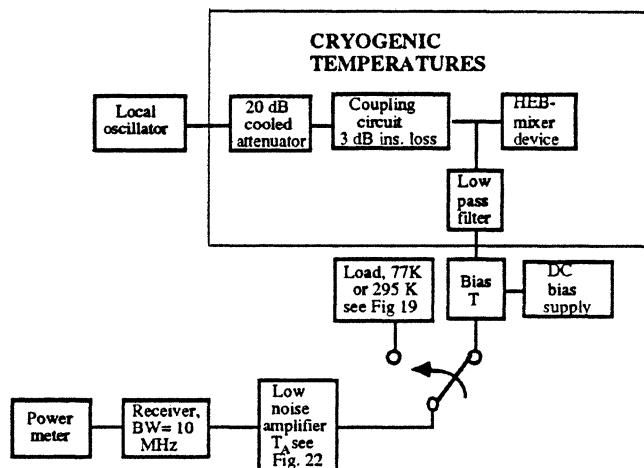


Fig. 21. Set-up for output noise measurement.

Since no isolator is available for the IF-range of interest, a coolable load was fabricated from lumped resistors and a capacitor, with values as shown in Fig. 19. The impedance of this load was checked with a network analyser, and agreed well with the measured data for the bolometer (see Fig. 18). This load was used as a hot and cold load for calibration of the room temperature low noise amplifier over the frequency range 1-100 MHz (Fig. 22).

The DSB receiver noise temperature of one of the HEB mixers was measured with a solid state noise source. The resulting mixer receiver noise temperature was between 470 and 690 K. A DSB mixer noise temperature between 100 and 450 K can be derived from these values, given the conversion loss in the biaspoint of 7 ± 1 dB. The influence of the components between the noise source and the mixer had to be subtracted, introducing an uncertainty in the determination of the mixer receiver noise temperature, thus the large interval quoted. The output noise from the mixer at intermediate frequencies of 20-90 MHz was measured to be 30-50 K (Fig. 22). For this measurement, the mixer was not biased at the optimum DC bias point. However, the optimum LO power was supplied. In this measurement, the conversion loss was 7 dB, and we can predict a DSB mixer noise temperature between 80 and 100 K, based on the measured output noise temperature. The predicted DSB mixer noise temperature is consistent with the above measurements of the mixer receiver noise.

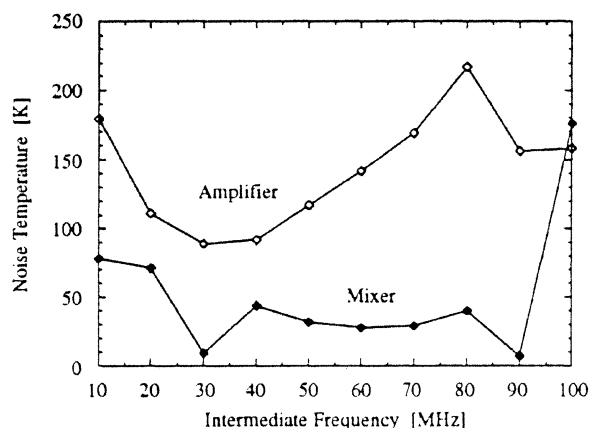


Fig. 22. Output noise temperature of mixer, and amplifier noise when connected to the mixer. $R_o = 26 \Omega$, $T_o = 2.1$ K. P_{LO} is optimised for maximum conversion gain

CONCLUSIONS

We have presented a simple phenomenological theoretical model for the bolometric mixer. This model allows us to derive conversion loss and bandwidths from knowledge of the pumped or unpumped IV-characteristic.

We do see very low conversion loss, which is related to negative resistance in the unpumped IV, and fits the theoretical model quite well.

The negative resistance is likely due to a bias dependent heating effect of the Nb lattice. When the bias is lowered, the temperature of the superconductor is lowered, and a larger current density possible. Hence the current can increase while the bias is decreased.

It is predicted that conversion gain can be achieved, if proper IF impedance load is chosen. The penalty for larger gain is smaller IF bandwidth.

The measured noise is quite low. We see noise temperatures out from the device typically around 50 K, and a double sideband noise temperature expected for an optimised mixer is calculated to about 100-150 K.

The impedance of the device at 20 GHz is bias dependent, which means that this frequency is lower than the bandgap frequency of the superconducting regions of the device.

The frequency dependence of the IF-impedance and conversion gain has been modelled and measured. The measurements are consistent with an electron energy relaxation time of 1.8-1.9 ns. This means that the maximum IF frequency for this particular device is about 100 MHz. It is pointed out that the IF-frequency dependence can be improved by a proper IF load circuit.

ACKNOWLEDGEMENTS

This work has been supported by the Swedish National Board of Industrial and Technical Development (NUTEK). The authors thank Profs. E.Gershenson and G.Gol'tsman for fruitful discussions.

REFERENCES

- [1] E.M.Gershenson et al, "Millimeter and Submillimeter Range Mixer Based on Electronic Heating of Superconducting Films in the Resistive State", *Sov.Phys.Superconductivity*, 3, pp.1582-1597, 1990.
- [2] G.N. Gol'tsman, et al., "Sensitive Picosecond NbN Detector for Radiation from Millimeter Wavelengths to Visible Light," *Supercond.Science and Technology*, 4, 453, 1991.
- [3] H.Ekström, B.Karasik, E.Kollberg, and K.S.Yngvesson, "A Microwave Mixer Using Superconducting Nb Films in the Resistive State", 1993 *Int.Semicond.Dev.Res.Symp.*, pp.475-478, 1993.
- [4] R. Blundell, C.E. Tong, "Submillimeter Receivers for Radio Astronomy," *Proc. IEEE*, 80, pp.1702-1720, 1992.
- [5] J.Mees, et al, "An Airborne SIS-Receiver for Atmospheric Measurements at 630 and 720 GHz", *Proceedings of the Fifth International Symposium on Space Terahertz Technology*, 1994
- [6] Zimmermann R&R&P, "All solid state radiometers for environmental studies to 700 GHz," *Proceedings of the Third International Symposium on Space Terahertz Technology*, pp. 706-723, 1992.
- [7] F.Arams, et al., "Millimeter Mixing and Detection in Bulk InSb", *Proc. IEEE*, 54, pp.308-318, 1966.
- [8] Phillips. T. G. & Jefferts K. B., "A low temperature bolometer heterodyne receiver for millimeter wave astronomy", *Rev. Sci. Instr.*, 44, 1009-1014, 1973.
- [9] Brown E. R., et. al., "A Heterodyne receiver for submillimeter wavelength region based on cyclotron resonance in InSb at low temperature", *Intern. J. Infrared and Millimeter Waves*, 6, 1121-1138, 1985.
- [10] Yang, J.-X. et. al., "Wide-bandwidth electron bolometric mixers,: a 2DEG prototype and potential for low-noise THz receivers", *IEEE Trans. Microwave Theory and Techniques*, May 1993.
- [11] J.-X. Yang, "Two dimension electron gas devices: applications in millimeter and submillimeter waves", Ph.D. Thesis, University of Massachusetts, Department of Electrical and Computer , Sept. 1992 Engineering
- [12] D.E. Prober, "Superconducting Terahertz mixer using a transition-edge microbolometer", *Appl. Phys. Lett.* 62 (17), April 1993.
- [13] J.C. Mather, "Bolometer Noise: Nonequilibrium Theory", *Appl. Optics*, 21, 1125, 1982.

Appendix

Modelling IV-characteristics.

For an IV-curve, with or without LO power, the model suggests that in the bias point V and I, we have

$$C_0 = \frac{dR_0}{dP} = \frac{1}{I_0^2} \cdot \frac{\frac{dV_0}{dI_0} - \frac{V_0}{I_0}}{\frac{dV_0}{dI_0} + \frac{V_0}{I_0}} \quad (A1)$$

Assume that for a certain bias voltage V_0 and current I_0 , the differential resistance $dV/dI = \infty$. Hence in this bias point we have $C_0 = 1/(I_0)^2$. Furthermore, C_0 is constant and the same for given ratio $V_0/I_0 = R_0$, i. e. a given device temperature (device isothermal). Hence

$$C_0 = \frac{dR_0}{dP} = \frac{1}{I_o^2} \cdot \frac{\frac{dV_0}{dI_0} - \frac{V_0}{I_0}}{\frac{dV_0}{dI_0} + \frac{V_0}{I_0}} = \frac{1}{I_{oo}^2} \quad (A2)$$

For simplicity and as an illustration, let us *assume* that for no LO power I is constant, $I = I_0$, independent of bias voltage ($v=0$ in Fig. 5 in paragraph 5). Since R_0 represents an isothermal, we have

$$\frac{P_{LO} + P_{DC}}{P_{DC}} = \frac{P_{LO} + R_o I_o^2}{R_o I_o^2} = \frac{R_o I_{oo}^2}{R_o I_o^2} \quad (A3)$$

Together with Eq. (A2), we now get

$$\frac{dV_0}{dI_0} = \frac{P_{LO}}{I_{oo}^2} \cdot \frac{1 + (I_o / I_{oo})^2}{(1 - (I_o / I_{oo})^2)^2} \quad (A4)$$

We define the parameter $v = P_{LO}/I_0$, where $I_0 = 1$ in this diagram.

$$\frac{P_{LO}}{P_{DC}} = \frac{P_{LO}}{R_o I_{oo}^2} = \frac{v}{R_o I_{oo}} = \frac{v}{V_o} \quad (A5)$$

where v_0 corresponds to the voltage where R_0 intersects $I = I_{00}$.

CYCLOTRON RESONANCE DETECTORS FOR THz FREQUENCIES

D. DAI, C.R. LUTZ, JR., C.F. MUSANTE, K.S. YNGVESSON, AND K.M. LAU

Department of Electrical and Computer Engineering
University of Massachusetts at Amherst, Amherst, MA 01003

E.S. JACOBS, E.R. MUELLER, AND J. WALDMAN

Submillimeter Technology Laboratory, University of Massachusetts at Lowell
Research Foundation, Lowell, MA 01854

and

M.A. TISCHLER

Advanced Technology Materials, Inc.
Danbury, CT 06810

ABSTRACT

Cyclotron resonance (CR) detectors, employing the two-dimensional electron gas (2DEG) medium at the hetero-interface between AlGaAs and GaAs, have been demonstrated from 94 GHz (3.2 mm wavelength) to 2.4 THz (119 μm wavelength). Both MBE material and in-house OMVPE grown material were tested. Responsivity as high as 5,000 V/W was measured at 1.8 THz, with an estimated detector NEP about 3.3×10^{-12} W/ $\sqrt{\text{Hz}}$. In addition to the CR response, strong detection due to a Shubnikov-de Haas like effect was also demonstrated. Detection of fast laser pulses at 600 GHz (496 μm) and 1.2 THz (256 μm) at cyclotron resonance, showed that the time-constant of the detector is ≤ 4 ns. The time-constant when the Shubnikov-de Haas effect is employed is somewhat slower, of the order of 12-15 ns.

I. INTRODUCTION

Applications such as astronomy, remote sensing, and laboratory experiments with pulsed laser sources, require a sensitive and fast detector for frequencies from 0.5 THz to several THz. Typical direct detectors are too slow for these tasks. One of the most sensitive detectors in the submillimeter region is the InSb hot electron bolometer. This device relies on the heating of electrons, and the subsequent change of the resistance, for detection. The InSb device can be tuned in frequency by using a magnetic field, and the peak response then occurs at the frequency for cyclotron resonance [1]. It can be used both in the direct detection mode and in the heterodyne mode. As a direct detector, it has high responsivity and a response time of about 10^{-7} seconds. It has also been operated as a heterodyne detector up to 2.4 THz. A similar detector using the two-dimensional electron gas (2DEG) medium was proposed by Smith et al. [2]. We have investigated the 2DEG cyclotron resonance detector over a wide frequency range (94 and 238 GHz, as well as 1.0, 1.8, and 2.4 THz), employing the 2DEG formed at a heterojunction between AlGaAs and GaAs. The 2DEG CR detector is projected to have a response time from 10^{-10} to 10^{-9} seconds, and thus be considerably faster than earlier detectors of this type. Smith et al. also proposed a heterodyne detector based on the 2DEG device. The potential bandwidth is predicted to be from 0.2 GHz to 2 GHz, and the 2DEG device also has the potential for very low noise. This paper briefly reports the experimental results of our current research on millimeter and submillimeter detection using 2DEG devices.

II. DEVICE FABRICATION

The 2DEG devices were fabricated on $\text{Al}_x\text{Ga}_{1-x}\text{As}/\text{GaAs}$ epi-layers grown on semi-insulated GaAs wafers by MBE and OMVPE. The detector geometry at millimeter waves is a simple bar between two contact pads with a typical size of $200\mu\text{m} \times 50\mu\text{m}$, as shown in Figure 1. The nonlinear 2DEG element consists of a planar sheet of 2DEG, formed at the interface between AlGaAs and GaAs, similar to the medium used in HEMTs, but without the gate. At THz frequencies, two types of square detector configurations, with

overall size of $1\text{mm} \times 1\text{mm}$ were designed (Figure 2). One has an open faced structure, and the other has an interdigitated contact structure. The interdigitated contact structure has six fingers total; the space between the fingers is $180\text{ }\mu\text{m}$, and the width of a finger is $40\text{ }\mu\text{m}$.

In order to successfully demonstrate the cyclotron resonance detection/mixing effect, the mobility of the device should be high, and the sheet charge density should be $\sim 3 - 4 \times 10^{11}\text{ cm}^{-2}$. It may also require a unique combination of materials parameters. In our detector experiments, the 2DEG devices are fabricated on several high mobility samples grown both by MBE and OMVPE. The mobilities of these samples are as high as $2 \times 10^6\text{ cm}^2/\text{V}\cdot\text{s}$, and the sheet charge densities are in the low 10^{11} cm^{-2} range, at 4.2K. The material parameters of these samples are listed in Table 1.

Table 1: 2DEG Material Parameters

Material	77 K		4.2 K	
	N_s ($\times 10^{11}\text{ cm}^{-2}$)	μ ($\text{cm}^2/\text{V}\cdot\text{s}$)	N_s ($\times 10^{11}\text{ cm}^{-2}$)	μ ($\text{cm}^2/\text{V}\cdot\text{s}$)
TDEG33(OMVPE)	4.7	171,000	4.95	728,400
T 7591 (MBE)	4.5	173,240	4.23	790,610
G 587 (MBE)	5.2	202,000	3.64	1,410,000
G 585 (MBE)	2.4	205,000	3.35	2,410,000

In our 2DEG device fabrication processing, wet chemical etching is used for device isolation. The height of the mesa is about $1.5\text{ }\mu\text{m}$. The 2DEG sheet is then located within the mesa, which is surrounded by semi-insulating GaAs for isolation of the device. The metallization of the devices consists of a standard sequence of evaporated layers for forming AuGe ohmic contacts, and the device pattern is defined by a lift-off process. In order to reduce the millimeter wave loss due to the dielectric reflection, the millimeter wave devices are thinned down to 5 mil.

III. EXPERIMENTAL RESULTS

A. Detection of CW Radiation

The experimental system at UMass/Amherst for the 2DEG CR detector measurements is shown in Figure 3. A liquid helium dewar with a superconducting magnet provides cooling to 4.2 K and a magnetic field of up to 5 Tesla. Different millimeter wave and submillimeter wave sources are used: (1) for 94 GHz and 238 GHz, we employ a Gunn oscillator, and a BWO with a varactor tripler, respectively, fed through an over-size waveguide; (2) at the THz frequencies, we use the $163\mu\text{m}$ (1.8 THz), and $119\mu\text{m}$ (2.4 THz) lines of a CO_2 -laser pumped molecular laser, guided to the sample through light pipes. At 94 and 238 GHz, the detector device is mounted as flip-chips on a printed circuit on a 5 mil quartz substrate, which is inserted into a waveguide block. For the THz experiment, the detector is placed in an integrating cavity.

We have investigated a number of high-mobility samples grown by MBE ($\mu_{4\text{K}}$ up to $2.4 \times 10^6 \text{ cm}^2/\text{V-s}$) and OMVPE ($\mu_{4\text{K}}$ up to $7.4 \times 10^5 \text{ cm}^2/\text{V-s}$) at the frequencies mentioned above. The responsivity at 1.8 THz is as high as 5,000 V/W (Figure 4), much higher than at 94 or 238 GHz (100-200 V/W) (Figure 5). The characteristics of the detector can be very different for devices fabricated from different wafers, indicating the complicated scattering processes occurring in the 2DEG medium biased with a magnetic field. The device configuration also plays an important role in the detector performance. In general, the open-faced devices show a single CR line only, whereas the interdigitated devices also show a detected pattern which is periodic as a function of inverse magnetic field ($1/B$), see Figure 6. The latter effect is similar to the Shubnikov-de Haas oscillations which can be seen in the resistance of the device, also shown in Figure 6. Our experimental results are summarized in Figure 7, showing the approximate detector responsivity versus frequency. To find the responsivity, we measured the output power of the laser, and also estimated the loss of the light pipe. Our superconducting magnet was limited to a maximum field of 5 Tesla; therefore we could not reach the cyclotron resonance field at 2.4 THz. Instead, we were able to demonstrate detection due to a Shubnikov-de Haas like effect at this frequency (Figure 8).

The samples with the highest responsivity (R) at 1.8 THz were grown by MBE, and have mobilities of about $790,000 \text{ cm}^2/\text{V-s}$. An OMVPE grown sample with similar mobility yielded $R=600 \text{ V/W}$ at 1.8 THz. These responsivities are much higher than those previously measured for this type of detector [2]. Further increase of R is possible by using lens coupling to a small detector.

B. Detection of Pulsed Radiation

This investigation was started with the motivation of developing a sensitive THz detector with fast response. We have performed a preliminary test which shows that the CR/2DEG detector is about two orders of magnitude faster than the InSb detector. We employed a pulsed laser system at the Submillimeter Technology Laboratory, University of Massachusetts/Lowell. A TEA CO_2 laser was used to pump a cavity-dumped THz gas laser with NH_3 as the active medium. The cavity-dumping was accomplished by directing a Q-switched pulse from a frequency-doubled YAG laser at a silicon etalon inside the THz laser cavity. A THz pulse with a FWHM of about 7 ns and peak power 100-200 W was created by this system (see the diagram in Figure 9). A Schottky diode detector in a corner-cube mount served as a comparison detector, which was assumed to be fast enough so as not to distort the THz pulse.

The laser was tuned to two different frequencies: (1) 1.2 THz ($256 \mu\text{m}$), and (2) 600 GHz ($496 \mu\text{m}$). The cyclotron resonance fields were 2.9 Tesla and 1.5 Tesla for these two frequencies. The detectors were grown by MBE, and had mobilities of $790,000 \text{ cm}^2/\text{V-s}$ and $1,410,000 \text{ cm}^2/\text{V-s}$, respectively. Both samples gave pulse-widths of about 12-15 ns at the higher frequency, substantially broadening the pulse detected by the Schottky-diode (FWHM = 7 ns, see Figure 10). The width of the CR-detected pulse was essentially independent of the bias current, up to $600 \mu\text{A}$. At the lower frequency, the CR detector produced a pulse only slightly broader than the Schottky-detector, see Figure 11. A CR detector time-constant of 4 ns is consistent with the data. This time is an upper limit, since the pulses from the CR detector may have been further lengthened by circuit effects, compared with the Schottky detector. These effects will be investigated further. The fastest response was found for larger bias currents, with a constant pulse

width being observed from 150 μA to 5.7 mA. Tuning the magnetic field to 2.9 Tesla, and still using the 600 GHz line, we found a much longer pulse-width of about 15 ns. We believe that this detection is due to the Shubnikov-de Haas (SdH) effect. One should note that the SdH detections are located at specific magnetic fields, periodic in $1/B$ (compare Figure 6), and that these positions are independent of the laser frequency. Since the cyclotron resonance field for 1.2 THz was also 2.9 Tesla, there must have been a coincidence between the CR field and the SdH field in the 1.2 THz measurements. This could explain why the time constant was so much slower at 1.2 THz. We tentatively conclude, then, that the time-constant for CR detection in the 2DEG medium is ≤ 4 ns, while the SdH effect time-constant is of the order of 12-15 ns.

IV. DISCUSSION AND CONCLUSIONS

A. Mechanism of Detection

Detectors of millimeter waves/submillimeter waves which utilize cyclotron resonance in a 2DEG have been explored in a number of earlier papers [3-7]. Most of this work has been aimed at understanding the physics of the 2DEG medium in a magnetic field, and only mentions the possibility of developing a detector as an aside. The quoted responsivity has often been quite low (about 1 V/W), and the response time has usually not been measured. It is not clear from most of these experiments how the responsivity and the NEP vary with parameters such as mobility, detector configuration, bias current, or frequency of the detected radiation.

Thiele et al.[8] used a thin gate to control the density of the 2DEG, and to pick up a detected, photo-voltaic response. A voltage is induced on the gate, as the Fermi energy in the 2DEG changes abruptly on passage through a Landau level. To interpret the shape of the cyclotron resonance response versus magnetic field, one must introduce an inhomogeneous electron density, which gives rise to states in between the Landau levels. The inhomogeneity of the electron density is likely to be related to a non-uniform distribution of the ionized impurities (donors) in the AlGaAs and in the quantum well. Non-uniform distribution of the donors is likely to be important in our devices as well.

The responsivity of Thiele et al.'s detector appears to be about 25 V/W. A radiation-induced increase in electron temperature by about 10 K was deduced.

Dießel et al.[9] introduced a different principle for detection, i.e. scattering of the electrons between edge states is promoted by the absorption of the submillimeter waves. This scattering is made possible by introducing two gates which deplete the electron gas over part of the width of the detector. The sub-mm-induced scattering then occurs between the two gates. This detector operated at 1.2 K, and a responsivity of close to 10,000 V/W was estimated. The optimum bias current was only about 100 nA.

Our own experiments show that comparable responsivity to that obtained by Dießel et al. can be obtained in a much simpler detector configuration. Also, the response time has now been measured for the first time. The following major experimental conclusions were obtained:

- (1) The optimum responsivity obtained so far increases by one to two orders of magnitude as the frequency of the detected radiation goes from 100-200 GHz to 1.8 THz.
- (2) As the electron mobility varies from 200,000 to about 10^6 cm²/V-s, the responsivity at 100-200 GHz increases from about 1V/W to 200 V/W. The optimum mobility for 1.8 THz detection is close to 10^6 cm²/V-s. The optimum electron density is likely to be the one which results in the maximum mobility, i.e. $3\text{-}4 \times 10^{11}$ cm⁻².
- (3) Due to incomplete data, we can not determine if the highest mobility sample ($\mu = 2.4 \times 10^6$ cm²/V-s) yields the highest responsivity.
- (4) "Shubnikov-de Haas type" detection occurs, with somewhat lower responsivity, but only in the interdigitated devices.
- (5) For the CR mode, we find a response time of ≤ 4 ns while the SdH effect detection is considerably slower, about 12-15 ns.

From (1), we deduce that the Landau levels have to be well separated in order for the detection mechanism to work optimally. At 94 and 238 GHz, this is not the case, judging from the measured cyclotron resonance linewidths.

From (2), we can see that the samples with optimum responsivity in general are those with high mobility. High mobility is known to be related to low impurity concentration in and near the channel; also, the remote impurities in the AlGaAs separated from the channel by a fairly thick (400 Å) spacer. This rule is not universal, however, indicating that the exact nature and location of the impurities can influence the mobility and the detector responsivity differently. An example of this effect is that detectors fabricated on OMVPE and MBE wafers with similar mobility and density yielded quite different responsivity results.

A very tentative explanation of our results can be formulated as follows: Due to local fluctuations in the potential related to the distribution of impurities, a given Landau level will fluctuate through the device, in relation to the Fermi level. At least in the interdigitated devices, conducting channels may form across the detector when the local energy is equal to the Fermi energy (or higher), as indicated by Büttiker [10]. At energies well separated from the Fermi energy, only localized states are possible, similar to the inter-Landau level states discussed by Thiele et al.[8]. An increase in the electron temperature, caused by absorption of submillimeter wave radiation, will change the number of channels which are able to percolate across the entire detector. It is not clear if this mechanism is feasible in the open-face detectors, since these are about 1×1 mm in size. Adiabatic electron transport has been observed in edge channels in long, narrow geometries over distances of 200-400 μm [10]. Future investigation will have to further clarify these tentative ideas about the detection mechanism in cyclotron resonance detectors.

Whether the above tentative explanation is correct or not, it is likely that hot electron phenomena are involved. We then expect the time-constant to be of the order of the energy relaxation time, τ_e . This relaxation time is known to be close to 1 ns from Shubnikov-de Haas measurements [11], which is consistent with the upper limit of 4 ns estimated from our pulse measurements. It is also noteworthy that the detector operated well even with a bias as high as 5.7 mA. At this bias, the electron temperature can be estimated to be in the range 50-80 K [5], an unusually high temperature for observing the CR effect.

B. Design of a Heterodyne Detector

By analogy with the InSb hot electron detector, we expect that the 2DEG detector will also operate in the heterodyne mode. The measured response time (τ) indicates that the heterodyne version should have a minimum IF bandwidth equal to $1/2\pi\tau = 50$ MHz based on our pulse measurements. Further measurements of actual mixing are needed to confirm what the bandwidth will be under optimum heterodyne detector conditions, which may be different from those in the pulse experiments. The device output noise temperature is expected to be of the order of the electron temperature (15 K), with a possible extra term due to electron temperature fluctuations (compare to the superconducting mixer case, see [12]). With a conversion loss similar to what is obtained for InSb mixers (10-13 dB), we then predict a DSB receiver noise temperature of roughly 100-200 K. Judging from our direct detector results, it will be difficult to obtain low conversion loss in the millimeter wave range; this is an experiment which must be attempted in the actual THz range. Initially, it may be useful to employ the same "open" optical coupling method which we have used for the direct detectors. However, a more optimum solution would be to couple via an extended hemi-spherical lens, as shown in Figure 12. Further development is ongoing to realize a lower resistance detector element, which can be matched to the antenna element behind the lens. Typical antenna elements can be a log-periodic spiral, or a double-dipole or double-slot antenna. These present an impedance of 50-100 ohms, whereas the present version of the detector has a typical resistance of 1.5 kohms, due to the magneto-resistive effect. The responsivity in the straight detector case will increase in inverse proportion to the linear size of the device: It is thus possible to reach responsivities of the order of 10^5 V/W, and NEPs of 10^{-13} to 10^{-14} W/ $\sqrt{\text{Hz}}$.

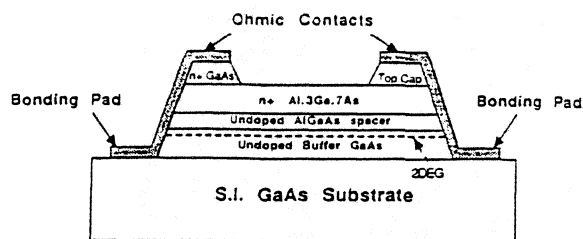
ACKNOWLEDGMENTS

This work was supported by NSF under grant ECS-9208752. The authors would like to thank Dr. N. Cronin of University of Bath, UK, for providing MBE samples for this work. Technical assistance by F. Agahi and R. Basco is also acknowledged.

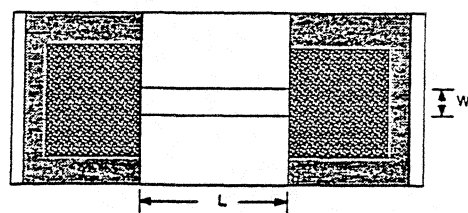
REFERENCES

- [1] E.R. Brown, J. Keene, and T.G. Phillips, "A Heterodyne Receiver for the Submillimeter Wave Region Based on Cyclotron Resonance in InSb at Low Temperatures," *Intern. J. Infrared and Millimeter Waves*, **6**, 1121 (1985).
- [2] S.M. Smith, N.J. Cronin, R.J. Nicholas, M.A. Brummel, J.J. Harris, and C.T. Foxon, "Millimeter and Submillimeter Detection Using $\text{Ga}_{1-x}\text{Al}_x\text{As}/\text{GaAs}$ Heterostructures," *Intern. J. Infrared and Millimeter Waves*, **8**, 793 (1987).
- [3] K.S. Yngvesson, J.-X. Yang, F. Agahi, D. Dai, C. Musante, W. Grammer, and K.M. Lau, "AlGaAs/GaAs Quasi-Bulk Effect Mixers: Analysis and Experiments," *Proceedings of the Third International Symposium on Space Terahertz Technology*, University of Michigan, Ann Arbor, MI, p.688 (1992).
- [4] J.-X. Yang, F. Agahi, D. Dai, C. Musante, W. Grammer, K.M. Lau, and K.S. Yngvesson, "Wide-Bandwidth Electron Bolometric Mixers: A 2DEG Prototype and Potential for Low-Noise THz Receivers," *IEEE Trans. on Microwave Theory and Techniques, Mini-Special Issue on Space THz Technology*, **MTT-41**, 581 (1993).
- [5] J.-X. Yang, "AlGaAs/GaAs Two Dimensional Electron Gas Devices: Applications in Millimeter Waves and Submillimeter Waves," Ph.D. Thesis, University of Massachusetts at Amherst, Department of Electrical and Computer Engineering, Sept. 1992.
- [6] J.C. Maan, Th. Englert, D.C. Tsui, and A.C. Gossard, "Observation of Cyclotron Resonance in the Photoconductivity of Two-Dimensional Electrons," *Appl. Phys. Lett.*, **40**, 609 (1982).
- [7] M.J. Chou, D.C. Tsui, and A.Y. Cho, "FIR Photoconductivity in the Integral Quantum Hall Regime in GaAs/AlGaAs," *Proc. 18th Int. Conf. on the Phys. of Semiconductor*, 437 (1986).
- [8] F. Thiele, E. Batke, J.P. Kotthaus, V. Dolgoplov, V.N. Ovsyuk, G. Gusev, G. Weimann, and W. Schlapp, "Far-Infrared Radiation Induced Photovoltage of Inversion Electrons on GaAs and Si," *Solid State Electronics*, **32**, 1503 (1989).
- [9] E. Dießel, G. Müller, D. Weiss, K. von Klitzing, K. Ploog, H. Nickel, W. Schlapp, and R. Löscher, "Novel Far-Infrared-Photoconductor Based on Photon-Induced Interedge Channel Scattering," *Appl. Phys. Lett.* **58**, 2231 (1991).
- [10] M. Büttiker, "The Quantum Hall Effect in Open Conductors," in *Semiconductors and Semimetals*, Vol. **35** (M. Reed, Ed.), Chapter 4, p. 191 (1992).

- [11] H. Sakaki, K. Hirakawa, J. Yoshino, S.P. Svensson, Y. Sekiguchi, and T. Hotta, "Effects of Electron Heating on Two Dimensional Magnetotransport in AlGaAs/GaAs Heterostructures," *Surface Science*, **142**, 306 (1984).
- [12] E.M. Gershenzon, G.N. Gol'tsman, I.G. Gogidze, Y.P. Gusev, A.I. Elant'ev, B.S. Karasik, and A.D. Semenov, "Millimeter and Submillimeter Range Mixer Based on Electronic Heating of Superconducting Films in the Resistive State," *Soviet Physics: Superconductivity*, **3**, 1582 (1990).

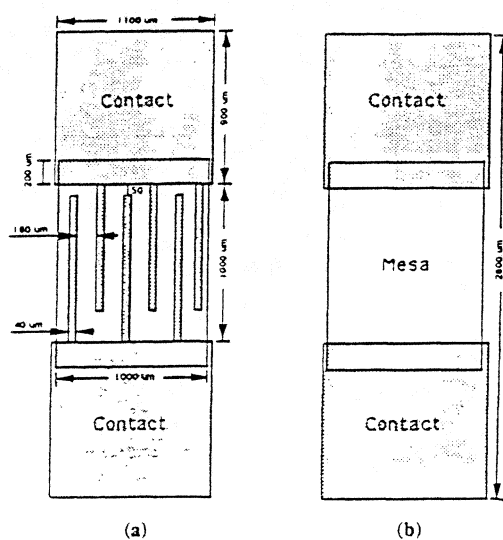


(a)



(b)

Figure 1: Millimeter wave device configurations: (a) side view; (b) top view.



(a)

(b)

Figure 2: THz detector configurations: (a) interdigitated; (b) open faced.

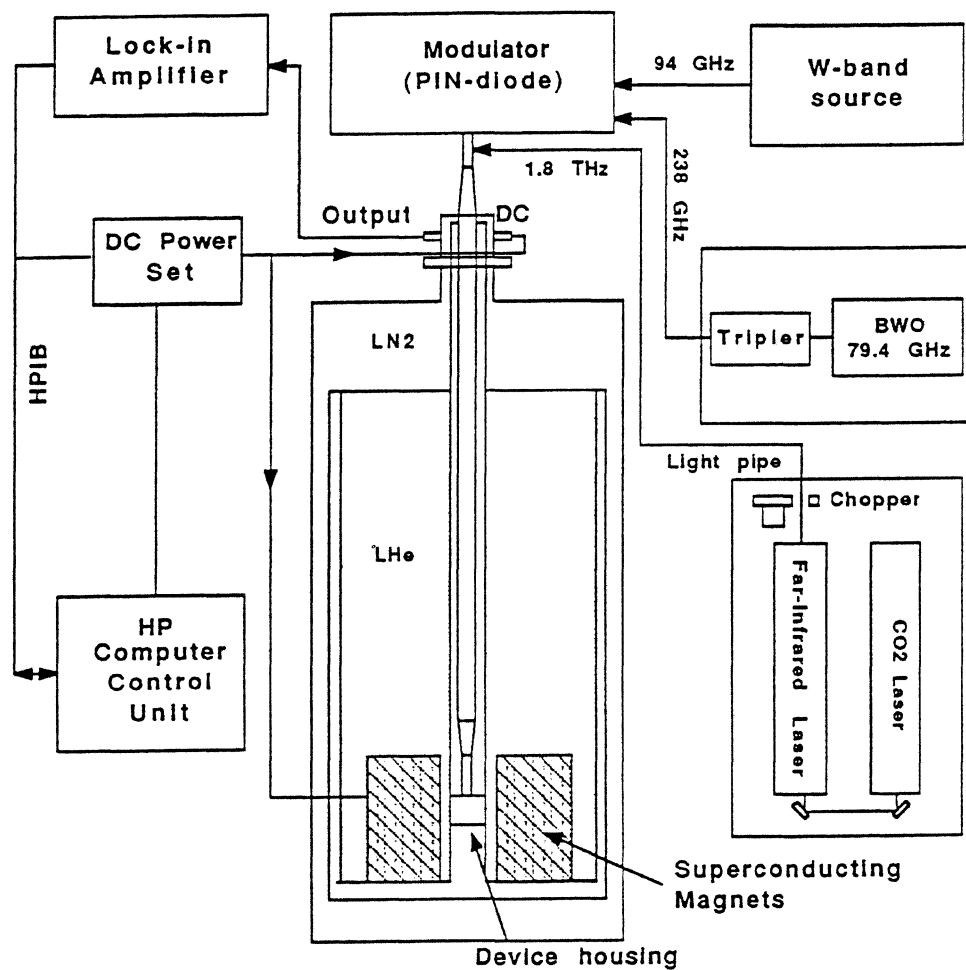


Figure 3: Schematic diagram of the experimental system set up.

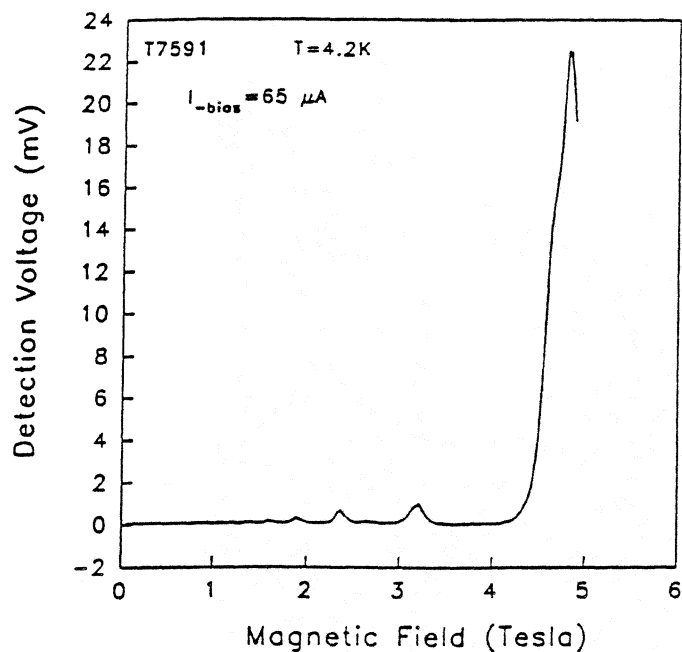


Figure 4: Detector response at 1.8 THz; MBE sample with $\mu_{4K} = 7.9 \times 10^5 \text{ cm}^2/\text{Vs}$.

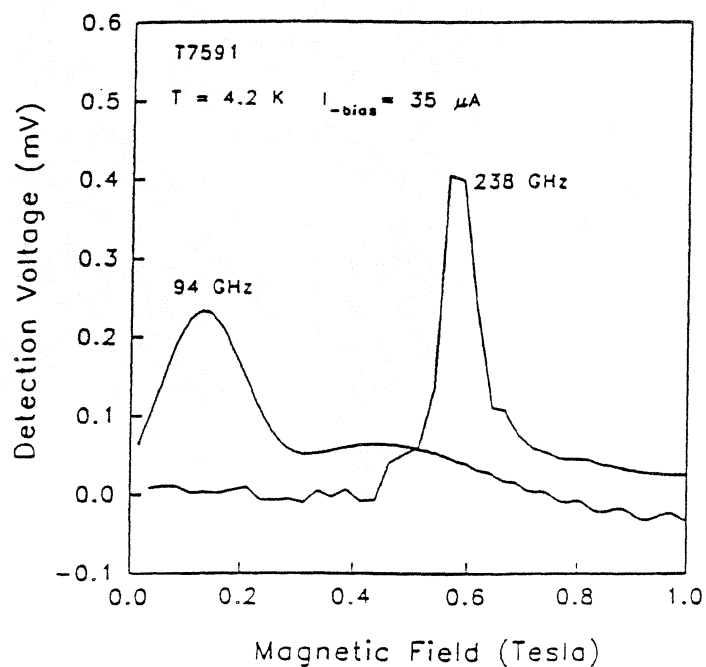


Figure 5: Detector responses at 94 GHz and 238 GHz, same material as in Figure 4.

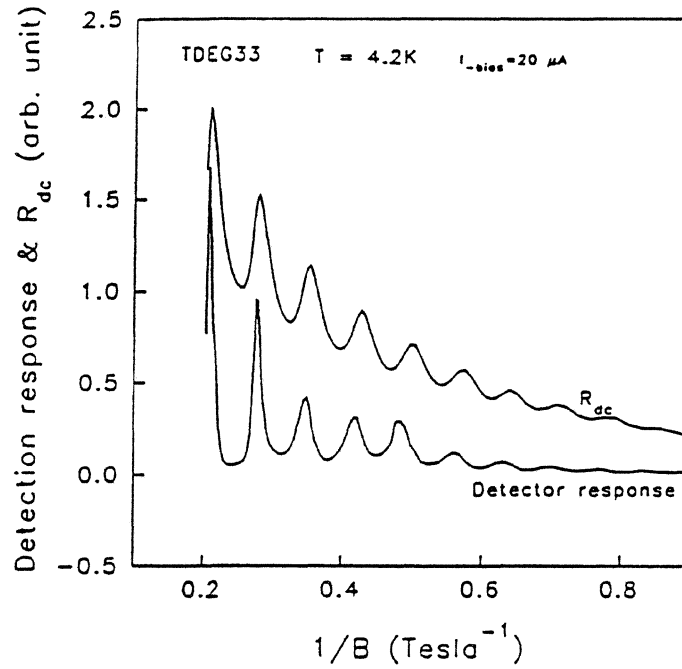


Figure 6: Detector response and device resistance vs. $1/B$; OMVPE sample with $\mu_{4K} = 7.4 \times 10^5 \text{ cm}^2/\text{Vs}$.

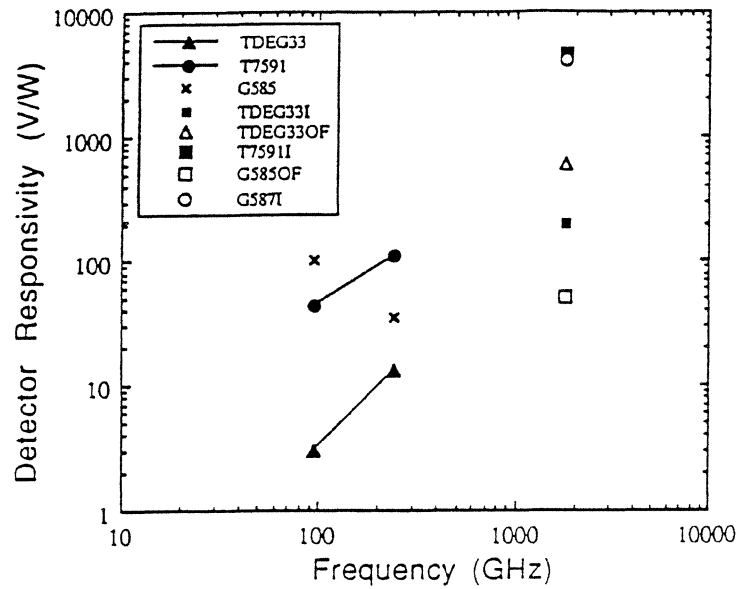


Figure 7: Detector Responsivity vs. Frequency for several different samples.

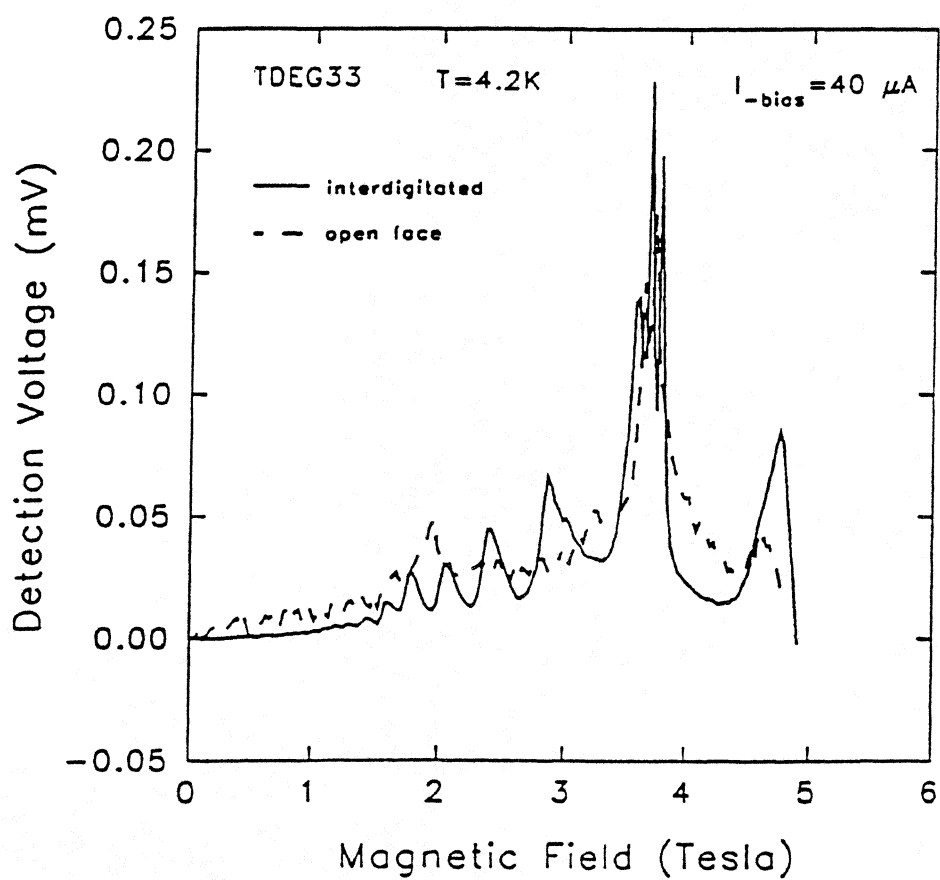


Figure 8: Detector response at 2.4 THz; same OMVPE material as in Figure 6.

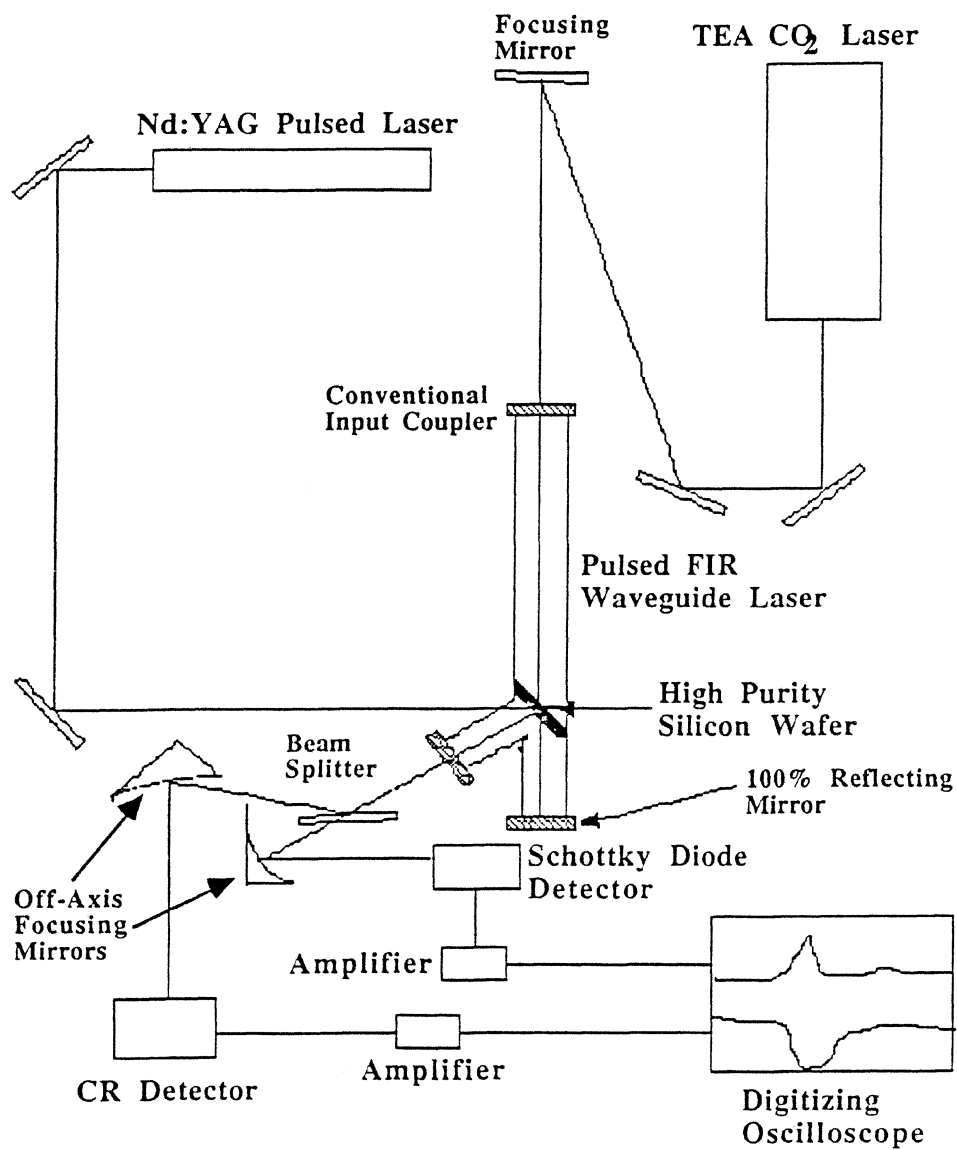
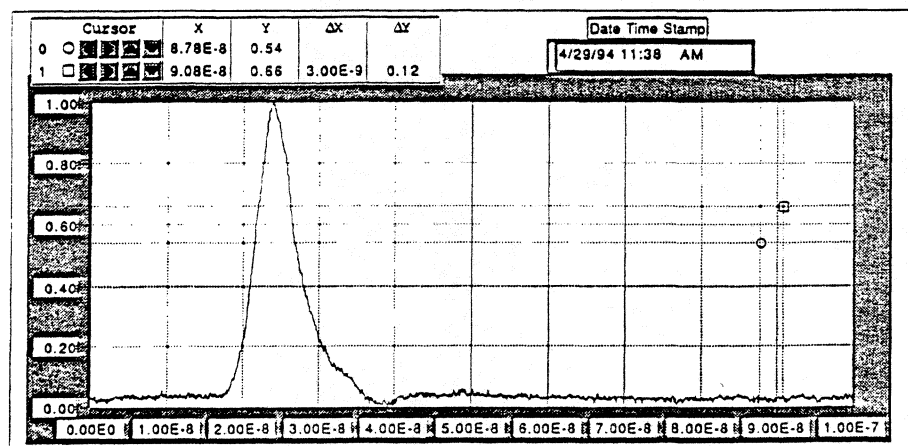
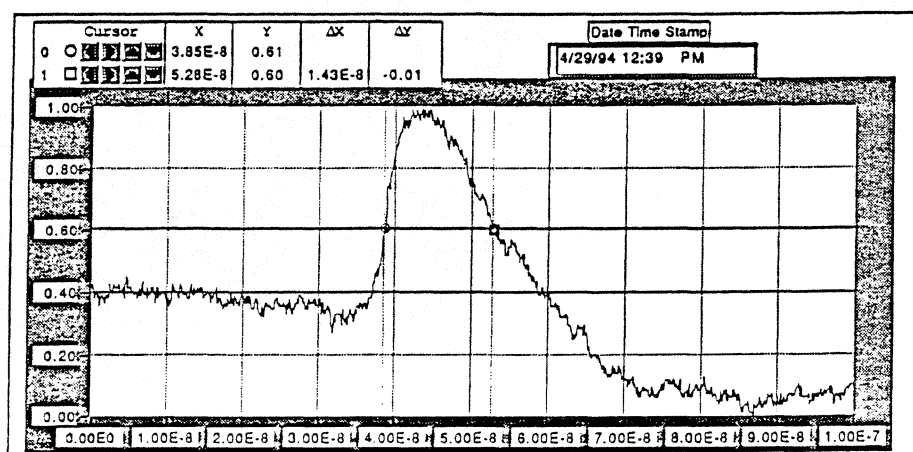


Figure 9: Diagram of the pulsed laser setup.

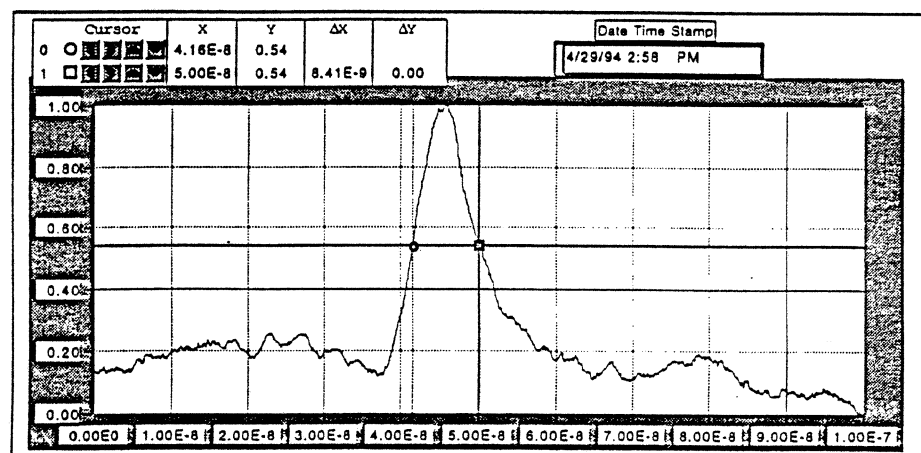


(a)

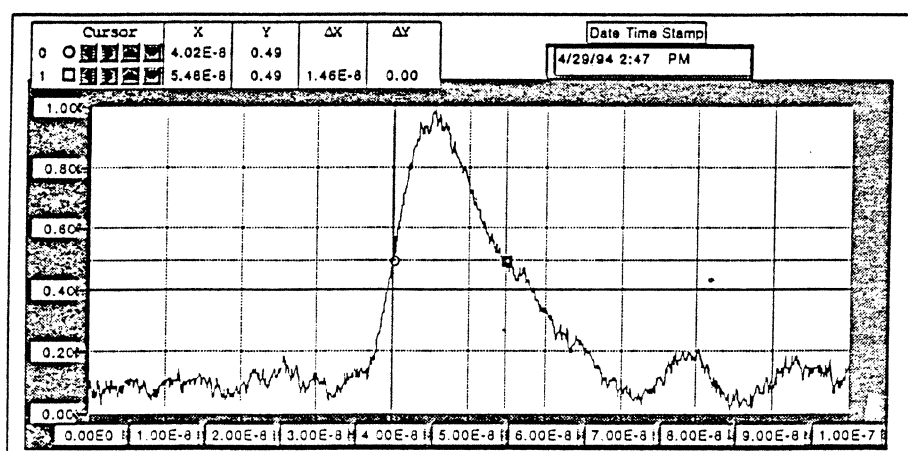


(b)

Figure 10: Pulse detection at 1.2 THz; (a) Schottky detector; (b) CR detector.



(a)



(b)

Figure 11: Pulse detection at 0.6 THz, employing the CR detector with a magnetic field of (a) 1.5 Tesla; (b) 2.9 Tesla.

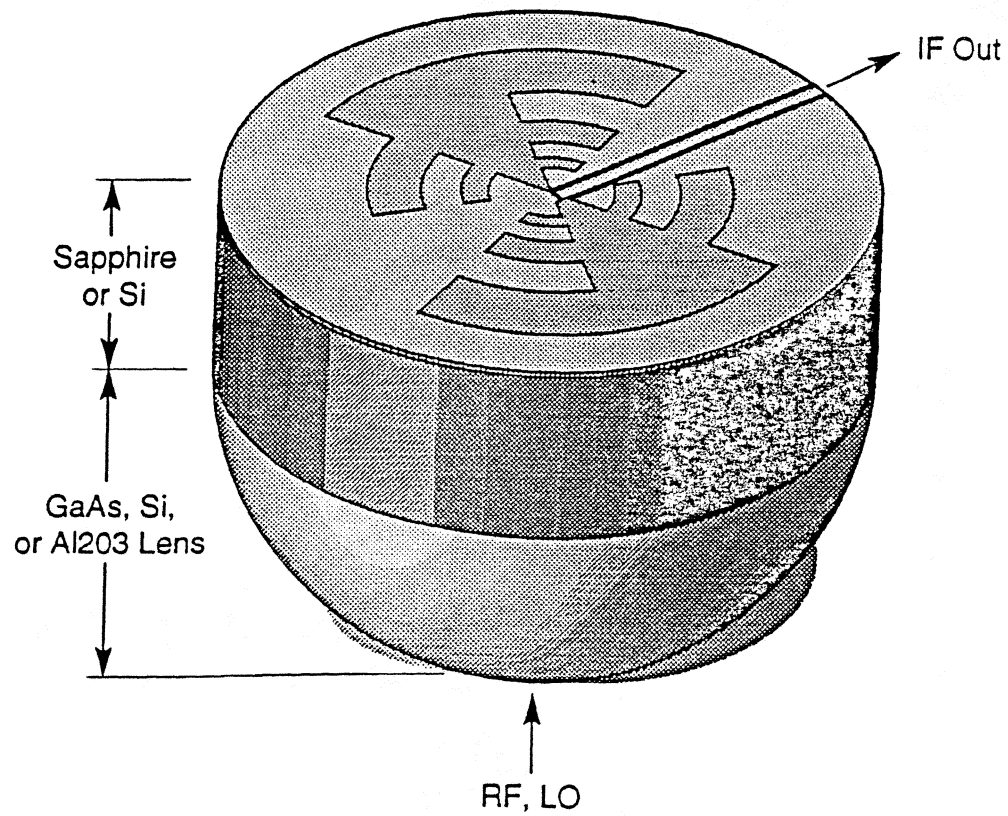


Figure 12: Quasi-optical coupling structure for the THz 2DEG hot electron heterodyne detector.

Slot-Line Tapered Antenna with NbN Hot Electron Mixer for 300-360 GHz Operation

G.Gol'tsman*, S.Jacobsson**, H.Ekstrom**, B.Karasik*, E.Kollberg**
and E.Gershenzon*.

NbN hot-electron mixers combined with slot-line tapered antennas on Si oxinitride membranes had been fabricated. Several strips of $1\ \mu\text{m}$ wide and $5\ \mu\text{m}$ long made from $100\ \text{\AA}$ NbN film are inserted into the slot antenna. IV-curves under local oscillator power in 300-350 GHz frequency range and conversion gain dependencies on intermediate frequency in the 0.1-1 GHz range are measured and compared with that for 100 GHz frequency band.

Our results show that pumped IV-curves and intermediate frequency bands are different for 100 GHz and 300 GHz frequency ranges. The interpretation exploits the fact that for the lowest radiation frequency the superconducting energy gap is larger than the radiation quantum energy while they are comparable at the higher frequency. The results show that such mixers have good perspectives for terahertz receiving technology.

For hot electron mixers based on thin superconducting films the interesting problem is to trace the transition from the condition $h\nu < 2\Delta$ to the opposite one. Here $h\nu$ is the quantum energy of the receiving radiation and 2Δ is the superconducting energy gap of the mixing element. The frequency corresponding to the energy gap of bulk NbN at $T = 0$ lies in terahertz range. For thin film mixing element under operation condition it may be much smaller due to electron heating produced by the LO power and biasing current. The study of the transition region can be carried out using wide quasioptical technique rather than waveguide technique which provides relatively narrow frequency band. In this work we study hot electron NbN film mixers matched to a slot-line tapered antenna (Fig. 1). Seven strips $1\ \mu\text{m}$ wide and $5\ \mu\text{m}$ long made from $100\ \text{\AA}$ thick NbN film are inserted into the antenna slot. The third (314 GHz) or the fourth (360 GHz) harmonic of a 100 GHz range Gunn oscillator was used as a signal source. As a local oscillator we used a backward wave oscillator (BWO).

Figures 2,3 show IV-curves under LO radiation for frequencies 100 GHz and 314 GHz. At higher frequency (Fig. 2) the transformation of IV-curves with the increase of LO power is quite similar to that occurring when the temperature of the mixer increases. The rise of LO power smears hysteresis and voltage steps that flattens IV-curves. The optimal operating point of the mixer belongs to the relatively flat IV-curve (around point M, Fig. 2). The different behaviour of IV-curve was observed for lower frequency (100 GHz). Although the increase of LO power causes the drop of both the critical current and the reverse critical current, the former decreases faster. Thus the hysteresis becomes more pronounced. When the critical current reaches zero IV-curve becomes flat. The optimal operating point belongs to the flat branch of IV characteristic and is located near the reverse critical current (around point M).

Intermediate frequency dependencies of the conversion gain are also different for lower and higher frequencies (Fig. 4,5). For the 100 GHz local oscillator the intermediate frequency band decreases from ≈ 2 GHz to 0.6 GHz when the operating point approaches the critical current. For the higher LO frequency the intermediate frequency band in the operating point is more than 1 GHz.

Features reported here can be qualitatively interpreted taking into account that the energy gap of the mixer film driven into the operating point is less compared to the energy gap of bulk NbN ($2\Delta = 6.5$ meV^[1]). At 300 GHz the IV-curve dynamics under the LO power shows that the radiation quantum energy may be close to the energy gap value in the operating point. For 100 GHz the transformation of IV-curves is obviously non thermal, which is a consequence of the condition $h\nu < 2\Delta$. In this case electrons are heated up by RF current in the same manner as by dc current, namely the electron heating occurs only in the normal state regions of the film. In superconducting regions RF currents are

transported by Cooper pairs. Contrary, for 300 GHz LO frequency the electron heating is likely more uniform.

In conclusion, it is shown that IV-curves of the hot electron NbN thin film mixer becomes more stable and the intermediate frequency band of such a mixer increases with the increase of LO frequency.

This work was supported by the Swedish National Board of Industrial and Technical Development and by the Russian Scientific Council on High- T_c Problem (Pr. No. 93169).

* G. Gol'tsman, B. Karasik and E. Gershenzon are with Moscow State Pedagogical University, Moscow, Russia.

** S. Jacobson H. Ekstrom and E. Kolberg are with Chalmers University of Technology, Göteborg, Sweden.

[1] D.R.Kareski et al., Phys. Rev. B, Vol. 27, No. 9, May, 1983, pp. 5460-5466.

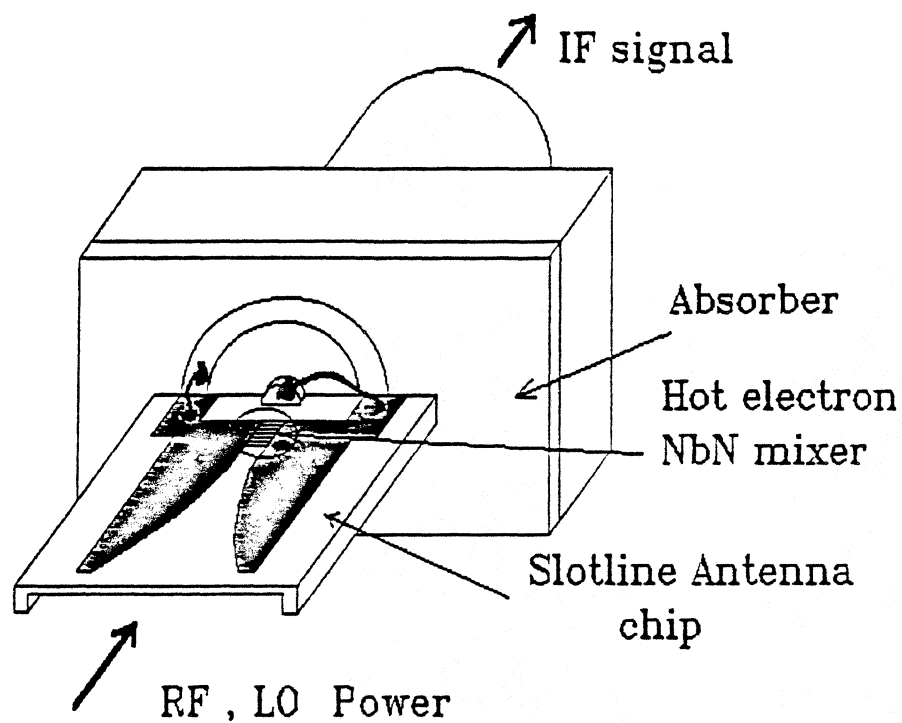


Fig. 1. Design of the antenna-coupled mixer mount.

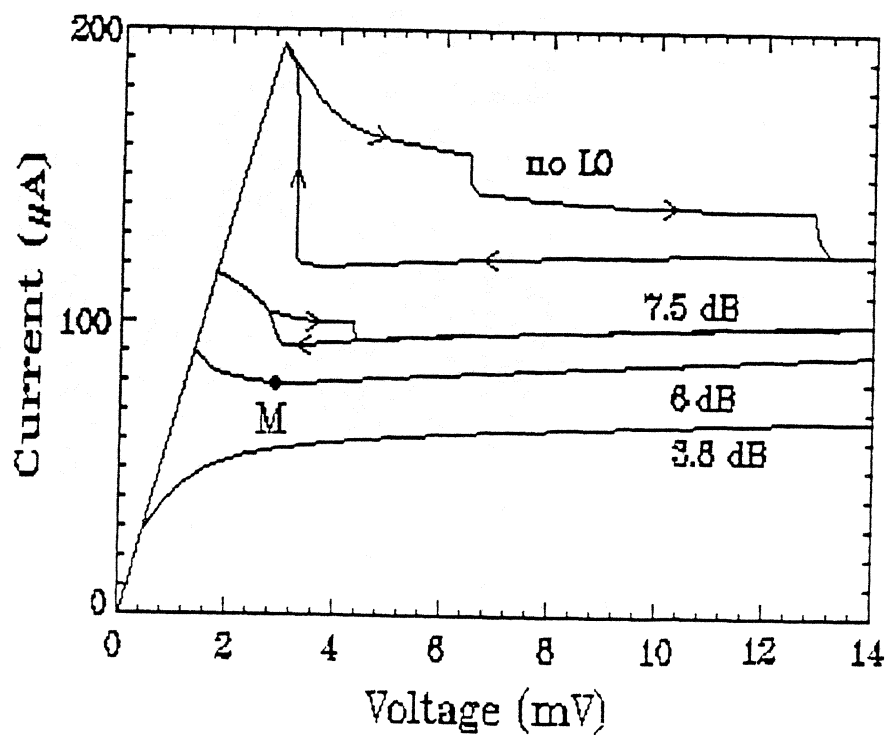


Fig. 2. IV-curves under LO power at 314 GHz.

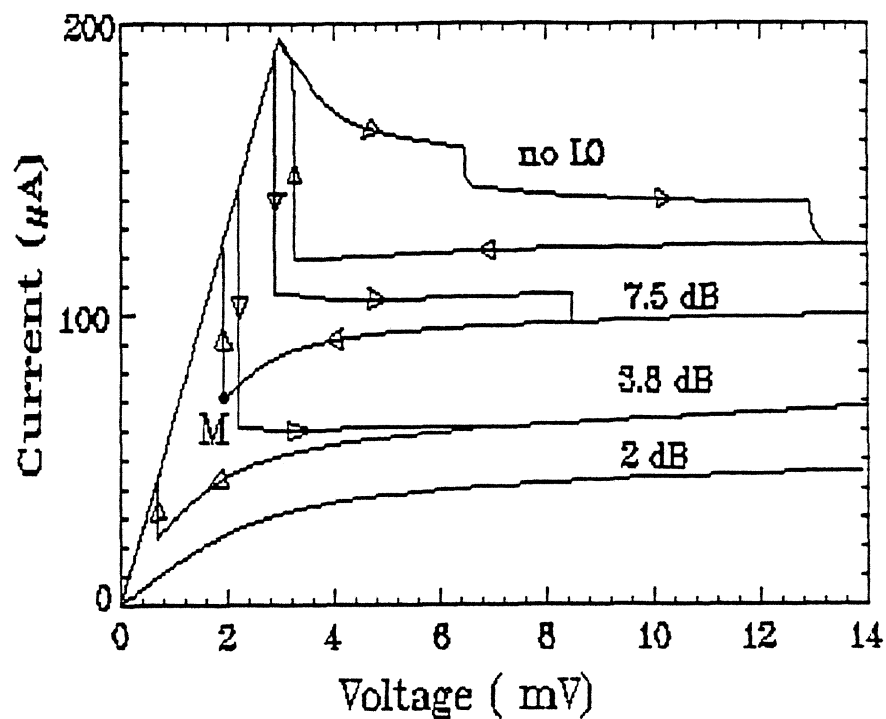


Fig. 3. IV-curves under LO power at 100 GHz.

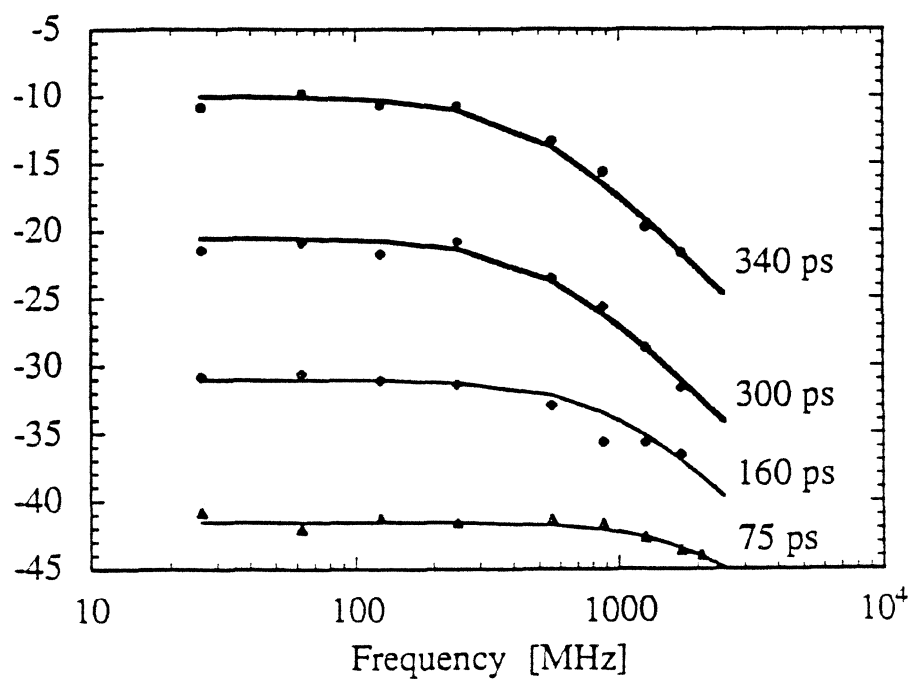


Fig. 4. Conversion gain versus intermediate frequency for 100 GHz LO frequency and three bias points.

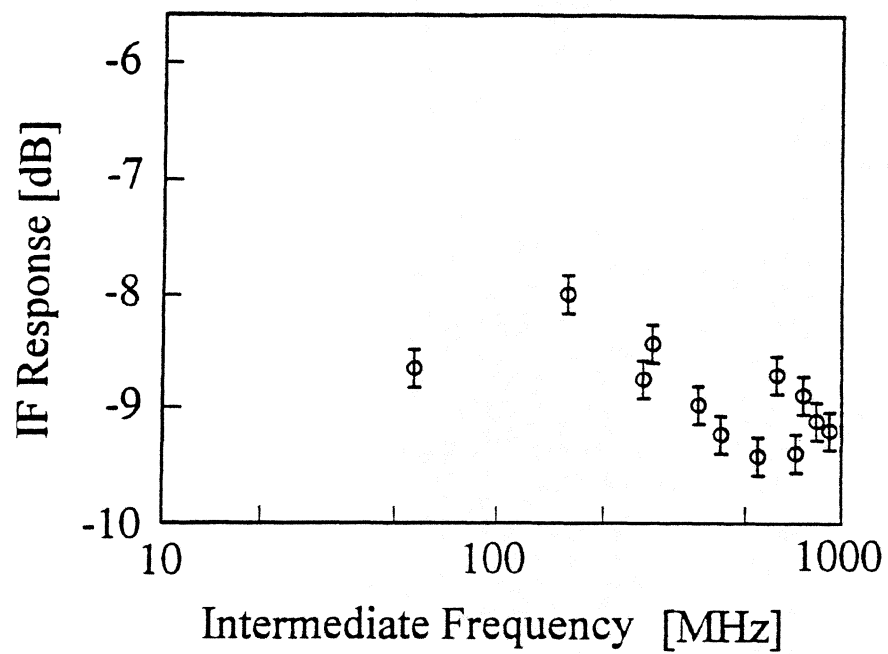


Fig. 5. Conversion gain versus intermediate frequency at 314 GHz.

NbN Hot Electron Waveguide Mixer for 100 GHz Operation

O.Okunev*, A.Dzardanov*, H.Ekstrom**, S.Jacobsson**, E.Kollberg**,
G.Gol'tsman* and E.Gershenzon*.

NbN is a promising superconducting material used to develop hot-electron superconducting mixers with an IF bandwidth over 1 GHz. In the 100 GHz frequency range, the following parameters were obtained for NbN films 50 Å thick: the noise temperature of the receiver (DSB) ~ 1000 K; the conversion losses ~ 10 dB; the IF bandwidth ~ 1 GHz; the local oscillator power ~ 1 μ W. An increase of NbN film thickness up to 80-100 Å and increase of working temperature up to 7-8 K, and a better mixer matching may allow to broaden the IF band up to 3 GHz, to reduce the conversion losses down to 3-5 dB and the noise temperature down to 200-300 K.

In the submillimeter waverange hot electron mixers can have high conversion coefficient and low noise temperature. The main limitation in using this kind of mixers is restricted IF band. For example, for the mixers based on n-InSb cooled to 4,2 K, the IF band is about 1 MHz [1]. A mixer based on superconductive thin Nb film in the resistive state gives an IF band less than 500 MHz [2]. The width of the IF band is restricted by the electron-phonon relaxation time τ_{eph} . To improve heat removal from the working area, mixing elements based on thin superconductive films are manufactured in the form of narrow strips. A possible way of extending the IF band is to reduce the strip length to the value of $L \leq \sqrt{D\tau_{eph}}$ [3]. In this case the IF band can be determined by the time of hot carriers escape from the strip.

An alternative way to extend the band is using superconductors with small τ_{eph} . In [4], τ_{eph} was studied in thin NbN films at various temperatures of the electrons Θ . The measurements were taken in a state close to equilibrium. τ_{eph} was determined from film resistance relaxation time in the resistive state. The resistivity was created by an external magnetic field $H \simeq H_{c2}$. The chosen levels of bias current and microwave

radiation power applied to the strip were so small that Θ was practically equal to the working temperature T of the thermostat. Fig. 1 shows how τ_{eph} depends on T for two samples with different mean free paths of electrons. At a temperature of 10 K, which approximately corresponds to the superconductive transition temperature in very thin NbN films $\tau_{eph} \simeq 15$ ps. This value of τ_{eph} must secure an IF band of 10 GHz. If the superconducting strip acts in the resistive state as an electromagnetic radiation mixer, then the state of its electron subsystem is far from equilibrium. In this case the magnetic field is absent and the resistivity is created by transport current and local oscillator power which cannot be considered as small. Nonetheless, the electron-electron interaction grows in films with a small electron mean free path, which leads to the fact that electron distribution function become a Fermi function so that the state of electrons may be described by the electron temperature $\Theta > T$.

The parameters of 100 GHz range mixers based on thin NbN films were studied using an experimental setup whose block scheme is shown in Fig 2. The samples to be studied were placed in a microwave mixer block, which was located in a helium cryostat at a working temperature of 4.2 K. Microwave radiation was applied to the mixer block along a circular waveguide with conical transition. Losses which occurred between the cryostat input and the input to the mixer block did not depend on frequency in the 80-120 GHz and amounted to 2 dB. Local oscillator and signal radiation were merged into a single channel using a directional coupler. A backward wave tube generator was used as the source of signal, while a Gunn generator served as local oscillator. Radiation power, which had been previously measured using a thermistor, was varied by calibrated attenuators. To measure the noise temperature of the mixer, a noise generator (discharge tube) with calibrated noise temperature was switched instead of the BWO generator. The voltage source

created a bias current flowing through a sample. The frequency and the amplitude of the converted signal were measured by a spectrum analyzer after a 50 dB amplification. The installation allowed to measure IV-curves of samples, conversion coefficient and its IF dependence, as well as the noise temperature of the mixers.

The studied structures, used as mixers, were manufactured from thin NbN films 50 Å thick, which had been produced by reactive magnetron sputtering of an Nb target in an argon/nitrogen mixture onto a polished substrate made of crystalline quartz. The configuration of strips and the design of the mixer block are shown in Fig. 3. Contact pads and a microstrip filter were sputtered onto the same substrate. The element thus produced was mounted in the middle of the waveguide. One contact pad was grounded in the mixer block, while an IF signal was taken from the mixer through the filter over a coaxial cable. A direct bias current was applied over the same cable. To match the mixer with the radiation, a mobile backshort was placed into the mixer block.

While manufacturing mixers our purpose was to thoroughly study the form of the IV-curves of the mixing element and its radiation induced change. This will help to select an optimal working point and to estimate the extent of input/output matching of the mixer. Fig. 4 shows the IV-curves of the first sample. For all curves, corresponding levels are given of radiation power at which they were derived. At power levels less than -20 dBm, these curves have a hysteretic shape. In this case, if a constant bias is applied to the sample, its resistance is determined by the resistance of the contacts until the current reaches the value of I_c . After that, a sharp growth of sample resistance occurs. A further monotonic growth of sample resistance continuous until normal resistance is achieved. It is impossible to bring the sample into the intermediate state at the "critical" point even for relatively low resistance values of the power supply. This type of instability is

connected with the hysteresis of the currents. Under radiation, the I_c current is reduced and, starting from a certain radiation power level, the IV-curves lose this shape. The optimal working point (marked as M) corresponds to local oscillator power of -25 dBm and is located near the resistive/superconductive state breaking point. The IV-curves of sample No 2 are shown in Fig. 5. The samples differ in the quality of the superconductive film. Sample No 2 has a greater normal resistance and smaller working currents and LO radiation power, the current hysteresis is absent. In table 1, parameters of the mixers produced from samples No 1 and 2 are listed. Total conversion losses of the mixer L_{total} are composed of unmatch $L_{mizerblock}$ and dissipation losses $L_{waveguide}$ in microwave input, internal conversion losses of the mixer $L_{internal}$, and unmatch losses in IF output L_{IF} . Total conversion losses of the mixer are directly measured as the ratio of microwave signal and the IF conversion signal. Input and output mismatch losses calculable from the IV-curves, taken under various levels of radiation.

It is to be noted that, in hot electron mixers, radiation has the same heat effect on the electron subsystem the direct electric current flowing in the sample. The sample resistance is determined by the value of Θ alone. Fig 6 clarifies the plan of calculating losses at mixer input $L_{coupling}$. The figure schematically shows the IV-curves for different LO power levels. Straight lines A and B correspond to two different electron temperatures. If one were to advance along the isotherm from low microwave power levels to higher levels, then the reduction of direct current power emitted in the sample should equal the increase of the microwave radiation power absorbed by the sample. Hence, the input mismatch losses can be defined as

$$L_{coupling} = \frac{P_{RFn} - P_{RFn-1}}{P_{DCn} - P_{DCn-1}}, \quad (1)$$

where P_{RFn} is the radiation power in point n and P_{DCn} is the direct

current power in point n.

IF output mismatch losses are calculated from the value of differential resistance at working point R_d :

$$L_{IF} = \frac{4R_d R_L}{(R_d + R_L)^2}, \quad (2)$$

where R_L is the input resistance of the IF amplifier.

In this case, internal conversion losses will be defined as follows:

$$L_{int} = L_{total} / L_{coupling} \cdot L_{IF}. \quad (3)$$

A phenomenological calculation of the conversion coefficient of the hot electron mixer was made by Arams^[1]. According to his calculations, the conversion gain is defined as follows:

$$G = 2C \frac{P_{LO}}{P_{DC}} \frac{R_L R_B}{(R_L + R_B)^2} \left[1 - C \frac{R_L - R_B}{R_L + R_B} \right]^2, \quad (4)$$

$$C = \frac{dR}{dP} I_{DC}^2$$

For mixers based on electron heating effect in thin superconductive films in the resistive state, C is found from^[2]:

$$C = \frac{dR}{d\Theta} \frac{\tau_{eph}}{c_e V} I_{DC}^2. \quad (5)$$

IF bandwidth is determined by the time τ , which depends on τ_{eph} and the parameters of circuit:

$$\tau = \frac{\tau_{eph}}{1 - C \frac{R_L - R_B}{R_L + R_B}}. \quad (6)$$

Experimental conversion losses may be compared with those calculated by defining the parameter C. This can be done by measuring the frequency dependence of the conversion gain for different working points. Fig. 7 shows such dependences for sample No 1 at three different working points. According to formula (6), a sharp growth of τ is to be expected

when the denominator becomes zero. Fig 7 demonstrates such a growth. The value of $\tau = 110$ ps close to τ_{eph} at 4.2 K for this sample corresponds to the characteristic with the maximum IF band. Therefore, a reduction of τ may only take place as a result of circuit factor effect, accounted for in (6). When the value of C was defined in this way, the conversion gain was calculated whose value corresponded to that measured.

Internal conversion losses of the mixers under study amounted to 3-6 dB, while the noise temperature of sample No 2 was 1200 K. As seen from Table 1, noise temperature may be reduced considerably by improving the input/output matching of the mixer and reducing dissipation losses at microwave input. Better matching can be achieved by varying the number of strips in the superconductive mixer.

The 100 GHz radiation frequency is low for NbN, $\hbar\omega < 2\Delta$. The impedance Z of the mixer is much less than its normal resistance. In a higher frequency range, the mixer based on electron heating effect in thin NbN films can be matched better and can have smaller conversion losses. IF bandwidth may be made wider by reducing τ with increasing the working temperature. This method allows to achieve the value of $\Delta f_{IF} = 2-3$ GHz at $T = 7-8$ K while preserving the remaining parameters of the mixer.

This work was supported by the Swedish National Board of Industrial and Technical Development and by the Russian Scientific Council on High- T_c Problem (Pr. No. 93169).

* O. Okunev, A. Dzardanov, G. Gol'tsman and E. Gershenzon are with Moscow State Pedagogical University, Moscow, Russia.

** H. Ekstrom, S. Jacobson and E. Kolberg are with Chalmers University of Technology, Göteborg, Sweden.

- [1] Arams F. et al. *IEEE Proc.*, Vol. 54, 1966, pp. 612-622.
- [2] Gershenzon E.M. et al., *Sov. Phys. Superconductivity*, Vol. 3, 1990, pp. 1582-1597.
- [3] Prober D., *APL*, Vol. 62, No. 17, 1993, pp.
- [4] Yu.P.Gousev et. al., *J. Appl. Phys.*, Vol. 75, No. 7, April, 1994, pp. 3692-3697.

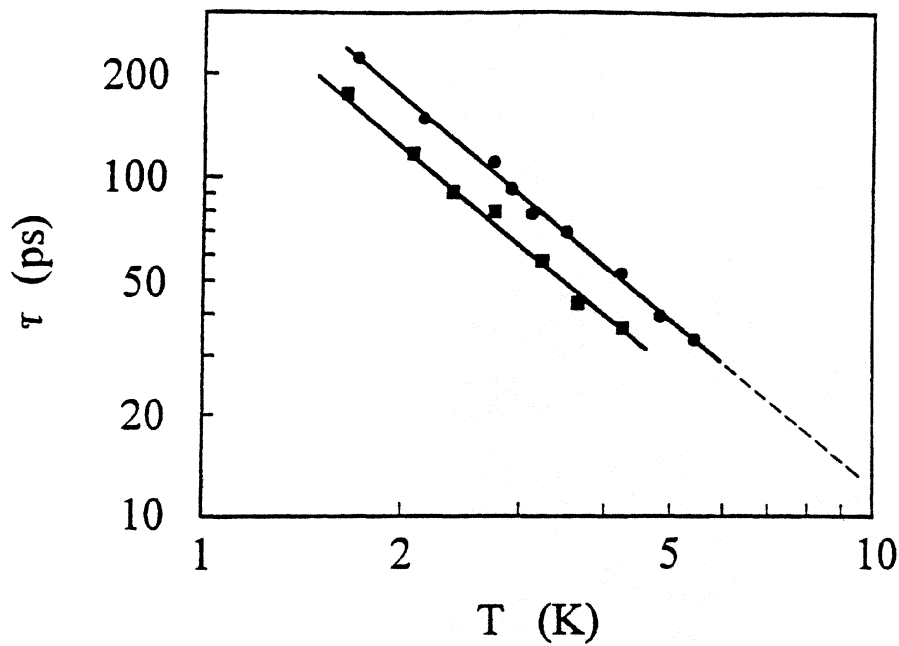


Fig. 1. Temperature dependence of electron-phonon interaction time for two NbN films ($H \simeq H_{c2}$, $\Theta \simeq T$)

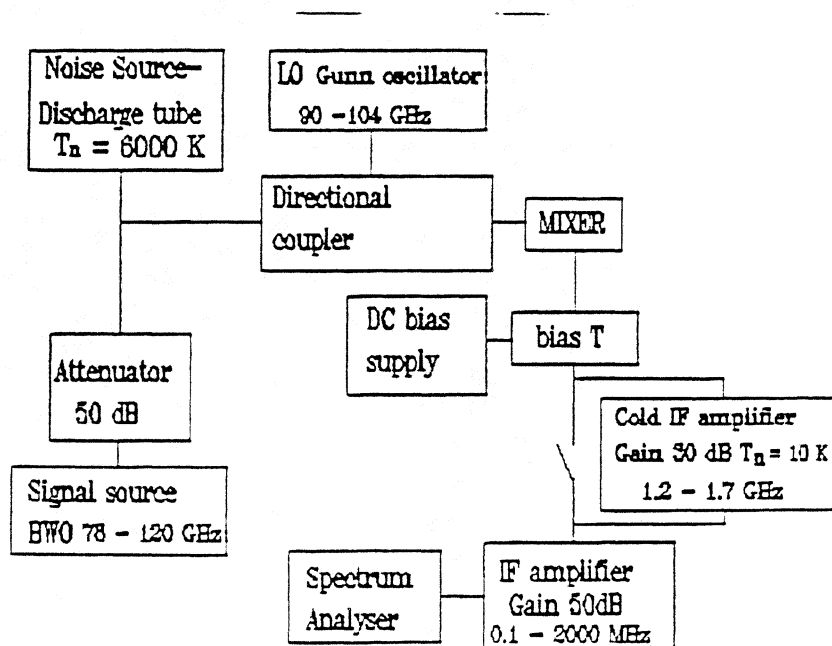


Fig. 2. Experimental setup.

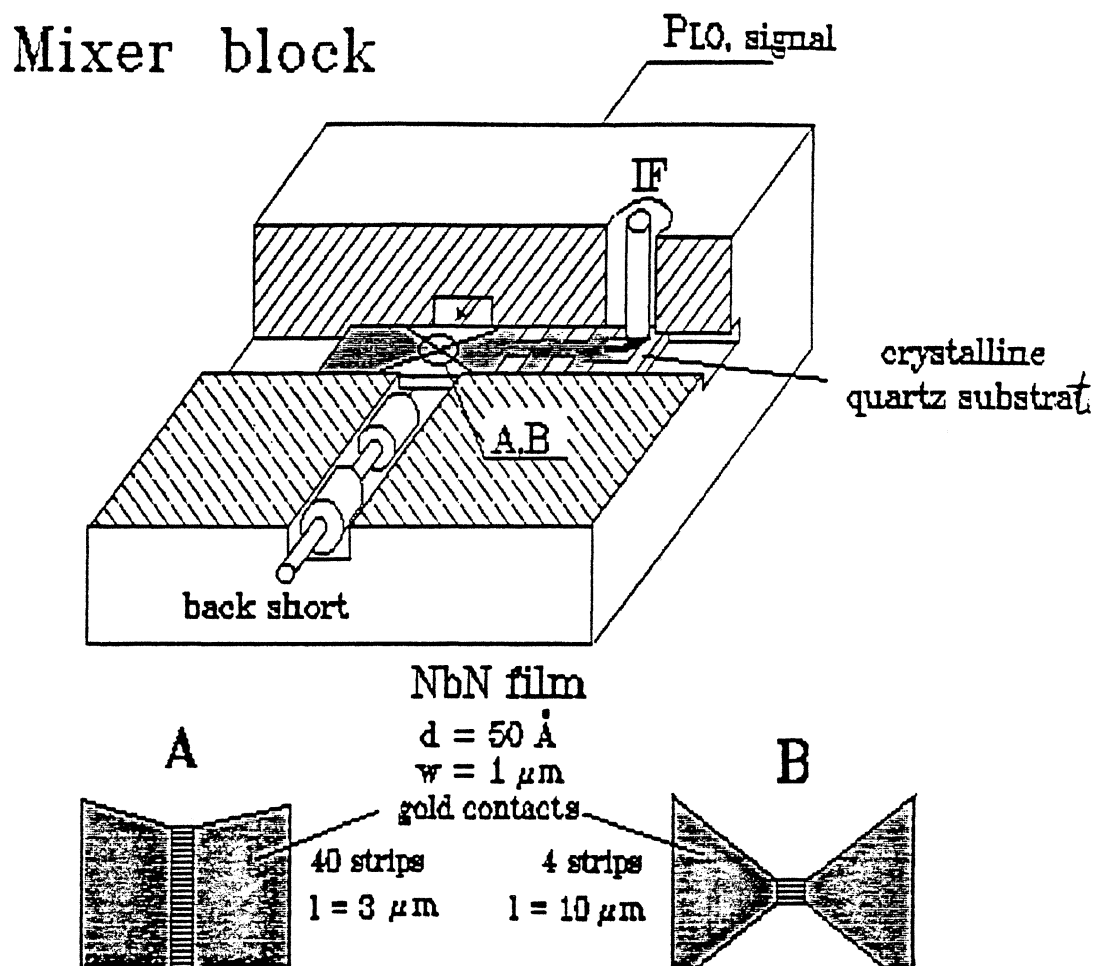


Fig. 3. Design of the mixer block and configuration of mixer chips.

Table I

No	L_{total}	$L_{coupling}$ $L_{waveguide} + L_{mizerblock}$	L_{mizer} $L_{int} + L_{IF}$	T_N	P_{LO}	Δf_{IF}
1	10dB	7dB = 2dB + 5dB	3dB = 3dB + 0dB	-	-28 dBm	0.6 GHz
2	14dB	6dB = 2dB + 4dB	8dB = 6dB + 2dB	1200 K	-45 dBm	1.4 GHz

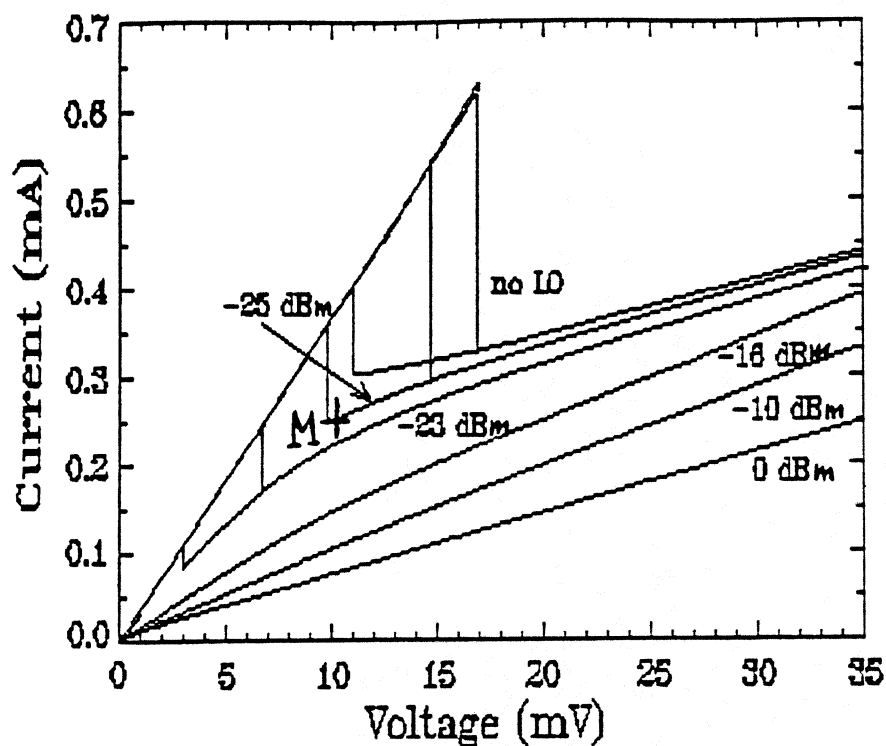


Fig. 4. IV-curves under LO power for sample No. 1.

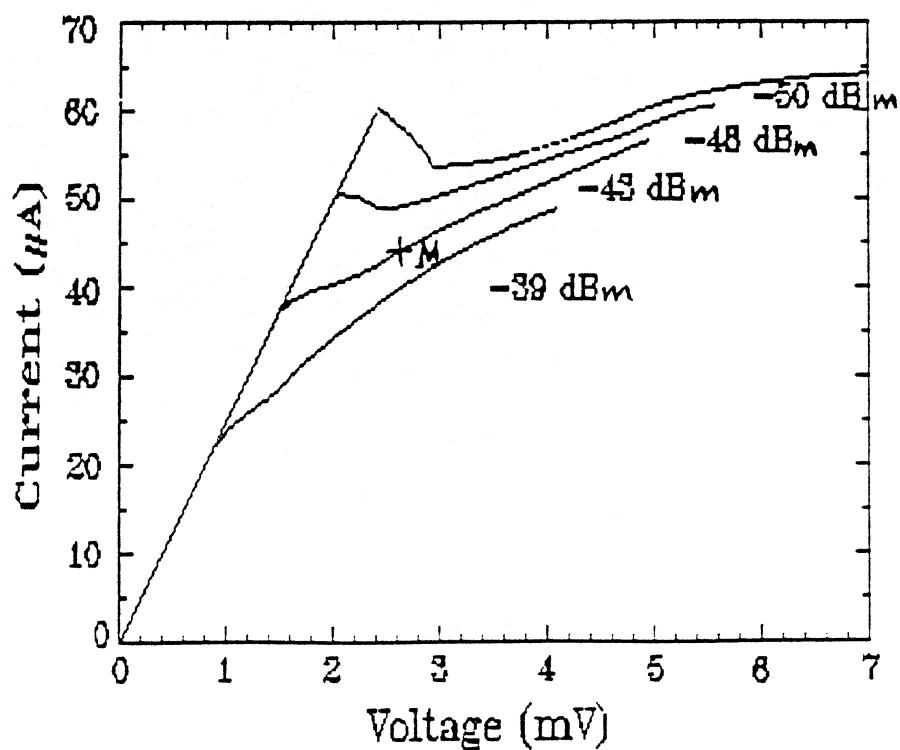


Fig. 5. IV-curves under LO power for sample No. 2.

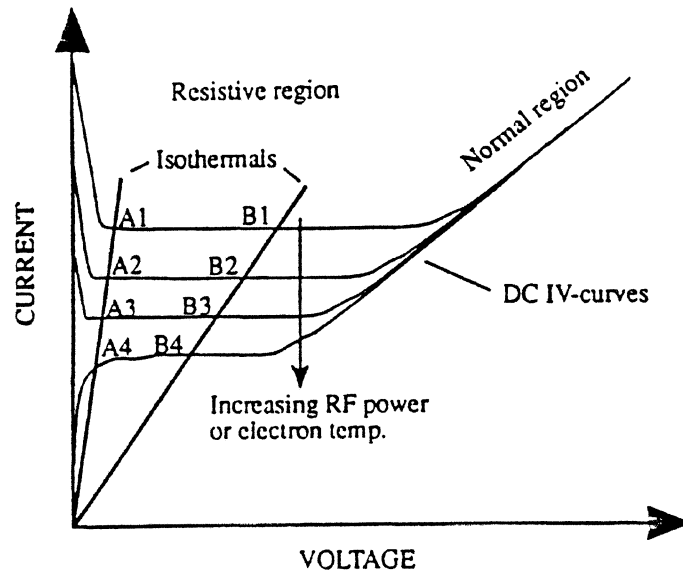


Fig. 6. Schematic IV-curves for different LO power. Straight lines A and B correspond to two different electron temperatures.

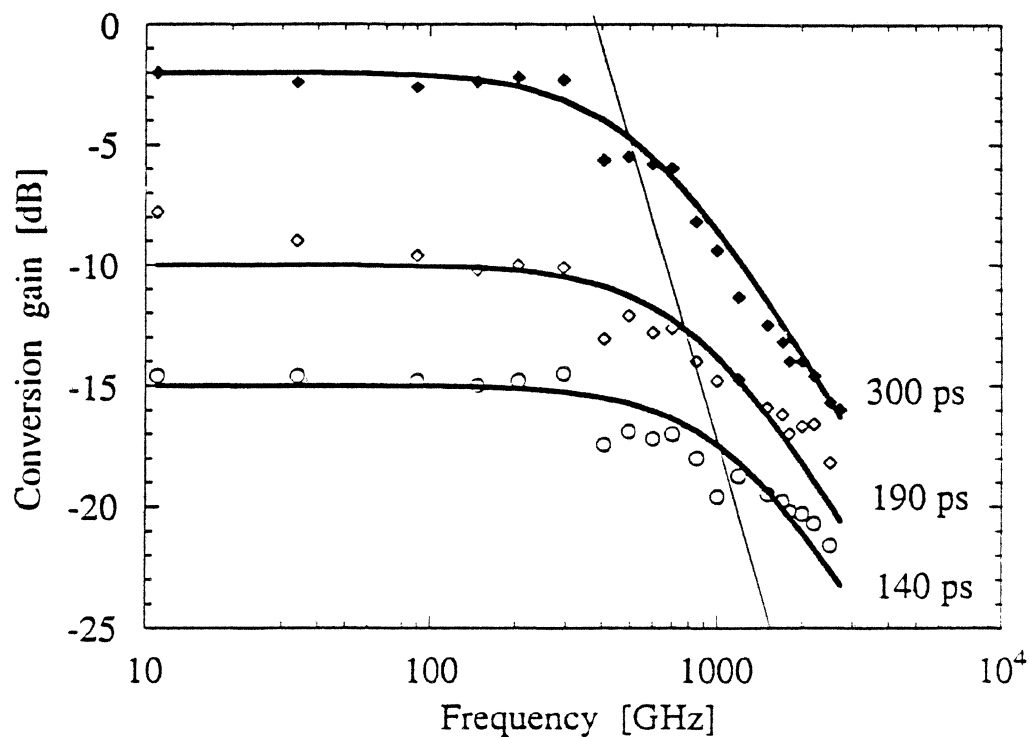


Fig. 7. Conversion gain versus intermediate frequency for three bias points, sample No. 1.

Noise Temperature of a Superconducting Hot-Electron Mixer

Andrey I. Elantev* and Boris S. Karasik*

The receivers based on the electron heating in superconducting films are becoming very attractive for terahertz applications. Due to the absence of spectral limitations and low parasitic reactances the hot-electron mixer may take an advantage over the traditional devices, e.g. SIS mixer and Schottky diode.

Only a few works are known^[1-3] where the performance of such a mixer was studied experimentally. The availability of the conversion loss at least less than 10 dB at microwaves and millimeter waves has been demonstrated. Along with this the theoretical evaluation of the conversion gain and noise temperature of a hot-electron mixer has been done in a number of papers^[1,4,5]. The results obtained by different authors are not consistent.

In the present paper we calculate the noise temperature of a hot-electron superconducting mixer assuming the Johnson noise and electron temperature fluctuations to dominate over other noise sources. We show that for superconductors with a broad transition $\Delta T_c \approx T_c$ (ΔT_c is the width of superconducting transition, T_c is the critical temperature) the noise temperature $T_M \propto \Delta T_c$ in contrast to [5]. For sharp superconducting transition the noise temperature does not depend on ΔT_c and can be given by the following expression:

$$T_M = 16T_c^3(T_c - T)^{-1}(2B_0 / B - 1)^{-1}$$

where T is the bath temperature, B_0 is the inherent in the superconductor frequency bandwidth determined by the electron-phonon relaxation time τ_{c-ph} at $T = T_c$, B is the mixer bandwidth.

Assuming $B_0/B = 5$ one can obtain for Nb mixer with $T = 4$ K and $T_c = 5$ K $T_M \approx 40$ K and also for NbN mixer with $T_c = 10$ K $T_M \approx 25$ K.

The difference between B_0 and B arises when the mixer is biased at the point of high conversion gain. The attainment of such an operation mode depends strongly on the film homogeneity.

[1]E. Gershenzon et al., Sov. Phys. Superconductivity 3, 1582 (1990)

[2]H. Ekström et al., Proc. of the 23rd European Microwave Conf., p. 787, 1993

[3]A. Dzardanov et al., Proc. of the Int. Conf. on Millimeter and Submillimeter Waves and Applications, 10-14 Jan. 1994, San Diego, CA, p. 276

[4]F. Arams et al., Proc. IEEE 54, 308 (1966)

[5]D.E. Prober, Appl. Phys. Lett. 62, 2119 (1993)

*Andrey I. Elantev and Boris S. Karasik are with the Moscow State Pedagogical University, 29 Malaya Pirogovskaya str., Moscow 119435, RUSSIA.

Radiation from a Quasioptical Josephson Junction Array

Michael J. Wengler and Boran Guan
Electrical Engineering Department, University of Rochester, NY 14627

Elie K. Track
HYPRES Inc., 175 Clearbrook Rd., Elmsford NY 10523

Abstract

At 190 GHz, 0.36 μ W has been detected from an 11×58 array of niobium Josephson junctions. The power is radiated directly into free space above the surface of the two-dimensional array of junctions. Detection is made by a commercial bolometer outside the array cryostat. The junctions in the array are closely spaced in the y-dimension, but spaced by more than one-half wavelength in the x-direction. This asymmetry results in mutual phase-locking between adjacent junctions suitable for the production of y-polarized radiation. The resonance and asymmetry also result in a reasonable impedance match between the Josephson junctions and the free-space radiation mode.

Introduction

Large two-dimensional arrays of Josephson junctions were proposed as submillimeter wavelength oscillators because of some attractive properties[1]. Large two-dimensional arrays have been successfully demonstrated with semiconducting devices for a variety of microwave applications[2-5]. In this context, large means the overall dimensions of the arrays are larger than a wavelength of the radiation.

The arrays proposed[1] have a number of properties useful for power combining applications. First, the impedance they present to the attached device can be controlled by their design. Second, they allow the coherent addition of power from many devices in the array so that arrays can handle or provide orders of magnitude more power than single devices. Finally, because they are large compared to a wavelength, they couple radiation directly into a free-space mode propagating normal to the array. Because of this last property, we refer to the Josephson junction array described here as a Quasioptical Josephson Oscillator, or QJO.

Our main goals in pursuing two-dimensional arrays are the possibility of higher radiated power from a larger number of junctions, and the possibility of higher frequency operation. In a one-dimensional array, radiation must travel through an increasing length of microstrip line as more junctions are added to the array. Both superconducting and normal metal microstrip lines have loss which increases as operation frequency is raised. In the QJO, however, generated radiation does not propagate any significant distance through on-chip wiring. Instead, it goes into a free-space mode propagating away from the array. If the QJO is extended by adding more junctions, it has a larger area from which its total power is radiated. It is not necessary for the added junctions' radiation to propagate through the longer lengths of wires on the extended QJO.

We have detected power from a number of fabricated arrays. The largest power detected is 0.36 μ W at a frequency of 190 GHz from an array of 638 junctions. The superconducting oscillator chip is in one liquid helium cryostat, and the bolometer we use for power detection is in another. The free-space radiation power we observe is uncorrected for any loss or beam dilution as it travels through a quartz lens, vacuum windows, and a few cm of air between the two cryostats.

This paper describes our work on these arrays. We recently reported the detection of significant power from these arrays. It is only the third time that near- μ W power levels of Josephson junction radiation propagating in free space have been observed. Martens *et al.* observed close to 1 μ W at 110 GHz from their largest symmetric array[6]. Booi and Benz observed 0.2 μ W from 53 to 230 GHz from a small symmetric array that couples to a stripline circuit which is then coupled to a waveguide radiator[7]. Higher output powers of tens of μ W at

frequencies near 500 GHz have been reported from one-dimensional Josephson arrays, but all of that power was dumped directly from the microstrip generator into an on-chip resistor[8].

QJO Particulars

A simplified schematic of our most successful QJO array is shown in Fig. 1. It is a variation of the array originally proposed by Wengler *et al.*[1]. The QJO tested had 11 columns of 58 junctions each for a total of 638 junctions. Junctions are spaced by $260\text{ }\mu\text{m}$ horizontally, but by only $56\text{ }\mu\text{m}$ vertically. This gives the array an active area of $2.86 \times 3.25\text{ mm}$ or about $1.8 \times 2.0\lambda_0$ where λ_0 is the free-space wavelength at the oscillation frequency.

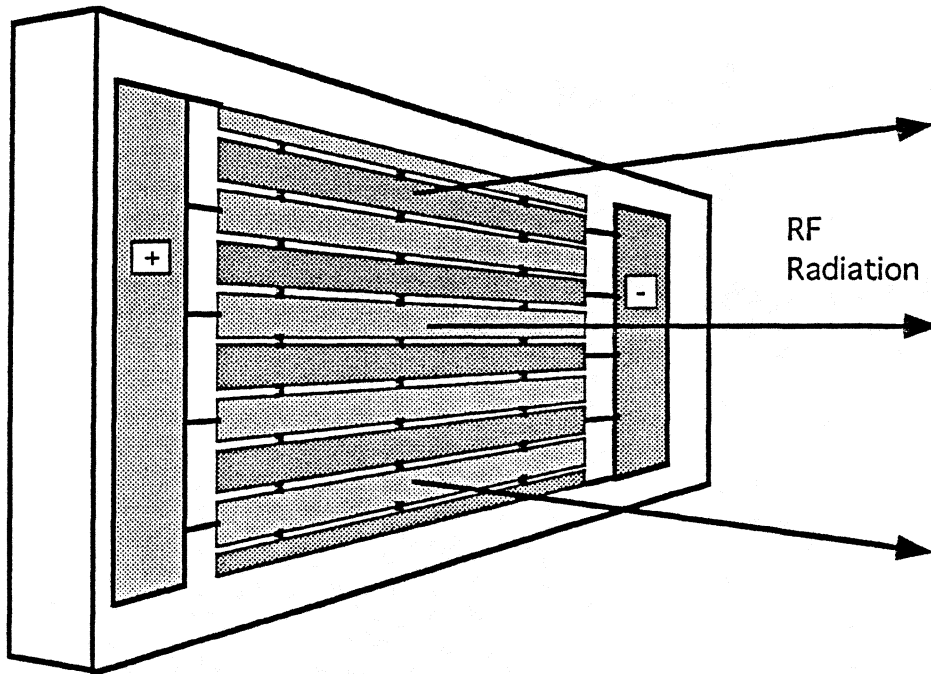


Figure 1. The figure illustrates an array with only 27 Josephson junctions. The array reported here has 638 junctions in it. However, the basic circuit idea is the same as shown in this figure.

Dc connections are made to alternating rows, from the sides, so that all junctions in the QJO are dc biased in parallel. All wires in the circuit are superconductors. In operation, every junction in the array sees *exactly* the same dc bias voltage, so that the Josephson frequency of oscillation of each junction, $f_J = 2eV_0/h$, is *exactly* the same. However, it is not necessarily the case that all junctions will oscillate in the same phase: this result must be brought about through circuit design, as described below.

A micrograph of the fabricated array in the vicinity of two of the SIS's is shown in Fig. 2a. The large white band crossing the picture is one of the +DC biased lines shown in Fig. 1. The edges of two -DC biased lines are seen in gray at the top and bottom of the micrograph. The Josephson junctions are Nb/Al₂O₃/Nb Superconductor-Insulator-Superconductor (SIS) tunnel diodes, shunted by resistors. The two SIS's in Fig. 2 are under the small dots which are seen in the two gaps between the + and -DC bias lines. The visible small feature is actually a $2 \times 2\text{ }\mu\text{m}$ square via hole to allow contact to the top of the $3 \times 3\text{ }\mu\text{m}$ SIS. We measure a current density for these SIS's of $3,900\text{ A/cm}^2$.

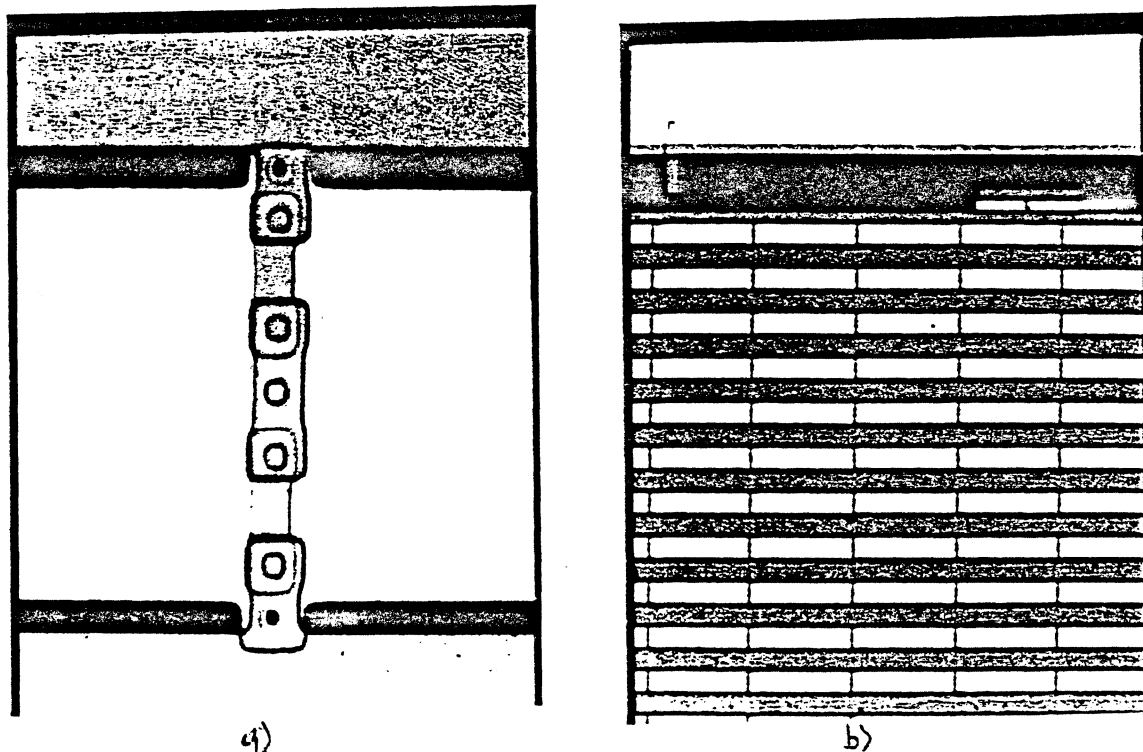


Figure 2. Micrographs showing details of the fabricated array. a) Detail in the vicinity of two junctions. The SIS's are under the small via holes which are topmost and bottommost in the figure. The rest of the structure shows the two shunt resistors, and the vias necessary to contact them. b) Detail showing about 22 rows and 5 columns of the array. A witness junction is seen just above the array.

The rest of the structure seen on the white bias line are the two $2\ \Omega$ shunt resistors, one for each of the SIS's, and the various via holes needed to make contact to the resistors. Those via holes are $3 \times 3\ \mu\text{m}$. The resistors are fabricated on top of the +DC line, and as close to the SIS as possible, to minimize their parasitic series inductance.

The RF Circuit

In the event that all of the junctions do oscillate in the same phase, we will have strong radiation in a direction perpendicular to the plane of the array. This can be understood by comparing this array with a phased-array antenna. Consider each small part of the array local to each junction as an independent radiator. With no phase difference between elements of the array, the direction in which all the junctions' radiation adds up in phase is perpendicular to the array.

The driving point impedance of the array, Z_A , should be chosen close to $2\ \Omega$ so that the shunted Josephson junctions will couple efficiently to it. Of the four different phased-array antennas investigated by Pance and Wengler[9], the Slot Array presented the lowest value of Z_A . The Slot Array they modelled had a resonant minimum value of Z_A when horizontal spacing between junctions was close to $\lambda/2$. λ is the wavelength of radiation on the slot-line formed by the horizontal dc bias wires connecting adjacent junctions. For the array reported here, that resonant condition is met for a frequency near 170 GHz. This is calculated using the index of refraction $n = 3.4$ of silicon to characterize the slot-line. Near resonance, the Slot Array had $Z_A \sim 10\ \Omega$, but the QJO reported here has somewhat different dimensions than the Slot Array[9].

Mutual Phase Locking at High Frequencies in the Array

Although all junctions must oscillate at the same frequency because of dc parallel biasing through superconducting wires, this does not constrain them to oscillate in phase. The most important mutual phase-locking mechanism in the arrays presented here is due to the mutual interaction between adjacent junctions at high frequencies. In the vertical dimension, junctions are connected by superconducting metal through a path which is much shorter than any of the wavelengths of interest in this problem. This results in some net series inductance between vertically separated junctions. Both small-signal[10] and large-signal[11] analyses show that an inductive coupling element forces the rf current to flow in series through the adjacent junctions. So within each column of the array, all of the junctions will have the same phase of oscillating current. This does not address the question of the relative phase of adjacent columns.

In the horizontal direction, adjacent junctions are connected by the slot-line transmission line structure formed by the dc bias lines. If the devices are closer together than $\lambda/2$ on this slot-line, the slot-line could be replaced by a series inductor. In that case, the rf current would flow up through one junction, across the top wire of the slot-line, and then down through the next junction. This is NOT the phase-locking we need. This would result in half the columns in the array being in one phase, and the other half being 180° out of phase.

However, for frequencies high enough so that the length of the slot-line between junctions exceeds $\lambda/2$, the equivalent circuit of the slot-line presents a capacitive reactance in series[11,12]. Conceptually, the rf current being pushed into the slot line by one junction goes through a phase-shift of more than 180° before it reaches the next junction. As far as the next junction can tell, it is just as though that current were coming from a junction with 180° phase than is actually the case. The result is that adjacent rows of the array will oscillate in phase, with the net result that every junction in the array is locked in phase, and significant radiation should be developed perpendicular to the plane of the array.

The array presented here shows significant output power at 190 GHz. The slot-line between adjacent junctions exceeds length $\lambda/2$ for frequencies above approximately 170 GHz. The fact that we see no radiation from the array below that frequency is evidence that our design for mutual phase locking in the horizontal and vertical directions is correct.

Long-range phase-locking between junctions may also be important in this array. In the original proposal[1], the array on the front surface, and metallization on the back surface of the QJO chip were intended to create a resonant cavity in the chip. The idea was that radiation building up in this cavity would be intense enough to injection-lock all the junctions in the array. Since then, it has been determined that with proper design, the array will have a tendency to properly phase-lock simply due to nearest-neighbor interactions[12]. We have designed the arrays so that mutual phase-locking would occur even in the absence of a long-range effect. However, the chip-cavity still exists in our circuit. We need to do experiments where we have a variable cavity behind the QJO so that we can determine how important this is to QJO operation.

DC Magnetic Flux and Mutual Phase Locking

In addition to high frequency, there are also dc phase-locking mechanisms[10]. These effects are analyzed by Pance for the quasioptical array[13]. Two horizontally adjacent junctions in this array participate in a closed superconducting loop. There will, in general, be dc magnetic flux, Φ , in each such loop in the array. For in-phase oscillation of adjacent junctions, it is required that $\Phi = n\Phi_0$, where n is an integer and $\Phi_0 = 2.07 \times 10^{-15}$ Webers is the quantum of magnetic flux called a fluxon.

The dc magnetic flux, Φ , in our array arises from the dc biasing currents. The inductance of each horizontal loop is in the neighborhood of 500 pH. This is calculated using a characteristic impedance of 163Ω for the slot-line, as measured for the Slot Array[9]. The critical current of each junction in the array is $I_C \sim 350 \mu\text{A}$. Thus, the dc flux condition for in-phase operation of the array is met $LI_C/\Phi_0 = 85$ times as the bias current of a junction is adjusted through the full range of I_C . With only a small change of dc bias current, the QJO circuit can relax to any required flux

quantization condition. For this reason, we believe that dc flux quantization places no real constraint on phase-locking in this array.

Experimental Technique

RF Power is measured using a bolometer operating at 4.2 K which is commercially available from Infrared Laboratories, Inc. The Josephson array and the bolometer are in separate dewars. The QJO dewar layout is shown in fig. 3. The array is mounted on a hyperhemispherical quartz lens to provide a narrower output beam, just as is done with some SIS submillimeter wavelength detectors[14]. The extra quartz windows serve to block infrared radiation from heating the QJO.

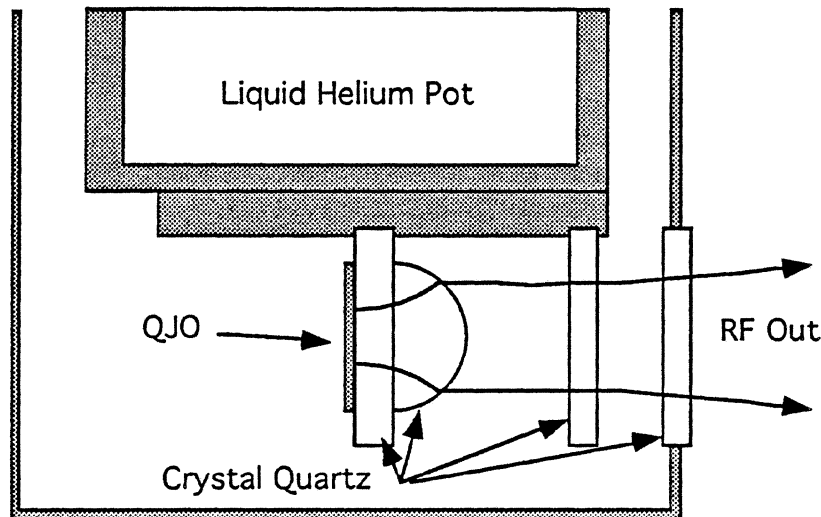


Figure 3. A schematic diagram of the QJO mounted in a dewar.

To detect the power, a lock-in amplifier is used. A chopper wheel interrupting the beam between the oscillator dewar and the bolometer dewar was tried, and then abandoned. In one position of the chopper wheel, the bolometer is seeing the QJO plus the very cold thermal radiation of the inside of the QJO dewar. In the other position of the chopper wheel, the bolometer is illuminated by 295 K room temperature radiation. The bolometer is very broad band, and the thermal difference between 295 K and looking in the QJO dewar corresponds to about $5 \mu\text{W}$ on the bolometer. It was impossible to detect nW power levels from the QJO with this large thermal signal. To fix this, we removed the physical chopper so the bolometer stares directly into the cold QJO dewar. The bias to the QJO is chopped between 0 mV and the bias voltage under test, and the bolometer signal is detected with a lock-in amplifier locked to this chopped bias. We appear to have sensitivity to about 1 nW power levels using this method.

Experimental Results

The experimental results for our array are summarized in fig. 4. The peak power detected is $0.36 \mu\text{W}$ at a bias voltage of 0.37 mV. This power is detected in the bolometer with no corrections made for any losses in coupling between the QJO array and the bolometer. The bias voltage corresponds to a Josephson frequency of 179 GHz.

We measure the frequency of the radiation at the power peak in two different ways. The first is using the witness junction which is fabricated next to the QJO array as shown in fig. 2b. When the array is biased so as to emit its maximum power, the IV curve of the witness junction shows constant voltage Shapiro steps at voltages 0.4 and 0.8 mV, as shown in Fig. 5. These are only produced if the radiation is at 193 GHz.

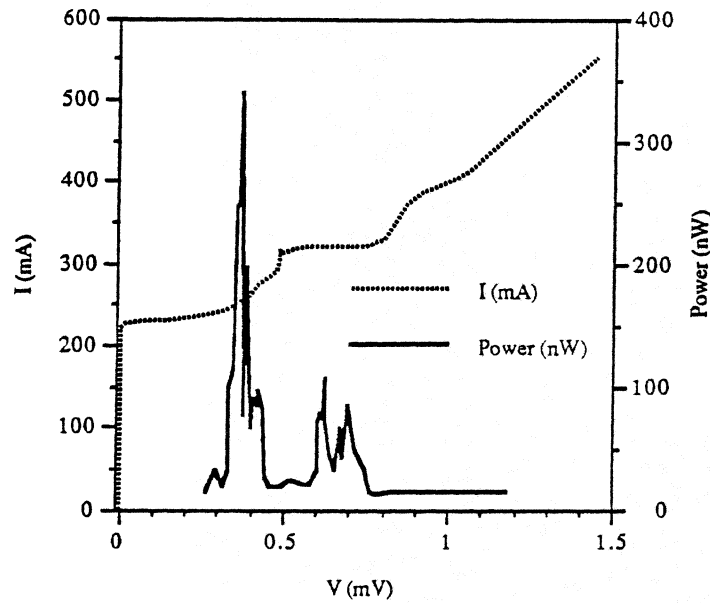


Figure 4. I-V curve and Power-V curve for the array. The tallest power peak occurs at frequency 190 GHz. The secondary peaks near $V = 0.6$ mV have not had their frequency measured.

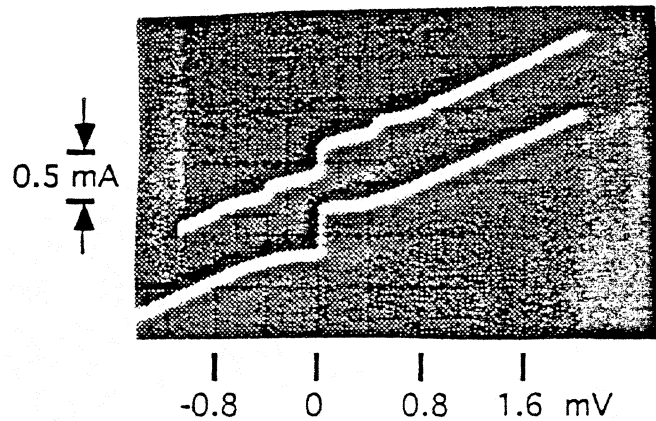


Figure 5. The I-V curve of the witness junction. For the bottom trace, the QJO array is turned off, so the witness junction I-V is RSJ. In the top trace, the QJO array is biased so that its radiation is detected in the external bolometer. The QJO radiation induces Shapiro steps in the witness junction I-V curve..

The second way we measure frequency of the radiation is by inducing standing waves in the radiation traveling between the QJO dewar and the bolometer dewar. This is done with a partially reflecting mesh on a translation stage. As the mesh is moved, the power coupled into the bolometer is modulated. Successive peaks are spaced by 0.8 mm. If this is half a free space wavelength, the radiation is at frequency 187 GHz.

The two measurements of frequency give 193 and 187 GHz for an average of 190 GHz. The apparent Josephson oscillation frequency for the QJO is 179 GHz. The QJO dc voltage is

calculated from an X-Y recorder output which is digitized by hand, and it must be corrected for a parasitic series resistance of about 7 m Ω . We believe the array is delivering power at about 190 GHz, and that this is the actual Josephson oscillation frequency of the array.

The QJO also has significant radiated power for bias voltages near 0.63 and 0.7 mV. When biased at the power peaks, no Shapiro steps are seen in the witness junction. This suggests, that radiation at these bias voltages is at some frequency other than 190 GHz, where the witness junction is proved to be a sensitive detector of radiation. The most likely situation is that the QJO array is radiating at its Josephson oscillation frequencies which are 305 and 340 GHz for these bias voltages. However, we are concerned that complicated dynamical effects can take place in a large array of coupled Josephson junctions, so we will not yet report for sure that we are seeing radiation at 300 GHz.

Conclusions

We have demonstrated radiated power from a quasioptical Josephson oscillator (QJO) at 190 GHz. The success of this circuit suggests that the QJO is a good candidate for submillimeter wavelength investigation.

Acknowledgments

Circuit design and fabrication were supported at HYPRES, Inc. by the Ballistic Missile Defense Organization through the U. S. Army under contract DASG60-93-C-0091. Design work was partially supported at the University of Rochester by the Air Force Office of Scientific Research under grant AFOSR 90-0233. We gratefully acknowledge Professor Dan M. Watson for the loan of the bolometer and advice on measurement techniques.

References

- [1] M. J. Wengler, A. Pance, B. Liu and R. E. Miller, "Quasioptical Josephson oscillator," *IEEE Trans. Magn.*, vol. 27, pp. 2708-2711, March, 1991.
- [2] C. F. Jou, W. W. Lam, H. Z. Chen, *et al.*, "Millimeter-wave diode-grid frequency doubler," *IEEE Trans. on Microwave Theory and Techniques*, vol. MTT-36, pp. 1507-1514, 1988.
- [3] W. W. Lam, C. F. Jou, H. Z. Chen, *et al.*, "Millimeter-wave diode-grid phase shifters," *IEEE Trans. on Microwave Theory and Techniques*, vol. MTT-36, pp. 902-907, 1988.
- [4] Z. B. Popovic, R. M. W. II, M. Kim and D. B. Rutledge, "A 100-MESFET planar grid oscillator," *IEEE Trans. Microwave Theory and Techniques*, vol. 39, pp. 193-200, February, 1991.
- [5] D. B. Rutledge, Z. B. Popovic, R. M. Weikle, *et al.*, "Quasi-optical power-combining arrays," in *Proc. 1990 IEEE MTT-S International Microwave Symposium Digest*, 1990.
- [6] J. S. Martens, A. Pance, K. Char, *et al.*, "Superconducting Josephson arrays as tunable microwave sources operating at 77 K," *Appl. Phys. Lett.*, vol. 63, pp. 1681-1683, 20 September, 1993.
- [7] P. A. A. Booij and S. P. Benz, "Emission linewidth measurements of two-dimensional array Josephson oscillators," *Appl. Phys. Lett.*, vol. 64, pp. 2163-2165, 18 April, 1994.
- [8] S. Han, B. Bi, W. Zhang and J. E. Lukens, "Demonstration of Josephson Effect Submillimeter Wave Sources with Increased Power," *Appl. Phys. Lett.*, In Press, 1994.

- [9] A. Pance and M. J. Wengler, "Microwave modelling of 2-D active grid antenna arrays," *IEEE Trans. Microwave Theory Tech.*, vol. 41, pp. 20-28, January, 1993.
- [10] A. K. Jain, K. K. Likharev, J. E. Lukens and J. E. Sauvageau, "Mutual phase-locking in Josephson junction arrays," *Physics Reports*, vol. 109, pp. 309-426, 1984.
- [11] B. Liu, "2-D Quasi-Optical Josephson Junction Arrays for THz Oscillators," Ph. D. Thesis, University of Rochester, 1993.
- [12] B. Liu, "Design of a Two-Dimensional Distributed Josephson Junction Array Emitting 190 GHz Free Space Radiation," *Appl. Phys. Lett.*, submitted, 1994.
- [13] A. Pance, "Two-Dimensional Josephson Arrays for Submillimeter Coherent Sources," Ph. D. Thesis, University of Rochester, 1992.
- [14] M. J. Wengler, "Submillimeter wave detection with superconducting tunnel diodes," *Proc. IEEE*, vol. 80, pp. 1810-1826, November, 1992.

CHARACTERIZATION OF THE EMISSION FROM 2D ARRAY JOSEPHSON OSCILLATORS *

P. A. A. Booij and S. P. Benz

Abstract-- We present experimental results on the emission from phase-locked two-dimensional arrays of Josephson junctions. We have coupled the emission from 10×10 arrays to a room-temperature mixer through a fin-line antenna and WR-12 waveguide. A single voltage-tunable peak was detected up to 230 GHz. A stripline resonance in the antenna reduced the array's dynamic resistance and thereby the emission linewidth to as low as 10 kHz. We extract an effective noise temperature of 14 K from the linewidth data. When the array's emission was coupled to an on-chip detector junction through a dc blocking capacitor, we detected voltage-tunable emission from 75 GHz up to 300 GHz, and in some circuits emission above 400 GHz. The coherent power spectrum depends primarily on internal resonances.

I. INTRODUCTION

Josephson junctions are natural voltage-tunable oscillators with characteristic frequencies in the GHz and THz frequency range. For applications such as on-chip local oscillators (LOs) for mixers, powers of $\sim 1 \mu\text{W}$ and linewidths less than 1 MHz are required. Three types of Josephson oscillators, flux flow oscillators (FFOs),^{1,2} one-dimensional (1D) arrays,³⁻⁵ and two-dimensional (2D) arrays of Josephson junctions,⁶⁻⁹ have generated enough power to pump an on-chip mixer. For off-chip applications, higher power, $> 1 \text{ mW}$ coupled to a 50Ω load, is required. 1D and 2D arrays are theoretically capable of delivering such power at GHz and THz frequencies.

Since the demonstration of coherent voltage-tunable emission from phase-locked 2D arrays,⁶ considerable research has been devoted to understanding the phase-locking mechanism. Wiesenfeld *et al.*¹⁰ analytically showed that unloaded 2D arrays exhibit stable phase locking between parallel junctions in a given row, but only neutrally stable phase locking between rows. This result is reminiscent of unloaded 1D series arrays where the phase-locked state is neutrally stable.¹¹ In 1D arrays, a weak interaction, such as feedback through a load, can induce phase locking. Similarly, phase locking between the N rows (each having M junctions in parallel in the voltage state) in 2D arrays can be stabilized by a load. Darula *et al.*¹² and Kautz¹³ have observed

* U.S. Government work not protected by U.S. copyright.

This work was partially supported by the BMDO Office of Innovative Science and Technology with technical program management from Rome Laboratory, and partially supported by the Office of Naval Research. P. A. A. Booij acknowledges the support of the University of Twente in The Netherlands.

The authors are with the National Institute of Standards and Technology, Boulder, CO 80303.

stable in-phase states in simulations of 2D arrays coupled to resistive loads. 2D arrays can compensate for \sqrt{M} times more critical current disorder than 1D arrays.¹³ This results from the inherent ability of current redistribution in 2D arrays to compensate for non-uniformities in the junction parameters.

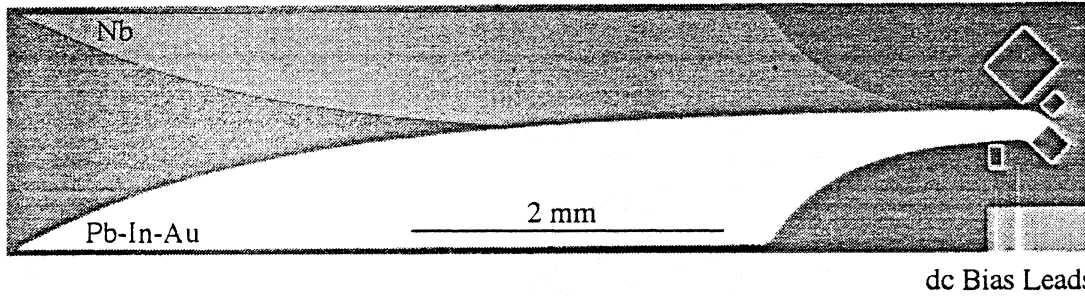


Fig. 1: Photograph of a 10 x 10 array (right) coupled to a fin-line antenna (left). The photograph also shows other arrays that are connected to antennas on other chips on the 7.62 cm (3 in) wafer.

We have characterized the emission from 2D array oscillators coupled to two different detection circuits. In the off-chip detector circuit (see Fig. 1), the arrays are coupled to a room-temperature mixer through a fin-line antenna and WR-12 (60-90 GHz) waveguide.¹⁴ For on-chip detection, the arrays are coupled to a detector junction through a dc blocking stripline capacitor.¹⁵ All arrays discussed in this paper use ground planes to reduce self-field effects and $4 \times 4 \mu\text{m}^2$ junctions (unless mentioned otherwise). Linewidth, power, and tunability of the emission are discussed in terms of circuit resonances. These data provide useful design criteria for higher-power array designs.

II. TWO-DIMENSIONAL ARRAYS OF JOSEPHSON JUNCTIONS

When current-biased at average voltage V , the supercurrent of a single resistively shunted junction (RSJ) oscillates at frequency $\nu_j = V/\Phi_0$, where $\Phi_0 = h/2e$, h is Planck's constant, and $-e$ is the elementary electron charge. For low normalized bias voltages $v = V/I_c R < 1$ (I_c is the critical current and R is the resistance of the RSJ), the junction generates harmonics with frequencies $\nu_n^j = nV/\Phi_0$, where $n = 1, 2, 3, \dots$. The junction can deliver a power

$$P_n^j = \frac{(v_n I_c R)^2 R_L}{2(R + R_L)^2} \quad (1)$$

to a resistive load R_L for each n th harmonic at a given bias voltage.³ The normalized harmonic amplitudes v_n are given by

$$\nu_n = \frac{2\nu}{(i+\nu)^n}, \quad (2)$$

where $i = I/I_c$, I is the bias current, and ν is defined as $\nu = V(R+R_L)/I_c R R_L$ when the load directly shunts the junction. For $\nu > 1$, thus ν greater than the characteristic frequency $\nu_c = I_c R / \Phi_0$, the junction oscillations are almost sinusoidal (higher harmonics are negligible) and the junction can deliver a fundamental power $P_1^j = I_c^2 R / 8$ to a matched load $R_L = R$. The theoretical linewidth of the oscillations, given by the full width at half-maximum power, is^{16,17}

$$\Delta\nu_1^j = \pi (nR_d/\Phi_0)^2 \{S_I(0) + [S_I(V)/2i^2]\} \quad (3)$$

where $S_I(V) = (4eV/R) \coth(eV/kT)$, $R_d = dV/dI$ is the dynamic resistance of the RSJ, k is Boltzmann's constant, and T is the temperature. Equation (3) describes the linewidth in terms of the low-frequency noise spectrum, where Johnson noise $S_I(0) = 4kT/R$ and noise mixed down from the harmonic frequencies ν_n^j are included.

The inset of Fig. 2 shows a schematic of a 4×3 ($M \times N$) array where 12 junctions can be in the voltage state and thus contribute to the emission. When $M \times N$ junctions in an array of RSJs phase lock, the power at array oscillation frequency ν_1^A delivered to a matched load $R_L = NR/M$ increases in proportion to $(M \times N)$ and the linewidth decreases in proportion to $1/MN$.^{3,7} Thus, for $\nu > 1$,

$$P_1^A = MN I_c^2 R / 8 = M^2 I_c^2 R_L / 8, \quad (4a)$$

$$\text{and } \Delta\nu_1^A = \frac{\Delta\nu_1^j}{MN}. \quad (4b)$$

Eq. (4b) holds provided that the individual junctions are identical (the array dynamic resistance $R_d^A = R_d$) and the array dimensions are much smaller than the fundamental wavelength, so that the array can be considered a lumped element.

Next we present experimental results that demonstrate the influence of junction parasitics and complex loads on the behavior of 2D array oscillators. When junction parasitics, such as the junction capacitance C_j and the inductance of each junction's shunt resistor L_s , are included, the equations that describe the junction dynamics cannot be solved analytically. Wiesenfeld *et al.*¹⁰ have derived an analytic approximation for ν_1 which we use to estimate the power coupled to the detectors.

III. RESULTS

A. Off-chip detection of 2D array emission

Figure 1 shows a photograph of a 10 x 10 array. The array design has been discussed elsewhere.^{7,11} The array is coupled to a 6.3 mm long antipodal fin-line antenna. The antenna is used to couple the array emission to the TE₁₀ mode in WR-12 waveguide. The antenna transforms the array impedance into the waveguide impedance through two exponentially tapered fins.

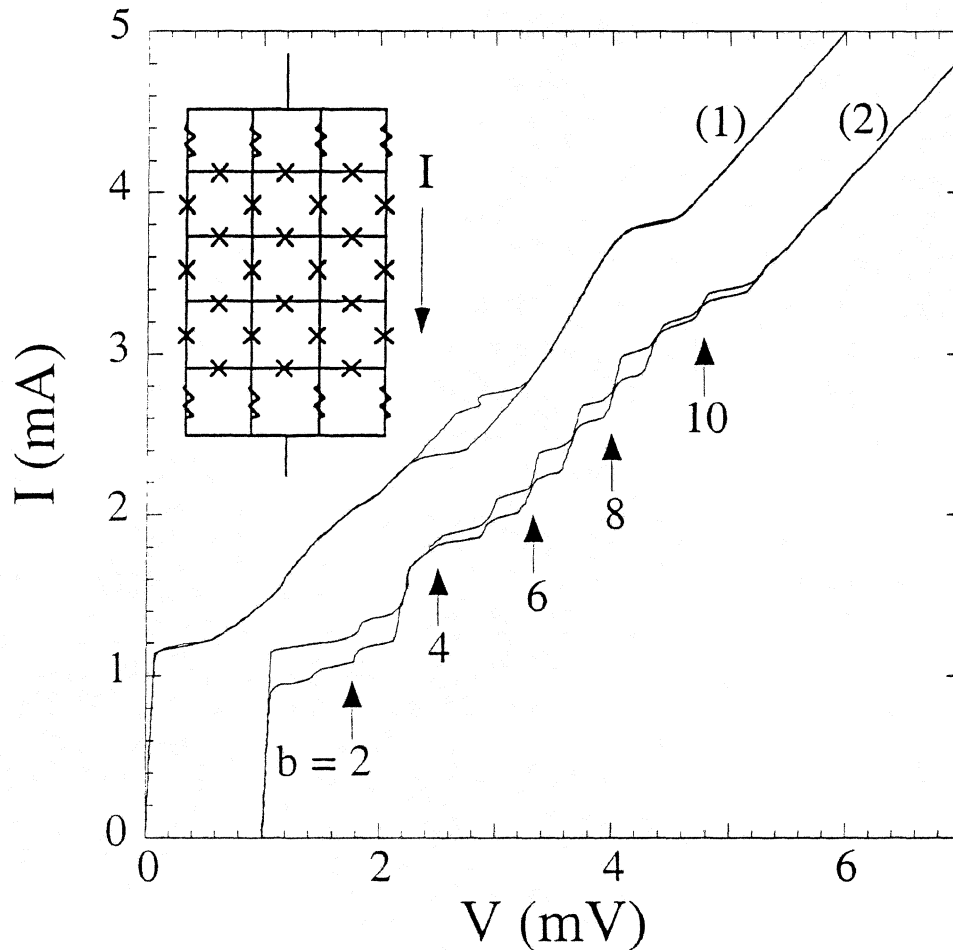


Fig. 2: I-V curve of a 10 x 10 array without (1), and with (2) the antenna. Curve (2) is displaced by 1 mV. Some of the resonance bands b are indicated with arrows. The inset shows a schematic of a 4 x 3 array where the junctions are shown as crosses.

Figure 2 compares the current-voltage (I-V) curves for an array with and without the antenna. The antenna induces in the I-V curve resonant steps that are independent of chip placement in the waveguide. The structure results from resonances in the ~3.3 mm overlapping region of the two fins at frequencies $\nu_R = b c_0 / (6.6 \text{ mm}) = b \times 17.4 \text{ GHz}$. Here, $c_0 = 1.15 \times 10^8 \text{ m/s}$ is the phase

velocity and b is the number of half-wavelengths in the overlapping region. The resonances induce small tunable frequency bands (bands b identified in Fig. 2) with reduced dynamic resistance R_d^A in the I-V curve. Coherent emission is observed from these bands.

We detected a single voltage-tunable peak at frequencies up to 230 GHz for each bias voltage. The detection methods are discussed in Ref. 14. The frequencies of the emission peaks agree through the Josephson relation with the bias voltages. In Fig. 3, an example spectral peak from band 5 with a linewidth of ~ 13 kHz is shown. In general, the linewidth varies by an order of magnitude over the bands. For low b , we found that the measured linewidth scales with $(R_d^A)^2/R$ at each bias point. The proportionality factor between Δv_1^A and $(R_d^A)^2/R$ (see Eqs. (3) and (4)) corresponds to an effective noise temperature of 14 ± 2 K.¹⁴

We detected a power of -88 ± 2 dBm across band 5 with a WR-10 harmonic mixer. We estimate the stripline-to-mixer loss of 8 ± 1 dB (including the stripline-to-waveguide loss of 4 ± 1 dB) from Shapiro steps induced in the I-V curve at 75 GHz with a Gunn LO. When corrected for this loss, and a mixer conversion and insertion loss of 43 dB, we arrive at an emitted power of -37 ± 3 dBm. The emitted power agrees with the theoretical power of -36.9 dBm (about $0.2 \mu\text{W}$) from Eq. (4a). In general, we found the emitted and theoretical powers to be within a factor of 2.

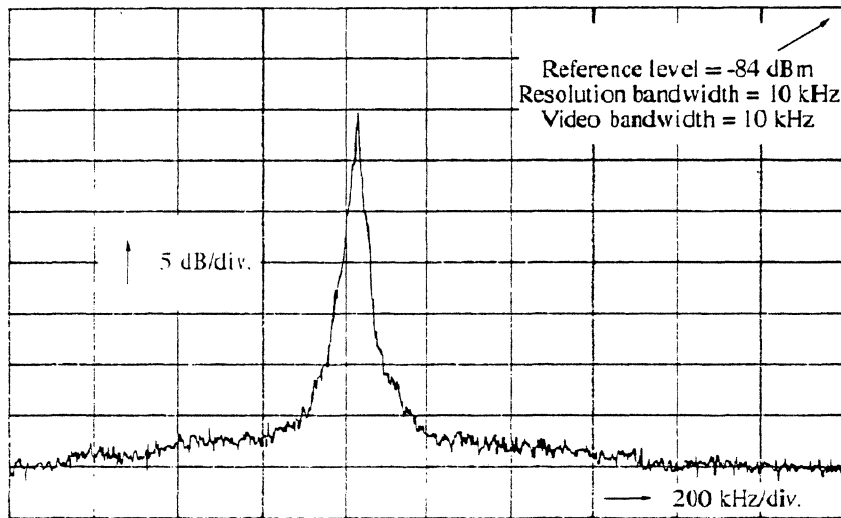


Fig. 3: Emission peak from band 5 after 100 video averages at 88.844 GHz showing a ~ 13 kHz linewidth.

The measured power and linewidth are consistent with the theoretical model in which all junctions phase lock. We detected linewidths as low as 10 kHz, which are the lowest linewidths reported for Josephson oscillators. Coherent emission was observed up to 230 GHz. This frequency range is limited by the low-pass character of the junction capacitance $C_j \sim 0.64$ pF. We expect stripline losses to limit the frequency range of arrays with smaller junctions (smaller C_j).

B. On-chip detection of 2D array emission

Next, we discuss circuits where external resonances are eliminated. For example, the stripline capacitors (that are used to couple the array's emission to a detector junction) were designed so that no standing waves occurred at the frequencies of interest.⁸ In this way, the measured spectra reflect array characteristics but no external resonances. The data show no significant features introduced by the load that are not related to internal resonances. This does not mean that the phase-locked state is not influenced by feedback through an external load, but that the main features of the emission spectrum are determined by internal resonances.

Figure 2 shows the I-V curve of an unloaded 2D array [curve (1)]. The structure in this I-V curve results from resonances between C_j and a combination of L_s and the array cell inductance L . Similar structure is observed in the I-V curves of loaded arrays. Figure 5, for example, shows the measured I-V curve of a 20×20 array coupled to a detector junction through a $75 \times 300 \mu\text{m}^2$ stripline capacitor.

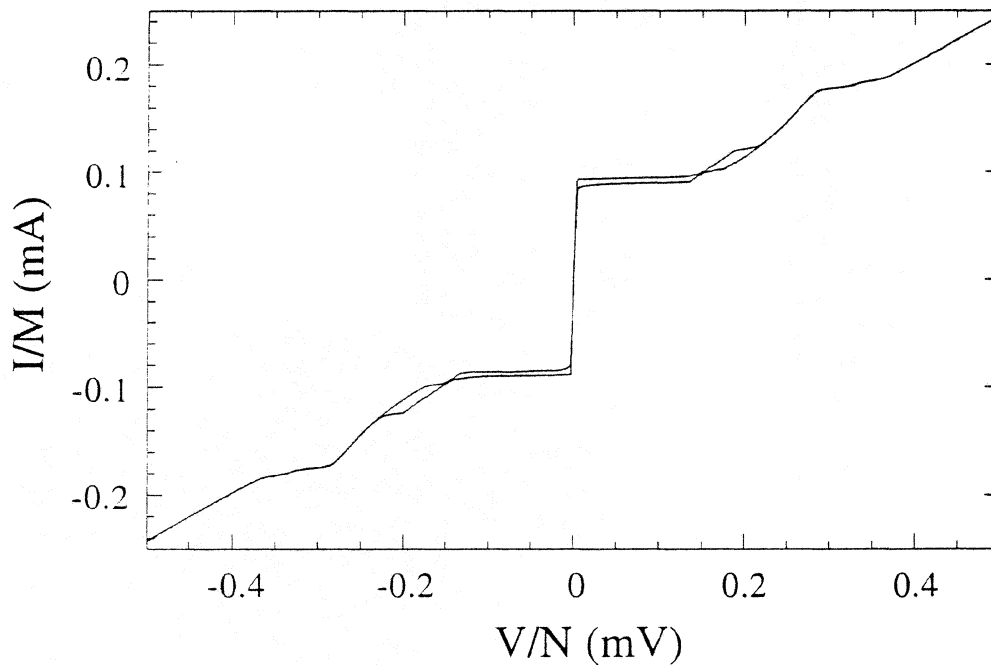


Fig. 5: Measured I-V curve of a 20×20 array coupled to a detector junction.

Figure 6 shows $R_d^A = dV/dI$ and the direct-detected power from the 20×20 array versus normalized array voltage V/N . The direct-detected power is determined by biasing the detector junction below (or above) the gap voltage (2.75 mV for Nb/AlO_x-junctions), so that emission is detected when the detector voltage V_d decreases (or increases).¹⁹ Emission observed from such arrays at frequencies above 400 GHz is not shown in Fig. 6.

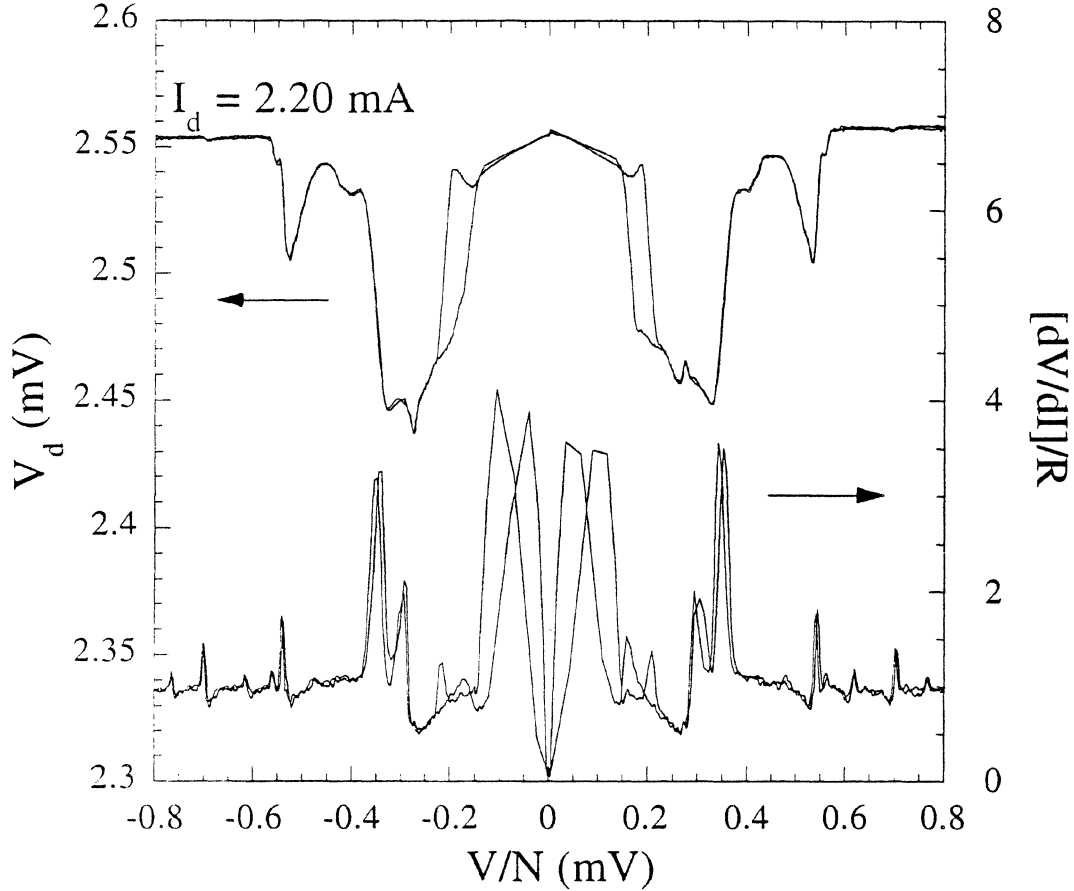


Fig. 6: Measured direct-detected power (modulation of V_d) and $R_d^A = dV/dI$ (normalized to R) of the 20×20 array.

The low-voltage structure ($V/N < 0.2$ mV) in Fig. 5 which displays metastable states is thought to be related to vortex and anti-vortex propagation going back and forth across the array.¹⁸ No coherent emission is detected at these voltages. This vortex motion may be similar to zero-field steps in 1D parallel arrays (which depend on L and C_j) and will be discussed in Ref. 15. Coherent emission is observed for $V/N \geq 0.2$ mV ($v \geq v_c$).

The structure in Fig. 5 for $V/N \geq 0.2$ mV is predominantly determined by a (junction) resonance between the shunt resistor's inductance L_s and the junction's capacitance C_j ; this resonance determines the primary (coherent) emission band. Fig. 6 shows that this primary emission band occurs for V/N (approximate frequency) varying from 0.2 (90 GHz) to 0.35 mV (170 GHz). This range is the same for 6×6 and 10×10 arrays, both with and without horizontal junctions perpendicular to the bias direction. This feature also occurs for arrays with different cell inductance, and in circuits with different coupling structures.

Our data indicate that the low frequency limit of the primary emission band is ν_c , and the high-frequency limit is approximately the parasitic junction resonance near $\nu_r = 1/2\pi\sqrt{L_s C_j} = 152$ GHz ($L_s = 1.7$ pH and $C_j = 0.64$ pF). Beyond this resonance, the I-V curve shows a high- R_d^A transition back to $V = RI$ (near $V/N = 0.35$ mV in Fig. 6). For arrays with larger $L_s = 2.4$ pH (larger dielectric thicknesses), ν_r decreased to ~ 128 GHz. For arrays with smaller junctions (smaller C_j), the primary emission band occurred up to higher ν_r ; for example, arrays with $2 \times 2 \mu\text{m}^2$ junctions have a primary emission band up to 300 GHz. For arrays with larger ν_c , the onset of coherent emission is shifted to higher frequencies, which explains the lack of coherent emission observed from arrays with high junction I_c when $\nu_c > \nu_r$.⁷

From the quality factor of the junction resonance $Q = \nu_r/\Delta\nu = \sqrt{L_s/R^2 C_j}$, we obtain a corresponding bandwidth $\Delta\nu = R/2\pi L_s = 133$ GHz. Above the primary emission band, emission is observed predominantly at multiples of ν_r with detected powers decreasing as $(\nu/\nu_r)^{-2}$. This decreased power for higher frequencies follows the transfer characteristic of the parasitics.

Our data from on-chip detection circuits show no significant features introduced by the load that are not related to resonances intrinsic to the array circuit. Frequency bands of coherent emission seem to be determined primarily by the resonance between junction parasitics L_s and C_j . The detected power at all frequencies corresponds to all junctions being phase locked. The oscillator is tunable over a primary emission band that ranges in frequency from approximately ν_c to slightly beyond ν_r . Thus, the desired emission characteristics of 2D arrays based on shunted tunnel junctions can be determined through modeling of the resonances between these parasitics.

IV. DISCUSSION AND CONCLUSIONS

The emission spectra of 2D arrays are strongly dependent on resonances external and internal to the array. We observe coherent emission near multiples of the resonance frequencies. When the arrays are coupled to antennas, the emission is dominated by the external resonances in the antenna. When the arrays are not coupled to the antenna, for example, when the arrays are coupled to on-chip detector junctions, internal resonances in the array due to junction parasitics determine the emission spectra. Characterization of external and internal resonances is necessary for accurate determination of power, linewidth, operating frequency, and tunability of phase-locked Josephson oscillators.

The $L_s C_j$ resonance can be useful in maximizing the power delivered to a load, but at high operating frequencies this will limit tunability. Minimization of circuit parasitics is necessary for higher-power, higher-frequency Josephson oscillators so that both the tunability and operation frequency of 2D array Josephson oscillators are increased. Thus, understanding junction parasitics is essential for designing stable phase-locked 2D arrays.

ACKNOWLEDGMENTS

We thank E. N. Grossman, C. A. Hamilton, R. L. Kautz, R. H. Ono, C. D. Reintsema, A. V. Ustinov, M. P. Weidman, and K. A. Wiesenfeld for advice, discussions, and the use of equipment.

REFERENCES

- ¹ A. V. Ustinov, T. Doderer, R. P. Huebener, J. Mygind, V. A. Oboznov, and N. F. Pedersen, "Multi-fluxon effects in long Josephson junctions," *IEEE Trans. Appl. Supercon.*, vol. 3 (1), pp. 2287-2290, March 1993.
- ² Y. M. Zhang, D. Winkler, and T. Claeson, "Linewidth measurements of Josephson flux-flow oscillators in the band 280-330 GHz," *Appl. Phys. Lett.*, vol. 62 (24), pp. 3195-3197, June 1993.
- ³ A. K. Jain, K. K. Likharev, J. E. Lukens, and J. E. Sauvageau, "Mutual phase-locking in Josephson junction arrays," *Phys. Rep.*, vol. 109 (6), pp. 309-426, 1984.
- ⁴ B. Bi, S. Han, and J. E. Lukens, "Radiation linewidth of phase-locked distributed array in the submillimeter wave range," *Appl. Phys. Lett.*, vol. 62 (22), pp. 2745-2747, May 1993.
- ⁵ S. Han, B. Bi, W. Zhang, and J. E. Lukens, "Demonstration of Josephson effect submillimeter wave sources with increased power," *Appl. Phys. Lett.*, vol. 64 (11), pp. 1424-1426, March 1994.
- ⁶ S. P. Benz and C. J. Burroughs, "Coherent emission from two-dimensional Josephson junction arrays," *Appl. Phys. Lett.*, vol. 58 (19), pp. 2162-2164, April 1991.
- ⁷ S. P. Benz and C. J. Burroughs, "Two-dimensional arrays of Josephson junctions as voltage-tunable oscillators," *Proceedings of the Third International Superconductive Electronics Conference*, Glasgow, pp. 230-237, June 1991; *Supercon Sci. Technol.*, vol. 4, pp. 561-567, 1991.
- ⁸ P. A. A. Booij, S. P. Benz, T. Doderer, D. Hoffmann, J. Schmidt, S. Lachenmann, and R. P. Huebener, "Frequency dependence of the emission from 2D array Josephson oscillators," *IEEE Trans. Appl. Supercon.*, vol. 3 (1), pp. 2493-2495, March 1993.
- ⁹ M. J. Wengler, B. Guan, B. Liu, and E. K. Track, "190 GHz radiation from a quasioptical Josephson junction array," *Appl. Phys. Lett.*, submitted, 1994.
- ¹⁰ K. Wiesenfeld, S. P. Benz, and P. A. A. Booij, "Phase-locked oscillator optimization for arrays of Josephson junctions," *J. Appl. Phys.*, submitted, 1994.
- ¹¹ P. Hadley, "Dynamics of Josephson junction arrays," *PhD thesis*, Stanford University, unpublished, 1989.

- ¹² M. Darula, P. Seidel, J. von Zameck Glyscinski, A. Darulova, F. Busse, and S. Benacka, "The stability of the phase-locked state in structures containing arrays of Josephson junctions," *EUCAS'93*, Göttingen, submitted, 1993.
- ¹³ R. L. Kautz, "Phase locking in two-dimensional Josephson-junction arrays: Effect of critical-current nonuniformity," to be presented at *ASC'94*, Boston, MA, October 1994.
- ¹⁴ P. A. A. Booï and S. P. Benz, "Emission linewidth measurements of two-dimensional array Josephson oscillators," *Appl. Phys. Lett.*, vol. 64 (16), pp. 2163-2165, April 1994.
- ¹⁵ P. A. A. Booï and S. P. Benz, "Resonances in two-dimensional Josephson-junction arrays," *J. Appl. Phys.*, submitted, 1994.
- ¹⁶ K. K. Likharev and V. K. Semenov, "Fluctuation spectrum in superconducting point junctions," *JETP Lett.*, vol. 15, pp. 442-445, 1972.
- ¹⁷ R. H. Koch, D. J. Van Harlingen, and J. Clarke, "Quantum-noise theory for the resistively shunted Josephson junction," *Phys. Rev. Lett.*, vol. 45 (26), pp. 2132-2135, December 1980; "Observation of zero-point fluctuations in a resistively shunted Josephson tunnel junction," *ibid.* vol. 47 (17), pp. 1216-1219, October 1981.
- ¹⁸ S. G. Lachenmann, T. Doderer, R. P. Huebener, P. A. A. Booï, and S. P. Benz, Observation of vortex motion in two-dimensional Josephson junction arrays, *Phys. Rev. B*, accepted, 1994.
- ¹⁹ A. Barone and G. Paterno, *Physics and applications of the Josephson effect*. New York: John Wiley & Sons, chapter 11, 1982.

Heterodyne Mixing and Direct Detection in High Temperature Josephson Junctions*

Erich N. Grossman and Leila R. Vale
National Institute of Standards and Technology
Boulder, CO 80303

Abstract

We have examined various properties of high characteristic frequency YBCO superconductor-normal-superconductor (SNS) Josephson junctions that are important to their performance as low-noise THz frequency mixers. Without far-infrared laser illumination, the microwave frequency noise temperature of our lowest noise device shows good agreement with the predictions of the resistively shunted Josephson model in applicable regions of bias. It has a maximum noise temperature of 36 ± 4 K at a physical temperature of 4 K. When illuminated with a 404 GHz far-IR laser local oscillator (LO) and a chopped 77 K blackbody signal, strong modulation of the 1 GHz IF noise power is observed. However, certain features of the modulated IF power signal strongly suggest that a large fraction of it is not true heterodyne detection. The spurious component is probably due to direct detection of the broadband hot load/cold load signal. We believe that reliable measurement of heterodyne performance will require narrowband signal sources.

I. Introduction

The importance of investigating high-critical temperature (high- T_C) Josephson junction mixers arises chiefly from the possibility of approaching quantum-limited noise performance at frequencies far higher than is possible with conventional quasiparticle mixers. Higher frequency performance can be reasonably hoped for because the energy gaps of high- T_C superconductors, though not measured (and perhaps not well-defined), would be expected to lie >10 times higher than those of low- T_C materials, based on the respective critical temperatures and the relation $E_{\text{gap}} = C k T_C$, ($C = 3.52$ for classic BCS superconductors). The possibility of mixer operation at higher temperatures is also an important secondary motivation for investigating high- T_C mixers, particularly for

* Publication of the U.S. Government. Not subject to copyright.

applications in remotely operated or spaceborne receiver systems. For these reasons, as techniques for fabricating Josephson junctions from the high- T_C materials have been developed, a number of groups^{1,2} have been examining their characteristics at high frequencies (≥ 100 GHz) and their suitability as terahertz-frequency mixers.

All high- T_C Josephson junctions fabricated to date are in the "shunted", or low capacitance regime, defined by a dimensionless capacitance $\beta_C = 2\pi(2e/h) I_C R_N^2 C \ll 1$, where I_C is the critical current, R_N the normal-state resistance, and C the capacitance of the junction, and $(2e/h) = 1/\phi_0 = 483$ GHz/mV is the Josephson constant. This gives them non-hysteretic current-voltage (I-V) characteristics with no sharp feature at the gap voltage. Conventional low- T_C tunnel junctions, because of their trilayer or "sandwich" geometry are in the $\beta_C \gg 1$ regime, which gives them a hysteretic I-V curve with a sharp non-linearity at the gap voltage due to the onset of quasiparticle tunneling. Mixing in conventional low- T_C junctions is based on this resistive non-linearity in the quasiparticle tunneling; mixing in non-hysteretic junctions ("Josephson mixing") on the other hand, is based on the non-linearity in the tunneling of Cooper pairs. In the late 1970's and early 1980's, low- T_C quasiparticle and Josephson mixers for millimeter wavelengths were developed in parallel, and a considerable body of knowledge about the physics of Josephson mixers was acquired,³ much of it based on the standard "resistively-shunted junction" (RSJ) model. Although a vague opinion arose that Josephson mixers always show large "excess" noise, the chief reason for the eventual predominance of quasiparticle mixers over Josephson mixers was that, at that time, the only experimental realization of Josephson mixers was in point contacts, which are mechanically and electrically extremely unstable and irreproducible. The theoretical properties of Josephson mixers are now being carefully re-examined⁴ and compared with experiment using well controlled (low- T_C) lithographic junctions. In fact, the "excess" noise of optimized Josephson mixers should be only a factor of a few (~ 10 or less) above the thermal noise level.

The natural or characteristic frequency f_C for any superconducting junction is set by the junction's $I_C R_N$ product via the definition $f_C = (2e/h) I_C R_N$. The characteristic frequency can never exceed the energy gap frequency of the superconducting material forming the

¹ J. P Hong, H. R. Fetterman, R. J. Forse, and A. H. Cardona, "Double Step-edge Weak Links Integrated with Spiral Antenna Structure in Epitaxial $Tl_2CaBa_2Cu_2O_8$ Films for Millimeter Wave Mixing", *Appl. Phys. Lett.*, 62, pp 2865-2867 (1993)

² R. Gupta, Q. Hu, D. Terpstra, G. J. Gerritsma, and H. Rogalla, "Near-millimeter-wave Response of high T_C Ramp-type Josephson Junctions", *Appl. Phys. Lett.* 62, pp.3351-3353 (1993)

³ J. H. Claassen and P. L. Richards, "Performance Limits of a Josephson-junction Mixer", *J. Appl. Physics*, 49, pp. 4117-4129 (1978)

⁴ R. J. Schoelkopf, T. G. Phillips, and J. Zmuidzinas, "A 100 GHz Josephson Mixer Using Resistively Shunted Nb Tunnel Junctions", *IEEE Trans. Appl. Supercon.*, in press

junction. In the low- T_C junctions used in conventional SIS mixers, the full energy gap-limited characteristic frequency is attained. However, in all high- T_C junctions fabricated to date, the characteristic frequencies lie well below any reasonable estimate of the gap frequency. Indeed, all high- T_C Josephson junctions yet reported, except ours, have characteristic frequencies which are only comparable to, or less than, those of the low- T_C junctions. About a year ago however, we developed a technique for producing high- T_C junctions with characteristic frequencies as high as 5 THz.⁵ In addition to high f_C , a low-noise Josephson mixer requires a normal state resistance that is at least comparable to the impedances of quasi-optical or waveguide RF coupling structures and to the impedance of the microwave IF circuits. Our high- f_C junctions typically have resistances of 10-30 Ω , which is quite reasonable for both RF and IF matching. They are therefore excellent candidates for low-noise mixers at THz frequencies. In the original work, these junctions were integrated with lithographic antennas and illuminated with far-infrared (far-IR) laser radiation. The resulting DC current-voltage characteristics showed Shapiro steps up to 17 mV, corresponding to locking of the internal Josephson currents with harmonics of the laser radiation to >8 THz.⁶ These results were described at the last Space Terahertz Symposium.

Since then, we have modified our device layout and the measurement apparatus to allow the coupling of 1 GHz intermediate frequency (IF) signals from the junction off the chip and into a low noise amplification and measurement system. Using this, we have directly measured mixer noise, both in the dark and with far-IR laser illumination. We have also performed heterodyne mixer measurements using the conventional hot load/cold load (H/C) technique. Although the noise of a related type of high- T_C Josephson junction has been examined indirectly through the rounding of Shapiro steps in the DC current-voltage characteristic,⁷ the work reported here is, to our knowledge, the first describing direct measurement of the IF-frequency noise in high- T_C junctions, and the first describing H/C load response from a high- T_C mixer at submillimeter frequencies.

⁵ P. A. Rosenthal, E. N. Grossman, R. H. Ono, and L. R. Vale, "High Temperature Superconductor-Normal-metal-Superconductor Josephson Junctions with high Characteristic Voltages", *Appl. Phys. Lett.*, 63, pp. 1984-1986 (1993)

⁶ P. A. Rosenthal and E. N. Grossman, "Terahertz Shapiro Steps in High Temperature SNS Josephson Junctions", *IEEE Trans. on Micr. Theory and Tech.*, in press

⁷ R. Gupta, Q. Hu, D. Terpstra, G. J. Gerritsma, and H. Rogalla, "A Noise Study of a High- T_C Josephson Junction under Near-millimeter-wave Irradiation", *Appl. Phys. Lett.*, in press

II. Mixer Fabrication, Experimental Setup, and Calibration

A. Mixer Fabrication

The technique for fabricating our high $I_c R_N$ junctions has been described in detail elsewhere.^{5,6} Briefly, the mixers are fabricated on 1 cm square substrates of either single-crystal lanthanum aluminate (LAO) or neodymium gallate (NGO). An 80-100 nm deep step is formed by ion-milling, in some cases milling directly into the substrate, but in most cases, milling into a previously deposited 300 nm thick film of strontium titanate (STO) (see table 1.) YBCO is then deposited by laser ablation at a 40° angle to the chip normal, from the high side toward the low side of the step, so that the YBCO film breaks at the step. The difference between the step height and the YBCO film thickness is thought to be crucial in determining the critical current density of the junction. Then, Au is sputtered in-situ from the opposite angle so as to fill in the break and create the SNS structure. This YBCO/Au bilayer is the basic building block for our mixer circuits. The bilayer is patterned into a strip as it crosses the step in order to define the junction width, which is 4 μm for all the mixer junctions described here (as opposed to 6 μm for the junctions in refs. 5,6). The crucial fabrication step for raising the junction's characteristic frequency and normal-state resistance is performed at the end. A small window directly above the junction is opened in photoresist and an angled ion-mill (from high side to low side) is performed to remove the Au of the bilayer that remains directly atop the YBCO, but not to remove the Au that lies in the shadow of the step and which forms the normal section of the SNS bridge. Removing this Au eliminates a large parasitic shunt conductance, and typically raises the junction resistance from $\sim 5 \Omega$ to $>10 \Omega$.

Table 1

	Substrate	$I_c(4K)$	R_N	f_c	$T_n(\text{max}), 4K$
THz 3	LAO/STO	145 μA	1.25 Ω	87.5 GHz	-
THz 4	LAO/STO	32 μA	37 Ω	520 GHz	-
THz 5	NGO/STO	25 μA	20 Ω	242 GHz	$36 \pm 4 \text{ K}$
THz 6	NGO	4 μA	150 Ω (!)	290 GHz	$100 \pm 20 \text{ K}$
THz 9	NGO/STO	315 μA	14 Ω	2.13 THz	850 K

For all our mixer chips except THz 9, the lithographic antenna was formed from electron-beam evaporated Ag, patterned by liftoff. This was done in a separate step, after

patterning the bilayer but before the final angled ion-mill. For THz 9, the antenna was formed from the same YBCO/Au bilayer. The rationale for a separately fabricated Ag antenna was that the antenna efficiency would be higher, because the ohmic loss in a high conductivity normal metal is substantially lower than in superconducting YBCO at high frequencies. However, since we recently directly measured a respectable optical coupling efficiency of 25 % over a 0.2 - 3 THz bandwidth from a YBCO/Au bilayer antenna of very similar design,⁸ we adopted a bilayer antenna for THz 9 for the sake of the simpler fabrication. The antenna used for our mixer junctions is of the same toothed log-periodic design⁹ as was used in refs. 5 and 6. The only difference is in the innermost tooth size - in the present case its inner radius is 10 μm . The outer radius of the outer tooth is 1000 μm . This results in an antenna bandpass of approximately 0.027 - 2.7 THz.

B. Experimental Setup

The overall layout of our experiments is illustrated in Fig. 2. A homemade, optically pumped, far-infrared molecular gas laser serves as our local oscillator (LO). In these experiments, the laser was operated on either the 404 or 992 GHz line of formic acid, on which it produces 1 - 4 mW. The substrates were mounted, circuit side up, against a 1 cm diameter hyperhemispherical Si lens.¹⁰ In general, 0.65 of Si spacer plates were placed between the chip substrate and the lens surface, placing the mixer somewhat behind the aplanatic hyperhemispherical focus. The mixer block was mounted on a thermally isolated platform whose temperature could be varied with a heater and monitored on a Ge resistance thermometer. A cooled low-pass filter with a measured 3 dB cutoff frequency of 3.3 THz and a measured passband insertion loss of -1.55 dB was used to reduce the thermal IR background to a manageable level. The total insertion loss due to the dewar window, low-pass filter, and reflection off the Si substrate lens was -4.7 dB. For most of the measurements, the LO and signal beams were focused into the cryostat and onto the mixer with a 90° off-axis paraboloidal mirror (40 mm on-axis focal length). Loss due to mismatch between the antenna beam and the focused signal beam is unknown, but we have measured an efficiency of 18 % for coupling the focused far-IR laser beam onto a room-temperature bolometer at the feed of an identical log-periodic antenna. Si wafers of various thicknesses were used as beamsplitters to combine LO and signal beams for heterodyne

⁸ J. P. Rice, E. N. Grossman, and D. A. Rudman, "Antenna-coupled High- T_c Microbolometer on Silicon", submitted to Appl. Phys. Lett.

⁹ R. H. DuHamel and D. E. Isbell, "Broadband Logarithmically Periodic Antenna Structures", IRE Natl. Conven. Rec. Pt. 1, p. 119-128 (1958)

¹⁰ D. F. Filipovic, S. S. Gearhart, and G. M. Rebeiz, "Double-slot Antennas on Hyperhemispherical, Elliptical, and Extended Hemispherical Dielectric Lenses, IEEE Trans. Microw. Theory and Tech. June 1992

mixing experiments. At 404 GHz, one of our standard thickness wafers is almost exactly 1 dielectric wavelength thick, providing >98 % transmission for the signal beam. For devices with high critical current (i.e. THz 9, see table 1), this beamsplitter did not couple sufficient LO power into the mixer, and a thicker beamsplitter was used, whose transmission for the signal beam was only 30 %. For H/C load measurements, we found the drift in the laser power was too great to allow reliable measurements of the H/C difference in IF power, ΔP_{IF} , to be made at DC. Therefore, the signal beam was mechanically chopped at 17 Hz and the signal of interest, P_{IF} or V , synchronously detected.

Both the DC and microwave frequency contacts to the chip are made by Au-plated, BeCu circuitboard traces. The mixers are DC biased by a battery powered, 1 k Ω output impedance supply (i.e. approximately a current bias). The microwave contacts are patterned into 50 Ω coplanar waveguide (CPW) on both the circuitboard and chip. A short length of semi-rigid coaxial cable is soldered at one end to the circuitboard's CPW and at the other to an SMA connector, which defines a convenient reference plane for the output of the mixer block. From there, the microwave signals pass through a DC block and isolator to an ultra-low noise 0.7 - 1.4 GHz HEMT amplifier. These three components remain at 4 K, even when the mixer block platform is raised to higher temperatures. For the measurements on THz 3 and THz 4, the cryogenic isolator was omitted. The output of the HEMT amplifier then passes through further room temperature amplification and a 50 MHz wide bandpass filter centered at 1 GHz. The filtered signal is then measured by a commercial microwave power meter.

In order to obtain 4-terminal DC contact to the mixer junction without series resistance from normal metal CPW and coax, the CPW ground return is broken to allow a DC current and voltage line to pass through. A primitive crossover is formed by patterning photoresist into a patch covering the DC lines, then overlaying the photoresist with In foil to complete the CPW ground return. The (room-temperature) 1 GHz return loss of the mixer block, as measured from the output reference plane, on a commercial microwave network analyzer, with an open circuit at the chip contacts, was -0.35 dB. The mixer block return loss with a chip in place, and with the In foil crossover arrangement, but an open circuit at the junction position, was -1.3 dB.

C. Calibration

In order to perform quantitative measurements of microwave mixer noise, it is essential to accurately calibrate the gain and noise of the IF system. We do not have a system of cryogenic microwave switches, directional couplers, etc. incorporated into the

cryostat that would allow the injection of calibrated signals into the IF system during the course of a measurement run. Therefore, we have performed our calibration by disconnecting the IF system input from the mixer block output, and connecting it instead to a 50 Ω termination mounted on the variable-temperature platform. Then, during a separate cooldown, we measure the IF system output power as a function of the platform temperature. The dependence is linear, with the slope yielding the IF system gain and the intercept yielding the IF system noise : $P_{out} = kB(G_{IF}T_{50} + T_a)$, where B is the 50 MHz system bandwidth, T_{50} is the temperature of the 50 Ω termination, and G_{IF} and T_a the desired gain and noise temperature of the IF system (the latter being essentially that of the HEMT amplifier). The accuracy of this calibration method is limited by the IF system's stability and reproducibility from cooldown to cooldown. Independent calibration runs done two weeks apart yielded gains which agree within 0.15 dB (3.4 %), and noise temperatures which agree within 0.8 K.

For converting system output powers to junction noise temperatures, the impedance mismatch between the mixer and 50 Ω IF system needs to be accounted for. This can be a very large effect as the junction's dynamic resistance $R_d = dV/dI$ can vary from 0 (in the 0-voltage state) to $\gg 50 \Omega$. We use a relation¹¹ expressing the scattering matrix formulation of the dependence of amplifier output noise on input match :

$$T_{out} = P_{out}/kB = G_{IF} \left[\left(1 - |\Gamma_1|^2 \right) T_1 + T_a + T_{rev} |\Gamma_1 - \beta|^2 \right] \quad (1)$$

where T_{rev} is the temperature of the reverse wave emitted from the amplifier input, and β the complex reflection coefficient for optimum amplifier noise match. Using an isolator effectively sets β to 0 and T_{rev} to the physical temperature of the isolator, 4 K. T_1 and Γ_1 are the noise temperature and complex reflection coefficient at the mixer block reference plane. If the IF line from the junction to the reference plane were perfectly lossless, then T_1 would just be the junction noise temperature T_j , and if, in addition, its impedance were exactly 50 Ω , then Γ_1 would just be the reflection coefficient of the junction $\Gamma_j = (R_d - 50\Omega)/(R_d + 50\Omega)$. In the remainder of this paper, we will make these assumptions and set $T_1 = T_j$ and $\Gamma_1 = \Gamma_j$. Experimentally however, we know the IF line has some loss because T_{out}/G_{IF} does not exactly reduce to $T_a + 4$ K in the 0-voltage state, independant of the junction's physical temperature. Rather, we find T_{out}/G to have a small linear dependance on temperature, with $\frac{d}{dT}(T_{out}/G) = 0.2$, suggesting approximately 1

¹¹D. Wait and G. F. Engen, "Application of Radiometry to the Accurate Measurement of Amplifier Noise", IEEE Trans. on Instrumentation and Measurement, 40, p.433-437, (1991), Eqn. (8)

dB of loss in the IF line, consistent with the 300 K network analyzer measurement of 1.3 dB loss.

III. Results

Five separate mixer chips have been fabricated and tested so far. For various ill understood reasons related to fabrication changes made in the last year, all but one mixer, THz 9, have had characteristic frequencies well below 1 THz (see table 1). For this reason, nearly all of the optical testing was done at 404 GHz. Two of the mixer junctions, THz 3 and THz 6 were clearly anomalous. The former did not receive a proper final angled ion-mill due to imperfect alignment of the milling window; its parasitic shunt conductance was therefore not fully removed. The latter had an exceptionally low critical current and high normal-state resistance, although its $I_c R_n$ product was quite in line with those of THz 4 and 5. We speculate that this junction's effective width was much less than those of all the others. In general, the attainment of reasonably high junction resistances ($>10 \Omega$) has not proven a problem. The difficulty has been in obtaining high and controllable I_c 's. We now believe our difficulties are related to accurate measurement and control of the difference between step height and YBCO film thickness. Beginning with THz 9, we expect our junctions to now be fairly close in their electrical characteristics to those described in refs. 5 and 6. Based on the hysteresis observed in those earlier devices, we had derived an approximate value of junction capacitance of 4.5 fF for 6 μm wide junctions. Scaling by the junction width, the current devices should have capacitances around 3 fF, leading to β_c in the range 0.09 - 0.8 (except for THz 3).

At the top of Fig. 3 we show the DC current and dynamic resistance of THz 5 as a function of DC voltage, without laser illumination. The dynamic resistance was measured by superimposing a small ($\sim 0.3 \mu\text{A}$ rms) AC current on the DC current, and synchronously detecting the resulting AC voltage. At the bottom of Fig. 3 is the raw IF system output power as a function of junction voltage on the same scale. There is an obvious correspondance between the peaks and dips in $P_{\text{out}}(V)$ and those in $R_d(V)$. This is largely just a manifestation of better matching to the IF system with higher dynamic resistances. The main features of $P_{\text{out}}(V)$ are (a) a value in the 0-voltage state that reflects the instrumental noise, as discussed above, (b) an initially linear rise out of the 0-voltage state, (c) a peak at a relatively low voltage, (d) a gradual rolloff at higher voltages, with a small number of peaks and dips superimposed, eventually converging on a constant value not far different from the noise in the 0-voltage state.

Analytic expressions exist for the RSJ model's predictions of junction noise in the regimes of (d) and (b). Specifically, RSJ quantum-noise theory^{12,13} yields, for the low-frequency, noise voltage spectral density $S_V(0)$ (in V^2/Hz),

$$S_V(0) = \frac{R_d^2}{R_n} \left[4kT + 2eV \left(\frac{I_c^2}{I} \right) \coth \left(\frac{eV}{kT} \right) \right] \quad (2)$$

when the following conditions are met : low capacitance, i.e. $\beta_c \ll 1$, low frequency, i.e. $f (= 1 \text{ GHz}) \ll f_J = (2e/h)V$, and current $I > I_c$, so that noise rounding can be neglected. These conditions are well satisfied for our junctions in the regime (d) where the noise gradually rolls off at high voltages. A further implicit assumption made in this RSJ-based noise theory is that the junction is current biased (i.e. embedding impedance $\gg R_n$) at all frequencies at which the Josephson currents are significant, i.e. up to the THz range. This condition is not so well satisfied for our junctions since we have (deliberately) aimed to make the junction resistance R_n comparable to the antenna impedance to obtain good RF coupling. Determining and accounting for finite embedding impedance at the Josephson frequencies is the main obstacle to obtaining a quantitative yet intuitive understanding of Josephson noise, and the issue was never thoroughly explored in the early work on Josephson mixers. Eqn. (2) is applicable to the gradual rolloff in the experimental noise at high voltages. On the other hand, the initial linear rise in the noise coming out of the 0-voltage state, where $I < I_c$ and noise rounding entirely accounts for the finite voltage, can be described¹⁴ by a model of thermally activated phase diffusion. In this case, the noise is the "fluxonic" equivalent of the usual electronic shot noise, and

$$S_V(0) = 2\phi_0 V \quad (3)$$

where $\phi_0 = h/2e$ is the flux quantum. This again assume $\beta_c \ll 1$. The regime intermediate between these two cases, in which the noise power peaks, and the case of finite capacitance $\beta_c \sim 1$ or $\beta_c \geq 1$, can only be modeled by numerical simulation.

The junction's equivalent circuit is a random voltage generator with voltage spectral density $S_V(0)$, in series with its dynamic resistance R_d . Therefore, the power spectral density delivered to a load resistance $R_L = 50 \Omega$ is given by

¹² R. H. Koch, D. J. Van Harlingen, and J. Clarke, "Quantum-Noise Theory for the Resistively Shunted Josephson Junction", *Phs. Rev. Lett.*, 45, p2132-2135 (1980)

¹³ K. K. Likharev and V. K. Semenov, *JETP Lett.*, 15, p.442 (1972)

¹⁴ R. F. Voss, "Noise Characteristics of an Ideal Shunted Josephson Junction", *J. Low Temp. Phys.*, 42, pp. 151-163, (1981)

$$P_{del} = (1 - |\Gamma|^2) kT_1 = \frac{R_L}{(R_L + R_d)^2} S_V(0). \quad (4)$$

In Fig. 4 we show a comparison between the experimental junction noise temperature T_1 , (derived from the raw IF system output power via Eqn. (1)), and the theoretical junction noise temperature derived from Eqns. (2)-(4) and the experimental I-V and R_d -V data. The agreement is remarkably good in the voltage regions where the theoretical expressions apply. In the region of the noise peak, the experimental noise is significantly higher than predicted by simply applying Eqn. (2).

This data on THz 5 constitutes an existence proof : it shows that high- T_c Josephson junctions can be experimentally realized that have resistances suitable for matching to $\sim 50 \, \Omega$ microwave and quasi-optical circuits, and which have noise temperatures comparable to the RSJ predictions, namely a few times the physical temperature. The next question is whether low noise temperature and high characteristic frequency (ICRN product) can be attained in the same junction. To give a crude idea of the noise level of different junctions, we have tabulated in table 1, along with f_c , the maximum junction noise temperature observed in the $P_{IF}(V)$ data without laser illumination. Unfortunately, we do not have sufficient statistics to answer the question yet. The only legitimate comparison we can make among our junctions that is relevant is between THz 5, which had low noise, but also low f_c (240 GHz), and the most recent device, THz 9, which had high f_c (2.1 THz) but also much higher noise. (THz 6 also had higher noise than THz 5, but this is largely expected due to its extremely small critical current. Its Josephson noise parameter $\Gamma = 2\pi \left(\frac{2e}{h} \right) \frac{kT}{I_c}$ is high enough that significantly higher noise would be expected just from the RSJ model.) We suspect that the correlation between high f_c and high noise suggested by comparing THz 5 with THz 9 is not genuine and general, however, because the I-V curve of THz 9 displays dramatic non-RSJ structure, whereas we already know from the devices described in ref. 6 that high characteristic frequencies can be attained simultaneously with I-V curves much closer to the ideal RSJ type.

There is definite evidence that, in the junctions with higher I_c (THz 3 and THz 9), the junction noise depends strongly on magnetic field. We have taken no special precautions to eliminate or shield the junction from magnetic components (particularly the 1 GHz isolator, in cases when it was used) inside the Dewar. The main manifestation of these effects is asymmetry in the measured junction noise between positive and negative current biases. Fig. 5a, for example, shows 2 sweeps of junction noise versus voltage for THz 3, the first taken in ambient field, and the second taken with the entire cryostat placed inside a magnetic shield. Moreover, for THz 9, we have seen apparent evidence of trapped

flux within the junction (Fig. 5b). Independent of whether the measurement was made with the cryostat in ambient field or in a magnetic shield, sweeps of junction noise after the cryostat had been cooled in ambient field showed very large asymmetry, while sweeps made a few days later, after the cryostat was cooled in zero field, were perfectly symmetric. In addition, larger, externally applied magnetic fields strongly modulate the critical current of most of the junctions. THz 6 however, which had anomalously I_C , showed no dependence of either critical current or junction noise with magnetic field. Thus, based on our admittedly limited statistics, there appears to be a strong correlation between critical current and sensitivity of critical current and junction noise to magnetic field.

When the mixer is illuminated with far-IR radiation, strong Shapiro steps appear in the DC I-V curve. Alongside this, the overall shape of the noise sweep versus voltage which is displayed in the dark measurements around zero voltage is reproduced around every Shapiro step voltage when the laser is incident. The height of the noise peak scales with the Shapiro step height. These general features of the $P_{IF}(V)$ dependence when LO radiation is applied are illustrated in Fig. 6. In most cases, we find a minimum in $P_{IF}(V)$ occurs approximately halfway between steps. This would suggest, as has been found in numerical RSJ simulations⁴, that approximately halfway between steps is the optimum bias point for heterodyne noise. On the other hand, in some cases, we find a maximum in $P_{IF}(V)$ halfway between steps. We do not presently have an explanation for this. Contrary to our expectation, the extrema in $P_{IF}(V)$ do not always correspond to matching extrema in $R_d(V)$; we have observed strong minima (factor of 2 peak-to-valley) in $P_{IF}(V)$ between steps with very little, if any curvature in the I-V curve at the same point.

Finally, we illuminated the mixer with both the LO beam from the laser and a signal beam from a chopped 77 K black body. Fig. 7 shows the total IF noise power as a function of mixer voltage, $P_{IF}(V)$, and the demodulated difference in IF noise power $\Delta P_{IF}(V)$ due to the chopped signal. Within the context of the usual H/C load measurement technique, the latter is proportional to the receiver's heterodyne conversion gain. If the demodulated signal shown in Fig. 7 is naively interpreted as entirely due to heterodyne detection, then its maximum value, $\Delta P_{IF} = 22 \mu\text{W}$ would correspond to a DSB receiver conversion gain of -12 dB, and the 950 μW total IF noise power at the same point would correspond to a DSB noise temperature of approximately 9000 K. In H/C measurements on THz 4 we have observed demodulated ΔP_{IF} signals corresponding to noise temperatures as low as 3000 K. To our knowledge, these are the first observations of H/C load response of a high- T_C mixer at frequencies above 100 GHz.

Unfortunately, we believe that use of the demodulated ΔP_{IF} signal to derive heterodyne conversion gain and noise temperature is by no means as straightforward as

outlined above, even though this H/C measurement technique is the most widely used one for characterizing heterodyne receivers in general, and was used in the Josephson mixer experiments in refs. 1 and 4. Two observations cast the primary doubt on this simple interpretation of the H/C signals. The first is that the demodulated ΔP_{IF} displays large signals of both signs. That is, at certain biases the IF power is larger with the hot load in the signal beam than with the cold load, but at other biases the IF power is larger, by a comparable amount, with the cold load in place than with the hot load. For a true heterodyne signal, the IF power must always increase as the signal power is increased (load switched from C to H). Secondly, in some cases we have observed ΔP_{IF} signals - signals substantially above the noise level - with the laser LO blocked. (This latter effect is common in conventional SIS mixers operated at high frequency. Recall that in the case of Josephson mixers however, there is the possibility of bona-fide "internal-mode" heterodyne mixing, between the junction's internal Josephson oscillations and the signal, which would manifest itself in just this way.)

An effect that would explain both these observations is direct (or "video") detection of the broadband H/C signal. Direct detection produces a small change in the DC I-V curve of the junction; since we use a DC current bias in our setup, this is manifested as a modulation of the junction voltage that is synchronous with the chopping of the H/C signal. Since the IF noise power, with or without laser illumination, varies rapidly with voltage at some voltages (see Figs. 5,6), the small voltage modulation due to direct detection produces a small modulation in P_{IF} . This appears just like a heterodyne signal, except that, since the IF noise power sometimes increases and sometimes decreases with voltage, the modulation in P_{IF} can be of either sign, i.e. $P_{IF}(H) > \text{or} < P_{IF}(C)$. A third observation suggests that this effect is indeed likely to be significant. It is that the voltage dependence of $\Delta P_{IF}(V)$ appears by eye to track, at least roughly, that of the derivative of the noise power, $dP_{IF}(V)/dV$. See Fig. 7. In principle, it would be possible to subtract this effect out of the measurements, by directly measuring both $dP_{IF}(V)/dV$ and the demodulated junction voltage ΔV , and subtracting their product from the measured $\Delta P_{IF}(V)$. Indeed, we can detect, and measure with reasonable signal-to-noise ratio, the demodulated junction voltage (not shown), while $dP_{IF}(V)/dV$ can be obtained from plots like Fig. 6. However, in practice, with realistic levels of signal-to-noise ratio, drifts in LO power, etc., we do not believe it likely that this subtraction of the spurious component of $\Delta P_{IF}(V)$ can be done very reliably or accurately. Furthermore, although we have described the effect for the case of a DC current bias, as used in our setup, the use of a DC voltage bias would not materially affect the situation. Therefore, we are presently not at all confident that the H/C load measurement technique can be used with broadband sources to accurately evaluate

heterodyne performance of Josephson mixers. This conclusion was also reached by Blaney et al.¹⁵ who did some of the most careful of the early work on point-contact Josephson mixers. The only completely reliable way to measure Josephson mixer heterodyne performance is to use a narrowband source (e.g. a spectral line, or a thermal source with a narrowband filter) as the source.

IV. Conclusions

We have performed a number of experiments directed toward measuring the heterodyne noise performance of high- T_C Josephson mixers at high frequencies. The experiments fall into 2 main categories: measurements of the 1 GHz (IF) noise power of bare, non-illuminated junctions, and H/C load heterodyne measurements with an external laser LO. We have fabricated and performed measurements on 5 devices, although only one of these actually had the high characteristic frequency of which our fabrication technique is capable. Substantial differences between junctions were observed in the non-illuminated noise power, but we do not have sufficient statistics to form general conclusions. In at least one case, the non-illuminated mixer noise temperature is consistent with the predictions of the general, current-biased RSJ noise theory. Most importantly for heterodyne receiver applications, the mixer noise temperature in this case is fairly low - it never rises above 36 ± 4 K (at a physical temperature of 4 K). The celebrated "excess noise" of Josephson mixers is simply not that large. The heterodyne measurements showed strong difference signals in the IF noise power from a chopped H/C load source, and naive interpretation of the signal amplitude would imply a DSB heterodyne receiver temperature of 9000 K (for THz 9) and 4000 K (for THz 4) at 404 GHz. However, observation of the signs of the difference signal at different biases, and of the fact that difference signals in IF noise power are still observable with the laser LO blocked, cast strong doubt on the reliability of the H/C load measurement technique for evaluating heterodyne receiver performance for Josephson mixers. Spurious difference signals in the IF power due to direct detection of the chopped signal are the likely cause of the problem, and are difficult, if not impossible, to subtract from the data. For this reason, we currently believe the only foolproof method for demonstrating low noise Josephson mixer performance with high- T_C junctions will be by using narrowband signal sources, e.g. by the observation of spectral lines.

¹⁵ T. G. Blaney, N. R. Cross, and R. G. Jones, "The Properties of a Heterodyne Receiver at 450 GHz using a Josephson Point-contact Mixer and an External Local Oscillator", *J. Phys. D: Appl. Phys.*, pp. 2103-2124, (1982)

We are very grateful to D. A. Rudman, C. D. Reintsema, R. H. Ono and L. J. Borchardt for assistance in junction fabrication and advice on junction characteristics. Heterodyne mixer development at NIST has been partially supported by the BMDO Office of Innovative Science and Technology, through ONR, and by NASA, Astrophysics Division.

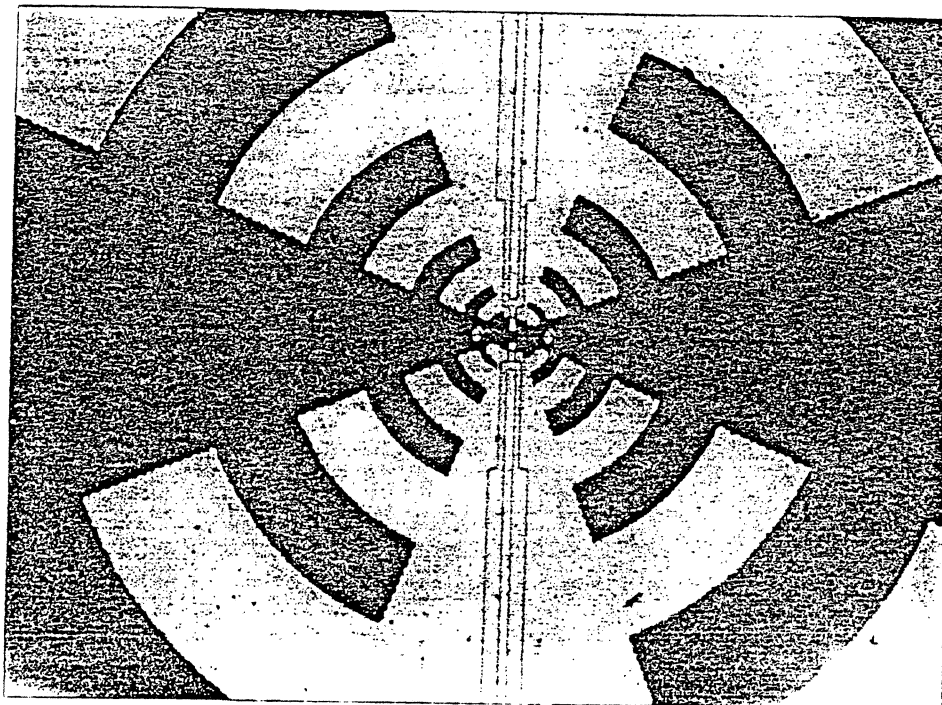


Figure 1. Photograph of THz 6. The step edge runs horizontally through the junction. The dark region at the center is the part of the bilayer which has been ion-milled to raise the junction resistance.

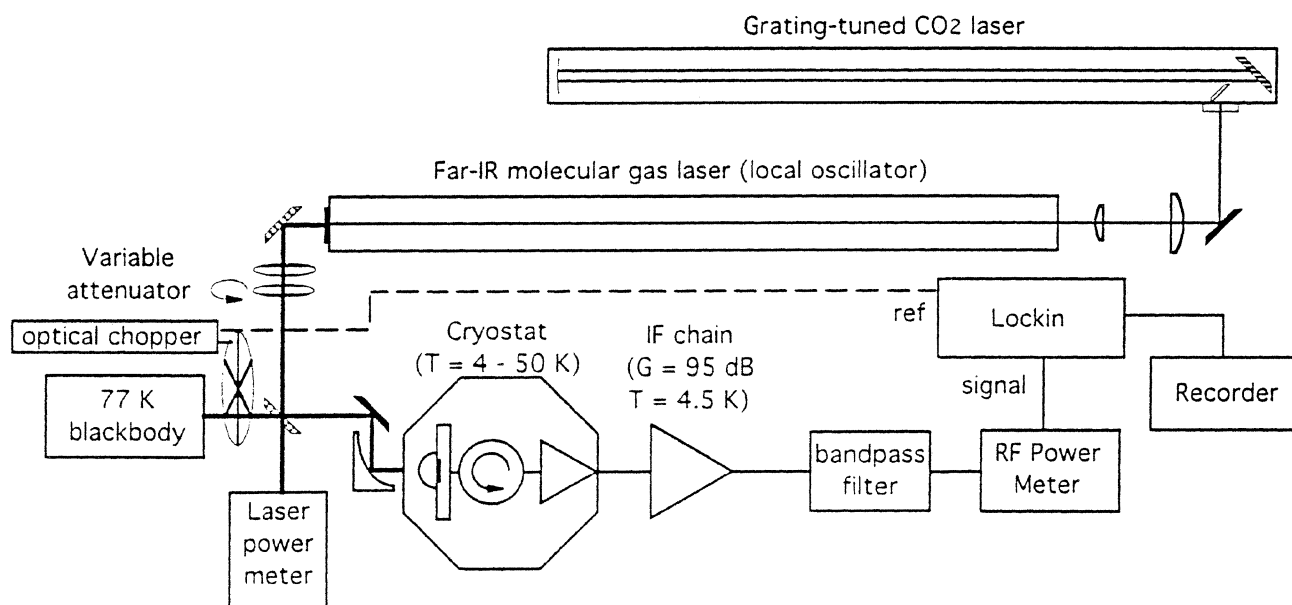


Figure 2. Experimental setup for heterodyne mixer measurements.

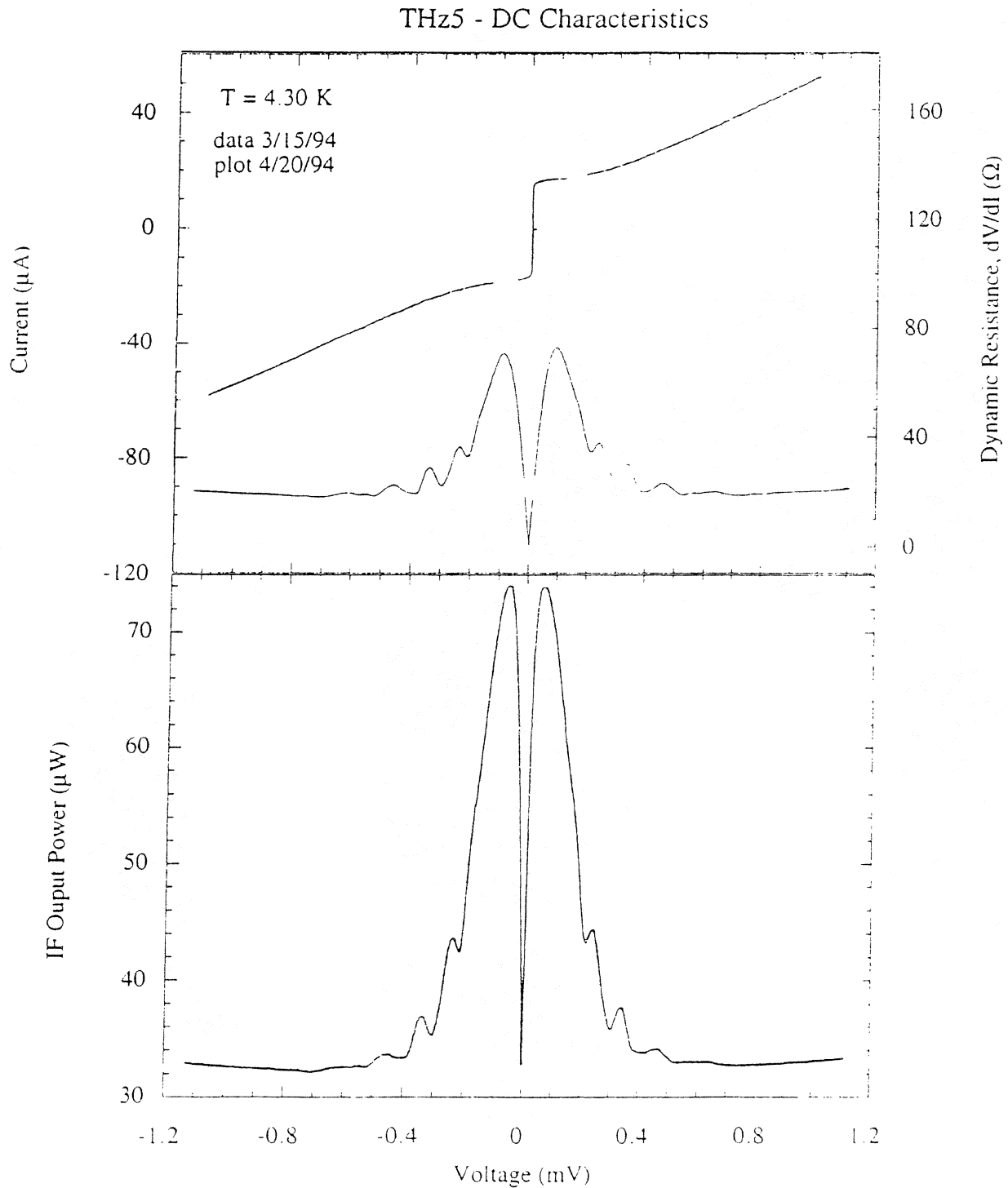


Figure 3. (top) Current-voltage characteristic and dynamic resistance $R_d = dV/dI$ versus voltage for THz 5. (bottom) The raw 1 GHz IF output power versus voltage, on same scale. The gain-bandwidth product of the IF system is $G_{IF}B = 1.76 \mu\text{W/K}$ (see text for IF calibration procedure).

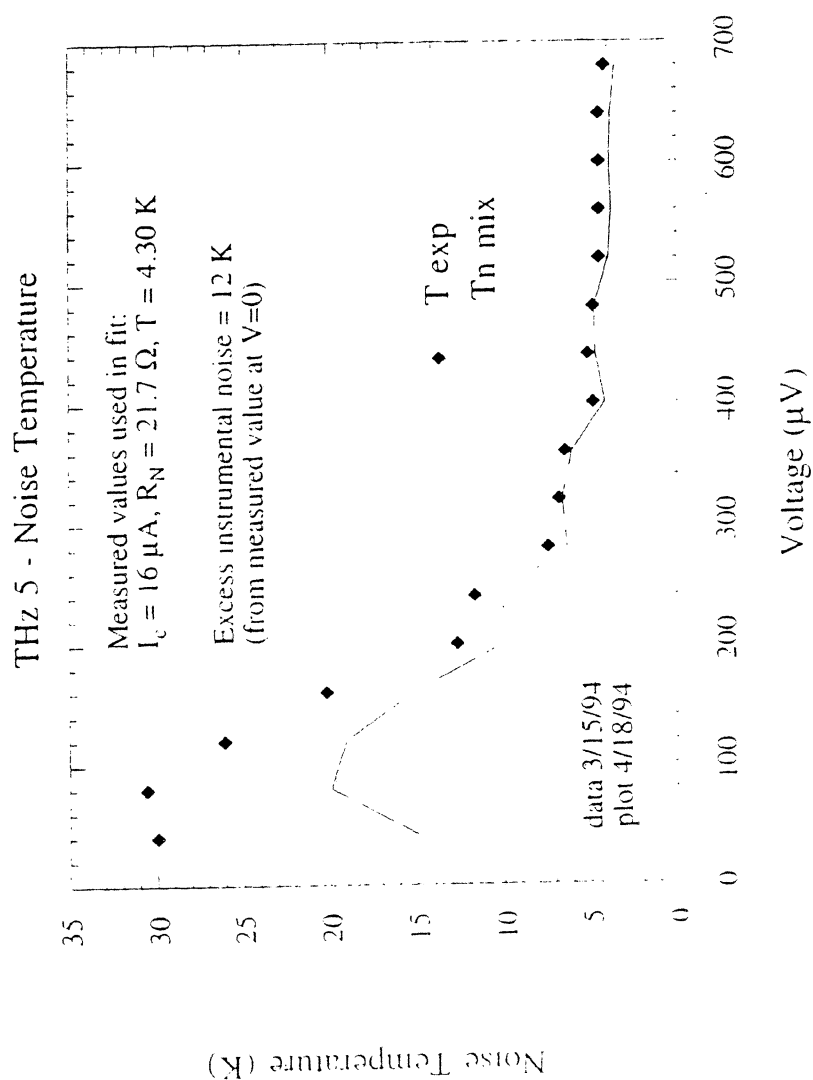


Figure 4. Theoretical junction noise temperature (solid line) using the measured I-V and R_d -V curves shown in Fig. 3, and the RSJ expression Eqn. (2). The solid points are the experimental data.

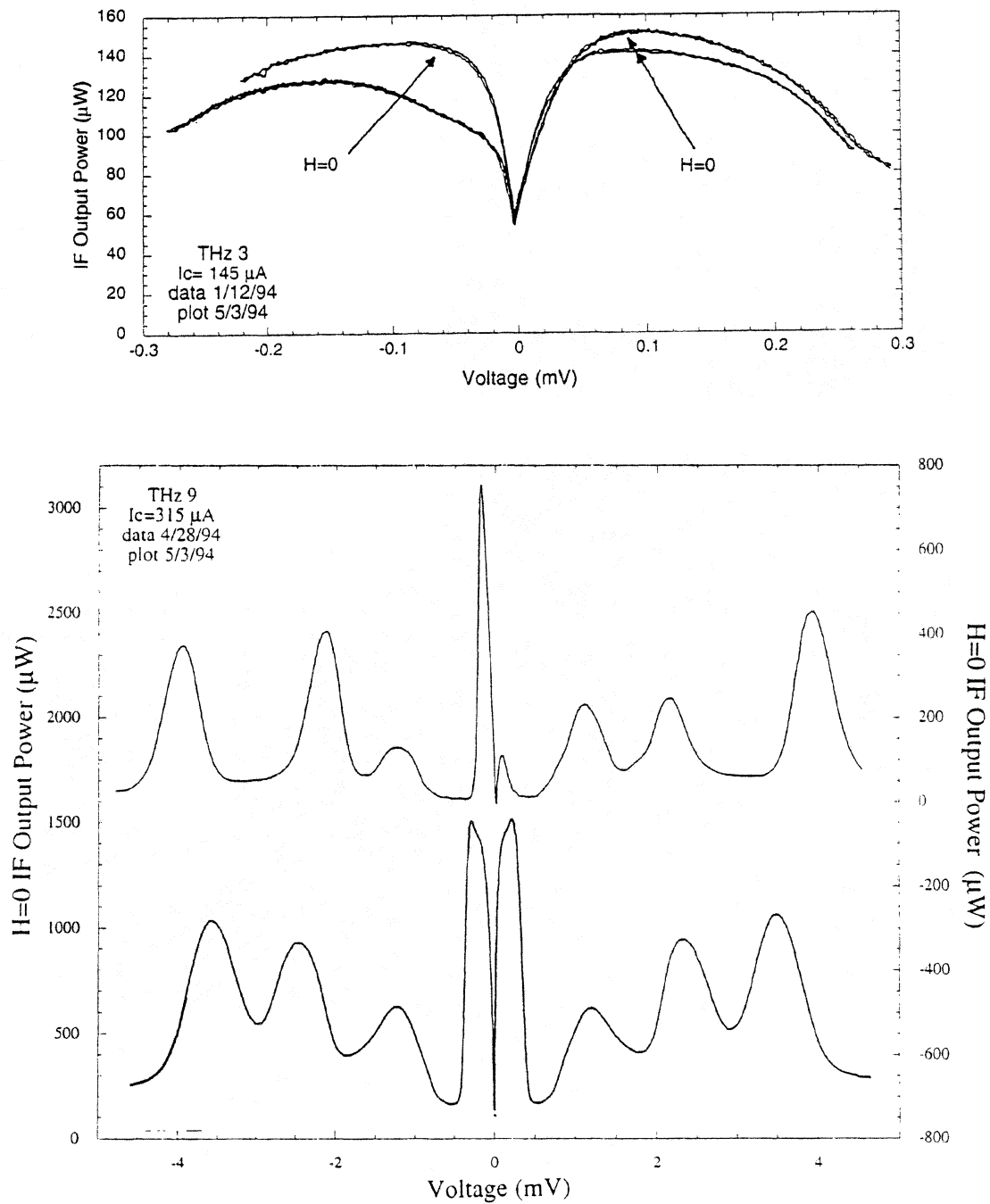


Figure 5. IF output power versus junction voltage for the two highest I_c devices in different magnetic field configurations (see text).

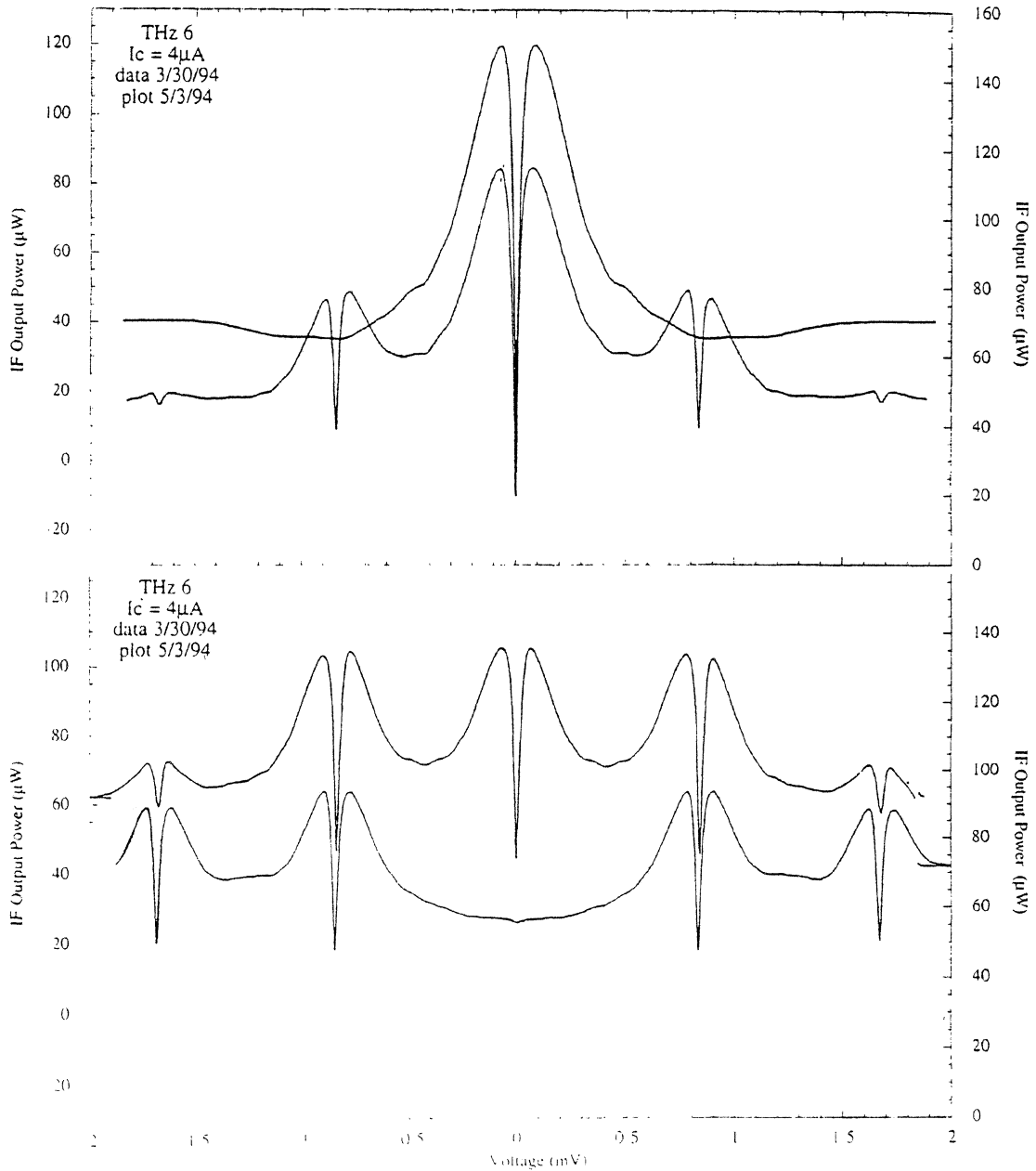


Figure 6. IF output power versus voltage under 404 GHz laser illumination at various power levels. (top) laser off, (second from top) intermediate laser power, (third from top) laser power sufficient to make 1st Shapiro step amplitude equal to I_c , (bottom) laser power sufficient to drive I_c to zero.

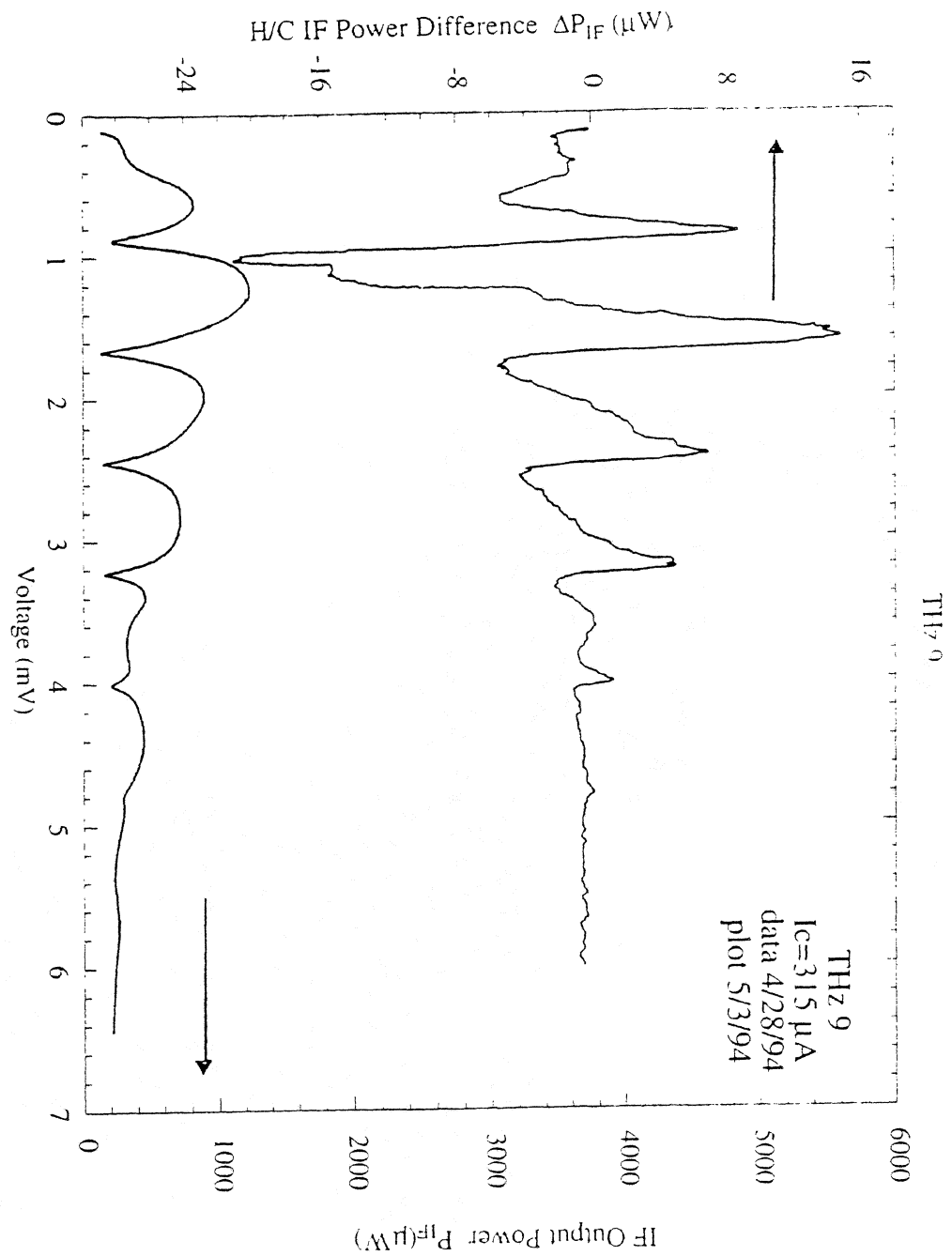


Figure 7. (Bottom) IF output power versus junction voltage, with 404 GHz illumination. (Top) Difference in IF output power ΔP_{IF} with signal beam chopped between 300 K and 77 K blackbody sources. The minima in IF output power occur at the Shapiro step voltages, and line up with zero-crossings in ΔP_{IF} .

MEASUREMENTS OF NOISE IN JOSEPHSON-EFFECT MIXERS

R.J. Schoelkopf, J. Zmuidzinas, and T.G. Phillips

Downs Laboratory of Physics, 320-47
California Institute of Technology, Pasadena, CA 91125

We present new heterodyne receiver results obtained at 100 GHz using resistively-shunted Nb and NbN tunnel junctions. In addition, we have carried out accurate measurements of the available noise power of these devices at the L-band (1.5 GHz) IF frequency. Both the heterodyne and the output noise measurements show that the noise of these devices can be a factor of five or more higher than that predicted by the simple current-biased RSJ model. The noise approaches the appropriate thermal or thermal and shot noise limits for bias voltages where the nonlinearity is not strong (i.e. $V > I_C R_N$), but as expected from the RSJ model, can be significantly higher at the low voltages where the mixers are typically biased. The bias voltage dependence of the noise shows structure which is associated with resonances in the RF embedding circuit. Surprisingly, we find that changes in the high-frequency (100 GHz) impedance presented to the junction can dramatically affect the magnitude and voltage dependence of the low-frequency (1.5 GHz) noise.

I. Introduction

While Josephson-effect mixers have been shown to have low conversion loss and low local oscillator power requirements as millimeter-wave mixers, their sensitivity is not as good as SIS mixers which utilize the quasiparticle nonlinearity of superconducting tunnel junctions. Josephson mixers are known to suffer from an “excess” noise, whose origin and magnitude has been clarified by recent simulations based on the RSJ (resistively-shunted junction) model¹. Recent progress in fabrication of high- T_C Josephson devices (mostly of SNS weak link types) has produced $I_C R_N$ products of up to ten millivolts². These devices may be suitable for producing heterodyne receivers well into the terahertz frequency range. However, in order to draw conclusions about the expected sensitivity and technological potential of Josephson-effect mixers in this frequency regime, a firm understanding of the noise processes and their scaling will be required.

We have been engaged in studies of the noise which is present in numerical simulations using the RSJ model, and in measurements of the heterodyne performance of well-characterized, lithographically-controlled Josephson devices using Nb and NbN shunted tunnel junctions. The heterodyne measurements suggest that the output noise of the devices can be even larger than the “excess” predicted by the RSJ model. We have therefore undertaken accurate measurements of the output noise of these shunted junctions at the receiver intermediate frequency (IF) of 1.5 GHz, including calibration of the contributions of the IF amplifier and corrections for the power coupling to the junction.

II. Junction Fabrication

The devices used in the experiments described here were made using a process for resistively-shunted tunnel junctions described previously³. A submicron, high current-density tunnel junction⁴ is fabricated along with a AuGe resistor in close proximity. Junctions based both on Nb/AlO_x/Nb and NbN/MgO/NbN trilayers are used. The shunt resistor reduces the junction normal state resistance as well as the $I_C R_N$ product, by a factor of typically three to five. The shunted junctions have normal resistances (after shunting) of 30-40 Ohms, critical currents of 10-20 microamps, $I_C R_N$ products of about 0.5 mV, and are very stable with time and thermal cycling. The current-voltage characteristics are non-hysteretic and very RSJ-like, the critical current scales with junction area, and the critical current can be modulated with a magnetic field. The junctions have current rises at the superconducting gap of the material (2.9 mV for Nb and approximately 4.5 mV for NbN), but this effect is small, since most of the current flows through the shunt resistor. Because the shunting reduces the $I_C R_N$ product and thus the critical frequency ($\omega_c = 2eI_C R_N / \hbar$), these devices should be nearly optimal for heterodyne detection at 100 GHz, but may not be suitable for higher frequencies.

III. Heterodyne Receiver Measurements

We have performed heterodyne detection tests using the shunted Nb and NbN junctions fabricated using the technique described above. The devices are fabricated on 100 μm thick quartz substrates and mounted in a full-height rectangular-waveguide mixer mount. The mixer mount incorporates two mechanically-adjustable, non-contacting backshorts, which allow a wide variation of the impedance presented to the junction. The waveguide has a transition to a corrugated scalar feedhorn, whose beam is then coupled outside of the dewar through a series of cooled IR filters and a polyethylene lens. Local oscillator (LO) radiation from a Gunn diode oscillator is injected into the beam through a mylar beam splitter. The beam pattern has been measured outside the dewar, and there is negligible spillover of the receiver beam onto dewar windows and filters. All measurements were performed with the devices cooled to 4.2 K.

The junction is biased with a combination bias tee and intermediate frequency (IF) matching network, which provides an optimum match for impedances of about 90 Ohms into the 50 Ohm IF circuit. The IF signal is amplified by a HEMT low-noise amplifier (LNA) on a 12 K stage, which has a gain of 30 dB and noise temperature of approximately 10 K. The amplifier bandpass is 500 MHz, centered at 1.5 GHz. The IF signal is then coupled to filters and room temperature amplifiers, and then finally led to a power detector. The bias electronics can be controlled using a personal computer, and current-voltage characteristics and IF power levels can be digitized and recorded for later analysis.

When illuminated with LO power, the devices develop strong Shapiro steps at the quantized voltages $V_n = nhv / 2e$, and the IF power shows smooth peaks between the current steps (see Fig. 1). Receiver response is measured using the standard hot/cold load technique, typically with room temperature and liquid nitrogen cooled absorbers which fill the receiver beam outside the dewar. Best response is always obtained between the zeroth and first Shapiro steps,

and for a local oscillator power which suppresses the critical current by approximately 50 percent. All of this behavior is in agreement with the predictions of the RSJ model.

A representative pumped I-V curve and hot/cold load response for a Nb shunted junction at 102 GHz is pictured in Figure 1. When biased at the optimum voltage, this receiver has a Y-factor of 1.8, and a double-sideband receiver noise temperature of 200 K. The best sensitivity seen to date with NbN devices is 270 K (DSB), and the general receiver behavior is very similar for devices with either superconductor. The conversion efficiency is approximately -6.5 dB, and therefore the mixer noise temperature, including any front-end losses, was about 150 K. Since this device was expected to be nearly optimal based on its observed DC characteristics, the mixer noise temperature expected from RSJ model simulations is closer to 30 K (DSB), with about -3 dB conversion loss. Even when accounting for the slight saturation and possible single-sideband operation of the receiver as described below, and including estimates of the front-end optical losses, the mixer output noise is probably still a factor of 2-5 times higher than expected.

The mixer sensitivity is strongly dependent on the position of the adjustable RF tuners, with best response coming near the positions which yield the maximum output power, and also close to optimum LO power match into the device. If we measure the instantaneous bandwidth of the mixer by changing the LO frequency while keeping the tuner positions fixed, the noise temperature degrades by about 50 percent after the frequency has been displaced by the 3 GHz separation between the sidebands, and then continues to increase roughly linearly with the frequency displacement. Note that this variation in receiver temperature is not due to compensation for the junction capacitance, as these devices have $\omega RC \approx 0.5$ at 100 GHz. This variation must instead be due to the intrinsic dependence of the mixer temperature on the RF port impedance. The observed dependence may indicate that the receiver is being tuned to a largely single-sideband mode, with a corresponding overestimate of the DSB mixer noise temperature from hot/cold load measurements.

We have also made a crude measurement of mixer linearity by plotting receiver output power as a function of input load temperature for liquid nitrogen, dry ice ($\cong 200$ K), room temperature, and heated ($\cong 350$ K) RF loads. The data indicate that the mixer is approximately 20 percent saturated for a room temperature input, and this effect probably accounts for a roughly 1 dB overestimate of the conversion loss. The size of this effect is reasonable given the experience with low-conversion-loss SIS mixers at these frequencies⁵. Saturation probably arises in the output because the IF voltage swings are limited to the size of a photon step. One would expect that this effect should be significantly (up to a factor of 4) stronger in Josephson-effect mixers, since the photon steps are half as wide. The larger conversion loss, relative to SIS mixers, that we observe probably tends to reduce the saturation.

The shape of the pumped I-V curves can be varied radically as the mechanical tuners are adjusted. Several example curves for a single device under illumination with 98 GHz LO radiation and varying tuner positions are shown in Figure 2. The strong variation in output impedance verifies that a wide range of driving impedances can be presented to the junction. Negative differential resistance such as that seen in Figure 2 is expected when the junction is driven with a largely inductive impedance⁶, and the low output impedance probably corresponds to a capacitive drive. Both of these curves were taken for tuner positions which were far away from LO power match and therefore required significantly more LO power to yield equivalent suppression of the critical current. Best receiver performance is always observed for a more intermediate output impedance similar to that expected for a real drive impedance, which is again consistent with RSJ model predictions that optimum mixer performance should be possible with mostly real RF impedances.

IV. Noise Measurement Technique

In order to verify that higher output noise is responsible for the degraded receiver sensitivity and to examine whether this noise can be reduced or eliminated, we undertook accurate measurements of available noise power produced by the junction under a variety of conditions, both with and without LO power applied. We report here only measurements in the absence of LO power, and with the optics removed so that the junction sees only 4.2 K thermal radiation at all frequencies. A block diagram of the microwave apparatus is displayed in Figure 3. A coaxial switch⁷ was inserted between the junction and the amplifier so that a variable temperature termination, similar to that described by McGrath et al.⁸, could be substituted for the junction. Two isolators⁹, each with a directivity of about 20 dB, ensure that no reflected noise waves from the amplifier contaminate the measurements. Finally, a bi-directional coupler¹⁰ allows a test signal to be introduced in order to measure the power reflection coefficient from the junction using a procedure described below. A similar technique has been used recently by Dubash¹¹ to measure the output noise of SIS mixers to high accuracy.

By heating the termination and observing the output power as a function of temperature, the noise of the IF chain and the gain of the system could be determined. A typical calibration is displayed in Figure 4. The termination was measured to have a return loss at cryogenic temperatures of about -14 dB. The chief uncertainty in calibration is in the accuracy of the diode temperature sensor¹² used to read the load temperature. The diode was calibrated by suspending it in a liquid helium storage dewar, and we estimate the error on the IF system noise determination to be ± 0.5 K. The IF system temperatures were typically about 10 K, varying slightly depending upon the bias conditions of the low noise amplifier and the bandpass selected by using room temperature filters.

To determine the available noise power from the junction and thus the junction output noise temperature, it is necessary to correct for any losses and mismatch between the junction and LNA. The bi-directional coupler allowed the introduction of a signal from a noise tube to be launched towards the junction. This signal was limited to a 500 MHz band centered at the 1.5 GHz IF frequency, and typically increased the total noise by about 20 percent. No difference in the shape of the I-V curve was observed between noise tube on and off states, verifying that the noise did not grossly affect the junction properties. Because of the weak (-30 dB) coupling, very little noise is added when the noise tube is off, and merely causes an increase in the measured IF system temperature by a small (< 0.5 K) amount. The directivity of the coupler at cryogenic temperatures was measured to be greater than 23 dB.

The difference in IF power with and without the noise source applied gives a measure of the reflection coefficient. When the junction is biased in the zero-voltage state, where the dynamic resistance is zero, it can serve as a reference short-circuit. The power reflection coefficient of the junction, ρ , is therefore given by

$$\rho(V) = \frac{P_{On}(V) - P_{Off}(V)}{P_{S-On} - P_{S-Off}}$$

where $P_{On}(V)$ is the power (as a function of the junction bias voltage, V) measured when the noise tube is on, and $P_{Off}(V)$ is the measured power when it is off. The denominator, $P_{S-On} - P_{S-Off}$, is the difference between those powers when the junction is in the zero-voltage state; this quantity is proportional to the strength of the coupled test signal from the noise tube. By reversing the port of the coupler through which the test signal is introduced, we can measure any loss, L , between the coupler and junction

$$L = 1 - \sqrt{\frac{P_{S-On} - P_{S-Off}}{P_{S-Rev} - P_{S-Off}}}$$

where P_{S-On} and P_{S-Off} are as defined above, and P_{S-Rev} is the power with the noise tube signal coupled in the *reverse* direction, towards the LNA. This loss was determined to be about 0.6 dB, which is probably due to the small reflections in the coaxial switch and loss in the cabling to the bias tee. No correction for this loss is made to the estimate of the IF system temperature, which is measured including the switch. Any difference in the loss between the junction and the amplifier (for example, unequal cable lengths) relative to the loss between the variable load and the amplifier causes a small systematic error (< 0.4 K) in the estimate of the amplifier contribution to the noise.

Having measured the IF reflection coefficient to the junction as a function of bias voltage, and having determined the IF system temperature through calibration with the variable temperature load, the available noise power or output noise temperature of the junction, in Kelvins, can be expressed as

$$T_{Junction} = \frac{1}{(1 - \rho(V))} \left(\frac{P_{Off}(V)}{G} - T_{IF} - \rho(V)T_{Physical} \right)$$

where $P_{Off}(V)$ is the measured IF system output with only the junction's noise at the input, G and T_{IF} are the measured IF system gain and noise temperature, and $T_{Physical}$ is the physical temperature of the isolators, whose terminations radiate thermal noise towards the junction which is partially reflected back into the LNA. The errors in the junction noise temperature are dominated by systematic errors in the determination of the IF system temperature, and in systematic errors in the measurement of the reflection coefficient due to the finite directivity of the directional coupler, which are more severe for large reflection coefficients.

V. Junction Noise Measurements

The apparatus and techniques described above have been used to measure the output noise temperature of both Nb and NbN shunted junctions. A plot of $T_{Junction}$ as a function of bias voltage for a NbN device with a magnetic field applied is shown in Figure 5. This curve displays several representative features seen in all of the measurements. First, the noise temperature above voltages

comparable to the $I_C R_N$ product (in this case, about 100 μV), where the junction I-V curve is linear but below the superconducting gap of the underlying tunnel junction, is nearly constant with a value of about 4.6 K. One would expect that in this region the noise would be mostly Johnson noise with a noise temperature equal to the physical temperature of 4.2 K. Other devices show similarly increased noise temperatures in this region, which could be due to systematic errors in the measurements, a slightly elevated temperature for the device itself, or perhaps some shot noise due to subgap leakage of the tunnel junction. Above the gap voltage of the junction (not shown), the noise temperature increases linearly with bias voltage (or current), and the slope of this line is approximately 1.5-2 K per mV of bias voltage. This is as expected for our devices from shot noise. Recalling that the junction has been shunted with a normal resistor such that its resistance is reduced, the circuit at high voltages should be a normal resistor with Johnson noise (not bias-dependent) in parallel with a shot-noise-producing tunnel junction. Therefore the noise should rise linearly with voltage, but with a slope reduced from the full shot-noise value* of 5.8 K/mV by the same factor of three to five as the resistance has been reduced. Both the observed noise floor and the behavior above the gap confirm that the calibration and measurement procedure are accurate to within the expected systematic uncertainties.

There is also a large noise spike, either positive or negative, located exactly at zero bias voltage. In all cases, the noise at zero bias is consistent with the contribution of the IF system

* The "effective shot noise temperature" is actually given by taking the current power spectral density for pure shot noise, $S_I = 2eI$, and comparing with the current spectral density for thermal noise, $S_I(\text{Johnson}) = 4k_b T/R$, giving a noise temperature, $T_{\text{shot}} = 2eI R / 4k_b$. For a tunnel junction with no significant excess current in the linear region above the gap, however, I times R is just the bias voltage, so that T_{shot} becomes $eV/2k_b$, or 5.8 K/mV.

alone. However, the coupling of the junction also vanishes (by definition) at this point, where the dynamic resistance is zero, so that the available power at this point is undefined. This divergence can be ignored and is not of consequence for any of the discussions below. Finally, one notices a substantial asymmetry of approximately 10 percent in the maximum noise value attained by the junction at equivalent positive and negative bias voltages. This asymmetry is orders of magnitude larger than the *statistical* errors in the measurement, and is reproducible and not dependent on the direction in which the voltage is swept. However, the sign of the asymmetry (i.e. whether the higher peak is at positive or negative voltage) can easily be reversed by changing the direction of the externally applied magnetic field. This effect must therefore be a self-field effect due to the addition of the external field with the field caused by the current through the junction or shunt resistor. The current-voltage characteristics between the two states also show small related asymmetries.

The most important feature seen in the plots are the smooth maxima in output noise temperature seen at both positive and negative voltages. These peaks occur at voltages where the device is strongly nonlinear (i.e. V less than about $I_C R_N$), and are due to noise which is converted downwards in frequency due to the Josephson effect, and also to power from the tails of the AC Josephson oscillations which can appear at the IF frequency. A theoretical curve which is obtained from the RSJ model with thermal noise, using the parameters determined from the best fit to the I-V curve, is shown for comparison. It compares relatively well with the observed behavior, showing roughly the correct magnitude for the noise and the reproducing the dependence on bias voltage. Some of the sharp ripples in the experimental data are not expected, and these are related to small ripples in the I-V curve which are not present in the RSJ model.

Another similar set of curves, in which the magnetic field and the critical current suppression are minimal, are displayed in Figure 6. Here the junction noise temperature attains much larger values before settling to the same thermal noise floor. In addition, the noise shows

departures from the smooth, single maximum on either side of zero voltage which is always predicted by the RSJ model. The features in the noise again seem to be correlated with voltage where there are resonances and variations in the dynamic resistance of the junction, as seen in the current-voltage characteristic. Similar features are seen in the IF reflection coefficient of the junction, but the noise temperatures have been corrected for this variation. There must therefore be a variation in the output noise. In addition, the RSJ model predicts a maximum output noise of only about 10 times the physical temperature, or about 50 K, for realistic parameter values corresponding to this junction. The observed noise is therefore seen to be a factor of five to ten times higher than expected, which is roughly consistent with the conclusions drawn from the heterodyne measurements of these devices. While the details of the shape of the curve depend on the junction parameters, this type of behavior, i.e. large noise and strong, non-RSJ variations with bias voltage, have been observed in several devices and both superconducting materials systems investigated.

The four superposed curves in Figure 6 are taken with the same NbN junction on subsequent cooldowns. In between cooldowns, the choke structure for the waveguide system which is deposited along with the junction onto the quartz substrate was trimmed away. This choke structure consists of an alternating series of microstrip sections which are approximately a quarter-wavelength at 100 GHz, and serve to couple the device to the waveguide. Most of the first section remained in order to provide a location to contact the junction. Comparison of the I-V curves (although there are slightly different amounts of trapped magnetic flux in the two cases) show that the strong resonance at about 0.4 mV has been weakened and moved to slightly higher voltage. Surprisingly, the shape of the junction noise temperature has also been altered, and the distinctive double-humped shape could not be reproduced for any applied magnetic field. Again we see that the shape of the I-V curve, the presence of resonances, and the low-frequency output noise of the device can be strongly influenced by the RF impedance presented to the junction at fairly high

frequencies. This dependence must be due to the nonlinear interaction of the junction and its embedding circuit.

VI. Discussion and Conclusions

We have performed heterodyne measurements using shunted tunnel junctions at 100 GHz, which show fairly good performance, but suggest that several non-ideal effects, including weak saturation and possible single-sideband operation are present. There is also a strong dependence of receiver performance and dynamic resistance on the RF embedding impedance. Most importantly, however, these heterodyne measurements indicate that the receiver performance is probably degraded because of elevated output noise from the devices. While the RSJ model predicts that the junction noise should be a factor of five to ten above the thermal noise limit (i.e. T_N for the junction is several times T_{Physical}), we observe noise levels under some conditions which are higher than the RSJ predictions by another factor of about five.

Accurate measurements of the junction output noise at the intermediate frequency of 1.5 GHz have been performed to verify this hypothesis. The output noise of the junctions, even without local oscillator power applied, are observed to attain values higher than predicted from the RSJ model, and also show a complicated behavior with bias voltage which can not be reproduced without inclusion of the external circuit into the nonlinear modeling of the RSJ circuit. Surprisingly, we have shown that the low-frequency (1 GHz) output noise, and its voltage dependence, can be radically altered simply by changing the high frequency (100 GHz) impedance presented to the junction. Inspection of the I-V curves shows that the peaks in junction noise temperature are correlated with regions of high dynamic resistance, where the Josephson oscillation linewidth, and hence the “excess” noise, according to our picture for its generation¹, might be expected to be at a maximum.

It remains somewhat unclear what the implications are for the development of low-noise Josephson-effect mixers. Elevated output noise, if only a factor of five to ten times the physical

temperature, would not preclude interestingly low mixer temperatures, particularly at the higher frequencies where SIS mixers are not yet available. However, our measurements show that the noise can be sensitive to the RF design of the mixer and to unanticipated resonances at high frequencies. Antenna-coupled mixer designs which are able to present a well-behaved, real impedance over a wide frequency range (e.g. self-similar structures such as log-periodic spirals¹³) should probably be used in the future.

Acknowledgments

We would like to thank J. Stern and R. LeDuc for the kind use of the facilities and their assistance in fabrication of the junctions used in these measurements, N. Dubash, R. McGrath, and T. Kerr for helping to find suppliers of microwave equipment suitable for low temperatures, J. Kooi and P. Schaffer for assistance with design and fabrication of the cryostat, and G. Ugras, E. Grossman, and T. Groesbeck for helpful discussions. This research was supported by NASA grant NAGW-107, and BMDO. R. Schoelkopf would like to acknowledge support from a NASA Graduate Student Researcher Fellowship.

References

- [1] R.J. Schoelkopf, J. Zmuidzinas, and T.G. Phillips, in preparation.
- [2] P.A. Rosenthal, E.N. Grossman, R.H. Ono, and L.R. Vale, *Appl. Phys. Lett.*, **63**, pp. 1984-1986, 1993; P.A. Rosenthal and E.N. Grossman, *IEEE Trans. on Microwave Theory*, in press.
- [3] R.J. Schoelkopf, T.G. Phillips, and J. Zmuidzinas, *IEEE Trans. on Applied Superconductivity*, **3**, pp. 2250-2253, 1993.
- [4] H.G. LeDuc et al., "Submicron area Nb/AlO_x/Nb Tunnel Junctions," in *Proceedings of the 3rd Intl. Symposium on Space Terahertz Technology*, Ann Arbor, MI, March 1992; J.A. Stern, H.G. LeDuc, and A.J. Judas, "Fabrication and Characterization of High Current-Density, Submicron NbN/MgO/NbN Tunnel Junctions," *ibid.*
- [5] L. D'Addario, *Intl. J. of IR and MM Waves*, **5**, pp. 1419-1442, 1984; and D. Woody, private communication.
- [6] Y. Taur, *IEEE Trans. on Electronic Devices*, **ED-27**, pp. 1921-1928, 1980.
- [7] SPDT latching coaxial switch, part #909C70200, Daytron/Transco, Simi Valley, CA.
- [8] W.R. McGrath, A.V. Raisanen, and P.L. Richards, *Int. J. of IR and MM Waves*, **7**, pp. 543-553, 1986.
- [9] Pamtech 1.25-1.75 GHz isolator, Pamtech, Inc., Canoga Park, CA.
- [10] Directional coupler, model DCS-305, Technical Research and Manufacturing, Inc., Bedford, NH.
- [11] N.B. Dubash, G. Pance, and M.J. Wengler, "Photon Noise in the SIS Detector," *Proceedings of the 4th Intl. Symposium on Space Terahertz Technology*, Los Angeles, CA, April, 1993.
- [12] Diode temperature sensor model DT-500, Lake Shore Cryotronics Inc., Westerville, OH.
- [13] T.H. Buettgenbach et al., *IEEE Trans. on Microwave Theory and Techniques*, **36**, pp. 1720-1726, 1988.

List of Figures

Figure 1: Shows receiver response to hot/cold absorbers at input. Solid curve is I-V curve under 102 GHz LO radiation, dashed curve is IF output power (in arbitrary units) when receiver views a room temperature load, dotted curve is power when viewing an IN_2 soaked absorber. Horizontal axis is junction bias voltage in mV. Only the positive half of the symmetric I-V curve is shown.

Figure 2: Displays several I-V curves of the same junction obtained under illumination with 98 GHz local oscillator power. The different curves and the dramatically different dynamic resistances between photon steps is a result of the different positions used for the mechanical waveguide tuners. Different amounts of LO power have been used to render approximately the same degree of critical current suppression. The full line probably corresponds to an inductive driving impedance, the dashed line to a capacitive drive, and the dotted line to a real drive impedance.

Figure 3: A block diagram schematic of the apparatus used for noise measurements. Junction is connected to a coaxial switch, through a bi-directional coupler and two isolators. Coupler allows calibration of junction reflection coefficient, and switch enables a variable-temperature termination to be connected to the IF input for calibration of system gain and noise.

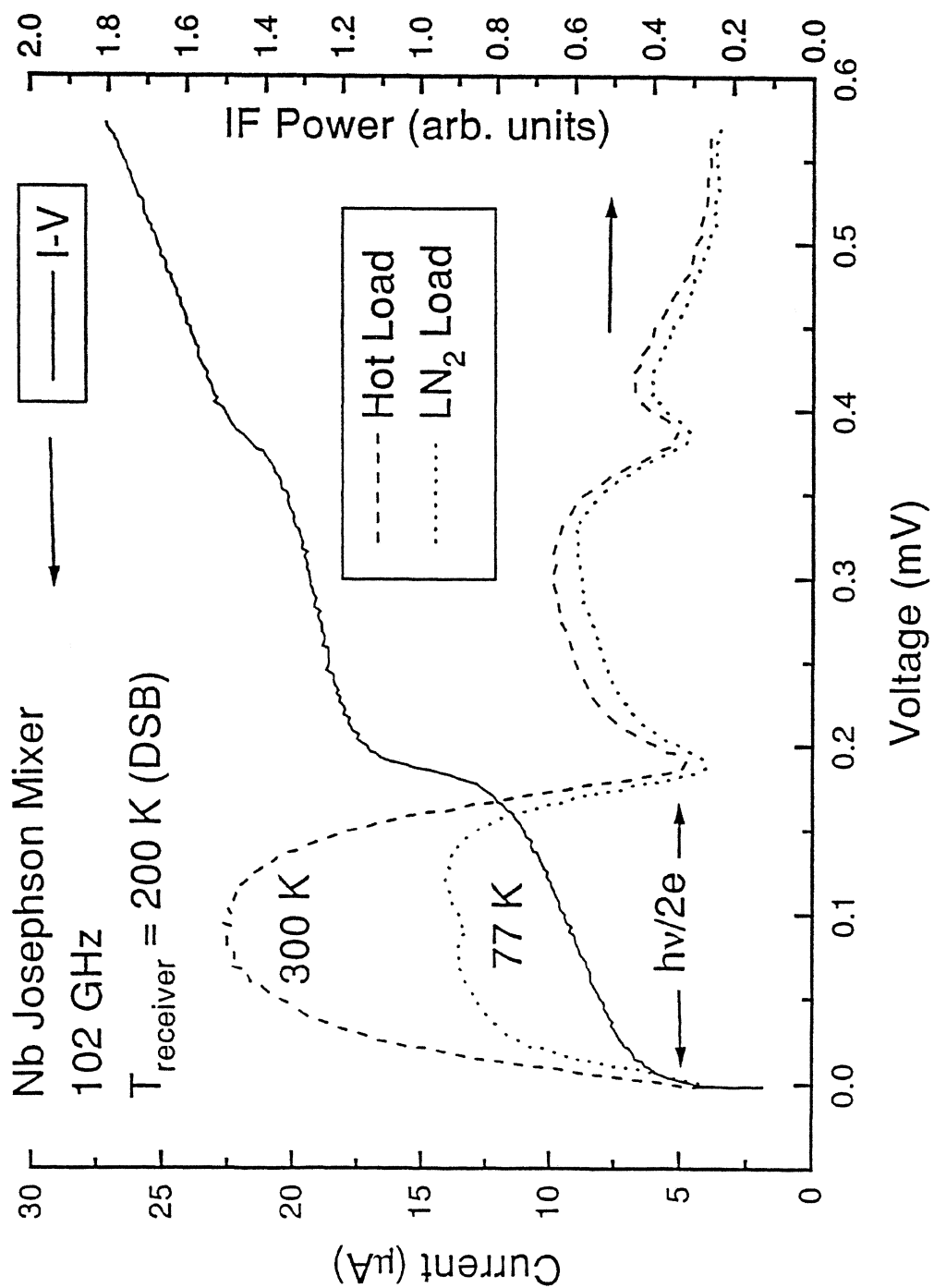
Figure 4: A typical IF calibration using variable-temperature load. Horizontal axis shows measured load temperature, and output power in arbitrary units, corresponding to the voltage on total power detector, is displayed on vertical axis. Data points are shown along with best-fit linear regression to data and parameters corresponding to fit. Statistical errors for fit

shown are determined by equally weighting all points and assuming that the deviations from linear fit represent the uncertainties. Fits are dominated by systematic errors (not shown).

Figure 5: Measured junction noise temperature and value calculated from RSJ model are displayed as a function of bias voltage. The parameters for the RSJ simulation have been derived from fitting the DC I-V curve, and assuming only thermal noise at 4.2 K is input into model. An external magnetic field has been applied to suppress the critical current to about one-fifth its usual value. The DC supercurrent occurs at zero voltage, in the center of the horizontal axis. This data shows behavior similar to the RSJ model predictions, and approaches a value consistent with thermal noise at voltages above about 0.5 mV.

Figure 6: Shows the effect of removing the RF choke from an NbN junction. Left axis is current, and the full and dash-dotted curves show the I-V curves on subsequent cooldowns; full line is with the choke, dash-dotted is without choke. A slight variation in the amount of external magnetic field is responsible for the discrepancy in critical current. The removal of the choke has weakened the resonance visible at about 0.3 mV, and displaced it slightly. Right axis displays the junction effective noise temperature (in K); the spikes at zero voltage (see text) have been removed for clarity. Full line is with choke present, dotted line is after choke removal. Notice the change in the maximum value attained by the noise, and the qualitative change in the shape (i.e. largest and second-largest peak change location).

Figure 1: Receiver Response



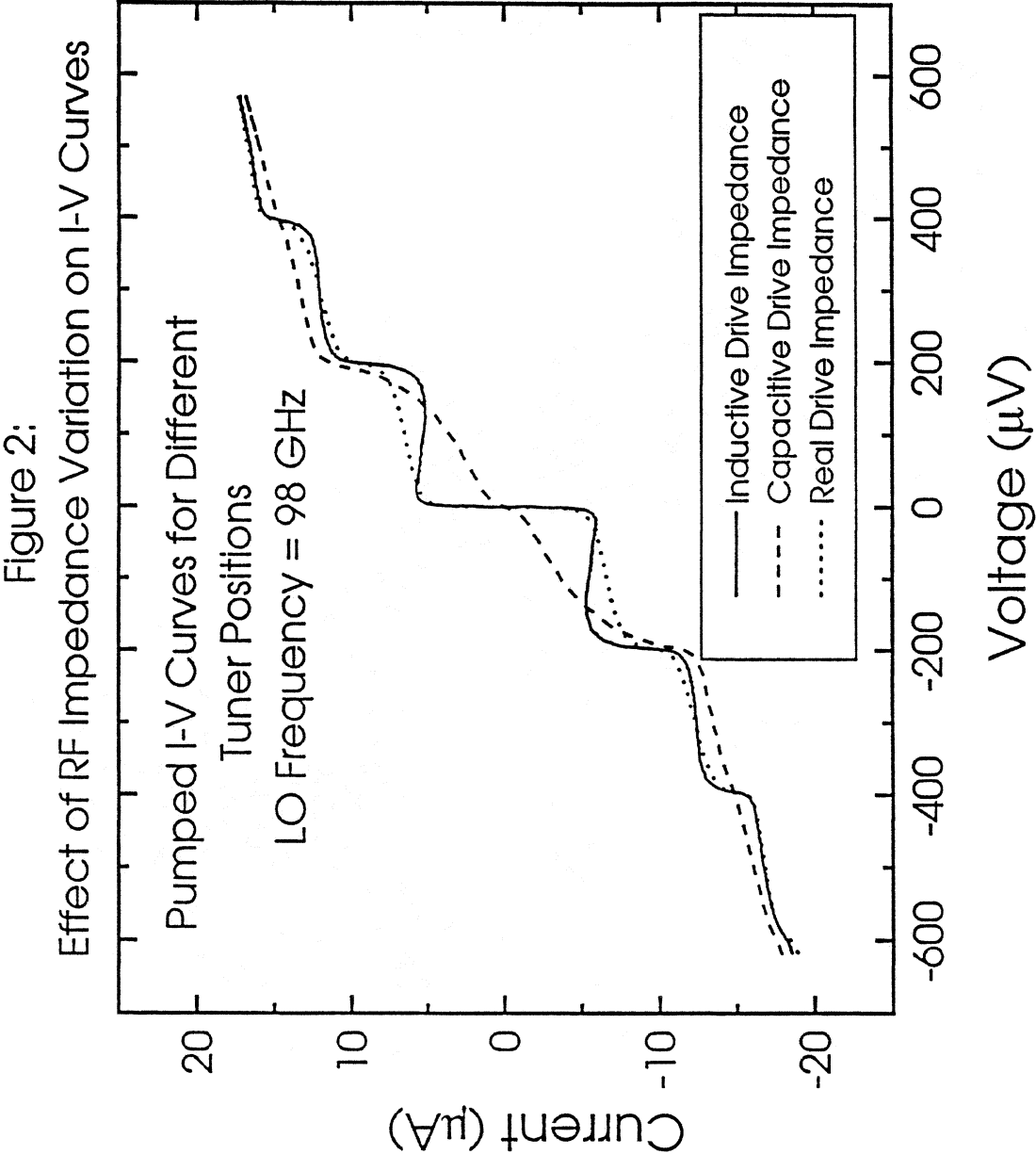


Figure 3: Noise Measurement Apparatus

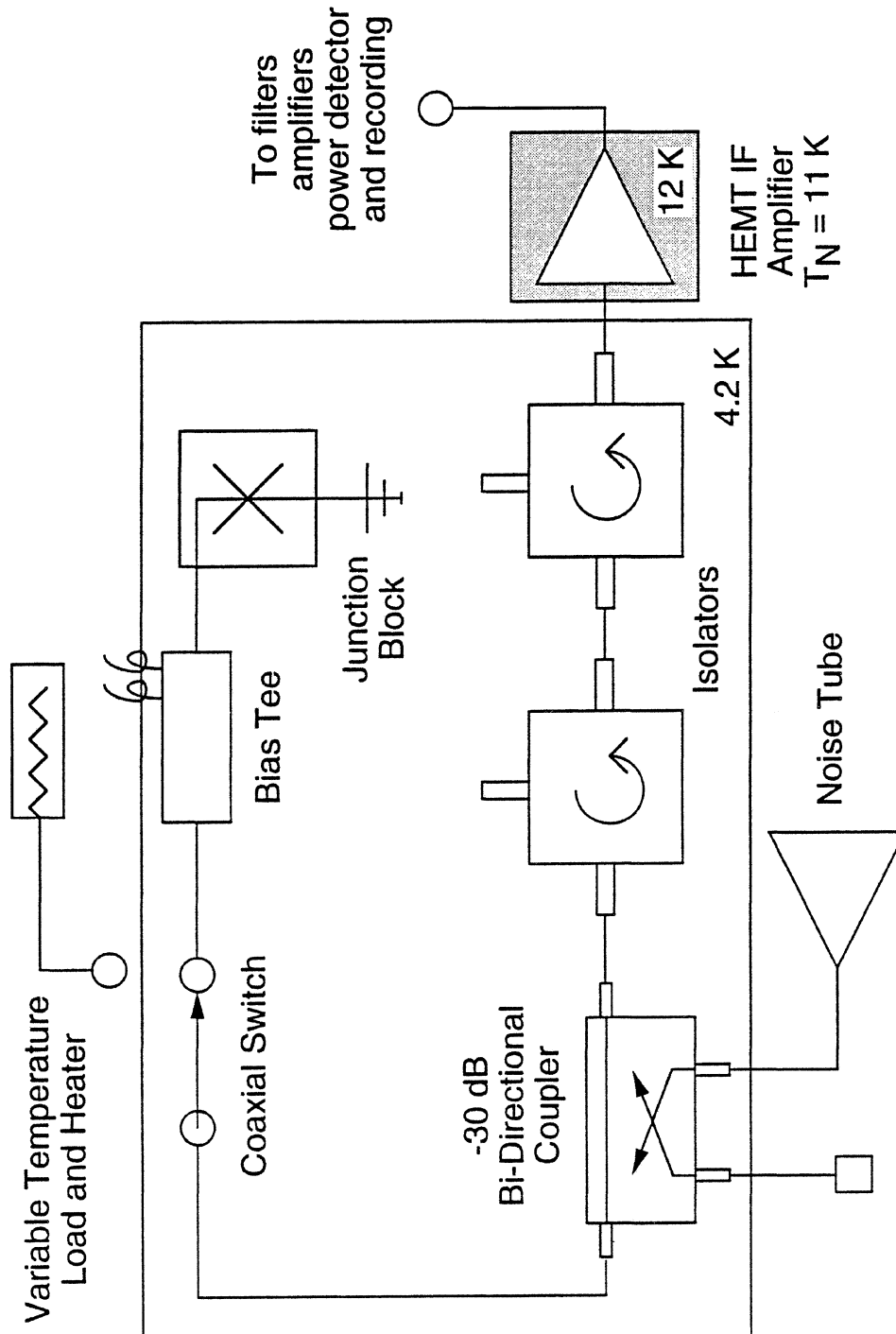


Figure 4: IF System Calibration

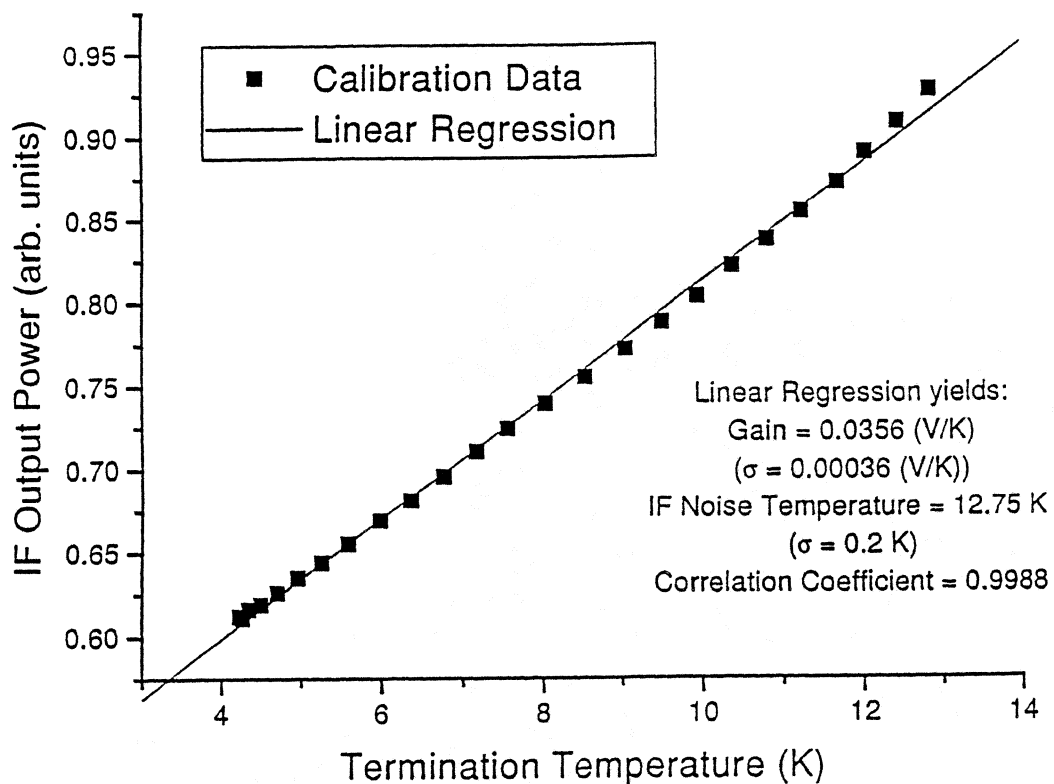


Figure 5: Measured and Predicted Noise

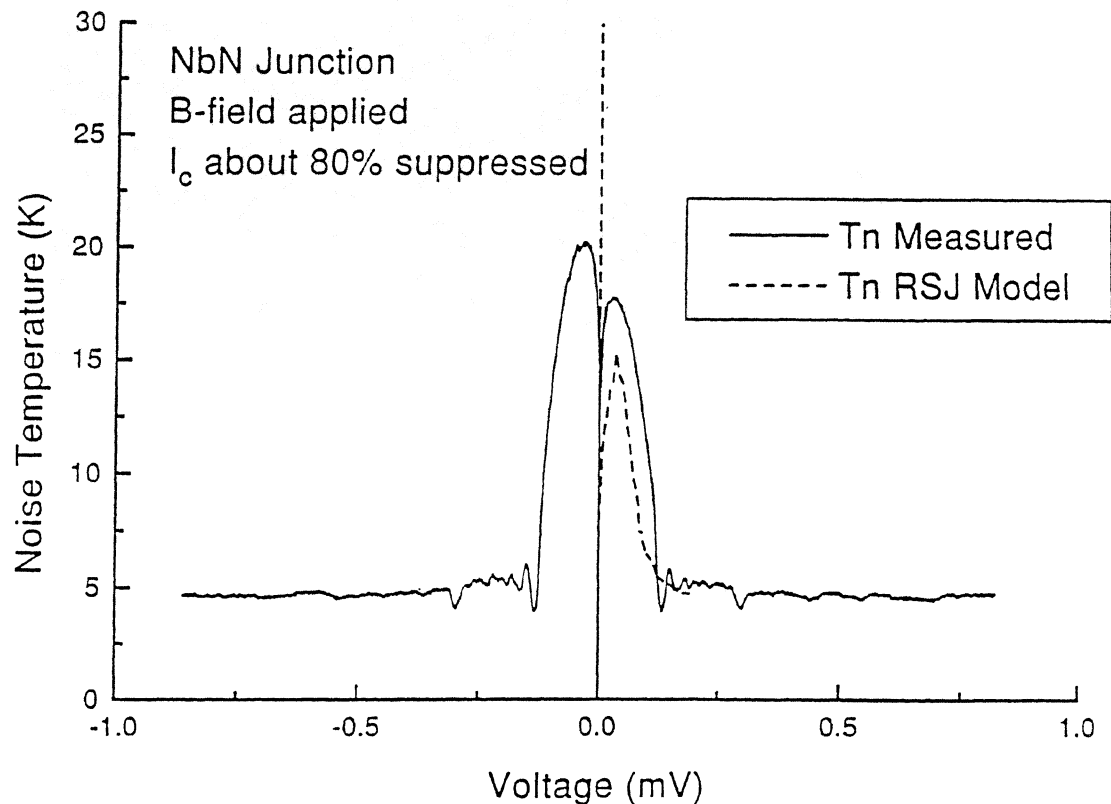
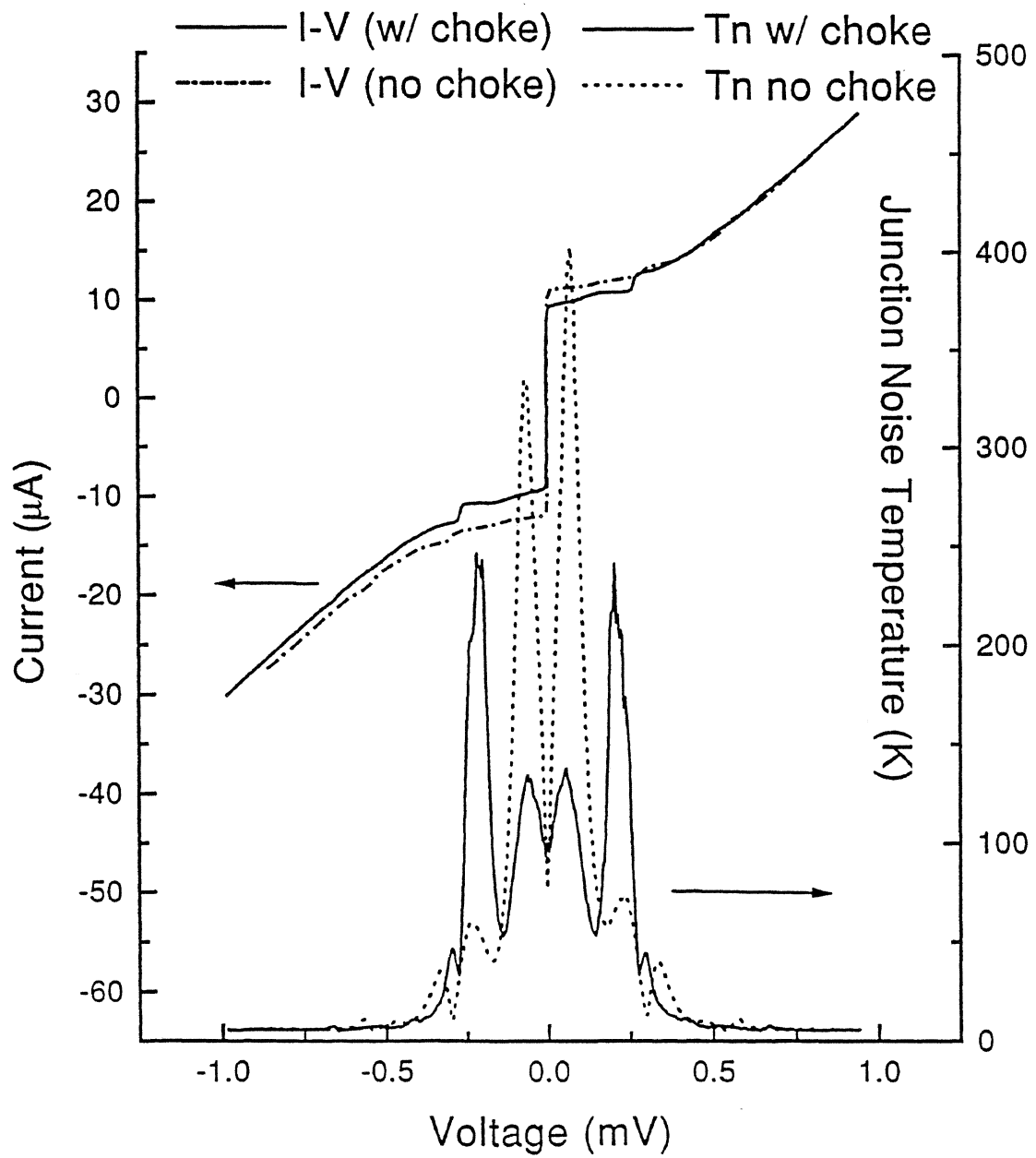


Figure 6: Effect of RF Impedance on Noise



High Power Impulse Generation Using Lateral Stacked Nonlinear Transmission Lines

H. Shi^{*}, C. W. Domier^{**}, and N. C. Luhmann, Jr.^{**}

Abstract

Our modeling studies predict that a nonlinear transmission line employing heterojunction stacked barrier devices and a novel lateral stacking configuration can produce impulses with up to 45 V pulse amplitude (equivalent to 20 W for a 50 Ω line) with 8.5 ps FWHM pulse duration. Two 45-section tapered coplanar wave guide lines have been designed and are currently being fabricated for proof-of-principle experiments.

High Power Impulse Generation Using Lateral Stacked Nonlinear Transmission Lines

H. Shi^{*}, C. W. Domier^{**}, and N. C. Luhmann, Jr.^{**}

I. Introduction

In work reported by other researchers, it has been experimentally demonstrated that pulses with picosecond duration and ~ 12 V peak value can be obtained on a nonlinear transmission line (NLTL) utilizing Schottky varactors as the nonlinear element [1]. More recent theoretical studies by our group predict that the use of heterojunction stacked barrier devices [2] such as the Multi-Quantum Barrier Varactor (MQBV) and the Schottky Superlattice Quantum Barrier Varactor (SSQBV) can significantly improve the performance of an NLTL [3], especially the voltage level. However, the increase in leakage current at large signal levels for these GaAs quantum barrier devices (due to the low barrier height) makes it difficult to improve the signal level beyond ≈ 20 V for a total of six barriers [4]. It is possible to further increase the signal level by using InP based material which has a higher barrier height, or by increasing the number of barrier. But they increase fabrication difficulty as well. On the other hand, the symmetric C-V characteristics of these new devices, naturally fit a back-to-back layout configuration [5], make it possible to lateral, rather than vertical as mentioned above, stacking devices to further improve the signal level. This lateral stacking configuration can double or triple the voltage handling capability of the device. The degree of the multiplication depends upon the final signal pulse width required.

II. Design of lateral stacked NLTLs and simulation results

In applications such as wide band radar, magnetic fusion plasma diagnostics and current sources for diode lasers, picosecond duration pulses with amplitudes of tens, or even hundreds of, volts, are required. The lateral stacking design can double or triple the signal amplitude, depending upon the level of lateral stacking introduced. However, as the stacking number, M , increases, the required device layout area increases by a factor of M^2 which introduces parasitic capacitance, C_p .

Therefore, the effective minimum device capacitance in the line with lateral stacking structure is $C_{min} + C_p$, where C_{min} is the device minimum capacitance without the line effect. Since the device cutoff frequency,

$$f_d = \frac{1}{2\pi C_{min}} \left(\frac{1}{C_{min}} - \frac{1}{C_{max}} \right),$$

is inversely proportional to $C_{min,eff}$, f_d is degraded by approximately a factor of $(1 + C_p/C_{min})$. For a pulse generating NLTL, the highest Bragg cutoff frequency, f_B , that can be designed is three to five times smaller than f_d . Therefore, the highest value of f_B is reduced by approximately a factor of $(1 + C_p/C_{min})$ as well. Since the final pulse width is inversely proportional to f_B , the narrowest pulse which can be obtained on a line with the lateral stacking structure is increased by approximately a factor of $(1 + C_p/C_{min})$. For $M=2$ and a line with $f_B=120$ GHz, following the NLTL design procedures in [6], the required device layout area can be found. Assuming that an interdigitated configuration, as shown in Fig. 1, is utilized in the device layout, C_p is computed. In this case, $C_p/C_{min}=0.45$ and the final pulse width is increased from 8.4 ps to 11.8 ps. This shows that for an NLTL with a final pulse duration of > 8.5 ps, we can laterally stack up to a factor of two without introducing significant parasitics.

Two 45-section tapered lines utilizing SSQBV's and lateral stacking of two devices have been designed and are currently being fabricated for proof-of-principle experiments. Coplanar waveguide is chosen to suit the test system described in Sec. III. Figure 1 shows the layout of a single section of the lines. The unloaded line impedance is 90Ω and the loaded line impedance is 50Ω to match the instrumental impedances. A tapered structure is applied to these lines to obtain smooth pulse compression. From what we have achieved in making the ohmic contact in our previous multiplier array and Schottky diode image mixer array fabrications, the device cutoff frequency is assumed to be 1.6 THz, the line Bragg cutoff frequency is increased geometrically nine times, the relative increment is the same in each step, for every five sections from 20 GHz to 125 GHz for Line (1) and to 50 GHz for Line (2). For an input signal of 20 V amplitude and 50 -100 ps pulse duration, the predicted output is a pulse of 45 V amplitude and 8 ps pulse duration and 20 ps pulse duration for Line (1) and Line (2), respectively. Figure 2 shows the equivalent

circuit model used in the simulation. Figures 3 and 4 show the simulation results for Lines (1) and (2), respectively.

III. Test Arrangement

The test system involves the use of as input pulse with a 15-20 V amplitude and 50-100 ps duration. Here, a circuit was built which employs a step-recovery diode as the output device . The circuit can compress a slow input signal into a step-like signal with a fall time of approximately the diode cutoff time (≈ 50 -100 ps) and a amplitude of 50 V. Finally, the output is differentiated into a pulse with a duration of the diode cutoff time and a amplitude ≈ 15 -20 V. The rest of the testing system includes Cascade Microtech probe holders with WPH-405 probe heads (65 GHz) and a Tektronix 11802 digital sampling oscilloscope with 50 GHz sampling plug-in. The input and output signals will be brought onto and off the chip by cascade probes.

IV. Acknowledgment

We thank Tom McEwan and Greg Dallun of LLNL for giving us the ideal of the step-recovery diode circuit and many help in building the circuit. This work is supported by Department of Energy under contracts DE-FG03-86-ER53225 and W-7405-ENG-48, and the UCLA Joint Services Electronics Program under contract F49620-C-0055.

Reference

- [1] M. Case, E. Carman, R. Yu, and M.J.W. Rodwell, *Appl. Phys. Lett.*, vol. **60**, p. 3019-3021, 1992.
- [2] H-X.L. Liu, L.B. Sjogren, C.W. Domier, N.C. Luhmann, Jr., D.L. Sivco, A.Y. Cho, *IEEE Electron Device Letters*, vol. **14**, p. 329-331, 1993.
- [3] H. Shi, W-M Zhang, C.W. Domier, N.C. Luhmann, Jr., L.B. Sjogren, H-X. L. Liu, *Submitted to IEEE Transactions on Microwave Theory and Techniques*.
- [4] W-M Zhang and etc., *Fifth International Symposium on Space Terahertz Technology*,

May 10-12, 1994, Ann Arbor, MI

- [5] U. Lieneweg, B.R. Hancock, and J. Maserjian, 1987 *IEEE Twelfth International Conference on Infrared and Millimeter Waves*, p. 6-7, 1987.
- [6] Mark J.W. Rodwell, Ph.D Dissertation, Stanford University, 1988.

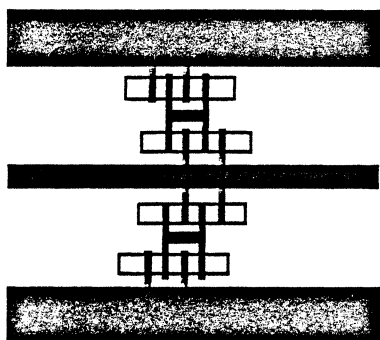


Figure 1. Layout for lateral stacking of two devices. Each solid rectangle includes a pair of back-to-back connected SSQBV's.

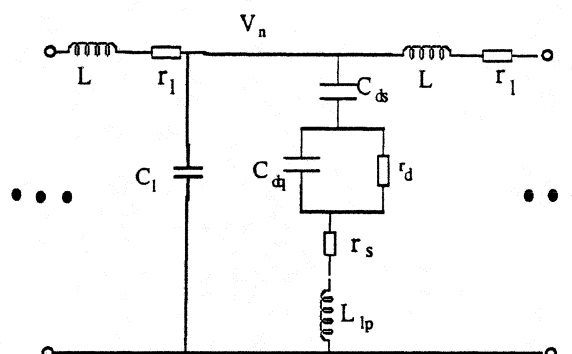


Figure 2. Equivalent circuit model employed in simulations.

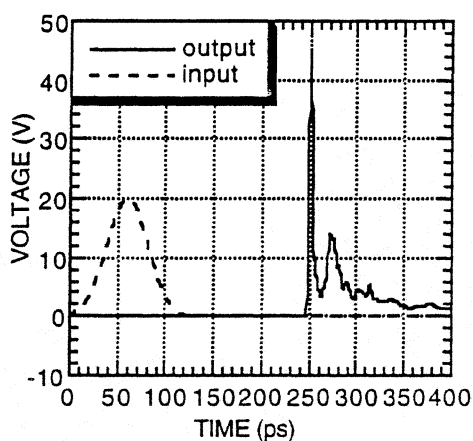


Figure 3. Simulation result for the input and output waveforms on Line (1).

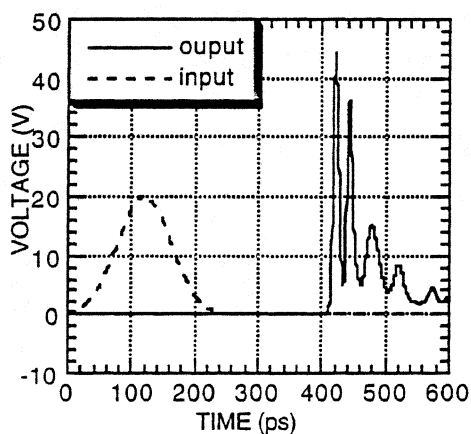


Figure 4. Simulation result for the input and output waveforms on Line (2).

Millimeter-Wave On-Wafer Waveform and Network Measurements Using Active Probes

Ruai Y. Yu^{*}, Madhukar Reddy, Joe Pusi^{**}, Scott T. Allen, Michael Case^{***},
and Mark J. W. Rodwell

Department of Electrical and Computer Engineering
University of California, Santa Barbara, CA 93106

I. Introduction

Recent advancement in III-V technology has led to significant improvements in transistor and monolithic millimeter-wave integrated circuit (MMIC) bandwidths [1,2]. Due to the lack of high frequency instrumentation, reports of transistors with high f_{\max} (400-500 GHz) are based on extrapolation of measurements below 120 GHz. More importantly, circuit design of MMICs demands accurate transistor and passive element models which cannot be determined with great confidence from extrapolation of measurements made at lower frequencies.

We have developed nonlinear transmission line (NLTL) [3] pulse generators with transition times more than a factor of 30 shorter than the SRDs [4]. The pulse trains generated by NLTLs have significant spectral content to sub-millimeter-wave frequencies and can serve as convenient signal sources for network measurements. Using NLTLs as strobe pulse generators, sampling circuits with mm-wave bandwidths have been realized [3-6]. Combining the mm-wave NLTL signal sources and sampling circuits, integrated circuits for network analysis have been fabricated [6,7]. Active probes incorporating the network analyzer integrated circuits (NWA ICs) and low loss probe tips permit signal delivery to and signal detection from devices under test (DUTs) at mm-wave frequencies, and can be used conveniently for both waveform and network measurements.

II. Base technology: NLTLs and NLTL-gated sampling circuits

The NLTL and the NLTL-gated sampling circuits permit generation and detection of transient signals with 300 GHz bandwidth. Proper design of the NLTL and the sampling circuits is essential for high performance active probes.

^{*} Currently with Rockwell International Science Center, Thousand Oaks, CA.

^{**} Currently with Hughes Aircraft Company, Space and Communication Group, El Segundo, CA.

^{***} Currently with Hughes Aircraft Company, Hughes Research Laboratory, Malibu, CA.

2.1. The shock-wave nonlinear transmission line.

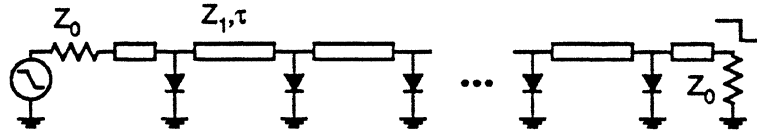
The NLTL is an electrical pulse (wavefront) compressor. The NLTL (Fig. 1(a)) is a high impedance transmission line periodically loaded by reverse-biased Schottky diodes acting as voltage-variable capacitors. The wave propagation velocity varies as the inverse square root of the total (diode plus transmission line) capacitance per unit length and hence increases as the diode reverse bias voltage is increased. For a negative-going step function (wavefront) input, the initial portions of the wavefront, near zero volts, propagate more slowly than the final, more negative, portions of the wavefront. The wavefront transition time (falltime) will progressively decrease with propagation distance. An asymptotic (minimum) compressed falltime is eventually reached at which the NLTL compression is balanced by various bandwidth limits in the structure. The two dominant bandwidth limits are the varactor diode cut-off frequency and the periodic-line (Bragg) cut-off frequency. The NLTLs employed in this work use hyperabrupt varactor diodes. Hyperabrupt varactors have larger capacitance variation than uniform-doped diodes, thereby increasing the NLTL compression rate, decreasing the required NLTL length and hence both the skin loss and the die area. When driven by a sinewave, the NLTL output is a sawtooth waveform with picosecond transition time. Its output therefore has a Fourier spectrum with power at high harmonics of its drive frequency.

2.2. The NLTL-gated sampling circuit

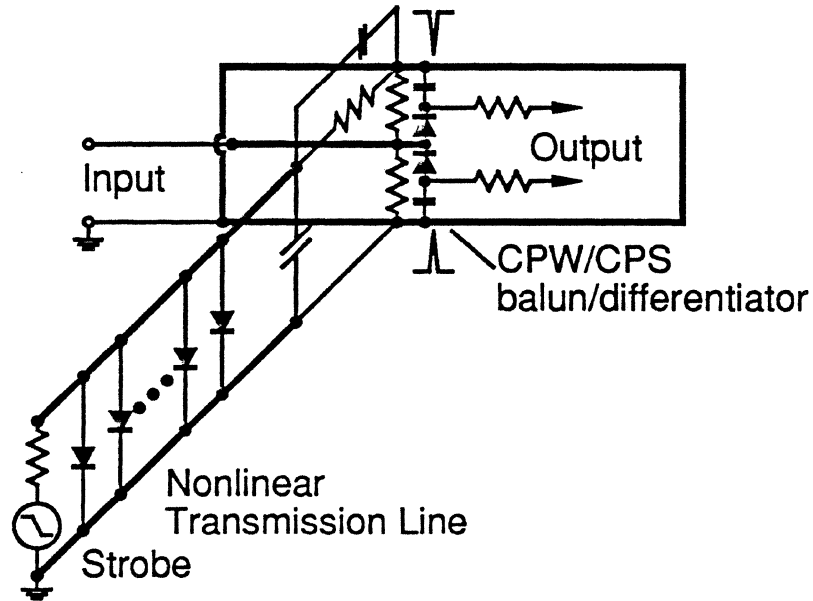
The active probe uses sampling circuits to downconvert in frequency the incident and reflected millimeter-wave signals. The sampling circuit (Fig. 1(b)) [5] consists of a strobe pulse generator, a diode/resistor bridge, and a balun/differentiator. An NLTL compresses an input strobe signal, either a step function or a ≈ 10 GHz sinewave, to picosecond falltimes. The sampling diodes are gated by a pair of symmetric positive and negative impulses generated from the strobe NLTL output using a balun/differentiator implemented using the coplanar strip (CPS) mode of the input signal coplanar waveguide (CPW). Coupled through series hold capacitors, the complementary strobe pulses drive the sampling diodes into forward conduction. During this period, the aperture time, the input (RF) signal partially charges the hold capacitors. If the RF frequency is then offset by Δf from a multiple nf_o of the strobe frequency f_o , the sampled (IF) signal is mapped out at repetition frequency Δf . The sampled signal can subsequently be measured by a digitizing oscilloscope. Sampling circuit bandwidth is limited by the sampling diode capacitance and by the duration of the strobe pulses.

To evaluate the NLTL and sampling circuit falltime, the output of an NLTL shock generator is connected to an on-wafer NLTL-gated sampling circuit. The convolved

(a)



(b)



(c)

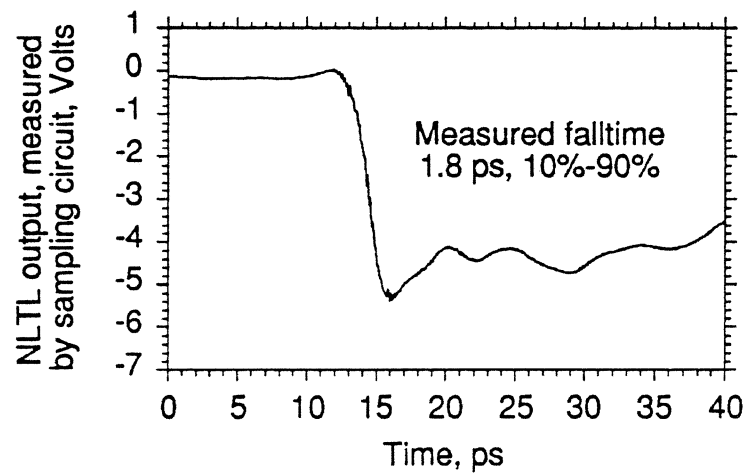


Figure 1: (a) NLTL circuit diagram, (b) circuit diagram of an NLTL-gated sampling circuit, and (c) NLTL output measured by an NLTL-gated sampling circuit, both using hyperabrupt diode technology.

responses of sampling circuit and NLTL shock-wave generator is thus measured. With an NLTL using 1.7 THz exponential hyperabrupt diodes (Fig. 1(c)), a 1.8 ps falltime is measured. From this, a 1.3 ps deconvolved NLTL falltime and a 275 GHz sampling circuit bandwidth are estimated; NLTLs and sampling circuits with approximately twice this bandwidth have been reported [4,8].

III. The active probes

In commercial sampling oscilloscopes and coaxial-based network analyzers, connections between the measurement apparatus and the DUTs are provided with coaxial cables and connectors. 110 GHz coaxial connectors were introduced in March 1993 with earlier connectors limited to 65 GHz. To obtain broadband measurements beyond this frequency, we have constructed active probes which place a mm-wave measurement IC in close proximity to the device under test (DUT). An NWA IC is mounted directly on a probe with its high-frequency test ports connected to a short low-loss coplanar waveguide (CPW) quartz probe tip, as shown in Fig. 2. The NWA IC and probe tip are connected by very short gold ribbon bonds. High-frequency signals (≈ 7 -200 GHz) propagate only on the probe tip connecting the NWA IC and the DUT. A signal routing substrate provides the signal paths for the 10-500 kHz IF signals and the 7-14 GHz NLTL drive signals. With proper probe tip design, an NLTL-based NWA IC, and low inductance ribbon bonds, the active probe can attain wider bandwidths than obtainable with instruments using coaxial connectors. Shakouri et. al. [8] has also reported an active probe for high speed on-wafer waveform measurements, as opposed to network measurements; in contrast, the work reported here focuses primarily on network (S-parameter) measurements.

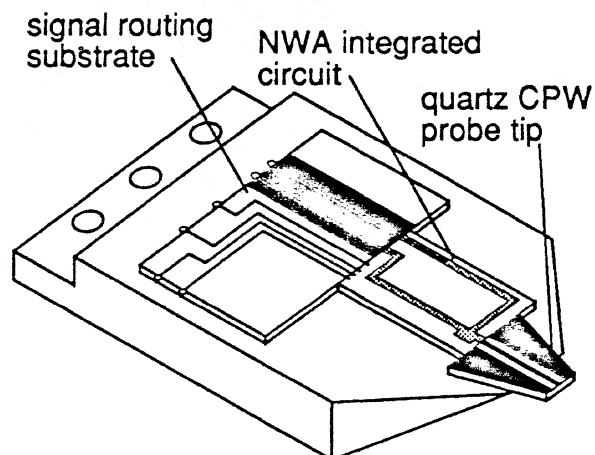


Figure 2: Active probe hybrid assembly.

3.1. Network analyzer integrated circuit design.

The network analyzer IC generates mm-wave stimulus signals and measures mm-wave incident and reflected waves. The NWA IC (Fig. 3) consists of a directional sampling circuit, two NLTLs, and a 25-dB attenuator. For network analysis, the active probes must be able to measure independently forward and reflected signals. Broadband coupled-line directional couplers are too large to incorporate within a monolithic IC. Instead, a 6-dB attenuator is used as the directional device. The directional sampling circuit consists of a pair of 2-diode sampling circuits measuring the input and output port voltages of a 6-dB attenuator placed between the stimulus signal generator and the device under test (DUT). The attenuators (25 dB and 6 dB) are chosen to keep both the sampling circuit and the device under test in their linear operating ranges. The peak to peak voltage at the input and output ports of the 6 dB attenuator are ≈ 280 mV and 140 mV, respectively; the sampling circuits have a linear dynamic range of $\approx \pm 500$ mV. The incident (V^+) and reflected (V^-) voltages can be extracted from the measured input (V_1) and output (V_2) port voltages of the 6-dB attenuator as:

$$V^+ = (1/3)(2V_1 - V_2)$$

$$\text{and,} \quad V^- = (2/3)(2V_2 - V_1)$$

We emphasize that the directional sampling circuit does not obtain independent measurements of the forward and reverse waves through time-separation of pulsed signals, as in a time-domain reflectometer. Errors associated with time-gating (uncorrected terms in source and load reflections, and time truncation of the long-duration impulse responses of narrowband resonators) are therefore avoided.

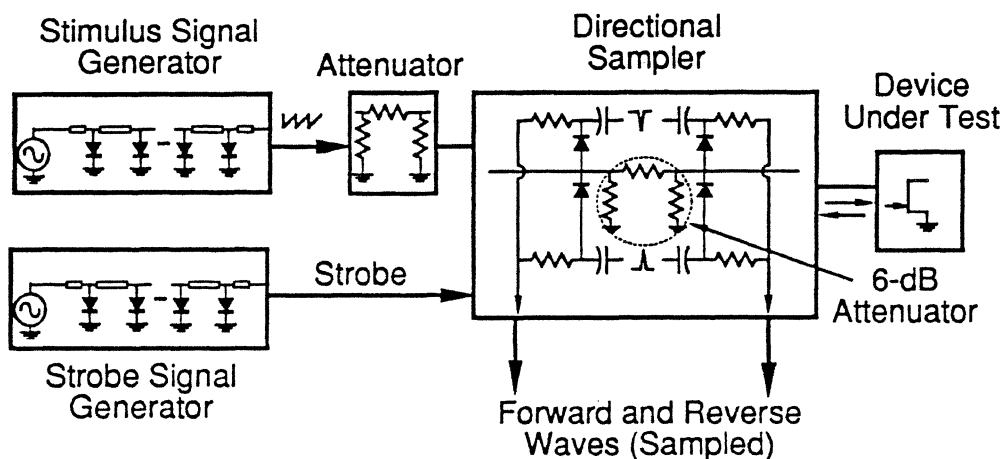


Figure 3: NWA IC block diagram.

In the integrated circuit, one NLTL generates the strobe pulses which operate the directional sampling circuit. A second NLTL generates a sawtooth waveform as the stimulus signal for network analysis. This sawtooth waveform has a 5 V amplitude and a ≈ 2 ps transition time, thus has Fourier components at harmonics of the NLTL drive frequency with the spectrum extending from the drive frequency to approximately 200 GHz. A 7-200 GHz frequency coverage is not readily obtained with the swept-frequency sources used in commercial network analyzers. The stimulus signal is attenuated by an attenuator to levels suitable for linear characterization of transistor circuits, and is passed through the directional sampling circuit to the DUT. IC fabrication is described in [7].

3.2. Probe tip design.

The CPW probe tip limits the probe bandwidth, hence its design is critical. Probe tips in commercial microwave wafer probes are long (≈ 1.5 cm) and are fabricated on alumina ($\epsilon_r=9.8$) substrate. Consequently, these have large attenuation above 65 GHz. Signal attenuation on the CPW probe tips arises from skin and radiation losses. For a given line impedance, skin loss is [9]:

$$\alpha_{skin} = \frac{\sqrt{\pi f \mu_0 / \sigma} \sqrt{(1 + \epsilon_r) / 2}}{4 \eta_0 d K(k) K(k') [1 - (w/d)^2]} \times \left\{ \frac{2d}{w} \left[\pi + \ln \left(\frac{4\pi w(1 - w/d)}{t(1 + w/d)} \right) \right] + 2 \left[\pi + \ln \left(\frac{4\pi d(1 - w/d)}{t(1 + w/d)} \right) \right] \right\}$$

where f is the frequency in Hz, ϵ_r the substrate dielectric constant, d the CPW ground-ground spacing, w the center conductor width, t the metal thickness, μ_0 the permeability of vacuum, σ the metal (gold) conductivity, $\eta_0=377 \Omega$ the free space impedance, $k = w/d$, $k'^2 = 1 - k^2$, and $K(k)$ the complete elliptic integral of first order. Radiation loss is [10]:

$$\alpha_{rad} = \left(\frac{\pi}{2} \right)^5 \frac{1}{\sqrt{2}} \frac{(1 - \epsilon_r)^2}{\sqrt{1 + \epsilon_r}} \frac{f^3 d^2}{c^3 K(k) K(k')}$$

where c is the speed of light. The total attenuation is then:

$$\alpha_{total} = \alpha_{skin} + \alpha_{rad}$$

Consequently, with appropriate scaling of line dimensions, CPWs on substrates with lower ϵ_r can attain lower attenuation. Further, for a given substrate, d can be chosen such that α_{total} is minimized at a particular frequency. Shown in Fig. 4 are the computed attenuation-frequency characteristics of CPW of different dimensions on alumina ($\epsilon_r=9.8$) and on

quartz ($\epsilon_r=3.8$) substrates. For the same d , CPWs on quartz substrates have lower attenuation due to smaller ϵ_r . For a given substrate (ϵ_r), CPWs with a larger d have smaller attenuation at lower frequencies and larger attenuation at higher frequencies, indicating that skin losses dominate at lower frequencies while radiation losses dominate at higher frequencies. At 200 GHz, $d=100\text{ }\mu\text{m}$ results in a minimum attenuation of 0.57 dB/mm on a quartz substrate. For the 2 mm-long quartz probe tips used in the current probes, the calculated round-trip attenuation is 2.3 dB at 200 GHz.

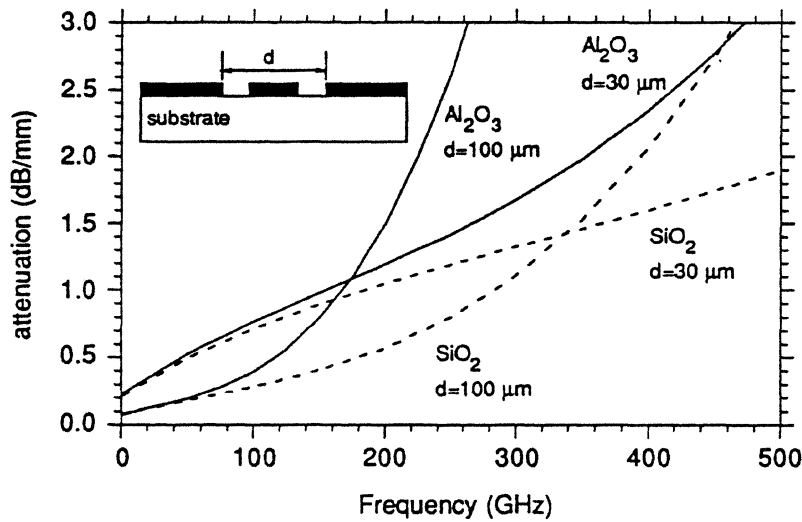


Figure 4: Computed total (skin plus radiation) losses for coplanar waveguide probe tips on quartz and alumina substrates.

To fabricate the probe tips, CPW lines are patterned on a quartz substrate with a lift-off of electron-beam evaporated $300\text{ }\text{\AA}$ Ti / $1\text{ }\mu\text{m}$ Au. A standard airbridge process is used to fabricate airbridges to connect the ground planes of the CPW, thereby suppressing the propagation of parasitic slotline modes [9]. $10\text{-}\mu\text{m}$ thick Ni is electro-plated at the contact points. The probe tips are sawed and angle-lapped so that the contact points are visible during probe placement.

3.3. Hybrid assembly and mechanical design.

The NWA IC is mounted adjacent to the probe tip on a gold-plated brass probe body. Gold ribbon bonds connect the NWA IC to the probe tip. To minimize the ribbon length and hence the bond wire inductance, the NWA IC substrate and the probe tip quartz

substrate have the same 20 mil thickness. The inductance of gold ribbon of thickness t , width w , and length l can be calculated as [11]:

$$L = 5.08 \times 10^{-3} l \left[\ln \left(\frac{l}{w+t} \right) + 1.19 + 0.22 \times \left(\frac{w+t}{l} \right) \right] \text{ nH/mil}$$

So for our $t \times w \times l = 0.25 \text{ mil} \times 2 \text{ mil} \times 4 \text{ mil}$ ribbons, $L = 40 \text{ pH}$. The circuit includes one bond in the center (signal) conductor and two parallel bonds for the ground connection, hence the total inductance of the ribbon bonds is 60 pH ($1.5 \times L$). The calculated 60 pH bond inductance was experimentally verified by using the NWA IC to measure the magnitude of the reflection from the wire bond. The ribbon connection limits the probe bandwidth to $100\Omega / (2\pi \cdot 60\text{pH}) = 265 \text{ GHz}$.

Because the probe tips are very short (2 mm), they do not flex when the probe is brought into contact with the DUT. Instead, the necessary mechanical flexure for reliable probe-DUT contacts is provided through elastic materials (i.e. a rubber joint) placed at the interface between the probe and its supporting arm.

3.4. Active probe bandwidth measurement.

When the active probes are used for waveform measurements, the bandwidth (BW) of the probes can be determined by falltime measurements with the probes measuring signals which have much smaller falltimes than that of the probes. In contrast, when the active probes are used for network measurements, the stimulus signal for the DUT is supplied through the probes, thus the probe falltime measurements should include the contribution from the probe's NLTL stimulus signal generator. Fig. 5 shows the step response of the active probes with the probes measuring an NLTL with a 0.7 ps falltime [4]. If the measured 2.7 ps is deconvolved from the 0.7 ps input signal falltime, a probe falltime of 2.6 ps is estimated, corresponding to a probe -3-dB bandwidth of 135 GHz for waveform measurements. To determine the uncorrected (pre-calibration) bandwidth of the active probe for network measurements, we measured the falltime of the reflection from an open circuit load with the active probe providing its own stimulus signal. The measured 3 ps reflection falltime, corresponding to an active probe -3-dB BW of 110 GHz for network measurements, includes the convolved contributions of the NLTL pulse generator falltime, the capacitance charging time of the two sampling circuits, the probe tip losses, and the inductance of bond wires connecting the probe tip to the NWA IC. As with conventional VNAs, measurements can be obtained significantly beyond the uncorrected -3-dB BW after calibration.

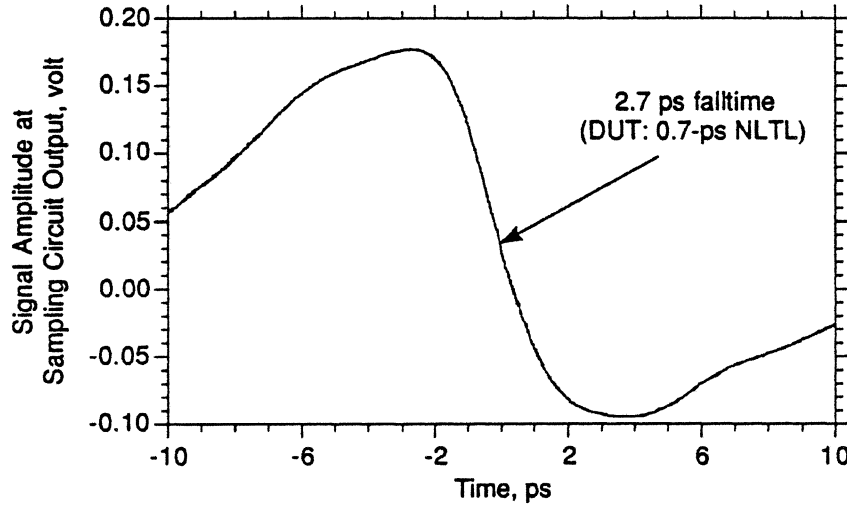


Figure 5: Step response of active probes for waveform measurement.

IV. Waveform measurements using active probes

For waveform measurements, the strobe NLTL on the probe is driven at f_o with a microwave frequency synthesizer, the input of the device under test is excited at $nf_o + \Delta f$, and the active probe measures the DUT output waveform. The DUT output waveform is downconverted by the NWA IC to an IF frequency Δf and measured with a low-frequency digitizing oscilloscope. In addition to the NLTL measurement above, we have also used the active probe to measure traveling-wave resonant tunnel diode (TWRTD) pulse generators [12]. The TWRTD pulse generator is excited at 40 GHz plus 1 kHz, and the active probe's strobe NLTL is driven at 10 GHz. A 3.5 ps, 400 mV transition is measured. If the 2.5 ps probe response time is deconvolved from the measured 3.5 ps transition time of the TWRTD pulse generator, a transition time of 2.5 ps is calculated.

V. Network measurements using active probes

Certain system level issues not as important for waveform measurements become critical for network measurements, and careful design and arrangement of the measurement system is essential for accurate and reproducible network analysis.

5.1. Measurement setup.

The setup of the network measurement using the active probes is shown in Fig. 6. A synthesizer provides the 7-14 GHz drive signal for the NLTL to generate the stimulus signal on the active probe. The drive signal is switched between the two active probes through a computer-controlled microwave switch to provide the stimulus signal to either port 1 or to port 2. A second synthesizer with the same phase reference provides the drive signals for the sampling circuit strobe NLTLs on the active probes. The active probes generate the 7-200 GHz stimulus signals for the DUT, and the response signals from the DUT, also in 7-200 GHz bandwidth, are downconverted by the active probes to 10-500 kHz IF signals. The IF signals first pass through buffering and summing circuits, then digitized with a digitizing oscilloscope and transferred to a workstation controller for data processing via a GPIB interface. Raw S-parameters are calculated from these measurements after Fourier transformation of the time waveforms. The corrected S-parameters of the DUT are obtained from a LRM calibration technique [13].

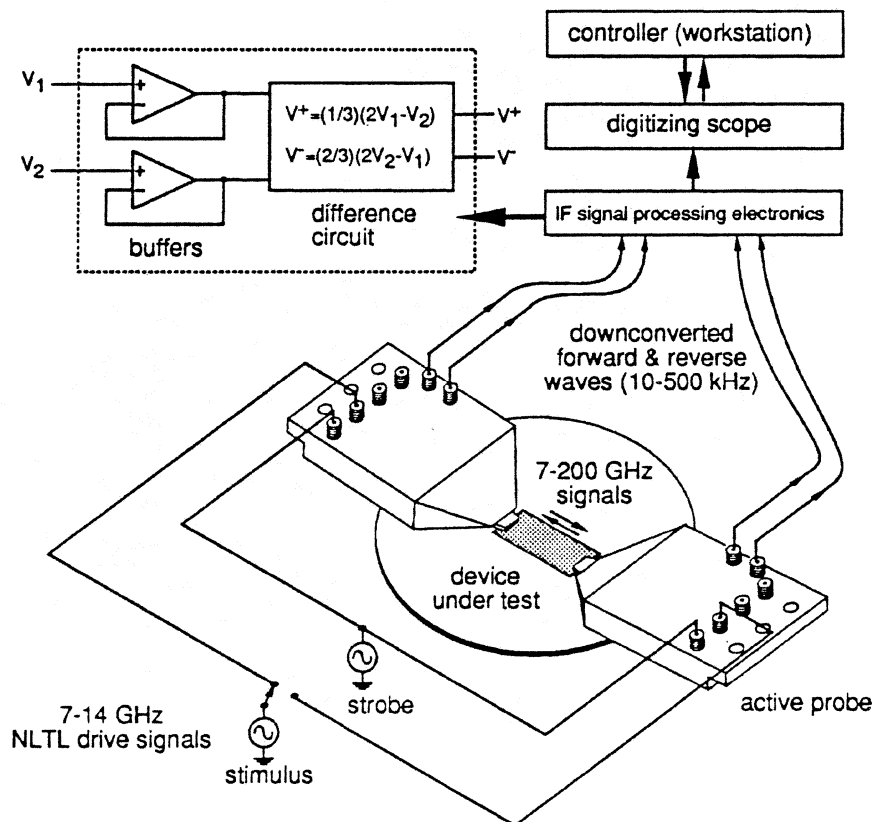


Figure 6: System setup for network analysis using active probes.

Since the active probes function correctly over a stimulus drive frequency range of 7-14 GHz, a complete octave in frequency, S-parameter measurements are possible over the entire frequency spectrum from 7-200 GHz. The LRM calibration was performed using the Cascade Microtech calibration standards consisting of a 1 ps through line, a 50 Ω match load, and a short circuit [14].

5.2. Measurement bandwidth, accuracy, and reproducibility.

As distinct from the -3 dB bandwidth of an electronic device or circuit, the bandwidth of a network analyzer is defined by the required accuracy and by the measurement reproducibility. There are five major limitations to the network measurement accuracy and reproducibility.

The first limitation arises from the two microwave synthesizers used to drive the NLTL strobe and stimulus signal generators on the active probes. Although the two synthesizers share a common 10 MHz frequency standard, they have significant relative phase fluctuations. These phase fluctuations produce phase noise sidebands about each harmonic of the RF fundamental frequency [15]. As illustrated in Fig. 7, sampling of the RF signals (at f_o and its harmonics) downconverts the RF signal spectrum (Fig. 7(a)) to much lower IF frequencies (Δf and its harmonics). Depending on the bandwidth of the phase noise sidebands and the IF fundamental frequency, significant overlap of phase noise sidebands can occur (Fig. 7(b)). Therefore, a given Fourier component of the RF signal is detected against a noise background set by the collective phase modulation sidebands of all other Fourier components. To reduce this effect, the IF fundamental frequency should be larger than the phase noise bandwidth (Fig. 7(c)). We have measured the synthesizer single-sideband phase noise spectral density in unit of dBc (1 Hz). We emphasize that the phase noise spectral density is the relative phase noise measured with the synthesizers operating from the same crystal oscillator fundamental frequency reference, which is the relevant quantity. The phase noise is significant (≈ -80 dBc per Hz) at frequencies close to the carrier frequency, and phase modulation due to power line harmonics contributes large phase noise components at 60 Hz and its first several harmonics. The phase noise spectrum decreases rapidly for $f > 10$ kHz (< -95 dBc per Hz), therefore IF frequencies Δf of > 10 kHz should be used. The mm-wave signal at nf_o is downconverted by the probe to an IF frequency $n\Delta f$, and $n\Delta f$ must therefore be less than the IF port bandwidth. The probe IF output impedance is high (≈ 100 k Ω) and the IF signal bandwidth is limited by capacitance of cables connecting the active probes to the digitizing oscilloscope. To obtain a > 500 kHz IF signal bandwidth (necessary for > 10 kHz IF fundamental frequencies), an

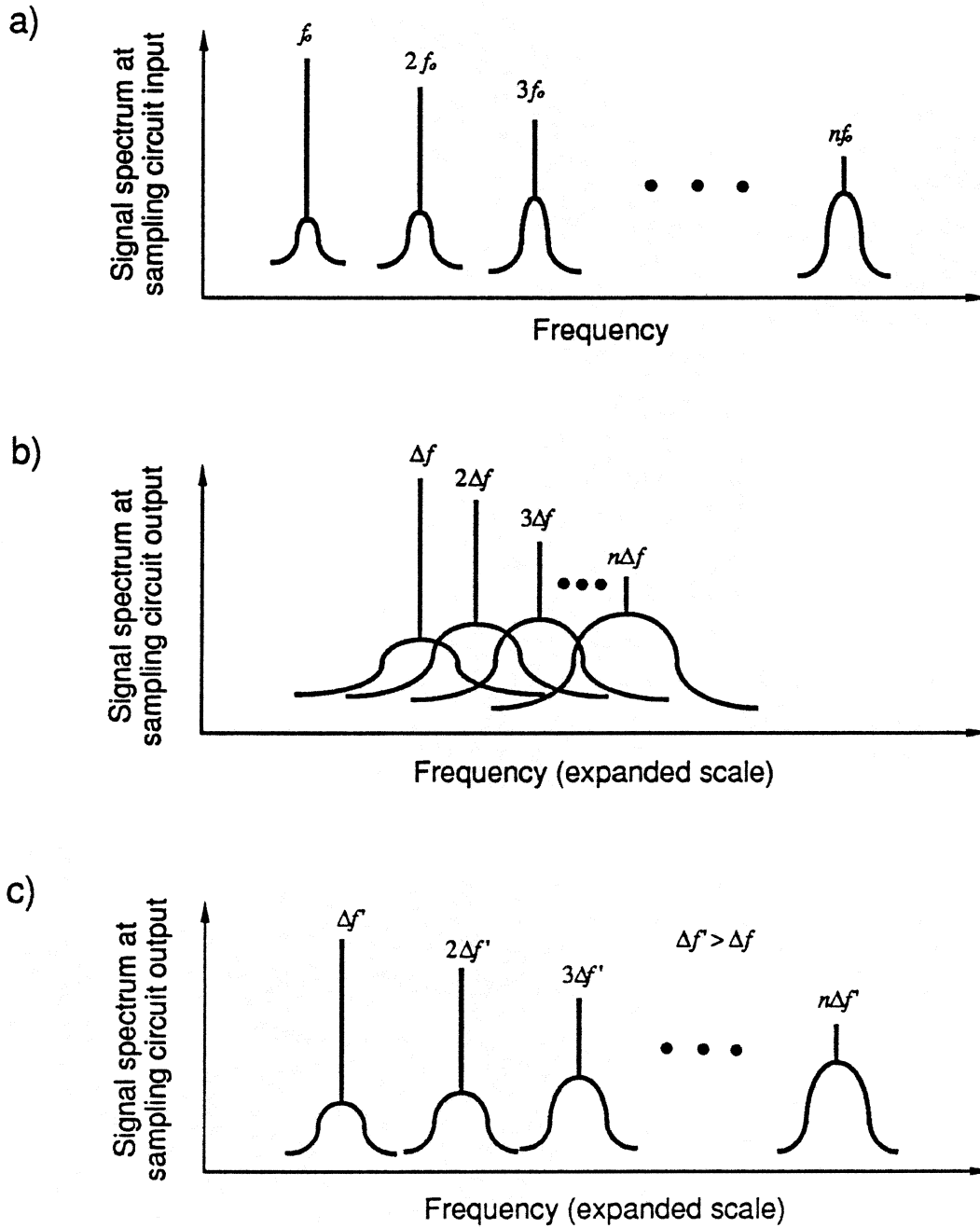


Figure 7: Phase noise sideband overlap due to downconversion of frequency spectrum by the sampling circuits: (a) spectrum at the input of the sampling circuit with RF fundamental frequency f_0 , (b) spectrum at the output of the sampling circuit with IF fundamental frequency Δf , and (c) spectrum at the output of the sampling circuit with IF fundamental frequency $\Delta f'$ where $\Delta f' > \Delta f$.

IF buffer circuit (Fig. 6) is mounted close to the active probe on the probe arm thereby reducing the interconnecting cable length (hence parasitic capacitance).

The second limitation arises from the 8-bit digitizing oscilloscope. During data acquisition, the IF waveform is digitized with 8-bit resolution. Since the stimulus (incident) time waveforms are approximately sawtooth waveforms, their spectral content decreases as $1/\pi n$ (normalized to the peak to peak amplitude of the time waveform), where n is the n^{th} harmonic of the fundamental frequency, hence the resolution for signal at higher frequencies are much less than 8-bit, severely limiting the accuracy, directivity, and dynamic range of the VNA at higher frequencies. For a waveform at 8 GHz fundamental drive frequency, for example, the signal amplitude at 200 GHz (25th harmonic) is $1/25\pi$, corresponding to a signal/quantization error ratio of 21 dB at 200 GHz. Because the NWA IC measures the sum of the incident and reflected signals, the quantization error becomes particularly severe when measuring reflections from DUTs with $\approx 50\ \Omega$ impedance where the small reflected signal is much smaller in magnitude than the large incident signal. To improve the system directivity, the approximate incident and reflected signals are obtained by a difference circuit (Fig. 6) before data acquisition by the digitizing oscilloscope. The sampling circuits also contribute noise to the network measurements. The measured noise figure of the sampling circuits is 65 dB [15]. Despite the high noise figure, the sampling circuit noise is negligible compared to the quantization error and phase noise.

The third limitation is due to the LRM calibration standards. In the LRM calibration technique, the transmission matrices of the 1 ps through line and the $50\ \Omega$ match load must be accurately defined while that of the reflect standard (with reflection coefficient of ≈ 1) needs only be known approximately. The 1 ps CPW through line is defined as a lossless, dispersionless transmission line, which is still a good approximation to 200 GHz. For higher frequencies, the non-ideality must be incorporated into the model for the 1 ps through line. The $50\ \Omega$ standard is modeled as a perfect $50\ \Omega$ in series with a variable inductor whose inductance depends on the amount of probe-standard overlap [16]. This model is not verified beyond 110 GHz. Use of offset calibration standards and offset DUTs results in similar probe to calibration standard/DUT launching characteristics and may improve calibration standard (hence measurement) accuracy [17].

The fourth limitation is due to crosstalk/isolation between the active probes. Currently, the NWA ICs and the probe tips on the active probes are exposed to air. When two probes are brought within 200 μm of each other, some degree of electromagnetic coupling is observed. The probe crosstalk cannot be eliminated by calibration because the magnitude of the coupling depends upon probe placement. Better shielding of the NWA ICs and probe tips should reduce this effect.

Finally, the network measurement bandwidth is ultimately limited by the active probe bandwidth as the mm-wave signals are attenuated beyond the -3 dB bandwidth of the active probe. The bandwidth limits of the active probes arise from the NWA ICs, the probe tips, and the interconnection between the ICs and the tips. The current NWA ICs use 275 GHz-bandwidth sampling circuits and 1.8 ps NLTLs. 515 GHz bandwidth sampling circuits and 0.68 ps NLTLs have been fabricated [4]; using these, the NWA IC bandwidth can be extended to at least 400 GHz. The bandwidth of the active probes would then be limited by the probe tips and the interconnection bandwidth, currently 260 GHz. Probe tip losses and bond inductances can be reduced through use of beam lead technology to mount NWA ICs close to probe tips, thereby minimizing both the CPW probe tip length and eliminating bond wire inductance.

We emphasize that the network measurement bandwidth is not the same as the -3 dB bandwidth of the active probes. Instead, the network measurement bandwidth is limited by the collective contribution of all the factors describe above.

5.3. Measurement results.

To verify the repeatability of the vector network analyzer (VNA), the VNA was calibrated and the 1-ps through line calibration standard was subsequently remeasured. The measured and calculated S-parameters are shown in Fig. 8. Two measurements were performed 30 minutes apart with the same calibration. As shown in Fig. 8(a), the reproducibility in transmission measurement is within ± 0.3 dB to 160 GHz, and degrade to ± 1 dB around 200 GHz; the phase repeatability, also shown in Fig. 8(a), is within 0.1 ps to 200 GHz; the return loss, shown in Fig. 8(b), is less than -30 dB to 160 GHz, and becomes -10 dB around 200 GHz. Measurements of the 50 Ω plus 7.5 pF calibration standard show only small deviations from the expected characteristics from 7 to 150 GHz, showing larger deviations between 150 GHz and 200 GHz because of the reduced system directivity, as is also apparent in the measurements of the 1-ps through line (Fig. 8). However, when the probes are raised (open circuit termination), the measured S-parameters (not shown) have as much as 1 dB error above 100 GHz. While measurement reproducibility is limited by phase noise, quantization errors, and probe crosstalk, measurement accuracy includes the effect of errors in the calibration standards. S-parameter measurements of the calibration standards themselves give good indications about system reproducibility (hence system phase noise, quantization errors, and probe coupling) regardless the correctness of the models for the calibration standards. Therefore, because less accurate measurements are obtained for an open circuit load than for the 1-ps

through line (a pre-defined standard), errors in the calibration standards themselves are currently the dominant source of measurement error.

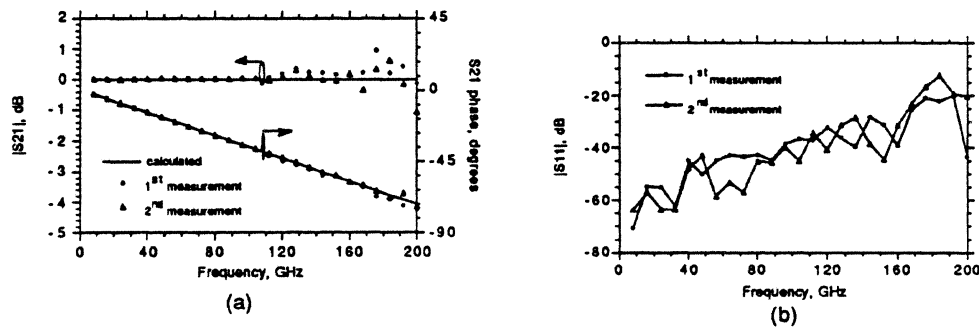


Figure 8: 2-port S-parameter measurements (taken at 30 minutes time intervals) of a 1-ps through line calibration standard: (a) magnitude and phase of S_{21} , and (b) magnitude of S_{11} .

With this VNA, we measured 2 MMICs fabricated with a 0.16 μm pseudomorphic MODFET technology. The S-parameters were obtained with NLTL drive frequencies varied from 7 to 9 GHz in 0.2 GHz steps, hence the resulting measured data points were at these drive frequencies and their harmonics. For measurements at any other frequencies in the 7-200 GHz range, appropriate NLTL drive frequencies can always be chosen so that these frequencies of interest are covered by certain harmonics of the selected NLTL drive frequencies. The first MMIC is a 5-stage traveling-wave amplifier (TWA) [18,19]. Fig. 9 shows the gain and return losses of the TWA measured by the active probes. The gain of the TWA is typically 8 dB over the full 7-80 GHz band, and drops off rapidly beyond 80 GHz; the input and output matching is better than -5 dB over the full 7-80 GHz. S-parameter measurements of the LNA were also performed on a similar LNA chip with a commercial coaxial 50 GHz network analyzer extended to 78 GHz by a waveguide test set [20]. The second MMIC is a medium power amplifier (MPA) that is designed to provide gain from 60-80 GHz. Fig. 10 shows the gain and return losses of the MPA measured by the active probes and by the commercial network analyzer. The MPA has more than 8 dB gain in the 60-80 GHz band, and, as measured by the active probes, the gain is greater than 5 dB to 90 GHz; the return losses are better than -8 dB in the 65-85 GHz band. Both amplifiers were susceptible to radio-frequency bias-circuit oscillations during measurements, oscillations which could be suppressed by small adjustments of the circuit DC bias voltages. Consequently, the MMIC bias conditions during measurements with the

commercial network analyzer were slightly different from those used during measurements with the active probes.

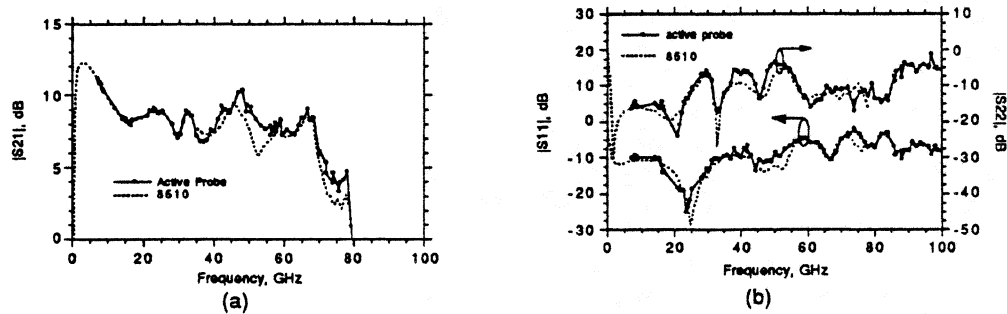


Figure 9: S-parameter measurements of a 5-stage traveling-wave amplifier: (a) gain, and (b) return losses.

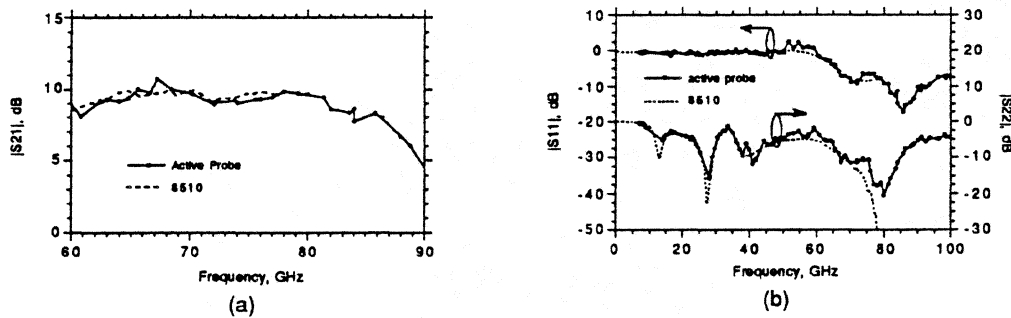


Figure 10: S-parameter measurements of a medium power amplifier: (a) gain, and (b) return losses.

As is apparent from these MMIC S-parameter measurements, good agreement between those measured by the active probes and by the commercial network analyzer is obtained in the 7-80 GHz band. Discrepancies between these measurements may be due to instrument errors, differences in circuit bias conditions, and circuit-circuit variations across the wafer. Beyond 80 GHz, the MMIC can only be measured by the active probes (we do not have access to a commercial 75-110 GHz network analyzer).

V. Conclusion

Commercial sampling scopes and network analyzers bandwidths are limited to 120 GHz, significantly below the state-of-the-art transistor and MMIC bandwidths. With NLTL technology, we have fabricated active probes incorporating GaAs NWA ICs and low loss, rugged quartz probe tips. Using the active probes, we have measured waveforms with 2.5 ps transition times, and we have demonstrated, with measurement of a 1-ps through line, a VNA with ± 0.3 dB reproducibility and better than 30 dB corrected directivity to 160 GHz, and with ± 1 dB reproducibility and better than 10 dB corrected directivity to 200 GHz. With this VNA, we have characterized 3 MMICs, and the S-parameters show good agreement with those measured by a commercial network analyzer from 7-78 GHz. The active probes are convenient tools for broadband on-wafer characterization of transistors and MMICs. With improvement in calibration standards, quantization errors, microwave synthesizer noise, probe crosstalk, and active probe bandwidths, more accurate and reproducible network analysis beyond 200 GHz is possible.

Acknowledgment: This work was supported by an AFOSR grant (grant number: F49620-92-J-0469), an AFOSR/AASERT grant (grant number: F49620-92-J-0365), an NSF Presidential Young Investigator Award, and a California/Hughes Micro contract. We are grateful to Dr. P. Tasker, Dr. M. Schlechtweg, and Dr. J. Braunstein at Fraunhofer Institute for supply of the MMICs.

References:

- [1] U. K. Mishra, A. S. Brown, and S. E. Rosenbaum, "DC and RF performance of 0.1 μ m gate length AlInAs-GaInAs pseudo-morphic HEMT's", Technical Digest, 1988 International Electron Device Meeting, Dec. 4-11, San Francisco.
- [2] R. Majidi-Ahy, C. Nishimoto, M. Riaziat, M. Glenn, S. Silverman, S. Weng, Y. Pao, G. Zdasiuk, S. Bandy and Z. Tan, "100 GHz High-Gain InP MMIC Cascode Amplifier", 1990 GaAs IC Symposium, Oct. 7-10, New Orleans.
- [3] M. J. W. Rodwell, M. Kamegawa, R. Yu, M. Case, E. Carman, and K. S. Kiboney, "GaAs Nonlinear Transmission Lines for Picosecond Pulse Generation and Millimeter-Wave Sampling", IEEE Trans. on Microwave Theory and Techniques, Vol. 39, No.7, July 1991.
- [4] S. T. Allen, U. Bhattacharya, and M. J. W. Rodwell, "4 THz sidewall-etched varactors for sub-mm-wave sampling circuits," Technical Digest, 1993 GaAs IC Symposium, Oct. 10-13, San Jose.

- [5] R. Y. Yu, M. Case, M. Kamegawa, M. Sundaram, M. J. W. Rodwell, and A. W. Gossard, "275 GHz 3-mask integrated GaAs sampling circuit," *Electronics Lett.*, vol. 26, No. 13, June 21, 1990, pp. 949-951.
- [6] R. A. Marsland, V. Valdivia, C. J. Madden, M. J. W. Rodwell, and D. M. Bloom, "Monolithic integrated circuits for millimeter-wave instrumentation," *Technical Digest, 1990 GaAs IC Symposium*, Oct. 7-10, New Orleans.
- [7] R. Y. Yu, M. Kamegawa, M. Case, M. J. W. Rodwell, and J. Franklin, "A 2.3-ps time-domain reflectometer for millimeter-wave network analysis," *IEEE Microwave and Guided Wave Lett.*, vol. 1, no. 11, Nov. 1991, pp. 334-336.
- [8] M. S. Shakouri, A. Black, B. A. Auld, and D. M. Bloom, "500 GHz MMIC sampling wafer probe," *Electronic Letters*, vol. 29, no. 6, pp. 557-558, March 18, 1993.
- [9] R. K. Hoffmann, "Handbook of microwave integrated circuits," Artech House Inc., 1987.
- [10] D. B. Rutledge, D. P. Neikirk, and D. P. Kasilingam, "Integrated-Circuit Antennas" in *Infrared and Millimeter Waves*, Ed. by K. J. Button, Vol. 10, pp. 1-90, New York: Academic Press, 1984
- [11] M. Caulton, "Lumped elements in microwave integrated circuits," in *Advances in Microwaves*, Ed. by Leo Young and H. Sobol, pp. 143-167, Academic Press, 1974
- [12] R. Y. Yu, Y. Konishi, S. Allen, M. Reddy, and M. J. W. Rodwell, "A traveling-wave resonant tunnel diode pulse generator," submitted to *Microwave and Guide Wave Lett.* for publication.
- [13] H. J. Eul and B. Schiek, "Thru-Match-Reflect: One Result of A Rigorous Theory for De-embedding and Network Analyzer Calibration," *Proceedings of the 18th European Microwave Conference*, Stockholm, Sweden, 1988.
- [14] Specification Sheet for Calibration Kit 25, Cascade Microtech, Inc., PO Box 1589, Beaverton, OR, 97075-1589.
- [15] Y. Konishi, M. Kamegawa, M. Case, R. Yu, S. Allen, and M. J. W. Rodwell, "A broadband free-space millimeter-wave vector transmission measurement system," to be published in *IEEE Transactions on Microwave Theory and Techniques*.
- [16] A. Davidson, K. Jones, and E. Strid, "LRM and LRRM calibrations with automatic determination of load inductance", Application Note, Cascade Microtech, 14255 SW Brigadoon Ct., Beaverton, OR 97005.
- [17] S. M. J. Liu, K. H. G. Duh, S. C. Wang, O. S. A. Tang, and P. M. Smith, "75-110 GHz InGaAs/GaAs HEMT high gain MMIC amplifier", *Tech. Digest, GaAs IC Symposium*, San Jose, Oct. 10-13, 1993.

- [18] M. Schlechtweg, P. Tasker, W. Reinert, J. Braunstein, W. Haydl, A. Hulsmann, and K. Kohler, "High gain 70-80 GHz MMIC amplifiers in coplanar waveguide technology," *Electronics Lett.*, vol. 29, no. 12, June 1993, pp. 1119-1120.
- [19] J. Braunstein, M. Schlechtweg, P. J. Tasker, W. Reinert, A. Julsmann, K. Kohler, W. Bronner, R. Bosch, and W. Haydl, "High performance narrow and wide bandwidth amplifiers in CPW-technology up to W-band," *Technical Digest, 1993 GaAs IC Symposium*, Oct. 10-13, San Jose.
- [20] P. J. Tasker, M. Schlechtweg, and J. Braunstein, "On-wafer single contact S-parameter measurements to 75 GHz: calibration and measurement system," *23rd European Microwave Conf.*, Madrid, 1993

CRYOGENIC PERFORMANCE OF MONOLITHIC AMPLIFIERS FOR 85–115 GHz

N.R. Erickson

Five College Radio Astronomy Observatory

Department of Physics and Astronomy

University of Massachusetts

Amherst, MA 01003

and

S. Weinreb and B.C. Kane

Martin Marietta Laboratories

1450 S. Rolling Road

Baltimore, MD 21227

Abstract

MMIC amplifiers designed for low noise room temperature operation at 100 GHz have been tested at 13–25 K over the 85–115 GHz range. All measurements have been made in waveguide test fixtures in which a short length of either microstrip or CPW line connects a waveguide probe to the amplifier input terminals. A scalar feed horn and dewar window complete the input circuit. The lowest noise temperature measured has been 110 K at 103 GHz, with no correction for input loss. Better results are expected with other chips from this batch and with improvements in the input circuit.

Introduction

Cryogenic HEMT amplifiers have achieved noise temperatures nearly as low as any of the competitive techniques (including masers) at frequencies up to 50 GHz. These amplifiers are far easier to use than any of the alternatives, and so are preferred for almost all applications. Recently, very good room temperature results have been reported with monolithic amplifiers for the 100 GHz range, and these suggested that the cryogenic performance could be exceptional. These amplifiers have now become available in sufficient numbers that they could be used in a fairly large array receiver, and the ease of use makes such a receiver practical.

We have evaluated the cryogenic performance of one batch of monolithic amplifiers for the 100 GHz range. The amplifiers were built at Martin–Marietta Labs, and tested at the FCRAO at UMass. The amplifiers use four gain stages, each a $0.1\ \mu\text{m}$ gate length AlGaAs/InGaAs/GaAs pHEMT [1], with all interconnections using grounded CPW line on a $100\ \mu\text{m}$ substrate. Via holes at less than quarter wave spacing are used to prevent substrate modes. The chips are wired with all drains connected to a common terminal, while the gates may be biased separately. While the evaluation is still ongoing, the initial tests of these amplifiers are very encouraging. We have tested several devices at cryogenic temperatures, and all have operated with comparable performance. Four devices were in carriers built by Martin–Marietta, while two have been in a mount designed at FCRAO for these tests. In both the amplifier has waveguide inputs and outputs, with probe transitions to either 50 ohm CPW line or 50 ohm microstrip.

The waveguide to CPW transitions were built on GaAs, as with the rest of the chip so that matching to the MMIC was easy. However, the high dielectric constant made the transition to waveguide difficult at 115 GHz (with WR–10 waveguide), and the VSWR over the full band was not very low. This degrades the noise outside the 100–115 GHz range.

The waveguide to microstrip transitions use 0.13 mm duroid substrates aligned along the E plane of the waveguide. They were designed with the aid of the Hewlett Packard HFSS program, and worked exactly as designed, with a VSWR < 1.2 from 85–115 GHz. This mount is shown in Fig. 1. The transition from microstrip to CPW is predicted to be have a low VSWR, but the HFSS program shows that there is a potential for a resonance in the gap where the microstrip box meets the CPW. This can be suppressed by bridging the CPW ground plane over to the box around the microstrip.

The minimum noise temperature measured so far (in the mount with the duroid probes) is 110 K at 103 GHz (including window loss and second stage contributions) at a physical temperature of 13 K. The peak gain is about 30 dB. These results are shown in Fig. 2. The noise is higher than projected for optimized devices at this frequency (about 50 K), but these may not represent the best results obtainable. This same amplifier had a noise temperature of 160 K at 109 GHz at a physical temperature of 25 K, when measured earlier, with the results shown in Fig. 3. In between these measurements the amplifier suffered some damage that affected its tuning, and thereafter the optimum frequency was lowered by ~ 7 GHz. However, in this process the minimum room temperature noise was unaffected, so the most likely explanation for the lower noise in the later measurements is the lower physical temperature. However there is also the possibility that some other problem affected the poorer set of data such as an out-of-band oscillation. This

amplifier shows a significant variation in the optimum bias with frequency. The results of Fig. 3 are for optimum bias at each frequency, while Fig. 2 is for fixed bias (set for minimum noise at 103 GHz). At extreme frequencies varying the bias is quite important; in the data in Fig. 3, if the bias is optimized at 112 GHz, then the noise at 85 GHz is 400 K (rather than 280 K as shown with optimum bias).

The minimum measured noise temperature of an amplifier with the CPW probes is 127 K at 109 GHz, at a physical temperature of 25 K. The dewar window and the following mixer add very little noise (1–3 K each), but the input CPW transition plus the waveguide and horn have a loss of ~ 0.8 dB (all at 25 K) which is difficult to accurately measure. Assuming this loss, the noise of the amplifier referenced to its input is ~ 100 K. If this amplifier were cooled further to 13 K with results similar to the amplifier above, the expected noise would be 70 K. This suggests that there may be a some variation in performance between amplifiers. The gain peaks at 100 GHz, with 27 dB available at minimum noise bias. Illumination has only a small effect, which varies with frequency.

The MMIC is followed by a low noise cooled mixer with a tunable LO. This mixer has an IF of 1.15 GHz, so there is some loss of detail in the performance vs frequency, and a tendency for the noise data to be weighted toward the sideband with higher gain. The amplifier is preceded by a scalar feed horn and a very low loss vacuum window made of a sandwich of plastic film and GoreTex fabric. The noise temperature is measured using hot and cold loads outside this window.

The present technology for building monolithic amplifiers makes it difficult to predict the exact parameters that will be achieved with the HEMTs, particularly gate capacitance, and other circuit parameters have some potential variation. Thus the design of a monolithic amplifier for a precise application can involve some trial and error. It seems practical (and much less expensive) at present to take amplifiers whose performance is close to our needs, and then modify them. Such modifications are possible because typical circuit dimensions on these chips are reasonably large (1–2 mils), and cutting conductors and adding bond wires is well within the range of microassembly techniques. The advantage of starting with a MMIC is that nearly all of the circuitry can be used, saving considerable effort. Work now is aimed at characterizing the noise of these existing amplifiers, to see if it can be improved over much of the 85–115 GHz range. This characterization is done by presenting the amplifier with a known mismatch, in this case produced by a .020" thick plug of teflon in the waveguide ahead of the amplifier. The noise is measured at several positions of this plug (which is actually an impedance transformer), and the results fit to the standard four parameter noise model. Data for one amplifier is shown in Fig. 4, with the raw data in the upper graph, and the minimum

possible noise temperature in the lower. The smooth behavior in the minimum noise shows that this technique works very well, since data at each frequency is independent. The scatter in values is an indication of the errors in the fit. The other three noise parameters are uniquely determined as well, with similar accuracy.

In order to improve the wideband noise, it is necessary to eliminate some of the line length ahead of the first HEMT. In these chips, this extra line has little effect on the noise, since it is close to $50\ \Omega$, but is $\lambda/2$ long. This line can simply be sawed off, without too much extra complexity in the use of the chip, except that it is necessary to provide a new gate bias connection. The process is essentially the same as building the input network for a discrete amplifier, except that we can use part of the existing input circuit, which makes assembly easier. We have successfully sawed off one chip, and installed it in a test block with gate bias. This chip operated much as expected except for a tendency to oscillate. Minimum noise was $\sim 115\ \text{K}$ at $117\ \text{GHz}$, but this might not be optimum because of the constraints on bias needed to prevent oscillation. Noise at lower frequencies showed a monotonic increase. In the process of stopping the oscillation, the chip was damaged, so no conclusive results were obtained.

Based on a preliminary analysis, a modified amplifier could have significantly flatter noise from 100 to $115\ \text{GHz}$, with a value close to the present minimum. For lower frequencies, down to $90\ \text{GHz}$, there should be some improvement, while noise at $85\ \text{GHz}$ may be unchanged. Varying the bias should reduce the noise at $85\ \text{GHz}$ down to $\sim 200\ \text{K}$. This should largely meet the needs of radio astronomers, for whom the most important frequencies are 108 – $115\ \text{GHz}$. Other frequencies are used much less of the time.

Conclusions

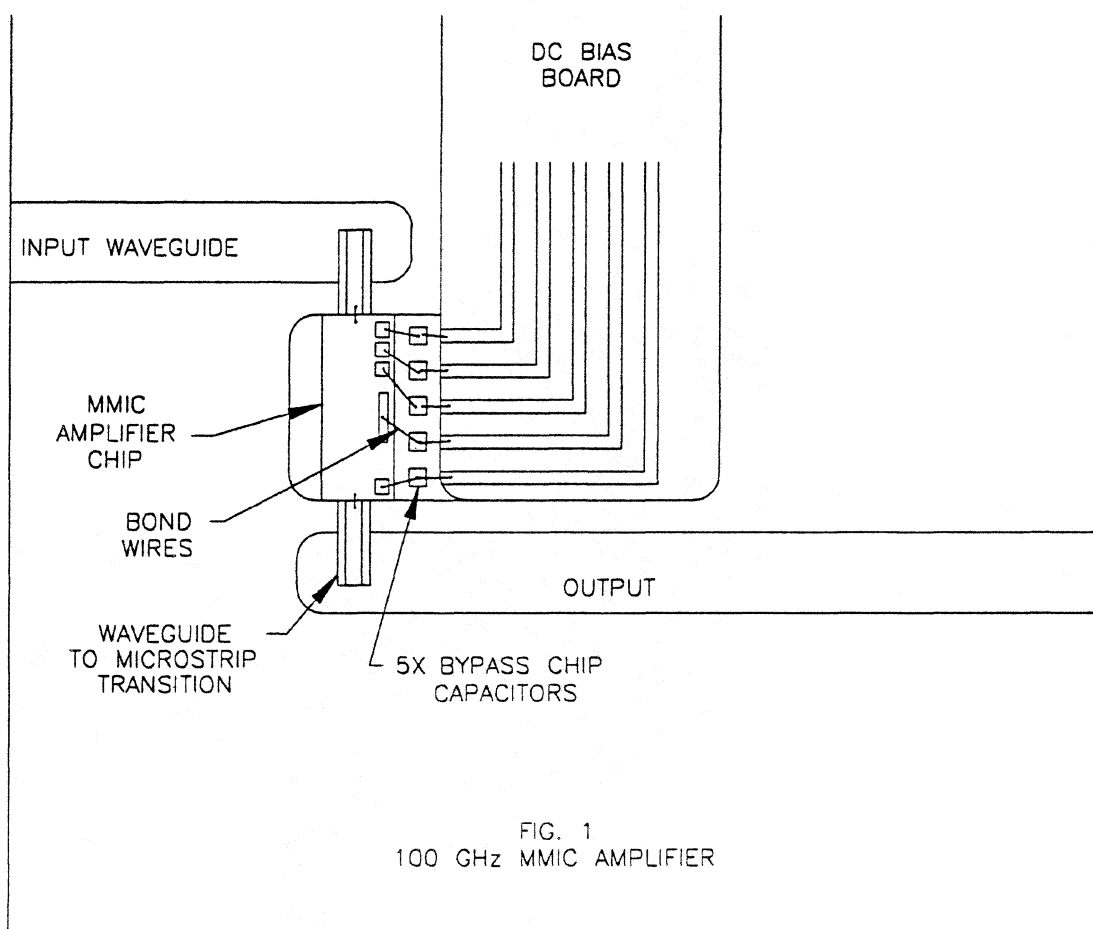
Monolithic amplifiers have demonstrated low noise operation over moderate bandwidths in the $3\ \text{mm}$ region. Noise temperatures below $100\ \text{K}$ are expected with optimized input tuning. The amplifiers are fairly easy to use, and may be modified to tune over wider bandwidths. Gain is high enough over most of the band that they may be followed by relatively noisy mixers.

Acknowledgements

This work was supported by the National Science Foundation under grant AST-9217677. We would like to thank N. Horner of NRAO for his help in the fabrication of the amplifiers.

Reference

- [1] "High Gain Monolithic pHEMT W-band Four-stage Low Noise Amplifiers," D-W Tu, W.P. Berk, S.E. Brown, N.E. Byer, S.W. Duncan, A. Eskandarian, E. Fisher, D.M. Gill, B. Golja, B.C. Kane, S. Svensson, and S. Weinreb, to be published in *1994 IEEE Microwave and Millimeter Wave Monolithic Circuits Symposium*, San Diego, May 1994.



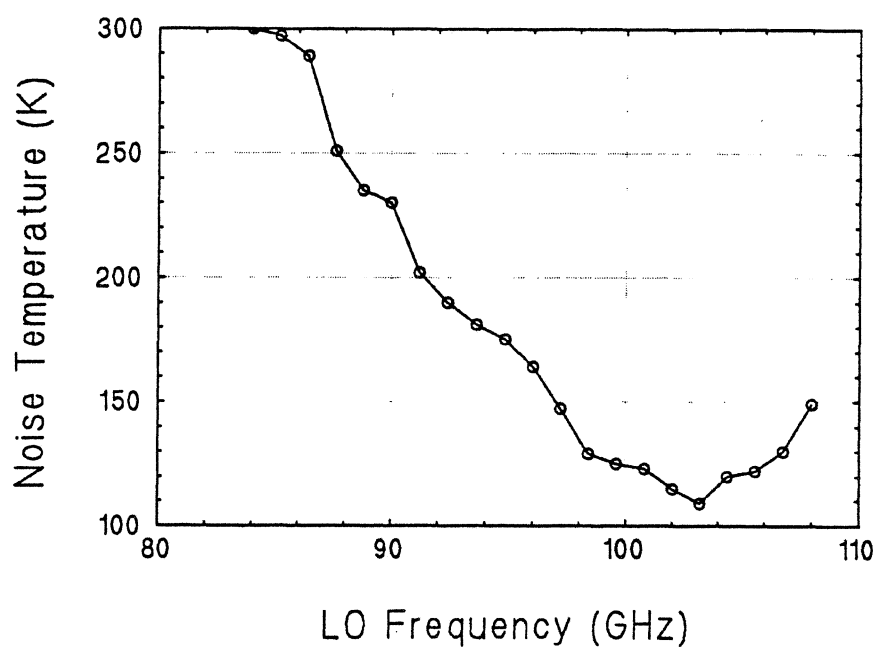


Fig. 2 Noise temperature of MMIC amplifier at 13 K. No corrections have been made for input losses or second stage contribution. Bias is fixed at all frequencies.

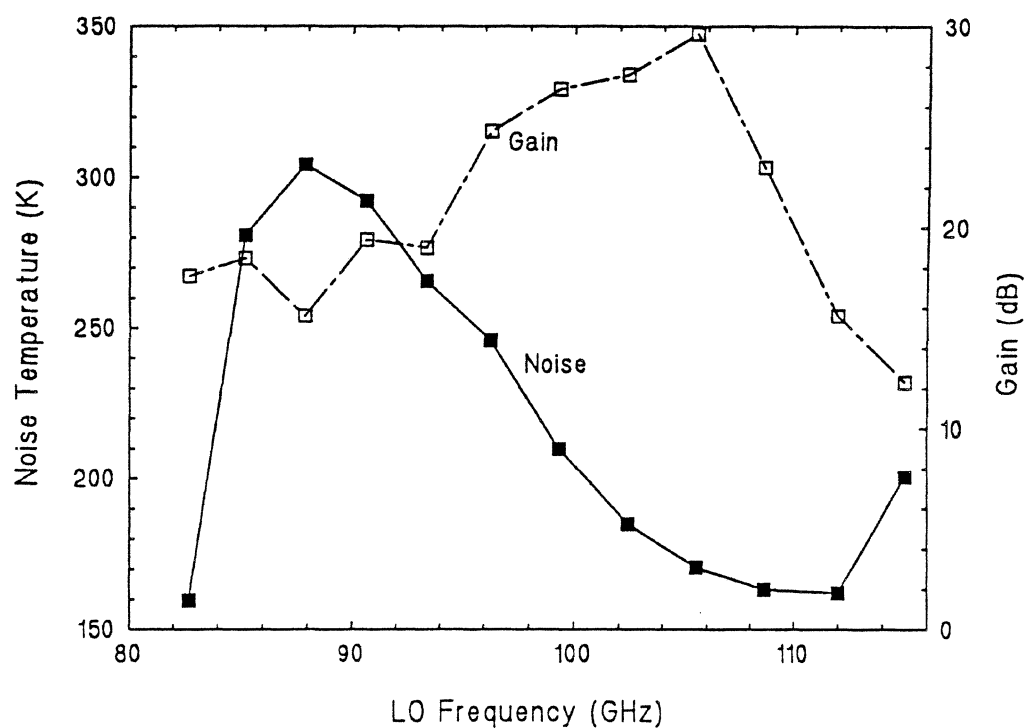


Fig. 3 Noise temperature and gain of MMIC amplifier at 25 K. Bias optimized at each frequency for minimum noise. No correction for input loss or second stage.

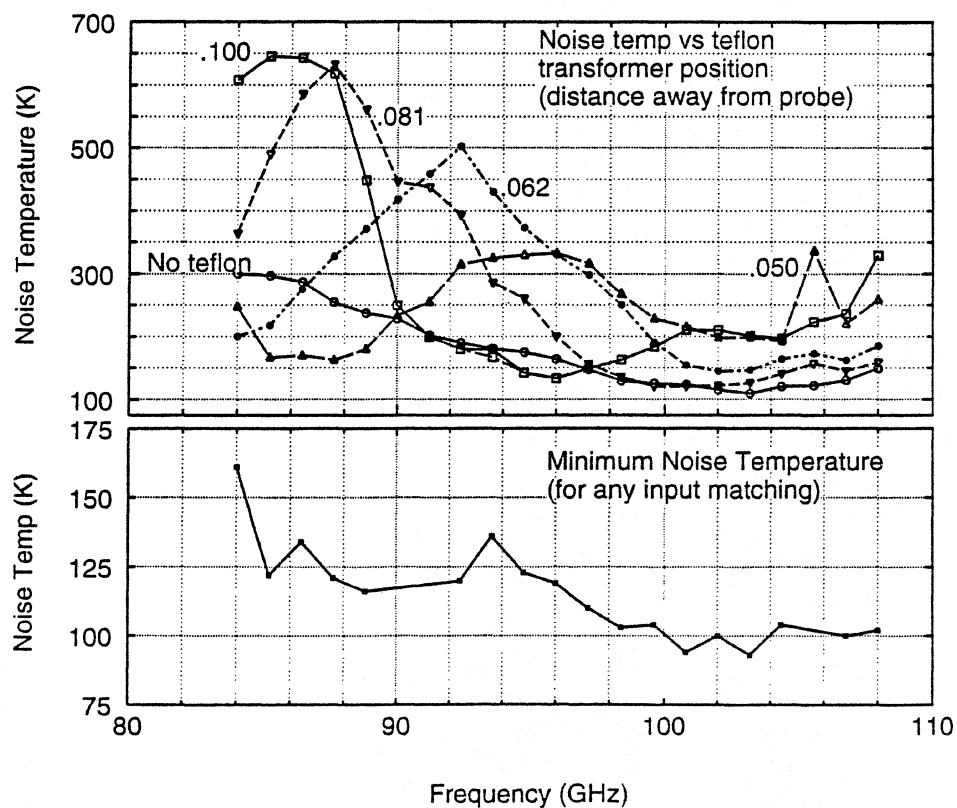


Fig. 4 Upper graph: Noise temperature of MMIC amplifier for various positions of an input transformer consisting of a $\lambda/4$ teflon slab.

Lower graph: Derived minimum noise temperature of amplifier for any input matching network. Graph includes corrections for second stage, but not for input loss.

This article is presented here as a review only and has been accepted for presentation at the 1994 IEEE-MTT Symposium, San Diego.

Monolithic 155 GHz and 213 GHz Quasi-Optical Transistor Oscillators

**Brian K. Kormanyos*, Steven E. Rosenbaum⁺, Linda P. Katehi*
and Gabriel M. Rebeiz***

* NASA/Center for Space Terahertz Technology
Electrical Engineering and Computer Science Department
University of Michigan, Ann Arbor, MI 48109-2122

⁺Hughes Malibu Research Laboratory
Malibu, California 90265

ABSTRACT

We report on the design and measurement of monolithic 155 GHz and 213 GHz quasi-optical slot antenna transistor oscillators. The oscillators were fabricated by the Hughes Malibu Research Laboratory [1]. The output signals were detected with an interferometer in front of an InSb hot electron bolometer and accurate frequency measurements were obtained by heterodyne detection using a wideband quasi-optical harmonic mixer-receiver. The circuits represent the highest frequencies achieved to date for a fundamental source using a three terminal device.

I. INTRODUCTION

Coplanar waveguide (CPW)-fed quasi-optical slot oscillators have been investigated by Kormanyos et al. [2,3] and Moyer et al. [4]. The uniplanar circuit requires no via holes and is compatible with the monolithic integration of high speed transistors. This allows oscillators to be designed to the highest frequency limit of the device. The oscillator is placed on a dielectric substrate lens for proper operation. The substrate lens simulates an infinite dielectric medium, eliminates power loss to substrate modes, and results in a unidirectional pattern [5]. The antenna impedance in this environment

is accurately calculated using the space domain integral equation technique [6], a full wave method of moments approach.

II. OSCILLATOR DESIGN

The transistor used is an AlInAs-GaInAs InP based HEMT fabricated at Hughes Malibu Research Laboratory and described elsewhere [7]. The device employs a self aligned T-gate defined by an electron beam process. The gate length is $0.05\mu\text{m}$ and the gate width is $10\mu\text{m}$. To obtain a small signal model for the $10\mu\text{m}$ transistor, a larger device with a $50\mu\text{m}$ gatewidth was built and tested to 40 GHz. A model was extracted and the results mathematically scaled for the smaller $10\mu\text{m}$ device. The scaled device model for the $10\mu\text{m}$ device is shown in Fig. 1. Since it was derived from measurements on a $50\mu\text{m}$ device, a large uncertainty exists in the $10\mu\text{m}$ device model parameters. The parasitic elements $L_g, L_d, L_s, C_{pgs}, C_{pgd}$, and C_{pds} associated with the extrinsic contact metalizations are known to about $\pm 5\text{pH}$ or fF which is greater than 100% in most cases. Values of the intrinsic elements $R_{gs}, C_{gs}, R_{gd}, C_{gd}, g_m, \tau, C_{ds}$, and g_{ds} are thought to be accurate to $\pm 20\%$. However, DC measurements of the smaller devices indicate that the transconductance is closer to 10mS than the scaled value of 16mS.

The oscillator design follows the reflection amplifier approach presented in [8]. Oscillator designs were carried out at frequencies from 150GHz to 550GHz in 50GHz increments. Due to the uncertainty existing in the device model, several designs were done at each frequency. The cases considered were with parasitics at their nominal values (low parasitics) and at twice these values (high parasitics). The transconductance was also taken to be either 16mS or 10mS. Varying the frequency and the model parameters resulted in 28 significant design cases of which 16 were selected for fabrication. The CPW layout for the oscillator circuit is shown in Fig. 2.

The transistors were integrated simultaneously with the CPW circuits. An etch was performed to remove conductive material which exists in the region of the slot antenna and in the gap between the CPW metalizations. DC biasing of the transistor is made possible by slits in the ground plane which isolate the gate, drain and source. These

slits are capacitively bypassed to create an uninterrupted ground plane for the RF circuit [3].

III. MEASUREMENTS

The oscillators were positioned on a 2.54 cm diameter elliptical silicon substrate lens for testing. Operational checks and rough frequency measurements were obtained by aligning the oscillators in front of an InSb hot electron bolometer with an interferometer and mechanical chopper in the beam path. Two of the designs were found to oscillate with about 50% yield (Table 1). The 150 GHz design case assuming high parasitics and 10mS transconductance (150H10) oscillated near its design frequency generating an output signal at 155 GHz. The 500 GHz case assuming high parasitics and 16mS transconductance (500H16) generated an output at an unexpected frequency near 213 GHz. The other 14 cases generated no output. This situation is not surprising considering the large uncertainty which exists in the device model.

The oscillator frequencies were accurately measured and their spectrums were observed using a quasi-optical wideband harmonic mixer [9] setup shown in Fig. 3. The measured spectrums of a 155 GHz and a 213 GHz oscillator are shown in Fig 4. The LO frequency was varied to observe both upper and lower sidebands and different IF frequencies were used to insure that the harmonic numbers and RF frequencies are correctly determined. To be certain that the observed signal corresponds to the fundamental oscillation frequency, the LO was adjusted to search for any signals at $1/2$ and $1/3$ of the oscillator frequency and no signals were observed.

The oscillator output power was estimated with a quasi-optical setup using calibrated waveguide diode detectors and a lock-in amplifier. The slot-oscillator power is determined from the amplitude of the signal at the calibrated detector and the Friis transmission equation. An estimate of the directivity of the slot oscillator is made by assuming an aperture efficiency of 40% [3]. The total output power is found to be no less than $10 \mu\text{W}$ for the 155 GHz oscillator and no less than $1 \mu\text{W}$ for the 213 GHz oscillator. The corresponding (minimum) DC to RF efficiencies are 0.13% at 155 GHz and 0.014% at 215 GHz. The 155 GHz power measurements are consistent with the fact that the transistor is very small with only a $10 \mu\text{m}$ gate width and the

circuits are operating close to f_{max} . The circuits were optimized for high loop gain not maximum power and there is a lot of uncertainty in the device model.

IV. CONCLUSION

This paper presents the highest frequency achieved to-date for a quasi-optical oscillator using a three terminal device. A large number of these devices could be used in quasi-optical power combining designs at millimeter wave frequencies to generate milliwatt power levels. The successful development of these monolithic oscillators demonstrates the high frequency capabilities of the sub-micron gate InP based HEMT which should also find applications as a small signal millimeter-wave and submillimeter-wave amplifier.

ACKNOWLEDGMENTS

This work is supported by the AFOSR under contract F19628-90-C-0171 and the NASA Center for Space Terahertz Technology at the University of Michigan.

REFERENCES

- [1] S. E. Rosenbaum et al., "Fabrication of a 213 GHz AlInAs/GaInAs/InP HEMT MMIC Oscillator," submitted to *IEEE Microwave and Guided Wave Letters*, April 1994.
- [2] B. K. Kormanyos and G. M. Rebeiz, "Quasi-optical CPW-fed slot-antenna oscillators," Proceedings of the *Third Int. Conf. on Space Terahertz Technology*, Ann Arbor, Michigan, March 24-26, 1992, pp.32-36.
- [3] B. K. Kormanyos, W. Harokopus Jr., L.P.B. Katehi, and G.M. Rebeiz, "CPW-Fed active slot-antennas," to appear in *IEEE Transactions on Microwave Theory Tech.*, April 1994.
- [4] H. P. Moyer and R. A. York, "Active cavity backed slot antenna using MESFET's," *IEEE Microwave and Guided Wave Letters*, vol. 3, no. 4, April 1993.
- [5] G. M. Rebeiz, "Millimeter-wave and terahertz integrated circuit antennas," *Proceedings of the IEEE*, vol. 80, no. 11, pp. 1748-1770, Nov. 1992.
- [6] N.I. Dib and P.B. Katehi, "Modeling of shielded CPW discontinuities using the space domain integral equation method (SDIE)," *Journal of Electromagnetic Waves and Applications*, vol. 5, no. 4/5, pp. 503-523, 1991.
- [7] L.D. Nguyen, A.S. Brown, M.A. Thompson, and L.M. Jelloian, "50-nm self aligned gate pseudomorphic AlInAs/GaInAs high electron mobility transistors," *IEEE Transactions on Electron Devices*, vol. 39, no. 9, Sept. 1992.
- [8] G. R. Basawapatna and R. B. Stancliff, "A unified approach to the design of wide-band microwave solid-state oscillators," *IEEE Trans. Microwave Theory Tech.*, vol. MTT-27, no.5, pp. 379-385, May 1979.
- [9] B. K. Kormanyos and G.M. Rebeiz, "A 26 to 220 GHz harmonic mixer-receiver," *Microwave Journal*, Vol. 36, No. 7, pp. 103-108, July 1993.

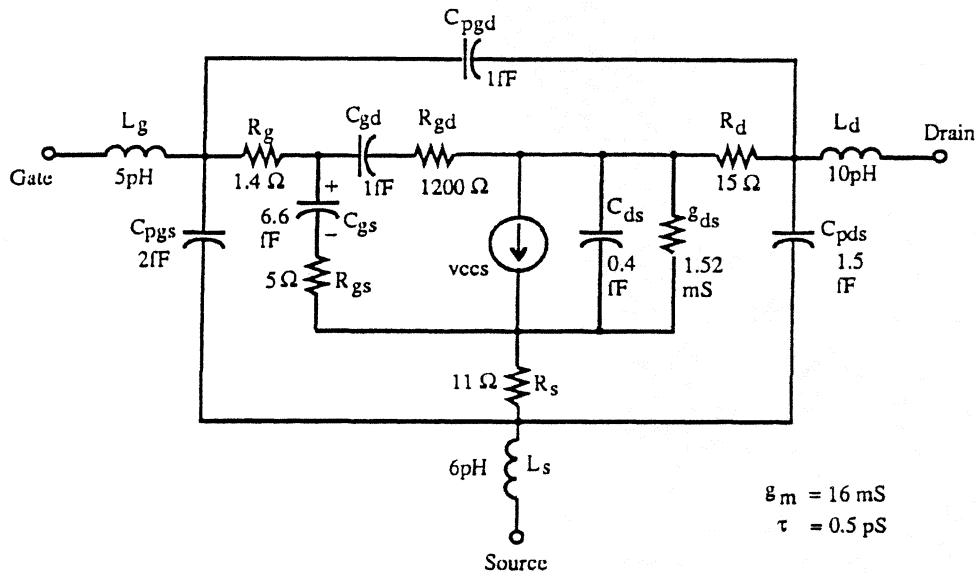


Figure 1: Small signal model for the InP based HEMT with $0.05\ \mu\text{m}$ gate length and $10\ \mu\text{m}$ gate width.

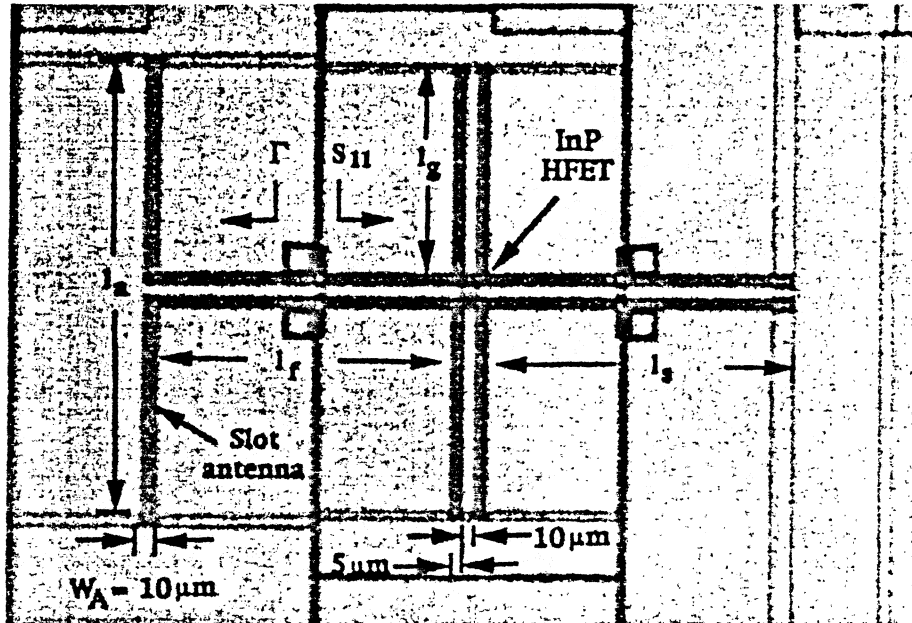


Figure 2: CPW layout for the high frequency quasi-optical slot oscillators.

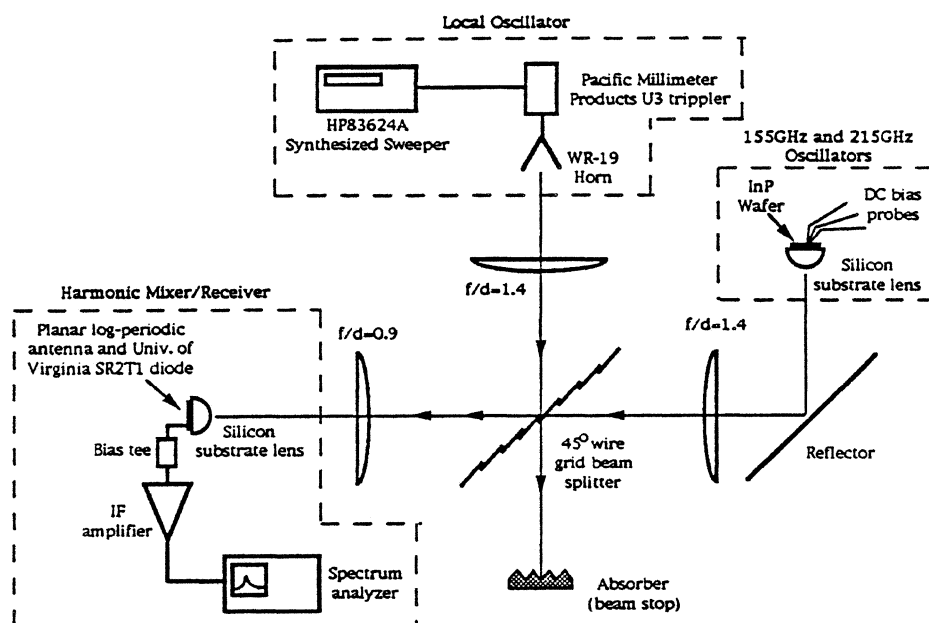


Figure 3: Wideband quasi-optical harmonic mixer setup for accurate frequency determination and spectrum measurements.

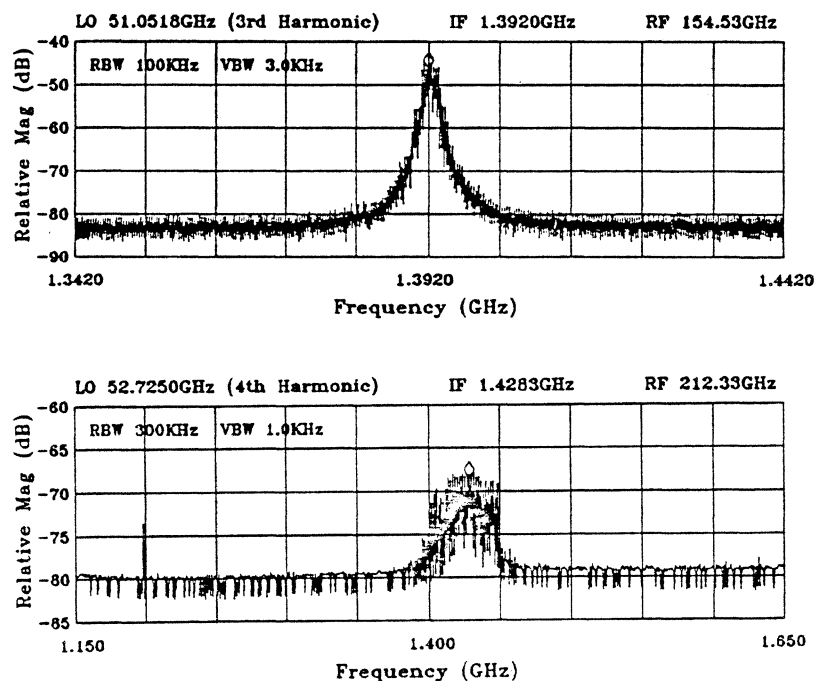


Figure 4: Measured down converted spectra of the 155 GHz and 213 GHz oscillators.

F^* (GHz)	L_p, C_p^{**}	g_m (mS)	l_s (μm)	l_g (μm)	l_f (μm)	l_a^{**} (μm)	$1/S_{11}$ (mag,ang)	Γ (mag,ang)
150	High	10	239	164.5	230.5	360	0.188, 164.4	0.595, 164
500	High	16	107	86.5	71	70	0.323, -147	0.897, -146.5

Table 1: Design parameters for the two successful monolithic millimeter-wave oscillators. (*F is the small signal design frequency, **Lp, Cp are the extrinsic parasitic inductors and capacitors in the device model where high parasitics corresponds to two times the nominal values shown in Fig. 1).

Monolithic Nonlinear Transmission Line Using Multi-barrier Devices

W-M. Zhang^{*}; X-H. Qin^{*}; J. Y. Liao^{*}; R. P. Hsia[®]; R. W. Geck^{*};

F. Jiang[®]; Y. Li[®]; C. W. Domier[®] and N.C. Luhmann, Jr. [®]

[ABSTRACT]

Schottky Quantum Barrier Varactors are employed as nonlinear elements in monolithic nonlinear transmission line (NLTL) applications. The epitaxial stacking structure together with the zero built-in voltage of the quantum barrier results in this device having a higher cut-off frequency and an enhanced breakdown voltage as compared to Schottky varactors. To reduce the leakage current associated with the quantum barrier, an AlAs/GaAs superlattice barrier is utilized instead of an $\text{Al}_x\text{Ga}_{1-x}\text{As}$ quantum barrier. Two monolithic NLTLs have been designed and fabricated. Hybrid NLTLs have been employed to pre-compress the input pulses.

^{*} University of California, Los Angeles, CA 90024

[®] University of California, Davis, CA 95616

[INTRODUCTION]

Monolithic Nonlinear Transmission Lines have been made by several groups utilizing coplanar wave guide and GaAs Schottky diodes. Pulses with ~ 0.8 ps rise time and $V_{pp} \sim 3$ V have been obtained at 77K, and ~ 1.4 ps rise time with $V_{pp} \sim 6$ V and ~ 4.5 ps rise time with $V_{pp} \sim 12.6$ V has been obtained at room temperature [1-4]. The output power and pulse width are limited by the breakdown voltage and the diode cut-off frequency. The trade-off between the breakdown voltage and the cut-off frequency of Schottky diodes makes it difficult to simultaneously achieve high voltage ($V_{pp} > 15$ V) and ultrashort pulsewidth (< 3 ps). With modern MBE technology, however, it is possible to vertically stack several devices in series and to obtain much higher power handling ability. Two such structures, Multi-Quantum Barrier Varactor (MQBV) and Schottky Quantum Barrier Varactor (SQBV), were conceived by our group which have proven to have higher cut-off frequency and increased power handling ability as compared to conventional Schottky diodes in frequency multiplier applications[5]. The MQBV is a stacked quantum barrier varactor, as shown in Fig. 1. The zero built-in voltage of the quantum barrier and the epitaxial stacking structure results in the MQBV having a high cut-off frequency and high breakdown voltage. The SQBV is comprised of a Schottky barrier on top of an MQBV structure, as shown in Fig. 2. A δ doping layer is added to increase the nonlinearity of the SQBV. With a Schottky contact instead of an ohmic contact, the SQBV has a higher diode cut-off frequency but reduced nonlinearity compared to the MQBV. By using a back-to-back layout configuration, the MQBV and SQBV varactors have symmetric C-V curves; hence, these devices have strong nonlinearities for both positive and negative voltages. The cut-off frequency of these devices is predicted to exceed 2 THz. Using MQBV and SQBV structures, $V_{pp} > 20$ V and 1-3 picosecond pulses appear to be readily achievable. In this work, the SQBV structure is utilized. To reduce the leakage current associated with quantum barriers, we also employed superlattice barriers instead of quantum barriers[6], as shown in Fig.3.

[DESIGN AND DISCUSSIONS]

A monolithic nonlinear transmission line is a coplanar transmission line loaded with varactors as nonlinear elements. The nonlinearity of the transmission line arises from the variable depletion layer width which depends on the DC bias voltage and on the AC voltage of the propagating wave. The voltage dependency of diodes causes the waveform steepening, and periodic loaded transmission line has strong dispersion near the Bragg cut-off frequency. The balance between these two factors causes the formation of short pulses. Each NLTL is comprised of many sections. An equivalent circuit of our NLTL is shown in Fig. 4, which serves as the basis of our designs and simulation. The coplanar transmission lines are modeled as an RLC ladder network, where L and C_{line} are, respectively, the inductance and capacitance per section, and R represents the skin loss. The SQBV is modeled as an MQBV (C_2) in series with a pair of back-to-back barrier-N-N+ (BNN) varactors (C_1 , C_3). Here R_s is the series resistance, while R_1 , R_2 , and R_3 stand for the leakage current over the barriers. To match external circuits, the input and output impedances are traditionally chosen as 50Ω , so are the large signal impedances of our NLTLs. To reach a high nonlinearity, high impedance coplanar transmission lines are preferred. Also, to emphasize the nonlinearity of the NLTL, wafer profiles are designed to have a large $C_{\text{max}}/C_{\text{min}}$ ratio.

Two monolithic nonlinear transmission lines have been designed to generate waveforms with 10ps and 20ps fall time. The transmission line impedance is chosen as 85Ω , the diode areas are $144\ \mu\text{m}^2$, and $288\ \mu\text{m}^2$, and the section lengths are $200\ \mu\text{m}$ and $400\ \mu\text{m}$.

[PRELIMINARY TEST RESULTS]

Monolithic NLTLs have been fabricated on SQBV and SSQBV wafers with a three mask process. Both wafers were grown by Quantum Epitaxial Designs. DC characteristic measurements have been performed with a HP4140B pA meter (I-V) and a HP4279 CV meter. As shown in Fig. 5, both devices have similar C-V curves. For SQBV device, the C_{\max}/C_{\min} ratio is 3.8, while for SSQBV, the ratio is 3.9. The I-V curves of SQBV and SSQBV devices are shown in Fig. 6. The breakdown voltages for both devices are $>17V$. At low voltage levels ($<15V$), the SSQBV has less leakage current, and at higher voltages ($>15V$), the SQBV has less leakage current.

A initial test system has been setup, which includes Cascade WPH-405 Microwave Probes (DC-65GHz), an Avtech impulse generator (350 ps FWHM pulses) and a Tektronix 11802A digital sampling oscilloscope equipped with a 50 GHz plug-in, as shown in Fig. 7. A hybrid nonlinear transmission line has been fabricated utilizing MA46580-992 GaAs beam-lead varactor diodes. The hybrid NLTL is employed to pre-compress the input pulses. The output of the hybrid NLTL is a shock wave with fall time 60-90ps and $V_{\min} \sim -22V$. The monolithic lines are current under test.

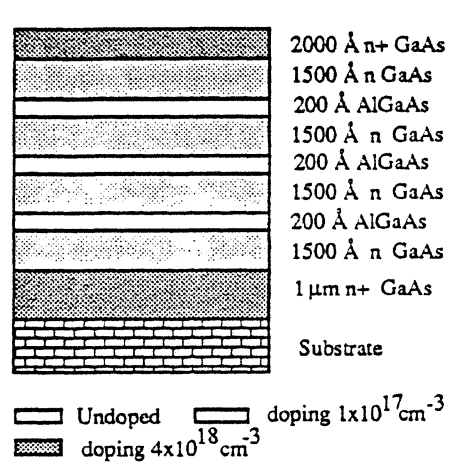


Fig.1 GaAs MQBV Doping Profile

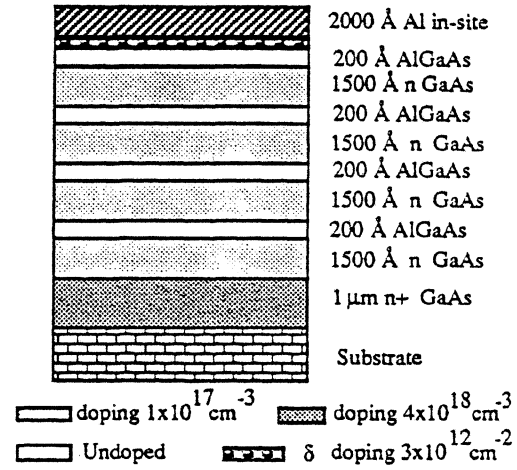


Fig.2 GaAs SQBV Doping Profile

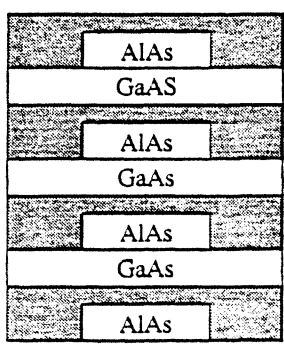


Fig.3 Superlattice Structure

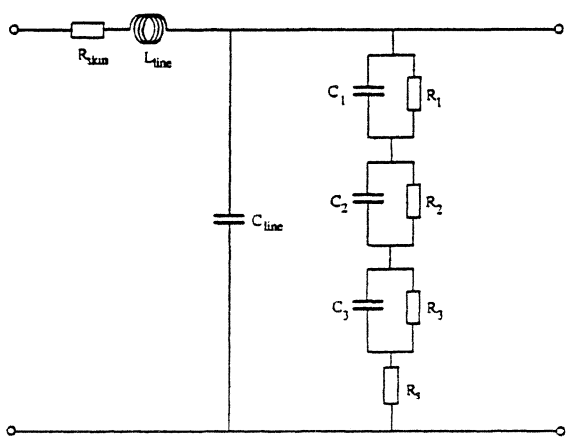


Fig. 4 Equivalent Circuit of One Section of an NLTL

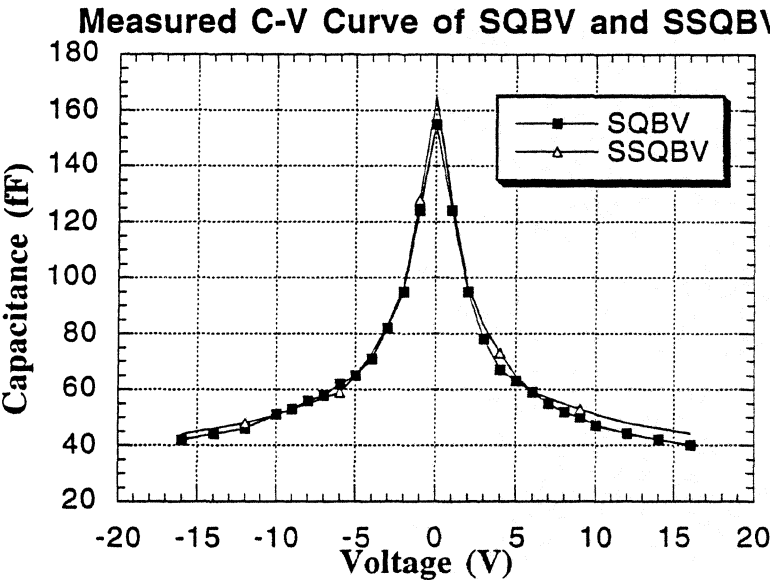


Fig. 5 Measured C-V Curves

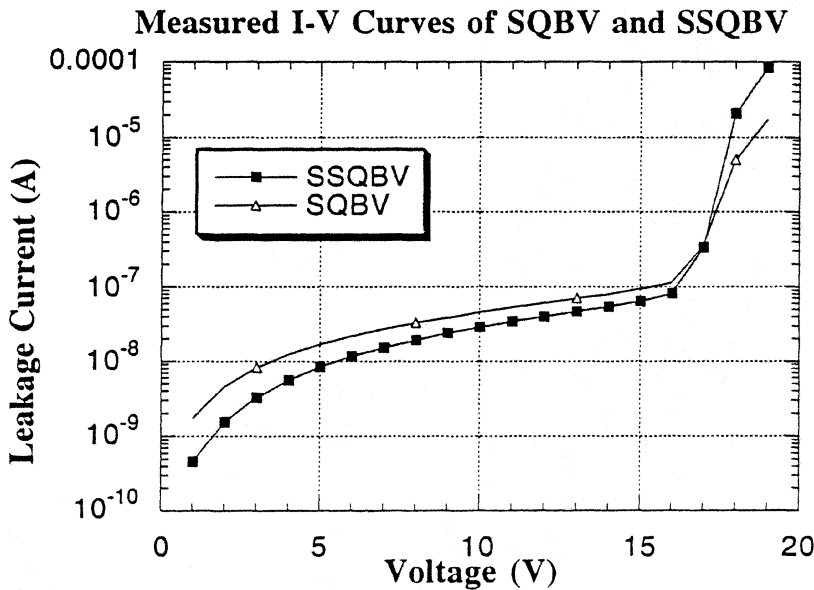


Fig. 6 Measured I-V Curves

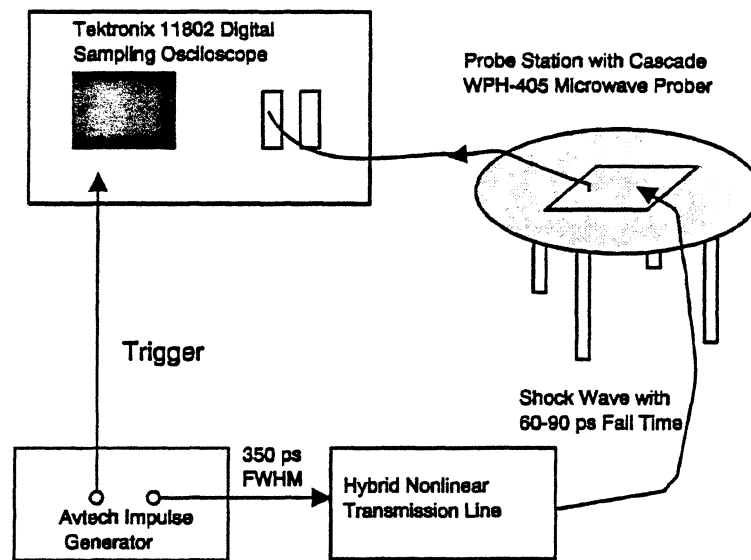


Fig. 7 Initial Test Setup

[REFERENCES]

- [1] M. Rodwell, M. Kamegawa, Ruai Yu, M. Case, E. Carman, K. Giboney, *IEEE Trans. on Microwave Theory and Techniques*, Vol. 39, 1194, (1991).
- [2] D. W. Van Der Weide, J. S. Bostak, B. A. Auld, and D. M. Bloom, *the 17th International Conference on Infrared and Millimeter Waves, Pasadena*, 97, (1992)
- [3] E. Carman, M. Case, M. Kamegawa, R. Yu, K. Giboney and M. Rodwell, *IEEE Trans. on Microwave Theory and Techniques*, Vol. 40, 819, (1992)
- [4] C. Raman, J. P. Sun, W. L. Chen, G. Munns, J. East, G. Haddad, *Third International Symposium on Space Terahertz Technology*, 146 (1992)
- [5] H-X. Liu, L. B. Sjogren, N. C. Luhmann, Jr., D. B. Rutledge, *International Journal of Infrared and Millimeter Waves*, Vol. 13, 251, (1992)
- [6] W-M. Zhang, H. Shi, C.W. Domier, N.C. Luhmann, Jr., *the 17th International Conference on Infrared and Millimeter Waves, Pasadena*, 408 (1992).

MONOLITHIC MILLIMETER WAVE BEAM CONTROL GRID

Xiaohui Qin*, W-M. Zhang*, J.Y. Liao*, R.P. Hsia**, W.R. Geck*, C.W. Domier**,
N.C. Luhmann, Jr.**, W. Berk†, S. Duncan† and D.W. Tu†

[ABSTRACT]

Monolithic integrated diode grid beam controllers can perform beam steering/focusing, switching and phase/amplitude modulation functions at relatively high power levels. Wide angle reflection beam steerer arrays have been designed for use at 60 GHz. In our design, a stacked grid pair with an optimum unit cell size is predicted to provide an $\sim 360^\circ$ phase range with a constant insertion loss of ~ 1.5 dB (average loss of 1.0 dB) in the reflection mode when a back reflector is employed. Such a stacked grid pair can function as a beam focuser and modulator as well as a beam switch (45 dB contrast ratio at 60 GHz and a minimum loss of 0.5 dB).

[INTRODUCTION]

Numerous application areas of current interest require electronic systems operating in the millimeter and submillimeter-wave frequency regime. Examples of such applications include fusion plasma diagnostics, radar (including automobile collision-avoidance radar), communications and imaging [1,2]. Both transmitters and receivers are required, with high speed electronic scanning capabilities highly desirable. A diode grid phase shifter has been successfully fabricated by W. Lam [3,4], with a measured 70° phase shift with 6.5 dB loss, at 93 GHz. To expand the phase range to 360° , a quasi-optical version of a method used in microwave circuits was suggested [5,6], in which two such arrays were stacked together. Electronically-controlled beam control arrays for use at D-band (110-170 GHz) have been built and have demonstrated amplitude modulation of the transmitted beam at 165 GHz. This was not designed for high switching speed but still resulted in a measured modulation response which was flat up to 50 MHz, with a 3 dB point of ≈ 150 MHz. The transmittance control is over the range of 20% to 50% at 99 GHz, and 20% to 70% at 165 GHz. A usable "flat amplitude" phase shift of 70° has been observed with a measured insertion loss of 3.5 dB of the reflected beam. Limited beam steering and beam focusing/defocusing has also been experimentally demonstrated at 120 GHz [7]. In addition, a high speed transmission beam switch array has been designed and built employing a coplanar waveguide bias arrangement, resulting in 300 MHz switching speed at V band and D band [8]. Finally, an initial demonstration of Schottky photodiode transmitted beam controller has been successfully performed albeit with further work required to produce the low loss, large phase range and contrast ratio necessary for practical applications. [9] The above experimental results were in good agreement with theoretical predictions, thereby motivating the current work where high performance beam

control arrays have been designed, and fabricated with testing underway. These are predicted to provide the performance parameters required for actual applications.

Figure 1. illustrates a section of an array fabricated in these studies. The two dimensional periodic grids loaded with Schottky varactor diodes comprise a surface whose reactance is controlled by the bias imposed on the individual diodes. In transmission, the changing reactance with bias allows the amplitude of the transmitted wave to be electronically modulated. In reflection, the changing reactance with bias controls the phase of the reflected wave such that a uniform variation of the phase across the grid performs phase shift, a linear variation sets the direction of the reflected beam and a quadratic variation of the phase focuses the reflected beam.

[DESIGNS AND DISCUSSIONS]

A monolithic millimeter wave beam control array consists of thousands of Schottky varactor diodes (shown partly in Fig. 1). The capacitance of the varactor changes with the applied bias voltage, resulting in an associated change in the varactor grid reactance. This capacitance-voltage (C-V) variation allows the array to function as an electrically or optically controlled phase shifter, amplitude modulator, beam focuser/defocuser, and beam steerer, etc. in either the reflection or transmission mode.

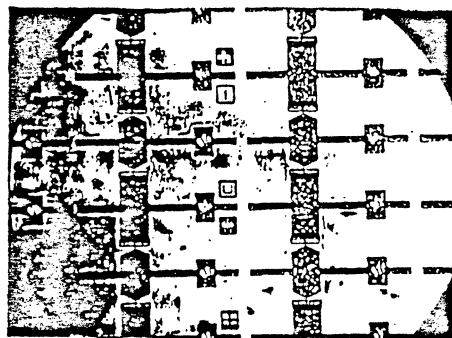


Figure 1. Photograph of a section of an array fabricated at Martin Marietta Laboratories, (Baltimore.)

Four beam control arrays have been fabricated on 3" diameter GaAs substrates. The primary goal for the device profile is to provide a suitable C-V characteristic with a minimum of conduction current and a large capacitance variation range over the useful bias voltage range. The varactor diode consists of Au/Ti/Pt as the Schottky contact, a $0.7\ \mu\text{m}$ thick, $6.0 \times 10^{16}\ \text{cm}^{-3}$ doped n type epi-layer and a $2.5\ \mu\text{m}$ thick, $6 \times 10^{18}\ \text{cm}^{-3}$ heavily doped n⁺ type epi-layer. The measured C_{max} value is $\sim 80\ \text{fF}$, C_{min} is $\sim 10\ \text{fF}$, and $C_{\text{parasitic}}$ is $\sim 8\ \text{fF}$ for the $8\ \mu\text{m}$ diameter diodes. The typical breakdown voltage is $\sim 12\ \text{V}$. Simulations show that a low loss transmission switch and wide angle reflection beam steerer can be achieved with a stacked grid pair of such diodes in an optimum grid structure design. The grid is a two dimensional periodic grid loaded with Schottky varactor diodes. The symmetry of the grid imposes boundary conditions, which define a unit cell as shown in Fig. 2. This reduces the problem of analyzing the grid to that of analyzing an equivalent waveguide. The equivalent waveguide has electric walls on the top and bottom, and magnetic walls on the sides, which extend along the z axis. The varactor resides in the $z=0$ plane. An accurate solution has been obtained by L.B. Sjögren [10] by segmenting the current and applying the method of moments to construct an equivalent circuit model of the

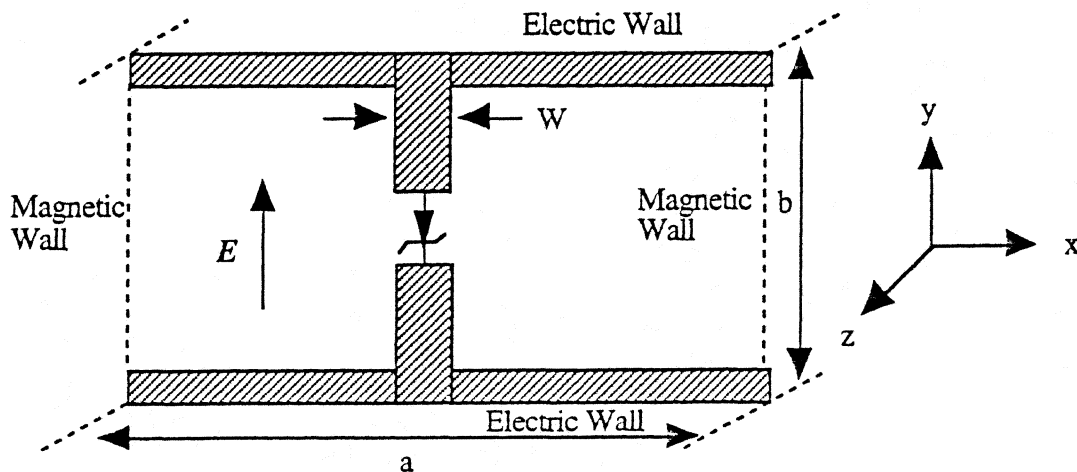


Fig. 2 Illustration of the unit cell of the beam control grid (E field and current are oriented parallel to the vertical diode embedding strip).

unit cell as shown in Fig. 3. The horizontal leads are bias lines, and the vertical lines serve as antennas. The equivalent impedance of the grid is represented by Z_g .

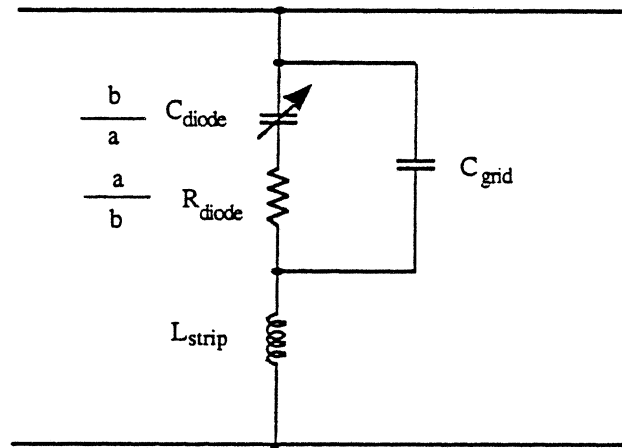


Fig. 3. An equivalent circuit model of the unit cell of beam control grid

The basic operation of the array can be explained by the quasi-optical plane wave approximation. A millimeter-wave beam incident upon the array is modeled as a TEM wave propagating on a transmission line representing the medium through which the beam is propagating. Simulations have demonstrated that for a stacked pair of varactor grids, large reflected beam phase range and transmitted beam amplitude On/Off contrast ratio can be achieved at the design frequency due to the composite effect of the two grids.[4] Figures 4 and 5 illustrate the stacked configuration for reflected and transmitted beam control. Simulations have been performed to optimize the grid structure for high performance of the reflection phase shifter, beam steerer and transmission amplitude switch at the design frequency of 60 GHz. A unit cell size of $900 \times 360 \mu\text{m}^2$ with a vertical strip width of $150 \mu\text{m}$ is found to represent the optimum grid design. A stacked grid pair of such structures provides a large phase range of $\sim 320^\circ$ at ~ 61 GHz with a maximum insertion loss of 3.5 dB.

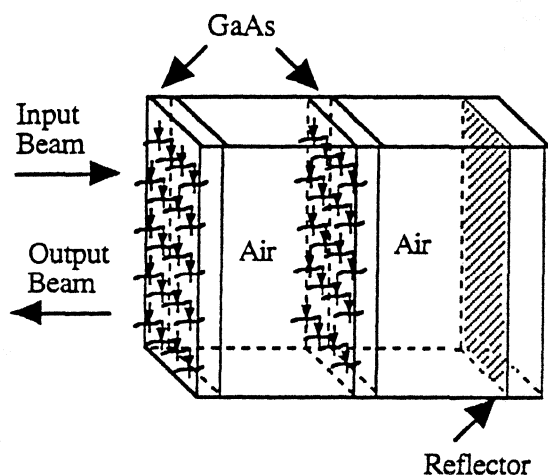


Fig. 4 Stack configuration for reflected beam control

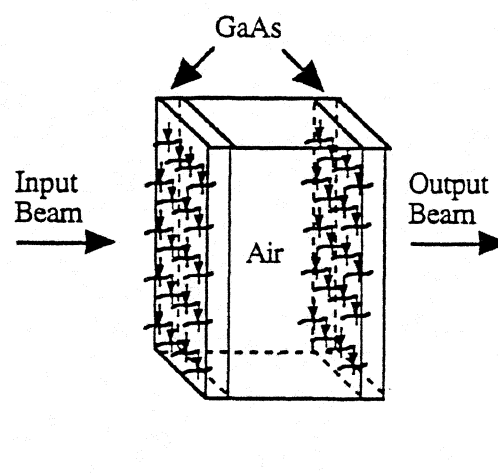


Fig. 5 Stack configuration for transmitted beam control

This grid pair configuration will also serve as a good transmission switch with a contrast ratio of ~ 45 dB (the contrast ratio is defined as the ratio of the transmitted power in the ON state to the transmitted power in the OFF state). The minimum insertion loss is ~ 3 dB at 60 GHz and ~ 0.5 dB at 45 GHz. The present dc bias arrangement is predicted to result in a switching speed of ~ 100 MHz. For fast switching application, coplanar waveguide bias lines will be employed. Here, it is projected that switching speeds as fast as several hundred picoseconds may be obtained. Automated low frequency characterization has been performed, using a computer controlled measurement system. Figure 6 illustrates the I-V mapping of the varactor diodes contained in a small section of the array. All diodes have been mapped and all detected shorted diodes have been removed from the arrays.

The typical measured diode breakdown voltage is ~ 10 V. Typical C-V characteristics are shown in Fig. 7, together with the envelope (spread) in parameters.



Fig. 6 I-V map of an array section 47 mm X 5.4 mm, (810 elements), where "@,A,B,C,D,*" represent different diode breakdown voltages.

Simulation results employing the measured low frequency and dc parameters of the diodes are illustrated in Figs. 8, 9(a) & 9(b). An ON/OFF contrast ratio of ~50 dB is predicted when the array serves as an transmission switch at 60 GHz. A reflection phase range of ~330° with a maximum insertion loss of ~3 dB (average loss of ~2.5 dB) is predicted at ~60 GHz.

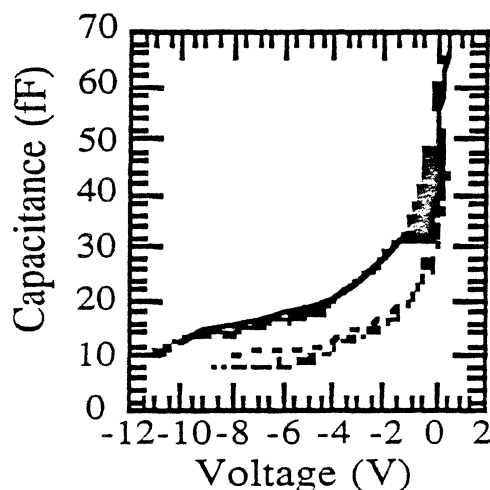


Fig. 7 Typical C-V Characteristics.

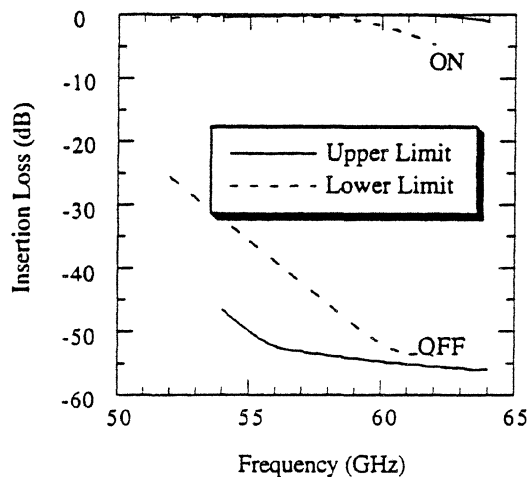


Fig. 8 Insertion Loss Envelope of Transmitted Beam.

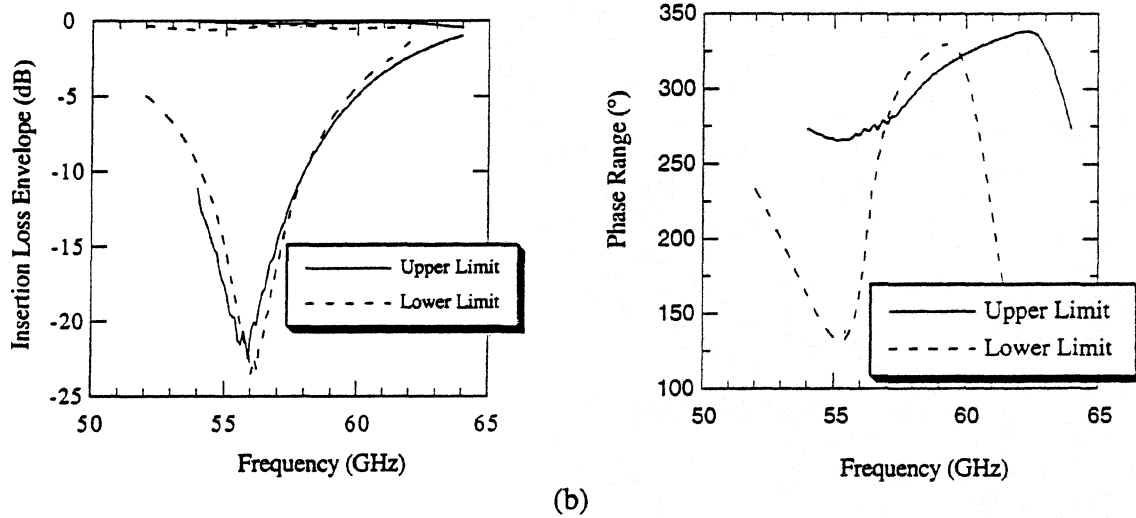


Fig. 9 (a) Insertion Loss Envelope, (b) Phase Range of Reflected Beam.

By non-identically biasing the two grids, a full 360° is predicted with a flat insertion loss of 1.5 dB. (see Figs. 10 (a) & (b))

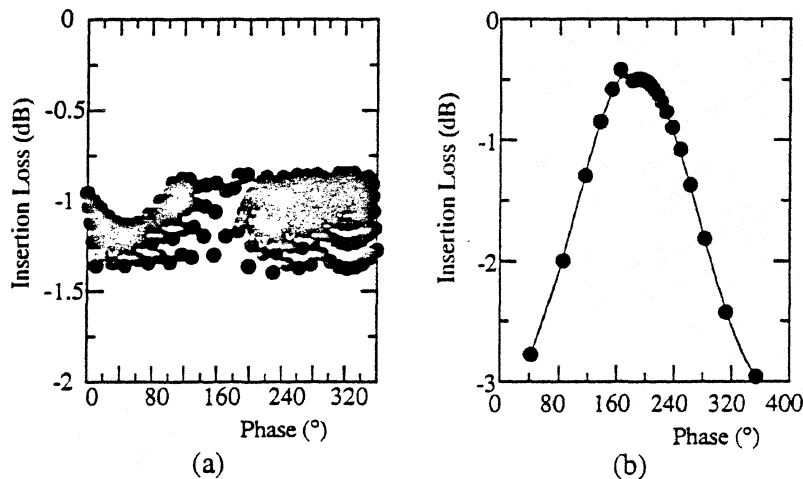


Fig. 10 Simulation results of reflected beam with non-identical (a) and identical bias (b) of the beam control grid pair

[MILLIMETER WAVE TESTING]

Reflection measurements of single grid and two grid configurations, including reflected phase shifting, beam steering, beam focusing/defocusing and frequency shifting are

underway. Transmission measurements of single and two grid configurations, including transmitted beam switching and modulation are also being performed currently. All the above testing utilizes a computer controlled system. The biasing is also controlled by an IBM PC computer through 64 channels of D/A converters for optimization of the bias voltage across the grids to maximize the On/Off contrast ratio for the switching and the phase range of the reflected phase shifter with minimum insertion loss envelope. The millimeter wave steering testing will be performed with a 6-axis computer controlled arm with control over the desired beam direction obtained by varying the bias across the grids linearly. Antenna patterns for the steered beam can be measured with the arm. Overmoded waveguide may be used to test the transmitted power for amplitude modulators. [8]

High performance 60 GHz two-grid Schottky varactor beam control arrays (including reflection beam phase shifters, steerers, transmission beam modulators and switches) have been designed. 3-4 dB insertion loss, 330° phase shift, 45 dB contrast ratio have been predicted by identically biasing the two grids pair. ~ 1.5 dB constant insertion loss, 360° phase shift can be theoretically achieved by biasing the two grids pair nonidentically. Millimeter wave testing in reflection/transmission modes are underway.

This project is supported by the Department of Energy at UCLA under contract DE-FG03-86ER-53225 and U.S. DOE at LLNL under contract W-7405-ENG-48 and the Joint Services and Electronics Program under contract F4962092-C-0055.

*Dept. of Electrical Engineering, University of California, Los Angeles, CA 90024

**Dept. of Applied Science, University of California, Davis, CA 95616

†Martin Marietta Laboratories, 1450 S. Rolling Road, Baltimore, Maryland 21227

References

1. K. Miyauchi, "Millimeter-Wave Communications," in Kenneth J. Button, Ed., *Infrared and Millimeter Waves*, 9 (Millimeter Components and Techniques, part 1), Ch. 1, pp. 1-93, Academic Press, New York, 1983.
2. D.B. Rutledge and S.E. Schwartz, "Planar Multimode Detector Arrays for Infrared and Millimeter-Wave Applications," *IEEE Journal of Quantum Electronics*, 17 (N. 3), pp. 407-414, March, 1981.
3. W.W. Lam, H.Z. Chen, K.S. Stolt, C.F. Jou, N.C. Luhmann, Jr., and D.B. Rutledge, "Millimeter-Wave Diode -Grid Phase Shifters," *IEEE Trans. Microwave Theory Tech*, 36 (N. 5), pp. 902-907, 1988.
4. W.W. Lam, "Millimeter-Wave Monolithic Schottky Diode-Grid Phase shifter," Ph.D thesis, California Institute of Technology, 1987.
5. W.W. Lam, C.F. Jou, N.C. Luhmann, Jr., and D.B. Rutledge, "Diode Grids for Electric Beam Steering and Frequency Multiplication," *Intl. J. of Infrared and Millimeter Waves*, 7, pp. 27-41, 1986.
6. Robert V. Garver, "360 Degree Varactor Linear Phase Modulator", *IEEE Trans. Microwave Theory Tech*, 17 (N. 3), pp. 137-147, 1969.
7. L.B. Sjogren, "Diode Array Beam Controllers," Ph.D thesis, University of California, Los Angeles, 1993.
8. T.Y. Liu, "Monolithic Schottky Diode Switching Array," M.S thesis, University of California, Los Angeles, 1994.
9. F. Wang, "Monolithic Schottky Photodiode Millimeter Wave Beam Control Arrays," M.S thesis, University of California, Los Angeles, 1994.

A NOVEL BIASED ANTI-PARALLEL SCHOTTKY DIODE STRUCTURE FOR SUBHARMONIC MIXING[‡]

Trong-Huang Lee[†], Chen-Yu Chi[‡], Jack R. East[‡],
Gabriel M. Rebeiz[‡], and George I. Haddad[‡]

[†]Jet Propulsion Laboratory
California Institute of Technology
Pasadena, California

[‡]NASA/Center for Space Terahertz Technology
The University of Michigan
Ann Arbor, Michigan 48109

ABSTRACT

Subharmonically-pumped mixers using zero-biased anti-parallel Schottky diode pairs produce good results but require a larger LO power than biased Schottky diodes. Presented here is a novel planar-diode anti-parallel pair that allows independent biasing of the two diodes. This diode pair is integrated into a quasi-optical wideband receiver and the RF measurements on a 1.2 μm anode diameter pair show a reduced LO power requirement at 180 GHz by a factor of 2 to 3 with a similar DSB conversion loss and noise temperature (9.7 dB and 1850°K) to an unbiased Schottky diode pair. This structure has potential for applications at submillimeter-wave frequencies where a large amount of LO power is not easily available.

I. INTRODUCTION

Space-borne receivers operating in the submillimeter region of the electromagnetic spectrum employ subharmonically-pumped (SHP) mixers because of the lack of adequate

[‡] This work is supported by NASA under Grant no. NAGW-1334.

local oscillator (LO) power at fundamental frequencies. Such mixers utilize local oscillators at one half the signal frequency where more LO power is usually available [1,2]. Recently, SHP mixers that were realized by a pair of anti-parallel Schottky diodes using planar-diode technology have produced excellent results at 200 GHz [3,5]. However, most of these diodes are zero-biased, and require a comparably large LO power. The use of an individually-biased diode pair has the advantages of lowering the turn-on voltage in the RF equivalent circuits and effectively reducing the LO power requirement. This scheme can be easily realized using a novel anti-parallel planar diode pair on a planar antenna with a biasing split as introduced in this paper.

II. DEVICE AND ANTENNA DESIGN

The anti-parallel diode pairs contain two identical GaAs Schottky diodes with opposite polarities. The anodes are formed by evaporating Ti/Pt/Au (500/500/1000 Å) on a $3 \times 10^{17} \text{ cm}^{-3}$ n⁺ epitaxial layer. The initially fabricated diodes are 4, 2, and 1.2 μm in diameter, resulting from an optical exposure system. The devices were fabricated using planar-diode technology proposed in [4], modified to include a biasing structure. The device layout is illustrated in Figure 1. This includes a surface channel, air-bridges, bias arms, and an overlay capacitor for RF coupling. The two bias arms are DC isolated by a 2.5 μm deep etched trench, but are RF shorted by the overlay capacitor. The overlay capacitor is a sputtered SiO₂/metal/SiO₂ tri-layer fabricated via a lift-off process after the trench is formed. The sandwiched metal layer is 6000 Å thick, enough to provide two skin depths at 90 GHz. The underlying GaAs device substrate is completely removed and replaced with a 3 mil quartz support, which is then diced into single devices. Additional fabrication details are given in [5].

The chip dimensions of a diced device on the quartz carrier are 300 μm long by 120 μm wide by 75 μm high. The quartz carrier, which has a lower dielectric constant than GaAs, reduces the pad-to-pad parasitic capacitance. The flip-chip mounting technique is used to epoxy single devices down to a log-periodic antenna.

The log-periodic antenna for the separately biased Schottky diodes is modified from the design described in [6]. This log-periodic antenna covers 35 GHz to 350 GHz with $\sigma=0.707$ and $\tau=0.5$. The angles of the metal teeth (α) and the trunk (β) are 30° and 60° , respectively. The antenna input impedance is independent of frequency and is 74 Ω on a silicon substrate ($\epsilon_r=11.7$). The layout is given in Figure 2. This includes one arm of the antenna without a split connecting to a quarter-wavelength transmission line at the IF (1.4 GHz) and an RF choke to provide a DC ground as IF ground. The other arm has a 20 μm split for biasing considerations, covered by a sputtered SiO_2 /metal/ SiO_2 tri-layer fabricated by a lift-off process to provide RF coupling to the antenna. This tri-layer is 1200/6000/500 \AA in thickness, similar to the overlay capacitor used in the AC short in the device contact pad.

The log-periodic antenna is placed on the back of a 12.7 mm-diameter hemispherical silicon dielectric lens and spacing wafers for 2400 μm extension [7]. The use of the silicon lens and extension wafers helps to eliminate substrate mode propagation and enhance gain and Gaussian coupling efficiency. The measured antenna patterns at 90 GHz are shown in Figure 3. The log-periodic antenna is linearly polarized but considerable cross-polarization components are found in the E- and H-planes (-5 to -10 dB). The antenna directivity calculated from full 2-dimensional pattern measurements is 138 at 90 GHz.

III. DC AND 180 GHz PERFORMANCE

Listed in Table 1 are the extracted DC parameters from measured data for 2 and 1.2 μm diodes from a Schottky diode pair. The measured DC parameters from adjacent diodes in an anti-parallel diode pair are very similar. All parameters except capacitances are obtained from the least-squares fitting of experimental $\ln(I)$ - V curves. All diodes have a barrier height close to 0.7 V, resulting from the evaporated Ti/Pt/Au Schottky metals. The diode capacitance, which consists of the zero-bias junction capacitance and pad-to-pad and finger-to-pad parasitic capacitances, was measured at 1 MHz using the high resolution mode of an HP 4275 LRC meter. The pad-to-pad capacitance was measured by removing the air-bridges. The zero-biased junction capacitance was estimated from the anode area and the depletion width of a 0.7 V barrier height, considering the effect of image force lowering. The replacement of a GaAs substrate with a quartz substrate results in a reduction of 10 ± 4 fF in parasitic capacitances.

The video detection measurement at 90 GHz was described in [5] and [6]. This is performed for both diodes to verify their similarity at 90 GHz. The measured and calculated video responsivity vs. bias current for a 1.2 μm -diameter diode pair are shown in Figure 4. The peak video responsivity is about 2600 V/W at a bias current of 10 μA .

The mixer performance of a 1.2 μm diameter diode pair was measured at 180 GHz using the hot-and-cold load method. The setup, conversion loss and noise temperature calculations are essentially identical to the one discussed in [6]. The IF mismatch loss is measured by the power reflection technique. The measured DSB diode conversion loss is shown in Figure 5. At 180 GHz, a minimum DSB conversion loss of 9.7 dB is found at a bias current of 100 μA per diode with an estimated available LO power from a 74

Ω source at the antenna terminals of 4.5 mW. The corresponding DSB noise temperature minimum is 1850°K. It is important to note that this log-periodic antenna on an extended silicon substrate lens contributes approximately 3 dB of loss in a Gaussian beam quasi-optical system (see [6] for more details). This means that the anti-parallel diode conversion loss is around 9.7 dB SSB from a 74 Ω RF source. Increasing the bias to 400 μ A reduces the LO power requirement to about 3 mW, as compared to 9 mW resulting from a zero-biased diode pair using an identical setup [6]. The DSB conversion loss (9.8 dB) and noise temperature (1890°K) remain essentially the same.

IV. CONCLUSION

In this paper, we have shown a novel structure for a separately biased Schottky diode pair that has a good video responsivity and a factor of 3 reduction in LO power requirement at 90 GHz. At 180 GHz a quasi-optical receiver results in a minimum DSB conversion loss of 9.7 dB and noise temperature of 1850°K at a bias current of 100 μ A. The fabrication of such devices only requires an extra tri-layer lift-off process in addition to the usual planar-diode technology, and is suitable for integrated receiver fabrication. This structure is well suited for higher frequency applications where LO power requirements become a limiting factor in mixer operation.

REFERENCES

- [1] M. V. Schneider, and W. W. Snell, "Harmonically Pumped Stripline Downconverter," *IEEE Trans. Microwave Theory Tech.*, vol. MTT-23, pp. 271-275, Mar. 1975.
- [2] M. Cohn, J. E. Degenford, and B. A. Newman, "Harmonic Mixing with an Antiparallel Diode Pair," *IEEE Trans. Microwave Theory Tech.*, vol. MTT-23, pp. 667-673, Aug. 1975.
- [3] P. H. Siegel, R. J. Dengler, I. Mehdi, W. Bishop, and T. W. Crowe, "A 200 GHz Planar Diode Subharmonically Pumped Waveguide Mixer with State-of-the Art Performance," *IEEE MTT-S Int. Symp.*, pp. 595-598, June 3, 1992.
- [4] W. L. Bishop, E. R. Meiburg, R. J. Mattauch, and T. W. Crowe, "A Micron Thickness, Planar Schottky Barrier Diode Chip for Terahertz Applications with Theoretical Minimum Parasitic Capacitance," *IEEE MTT-S Int. Symp.*, pp. 1305-1308, May 1990.
- [5] T. H. Lee, J. R. East, C. Y. Chi, G. M. Rebeiz, R. J. Dengler, I. Mehdi, P. H. Siegel, and G. I. Haddad, "The Fabrication and Performance of Planar Doped Barrier Diodes as 200 GHz Subharmonically-Pumped Mixers," to be published in *IEEE Trans. Microwave Theory Tech.*, Apr. 1994.
- [6] B. K. Kormanyos, P. H. Ostdiek, W. L. Bishop, T. W. Crowe, and G. M. Rebeiz, "A Planar Wideband 80-200 GHz Subharmonic Receiver," *IEEE Trans. Microwave Theory Tech.*, vol. 41, no. 10, pp. 1730-1737, Oct. 1993.
- [7] D. F. Filipovic, S. S. Gearhart, and G. M. Rebeiz. "Double-Slot Antenna on Extended Hemispherical and Elliptical Silicon Dielectric Lenses," *IEEE Trans.*

Microwave Theory Tech., vol. 41, no. 10, pp. 1738-1749, Oct. 1993.

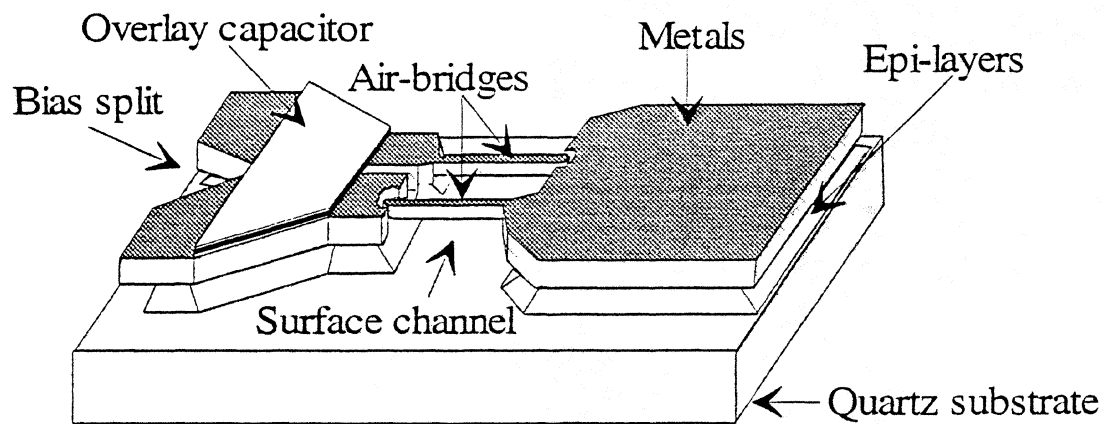


Figure 1: The novel anti-parallel diode structure with a biasing split and overlay capacitor before mounting on a log-periodic antenna. The GaAs substrate has been removed completely and replaced with a 3 mil quartz substrate.

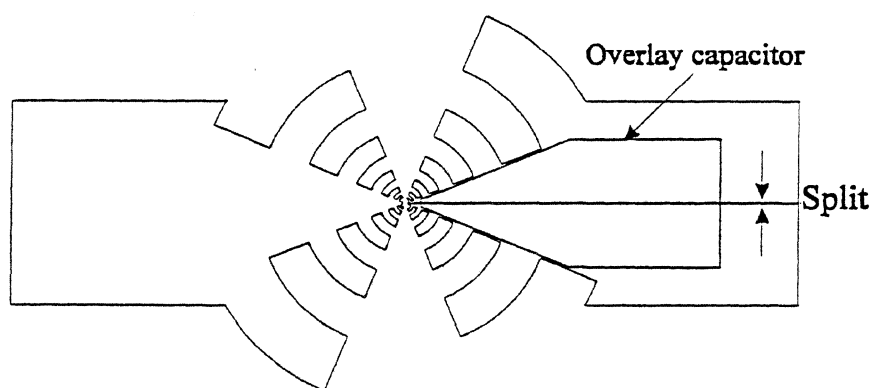


Figure 2: The layout of a log-periodic antenna with a split and an overlay capacitor.

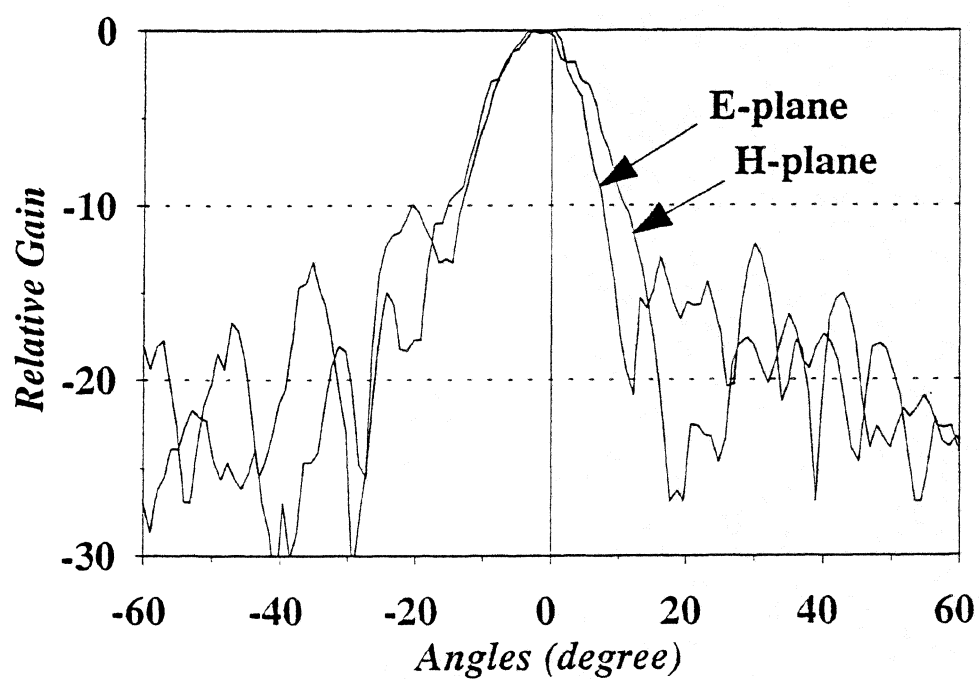


Figure 3: Measured E and H-plane patterns of a log-periodic antenna on 12.7 mm diameter silicon substrate lens at 90 GHz.

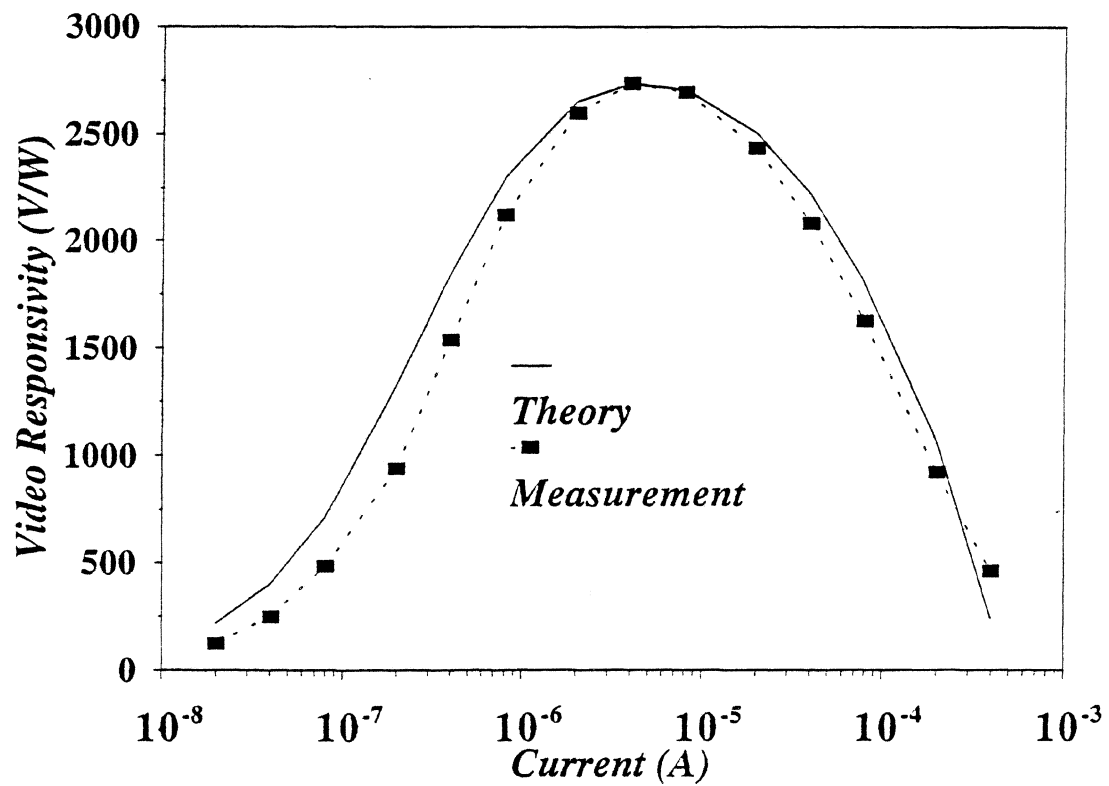
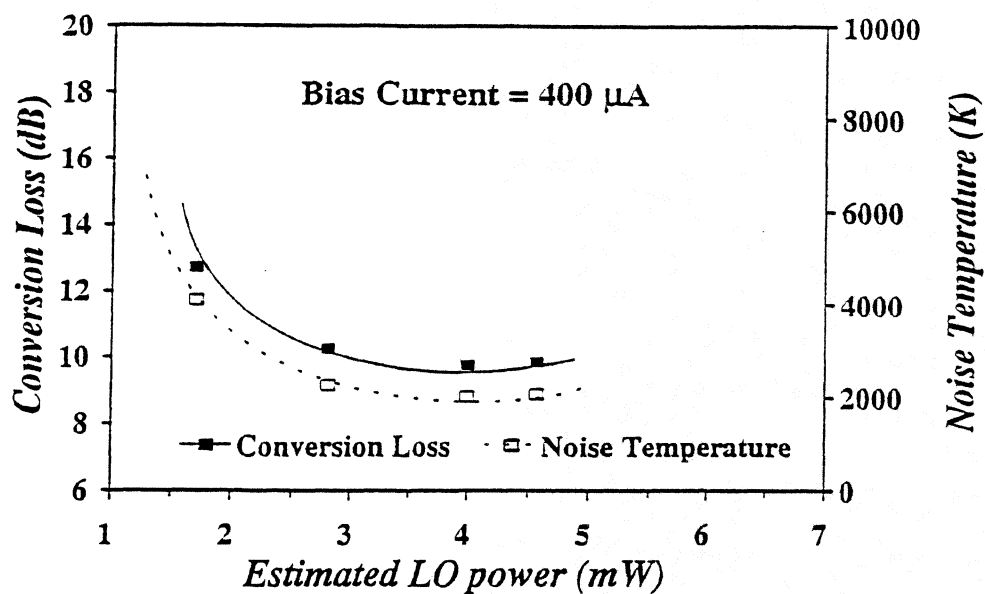
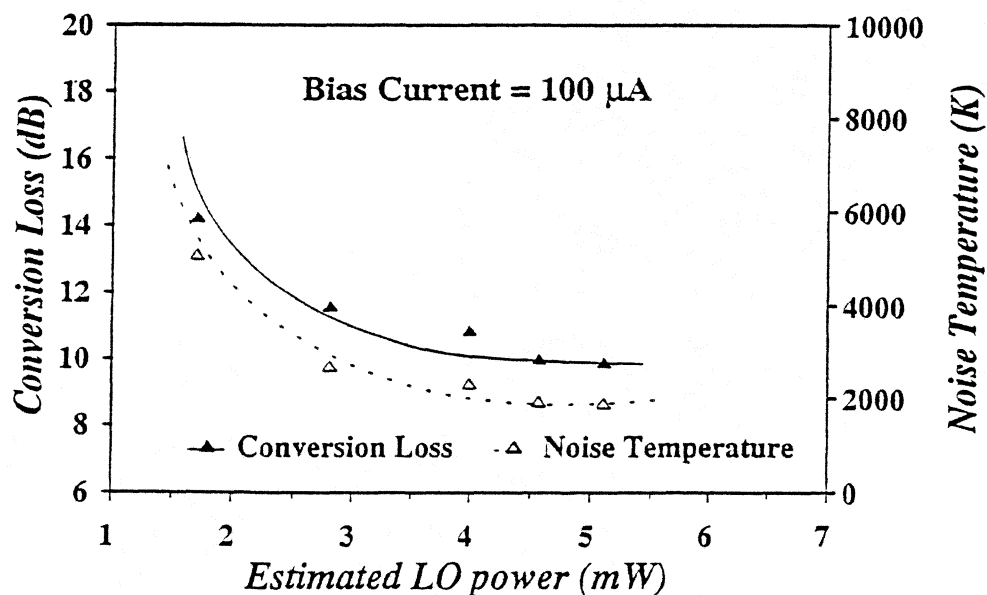


Figure 4: The measured and theoretical video responsivity (measured voltage over RF power available at log-periodic antenna terminals) for a 1.2 μm diameter Schottky diode at 90 GHz.



(a)



(b)

Figure 5: Measured conversion loss and noise temperature at 184 GHz vs. estimated LO power at 90 GHz for 1.2 μ m diameter anti-parallel diodes, biased at (a) 400 and (b) 100 μ A.

Parameters	R_s (Ω)	n	I_s (A)	ϕ_{barrier} (V)	Capacitance (fF)		
					C_j	$C_{\text{pad-to-pad}}$	$C_{\text{finger-to-pad}}$
2.0 μm	7.8	1.17	2.0×10^{-14}	0.716	6.3	< 4 fF	< 3 fF
	5.1	1.18	5.1×10^{-14}	0.693			
1.2 μm	14	1.15	6.7×10^{-15}	0.719	2.3	< 4	< 2
	15	1.20	1.2×10^{-14}	0.704			

Table 1: Anti-parallel Schottky diode DC parameters extracted from I-V and low frequency capacitance measurements.

GaAs Schottky Diodes for Atmospheric Measurements at 2.5 THz

Perry A. D. Wood, David W. Porterfield,
William L. Bishop and Thomas W. Crowe

*Semiconductor Device Laboratory
Department of Electrical Engineering
University of Virginia
Charlottesville, VA 22903*

ABSTRACT

OH is an important molecule in the chemistry of the upper atmosphere, and is most easily observed at 2.5 THz. GaAs Schottky diodes are currently the most sensitive heterodyne receiver elements for applications above 1 THz.

The 1T15 is a whisker contacted 0.25 micron anode diameter Schottky diode with an epilayer doping and thickness of 10^{18} cm^{-3} and 300 Å, respectively. At 2.5 THz and an LO pump power of 6 mW, the 1T15 achieved a DSB mixer temperature of 9300K and conversion loss of 13.2 dB. The LO power can be reduced to 3.4 mW with only a 5% increase in receiver noise temperature. It can be further reduced to about 2 mW and still maintain a receiver noise temperature of less than 15000K.

A discussion of improvements for whisker contacted diodes is presented. The use and fabrication of planar diodes at 2.5 THz is also considered.

BACKGROUND

In recent years studies of the upper atmosphere have become a priority for the scientific community. This has come about in part due to concerns about ozone depletion. There are many chemicals and processes involved in the ozone depletion cycle and each one of these must be studied. OH is a particularly important molecule which has yet to be studied on a global basis. This molecule can be most easily measured at 2.5 THz. NASA has planned a Microwave Limb Sounder (MLS) which will be flown as part of the Earth Observing System (EOS) [1]. This mission will require receivers at 215 GHz, 440 GHz, 640 GHz and 2.5 THz. It is the latter frequency that this paper will address.

SIS receivers have made tremendous improvements recently and now outperform Schottky mixers at frequencies up to around 600 GHz [2][3][4]. However, whisker contacted Schottky diodes mounted in a corner cube are the most sensitive detectors at 2.5 THz. The 1T15 Schottky diode, fabricated by the Semiconductor Device Laboratory of the University of Virginia, is a whisker contacted Schottky diode designed for mixing applications above 1 THz. The anode diameter has been reduced to 0.25 microns to reduce the junction capacitance. The epilayer doping density was increased to offset the increase in series resistance that would have resulted from the smaller anode as well as increasing the current where hot-electron noise begins to dominate. Also the epilayer thickness was reduced to

more closely match the thickness of the depletion layer during normal operation. The fabrication and design of the submicron anode diameter diodes is discussed in the literature [5][6].

Planar diodes offer an attractive alternative to whisker contacted diodes. They are inherently more rugged and allow for easier integration of antennas and matching structures. Bishop et al [7] have described the fabrication of such devices. Fabrication issues for 2.5 THz will be presented in a later section.

RESULTS

Three 1T15 diodes were tested at 2.5 THz. The physical specifications for these diodes are given in Table 1. The series resistance was calculated using a three point voltage measurement at 10, 100 and 1000 μA .

The video responsivity for these diodes was measured using a Keating PM103 power meter as a reference. Fig. 1 is a schematic of the optical layout used to measure video

Table 1. Physical specifications of the tested 1T15 diodes.

Diode	Epilayer Thickness (\AA)	Epilayer Doping (cm^{-3})	Series Resistance (Ω)	Zero-Bias Capacitance (fF)	ΔV at 10-100 μA (mV)	Ideality Factor
1T15#47	300	10^{18}	18	0.22	105	1.6
1T15#12	300	10^{18}	20	0.25	102	1.6
1T15#50	300	10^{18}	20	0.27	99	1.6

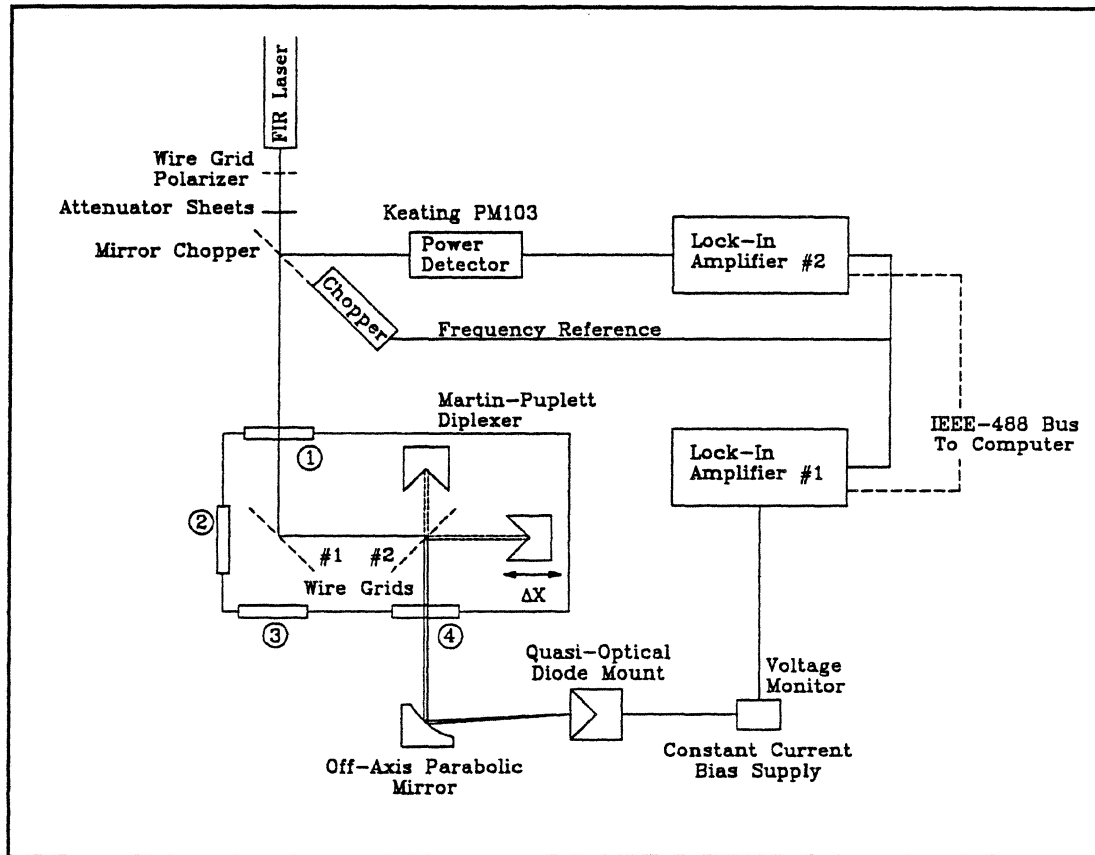


Figure 1. Optical schematic for video responsivity measurements.

responsivity. The distance to the Keating PM103 and to the diode mount were kept the same so that the incident power would be the same on both. All video responsivities were measured with a bias current of $1 \mu\text{A}$. The video responsivities for the three diodes are: 1T15#47, $R_v = 111 \text{ V/W}$; 1T15#12, $R_v = 102 \text{ V/W}$; and 1T15#50, $R_v = 87 \text{ V/W}$. We expect that a diode with a higher junction capacitance will have a lower video responsivity and our data fits this expected trend. However, because of the uncertainties in the capacitance and video responsivity measurements, this trend may be fortuitous.

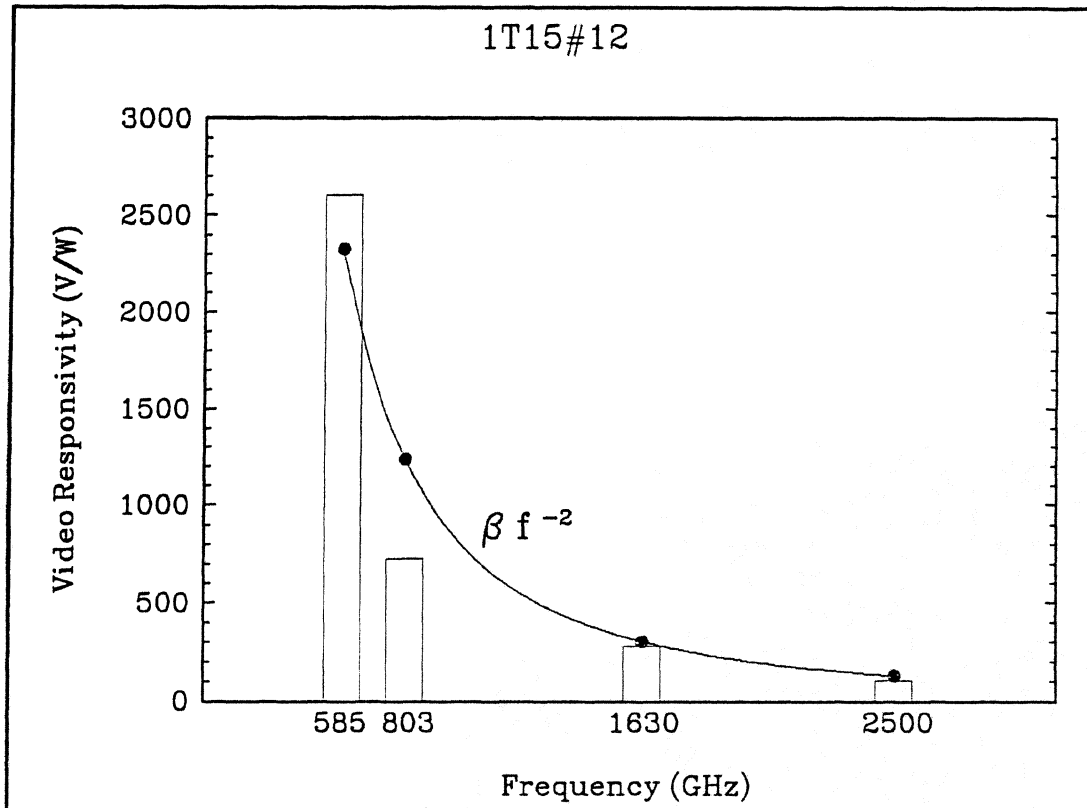


Figure 2. Video responsivity versus frequency for the 1T15#12 diode.

Video responsivity data for the 1T15#12 diode at lower frequencies is shown in Fig.

2. There is an approximate $1/f^2$ decrease in the responsivity as the frequency increases.

Video responsivity is a good indicator of LO power requirements as we shall see that the required LO power increases as f^2 .

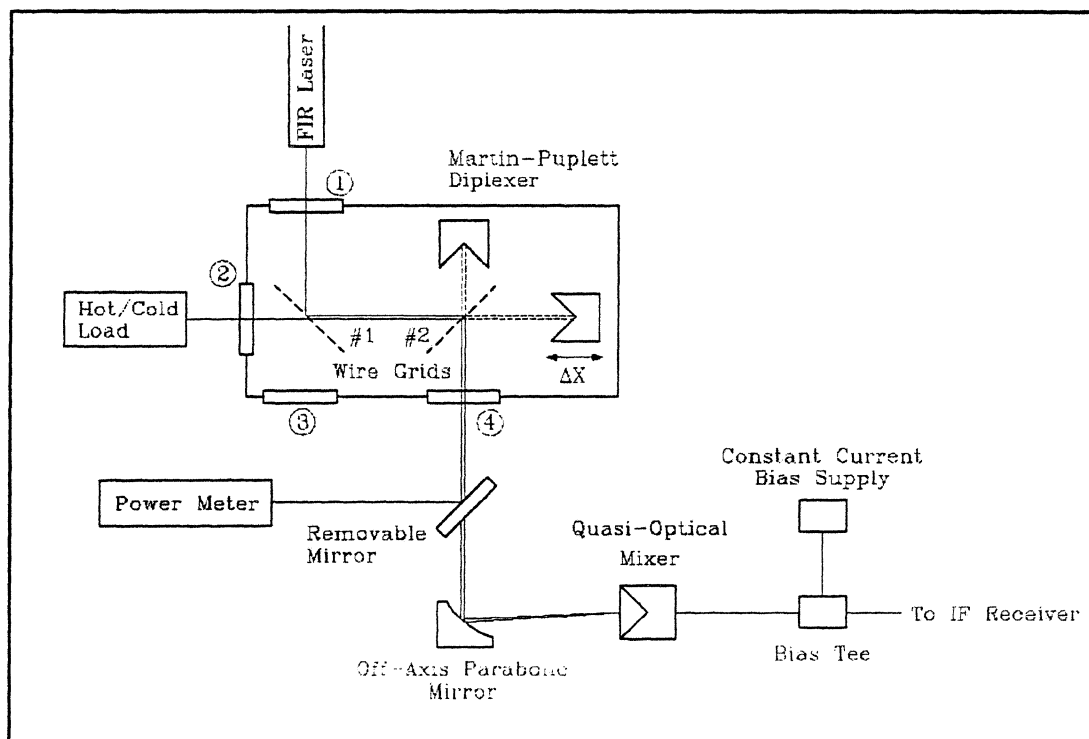


Figure 3. Optical layout used to measure receiver noise temperature.

Receiver noise measurements were made using the optical layout shown in Fig. 3. A Scientech 365 power meter was used because the noise measurements require an unchopped LO and the Scientech 365 meter, unlike the Keating PM103 meter, requires an unchopped signal. The Scientech 365 meter was placed so that the distance from the laser to the power meter was the same as the distance from the laser to the diode. Receiver noise temperature as well as mixer conversion loss and temperature were double sideband measurements. The IF receiver was operated at room temperature and had a noise temperature of 103K. An atmospheric absorption of 1 dB was measured over the signal path. This was calculated from the power difference as measured by the Scientech 365 meter over a 50 cm path length. The

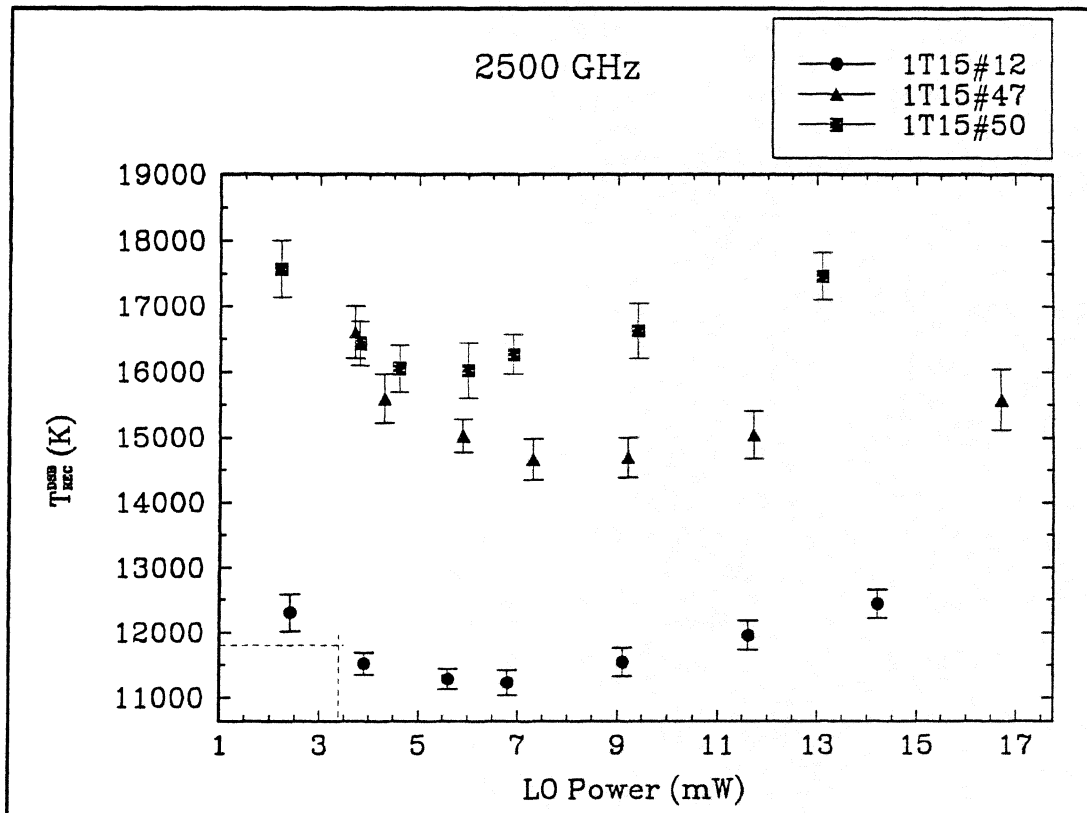


Figure 4. Graph of receiver temperature versus LO power for three 1T15 diodes. The dashed line in the lower left corner represents the minimum LO power for a 5% increase in receiver noise temperature.

hot/cold load was made from room temperature FIRM (Far Infrared Absorbing Material) and 77K FIRM. FIRM, developed at the University of Massachusetts Lowell, is a silicone based anechoic with low reflection at 2.5 THz [8].

The goals for these measurements were to achieve a receiver noise temperature of less than 15000K [9] and to determine the minimum LO power required to realize that result. A graph of LO power versus DSB receiver noise temperature is shown in Fig. 4. The 1T15#12

diode achieved the lowest receiver noise temperature, 11400K. Fig. 4 represents the best contacts out of three attempts for each diode. For the 1T15#47 and 1T15#50, these results were obtained once, while for the 1T15#12 these results were achieved with two different contacts. For all the diodes there was evidence of LO saturation because of the increase in receiver noise temperature at the higher power levels. The dashed lines in the lower left corner of Fig. 4 represent the power level (3.4 mW) where the receiver noise temperature of the 1T15#12 is only 5% higher than the minimum (11400K). We define this as the minimum

Table 2. Mixer results at 2.5 THz

Diode	P_{LO} (mW)	L'_m (dB)	T'_m (K)	T_{rec} (K)
1T15#47	9.6	14.1	12000	14700
	4.9	13.8	11600	14200
	2.3	14.4	12200	15000
1T15#12	6.2	13.1	9300	11400
	2.4	14.1	9900	12600
1T15#50	6.0	15.0	12900	16200

required LO power for optimum performance. Table 2 shows a breakdown of mixer temperature and conversion loss for different power levels. Both the 1T15#47 and 1T15#12 achieve a receiver noise temperature below 15000K even down to power levels near 2 mW. While the 1T15#50 diode had a receiver noise temperature greater than 15000K, it would have been less than 15000K had the IF noise temperature been 65K rather than 103K.

Fig. 5 shows the minimum LO power requirement versus frequency for the 1T15#12 diode. The required LO power increases approximately as the frequency squared. This is the inverse of the video responsivity trend. From this data we conclude that diodes with higher video responsivity generally have lower LO power requirements.

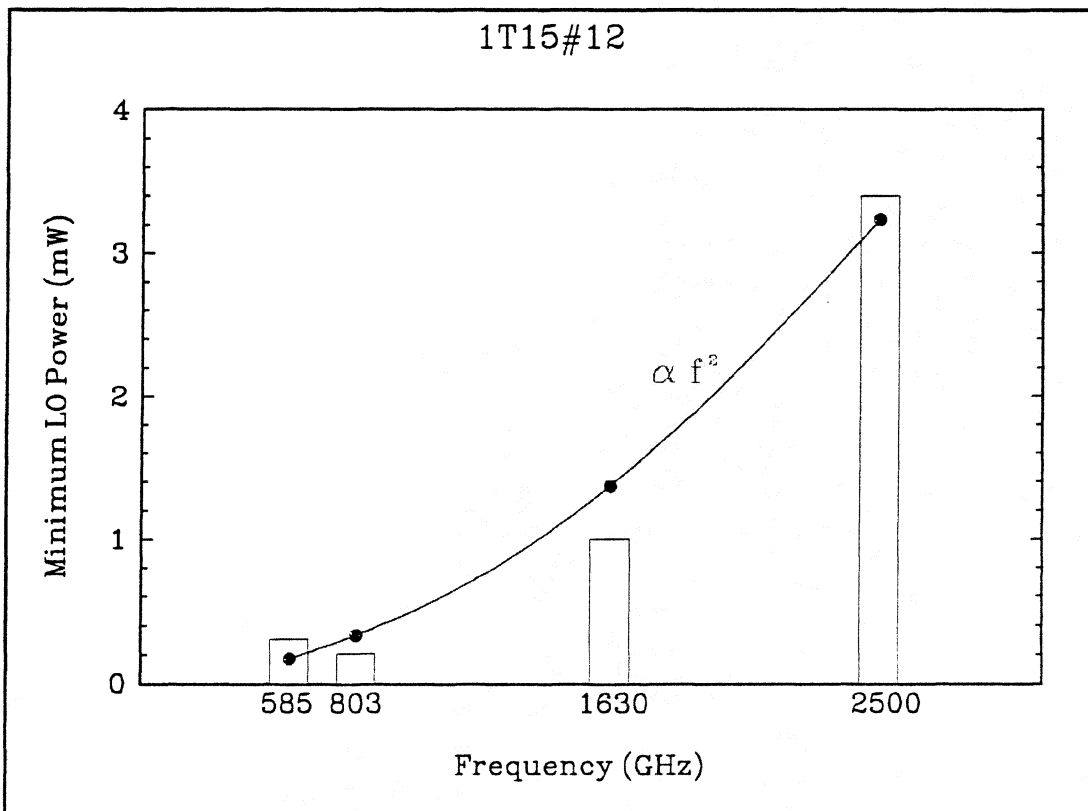


Figure 5. Minimum LO power versus frequency for the 1T15#12 diode.

The corner cube mixer mount has been designed with an IF impedance transformer. This transformer was designed for lightly doped ($2-4 \times 10^{17} \text{ cm}^{-3}$) and higher capacitance diodes. For the 1T15, S_{11} is about -7 to -9 dB. This mismatch was measured for each diode at the optimum operating point (lowest receiver noise temperature). Using the analysis of

Harris et al [10], we can remove the effect of the IF mismatch. To remove only the effect of the IF mismatch, we will assume that the optical coupling is perfect. Then we have;

$$T'_m = L'_m \Gamma^2 T_{\text{cir}} + T_m$$

$$L'_m = \frac{L_m}{1 - \Gamma^2}$$

where L'_m and T'_m are the uncorrected mixer conversion loss and temperature, respectively (see Table 2). T_{cir} is the temperature of the circulator resistor (300K), Γ is the reflection coefficient and L_m and T_m are the corrected mixer conversion loss and temperature, respectively. This analysis is shown in Table 3. The corrected mixer temperatures are about 10% lower, while the corrected conversion losses are about 0.6 to 0.9 dB lower.

Table 3. Correction for IF mismatch

Diode	Zero Bias C_{j0} (fF)	Receiver Noise T_{rec} (K)	Mixer Noise T_m (K)	Mixer Loss L'_m (dB)	S_{11} (dB)	LO Power (mW)	Corrected Mixer Noise T_m (K)	Corrected Mixer Loss L_m (dB)
1T15#12	0.25	11500	9300	13.2	-8.7	6.2	8500	12.6
1T15#47	0.22	14200	11600	13.9	-7.2	4.9	10300	13.0
1T15#50	0.27	16300	13000	15.1	-9.2	6.0	11800	14.5

DISCUSSION: PLANAR DIODES

Planar diodes are very attractive for space applications because of their inherent ruggedness compared to whisker contacted Schottky diodes. However, they are currently unable to be used at 2.5 THz. To achieve results comparable to whisker contacted diodes, the planar diodes need to be constructed using the same ideas, i.e., decrease the anode diameter to 0.25 microns or less and increase the epilayer doping. Fabricating sub micron anodes is possible, but the fabrication of the integrated antenna and the substrate present a challenge.

The radiation from an antenna on a substrate will be strongest through the higher dielectric substrate. The planar diode is made on a semi-insulating GaAs substrate. Between the metal antenna and substrate is a layer of n+ material. This n+ layer is conductive and therefore introduces losses. As the frequency of operation is increased this layer becomes a more significant parasitic. The n+ layer can be removed or thinned, except in a small area around the anode. This would bring the antenna structure closer to the semi-insulating substrate.

Decreasing the anode diameter is also important. This will present a challenge for alignment during fabrication. The finger across the air gap should be no larger than the anode itself to minimize parasitic capacitance.

CONCLUSIONS

The 1T15 diode is a very sensitive mixer at 2.5 THz. We measured a mixer temperature of 9300K and mixer conversion loss of 13.2 dB with an LO power of 6.2 mW. The minimum LO power for an increase of 5% in the minimum receiver noise temperature is 3.4 mW. The LO power can be further reduced to 2 mW for a receiver noise temperature of 15000K. Operation with small LO powers is important for satellite work where power is tightly budgeted.

Possible changes and improvements for the 1T15 include;

- Decrease the anode diameter: It is possible that a further reduction in anode diameter will improve noise performance and will certainly reduce LO power requirements.
- Improve the IF match: This can decrease the noise by about 10% and the conversion loss by 0.6 to 0.9 dB.
- Better coupling: The corner cube couples about 1/2 of the incident power. Improving the coupling will decrease the LO power requirements and decrease the noise temperature and conversion loss.
- Cooling: Cooling the 1T15 does not appear to alter the IV curve. Since the IV curve has not changed, then the diode should not be any more efficient as a mixer than it was at room temperature.

Planar diodes, though not currently viable at 2.5 THz, will no doubt be improved. The challenges to making efficient planar diodes at 2.5 THz are solvable and are being actively investigated.

ACKNOWLEDGEMENTS

This work has been supported by the National Science Foundation (ECS-9113123) and the U. S. Army Foreign Science Technology Center (DAHC90-91-C-0030).

REFERENCES

- [1] J. W. Waters and P. H. Siegel, "Applications of Millimeter and Submillimeter Technology to Earth's Upper Atmosphere: Results to Date and Potential for the Future," Fourth International Symposium on Space THz Technology, Los Angeles, CA, March 1993.
- [2] G. De Lange, C. E. Honingh, M. M. T. M. Dierichs, H. H. A. Schaeffer, H. Kuipers, R. A. Panhuyzen, T. M. Klapwijk, H. van de Stadt, M. W. M. de Graauw, E. Armandillo, "Quantum Limited Responsivity of a Nb/Al₂O₃/Nb SIS Waveguide Mixer at 460 GHz and First Results at 750 and 840 GHz," Fourth International Symposium on Space THz Technology, Los Angeles, CA, pp. 41-49, March 1993.
- [3] W. R. McGrath, P. Febvre, P. Batelaan, H. G. LeDuc, B. Bumble, M. A. Frerking, J. Hernichel, "A Submillimeter Wave SIS Receiver for 547 GHz," Fourth International Symposium on Space THz Technology, Los Angeles, CA, pp. 50-58, March 1993.
- [4] F. Schäfer, E. Kreysa, T. Lehnert, K. H. Gundlach, "A Planar SIS Receiver with Logperiodic Antenna for Submillimeter Wavelengths," Fourth International Symposium on Space THz Technology, Los Angeles, CA, pp. 661-665, March 1993.
- [5] T. W. Crowe, R. J. Mattauch, H. P. Röser, W. L. Bishop, W. C. B. Peatman, "GaAs Schottky Diodes for THz Mixing Application," Invited paper, Proc. of the IEEE, Special Issue on Terahertz Technology, Vol. 80, No. 11, Nov. 1992.
- [6] W. C. B. Peatman, P. A. D. Wood, D. Porterfield, T. W. Crowe, "Quarter-micrometer GaAs Schottky barrier diode with high video responsivity at 118 μm ," Appl. Phys. Lett., Vol. 61, No. 3, pp. 294-296, 20 July 1992.
- [7] W. L. Bishop, T. W. Crowe, R. J. Mattauch, "Planar GaAs Schottky Diode Fabrication: Progress and Challenges," Fourth International Symposium on Space THz Technology, Los Angeles, CA, pp. 415-429, March 1993.

- [8] R. H. Giles, A. J. Gatesman, J. Fitzgerald, S. Fisk, J. Waldman, "Tailoring Artificial Dielectric Materials at Terahertz Frequencies," Fourth International Symposium on Space THz Technology, Los Angeles, CA, pp. 124-133, March 1993.
- [9] J. W. Waters, "A Focused MLS for EOS," December 1991.
- [10] A. I. Harris, U. U. Graf, R. Genzel, "Measured Mixer Noise Temperature and Conversion Loss of a Cryogenic Schottky Diode Mixer Near 800 GHz," *Int. J. of Infrared and Millimeter Wave*, Vol 10, No. 11, pp. 1371-1376, Nov. 1989.

A MONOLITHIC DOUBLE-SLOT SCHOTTKY-DIODE RECEIVER

Steven S. Gearhart, and Gabriel M. Rebeiz

NASA/Center for Space Terahertz Technology
Electrical Engineering and Computer Science Department
University of Michigan
Ann Arbor, MI 48109-2122

ABSTRACT

A 250 GHz monolithic Schottky-diode receiver based on a double-slot antenna is presented. The double-slot antenna is placed on an extended hemispherical high-resistivity silicon substrate lens. The measured DSB conversion loss and noise temperature at 258 GHz are 7.8 ± 0.3 dB and 1600 ± 100 K for the antenna-mixer, respectively. A non-optimal polyethylene $\lambda_d/4$ matching-cap layer for the silicon lens improves the conversion loss and noise temperature by 1 dB, and another 0.7 dB improvement could be obtained with the use of a more optimal matching cap layer. The uniplanar double-slot antenna receiver is less than 0.3x1mm in size including the IF filter and represents the first fully monolithic 250 GHz receiver to-date. The measured performance is within 2-3 dB of the best 200+GHz waveguide receivers using planar Schottky diodes [1].

I. INTRODUCTION

Integrated-circuit receivers consisting of a planar antenna integrated with a matching network and a planar Schottky-diode or a three terminal device offer many advantages over waveguide-based receivers at millimeter-wave frequencies. They are smaller, lighter and less expensive to build than waveguide systems and can be easily produced in large numbers for millimeter-wave applications. A potential candidate for excellent millimeter-wave performance is the double-slot antenna [2-4]. This paper presents an improved double-slot receiver design by 1) monolithically integrating a planar Schottky diode with the double-slot antenna so as to result in minimum parasitic capacitance and series resistance and 2) placing the slot antenna on an extended hemispherical high-resistivity silicon substrate lens to result in high gain patterns with high Gaussian coupling efficiency [5]. This design requires no via holes or a backing ground-plane. The GaAs substrate is therefore not thinned down to $100\mu\text{m}$ (or less) thereby increasing the yield of the fabrication process. The application areas for this receiver are in millimeter-wave imaging arrays for remote-sensing and radio-astronomical systems.

II. RECEIVER DESIGN

The monolithic CPW-fed double-slot antenna receiver is shown in Figure 1. The design of the double-slot receiver is a compromise between an antenna geometry that will result in a high efficiency Gaussian beam pattern, an input impedance that will result in high RF coupling to the planar diode, and a physical circuit that is relatively insensitive to fabrication variations. In the double-slot antenna design, the length of the slots control the H-plane pattern and the separation between the slot antennas controls the E-plane pattern [5]. The slot antennas are chosen to be $0.30\lambda_0$ -long ($354\mu\text{m}$) with a separation of $0.16\lambda_0$ ($190\mu\text{m}$) where λ_0 is the free-space wavelength at 250 GHz. This design yields theoretical E-, H-, and 45°-plane 10 dB beamwidths of 48°, 49°, and 53° and a maximum cross-polarization level of -30dB into an infinite GaAs dielectric ($\epsilon_r=12.8$) at 250GHz. The receiver is mounted on a high-resistivity Silicon lens, eliminating the power loss to substrate modes and making the pattern unidirectional into the dielectric lens [6]. From previous experience [7,8], the relative dielectric constants of silicon ($\epsilon_r=11.7$) and GaAs ($\epsilon_r=12.8$) are close enough that no substrate modes and associated power loss occur when a GaAs wafer is placed on a silicon lens. The power radiated to the back-side is minimal, only 9% (-0.4 dB), and therefore no backing-cavity is used to recover this power loss. In this work, the double-slot receiver is centered on a 13.7 mm diameter extended hemispherical silicon lens. An extension length, defined as the distance from the planar surface of the antenna to the hemispherical plane of the silicon lens, of $2300\mu\text{m}$ is chosen to yield an antenna pattern with high Gaussicity and high directivity [5]. The resulting radiation pattern has a directivity of 29 dB and a 90%

Gaussian-coupling efficiency at 250 GHz. The Gaussian-coupling efficiency does not include power loss to the back-side (-0.4 dB) or the reflection loss at the silicon-air interface. The reflection loss is calculated to be -1.7 dB for no matching-cap layer on the silicon lens and -0.2 dB for a $\lambda_d/4$ polyethylene matching-cap layer with uniform thickness [5,9].

The Schottky-diode is placed in series between the slot antenna, resulting in a sum-mode antenna pattern (Fig. 2). The $0.30\lambda_0$ -long slot antennas (at 250 GHz) are $15\mu\text{m}$ wide and are near the second resonance region of a slot antenna on a silicon or GaAs half-space [10]. The input impedance of the double-slot antenna is the sum of the slot self-impedance (Z_{11}) and the double-slot mutual impedance (Z_{12}) since the two slots are fed in phase. The self and mutual impedances of a slot antenna on a semi-infinite dielectric have been calculated recently by Zmuidzinas [3] and Eleftheriades [10]. Using the program of Eleftheriades at the design frequency of 250 GHz, $Z_{11}=25.5+j0.4\ \Omega$, $Z_{12}=2.4-j9.7\ \Omega$, and $Z_{ant}=Z_{11}+Z_{12}=27.9-j9.3\ \Omega$ [10]. The RF matching network consists of two short sections ($90\mu\text{m}$) of 35Ω CPW-line. The 35Ω CPW-line dimensions are $s=18\mu\text{m}$ and $w=6\mu\text{m}$ at the antenna feed point with a metal thickness (gold and n^+ -layer) of $2.5\mu\text{m}$. The CPW line widens to $s=30\mu\text{m}$ and $w=10\mu\text{m}$ near the diode, and the impedance remains $35\ \Omega$ on the line. For the $90\mu\text{m}$ -long CPW line, λ_{eff} is equal to $490\mu\text{m}$, and the line has an electrical length of 66° at 250 GHz found using EEsoff Linecalc [19]. The maximum total width of the CPW-line ($s+2w=50\mu\text{m}$) may allow some loss to radiation [11], but this width is necessary to accommodate the ohmic contact of the planar Schottky diode. The antenna input impedance Z_{ant} is transformed across the $90\mu\text{m}$ -long CPW line to Z_1 . The diode embedding impedance, defined as the impedance seen at the diode terminals, is then $2Z_1$ since the diode is in series with the CPW-line. At 250 GHz, $Z_1=29.3+j10.6\ \Omega$ and $2Z_1=59+j21\ \Omega$. Since the slots have a wideband input impedance in this region and the matching networks are short, the diode embedding impedance $2Z_1$ is also relatively wideband. The antenna input impedance Z_{in} and diode embedding impedance $2Z_1$ are displayed over a 20% bandwidth from 225 to 275 GHz in figure 3.

The theoretical receiver performance was analyzed using the reflection algorithm of Held and Kerr [12]. The diode parameters are assumed to be $I_o=1 \times 10^{-14}\ \text{A}$, $n=1.15$, $C_{jo}=3\ \text{fF}$, $V_{bi}=0.76\ \text{V}$ and $R_s=15\ \Omega$. A parasitic capacitance of $C_p=2\ \text{fF}$ is included in parallel with the embedding impedance $2Z_1$. These diode parameters are typical of a good monolithic $1.2\mu\text{m}$ -anode Schottky diode with an etched surface channel. By varying the RF embedding impedance, it is determined that minimum conversion loss occurs with an RF embedding impedance of approximately $60+j50\ \Omega$ and a minimum noise temperature occurs for an RF embedding impedance of $40+j40\ \Omega$ with an available LO power of 2.0-2.5 mW. The effects of the embedding impedances at the 2nd, 3rd, and 4th harmonics of the RF and LO were

tested by making them open circuits, short circuits, and reactive loads in the analysis. While varying the higher order harmonic embedding impedances caused the conversion loss and noise temperature to change by ± 0.5 dB, the regions of minimum conversion loss and noise temperature remained constant. However, due to the CPW lines which would tend to radiate at the higher harmonics (500 GHz, 750 GHz), the embedding impedances at these harmonics are set to 50Ω for the remainder of the analysis. The diode IF impedance is typically 100 to 120Ω . For the designed embedding impedance of $2Z_1 = 59 + j21 \Omega$ at 250 GHz with an available LO power of 2.5 mW, the diode RF impedance is $71 - j45 \Omega$, the diode LO impedance is $57 - j53 \Omega$, and the IF impedance is 105Ω . The corresponding diode bias is $V_b = 500$ mV and $I_b = 3.5$ mA. This results in a theoretical LO reflection loss of 0.8 dB, a SSB conversion loss of 6.2 dB, and a SSB noise temperature of 830K. The receiver design is wideband. Over the 20% bandwidth from 225 GHz to 275 GHz, the theoretical SSB conversion loss is less than 7.2 dB and the SSB noise temperature is less than 1500K.

The CPW line is short-circuited to the ground-plane at the left slot antenna, providing the DC return for biasing the diode. On the right slot-antenna, the CPW line is connected to a low-pass IF filter. The IF network consists of a 4-section low-pass CPW filter with a 3-dB corner frequency of 150 GHz and a short-circuit rejection of -13 dB from 220 to 280 GHz. A six-section filter with a rejection of -20 dB could have been included but was too large for the integrated circuit. The IF filter is followed by a $\lambda/4$ CPW matching network at 1.4 GHz on a low-loss Duroid 6006 ($\epsilon_r = 6.5$) substrate [13] with an impedance of 75Ω to match the 110Ω IF impedance of the LO pumped diode.

III. MILLIMETER-WAVE MEASUREMENTS

During the fabrication process, the anode diameter increased to $1.5 - 1.6 \mu\text{m}$. The diode junction capacitance is therefore $C_{j0} = 4$ fF. One major advantage of the monolithic design is the elimination of the pad-to-pad parasitic capacitance. This capacitance becomes part of the RF transmission line which is connected to the diode terminals. The small remaining parasitic capacitance is due to the region under the finger and around the anode and is estimated to be $C_p = 2$ fF.

The DC parameters are calculated by measuring the current-voltage characteristic and curve fitting to the standard IV equation. The measured DC parameters of the *fabricated* diode are $R_s = 13 \Omega$, $n = 1.2$, $\Phi_b = 0.68$ V and $I_s = 1.0 \times 10^{-13}$ A. This yields a cutoff frequency given by $f_T = 1/2\pi R_s(C_{j0} + C_p)$ of 1700 to 2000 GHz.

A polyethylene ($\epsilon_r = 2.3$) matching cap was developed to reduce the RF reflection at the silicon ($\epsilon_r = 12$) lens-air interface. Ideally, the matching cap should be $\lambda_d/4 = 200 \mu\text{m}$ thick [9], where λ_d is the wavelength in the polyethylene at 250 GHz. The matching cap is fabricated

by melting 220 μ m-thick polyethylene over the silicon lens on a hotplate at 225°C. Several matching caps were fabricated and then removed to measure their thickness. Typically, the matching caps were $190 \pm 15\mu$ m-thick in the center and $175 \pm 15\mu$ m-thick on the edge.

The double-slot antenna is centered on a 13.7 mm diameter extended hemispherical silicon lens with the polyethylene matching cap. The patterns are measured by DC biasing the diode and using it as a video detector. Figure 2 shows the measured E and H-plane patterns at 258 GHz, which agree well with theory [5]. A small cross-polarization peak of -20 dB at broadside was measured in the E, H and 45°-planes due to the widening of the CPW line at the center of the slot-antennas. The forward pattern directivity is calculated to be 28.5 dB at 258 GHz by averaging the measured E, H and 45°-plane patterns and agrees well with the predicted value of 29 dB [5]. This results in a measured aperture efficiency (coupling to a plane wave) of 55%. The radiation patterns were also measured at 237 GHz and 280 GHz to test the bandwidth of the double-slot antenna. The patterns are symmetric at 237 GHz, but the 280 GHz E-plane shows unsymmetric sidelobes. This is probably due to the absence of air-bridges for the IF filter. A similar antenna has been tested at 220-280 GHz with a polyimide capacitor replacing the IF filter next to the right antenna [5]. This version of the double-slot antenna had a symmetric mainbeam with low sidelobes at 280 GHz.

The video responsivity, defined as the detected diode voltage divided by the total RF power incident on the 13.7 mm lens aperture, of the receiver was tested with and without the polyethylene matching cap. The RF power was measured using a large area bismuth bolometer on a dielectric membrane [16], and the detected diode voltage is measured across a 100 k Ω load. The matching cap was found to increase the video responsivity by 1.0 ± 0.2 dB from 246 to 258 GHz while having no measured effect on the antenna radiation patterns. The measured video responsivity at 246 GHz is 410 V/W and at 258 GHz is 330 V/W. The video responsivity referenced to the diode junction may be calculated with the inclusion of the following losses: the antenna aperture efficiency (coupling to a plane wave, estimated to be 55%), the silicon-lens reflection loss with a matching cap-layer (-0.7 dB), the absorption loss in the high-resistivity silicon lens (-0.2 dB), and power lost to the backside of the antenna (-0.4 dB). The resulting video responsivity at the diode terminals is 1000 V/W at 246 GHz and is competitive with the performance of whisker-contacted diodes at 250 GHz.

The quasi-optical measurement is designed for 258 GHz, because the LO source has a peak power at this frequency. The Mach-Zender interferometer (designed for a center frequency of 250 GHz) allows the RF and LO signals to be combined at the receiver, and the two teflon objective lenses focus all of the LO power supplied by the corrugated LO feedhorn to the phase center of the double-slot antenna on the extended silicon lens. A tunable Gunn diode with a tripler is the 258 GHz LO source. The corrugated LO feedhorn has a

beamwaist of 2.0mm. A 65mm-diameter $f/0.85$ objective lens is located 60mm from the horn aperture. This lens focused the Gaussian beam through the interferometer to the second teflon objective lens, a 65mm-diameter $f/1.4$ lens. Finally, the Gaussian beam is focused 107mm behind the $f/1.4$ lens to the 3.1mm minimum beamwaist of the double-slot antenna on the extended hemispherical silicon lens. This minimum beamwaist is 38mm behind the surface of the substrate lens.

The Mach-Zender interferometer is tuned to an IF of 1.4GHz. The 1.4 GHz IF-chain has a noise temperature of 105K and a gain of 97 dB with a bandwidth of 100 MHz. The measured DSB conversion loss and noise temperature vs. bias and available LO power are presented in figure 4. The best performance was achieved at a DC bias of 0.73 V and a DC current of 1.2 mA. The available maximum LO power at the silicon-lens aperture is 1.65 mW. The available LO power at the diode terminals is calculated by multiplying the above power by the antenna back-side power loss (0.4 dB) and Gaussian-coupling efficiency (0.5 dB), the lens-air reflection loss with the matching cap (0.7 dB) and the silicon lens absorption loss (0.2 dB). This results in a maximum available LO power at the diode terminals of 1.1 mW, which is just enough to optimally pump the diode (Fig. 4b). The reflection and absorption loss (estimated at 0.3 dB and 0.3 dB, respectively) of the 65mm-diameter $f/1.4$ teflon objective lens and a 0.2dB insertion loss in the interferometer have been normalized out of the measurements. The measured DSB conversion loss and noise temperature of the antenna/mixer is 9.0 ± 0.3 dB and 2000 ± 100 K at 258 GHz without a matching cap layer and 8.0 ± 0.3 dB and 1600 ± 100 K with the polyethylene matching cap layer. The measured IF reflection coefficient is 0.2 dB at a bias current of $I_b=1.0$ -1.2 mA and can be normalized out of the receiver measurements. The minimum DSB antenna-mixer conversion loss and noise temperature is therefore 7.8 ± 0.3 dB and 1600 ± 100 K. These results are within 2-3 dB of the best tuned waveguide mixers using planar diodes [1] and represent the first monolithic 250 GHz receiver to date.

The theoretical receiver performance is analyzed using the reflection algorithm of Held and Kerr [12] with the actual diode parameters of $I_o=1 \times 10^{-13}$ A, $n=1.2$, $C_{j_o}=4$ fF, $C_p=2$ fF, $\Phi_b = 0.68$ V and $R_s=13 \Omega$ with an RF embedding impedance of $2Z_1=72+j28 \Omega$ at 258 GHz and an IF impedance of 110Ω . For an LO pump power of 3.5 mW and a bias current of 1.4 mA the theoretical single sideband conversion loss is 6.9 dB and the single sideband noise temperature is 1930K. Note that these figures do not include the silicon lens-air reflection loss of 0.7 dB, the silicon lens absorption loss of 0.2 dB, the back-side power loss of 0.4 dB, or the Gaussian coupling efficiency loss of 0.5 dB. Including these losses employing the equivalent noise temperature of an attenuator [17], the overall theoretical single sideband conversion loss is 8.7 dB and a noise temperature is 3075K. Assuming that the receiver responds to both

sidebands identically, these results correspond to a double-sideband conversion loss of 5.7 dB and a noise temperature of 1540K. This discrepancy between the predicted and measured receiver performance is probably due to the increased series resistance due to the skin effect at 258 GHz. Additionally, it has been shown that the parasitic shunt capacitance for a planar Schottky diode increases with frequency at millimeter-wave frequencies [18]. Regardless, the agreement between experiment and theory is quite good for a 250 GHz receiver.

ACKNOWLEDGEMENTS

This work has been supported by the NASA Center for Space Terahertz Technology. The authors would like to thank Dan Filipovic of the University of Michigan and George Eleftheriades, formerly at the University of Michigan and currently at EFPL in Switzerland for their excellent theoretical support. We also thank the talented William Bishop of the University of Virginia for his suggestions about Schottky-diode fabrication procedures.

REFERENCES

- [1] P.H. Siegel, R.J. Dengler, I. Mehdi, J.E. Oswald, W.L. Bishop, and T.W. Crowe, "Measurements on a 215 GHz subharmonically pumped waveguide mixer using planar back-to-back airbridge Schottky diodes," *IEEE Trans. on Microwave Theory Tech.*, vol.41, pp.1913-1921, Nov. 1993.
- [2] A.R. Kerr, P.H. Siegel, and R.J. Mattauch, "A simple quasi-optical mixer for 100-120 GHz," *IEEE-MTT Int. Microwave Symp. Digest*, pp.96-98, 1977.
- [3] J. Zmuidzinis, "Quasi-optical slot antenna SIS mixers," *IEEE Trans. on Microwave Theory Tech.*, vol.40, pp.1797-1804, Sept. 1992.
- [4] G. Gauthier, T.P. Budka, W.Y. Ali-Ahmad, D.F. Filipovic, and G.M. Rebeiz, "A low-noise 86-90GHz uniplanar Schottky-receiver," *IEEE Int. Microwave Theory Tech. Symposium*, Atlanta, Georgia, pp.325-328, June 1993 .
- [5] D.F. Filipovic, S.S. Gearhart and G.M. Rebeiz, "Double-slot antennas on extended hemispherical and elliptical silicon dielectric lenses," *IEEE Trans. Microwave Theory Tech.*, vol.41, pp.1738-1749, Oct. 1993.
- [6] D.B. Rutledge, D.P. Neikirk and D.P. Kasilingam, "Integrated Circuit Antennas," in *Infrared and Millimeter-Waves*, vol.10, pp.1-90, K.J. Button, Ed., New York, Academic Press, 1983.
- [7] B.K. Kormanyos, P.H. Ostdiek, W.L. Bishop, T.W. Crowe, and G.M. Rebeiz, "A planar wideband 80-200 GHz subharmonic receiver," *IEEE Trans. Microwave Theory Tech.*, vol.41, pp.1730-1737, Oct. 1993.
- [8] S.S. Gearhart, J. Hesler, W.L. Bishop, T.W. Crowe, and G.M. Rebeiz, "A wideband 760GHz planar integrated schottky receiver," *IEEE Microwave Guided Wave Lett.*, vol. 3, pp.205-207, July 1993.

- [9] C.E. Zah and D.B. Rutledge, "A polystyrene for matching a silicon lens at millimeter wavelengths," *Int. J. Infrared Millimeter Waves*, vol.6, pp.909-918, Sept. 1985.
- [10] G. Eleftheriades and G. M. Rebeiz, "Self and mutual admittance of slot antennas on a dielectric half-space," *Int. J. Infrared Millimeter-Waves*, vol.14, No.10, pp.325-328, Oct. 1993.
- [11] M. Riaziat, R. Majidi-Ahy, and I. Feng, "Propagation modes and dispersion characteristics of coplanar waveguides," *IEEE Trans. Microwave Theory Tech.*, vol.38, pp.245-251, Mar. 1990.
- [12] D.N. Held and A.R. Kerr, "Conversion loss and noise temperature of microwave and millimeter-wave receivers: part I-theory; part II-experiment," *IEEE Trans. Microwave Theory Tech.*, vol.MTT-26, pp.49-61, Feb. 1978.
- [13] Duroid is a trademark of the Rogers Corporation. (We thank Rogers Co. for the donation of the substrate.
- [14] T.W. Crowe and R.J. Mattauch, "Analysis and optimization of millimeter-and submillimeter-wave mixer diodes," *IEEE Trans. on Microwave Theory Tech.*, vol.MTT-35, pp.159-168, Feb. 1987.
- [15] W.L. Bishop, K. McKinney, R.J. Mattauch, T.W. Crowe and G. Green, "A novel whiskerless schottky diode for millimeter and submillimeter wave applications," *proc.IEEE MTT-S Int'l Symp.*, pp.607-610, June 1987.
- [16] C.C. Ling and G.M. Rebeiz, "A wide-band monolithic quasi-optical power meter for millimeter- and submillimeter-wave applications," *IEEE Trans. on Microwave Theory Tech.*, vol.39, pp.1257-1261, Aug. 1991.
- [17] F.T. Ulaby, R.K. Moore, and A.K. Fung, *Microwave Remote Sensing-Active and Passive*, Vol. I, Reading, MA , 1981.
- [18] J.A. Wells and N.J. Cronin, "Frequency dependant simulation of planar millimeter-wave mixer diodes," *17th. Int. Conf. Infrared Millimeter Waves*, pp.214-215, Dec. 1992.
- [19] EEsof, Inc.; Westlake Village, CA.

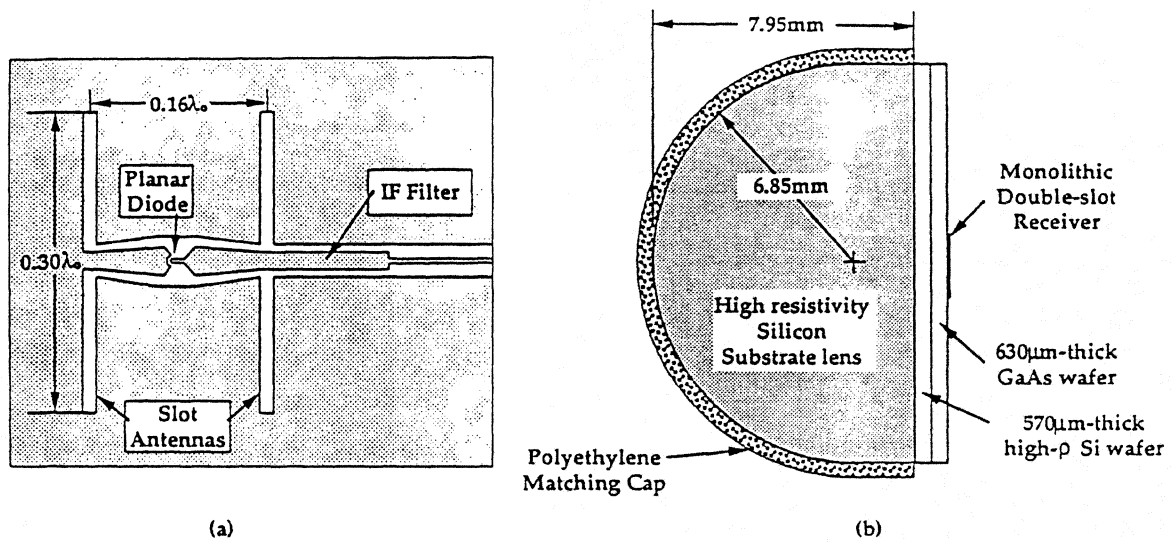


Figure 1: The 250 GHz monolithic double-slot antenna receiver: (a) top view, (b) side view illustrating the high resistivity silicon lens, polyethylene matching cap, and GaAs wafer.

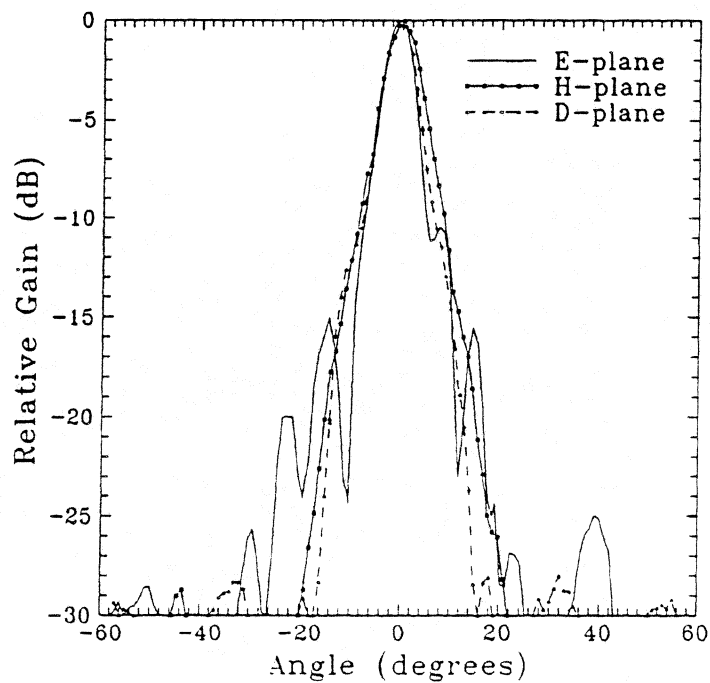


Figure 2: Measured E-, H-, and 45°-plane patterns at 258 GHz on a 13.7-mm extended hemispherical lens.

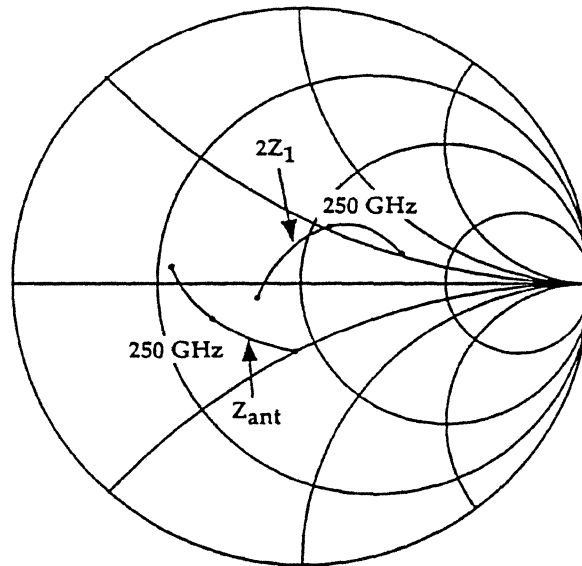


Figure 3: Theoretical impedance design over a 20% bandwidth: (a) antenna input impedance Z_{ant} , (b) the RF embedding impedance $2Z_1$ as seen by the diode.

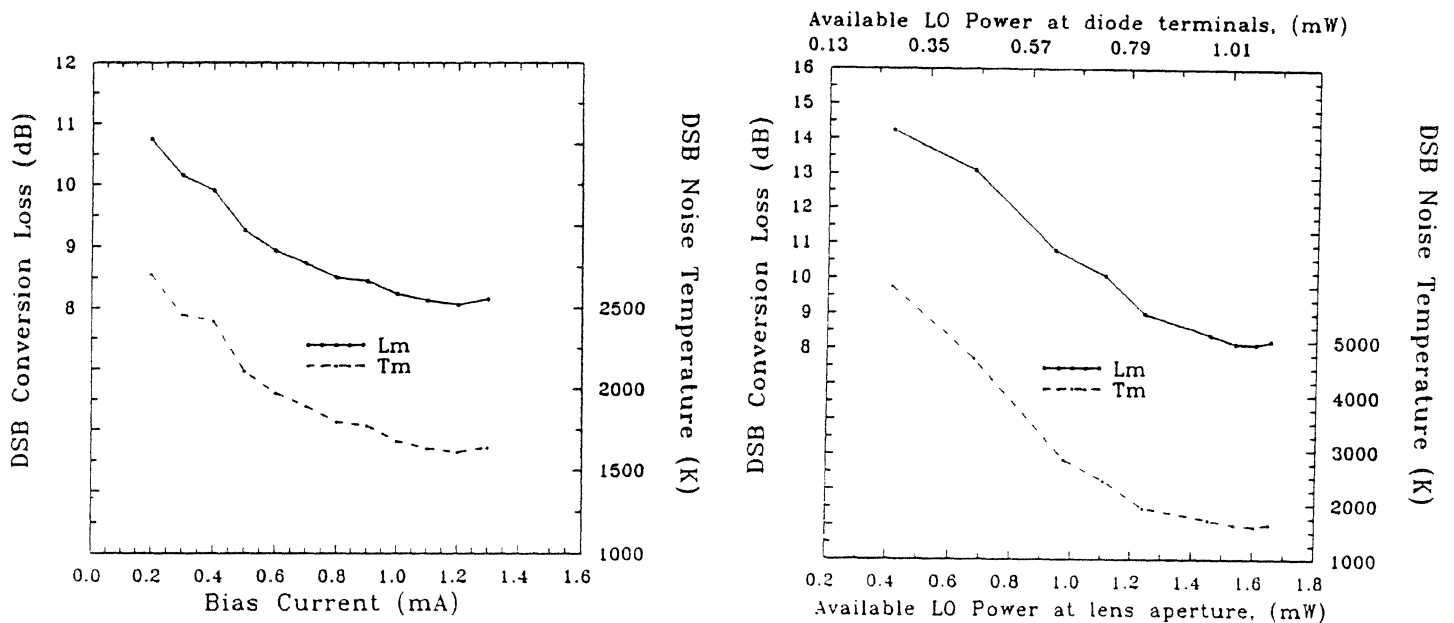


Figure 4: Measured antenna-mixer conversion loss and noise temperature (including the IF-chain contribution) at 258 GHz versus: (a) bias current at an available LO power of 1.65mW at the lens aperture, (b) available LO power at a bias of 1.2mA.

Effect of Parasitic Capacitance on the Performance of Planar Subharmonically pumped Schottky Diode Mixers

I. Mehdi and P. H. Siegel
California Institute of Technology
Jet Propulsion Laboratory,
Pasadena, CA 91109

ABSTRACT

Planar integrated Schottky diodes represent a robust alternative to whisker contacted diodes for space borne applications. However, compared to whisker contacted diodes, today's planar diodes possess larger values of parasitic capacitance. The effect of parasitic capacitance on the performance of a subharmonically-pumped antiparallel-pair planar Schottky-barrier-diode mixer is investigated. It is shown, that with appropriate design, one can obtain mixer performance from planar diodes that is comparable to the performance of low parasitic whisker contacted diode circuits at least up to 200 GHz.

I. INTRODUCTION

In recent years there has been a considerable amount of interest in utilizing planar integrated diodes in millimeter and sub-millimeter wave radiometers[1-5]. Perhaps the main driving force behind this interest has been the apparent reliability problems associated with whisker contacted devices in such risk prone systems as space-borne instruments. It is also hoped that by using an integrated

device the rf circuit would attain some repeatability enabling one to optimally design the embedding circuit. Use of integrated devices also enables one to utilize circuit topologies requiring more than one diode since it is easier to fabricate a chip with two similar anodes than to design with two whisker contacted anodes.

The physical difference between an integrated whisker-less diode and a whisker contacted diode lead the two circuits to have different associated parasitics even though the metal-semiconductor contact is essentially the same. The nonlinear behavior of a mixer circuit makes the prediction of the effect of particular elements non trivial. In this paper the effect of parasitic capacitance and inductance on the performance of a 200 GHz subharmonically pumped mixer with anti-parallel pair Schottky diodes is investigated.

II. DEVICE AND CIRCUIT MODEL

A number of technologies are available that enable one to fabricate whisker-less planar Schottky diodes. In [6], some of these technologies, such as mesa etching and proton bombardment, have been discussed and it is concluded that due to the ease of fabrication and relatively low parasitics the Surface Channel Technology (SCT) presents the best potential. This technology has been developed at the University of Virginia and has been discussed in detail in [1,3,6,7]. In the SCT diodes, the Schottky anode is first contacted by a metal finger akin to an air bridge and then the anode and cathode pads are isolated by etching a channel in the highly doped semiconductor. Fig. 1(a) depicts a schematic of a planar SCT diode showing the various components of the parasitic capacitance. In a whisker contacted diode, the whisker is perpendicular to the anode and the capacitance between the whisker and the diode cathode is rather small [8]. The total shunt

capacitance for a whisker diode has been reported to be as low as 1 fF [6]. However, in the planar device, the metal contact finger is horizontal to the anode and thus the parasitic capacitance between the metal finger and the semiconductor tends to be much higher. This parasitic capacitance has several components as shown in Fig. 1(a). C_{pp1} is the capacitance between the cathode and anode pad. C_{pp2} is the capacitance between the cathode pad and the n+ GaAs material under the Schottky anode. C_{pp3} is the capacitance between the two n+ GaAs regions of the device separated by the surface channel. Thus C_p which, we will call the parasitic capacitance from pad-to-pad, can be defined as $C_p = C_{pp1} + C_{pp2} + C_{pp3}$. C_f is defined as the capacitance between the anode contact finger and the n/n+ GaAs and we divide it into two components. C_{fp1} is the part of the capacitance that results primarily from the finger overlap on the anode pad, while C_{fp2} is the capacitance due to the overlap between the finger tip and the generally smaller anode. The total of C_{fp1} and C_{fp2} we will call C_f . The capacitance between the finger and the GaAs, is divided between C_{pp2} and C_{fp1} . It is assumed that since the finger gets closest to the GaAs around the Schottky anode most of the finger-to-pad capacitance should be accounted for by C_{fp1} . At high frequencies, these capacitances, especially C_{pp2} , are distributed, however in this study it has been treated as lumped elements and the equivalent circuit shown in Fig. 1(b) has been used.

Another important difference between the whisker contacted diode and the planar diode is the value of L_s . For whisker contacted diodes the whisker generally is fairly thick (10-20 microns) and the inductance per unit length is expected to be fairly small, although the whisker length tends to be large (100 microns or more). In integrated devices the fingers are typically 2-4 microns wide and perhaps a micron thick. This causes the integrated device to have non-negligible inductance even though it is very short (10-50 microns). This inductance is of paramount interest because of the role

it plays in the subharmonic mixer circuit where it has been shown [9,10] that the loop inductance causes the mixer circuit to resonate with the chip capacitance.

For this analysis the semiconductor-metal junction (Schottky anode) is modeled in the usual way as a nonlinear capacitor in parallel with a nonlinear resistance. The capacitance and resistance of the device are related to the semiconductor doping, epi-layer thickness and anode geometry. R_s is the parasitic series resistance associated with the undepleted epi layer, n^+ GaAs and the ohmic contact. This resistance is assumed to be constant with voltage. The diode I-V relationship is assumed to follow the standard thermionic emission theory. The capacitance of the diode is given by

$$C_j(V) = C_{j0} \left(1 - \frac{V}{\phi_b} \right)^{-\gamma},$$

where V is the applied voltage, C_{j0} is the zero bias capacitance, γ is 0.5, and ϕ_b is the barrier height.

In order to accurately simulate the performance of a mixer with the circuit of Fig. 1(b) it is essential to use circuit parameters that are consistent with presently available device technology. The total measured capacitance for an anti-parallel pair diode chip can be written as

$$C_{tot} = C_j + C_j + C_p + C_f + C_f,$$

where finger to finger capacitance is assumed to be small and has been neglected. C_{tot} can be directly measured with a capacitance bridge on the actual circuit. The junction capacitance, C_j , can be extrapolated by measuring the total capacitance of various size anodes with all other geometrical

parameters a constant. C_p can be measured by knocking off the fingers on a chip and measuring the capacitance across the contact pads. To distinguish between C_p and C_f we have made devices with metal fingers but no anode contact. Measuring the total capacitance of such a device and then subtracting the C_p gives us an upper limit to C_f .

The parasitic capacitance is dependent on a number of fabrication parameters. The surface channel width, the finger width, finger length, the GaAs pad sizes, and the quality of the dielectric constant will all effect the C_{tot} . These parameters can vary considerably from laboratory to laboratory and even from batch to batch. Typical values of C_p range from 3 fF to 12 fF. Typical values for C_f range from 0.7 fF to 3 fF. Based on this data a reasonable parameter space can be defined which would encompass present day diode fabrication technology. The correct value for the finger inductance remains a bit uncertain till direct measurements can be successfully conducted. The model measurements of [11] give the finger inductance as 0.53 pH per micron plus 18 pH attributed to fringing current inductance associated with the abrupt change in metallization width. Thus for a finger that is 50 microns long the total inductance according to [11] would be about 45 pH.

III. MIXER SIMULATIONS

The circuit used for the subharmonically pumped mixer is shown in Fig. 2(a) [9,10]. The planar diode is represented with the equivalent circuit of Fig. 1(b). The diode electrical characteristics have been discussed earlier and it is assumed that both diodes are identical and are connected with opposite polarity so they conduct on alternate half-cycles of the local oscillator (LO). For even harmonics and DC the diodes are out of phase and thus produce zero voltage across Z_3 . This is shown in Fig 2(b). For odd harmonics the circuit of Fig. 2(a) simplifies to the circuit of Fig.

2(c). During simulations, all linear elements are incorporated into the embedding network as shown in Fig. 2(a) and Z_3 represents the source or load impedance. The IF load $Z_3(\text{IF})$ is conjugate matched to the output impedance of the mixer. The embedding impedance is set to 50 Ohms for the first and second harmonics while at other harmonics a short circuit is assumed.

The mixer simulation that has been developed follows the procedure described by Kerr in [9,10]. Obviously the admittance matrix of the mixer is slightly different from the admittance matrix developed in [10] because of the addition of the parasitic capacitance. The admittance matrix of the mixer circuit of Fig. 2 (a), taking into account the parasitic capacitance, is as following:

$$Y = \begin{bmatrix} Y_{11} & 0 & Y_{13} \\ 0 & Y_{11} & Y_{13} \\ -Y_{11} & -Y_{11} & Y_{33} \end{bmatrix}$$

where

$$Y_{11} = \frac{1 - \omega^2 L_s C_f}{R_s - \omega^2 R_s L_s C_f + j\omega L_s}$$

$$Y_{13} = \frac{1 - \omega^2 L_s C_p + j\omega [R_s C_f + R_s C_p - \omega^2 C_p R_s C_f L_s]}{R_s + j\omega L_s - \omega^2 R_s L_s C_f}$$

$$Y_{33} = -Y_{13} - Y_{23} + \frac{1}{Z_3}$$

The mixer simulation assumes that both diodes are identical and only eight harmonics of the LO are considered. The rectified current in the diodes is set at 1 mA and the LO power is varied to obtain the desired current flow. LO, signal and IF are 108, 216 and 1.4 GHz respectively. Fig. 3

shows the effect of C_p on the performance of the subharmonic mixer for a diode with ideality factor, $\eta=1.25$, saturation current $I_s=2.5E-16$ A, barrier height $\phi_b=1.10$ V, series resistance $R_s=12\ \Omega$ and zero bias junction capacitance $C_{j0}=3$ fF. The single sideband (SSB) conversion loss, input noise temperature and the real part of the IF output impedance are plotted as a function of the finger inductance, L_s present in the circuit. One can clearly observe that the mixer performance is a strong function of the loop inductance. The observed peaks in the conversion loss and noise temperature occur at even harmonics of the LO when the loop inductance resonates with the device capacitance. Note that the resonance is getting broader as C_p is increased from 0 fF to 12 fF. As is evident from the equivalent circuit in Fig. 2, as C_p increases it essentially provides a short for the RF power. Fig. 3(b) shows the effect of C_f on the mixer performance in the absence of C_p . The main effect of increasing C_f is to reduce the value of the inductance necessary for resonance thus restricting the values of loop inductance that can be tolerated.

Figure 4 shows the mixer performance for an identical circuit with a diode whose series resistance has been halved to 6 Ohms and whose zero bias junction capacitance has been doubled to 6 fF (maintaining a constant RC product). Figure 4(a) shows the effect of C_p on this mixer. Again, the resonance is broadened but now they occur at smaller values of L_s as compared to Fig. 3(a). Fig. 4(b) shows the effect of C_f on the mixer. As before, increasing C_f moves the resonance towards smaller values of L_s , thus restricting the range that can be tolerated.

Figure 5 shows the computed mixer performance, using a diode with $R_s=12$ Ohms and $C_{j0}=3$ fF, for two different sets of parasitic values. The solid curve shows a circuit whose parasitic capacitance is zero, approximately simulating a whisker contacted diode. The dashed curve uses a

C_p of 4 fF and C_f of 1 fF simulating a planar SCT diode, which in fact has been tested as a 200 GHz subharmonic mixer [3]. From Fig. 5 it can be seen that for a loop inductance below 45 pH the performance of the planar diode mixer and the whisker contacted diode are similar at least up to 200 GHz.

An exact comparison with experimentally obtained mixer results is not possible due to a lack of measurements on the actual value of L_g . The performance of whisker contacted diodes and planar diodes with similar characteristics in fundamental mixers is now equivalent up to 300 GHz [7,12]. Similarly, it has been shown that at least up to 200 GHz, planar diode subharmonically pumped mixer perform as well, if not better than, their whisker contacted counterparts [3].

IV. CONCLUSION

The equivalent circuit of a planar SCT Schottky diode chip with two diodes in anti-parallel configuration has been used to study the effect of parasitic capacitance on the mixer performance. The model incorporates realizable values of the parasitic capacitance that have been reported previously. Based on computer simulations it is shown that reasonable values of the parasitic capacitance can be tolerated at least up to 200 GHz as long as the loop inductance is low enough so that it does not resonate with the device capacitance. This study also stresses the need for measuring or precisely calculating the inductance associated with the planar device.

V. ACKNOWLEDGEMENT

The research described in this talk was carried out at the Jet Propulsion Laboratory, California Institute of Technology, under contract with the National Aeronautics and Space Administration.

REFERENCES

- 1 D. Garfield, R. Mattauch, and S. Weinreb, "RF Performance of a Novel Planar Millimeter-Wave Diode Incorporating an Etched Surface Channel," *IEEE-MTT* , vol. 39, no. 1, pp.1-5, January 1991.
- 2 T. Newman, W. L. Bishop, K. T. Ng, S. Weinreb, "A Novel Planar Diode Mixer for Submillimeter-Wave Applications," *IEEE-MTT* vol. 39, no. 12, pp. 1964-1971, December 1991.
- 3 P. H. Siegel, R. J. Dengler, I. Mehdi, J. E. Oswald, W. Bishop, T. Crowe, and R. J. Mattauch, "Measurements on a 215 GHz Subharmonically Pumped Waveguide Mixer using Planar back-to-back Air Bridge Schottky Diodes," *IEEE-MTT* Vol. 41, No. 11, November 1993.
- 4 T.-H. Lee, PhD dissertation, University of Michigan, May 1994.
- 5 P. H. Siegel, I. Mehdi, R. J. Dengler, J. E. Oswald, A. Pease, T. W. Crowe, W. Bishop, F. Li, R. J. Mattauch, S. Weinreb, J. East and T. H. Lee, "Heterodyne Radiometer Development for the Earth Observing System Microwave Limb Sounder," *SPIE Conference Proc. #1847-Infrared and Millimeter-Wave Engineering*, May 1993.
- 6 W. Bishop, K. McKinney, R. Mattauch, T. Crowe, and G. Green, "A Novel Whiskerless Diode for Millimeter and Submillimeter Wave Applications," 1987 *IEEE-Int. Microwave Symposium Digest*, pp. 607-610, June 1987.
- 7 R. J. Mattauch, et. al., "Recent results on : Surface-channel Schottky, InGaAs Schottky, and Nb based SIS mixer element research," *First International. Swamp. on Space Terahertz*

Technology, p. 279, March 1990.

- 8 A. R. Kerr, J. A. Grange, J. A. Lichtenberger, "Contact whiskers for millimeter wave diodes," NASA Technical Memorandum no. 79616, Goddard Space Flight Center, Institute for Space Studies, Aug. 1978.
- 9 A. R. Kerr, "Noise and Loss in Balanced and subharmonically pumped mixers: Part I--Theory," IEEE-MTT, vol. 27, no. 12, December 1979.
- 10 A. R. Kerr, "Noise and Loss in Balanced and subharmonically pumped mixers: Part II--Application," IEEE-MTT, vol. 27, no. 12, December 1979.
- 11 R. T. Newman, Jr., PhD dissertation, University of Virginia, August 1991.
- 12 T. Newman, W. L. Bishop, K. T. Ng, and S. Weinreb, "A novel planar diode mixer for submillimeter-wave applications," IEEE-MTT vol. 39, no. 12, pp.1964-1971, December 1991.

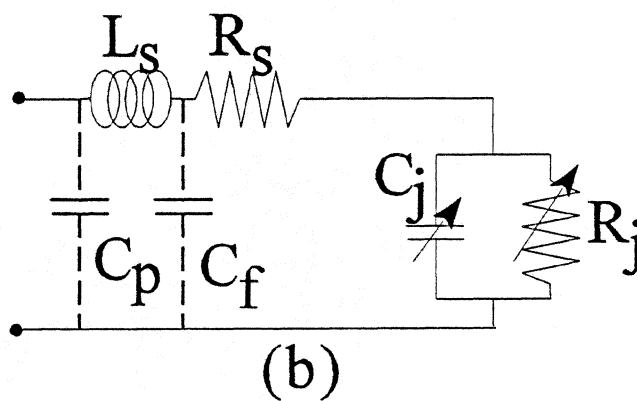
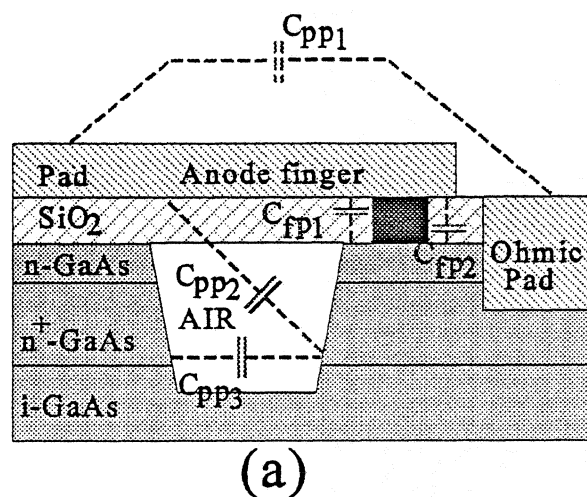
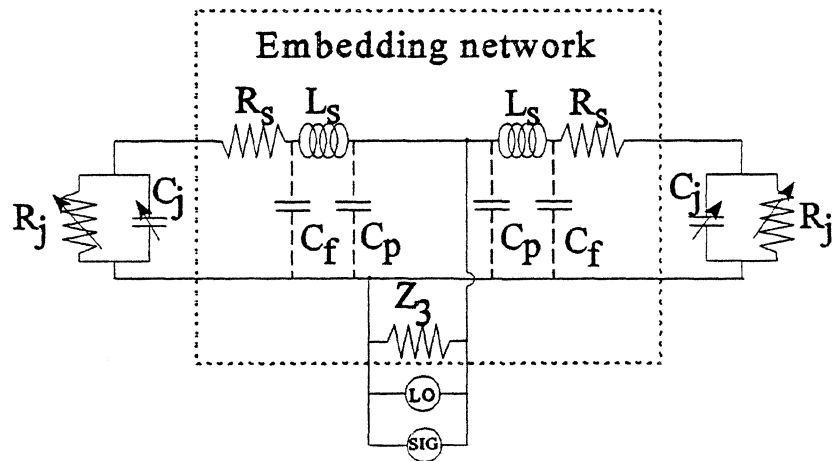
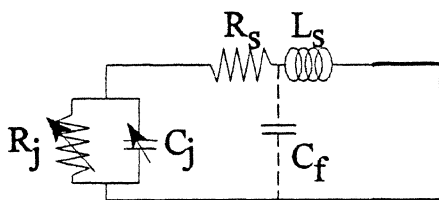


Figure 1: (a) Schematic of a planar integrated Schottky diode chip using Surface Channel Technology. (b) A representative equivalent circuit using lumped elements. $C_p = C_{pp1} + C_{pp2} + C_{pp3}$ and $C_f = C_{fp1} + C_{fp2}$.



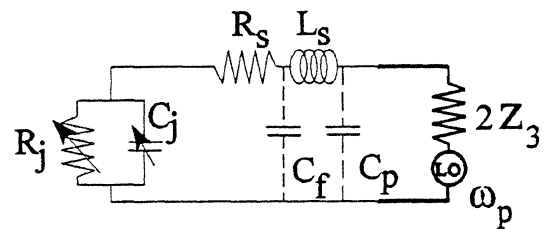
(a)

Even Harmonics & DC



(b)

Odd Harmonics



(c)

Figure 2 (a) Subharmonic mixer circuit used in simulation after [9,10], (b) assuming identical diodes the equivalent circuit for DC and even harmonics of the LO, (c) equivalent circuit for odd harmonics of the LO.

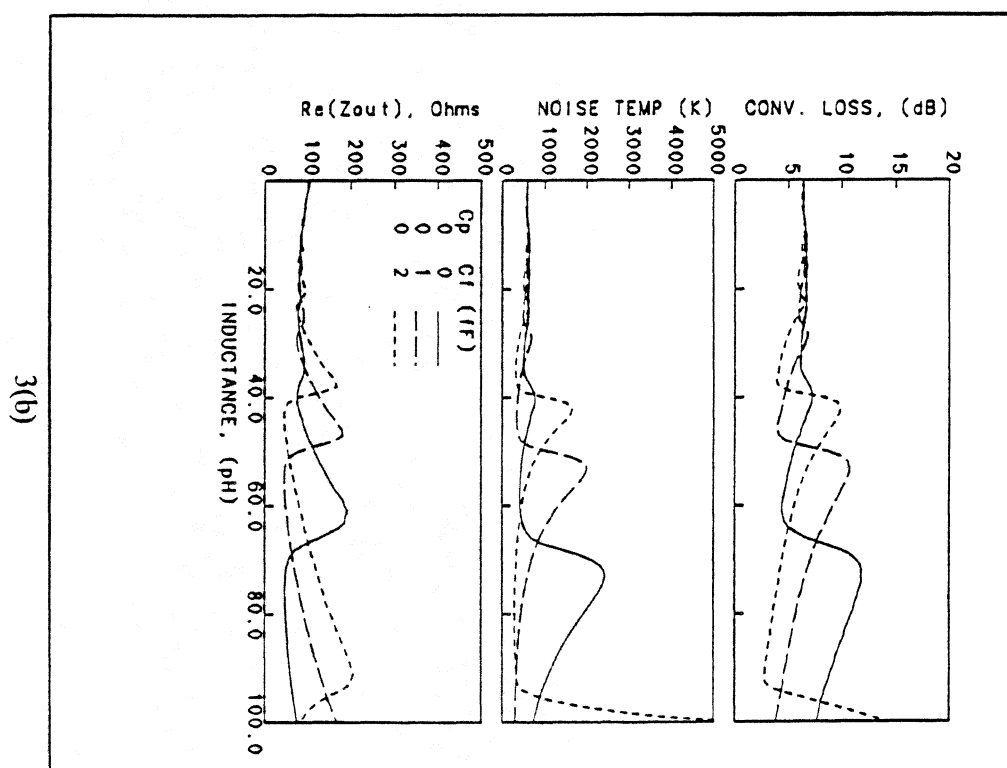
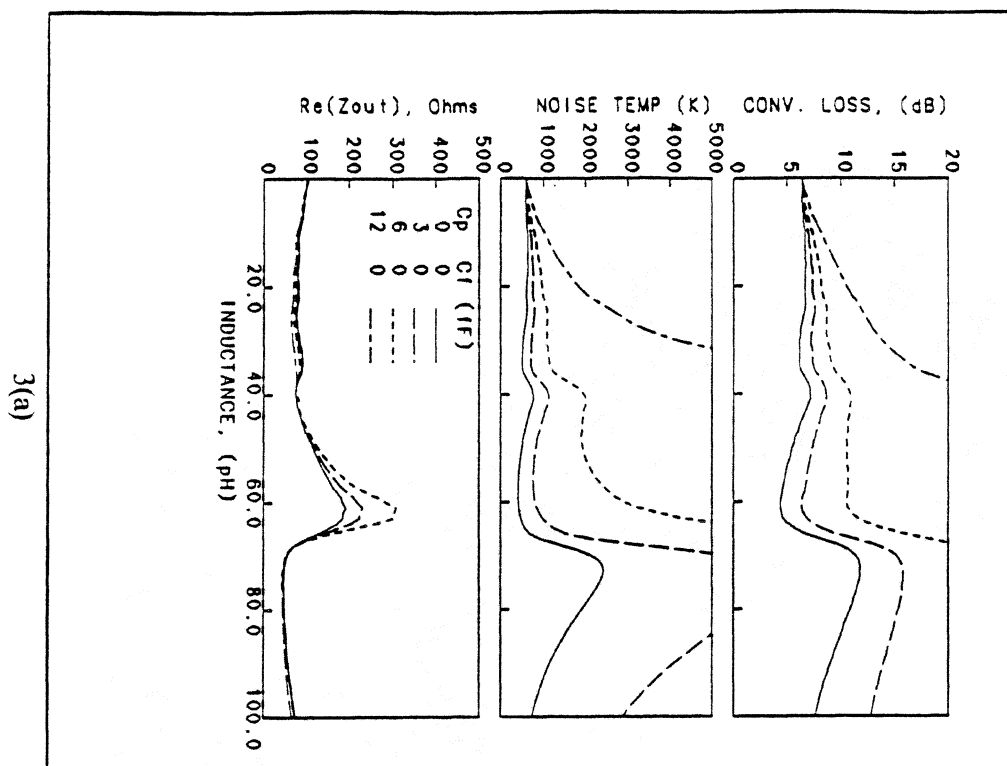


Figure 3: Effect of the parasitic capacitance on the performance of a 216 GHz subharmonically pumped mixer as a function of loop inductance for a diode with $R_s = 12 \, \Omega$ and $C_{j0} = 3 \, \text{fF}$. (a) C_p is varied from 0 fF to 12 fF, (b) C_l was varied from 0 fF to 2 fF.

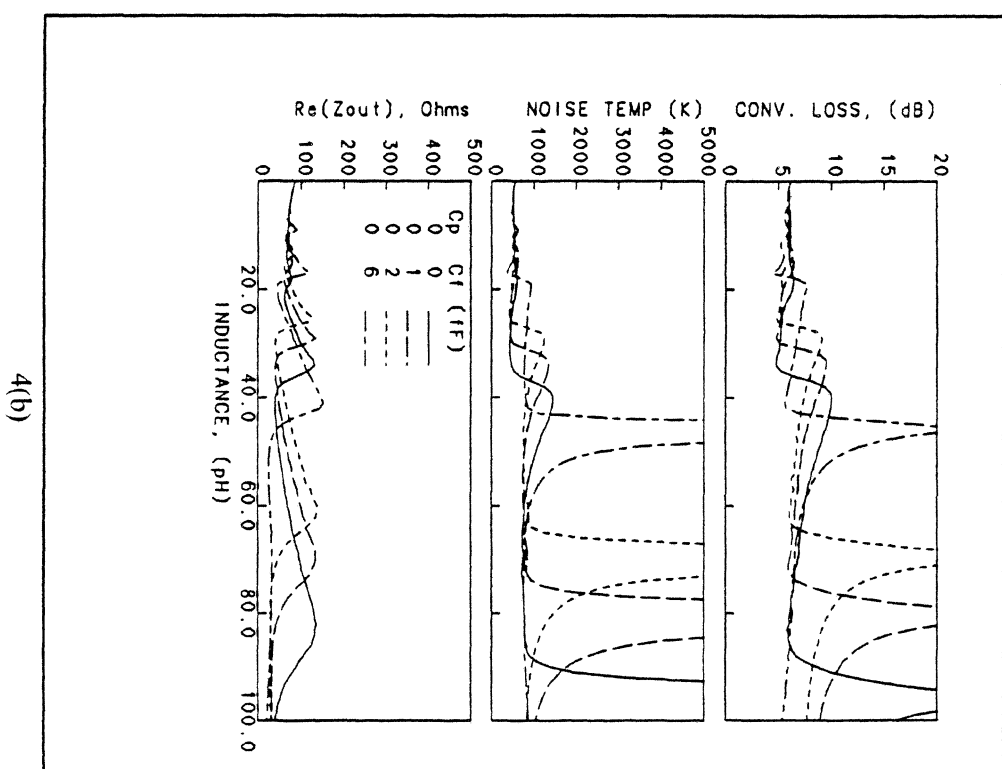
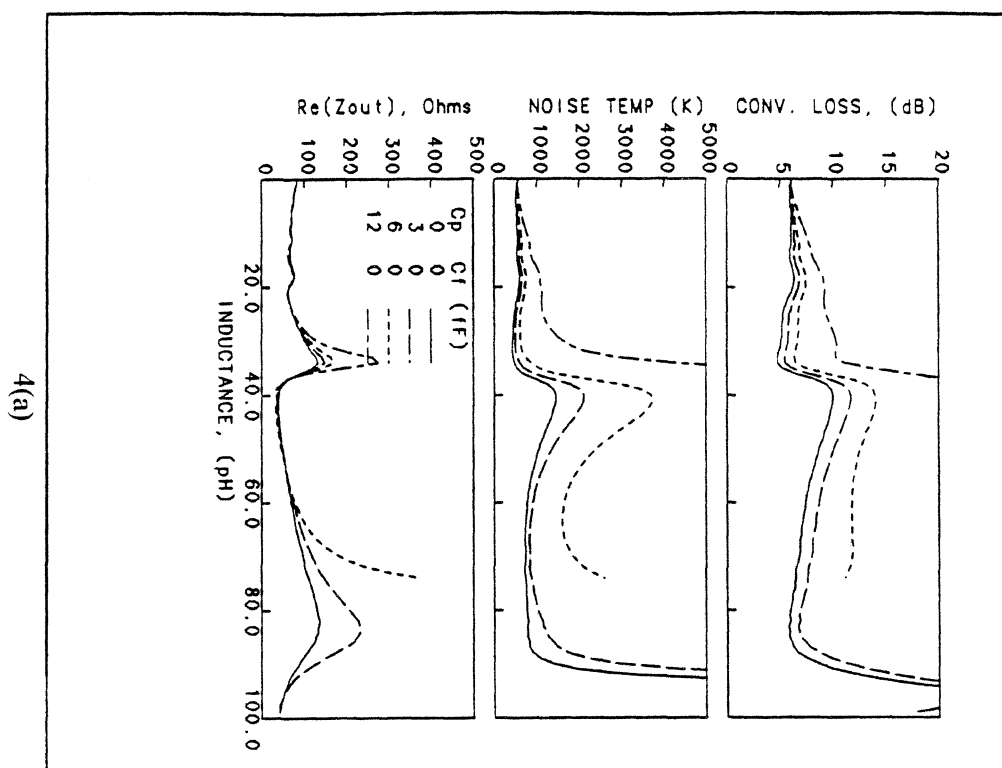


Figure 4: Effect of the parasitic capacitance on the performance of a 216 GHz subharmonically pumped mixer as a function loop inductance for a diode with $R_s = 6 \Omega$ and $C_{jo} = 6$ fF. (a) C_p varied from 0 fF to 12 fF. (b) C_f varied from 0 fF to 2 fF.

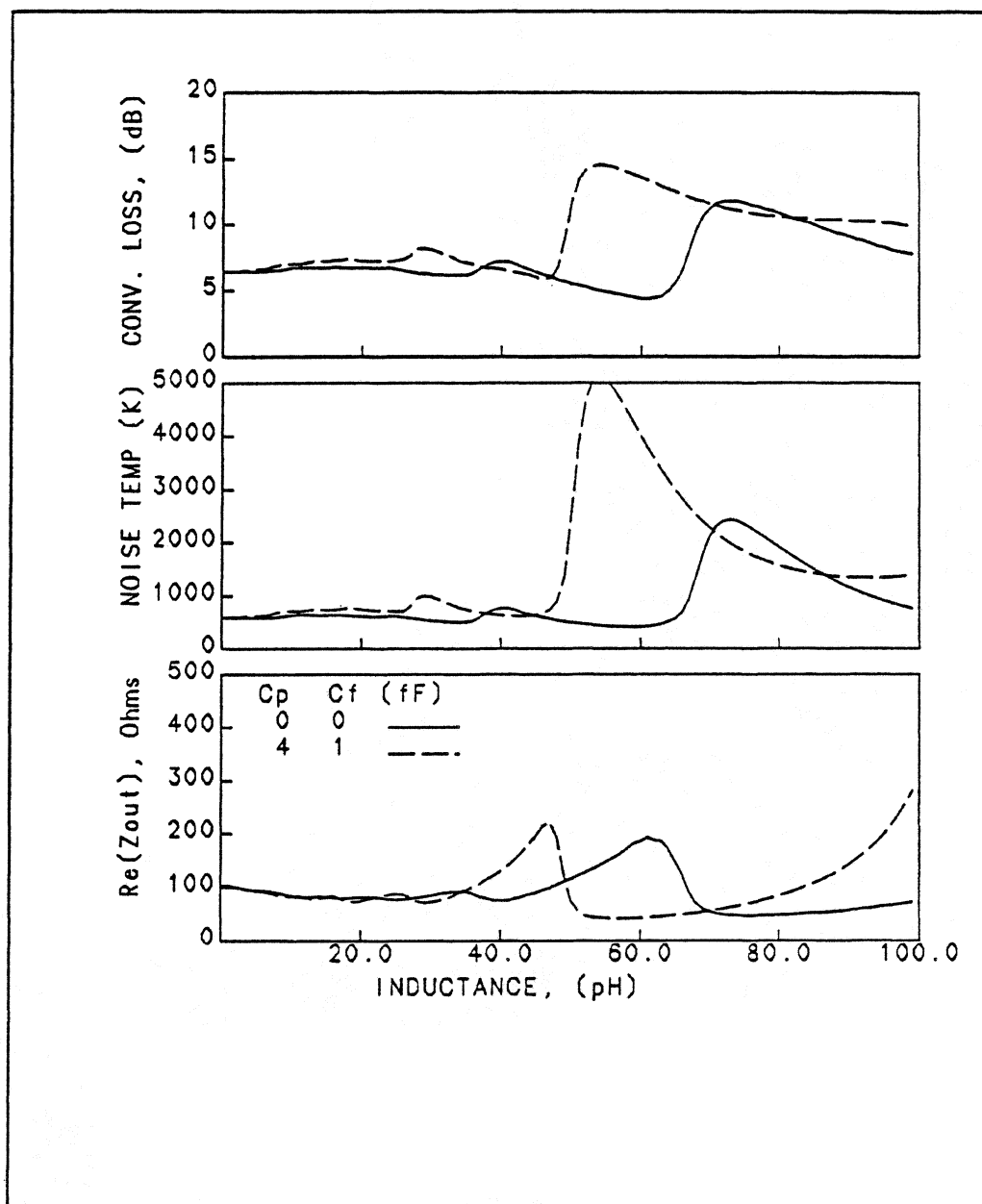


Figure 5: Subharmonic mixer performance comparison between a low capacitance (whisker contacted) and a higher capacitance (planar) diode. The solid curve represents the whisker contacted diode. LO, signal and IF are 108, 216, and 1.4 GHz respectively. $R_s = 12 \Omega$ and $C_{j0} = 3$ fF for both diodes. $C_p, C_f = 0$ for the whiskered diode and 4 and 1 fF respectively for the planar diode.

Design Optimization of Schottky Barrier Diodes at THz Frequencies

A. Grüb, V. Krozer, A. Simon, H.L. Hartnagel

Institut für Hochfrequenztechnik, Technische Hochschule Darmstadt, Merckstr. 25, D-64283 Darmstadt, Germany, Phone: +49 6151 162162, Fax: +49 6151 164367

Abstract

Whiskered GaAs Schottky barrier diodes are still the key elements in mixing applications at frequencies higher than 1000 GHz. It is obvious that envisaged operating frequencies of e.g. 2.5 THz, which are necessary for environmental studies, require sub-halfmicron anode diameters with all the encountered problems such as whisker stability, fabrication and reliability. Therefore, it is essential to optimize diode parameters such as epi layer thickness and doping concentration in order to achieve improved performance of the device and the overall receiver system.

The common optimization approaches make use of the cut-off frequency f_c which has several drawbacks. Therefore, we propose a new optimization procedure which takes into account the complete diode equivalent circuit. The I/V, C/V, and noise characteristics are calculated and a new cut-off frequency f_{cn} is defined. The calculations are based on an analytical diode model [1,2]. The new cut-off frequency f_{cn} is bias dependent and takes into account $R_s(I)$, $R_j(I)$ and $C_j(I)$. f_{cn} in conjunction with the diode noise temperature $T_n(I)$ is utilized to obtain a design procedure for the fabrication of whisker contacted as well as planar diode structures.

The results demonstrate that the epi layers should be thinner than currently used for the fabrication of THz Schottky diodes in order to improve the diode performance.

Introduction

The requirement of atmospheric studies (ozone depletion) has caused a strongly increased interest in heterodyne receivers for applications at frequencies higher than 1 THz. The OH molecule for example plays an important role in the catalytic ozone destruction process. This molecule has a transition frequency of 2514.3 GHz which corresponds to the lowest energy level. Other important molecules in this respect are O_3 (2510.6 GHz) and H_2O (2529.3 GHz) [3].

Heterodyne receivers at frequencies above 1 THz have to use whisker contacted Schottky barrier diodes as mixing element. The application of SIS junctions as well as planar Schottky diodes are presently restricted to lower frequencies due to material and technology problems.

The application of whisker contacted Schottky diodes at THz frequencies requires an optimized diode design in order to achieve the optimum mixer performance. The diode design parameters are the anode diameter d_{an} , the epi doping concentration N_e and the epi thickness t_e . Recently, several groups have made contributions to the optimization of Schottky diodes [2,4,5,6,7]. The main task of the optimization procedure is to define an appropriate criterium for the parameter optimization. Commonly accepted is the figure-of-merit cut-off frequency which makes use of constant values of the diode series resistance and the zero bias junction capacitance for the optimization. It is obvious that these assumptions are very different from the conditions in a mixer where the diode is biased strongly in the forward direction. This paper introduces a more realistic cut-off frequency which is based on bias dependent parameters and takes into account all elements of the diode equivalent circuit.

Diode model

A diode model for the simulation of THz Schottky diodes has to include the following items:

- field emission and thermionic field emission
- current spreading in the different layers
- current dependent recombination velocity
- field dependent electron mobility
- equations for R_j and C_j which are valid near flat-band

Our analytical diode model has the above mentioned features and details have been presented earlier [1,2].

Optimization Approaches

For a successful diode parameter optimization procedure one has to know how a variation of the parameters affects the diode performance. One possibility is to investigate the influence on the elements of the diode equivalent circuit which is shown in fig.1 . For the resistive down conversion of a THz signal only the nonlinear junction resistance R_j is necessary. All other elements such as the junction capacitance C_j and the series resistance R_s which has contributions due to the resistance of the undepleted epi layer R_{epi} , the substrate resistance R_{sub} and the contact resistance R_{con} are parasitics which influence the diode performance negatively and therefore have to be minimized. Additionally, noise sources due to thermal noise u_{th} , hot electron noise u_{hot} , shot noise i_{shot} and noise due to traps i_{trap} have to be considered.

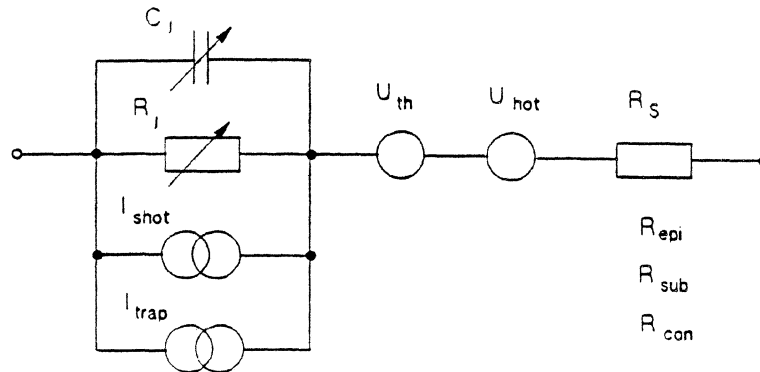


Fig.1: The diode equivalent circuit

The basic influence of the diode design parameters on the different elements of the diode equivalent circuit is summarized in the following table:

	R_j and η	C_j	R_s	i_{shot}	u_{th}	u_{hot}
d_{an}	+	-	+			
N_e	-	-	+	-	+	+
t_e	(+)	+	-		-	

The $+/-$ in the table mean that the corresponding design parameter should be chosen as large/small as possible in order to minimize the parasitics. The first column corresponds to the nonlinearity of

the junction resistance which should be as large as possible. In every row there exist + and - at the same time which means that a compromise has to be found. The problem of diode optimization finally focusses on the question of defining an appropriate criterium for these compromises. In the following sections two optimization criteria will be described and discussed.

The figure-of-merit cut-off frequency f_c (in the following referred to as standard cut-off frequency) is a wellknown and commonly accepted parameter for the optimization of high-frequency devices. For Schottky diodes the cut-off frequency is defined as follows.

$$f_c = \{2\pi R_s C_{j0}\}^{-1} \quad (1)$$

The above definition takes into account only constant values for the series resistance R_s and the zero bias junction capacitance C_{j0} of the diode. These two parameters are both dependent on the anode diameter, the epi layer doping concentration and thickness. The cut-off frequency f_c can be determined by either measuring the corresponding values of R_s and C_{j0} or by utilizing a diode model for the calculation. The diode design parameters are then chosen such that the cut-off frequency becomes as large as possible.

This approach has several drawbacks which make the use as optimization procedure questionable:

- R_j is neglected
- no bias dependence is considered

Since THz Schottky diodes have to be biased at large forward currents near the flat-band condition, these drawbacks are quite severe. At the operating bias the diode junction resistance is only a few times larger than the series resistance and, therefore, has to be considered in the optimization procedure. Furthermore, the elements of the diode equivalent circuit such as junction resistance, junction capacitance and series resistance are strongly bias dependent. Therefore, the cut-off frequency varies also with the applied bias.

The new approach takes into account all elements of the diode equivalent circuit. The impedance of the diode is given by

$$Z_d = R_s + \frac{R_j}{1 + j\omega R_j C_j} \quad (2)$$

For the definition of a new cut-off frequency the following relationship is used which is similar to the definition of the standard cut-off frequency.

$$\operatorname{Re}\{Z_d\} = \operatorname{Im}\{Z_d\}$$

This condition leads to a second order equation. The solution provides a condition for the junction resistance (eq. 3) and results in an efficient definition of a new cut-off frequency f_{cn} (eq. 4).

$$R_j \geq (2 + \sqrt{8}) R_s \quad (3)$$

$$f_{cn} = \{4\pi R_s(I) C_j(I)\}^{-1} \quad (4)$$

The smallest value for the junction resistance which is equal to $R_j = (2 + \sqrt{8}) R_s$ defines an operating bias which corresponds perfectly to experimentally obtained values in receiver systems. Therefore, this smallest value of R_j is used to define the diode operating bias. The proposed optimization process includes the following steps:

1. choose a set of design parameters d_{an} , N_e , t_e
2. calculate diode I/V, C/V and noise characteristics
3. extract R_s for high currents
4. define operating bias
5. check current density and noise temperature at this bias
 if $J \geq 10000 \text{ A/mm}^2$ or $T_n \geq 250 \text{ K}$ goto 1.
 else
6. calculate new cut-off frequency

Discussion

This section shows the results which have been obtained by applying of the two previously described optimization procedures. All calculations are made for a substrate doping concentration of $2 \cdot 10^{18} \text{ cm}^{-3}$ and a substrate thickness of $50 \text{ }\mu\text{m}$ (including a $1 \text{ }\mu\text{m}$, $3 \cdot 10^{18} \text{ cm}^{-3}$ buffer layer). These are also the values currently used for diode fabrication in our laboratory.

Standard cut-off frequency:

Fig.2 and fig.3 show the standard cut-off frequency as a function of the epi thickness and epi doping for an anode diameter of 0.8 and 0.4 μm .

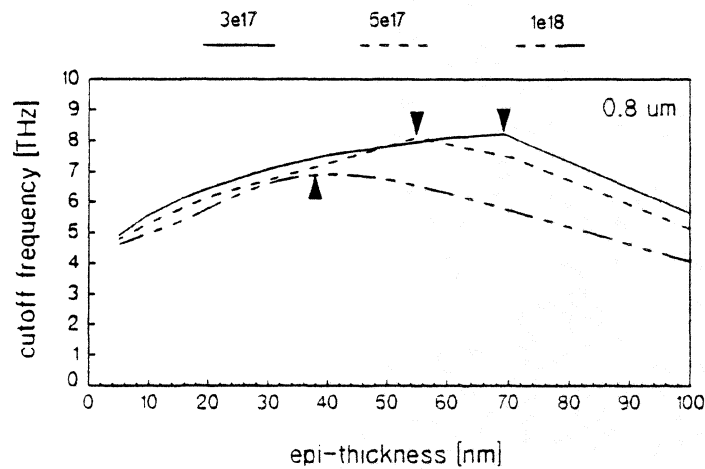


Fig.2: Standard cut-off frequency for 0.8 μm anode diameter

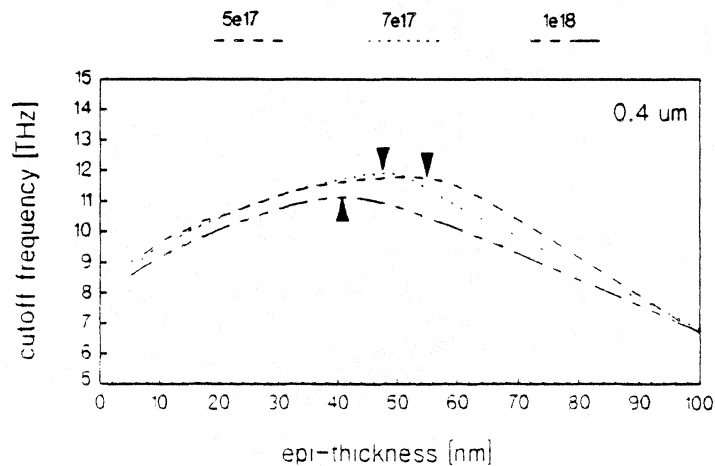


Fig.3: Standard cut-off frequency for 0.4 μm anode diameter

The first result is that the maximum of the cut-off frequency for all epi doping concentrations and anode diameters is obtained for an epi layer thickness which is equal to the zero bias depletion width (dark triangles in fig.2,3). A comparison to some of the commercially available diodes reveals

that so far all these diodes have been designed according to this optimization criterium.

diode	d_{an} [μm]	N_e [$10^{17} cm^{-3}$]	t_e [nm]
1I7*	0.8	3	70
1T12*	0.5	4	75
1I12*	0.45	4.5	60
1T14*	0.25	10	60
DAC3 – 08 ⁺	0.8	3	70
DAC10 – 08 ⁺	0.8	10	30

* fabricated at the University of Virginia

+ fabricated at the University of Darmstadt

It can also be seen that with decreasing anode diameter the maximum cut-off frequency is achieved with higher epi doping densities which approach a value of $10^{18} cm^{-3}$ for sub-halfmicron diodes.

New cut-off frequency:

The situation is quite different for the new cut-off frequency. Fig.4 and fig.5 show the new cut-off frequency as a function of the epi thickness and epi doping for an anode diameter of 0.8 and 0.4 μm .

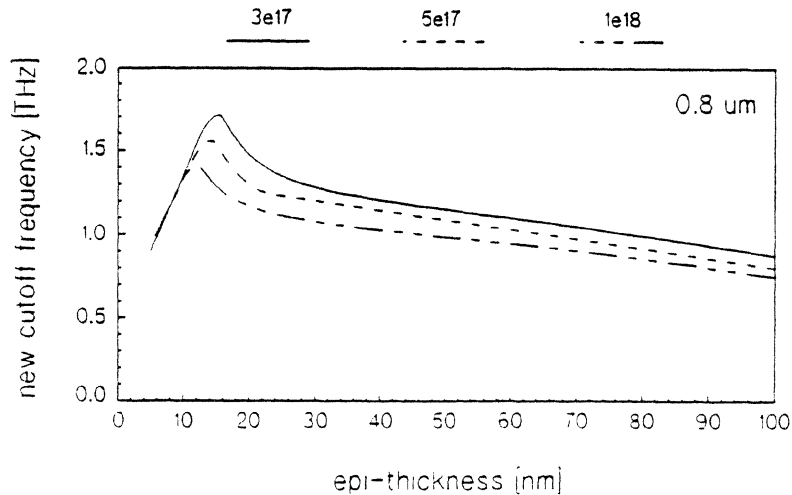


Fig.4: New cut-off frequency for 0.8 μm anode diameter

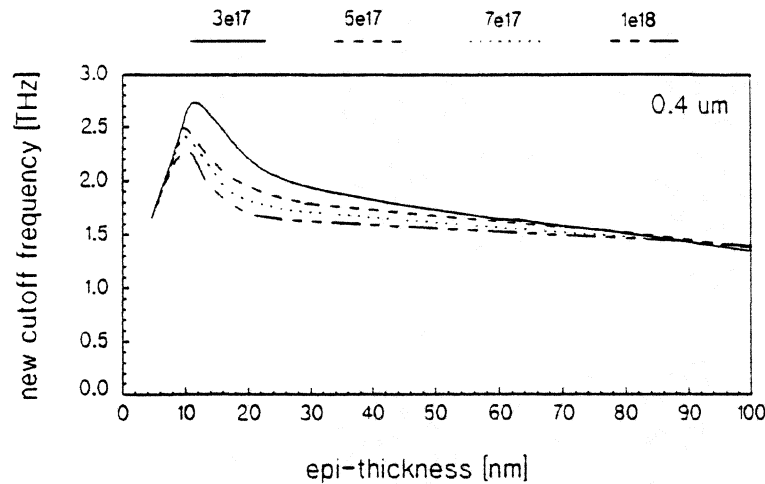


Fig.5: New cut-off frequency for 0.4 μm anode diameter

First, one can see that for epi layers thinner than $\approx 10 \text{ nm}$ f_{cn} does not depend on the doping concentration any more because the junction capacitance is more or less dominated by the substrate doping. The maximum of the cut-off frequency f_{cn} occurs at values for the epi layer thickness between 11 and 15 nm. A closer look at the simulation results reveals that these values correspond to an epi layer which is just becoming depleted at the operating bias. This epi layer depletion leads to a minimization of the series resistance because R_{epi} becomes zero for this special bias condition.

A second important result is that lower doping concentrations lead to higher cut-off frequencies f_{cn} . This is different from the results which are obtained from the standard approach where high doping concentrations are preferred. Since the noise due to hot electrons increases inversely to the doping concentration, which has to be considered, the optimum N_e should be $3 \cdot 10^{17} \text{ cm}^{-3}$. For this doping concentration the noise contribution due to hot electrons is still neglectable at the calculated bias. Currently, no diodes with such thin epi layers have been fabricated but similar simulation results have been obtained by a different approach [6].

Fig.6 illustrates the dependence of the standard and new cut-off frequency on the anode diameter for a given epi doping concentration. Both cut-off frequencies increase with decreasing anode diameter, as expected. Even for anode diameters as small as 0.1 μm there is no saturation visible. However, anodes smaller than 0.1 μm are not reasonable. Besides the difficulties of reliable fabrication and contacting, the required operating current densities exceed 10000 A/mm² leading to a degradation

of the Schottky contact during operation [8].

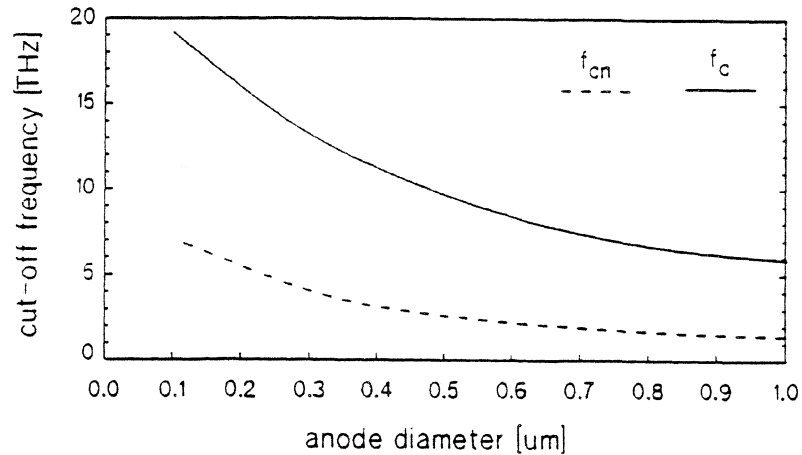


Fig.6: Standard and new cut-off frequency as function of the anode diameter

Conclusions

A new optimization approach for THz Schottky diodes has been presented. This approach makes use of a new cut-off frequency which is based on the complete diode equivalent circuit. The bias dependence of every single circuit element is taken into account. The results show that the thickness of the epi layer should be chosen such that at the operating point the epi layer is just depleted. Currently, diodes with epi layers of about 15 nm are under fabrication for a comparison with diodes designed according to the standard approach.

Acknowledgements

This work has been funded by the Deutsche Forschungsgemeinschaft DFG whose support is gratefully acknowledged. The authors would like to thank Dipl.-Ing. K. Beilenhoff for stimulating discussions.

References

- [1] V. Krozer, A. Grüb: A Novel Fabrication Process and Analytical Model for Pt/GaAs Schottky Barrier Mixer Diodes, *Solid-State Electronics*, Vol. 37, No. 1, pp. 169–180, 1994.
- [2] A. Jelenski, A. Grüb, V. Krozer, H.L. Hartnagel: New Approach to the Design and the Fabrication of THz Schottky Barrier Diodes, *IEEE MTT-41*, Vol. 41, No. 4, 549–556, 1993.
- [3] R. Titz, M. Birk, D. Hausamann, R. Nitsche: 2.5 THz Receiver for Stratospheric Measurements, *International Seminar on THz Electronics*, March 28–29, Darmstadt, Germany, 1994.
- [4] W.C.B. Peatman, T.W. Crowe: Design and Fabrication of 0.5 Micron GaAs Schottky Barrier Diodes for Low-noise Terahertz Receiver Applications, *Int. J. Infrared and Millimeter Waves*, Vol. 11, No. 3, 355–365, 1990.
- [5] T.W. Crowe, W.C.B. Peatman, P.A.D. Wood, X. Liu: GaAs Schottky Barrier Diodes for THz Applications, *Proc. IEEE Int. Microwave Symposium*, Albuquerque, USA, 1992.
- [6] K. Mizuno, T. Suzuki, J.J. Chang, T. Nozokido, C.M. Mann, Y. Kuwano: Development of GaAs Schottky Barrier Diodes for the Submillimeter Wave Region, *Proc. Int. Conf. Advanced Microelectronic Devices and Processing*, 253–258, Sendai, Japan, 1994.
- [7] S. Mukhopadhyay, A.N. Daw: On the Dependence of Cut-off Frequency of a Schottky Diode on Epilayer Doping, *Solid-State Electronics*, Vol. 37, No. 1, 192–194, 1994.
- [8] A. Grüb, V. Krozer, A. Simon, H.L. Hartnagel: Reliability and Microstructural Effects of GaAs Schottky Diodes for Submillimeter-Wave Mixing Applications, *Solid-State Electronics*, accepted for applications.

NOVEL CHIP GEOMETRIES FOR THz SCHOTTKY DIODES

W. M. Kelly, Farran Technology Ltd., Cork, Ireland

S. Mackenzie and P. Maaskant, National Microelectronics Research Centre,
University College, Cork, Ireland

Introduction

For THz applications involving low noise heterodyne receivers, the whisker-contacted Schottky barrier diode provides excellent room temperature and cryogenic performance. The traditional chip structure consists of a honeycomb anode array on top of a chip which is typically 100 μ m square and 100 μ m thick, with ohmic contacts on the back, or occasionally on the side, so-called notch-front chips [1]. The chip is mounted in a variety of structures such as across waveguides, on planar filter metallisations, or at the end of coaxial filters, and the ideal chip shape for these differs. It is important to build the chip structure into the electrical design, especially at short wavelengths where chip dimensions are comparable to waveguide dimensions.

Fabrication Options

In light of the above, we explore in this paper the possibilities for fabricating new or improved chip structures using advanced processing techniques such as reactive ion etching (RIE), etch-stop layers, epitaxial lift-off (ELO), and bonding by atomic rearrangement (BAR). RIE enables the etching of deep features (up to hundreds of micrometers) into the surface of the semiconductor wafer [2]. Additionally, the side profiles of the etched features can be controlled, varying between purely isotropic to highly anisotropic. Etch-stop-layers are often used to enable accurate control of vertical etching. ELO is a technique involving the use of chemical etching and often etch-stop-layers, in which the surface layers including the active devices are lifted off one substrate and transferred to another [3]. For example, active optoelectronic devices can be fabricated on InP or GaAs substrates and transferred to Si wafers where they can be interconnected with electronic circuitry [4]. In respect to millimetre wave devices, it can be envisaged as a good technique for producing very thin planar chips. BAR [5] is an alternative for achieving this result, in which pieces of one semiconductor can be

attached to another using a high temperature controlled environment anneal to create the bond. These various techniques enable processes to be developed for the fabrication of chips with arbitrary cross-sectional shape with high yield and with little if any limitation on the electrical characteristics of the anode junction.

Fabrication Process

The most straightforward technological solution involves RIE. We have developed a process which allows diode chips of circular, square or rectangular cross-section to be fabricated in thicknesses down to about $20\mu\text{m}$. The process commences by the deposition of a layer of passivation, usually SiO_2 , to a thickness of about $0.5\mu\text{m}$. This is followed by the lithography for the anode definition. We use an electron beam lithographic system along with dry-developable silylated resist technology for this step. The anode holes are defined in the SiO_2 layer using RIE with CHF_3/Ar gas. The chip shape is then defined by a second level of lithography, $30\mu\text{m}$ circles in the case of the chips described here, followed by deep RIE in SiCl_4 gas. An ohmic contact is electroplated on to the mesa sidewalls and alloyed prior to Pt/Au anode metallisation. The substrate is removed by a chemical/grinding process and a back contact metallisation is evaporated on to the chips before separation for electrical characterisation.

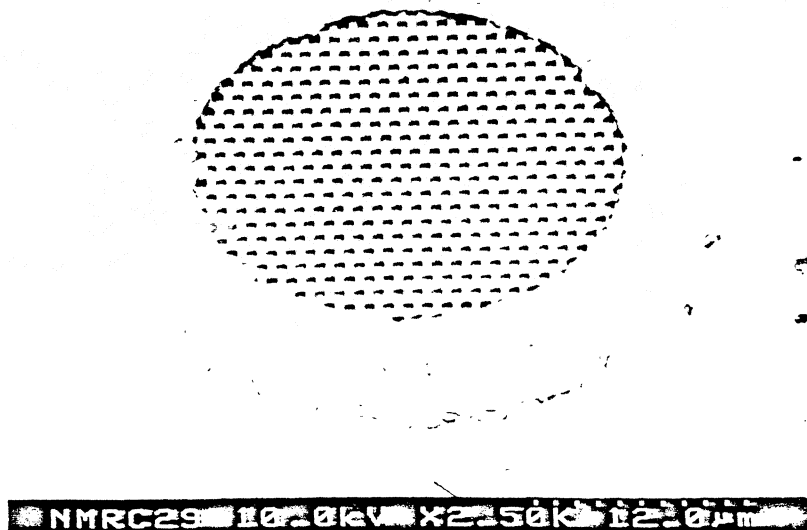


Figure 1. Micrograph of $30\mu\text{m}$ diameter cylindrical Schottky diode chip.
The chip is $30\mu\text{m}$ high and is patterned with $0.9\mu\text{m}$ anodes.

The micrograph in figure 1 shows for example a single 30 μm diameter by 30 μm high cylindrical diode chip with an array of micron-sized Schottky anodes on the top surface. This chip is ideally shaped for location at the end of a coaxial RF choke filter.

Device Characteristics

The above procedure has been used to fabricate a batch of demonstrator cylindrical diode chips with anode diameter of 1.3 μm on MOVPE grown GaAs. This material had a 5 μm buffer layer of doping $4 \times 10^{18} \text{ cm}^{-3}$, with a 600 \AA epilayer doped to $5 \times 10^{17} \text{ cm}^{-3}$. DC electrical characteristics of a typical diode are shown in figure 2.

The data is presented as a plot of $\log(I)$ against V , together with a curve of $I = I_0 \exp(q(V - IR_s)/\eta kT)$. The series resistance of the device has been measured as $R_s = 5.5 \Omega$ at a current of 10mA, consistent with the expected epilayer resistance and ohmic contact area. The diodes exhibit an ideality factor of $\eta = 1.2$ and a zero-bias junction capacitance of 6fF. Thus it can be seen that this new process can be used for the fabrication of smaller chip geometries without adversely affecting the electrical characteristics of the resulting devices.

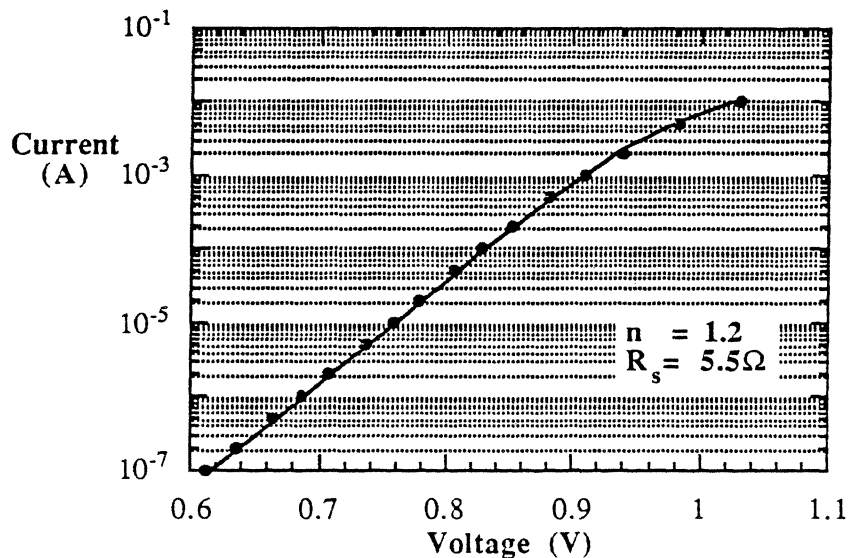


Figure 2. I-V characteristic of 1.3 μm diameter diode on cylindrical chip

We have also made devices with square anodes and high packing density as in figure 3, allowing for easy whisker contacting.

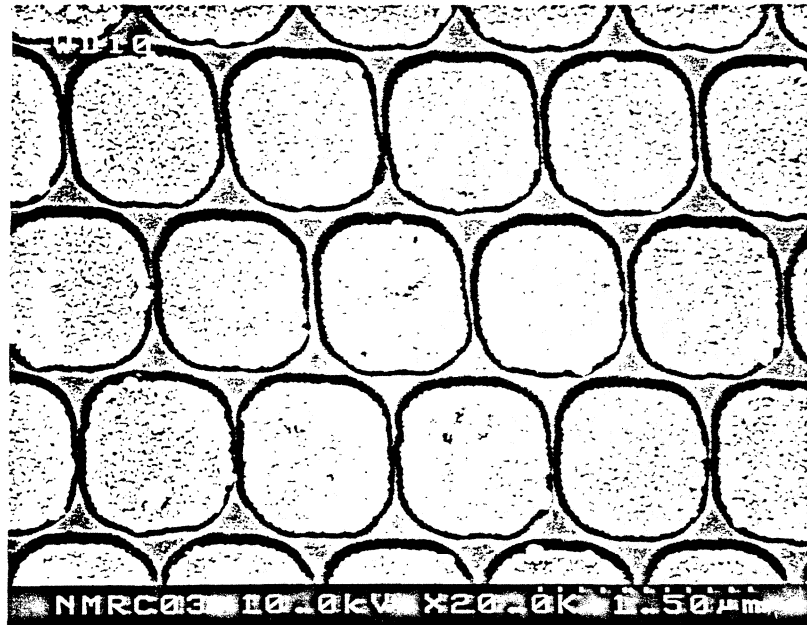


Figure 3. Densely packed 0.9 μ m square anodes with Pt/Au metallisation

Conclusions

An advanced process for the fabrication of new Schottky barrier diode chip geometries has been developed. The technique facilitates the production of chips with arbitrary cross-section and is especially suited to the fabrication of chips with dimensions less than the 80 μ m limit allowed by dicing. The devices are mechanically robust and exhibit no adverse effects on their electrical characteristics as a result of the fabrication procedure. Using this process, the structure of the diode chip can be matched to that of the circuit components, representing a significant advance for optimising the performance of submillimetre systems incorporating Schottky diode technology.

Acknowledgements

The authors would like to thank the EU Environmental Programme Contract No. EV5V-CT92-0081 for part support of this work.

References

1. Verlangieri P.A. and Schneider M.V., Intl. J. Infrared and Millimeter Waves, Vol.6, No. 12, pp 1191-1202, 1985
2. Gorowitz B. and Saia R.J., in *VLSI Electronics Microstructure Series*, Vol.8, Einspruch N.G. and Brown D.M., Eds., Academic Press Inc, San Diego, 1984
3. Chan W.K., Yi-Yan A. and Gmitter T.J., IEEE J. Quant. Electron., Vol. 27, No. 3, pp 717-725, 1991
4. Ersen A., Schnitzer I., Yablonovitch E. and Gmitter T., Solid State Electron., Vol. 36, No. 12, pp 1721-1739, 1993
5. Liao Z.L. and Mull D.E., Appl. Phys. Lett., Vol. 56, No. 8, pp 737-739, 1990

A Balanced Doubler Using a Planar Diode Array for 270 GHz

N.R. Erickson and J. Tuovinen
Five College Radio Astronomy Observatory
Dept. of Physics and Astronomy
University of Massachusetts
Amherst, MA 01003

and

B.J. Rizzi and T.W. Crowe
Semiconductor Device Laboratory
Dept. of Electrical Engineering
University of Virginia
Charlottesville, VA 22903

ABSTRACT

A balanced doubler for 270 GHz has been built using a planar array of four varactor diodes. The maximum output power is 5.5 mW, with 45 mW input, corresponding to an efficiency of 12%. Much higher efficiencies should be possible given the measured device parameters, but circuit or device parasitic losses appear to be a limitation at present.

INTRODUCTION

In the frequency range above 100 GHz, frequency multipliers can achieve high conversion efficiency at low input power, but tend to saturate at a rather low output power. The saturation mechanism is believed to be due to the limited carrier velocity in the GaAs epitaxial layer [1], which leads to a maximum displacement current in the varactor. Since the current increases with frequency for a given voltage swing, this becomes a major limitation for submillimeter applications.

One of the most attractive solutions to this problem is to use series arrays of diodes, because they allow one to increase both the area and the number of diodes, while they may be treated as a single diode so far as circuit design is concerned. In an array having the same impedance level and total power handling as a single diode, the current density varies inversely with the number of diodes. In work reported previously [2], we were able to use this approach to build a doubler for 160–180 GHz using a four diode array which greatly exceeded the power capability of conventional whiskered diodes. The doubler described in this work, operating with an output frequency of 270 GHz, also uses four planar diodes fabricated on a single chip.

The diodes fabricated for this doubler have excellent parameters (as measured at low frequencies) and have been designed for optimized operation in the circuit. A doubler mount has been designed for their use, and the diodes successfully installed. The output power obtained is comparable to that expected from a pair of whiskered devices at the same frequency. However, the efficiency is much lower, apparently due to some presently unknown loss. While this demonstrates the potential for such arrays, work remains to understand the nature of the loss.

DIODE DESIGN AND CHARACTERIZATION

The doubler circuit used is close to a scaled version of the one reported previously [2]. This circuit is quite simple to fabricate, and the installation of planar diodes in the 170 GHz model was fairly easy. The primary design constraint for the diodes is that the chip must fit into this mount. Diodes for this work were fabricated using the surface channel process [3], and this constrains the geometry to be an array in a straight line. The diode layout is shown in Fig. 1, showing the connections to the doubler mount at three points. The large central pad serves as the ohmic contact for the two central diodes, as well as the output terminal. The ohmic contacts for the end diodes are the two small inner pads. The end pads are sized

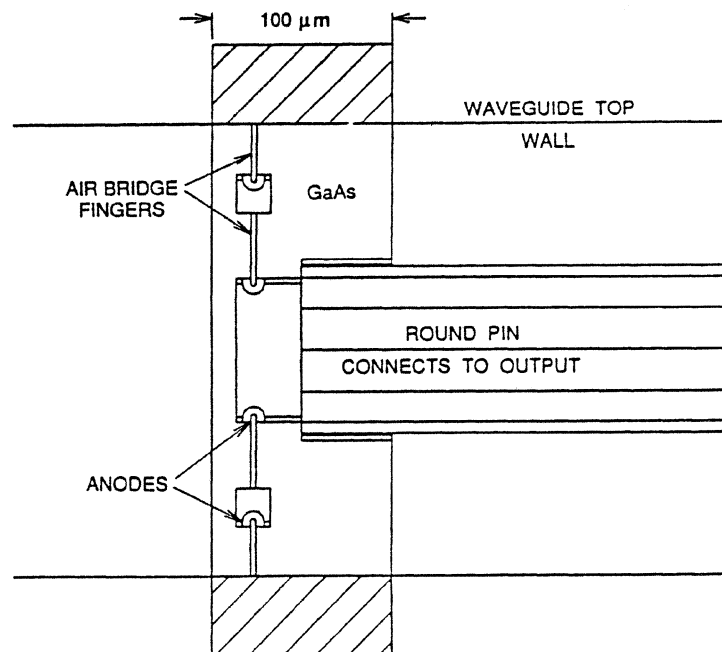


Fig. 1. Planar diode array, showing the method of installation into the circuit. The ends are soldered to the input waveguide walls, while the center pad solders to a pin connecting to the output waveguide. Chip is 370x100x25 μm, waveguide is 330 μm high.

to permit the chip to be soldered to the top and bottom walls of the waveguide. The diode layout was checked with the Hewlett Packard HFSS program to balance the power to the two diodes of each series pair, as well as to ensure reasonable power coupling to the chip. An effort was made to maximize the circuit inductance within the chip, since all varactors require substantial series inductance to tune out the average junction capacitance.

The series resistance of the parallel combination of the two pairs of diodes (equivalent to the resistance of a single diode) was measured in the doubler mount both at dc and using an HP 8720 network analyzer at 130 MHz [2]. The dc measurements gave a resistance of 6.4Ω , while the rf measurements were about 1Ω higher. The capacitance of each junction was measured at 1 MHz using a standard capacitance bridge. The junction capacitance was 16 fF with an additional pad to pad capacitance of 6 fF. The minimum value for the junction capacitance was 6 fF. The available pump power required a total breakdown voltage of only 15 V total for the two series diodes.

DOUBLER MOUNT AND TESTS

The doubler design is electrically equivalent to that in [2], but was scaled and slightly redesigned for use at 270 GHz. A cross section is shown in Fig. 2. All the waveguides were

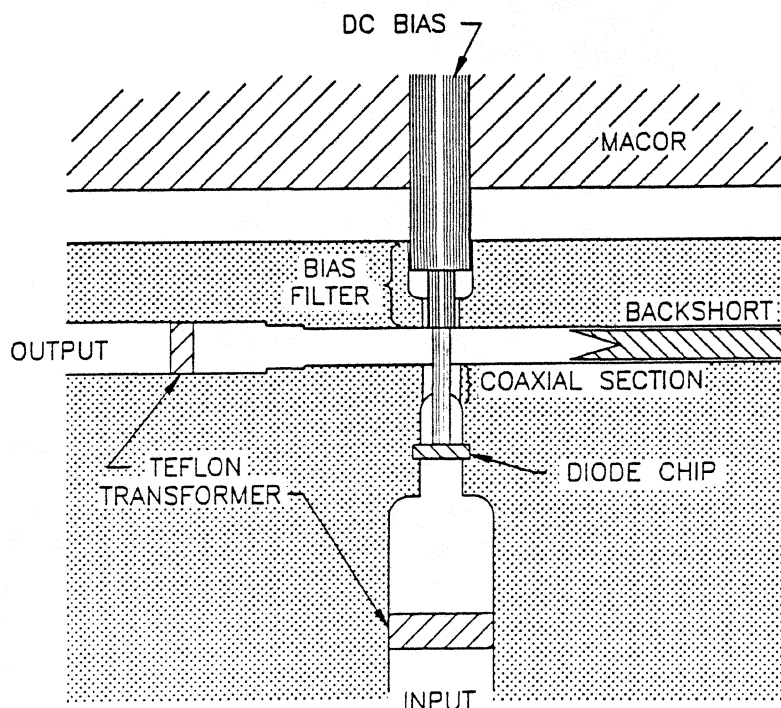


Fig. 2. Cross section through the balanced doubler mount.

milled symmetrically about the center line with the coaxial sections milled with a square outer section. The diode is soldered to the waveguide top and bottom walls as well as to the center pin in one operation, using low temperature indium solder. This operation was difficult with the small chip, but a technique was worked out in which the diode was placed on three thin solder preforms which ensured that the correct amount of solder was used. It is necessary to quickly cool the block after soldering since the solder tends to migrate along the surface of the device and bridge the anodes to the ohmic pads.

All tests were made with a 45 mW Gunn oscillator source tuning 125–145 GHz. The greatest output power was for 135 GHz input. At this frequency, no low loss isolators are available, so the interaction between the oscillator and the highly nonlinear load of the doubler can be severe. This is particularly a problem when neither the source nor the load is matched, as is the case here. To reduce the adverse interaction, a low loss adjustable phase shifter was included in the input circuit. A similar problem exists at the output, where the power sensor used (an Anritsu WR–8 sensor with taper to WR–3) also was poorly matched. The result is that it is difficult to determine the actual input and output powers, and whether the doubler is well matched. The Anritsu sensor was calibrated at both input and output frequencies with the same calorimeter built in WR–12 waveguide [4].

In these tests, the input and output match were optimized using teflon quarter-wave transformers positioned in the waveguide so that the output power was maximized. These transformers can correct a maximum VSWR of:

$$\epsilon(\text{teflon})[\lambda_g/\lambda(\text{air}) / \lambda_g/\lambda(\text{teflon})]^2 \cong 2.9 \text{ (typically).}$$

For the input circuit, the strong interaction with the oscillator made it impossible to determine the match obtained, but it was assumed that the maximum power from the oscillator was coupled to the doubler, since the addition of a second transformer was of little benefit. The improvement in power with the addition of the output transformer was only about 25%, meaning that the output match was fairly good. The available power was measured at 45 mW though the phase shifter, by placing a teflon transformer before the power sensor, and varying the phase for maximum power.

The peak output power was 5.5 mW, under bias conditions of 7.8 V and 0.3 mA. The efficiency is 12%, while the theoretical efficiency of the diode (assuming $\gamma = 0.4$, $R_s = 7.4 \Omega$, $C_j(0) = 16\text{fF}$ for each junction) is 35% at a total input power of 40 mW. While this operation corresponds to the expected varactor mode, only slightly less power (~ 5 mW) was obtained under very different bias conditions of 2.1 V and 7.4 mA. This is quite surprising since this mode of operation is inherently much less efficient due to the large dissipation of

power (15.5 mW) in the bias circuit. This would be the case if the diode had poor capacitance modulation, but this is inconsistent with the low frequency characterization of the diodes. The chip is not expected to show significant saturation at the input power level of 11 mW per junction, but no measurements of output vs. input power have been made. Another possibility is that some unmeasured parasitic loss is present, either in the diode chip or in the doubler mount, and that this loss is relatively more important when the diode is biased in the high Q varactor mode. This type of loss appears to be present on the 160–180 GHz planar diode doubler, and is discussed in ref [5]. Since these diodes are made in a very similar way, a full understanding of the lower frequency doubler should clarify these results.

CONCLUSIONS

A balanced doubler using a planar array of four varactors has been successfully built for 270 GHz. The output power is 5.5 mW at 12% efficiency. This efficiency is considerably lower than is expected from the diodes and work is presently directed at understanding the reason for this discrepancy.

ACKNOWLEDGEMENTS

This work was supported by NASA under grant NAGW-2430, and by JPL under contract 959206.

REFERENCES

- [1] E.L. Kollberg, T.J. Tolmunen, M.A. Frerking and J.R. East, "Current Saturation in Submillimeter Wave Varactors," *IEEE Trans. Microwave Theory Tech.*, Vol MTT-40, pp. 831–838, May 1992.
- [2] B.J. Rizzi, T.W. Crowe and N.R. Erickson, "A High-Power Millimeter-Wave Frequency Doubler Using a Planar Diode Array," *Microwave and Guided Wave Lett.*, pp. 188–190, June 1993.
- [3] W.L. Bishop, T.W. Crowe, R.J. Mattauch and P.H. Ostdiek, "Planar Schottky Barrier Mixer Diodes for Space Applications at Submillimeter Wavelengths," *Microwave and Optical Technology Lett.*, Vol. 3, No. 1, pp. 44–49, Jan. 1991.
- [4] B. Vowinkel, "Broad-Band Calorimeter for Precision Measurement of Millimeter- and Submillimeter-Wave Power," *IEEE Trans. Instrum. Meas.*, IM-29, pp. 183–189, 1980.
- [5] J. Tuovinen and N.R. Erickson, "Verification of the Finite Element Analysis and Study of Losses of a Planar Diode Doubler," this proceedings.

Planar Balanced Doubler Chip to 320 GHz

Brian J. Rizzi and Thomas W. Crowe
Semiconductor Device Laboratory
Department of Electrical Engineering
University of Virginia
Charlottesville, VA 22903-2442

I. INTRODUCTION

Schottky barrier varactor diodes are used as frequency multipliers in the local oscillator sources of heterodyne receivers at millimeter and submillimeter wavelengths. Whisker contacted GaAs Schottky barrier varactor diodes have been the most common frequency multiplier element, and have been used in heterodyne receivers extending well into the submillimeter wavelength range [1,2,3,4,5]. Although whisker contacted varactor diodes have proven very effective, much work has gone into developing varactor diodes which are more mechanically robust and have the potential to deliver larger amounts of power. This paper reviews the development of a planar varactor diode chip to be used in a balanced doubler to about 320 GHz.

The development of a multiplier chain to 1 THz using planar varactor diodes has continued. The proposed chain consists of two doublers (80 to 160 GHz and 160 to 320 GHz) and a tripler (320 to 960 GHz). The doubler chips incorporate multiple diodes for increased power handling ability, and are designed to be used in a balanced doubler circuit designed by Erickson [4]. The 320 GHz doubler chip is based upon the 160 GHz chip, which has been used in the balanced doubler circuit to generate record output power of 55 mW at 170 GHz [6,7,8].

The design goals for the 320 GHz doubler chip are reviewed in section II, and the DC characteristics for the prototype devices are described in section III. The results of

RF measurements are briefly described in section IV.

II. CHIP DESIGN GOALS

The 320 GHz balanced doubler chip is based upon the 160 GHz chip, however the design goals for the two devices are different. The primary goal in designing the first stage doubler was to generate as much output power as possible. The second stage doubler, however, must operate at twice the frequency, and is not required to handle as much input power. Therefore, the primary goal in designing the 320 GHz device is to achieve maximum diode efficiency while retaining moderate input power handling. An additional goal is to improve upon the power balance between the four junctions so maximum device efficiency is possible. The new device must also be designed so the chip fits in the 320 GHz doubler mount, requiring a chip length of only 500 μm . Sketches of the 160 GHz and 320 GHz devices are shown in Fig. 1 for comparison.

Since the goal is to develop an efficient doubler, the 320 GHz chips have considerably higher epitaxial layer doping densities and much thinner epitaxial layers compared to the 160 GHz diodes. The increased doping levels are required for reducing the device series resistance, which is especially important since the anode diameters are considerably smaller for the 320 GHz diodes. Although the higher doping density and thinner active layer result in a lower reverse breakdown voltage, this trade-off is acceptable since the input power requirement for the 320 GHz diodes is considerably lower than for the 160 GHz devices.

Similar to the 160 GHz doubler chip, the 320 GHz chip has two varactor diodes in series for each "leg" of the balanced doubler circuit. Since the doubler chip is soldered across the input waveguide, an initial constraint on the chip design is to fit the device into

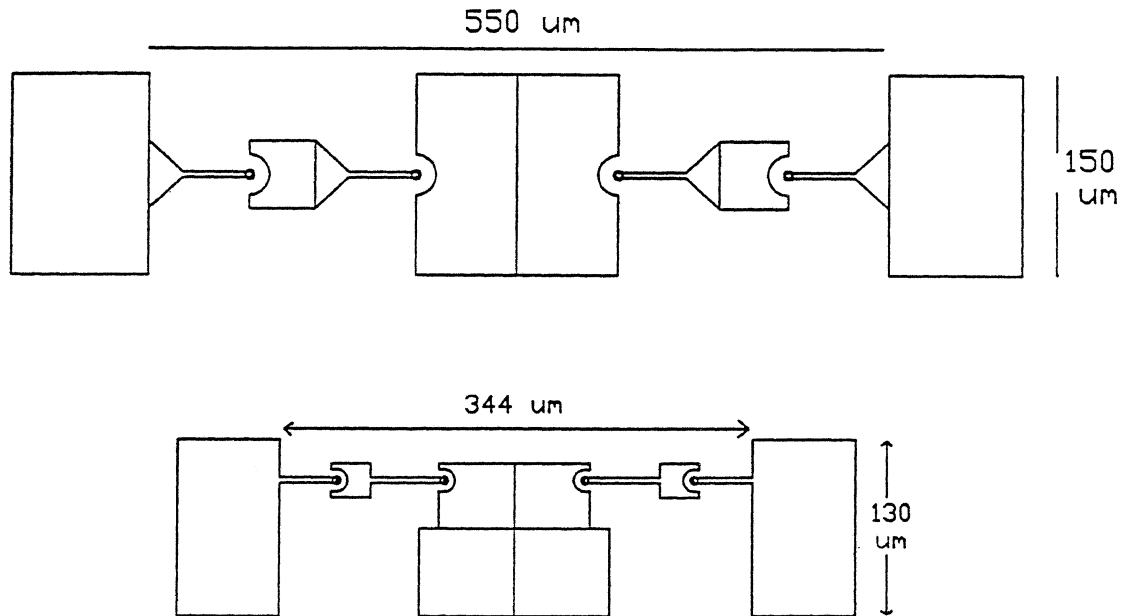


Fig. 1: Sketch of the 160 GHz (top) and 320 GHz (bottom) doubler chips.

the doubler mount. The Hewlett Packard High Frequency Structure Simulator (HFSS) has been used by J. Tuovinen (of the University of Massachusetts, Amherst) to help determine the chip dimensions for the prototype devices [9]. The 320 GHz chip is designed to span the input waveguide and is 500 μm in length by 130 μm in width. The ohmic contact pad size for the two inner diodes has been reduced to 25 μm x 25 μm and the center output pad and end contact pads have also been reduced in size compared to the 160 GHz chip. The smaller pads not only help lower the parasitic pad-to-pad capacitance, but they are necessary so that a total finger length of about 100 μm for each diode pair can be achieved for the reduced chip length. In order to reduce the ohmic pad size to 25 μm x 25 μm and obtain low series resistance, a contact resistivity of approximately $10^{-6} \Omega \text{cm}^2$ must be achieved for the 25 μm x 25 μm ohmic contact pads.

To achieve a good power balance between the four varactors on the doubler chip, each diode must have very similar characteristics. In addition to the junction capacitance, which is a function of the anode area, the pad-to-pad capacitance of each diode should also be approximately equal. Since the center output pad is considerably larger than the end contact pads, the finger length of the two center diodes (54 μm) is larger than that of the end diodes (42 μm) so the pad-to-pad capacitance seen by each diode is approximately the same. In addition, the center output pad is "flared" at the bottom so the bias pin can be soldered in place without having the solder come close to the center anodes.

The predicted chip parameters and DC characteristics for the planned 320 GHz diodes are listed in Table I. The 12 fF junction capacitance for each diode is designed to achieve a good match between the chip and circuit, and the series resistance is minimized while maintaining a breakdown voltage of approximately 8 V. The measured parameters for the 160 GHz SC10V2 doubler chips are also listed for comparison [6,7,8].

Table I: Predicted Parameters and DC Characteristics for 320 GHz Chip (single diode)							
type	t_{chip} (μm)	t_{epi} (μm)	N_{epi} (cm^{-3})	diam (μm)	C_{j0} (fF)	R_s (Ω)	V_{br} (V)
planned 320 GHz	25	0.40	1×10^{17}	4	12	7	8
measured 160 GHz	25	0.64	4.5×10^{16}	9	37	6	15

III. PROTOTYPE 320 GHZ DOUBLER CHIPS

Four batches of prototype 320 GHz balanced doubler chips have been fabricated, and an SEM photograph of a completed chip is shown in Fig. 2. As for the 160 GHz chip, the large central pad serves as the ohmic contact for the two central diodes, as well as the output terminal and bias connection. The ohmic contacts for the end diodes are the two small inner pads. The fabrication steps used for the 320 GHz doubler chips are based upon the surface channel process [10,11,12], and the 160 GHz planar doubler chip fabrication [6,7,8].

DC Characteristics

The measured DC characteristics of the four prototype batches of 320 GHz chips are shown in Table II. The SC3T1 and SC3T2 diodes have been fabricated with

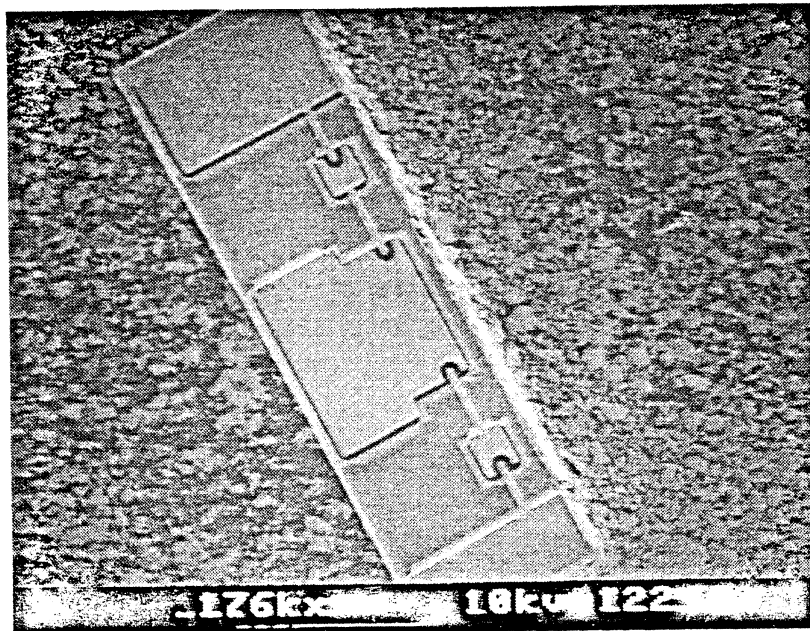


Fig. 2: SEM Photograph of the 320 GHz Balanced Doubler Chip.

evaporated ohmic contacts in an attempt to reduce the contact resistance, and have very similar DC characteristics. The zero bias capacitance, series resistance and breakdown voltage of these diodes are close to the predicted values given in Table I. However, the SC3T1 and SC3T2 diodes have very poor capacitance modulation (maximum capacitance/ minimum capacitance ratio) which severely limits the device RF performance. Diodes from these two batches have capacitance ratios ($\frac{C_{\max}}{C_{\min}}$) of approximately 1.2. A ratio of at least 2 is desired for frequency multiplication.

In the next batches of devices, steps have been taken to improve the capacitance modulation. The SC3T1 and SC3T2 diodes tend to punch-through before the maximum electric field for breakdown is reached, indicating a thicker active layer could yield improved performance. The SC3T3 devices have the same epitaxial doping density as the two previous batches, but the epitaxial thickness has been increased to 0.27 μm to allow for a greater applied reverse voltage and additional capacitance modulation. The

Table II: 320 GHz Balanced Doubler Chip Characteristics (single diode)

batch #	t_{chip} (μm)	t_{epi} (μm)	N_{epi} (cm^{-3})	diam (μm)	C_{j0} (fF)	R_s (Ω)	V_{br} (V)
SC3T1	25	0.25	1.5×10^{17}	3	14	8	7
SC3T2	25	0.25	1.5×10^{17}	3	15	9	7
SC3T3	25	0.27	1.5×10^{17}	4.5	28	8	8
SC3T4	25	0.40	1.0×10^{17}	3.5	15	6	9

SC3T4 diodes have a reduced epitaxial layer doping density of $1 \times 10^{17} \text{ cm}^{-3}$ in addition to an increased thickness of $0.40 \text{ }\mu\text{m}$. A lower active layer doping density should lead to a sharper capacitance variation. To eliminate possible sources of error and improve device yield, the evaporated ohmic contacts have been replaced with the proven SnNi/Ni/Au alloyed ohmic contact technology for the SC3T3 and SC3T4 diodes.

Capacitance measurements indicate the SC3T3 and SC3T4 diodes do have considerably improved capacitance modulation. The junction capacitance of the SC3T3 diodes, however, is quite large due to oversized anodes and they are not suitable for the 320 GHz doubler mount. The SC3T4 devices have a zero-bias junction capacitance of 15 fF, and a capacitance ratio of approximately 1.5. Often the pad-to-pad capacitance of planar diodes can be tuned out in the multiplier circuit. If the 4 fF pad-to-pad capacitance is subtracted from the SC3T4 diodes, the capacitance ratio improves to almost 2.

In addition to the pad-to-pad capacitance, the finger capacitance contributes to the total parasitics of the device. Most of the finger capacitance is caused by a portion of the contact finger overlying the oxide and the conductive GaAs near the anode. In an effort to reduce this capacitance, several SC3T4 chips have been etched an additional 12 minutes in the surface channel etch to undercut the contact finger length which covers the oxide and conductive GaAs. In Fig. 3 the capacitance-voltage characteristic of an SC3T4 single diode is shown before and after the additional surface channel etch. It is evident from the capacitance curve that the effect of the additional etching is a reduction in total capacitance by approximately 3 fF and an increase in the measured capacitance ratio from 1.5 to 1.7. If the pad-to-pad capacitance is now subtracted from the diode after the

additional etching, a capacitance ratio greater than 2 is obtained. The increased capacitance modulation of the SC3T4 diodes should lead to significantly improved RF performance.

IV. 320 GHz DOUBLER RF RESULTS

RF measurements for the SC3T2 and SC3T4 diodes have been performed by N. Erickson [13]. The planar doubler mount used for the 300 GHz tests is a scaled version

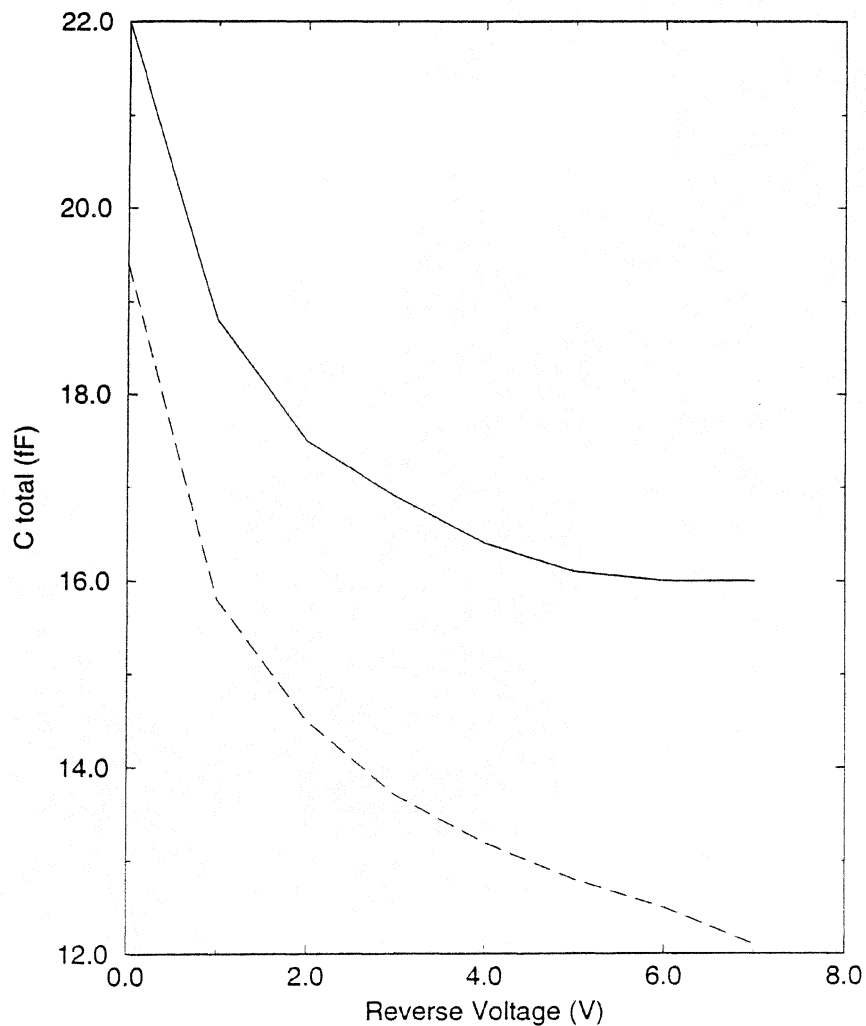


Fig. 3: C-V curve of SC3T4 diode before etching (solid) and after etching (dashed).

of the one used for the 160 GHz diodes [6,7,8]. The two doubler block cross-sections are essentially identical, and a sketch of the planar balanced doubler mount design is shown in Fig. 4. Matching for the 300 GHz tests was optimized using teflon quarter-wave transformers, which can be positioned in the input and output waveguides to achieve maximum output power. In addition, tuning is possible through the use of input and output backshorts. The substrates for the 320 GHz doubler chips have been thinned to approximately 25 μm to reduce the circuit loading caused by the bulk GaAs. The impedance match obtained for the planar chips is comparable to that for whiskered diodes in similar mounts.

Despite their small measured capacitance ratios, the SC3T2 diodes produced encouraging RF results. An output power of approximately 4 mW has been generated at

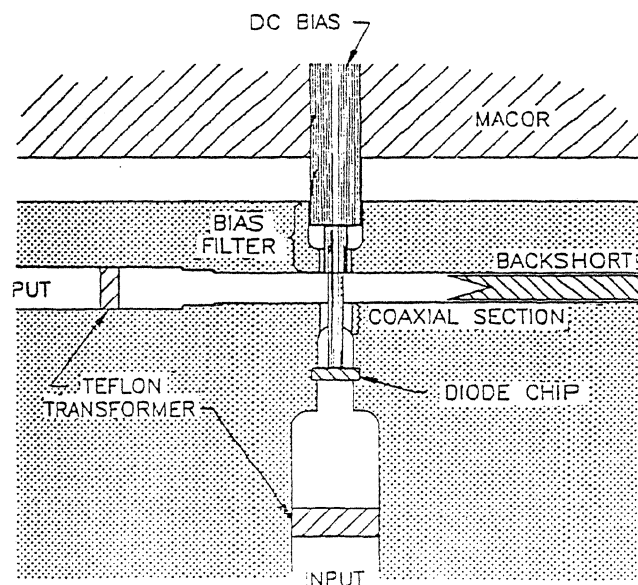


Fig. 4: Cross-section of the planar balanced doubler mount.

320 GHz with 30 mW input power supplied by a source consisting of a Gunn oscillator in conjunction with the 160 GHz planar balanced doubler. The SC3T2 diodes are certainly not optimized, as they produced the maximum output power of 4 mW at an applied bias between zero and -2 V, indicating much of the frequency multiplication occurred in a resistive, or "varistor" mode. In the "varistor" mode of operation, the forward I-V characteristic of the diode is used, and this is much less efficient than when operating as a varactor. Despite producing maximum output power with little to no applied reverse bias, this result matches the power output by Erickson's 300 GHz balanced doubler which uses two whisker contacted diodes [4]. The cause for the resistive mode operation is most likely due to the low breakdown voltage and small capacitance modulation of the SC3T2 diodes.

As expected, the SC3T4 diodes delivered improved performance compared to the SC3T2 devices due to increased capacitance modulation and breakdown voltage. A maximum output power of approximately 6 mW has been obtained at 270 - 300 GHz with the input power supplied by a Gunn oscillator. This result was achieved with 50 mW input power, for an efficiency of 12 %. Although this result is very impressive, the doubler does not appear to be operating at its fullest potential. The same output power obtained while operating in a "varactor" mode, which should be the most efficient, was also generated while operating in a "varistor" mode. A "varistor" mode of operation is normally not as efficient as pure varactor multiplication. The RF results indicate some parasitic element may be preventing the doubler from operating at its peak efficiency and causing it to operate equally as a varactor and a varistor. Despite this less than optimal operation, however, the generated output power equals the best doubler result at about 300 GHz.

V. SUMMARY

Improvements in planar chip and mount design have made the planar Schottky varactor diodes competitive with whisker contacted diodes at frequencies up to 320 GHz. By integrating several diodes on a single chip, increased power generation has been achieved.

Several design changes were implemented in the 320 GHz series diode array, including reducing the ohmic and anode contact pad sizes, staggering the finger lengths and reducing the overall chip dimensions compared to the 160 GHz devices. In addition, portions of the fabrication process were modified in the development of the smaller chips.

The first application of a planar array of varactor diodes in the 300 GHz frequency range has been demonstrated. The planar Schottky device has displayed superior performance to a pair of whisker contacted diodes used in a similar mount at a nearby frequency, thus demonstrating the potential for series diode arrays at millimeter and submillimeter wavelengths.

ACKNOWLEDGEMENT

The authors would like to thank Dr. Neal Erickson (U. Mass, Amherst) for supplying RF measurements on the balanced doubler. This work is supported by NASA (NGT-50725 and NAGW-2377) and JPL (#958202).

REFERENCES

- [1] R. Zimmermann, R. Zimmermann and P. Zimmermann, "All Solid-State Radiometers for Environmental Studies to 700 GHz," Third Int'l Symp. Space THz Tech., Ann Arbor, MI, March 1992.
- [2] H. Nett, S. Crewell, K. Kunzi, "A 625-650 GHz Heterodyne Receiver for Airborne Operation," 16th Int'l Conf. IR and MM Waves, Lausanne, Switzerland, August 1991.

- [3] S. Crewell and H. Nett, "Measurements of the Single Sideband Suppression for a 650 GHz Heterodyne Receiver," Third Int'l Symp. Space THz Tech., Ann Arbor, MI, March 1992.
- [4] N.R. Erickson, "High Efficiency Submillimeter Frequency Multipliers," 1990 IEEE MTT-S Int'l Microwave Symp., Dallas, TX, May 1990.
- [5] A. Rydberg, B.B. Lyons and S. Lidholm, "On the Development of a High Efficiency 750 GHz Frequency Tripler for THz Heterodyne Systems," IEEE Trans. Microwave Theory Tech., Vol. MTT-40, No. 5, pp. 827-830, May 1992.
- [6] B.J. Rizzi, T.W. Crowe and N.R. Erickson, "A High Power Millimeter Wave Frequency Doubler Using a Planar Diode Array," IEEE MTT-S Microwave and Guided Wave Letters, Vol. 3, No. 6, June 1993.
- [7] N.R. Erickson, B.J. Rizzi and T.W. Crowe, "A 174 GHz High Power Doubler Using a Planar Diode Array," Fourth Int'l Symp. Space THz Tech., Los Angeles, CA, March 1993.
- [8] B.J. Rizzi, K.K. Rausch, T.W. Crowe, P.J. Koh, W.C.B. Peatman, J.R. Jones, S.H. Jones and G. Tait, "Planar Varactor Diodes for Submillimeter Applications," Fourth Int'l Symp. Space THz Tech., Los Angeles, CA, March 1993.
- [9] J. Tuovinen, Private Communication, May 10, 1993.
- [10] W.L. Bishop, K. McKinney, R.J. Mattauch, T.W. Crowe and G. Green "A Novel Whiskerless Schottky Diode for Millimeter and Submillimeter Wave Applications," Proc. 1987 IEEE MTT-S Intl. Symp., Las Vegas, NV, 607-610, June 1987.
- [11] W.L. Bishop, T.W. Crowe, R.J. Mattauch and P.H. Ostdiek, "Planar Schottky Barrier Mixer Diodes for Space Applications at Submillimeter Wavelengths," Microwave and Optical Technology Lett., Special Issue on Space THz Tech., Vol. 3, No. 1, pp. 44-49, Jan. 1991.
- [12] W.L. Bishop, E.R. Meiburg, R.J. Mattauch and T.W. Crowe, "A Micron Thickness, Planar Schottky Barrier Diode Chip for Terahertz Applications with Theoretical Minimum Parasitic Capacitance," 1990 IEEE MTT-S Int. Microwave Symp., Dallas, TX, May 1990.
- [13] N.R. Erickson, J. Tuovinen, B.J. Rizzi and T.W. Crowe, "A Balanced Doubler Using a Planar Diode Array for 270 GHz," Fifth Int'l Symp. Space THz Tech., Ann Arbor, MI, May 1994.

On the Modelling of the Millimeter Wave Schottky Varactor

Jyrki T. Louhi and Antti V. Räisänen

Helsinki University of Technology, Radio Laboratory,
Otakaari 5 A, FIN-02150 Espoo, Finland

Abstract

Schottky varactor frequency multipliers are used to generate the local oscillator power at millimeter and submillimeter wavelengths. The aim of this study is to model the edge effects of the small-area circular anode in order to take them into account in all components of the equivalent circuit. The equivalent circuit contains a junction capacitance, a junction conductance, a series resistance and a model for electron velocity saturation. The correction factors due to the edge effect for the junction capacitance and for the series resistance are available in the literature. In this work we have modelled the electron velocity saturation by limiting the velocity of the transition front between the depleted and undepleted layer. By using this model the maximum current of the diode is given by the actual area of the transition front between depleted and undepleted layers. We have used our new model to analyse the two diode balanced doubler for 160 GHz constructed earlier by Erickson. The agreement between the theoretical results and the measurements is excellent, when the physical parameters of the epitaxial layer and the correction terms due to the edge effects are employed.

1 Introduction

Frequency multipliers are used to generate the all-solid-state local oscillator power of heterodyne receivers at millimeter and submillimeter wavelengths [1]. These local oscillators are needed in many near future scientific satellites (SWAS, Odin, FIRST and SMIM). At millimeter and submillimeter wavelengths a Schottky varactor is the most commonly used multiplier device, although several novel varactors have been proposed [2].

Although the equivalent circuit of the Schottky varactor has been widely studied, varactor fabrication technology has been greatly improved and many different kind of multiplier structures have been tried, the maximum output power of all-solid-state local oscillators remains low at submillimeter wavelengths. The aim of this work is to develop the equivalent circuit of the Schottky varactor in order to find a model, which is physically valid at millimeter and submillimeter wavelengths .

2 Model of Schottky varactor

The Schottky varactor consists of a circular metallic anode on top of a epitaxial GaAs as shown in Figure 1. The radius of the anode is R_0 and the thickness of the epitaxial layer is t_e . At millimeter and submillimeter wavelengths the radius of the varactor anode is not large compared to the thickness of the epitaxial layer and to the width of the depletion layer. Due to the small-area circular anode the potential of the epitaxial layer as well as the transition front between the depleted and undepleted layer are curved near the periphery of the circular anode as shown in Figure 1. This edge effect should be taken into account in the equivalent circuit of the Schottky varactor, which includes

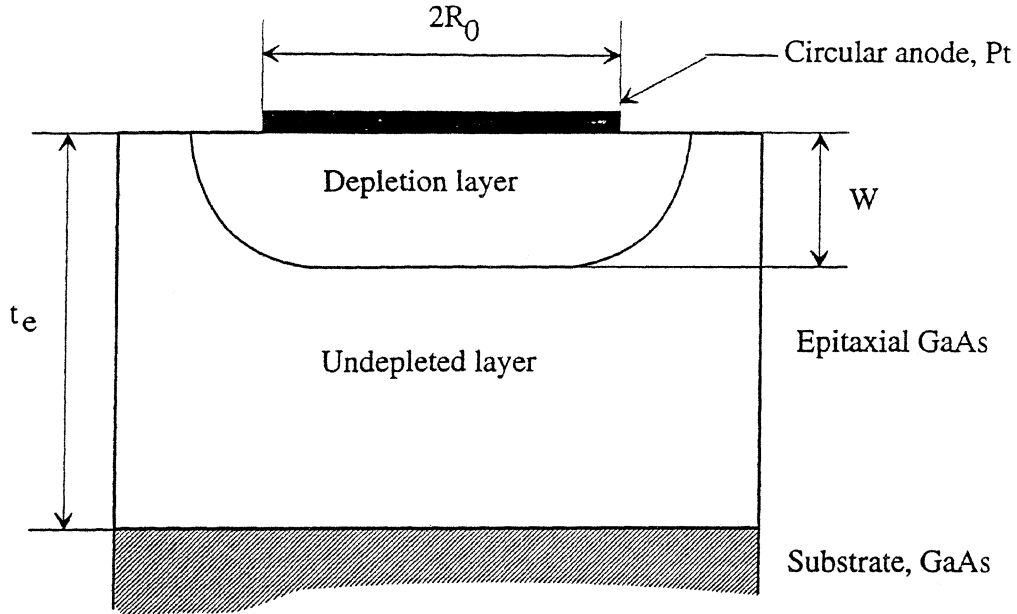


Figure 1: Schematic of a Schottky varactor.

typically a nonlinear junction capacitance, a nonlinear junction conductance and a linear or nonlinear series resistance [1]. At millimeter and submillimeter wavelengths a model of the electron velocity saturation should also be included to the equivalent circuit of the Schottky varactor.

2.1 Junction capacitance

The capacitance of the circular Schottky varactor can be found by calculating the net charge of the depletion layer from the numerically solved potential of the epitaxial layer [3, 4]. At millimeter wavelengths a first order correction term is normally included to the model of the junction capacitance as [3, 4, 5]

$$\begin{aligned}
 C_j &= \frac{\epsilon \pi R_0^2}{W} \left(1 + b \frac{W}{R_0} \right) \\
 &= \frac{\epsilon \pi R_0^2}{W} \gamma_C,
 \end{aligned} \tag{1}$$

where ϵ is the dielectric constant of the semiconductor, W is the width of depletion layer, b is numerical constant 1.5 and γ_C is the net correction term compared to the capacitance of the one-dimensional varactor. At submillimeter wavelengths an extra second order correction term should also be included in the model of the junction capacitance as [4]

$$C_j = \frac{\epsilon \pi R_0^2}{W} \left(1 + b_1 \frac{W}{R_0} + b_2 \frac{W^2}{R_0^2} \right), \quad (2)$$

where the numerical constants are $b_1 = 1.5$ and $b_2 = 0.3$.

2.2 Series resistance

The series resistance of the partially depleted epitaxial layer can be found from the geometrical resistance of the undepleted layer. The exact solution of the resistance depends from the width of the undepleted layer, which means that the series resistance is nonlinear [6]. However, if the nonlinearity of the series resistance is omitted, the efficiency of the multiplication is slightly decreased at low input power levels and remains almost the same at high power levels [7]. In computer simulations a constant series resistance is used in order to decrease the required time of the numerical analysis without decreasing the accuracy of the results too much. The resistance of the totally undepleted epitaxial layer with circular anode can be found analogically [8]

$$\begin{aligned} R_e &= \frac{\rho t_e}{\pi R_0^2} \frac{1}{t_e} \int_0^\infty \frac{\tanh(z t_e) \sin(z R_0) J_1(z R_0)}{z^2} dz \\ &= \frac{\rho t_e}{\pi R_0^2} \gamma_R, \end{aligned} \quad (3)$$

where ρ is the resistivity of the epitaxial layer and γ_R is the net correction term compared to the resistance of the one-dimensional varactor. For a varactor with a large anode compared to the thickness of the epitaxial layer ($R_0 \gg t_e$) the correction factor γ_R is 1 and for a very small anode the correction factor is

$$\gamma_R = \frac{\pi R_0}{4 t_e}. \quad (4)$$

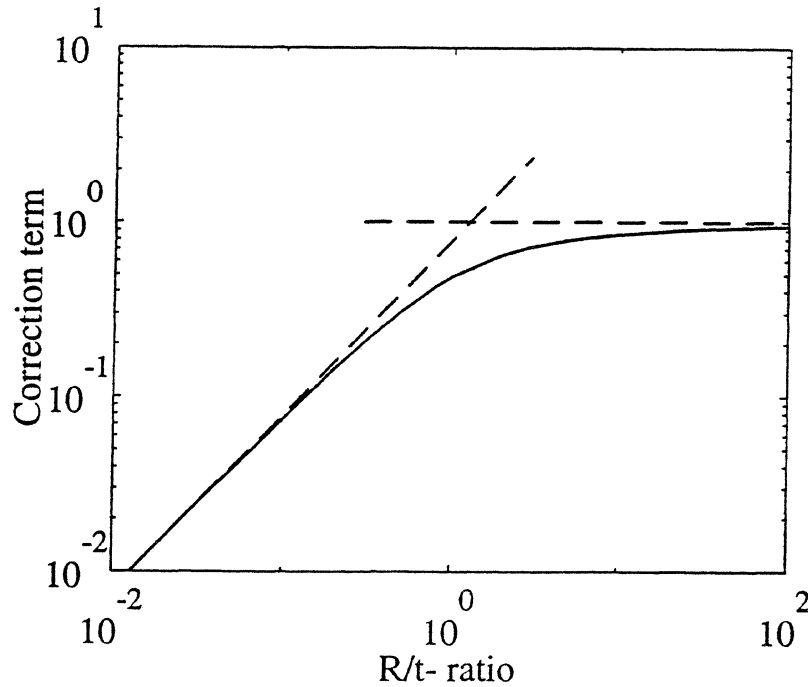


Figure 2: The net correction term of the series resistance γ_R .

For all R_0/t_e -ratios the net correction term can be easily found from the approximate formula

$$\gamma_R \approx \left[1 + \frac{4t_e}{\pi R_0} \right]^{-1}. \quad (5)$$

For a typical millimeter wave varactor the radius of the anode is about three times the thickness of the epitaxial layer and so the net correction term is about 0.73 (see Figure 2). The total series resistance of the varactor includes also the contact resistance (about 1Ω) and the series resistance of the substrate layer. At frequencies above 100 GHz the plasma resonance should also be included to the model of the series resistance [6].

2.3 Electron velocity saturation

At millimeter and submillimeter wavelengths the maximum output power of a Schottky varactor frequency multiplier is strongly affected by the electron velocity saturation,

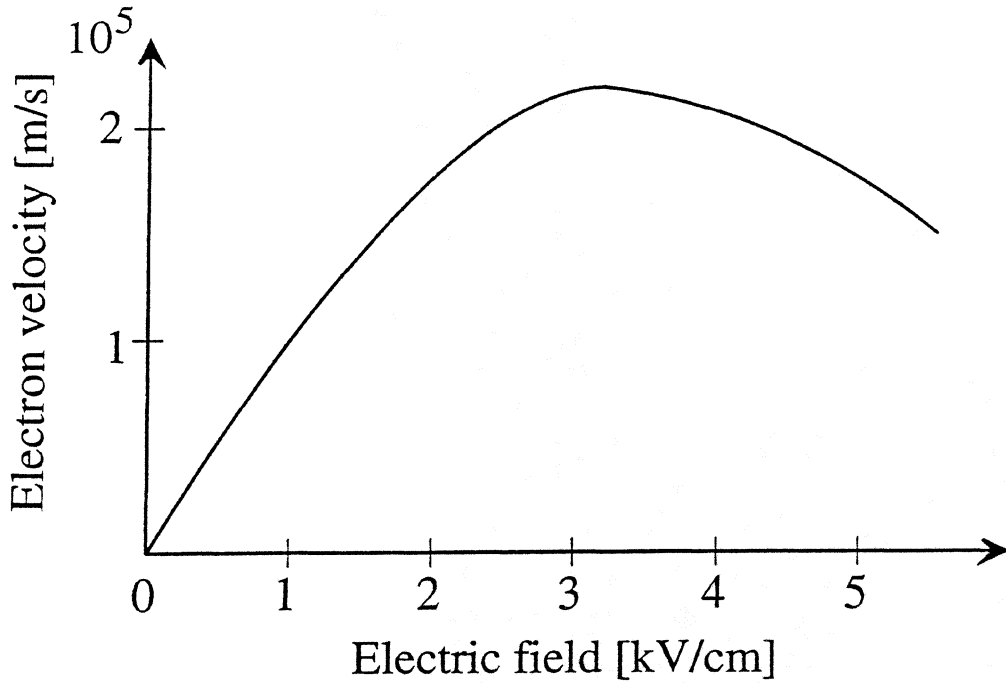


Figure 3: Schematic of the electron velocity in GaAs.

which takes place in GaAs at high electric fields (see Figure 3). At low electric fields the electron velocity is directly related to the electric field. In an intrinsic case the maximum electron velocity is about $2.2 \cdot 10^5$ m/s at electric field of 3.2 kV/cm. Kollberg *et al.* have modelled this saturation of the electron velocity by a nonlinear resistance, which increases as the function of the electron current of the varactor [9]. This model is empirical, because the formula of the nonlinear resistance ($R_i = aR_S i^6$) is found by fitting the results of numerical analyses to the experimental results. East *et al.* have recently presented a more physical model, where the electron conduction current has been limited by the maximum current of the varactor [10]

$$I_m = \pi R_0^2 N_D q v_m, \quad (6)$$

where N_D is the doping density, q is the charge of electron and v_m is the maximum velocity of electron. However this model is also empirical, because the value of maximum velocity ($3.5 \cdot 10^5$ m/s) has been obtained by fitting the results of the numerical analyses to the experimental results.

In this work a new model has been derived for the electron velocity saturation by limiting the velocity of the transition front between the depleted and undepleted layer by the maximum velocity of the electron

$$\left| \frac{\partial W}{\partial t} \right| < v_m. \quad (7)$$

The width of the depletion layer is given by

$$W = \sqrt{\frac{2\epsilon(\phi_{bi} - V)}{qN_D}}, \quad (8)$$

where ϕ_{bi} is built-in potential and V is the external voltage. When the electron conduction current required to pump the junction capacitance is

$$I = C_j \frac{\partial V}{\partial t} = C_j \frac{\partial V}{\partial W} \frac{\partial W}{\partial t}, \quad (9)$$

the maximum current of the diode is given by

$$\begin{aligned} I_m &= C_j \left| \frac{\partial V}{\partial W} \right| \left| \frac{\partial W}{\partial t} \right|_m \\ &= \frac{\epsilon \pi R_0^2 \gamma_C}{W} \frac{q N_D W}{\epsilon} v_m = \pi R_0^2 q N_D v_m \gamma_C. \end{aligned} \quad (10)$$

The edge effect is taken into account by the correction factor γ_C , which is also used for the junction capacitance. This means that the maximum current of the varactor depends on the actual area of the transition front between the depleted and undepleted layer. The maximum current of varactor given by equation (10) is always higher than the value obtained by using equation (6), because the area of the transition front is higher than the area of the varactor anode.

In static situation the maximum electron velocity in GaAs is about $2.2 \cdot 10^5$ m/s at electric field of 3.2 kV/cm as mentioned before. However, during fast transients the electron velocity in GaAs can overshoot the steady-state value by several times [11, 12]. This velocity overshoot increases the maximum electron velocity at high frequencies. At millimeter wavelengths the maximum velocity can be assumed to be about $2.9 \cdot 10^5$ m/s [13].

3 Multiplier performance

We have tested the new model by analyzing the two diode balanced doubler for 160 GHz constructed by Erickson [14]. The varactor used in the doubler is a whisker contacted UVA 6P4 Schottky varactor, whose parameters are shown in Table 1. The doubler has been analysed by using the multiple reflections technique, where the linear part of the circuit is solved in frequency domain and the nonlinear part is solved in time domain [15].

The results of our analyses are shown in Figure 4. The efficiency has been calculated with optimum embedding impedances and with optimum bias voltage. The results of our theoretical analyses agree well with the experimental results, when the 0.5 dB input losses and the 0.8 dB output losses are taken into account. The equality between the numerical and experimental result is very good at high power levels, when the effect of the electron velocity saturation is high. The disagreement between the numerical results and the experiments at low input power levels can be partly explained by the measured VSWR at the input waveguide (VSWR is about 1.9 – 2.7 at input power levels 20 – 10 mW per diode) [16].

According to the simulation results the maximum electron conduction current during a

Table 1: Parameters of the Schottky varactor UVA 6P4.

Radius of the anode	R_0	3.2 μm
Thickness of the epitaxial layer	t_e	1.0 μm
Doping density	N_D	$3.5 \cdot 10^{16}$ $1/\text{cm}^3$
Electron mobility	μ	0.61 m^2/Vs
Series resistance	R_s	10.5 Ω
Junction capacitance at zero bias	C_0	21 fF
Break-down voltage	V_B	-20 V

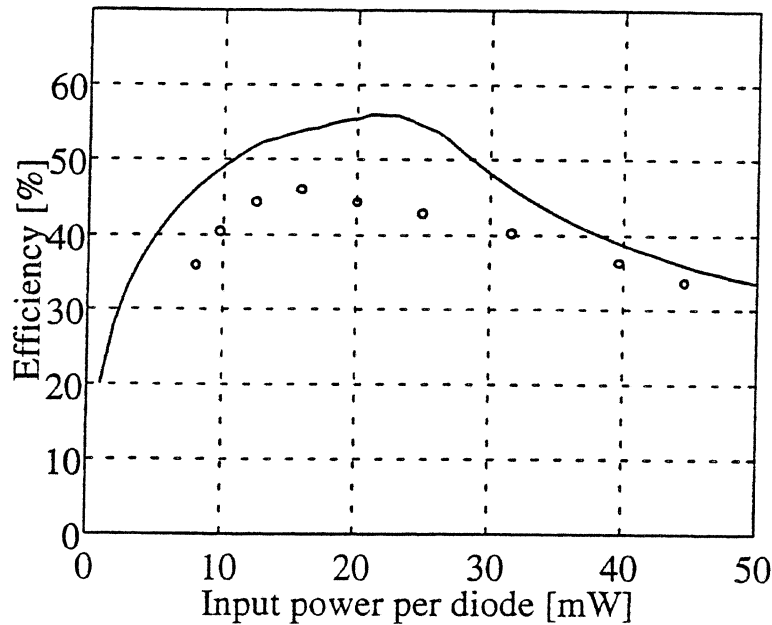


Figure 4: The maximum theoretical efficiency of a 160 GHz doubler. Measured results, after reduction of 0.5 dB input losses and 0.8 dB output losses, have also been plotted.

pump cycle is about 66 mA, when the input power is 60 mW per diode. This means that the maximum current obtained by using equation (6), which is about 52 mA, is exceeded by 25 %. In other words, when the edge effects have been taken into account, the increased area of the transition front between the depleted and undepleted layer helps to pump the junction capacitance of the Schottky varactor more efficiently than can be assumed, if equation (6) is employed. This means that our new model, which uses only physical parameters, works well without any extra fitting to the experimental results. Furthermore, our model can be used to analyse submillimeter wave frequency multipliers (doubblers, triplers, quadruplers, quintuplers etc.), because the model is based on the physical parameters of the varactor and is independent from the multiplication factor and from the type of the Schottky varactor.

4 Conclusions

The equivalent circuit of the millimeter and submillimeter wave Schottky varactor is strongly affected by the edge effects of the small-area circular anode. In this work the electron velocity saturation has been modelled by limiting the velocity of the transition front between the depleted and the undepleted layers. By using this model the maximum conduction current of the varactor is given by the actual area of the transition front, which is always larger than the area of the anode. The equivalent circuit of the Schottky varactor includes also correction terms for the junction capacitance and for the series resistance.

The agreement between the theoretical results and the experimental results is good in the case of the two diode balanced doubler for 160 GHz, when physical parameters of the varactor are employed. The model can be used to analyse any submillimeter wave Schottky varactor frequency multiplier, because the model is based on the physical parameters of the varactor and is independent from the multiplication factor and from the type of the Schottky varactor.

References

- [1] Räisänen A.V.: Frequency multipliers for millimeter and submillimeter wavelengths, *Proceedings of the IEEE*, vol. 80, no. 11, pp. 1842-1852, 1992.
- [2] Frerking M.A. and East J.R.: Novel heterojunction varactors. *Proceedings of the IEEE*, vol. 80, no. 11, pp. 1853-1860, 1992.
- [3] Wasserstrom E. and McKenna J.: The potential due to a charged metallic strip on a semiconductor surface, *The Bell System Technical Journal*, May-June, pp. 853-877, 1970.
- [4] Louhi J.T.: The capacitance of a small circular Schottky diode for submillimeter wavelengths. *IEEE Microwave and Guided Wave Letters*, vol. 4, no. 4, 1994.

- [5] Copeland J.A.: Diode edge effect on doping-profile measurements. *IEEE Transactions on Electron Devices*, vol. ED-17, no. 5, pp. 401-407, 1970.
- [6] Crowe T.W.: GaAs Schottky barrier mixer diodes for the frequency range 1-10 THz. *International Journal of Infrared and Millimeter Waves*, vol. 10, no. 7, pp. 765-777, 1989.
- [7] Räsänen A.V. and Sironen M.: Capability of Schottky-diode multipliers as local oscillators at 1 THz. *Microwave and Optical Technology Letters*, vol. 4, no. 1, pp. 29-33, 1991.
- [8] Schumann P.A. and Gardner E.E.: Application of multilayer potential distribution to spreading resistance correction factors. *Journal of the Electrochemical Society*, vol. 116, no. 1, pp. 87-91, 1969.
- [9] Kollberg E.L., Tolmunen T.J., Frerking M.A. and East J.R.: Current saturation in submillimeter wave varactors. *IEEE Transactions on Microwave Theory and Techniques*, vol. 40, no. 5, pp. 831-838, 1992.
- [10] East J., Kollberg E. and Frerking M.: Performance limitations of varactor multipliers. *Proceedings of the 4th International Symposium on Space Terahertz Technology*, pp. 312-325, 1993.
- [11] Ruch J.G.: Electron dynamics in short channel field-effect transistors. *IEEE Transactions on Electron Devices*, vol. ED-19, no. 5, pp. 652-654, 1972.
- [12] Maloney T.J. and Frey J.: Transient and steady-state electron transport properties of GaAs and InP. *Journal of Applied Physics*, vol. 48, no. 2, pp. 781-787, 1977.
- [13] Grondin R.O., Blakey P.A. and East J.R.: Effects of transient carrier transport in millimeter wave GaAs diodes. *IEEE Transactions on Electron Devices*, vol. ED-13, no. 1, pp. 21-28, 1984.
- [14] Erickson N.: High efficiency submillimeter frequency multipliers. *IEEE MTT-S International Microwave Symposium Digest*, vol III, Dallas, pp. 1301-1304, 1990.
- [15] Siegel P.H., Kerr A.R. and Hwang W.: *Topics in the Optimization of Millimeter - Wave Mixers*, NASA Technical Paper 2287, 1984.
- [16] Erickson N.: Private communication, November 1991.

VERIFICATION OF THE FINITE ELEMENT ANALYSIS AND STUDY OF LOSSES OF A PLANAR DIODE DOUBLER

Jussi Tuovinen and Neal R. Erickson

Five College Radio Astronomy Observatory
Department of Physics and Astronomy
University of Massachusetts
Amherst, MA 01003

Abstract

Microwave modeling using finite element analysis (FEA) is valuable for its flexibility and the ease with which modifications can be made to a structure. The focus of this paper is the verification of the accuracy of the results predicted by the FEA of a planar diode doubler from 85 to 170 GHz. Careful measurements with a slotted line were carried out to determine the diode terminal impedance at the input frequency. In the measurements, a commercial network analyzer could not be used due to the large input power requirement of the doubler. Good agreement between the measured and simulated the diode terminal impedance was observed, although full agreement requires the addition of an empirical loss term. Several options were considered for the source of the loss of the doubler structure. The most probable cause of the loss is the dislocation layer on the back side of the planar diode chip, which was formed when the diode was thinned mechanically. Full confirmation of this source of loss will be performed in the future.

1 Introduction

The design of high efficiency multipliers requires good modeling capabilities. This is particularly true in the case of multipliers with an array of planar diodes. Modeling based on the finite element analysis (FEA) has been chosen over conventional scale modeling in the work described here. The advantages of the FEA approach are that it makes it easy to study dielectric thickness effects, optimum inductances in the diode package, power balance between

the diodes, and the origin of parasitic effects. It also permits multiple probe ports, deletion of parts of the structure and splitting the structure in pieces. In this finite element analysis, the HFSS (High Frequency Structure Simulator by Hewlett Packard) software package was used.

This paper describes the work that was carried out to verify the accuracy of the results predicted by numerical simulations of a planar diode doubler from 85 to 170 GHz. This doubler is shown in Figure 1 and the full description of the FEA is given in [1]. Experimental tests on the doubler are explained in [2] and the details of the array of planar diodes in [3]. Careful measurements were carried out to determine the diode terminal impedance at the input frequency. The main problem in measuring the input impedance of a frequency multiplier (from which the diode terminal impedance can be calculated), is that it depends strongly on bias voltage and absorbed input (pump) power. The available input power for testing this doubler with an array of four planar varactors on a single chip should be at least 100 mW. This means that a commercial vector network analyzer can not be used to measure input impedances at frequencies around 85 GHz. Instead a WR-10 slotted line was used to measure the complex reflection coefficient, which was in turn used with the de-embedding circuit model to obtain the measured diode terminal impedances. Input reflection may greatly reduce the absorbed power, invalidating the “high power” measurement. Therefore, the input match was first optimized with a tuner consisting of a $\lambda_g/4$ thick piece of teflon properly placed in the input waveguide. The use of this simple matching transformer is convenient because its effect on the circuit can be easily predicted in the de-embedding process to obtain the diode terminal impedances. The output match was improved utilizing the same technique, since mismatch in the output affects the input impedance.

2 Measurement set-up

To verify the reliability of the simulated results, measurements of the input impedance of the doubler were carried out. Using the known input waveguide geometry, the de-embedded diode terminal impedance was calculated. The measurements were carried out between 79.7 and 90.6 GHz.

Before making the actual impedance measurements, matching in both the input and output port of the doubler were improved by adjusting the positions of two $\lambda_g/4$ thick teflon pieces in the respective waveguides. In this matching process the output power was

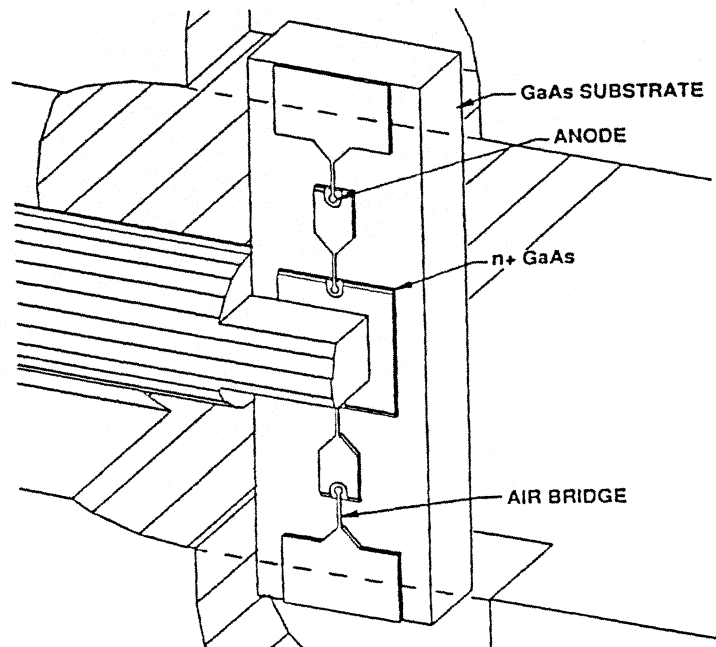
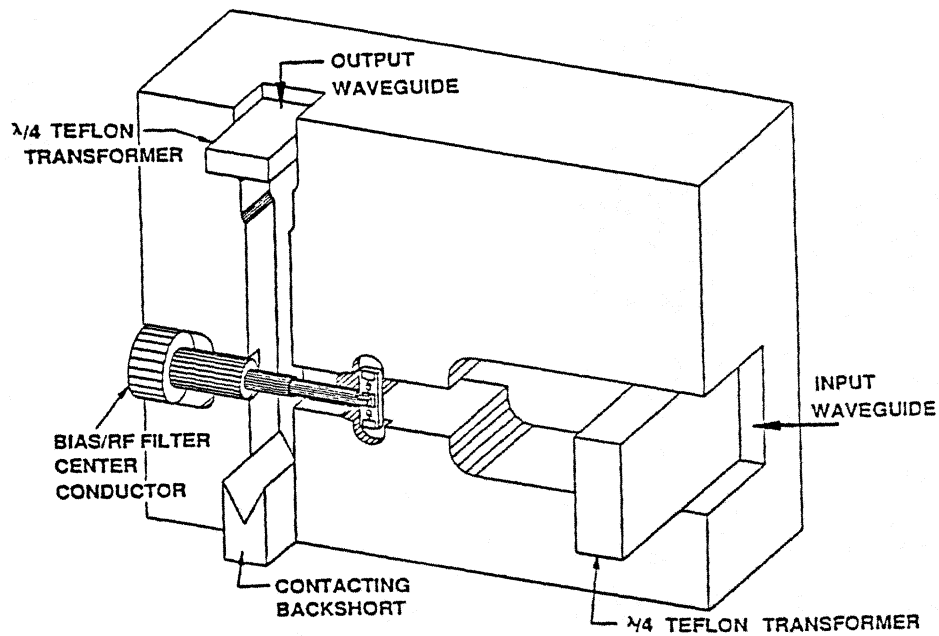


Figure 1: The planar diode frequency doubler from 85 to 170 GHz used in the tests and in the finite element analysis. The end pads of the diode are soldered to a mating half of the block.

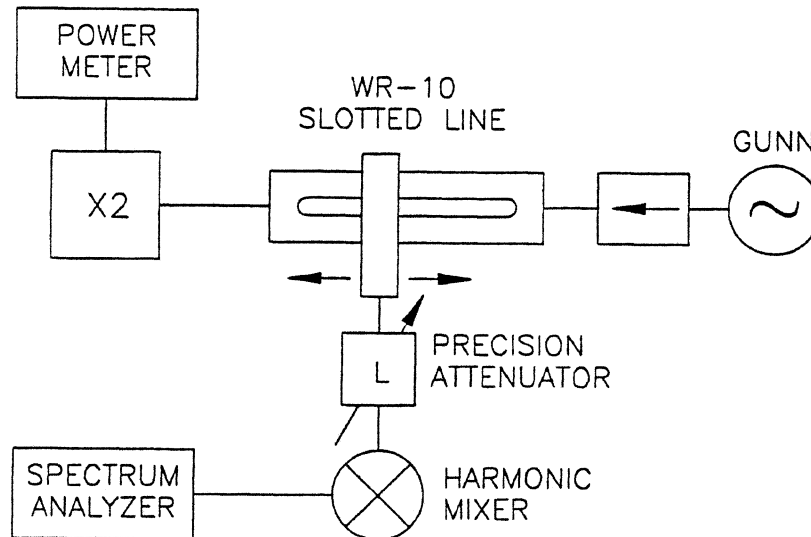


Figure 2: Set-up for measuring the input impedance of the doubler.

maximized and the reflected input power was minimized, with resulting VSWRs $< 2 : 1$ on both ports.

The input impedance measurement set-up is shown in Figure 2. At 79.7 GHz a fixed Gunn oscillator with an output power of 140 mW was used while at other frequencies a tunable Gunn oscillator with an output power of 100 – 120 mW was used. The maximum power with the latter Gunn was obtained around 82 GHz and the minimum at the high end of the measurement band. The Gunn oscillator was followed by an isolator, and a slotted line. The input waveguide of the doubler was connected to the other end of the slotted line and the output waveguide was connected to a power meter. The probe port of the slotted line was attached to a calibrated adjustable attenuator, which was followed by the harmonic mixer of a spectrum analyzer.

During the measurements, power coupled to the sliding probe was detected with the spectrum analyzer. The actual value of the power ratio was obtaining by adjusting the calibrated attenuator. This method of detection is more sensitive than a diode detector and also ensures that the oscillator is at the correct frequency.

The needed reference positions of the VSWR minima were obtained by placing a copper

plate between the flanges of the doubler and slotted line. Because of the limited isolation of the isolator in front of the Gunn oscillator, the Gunn had to be tuned (electrically or mechanically) slightly for the reference measurement. This is important for accurate measurements, because even a relatively small change in frequency causes a significant error in the location of the standing wave minimum and therefore in the phase of the reflection coefficient. This is because the probe of the slotted line is more than 15 wavelengths away from the short. During the measurements the frequency was kept fixed within few MHz.

With and without the short, three standing wave minimum locations were measured. The difference between the three minimum pairs were calculated and the average of the these differences was used to calculate the phase of the reflection coefficient. The magnitude of the coefficient was determined from the average of three power ratios.

3 Comparison of the simulated and measured results

Comparison of the measured and simulated de-embedded diode terminal impedances is shown in Figure 3. The results in this figure are based on the assumption that the planar diode can be modeled as a two terminal device. The need of modeling the diode as a three terminal device was also considered. The required series element in three terminal device were so small that the assumptions of two terminal is well justified. During the measurements the diode bias was kept at 11 V. The input power varied from 100 to 140 mW. The GaAs substrate thickness of the diode was measured to be about $22 \pm 2 \mu\text{m}$. The theoretical curve was calculated using above input power, bias voltage, and substrate thickness. The second harmonic termination was chosen at the value for optimum efficiency. The effect of different sources of errors on the measurement is show in Table 1. The overall accuracy (3σ) of the measurements is about ± 4.0 and $\pm 4.1 \Omega$ for the real and imaginary parts, respectively. The random errors were small; at a fixed frequency and doubler setting the real and imaginary parts were repeatable with in 1 and 2 Ω , respectively. Sources of systematic errors are the teflon matching transformer (position and tilt in the waveguide), frequency offset in the de-embedding, and output mismatch. Also, the assumption of no losses in the simulations causes systematic errors.

Figure 3 shows that the imaginary part of the impedance agrees very well with the simulations. The measured real part values are much more scattered and the difference between the measured and simulations can not be explained with the measurement errors.

Table 1: Sources of error in the slotted line measurement of the diode terminal impedance.

Source of error	Value of the error parameter at 3σ deviation	Value of error (\pm)	
		$\text{Re}(Z)/\Omega$	$\text{Im}(Z)/\Omega$
VSWR	Accuracy of power ratio 1 dB	0.3	1.5
Phase of ρ	$\Delta\text{ang}(\rho) = 30^\circ$	2.0	1.25
Losses in WG mount	10 % loss assumed	0.25	0.25
Input power inaccuracy	P changed from 100 to 40 mW	1.5	2.25
Output mismatch	Trans. moved $\lambda_g/4$ from opt. pos.	2.25	2.25
Input trans. not ideal shape	Real shape simulated with HFSS	-	-
Input trans. tilted	Tilted $102\ \mu\text{m}$ from one end	1.0	1.0
Input trans. position	Position changed $51\ \mu\text{m}$	1.5	1.25
Input trans. thickness	Thickness changed $51\ \mu\text{m}$	1.0	1.0
De-embedding frequency	Frequency changed 100 MHz	0.3	0.6
TOTAL ERROR (RSS) 3σ		± 4.0	± 4.1

The good agreement with the imaginary part of the measured and simulated values can be explained by the clear physical origin of the reactance. The reactance is mainly defined by the capacitance of the planar diode, which is due to the fringing fields in the planar structure and the junction capacitance. The origin of the real part of the terminal impedance is more complex. In addition to the series resistance of the junction the termination of the second and third harmonics affects the real part. In the simulation, an ideal open termination was assumed for the 3rd and higher harmonics.

The discrepancy between the measured and simulated real part of the diode terminal impedance implies the presence of a loss in the real doubler circuit that has been missed by lossless finite element simulations. A simple equivalent circuit of the planar diode is shown in Figure 4. This equivalent circuit includes a shunt resistance, which simulates the losses in the doubler structure. Comparison of the diode terminal impedance calculated using the equivalent circuit and the HFSS-MDS simulations is shown in Figure 5. This figure shows that a shunt resistance of $300\ \Omega$ could explain the higher measured real parts of the diode terminal impedance.

Four main sources of a possible loss in the doubler structure were foreseen: 1) waveguide losses, 2) limited conductivity of the n^+ region underneath the metal pads of the planar diode, 3) losses in the GaAs substrate, and 4) losses in the back surface of the planar diode chip (the rough ground surface formed during the thinning of the diode chip). Because of the first source of loss, a 10 % waveguide loss was included in the error analysis, which shows

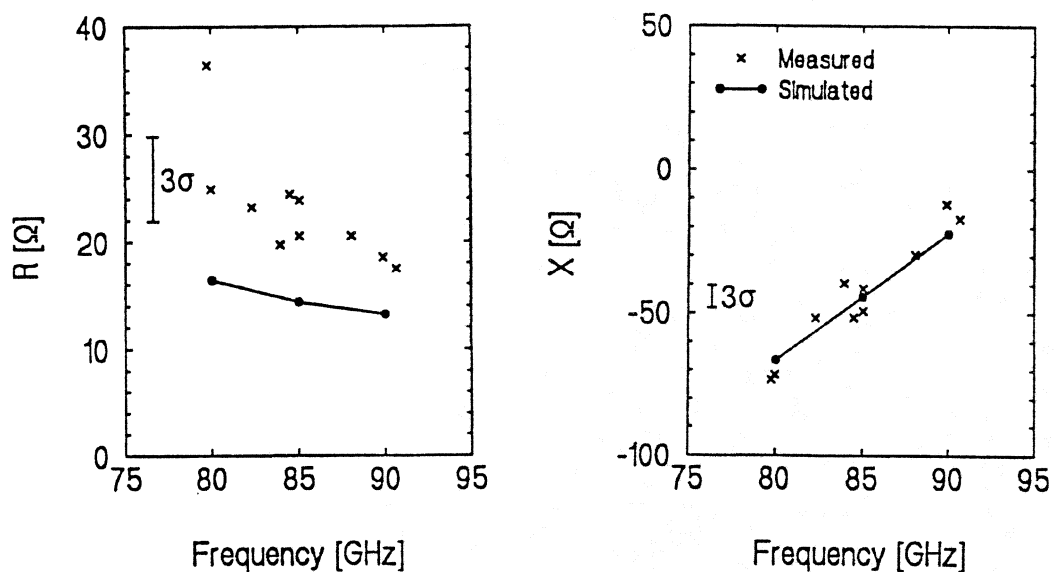


Figure 3: Real and imaginary part of the measured and simulated de-embedded diode terminal impedances. The simulated curve is calculated for a $22\ \mu\text{m}$ GaAs thickness and using real input power levels and bias voltages for the diode.

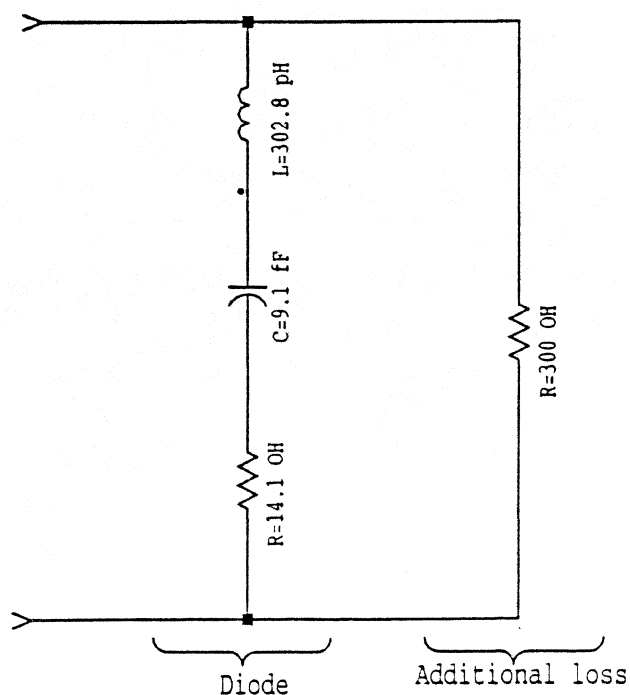


Figure 4: The equivalent circuit of the planar diode at the input frequency. This circuit includes also the shunt resistor, which can explain the measured real parts of the diode terminal impedance.

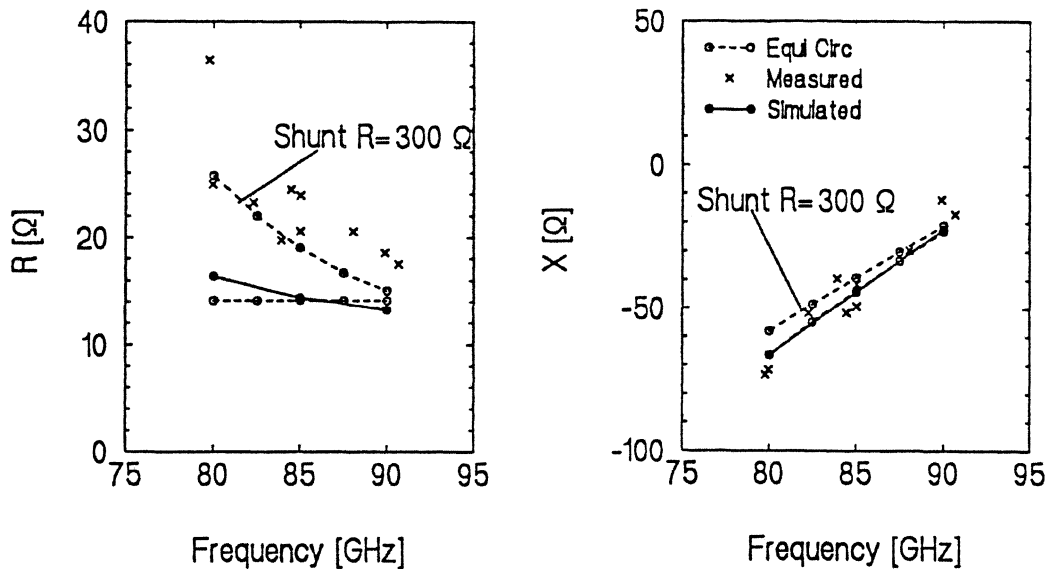


Figure 5: Real and imaginary part of the measured and simulated de-embedded diode terminal impedances with the impedances calculated using the equivalent circuit with and without the 300 Ω shunt resistor.

that the discrepancy between the measurements and simulations can not be explained by a reasonable waveguide loss. The effect of the limited n^+ region conductivity was studied by the FEA. In the analysis a conductivity of 1000 S/cm was used. No significant change was observed for the real part of the diode terminal impedance.

The results of the FEA of the loss in the GaAs are shown in Figure 6. This figure shows that a value of $\tan \delta = 0.3$ for the GaAs substrate does raise the simulated values quite close to the measured ones. However, because this unrealistically large value of $\tan \delta$ is required and because the slope of the simulated curve of the real part does not seem to agree very well with the measured values, the loss in the GaAs substrate is not assumed to be the main explanation for the loss in the doubler circuit.

Since the above three sources of loss did not seem to be very likely explanations, we finally considered the dislocation layer on the back side of the chip. This layer is due to the mechanical thinning process of the diode and we assume that the surface states at the many grain boundaries cause this surface to behave like a poor conductor. The dislocation layer was simulated in the FEA by placing an infinitely thin resistive layer on the back side of the diode chip. Figure 7 shows results of these simulations. The resistance values for the layer, shown in the figure, are over the full length of the diode. Figure 7 shows that the layer has a strong effect on both the real and imaginary part of the terminal impedance. On

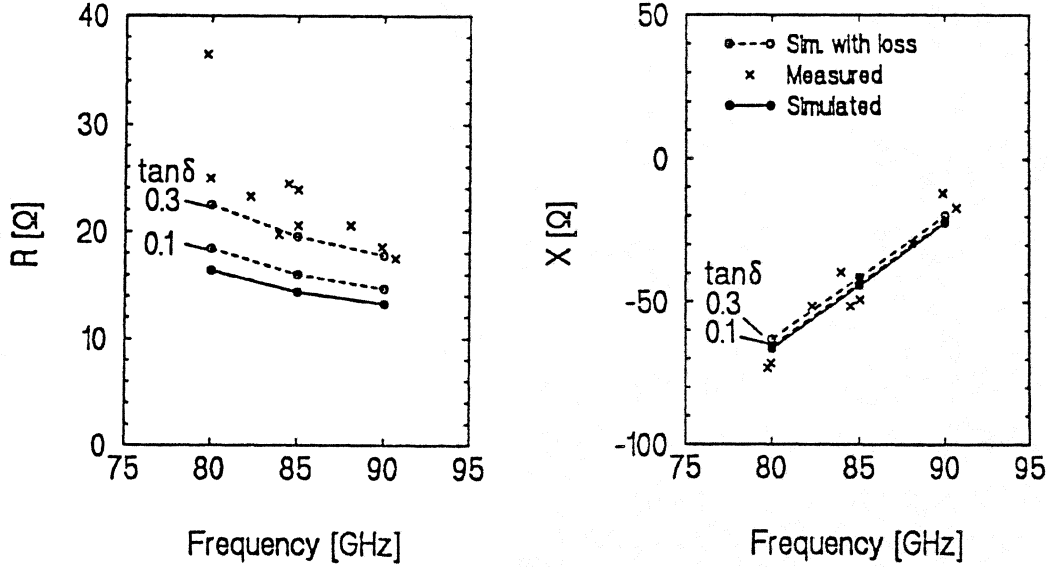


Figure 6: *Real and imaginary part of the measured and simulated de-embedded diode terminal impedances. The GaAs substrate loss is included to the simulated curves.*

the imaginary part, the layer has mainly reduced the capacitance by 23Ω at all frequencies and resistance values. The simulated real part of the impedance is sensitive for the actual value of the resistance of the layer. Simulations with a resistive layer of 800Ω predict very similar real part values with the measurements. This shows that the dislocation layer is a likely explanation for the high measured real parts of the diode terminal impedance. A thin and very lossy dielectric layer might better simulate the dislocation layer, because a constant shift in the imaginary part of the simulated results was caused by a lossy conductive layer.

Overall, the good agreement between the measured and simulated reactive parts has convinced us on the usefulness of finite element analysis. This is especially true after considering the great complexity of the doubler structure, simulations, and measurements.

4 Conclusions

The accuracy of previously described finite element analysis (FEA) of a planar diode multiplier [1] has been verified by careful measurements. The input impedance of the doubler, from which the diode terminal impedance was calculated, was measured between 80 and 90 GHz using a WR-10 slotted line. Before actual impedance measurements, the input match was optimized with a tuner consisting of a $\lambda_g/4$ thick piece of teflon placed in the waveguide. This was important to ensure high absorbed input power, i.e., the correct operating point

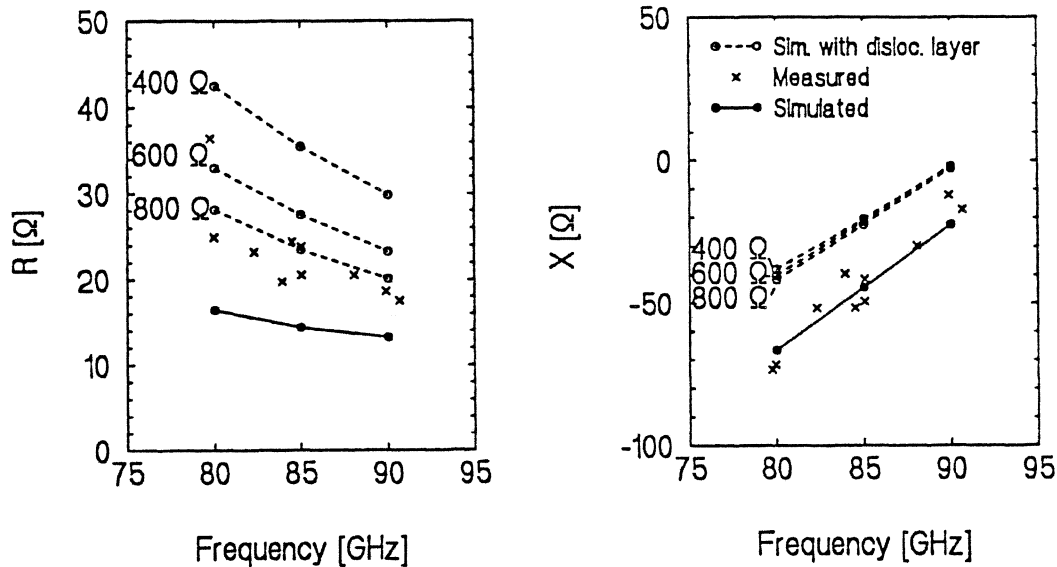


Figure 7: Real and imaginary part of the measured and simulated de-embedded diode terminal impedances. Dislocation layer simulated by a resistive layer.

for the doubler. The output match was optimized the same way. A good agreement was observed between the reactive part of the measured and simulated diode terminal impedances. The resistive part of the impedance did not show as good agreement as the reactive, which is due to the more complex nature of the origin of the real part, which may include losses in the diode itself. Different sources of this loss was considered. The best fit to the loss is a dislocation layer on the back side of the planar diode chip, which was formed during the mechanical thinning process of the diode.

Acknowledgment

We acknowledge the financial support of the European Space Agency through a ESA Fellowship for one of the authors, the National Aeronautics and Space Administration under grant NAGW2430, and Jet Propulsion Laboratory under contract 959 206.

References

- [1] J. Tuovinen, N. R. Erickson, "Finite element analysis of a planar diode doubler," *Proc. 4th Int. Symp. Space Terahertz Tech.*, Los Angeles, pp. 326-339, 1993.

- [2] N. R. Erickson, B. J. Rizzi, T. W. Crowe, "A 174 GHz high power doubler using a planar diode array," *Proc. 4th Int. Symp. Space Terahertz Tech.*, Los Angeles, pp. 287–296, 1993.
- [3] B. J. Rizzi, J. L. Hesler, H. Dossal, T. W. Crowe, "Varactor diode for millimeter and submillimeter wavelengths," *Proc. 4th Int. Symp. Space Terahertz Tech.*, Los Angeles, pp. 297–311, 1993.

SOLID-STATE LOCAL OSCILLATOR SOURCES FOR 600-900 GHz

P. A. Jaminet

Harvard-Smithsonian Center for Astrophysics
60 Garden St. MS-42
Cambridge, MA 02138

ABSTRACT

We have developed tunable, solid-state frequency sources covering the 600-720 GHz atmospheric window, and constructed another source for 780-880 GHz which is not yet functional. The sources are intended for use as local oscillators for SIS mixers. The sources are based upon a 120-147 GHz Gunn oscillator, and use crossed-waveguide multipliers for frequency multiplication. The first source, covering the 600-720 GHz window, uses a quintupler; the second, covering most of the 780-900 GHz window, cascades a doubler and a high-frequency tripler. The multipliers use 2T10 Schottky diodes obtained from the University of Virginia Semiconductor Device Laboratory. We discuss the multiplier designs, and report the results of tests of the 600-720 GHz source.

Introduction

With the recent development of sensitive SIS mixers operating in the 600-720 GHz atmospheric window[7, 12, 13], and the prospect of SIS mixers being developed for the last remaining submillimeter window at 780-920 GHz, the development of solid-state tunable local oscillator (LO) sources covering these windows has become important to submillimeter wavelength astronomy. Several commercial vendors offer sources for the 600-720 GHz band[8, 9], but these sources are often expensive and sometimes restricted in bandwidth. As part of the receiver development program for the Submillimeter Array Project, we have chosen to develop our own sources.

The scheme we have chosen to cover these frequency bands uses a Gunn oscillator obtained from J. E. Carlstrom Co.[2] which operates from 117-147 GHz with approximately 35 mW of output power. The cutoff at 147 GHz is determined by the WR-8 output waveguide. Tests have shown that this oscillator can readily be phase-locked throughout its operating band.

For the 600-720 GHz band the Gunn oscillator is followed by a quintupler of our design, built by Custom Microwave[4]. For the 780-900 GHz band we use a doubler purchased from Millitech[8] to generate radiation between 260 and 294

GHz, which then drives a tripler. The Millitech doubler generates about 2 mW of output power in the required range. With a cascaded tripler, it is possible to obtain radiation from 780 to 882 GHz. The tripler was built to our design by Custom Microwave.

High efficiencies for both triplers and quintuplers have been obtained in low frequency multipliers. A quintupler obtained peak efficiency of 4% at 168 GHz with efficiency greater than 1.5% from 165-170 GHz[15]. A tripler obtained peak efficiency of 28% at 107 GHz and greater than 10% efficiency from 100-115 GHz[14]. As these citations illustrate, published work has often concentrated on obtaining very high efficiencies, usually over narrow bandwidths and through the use of resonant structures that are difficult to fabricate at high frequencies. More useful for astronomical purposes, because the power requirements of SIS mixers are relatively low, are broadband multipliers with rather lower efficiencies. An example of a tripler which achieved broadband performance is that of Archer[1], which obtained 3% efficiency over 200-290 GHz. However, Archer's design would be very difficult to scale to high frequencies.

The power required from an SIS mixer local oscillator source can be calculated from the fact that conversion on the first photon peak below the gap varies roughly like $J_1(eV_{LO}/h\nu)$ [11]. Thus conversion is maximized when:

$$P_{LO} \approx 0.6 \times \frac{(h\nu/e)^2}{R_{junction}}$$

where $R_{junction}$ is the RF impedance the detector presents at the frequency ν . For typical receivers with $R_{junction} = 25 \Omega$, and adding a factor of 3 for optical coupling losses and a safety margin, this formula leads to optimal LO source powers of 0.5-1.0 μ W for the 600-900 GHz frequency band. To achieve a minimum source output power of 1 μ W with our scheme, efficiencies greater than 0.004% for the quintupler and 0.05% for the tripler are required. These efficiencies should be well within the capabilities of current multiplier diode technology. In fact, a multiplication efficiency of 0.003% has been obtained for 7th and 8th harmonic radiation at 800 GHz in a multiplier that was far from optimized for this frequency[10]. Thus, there is good reason to believe that output power levels well above the level needed to drive SIS mixers can be readily generated.

The high-frequency multipliers use 2T10 GaAs Schottky varactor diodes fabricated at the University of Virginia Semiconductor Device Laboratory. These diodes are identical in design to the earlier 2T2 diodes, which are the most successful submillimeter multiplier diodes yet made[3]. These diodes have a cutoff frequency of 4.8 THz; experience suggests that Schottky varactor diodes can multiply effectively up to about one-fifth the cutoff frequency[3], so it is reasonable to suppose that the 2T10 diodes can provide useable amounts of power through 900 GHz.

Design

Figure 1 illustrates the design of the 600-720 GHz quintupler; the design of the 780-900 GHz tripler follows similar principles.

The input waveguide is WR-8, chosen to match the Gunn oscillator. A non-contacting backshort is used in the input guide. A post of diameter approximately one-fifth the waveguide width extends into the middle of the guide. At DC the post is isolated from the multiplier body, because it carries the DC bias to the multiplier diode. At RF, an effective short is produced at the waveguide wall by a $\lambda/2$ transmission line (1.14 mm in length) terminated in an RF short by a parallel-plate capacitor defined with a 25 μm Mylar sheet.

At the end of the post is mounted the whisker. We use a 25 μm diameter, 78% Au and 22% Ni whisker, and etch it to the proper length and point it in a tenth-normal solution of HCl. The whisker forms a transmission line between the input and output guides, which is intended to act as a low-pass filter. At the multiplier output frequency, the coaxial section between the guides is a quarter wavelength; this forms a low-impedance section; the length of the whisker in the input and output guides is approximately a quarter wavelength, and these form high-impedance sections of a blocking filter for the RF. The post in the input guide may also be considered a low-impedance section of this line. Unfortunately, the impedance ratio between the low- and high-impedance sections is only about 1:2, and so the filter is of limited effectiveness. However, this structure is simple and easily fabricated at high frequencies; it is difficult to fabricate more effective structures by mechanical means. (Planar diodes may ultimately allow good high-frequency filters to be built.)

The output waveguide is chosen to be just small enough to cutoff the 4th harmonic radiation when operated at its highest useful astronomical frequency, 720 GHz. The nominal cutoff frequency is 579 GHz. The output waveguide uses a contacting backshort.

The 2T10 diode chip was quartered, forming individual chips in the shape of cubes 100 μm on a side. Each chip is soldered to the top of a gold-plated brass mounting post 190 μm in diameter. The diode post is moved by a differential screw approximately 58 μm per revolution. Contact is made with the diode partially in the waveguide.

In general, one desires highly inductive embedding impedances for the diode at the idler frequencies, that is, the frequencies of the lower harmonics. The main source of inductance in our design is that introduced by the waveguide below cutoff; a secondary source is the inductance of the whisker. This method works fairly well at providing good idler impedances in the tripler, but cannot work well in the quintupler. The impedance associated with the waveguide is highly inductive just below cutoff and decreasingly inductive as the frequency

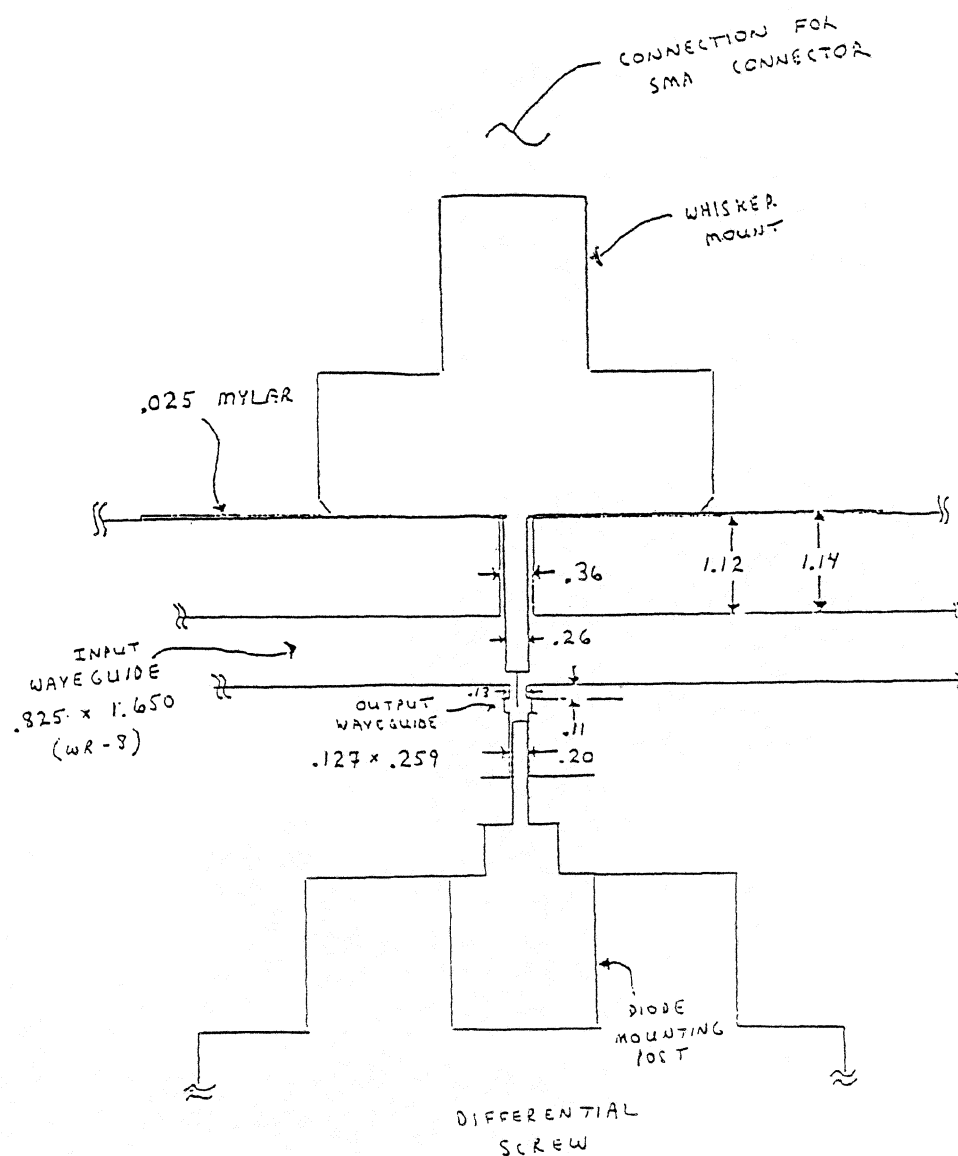


Figure 1: Layout and dimensions of the quintupler for 600-720 GHz. The dimensions are in millimeters.

is decreased. If the 4th harmonic is cutoff in the guide, then this leads to only mildly inductive terminations at the 2nd and 3rd harmonics. The whisker, too, introduces a reactance which increases with frequency. For this reason it is much harder to obtain theoretically optimal efficiencies from a quintupler than from a tripler.

A length of 2.21 mm of output waveguide lies between the multiplier diode and the beginning of the output horn; this length is necessary to adequately suppress both higher-order waveguide modes and evanescent modes from the lower harmonics. The horn is a pyramidal horn with apertures 1.88 mm and 2.72 mm and an axial length of 7.32 mm. These parameters give a gain of 23.5 dB.

Measurements

We have tested the 600-720 GHz source in two ways: measuring the total power radiated with an InSb bolometer system, and measuring the output spectrum to check for harmonic content using a Fourier Transform Spectrometer. Additional tests await the construction of an SIS mixer for these frequencies.

Output Power

The output power was measured using an InSb bolometer system purchased from Infrared Laboratories[5]. The bolometer was calibrated against a narrow-band, fixed-tuned 690 GHz source purchased from Radiometer Physics, which was in turn calibrated against a TK TeraHertz Absolute Power Meter System[6], and shown to produce about 80 μ W. The principal uncertainty in the power calibration is the estimate of the relative optical coupling of the two multipliers to the bolometer. Fortunately, the two multipliers have approximately the same gain. Although the Radiometer Physics multiplier uses a dual-mode conical horn while our multiplier use a pyramidal horn, the two horns have approximately the same slant length and aperture size. Thus, coupling coefficients are similar and should not introduce an uncertainty exceeding a factor of two.

The results of the output power measurements are summarized in Figure 2. The output power is in excess of 3 μ W from 615 to 720 GHz, except at 630 GHz where an atmospheric absorption line is responsible for the reduced power detected at the bolometer. This power level is more than adequate to drive a well-designed SIS mixer.

There are several causes for the fluctuations in the recorded output power. Broadly speaking, the output power follows the pattern of atmospheric transmissivity: at 630 and 730 GHz, atmospheric absorption lines reduce the signal reaching the bolometer. From 600-610 GHz, output power is disappointingly

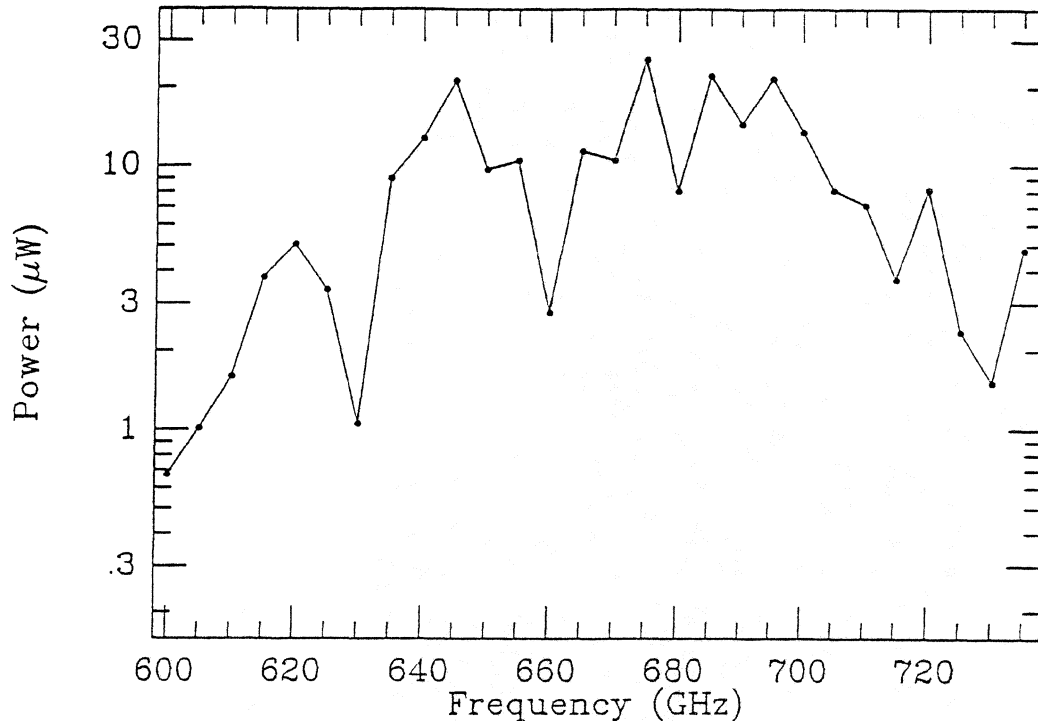


Figure 2: Output power as a function of frequency from the 600-720 GHz source.

low. This we attribute to the operation very close to the cutoff frequency of the guide (nominal cutoff frequency is 579 GHz), so that attenuation is high, and the embedding impedance seen by the diode is likely to be unusual. The cutoff frequency was chosen to be high so as to cutoff the 4th harmonic when the multiplier is radiating its 5th harmonic at 720 GHz. Two considerations — that no 4th harmonic radiation is seen even when the 5th harmonic is generated at 735 GHz, and that the output power should be so small at 600 GHz — both suggest that the output waveguide was built slightly smaller than its nominal design size.

At 660 and 715 GHz, the multiplication efficiency remains high, and the dips in output power are caused by reductions in the amount of Gunn oscillator radiation being coupled into the multiplier diode. The cause of these resonances is unclear. Finally, other variations, such as the dip in output power at 680 GHz inbetween strong signals at 675 and 685 GHz, largely reflect variations in the

effectiveness of the tuning backshort in the output waveguide. At 675 and 685 GHz, this backshort has a strong effect, and tunes through a sharp resonance at which output rises dramatically from about 10 μ W to over 25 μ W. At 680 GHz the performance is nearly the same at most backshort positions, but the resonance is absent. At 680 GHz there is less than a factor of two between the output power at the best backshort position and the output power at the worst. This mediocre performance is probably unavoidable with the contacting backshort design we used in the output guide, and in future we expect to use a non-contacting backshort, despite its added cost and fabrication difficulty.

Output Spectra

The Fourier Transform Spectrometer (FTS) used to observe the harmonic content of the multiplier was built by the Submillimeter Receiver Laboratory of the Smithsonian Astrophysical Observatory for tests of the optical properties of submillimeter materials and other laboratory measurements. It is quite sensitive, and signal-to-noise ratios of 50 dB were commonly achieved with the 600-720 GHz source.

Figure 3 shows spectra taken every 10 GHz from 600 to 720 GHz of the multiplier output. In these measurements the Gunn oscillator was free-running and the frequency numbers reflect the Gunn tuning values provided by the J. E. Carlstrom Co. Coupling between the multiplier and the Gunn oscillator was present — no isolator was used between the two devices — and this may account for the slight difference in frequency between the manufacturer's tuning values and the observed output frequency.

The FTS resolution was 18 GHz and the spacing of individual bins in Figure 3 is 7 GHz, so that unresolved lines are 2.5 bins wide. The free-running drifts of the Gunn are responsible for the line wings resolved in some frequencies at power levels of about -40 dB.

For a clearer view of typical spectra, Figure 4 shows an expanded view of the spectra for the astronomically important frequencies of 650 and 690 GHz. As these spectra show, it is not uncommon to see 6th harmonic radiation. Aside from 600 GHz, where the 5th harmonic radiation is heavily attenuated and 6th harmonic radiation at 720 GHz actually dominates at some backshort settings (with output power of almost a microwatt), the largest observed output of 6th harmonic radiation was at 780 GHz with the source tuned to 650 GHz. However, even at this worst case, the 6th harmonic is 20 dB lower than the 5th harmonic, which, when combined with suppression in receiver optics, would cause negligible contamination in astronomical receivers. More typically the 6th harmonic is 40 dB lower than the 5th harmonic. Also, backshort and bias voltage settings can be chosen to reduce the 6th harmonic output. Moreover, the 6th harmonic is

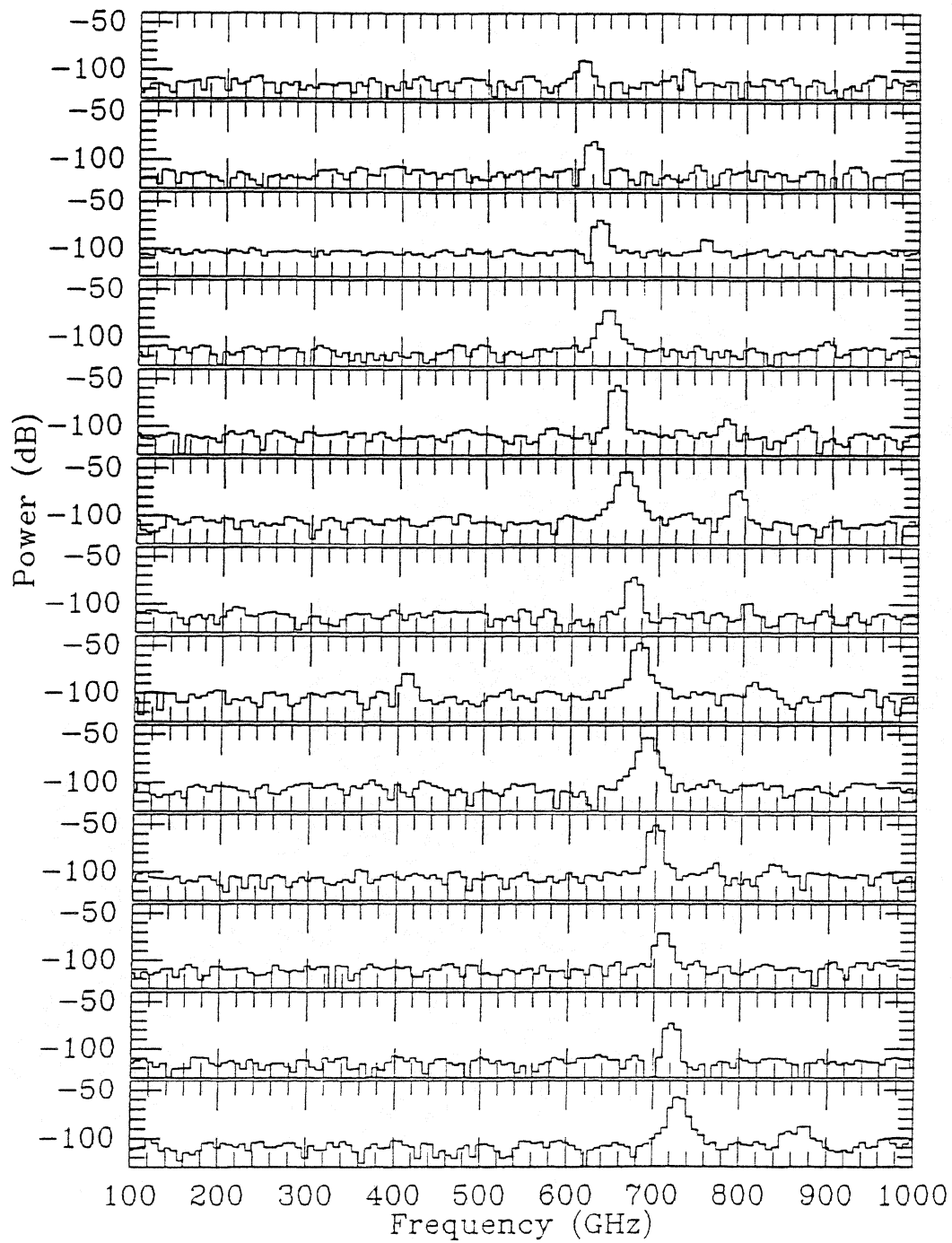


Figure 3: Spectra of the 600-720 GHz source, tuned to nominal frequencies of 600 GHz (top), 610 GHz (second panel), etc., through 720 GHz (bottom panel).

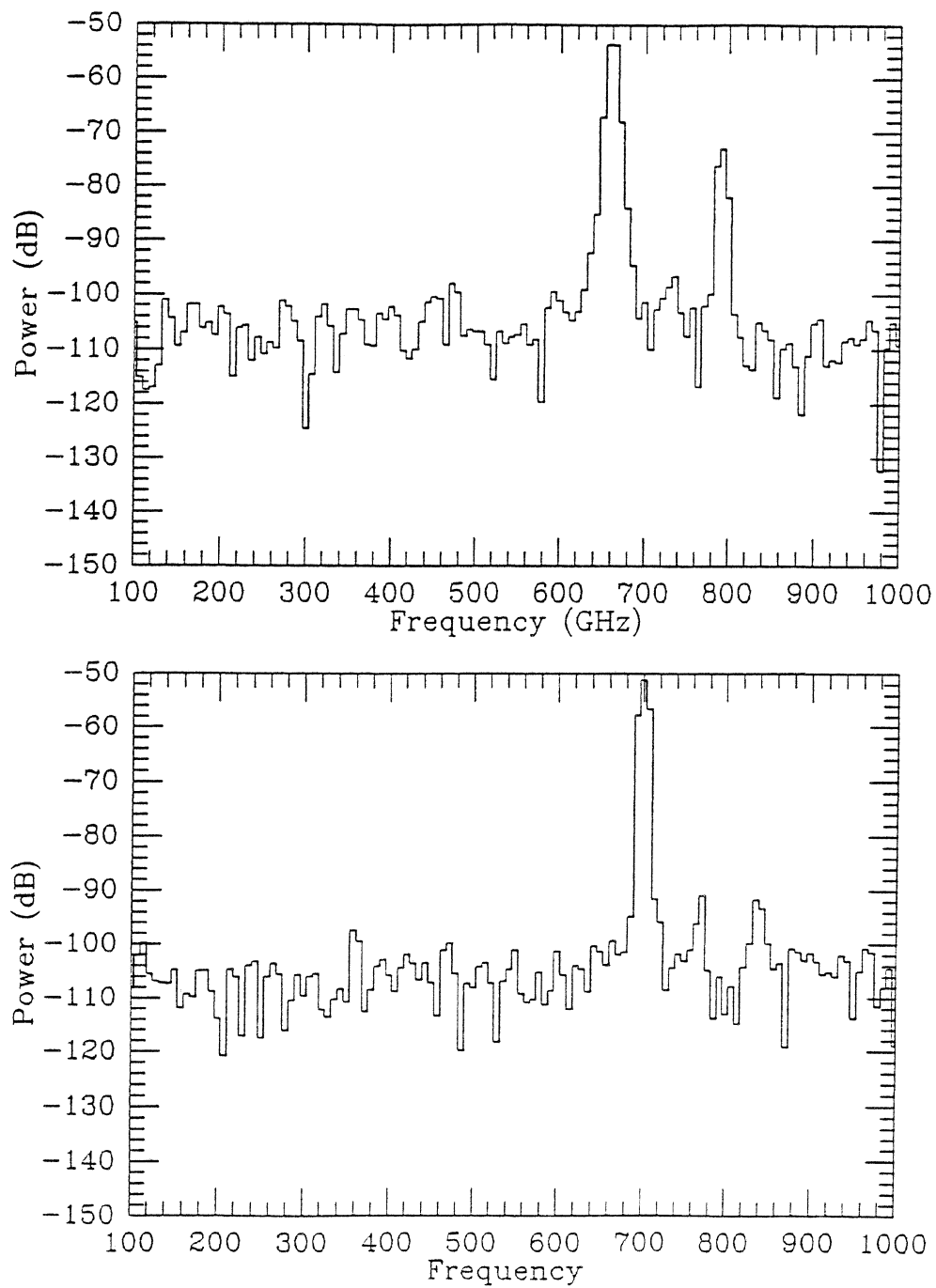


Figure 4: Top panel: Spectrum of source tuned to a nominal frequency of 650 GHz. Bottom panel: Spectrum of source tuned to a nominal frequency of 690 GHz.

suppressed much more rapidly than the 5th as the output power is reduced from the 20 μW level used in this measurement to the 1 μW level that would be used in an actual receiver. For these reasons, we are satisfied that there is no problem with contamination by higher harmonics from this source.

Nor is contamination by lower harmonics a problem. The only spectrum in which lower harmonics was detected is the 670 GHz spectrum, in which 3rd harmonic radiation appeared at a power level down by more than 30 dB from the 5th harmonic power. However, this level is inconsistent with the 3rd harmonic power level expected in the diode, considering the 60 dB suppression that the output waveguide contributes to this evanescent mode. It is conceivable that some power may be leaking out through the input guide or the diode post channel.

Possible Design Improvements

There are several ways in which the design of the high-frequency multipliers could be improved. One especially unsatisfactory feature of the quintupler was the poor performance of its output backshort, suggestive of a poor reflection coefficient. A non-contacting backshort design, though more difficult to fabricate, would be likely to significantly improve the multiplier performance.

A change with uncertain but potentially significant benefits would be to use a resonant blocking filter on the diode post. The 190 μm diameter diode post slides in a 200 μm hole, and is allowed to contact the sides. If contact is made then no TEM modes can propagate, but the cutoff frequency for higher-order modes is on the order of 300 GHz. Thus terminations at both idler and output frequencies may be affected, and power may leak out this port at the output frequency. Use of a proper blocking filter might improve the coupling to the output waveguide mode. In our design no resonant filters were inserted so that diodes and diode posts would be interchangeable between the two multipliers; however, this convenience saves only a modest expense in spare diodes.

It does seem that the output waveguide of the quintupler was slightly too small, making its use from 600-610 GHz problematic. Judging from the lack of 4th harmonic contamination at 735 GHz, a slightly larger waveguide size would allow operation throughout the 600-720 GHz atmospheric window.

As yet we have not investigated the dependence of performance on whisker length, which in our design also changes the location of the diode in the output waveguide. It may be that this parameter is not optimized.

An unclear issue is the cause of the resonances at 660 and 715 GHz, in which less power is coupled into the multiplier diode. It is unclear whether these resonances are a consequence of bad coupling between the input waveguide mode and the coupling post, or a problem with transmission down the whisker transmission line which is terminated by the diode. Probably scale model measurements would

be needed to resolve this issue. In any event, it is probably possible to improve the input guide post design.

Conclusion

We have developed an inexpensive solid-state local oscillator source capable of driving an SIS mixer between 610 and 720 GHz. Within that band, the source produces 3 to 50 times (typically 20 times) the power required to drive an SIS mixer. There is still room for improvement in the multiplier design, and this suggests that available Schottky diodes are capable of producing sufficient LO power for SIS mixers at still higher frequencies — very likely through the highest frequencies at which the atmosphere is still transmissive, about 900 GHz.

Acknowledgements

The author is grateful to Jon Kawamura for his assistance with the measurements. Also, thanks to Ken Zelin and Tom Crowe of the University of Virginia Semiconductor Device Laboratory for helpful advice on soldering diodes to crystal posts; and to Al Betz of the University of Colorado for advice on pointing whiskers. This work was supported by the Submillimeter Array Project of the Smithsonian Astrophysical Observatory.

References

- [1] J. W. Archer, *IEEE Trans. Microwave Theory and Techniques*, **MTT-32**, 416 (1984).
- [2] J. E. Carlstrom Co., 262 S. Greenwood Ave., Pasadena, CA 91107, USA.
- [3] T.W. Crowe, W.C.B. Peatman, and E. Winkler, *Microwave and Optical Technology Letters*, Jan. 1991.
- [4] Custom Microwave, Inc., 940 Boston Avenue, Longmont, CO 80501, USA.
- [5] Infrared Laboratories, Inc., 1808 East 17th St., Tucson, AZ 85719, USA.
- [6] Thomas Keating Ltd., Station Mills, Billingshurst. West Sussex, England RH14 9SH.
- [7] J. W. Kooi, C. K. Walker, H. G. Leduc, P. L. Schaffer, T. R. Hunter, D. J. Benford, and T. G. Phillips, *International Journal of Infrared and Millimeter Waves*, **15**, 477 (1994).

- [8] Millitech Corporation, P. O. Box 109, South Deerfield, MA 01373-9990, USA.
- [9] Radiometer Physics, Bergerwisen Straß 15, 53340 Meckenheim, Germany.
- [10] H. Rothermel, T. G. Phillips, and J. Keene, *International Journal of Infrared and Millimeter Waves*, **10**, 83 (1989).
- [11] S. Rudner, M. J. Feldman, E. Kollberg, and T. Claeson, *Journal of Applied Physics*, **52**, 6366 (1981).
- [12] Morvan Salez, Pascal Febvre, William R. McGrath, Bruce Bumble, and Henry G. Leduc, *International Journal of Infrared and Millimeter Waves*, **15**, 349 (1994).
- [13] K.-F. Schuster, A.I. Harris, and K.-H. Gundlach, *International Journal of Infrared and Millimeter Waves*, **14**, 1867 (1993).
- [14] Timo J. Tolmunen and Antti V. Räisänen, *International Journal of Infrared and Millimeter Waves*, **8**, 1337 (1987).
- [15] Timo J. Tolmunen and Antti V. Räisänen, *International Journal of Infrared and Millimeter Waves*, **10**, 505 (1989).

Novel Varactor Diode Structures for Improved Power Performance[†]

Fred T. Brauchler, Jack R. East, and George I. Haddad

NASA / Center for Space Terahertz Technology
The University of Michigan
Ann Arbor, Michigan 48109

ABSTRACT

This paper describes two novel varactor structures to improve the power performance of multiplier sources. The first structure is similar to the conventional Schottky diode varactor with the addition of a wider-bandgap semiconductor layer at the Schottky contact. The wider bandgap material presents a larger barrier to electron flow in forward bias and a larger breakdown voltage in reverse bias. The second device structure, the back-to-back Schottky Diode Varactor (bbSDV), is a lateral current flow device with a symmetric C-V characteristic. The structure is similar to two Schottky diode varactors connected cathode-to-cathode except the ohmic contacts are eliminated and the two Schottky barrier diodes share the same depletion region. Eliminating the contacts and some of the low-doped depletion material should reduce the series resistance. A bbSDV has been fabricated with less than 0.4 A/cm^2 leakage current and a $C_{\text{max}}/C_{\text{min}}$ ratio greater than 3 for a $\pm 20\text{V}$ voltage swing.

I. Introduction

Solid state power sources in the 100-3000 GHz frequency range are essential in heterodyne receivers used for radio astronomy and remote sensing. To obtain high spectral resolution in the millimeter and sub-millimeter wave regime, heterodyne receivers are implemented to convert an incoming signal to a much lower intermediate frequency for amplification. These systems require a mixing element and a local oscillator power source

[†] This work was supported by NASA under Grant No. NAGW-1334.

near the frequency of interest. Solid state fundamental oscillator sources are not available in the sub-millimeter wave range, so harmonic multipliers utilizing varactor diodes become a critical component. This paper will present two novel varactor structures to improve the power performance of multiplier sources. The first structure is similar to the conventional Schottky diode varactor but utilizes a wider-bandgap semiconductor layer at the Schottky contact. The second device structure, the back-to-back Schottky diode varactor (bbSDV), is a lateral current flow device with a symmetric C-V characteristic.

II. AlGaAs Barrier Structure

All varactors depend on a nonlinear capacitance-voltage relation for harmonic generation and some type of barrier to real current flow. The most common is the reverse biased Schottky diode. This diode consists of a Schottky contact on top of a doped semiconductor with a back ohmic contact. The metal-semiconductor junction forms a barrier to electron flow while the semiconductor depletion region forms a capacitor with the well known inverse-square-root voltage dependence. A large barrier height is desired to increase the voltage swing and reduce the leakage current.

The limitations on conventional varactor performance include (1) the capacitance ratio, (2) breakdown voltage and forward conduction, (3) velocity saturation [1], and (4) displacement current in the neutral region. With doping, a trade-off is made between items (1)&(2) and (3)&(4). In other words, a lower doping improves the capacitance ratio and voltage swing and a higher doping reduces the effects of velocity saturation and displacement current in the neutral region.

A variation of the conventional varactor described above is one with a heterostructure of two materials with different bandgaps. One such arrangement, as shown in figure 1, places a larger bandgap material (barrier region), AlGaAs, between the Schottky contact metal and the lower bandgap material (depletion region), GaAs. The advantages of this

structure include (1) an additional degree of freedom in the device design, (2) a higher breakdown voltages in reverse bias, and (3) a larger barrier to electron flow in the forward direction. Potential problems include poor transport in the barrier AlGaAs layer and possible Γ -X transport which would lower the effective barrier height.

Figure 2 shows the calculated breakdown voltage vs. doping for a uniform AlGaAs structure of four different Al-fractions. From Sze [2], breakdown is the point where

$$1 = \int_0^w \alpha_n(\epsilon) dx$$

with the ionization data from Chau [3]. As can be seen for a reasonable doping, an increase in the Al-fraction results in a significant increase in breakdown voltage. In figure 3, the heterostructure breakdown voltage vs. AlGaAs layer width is calculated for three doping levels with three Al-fraction levels each. At a given AlGaAs width, a substantial increase in breakdown voltage is possible.

An AlGaAs/GaAs heterostructure varactor has been fabricated and the I-V characteristics are shown in figure 4. The structure is a 300Å, $3.0 \times 10^{16} \text{ cm}^{-3}$ N-doped $\text{Al}_{0.3}\text{Ga}_{0.7}\text{As}$ barrier layer on a 6000Å, $3.0 \times 10^{16} \text{ cm}^{-3}$ N-doped GaAs depletion layer with an N+ doped GaAs layer. For comparison, a 5700Å, $3.0 \times 10^{16} \text{ cm}^{-3}$ N-doped GaAs depletion layer with an N+ doped GaAs layer structure is also shown. As can be seen, the heterostructure device has approximately a 0.5V larger turn on voltage and nearly a 3V greater breakdown voltage. The increase in the voltage swing should increase the power capability.

The added flexibility of a barrier layer can be used to increase the voltage swing, as shown above. However, by both adding the barrier layer and increasing the doping so as to keep the same breakdown voltage, the efficiency of the varactor can be increased. A performance analysis has been completed on a GaAs varactor doubler operating with an input frequency of 80GHz. The analysis, detailed in East *et. al.* [4], includes effects of

forward conduction currents, velocity saturation, displacement currents in the neutral region, and breakdown currents. Figure 5 shows the calculated efficiency vs. the input power for three conditions. The first condition for a 20V breakdown voltage and $3 \times 10^{16} \text{ cm}^{-3}$ doping represents a GaAs Varactor. The second represents a same doping but greater breakdown voltage as an AlGaAs capped sample. For the third condition, 20V breakdown and $4 \times 10^{16} \text{ cm}^{-3}$ doping, the addition breakdown voltage is exchanged for an increase in doping. As can be seen, by increasing the doping, the peak efficiency shifts from 42% to over 53%. The corresponding peak power levels can be seen in figure 6.

III. Symmetrical Structure

Symmetrical structure varactor diodes provide multiplication by 3 with a simpler circuit and require no bias. Some current approaches include the single barrier varactor (SBV) [5] and the back-to-back barrier-N-layer-N+ varactor (bbBNN) [6]. The proposed structure is a back-to-back Schottky diode varactor (bbSDV).

The bbSDV structure has a rectangular mesa with Schottky contacts on two opposite edges. The Schottky metal extends on each of the sides to form contact pads. Unlike most varactors where the current flow is normal to the epitaxial layers, this structure utilizes a lateral current flow. A drawing of the device is shown in figure 7. In figure 8, micrographs of a back-to-back Schottky diode varactor is shown with a cross-sectional area of $25 \mu\text{m}^2$ and mesa length of $4 \mu\text{m}$.

Electrically, the bbSDV can best be described as two back-to-back Schottky diodes that share a single depletion region. Under zero bias, each junction has a small depletion region and thus the capacitance is large. When biased, most of the voltage-drop will be across the reverse biased junction while the other junction will change only slightly.

A simple model of this device at low to moderate voltages is a capacitance, resembling the series combination of the depletion capacitance at each Schottky, in series with a

series resistance corresponding to the undepleted semiconductor between the two depletion regions. Under zero bias, the two capacitors are just the junction capacitances in series with the series resistance. When a bias is applied, one of the depletion regions expands causing an associated decrease in both the junction and total capacitance. Since the same occurs with the other junction in the opposite bias, the C-V characteristics are symmetrical about the zero bias point. The change in capacitance with bias requires a leakage current flow at the forward bias junction, because charge accumulation is not supported in this structure [7] [8]. This will limit the frequency response of the device.

A barrier layer at the Schottky contact interface can provide a potential solution to the leakage current requirement. Such a barrier has been demonstrated with the increased turn on voltage of figure 10 in which an Al_2O_3 barrier layer was placed at the interface of a single Schottky diode structure. The semiconductor material structure consisted of a 300\AA $1 \times 10^{18} \text{ cm}^{-3}$ N-doped GaAs epitaxial layer on an N+ doped GaAs ohmic layer.

A bbSDV without a barrier layer has been fabricated with the following properties. A GaAs semiconductor N-type epitaxial layer of doping $4.3 \times 10^{16} \text{ cm}^{-3}$ and thickness of $1\text{ }\mu\text{m}$ on a semi-insulating GaAs substrate was used in the device. The metal contacts were formed with a Ti/Au deposition. The I-V characteristic, as shown in figure 9, displays that for a large voltage swing, there is less than $1\text{ }\mu\text{A}$ of leakage current for a $75\text{ }\mu\text{m}^2$ cross sectional area. This corresponds to 1.3 A cm^{-3} of leakage current for a $\pm 20\text{V}$ swing. A $C_{\text{max}}/C_{\text{min}}$ ratio of greater than 3 is also in the C-V characteristics of figure 9.

The bbSDV has many advantages over other varactor devices. The fabrication process requires only two lithographic steps and no back side processing except substrate removal. This simplifies fabrication and hence increases throughput and device to device uniformity. A second advantage is the good control of capacitance via the contact area. In this structure, the contact area can be specified much more accurately than in a vertical structure since a small height dimension is already accurately defined. The third advan-

tage is a high voltage swing with low leakage current as the Schottky diode varactor. This larger voltage swing corresponds to a larger power handling capability. The bbSDV has the properties of two Schottky diode varactors connected cathode to cathode, except for the series resistance since the depletion region is shared.

IV. Conclusions

Two novel structures to improve the power performance of multiplier sources were presented. The first structure, very similar to a conventional Schottky diode varactor, utilized an AlGaAs barrier layer to provide an additional degree of freedom, a design trade off between the breakdown voltage and doping. Also the barrier increased the turn on voltage. Through a performance analysis, it was shown that doping dominates the efficiency.

The second structure presented is the bbSDV. The advantages of this device is the good control of capacitance, few fabrication steps, lower leakage current for a large voltage swing, and a symmetric C-V characteristic for 3rd harmonic multiplication. A potential problem exist at RF because charge accumulation is not supported. However, a similar structure is proposed with barriers that would circumvent such a problem.

List of Figures

1. AlGaAs barrier structure.
2. Calculated breakdown voltage vs. doping for a uniform AlGaAs structure
3. Calculated heterostructure breakdown voltage vs. AlGaAs barrier layer width for three doping levels each by three Al-fraction levels.
4. Measured current vs. voltage characteristics of an AlGaAs/GaAs heterostructure varactor and a similar GaAs structure for comparison.
5. A performance analysis calculation of efficiency vs. input power for three GaAs structures.
6. A performance analysis calculation of output power vs. input power for three GaAs structures.
7. Back-to-back Schottky diode varactor drawing.
8. Micrographs of back-to-back Schottky diode Varactors; Area $25\mu\text{m}^2$, Length $4\mu\text{m}$.
9. Measured current vs. voltage and capacitance vs. voltage characteristics of a $75\mu\text{m}^2$ cross sectional area back-to-back Schottky diode varactor.
10. Measured current vs. voltage characteristics of a Schottky diode with and without an Al_2O_3 barrier at the Schottky interface.

References

- [1] E. Kollberg, T.J. Tolmunen, M.A. Frerking, J.R. East, "Current Saturation in Submillimeter Wave Varactors," *Second International Symposium on Space Terahertz Technology*, 1991, pp. 306-322
- [2] S.M. Sze, *Physics of Semiconductor Devices*, 2nd ed. New York: Wiley 1969, pp. 100.
- [3] H.F. Chau, Ph.D. Dissertation, The University of Michigan, Ann Arbor, Michigan, USA, 1992, pp. 29.
- [4] J.R. East, E. Kollberg, and M.A. Frerking, "Performance Limitations of Varactor Multipliers," *Fourth International Symposium on Space Terahertz Technology*, 1993, pp. 312-325.
- [5] E. Kollberg and A. Rydberg, "Quantum-barrier diodes for high-efficiency millimeter-wave multipliers," *Electron. Lett.*, vol. 25, 1989, pp. 1696-1697.
- [6] U. Lieneweg, T.J. Tolmunen, M.A. Frerking, and J. Maserjian, "Modeling of Planar Varactor Frequency Multiplier Devices with Blocking Barriers," *IEEE Microwave Theory and Tech.*, vol. 40, no. 5, May 1992, pp. 839-845.
- [7] T. Crowe personal communication.
- [8] N. Erickson personal communication.

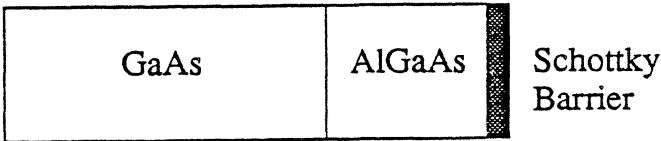


Figure 1

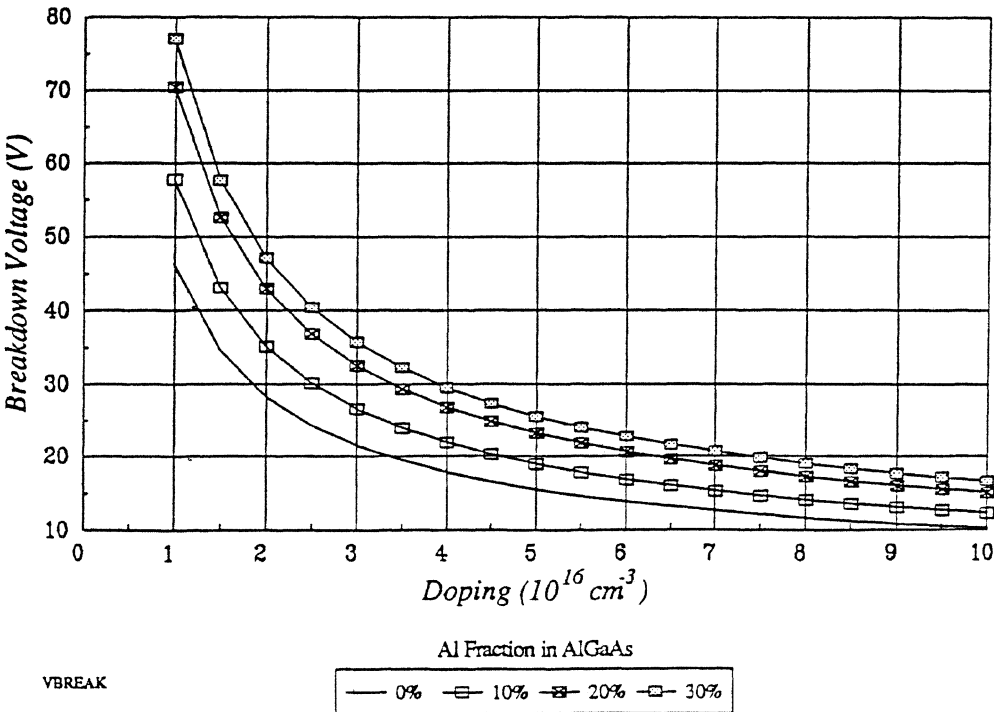


Figure 2

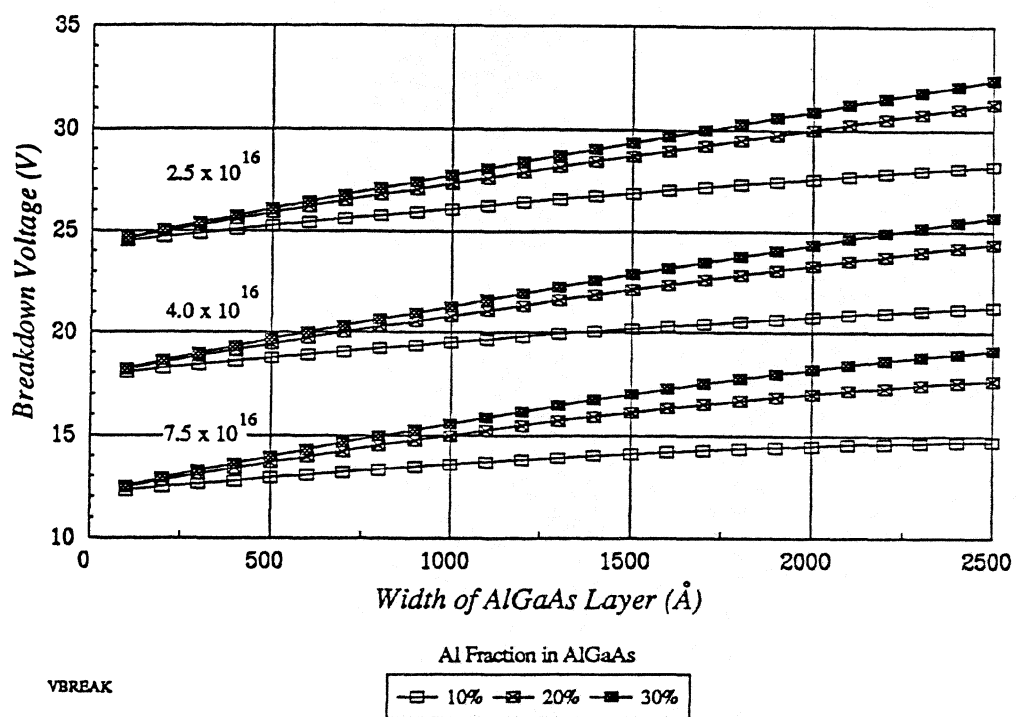


Figure 3

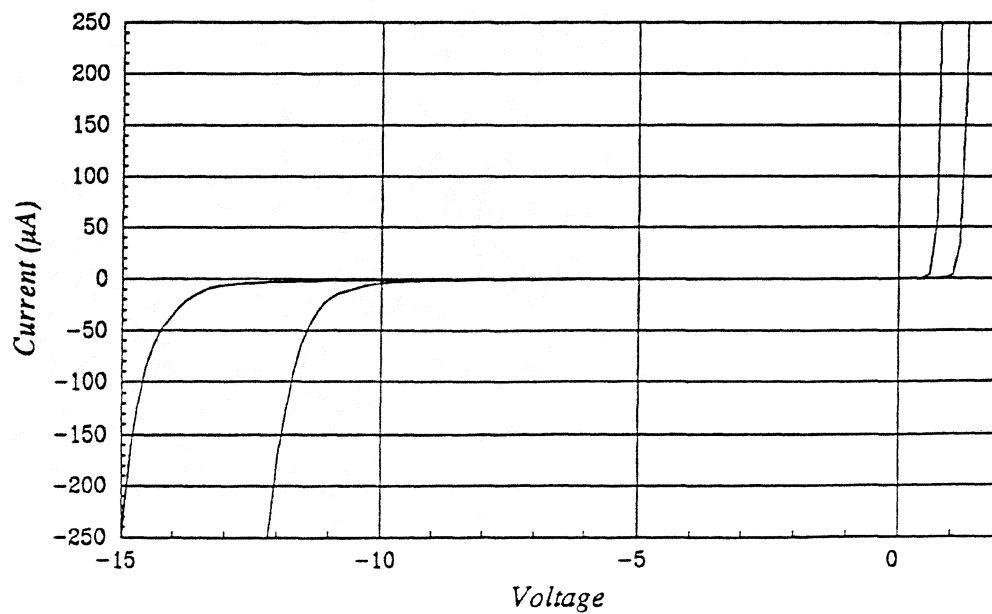


Figure 4

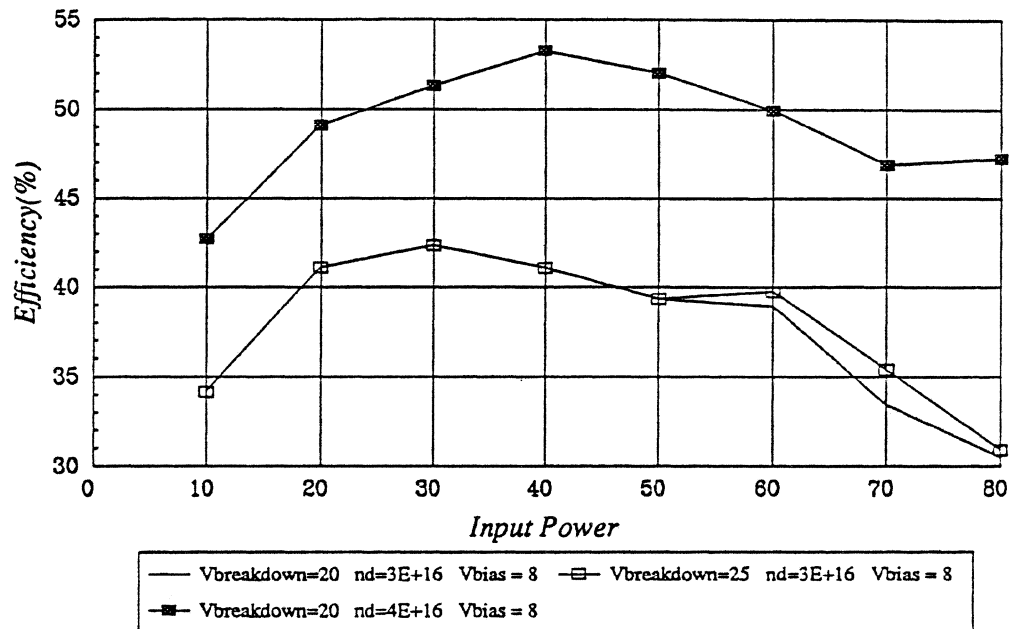


Figure 5

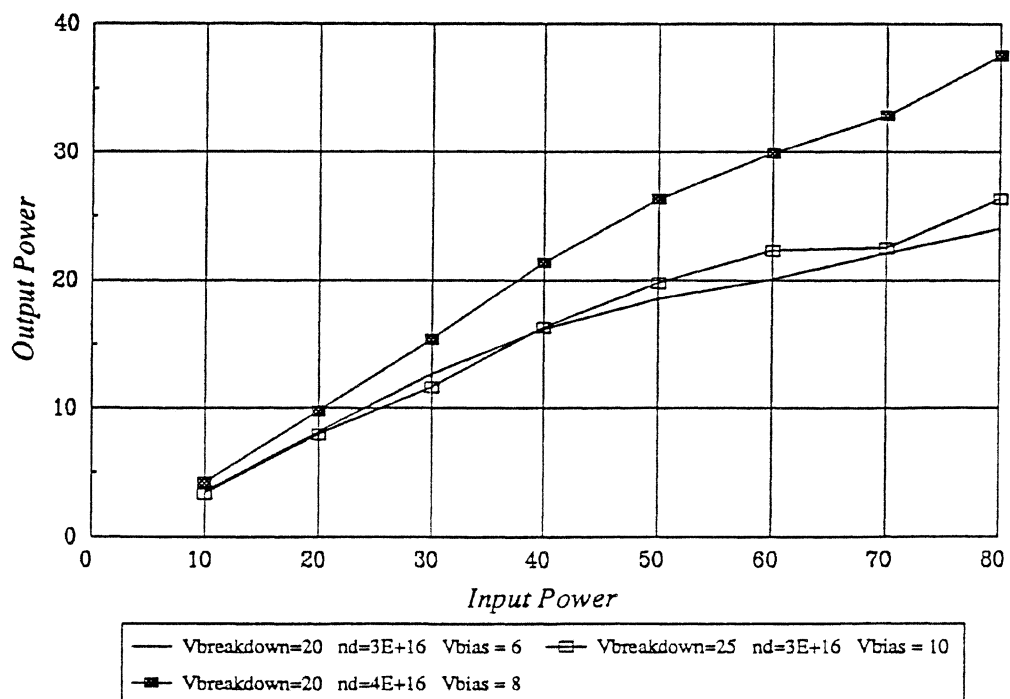


Figure 6

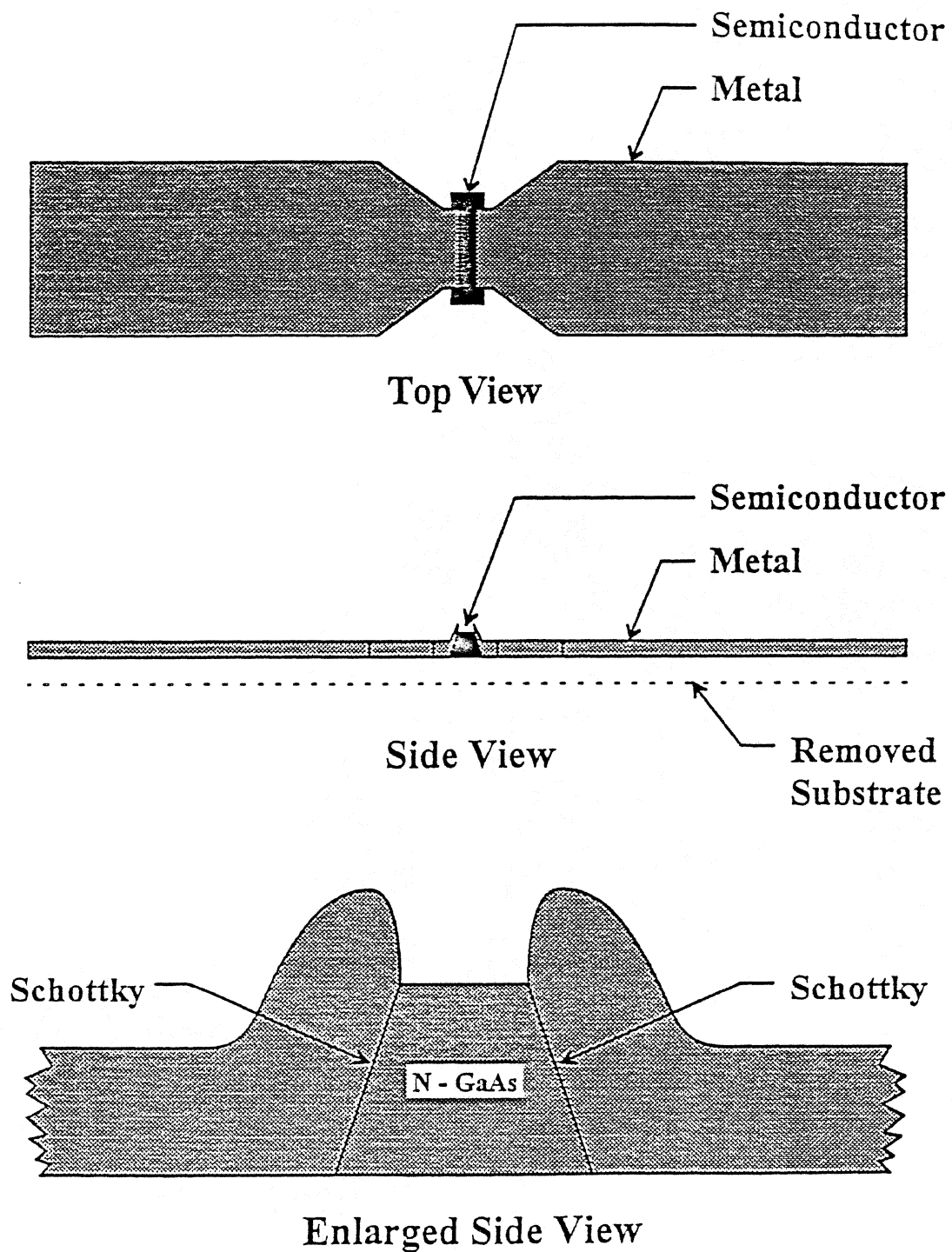


Figure 7

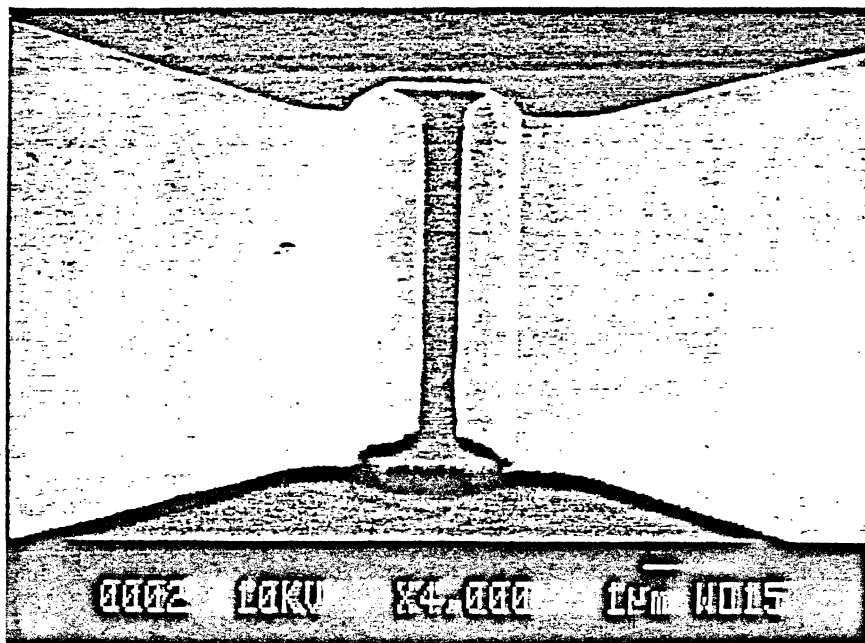
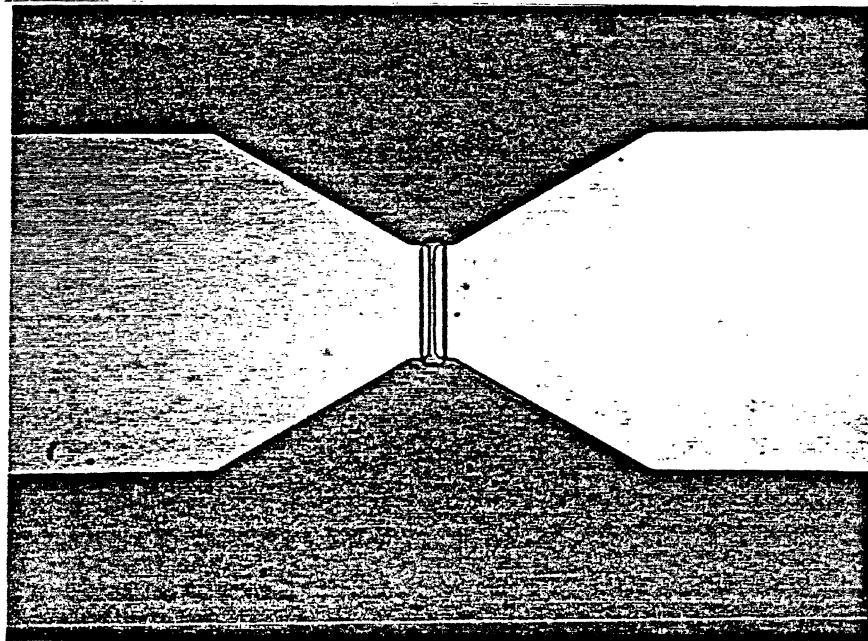


Figure 8

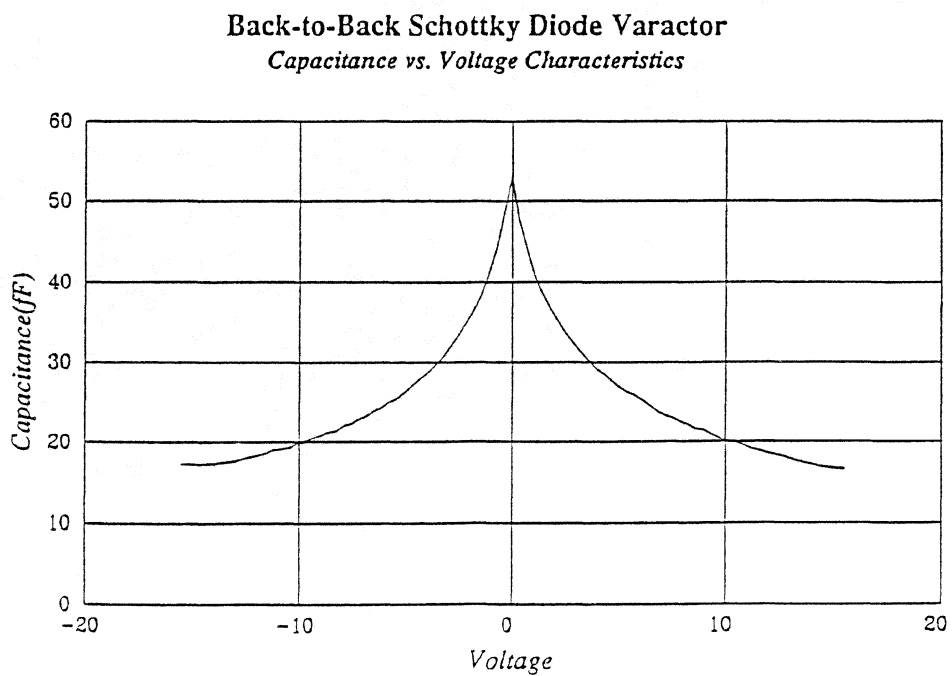
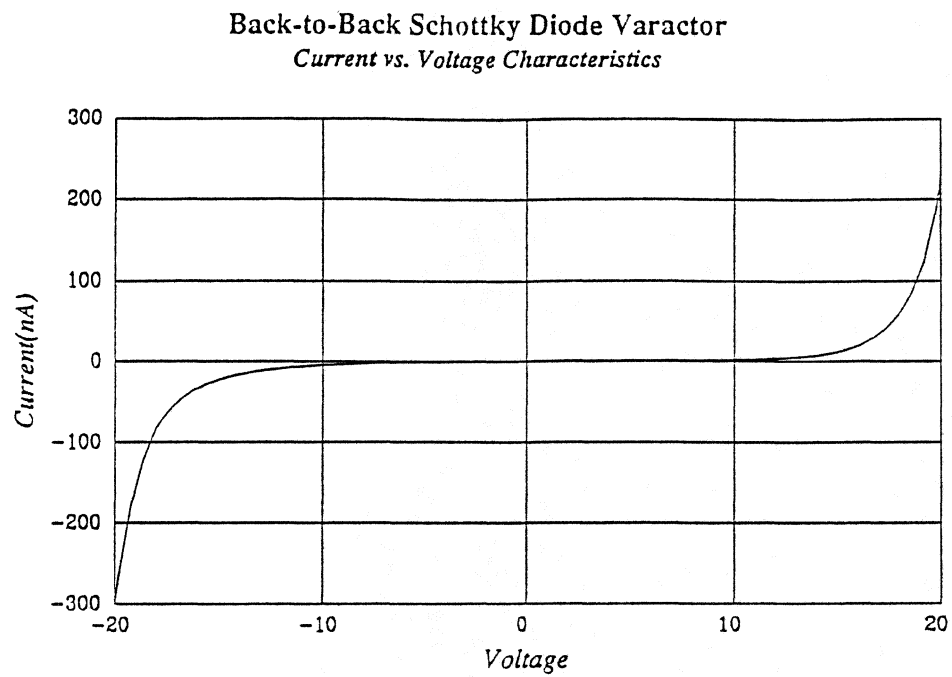


Figure 9

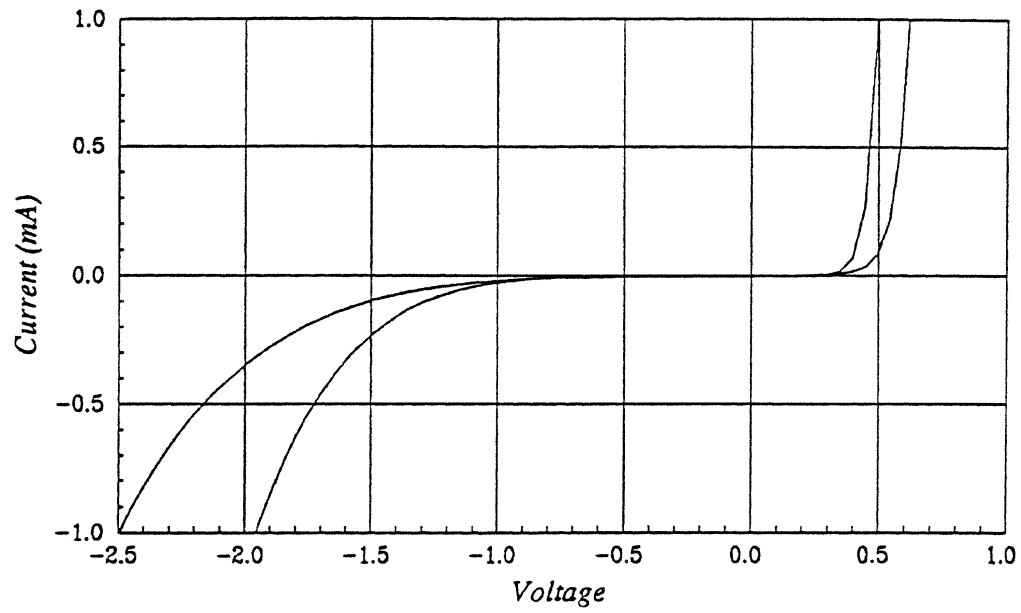


Figure 10

A TRIPLER TO 220 GHz USING A BACK-TO-BACK BARRIER-N-N⁺ VARACTOR DIODE

**DEBABANI CHOUDHURY, PETER H. SIEGEL, ANTTI V. RÄISÄNEN*,
SUZANNE C. MARTIN AND R. PETER SMITH**

Jet Propulsion Laboratory
California Institute of Technology
Pasadena, CA 91109

* Current Address: Helsinki University of Technology
Radio Laboratory
FIN-02150 Espoo, Finland

ABSTRACT

The back-to-back barrier-N-N⁺ (bbBNN) varactor is a nonlinear device being developed for frequency multiplier applications above 100 GHz. Its symmetrical C-V characteristic, low series resistance and suitability to planarization make it ideal choice for high frequency, low power, odd harmonic generation.

In this paper, the performance of a 220 GHz tripler using integrated planar bbBNN devices is presented. A new split-waveguide block design has been used to provide the proper embedding impedances to the device. The performance over 200-240 GHz has been measured and the

bbBNN device is shown to provide as much as 734 microwatts output power. This is believed to be the highest conversion efficiency yet reported for all planar tripler at this frequency. The performance is expected to be improved further with minor changes to the device and circuit parameters.

I. INTRODUCTION

The submillimeter-wave range of the spectrum holds enormous promise for spectral line studies of the interstellar medium, distant galaxies, solar system and earth remote sensing. To achieve the high sensitivity and spectral resolution requirements of observatory and exploratory stage missions, submillimeter-wave heterodyne radiometers are being developed [1,2]. One of the least developed technologies for submillimeter-wave heterodyne radiometry is the local oscillator source. Candidate technologies include harmonic generators, such as frequency multipliers pumped by millimeter-wave fundamental sources. Although the whisker contacted Schottky varactor diodes have proven very effective, there remains great interest in developing mechanically robust, planar device technologies which are capable of operating well into the submillimeter wavelength range and have the potential to deliver sufficient amounts of power [3]. To minimize the risk of failure, planar device technology is preferred for space applications. The goal of our work is to demonstrate that planar devices can replace whisker contacted devices without degrading performance.

One candidate planar diode is a planar back-to-back barrier-n-n⁺ (bbBNN) varactor [4,5]. This device has a very sharp C-V characteristic, which helps the device to be highly efficient at low input power levels. This is an advantage, particularly at THz frequencies, where the available input power is quite low. Its symmetric C-V characteristic offers significant benefits for odd harmonic multiplier applications since the idler circuits at the even harmonics are not needed. This device has a comparatively low series resistance and high cut-off frequency. It has low

substrate parasitics as all non-essential semiconductor materials are removed using a backside processing technique [6]. Although measurements on discrete planar bbBNN devices have been carried out earlier in a crossed waveguide mount [5], handling and mounting of the small discrete chips were very difficult. This motivated us to develop the technique to integrate RF microstrip filter circuitry with the planar bbBNN device [7].

Waveguide mounts can provide appropriate embedding impedances at the input and output frequencies to couple power in and out of a nonlinear device. In order to accommodate the necessary waveguide flanges and backshort tuning mechanisms, frequency multipliers commonly utilize a crossed waveguide design. Ease of fabrication and assembly, wide tunability of fundamental and harmonic embedding impedances and low loss are the desirable aspects of the multifrequency, multiwaveguide mount designs. To avoid the fabrication complexity of the crossed waveguide block and to facilitate easy mounting of planar integrated devices, a split-waveguide block has been proposed recently [8]. The present experiment has been carried out using this split-waveguide block.

II INTEGRATED bbBNN DEVICE

The integrated bbBNN device used in this experiment was developed at the Microdevices Laboratory of JPL. Fig.1 shows the schematic diagram of an integrated planar bbBNN varactor structure on a quartz substrate. All non-essential high dielectric semiconductors have been removed using the backside processing technique, so as to have only the small semiconductor mesa region in the final circuit structure. The fabrication procedure for the integrated device has been described in [6,7]. The semiconductor layer structure of the mesa is shown in Fig.2. The thinned wafer from the top surface down consists of, (i) a 2 nm thick GaAs cap layer, (ii) a 20 nm $\text{Al}_{0.45}\text{Ga}_{0.55}\text{As}$ barrier, (ii) a 3 nm GaAs spacer followed by $4 \times 10^{12} \text{ cm}^{-2}$ silicon planar doping, (iv) a 120 nm thick moderately doped GaAs layer (doping level = $1 \times 10^{17} \text{ cm}^{-3}$) and (v) a 1300

nm thick highly doped GaAs layer (doping level = $5 \times 10^{18} \text{ cm}^{-3}$). The active mesa region is covered by a silicon nitride layer.

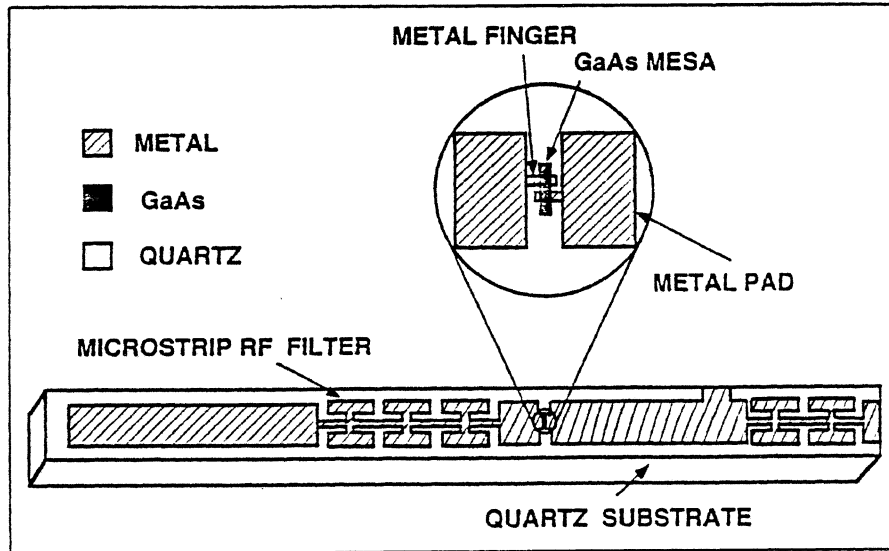


Fig.1 Schematic of a planar bbBNN varactor integrated with the microstrip filter structure on a fused quartz substrate

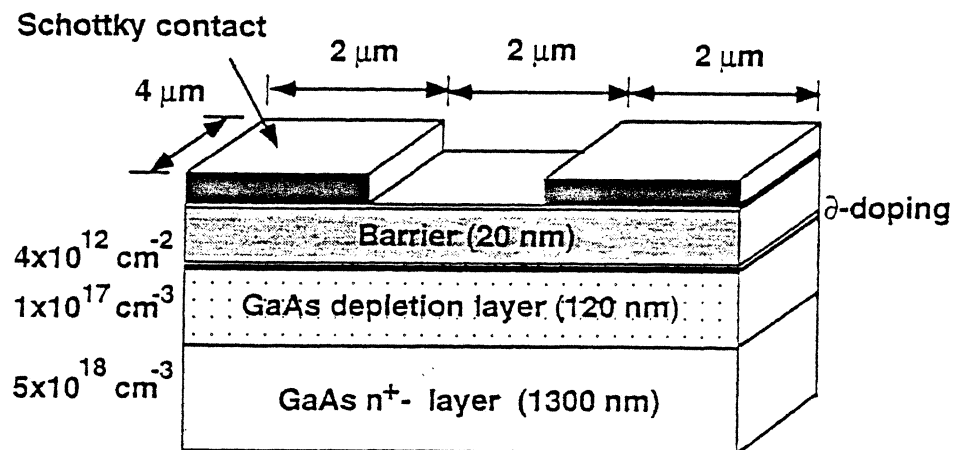


Fig.2 Semiconductor layer structure of the bbBNN device

Fig.3(a) and 3(b) show the capacitance-voltage (C-V) and current-voltage (I-V) characteristics of an $8 \mu\text{m}^2$ device integrated with RF

microstrip filter circuitry. This device has $C_{\max}/C_{\min} = 2.7$ and a breakdown voltage of 6.5 volts.

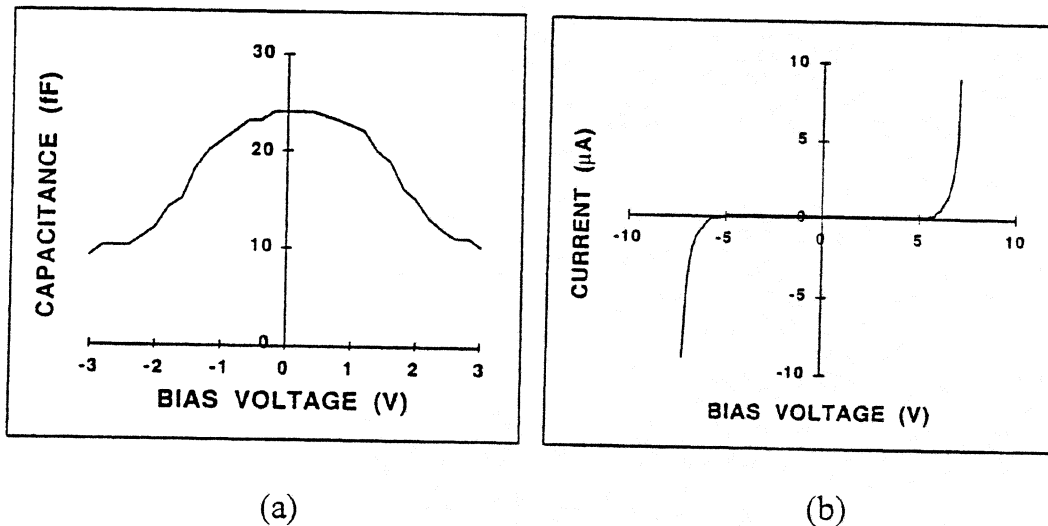


Fig.3 Measured (a) C-V and (b) I-V characteristics of a $8 \mu\text{m}^2$ integrated bbBNN varactor.

III. MOUNT DESCRIPTION

A split-waveguide mount [8] has been used to provide the proper embedding impedances to the integrated bbBNN device. This mount has been specially designed for planar devices integrated with filter tuning circuitry on a quartz substrate. Fig.4 shows one half of the 220 GHz tripler mount. Two halves of the block are mirror images of each other and input and output rectangular waveguides are split along the E-field. The input power is coupled to the quartz microstrip RF filter through a WR-12 E-plane arm. The bbBNN device is positioned at the center of the broadwall of a half height WR-4 waveguide (0.28 mm x 1.09 mm). A channel waveguide transformer [9] couples the output waveguide to standard WR-4 through an E-plane arm. The distances of the input and output E-plane waveguides from the microstrip filter are approximately $\lambda_{g,\text{fundamental}}/2$ and $\lambda_{g,\text{third-harmonic}}/2$ respectively. The mount has four sliding backshorts, two at the input side

and two at the output side. The backshorts provide both a series and parallel stub at the input and output and help to achieve the maximum coupling. The filter channel is 0.36 mm wide and 0.31 mm high and it extends across and beyond the output tuner waveguide. This allows DC and RF grounding at the end of a microstrip filter instead of at the waveguide wall. The bias voltage can be applied to the device through the bottom of the lower half of the block, via a SMA coaxial connector and a bias filter.

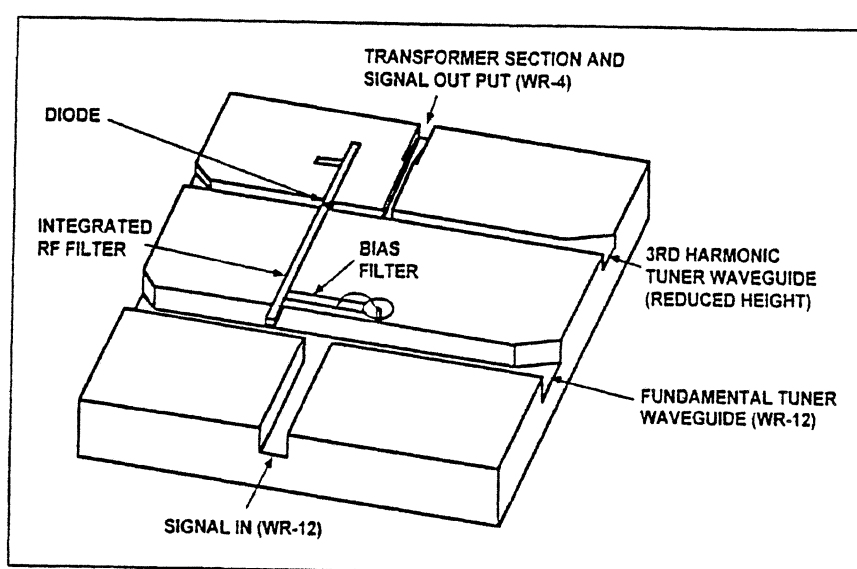


Fig.4 Schematic diagram of the lower half of the 220 GHz split-waveguide rippler mount with the integrated bbBNN device.

The integrated RF filter and the bias filter (Fig.4) help to achieve the signal separation. These microstrip hammerhead filters are fabricated on 0.33 mm wide and 0.152 mm thick fused quartz substrates. The bias filter and the RF filter are the three section hammerhead filters, similar to those presented in [10]. Fine tuning of the filter response was accomplished using the finite difference time domain (FDTD) method [11]. The bias filter rejects the input power 60-80 GHz. The RF filter passes the input frequency, but rejects the tripled output power. The filter on the far side of the output tuner waveguide presents a short circuit at the waveguide

wall at the third harmonic frequency and presents a reactive termination, via a side stub, at the fundamental frequency.

IV. RF PERFORMANCE

The tripler performance was measured using Gunn oscillators as pump source. Input frequencies in the range of 66-80 GHz were used. The device was biased at 0 volts during the measurements. The flange-to-flange efficiency of the bbBNN device with the C-V and I-V characteristics of Fig.3, was measured using the technique described in reference [12]. The best performance was achieved at an output frequency of 217.5 GHz. Fig.5(a) shows the measured flange-to-flange tripling efficiency versus input power for the integrated bbBNN in the 220 GHz split-waveguide mount. The flange-to-flange efficiency of the tripler reaches its maximum value of 7% at 8.8 mW input power and then begins to decrease as the pump power level is increased. Fig.5(b) shows the tripled output power versus input power for this device. A maximum output power of 734 μ W was measured for 14.3 mW input power.

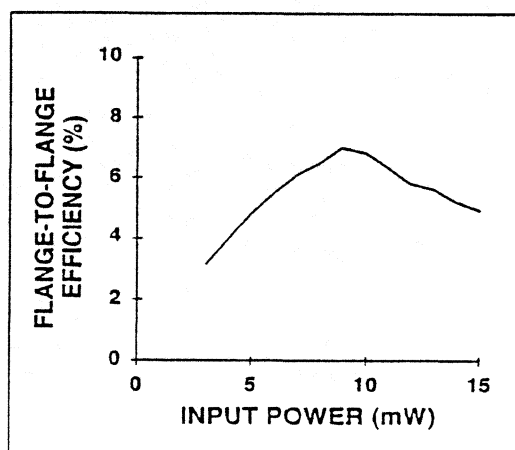


Fig.5(a) Measured flange-to-flange efficiency versus input power plot at 217.5 GHz.

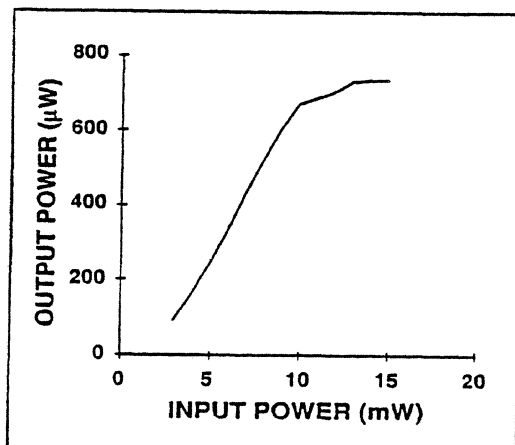


Fig.5(b) Measured output power versus input power plot at 217.5 GHz.

V. CONCLUSION

A flange-to-flange tripling efficiency of 7% has been reported for a planar bbBNN device integrated with microstrip tuning structures on a quartz substrate in 220 GHz split-waveguide mount. An output power of 734 μ W has been measured. This is the best performance for these integrated devices to date. The measured device had $C_{\max}/C_{\min} = 2.7$. Theoretical studies indicate that devices with higher C_{\max}/C_{\min} will give better efficiency [13]. The performance should improve with minor modifications of device and circuit parameters.

ACKNOWLEDGMENT

The work was carried out at the Jet Propulsion Laboratory, California Institute of Technology, under contract with the National Aeronautics and Space Administration. The authors would like to

thank Dr. Margaret Frerking for various useful discussions. Authors also specially thank Andrew Pease and Mark Natzic for their help in mounting the integrated device structures in the split-waveguide mounts. A.V.Räisänen was on sabbatical leave at JPL as senior research Fellow of the National Research Council, from Helsinki University of Technology, Finland.

REFERENCES

- [1] R.Zimmermann, R.Zimmermann, and P.Zimmermann, "All solid-state radiometers for environmental studies to 700 GHz", Proceedings of Third International Symposium on Space Terahertz Technology, pp.706-723, 1992.
- [2] M.A.Frerking, "Submillimeter heterodyne instrument concept for SMIM", Proceedings of SPIE Conference, 1874, Infrared and Millimeter Wave Engineering (1993).
- [3] B.J.Rizzi, K.K.Rausch, T.W.Crowe, P.J.Koh, W.C.B.Peatman, J.R.Jones, S.H.Jones and G.Tait, "Planar varactor diodes for submillimeter applications", Proceedings of Third International Symposium on Space Terahertz Technology, pp.297-311, 1992.
- [4] U.Lieneweg, T.J.Tolmunen, M.A.Frerking and J.Maserjian, "Modeling of planar varactor frequency multiplier devices with blocking barriers", IEEE Trans. Microwave Theory and Tech., vol.40, no.5, pp.839-845, May 1992.
- [5] D.Choudhury, A.V.Räisänen, R.P.Smith, M.A.Frerking, S.C.Martin and J.K.Liu, "Experimental performance of a back-to-back barrier-n-n⁺ (bbBNN) varactor tripler at 200 GHz", IEEE Trans. Microwave Theory and Tech., vol.42, no.4, April 1994.

- [6] R.P.Smith, D.Choudhury, S.C.Martin, M.A.Frerking, J.K.Liu and F.A.Grunthaner, "A new fabrication technique for back-to-back varactor diodes", Proceedings of Third International Symposium on Space Terahertz Technology, pp.158-163, 1992.
- [7] D.Choudhury, A.V.Räisänen, R.P.Smith, S.C.Martin, J.E.Oswald, R.J.Dengler, M.A.Frerking and P.H.Siegel, "Frequency tripler with integrated back-to-back barrier-n-n⁺ (bbBNN) varactor diodes in a novel split-waveguide block at 220 GHz", 1994 IEEE MTT-S Symposium Digest, San Diego, May 1994.
- [8] A.V.Räisänen, D.Choudhury, R.J.Dengler, J.E.Oswald and P.H.Siegel, "A novel split-waveguide mount design for millimeter- and submillimeter-wave frequency multipliers and harmonic mixers", IEEE Microwave and Guided Wave Letters, vol.3, no.10, pp.369-371, October 1993.
- [9] P.H.Siegel, D.W.Peterson and A.R.Kerr, "Design and analysis of channel waveguide transformer", IEEE Trans. Microwave Theory and Tech., vol.31, no.6, pp.473-484, June 1983.
- [10] P.H.Siegel, J.E.Oswald, R.J.Dengler, D.M.Sheen and S.M.Ali, "Measured and computed performance of a microstrip filter composed of semi-insulating GaAs on a fused quartz substrate", IEEE Microwave and Guided Wave Letters, vol.1, no.4, pp.78-80, April 1991.
- [11] J.E.Oswald and P.H.Siegel, "The application of the FDTD method to millimeter-wave filter circuits including the design and analysis of a compact coplanar strip filter for THz frequencies", 1994 IEEE MTT-S Symposium Digest, San Diego, May 1994.
- [12] D.Choudhury, M.A.Frerking and P.D.Batelaan, "A 200 GHz tripler using a single barrier varactor", IEEE Trans. Microwave Theory and Tech., vol.41, no.4, pp.595-599, April 1993.

- [13] D.Choudhury, A.V.Räisänen, R.P.Smith and M.A.Frerking,
"Study of the effect of the C_{\max}/C_{\min} ratio on the performance of back-to-back barrier-n-n⁺ (bbBNN) varactors for frequency multiplier applications",
IEEE Microwave and Guided Wave Letters, vol.4, no.4, April 1994.

EXPERIMENTS WITH SINGLE BARRIER VARACTOR TRIPLER AND QUINTUPLER AT MILLIMETER WAVELENGTHS

*Timo J. Tolmunen^{1,2}, Antti V. Räisänen¹, Elliot Brown³,
Hans Grönqvist⁴ and Svein Nilsen⁴*

¹ Radio Laboratory, Helsinki University of Technology, FIN-02150 Espoo, Finland

² Turku Institute of Technology, FIN-20700, Turku, Finland

³ Lincoln Laboratory, Massachusetts Institute of Technology, Lexington, MA 02173

⁴ Department of Applied Electron Physics, Chalmers University of Technology, S-41296 Göteborg, Sweden

Abstract

InGaAs/InAlAs single-barrier varactor diodes were tested as frequency triplers and quintuplers. Two different diodes, one made at MIT Lincoln Laboratory and the other made at the Chalmers University of Technology were tested in crossed-waveguide tripler and quadrupler/quintupler mounts.

In the tripler mount only the Lincoln diode was tested. The highest observed flange-to-flange tripling efficiency was 6.5 % with 2 mW of input power at an output frequency of 116 GHz. The highest measured output power was 200 μ W. The experimental results of the tripler are in a close agreement with theoretical simulations which predict 11 % peak efficiency with 2-3 mW of pump power. Beyond the peak the efficiency decreases quickly due to the leakage current.

In the quintupler mount both diodes were tested. The highest measured quintupling efficiency of the Lincoln diode was 0.93 % at 171.5 GHz with input power of 14 mW. The Chalmers diode was able to provide 0.65 % peak efficiency at 172.5 GHz with input power level of 22 mW. The highest observed output power was 137 μ W and 150 μ W for the Lincoln and Chalmers diode, respectively. The highest efficiency exceeds slightly and the highest output power exceeds by a factor of five the best results reported previously for single-barrier varactor quintuplers.

I INTRODUCTION

At millimeter wavelengths above 100 GHz frequency multipliers have been used extensively in generation of coherent LO power. Most commonly these multipliers are based on the back-biased GaAs Schottky-varactors due to their mature technology. However, recently interest has also grown in novel varactor diodes having symmetric capacitance versus voltage (C - V) characteristic about zero bias. The greatest benefit of the symmetry is the odd-harmonic power generation. This generally simplifies the design of triplers and especially quintuplers or other higher-order harmonic multipliers, because of the reduction in the number of idler circuits.

The devices having symmetric C - V characteristics include diodes such as back-to-back BNN (bbBNN), resonant tunneling diode (RTD) and single-barrier varactor (SBV). Due to its highly nonlinear C - V curve, the single-barrier varactor has been considered as one of the most attractive alternative for conventional Schottky-varactors in higher-order frequency multiplication [1].

In simplest form, the single-barrier varactor consists of two n -type semiconductor cladding layers separated by an electron barrier layer. The doping profile in the cladding layers is perfectly symmetric about the center of the barrier so that the C - V characteristics is symmetric about zero bias. With cladding layers made of GaAs and the barrier of AlGaAs, single-barrier varactors have been demonstrated as triplers with output between 200 and 300 GHz, yielding a maximum flange-to-flange efficiency of 5 % at 222 GHz [2] and 2 % at 192 GHz [3]. The device in Ref. 2 was also tested as a quintupler at 310 GHz, yielding a maximum efficiency of 0.2 %.

Recently, with InGaAs cladding layers and an InAlAs barrier, single-barrier varactors have been tested as a quintupler with output at 150–190 GHz [4], yielding maximum efficiency of 0.78 % at an output frequency of 172 GHz. The combination of InGaAs/InAlAs materials yields a larger barrier height with less excess conduction current compared to the GaAs/AlGaAs diodes.

In the present work two different InGaAs/InAlAs single-barrier varactors, one made at MIT Lincoln Laboratory and the other made at the Chalmers University of Technology, were examined. These diodes were tested as triplers for 115 GHz and as quintuplers for 170 GHz. In the experiments multiplier blocks originally designed for Schottky-varactors were used [5,6]

II MULTIPLIER DEVICES

Both the Lincoln and Chalmers diodes consisted of an $\text{In}_{0.53}\text{Al}_{0.47}\text{As}$ barrier embedded between n -type $\text{In}_{0.53}\text{Ga}_{0.47}\text{As}$ cladding layers. The epitaxial layers.

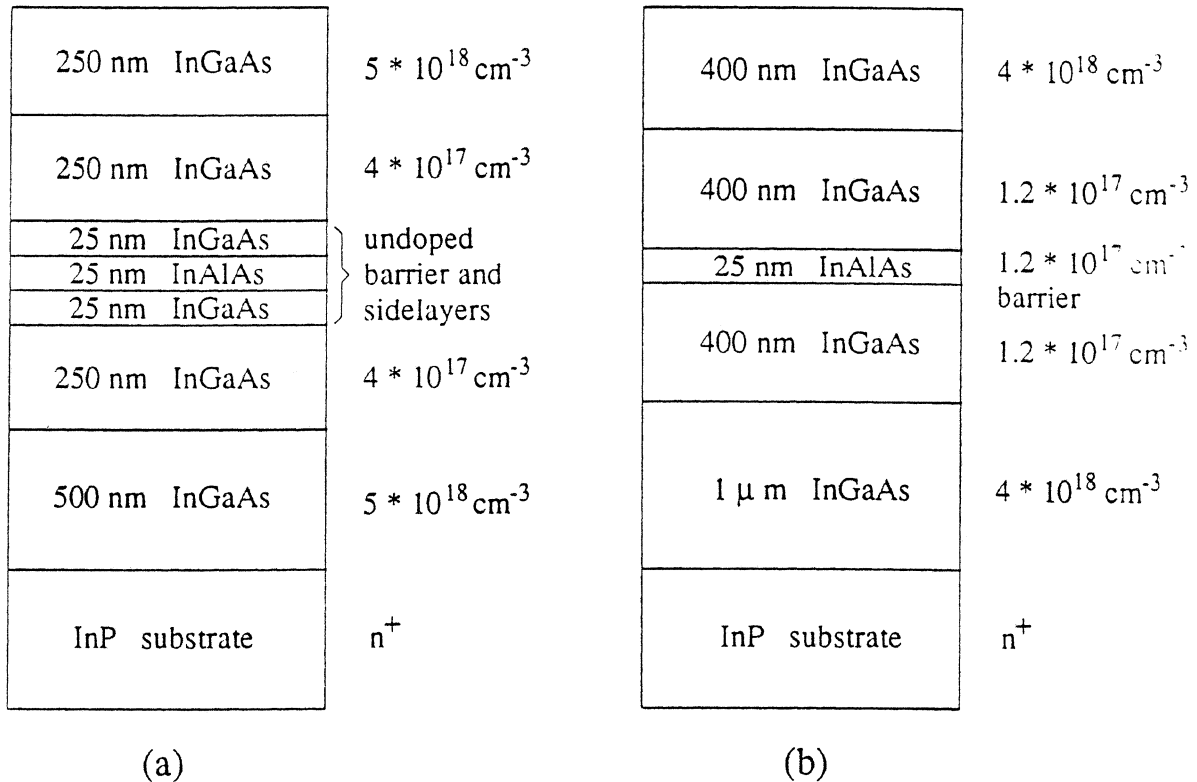


Figure 1. Epitaxial layer structure of the a) Lincoln diode and b) Chalmers diode.

depicted in Fig. 1, were grown by molecular beam epitaxy on an InP substrate.

In order to assist the whisker contacting of mesa diodes, the regions between mesas in the Lincoln diode were filled with Si_3N_4 . The same procedure was carried out on the Chalmers diode with photoresist instead of Si_3N_4 . The Lincoln and Chalmers diodes have areas of about $16 \mu\text{m}^2$ and $30 \mu\text{m}^2$, respectively. Figure 2a shows the theoretical and measured C - V characteristics of the Chalmers diode, Figure 2b shows the theoretical curve of the Lincoln diode and Figure 3 shows the measured I - V characteristics of the sample diodes used in these experiments. Note that only the positive half of the antisymmetric I - V curve is presented.

Figure 3 indicates clearly that the leakage current is remarkable especially in the case of the larger-area Chalmers diode. Therefore, the multiplication can be purely reactive only with relatively low input power levels. With higher pump power the multiplication is dominated by the resistive multiplication which results in considerably lower performance.

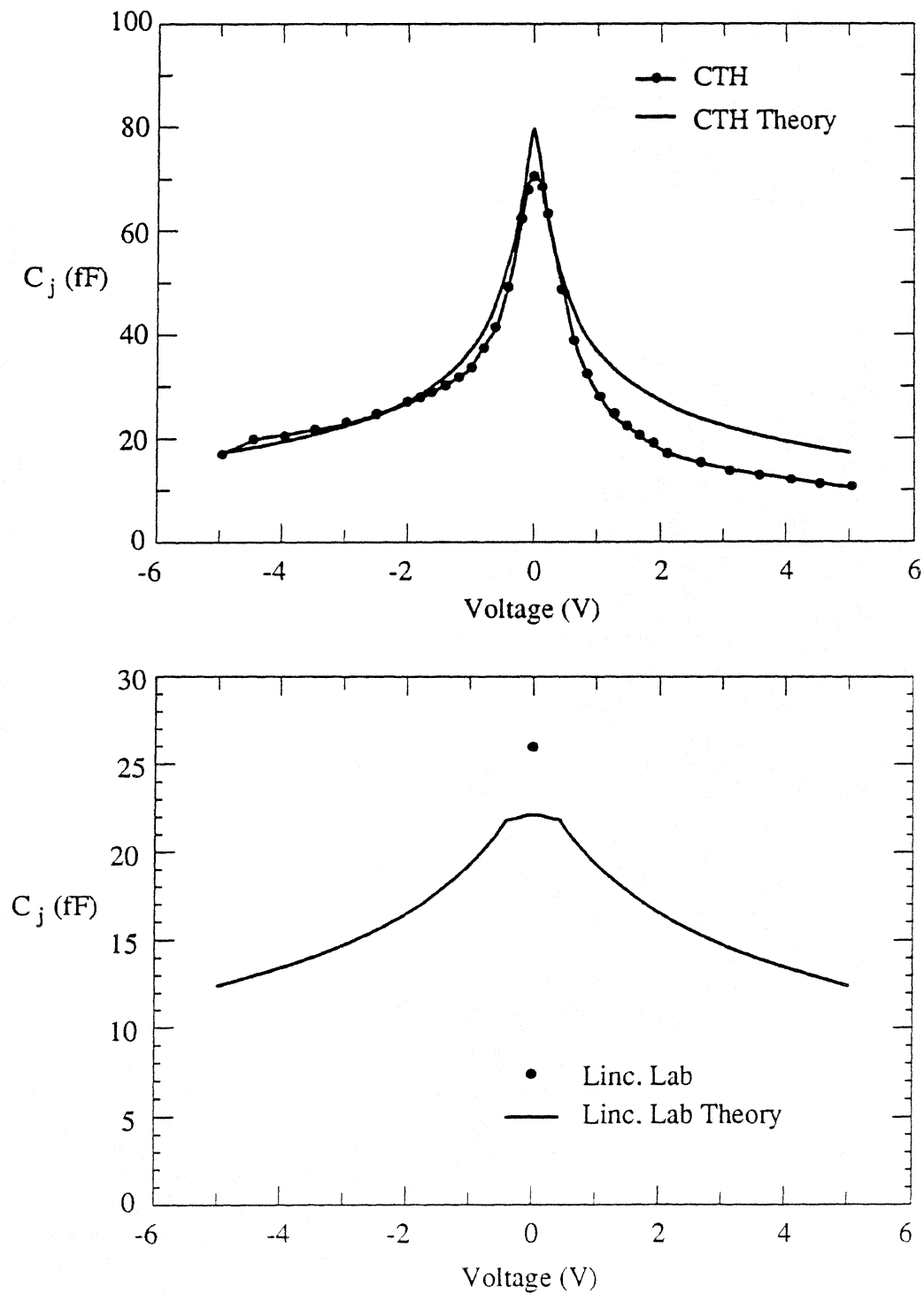


Figure 2. $C-V$ characteristics of the a) Chalmers diode and b) Lincoln diode. Solid line is theoretical and dotted line is measured.

III TEST MOUNTS

The single-barrier varactors were tested in a crossed-waveguide tripler and quadrupler/quintupler structure in which the input and output waveguides are separated by a low-pass filter. The mounts were originally optimized for conventional 5- μm -diameter Schottky-varactors [5,6]. In both mounts input power is coupled in through a half-height WR-22 waveguide and is impedance matched to the coaxial filter using a non-contacting sliding backshort. The diode is soldered to the far end of the filter pin and is located in an output waveguide having non-standard dimensions ($1.80 \times 0.45 \text{ mm}^2$) at the diode location. In the quintupler mount this non-standard waveguide also forms an idler cavity which is tuned by a non-contacting sliding backshort. The idler cavity and the output waveguide (WR-4) are coupled through a transition in the waveguide width. In the tripler mount the reduced-height non-standard dimensions are simply tapered in order to form a full-height output waveguide. In both mounts the diode is dc biased through a whisker contact across the output waveguide (or the idler cavity) and through the coaxial filter. More detailed descriptions of both crossed-waveguide mounts including the schematics are given in Refs. 5 and 6.

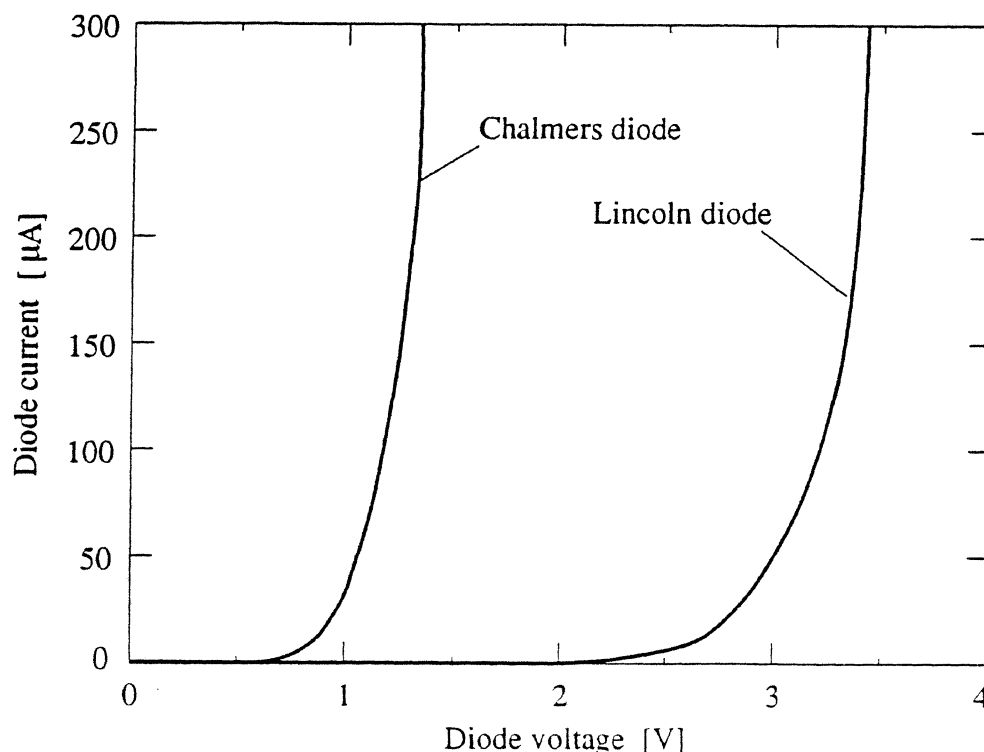


Figure 3. Measured I - V curve of the Chalmers and Lincoln diodes.

IV EXPERIMENTAL RESULTS

In the tripler mount only the Lincoln diode was tested. In the experiments $12.7\text{-}\mu\text{m}$ -diameter whiskers having lengths of $200\text{--}400\text{ }\mu\text{m}$ were used. In order to assist the input matching the whisker was soldered at the end of the center pin of a 1.4-mm -long coaxial resonator. The resonator was approximately $\lambda/6$ -long at the fundamental frequency. Therefore, it increased the embedding inductance. At the third harmonic the resonator was $\lambda/2$ -long and did not have any effect on the embedding impedance.

Figure 4 shows the measured flange-to-flange tripling efficiency versus output frequency at pump power levels of 2.0 and 6.0 mW . The best conversion efficiency was 6.5% with a pump power of 2 mW at an output frequency of 115.8 GHz . The results shown in Figure 4 were obtained with the whisker length of $250\text{ }\mu\text{m}$. It was also observed that the output power was saturated to around $200\text{ }\mu\text{W}$ at input power levels of $5\text{--}8\text{ mW}$. With higher input power levels the output power decreased slightly. This phenomenon was caused by the resistive multiplication process due to the leakage current which become dominating at these input power levels.

In the quintupler mount both devices were tested. In these experiments $12.7\text{-}\mu\text{m}$ -

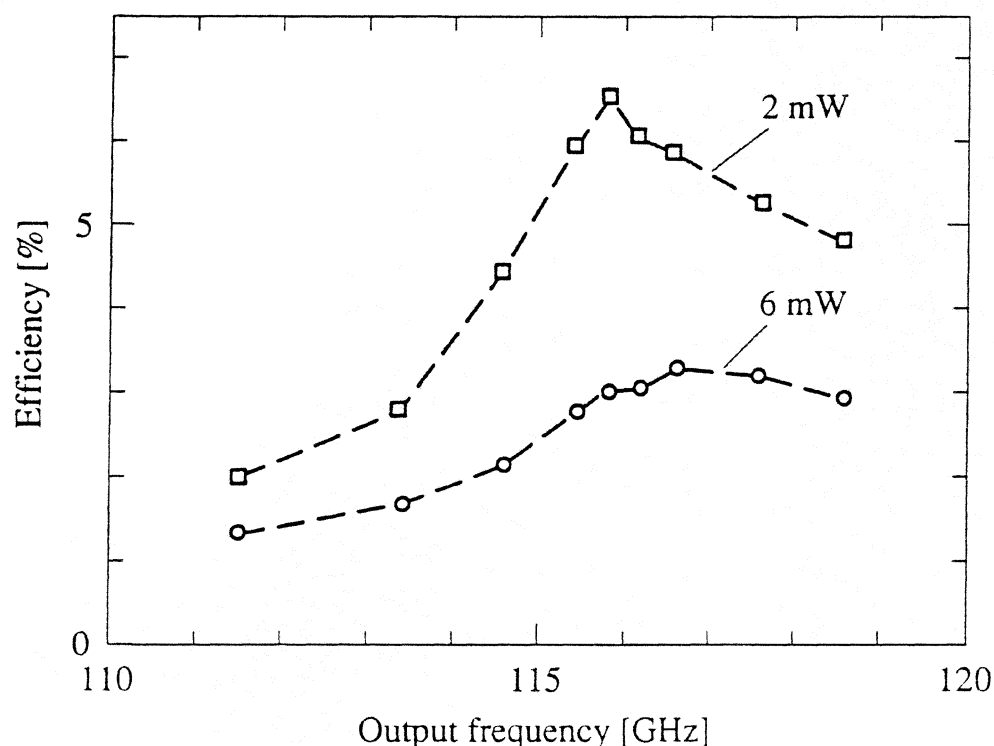


Figure 4. Measured flange-to-flange tripling efficiency versus frequency for the Lincoln diode.

diameter whiskers having lengths of 200–500 μm were used. Also the coaxial-resonator was used in order to assist input matching. In this case, however, the length of the resonator was chosen to be around $\lambda/5$ at the fundamental. This kind of resonator increased highly the fundamental and slightly the idler embedding inductance, but had no effect at the output frequency.

The highest measured quintupling efficiency of the Lincoln diode was 0.93 % at 171.5 GHz with pump power level of 14 mW. In the case of the Chalmers diode the highest efficiency was 0.65 % at 172.5 GHz with input power level of 22 mW. In both cases the whisker length of around 200 μm yielded the best performance. In Figure 5 the quintupling efficiency of both devices is illustrated versus input power level at frequencies where the efficiency peaks. The highest measured output power was 137 μW and 150 μW for the Lincoln and Chalmers diode, respectively.

V DISCUSSION

The performance of the tripler and quintupler was analyzed theoretically at the output frequencies where the peak efficiency was obtained. In the simulations

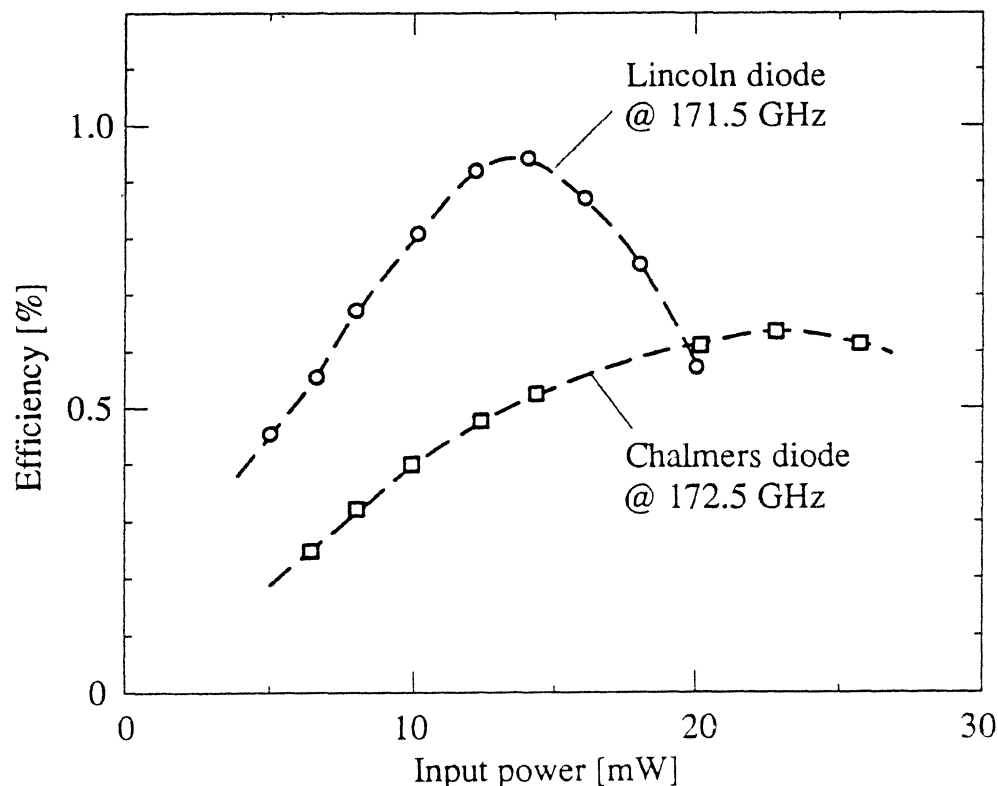


Figure 5. Quintupling efficiency versus input power at frequencies where the peak efficiency was obtained.

measured I - V and C - V curves (Figs. 2 and 3) of the sample diodes were used. In the case of the Lincoln diode, however, the C - V curve was theoretical.

In Figure 6 the theoretical performance of the Lincoln diode as a frequency tripler is presented together with experimental results as a function of input power. The theoretical results indicate that with perfect impedance matching and in the absence of waveguide losses, the tripling efficiency of the Lincoln diode would be about 11 % with 3 mW of pump power. Beyond the peak the efficiency decreases quickly due to the increasing leakage current. The difference between theoretical and experimental curves is around 2.5 dB. Based on earlier experiments with Schottky-varactors the embedding impedances provided by the tripler mount at various frequencies are rather well understood [5]. Therefore, it is believed that the impedance matching at the fundamental and output frequencies was nearly optimum. However, the total ohmic losses of the waveguide mount are estimated to reduce conversion efficiency by around 1.5 dB below the theoretical. Taking losses into account the agreement between theory and experiments is rather good.

It is interesting to compare single-barrier varactor tripler results to those obtained with a conventional Schottky-varactor in the same mount. A VD010 varactor by Farran Technology was able to provide 28 % peak efficiency at 107 GHz with pump power of 5 mW [5]. Also in this case the best results were approximately 2.5–3.0 dB

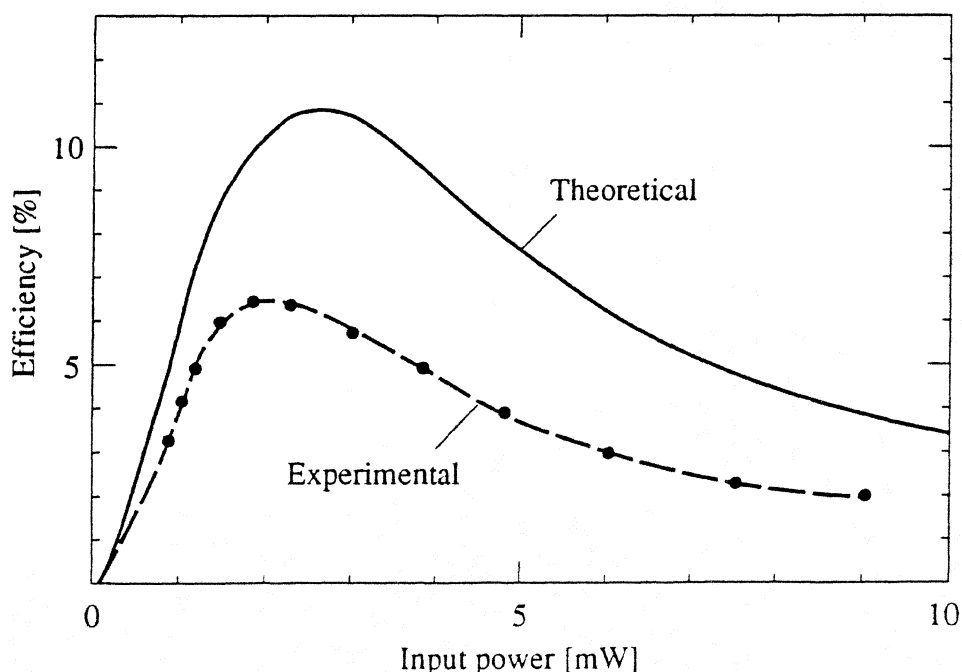


Figure 6. Experimental tripling efficiency of the Lincoln diode in comparison to theoretical performance.

below theoretical values. The peak efficiency of the Schottky-varactor was by a factor of four higher than that obtained with the single-barrier varactor diode. With 30 mW input power the output power of the Schottky-varactor tripler was 3.0–5.6 mW over 15 GHz frequency band and the maximum output power was around 6.5 mW obtained with (safe) input power levels of 40–50 mW. The maximum output power of the single-barrier varactor tripler was 150–200 μ W over 5 GHz band obtained with pump power of 5–8 mW. Input power levels higher than 15 mW typically resulted in the diode failure.

In Figure 7 the theoretical performance of the Lincoln diode and Chalmers diode as a quintupler is presented together with experimental results. The theoretical results indicate clearly that the efficiency peaks at 3.7 % for the Lincoln diode and at 2.8 % for the Chalmers diode with input power level of around 3 mW. It is not fully understood why the shape of the experimental curves are completely different at low input power

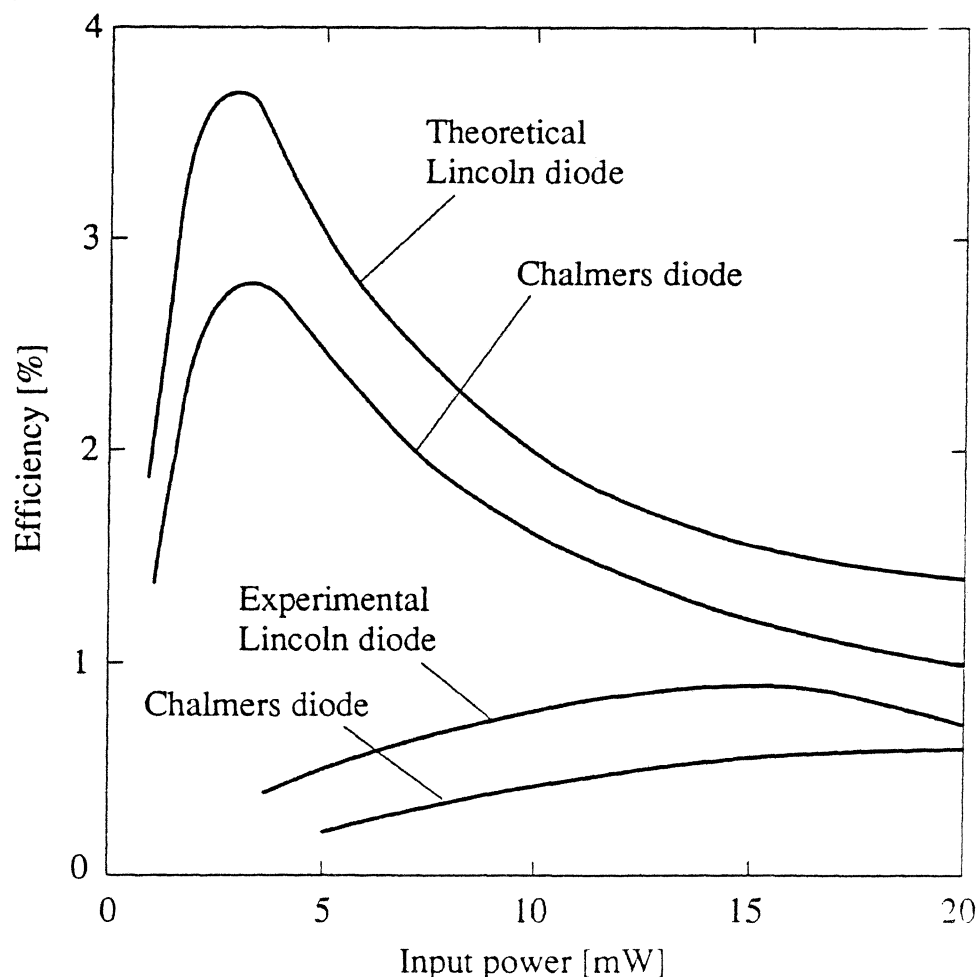


Figure 7. Experimental quintupling efficiency of the Lincoln and Chalmers diodes in comparison to theoretical performance.

levels. However, it is assumed that non-optimized terminations (especially at the idler frequency) results in this shortfall. It is well known that the multiplication efficiency of a varactor diode is critically dependent on the idler termination. The agreement is better at higher input power levels where the multiplication is mostly resistive and less sensitive to variations in the idler termination. At high input power levels the difference can be explained by the ohmic losses in the waveguide mount which are estimated to be around 2–3 dB.

Although the quintupling efficiency of the Lincoln diode exceeds that of the previous GaAs/AlGaAs single-barrier quintupler [2] by nearly a factor of five and that of the InGaAs/InAlAs diode slightly [4], it falls short of the best results for conventional Schottky-varactor quintuplers. In the same mount, a flange-to-flange quintupling efficiency of 4.2 % was measured from VD010 at 168 GHz with 10 mW of pump power [6]. Furthermore, with P_{in} of 40 mW an output power of 1.3 mW was available from VD010 at this same frequency and an output power over 700 μ W was measured over the range from 165 GHz to 170 GHz. The single-barrier varactor diodes were able to provide an output power of 100–150 μ W over 3–4 GHz frequency band.

VI CONCLUSIONS

A tripler for 115 GHz and a quintupler for 170 GHz with whisker-contacted single-barrier varactor diodes were tested. The highest observed tripling and quintupling efficiencies were 6.5 % and 0.93 %, respectively. These conversion efficiencies should improve considerably with better single-barrier varactor diodes having lower leakage current densities.

ACKNOWLEDGEMENTS

The authors wish to thank K. Herold and E. Laine for machining the multiplier mounts, and A. R. Calawa and M. J. Manfra for providing the Lincoln Laboratory InGaAs/AlAs materials used in this work. The Lincoln Laboratory portion of this work was sponsored by NASA through the Jet Propulsion Laboratory.

REFERENCES

- [1] T. J. Tolmune and M. A. Frerking, "Theoretical performance of novel multipliers at millimeter and submillimeter wavelengths", *Int. J. of Infrared and Millimeter Waves*, vol. 12, no. 10, pp. 1111–1134, Oct. 1991.

- [2] A. Rydberg, H. Grönqvist and E. Kollberg, "Millimeter- and submillimeter-wave multipliers using quantum-barrier-varactor (QBV) diodes". *IEEE Electron Device Letters*, vol. 11, no. 9, pp. 373–375, Sept. 1990.
- [3] D. Choudhury, M. A. Frerking and P. D. Batelaan, "A 200 GHz tripler using a single barrier varactor", *IEEE Trans. on Microwave Theory Tech.*, vol. 41, no. 4, pp. 595–599, April 1993.
- [4] A. V. Räisänen, T. J. Tolmunen, M. Natzic, M. A. Frerking, E. Brown, H. Grönqvist and S. M. Nilsen, "A single barrier varactor quintupler at 170 GHz." submitted for publication in *IEEE Trans. on Microwave Theory Tech.* 1993.
- [5] T. J. Tolmunen and A. V. Räisänen, "An efficient Schottky-varactor frequency multiplier at millimeter waves. Part II: Tripler." *Int. J of Infrared and Millimeter Waves*, vol. 8, no. 10, pp. 1337–1353, Oct. 1987.
- [6] T. J. Tolmunen and A. V. Räisänen, "An efficient Schottky-varactor frequency multiplier at millimeter waves. Part III: Quadrupler" and "Part IV: Quintupler." *Int. J of Infrared and Millimeter Waves*, vol. 10, no. 4, pp. 475–518, April 1989.

GaAs/InGaAs/AlGaAs HETEROSTRUCTURE BARRIER VARACTORS FOR FREQUENCY TRIPLING

J. R. Jones, S. H. Jones, and G. B. Tait[†]

Department of Electrical Engineering, University of Virginia, Charlottesville, VA 22903

[†]Electronics Science & Technology Division, Naval Research Laboratory, Washington, DC 20375

Abstract

Accurate and efficient calculations of the large-signal time-dependent behavior of GaAs/InGaAs/AlGaAs Heterostructure Barrier Varactor (HBV) frequency tripler circuits are presented. This is accomplished by combining a novel harmonic-balance nonlinear circuit analysis technique with a hydrodynamic device simulator based on the first two moments of the Boltzmann transport equation and Poisson's equation. The unified numerical device/harmonic-balance nonlinear circuit simulator allows HBV multiplier circuits to be co-designed from both a device and a circuit point of view by specifying the device geometry, doping profile, and alloy composition profile, as well as the parasitic impedances of the device and the embedding impedances of the circuit. Excellent correlation between the numerical device simulator and experimental DC I-V and static C-V data has been obtained for GaAs/AlGaAs, GaAs/InGaAs/AlGaAs, and InGaAs/InAlAs on InP HBVs. Harmonic-balance simulations of GaAs/Al_{0.7}Ga_{0.3}As and GaAs/In_{0.0-0.2}Ga_{1.0-0.8}As/Al_{0.7}Ga_{0.3}As HBVs indicate that an improvement in tripler performance can be achieved using the GaAs/graded InGaAs/AlGaAs structure. Third harmonic output power levels of several milliwatts and multiplying efficiencies of at least 7.0 % are obtainable from these two device structures, for frequency tripling from 100 GHz to 300 GHz, with nominal parasitic device impedances and realizable fundamental and third harmonic circuit embedding impedances.

I. Introduction

The Heterostructure Barrier Varactor (HBV), first proposed in 1989[1], has received considerable attention as a promising device for high efficiency frequency multiplication in the millimeter to submillimeter wavelength range because of its attractive device characteristics and large number of design parameters. A single barrier HBV consists of a large band gap semiconductor sandwiched between symmetric capacitive modulation regions of smaller band gap material such that the device has an evenly symmetric nonlinear capacitance-voltage (C-V) relationship at zero DC bias. The evenly symmetric device C-V characteristic eliminates the even harmonic components from the output current waveform so that high efficiency frequency multiplier circuits, which do not require DC bias and which require fewer idlers than standard Schottky varactor multipliers,

can be realized. These device characteristics make the HBV an ideal candidate for use in broadband frequency triplers and quasi-optical tripler arrays, especially since no idlers are required for frequency tripling. By epitaxially stacking several single barrier HBVs in series, further advantages are expected including higher device cut-off frequencies, for a given device area, due to reduced device capacitances, and higher power generation capabilities due to the distribution of pump power over several series devices. Furthermore, the HBV has a large degree of design flexibility in that the semiconductor alloy composition and doping profiles, barrier thickness, number of barriers, device geometry, and device area can be independently varied. Overall, the design flexibility and attractive device characteristics of the HBV suggest that a high efficiency frequency multiplier with excellent device/circuit impedance matching and near-optimum C-V relationship can be achieved with a single device.

The large number of device design parameters coupled with the circuit design constraints makes the task of designing HBV frequency multipliers a daunting one. With this in mind, a DC and large-signal time-dependent numerical device simulator, with excellent computational speed and convergence properties, has been developed for generic InGaAs/InAlAs on InP and GaAs/InGaAs/AlGaAs HBVs. The simulator is based on the first two moments of the Boltzmann transport equation and combines electron transport through the heterostructure bulk with electron transport across the abrupt heterointerfaces in a fully self-consistent manner. The simulator can model any combination of doping and InGaAs, AlGaAs, or InAlAs alloy composition profiles such that a systematic investigation of candidate HBV devices can be undertaken to illuminate the combination of device geometry, doping profile, and alloy composition profile which yields optimal device performance. Given the importance of both the nonlinear device and its embedding circuit in the design of frequency multipliers, the numerical device simulator has been combined with a efficient harmonic-balance nonlinear circuit analysis technique to provide a unified computer-aided design environment for the entire HBV multiplier circuit. HBV multiplier circuits can, therefore, be co-designed from both a device and a circuit point of view by specifying the device geometry, doping profile, and alloy composition profile, as well as the

parasitic impedances of the device and the embedding impedances of the circuit.

An overview of the DC and large-signal time-dependent numerical device simulator is given in Section II. Likewise, a brief overview of the harmonic-balance nonlinear circuit analysis technique utilized in this work is presented in Section III. Experimental and theoretical DC, large-signal time-dependent, and harmonic-balance results are discussed in Section IV. Finally, conclusions are given in Section V.

II. Numerical Device Simulator

Given the essentially one-dimensional geometry of the HBV and the majority carrier nature of HBV operation, carrier transport through the bulk regions of an HBV has been described by a set of coupled nonlinear differential equations for electrons derived from the first two moments of the Boltzmann transport equation and Poisson's equation. These equations are valid in regions with smoothly varying alloy composition, and hydrodynamically model the scattering and diffusive transport mechanisms of electrons within the device. The resulting equations governing DC and large-signal time-dependent transport are

$$\frac{\partial J_{n,p}(x,t)}{\partial x} = \frac{1}{q} \frac{\partial n(x,t)}{\partial t} \quad (1)$$

$$J_{n,p}(x,t) = -\tau_p(x) \frac{\partial J_{n,p}(x,t)}{\partial t} - \frac{q^2 \tau_p(x) n(x,t)}{m^*(x)} \frac{\partial \phi_n(x,t)}{\partial x} \quad (2)$$

$$\frac{\partial}{\partial x} \left[\epsilon(x) \frac{\partial \psi(x,t)}{\partial x} \right] = q [n(x,t) - N_D(x)] \quad (3)$$

where

$$n(x,t) = n_{i,ref} \exp \left[\frac{q}{kT} (\psi(x,t) + V_n(x) - \phi_n(x,t)) \right] \quad (4)$$

and where $J_{n,p}$ is the electron particle current density, n is the electron density, ϕ_n is the electron quasi-Fermi potential, ψ is the electrostatic potential, k is Boltzmann's constant, q is the electron charge, T is the absolute temperature, $n_{i,ref}$ is the intrinsic electron density in

the reference material (GaAs or InP), and τ_p , m^* , and ϵ are the spatially-dependent momentum relaxation time, electron conductivity effective mass, and dielectric permittivity, respectively. Furthermore, V_n is the spatially-dependent alloy potential, referenced to intrinsic GaAs or InP, which models the additional electric force, caused by gradients in the electron affinity and the effective conduction band density of states, that electrons are subjected to in compositionally nonuniform materials[2]. In all, equation (1) is the electron current continuity equation and equation (3) is Poisson's equation. Equation (2) is the electron particle current density expression derived from the first moment of the Boltzmann equation, and includes the time-dependent term not included in the standard drift-diffusion equations. This extra term has been retained to help model ballistic transport phenomenon in the thin barrier region of the HBV, and high frequency transport phenomenon throughout the device.

In order to accurately model the current in heterostructure devices, it has been found that careful consideration of carrier transport across abrupt material discontinuities is required[3,4]. As such, electron transport across the abrupt heterointerfaces of an HBV has been described by a set of nonlinear electron particle current density equations which couple together the quasi-Fermi potentials on both sides of the interfaces and act as constraints on the particle current density throughout the device. Electric displacement continuity, electrostatic potential continuity, and electron particle current density continuity complete the set of interface conditions required for a self-consistent solution at a given heterointerface.

For an HBV biased as shown in Figure 1, the particle current density constraint at $x = 0$ takes into account thermionic emission and thermionic-field emission (thermally assisted tunneling) of carriers over and through the abrupt barrier, and is derived from an evaluation of the net flux of carriers crossing the heterointerface as given by emission theory and assuming a Maxwell-Boltzmann electron distribution[4]. The resulting interface constraint on the electron particle current at this junction is

$$J_{n,p}(0) = \frac{A^* T^2}{N_c(0^*)} \left\{ \exp \left[\frac{q}{kT} (\phi_n(0^+) - \phi_n(0^-)) \right] - 1 \right\} \{ n_{i,ref} \exp \left[\frac{q}{kT} \left(\frac{\Phi}{q} + \psi(0) + V_n(0^+) - \phi_n(0^+) \right) \right] \} \quad (5)$$

where A^* is the effective Richardson constant, Φ is the effective barrier height lowering due to tunneling, and the last term in braces in equation (5) is the electron density on the barrier side of the junction, $n(0^+)$.

At the $x = W$ heterointerface of Figure 1, the thermionic emission/thermionic-field emission electron particle current density constraint of equation (5) becomes a “fluid-outflow” constraint on electron transport. Under such high field conditions, the particle current density constraint is, again, derived from an evaluation of the net flux of carriers crossing the heterointerface as given by emission theory, but a full drifted-Maxwellian electron distribution is utilized instead of a Maxwell-Boltzmann distribution. The resulting interface constraints on the electron particle current at this junction is

$$J_{n,p}(W) = \{ \langle v_x \rangle_{R \rightarrow L} \exp[\phi_n(W^-) - \phi_n(W^+)] - \langle v_x \rangle_{L \rightarrow R} \} \{ n_{i,ref} \exp[\psi(W) + V_n(W^-) - \phi_n(W^-)] \} \quad (6)$$

where the first term in braces in equation (6) is interpreted as an average interface collection velocity and the last term in braces in this equation is the electron density on the barrier side of the junction, $n(W^-)$. The left and right directed components of the average interface collection velocity are given by, respectively

$$\langle v_x \rangle_{R \rightarrow L} = \sqrt{\frac{kT}{2\pi m_{D-M}^*}} \quad (7)$$

$$\langle v_x \rangle_{L \rightarrow R} = \sqrt{\frac{kT}{2\pi m_{D-M}^*}} \exp\left[\frac{-h^2 k_o^2}{8\pi k T m_{D-M}^*}\right] + \frac{h k_o}{4\pi m_{D-M}^*} \left\{ 1 + \operatorname{erf}\left[\frac{h k_o}{2\pi \sqrt{2k T m_{D-M}^*}}\right] \right\} \quad (8)$$

where

$$k_o = \frac{-J_{n,p}(W)}{n(W^-)} \quad (9)$$

is the displacement of the Maxwellian distribution from equilibrium and m_{D-M}^* is a suitable average of electron effective masses on the two sides of the heterointerface. In all, the interface constraint given by equation (6) is similar to the boundary constraint of Adams and Tang for Schottky contacts at high forward bias when the flat-band condition is exceeded[5].

Electrons can tunnel through the tip of the heterojunction barrier under appropriate bias conditions, i.e. at the $x = 0$ heterointerface in Figure 1. Since this tip closely resembles a triangular barrier, the WKB approximation for tunneling through the tip of a triangular barrier has been used to estimate the contribution of tunneling electrons to the total electron particle current as given in equation (5). By using the WKB approximation, the barrier height is, in effect, reduced by an amount[6]

$$\Phi = \frac{-3\hbar\xi\ln(P)}{8\pi\sqrt{2qm_B^*}} \quad (10)$$

where \hbar is Plank's constant, ξ is the total electric field in the barrier, m_B^* is the electron effective mass in the barrier, and P is the tunneling probability, or the probability of the triangular barrier being penetrated by an electron with energy Φ less than the height of the barrier. The electric field dependency of Φ is self-consistently determined during the numerical simulations.

The carrier transport equations are solved in two steps. First, the thermal equilibrium values of the state variables are obtained from the discretized nonlinear Poisson equation using a globally convergent nonlinear iterative technique[7]. The carrier transport equations are then solved at a given bias value via the coupled equation Newton-Raphson method. For the initial bias value, the thermal equilibrium solution serves as the starting point for the method; for subsequent bias values, the previous solution serves as the starting point. This procedure is very important since good initial conditions are required for convergence of the Newton method, and initial conditions derived from analytical approximations are not available for complex heterostructures. In our implementation of the Newton method, an exact Jacobian operator is formulated from the continuous system of coupled nonlinear transport equations. The resulting linearized system of equations is then discretized using a trapezoidal rule finite-difference scheme over a nonuniform mesh and solved by LU decomposition. In order to enhance the convergence range of the method, the Newton correction vectors are damped.

The transport equations are subject to constraints at both the device domain boundaries and the heterointerfaces. In order to utilize existing numerical codes which

solve two-point boundary value problems, all of the constraints are mapped onto two boundary points by appropriately “folding/translating” portions of the device domain and rescaling the transport equations in these regions. For a single barrier HBV, this means “folding,” at the heterointerfaces, the barrier region back onto the first modulation region, and “translating” the second modulation region onto the first modulation region. Unfortunately, this technique triples the number of equations to be solved since solution of the transport equations is now required in three regions (one barrier and two modulation) of the device. In addition, careful mesh construction is required since the mesh of the first modulation region is imposed on the barrier and second modulation regions.

In order to develop a robust numerical device simulator which could be efficiently combined with a harmonic-balance nonlinear circuit simulator, careful consideration was given to developing a DC and large-signal time-dependent device simulator with excellent numerical convergence and accuracy properties. Potential problems and inefficiencies were minimized by, among others, the following considerations:

- 1) The electron quasi-Fermi potential is chosen as a state variable instead of the electron density. This provides improved scaling of the Jacobian matrix and, since the magnitudes of potentials do not change by more than an order of magnitude across the entire mesh, superior accuracy control is obtained. In addition, very small currents, down to zero current, can be accurately resolved when the electron particle current density equation is formulated using the electron quasi-Fermi potential.
- 2) A finely subdivided, nonuniform mesh is utilized for improved accuracy of the numerical results.
- 3) Poisson’s equation is reduced to two first-order differential equations such that an exact Jacobian matrix can be formulated.
- 4) In order to insure robust large-signal time-dependent simulations, the right-hand side of equation (1) is discretized using a fully implicit (backward Euler) finite difference discretization scheme. For DC simulations, the right-hand side of this equation reduces to zero, emphasizing the required constancy of the electron particle current density.

Overall, the two equations obtained from Poisson’s equation, along with equations (1) and (2), yield the state variable set $J_{n,p}$, ϕ_n , ψ , and D . After “folding/

translating” of the device domain, twelve carrier transport equations must be solved at a given bias value subject to the heterointerface constraints and ideal ohmic contact boundary constraints. In order to derive an entire I-V curve or time-domain current waveform, as well as to obtain information about the internal physics of the device as a function of bias, the DC or AC bias is incrementally changed from the zero-bias condition. At each bias value, Newton iterations continue until the maximum change in the electrostatic and electron quasi-Fermi potentials across the entire mesh is less than $10^{-5} kT/q$ at 300 K. A typical bias-point solution is obtained, with this level of convergence and over a mesh containing 500 grid points, in 3 to 5 Newton iterations. On an HP Apollo 9000 Series 735 workstation, this corresponds to an average CPU execution time of approximately two seconds.

Finally, static C-V characteristics are obtained from the state variables by calculating the change in charge with respect to the change in applied DC bias over the depletion side of the device for sufficiently small increments in the device bias. Likewise, the displacement current is obtained from the state variables by calculating the change in the electric displacement with respect to the simulation time step. Multiple barriers are modelled in an ideal fashion by assuming that the terminal voltage is equally divided among the barriers. Therefore, in the simulator, only one barrier is simulated with an terminal voltage equal to the total terminal voltage divided by the number of barriers. For asymmetric HBVs, which can suffer from self-biasing, the full multiple barrier structure would have to be simulated to self-consistently account for this phenomenon.

III. Harmonic-Balance Nonlinear Circuit Analysis Technique

The harmonic-balance nonlinear circuit analysis technique employed in this work is an extension of the multiple-reflection algorithm[8]. The time-domain current through the device is calculated by the numerical device simulator, for one period, as described in the previous section. The harmonic components of the current are extracted from the time-domain current waveform using a discrete fourier transform. A fixed-point iterative expression, derived from the robust multiple-reflection algorithm, is then used to update the total voltage applied directly across the active region of the device in terms of the circuit

embedding impedances, the harmonic components of the current, and the harmonic components of the voltage from the previous iteration. This iterative process continues until the harmonic components of the voltage converge to their steady-state values.

The novelty in the harmonic-balance algorithm utilized here is that, in deriving the fixed-point iterative voltage update expression, we use *a priori* knowledge, from Kirchhoff's voltage law, that the nonlinear device impedance will equal the negative of the linear circuit impedance for each of the undriven harmonics in the steady state. This eliminates the computationally intensive and possibly unstable Runge-Kutta numerical time-integration necessary in the multiple-reflection algorithm, and automatically calculates complex under-relaxation parameters for each harmonic component of the fixed-point iterative voltage update equation. A Steffenson numerical acceleration scheme, adopted from the secant methods of numerical analysis[9], is also utilized to greatly increase the computational speed and convergence properties of the harmonic-balance nonlinear circuit analysis. Unlike Newton-type techniques, the difficult and time-consuming numerical calculations needed to assemble Jacobian matrices and to solve large linear systems of equations are avoided, while a convergence rate nearly equal to that of Newton-type methods is maintained.

IV. Results and Discussion

A. DC Results

In order to verify the accuracy of the DC and AC numerical device simulators, and to investigate the relevant material parameters for an InGaAs/AlGaAs heterointerface, single barrier n GaAs/undoped GaAs/undoped $\text{Al}_{0.7}\text{Ga}_{0.3}\text{As}$ and n GaAs/n $\text{In}_{0.0-0.2}\text{Ga}_{1.0-0.8}\text{As}$ /undoped $\text{In}_{0.2}\text{Ga}_{0.8}\text{As}$ /undoped $\text{Al}_{0.7}\text{Ga}_{0.3}\text{As}$ HBV structures have been grown by the Naval Research Laboratory (NRL) using Molecular Beam Epitaxy (MBE). The GaAs/ $\text{Al}_{0.7}\text{Ga}_{0.3}\text{As}$ HBV structure has been processed into mesa-isolated whisker-contacted HBV devices using a process successfully employed to fabricate Alloy Ramp diodes and Gunn diodes. The process involves an ohmic contact lift-off process to form the device anodes, a mesa-isolation etch to electrically isolate the individual mesa devices, and

a polyimide passivation layer to protect and further isolate the individual mesa devices.

Four-wire measurements of the I-V characteristics of several devices from two different wafers are shown in Figure 2 along with the simulated I-V curve. Excellent correlation between the DC numerical device simulator and the experimental I-V results for the GaAs/Al_{0.7}Ga_{0.3}As HBVs has been obtained as shown by this figure. The simulated device consisted of a 200 Å undoped ($\approx 1 \times 10^{16} \text{ cm}^{-3}$) Al_{0.7}Ga_{0.3}As barrier surrounded by two 50 Å undoped ($\approx 5 \times 10^{15} \text{ cm}^{-3}$) GaAs spacer layers and two n-type GaAs modulation layers. The asymmetry in the I-V characteristics was attributed to an asymmetry in the doping and thicknesses of the modulation layers, and was verified by Secondary Ion Mass Spectroscopy (SIMS). One modulation layer was determined to have a length of approximately 2000 Å and a doping of approximately $9.5 \times 10^{16} \text{ cm}^{-3}$, while the other modulation layer was approximately 1750 Å in length and was doped approximately $6.0 \times 10^{16} \text{ cm}^{-3}$. The alloy composition of the 200 Å undoped AlGaAs barrier was also verified by SIMS to be 70% aluminum.

Excellent correlation between the DC numerical device simulator and experimental DC I-V and static C-V data from the literature has also been obtained for single barrier GaAs/Al_{0.7}Ga_{0.3}As, GaAs/Al_{0.4}Ga_{0.6}As, GaAs/In_{0.2}Ga_{0.8}As/Al_{0.4}Ga_{0.6}As, and In_{0.53}Ga_{0.47}As/In_{0.52}Al_{0.48}As on InP HBVs.

B. Large-Signal Time-Dependent Results

Before examining results from the unified numerical device/harmonic-balance nonlinear circuit simulator, it is instructive to examine how two candidate HBVs respond to a pure sinusoidal large-signal voltage excitation, i.e. in the absence of harmonic voltages impressed by an external circuit. Figure 3 shows the time-domain current waveforms for two such simulated HBVs subject to a 100 GHz, 6.0 V sinusoidal excitation voltage. The HBVs are 8 μm diameter, four barrier structures with 200 Å undoped ($\approx 1 \times 10^{16} \text{ cm}^{-3}$) Al_{0.7}Ga_{0.3}As barriers. Each barrier is surrounded by 50 Å undoped ($\approx 5 \times 10^{15} \text{ cm}^{-3}$) spacer layers and 3500 Å doped ($6 \times 10^{16} \text{ cm}^{-3}$) modulation layers. The first structure had GaAs spacer and modulation layers, while the second structure had 3000 Å GaAs/500 Å

$\text{In}_{0.0-0.2}\text{Ga}_{1.0-0.8}\text{As}$ modulation layers and $\text{In}_{0.2}\text{Ga}_{0.8}\text{As}$ spacer layers.

As Figure 3 shows, the total current from the $\text{GaAs}/\text{In}_{0.0-0.2}\text{Ga}_{1.0-0.8}\text{As}/\text{Al}_{0.7}\text{Ga}_{0.3}\text{As}$ HBV is larger than that from the $\text{GaAs}/\text{Al}_{0.7}\text{Ga}_{0.3}\text{As}$ for the same applied voltage. Fourier analysis of the applied voltage waveform and the resulting current waveforms has been utilized to obtain information about the fundamental and harmonic frequency components of the voltage and current, as well as about the complex device impedance at the fundamental frequency. The impedance of the $8\text{ }\mu\text{m}$ $\text{GaAs}/\text{Al}_{0.7}\text{Ga}_{0.3}\text{As}$ device is $Z(f_0=100\text{ GHz}) = 14.503 - j115.61\text{ }\Omega$; for the $8\text{ }\mu\text{m}$ $\text{GaAs}/\text{In}_{0.0-0.2}\text{Ga}_{1.0-0.8}\text{As}/\text{Al}_{0.7}\text{Ga}_{0.3}\text{As}$ device, the impedance is $Z(f_0=100\text{ GHz}) = 15.492 - j94.596\text{ }\Omega$. In terms of the harmonic content of the output current waveforms, the even harmonic components are negligible when compared to the components of the fundamental and third harmonic frequencies, as expected. This is especially clear from Figure 3 where the current waveforms are triangular in shape and, thus, primarily composed of odd harmonics. For the $8\text{ }\mu\text{m}$ $\text{GaAs}/\text{Al}_{0.7}\text{Ga}_{0.3}\text{As}$ device, the ratio of the current magnitude at $3f_0$ to that at f_0 is approximately 0.264; for the $8\text{ }\mu\text{m}$ $\text{GaAs}/\text{In}_{0.0-0.2}\text{Ga}_{1.0-0.8}\text{As}/\text{Al}_{0.7}\text{Ga}_{0.3}\text{As}$ device, this ratio is approximately 0.337. More importantly, the current magnitude at $3f_0$ is 6.788 mA for the $\text{GaAs}/\text{Al}_{0.7}\text{Ga}_{0.3}\text{As}$ device and increases to 10.54 mA for the $\text{GaAs}/\text{In}_{0.0-0.2}\text{Ga}_{1.0-0.8}\text{As}/\text{Al}_{0.7}\text{Ga}_{0.3}\text{As}$ device, an increase of approximately 55 % in the third harmonic component of the current waveform. As will be seen conclusively in the next section, these results indicate that the $\text{GaAs}/\text{In}_{0.0-0.2}\text{Ga}_{1.0-0.8}\text{As}/\text{Al}_{0.7}\text{Ga}_{0.3}\text{As}$ HBV should provide improved tripler performance when compared to the performance of the $\text{GaAs}/\text{Al}_{0.7}\text{Ga}_{0.3}\text{As}$ HBV. This is primarily because the $\text{GaAs}/\text{In}_{0.0-0.2}\text{Ga}_{1.0-0.8}\text{As}/\text{Al}_{0.7}\text{Ga}_{0.3}\text{As}$ HBV structure can be pumped harder before avalanche breakdown limits its performance. In addition, the slightly higher circuit embedding impedances required for near optimum performance indicate that broadband device/circuit matching should be possible.

C. Harmonic-Balance Results

The unified numerical device/harmonic-balance nonlinear circuit simulator was first compared to harmonic-balance results obtained using our harmonic-balance algorithm

in conjunction with a simple analytical device model. The device model used curve fits to the device I-V and static C-V characteristics as obtained from the numerical device simulator under DC excitation. The time-dependent device current $i(t)$ is, thus,

$$i(t) = I_{DC}(v(t)) + C_{Static}(v(t)) \frac{dv}{dt} \quad (11)$$

where the first term is the device particle current and the second term is the device displacement current.

Figure 5 shows a comparison of the current and voltage waveforms obtained from the full unified numerical device/harmonic-balance nonlinear circuit simulator with those obtained from the analytical device/harmonic-balance nonlinear circuit simulator for an 8 μm diameter, single 200 Å barrier GaAs/Al_{0.7}Ga_{0.3}As HBV subject to a 100 GHz, 30 mW pump signal. The parameters for this device are the same as those of the four barrier GaAs/Al_{0.7}Ga_{0.3}As HBV previously outlined. For the harmonic-balance simulations, a device parasitic series resistance of 4.0 Ω was assumed, and fundamental and third harmonic circuit embedding impedances of $Z(f_1=100 \text{ GHz}) = 12.0 + j56.0 \Omega$ and $Z(f_3=300 \text{ GHz}) = 12.0 + j20.0 \Omega$, respectively, were used. All other embedding impedances were set to short circuit values of $0.001 + j0.000 \Omega$. Although the resulting current and voltage waveforms have the same general shape, the sharpness and magnitudes of the waveforms differ substantially. More importantly, the predicted absorbed power, third harmonic output power, and multiplying efficiency are substantially overestimated by the analytical device/harmonic-balance nonlinear circuit simulator. In particular, the analytical device/harmonic-balance nonlinear circuit simulator predicted an absorbed power of 7.87 mW and a third harmonic output power of 0.95 mW (multiplying efficiency of 12.07 %) as compared to an absorbed power of 10.40 mW and a third harmonic output power of 0.43 mW (multiplying efficiency of 4.17 %) for the full unified numerical device/harmonic-balance nonlinear circuit simulator.

From these results, it is clear that the time-dependent behavior of electrons in HBVs is not adequately accounted for using a simple analytical device model in conjunction with the harmonic-balance nonlinear circuit analysis. As a consequence, the results obtained

with such an analytical device model are significantly different from those obtained with a full numerical device model utilizing hydrodynamic transport equations where the dynamic high frequency nonstationary behavior of carriers is more accurately modeled.

Finally, it is instructive to compare the harmonic-balance results from the full numerical device/harmonic-balance nonlinear circuit simulator with the results obtained for HBVs subject only to large-signal time-dependent *sinusoidal* (fundamental) excitation. The HBVs analyzed are the 8 μm diameter, four barrier GaAs/Al_{0.7}Ga_{0.3}As and GaAs/In_{0.0-0.2}Ga_{1.0-0.8}As/Al_{0.7}Ga_{0.3}As HBV structures outlined in the previous section. Figure 6 shows the steady-state harmonic-balance current and voltage waveforms for the GaAs/Al_{0.7}Ga_{0.3}As HBV structure with a parasitic series resistance of 8.0 Ω and circuit embedding impedances of $Z(f_1=100 \text{ GHz}) = 23.0 + j115.6 \Omega$ and $Z(f_3=300 \text{ GHz}) = 23.0 + j75.0 \Omega$. Likewise, Figure 7 shows the steady-state harmonic-balance current and voltage waveforms for the GaAs/In_{0.0-0.2}Ga_{1.0-0.8}As/Al_{0.7}Ga_{0.3}As HBV structure with a parasitic series resistance of 8.0 Ω and circuit embedding impedances of $Z(f_1=100 \text{ GHz}) = 30.0 + j90.0 \Omega$ and $Z(f_3=300 \text{ GHz}) = 30.0 + j38.0 \Omega$. These circuit embedding impedances are believed to be fairly optimum values, although a complete optimization has not yet been completed.

For both HBV structures, the predicted absorbed power is $\approx 34.4 \text{ mW}$ for a pump power of 35.0 mW, and the predicted third harmonic output power is $\approx 2.4 \text{ mW}$ for a multiplying efficiency of $\approx 7.0 \%$. These values should improve with lower parasitic device series resistances. An important thing to note is that the real parts of the circuit embedding impedances are higher and, thus, easier to realize for the GaAs/In_{0.0-0.2}Ga_{1.0-0.8}As/Al_{0.7}Ga_{0.3}As HBV structure. This may be an important consideration in the design of broadband frequency multipliers using HBVs since good device/circuit matching is required over a broad frequency range. It is also important to note that the GaAs/Al_{0.7}Ga_{0.3}As HBV structure, under the given pumping conditions and with the fairly optimum circuit embedding impedances cited above, is being pumped at its maximum level when avalanche breakdown is considered. The GaAs/In_{0.0-0.2}Ga_{1.0-0.8}As/Al_{0.7}Ga_{0.3}As HBV structure, on the other hand, is being pumped at only about 69 % of its maximum

level under the given pumping conditions and with the fairly optimum circuit embedding impedances cited above. As a result, improved tripler performance is expected from a $\text{GaAs/In}_{0.0-0.2}\text{Ga}_{1.0-0.8}\text{As/Al}_{0.7}\text{Ga}_{0.3}\text{As}$ HBV when compared to the performance of the $\text{GaAs/Al}_{0.7}\text{Ga}_{0.3}\text{As}$ HBV.

V. Conclusions

In conclusion, an accurate and fast DC and large-signal time-dependent numerical device simulator for generic $\text{GaAs/InGaAs/AlGaAs}$ and InGaAs/InAlAs on InP HBVs has been developed based on a physical model which combines current transport through the heterostructure bulk with current across the abrupt heterointerfaces in a fully self-consistent manner. The simulator can model any combination of doping and InGaAs , AlGaAs , or InAlAs alloy composition profiles, and provides an excellent tool for examining the DC and large-signal time-dependent characteristics of candidate HBV frequency multipliers. A novel and efficient harmonic-balance nonlinear circuit analysis technique has been developed which allows hydrodynamic-type device simulators to be used in place of typical analytical device or equivalent circuit models. The numerical device simulator has been successfully combined with the harmonic-balance nonlinear circuit simulator to provide a unified computer-aided design environment for the entire HBV multiplier circuit. HBV multiplier circuits can, therefore, be co-designed from both a device and a circuit point of view by specifying the device geometry, doping profile, and alloy composition profile, as well as the parasitic impedances of the device and the embedding impedances of the circuit.

Excellent correlation between the numerical device simulator and experimental DC I-V and static C-V data has been obtained for GaAs/AlGaAs , $\text{GaAs/InGaAs/AlGaAs}$, and InGaAs/InAlAs on InP HBVs. Large-signal time-dependent simulations of $\text{GaAs/Al}_{0.7}\text{Ga}_{0.3}\text{As}$ and $\text{GaAs/In}_{0.0-0.2}\text{Ga}_{1.0-0.8}\text{As/Al}_{0.7}\text{Ga}_{0.3}\text{As}$ HBVs under pure sinusoidal voltage excitation indicate that a significant improvement in the magnitude of the output current waveform can be obtained with the $\text{GaAs/In}_{0.0-0.2}\text{Ga}_{1.0-0.8}\text{As/Al}_{0.7}\text{Ga}_{0.3}\text{As}$ HBV structure. More importantly, harmonic-balance nonlinear circuit simulations of these two

HBV structures indicate that third harmonic output power levels of several milliwatts and multiplying efficiencies of at least 7.0 % are obtainable with realizable fundamental and third harmonic circuit embedding impedances. The harmonic-balance simulations also show that the $\text{GaAs/In}_{0.0-0.2}\text{Ga}_{1.0-0.8}\text{As/Al}_{0.7}\text{Ga}_{0.3}\text{As}$ HBV structure can be pumped significantly harder than the $\text{GaAs/Al}_{0.7}\text{Ga}_{0.3}\text{As}$ HBV. Overall, the use of graded InGaAs/GaAs modulation layers should yield improved tripler performance when compared to a typical GaAs/AlGaAs HBV.

Acknowledgments

J. R. Jones is supported by a United States Air Force Laboratory Graduate Fellowship under the sponsorship of the Solid-State Directorate, Wright Laboratory, WPAFB, OH. This work is also partially supported by the NSF Grant #ECS-8720850. The authors are grateful to Scott Katzer of the Naval Research Laboratory for growing the HBV MBE structures. The authors would also like to thank M. F. Zybura and T. W. Crowe of the University of Virginia, and N. R. Erickson of the University of Massachusetts for numerous technical discussions relevant to this work. SIMS analysis was performed by Charles Evans & Associates, Redwood City, California.

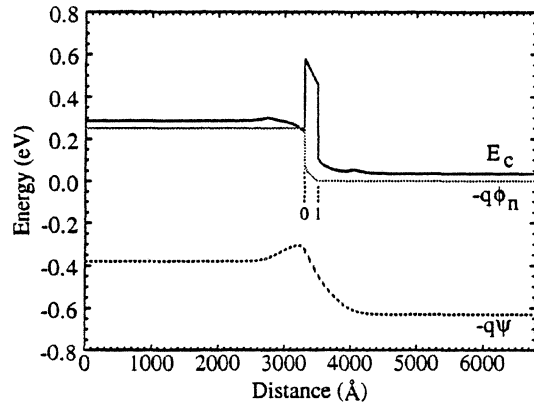


Figure 1. Band structure of n GaAs/ n $\text{In}_{0.0-0.2}\text{GaAs}/n$ $\text{In}_{0.2}\text{GaAs}/n$ $\text{Al}_{0.7}\text{GaAs}$ HBV biased at 0.25 V.

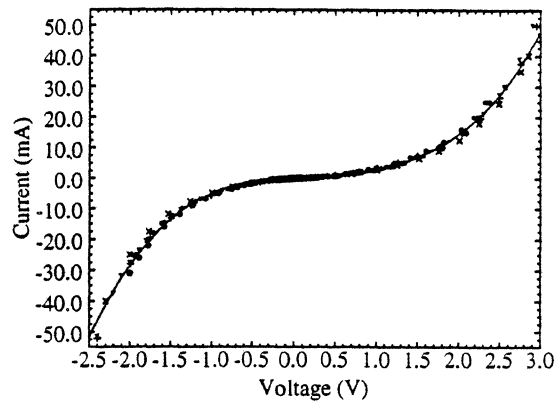


Figure 2. Experimental (symbols) and theoretical (solid line) I-V characteristics for 8 μm diameter mesa-isolated whisker-contacted n GaAs/ n GaAs/ n $\text{Al}_{0.7}\text{GaAs}$ HBVs.

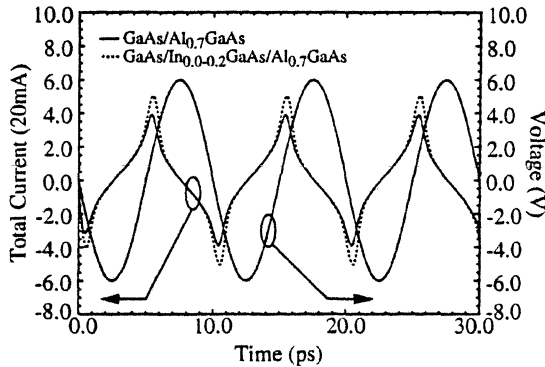


Figure 3. Current waveforms for 8 μm diameter, four 200 \AA barrier $6 \times 10^{16} \text{ cm}^{-3}$ GaAs/ $\text{Al}_{0.7}\text{GaAs}$ and $6 \times 10^{16} \text{ cm}^{-3}$ GaAs/ $\text{In}_{0.0-0.2}\text{GaAs}/\text{Al}_{0.7}\text{GaAs}$ HBVs subject to 100 GHz, 6.0 V sinusoidal excitation.

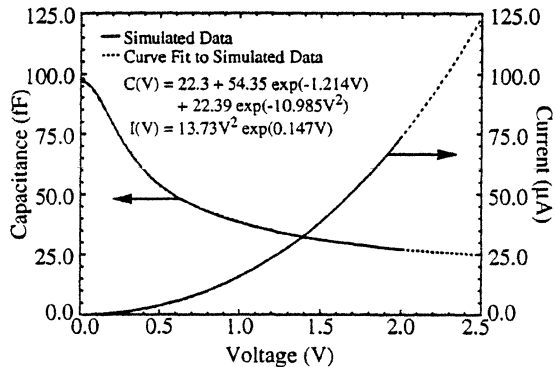


Figure 4. Simulated and curve-fit $I(V)$ and $C(V)$ characteristics for 8 μm diameter single 200 \AA barrier $6 \times 10^{16} \text{ cm}^{-3}$ GaAs/ $\text{Al}_{0.7}\text{GaAs}$ HBVs.

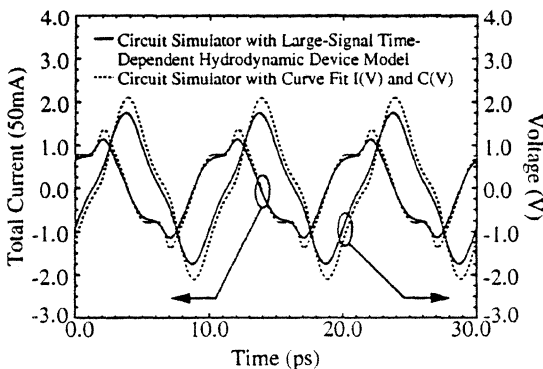


Figure 5. Steady-state harmonic-balance current and voltage waveforms for 8 μm diameter, single 200 \AA barrier $6 \times 10^{16} \text{ cm}^{-3}$ GaAs/ $\text{Al}_{0.7}\text{GaAs}$ HBVs subject to 100 GHz, 30 mW excitation.

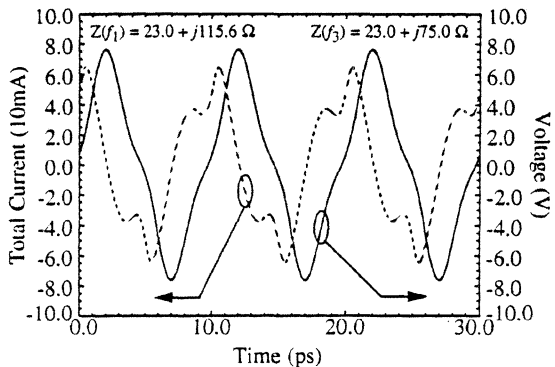


Figure 6. Steady-state harmonic-balance current and voltage waveforms for 8 μm diameter, four 200 \AA barrier $6 \times 10^{16} \text{ cm}^{-3}$ GaAs/ $\text{Al}_{0.7}\text{GaAs}$ HBVs subject to 100 GHz, 30 mW excitation.

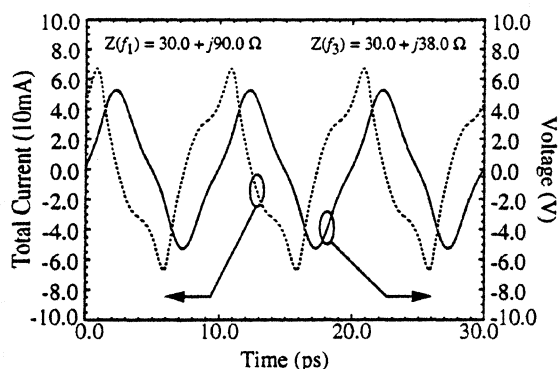


Figure 7. Steady-state harmonic-balance current and voltage waveforms for $8\text{ }\mu\text{m}$ diameter, four $200\text{ }\text{\AA}$ barrier $6 \times 10^{16}\text{ cm}^{-3}$ GaAs/ $\text{In}_{0.0-0.2}\text{GaAs}/\text{Al}_{0.7}\text{GaAs}$ HBVs subject to 100 GHz, 30 mW excitation.

References

1. E. Kollberg and A. Rydberg, "Quantum-Barrier-Varactor Diodes for High-Efficiency Millimetre-Wave Multipliers," *Electron. Lett.*, Vol. 25, No. 25, Dec. 1989, pp. 1696-1698. Originally called the Quantum Barrier Varactor (QBV), we prefer to call the device the Heterostructure Barrier Varactor (HBV) to emphasize the importance of the heterostructure alloy composition and doping profiles in the design and operation of the device.
2. M. S. Lundstrom and R. J. Schuelke, "Numerical Analysis of Heterostructure Semiconductor Devices," *IEEE Trans. Electron Dev.*, Vol. ED-30, No. 9, Sept. 1983, pp. 1151-1159.
3. K. Horio and H. Yanai, "Numerical Modeling of Heterojunctions Including the Thermionic Emission Mechanism at the Heterojunction Interface," *IEEE Trans. Electron Dev.*, Vol. 37, No. 4, Apr. 1990, pp. 1093-1098.
4. G. B. Tait and C. R. Westgate, "Electron Transport in Rectifying Semiconductor Alloy Ramp Heterostructures," *IEEE Trans. Electron Dev.*, Vol. ED-38, No. 6, June 1991, pp. 1262-1270.
5. J. Adams and T. W. Tang, "A Revised Boundary Condition for the Numerical Analysis of Schottky Barrier Diodes," *IEEE Electron Dev. Lett.*, Vol. ED-7, No. 9, Sept. 1986, pp. 525-527.
6. E. H. Rhoderick and R. H. Williams, *Metal-Semiconductor Contacts*, 2nd Edition, Oxford, England: Clarendon, 1988, pp. 109-111.
7. G. B. Tait, "Heterostructure Semiconductor Device Analysis: A Globally Convergent Solution Method for the Nonlinear Poisson Equation," *Solid-State Electron.*, Vol. 32, No. 5, May 1989, pp. 369-376.
8. P. H. Siegel, A. R. Kerr, and W. Hwang, "Topics in the Optimization of Millimeter-wave Mixers," *NASA Tech. Papers*, No. 2287, Mar. 1984.
9. J. Ortega and W. Rheinboldt, *Iterative Solution of Nonlinear Equations in Several Variables*, New York, New York: Academic Press, 1970.

Planar Varactor and Mixer Diodes Fabricated Using InP-Based Materials

P. Marsh, D. Pavlidis, and K. Hong

Center for Space THz Technology, Department of Electrical Engineering and Computer Science,
The University of Michigan, Ann Arbor, MI 48109

Abstract

This paper reports on a planar integrated technology which, unlike previous approaches, utilizes InP-based materials and airbridge technology to reduce parasitics by avoiding the use of a bridge-supporting dielectric. Vertical-heterojunction varactors (VHV) and mixers were grown by the in-house Metalorganic-Chemical Vapor Deposition (MOCVD) system on S.I. InP substrates. A novel process is presented which allows fabrication of planar diodes with very short airbridges, a low risk of anode/ohmic undercutting, and without need for replanarization. Methods have been investigated here for replacing the InP substrates with glass and quartz.

Systematic studies on VHV's revealed the effects of varying the barrier thickness (d_1), epilayer thickness (d_2) and barrier indium concentration (x). Control of C_{min} , C_{max}/C_{min} , reverse saturation current density (J_s), forward and reverse leakage, and Schottky barrier height (ϕ_{be}) was demonstrated via choice of device layer structure and alloy composition. The technology allowed demonstration of varactors with leakage currents which could be substantially reduced by design and material choice. Microwave characterization permitted the study of cutoff frequencies (f_c) as functions of anode diameter for several values of d_1 , d_2 , and x . One μm VHV's showed f_c 's in the THz range. First results on the $1\ \mu\text{m}$ InGaAs/InP mixers showed much lower forward turn-on voltages than for similarly-sized GaAs diodes. This suggests the possibility of diode mixing using smaller local oscillator power levels than GaAs diodes.

II. Introduction

Traditionally, whisker anode contacting technology has been the de-facto standard for submillimeter mixers and varactor multipliers. While whisker contacting produces low parasitics, it is suitable only for discrete devices, has limited reliability, and consequently is difficult to space qualify. To address these problems, GaAs planar diodes have been proposed and demonstrated [1]. In many GaAs-based planar diode technologies [1], [2], anode openings are etched through a film of SiO_2 which also supports the evaporated airbridges. Usually, isolation is achieved by laterally undercutting the n+ GaAs under the airbridge. In short-airbridge designs, the isolation etch runs the risk of undercutting the anode. In [2], a solution is proposed using a trench isolation technique in which the trench is anisotropically etched before the airbridge is fabricated. However the trench in [2] also requires a planarizing step.

Planar varactor and mixer diodes have traditionally relied on GaAs and AlGaAs/GaAs material systems to achieve high performance at submillimeter and THz frequencies. In recent years,

improvements in growth technology have made it feasible to utilize the performance advantages offered by the InP-based material systems. The high mobility and conductivity of InP-based materials (InGaAs) enables the reduction of access resistance (R_s). The low barrier heights (ϕ_{be}) of mixers using InGaAs and InP Schottky junctions are especially useful in reducing LO power requirements. The InAlAs/InGaAs heterojunction of InP-based varactors achieves an electron barrier of 0.5eV vs. 0.26-0.3eV for AlGaAs/GaAs, resulting in potentially reduced leakage relative to GaAs/AlGaAs varactors. A first demonstration of the InAlAs/InGaAs varactor principle was recently reported by the authors [3].

To gain full advantage of the InP-based system for planar diodes, the authors have developed a novel isolation technique that avoids the use of SiO_2 and the BHF SiO_2 etch, thus avoiding etching damage to the InAlAs barrier layers used in InP-based varactors. By avoiding use of the SiO_2 under the bridge this novel planar diode process also reduces parasitic capacitance by approximately 1fF, which is significant compared to the 3-6fF of $1\mu\text{m}$ diodes. Furthermore, this process avoids the need of undercutting the airbridge while not requiring a replanarization step.

Section III. of this paper covers layer structures of the demonstrated InP-based varactor and mixer diodes. A novel planar diode fabrication technique is discussed in section IV. Several advantages, such as reduction of parasitic capacitance and ease in dicing accrue from the replacement of the InP substrate. Therefore section V illustrates the replacement of the diodes' InP substrate with glass. Finally, sections VI and VII present measured dc and microwave performance of the planar varactors and mixers.

III. Varactor and Mixer Layer Structures

Figure 1. illustrates the layer structures for the varactor and mixer diodes. All structures covered here were grown in-house via Metalorganic-Chemical Vapor Deposition (MOCVD) on S.I. InP substrates. The $1\mu\text{m}$ thick n+ InGaAs layer serves to provide a low sheet resistance and good ohmic contacts.

The heterojunction varactors here use an undoped InGaAs active layer (thickness $d_2 = 400\text{\AA}$ and 800\AA) to support a variable-thickness depletion region. In all cases, the InGaAs is lattice-matched to the InP substrate. The $\text{In}_x\text{Al}_{1-x}\text{As}$ barrier layer thickness (d_1) is 100\AA or 200\AA . Decreasing x is expected to increase the electron barrier height, and decrease varactor leakage. To study the impact of x , some varactors have been fabricated with $x = 0.4$ (strained) and $x = 0.52$ (lattice-matched). Optimization of the InAlAs significantly affects performance and required a special study as reported in [4] and [5].

The mixer structure uses an 800\AA i-InP active layer. The InP/InGaAs heterojunction region is

highly n-doped in an attempt to render it transparent to electron flow so that the diode performs as an InP Schottky while taking advantage of the n+ InGaAs' low sheet and ohmic resistances.

IV. Topology and Fabrication

Diode topologies such as single-ended, wafer-probeable, antiparallel pair, back-back pair, and strip-anode diodes have been included on the same mask set. Pad sizes vary from $40 \times 70 \mu\text{m}$ to $80 \times 150 \mu\text{m}$. Wafer-probeable diodes have a pad configuration consisting of $50 \mu\text{m}$ wide ground, signal, and ground (GSG) pads having a $100 \mu\text{m}$ pitch compatible with Cascade® on-wafer microwave probes. These devices allow extraction of microwave characteristics. Antiparallel diode pairs have been designed for application in subharmonic mixers, where the LO frequency is approximately $1/2$ that of the RF. These devices consist of two diodes in parallel, with the anode of one connected to the cathode of the second. Back-back diodes provide a symmetric C-V curve useful for varactor tripling. Strip-anode diodes are used to experiment with R_s reduction via an elongated anode. Typical anode diameters vary from $1 \mu\text{m}$ to $5 \mu\text{m}$ diameter. A few large diodes ($48 \mu\text{m}$ and $100 \mu\text{m}$) allow low-frequency C-V characterization. The same mask set is used for both varactors and mixers. This mask set is also includes alignment marks that facilitate the use of

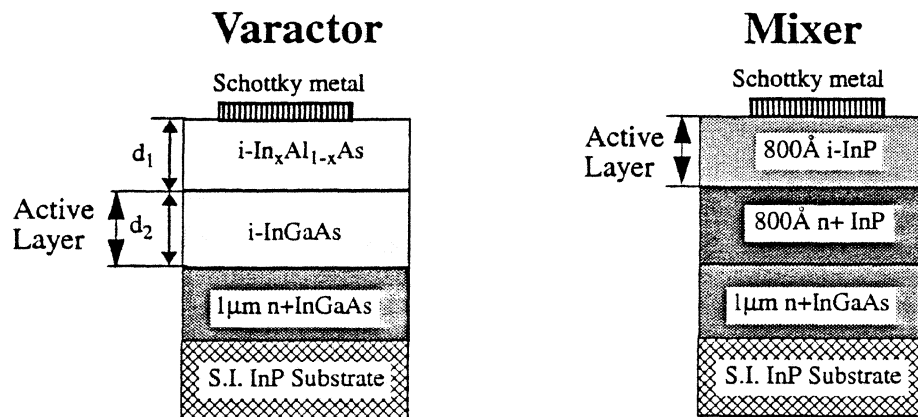


Figure 1. Layer structure of varactor and mixer diodes. The n+ InGaAs layer provides low sheet and ohmic contact resistance, while the i-InAlAs barrier layer provides an electron block for the varactors. In all cases, InGaAs is lattice-matched to InP, while the InAlAs composition is varied to explore the effects of indium content on the varactor leakage and saturation current. The mixer structure addresses the control of ϕ_{bc} via material choice.

in-house E-beam lithography for submicron diameter anode definition. Seven mask levels are used in the following order, namely: 1. Preposition metal, 2. Mesa etch, 3. Ohmic metal, 4. Interconnect metal, 5. Pillar, 6. Trench isolation etch, and 7. Airbridge. In some cases, mask level 2. is optionally eliminated and the mesa etch step (etch to n+ InGaAs) is replaced by etching of

the ohmic region only.

Figure 2. illustrates the main features of the planar diode process described in this paper. First, the preposition level is deposited. These metal patterns provide the diode alphanumeric labels and an E-beam alignment grid. Next, a mesa etch exposes the n+ InGaAs. Optionally, the mesa pattern may be eliminated. In this case, an ohmic etch exposes the n+ InGaAs beneath the ohmic contacts exclusively. Ohmic contacts of Ge/Au/Ni/Ti/Au are defined and evaporated onto the n+ InGaAs ohmic regions, then annealed via rapid thermal anneal (RTA). Interconnect pads are then defined and evaporated. After this, anodes and airbridge pad attachments are defined via the pillar mask. A conformal hotplate bake is performed, on the pillar photoresist, to ensure good coverage of the evaporated pillar metal. Next, the pillar photoresist is exposed for a second time using the isolation mask, which exposes the region beneath the future airbridge. Pillar metal is then evaporated and followed by airbridge photoresist spun over the pillar metal. The airbridge regions are then opened in the airbridge photoresist. A corner of the sample is also flood exposed and developed to insure a good electrical contact to the pillar metal for gold plating of the airbridges. The top pillar Ti is then removed and the airbridges are Au plated on to a thickness of approximately 3 μ m. Next, the airbridge photoresist is removed via flood exposure and development. Pillar metal is then etched away, exposing the pillar photoresist. Subsequently, the pillar photoresist is developed for a second time to reveal the isolation patterns. Finally, an isolation etch removes all n+ InGaAs between the diode pads to achieve electrical isolation. Unlike most conventional planar diode processes this novel planar diode process requires no lateral undercutting of the airbridge since the photoresist under the airbridge has been developed away. The probability of anode undercut is further reduced via utilization of device orientation in conjunction with the crystallographic nature of the isolation etch. Diode batches produced with the above process have demonstrated yields greater than 85-

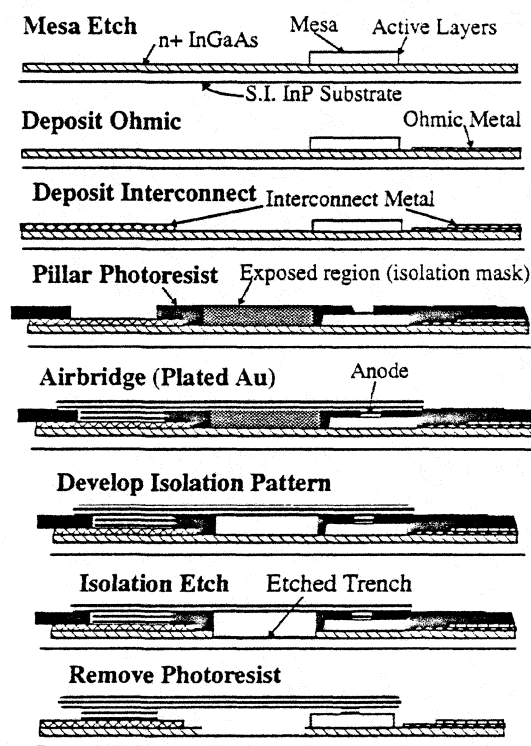


Figure 2. Side view of planar process for InP-based diodes. Active layers had thicknesses on the order of 1000Å. The n+ layer was near 1 μ m thick. Airbridges are 10-60 μ m long, 2-4 μ m wide, and 2-4 μ m thick. Note that all n+ InGaAs to be etched is uncovered before the isolation etch.

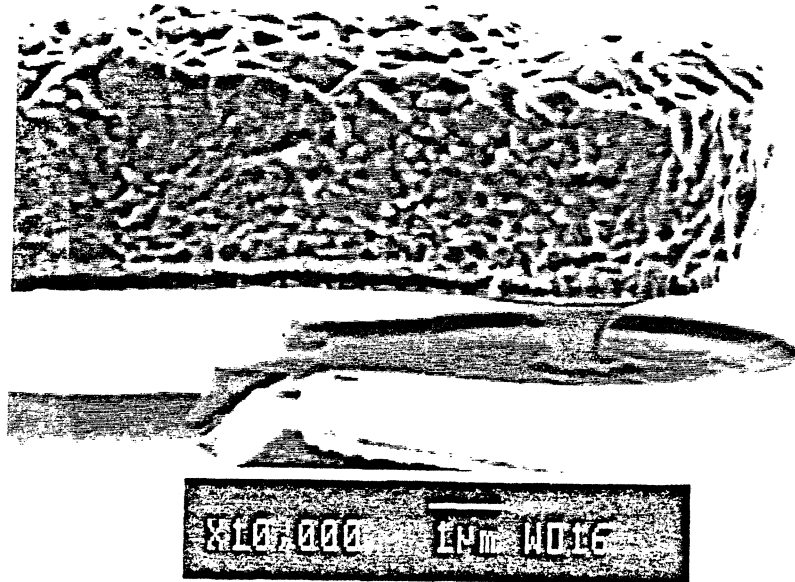


Figure 3. Side-view SEM of diode anode region. Here, the anode diameter is $0.6\mu\text{m}$. It appears that there is potential for controlling the anode diameter via exposure, development time, and conformal bake parameters.

90% for regions $\sim 2\text{mm}$ away from the edge (avoiding the photoresist edge bead). Figure 3 shows an InP-based varactor diode fabricated with the above described technology, except that its isolation etch was performed via undercutting the airbridge. Its anode diameter is $0.6\mu\text{m}$.

V. Epitaxial Lift-Off and Substrate Replacement

It has been found that the mechanical properties of InP give it a tendency towards unacceptable chipping during dicing via dicing saw. Also, the InP's $\epsilon_r \approx 13$ contributes significantly to pad-pad capacitance. A substrate replacement process using glass, has been studied, to address these problems. It has been found that the glass dices with much greater precision and very little chipping. Furthermore, the glass substrate may be easily removed via BHF or HF.

The wafer frontside is first protected with $4\text{-}6\mu\text{m}$ thick hardbaked photoresist. Next, $1\text{-}2\text{mm}$ thick black wax is cut to the wafer's size and oven-baked onto the wafer. The InP substrate is then removed via selective HCl etch under vigorous agitation. This leaves the InGaAs epitaxial layers and devices on the black wax. UV curable glue is then spun on a $50\mu\text{m}$ thick substrate of cover glass to yield a $2\text{-}5\mu\text{m}$ film. The glue side of the glass slide is then set on the diode side of the black wax and allowed to wet the diodes. A UV and adhesion cure follow next. Finally, the process is completed by removal of the black wax. Optionally, it should be possible to use quartz or another UV transparent substrate in place of the cover glass.

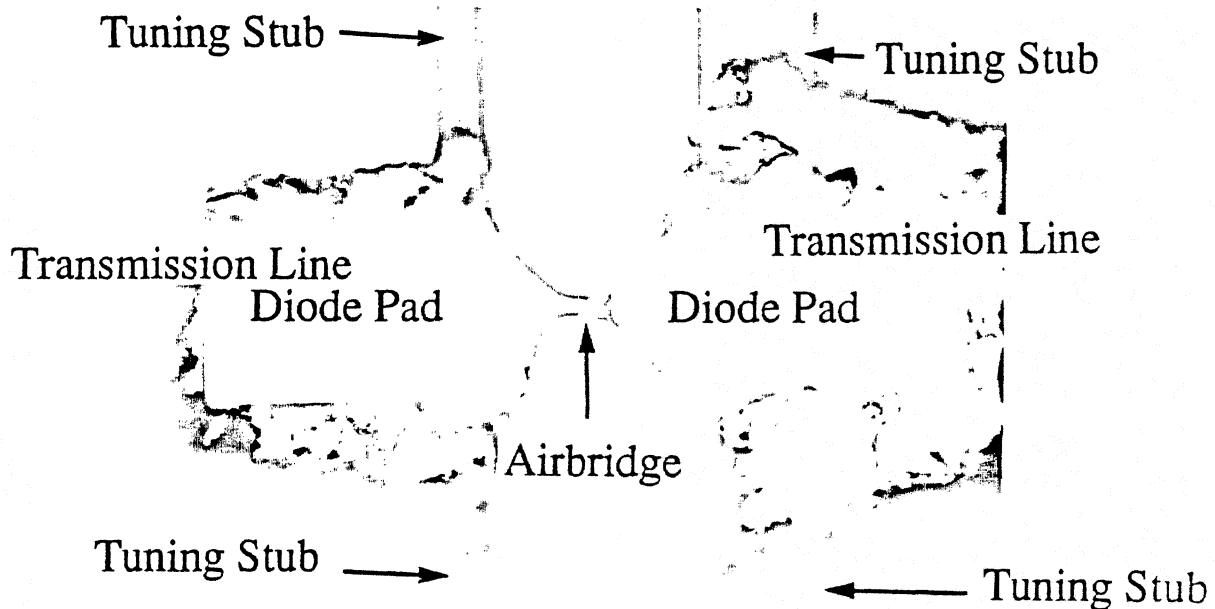


Figure 4. Photograph of varactor diode flip-chip mounted into a quartz multiplier circuit, using conductive epoxy. The active regions are protected with wax or photoresist during substrate removal.

After replacing the InP substrate, the devices may be chemically or mechanically diced and flip-chip mounted into their chip carriers for submillimeter testing. Figure 4 illustrates a diode that has been flip chip mounted using conductive epoxy. The diode's substrate has been etched away while the active layers were protected with photoresist.

VI. Varactor DC and Microwave Results

Leakage current and ohmic series resistance (R_s) both add losses to varactor multipliers which reduce their conversion efficiency. DC I-V characterization of varactors is useful mainly to evaluate their leakage current properties and low-frequency ohmic series resistance (R_s).

Varactor I-V curves were characterized at room temperature using an HP4145 parameter analyzer. Measured I-V curves (Figure 5) agree with theory in that for a given barrier thickness, increasing the barrier's Al content (decreasing x) results in reduced forward and reverse leakage currents. The varactor I-V curves also appear to imply the necessity of having the barrier thickness greater than 100\AA to obtain reasonable leakage performance. It should also be noted that the reverse current is more strongly affected by d_1 while the forward current is more strongly affected by x .

As expected, increasing the Al content (lower x) increases the barrier height. For example, decreasing x increased the effective ϕ_b from 0.48V to 0.54V and reduced J_s from 7.4mA/cm² to 250 μ A/cm².

TLM characterization of the 1 μ m n+ InGaAs layer indicated sheet resistances from 4.7 Ω/\square to 2.8 Ω/\square , ohmic contact resistances from 9.7 $\times 10^{-3}\Omega\cdot\text{mm}$ to 17 $\times 10^{-3}\Omega\cdot\text{mm}$ and specific ohmic contact resistances of 0.2 $\times 10^{-6}\Omega\cdot\text{cm}^2$ to 10 $\times 10^{-6}\Omega\cdot\text{cm}^2$.

C-V curves were characterized via two methods namely, low-frequency C-V meter at 4MHz and microwave S-parameters (1-25GHz) in conjunction with EESOF LIBRA[®] microwave simulation program to fit the S-parameters to the

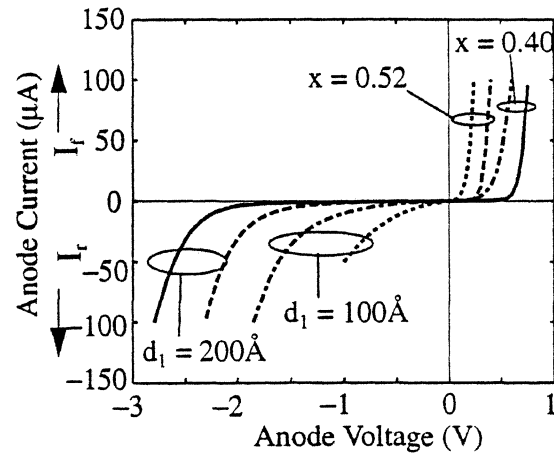


Figure 5. Impact of active layer thickness (d_1) and In mole fraction (x) on varactor I-V curves. Reverse current is highly sensitive to d_1 while forward current depends more on x . In all cases $d_2 = 800\text{\AA}$ and the anode was 2 μ m in diameter.

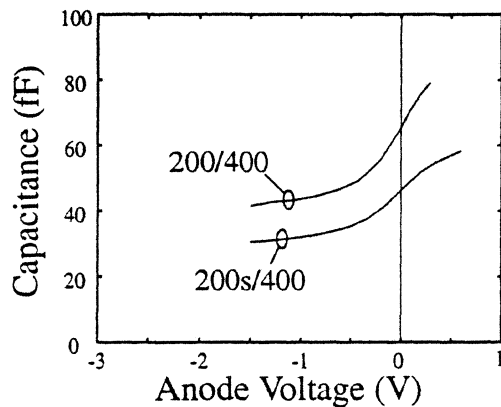


Figure 6a. C-V curves of VHV varactors having $d_1=200\text{\AA}$, $d_2=400\text{\AA}$, and 3 μ m anode diameters. The “s” designates higher Al content in the barrier.

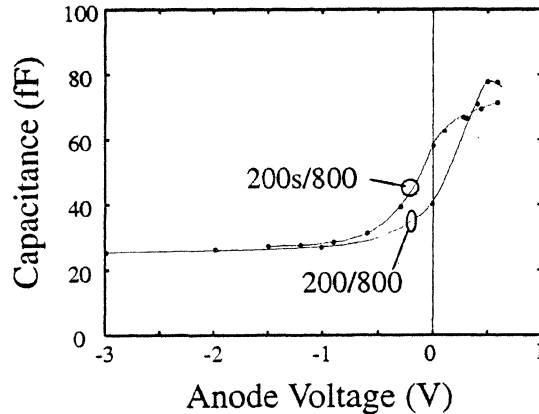


Figure 6b. C-V curves of VHV varactors having $d_1=200\text{\AA}$, $d_2=800\text{\AA}$, and 3 μ m anode diameters. The “s” designates higher Al content in the barrier.

diode model discussed above. The S-parameter derived C-V curves of Figures 6a and 6b illustrate the effects of d_1 , d_2 , and Al content on the S-parameter derived C-V characteristics. The useful operation range of these varactors, where leakage currents remained below about 10 μ A, extends from approximately -1.8V \rightarrow -1.4V to 0.26V \rightarrow 0.45V. The useful $C_{\text{max}}/C_{\text{min}}$ ratio of the 200/400, 200s/400, 200/800, and 200s/800 (d_1/d_2) (where s means $x = 0.4$ otherwise $x = 0.52$) varactors are 1.75, 1.8, 2.5, and 2.55 respectively. Increasing the Al content of the barrier layer increases the useful forward voltage swing and hence $C_{\text{max}}/C_{\text{min}}$ only slightly. Increasing d_2 from 400 \AA to 800 \AA

results in the expected trends of decreasing C_{\min} from 41.5fF to 26fF and increasing C_{\max}/C_{\min} from 1.7 to 2.5.

Microwave characterization permitted the study of cutoff frequencies (f_c) as functions of anode diameter for several values d_1 , d_2 , and x ,

where: $f_c \triangleq \frac{1}{2\pi R_s C_{ja}}$ and $C_{ja} \triangleq \frac{C_{\max} + C_{\min}}{2}$. Figure

7 shows f_c of the InGaAs/InAlAs varactors as functions of anode diameter and d_2 thickness. For large anode diameters, the perimeter/area ratio declines, making R_s decrease more slowly, whereas C_{ja} continues to increase proportional to

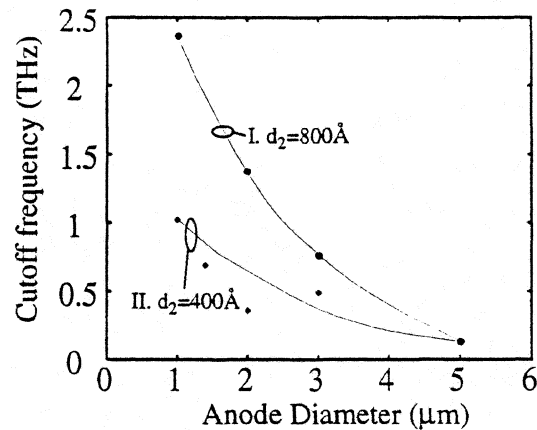


Figure 7. Cutoff frequency as a function of anode diameter and layer structure. In both layers, the In content, $x = 0.52$ and barrier layer thickness, $d_1 = 200\text{\AA}$.

anode area. Thus the decrease of $R_s \cdot C_{ja}$ with decreasing anode size, implies an inverse relation between f_c and anode size. The cutoff frequency increased with d_2 due to the inverse relation between d_2 and C_{ja} . One μm varactors, having $d_1 = 200\text{\AA}$ and $d_2 = 800\text{\AA}$ showed f_c 's up to 2.4THz.

Varactors were also characterized at 4MHz via a low-frequency C-V meter. When $1\mu\text{m}$, $3\mu\text{m}$, and $48\mu\text{m}$ varactors with $d_1, d_2 = 200\text{\AA}$ and 800\AA respectively, were tested, their diameters and pad capacitance could be adjusted to make their normalized C-V (C normalized to anode area) curves agree very well together. Thus, the low-frequency analysis showed that $1\mu\text{m}$ and $3\mu\text{m}$ varactors had nearly the same shape of C-V curve indicating that fringing capacitance effects were not significant.

VII. Mixer Diode Electrical Results

InP mixers were fabricated using the layer structure shown in figure 1 above. The InGaAs/InP heterointerface was submerged in n+ material so as to minimize its effective electron barrier. The Schottky barrier was 0.33eV, as expected for InP. Ideality factors were close to unity. Figure 8 shows that this diode design appears to be promising given its superior ideality factor and reverse

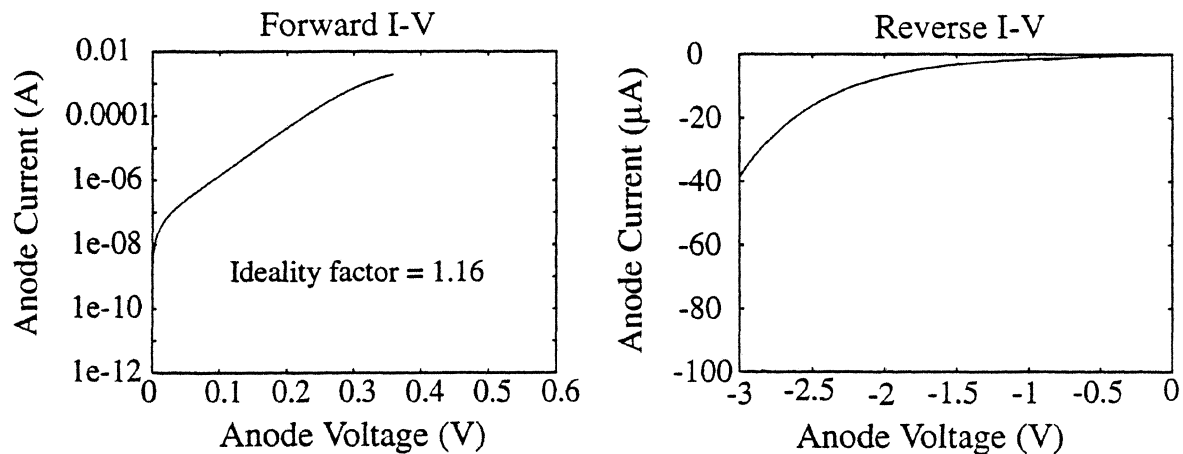


Figure 8. I-V characteristics of an InP/InGaAs mixer diode having an anode diameter = $1\mu\text{m}$ and the layer structure illustrated in figure 1 above. The ϕ_{be} is approximately 0.33eV. The diode exhibits a superior ideality factor lower reverse leakage relative to diodes having the heterointerface in the low-doped active region.

leakage relative to diode designs that have a heterointerface within the low-doped active region.

VIII. Conclusions

Varactor diodes having cutoff frequencies above 2THz based on InAlAs/InGaAs have been fabricated and characterized. Devices were fabricated using a planar diode process featuring plated airbridges. A novel isolation process has been applied that greatly increases the controllability of the isolation etch and reduces etch time and ohmic metal undercutting. This new isolation process should also nearly eliminate the isolation etch problems of diodes that have very short (10-20 μm) airbridges; as is the case for mixers integrated into log-periodic antennae.

An epitaxial lift-off process is under development that should allow the replacement of the InP substrate with glass or quartz substrates to ease dicing and reduce parasitic capacitance.

$C_{\text{max}}/C_{\text{min}}$ was seen to increase with active layer thickness (d_2). Leakage currents had been found to be reduced by increasing barrier thickness (d_1) and/or increasing the barrier's Al content. This study indicated that the cutoff frequency could be improved by moderate increases in active layer thickness and/or decreasing the anode diameter. Leakage currents can be reduced by using an Al mole fraction of 0.6 in the barrier layer.

InP/InGaAs mixer structures were also investigated. These results indicate that low ideality factors along with low reverse leakage can be obtained with InP diodes. Additionally, the $1\mu\text{m}$ InP mixer diode, investigated here, shows a forward current of 1mA at 0.316V which is much less bias than that required for a comparable GaAs diode. These mixer results indicate the possibility

of a substantial reduction of LO power requirements without the need for dc bias and are especially interesting relative to THz subharmonic mixers.

Acknowledgments:

The authors wish to thank A. Samelis for his help in diode characterization and Y. Kwon and G. NG for valuable discussion regarding development of the mask set and diode fabrication technology.

References:

- [1] W. L. Bishop, E. R. Meilburg, R. J. Mattauch, T. W. Crowe, and L. Poli, "A Micron-Thickness, Planar Schottky Diode Chip for Terahertz Applications with Theoretical Minimum Parasitic Capacitance", 1990 MTT-S Digest, Dallas, TX, May 8-10, 1990 PP-2.
- [2] W. L. Bishop, T. W. Crowe, and R. J. Mattauch, "Planar GaAs Schottky Diode Fabrication: Progress and Challenges", Fourth International Symposium on Space Terahertz Technology, UCLA, Los Angeles CA, March 30 - April 1 1993, P 415-429.
- [3] P. Marsh, G.I. Ng, D. Pavlidis, and K. Hong, "InAlAs/InGaAs Varactor Diodes with THz Cutoff Frequencies Fabricated by Planar Integrated Technology" Proceedings of the Sixth International Conference on Indium Phosphide and Related Materials, Santa Barbara, CA, March 28-31, 1994.
- [4] F. Ducroquet, G. Guillot, K. Hong, C. Hong, D. Pavlidis, and M. Gauneau, "Deep Level Characterization of LP-MOCVD Grown $\text{Al}_{0.48}\text{In}_{0.52}\text{As}$ " Proceedings of the MRS Fall Meeting, Boston, MA, November 1993.
- [5] K. Hong, D. Pavlidis, Y. Kwon, and C. H. Hong, "MOCVD Growth Parameter Study of InP-based Materials for High Performance HEMT's" Proceedings of the Sixth International Conference on Indium Phosphide and Related Materials, Santa Barbara, CA, March 28-31, 1994.

Frequency conversion to 368 GHz Using Resonant Tunneling Diodes

O. Tanguy*, D. Lippens*, J. Bruston**, J.C. Pernot**, G. Beaudin**
J. Nagle*** and B. Vinter***

Abstract: We report on measurements of quantum-well heterostructures diodes at millimeter and submillimeter wavelengths. The samples were fabricated from high quality strained layer epitaxies with design rules suitable for their characterisation at very high frequencies. The devices with barrier thicknesses ranging from 1.1nm to 1.7nm exhibit excellent dc characteristics with peak-to-valley current ratios up to 7:1 and peak current densities between 50 and 150 kA/cm². These structures have been mounted in a tripler cross-waveguide fixture and rf tested by measuring their impedance at millimeter-wavelengths and by investigating their rf properties in a frequency converter experiment. Harmonic multiplication to a frequency of 368 GHz with an output power of 0.8μW was achieved. These results are interpreted on the basis of non linear harmonic balance simulation codes which give some guidelines for optimizing the devices in terms of structures and operating conditions.

Introduction: Resonant tunneling diodes based on the resonant tunneling effect in double barrier heterostructures (DBH) are among the most promising solid state candidates for operating at very high frequencies due to the very short time response of the physical mechanisms involved. They exhibit strong negative differential conductance effects in their current-voltage characteristics so they can be used in non linear high speed applications such as oscillators^[1] and frequency harmonic multipliers^[2]. For these RTD-based analogue applications, one of the most important issue is the behaviour of the conductance not only as a function of voltage, defining by this means the resistive non linearity, but also as a function of frequency. This is particularly true in the context of the remarkable advancement in the crystal growth which makes now possible to grow ultra thin layers with atomically sharp interfaces, increasing by this means the frequency capability of devices. In this paper, we report on measurements carried out on such high performance diodes which have been successfully fabricated from strained-layer epitaxies. The frequency evaluation of samples has been carried out mainly in a frequency converter experiment starting from a 123 GHz input frequency and by tripling this fundamental oscillation for an output at 368GHz.

Design and fabrication: Figure 1 shows the new structure that we used for the design. For harmonic multiplier applications, it is imperative to optimize the current voltage characteristics to achieve high speed operation and simultaneously pronounced variations of the conductance in order to maximize the harmonic content. To achieve high frequency operation, we need to optimize the peak current density and the peak-to-valley current ratio which are the key parameters in the present application. Also, a decrease in the peak voltage can reduce the amount of power to pump the diode. To this aim, we used a double barrier in a triple-well configuration. In short, this layer is designed with local InGaAs potential perturbations forming buried wells on each side and within the DBH. By this means we take advantage of a lower effective mass with the associated benefit of a higher discontinuity at the heterointerfaces. Also, a decrease in the peak voltage can be expected because the quantum level of the DBH is lowered with respect to the emitter reference energy. The wells are filled up as a consequence of the charge transfer from the adjacent layers leading to the formation of dipoles as in any modulation doped structure. The first step in the design was thus to determine carefully the charges trapped in the wells and the escape times through the barriers. To deal with this issue, a self consistent numerical procedure was used with the potential profile

reported in Figure 1. The calculation of eigenstates and of their lifetimes permits one to deduce peak current densities and peak-to-valley current ratios[3].

Epilayers were fabricated by Molecular Beam Epitaxy starting from a GaAs semi insulating substrate. The growth sequence is given in Figure 2. The ultra thin barriers of AlAs with thicknesses between 1.1 nm and 1.7 nm allow us to achieve a relatively high tunneling transmission. The prewell and postwell are 5nm thick whereas the midwell is 4nm thick. We have intentionally limited the Indium content of InGaAs layers to 0.1 in order to avoid misfit dislocations. For each transition a 0.5nm thick GaAs spacer was systematically placed to recover good surface states. The triple well double barrier zone is then sandwiched between two 500nm thick n+ GaAs layers acting as electron reservoirs followed by 10nm thick cladding layers doped 10^{17} cm^{-3} . Before each series of tunneling wafers, a calibration was made to determine InGaAs and AlAs growth rates so that the layer thicknesses can be controlled accurately.

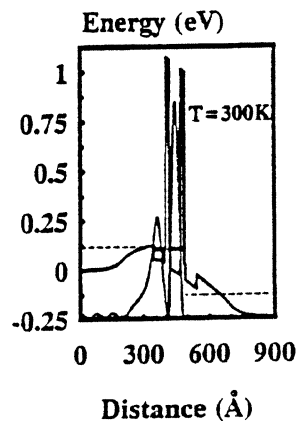


Fig. 1 Design of a Double Barrier Heterostructure in a triple well configuration

GaAs	$3 \cdot 10^{18} \text{ cm}^{-3}$	500 nm
GaAs	$1 \cdot 10^{17} \text{ cm}^{-3}$	10 nm
GaAs	Undoped (UD)	5 nm
In _{0.1} Ga _{0.9} As	UD	5 nm
GaAs	UD	0.5 nm
AlAs	UD	1.7 nm
GaAs	UD	0.5 nm
In _{0.1} Ga _{0.9} As	UD	4 nm
GaAs	UD	0.5 nm
AlAs	UD	1.7 nm
GaAs	UD	0.5 nm
In _{0.1} Ga _{0.9} As	UD	5 nm
GaAs	UD	5 nm
GaAs	$1 \cdot 10^{17} \text{ cm}^{-3}$	10 nm
GaAs	$3 \cdot 10^{18} \text{ cm}^{-3}$	500 nm
SI Substrate		

Fig. 2 Growth sequence

Devices were fabricated in a mesa-etched technology including patterning of $4\mu\text{m}$ -diameter dots on the epitaxial side of the wafer, deposition of AuGeNi metallization and alloying of these layers to make ohmic contacts. In order to avoid undercutting effects which are source of trouble in chemical etching, mesa isolation was performed with chlorine ion beam assisted etching (R.I.E.) using the patterned metal as a mask. Pillars with well-defined side-walls have thus been successfully fabricated. Figure 3 gives a scanning electron micrograph of a representative device. In view of rf testing some of the samples have also been thinned down to $100\mu\text{m}$ followed by a uniform deposition of material contact and alloying. Lastly, the wafer have been diced into chips of $100\mu\text{m}$ -side to be whisker-contacted in a rf test fixture.

An HP dc set-up was used for measuring the current voltage characteristics of the diodes and to calculate the small signal conductance of the samples from the derivative of the I-V curve at each bias point. Figure 4 gives an example of current voltage characteristics we obtained at room temperature. In the NDC region abrupt changes in G are apparent due to the well known shoulder-like I-V resulting from spurious low frequency self-oscillations. Also note the very good symmetry of the forward and reverse characteristics which reveals the quality of samples. For the three technological runs with barrier thicknesses of 1.1nm, 1.4nm and 1.7nm respectively we obtained current densities between 30 and 150kA/cm^2 and peak-to valley-current ratios up to 7:1. The peak voltage is 600mV in the best case and depends on J_p via the voltage drop across the series resistance.



Fig. 3 SEM view of diodes with mesa defined by RIE

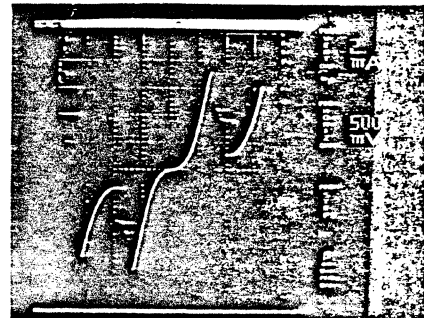


Fig. 4 Typical I-V at 300K

Frequency evaluation: For the rf probing, the thinned samples were inserted into a tripler mount which was designed for harmonic multiplication at sub-millimeter wavelengths. Isolation between the pump and the output frequency and matching at these frequencies are achieved by means of low pass and high pass filters and tuning elements. As seen previously, DBH's exhibit symmetric conductance variations $G(-V)=G(V)$. This property is also verified for the capacitance. This greatly simplifies the multiplier design by suppressing the idler at second harmonic. Figure 5 shows a cross section of the tripler mount we have fabricated. This is a cross-guide configuration based on the design of Archer for tripling to 366GHz. The input power is coupled to a microstrip low pass filter on a quartz substrate through a microstrip-waveguide transition. Special attention was paid to these passive elements by measuring the S parameters of low frequency scaled prototypes. For the high pass filter in the output branch we take benefit of the waveguide cutoff frequency ($F_c=300\text{GHz}$). The whisker also plays the role of antenna to couple the third harmonic power generated in the non-linear device to the output. Mobile contacting backshorts are used to match the diode to its embedding.

The effectiveness of the matching was verified by measuring a 2T2 varactor from the University of Virginia. Figure 6 shows the reflection coefficient plotted in a Smith chart, measured at the input and by tuning the position of the input backshort. These measurements were carried out at 109GHz with a HP 85109 Network analyzer with a very narrow span of about 350 MHz at a bias of 0.25V. It can be seen that a very good match can be obtained. Confidence in the fact that the input power is effectively coupled to the diode can also be found by biasing the device at the built-in voltage where self-biasing effects can be pointed out.

For the experimental set-up used in harmonic multiplication experiment the source is a carcinotron with an output power up to 200mW between 106 and 123 GHz. A reflectometer allows us to measure the return loss at the input. A corrugated horn radiates the output power which is then focused and filtered by means of quasi-optical lenses and dichroic filters. Power measurements were made using a Goly cell which is very sensitive but measures only relative values. This detector was calibrated at several high power points ($\sim 10\text{mW}$) with an Anritsu bolometer and a Thomas Keating calorimeter. The linear behavior of the Goly cell allows us to extrapolate this calibration to lower power levels and to achieve a sensibility of 100nW at 368GHz.

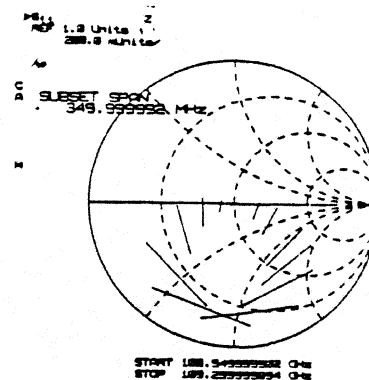


Fig. 6 Smith chart of S11 for a 2T2

Discussion: Further insight into the power balance can now be obtained by comparing this result with those obtained with conventional varactors despite the fact that DBH's make use of the singularities in the I-V curve whereas varactors work as non linear capacitive elements. The heterostructure has a cutoff frequency f_c of around 160GHz. An ideal varactor with a similar f_c would give an efficiency of $2 \cdot 10^{-4}$. The Schottky varactor 2T2 with a cut-off frequency of 2THz has a theoretical efficiency of 10%. Its best efficiency measured in our mount was 1%. If we apply the same ratio to the DBH diode we can expect that much higher efficiency can be obtained for samples with much higher current density and hence f_c . This increase in the conversion efficiency η as a function of J_p is exemplified in figure 8 which compares $\eta(f)$ calculated in the framework of harmonic balance simulation by using MDS codes. These results have been computed by means of a fitted form of the I-V characteristics of intraband tunneling structures such as those we fabricated. Four current density values were here considered between 50kA/cm² and 250kA/cm². This last value corresponds to the best results achieved up to now with InAs-based resonant tunneling structures such as InGaAs/AlAs double barriers grown on InP. One can note that the frequency capability of devices is dramatically improved at increasing current density notably at submillimeter wavelengths. Also crucial is the intrinsic capacitance of devices as demonstrated in Figure 9 which displays the variations of efficiency as a function of output power for various values of the intrinsic capacitance of devices C_d ranging from 40 fF down to 5 fF. A drastic decrease in efficiency and hence in output power is apparent at high frequencies in particular for devices with C_d of the order of a few tens of femtofarads.

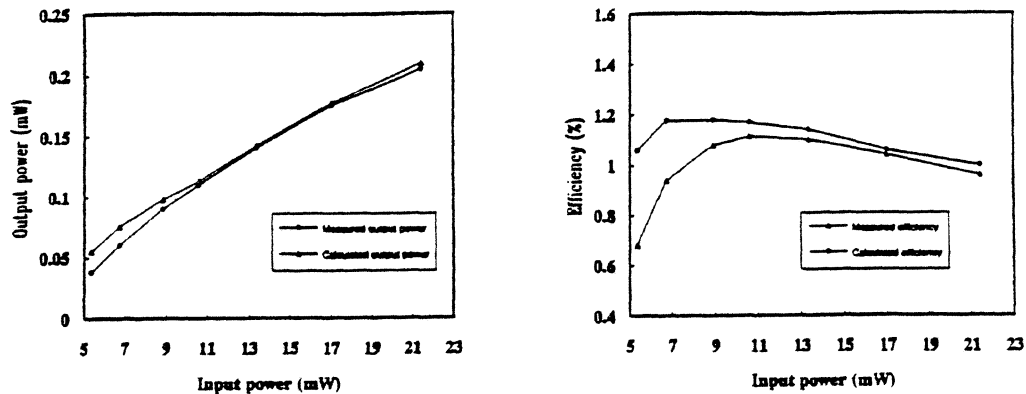


Fig. 7 Output power and efficiency for a 2T2
Comparison between calculated and measured values

Turning now to the influence of the parasitic self inductance due to the interconnecting metallization for a monolithic version or to the whisker for the devices under consideration we obtained the typical evolution $\eta(f_{out})$ reported in Figure 10. We have considered respectively the ideal case $L_s=0$, the situation corresponding to integration techniques with air bridged devices we published recently^[4] where $L_s=50\text{pH}$ and several values up to 1nH which are representative of the self inductance due to a whisker. As a general rules huge degradations can be pointed out at increasing L_s values.

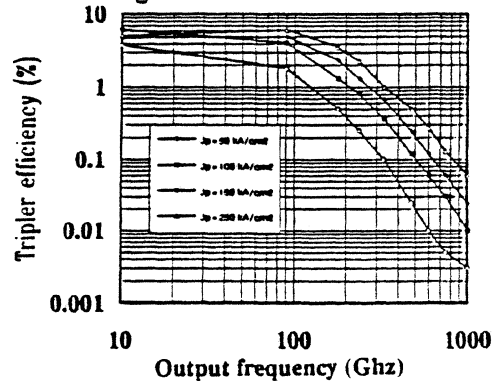


Fig. 8 Efficiency versus P_{in}
Influence of J_p

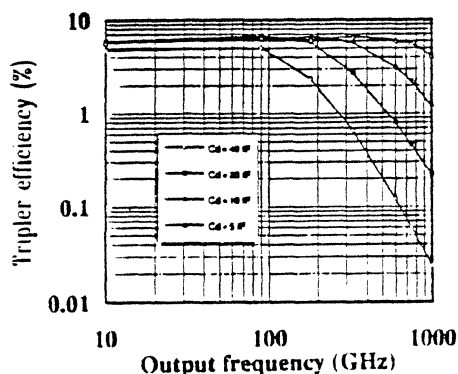


Fig. 9 Third harmonic conversion efficiency
Influence of C_d

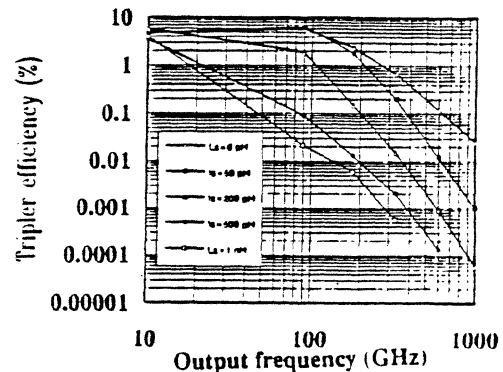


Fig. 10 Efficiency for tripling
Influence of L_s

Beyond the search of high current density to increase the capability of devices and of low parasitics in the recent context of planar integrated technologies^[5], the voltage range for Negative Differential Conductance effects appears also of prime importance. In order to consider this issue, we have compared three kinds of I-V characteristics by computing the variations of efficiency against P_{in} for frequency tripling and quintupling. Figure 11a shows the results we calculated by means of the large signal MDS simulation program for a resonant tunneling diode with $\Delta V=400\text{mV}$. As expected, one can observe an abrupt rise in efficiency in the NDC region with a maximum value for η_3 of 2.2%. As a consequence despite the presence of a negative differential resistance, we do not exceed the conversion efficiency limit $\eta_{max}=1/n^2$ (where n is the harmonic number) found by Page^[6] for diodes exhibiting a resistive non linearity. On the contrary, when one assumes that the devices exhibit NDC effects over a large ΔV , conversion efficiencies are enhanced as seen in Figure 11 b which was computed for $\Delta V=1\text{V}$. Let us recall that V_p should be as low as possible so that the peak amplitude of the voltage across the diode reaches the voltage corresponding to peak current very rapidly whereas ΔV should be increased. One way to enhance ΔV is to use extended spacer layers but subsequent amplification affects not only ΔV but also V_p .

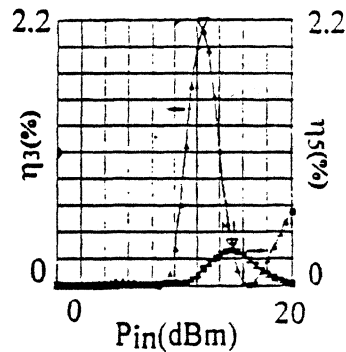


Fig. 11 (a) Efficiency versus rf voltage swing for Intra-band tunnelling devices

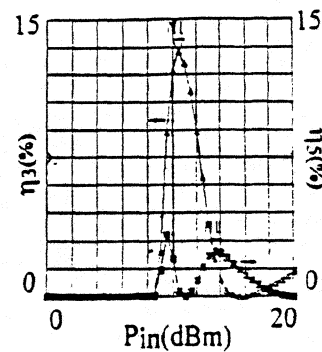


Fig. 11 (b) Efficiency versus V_{rf} $\Delta V=1\text{V}$

However these shortcomings can be alleviated by taking advantage of interband tunneling phenomena which have been observed for Sb-based material systems. In this case, the conduction (E_c) and valence (E_v) bands can overlap and a high conduction state can be established under forward and reverse conditions near equilibrium. The band offset between E_c and E_v states is typically of a few tens of millielectronvolts and as a consequence the conduction can be stopped very soon with a smooth decrease in the current values which reflects indeed the dispersion curve in the forbidden gap region. At higher voltages, other parasitic conduction mechanisms are involved and the current starts again to increase. Figure 12 gives an example of I-V characteristic which can be expected with these broken gap heterostructures such as InAs/GaSb. The variations are quite similar to those of conventional Esaki diodes except the fact that we do not need a highly doped active region as this is the case for homojunctions. This distinction was early recognized notably by Sollner et al.^[7]. The efficiency we calculated with a peak current density of 150kA/cm^2 and $V_p=100\text{mV}$ reaches 44% (Figure 13). It is clear that at such theoretical efficiency levels, resonant tunneling diodes are capable of providing adequate power for submillimeter wave applications and to compete with conventional varactors.

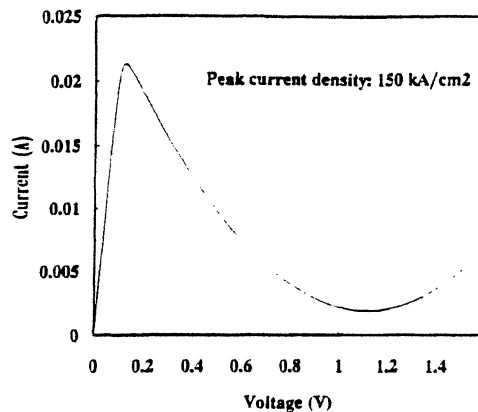


Fig. 12 Typical current voltage curve for interband tunneling diodes

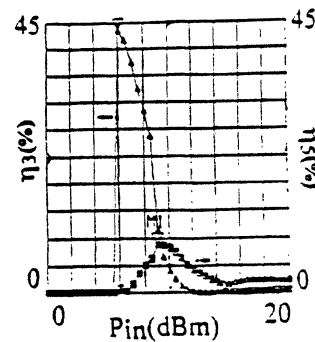


Fig. 13 Efficiency against V_{rf}

Conclusion: High-quality Double Barrier Heterostructures have been successfully fabricated and tested in a frequency conversion with output at submillimeter-wavelengths. Very sensitive power measurements were developed to this aim that permits us to measure an output power of 800nW at 386GHz. These results are discussed in terms of cut-off frequencies showing the requirement of further increase the current density for future improvements in the conversion efficiency and in the operating frequency. On the other hand, heterostructures which involved interband tunneling phenomena appear very promising owing to their current-voltage characteristics more favorable for relaxing the trade-off pointed out for intra-band tunneling structures.

This work was partially supported by the D.R.E.T.(Contract 91.099)

*O. Tanguy and D. Lippens are with
Institut d'Electronique et de Microélectronique du Nord
Avenue Poincaré, BP 69, 59652 Villeneuve d'Ascq Cedex, France

**J. Bruston, J.C. Pernot and G. Beaudin are with
Ecole Normale Supérieure 24 rue Lhomond 75231 Paris
Observatoire de Meudon, 5 Place Jules Janssen, 92195 Meudon Cedex, France

***J. Nagle and B. Vinter are with
Laboratoire Central de Recherches, Thomson CSF
Domaine de Corbeville, 91404 Orsay Cedex, France

[1] E. R. Brown, et al ; Appl Phys. Lett; Vol.58, No.20, May 1991, pp2291-2293

[2] R. Bouregba, et al., Electronics Letters, Vol. 26, No. 21, October 1990, pp1804-1805

[3] L. Burgnies, et al., To be published in J. Appl. Phys., May 1994

[4] E. Lheurette, et al., Electronics Letters, Vol. 28, No. 10, May 1992, pp937-338

[5] S. T. Allen, et al., IEDM proceedings, 1993, pp407-410

[6] C. H. Page, Proceedings of the IRE, October 1958, pp1738-1740

[7] T.C.L.G. Sollner, et al., Physics of quantum Electron Devices edited by F. Capasso

Springer-Verlag

QUASIOPTICAL MULTIPLIER ARRAY WITH SEPARATE WAVEGUIDE FEED

D. Steup / A. Weber

*Laboratories for High Frequency Technology
University of Erlangen-Nürnberg, D-91058 Erlangen, Cauerstraße 9, Germany*

1 Abstract

A new type of Submillimeterwave source is presented consisting of a high power pump oscillator, a power splitting network and a varactor multiplier compound with quasioptical output. Pump power is delivered by a Russian backward wave oscillator (BWO) up to a level of 500 mW at a frequency of 145 GHz. The multiplier setup contains four strictly parallel working varactor diodes in the quadrupling mode leading to an output frequency of the SMMW-source of 580 GHz. The diode output circuit is realized quasioptically simultaneously acting as a tunable power combiner. The idler terminations are impedance tuned by a quasioptical filter network.

2 Introduction

Low conversion loss in SMMW-heterodyne receivers requires sufficient local oscillator power in order to drive hard the nonlinearity. On the one hand a combination of a semiconductor oscillator and a subsequent frequency multiplier appears to be a proper solution of a compact and flexible local oscillator source. On the other hand the multiplier output power is limited because all available diode types show saturation effects driven with some mW of input power resulting in a maximum of multiplication efficiency of SMMW-varactors in dependence of their pump power [1,2]. Besides varactor design for high cut-off frequencies on the one hand and for high power handling capability on the other hand require a tradeoff of the diode parameters [3]. Therefore a promising approach to a higher output power of compact SMMW-multiplier sources could be the distribution of input power to several parallel working multiplying elements followed by an efficient power combination of the single output signals. In our approach a multiplier containing four parallel and synchronously working varactors has been built.

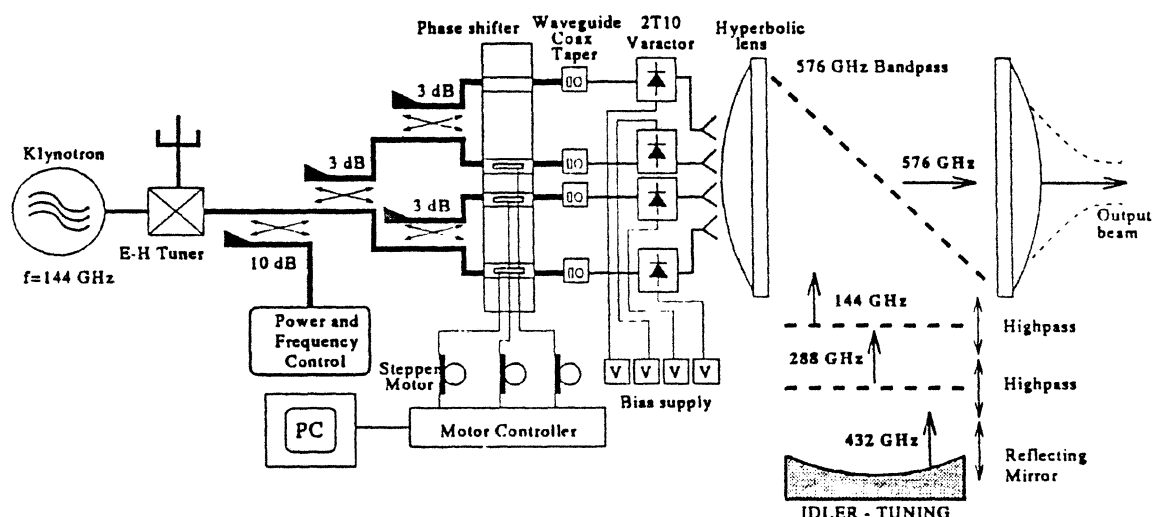


Figure 1: Principle circuit of the SMMW-source

3 General description of the source

Input pump power at the fundamental is delivered by a Russian BWO ($P_{max} = 500$ mW, $142 \text{ GHz} < f_{out} < 148 \text{ GHz}$) and divided into four phase coherent channels of equivalent power transmission by a waveguide network of three 3 dB directional couplers. This makes an independent adjustment of amplitude and phase for each fed device possible. In a computer-controlled four channel phase shifter the phase relations between all channels can be adjusted. Each diode of the multiplying array is fed separately via a semi-rigid coaxial line which operates in the fundamental mode up to a frequency of 894 GHz. Every transition from waveguide to coaxial line is tunable using a sliding contactless short [4]. The diodes (whisker contacted 2T10 UVA¹ varactors with honeycomb structure) are placed at the end of the inner coaxial conductor. The multiplying efficiency of each diode is controlled by a separate bias feed. The whiskers act as a quasioptical long-wire antenna array in the output circuit. The antennas are lined up in form of a broadside array with the main lobe perpendicular to the linear array geometry to avoid shielding effects. They are placed in front of a movable plane mirror to improve the directivity of radiation. Optimum power combining is achieved for a distance of 0.2 mm between the antennas and 0.3 mm spacing between array and reflector. Power combination can also be controlled by quasioptical interference effects which are controlled by the relative phase shift of the pump signals. The output beam is collimated using a hyperbolic lens; the fourth harmonic at 576 GHz is filtered by a bandpass (i.e. a resonant metallic mesh) and couples through a second lens into a quasioptical beam waveguide which finally leads to a cornercube mixer. The idler circuits at the second and third harmonic and the fundamental circuit are tuned by a quasioptical network consisting of two movable highpass filters and a movable mirror. This offers the possibility of an independent impedance termination adjustment for each

¹UVA : University of Virginia

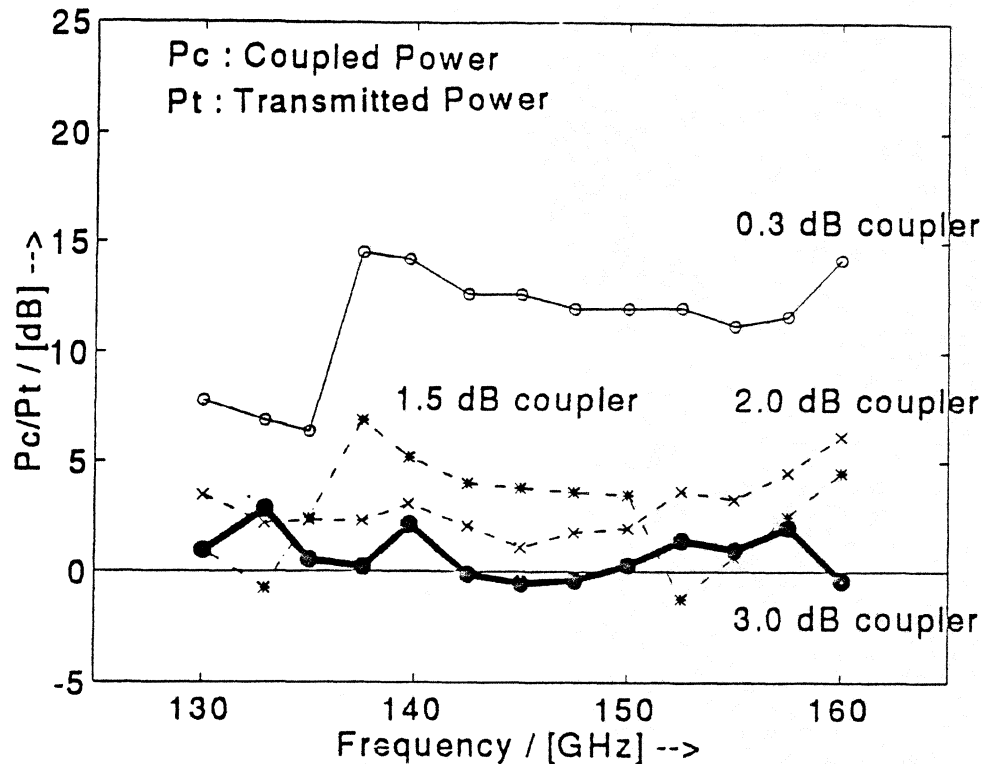


Figure 2: Measured power splitting of different directional couplers

frequency circuit.

4 Power-splitting network

Parallel and optimum operation of each diode requires separate pump signal feed. This is realized by a power-splitting WR-6 hollow waveguide network (1.651 mm * 0.8255 mm). The source is matched to the waveguide network by an E-H tuner. Feeding with a single high power source secures phase-coherent input signals for all active diode elements. Phase shift between the channels is controlled by a four channel phase shifter. Power is splitted into four channels with equal amplitude by 3 dB directional couplers. Phase shifter, E-H tuner and 3 dB directional couplers were developed and machined in our laboratories and are discussed in detail subsequently.

4.1 3 dB directional coupler

The directional couplers are realized as top wall couplers with circular holes [9] etched in a 12 μm thick, gold plated brass foil. For the 3 dB types we chose two perforation lines having Tschebyscheff design with hole diameters between 250 μm and 448 μm .

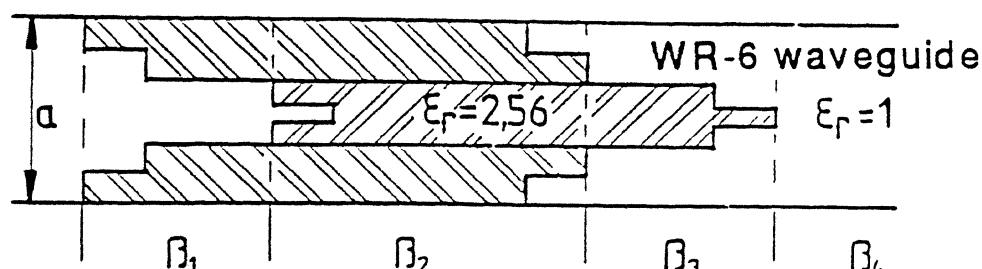


Figure 3: Schematic of four-channel phase shifter

Measurements of different couplers are shown in Fig.2. Here the relation between the power amounts at the two different output ports is displayed as a function of the input frequency. A coupling coefficient variation lower than 1 dB was achieved within a bandwidth of 15 GHz around the center frequency. The couplers were designed for an operating frequency of 145 GHz transmission loss being below 2 dB.

4.2 Four channel phase shifter

In principle the four feeding channels are designed to be of equal length. Manufacturing may cause deviations from the standard electrical length of the pump signal channels. For compensation of these deviations we constructed a four channel phase shifter making a relative phase shift between the different signal paths possible. Consequently, every defined phase relation between the single pump signals of the diodes can be adjusted according to an optimum power combining between the different antenna signals in the output circuit. Another feature is the possibility of an output beam steering (*Phased array*).

Phase shifting is achieved by moving dielectric stripes made of polystyrene ($\epsilon_r = 2.56$) inside the WR-6 waveguide. Every waveguide contains three dielectric stripes. The outer ones are fixed and a central stripe can be reproducibly moved relative to them by a computer controlled stepper motor. For matching dielectric filled waveguide and hollow waveguide, the stripes are equipped at their ends with $\frac{\lambda}{4}$ - transformers.

Generally the phase shifting structure consists of four waveguide sections with different phase constants β_i . Moving of the central stripe corresponds to a variation of the single line lengths or of the resulting phase constant of all sections respectively. A high similarity between the transmission characteristic of the different channels was realized. A highly linear phase shift was measured from 0 to 200 degrees in dependence of the stripe displacement (Fig.4). Transmission loss of each channel sums up to 3.5 dB.

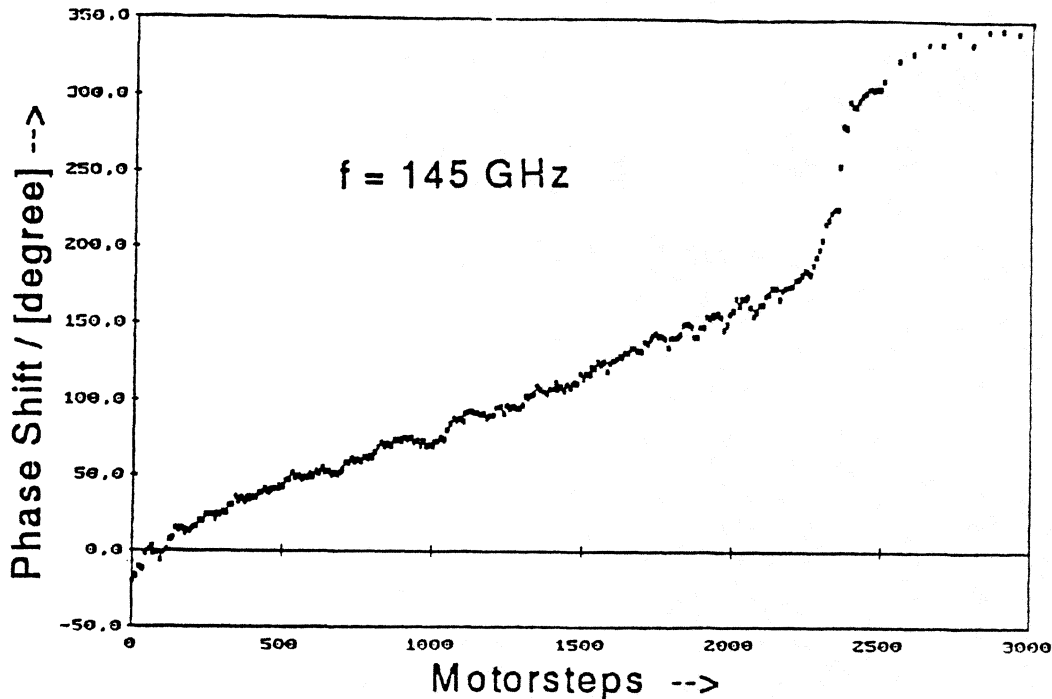


Figure 4: Measured phase shift

4.3 E-H tuner

The E-H tuner was also designed in our institute. For matching operation we use non-contacting shorts with cylindrical cross-section. The micrometer driven plunger contains seven sections with alternating characteristic impedance Z_l . We realized plunger diameters of 0.8 mm and 0.25 mm what corresponds to a Z_l of approximately 1.88 Ω and 71.7 Ω .

This leads to an impedance drop by a factor of $7.6 \cdot 10^{-9}$ for a given operating frequency of 145 GHz [4]. We measured a tuning-dynamic of more than 24 dB over a bandwidth of 10 GHz around a center frequency of 145 GHz as illustrated in Fig.5. The transmission loss of the device is lower than 1dB.

5 Coaxial-waveguide transition

Nearly all MMW- and SMMW multiplier setups contain a coaxial waveguide transition because the diode is usually mounted on a coaxial choke structure. The other end of the inner conductor is usually soldered with the waveguide bottom in order to close the bias circuit of the diode. Similarly the electric field of the H_{10} -mode in the rectangular waveguide is shortened at its maximum field strength what negatively affects the coupling efficiency from H_{10} - waveguide to TEM - coaxial mode. Therefore, we developed a new kind of transition which simultaneously combines a closed bias circuit and a more efficient mode conversion. In our model the coaxial line is elongated through the lower waveguide wall and is shortened at a distance of a quarter-wavelength away from the waveguide

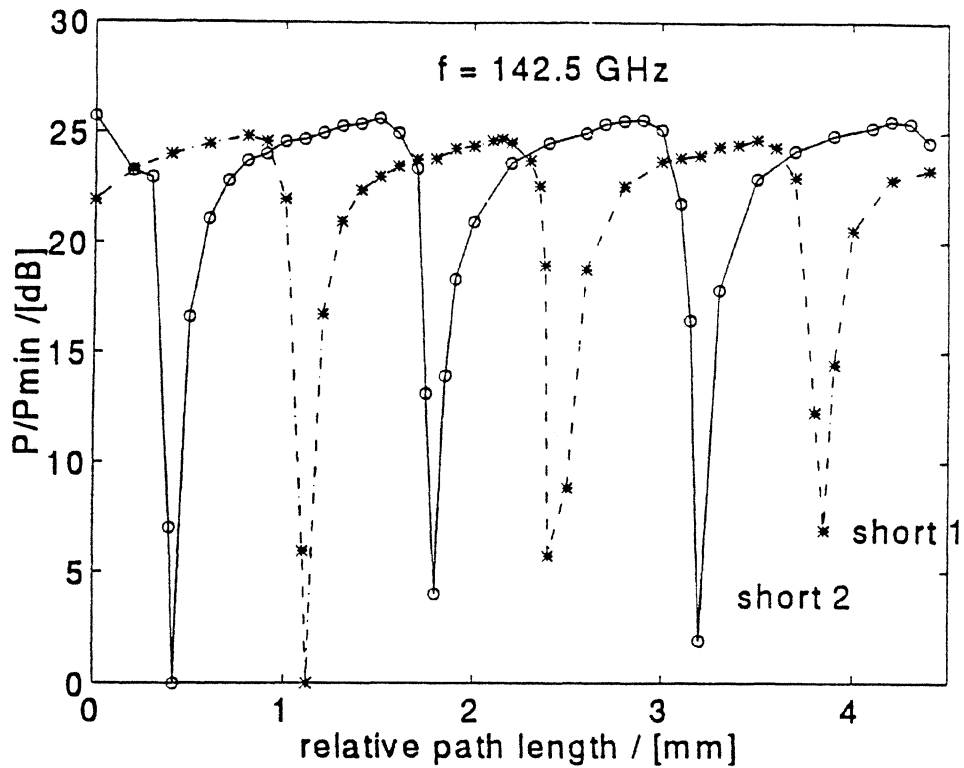


Figure 5: Reflection measurement of the E-H tuner

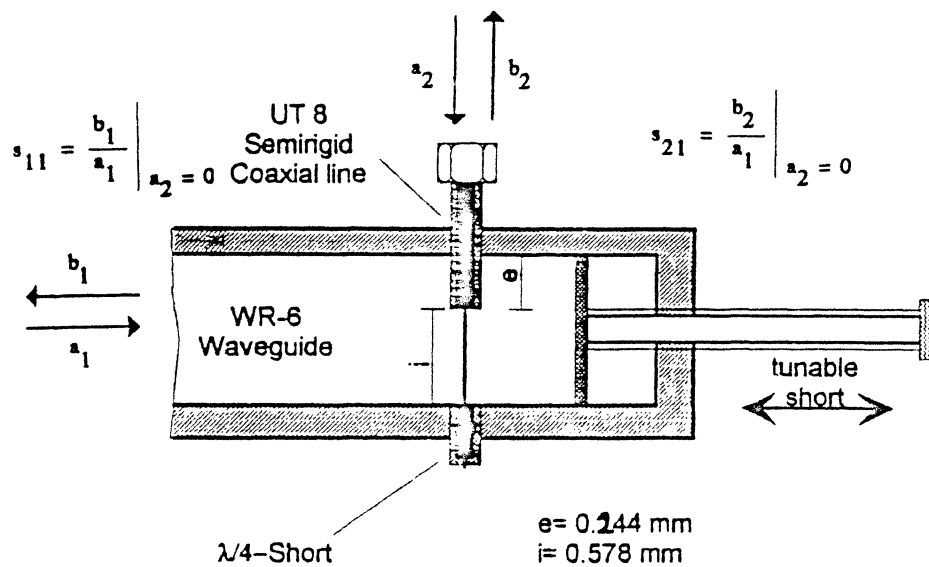


Figure 6: Schematic of waveguide-coaxial transition

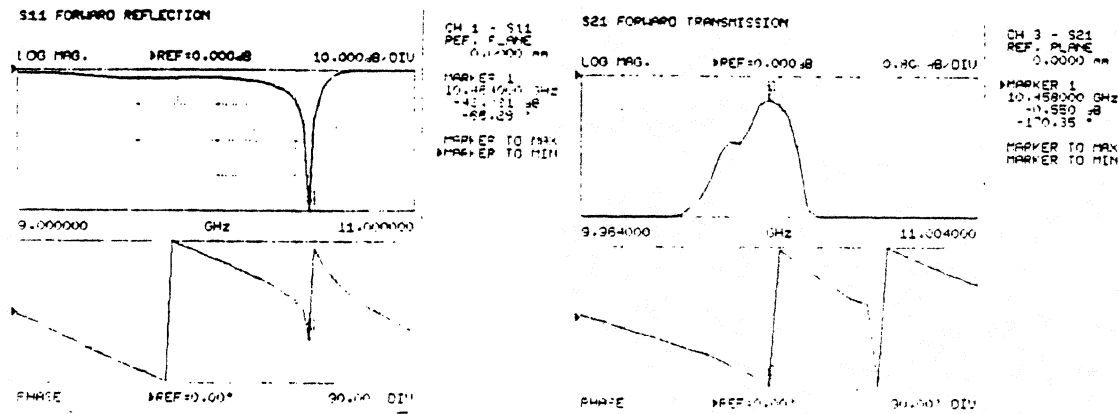


Figure 7: S-parameter measurement of waveguide-coaxial transition

bottom. So, the short is transformed approximately in an open circuit at the waveguide bottom and simultaneously the bias circuit is closed. Similarly the outer conductor of the coaxial line dips into the waveguide at a length of 0.244 mm. The transition from WR-6 waveguide (1.651 mm * 0.8255 mm) to the semi-rigid coaxial line ($d_i=0.05$ mm, $d_o=0.1$ mm) is shown in fig.6. The axial line profile in the transition region was realized using a photolithographic etching process. The dielectric is left standing in the area of the open laid inner conductor so as to achieve a higher coupling-bandwidth of the transition. The transition can be adjusted with a non contacting movable short. It was tested by measurements at X-band in a frequency range of 9 to 11 GHz as illustrated in fig.7. Here a transmission loss improvement of about 4 dB compared with the standard design was achieved (compare Table 1).

	Bandwidth	Power coupling
Standard	4.82 GHz	36.2 %
New transition	5.75 GHz	88.1 %

6 Quasioptical multiplier array

The varactor array is fed by four separate semi-rigid coaxial lines of about 1 cm length. They are monomode up to 894 GHz and have a transmission loss of about 1 dB/cm. The diodes (chipsize $100\ \mu\text{m} \times 100\ \mu\text{m} \times 100\ \mu\text{m}$) are soldered onto the end of the inner coaxial conductor. For mechanical stability the inner conductor is enlarged to a diameter of $150\ \mu\text{m}$ by soldering a $12\ \mu\text{m}$ thin brass bush onto its end. The semi rigid lines are bent as illustrated in fig.8 to realize a distance of 0.2 mm between the active elements. The lines are glued with epoxide resin inside the waveguide block to achieve high mechanical stability. As active elements we use 2T10 UVA honeycomb varactors ($C_{jo} = 5.5$ fF, $R_s = 9\ \Omega$) which are contacted with a 4λ whisker at 576 GHz. The coaxial lines were passed through an oblong hole drilled in a gold plated and polished brass plate. Consequently, the whiskers correspond to a long-wire antenna array on a reflecting ground plane. Every whisker is contacted and manipulated by its own adjuster which is simultaneously used to provide

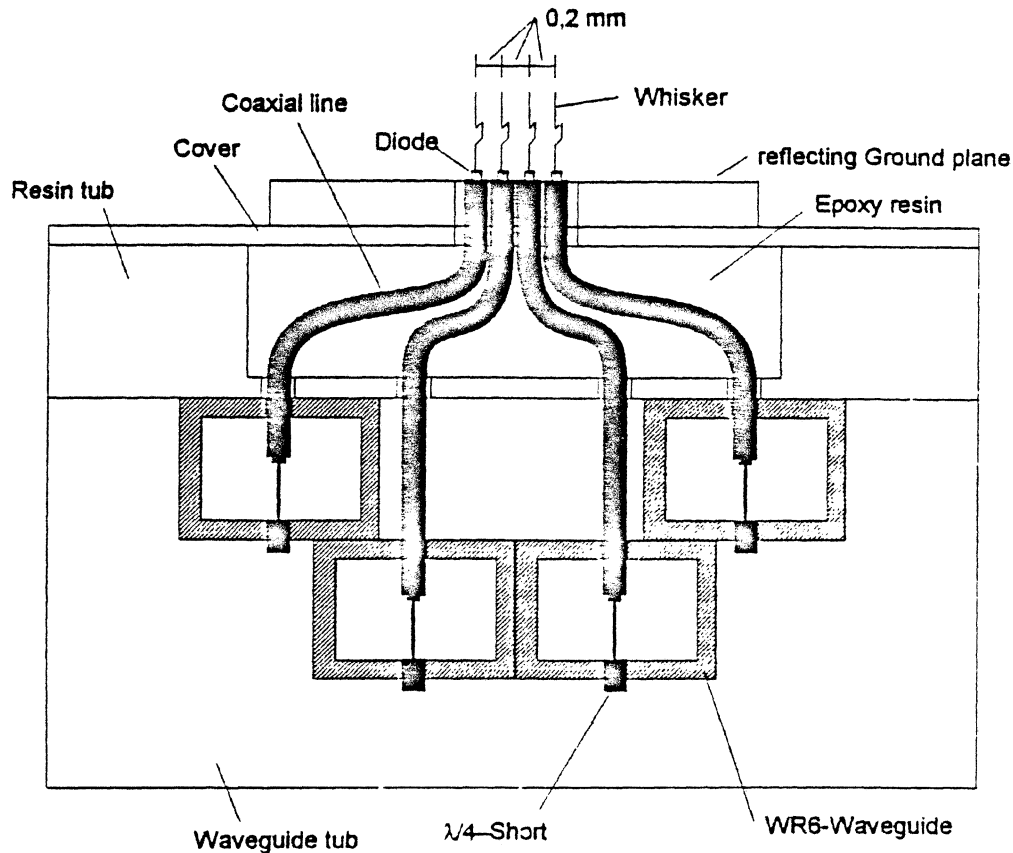


Figure 8: Schematic of coaxial feeding network

each diode with a separate bias. So, a suitable impedance level for each diode performing optimum multiplying efficiency can be selected. For a higher directivity of radiation the array is positioned in front of a plane reflector. This reflector is micrometer-driven to adjust an optimum power combining in the output circuit. Choosing this configuration the array results in four active and twelve virtual radiation elements. With the phase shifter integrated in the power splitting network we can enforce an in-phase steering of the single radiating elements leading to a 'broadside array' configuration. Consequently at the output all active elements are working strictly parallel because their main lobe is perpendicular to the linear array geometry avoiding any shielding effects between the active devices.

The array geometry was optimized according to power combining in the far field. The array pattern as illustrated in fig.11 was calculated from the electromagnetic vector potential and geometrical parameters as the distance between array and reflector as well as the distance between the single antennas were varied so as to get a high beam efficiency and a high sidelobe attenuation. The beam efficiency is hereby defined as the amount of power collimated in the main lobe related to the whole output power of the array. Optimum

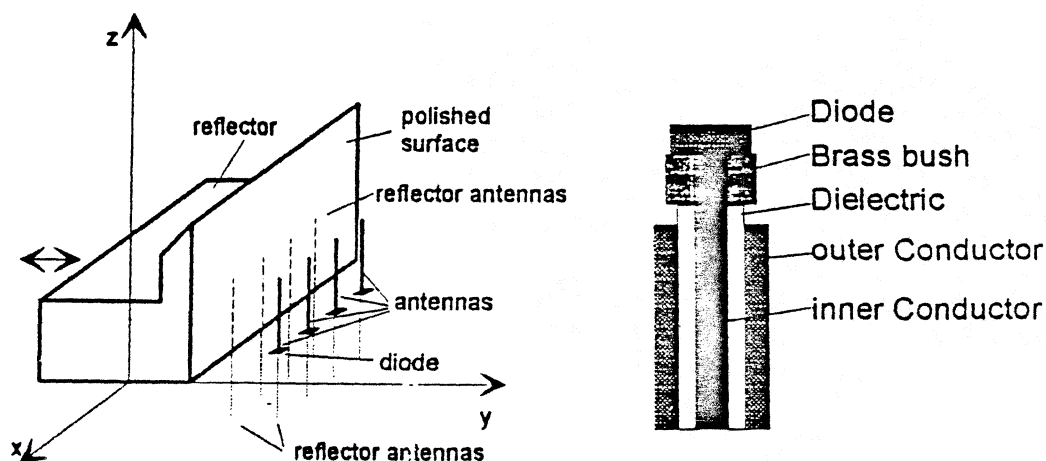


Figure 9: Schematic of diode array and diode mount

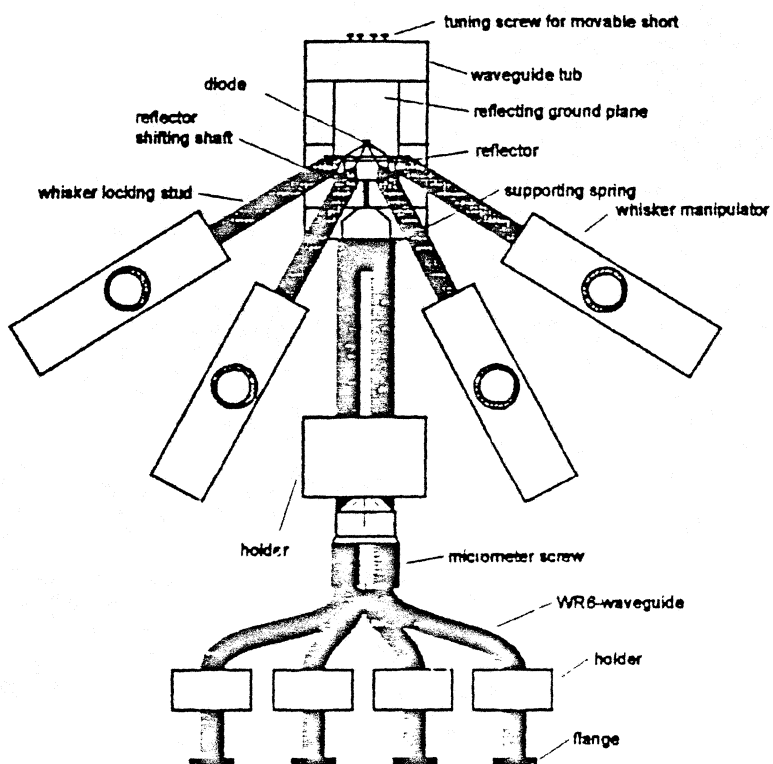


Figure 10: Setup of reflector and whisker manipulation

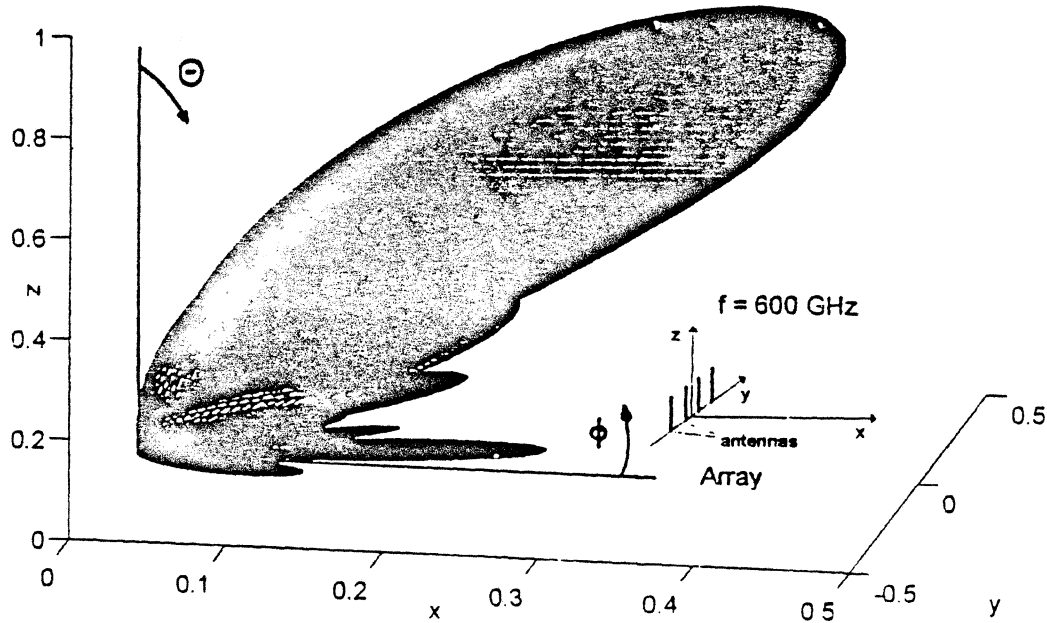


Figure 11: Beam pattern of the long-wire antenna array

values for our configuration are a beam efficiency of 89.8% and a side lobe attenuation of 9.5 dB. These optimums are coupled with a reflector distance from the array of 0.3 mm and an antenna distance of 0.2 mm.

Optimum beam coupling of the output pattern at 576 GHz to a fundamental Gaussian mode was depicted in Fig.12 in dependence of the distance between array center and coupling position as well as of the far field divergence angle Θ of the Gaussian beam. In the far field the coupling is nearly independent from position as expected. The output pattern at 576 GHz couples best to a Gaussian beam with a far field angle of 13 degrees what corresponds to a beam waist of 1.4λ . According to these beam parameters the lenses of the quasioptical output network are designed.

7 Quasioptical filter network

This quasioptical network has to fulfil two different aspects mainly: At first the output power at 576 GHz has to be coupled effectively to the load, in our case a corner cube mixer; secondly the input circuit and the idler terminations have to be adjusted to a certain impedance level in order to realize a low conversion loss of the quadrupling process. This is done by quasioptical bandpass filters, highpass filters and mirrors as shown in fig.13. Several realizations of a quasioptical filter network are possible. The main advantages of the presented setup are the negligible attenuation of output power by idler filters and the possibility of separate impedance tuning for each frequency circuit.

The principle of the output filter network works as follows: The first hyperbolic lens

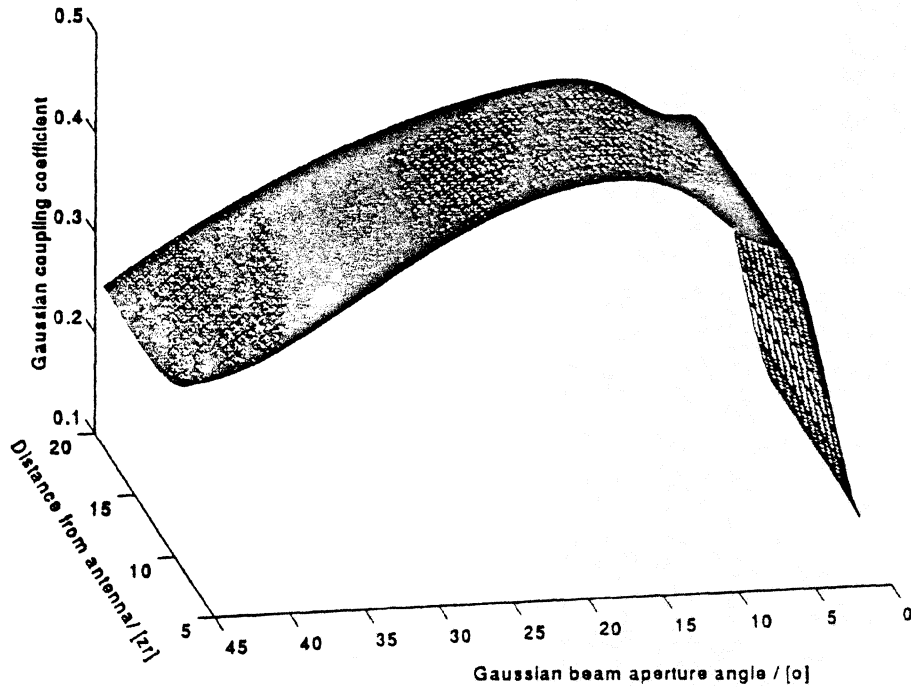


Figure 12: Gaussian beam coupling of the array

makes a transformation to a Gaussian beam of nearly plane phase surfaces. The band-pass filter is placed under an angle of 45° to the output beam. Consequently the power amount at 576 GHz is separated from the electromagnetic power of the other frequency circuits at 144, 288 (2×144), 432 (3×144), 720 GHz (5×144) and so on. The desired signal is matched by a second hyperbolic lens to the pattern of our corner cube mixer; the input and idler frequencies are reflected onto a cascade consisting of quasioptical highpass filters and a final mirror. The first filter is transparent for frequencies above 170 GHz, the second above 320 GHz (comp. Fig. 16b). Hereby a theoretical transmission of 50 % is assumed as frontier between reflection and transmission band. Consequently the impedance termination of the input frequency circuit can be adjusted by axial movement of the first highpass filter corresponding to a variation of the reflection resonator realized by the shorted quasioptical line. Considering the antenna as coupling link between diode and resonator (Fig. 14) the reflection coefficient at the diode output behaves like

$$r = \frac{s_{11} - \det S r_a e^{-2\gamma l}}{1 - s_{22} r_a e^{-2\gamma l}} \quad (1)$$

Hereby S describes the scattering matrix of the antenna and r_a the reflection coefficient of the highpass filter.

The second harmonic at 288 GHz is separately adjustable with the second highpass. This principle of the highpass filter cascade is extendable to all other higher idler circuits but because of their with higher order strongly decreasing power content and lower significance for the quadrupling process we only provided one variable idler termination in form of a mirror for all harmonics above 432 GHz.

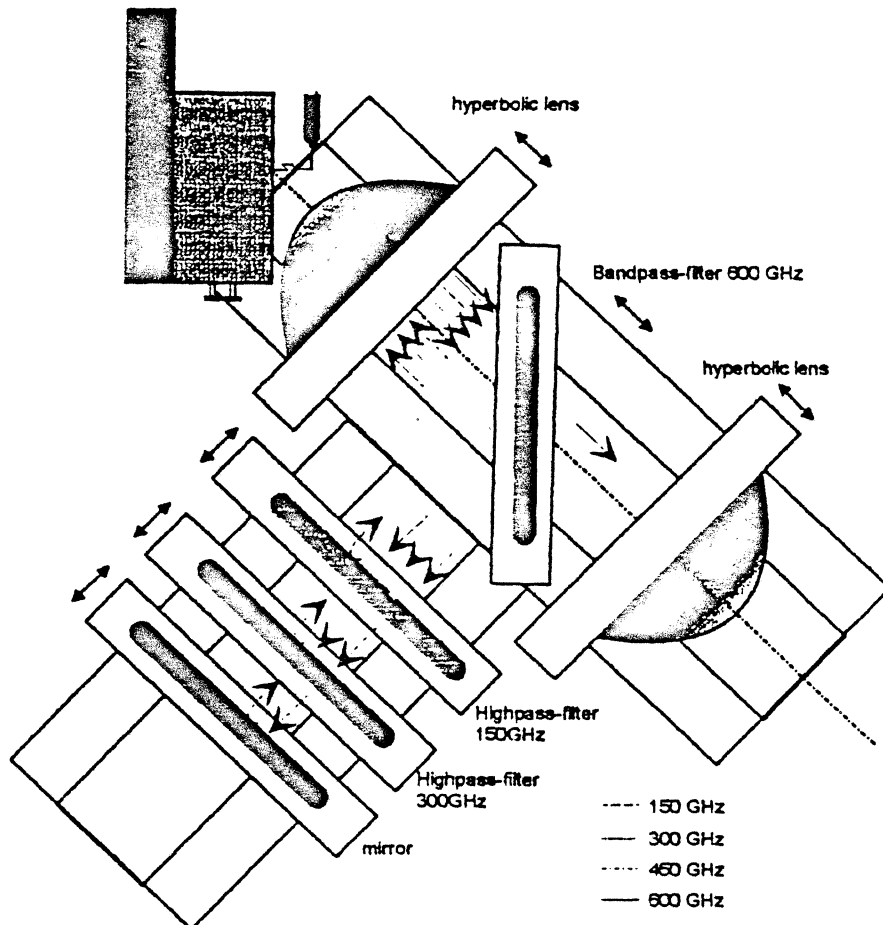


Figure 13: Schematic of the quasioptical filter network. The operating frequencies of 144, 288, 432 and 576 GHz are rounded off to values of 150, 300, 450 and 600 GHz

All components of the filter network can be swivelled independently in two orthogonal directions to make an optimum adjustment to the Gaussian beam profile possible. The edge taper of all components is greater than 35 dB to avoid diffraction loss in the beam waveguide.

For our lenses we measured a transmission loss of 0.9 dB slightly exceeding our calculated value of 0.3 dB.

The functionality of our quasioptical filter network was measured at frequencies of 144 and 288 GHz where signal generators were available. Instead of the multifrequency long-wire antenna array the quasioptical circuit was fed by test oscillator signals at discrete frequencies and the impedance tuning of the single filters was tested by measuring the power reflection coefficient at the input port of the quasioptical network. The measurements are

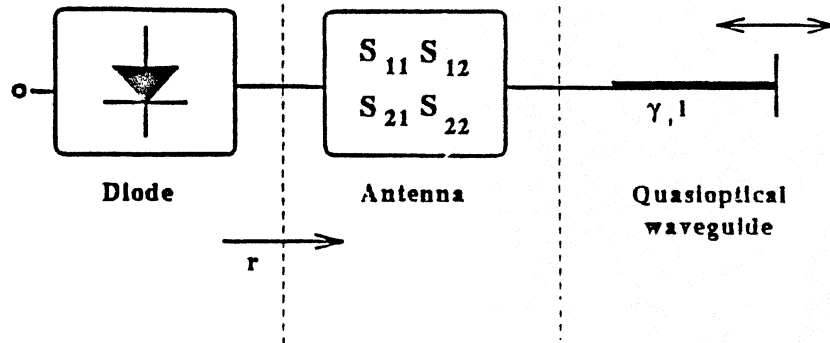
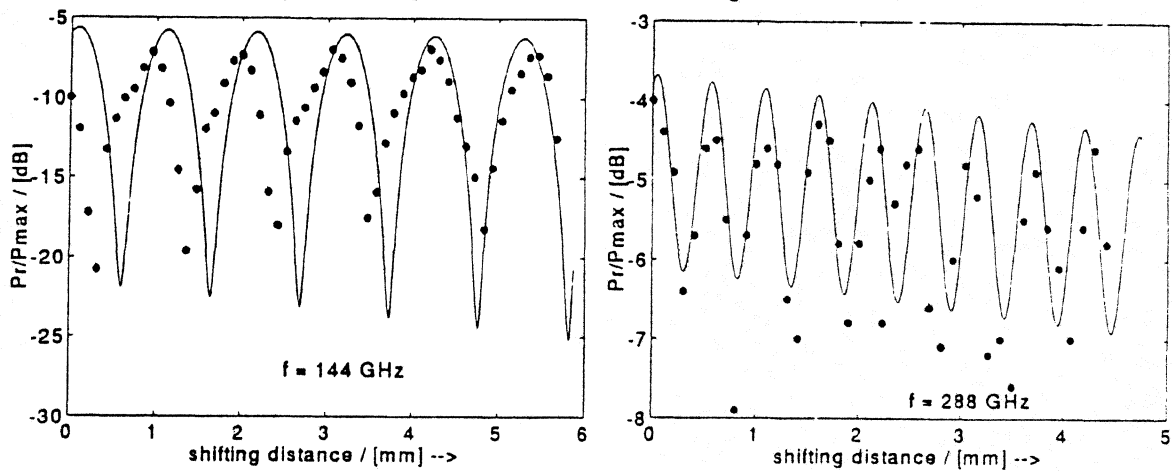


Figure 14: Equivalent network for a single idler circuit

Figure 15: Measurement of quasioptical impedance tuning, P_r : Reflected power

compared with a calculation according to Eq. 1. Hereby the unknown S-parameters of the antennas are fitted to a good agreement with our check points.

The results are presented in Fig.15. The power reflection coefficient is a periodic function of the axial filter position. Minima and maxima repeat at a displacement range of half a wavelength at the test frequency. A dynamic of the power reflection coefficient of 16 dB at 144 GHz and 5 dB at 288 GHz was realized with the corresponding highpass filters. The resistive losses in our idler circuits sum up to 5.5 dB at 144 GHz and 4 dB at 288 GHz respectively. These are due to not exactly plane phase surface of the electromagnetic wave resulting in geometrical walk-off of the reflected wave, to losses of lenses and meshes and to a imperfect reflection characteristic of the high pass filters. The interference between the idler circuits is lower than 0.5 dB meaning that the tuning filter for the first harmonic has a negligible influence at 288 and 432 GHz and the other way round.

8 Quasioptical filters

As frequency selective devices different types of metallic meshes are used. They differ in their apertures according to their filter characteristic. The high-passes consist of quadratic holes in a self-supporting brass structure.

The transmission characteristic of these inductive meshes depends on the lattice constant, the stripwidth, and the thickness of the brass foil. After a photolithographic process the holes are etched into a 70 μm thick copper foil being gold-plated for a reduction of ohmic losses. The transmission characteristic of the meshes was calculated according to [6]. For the first mesh ($g = 710 \mu\text{m}$, $\frac{a}{g} = 0.79$) we realized a reflection of 81 % at 144 GHz and a transmission of 91 % at 288 GHz. For the second filter ($g = 410 \mu\text{m}$, $\frac{a}{g} = 0.79$) a reflection of 75% at 288 GHz was reached.

The bandpass design shows cross-shaped apertures etched in brass foil of 12 μm thickness. These are equivalent to a cascade of an inductive mesh as mentioned above and a lowpass consisting of metallized patches on a dielectric substrate. The shape of the crosses is not symmetrical because it has to be placed under an angle of 45° into the beam guide. The theoretical transmission characteristic was calculated according to [7,8]. A high agreement between theory and measurement was obtained and the transmission loss for the desired signal is below 1 dB. Stop band attenuation for all powerful idler frequencies is higher than 20 dB what guarantees an efficient separation from the output mixer path.

9 Measurements

First measurements on the multiplier structure were carried out in order to test the operation of the device. Output power at 579 GHz was detected using a corner cube mixer and was displayed by a spectrum analyzer.

At first the symmetry of the power splitting network was tested. The deviation of an equal power distribution to the four channels was below 1 dB so that all diodes were assumed to be fed with nearly the same amount of input power.

In the beginning all channels of the source were tested separately. For each single channel a set of optimum parameters - plunger position and bias - was adjusted according to a maximum of the output signal. Subsequently the power splitting network was connected to the multiplier and the source was aligned to a maximum of output power by shifting the relative phase between the channels and slight corrections of the bias supply. Hereby bias voltages for the inner diodes of about -0.9 V and for the outer ones of 0.2 V guarantee an optimum quadrupling performance.

In the following the quasioptical output circuit was tuned due to a further maximization of the output. Measurement of output power as a function of the distance between the movable reflector and the antenna array shows a global maximum at a distance of 0.3 mm (Fig. 16a) which is consistent with our calculations predicting an optimum quasioptical power combining at this geometry [5].

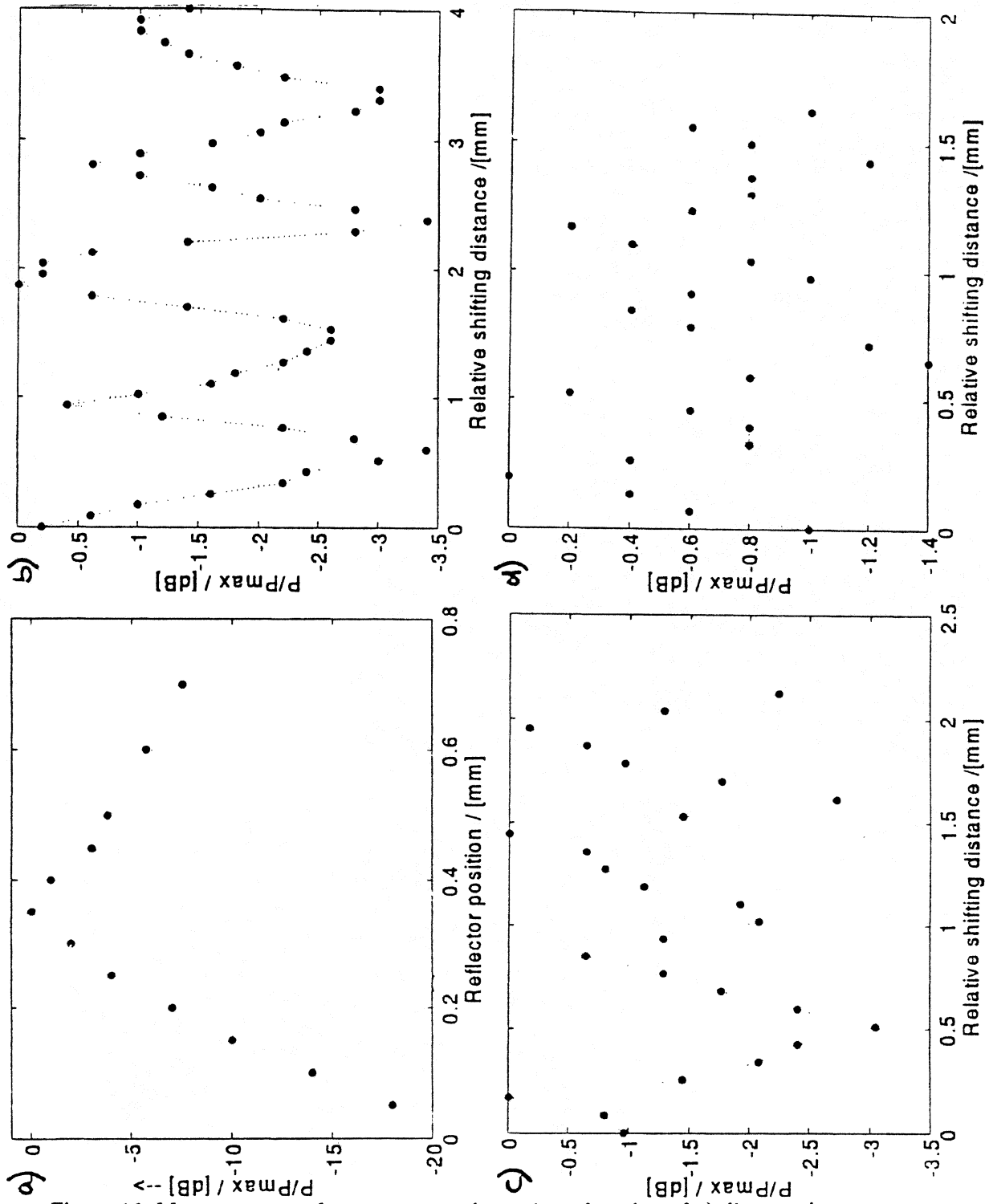


Figure 16: Measurements of output power dynamic as function of a) distance between array and plane reflector, b) Shifting distance of the first inductive mesh, c) Shifting distance of the second inductive mesh, d) Shifting distance of the mirror

An adjustment of the quasioptical filter network contains an output power dynamic of 3.5 dB in dependence of the impedance termination at the first harmonic (144.7 GHz). It is illustrated as function of the filter position in Fig. 16b. The periodicity of the output power characteristic is about 1mm what corresponds to half a wavelength of the pump frequency.

Tuning of the second harmonic with the other highpass filter shows an output power dynamic of 3.1 dB (Fig. 16c). The influence of the mirror reflecting the power amounts of all other higher harmonics is small. Here we measured a dynamic of about 1.3 dB and a periodicity at a shifting distance of 350 μm due to the third harmonic at 435 GHz. This periodicity is slightly disturbed pointing out fractions of power at other harmonics also being reflected (Fig. 16d).

Finally a maximum output power of 60 μW at quadrupling to 579 GHz was achieved due to a pump power of 280 mW. Compared with a single channel operation of the source where the whole input power was fed to one single channel and the other channels were terminated without reflection we stated an increase in output power of 4.5 dB. In this first laboratory setup we have to manage with one high power oscillator and a lossy power splitting network. Therefore it is probable that the input energy which effectively couples into each diode is too low for an optimum quadrupling performance. A multiplier setup with an integrated phase shifter in each channel driven by his own Gunn-oscillator and phase locked by a central Gunn-oscillator may guarantee a more effective diode fed and promises a further increase in output power compared with single diode operation.

10 References

- [1] A.V. Räisänen, 'Frequency Multipliers for Millimeter and Submillimeter Wavelengths', Proceedings of the IEEE, Vol.80, No.11, November 1992
- [2] T.W. Crowe, W.C.B. Peatman, R.Zimmermann, R.Zimmermann, 'Consideration of Velocity Saturation in the Design of GaAs Varactor Diodes', IEEE Microwave and Guided Wave Letters, Vol.3, No.6, June 1993
- [3] T.J. Tolmunen, M.A. Frerking, 'Theoretical Performance of Novel Multipliers at Millimeter and Submillimeter Wavelengths' International Journal of Infrared and Millimeter Waves, Vol.12, No.10, 1991
- [4] R.E. Collin, 'Grundlagen der Mikrowellentechnik', VEB Verlag Technik, Berlin, 1973
- [5] D.Steup, 'Whisker-Contacted Diode-Multipliers as Quasioptical SMMW-Arrays', International Journal of Infrared and Millimeter-Waves, Vol.14, No.12, 1993
- [6] L.C. Botten, R.C. McPhedran, J.M. Lamarre, 'Inductive Grids in the Resonant Region: Theory and Experiment', International Journal of Infrared and Millimeter-Waves, Vol.6, No.7, 1985
- [7] V.A. Soglasnova, B.P. Gorshunov, 'Amplitude and Phase Characteristics of Metal Meshes - The Elements of Submillimeter Interference Filters', International Journal of Infrared and Millimeter Waves.

Vol.14, No.1, 1993

[8] R. Ulrich, 'Interference filters for the Far Infrared', Applied Optics, Vol.7, No.10, October 1968

[9] R. Levy, 'Analysis and Synthesis of Waveguide multiaperture directional couplers', IEEE-MTT, Vol. MTT-16, No. 12, 1968

THEORETICAL AND PRACTICAL LIMITS ON THE RF BANDWIDTH OF SIS MIXERS*

A. R. Kerr

National Radio Astronomy Observatory**
Charlottesville, VA 22903

ABSTRACT

Most millimeter-wave mixers have an RF equivalent circuit that falls into one of the following categories: (i) Parallel R-C (the junction) connected to a resistive source with no broadband matching circuit. (ii) Parallel R-C, and possibly series L, followed by a broadband matching circuit. (iii) Parallel R-C-L, and possibly series L, followed by a broadband matching circuit. This paper examines the maximum (RF) bandwidths achievable by SIS mixers in each of these categories.

Fundamental limitations on the matching bandwidth between a resistive source and a capacitive load were derived by Bode in 1945. In 1950, Fano developed a more general theory which included capacitive devices with series inductance. To use the work of Bode and Fano to determine the useful bandwidth of a practical mixer, it is necessary first to know the range of (complex) source impedances within which acceptable performance is obtained. From SIS mixer theory it is found that acceptable performance results when the magnitude of the source reflection coefficient ρ , relative to the optimum source impedance, is less than some value. For Nb/Al-Al₂O₃/Nb SIS mixers in the 70-350 GHz range, $|\rho| \leq 0.4$ appears appropriate.

It is found that the inductance of a series array of junctions only limits the bandwidth if it exceeds a critical value. Otherwise the inductance must actually be augmented to achieve the theoretical maximum bandwidth.

*A more extensive version of this paper has been accepted for publication in *IEEE Transactions on Microwave Theory and Techniques*.

**The National Radio Astronomy Observatory is operated by Associated Universities, Inc. under cooperative agreement with the National Science Foundation.

Introduction

As SIS mixers achieve lower noise over wider frequency bands, it is interesting to examine the factors that limit their ultimate bandwidth. These can be divided into two categories: theoretical limits, and limits imposed by practical constraints such as conductor dimensions and tolerances. The term *bandwidth* here refers to the frequency range over which the LO can be tuned while maintaining satisfactory mixer performance without re-tuning the RF or IF circuits of the mixer. We assume here a low IF, so the junction sees the same embedding impedance in the upper and lower sidebands.

The performance of an SIS mixer, operating as a mixer, with given LO frequency, LO amplitude, and bias voltage, is governed by the embedding impedances seen by the junction at the sideband and intermediate frequencies, $f_{LO} \pm f_{IF}$ and f_{IF} . The first step in determining the maximum theoretical bandwidth is therefore to determine the desired IF load impedance and the acceptable range of RF embedding impedances. With a suitable normalizing impedance (characteristic impedance), the acceptable range of RF embedding impedances can be expressed as a maximum allowable reflection coefficient. This allows us to make use of the famous integral equations relating match and bandwidth, developed over 40 years ago by Bode [1] and Fano [2].

The Range of Acceptable Embedding Impedances

The performance of a typical 230 GHz double sideband Nb/Al-Al₂O₃/Nb SIS receiver is shown in Fig. 1. The contours are plotted on Smith charts of RF embedding admittance (i.e., in the $(-\rho)$ -plane). The embedding admittance includes the capacitance of the junction, and is assumed equal in the upper and lower sidebands. The mixer gain and receiver noise temperature are shown as single-sideband (SSB) quantities. The receiver includes an IF amplifier with $T_{IF} = 4$ K, and an IF isolator at 4 K. Admittances in the diagram are normalized to the optimum source conductance $1/R_{S,opt}$ where [3,4]

$$R_{S,opt} = \left(\frac{R_N}{2.4} \right) \left(\frac{f_{GHz}}{100} \right)^{0.72} \quad (1)$$

R_N is the normal resistance of the junction (or array of junctions). The IF load impedance Z_{IF} is fixed and equal to $R_{S,opt}$, and the pumping parameter $\alpha = eV_{LO}/\hbar\omega_{LO} = 1.2$, with the DC bias voltage at the mid-point of the first photon step. For Nb/Al-Al₂O₃/Nb SIS mixers operating up to at least 60% of the gap frequency, this set of operating conditions has been found to result in well behaved receivers with noise temperatures close to their minimum, and with contour plots similar in character to those in Fig. 1.

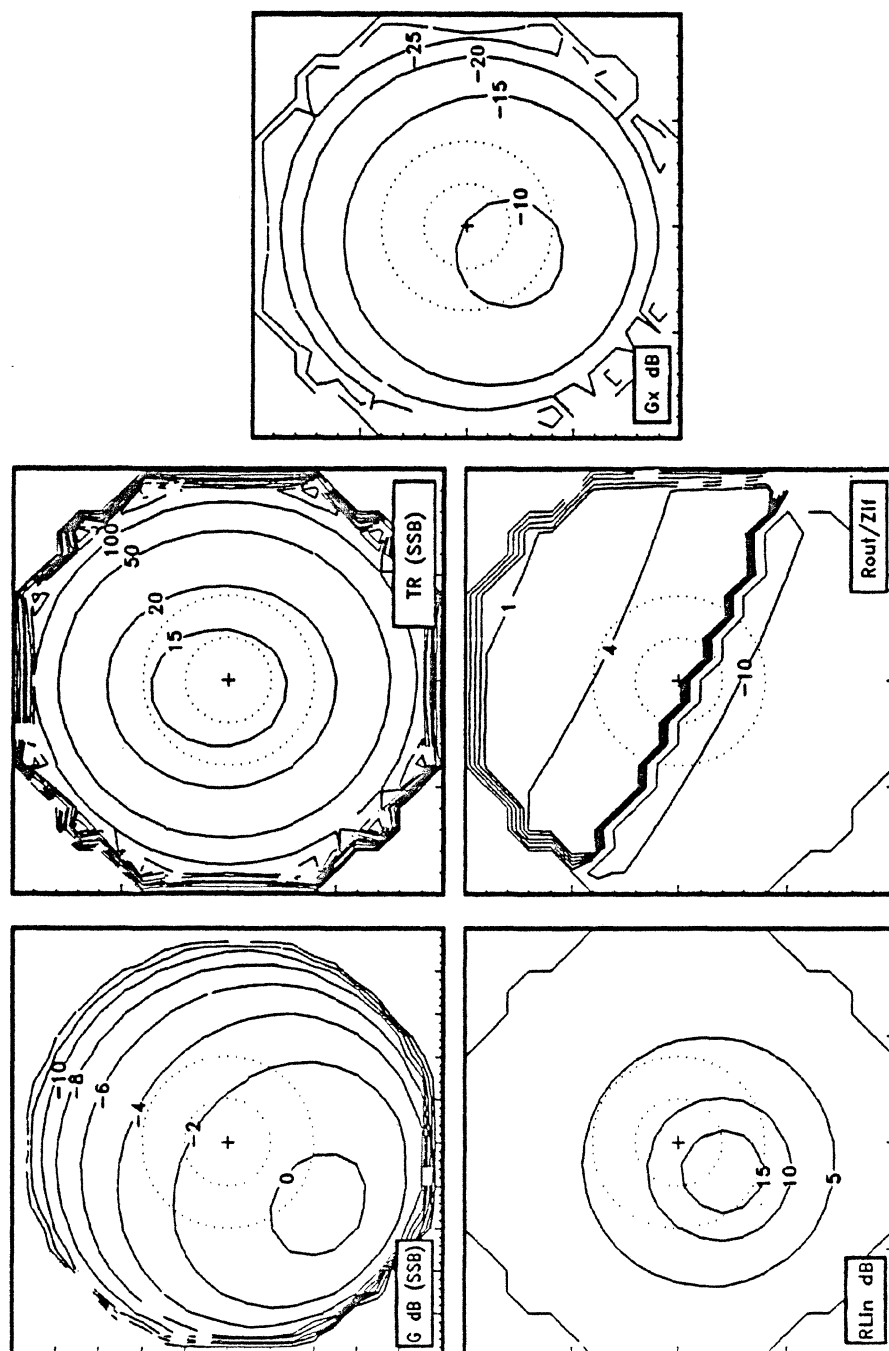


Fig. 1. Contour plots of mixer gain, receiver noise temperature, input return loss, IF VSWR, and signal-to-image conversion gain, for a 230 GHz SIS receiver using typical Nb/Al-Al₂O₃/Nb junctions. The contours are plotted on Smith charts of RF source admittance (*i.e.*, in the ($-\rho$)-plane). The dotted circles are $|\rho| = 0.2$ and $|\rho| = 0.4$. The receiver includes an IF amplifier with $T_{IF} = 4$ K, and an IF isolator at 4 K. The mixer gain and receiver noise temperature are shown as SSB quantities. (See text for further details.)

The dotted circles, $|\rho| = 0.2$ and 0.4 in the figure, indicate regions of embedding admittance within which two possible levels of acceptable performance are obtained – see Table I. Note that the choice of $R_{S,opt}$ as given by eq. (1), and of $Z_{IF} = R_{S,opt}$, are used here to elucidate the bandwidth theory in the following section but are not crucial to it; other values could equally well be used, as, for example, those given in [5].

TABLE I

	$ \rho \leq 0.2$	$ \rho \leq 0.4$
Mixer conversion gain (SSB)	-0.5 \rightarrow -1.5 dB	+0.5 \rightarrow -4.0 dB
Receiver noise temp (SSB)	12 \rightarrow 15 K	12 \rightarrow 20 K
Input return loss	> 8 dB	> 5 dB
Signal-to-image conv. loss	9 \rightarrow 11 dB	9 \rightarrow 13 dB
Output VSWR (R_{out}/Z_{IF})	-17 \rightarrow +6	-5 \rightarrow +3

Equivalent Circuit of the Practical SIS Junction

The simplest equivalent circuit of an SIS junction is shown in Fig. 2(a). Here C is the geometrical capacitance of the junction, and R represents the resistance of the tunneling barrier.

In most applications the connection between the SIS junction and the next element in the RF circuit will have some series inductance, as shown in Fig. 2(b), which might be expected to limit the ultimate bandwidth of the circuit. This inductance could be the inductance of a junction across a waveguide or the series inductance of an array of junctions.

Some SIS mixer designs have used a parallel inductance connected directly across the junction terminals [4,6-11] to resonate the junction capacitance, as in Fig. 2(c). In that case also, the inductance of the connection to the next RF circuit element may restrict the ultimate bandwidth of the mixer.

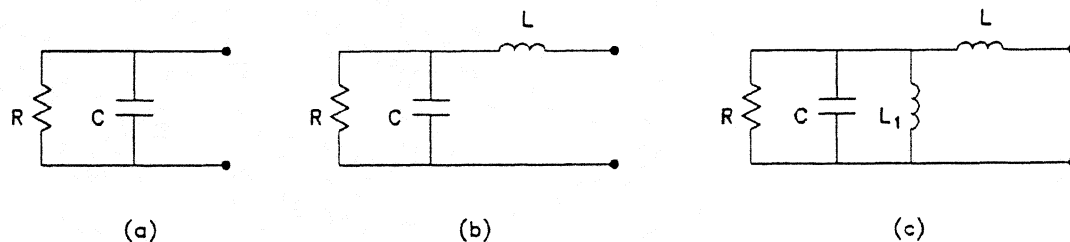


Fig. 2. Equivalent circuits of: (a) a capacitive device, (b) a capacitive device with series inductance, and (c) an inductively tuned device with series inductance.

The theoretical limits on the match-bandwidth of these three circuits will now be examined. It is assumed that each circuit is connected to a resistive source through a lossless matching circuit of arbitrary complexity.

Bode's Theory for the Circuit of Fig. 2(a)

In 1945 Bode at Bell Labs [1] showed that for the simple circuit of Fig. 2(a), connected via a lossless matching network to a resistive source, the reflection coefficient ρ is constrained by the integral equation:

$$\int_0^\infty \ln \left| \frac{1}{\rho(\omega)} \right| \cdot d\omega \leq \frac{\pi}{RC} . \quad (2)$$

This equation is derived solely from the conditions for physical realizability of the lossless matching circuit. Inspection of eq. (2) indicates that the lowest value of the upper bound of $|\rho|$ (ρ_a in Fig. 3) within the frequency band $\omega_1 \leq \omega \leq \omega_2$ is achieved when $|\rho| = \rho_a$ within that band, and $|\rho| = 1$ at all other frequencies. The optimum $|\rho(\omega)|$ therefore coincides with the solid curve in Fig. 3. The integral in eq. (2) is then simply evaluated, giving the well known result:

$$\ln \left[\frac{1}{\rho_{a, \min}} \right] = \frac{\pi}{RC} (\omega_2 - \omega_1) . \quad (3)$$

Analysis of the Circuit of Fig. 2(b)

In 1950, Fano at MIT published a broadband matching theory that applied to a wider range of circuits. For the RCL circuit of Fig. 2(b), physical realizability requires two integral equations to be satisfied:

$$\int_0^\infty \ln \left| \frac{1}{\rho_1} \right| \cdot d\omega = \pi \left(\frac{1}{RC} - \sum \lambda_{rl} \right) , \quad (4)$$

$$\int_0^\infty \omega^2 \ln \left| \frac{1}{\rho_1} \right| \cdot d\omega = -\frac{\pi}{3} \left(\frac{1}{R^3 C^3} - \frac{3}{RLC^2} - \sum \lambda_{rl}^3 \right) . \quad (5)$$

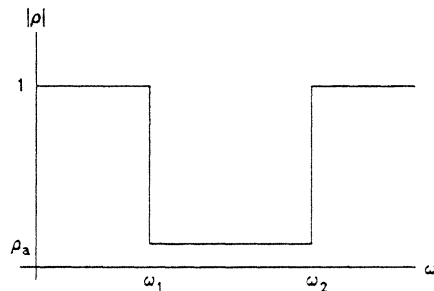


Fig. 3. $|\rho|$ is required to lie below the solid curve. The minimum possible value of ρ_a , in the given frequency band ω_1 and ω_2 , is to be determined.

Here the λ_{ri} are the zeros of the reflection coefficient of the embedding circuit that lie in the right half of the complex frequency (s) plane. Fano solved these equations to find the lowest possible reflection coefficient $|\rho_{a,min}|$ for a given bandwidth, but only for the low-pass case ($\omega_1 = 0$ in Fig. 3). We have extended his analysis to the band-pass case, with the result:

$$K^3 - \frac{6}{bQ_c}K^2 + \left[\frac{12}{b^2} \left(1 + \frac{1}{Q_c^2} \right) + 1 \right] K - \frac{24}{b^3Q_LQ_c^2} = 0, \quad (6)$$

where $K = (2/\pi)\ln(1/|\rho_{a,min}|)$, the fractional bandwidth $b = (\omega_b - \omega_a)/\omega_0$, $Q_c = \omega_0 RC$, and $Q_L = \omega_0 L/R$. Equation (6) is a cubic in K and b , and can be solved analytically.

Analysis of the Circuit of Fig. 2(c)

Here Fano's theory is used with the standard low-pass to band-pass mapping, $\omega \rightarrow \omega_x(\omega/\omega_x - \omega_x/\omega)$, giving

$$K^3 - \frac{6}{bQ_c}K^2 + \left(\frac{12}{b^2Q_c^2} + 4 \right) K - \frac{24}{b^3Q_LQ_c^2} = 0 \quad (7)$$

where, as above, $K = (2/\pi)\ln(1/|\rho_{a,min}|)$, the fractional bandwidth $b = (\omega_2 - \omega_1)/\omega_0$, $Q_c = \omega_0 RC$, and $Q_L = \omega_0 L/R$. Again, this equation is cubic in K and b .

Results and Discussion

For the circuits of Fig. 2, connected to a resistive source through a lossless matching network of arbitrary complexity, the above equations give the minimum possible value of $|\rho|$ that can be obtained over a fractional bandwidth b . In this section we choose the case of $\omega RC = 4$ and examine $|\rho_{a,min}|$ and b for several values of $\omega L/R$.

Results for the RCL circuit of Fig. 2(b) and the RCL₁L circuit of Fig. 2(c) are shown in Figs. 4(a) and (b) (solid curves). Also shown in Fig. 4 are: (i) the Bode limit for the case of $L = 0$ (i.e., Fig. 2(a)) – dashed curve; (ii) $|\rho_{a,min}|$ for a parallel RC circuit tuned by a parallel inductor and connected to a source resistance R_s chosen to maximize the bandwidth for each value of $|\rho_{a,min}|$, but with no additional matching (i.e., Fig. 2(c) with $L = 0$) – dotted curve; and (iii) $|\rho|$ for the RC device of Fig. 2(a) connected directly to a source of resistance R with no matching circuit – short horizontal line.

It is clear from Fig. 4 that for values of L less than some value L_B (whose value depends on the desired value of $|\rho_{a,min}|$ and the other elements of the equivalent circuit) the bandwidth is not limited by L , and the full Bode limit (dashed curve) is theoretically attainable. For such a circuit, the first element of the optimum matching network is an additional series inductance; in this case the inductance in Figs. 2(b) or

(c) can be regarded simply as part of the first element of the optimum matching network that would be used with the RC circuit of Fig. 2(a).

Mixers are not generally matched when connected to their optimum RF embedding impedance. In using these results to determine the maximum bandwidth of a mixer it is appropriate therefore to set the device resistance R equal to the optimum RF source resistance, $R_{S,opt}$, determined from mixer theory. The reflection coefficient of the embedding circuit is thus normalized to $R_{S,opt}$. Equations (3), (6), and (7) are then used to determine the bandwidth within which $|\rho| \leq |\rho_{max}|$, where $|\rho_{max}|$ is also determined from mixer theory to give acceptable receiver performance. The appropriate values of Q_C and Q_L are therefore $\omega R_{S,opt}C$ and $\omega R_{S,opt}/L$, respectively.

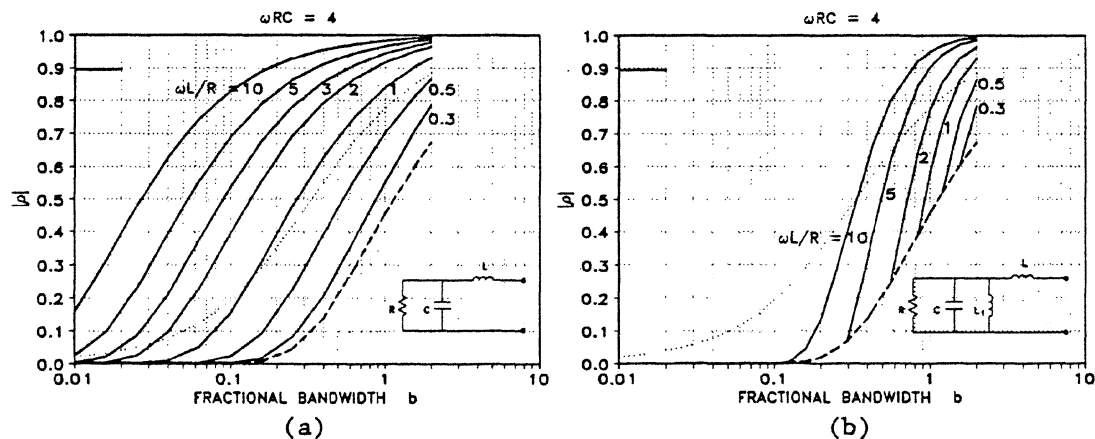


Fig. 4. The lowest upper bound $|\rho_{a,min}|$ on the reflection coefficient vs fractional bandwidth b , with $\omega_0 RC = 4$ and various values of $\omega_0 L/R$. The Bode limit for the simple RC device is indicated by the dashed curves. The dotted curves are for a parallel RC device tuned by a parallel inductor but with no additional matching. The short horizontal lines are for a parallel RC device connected to a source resistance R with no matching.

An Example

It is interesting to see how closely the theoretical bandwidth limit can be approached in a practical SIS mixer with a matching circuit of moderate complexity. As an example, we choose a 250 GHz mixer with a coplanar array of four SIS junctions, shown in Fig. 5, and a matching circuit consisting of a series capacitor and four transmission lines in series, similar, except for the capacitor, to the tuning circuit discussed in [12]. The complete circuit is shown in Fig. 6. Note that the electrical length of the array of junctions is small, so the coplanar line sections can be regarded as lumped inductances, and the equivalent circuit of Fig. 2(b) is applicable.

The capacitor C_A was initially adjusted to make the impedance of the SIS array real at the center frequency. Lines 1, 2, and 3 were set to a quarter wavelength, and the fourth line set to half a wavelength. The

microwave circuit design program MMICAD [13] was then used to optimize the elements of the matching network to give $|\rho| \leq 0.4$ over the widest possible bandwidth.

With the requirement, stated above, that the IF load $Z_{IF} = R_{S,opt}$, $R_{S,opt}$ was chosen for convenience as 50 ohms, corresponding to a normal resistance $R_N = 62$ ohms (from eq. (1)). The quantity $\omega R_N C$ was chosen as 5.0, corresponding to $\omega R_{S,opt} C = 4.0$. The resulting embedding admittance is shown in Fig. 7 on an admittance Smith chart ($(-\rho)$ -plane). The optimized values of the elements in the matching network are: $C_A = 75$ fF, $Z_{01} = 2.48 \Omega$, $Z_{02} = 2.34 \Omega$, $Z_{03} = 16.5 \Omega$, $Z_{04} = 61.2 \Omega$, $l_1 = 0.265 \lambda_{g0}$, $l_2 = 0.246 \lambda_{g0}$, $l_3 = 0.254 \lambda_{g0}$, and $l_4 = 0.516 \lambda_{g0}$.

The magnitude of the reflection coefficient $|\rho| \leq 0.4$ from 206-296 GHz, giving a fractional bandwidth $b = 0.36$. For comparison, the Fano bandwidth limit for the same mixer can be deduced from Fig. 4(a), using $\omega RC = 4$ and $\omega L/R = 0.4$, and is $b_{Fano} = 0.55$. The Bode limit for SIS junctions with $\omega RC = 4$ is $b_{Bode} = 0.85$. The bandwidth for an inductively shunted junction (i.e., with a parallel tuning inductor and no other matching elements) and the same value of ωRC , is $b_{isj} = 0.24$. These numbers are listed in Table II.

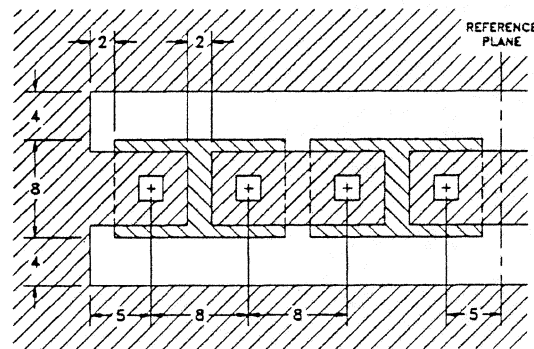


Fig. 5. Series array of four SIS junctions in coplanar waveguide. The substrate is fused quartz, with $\epsilon_r = 3.8$. Dimensions are in μm .

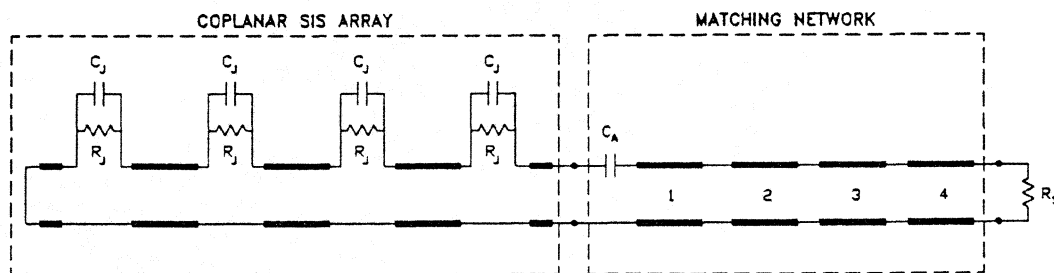


Fig. 6. Circuit of the 250 GHz SIS mixer used in the example. The matching network contains a capacitor C_A in series with four transmission line matching sections. The source resistance $R_S = 50 \Omega$.

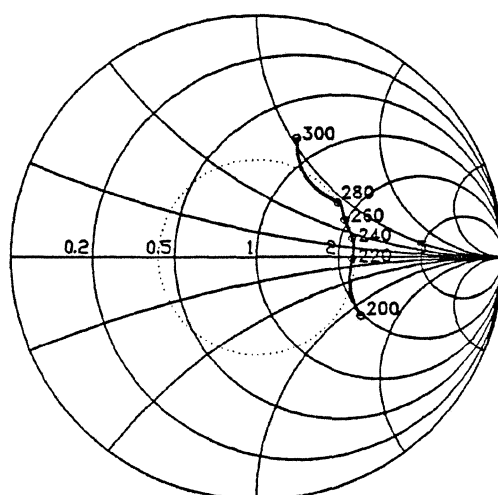


Fig. 7. Embedding admittance of the SIS mixer in Fig. 6 after optimizing the matching network to give the widest possible bandwidth with $|\rho| \leq 0.4$ (dotted circle). Admittances are normalized to the optimum source conductance of the array $1/R_{s,opt}$.

TABLE II

Circuit	b
Bode limit for parallel RC	85%
Fano limit with series L	55%
Circuit of Fig. 6	36%
RC with parallel L tuning	24%

Acknowledgements

The author would like to thank M. J. Feldman, J. Granlund, S.-K. Pan, and M. W. Pospieszalski for their helpful discussions and comments during the course of this work.

References

- [1] H. W. Bode, "Network analysis and feedback amplifier design," New York: Van Nostrand, 1945.
- [2] R. M. Fano, "Theoretical limitations on the broadband matching of arbitrary impedances," *J. Franklin Inst.*, vol. 249, pp. 57-83 and 139-155, Jan. and Feb. 1950.

- [3] A. R. Kerr and S.-K. Pan, "Some recent developments in the design of SIS mixers," *Int. J. Infrared Millimeter Waves*, vol. 11, no. 10, pp. 1169-1187, Oct. 1990.
- [4] A. R. Kerr, S.-K. Pan, A. W. Lichtenberger and D. M. Lea, "Progress on tunerless SIS mixers for the 200-300 GHz band," *IEEE Microwave and Guided Wave Letters*, vol. 2, no. 11, pp. 454-456, Nov. 1992.
- [5] Q. Ke and M. J. Feldman, "Optimum source conductance for high frequency superconducting quasi-particle receivers," *IEEE Trans. Microwave Theory Tech.*, vol. MTT-41, no. 4, pp. 600-604, April 1993.
- [6] A. R. Kerr, S.-K. Pan, and M. J. Feldman, "Integrated tuning elements for SIS mixers," *Int. J. Infrared Millimeter Waves*, vol. 9, no. 2, pp. 203-212, Feb. 1988. This paper was presented at the International Superconductivity Electronics Conference, Tokyo, Japan, Aug. 1987.
- [7] A. R. Kerr, S.-K. Pan, S. Whiteley, M. Radparvar, and S. Faris, "A fully integrated SIS mixer for 75-110 GHz," *IEEE Int. Microwave Symp. Digest*, pp. 851-854, May 1990.
- [8] F. Schafer, E. Kreysa, T. Lehnert, and K. H. Gundlach, "A planar SIS receiver with log-periodic antenna for submillimeter waves," *Proceedings of the Fourth International Symposium on Space Terahertz Technology*, pp. 661-665, March 1993.
- [9] A. Karpov, M. Carter, B. Lazareff, M. Voss, D. Billon-Peron, K. H. Gundlach, "Wideband fixed tuned and tuneable SIS mixers for 230 GHz and 345 GHz receivers," *Proceedings of the Fourth International Symposium on Space Terahertz Technology*, p. 11, March 1993.
- [10] W. R. McGrath, P. Febvre, P. Batelaan, H. G. LeDuc, B. Bumble, M. A. Frerking, and J. Hernichel, "A submillimeter wave SIS receiver for 547 GHz," *Proceedings of the Fourth International Symposium on Space Terahertz Technology*, pp. 50-58, March 1993.
- [11] J. Mees, A. Skalare, M. M. T. M. Dierichs, H. van der Stadt, R. A. Panhuyzen, Th. de Graauw, and T. M. Klapwijk, "Double dipole antenna SIS receivers at frequencies above 500 GHz," *Proceedings of the Fourth International Symposium on Space Terahertz Technology*, pp. 59-71, March 1993.
- [12] G. Pance and M. J. Wengler, "Integrated tuning elements for millimeter and submillimeter SIS mixers," *IEEE International Microwave Symposium Digest*, pp. 337-340, June 1992.
- [13] MMICAD is a microwave integrated circuit analysis and optimization program, and is a product of Optotek, Ltd., Ontario, Canada K2K-2A9.

JOSEPHSON NOISE IN SIS RECEIVERS

Brigitte Leridon

DEMIRM

Observatoire de Paris - 61, avenue de l'Observatoire

75014 Paris

Ecole Normale Supérieure - 24, rue Lhomond

75005 Paris

France

Abstract: The tunneling of Cooper pairs through the barrier of a superconductor-insulator-superconductor (SIS) junction (Josephson effect) is a major drawback for the operation of an SIS mixer (generation of instabilities and noise). For frequencies lower than 200 GHz, the junction capacitance is usually sufficient to shunt the rf Josephson currents. At higher frequencies however, an external magnetic field needs be used to suppress this effect.

I present here a calculation of the noise equivalent power generated by the high frequency Josephson currents fluctuating at the signal and image ports and mixed to the output, under the assumption that the Josephson currents are sufficiently small to allow stable bias. In this calculation, possible additional losses due to Josephson effects are neglected.

I - Introduction

In the Quantum Theory of Mixing developed by J. Tucker [1], the Josephson tunneling of Cooper pairs through the junction barrier is neglected. The Josephson currents are considered either shunted by the junction intrinsic capacitance or suppressed by external magnetic field.

This assumption is justified at detection frequencies lower than 200 GHz with no magnetic field applied, and at higher frequencies

each time a proper magnetic cancellation of the Josephson current is available.

If not suppressed, the Josephson currents are the source of drastic instabilities such as the drop-back effect, when non-zero voltage bias is not possible. In the better case, they are accountable for supplementary noise in the output power [2]. See figure 1 and 2 [10].

In experimental situations however, an intermediate situation is very often encountered: the Josephson currents are sufficiently small to allow stable bias but there is some residual Josephson current on the I-V curve at zero voltage. This is the case, for instance, in SIS junction arrays with small dishomogeneities between the junctions, and in space embarked devices where there is no possibility to adjust the current in the superconducting coils [3]. This is the reason why having an estimation of the Josephson noise mixed into the output of the receiver in this particular case is of great practical interest.

II - General formulation of pair and quasiparticle currents for the evaluation of mixer performances

The more general formulation of tunneling currents through an SIS junction has been derived by Werthamer [4] and includes contributions of the quasiparticle and pair currents:

$$\mathfrak{I}(t) = \mathfrak{I}_m \int_{-\infty}^{+\infty} \int_{-\infty}^{+\infty} d\omega d\omega' \left\{ W(\omega) W^*(\omega') e^{-i(\omega - \omega')t} j_1(\omega' + \frac{1}{2}\omega_0) + W(\omega) W(\omega') e^{-i(\omega + \omega')t + i\varphi + i\alpha} j_2(\omega' + \frac{1}{2}\omega_0) \right\}$$

where

$$\omega_0 = 2eV_0/\hbar$$

j_1 and j_2 are the quasiparticle and pair current amplitudes, $W(\omega)$ is related to the voltage impressed across the junction and is given by

$$\int_{-\infty}^{+\infty} d\omega W(\omega) e^{-i\omega t} = \exp \left\{ -i(e/h) \int_{-\infty}^t dt' \int_{-\infty}^{+\infty} dx E_x(x, t') \right\}$$

In the quantum theory of mixing, only the first term, i.e. the term related to single particle tunneling is used. Due to the expression of the voltage bias across the junction, the function $W(\omega)$ is identified to

$$W(\omega) = \sum_{n=-\infty}^{+\infty} J_n(\alpha) \delta(\omega - n\omega_0)$$

where

$$\alpha = eV_0/h\omega$$

$$V(t) = V_0 + V_\omega \cos \omega_0 t$$

These expressions enable to calculate the I-V characteristic of the junction in the presence of the local oscillator drive from the I-V characteristic without radiation applied. Including experimental parameters such as the source and load admittances, the small signal admittance matrix, the gain and the quasiparticle shot noise can be derived.

The expression of the quasiparticle shot noise in terms of the mixer noise temperature is given by

$$kT_M = \frac{1}{4G_S |\lambda_0|^2} \sum_{m,m'} \lambda_{0m} \lambda_{0m'}^* H_{mm'}$$

where $H_{mm'}$ is the quasiparticle current correlation matrix and the λ_{0m} are related to the small signal impedance matrix coefficients

$$\lambda_{0m} = Z_{0m}/Z_{00}$$

The quasiparticle current correlation matrix can be expressed in terms of the power spectral density of the quasiparticle current fluctuations which is related to the quasiparticle response function via a fluctuation-dissipation relation. This leads to the following expression [1-5]

$$H_{mm'} = e \sum_{n,n'=-\infty}^{+\infty} J_n(\alpha) J_{n'}(\alpha) \delta_{m-m',n'-n} \times \\ \left(\coth \left[\frac{\beta}{2} (eV_0 + n'h\omega_{l0} + h\omega_{m'}) \right] I_{qp} \left(V_0 + \frac{n'h\omega_{l0}}{e} + \frac{h\omega_{m'}}{e} \right) + \coth \left[\frac{\beta}{2} (eV_0 + nh\omega_{l0} - h\omega_{m'}) \right] I_{qp} \left(V_0 + \frac{nh\omega_{l0}}{e} - \frac{h\omega_{m'}}{e} \right) \right)$$

Using these equations it is possible to compute the mixer noise temperature for a given experimental situation. The thermal noise due to the physical temperature of the signal and image ports can be added without difficulty, but it is not the purpose here, since we want to compare an estimation of the Josephson noise to the quasiparticle shot noise.

III - Calculation of the Josephson noise

Following a similar approach, it is possible to express the pair current correlation matrix in terms of the pair (and quasiparticle-pair) current response function I_{pair} and $I_{qp-pair}$. See figure 3.

A complete expression for the quasiparticle and pair mixing process is given by Shen [5]. However his equations can not be solved analytically because of the hysteretic behavior of the junction.

The pair current fluctuations arise from the interaction of the pair current with the blackbody radiation field of the junction. The power spectrum of these fluctuations has been derived by Rogovin and Scalapino in the case of linear first-order process [6].

$$P_{I_{\text{pair}}}(\omega) = \frac{e}{\pi} \left\{ I_{\text{pair}}(V_0 + \hbar\omega/2e) \coth\left(\beta(eV_0 + \hbar\omega)/2\right) \right. \\ \left. + I_{\text{pair}}(V_0 - \hbar\omega/2e) \coth\left(\beta(eV_0 - \hbar\omega)/2\right) \right\}$$

$$P_{I_{\text{qp-pair}}}(\omega) = \frac{e}{\pi} \left\{ I_{\text{qp-pair}}(V_0 + \hbar\omega/2e) \coth\left(\beta(eV_0 + \hbar\omega)/2\right) \right. \\ \left. + I_{\text{qp-pair}}(V_0 - \hbar\omega/2e) \coth\left(\beta(eV_0 - \hbar\omega)/2\right) \right\}$$

These expressions are used to calculate $H_{mm'}$ with the following approximations.

The voltage sweep impressed accross the junction should be changed by the presence of Josephson currents and a rigorous derivation should include self consistent derivation of this voltage [7], hence the $W(\omega)$ functions should be changed from the simple quasiparticle mixer. The above-made assumption that the Josephson currents remain small allows to keep the same expression for the $W(\omega)$ functions since we state that the voltage bias remains stable. The formula giving the mixer noise temperature for quasiparticle, where the normalised impedances λ_{0m} are assumed to remain unchanged from the zero-Josephson effect case, is then used.

The physical interpretation for doing such, is that there is a possibility, frequently encountered in practice, to operate a receiver even in the case of non totally suppressed Josephson effect, without any strong modification of the mixer's behavior but with additional noise. Of course this calculation is expected to give an order of magnitude of the Josephson noise only in the case of small currents.

IV - Computer simulation results

The Josephson noise is calculated for a junction with normal resistance $R_n = 60 \, \Omega$ and gap voltage $V_g = 2.8 \, \text{mV}$, for a local oscillator frequency of 540 GHz. In the results presented below, the shunting effect of the junction capacitance is not considered because we assume that the matching conditions are optimized at the signal and image frequencies.

	$V_0 = 1.12 \, \text{mV}$ (1 st Shapiro step)	$V_0 = 2.23 \, \text{mV}$ (2 nd Shapiro step)
TM (quasiparticle)	110 K (SSB)	33 K (SSB)
TM (1% Jos. eff.)	32 K (SSB)	40 K (SSB)
TM (5% Jos. eff.)	160 K (SSB)	200 K (SSB)

V - Interpretation of excess noise in arrays

The experimental mixer noise temperature in arrays is always found higher than in theoretical predictions. Small surface discrepancies could slightly change the magnetic conditions from one junction to the other and some residual Josephson current in one junction could be accountable for the excess noise.

VI- Interpretation of excess shot noise in non-irradiated SIS junctions

Dubash et al. [8] measured shot noise in SIS junctions with no radiation applied. See figure 4.

For simple quasiparticle shot noise, the noise power as a function of bias voltage should be directly proportional to the I-V curve. However, they found an important excess noise at the gap voltage, sensitive to magnetic field.

Taking into account the pair shot noise, shown to be proportional to the pair response function plotted on figure 3, the excess noise is perfectly understandable. However, the junction capacitance has to be considered here, as it lowers the sub-gap Josephson currents [7] and decreases significantly the Josephson noise for voltages smaller than the gap voltage.

VII - Conclusion

This way of calculating the contribution of Josephson currents to the receiver noise temperature is really a first step, as many approximations have been made. The quantitative results, however, prove very interesting as they tend to demonstrate that the occurrence of even small Josephson currents rises significantly the total mixer noise temperature.

This enables to attribute the excess noise in arrays to Josephson noise, and probably also some excess noise in single-junction detectors.

The role of the capacitance of the junction has not been detailed here, since we assumed that it was shunted by some integrated tuning structures, but the twofold role of the matching structures has to be investigated in details.

Further investigations would also include the evaluation of additional losses due to Josephson currents, or maybe the possibility of additional gain as observed in ref [2].

Acknowledgments:

Thanks are to P. Febvre for collaboration to the computational work and to P.J. Encrenaz and G. Beaudin for continued support.

The author also acknowledges Matra Marconi Space for financial support.

References:

- [1] J. R. Tucker and M. J. Feldman
Rev. Mod. Phys. 57, n° 4, Oct. 1985
- [2] M. J. Wengler, N. B. Dudash, G. Pance and R. E. Miller
IEEE Trans. on Microwave Th. and Techn. , 40, n° 5,
May 1992
- [3] B. Leridon and R. Maoli
J. Appl. Phys., vol. 74, n° 9, Nov. 1993
- [4] N. R. Werthamer
Phys. Rev. 147, n° 1, July 1966
- [5] T.-M. Shen
IEEE J. of Quantum Electron. QE-17, n° 7, July 1981
- [6] D. Rogovin and D. J. Scalapino
Ann. of Phys. 86, pp. 1-90, 1974
- [7] D. G. McDonald, E. G. Johnson and R. E. Harris
Phys. Rev. B, vol. 13, n° 3, Feb. 1976
- [8] N. B. Dubash, G. Pance and M. J. Wengler
Fourth Int. Symp. on Sp. Terahertz Technol., p. 19,
March 1993
N. B. Dubash, G. Pance and M. J. Wengler
IEEE-MTT, March 1994 (in press)
- [9] P. Febvre, W. R. McGrath, P. Batelaan, B. Bumble,
H. G. LeDuc , S. George, P. Feautrier
To appear in: Int. J. of Infrar. and Millim. Wav., vol. 15
n° 6, June 1994

- [10] P. Febvre, W. R. McGrath, B. Bumble, and H. G. LeDuc, unpublished data.

Figure caption:

Figure 1: I-V characteristic of a two-junction array, with 380 GHz radiation applied, with Josephson current not suppressed (solid line) and suppressed by external magnetic field (dashed line).

(After Febvre et al., 3rd Int. Symp. on Space Terahertz Technol., March 1992)

Figure 2: Receiver output power (hot load) for 540 GHz radiation with: a) $I_{\text{coils}} = 389$ mA (Josephson current well suppressed), b) $I_{\text{coils}} = 361$ mA, c) $I_{\text{coils}} = 513$ mA, d) $I_{\text{coils}} = 458$ mA. After Febvre et al. [10]. Junction tests reported in [9].

Figure 3: Normalized pair (solid line), quasiparticle-pair (dotted line) and sum (dashed line) response functions as derived in ref. [6]

Figure 4: Shot noise measured in SIS junction. After Dubash et al. [8].

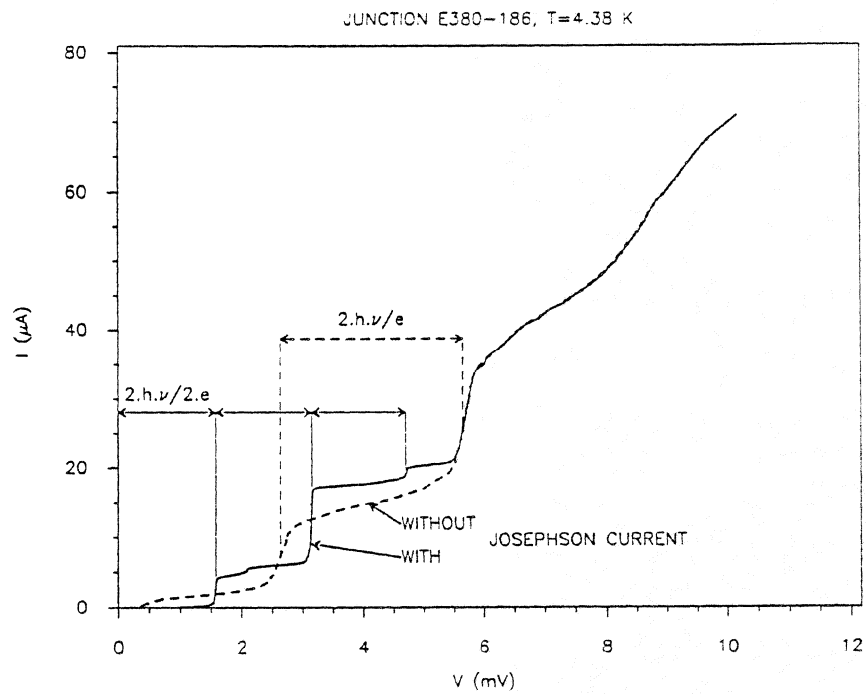


Figure 1

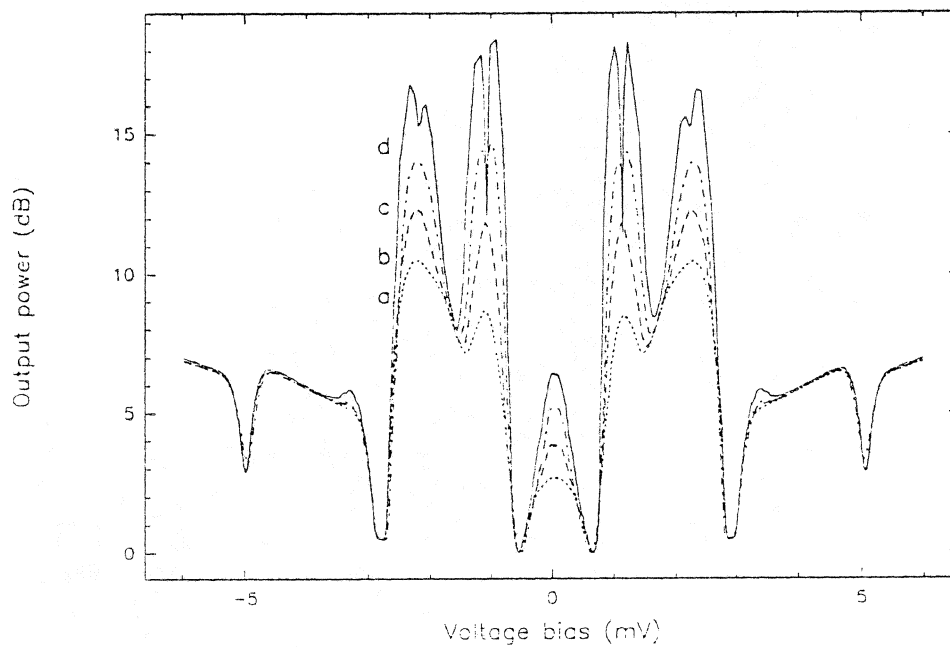


Figure 2

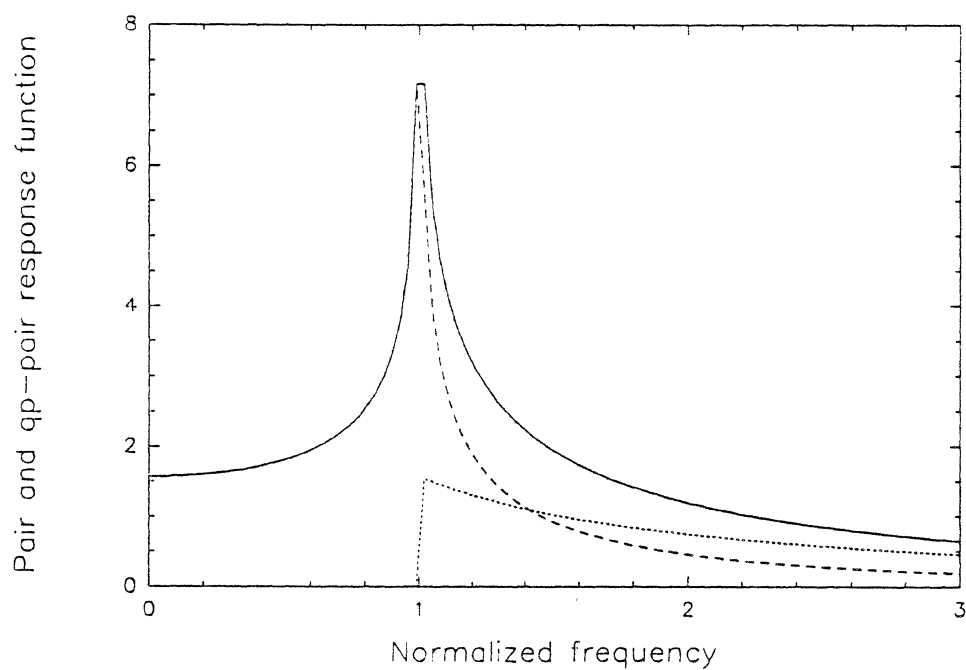


Figure 3

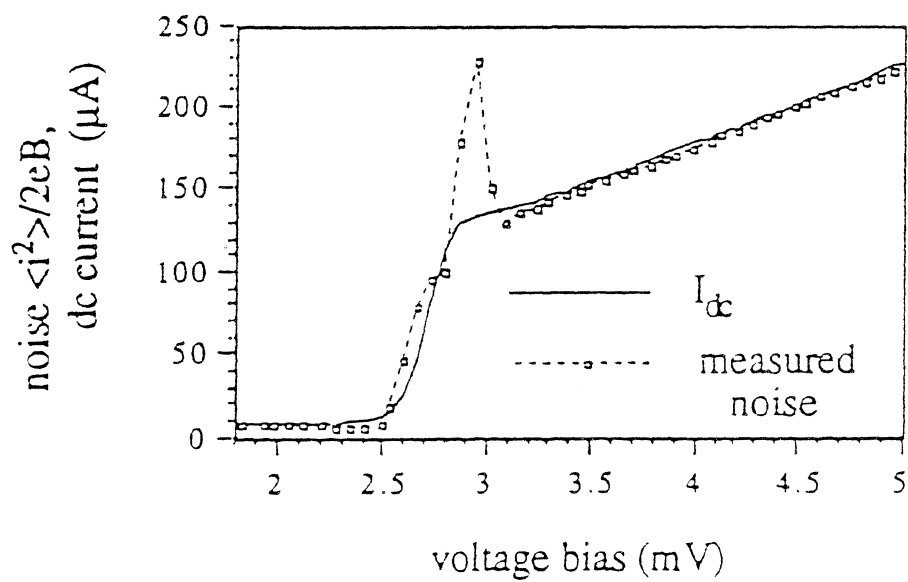


Figure 4

SIGNAL AND IMAGE PORT OUTPUT POWER IN THE QUANTUM THEORY OF MIXING

Qing Ke and M. J. Feldman

Department of Electrical Engineering
University of Rochester, Rochester, NY 14627

ABSTRACT

The quantum theory of mixing is essential for the *interpretation* of experimental superconducting quasiparticle (SIS) mixers. When the bias and tuning parameters are known, the theory is quite successful at predicting the mixer performance, gain and noise temperature. However, the theory usually predicts much higher conversion gain for some other set of bias and tuning parameters, and this is not seen in experiment. Thus the theory is less useful for engineering *design* of SIS mixers. We believe we have resolved this longstanding discrepancy. We find there are two distinct "optimum" operation modes for ideal SIS mixers. The high gain mode predicted by the theory will not be accessible in real experiments. To understand this, we present the equations of a DSB SIS mixer in a novel form, in terms of the complex-plane phase angle between the amplitude modulation input admittance vector and the local oscillator input admittance vector.

INTRODUCTION

Classical mixer theory does not apply to heterodyne mixers operating at a frequency ω high enough that the voltage scale of the resistive nonlinearity is smaller than $\hbar\omega/e$. The quantum theory of mixing [1] developed by J.R. Tucker must be used. Tucker's theory is very successful in describing the superconductor-insulator-superconductor (SIS) quasiparticle mixer. In particular, if the operating parameters of an optimized mixer can be independently determined, the theory predicts the IF conversion gain quite precisely [2,3].

Yet there is a major discrepancy between the theory's predictions and the experiments. From the earliest attempts [4], the best SIS mixers have had low to moderate conversion gain (as high as 10 dB in two experiments [5,6]), but *optimized* computer fits to these experiments often predict very high to infinite gain. In fact, it appears that for some set of bias and tuning parameters the quantum theory of mixing always predicts considerably higher conversion gain for high quality SIS junctions than can actually be achieved in experiment. This is true even when harmonic effects and saturation are taken into account.

One clear early example of this is Ref. [7]. There the highest conversion gain achieved was 4.3 dB, and the theory reasonably predicted that value using measured operating parameters. However, the theory also predicted conversion gain higher than 20 dB for a different set of operating parameters. In this experiment the junction capacitance was large, so harmonic effects could be safely ignored.

We believe we have resolved this longstanding mystery. We find there are two distinct and disjoint "optimum" operation modes for ideal SIS mixers which are predicted by the quantum theory of mixing. One mode has very high or infinite IF conversion gain, and the "reflected" power (the signal reflection gain and the signal-to-image conversion gain) is extremely high as well. The other mode has moderate IF conversion gain, but the reflection gains tend to be very small. The high reflected power implies that the high gain mode will not be accessible in real experiments. Therefore, eliminating the high gain solution in computer simulations should give much better agreement with experiments.

CALCULATIONS

In a typical experiment the gain of an SIS mixer is maximized by varying the dc bias, the LO power, the embedding impedances, etc. When this procedure is attempted in calculations, however, the quantum theory of mixing predicts infinite gain for high quality SIS junctions over a wide range of parameter values. There is no unique optimum bias point. To avoid this difficulty, and to make our calculation as realistic as possible, we take as our figure of merit not the gain but the minimum value of the SSB (single sideband) receiver noise temperature

$$T_R = T_M + T_{IF}/\mathcal{G}_{IF}. \quad (1)$$

Thus our calculation involves a trade-off between minimizing the mixer noise temperature T_M and maximizing the mixer conversion gain \mathcal{G}_{IF} , which is mediated by the noise temperature of the IF amplifier T_{IF} .

The equations used to calculate T_R are taken from Ref. [1]. Only a few are presented here. We consider a DSB (double sideband: equal signal and image termination) mixer in the three-frequency low-IF approximation, which should be a fairly good representation of most well-designed experimental mixers. For a DSB mixer the thermal noise from the image termination does not affect receiver optimization, so for convenience we assume zero physical temperature and the thermal noise simply reduces to the quantum noise temperature of the mixer, $\hbar\omega/2k$. We ignore the thermal noise from the IF termination which is reflected from the mixer back into the IF amplifier, although this can be an important factor for real SIS receivers. We ignore any interference from the Josephson effect.

The standard SSB IF conversion gain of a DSB SIS mixer (Ref. [1], Eq. 4.74) can be written in the novel form:

$$\mathcal{G}_{IF} = \frac{G_L G_{01}^2}{(G_{00} + G_L)^2} \frac{4G_s}{|Y_s + Y'_s| \cos\theta|^2}, \quad (2)$$

$$Y'_s = G'_s + jB'_s = G_{11} + G_{1-1} - \frac{2G_{01}G_{10}}{G_{00} + G_L} + j(B_{11} + B_{1-1} - \frac{2G_{01}B_{10}}{G_{00} + G_L}). \quad (3)$$

\mathcal{G}_{IF} depends upon $Y_s = G_s + jB_s$, the source admittance seen by the SIS junction at the signal and the image frequencies, and upon the load conductance G_L which represents the conductance of the IF amplifier circuitry as seen by the junction. The explicit dependence of \mathcal{G}_{IF} upon Y_s in Eq. 2 is given by a simple impedance matching formula which has its maximum at $Y_s = |G'_s| - jB'_s$. Note that G'_s , which can be negative, is not the input conductance of our mixer. (Y'_s is the input admittance in the simple amplitude modulation model of the SIS mixer, in which the signal results from an amplitude modulation of the LO, as described in Ref. [1], Sec. III.B.) The input admittance of the mixer at the local oscillator frequency ω is

$$Y_{LO}^o \equiv I_{LO}/V_{LO} = G_{LO}^o + jB_{LO}^o = G_{11} - G_{1-1} + j(B_{11} - B_{1-1}), \quad (4)$$

where I_{LO} is the (complex) amplitude of the current and V_{LO} is the (real) amplitude of the voltage across the junction at frequency ω . Of course $G_{LO}^o > 0$. \mathcal{G}_{IF} also depends upon Y_s , implicitly, through the angle θ . θ is the relative phase angle between the vectors $(Y_s + Y'_s)$ and

$(Y_s + Y_{LO}^\circ)$ in the complex plane. Thus $|(Y_s + Y_s')| \cos \theta$ is the projection of the vector $(Y_s + Y_s')$ in the direction of $(Y_s + Y_{LO}^\circ)$.

Equations 2 - 4 are expressed in terms of the elements of the small-signal admittance matrix [1], $Y_{ij} = G_{ij} + jB_{ij}$. Each G_{ij} is evaluated as an infinite sum over index n of the currents $I_n \equiv I_{dc}(V_n)$ weighted by a combination of Bessel functions of argument $\alpha \equiv eV_{LO}/\hbar\omega$, where $I_{dc}(V)$ is the unmodulated dc I-V characteristic of the SIS junction, $V_n \equiv V_0 + n\hbar\omega/e$, and V_0 is the dc bias voltage.

We pay close attention to the reflected power. The signal reflection gain and the signal-to-image conversion gain of a DSB mixer in the three-frequency low-IF approximation are respectively:

$$\mathcal{G}_S = \frac{1}{4\cos^2\theta} \left| \frac{Y_s - Y_s'^*}{Y_s + Y_s'} + \frac{Y_s - Y_{LO}^{\circ*}}{Y_s + Y_{LO}^\circ} \right|^2, \quad (5)$$

$$\mathcal{G}_I = \frac{1}{4\cos^2\theta} \left| \frac{Y_s^* - Y_s'}{Y_s + Y_s'} - \frac{Y_s^* - Y_{LO}^\circ}{Y_s + Y_{LO}^\circ} \right|^2. \quad (6)$$

Note that the explicit dependence of \mathcal{G}_S and \mathcal{G}_I upon Y_s is given by the interference of two voltage reflection coefficients. Although high IF conversion gain might seem advantageous in the context of Eq. 1, when \mathcal{G}_{IF} is infinite both \mathcal{G}_S and \mathcal{G}_I (and in fact the output power at all sideband frequencies [8]) are infinite as well, clearly an unstable situation. In this paper we will show that the IF conversion gain can be sizable even if an SIS mixer is operated far from instability, with very small reflected power.

There has been little appreciation of \mathcal{G}_S and \mathcal{G}_I in the literature. An exception is Ref. [9], which enforced an approximate signal input impedance match. But a preliminary version of the present paper [10] is the first to mention the signal-to-image conversion gain of an SIS mixer in any context.

To simplify our calculations we will ignore all reactances: in Eqs. 2 - 6 each admittance Y is replaced by its conductance G , and $\cos \theta = 1$. This entails the controversial assumption that the quantum susceptance has no significant effect. It has recently been argued that the quantum susceptance is a central element of the behavior of SIS mixers [11]. Nevertheless, we believe that this nonlinear reactance has little effect on the performance of an optimized SIS receiver except insofar as it affects LO impedance matching. This question will be further addressed below.

We calculated the minimum noise temperature of the SIS receiver at each frequency. At each frequency the optimum values of G_s , V_0 , and α were calculated given discrete values for the remaining parameters and an assumed SIS junction I-V curve. We have performed these calculations for a wide range of parameters, but only a few illustrative results are presented here. We normalize voltages to the energy gap voltage V_g , conductances to the normal state resistance R_N , and frequencies to the energy gap frequency $\omega_g \equiv eV_g/\hbar$.

RESULTS

The dotted curve of Fig. 1 shows the minimum theoretical noise temperature of an SIS receiver for frequencies up to $\omega = 0.2 \omega_g$, using an SIS I-V curve corresponding to the best experimental junctions (see Ref. [12], Fig. 1, "sharp"), with $G_L = 0.3/R_N$, $T_{IF} = 3$ K, and $V_g = 3$ mV. The smoothness of this curve hides the fact that it includes two distinct and disjoint types of behavior. The thick lines in Fig. 2 represent the three corresponding small-signal gains. It is seen that \mathcal{G}_{IF} is extremely high, and \mathcal{G}_S and \mathcal{G}_I are even higher, for normalized frequencies between 0.03 and 0.12. For other frequencies \mathcal{G}_{IF} is more moderate but still sizable, while \mathcal{G}_S and \mathcal{G}_I are quite small.

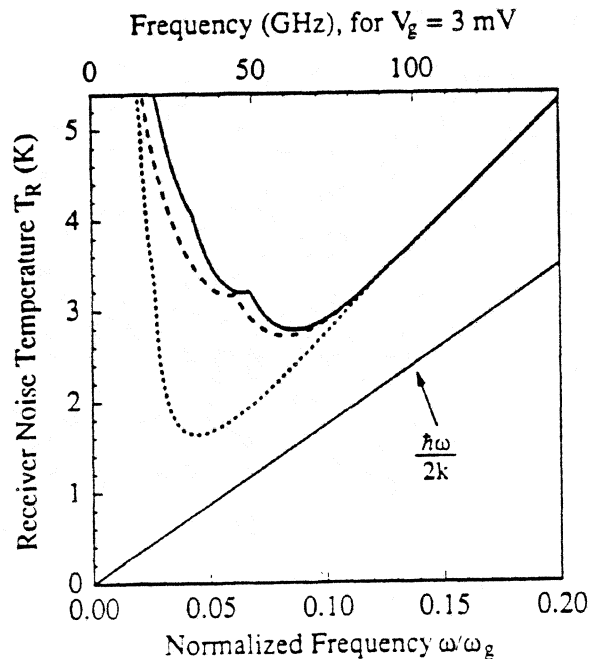


Fig. 1. The SSB noise temperature of a DSB SIS receiver optimized at each frequency. The computation assumes a sharp I-V curve, $G_L = 0.3/R_N$, $T_{IF} = 3$ K, and $V_g = 3$ mV. The dotted curve is the universal minimum of T_R , the dashed curve is calculated with the constraint $G'_s > 0$, and the solid curve is calculated with the constraint $\mathcal{G}_I \leq 1/4$.

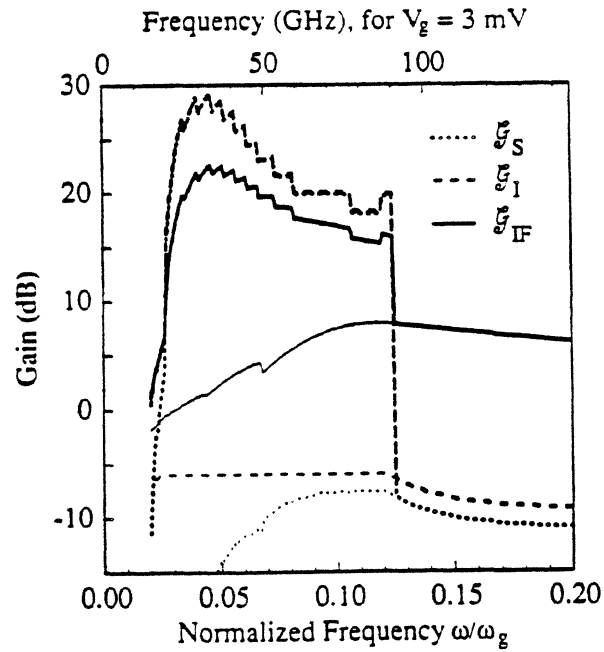


Fig. 2. The thick lines represent the IF conversion gain \mathcal{G}_{IF} , the signal reflection gain \mathcal{G}_S , and the signal-to-image conversion gain \mathcal{G}_I , which correspond to the dotted curve of Fig. 1. The thin lines represent the gains which correspond to the solid curve of Fig. 1.

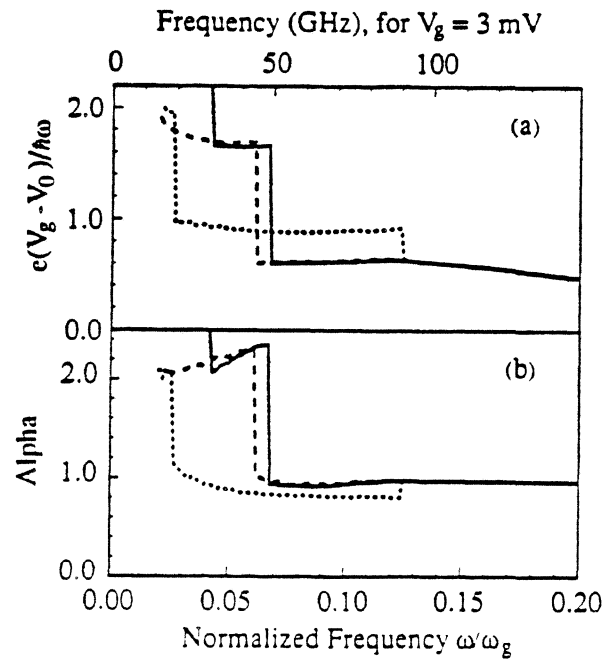


Fig. 3. Bias voltages for the optimized receiver of Fig. 1. a) The dc bias voltage presented in units of "photon step number" (see Eq. 7), b) The normalized LO voltage amplitude $\alpha \equiv eV_{LO}/\hbar\omega$. The three line styles correspond to those of Fig. 1.

We performed the same receiver optimization calculations subject to the constraint $\mathcal{G}_I \leq 1/4$. In other words, we eliminate all results giving significant output power at the image frequency. This results in the solid curve of Fig. 1 and the thin lines in Fig. 2. It is clear that the reflected power constraint eliminates the high gain operating mode and so the moderate gain mode extends continuously across the entire frequency region.

This illustrates a general feature of our results: For a wide range of parameter values there are two distinct minima for T_R corresponding to two distinct receiver operation modes. One mode has very high IF conversion gain, and the reflected power is very high as well. The other has moderate IF conversion gain, but the reflected power tends to be very small.

Figures 3 and 4 show that the bias and tuning parameters are very different for the two modes. As a measure of the dc bias voltage V_0 we define the non-integer generalization of the photon step number,

$$N_{\text{step}} \equiv e(V_g - V_0)/\hbar\omega, \quad (7)$$

so that $0 < N_{\text{step}} < 1$ can be called the "first photon step," etc. Fig. 3a shows that the moderate gain mode is well approximated by $N_{\text{step}} \approx 0.6$ on the first photon step. At lower frequencies the optimum bias point moves to the second photon step and the moderate gain mode has $N_{\text{step}} \approx 1.6$. This behavior continues to lower frequency and is in fact a general feature of our results: The optimum dc bias voltage for the moderate gain operating mode (for low frequency) is always slightly below the middle of a photon step. For the high gain mode, however, $N_{\text{step}} \geq 0.9$ on the first photon step and 1.9 on the second photon step.

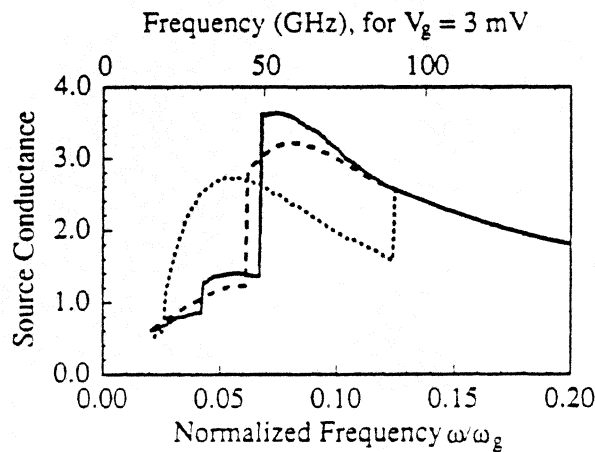


Fig. 4. The normalized source conductance $G_s R_N$ for the optimized receiver of Fig. 1. The three line styles correspond to those of Fig. 1.

Again, this is a general feature of our results: The optimum dc bias voltage for the high gain mode (unlike most experiments) is always at the beginning of a photon step. Fig. 3b shows that the frequency dependence of α is quite similar to that of N_{step} .

The source conductance G_s for minimum noise temperatures is also very different for the two modes (Fig. 4). For the high gain mode G_s is almost exactly equal to $-G'_s$, as required by Eq. 2. The G_s for the moderate gain mode, however, has a very different character; it is quite close to the value which minimizes the shot noise, and this in turn follows closely the LO input conductance G_{LO}^o [12]. Note that the optimum source conductance is in every case experimentally convenient: G_s is roughly of order $1/R_N$.

It is instructive to consider the mixer output conductance, G_L^o , of our optimized receiver (Fig. 5). The high gain mode generally but not exclusively has negative G_L^o . The moderate gain mode always occurs with positive G_L^o . Note that in the lower half of the frequency range of Fig. 5 the output impedance match is surprisingly good.

An important general feature of our results is that the moderate gain mode is quite insensitive to the level of reflected power allowed. In fact, for the parameters used for Figs. 1 to 5, *any* reasonable constraint on the maximum allowed \mathcal{G}_I , from 0.1 to 10, serves to eliminate the high gain mode but has very little effect on the moderate gain mode. This is persuasive evidence that these two operating modes are indeed distinct. [This explains why the $G'_s > 0$ -constrained case (dashed lines in Figs. 1, 3, 4, and 5) lies quite close to the reflected-power-constrained case (solid lines).]

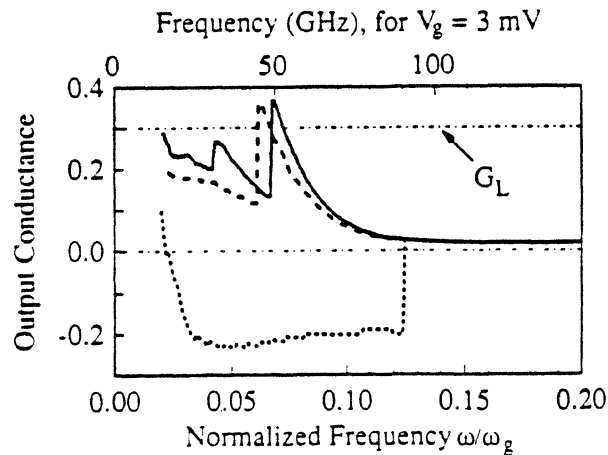


Fig. 5. The normalized output conductance $G_L^o R_N$ for the optimized receiver of Fig. 1. The three line styles correspond to those of Fig. 1. The load conductance $G_L = 0.3/R_N$ is also shown.

The behavior we have described is quite widespread. In fact, if we had chosen a larger value for T_{IF} , if we had assumed some leakage current, if we had included the quantum susceptance in generating Figs. 1 to 5, the high gain mode would predominate over a much wider frequency range.

DISCUSSION

We understand our results in the following way. T_M and \mathcal{G}_{IF} in Eq. 1 are in general slowly varying functions of their various parameters. The exception is that when G'_S is negative the quantity $G_S + G'_S$ can go to zero, giving analytically infinite \mathcal{G}_{IF} in Eq. 2. Near exact cancellation occurs over only a small region of parameter space. Thus we can picture a display of T_R in a multi-parameter space as having a rather sharp minimum near $G_S + G'_S = 0$ and more gradual behavior, including a broad minimum, elsewhere. These two minima correspond to our two operating modes. Near $G_S + G'_S = 0$ both \mathcal{G}_S and \mathcal{G}_I will be very large (cf. Eqs. 5 and 6). If the vicinity of $G_S + G'_S = 0$ is forbidden (by constraining \mathcal{G}_I), the remaining minimum will be quite insensitive to the operating parameters.

This analysis supports our conclusion that, were we to include the quantum susceptance and a tuning susceptance in our calculations, the result would be very much the same. Equation 2 shows two possibilities for analytically infinite \mathcal{G}_{IF} . First, $Y_S + Y'_S$ can go to zero. But even if $G'_S > 0$, it is possible for the vector $(Y_S + Y'_S)$ to be perpendicular to $(Y_S + Y_{LO}^0)$, giving $\cos\theta = 0$. This means that the quantum susceptance widens the range of possibility of infinite gain in SIS mixers (as noted in Ref. [11]), so that infinite gain can be predicted for instance for poorer quality I-V curves and over a wider frequency range. Nevertheless, the discussion of the above paragraph still exactly applies, but for the quantity $(Y_S + Y'_S)\cos\theta$ rather than $G_S + G'_S$. Thus considering the quantum susceptance underlines the importance of removing the high gain solutions in computer simulations.

In Fig. 2 that \mathcal{G}_I is always larger than \mathcal{G}_S . This is true for all of our simulations: for an optimized SIS receiver there is always more power returned to the source at the image frequency than at the signal frequency! We do not know the physical reason for this. Mathematically, it is clear from inspection of Eqs. 5 and 6 that this is a simple consequence of the fact that the optimum G_S is always intermediate between G_{LO}^0 and G'_S . In fact \mathcal{G}_S can be extremely small while \mathcal{G}_I is still sizable; an example is seen at low frequencies in Fig. 2. Thus the signal-to-image gain \mathcal{G}_I is a crucial parameter.

It is clear that the high gain mode should not be experimentally accessible. The very large returned power makes the mixer extraordinarily sensitive to small variations in the signal and image terminations. The high output power (at higher sideband frequencies as well, unless they are perfectly terminated) is extremely conducive to mixer saturation. The sensitivity of the high gain mode to mixer operating parameters implies that these solutions are near instability and will be obliterated by noise and other processes. It appears that the high gain mode is a mere mathematical curiosity, forgoing a direct experimental assault.

On the other hand, we show that it is possible to have moderately high gain, 8 dB for the particular example of Fig. 2, for stable mixer operation with low noise and very low returned power. We believe that this resolves the mystery outlined in the Introduction. Since the high gain mode is not accessible, constraining the reflected power in computer fitting should give much better agreement with experiments. .

CONCLUSION

It is important to consider the signal reflection gain and especially the signal-to-image conversion gain in computer simulations of SIS mixers. The computed minimum receiver noise temperature often entails extremely high signal and image returned power, and this type of solution is likely inaccessible in real experiments. If this mode of operation is eliminated, it is possible to have moderately high gain with very low returned power and low noise temperature, as seen in experiment.

Acknowledgment: This work was supported in part by NSF grant # AST-8922301.

REFERENCES

- [1] J.R. Tucker and M.J. Feldman, "Quantum detection at millimeter wavelengths," *Rev. Mod. Phys.* 57, 1055-1113 (Oct. 1985).
- [2] M.J. Feldman, S.-K. Pan, A.R. Kerr, and A. Davidson, "SIS mixer analysis using a scale model," *IEEE Trans. Magnetics* MAG-19, 494-497 (May 1983).
- [3] C.A. Mears, Qing Hu, P.L. Richards, A.H. Worsham, D.E. Prober, and A.V. Räisänen, "Quantum limited quasiparticle mixers at 100 GHz," *IEEE Trans. Magnetics* MAG-27, 3363-3369 (March 1991).
- [4] T.-M. Shen, P.L. Richards, R.E. Harris, and F.L. Lloyd, "Conversion gain in mm-wave quasiparticle heterodyne mixers," *Appl. Phys. Lett.* 36, 777-779 (1 May 1980).
- [5] A.V. Räisänen, D.G. Crété, P.L. Richards, and F.L. Lloyd, "A 100 GHz SIS mixer with 10 dB coupled gain," in *1987 IEEE MTT-S Int. Microwave Symp. Dig.*, 929-930.
- [6] J.A. Carpenter, A.D. Smith, E.R. Arambula, L.P.S. Lee, T. Nelson, and L. Yujiri, "100 GHz SIS mixer with improved rf matching," *IEEE Trans. Magnetics* MAG-27, 2654-2657 (March 1991).
- [7] W.R. McGrath, P.L. Richards, A.D. Smith, H. van Kempen, R.A. Batchelor, D.E. Prober, and P. Santhanam, "Large gain, negative resistance, and oscillations in superconducting quasiparticle heterodyne mixers," *Appl. Phys. Lett.* 39, 655-658 (Oct. 1981).
- [8] M.J. Feldman, "Some analytical and intuitive results in the quantum theory of mixing," *J. Appl. Phys.* 53, 584-592 (Jan. 1982).
- [9] A.R. Kerr and S.-K. Pan, "Some recent developments in the design of SIS mixers," *Int. J. Infrared Millimeter Waves* 11, 1169-1187 (Oct. 1990).
- [10] Qing Ke and M.J. Feldman, "Reflected power effects in computer simulations using the quantum theory of mixing," in *1992 IEEE MTT-S Int. Microwave Symp. Dig.*, 1425-1428.
- [11] C.A. Mears, Qing Hu, and P.L. Richards, "The effect of the quantum susceptance on the gain of superconducting quasiparticle mixers," *IEEE Trans. Magnetics* MAG-27, 3384-3387 (March 1991).
- [12] Qing Ke and M.J. Feldman, "Optimum source conductance for high frequency superconducting quasiparticle receivers," *IEEE Trans. Microwave Theory Tech.* MTT-41, 600-605 (April 1993).

ANALYTICAL DESCRIPTION OF THE INFLUENCE OF THE QUANTUM SUSCEPTANCE ON THE PERFORMANCE OF SIS MIXERS

Pascal FEBVRE

DEMIRM - Observatoire de PARIS-MEUDON
5, place Jules JANSSEN - 92195 Meudon Cedex - FRANCE

ABSTRACT

A new analytical formalism has been used to describe the contours of constant mixer output conductance and constant available conversion gain in the source admittance plane. This analysis is valid for Double Side-Band mixers in the three-frequency approximation using the low IF limit. The influence of the small-signal admittance matrix reactive terms and of the quantum susceptance is studied in the particular case of SIS mixers. The three different regimes of operation of an SIS mixer are described. The regions in the source admittance plane for optimum receiver performance are discussed. It is shown that the optimum $\omega R_N C$ product is dependent on the losses of the microwave environment of the mixer. This analytical and graphical formalism is shown to be an efficient tool to understand the behaviour of mixers and ease their design.

I. INTRODUCTION

The quantum theory of mixing developed by Tucker [1, 2] has been widely used to predict the performance of SIS mixers using either the three or five-frequency approximations. Good agreements between theory and experiments have been found up to 100 GHz [3-5]. But the complexity of the quantum theory of mixing associated with the large number of free parameters (Local Oscillator power, DC bias voltage, IF and RF port admittances, frequency of operation, quality of the I-V curve) makes difficult the prediction of performances in the general case. Computer simulations are generally used to find the parameters of SIS mixers which give optimum performance [6-9] or to compare a posteriori theoretical predictions with experimental results [3-5, 10-11]. Some attempts to describe analytically the behaviour of SIS mixers have been made in the low LO limit [12-14], but the quantum reactive terms of the small-signal matrix are sometimes neglected to simplify the analysis since it has been argued that they have little

effect on the performance of SIS mixers [13,15]. But this last approximation has been a controversial subject [16, 17].

One presents here a different analytical formalism which allows to understand how the performance of an SIS mixer is affected by several free parameters accessible to the experimentalists. The quantum reactive terms of the small-signal matrix are taken into account and their influence is studied quantitatively. In this treatment the interferences from Josephson effects are not considered and the analysis is limited to Double Side-Band SIS mixers in the low IF limit using the three-frequency approximation. These assumptions are commonly used since they correspond to most of the practical mixers in operation and under development up to 700 GHz. Moreover, most of the current SIS receiver developments above 300 GHz use tuning circuits to resonate the SIS intrinsic parasitic capacitance at the operating frequency [18-21]. The three-frequency approximation is then a good assumption since the harmonics of signal, image and Local Oscillator (LO) frequencies are shunted by the SIS specific capacitance which is not resonated any more by the tuning circuit. Besides the SIS mixer is operated as a Double Side-Band (DSB) mixer since the Intermediate Frequency is lower than the instantaneous RF bandwidth at the resonance frequency of the SIS junction specific capacitance with the tuning circuit.

With these assumptions the IF output impedance of the mixer as well as its conversion gain can be calculated analytically [2]. These quantities are expressed in this paper in a more convenient form to be easily treated analytically and graphically. One shows that such an analytical investigation in the general case is of great help to get an intuitive understanding of the behaviour of SIS mixers, to predict their optimum performance and to ease the design of practical receivers.

In this treatment the source and load admittances of the environment are not fixed but are free parameters in order to allow their determination for optimum performance. It is then possible to determine the contours of constant IF output admittance and constant available conversion gain in the source admittance plane. The regions of infinite available conversion gain and negative output differential resistance will be treated as particular cases of this analysis. A close analysis has been performed by Pan & Kerr [22] to determine analytically the regions of infinite available gain and negative output differential resistance in the same plane for Double Side-Band mixers. They also performed the calculations of the contours of constant conversion loss and the expression of the IF output admittance for Single Side-Band mixers. This last case will not be treated in this work.

The analytical expression of the IF conductance is presented and the corresponding graphical representation is described in part II. The ranges of LO powers and bias voltages for which the quantum reactive terms are necessary to correctly predict the mixer performance are determined in Part III for different LO frequencies. Part IV performs the analysis to determine the contours of constant mixer available conversion gain. Part V discusses the case of the optimum $\omega R_N C$ product and finally the conclusion will be drawn in part VI.

II. CONTOURS OF CONSTANT IF CONDUCTANCE IN THE (G_S, B_S) PLANE

A mixer consists of a Local Oscillator at frequency ω_{LO} applied on a non-linear device which is mixed with the sideband frequencies $\omega_m = m \omega + \omega_0$, $m = -1, 0, 1$ in the three-port approximation. Each sideband is assumed to be terminated by Y_i which is the admittance of the external microwave environment of the mixing device at port i . With the assumption of a Double Side-Band mixer with the low IF limit, one has the same admittance $Y_S (= G_S + j B_S) = Y_1 = Y_{-1}^* = Y_{LO}$ at the signal, image and LO frequencies. These last three frequencies will be called RF frequencies in the following. The admittance of the environment at the Intermediate Frequency (IF) is noted $Y_L = Y_0$. Its real part is noted G_L .

The small-signal currents and voltages at each sideband are related by the small-signal admittance matrix terms which are written $Y_{ij} = G_{ij} + j B_{ij}$ where $i, j = -1, 0, 1$ in the three-port approximation. The values of B_{ij} are called the quantum reactive terms of the small-signal admittance matrix. The values of G_{ij} and B_{ij} have been given for SIS mixers in a convenient way in [2] with expressions (4.72) and (4.73). The augmented matrix $\|Y'\|$ is defined by the terms $Y'_{ij} = Y_{ij} + Y_i \delta_{ij}$. Using some basic principles of frequency conversion the mixer IF admittance as well as the conversion gain can be estimated by inverting the augmented matrix [1, 2, 23]. One obtains: $\|Z\| = \|Y'\|^{-1}$. The IF impedance can be expressed as [2, 23]:

$$Y_{IF} = \frac{1}{(Z_{00})_{Y_L=0}} \quad (2.1)$$

In the case of a Double Side-Band Mixer, this admittance is real, it will be noted G_{IF} in the following. One sees from equation (2.1) and from the formalism of the augmented matrix that G_{IF} is a function of the values of Y_{ij} and Y_S only. This conductance is also the slope of the pumped I-V curve [2]. It can be expressed under the form:

$$G_{IF} = G_{00} - 2 G_{01} \frac{g_1^- G_{10} + b_1^- B_{10}}{g_1^- g_1^+ + b_1^- b_1^+} \quad (2.2)$$

where:

$$\begin{aligned} g_1^+ &= G_s + G_{11} + G_{1-1} \quad \text{and} \quad g_1^- = G_s + G_{11} - G_{1-1} \\ b_1^+ &= B_s + B_{11} + B_{1-1} \quad \text{and} \quad b_1^- = B_s + B_{11} - B_{1-1} \end{aligned} \quad (2.3)$$

It is can be easily shown that expressions (2.2) with (2.3) are identical to the expressions (4.77) with (4.75) given by Tucker and Feldman in Ref. [2].

From this simple analytical formulas, it is straightforward to show that the contour of constant IF conductance G_{IF} in the source admittance plane (G_s, B_s) is a circle of center (X_G, Y_B) and radius R_0 with:

$$X_G = \frac{G_{01} G_{10}}{G_{00} - G_{IF}} - G_{11} \quad (2.4)$$

$$Y_B = \frac{G_{01} B_{10}}{G_{00} - G_{IF}} - B_{11} \quad (2.5)$$

$$R_0 = \sqrt{R_G^2 + R_B^2} \quad (2.6)$$

$$R_G = \frac{G_{01} G_{10}}{G_{00} - G_{IF}} - G_{1-1} \quad (2.7)$$

$$R_B = \frac{G_{01} B_{10}}{G_{00} - G_{IF}} - B_{1-1} \quad (2.8)$$

It is important to notice that this description is not specific to SIS mixers but **it is valid for all Double Side-Band mixers using the three-frequency approximation in the low IF limit.**

The regions in the source admittance plane which give negative IF output conductance G_{IF} are also associated with infinite available conversion gain (see paragraph IV) and the above expressions (2.4) to (2.8) reduce to the expressions given in [22] if one takes $G_L = -G_{IF}$. In the present case the IF output admittance Y_L is not fixed and, as a consequence, though the available conversion gain is infinite, the coupled gain can vary depending on the value of Y_L .

This description in terms of contours in the (G_s, B_s) plane is valid for any set of Y_{ij} . The terms Y_{ij} of the small-signal matrix vary of course as a function of the shape of

the I-V curve, the RF frequencies, the LO power and the DC bias voltage. One will examine the influence of these parameters later.

Also, the radius of the circles is the square root of the sum of two terms. If the reactive terms of the small-signal admittance matrix are neglected, one clearly sees that the radius is smaller. This remark will be of particular importance for the following.

Figure 1 shows the geometrical construction of these circles in the (G_S, B_S) plane.

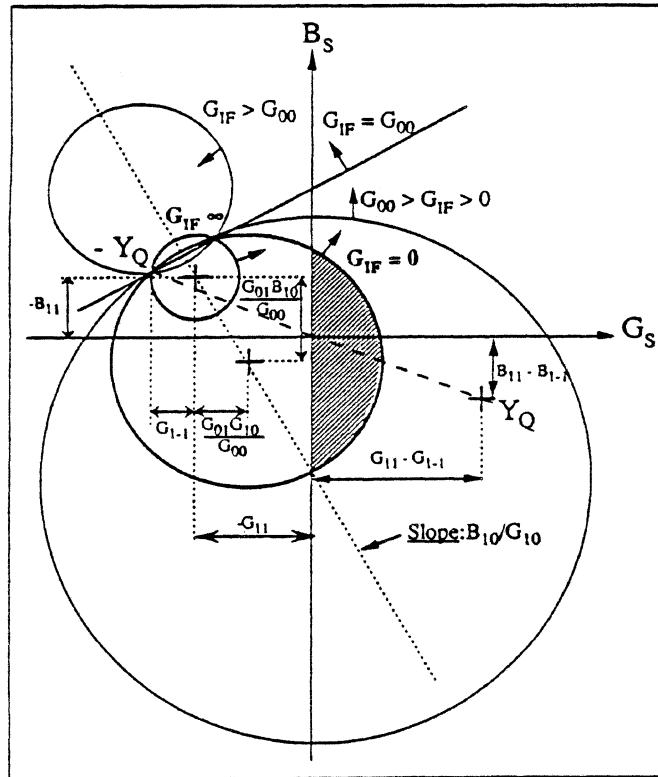


Figure 1: Contours of constant mixer IF output conductance G_{IF} . The hatched region corresponds to negative output conductance and infinite available gain. Y_Q is the large-signal admittance of the mixer at the LO frequency.

To understand this figure one can notice a few interesting features of these circles according to equations (2.4) to (2.8).

First, when the IF conductance varies, the centers of the circles in the (G_S, B_S) plane are located on a line whose slope is constant and given by B_{10}/G_{10} .

Second, the contour for $G_{IF} = G_{00}$ is a line perpendicular to the line on which the centers of the circles are located. It corresponds to a circle of infinite radius.

At last, all these circles cross two particular points located on the $G_{IF} = G_{00}$ line . One of these points is located at the admittance $-Y_Q$ where Y_Q is the large-signal admittance of the mixer which is also called the quantum admittance. The real part of Y_Q is called the quantum conductance and named G_Q . The imaginary part is the quantum susceptance and called B_Q . They can be expressed as a function of some terms of the small-signal admittance matrix [23] according to the relations (2.9) and (2.10):

$$G_Q = G_{11} - G_{1-1} \quad (2.9)$$

$$B_Q = B_{11} - B_{1-1} \quad (2.10)$$

The zero IF output conductance circle, which is also a circle of infinite available gain has a particular importance: the region in the source admittance plane having a physical meaning and for which G_{IF} is negative is comprised inside this circle and in the half-plane corresponding to $G_s > 0$ as it has been also noticed in Ref. [22]. It corresponds to the hatched region of figure 1. This circle is the border between two dual regions in the $G_s > 0$ half-plane. Indeed, outside the hatched region the maximum coupled conversion gain is the available non-infinite conversion gain. Any source admittance in this region corresponds to a given positive IF output conductance of the mixer - i.e. to a given positive slope of the DC pumped I-V curve- and is located on one contour of constant IF mixer conductance G_{IF} . In this region the IF load conductance G_L must be equal to G_{IF} to reach the available conversion gain. Let us call these values $G_{L,pos}$ and $G_{avail,pos}$.

But it is possible to find an other (dual) source admittance inside the hatched region (see figure 1) which gives **the same coupled conversion gain $G_{avail,pos}$ with the same load admittance $G_{L,pos}$** . Indeed, once $G_{L,pos}$ is fixed, there is a source admittance in the hatched region of negative output differential resistance G_{IF} which gives the right output coupling γ with $G_{L,pos}$ where γ is expressed under the form:

$$\gamma = \frac{4 G_{IF} G_{L,pos}}{|G_{IF} + G_{L,pos}|^2} \quad (2.11)$$

to provide a coupled gain equal to $G_{avail,pos}$ since the available conversion gain is infinite (and corresponds to $G_{IF} = -G_{L,pos} < 0$). The only difference in terms of mixer performance comes from the mixer noise which has no reason to be the same for these two different source admittances. Also, the hatched region corresponds to negative differential resistance in the I-V curve which is associated with possible oscillations and instabilities [3] and is not desirable for stable operation of a practical receiver. Then, two different modes of operation can be distinguished: one is unstable and corresponds to non

desirable conditions of operation of the receiver, the other one, corresponding to a positive differential resistance of the pumped I-V curve is more likely to be obtained in practical experiments and can be associated to high but not infinite available conversion gain.

It is interesting to mention that the condition given in Ref. [15] and expressed as:

$$G_S + G'_S = 0 \quad (2.12)$$

which allows to determine two different modes of operation does exactly correspond to the source conductances within the hatched region of figure 1 when the quantum reactive terms are neglected. Indeed the expression of G'_S given in Ref. [15] is $-(X_G + R_G)$ with expressions (2.4) and (2.7) and corresponds to the maximum source conductance of the circles of negative G_{IF} . Then the two different modes of operation described in Ref. 15 when the quantum reactive terms are neglected correspond to the two different regions (hatched and not hatched) shown in figure 1.

III. INFLUENCE OF THE QUANTUM REACTIVE TERMS

Once the analytical description of the contours of constant IF output conductance G_{IF} of the mixer is performed, it is straightforward to study the influence of the quantum reactive terms. To do that, one will first neglect them. In that case the circle of zero G_{IF} is smaller as is shown in figure 2 which is the same figure as figure 1 where all the B_{ij} 's have been set to zero. By comparing these two figures, one clearly sees that the regions in the source admittance plane (G_S , B_S) for which there is a possibility of infinite available gain and negative differential output conductance are shrunk when quantum reactive terms are neglected. It means that the reactive terms and, as a consequence, the quantum susceptance obtained with (2.10), increase the range of possibilities for infinite available gain. This corroborates some conclusions of Ref. [16-17] and makes the case very general. Also one can argue that the quantum susceptance is not directly responsible for that effect but is more a consequence of the presence of quantum reactances in the small-signal admittance matrix. Indeed, one sees in figure 1 that the quantity $(G_{01} B_{10})/G_{00}$ is of particular importance to account for the smaller radius of the circle of zero G_{IF} .

One will now choose the criterium of the possibility of infinite available gain to determine the influence of the reactive terms. As any criterium, it is questionable but it allows to determine the ranges of parameters for which a typical quantum effect of a

mixer like negative differential output conductance can occur. A good other criterium could have been the possibility to get conversion gain versus conversion loss.

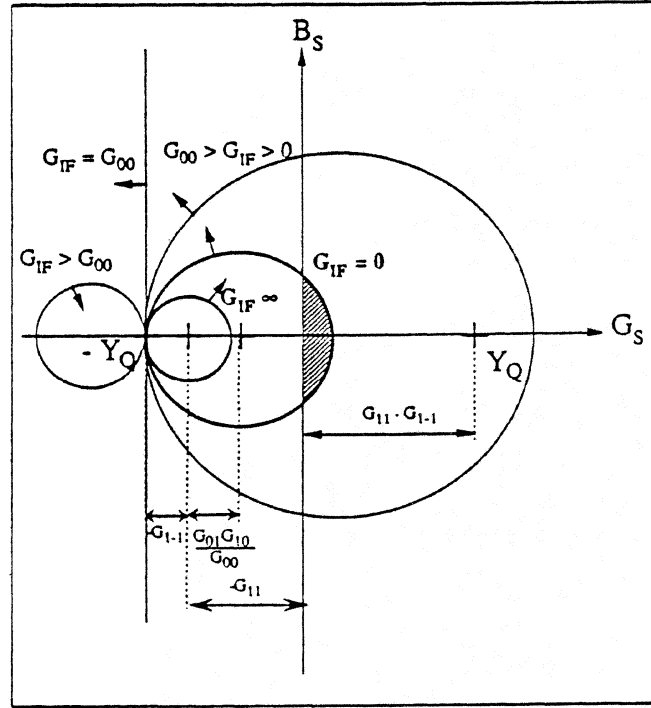


Figure 2: Contours of constant mixer IF output conductance G_{IF} . In this figure the quantum reactive terms B_{ij} have been set to zero. The hatched region corresponds to negative output conductance and infinite available gain, it is smaller than in figure 1.

Though the analysis of the ranges of parameters for which infinite available gain is possible does not allow to predict the parameters for optimum performance, it is a useful tool to target the regions in the source admittance plane where good mixer performance is possible and then to ease their design.

III.1 Quantum reactive terms neglected

When the reactive terms are neglected it is possible to have infinite available gain if part of the $G_{IF} = 0$ circle crosses the half-plane $G_S > 0$ in the source admittance plane. Analytically it corresponds to the relation:

$$(X_G + |R_G|)_{G_{IF}=0} \geq 0 \quad (3.1)$$

which can be rewritten:

$$\frac{G_{01} G_{10}}{G_{00}} \geq \frac{G_{11} + G_{1-1}}{2} \quad (3.2)$$

If one calls:

$$\eta = \frac{2 G_{01} G_{10}}{G_{00} (G_{11} + G_{1-1})} \quad (3.3)$$

the inequality (3.2), which is the criterium of possibility of infinite available gain when quantum reactive terms are neglected, can be expressed under the form

$$\eta \geq 1 \quad (3.4)$$

This is the relation given by Tucker & Feldman in Ref. [2] to predict the same possibility of unlimited gain and negative differential resistance.

III.2 Quantum reactive terms taken into account

In this case, the inequality (3.1) must be replaced by:

$$(X_G + R_0)_{G_{IF}=0} \geq 0 \quad (3.5)$$

where the radius is now a function of conductive and reactive terms. Inequality (3.5) becomes:

$$\frac{G_{01} G_{10}}{G_{00}} \geq \frac{G_{11} + r G_{1-1}}{1 + r} \quad \text{or} \quad \frac{G_{01} G_{10}}{G_{00}} \leq \frac{G_{11} - r G_{1-1}}{1 - r} \quad (3.6)$$

with:

$$r = \sqrt{1 + \frac{R_B^2}{R_G^2}} \quad (3.7)$$

The two inequalities of (3.6) cannot be true at the same time, they represent the general condition to obtain infinite available conversion gain, they reduce to (3.2) or (3.4) if one neglects the reactive terms.

III.3 Description of the different regimes of operation of SIS mixers

The influence of the quantum reactive terms can be examined by finding the ranges of parameters for which inequalities (3.2) and (3.6) are true or false. These parameters are the I-V curve quality, RF frequencies, DC bias voltage V_0 and RF voltage V_{LO} through the parameter $\alpha = (e V_{LO}) / (h \nu)$. They influence the mode of operation of the mixer through the terms G_{ij} and B_{ij} .

It is straightforward to see using (3.2) and (3.6) that if (3.6) is false then (3.2) is also false. Practically it means that if it is not possible to predict infinite available conversion gain by including the reactive terms in the calculation then, a fortiori, there is no possibility to predict infinite gain if these terms are neglected. Then three different cases remains, they correspond to three different regimes of operation of the mixer.

1) (3.2) and (3.6) are false: it means that there is no possibility of infinite available gain. One will call this regime of operation "classical regime" since the mixer basically behaves like a classical mixer though, in that case, the criterium of unity conversion gain would have been better than this criterium of infinite available gain since there is still some possibility for absolute conversion gain. This case is illustrated in figure 3-a. The dashed circle is the zero IF conductance contour when reactive terms are neglected and the solid circle represents the contour for the same zero G_{IF} with reactive terms included in the calculation. Since none of these circles crosses the half-plane $G_S > 0$ then there is no possibility for infinite available gain.

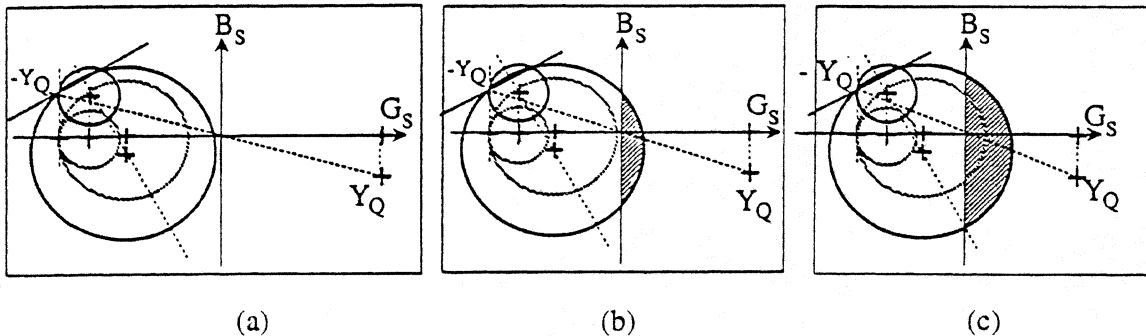


Figure 3: Contours of zero mixer IF output conductance G_{IF} with reactive terms included (solid circle) and neglected (dashed circle). Figure 3-a corresponds to the classical regime since there is no possibility of negative resistance on the half-plane $G_S > 0$. Figure 3-b shows the quantum reactive regime. At last figure 3-c displays the case of pure quantum regime where one can clearly see that the reactive terms increase the size of the hatched region for which infinite available gain is possible.

2) (3.2) is false and (3.6) is true: in that case it is not possible to predict infinite available gain if one neglects the quantum reactive terms but there are some source admittances for which infinite available gain is possible. see figure 3-b. It means that the quantum reactive terms are essential to account for unlimited gain and negative output differential resistance as it has been noticed in Ref. [16, 17]. One will call this mode of

operation "quantum reactive regime" since the reactive terms are necessary to provide infinite available gain. Infinite available gain occurs in the hatched region of figure 3-b.

3) (3.2) and (3.6) are true: infinite available gain is predicted even if the quantum reactive terms are neglected which corresponds to a "quantum conductive regime" since the conductive terms are sufficient to explain unlimited gain. These cases have been theoretically considered by Feldman in Ref. [13]. But the reactive terms widen the region in the source admittance plane for which infinite gain is possible. It means that both conductive and reactive terms influence the mixer behaviour. This regime is called "pure quantum regime". One can see in figure 3-c how the reactive terms increase the size of the hatched region of unlimited gain.

It is now possible to determine in which regime the mixer operates as a function of the parameters which control the values of the small-signal admittance matrix terms.

One will examine here only the influence of the RF frequency, α and V_0 for a given I-V curve shown in figure 4-d. Three graphs showing the different regimes of operation are shown in figures 4-a, 4-b and 4-c at three frequencies normalized to the gap frequency which are respectively 0.15, 0.84 and 1.09. They correspond to 100 GHz, 540 GHz and 700 GHz respectively for Nb/AlOx/Nb junctions. The abscissa axis shows the DC bias voltage V_0 normalized to the gap voltage of the junction and the ordinate axis displays the RF voltage through the parameter α in figures 4-a, 4-b and 4-c. The corresponding calculated pumped I-V curves are shown in figures 4-d, 4-e and 4-f.

The white regions of figures 4-a, 4-b and 4-c correspond to the classical regime of the SIS mixer, the hatched regions show the quantum reactive regime and the darken regions correspond to the pure quantum regime for which the quantum reactive terms are not necessary to predict unlimited gain.

One can first notice that it is possible to predict most of the regions of infinite available gain by neglecting the reactive terms at 100 GHz since the darken regions fill most of the hatched regions on the first two photon steps. It is not the case any more at 540 and 700 GHz where most of the V_0 and α ranges for which infinite gain is possible correspond to the quantum reactive regime.

An interesting feature appears at 540 GHz for a reduced voltage of about 0.7 indicated in figures 4-b and 4-e by a dashed line. One can see that there is an inflection point in the pumped I-V curve of figure 4-e which can be understood as the overlap of the second-order photon step from the negative voltage part of the I-V curve [20, 24]. In the following one will call overlap voltage the voltage at the inflection point in the pumped I-V curve. For voltages higher than this overlap voltage one sees that the range of values

of α for which unlimited gain is possible is larger than below the overlap voltage. It means that good performance is still possible for lower voltages but for a limited range of values of α corresponding to lower LO powers. As a consequence a mixer operating with LO powers corresponding to values of α around 1.2 in this particular case will perform better for voltages higher than the overlap voltage [20,24]. Such an inflection point has also been observed at 540 GHz in figure 9 of Ref. [21] and was associated to a dip in the IF power versus DC voltage curve.

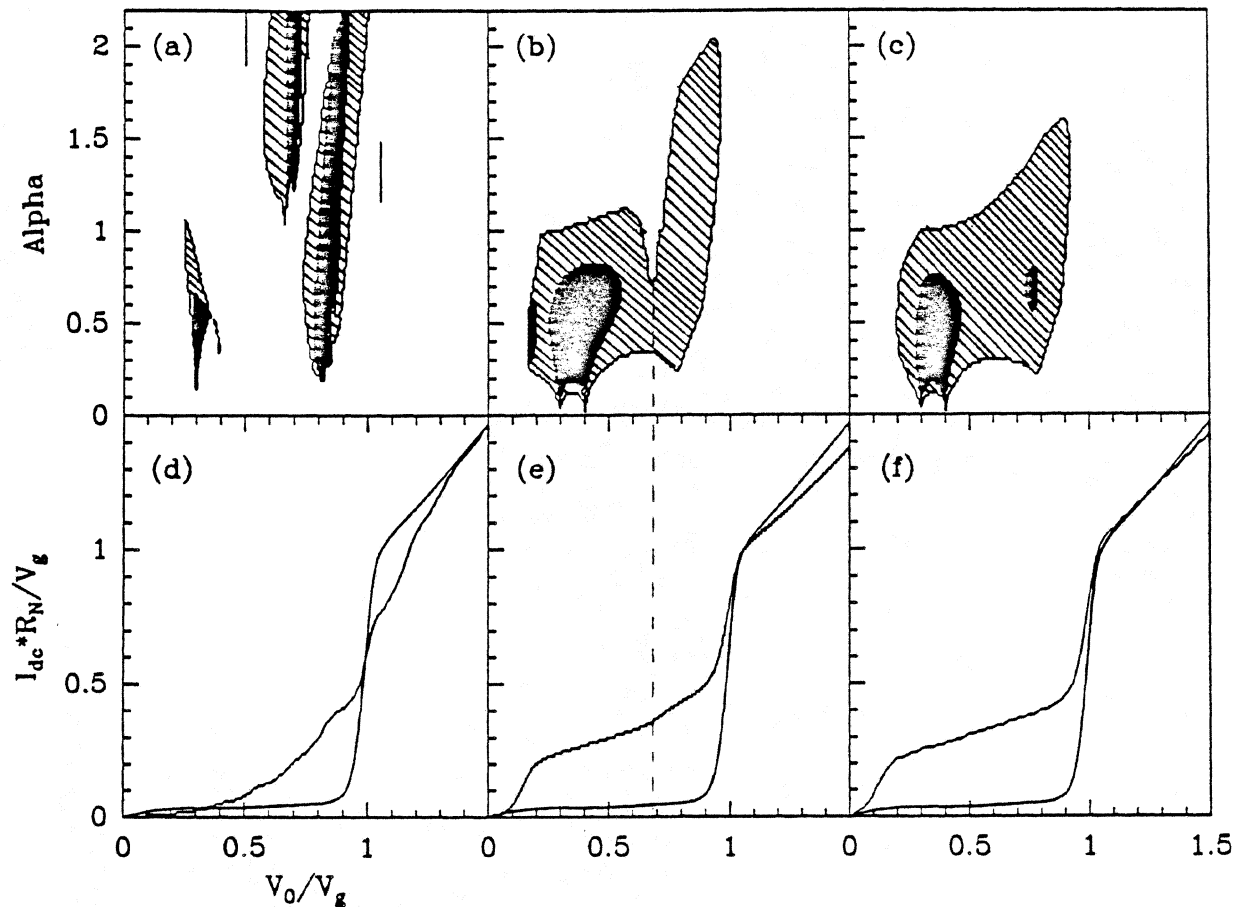


Figure 4: Regions of classical regime (white regions), quantum reactive regime (hatched regions) and pure quantum regime (darken regions) in the (V_0, α) plane for three different frequencies: 100 GHz in figure 4-a, 540 GHz in figure 4-b, 700 GHz in figure 4-c. The corresponding calculated pumped I-V curves are shown respectively in figures 4-d, 4-e and 4-f.

Remark: Some darken and hatched regions appear at 100 GHz for reduced voltages close to 0.2-0.3, the physical reason for that is not known but may be due to computational errors caused by a too strong smoothing of the unpumped I-V curve at these voltages.

IV. CONTOURS OF CONSTANT AVAILABLE CONVERSION GAIN

The knowledge of the contours of constant conversion gain are of particular importance to study the behaviour of a mixer. Some analytical formulas have been derived for Single Side-Band mixers [22]. One presents here analytical formulas for Double Side-Band mixers. In the general case the contours of constant conversion gain do not have simple geometrical expressions. But it is possible to make some additional assumptions which are true in most of cases. These assumptions are the following:

$$|G_{1-1}| \ll G_{11} \quad (4.1)$$

$$|B_{1-1}| \ll |B_s + B_{11}| \quad (4.2)$$

(4.1) is true most of time and (4.2) means that the contours of constant conversion gain slightly deviates from the analytical form given below inside a strip of susceptances B_s centered at the susceptance $-B_{11}$ and of width $2|B_{1-1}|$ in the source admittance plane.

The conversion gain can be expressed under the form:

$$G_m = \gamma \frac{G_s G_{01}^2 \left((g_i^-)^2 + (b_i^-)^2 \right)}{(g_i^- g_i^+ + b_i^- b_i^+)^2} \frac{1}{G_{F1}} = \gamma G_m^0 \quad (4.3)$$

where the output coupling factor γ is defined by (2.11). The available conversion gain is $G_m^0 = (L_m^0)^{-1}$. It is possible to show that, according to the assumptions (4.1) and (4.2), the contours of constant available gain are circles of center (x_g, y_b) and radius r_0 with:

$$x_g = \frac{G_{01}}{G_{00}} \left(G_{10} + \frac{G_{01}}{2} L_m^0 \right) - G_{11} \quad (4.4)$$

$$y_b = \frac{G_{01} B_{10}}{G_{00}} - B_{11} \quad (4.5)$$

$$r_0 = \sqrt{r_g^2 + r_b^2} \quad (4.6)$$

$$r_g^2 = \left(\frac{G_{01}}{G_{00}} \right)^2 \left[\left(G_{10} + \frac{G_{01}}{2} L_m^0 \right)^2 - L_m^0 G_{00} G_{11} \right] \quad (4.7)$$

$$r_b = \frac{G_{01} B_{10}}{G_{00}} \quad (4.8)$$

When there is a possibility of infinite available gain these circles always cross the same two points on the B_s axis which are located on the contour of zero IF conductance as is shown in figure 5. One can notice that the circle of infinite available gain ($L_m^0 = 0$) is also the circle of $G_{IF} = 0$. When $L_m^0 < 0$ the available gain is still infinite through the parameter γ which can be infinite if the IF output match is such that $G_L = -G_{IF}$.

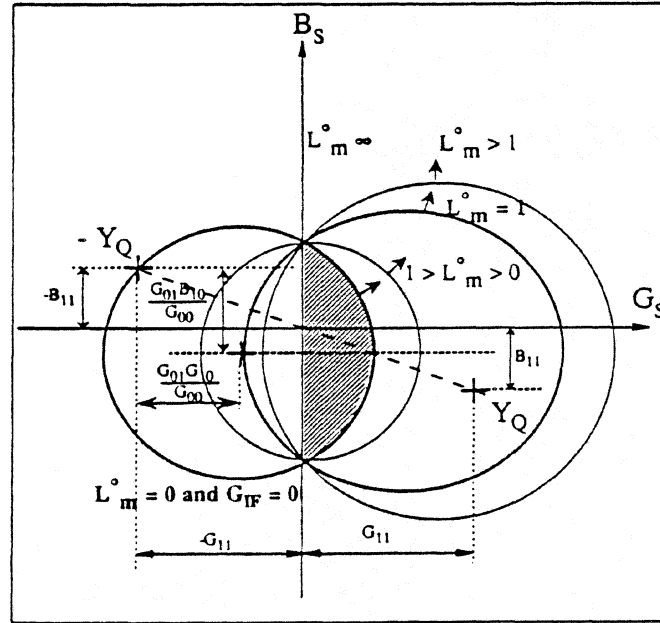


Figure 5: Contours of constant mixer available conversion gain. The hatched region corresponds to negative output conductance and infinite available gain. The centers of the circles are located on a line of constant susceptance and all circles cross two particular points on the $G_s = 0$ axis.

One can notice that all these circles have their center on a line of constant susceptance equal to y_b . It is not the case for the circles of constant IF conductance whose centers are located on a line of slope B_{10}/G_{10} . This feature has been noticed in a particular case in [4]. It is in fact a very general behaviour of Double Side-Band mixers.

Also some contours of constant available conversion gain calculated by computer in [25] to be compared with experiments exhibit the same feature.

It is interesting to mention that this constant susceptance is the sum of two terms: the opposite of the quantum susceptance and $(G_{10} B_{10})/G_{00}$. On the other hand the mixer noise is minimized for source admittances close to the complex conjugate of the large-signal admittance which is also the quantum admittance [9, 26]. Since the receiver optimum performance is a trade-off between optimum mixer noise and optimum mixer gain, the susceptance for optimum receiver performance lies between B_Q^* with B_Q given by (2.10) and y_b where y_b is given by (4.5) as it can be seen in figure 5.

V. OPTIMUM $\omega R_N C$ PRODUCT

The optimum $\omega R_N C$ product is an important parameter of SIS junctions and it has been argued in Ref. [27] that it should vary as $1/\omega$. But this optimum value has been a controversial subject and it is argued in Ref. [26] that the choice of $\omega R_N C$ product has to be made on technological grounds. One shows here that the optimum value is clearly dependent on the losses in the microwave environment of the junction. These losses can be due to the waveguide and backshort losses for waveguide mixers, dielectric losses for quasi-optical mixers but they are present also in the tuning circuits above the gap frequency of the superconductor, ...etc...

In any case the minimum normalized conductance which can be provided to the junction is $1/R_{\text{loss}}$ if one calls R_{loss} the losses of the microwave environment normalized to the normal resistance of the junction R_N . In the source admittance plane (G_S, B_S) it means that the accessible environment admittances lie inside a circle of diameter $1/R_{\text{loss}}$ centered on the $B'_S = 0$ axis as is shown in figure 6. B'_S is the source admittance of the environment without the SIS junction capacitance C which has been included with the junction non-linear admittance. All admittances of figure 6 have been normalized to the normal conductance of the junction and, as a consequence, the $\omega R_N C$ product is the distance between the $B'_S = 0$ axis and the $B_S = 0$ axis. This last axis was used for the construction of the contours of constant mixer IF conductance G_{IF} of figure 1 and constant available conversion gain of figure 5. They have been reproduced for clarity in figure 6. In this figure it appears that it is possible to get good performance if there is a common region between the disk of diameter $1/R_{\text{loss}}$ and the admittances close to Y_Q^* where the mixer noise is minimum and close but outside the hatched region where the conversion gain is high. Then, if the losses are high, the accessible regions in the source admittance plane where it is possible to tune the mixer are inside a small circle which

performance by providing source admittances closer to Y^*_Q and outside the hatched region of negative output conductance. It means that, in practice, the receiver must be optimized for maximum Y-factor and not for maximum IF power level. But if the losses or the mixer mount do not allow to reach the hatched region, then the maximum IF power levels roughly correspond to minimum noise then the technique which consists of maximizing the IF power is valid for most of cases when the slope of the I-V curve is positive.

VI. CONCLUSION

Some graphical representations have been used to display in the source admittance plane the contours of constant IF output conductance and constant available gain of Double Side-Band mixers using the three-frequency approximation in the low IF limit. These contours have been determined analytically and are circles. Their properties are only dependent on the terms of the small-signal admittance matrix. This analysis applies to any mixer operated under the above assumptions, it has been used here for the case of SIS mixers. It is shown that this way of understanding the behaviour of a mixer allows to easily interpret many experimental facts like the influence of the quantum reactive terms with, in particular, the quantum susceptance or the $\omega R_N C$ product. The two different modes of operation stated in Ref. [15] can also be easily visualized. Such an analytical tool is very useful to help the design of SIS mixers since it allows to determine analytically the regions in the source admittance plane for optimum mixer performance of a given DC I-V curve.

ACKNOWLEDGEMENTS

The author wants to thank Gérard Beaudin and Pierre Encrenaz for continuing support. He also appreciated useful discussions with S.K. Pan, Qing Ke, M.J. Feldman, W.R. McGrath and M. Salez. The experimental I-V curve shown in this paper comes from an SIS junction fabricated by Sébastien George and Philippe Feautrier. This work has been performed at the DEMIRM of the Observatoire de Paris-Meudon - France.

REFERENCES

- [1] J.R. Tucker, "Quantum limited detection in tunnel junction mixers," IEEE J. Quantum Electron., vol. QE-15, pp. 1234-1258, Nov. 1979.

- [2] J.R. Tucker and M.J. Feldman, "Quantum detection at millimeter wavelengths," *Rev. Mod. Phys.* **57**, pp. 1055-1113, Oct. 1985.
- [3] W.R. McGrath, P.L. Richards, A.D. Smith, H. van Kempen, and R.A. Batchelor, "Large gain, negative resistance, and oscillations in superconducting quasiparticle heterodyne mixers," *Appl. Phys. Lett.*, vol. 39, no. 8, pp. 655-658, Oct. 1981.
- [4] M.J. Feldman, S.K. Pan, A.R. Kerr, and A. Davidson, "SIS mixer analysis using a scale model," *IEEE Trans. Magnetics*, vol. MAG-29, pp. 494-497, May 1983.
- [5] C.A. Mears, Qing Hu, P.L. Richards, A.H. Worsham, D.E. Prober, and A.V. Räisänen, "Quantum limited quasiparticle mixers at 100 GHz," *IEEE Trans. Magnetics*, vol. MAG-27, pp. 3363-3369, March 1991.
- [6] S. Withington and E.L. Kollberg, "Spectral-Domain Analysis of Harmonic Effects in Superconducting Quasiparticle Mixers," *IEEE Trans. MTT*, vol. 37, no. 1, pp. 231-238, Jan. 1989.
- [7] C.E. Tong and R. Blundell, "Simulation of the Superconducting Quasiparticle Mixer Using a Five-Port Model," *IEEE Trans. MTT*, vol. 38, no. 10, pp. 1391-1398, Oct. 1990.
- [8] M.J. Feldman, "Theoretical considerations for THz SIS mixers," *Int. J. of Infrared and Millimeter Waves*, vol. 8, pp. 231-238, Jan. 1989.
- [9] D.P. Woody and M.J. Wengler, "Optimizing double-sideband SIS quasiparticle mixers," *IEEE Trans. Mag.*, vol. 27, pp. 3388-3390, March 1991.
- [10] C.E. Honingh, D. de Lange, M.M.T.M. Dierichs, H.H.A. Schaeffer, J. Wezelman, J. v.d. Kuur, Th. de Graauw and T.M. Klapwijk, "Comparison of Measured and Predicted Performance of a SIS Waveguide Mixer at 345 GHz," *Proceedings of the 3rd International Symposium on Space Terahertz Technology*, pp. 251-265, Ann Arbor, MI, March 24-26, 1992.
- [11] N.G. Ugras, A.H. Worsham, D. Winkler, D.E. Prober, "A superconducting Mixer Tuned by the Quantum Susceptance," *Proceedings of the 4th International Symposium on Space Terahertz Technology*, pp. 629-638, U.C.L.A., Los Angeles, CA, March 30-April 1, 1993.
- [12] T.M. Shen, "Conversion Gain in Millimeter Wave Quasi-Particle heterodyne Mixers," *IEEE J. Quantum Electron.*, vol. QE-17, pp. 1151-1165, July 1981.
- [13] M.J. Feldman, "Some analytical and intuitive results in the quantum theory of mixing," *J. Appl. Phys.*, vol. 53, no. 1, pp. 584-592, Jan. 1982.
- [14] M.J. Feldman, "An analytical investigation of the superconductor quasiparticle mixer in the low power limit," *IEEE Trans. Mag.*, vol. 27, no. 2, pp. 2646-2649, March 1991.
- [15] Q. Ke and M.J. Feldman, "Reflected power effects in computer simulations using the quantum theory of mixing," *IEEE MTT-S International Microwave Symposium Digest*, vol. 3, pp. 1425-1428, 1992 and Q. Ke and M.J. Feldman, "Signal and image port output power in the quantum theory of mixing," *this Symposium Proceedings*.

- [16] C.A. Mears, Q. Hu and P.L. Richards, "The effect of the quantum susceptance on the gain of superconducting quasiparticle mixers," *IEEE Trans. Mag.*, vol. 27, no. 2, pp. 3384-3387, March 1991.
- [17] Qing Hu, C.A. Mears and P.L. Richards, F.L. Lloyd, "Quantum susceptance and its effects on the high-frequency response of superconducting tunnel junctions," *Phys. Rev. B*, vol. 42, no. 16, pp. 10250-10263, December 1990.
- [18] J. Zmuidzinas and H.G. LeDuc, "Quasioptical slot antenna SIS mixers," *IEEE Trans. Microwave Theory Tech.*, vol. 40, no. 9, pp. 1797-1804, September 1992.
- [19] G. de Lange, C.E. Honingh, M.M.T.M. Dierichs, H.H.A. Schaeffer, H. Kuipers, R.A. Panhuyzen, T.M. Klapwijk, H. van de Stadt, M.W.M. de Graauw, E. Armandillo, "Quantum limited responsivity of a Nb/Al₂O₃/Nb SIS waveguide mixer at 460 GHz and first results at 750 and 840 GHz," *Proceedings of the 4th Int'l Symp. Space Terahertz Tech.*, pp. 41-49, U.C.L.A., Los Angeles, CA, March 30-April 1, 1993.
- [20] M. Salez, P. Febvre, W.R. McGrath, B. Bumble, H.G. LeDuc, "An SIS waveguide heterodyne receiver for 600 GHz to 636 GHz," *Int. J. of Infrared and Millimeter Waves*, vol. 15, no. 2, pp. 349-368, February 1994.
- [21] P. Febvre, W.R. McGrath, P. Batelaan, B. Bumble, H.G. LeDuc, S. George, P. Feautrier, "A low-noise SIS receiver measured from 480 GHz to 650 GHz using Nb junctions with integrated RF tuning circuits," to appear in: *Int. J. of Infrared and Millimeter Waves*, vol. 15, no. 6, June 1994.
- [22] S.K. Pan and A.R. Kerr, "A superconducting Tunnel Junction Receiver for Millimeter-Wave Astronomy," *NASA Technical Memorandum 87792*, pp. 52-67, 1986.
- [23] H.C. Torrey and C.A. Whitmer, *Crystal Rectifiers*. New-York: McGraw-Hill, 1948, M.I.T. Rad. Lab. Series, vol. 15.
- [24] M. Salez, P. Febvre, W.R. McGrath, B. Bumble, H.G. LeDuc, "High frequency effects and performance of a 600 GHz- 635 GHz SIS receiver using Nb/AlO_x/Nb junctions," this symposium proceedings.
- [25] W.R. McGrath and P.L. Richards, D.W. Face and D.E. Prober, F.L. Lloyd, "Accurate experimental and theoretical comparisons between superconductor-insulator-superconductor mixers showing weak and strong quantum effects," *J. Appl. Phys.*, vol. 63, no. 8, pp. 2479-2491, April 1988.
- [26] Q. Ke and M.J. Feldman, "Optimum source conductance for high frequency superconducting quasiparticle receivers," *IEEE Trans. MTT.*, vol. MTT-41, pp. 600-605, April 1993.
- [27] A.R. Kerr and S.K. Pan, "Some recent developments in the design of SIS mixers," *Int. J. of Infrared and Millimeter Waves*, vol. 11, no. 10, pp. 1169-1187, October 1990.

CANCELLATION OF JOSEPHSON CURRENTS IN SUPERCONDUCTING JUNCTION ARRAYS

Roberto MAOLI and Brigitte LERIDON

DEMIRM

Observatoire de Paris
61, Avenue de l'Observatoire
75014 Paris

Abstract

We propose a method to investigate the possibility of a total suppression of the Josephson currents in junction arrays. Using a tunable external magnetic field and correctly interpreting the Josephson peaks in the I-V curve, it is possible to separate the individual behavior of the junctions and to study the magnetic dependence of their critical Josephson current. This way we can investigate some intrinsic properties of the junctions like the difference between their barrier thicknesses and between their surfaces and the polluting effect of the magnetic environment.

1 Introduction

Suppression of Josephson current is one of the main problems in SIS heterodyne receivers working at frequencies greater than 200 GHz. It is responsible for excess of noise and bias instabilities [1]. For these reasons most of the radiometers use a tunable external magnetic field generally produced by a couple of superconducting coils.

The aim of this paper is to suggest a method that uses this facility to study the evolution of the critical Josephson currents in SIS junction arrays as a function of the field produced by the coils [2].

Separating the individual behavior of each junction it is possible to investigate their intrinsic properties and the influence of the magnetic environment.

In section 2 we describe the DC I-V curve of an SIS array emphasizing the interpretation of Josephson peaks; in section 3 we recall the theoretical behavior of Josephson current under a variable magnetic field and we extend it to the case of an SIS array; in section 4 we apply our method to study an array of four Nb/Al-AlOx/Nb junctions.

2 I-V curve

Two different kinds of charge carriers are present in a superconductor: Cooper pairs and quasiparticles. As a consequence two different current regimes can be distinguished in the I-V curve of an SIS junction: the Josephson current branch at $V=0$ and the quasiparticle current branch for $V \geq 2\Delta/e$, where Δ is the energy gap of the superconductor and e is the electron charge.

When varying the bias current from zero to above the gap current, the junction describes an hysteretic cycle (see figure 1a). It starts in the Josephson branch and switches to the quasiparticle regime for a transition value given by

$$I_{jos} = I_{max} \sin(\varphi_0) \quad (1)$$

where I_{max} is the critical Josephson current and φ_0 is the difference of phase between the two superconductors.

As a statistical rule (see figure 2) for small variation of the bias current the junction in the pair regime prefers to accord its phase difference rather than changing its physical state. As a consequence the transition happens almost every time for a bias value equal to the critical Josephson current that is for $\varphi_0 = \pi/2$.

In an SIS array (see figure 1b) the junctions have different values of the critical Josephson current. Then the transition between the

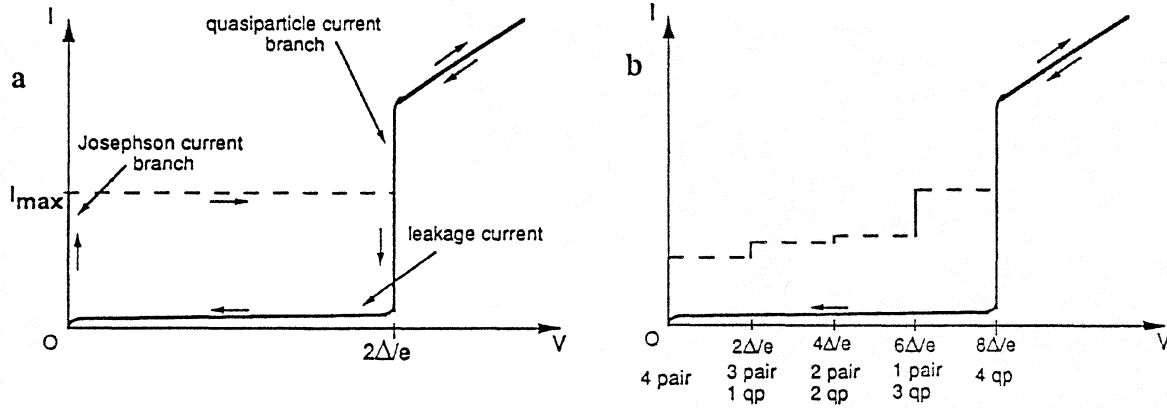


Figure 1: (a) Typical DC I-V curve for a current biased SIS single junction showing the hysteric behavior between the two current regimes. (b) Typical DC I-V curve for a four junction array. Each peak is associated to a different physical state of the array where some junctions are in the pair regime and the others are in the quasiparticle one.

pair regime and the quasiparticle regime occurs in the different junctions for different values of the bias current. There are $(n+1)$ regimes for the array and n peaks in the I-V curve before the gap at $V=2n\Delta/e$ where all the junctions are in their quasiparticle regime.

The i^{th} peak is associated to a physical state with $(i-1)$ junctions in the quasiparticle regime and $(n-i+1)$ junctions in the pair regime; its height corresponds to the critical Josephson current of the i^{th} junction where the junctions are sorted for growing values of their I_{max} .

The absence of some intermediate peak can be interpreted as the simultaneous transition to the quasiparticle regime of more than one junction, due to the almost equal value of their critical currents.

3 Josephson current and magnetic environment

The theoretical magnetic field dependence of the critical Josephson current is well known [3]. Assuming that the magnetic field produced by the coils is in the x direction we have

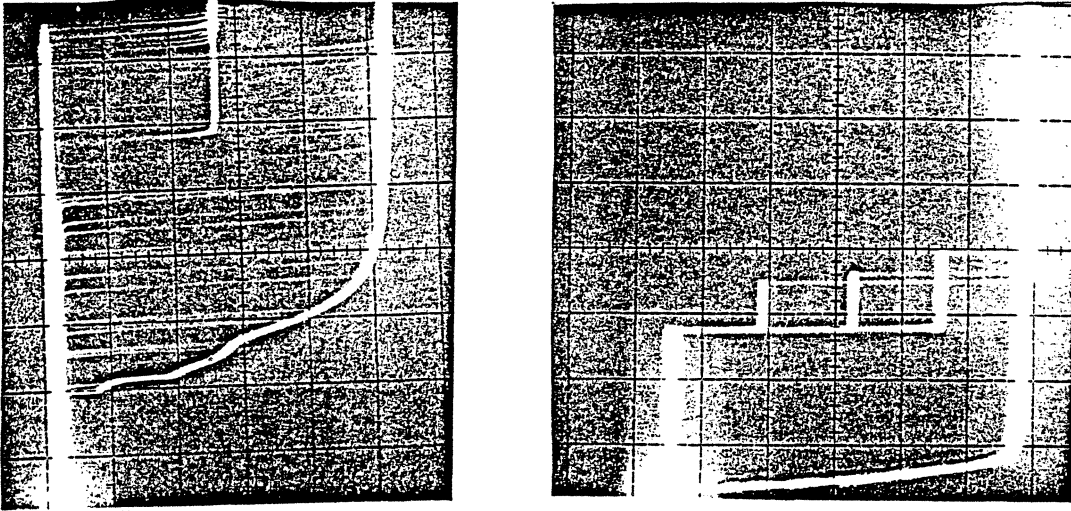


Figure 2: Transitions between different regimes of an array. (Left) I-V curve of a two junction array: even if statistically unlikely transitions between the two regimes of a junction can happen also for a bias current smaller than the critical Josephson current, as shown by the presence of numerous horizontal lines. (Right) I-V curve for a four junction array: the transition of a junction to its quasiparticle regime can induce a premature switch of the other junctions.

$$I_{\max} = I_0 \left| \frac{\sin\left(\pi \frac{\phi_x}{\phi_0}\right)}{\pi \frac{\phi_x}{\phi_0}} \right| \left| \frac{\sin\left(\pi \frac{\phi_y}{\phi_0}\right)}{\pi \frac{\phi_y}{\phi_0}} \right| \quad (2)$$

for rectangular junctions, and

$$I_{\max} = I_0 \left| \frac{J_1\left(\pi \frac{\sqrt{\phi_x^2 + \phi_y^2}}{\phi_0}\right)}{\frac{\pi}{2} \frac{\sqrt{\phi_x^2 + \phi_y^2}}{\phi_0}} \right| \quad (3)$$

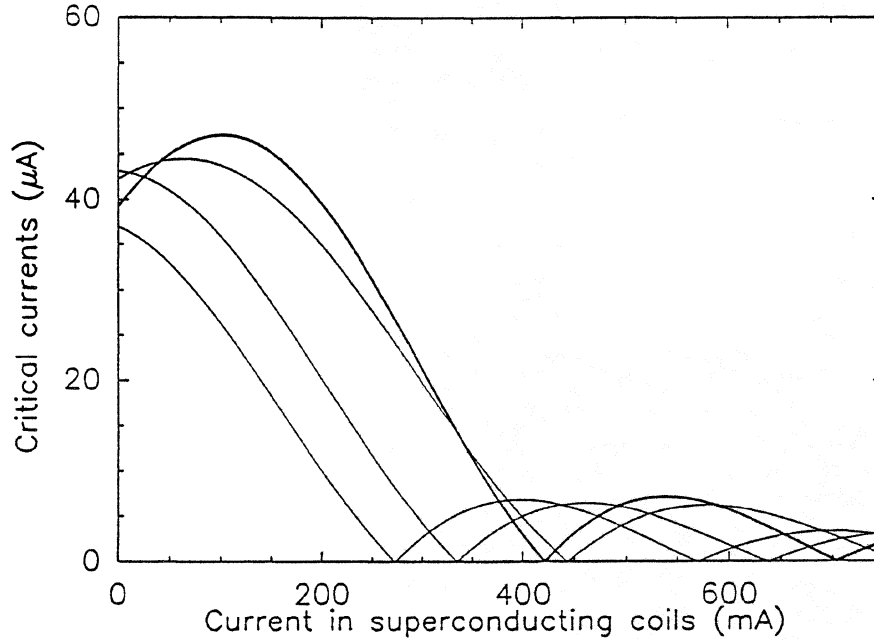


Figure 3: Simulation of the magnetic dependence of the critical Josephson currents for a four junction array. We allowed for each junction a variation of 10% for the I_0 and ϕ_0 values as well as trapped fluxes between 0 and $\phi_0/2$ in the x and y direction.

for circular junctions. In these formulas, $\phi_x = \phi_{\text{coil}} + \phi_{\text{ext},x}$ is the flux generated by the superconducting coils plus the external flux trapped along the coils axis, $\phi_y = \phi_{\text{ext},y}$ is the flux trapped along the perpendicular direction in the junction plane, $\phi_0 = hc/2e$ is the flux quantum ($2.07 \cdot 10^{-7} \text{ G cm}^2$), I_0 is the critical Josephson current in absence of magnetic fields, J_1 is the Bessel function of the first kind.

In figure 3 we plotted the theoretic behavior of a four circular junction array. In this simulation we took different values of I_0 , ϕ_0 , $\phi_{\text{ext},x}$ and $\phi_{\text{ext},y}$ for the different junctions.

Following one junction, for example that one plotted in bold line and keeping in mind that the peaks in the I-V curve are sorted for growing value of the critical current, we can see that the junction is not associated to the same peak for all the values of the current producing the tunable magnetic field. For example it is associated to

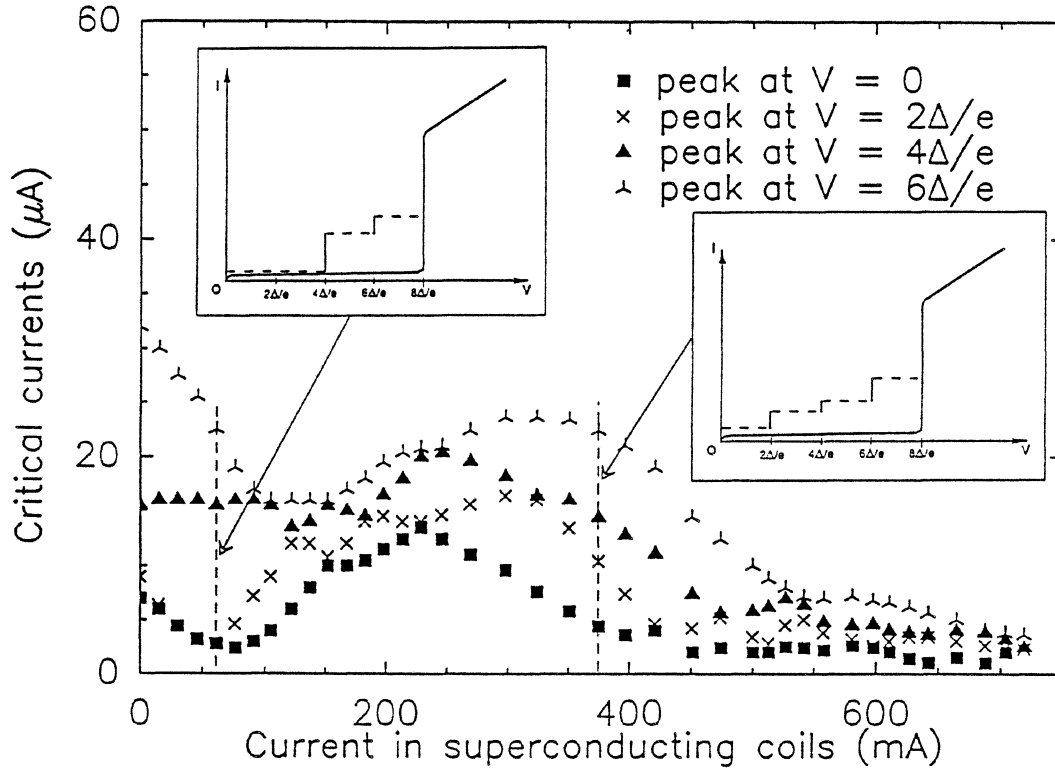


Figure 4: Critical Josephson currents vs tunable magnetic field for a four junction array in the case of a very polluting magnetic environment. The insets show the I-V curve associated to two different fixed values of the coils field.

the second peak for $I_{coil} \leq 20$ mA, to the fourth peak for 40 mA $\leq I_{coil} \leq 330$ mA and to the first one for 390 mA $\leq I_{coil} \leq 430$ mA.

As a general rule, when changing the value of the tunable magnetic field, the relative order of the critical currents changes too and it is not possible to associate a given peak always to the same junction.

Then to reconstruct the individual behavior of each junction in an external magnetic field we have to search for continuity of the theoretical function in the adjacent peaks.

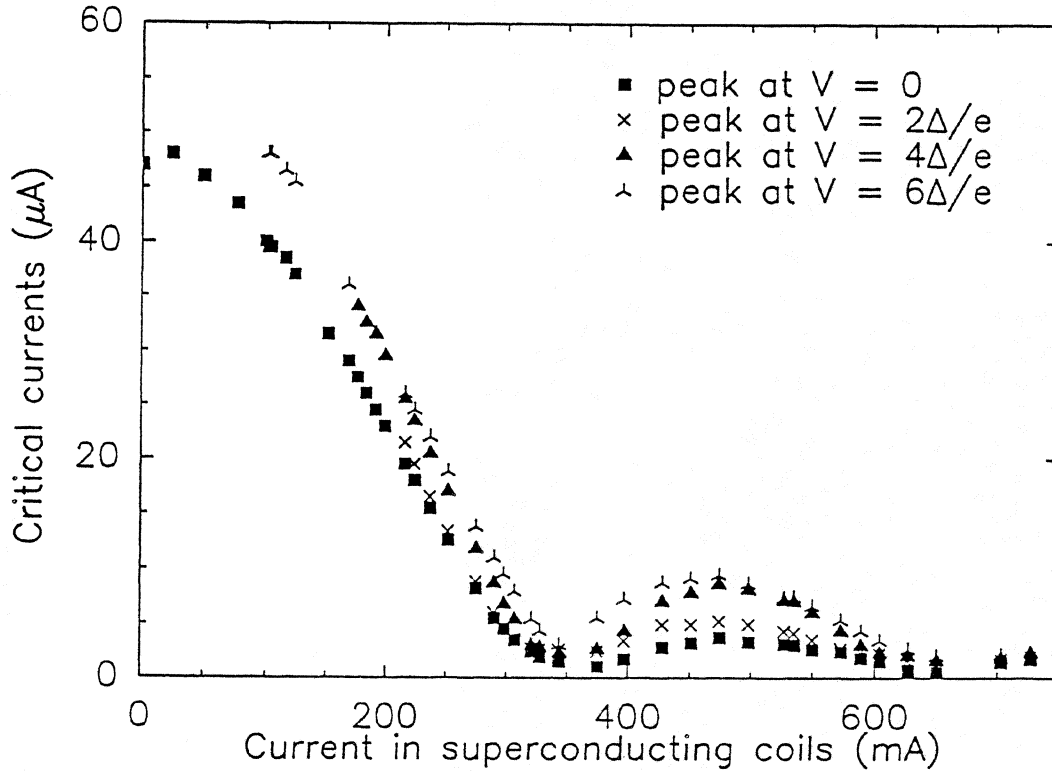


Figure 5: Critical Josephson currents vs tunable magnetic field for a four junction array in a clean magnetic environment.

4 Experimental results

In order to apply this method to a practical case we tested an array of four Nb/Al-AlOx/Nb junctions [4]. The junctions have circular shape with a diameter of $1.9 \mu m$ and a normal resistance for the array of 115Ω . The array was placed in a cryogenerator at 4.2 K and a couple of superconducting coils was used to produce the tunable magnetic field.

The method consists in plotting the height of the I-V curve peaks for different values of the magnetic field produced by the coils (see figure 4).

When we measure the dependence of the critical Josephson current from the current in the superconducting coils the formula (3) becomes

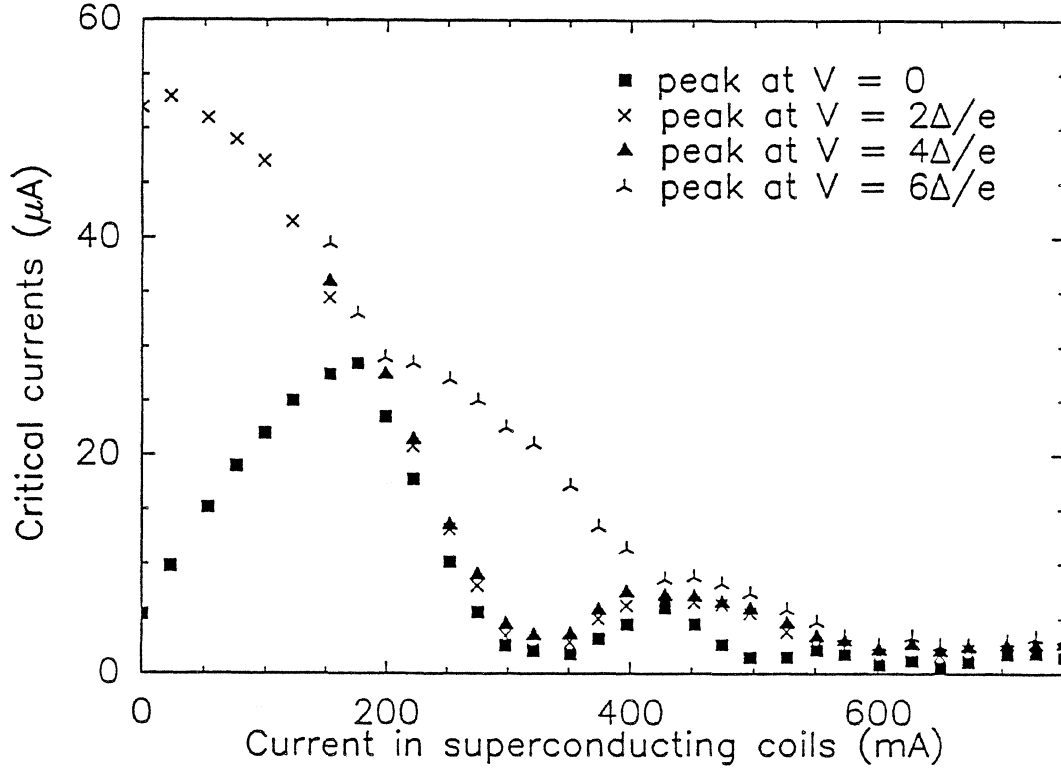


Figure 6: Critical Josephson currents vs tunable magnetic field for a four junction array. One of the junction has some trapped flux. Its maximum critical current is lower and its behavior is shifted along the x axis compared to the other junctions.

$$I_{\max} = I_0 \frac{\left| J_1 \left(k \pi \sqrt{(I_{\text{ext},x} + I_{\text{coil}})^2 + I_{\text{ext},y}^2} \right) \right|}{\left| k \frac{\pi}{2} \sqrt{(I_{\text{ext},x} + I_{\text{coil}})^2 + I_{\text{ext},y}^2} \right|} \quad (4)$$

where k is the inverse of the coils current that produces a flux in the junction equal to ϕ_0 while $I_{\text{ext},x}$ and $I_{\text{ext},y}$ are the coils current values that produce a flux equal to the trapped one.

In figure 4, 5 and 6 we represent some examples of the peaks evolution in different conditions of the magnetic environment.

$\Delta k \Delta I_0$	- 2 0	- 1 0	- 5	0	5	1 0	2 0
0	0.0	0.0	0.0	0.0	0.0	0.0	0.0
1	0.4	0.4	0.4	0.4	0.4	0.4	0.4
2	0.7	0.8	0.8	0.8	0.8	0.8	0.9
3	1.0	1.1	1.2	1.2	1.2	1.2	1.3
5	1.7	1.8	1.9	1.9	2.0	2.0	2.1
7	2.4	2.5	2.6	2.6	2.7	2.8	2.9
1 0	3.3	3.5	3.6	3.6	3.7	3.8	4.0
1 5	4.7	5.0	5.1	5.2	5.3	5.4	5.6
2 0	5.9	6.3	6.4	6.6	6.7	6.9	7.1
2 5	7.0	7.5	7.6	7.8	8.0	8.1	8.4
3 0	8.0	8.5	8.7	8.9	9.1	9.2	9.5
4 0	9.7	10.3	10.5	10.7	10.9	11.1	11.4

Table 1: Residual Josephson current as a function of the k and I_0 mismatches between the junctions. The values are given in percentage of the critical Josephson current in a zero magnetic field.

4.1 Intrinsic properties

In figure 5 the array is in a clean magnetic environment. For $I_{coil} < 100$ mA only one peak is present due to the quite identical value of the critical currents. The junctions reach the first minimum for almost the same magnetic flux.

This situation is the most favourable for the receiver to work. It is possible to strongly suppress the Josephson currents in all the junctions of the array at the same time and with a small magnetic field.

In this situation we can investigate about some intrinsic properties of the junctions. Using a χ^2 test with I_0 and k as free parameters to fit the theoretical behavior we found a maximum mismatch of 20% for I_0 and 8% for k . From the former we get qualitative information about the barrier thicknesses of the junctions while from the latter we directly measure the mismatch between their linear dimensions.

The k mismatch gives the intrinsic limit for a specific array concerning the Josephson current suppression (see table 1). This limit is important in the choice between single junctions or arrays as non linear elements for high-frequency operating SIS mixers [5].

Approaching the gap frequency (~ 700 GHz for Niobium) the receiver performances become more sensitive to the presence of a residual Josephson current [6] and single junctions should be preferred to junction arrays.

4.2 Magnetic environment

In figure 6 one of the junctions has some trapped flux. Performing a χ^2 test with two more free parameters, $I_{\text{ext},x}$ and $I_{\text{ext},y}$, we estimated a trapped flux equal to ϕ_0 due to a magnetic field at 45° with respect to the coils axis.

An example of important magnetic pollution is shown in figure 4. All the junctions have some trapped flux, consequently their maximum critical currents are decreased and shifted along the x axis.

In both situations, the minima are displaced as well, hence, it is not possible any more to find a value of the current in the coils for which the Josephson current is suppressed in all the junctions.

If the Josephson currents remain too high for acceptable values of the magnetic field there is no way to bias the junction properly because of the drop-back effect.

Using large magnetic fields can generally reduce the Josephson currents but degrades the quality of the I-V curve and therefore the mixing performances.

The only solutions are to warm up the junction in order to expel the flux and to shield the mixer block from external magnetic pollution.

5 Conclusion

Studying the evolution of the Josephson peaks of SIS junction arrays as a function of an external magnetic field it is possible to investigate the impediments to a total suppression of the Josephson current.

We can distinguish an intrinsic impossibility due to area discrepancies between the junctions and an external impossibility due to the sensitivity of the array to the magnetic environment.

The first decides the limit where the technology becomes not good enough to continue using junction arrays and suggests the choice of single junctions for SIS receiver working above 500 GHz.

The second one may be important for studying the efficiency of mixer shielding especially in view of space qualified receivers where heating the system might not be possible and generally human interventions are limited to remote control systems.

Acknowledgment

The authors like to thank P. J. Encrenaz and G. Beaudin for their continued support and P. Feautrier for supplying the junction arrays. We acknowledge the financial support of the European Space Agency through an ESA Fellowship for R.M. and of Matra Marconi Space for B. L.

References

- [1] M. J. Wengler, N. B. Dubash, G. Pance, and R. E. Miller, "Josephson effect gain and noise in SIS mixers," *IEEE Trans. MTT*, pp. 820-826, **40**, 1992.
- [2] B. Leridon and R. Maoli, "Critical Josephson current as a characterization tool for superconducting junction arrays," *J. of Appl. Phys.*, pp. 5648-5651, **74**, 1993.

- [3] A. Barone and G. Petero, "Physics and Applications of the Josephson Effect," ed. Wiley, New York, pp. 69-79, 1982.
- [4] P. Feautrier, M. Hanus, and P. Febvre, "Nb/Al-AlO_x/Nb junctions for a 380 GHz SIS Receiver," *Supercond. Sci. Technol.*, pp. 564-568, **5**, 1992.
- [5] P. Febvre, B. Leridon, R. Maoli, S. George, P. Feautrier, G. Ruffié, W. R. McGrath, and G. Beaudin, "New Elements for Analysis of Series Arrays of Superconducting Junctions for Submillimeter Heterodyne Detection," *Proc. of the First European Workshop on Low Temperature Electronics (WOLTE 1)*, to be published in *Journal de Physique - Colloque* by Les Editions de Physique.
- [6] B. Leridon, "Josephson noise in SIS Heterodyne Receivers," *This proceedings*.

DESIGN AND REALIZATION OF GaAs D-BAND IMPATT OSCILLATORS

M. Tschernitz and J. Freyer

Lehrstuhl für Allgemeine Elektrotechnik und Angewandte Elektronik

Arcisstr. 21, 80290 München, Germany

Abstract

GaAs IMPATT oscillators for cw operation at D-band frequencies are designed and fabricated. The active devices are encapsulated using the novel module technique on diamond heat sinks. For the design of the module a CAD-software package is applied which considers the complete outer waveguide resonator structure as well as the module encapsulation structure. As active devices GaAs single-drift flat-profile IMPATT diodes and Read-type IMPATT diodes are investigated. The Read-type diode structure is designed by the help of a numerical program for calculation of the device impedance. The main design feature is low dc input voltage yielding high dc current density. Experimental results for rf output power and noise behaviour are given for both types of diodes in the frequency range from 110-150 GHz.

1 Introduction

Avalanche transit-time devices are keyelements for power generation at mm-wave frequencies and can be applied in various systems, for example as low-noise local oscillator or self-oscillating mixer. For the realization of mm-wave oscillators the most critical parameter that determines rf-performance is the

impedance matching of the active diode to the resonant circuit. In particular at elevated mm-wave frequencies the rf-behaviour predominantly is determined by the diode encapsulation structure. Up to now, the encapsulation structure mainly is realized with the help of quartz stand-offs and gold bond ribbons. Because of the intricate encapsulation process high failure rates occur and the reproducibility of the rf-behaviour is a critical task. A decisive improvement is achieved from MMIC-technique for the fabrication of mm-wave oscillators which yields excellent reproducibility due to the applied photoresist technology (see for example [1][2]). In order to bring forward the advantage of photoresist technology for encapsulation of two-terminal devices also on diamond heat-sinks an encapsulation module representing a monolithic integration of active diode and surrounding standoff structure has been developed [3]. Good rf-performance achieved by the help of this technique is demonstrated at W-band frequencies, yielding a conversion efficiency of more than 10 % at 90 GHz with a GaAs IMPATT diode [4].

This work is concerned with the design and fabrication of modules and resonator structures for D-band frequencies. Resonator and module are optimized using a finite element CAD software package for calculation of the entire impedance. As active devices conventional applied single-drift flat-profile GaAs IMPATT-diodes as well as Read-type diodes are investigated. Experimental values for rf-output power and noise measure for the frequency range from 110-150 GHz are reported.

2 The encapsulation module

The principal cross-section of the module can be seen in Fig. 1. Initial material for the fabrication is semiinsulating GaAs on which a GaAlAs etch-stop layer

followed by the desired layer sequence for the active diode is grown. For the epitaxial growth standard molecular beam epitaxy is used. The semiinsulating GaAs material is used for electrical isolation of the diode from the stand-off structure and replaces separately mounted quartz stand-offs. The diode top contact structure is realized by selective etching technology for GaAs substituting the gold bond ribbons (see Fig. 1). The REM-photograph in Fig. 2 shows a module seen from the epitaxial layer side, i.e. the side which has to be bonded onto the heat-sink. The stand-off structure guarantees the mechanical fixing of the module on the diamond heat-sink. Photoresist technology applied for the realization of all critical dimensions of the module results in high reproducibility. Instead of thermocompression bonding of a tiny single diode (diameter $\simeq 15\text{-}20\text{ }\mu\text{m}$) on a diamond heat sink and contacting this device with gold bond ribbons the whole module is bonded in one step on the diamond heat sink.

3 The resonator structure

The modules are incorporated into a D-band waveguide resonator terminated at one end with a sliding short for tuning. A disk-type radial resonator structure is mounted directly on the module top-metallization. This leads to a height of the resonant disk above the waveguide bottom which is equal to the module height (module dimensions: see Fig. 1). This distance is much lower as compared to conventionally encapsulated devices with quartz stand-offs. Therefore, the resonant structure was investigated in order to ensure that impedance matching between active device and resonator is possible. For the computer simulation a finite element CAD software package is used ('HFSS', Hewlett Packard). The program considers the complete outer resonator struc-

ture as well as the module encapsulation structure. The result shows that a typical negative resistance from -0.2 up to -2.0Ω can be matched in the frequency range from 110-150 GHz if the cap diameters are between 0.6-1.4 mm.

4 Diode structures

The GaAs single-drift flat-profile IMPATT diodes are realized with an doping concentration in the active region between $3.0 \cdot 10^{17} \text{cm}^{-3}$ and $3.4 \cdot 10^{17} \text{cm}^{-3}$ [5]. Generally, the maximum dc input power of the devices is thermally limited due to the relatively poor thermal conductivity of GaAs. This limits the maximum dc current density which, however, is necessary for efficient operation at elevated frequencies. The current density can be increased only if the operation voltage is reduced. This demand results in a Read-type diode structure [6]. For the design of this structure a numerical program for calculation of the device impedance has been applied. Drift,- diffusion,- impact ionization- and space charge effects as well as tunnel induced current are taken into account. The resulting diode structure together with the principal electric field distribution is shown in Fig. 3. The design of the high field region is suggested from Monte-Carlo simulation of Read-type structures [9] pointing out that suppression of tunneling is achieved from this design for ensuring operation predominantly in IMPATT-mode. The calculated negative resistance for the Read-type structure in comparison to a flat-profile structure optimized for 140 GHz is shown in Fig. 4 as function of the operation frequency (small-signal operation). A constant dc input power density of 500 kW/cm^2 is assumed leading to a device temperature of 450 K. It can be seen that the Read-type diode offers almost twice the negative resistance as compared to the flat-profile

structure.

For ensuring low-ohmic contacts a well established contact system for GaAs has been applied for all diodes investigated: TiPdAu for the p^+ -ohmic contact and AuGeNi/Au for the n^+ -ohmic contact.

5 Experimental results

The measured breakdown voltage for the flat-profile diodes is between 7.8-8.2 V. The value of 6.2 V for the Read-type diode demonstrates the achieved reduction of operation voltage. Thus, the maximum dc current density for long-time stable operation is about 65 kA/cm^2 for a flat-profile diode and 80 kA/cm^2 for a Read-type diode (diode diameter: $20 \text{ }\mu\text{m}$). For the rf measurements, all modules are fabricated with identical dimensions but active diodes having different diameters. The best results for rf output power are depicted in Fig. 5. Flat-profile diodes lead to 80 mW at 111 GHz and 63 mW at 118 GHz (diode diameter: $18\text{-}23 \text{ }\mu\text{m}$). The highest oscillation frequency observed from a flat-profile diode is 131 GHz (diode diameter $18 \text{ }\mu\text{m}$). As expected, the Read-type diodes lead to essentially better rf-performance. At 122 GHz 75 mW are realized, the highest oscillation frequency for cw-operation is 150 GHz (1mW output power). The diode diameters applied for 120-150 GHz are in the range from 17 to $27 \text{ }\mu\text{m}$.

The noise measure represents a characteristic quantity for the principal noise behaviour of a device as it is independent from the resonator behaviour and the diode area. Evaluation of the noise measure requires measurement of the external Q-factor and the rms-frequency deviation. Several oscillators fabricated are used for investigation of the noise behaviour. The noise-to-carrier ratio for evaluation of the rms-frequency deviation has been measured with

the help of a spectrum analyzer. For determination of the external Q-factor a self-injection method has been applied [10]. The measured values are in the range from 30-500 for various resonator configurations tested. In Fig. 6 the experimental as well as theoretical values for the noise measure are presented. The measurements are performed at relatively low rf output power levels ($P_{rf} \simeq 2-5$ mW) allowing the quantitative comparison with theoretical small-signal results [11]. For the calculations a dc current density of 50 kA/cm^2 and a device temperature of 450 K are assumed, which are in correspondence to the experimental values. For a flat-profile diode at 131 GHz a minimum noise measure of 27 dB is observed. The noise measure for a Read-type diode leads to a value of 26 dB at 144 GHz.

6 Conclusion

In this paper the investigation of GaAs IMPATT diodes for the frequency range from 110 up to 150 GHz is presented. The achieved results for the rf-output power point out that the module technique is a practical tool for the encapsulation of GaAs transit-time devices for D-band frequencies. The advantage resulting from this technique is high reproducibility and easy device handling. The measured power levels for the Read-type diodes, compared to flat-profile diodes, demonstrate that the reduction of dc input voltage leads to superior rf-performance at elevated frequencies. The good noise behaviour of the GaAs IMPATT devices is demonstrated by noise measurements performed up to 144 GHz.

ACKNOWLEDGEMENT

The authors kindly acknowledge D. Liebig for performance of the Monte-Carlo simulation, H. Grothe for the epitaxial growth of the MBE-wafers and W. Harth for encouragement and many stimulating discussions. Financial support is provided by the Deutsche Forschungsgemeinschaft (SFB 348).

References

- [1] Bogner, W. and Freyer, J.: V-band monolithic GaAs IMPATT oscillator, 21 th. European Microwave Conference, Vol. 1, pp. 358-363, 1991.
- [2] Luy, J. F., Strohm K. M., Buechler. J. and Russer, P.: Silicon Monolithic Millimeter Wave IMPATT Oscillator, IEE Proceedings-H, Vol. 139. No. 3, pp. 209-216, 1992.
- [3] Tschernitz, M., and Freyer, J.: New Encapsulation Modules for mm-Wave GaAs Transit-Time Devices, Electronics Letters, Vol. 28, p. 2125, 1992.
- [4] Tschernitz, M., and Freyer, J.: GaAs modules for power generation at W-band frequencies, Proc. of the 23th European Microwave Conference (Madrid), pp. 446-447, 1993.
- [5] Eisele, H., and Haddad, G. I.: 'GaAs Single-Drift Flat-Profile IMPATT Diodes for CW Operation at D Band', Electronics Letters, Vol. 28, p. 2176, 1992.
- [6] Tschernitz, M., Freyer, J., and Grothe. H.: GaAs Read-type IMPATT diodes for D-band, submitted for publication in Electronics Letters.

- [7] Gaul, L.: Großsignal und Stabilitätsanalyse von GaAs- Lawinendioden für Puls- Leistungsschaltern im Millimeterwellenbereich, Ph.D. Theses, TU-München. 1993.
- [8] Freyer, J., Mayer, B. and Tschernitz, M.: CAD for mm-wave resonators, to be published at 24th European Microwave Conference (Cannes), 1994.
- [9] Liebig, D.: private communication.
- [10] K. Kurokawa, IEEE Trans. Microwave Theory Techn. MTT-16, p. 234, 1968.
- [11] Harth, W., Bogner, W., Gaul, L. and Claassen, M.: A comparative study on the noise measure of millimetre-wave GaAs Impatt diodes, Solid State Electronics, 37, pp. 427-431, 1994.

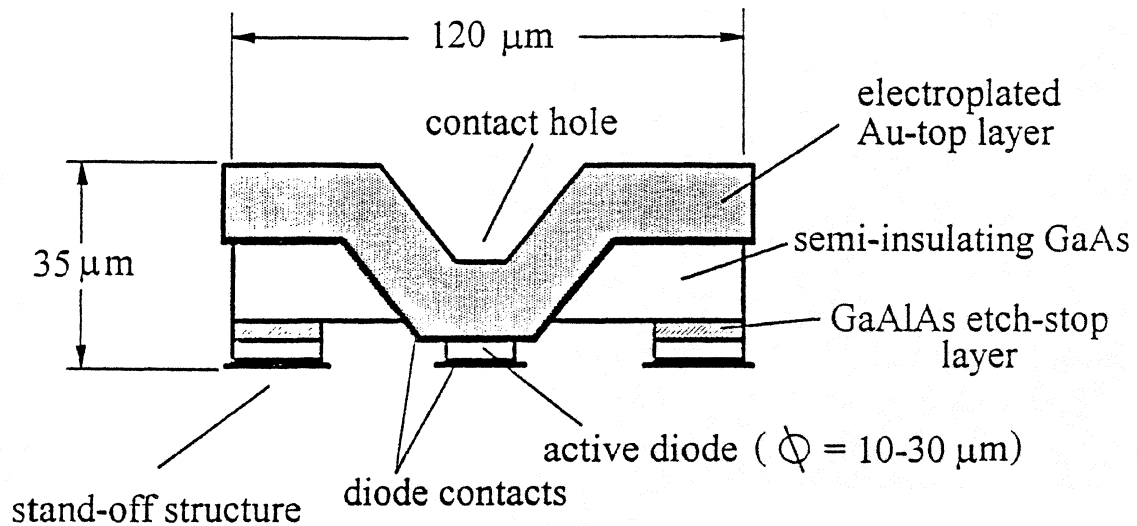


Figure 1: Principal cross-section of an encapsulation module (dimensions are for D-band frequencies)

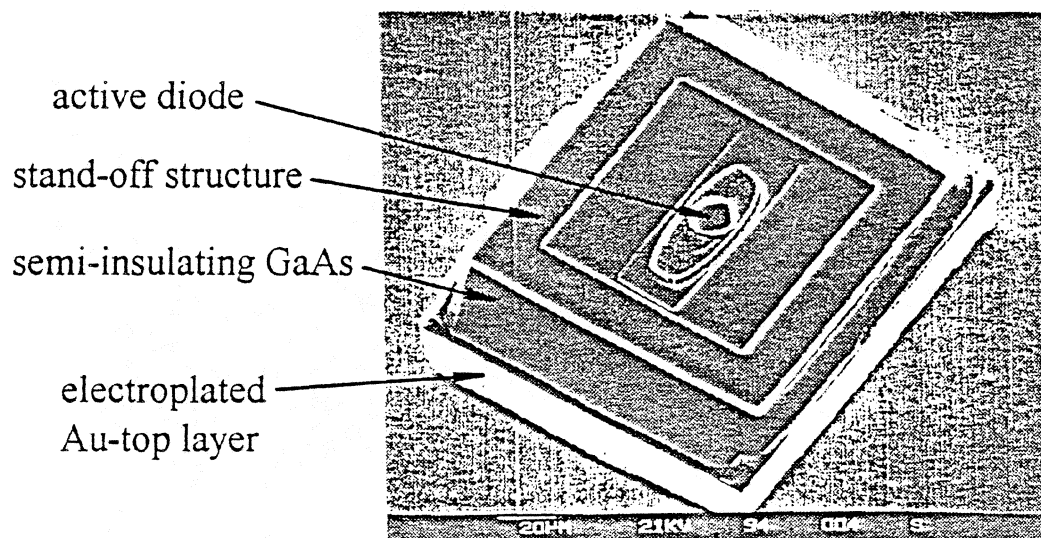


Figure 2: REM-Photograph of an encapsulation seen from the epitaxial layer side

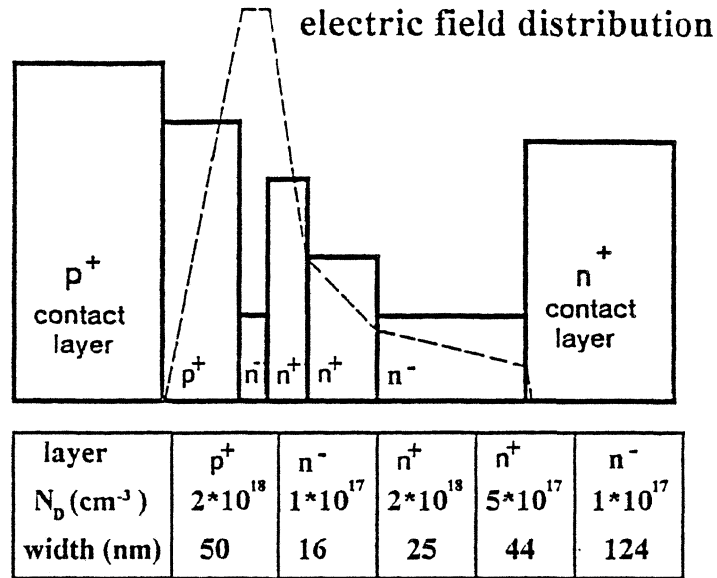


Figure 3: Read-type IMPATT diode structure for D-band frequencies with the electric field distribution

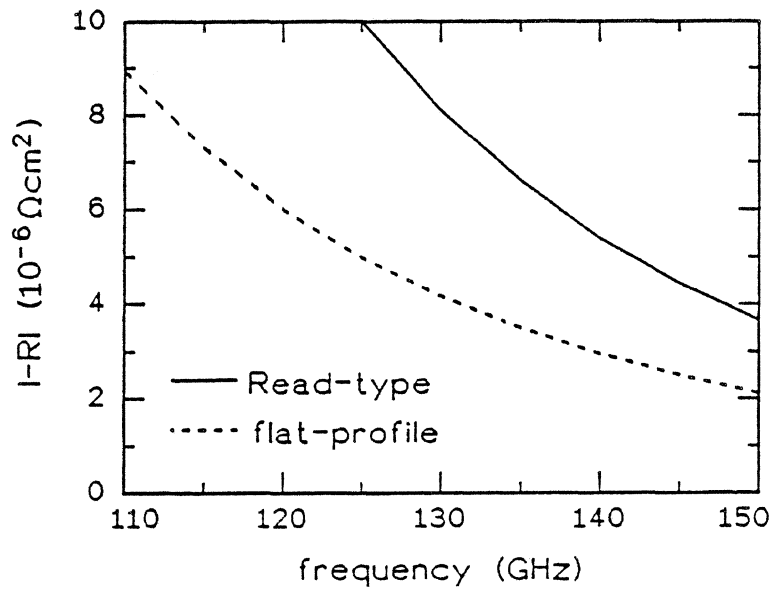


Figure 4: Negative resistance of the Read-type diode structure and a flat-profile diode structure optimized for 140 GHz (dc input power density = 500 kW/cm^2)

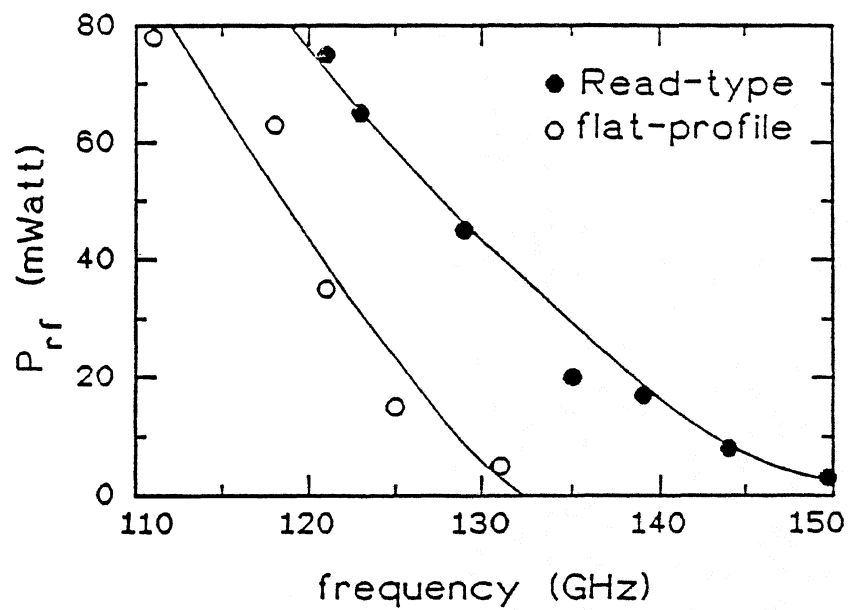


Figure 5: Rf-output power for flat-profile and Read-type diodes

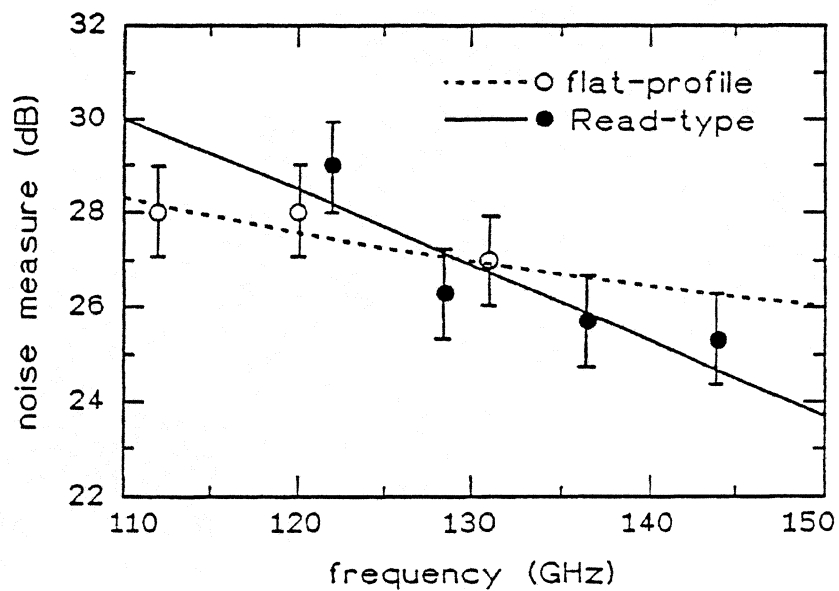


Figure 6: Experimental and theoretical values for the noise measure (small-signal operation)

PERFORMANCE OF GaAs TUNNETT DIODES AS LOCAL OSCILLATOR SOURCES

H. Eisele, C-C. Chen, R. Mains, G. I. Haddad

Solid-State Electronics Laboratory
Department of Electrical Engineering & Computer Science
The University of Michigan
Ann Arbor, Michigan 48109-2122

Abstract

Improved heat dissipation in TUNNETT diodes on diamond heat sinks has lead to RF power levels of up to 95 mW and dc to RF conversion efficiencies of up to 5.9 % between 104 GHz and 111 GHz. These values for power and efficiency exceed those of Gunn devices in this frequency range and together with the clean spectra and demonstrated phase-locking capabilities make GaAs TUNNETT diodes suitable for local oscillator applications. TUNNETT diodes in second-harmonic mode yielded an RF output power of up to 0.6 mW between 210 GHz and 220 GHz. Diodes on diamond heat sinks show clear signs of saturation in the dc to RF conversion efficiency, which can be attributed to about 60 % higher bias current densities than originally assumed in the structure design. Extensive numerical simulations using a computer program with an energy-momentum model show good agreement between predictions and experimental results and can provide realistic estimates for the RF performance at higher submillimeter-wave frequencies.

1. Introduction

Tunnel injection transit-time (TUNNETT) diodes for power generation at high frequencies were first proposed in 1958 [1], but the lack of refined growth techniques required for the high doping levels and steep transitions in the doping profile impeded significant power levels in CW operation of TUNNETT diodes until a few years ago. Commercially available systems for epitaxial growth, such as molecular beam epitaxy (MBE) or metallorganic chemical vapor deposition (MOCVD), now routinely provide the necessary material quality. Better understanding of the device characteristics have lead from the first experimental results [2,3] to RF power levels of up to 95 mW at 104.2 GHz, which clearly demonstrate the potential of GaAs TUNNETT diodes as powerful oscillators at submillimeter-wave frequencies. This paper reviews the fabrication processes and their impact on the device performance and compares the experimental results with the predictions of detailed device simulations.

2. Fabrication technologies and their impact on the RF performance

W-band GaAs TUNNETT diodes were first designed for operation on integral heat sinks at oscillation frequencies around 100 GHz. A versatile selective etching technology [4,5] was employed to fabricate

diodes on integral heat sinks. These diodes yielded an RF output power of up to 40 mW around 103 GHz and dc to RF conversion efficiencies over 4 %. Since neither RF output power nor dc to RF conversion efficiency saturated up to the maximum applied bias, diodes on integral heat sinks were considered to be thermally limited and RF power levels were expected to increase significantly on better heat sinks. Therefore, a selective etching technology that has been successfully used to fabricate GaAs W- and D-band impact ionization avalanche transit-time (IMPATT) diodes on diamond heat sinks was adopted [5,6]. This well-established fabrication process was slightly modified [7] to obtain diodes on integral heat sinks as well as diodes for mounting on diamond heat sinks in one batch. All GaAs TUNNETT diodes were packaged in the same open structure with quartz standoffs and tapered leads and tested in several identical full-height waveguide cavities with resonant caps for frequency and impedance tuning.

RF output power levels up to 95 mW and corresponding dc to RF conversion efficiencies up to 5.9 % were achieved with diodes on diamond heat sinks, whereas diodes on integral heat sinks of the same batch showed performance similar to previously tested diodes. Figure 1 summarizes the best results of all tested diodes on diamond heat sinks and compares them with the best results of about 70 % of the tested diodes on integral heat sinks. RF power levels are more than doubled through the improved heat dissipation whereas dc to RF conversion efficiencies typically increase by a factor of 1.5. All diodes on diamond heat sinks exhibit clear signs of saturation in the efficiency and, therefore, must be considered electronically limited.

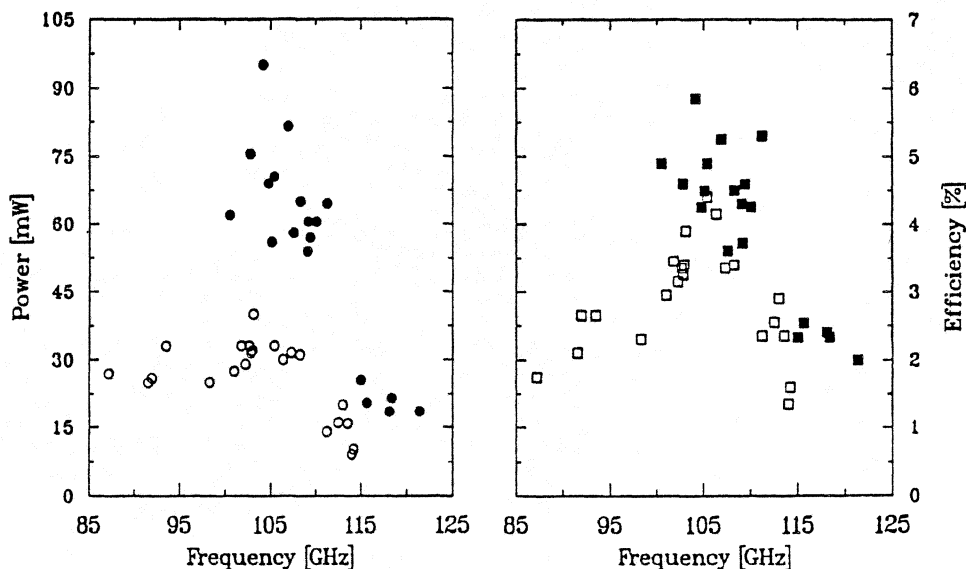


Fig. 1: RF output power (●, ○) and dc to RF conversion efficiency (■, □) vs. oscillation frequency for GaAs TUNNETT diodes on integral (closed symbols) and diamond (open symbols) heat sinks.

A detailed thermal analysis that also included the experimental results of W- and V-band IMPATT diodes predicts thermal resistances between 80 KW⁻¹ and 100 KW⁻¹ for nominal diameters between 20 μm and

25 μm . Since the dc input power for diodes on diamond heat sinks typically ranges from 1.4 W to 1.7 W for a maximum RF output power above 50 mW, the operating junction temperature can be safely assumed to be well below 200 °C for a cavity at room temperature.

Different diodes on diamond heat sinks were more similar in RF performance than their counterparts on integral heat sinks, but several pairs of diodes on both types of heat sinks were sufficiently matched to attempt power combining in a dual-cavity configuration [8]. Combining efficiencies were typically around 80 % and more than 140 mW were measured with the best pair on diamond heat sinks at an oscillation frequency of 103.9 GHz. In this case the overall dc to RF efficiency was 4.3 % and the combining efficiency exceeded 85 %.

GaAs TUNNETT diodes can be phase locked as shown by the spectrum in Figure 2 for a configuration with a narrow loop bandwidth (< 25 kHz) [9]. The spectrum was measured at the intermediate frequency of the phase-locked loop to bypass the upconverted phase noise of the spectrum analyzer.

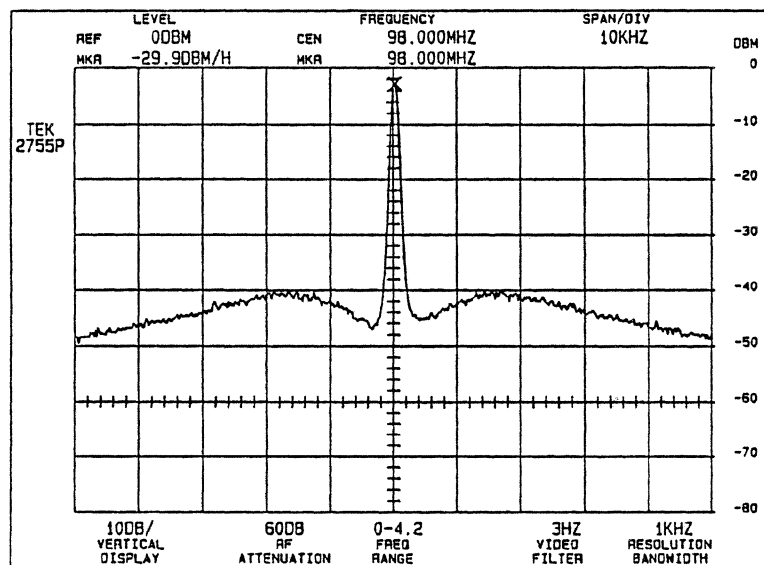


Fig. 2: Spectrum of a phase-locked GaAs TUNNETT diode oscillator at 107.758 GHz, power level 40 mW, center frequency 98.000 MHz, vertical scale 10 dB/div, horizontal scale 10 kHz/div, BW 1 kHz, VideoBW 3 Hz.

The improved heat dissipation on diamond heat sinks also increased the available RF output power in second-harmonic mode and up to 0.6 mW was measured at 209.5 GHz. A similar setup for these measurements was reported recently [10], and it should be noted again that the available RF power levels of diodes on both types of heat sinks might be significantly higher. Figure 3 shows the measured spectrum of a free-running TUNNETT diode oscillator in second-harmonic mode with an RF output power of 0.57 mW. This demonstrates that clean spectra can be achieved in second-harmonic mode although the

noise floor of the harmonic mixer and spectrum analyzer inhibit accurate phase noise measurements. Oscillations up to 235 GHz in second-harmonic mode are the highest reported to date for CW operation of any GaAs transit-time device.

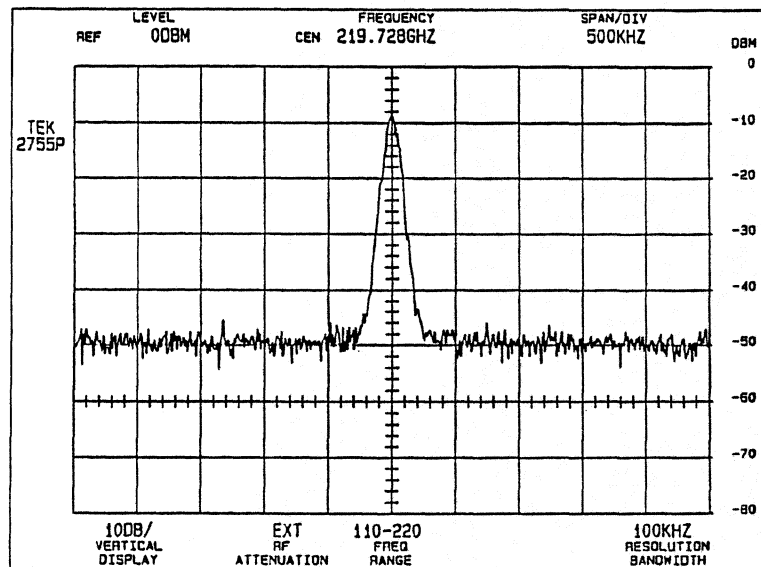


Fig. 3: Spectrum of a GaAs TUNNETT diode free-running oscillator, power level 0.57 mW, center frequency 219.728 GHz, vertical scale 10 dB/div, horizontal scale 500 kHz/div, BW 100 kHz.

3. Predicted performance vs. experimental results

Numerical simulation programs that are based on the drift-diffusion and energy-momentum transport models and include interband tunneling have been developed to predict the performance of two-terminal transit-time devices. A detailed description of the models can be found in Reference 11 and an accompanying paper [12] describes its application to InP transit-time devices. The material parameters such as band gap lowering or drift velocities, diffusion coefficients, ionization and tunneling rates of electrons and holes, need to be chosen carefully to ensure realistic estimates from the simulations. Diffusion coefficients and drift velocities were taken from Monte-Carlo simulations and "curve fitted" to published or unpublished results of measurements [13] or simulations. The high-field ionization rates were assumed to be equal and derived from breakdown voltages of various GaAs IMPATT diodes [6,13]. Previous simulations of GaAs W- and D-band IMPATT diodes predicted bias voltages typically within $\pm 5\%$ of the measured values at the maximum RF output power and provided good agreement between predicted and measured RF performance as well if contact resistances were taken into account [14]. Tunneling rates were based on a simple theoretical model [15] and adjusted accordingly to match the bias voltages of diodes on integral heat sinks as well as on diamond heat sinks typically within 10 %. In addition to an accurate prediction of the bias voltages, the chosen tunneling rates ensure that about the same portion of

the total bias current is generated through tunneling as can be extrapolated from the measured current-voltage characteristics under operating conditions [7].

The aforementioned fabrication process leads to some undercut in the diodes and impedes an accurate measurement of the actual diode diameter unless the packaged diode is destroyed. Therefore, the current densities were estimated to be in range of 40 kAcm^{-2} to 45 kAcm^{-2} . Figure 4 shows the predicted dc to RF conversion efficiencies as a function of the RF voltage for the lower and upper limit of the estimated current densities. The terminals of the diode are not accessible inside the package at millimeter-wave frequencies to measure the actual RF voltage between the p^+ and n^+ contacts of the diode or to verify the embedding impedance. Although the embedding impedance could be determined with acceptable accuracy using scale models and S-parameter measurements or could be calculated using appropriate models for the resonant cap structure or the versatile HFSS (high-frequency structure simulator by Hewlett Packard) software package, the strong back bias effect in TUNNETT diodes itself gives an accurate estimate of the actual RF voltage across the terminals. The predicted change of the bias voltage in percent is plotted in Figure 4 as a function of the RF voltage and compared with the measured change of a diode that yielded an RF output power of more than 80 mW at an oscillation frequency of 106.9 GHz. The predicted dc to RF conversion efficiencies between 5.43 % and 5.61 % for a typical RF voltage of 6.5 V are close to the measured value of 5.3 % for this particular diode and actually tend to saturate as

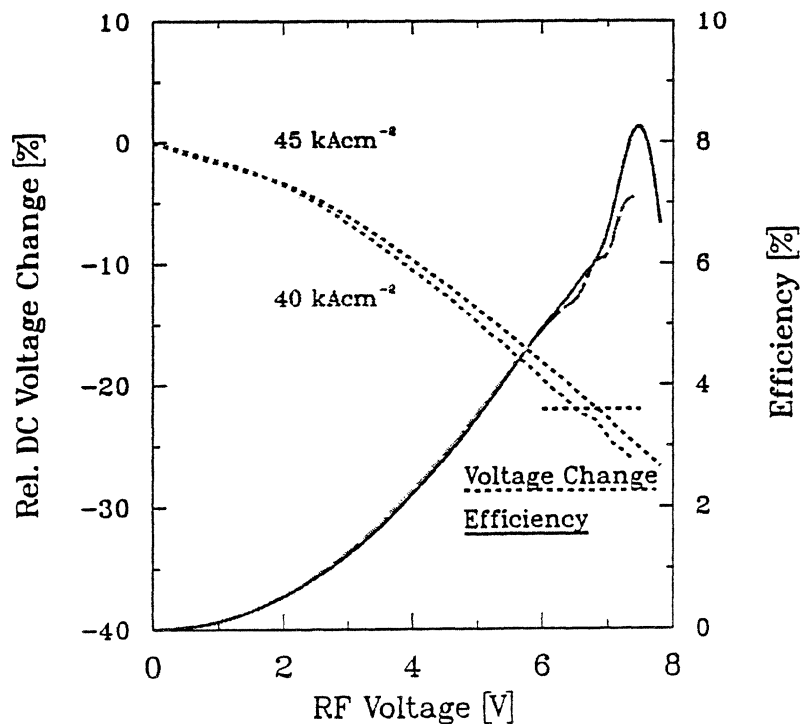


Fig. 4: Predicted dc to RF conversion efficiency and relative change of bias voltage as a function of RF voltage.

seen in all tested diodes on diamond heat sinks. The predicted RF power levels exceed the measured values of the three best diodes by no more than 2 dB and demonstrate the validity of the simulations. The simulations also reveal that the peak in the injected current occurs within 10 degrees of the maximum in the RF voltage and that the mode of operation is very close to the mode of in-phase carrier injection as proposed in Reference 1. The good agreement between experiment and numerical simulations shows that these simulation programs can be used as a powerful tool to find a more optimized device structure and to predict the performance at higher submillimeter-wave frequencies [11].

Acknowledgment

This work was supported by NASA under contract No. NAGW 1334.

References

- [1] Nishizawa, J., Watanabe, Y.: "High Frequency Properties of the Avalanching Negative Resistance Diode", *Science Report Research Institute Tohoku University*, **10**, 1958, pp. 91-108.
- [2] Pöbl, M., Dalle, C., Freyer, J., Harth, W.: "CW mm-Wave GaAs TUNNETT Diode," *Electronic Letters*, **26**, 1990, pp. 1540-1542.
- [3] Kidner, C., Eisele, H., and Haddad, G. I.: "Tunnel Injection Transit-Time Diodes for W-Band Power Generation", *Electronics Letters*, **28**, 1992, pp. 511-513.
- [4] Kamoua, R., Eisele, H., Haddad, G. I.: "D-Band (110 GHz - 170 GHz) InP Gunn Devices", *Solid-State Electronics*, **36**, 1993, pp. 1547-1555.
- [5] Eisele, H.: "Selective Etching Technology for 94 GHz GaAs IMPATT Diodes on Diamond Heat Sinks", *Solid-State Electronics*, **32**, 1989, pp. 253-257.
- [6] Eisele, H., Haddad, G. I.: "GaAs Single-Drift Flat-Profile IMPATT Diodes for CW Operation in D Band", *Electronics Letters*, **28**, 1992, pp. 2176-2177.
- [7] Eisele, H., Haddad, G. I.: "GaAs TUNNETT Diodes on Diamond Heat Sinks for 100 GHz and Above", to be published in *IEEE Transactions on Microwave Theory and Techniques*.
- [8] Eisele, H., Haddad, G. I.: "Enhanced Performance in GaAs TUNNETT Diode Oscillators Above 100 GHz Through Diamond Heat Sinking and Power Combining", presented at the *1994 IEEE MTT-S International Microwave Symposium*, May 23-27, 1994, San Diego, California.
- [9] Eisele, H., Haddad, G. I.: "Recent Experimental Results from GaAs TUNNETT Diodes Above 100 GHz", *Proceedings of the International Conference on Millimeter and Submillimeter Waves and Applications*, San Diego, California, 1994.

- [10] Eisele, H., Kamoua, R., Haddad, G. I., Kidner, C.: "Active Two-Terminal Devices as Local Oscillators for Low-Noise Receiver Systems at Submillimeter Wave Frequencies", *Archiv für Elektrotechnik*, **77**, 1994, pp. 15-19.
- [11] Chen, C-C., Mains, R. K., Haddad, G. I., Eisele, H.: "Numerical Simulation of TUNNETT and MITATT Devices in the Millimeter and Submillimeter Range", *Proceedings of the 4th International Symposium of Space Terahertz Technology*, March 30 - April 1, 1993, Los Angeles, California, pp. 362-376.
- [12] Chen, C-C., Mains, R. K., Haddad, G. I., Eisele, H.: "High-Efficiency InP IMPATT Diodes for High-Frequency Power Generation", these proceedings.
- [13] Eisele, H.: "Electron Properties in GaAs for the Design of mm-Wave IMPATTs", *International Journal of Infrared and Millimeter Waves*, **4**, 1991, pp. 345-354.
- [14] Eisele, H., Mains, R. K., Haddad, G. I., Chen, C-C.: "GaAs IMPATT Diodes for Frequencies Above 100 GHz: Technology and Performance", *Proceedings of the 2nd International Symposium on Space Terahertz Technology*, February 26-28, 1991, Pasadena, California, pp. 145-153.
- [15] Kane, E. O.: "Zener Tunneling in Semiconductors", *Journal Phys. Chem. Solid*, **12**, 1959, pp. 181-188.

Second Harmonic 210 GHz InP Millimeter Wave Transferred Electron Oscillators

M.F. Zybura, S.H. Jones, G.B. Tait[†]

Applied Electrophysics Laboratories
Department of Electrical Engineering
University of Virginia
Charlottesville, VA 22903-2442

[†]Electronics Science and Technology Division
Naval Research Laboratory
Washington, DC 20375

Abstract

Accurate and efficient calculations of the large-signal AC behavior of second- and third-harmonic InP Transferred Electron Oscillators (TEOs) are presented. This is accomplished by combining a novel harmonic balance circuit analysis technique with a hydrodynamic device simulator employing the temperature dependent drift and diffusion equations. The electron transport simulations include a detailed heat flow analysis to update the temperature profile in the device. The nonlinear circuit analysis utilizes a fixed-point iterative method derived from the robust multiple reflection algorithm. To expedite the process and aid in convergence, an acceleration technique is also employed in this algorithm. The associated reduction in computation time allows for the inclusion of a full hydrodynamic treatment of the Transferred

Electron Device (TED) using the first two moments of the Boltzmann transport equation. Comparisons are made with the published experimental data reported by Rydberg on second- and third-harmonic 200-300 GHz InP TEOs. Simulation results for TEOs designed specifically for 210 GHz second harmonic, and 315 GHz third harmonic are presented.

1 Introduction

Rydberg [1] has demonstrated as much as 0.6 mW of power at 270 GHz using third-harmonic InP devices. To optimize future harmonic device designs for increased power and higher frequencies, a design tool that efficiently determines power at all harmonics, as a function of the device characteristics, embedding circuit, and packaging parameters is required. Presently, computer aided design programs are available for microwave nonlinear circuit analysis based on the harmonic balance numerical technique [2]. These codes reduce the nonlinear semiconductor devices to equivalent circuit elements with closed form analytical approximations for the current-voltage characteristics making the nonlinear circuit analysis possible. This approach is powerful for lower frequency design, and has been a critical factor in the design of integrated microwave circuits. For more complex and higher fre-

quency millimeter wave circuits however, the approximate equivalent circuit technique is not sufficiently accurate. In this work, an efficient fixed point iteration method derived from the multiple reflection technique [2] is employed facilitating the use of a full hydrodynamic device simulator using the drift and diffusion equations. The drift and diffusion equations utilize both field (0.1-100 kV/cm) and temperature (300-500K) dependent mobility and diffusivity derived from monte carlo simulations, and a thermal analysis which includes all regions of the device. Every aspect of the linked nonlinear circuit/ hydrodynamic device simulator has been designed for accuracy, computational speed, and robust convergence properties.

2 Thermal Model

Since the dc-microwave conversion efficiency in TEDs can degrade substantially if the device active-region temperature approaches 500K, temperature effects must be considered to optimize high power oscillator design. During operation, heat is generated in all regions of the device, however most of the power dissipation occurs across the device active-region due to both its relatively high resistivity and low dc-rf conversion efficiency. Given the extremely low thermal conductivity of the air surrounding the mesa, es-

essentially all the heat generated in the packaged device will flow into the highly conductive gold plated copper heat sink through the device layers and contacting regions. Thus, the thermal analysis can be reduced to one dimension, with no heat loss through the sides or top of the mesa. In our model, heat generation is considered in all layers of the packaged device [3]. Integrating the associated one dimensional heat equation, and solving the resultant set of linear equations yields an expression for the temperature across a given layer as a function of the interface temperatures that bound that region. The continuity criterion is applied at every interface giving a system of linear equations with a tri-diagonal matrix for the determination of the unknown interface temperatures. To complete the mathematical description, specifications of boundary conditions at both the mesa to air, and contact to heat sink interfaces are required. At the heat sink interface the flow of heat from the semiconductor into the stud can be approximated as heat transfer into an infinite half plane. At the top of the mesa, as mentioned, it is assumed that there is no heat flow ($\frac{\partial T}{\partial x} = 0$). The symbolic solution to these equations gives closed form expressions for T and $\partial T/\partial x$ in each layer given the layer dimensions, the ohmic contact resistance, and the power dissipated per unit volume (Q) in that layer. As described below, Q is calculated in all layers from the large signal ac numerical calculation of

the device current and power.

3 Device Simulator

The device simulator employed here is a slightly modified version of a previously described simulation program [3, 4]. The phenomenological hydrodynamic equations governing the physical model are the reduced, one dimensional forms of the first two moments of the Boltzman Transport Equation (BTE) and Poisson's equation,

$$\frac{\partial n}{\partial t} = \frac{1}{q} \frac{\partial J}{\partial x} \quad (1)$$

$$J = qnE\mu(E, T) + qD(E, T)\frac{\partial n}{\partial x} + qnD_n^T\frac{\partial T}{\partial x}, \quad (2)$$

and

$$\frac{\partial^2 \phi}{\partial x^2} = -\frac{q}{\epsilon}(N_D(x) - n), \quad (3)$$

where n , q , and J are the electric charge density, the electron charge, and the particle current density, respectively. In equation 2, E , μ , D , D_n^T , and T are the electric field, the temperature and field dependent mobility and diffusivity, the thermal diffusivity, and the lattice temperature, respectively. In equation 3, ϕ is the scalar potential, ϵ is the dielectric permittivity of the device material, and $N_D(x)$ is the donor impurity concentration. The

electric field is calculated from Poisson's equation, and the thermal gradient, $\partial T/\partial x$, is analytically determined from the aforementioned thermal analysis.

The GaAs and InP electric field and temperature dependent mobility, $\mu(E, T)$, and diffusivity, $D(E, T)$, were calculated from over 300 three-valley monte carlo simulations. These simulations were performed using 10,000 superparticles at 50 degree increments from 300K to 500K with a uniform donor concentration of 10^{16}cm^{-3} . The monte carlo code is similar to the code used in [5], however to account for high temperature effects, along with lattice temperature, several material parameters were modified to be temperature dependent [6, 7]. These include: the energy gaps and conduction valley minima separation of Γ , L, and X valleys, the gamma valley electron effective mass, the density and lattice constant, and the high and low frequency dielectric constants. Both the mobility and diffusivity data has been numerically fit using equation (6-2-8) of reference [8], and the accompanying fit parameters are again fit versus temperature yielding surface contours for both mobility and diffusivity versus electric field and temperature. Closed form expressions for $\mu(E, T)$ and $D(E, T)$ serve to enhance computation speed. The above drift and diffusion transport equations form a set of coupled nonlinear partial differential equations, which are solved by the half-implicit Crank Nicolson finite difference scheme. Spatial and tem-

poral increments typically are on the order of the length and time over which charge imbalances grow or decay. Spatially, the Debye length is suitable, and temporally, the dielectric relaxation time is appropriate. This technique offers substantial reductions in CPU time while retaining some important hot electron effects since $\mu(E, T)$ and $D(E, T)$ have been extracted from prior monte carlo analysis. The frequency dependent parasitic resistances of the device (DC- n^{th} harmonic) are also calculated [9] and added to the respective embedding impedances also included in the nonlinear circuit analysis described below.

4 Harmonic Balance

To fully design transferred electron oscillators (TEOs) equal design consideration must be given to both the device and the circuit in which it is mounted. With a hydrodynamic device simulator, one can determine the optimal embedding impedances of the cavity presented to the device by optimizing the power generation as a function of the ac voltage. However, such an optimization is virtually impossible when considering higher harmonic components of the driving voltage. Similarly, finding a device design which has some pre-specified operating impedance is difficult, when considering second- or

third-harmonic operation. By linking both the device and circuit simulators this problem can be overcome. The harmonic balance nonlinear circuit analysis technique employed here is an extension of the Siegel and Kerr multiple reflection algorithm [2]. A fixed-point iteration is used to update the total voltage at the device terminals. The current through the device then is numerically calculated as described above. In our algorithm, we use *a priori* knowledge of the solution from Kirchhoff's voltage law that the nonlinear device impedance will equal the negative of the linear circuit impedance for each undriven harmonic in steady state ($Z_n^{NL} = -Z_n^L, n = 2, 3, \dots, 6$). This eliminates the computationally intensive and possibly unstable Runge-Kutta numerical integration necessary in the multiple-reflection technique, and automatically calculates the complex under-relaxation parameters for each harmonic component of the fixed point update equation. Included with the fixed-point iteration is a Steffenson acceleration scheme adopted from the secant methods of numerical analysis [10]. Unlike Newton techniques, the difficult and time consuming numerical calculations needed for the assembly of Jacobian matrices and the solutions of large linear systems of equations are avoided, while maintaining a convergence rate nearly that of Newton-type methods.

5 Results and Discussion

Figure 1 illustrates the algorithm by which the TEO simulations are performed. The operating frequency, DC bias, circuit embedding impedances ($2^{nd} - 6^{th}$ harmonic), doping profile, and chip characteristics are adjustable inputs. The ac driving voltage, V_1 , is allowed to sweep over a given range where optimal power, stability, and sufficient device impedances at the fundamental are anticipated. This limits the optimization to the DC and fundamental driving voltages. After each fixed-point iterative update of the voltage, the device current is numerically calculated, and the circuit and device impedances at each harmonic are tested for convergence ($Z_n^{dev} = -Z_n^{ckt}$, $n = 2, 3, \dots, 6$). Outputs include current and voltage waveforms, electric field and electron concentration profiles versus time and position, the temperature profile and output power (DC-6th harmonic). In order to demonstrate the correlation between simulation and experimental results, comparisons have been made with published experimental data of Rydberg [1]. The InP TED simulated and described in reference [1] has a $1.1\mu\text{m}$ graded active region from $1.4 \times 10^{16} \text{cm}^{-3}$ at the cathode to $1.6 \times 10^{16} \text{cm}^{-3}$ at the anode, and a $50\mu\text{m}$ mesa diameter. At a fundamental frequency of 94 GHz and DC bias of 4-V, the simulations indicate peak power and stability for an impressed

2-V ac signal directly across the device. This gives a device impedance at the fundamental of $Z_1^{dev} = -0.8 - j6.6\Omega$. Figure 2 shows the resultant power versus circuit impedance surface contour for a domain of second harmonic (188 GHz) circuit impedances ranging from $1.55\Omega \leq R_2 \leq 10.55\Omega$ and $0\Omega \leq X_2 \leq 10.0\Omega$. Because the device is typically capacitive, only positive reactances are considered. Six harmonics are considered and in this case the embedding impedances of the higher harmonics ($3^{rd} - 6^{th}$) are set to 0.001Ω for both resistive and reactive components. The frequency dependent parasitic resistances are added to the corresponding linear embedding impedances. Peak performance of 6.4 mW is predicted for a second harmonic circuit impedance, $Z_2^{ckt} \approx 2.3 + j3.0\Omega$. Power generation near 2 mW is expected for circuit impedances as large as $Z_2^{ckt} = 10 + j10$. Experimentally, Rydberg has demonstrated ≈ 5 mW of power generated at 188 GHz in second-harmonic operation.

To simulate third harmonic performance, the stable second harmonic operating impedance $Z_2^{ckt} = 2.0 + j3.5\Omega$ is selected. The third harmonic (282 GHz) power versus corresponding third harmonic circuit impedances is shown in Figure 3. Again optimal performance is predicted for a low circuit impedance, $Z_3^{ckt} \approx 2.4 + j2.0\Omega$. The anticipated output power varies from $\approx .1 - 0.76$ mW over the selected range of third harmonic circuit

impedances. At 280 GHz rydberg has shown 0.2 mW of output power. Electron concentration profiles for this device operating in third-harmonic mode with $Z_1^{ckt} = 0.8 + j6.6$, $Z_2^{ckt} = 2.0 + j3.5\Omega$, and $Z_3^{ckt} = 2.0 + j2.5$ are shown in Figure 4. The active region is bordered by regions of higher doping ($N_D = 8 \times 10^{16} \text{cm}^{-3}$) to mimic the n^+ regions which bind it. Snapshots of the electron concentration are given in increments of one fifth of the fundamental frequency period. It is apparent that the device operates in an accumulation mode with the charge instabilities nucleating $\approx 0.5 \mu\text{m}$ from the cathode. Figure 5 show the 210 GHz second harmonic power versus the resistive part of the circuit impedance for a $2.1 \mu\text{m}$ long InP TED. The device doping slopes from $1.5 \times 10^{16} \text{cm}^{-3}$ at the cathode to $2.0 \times 10^{16} \text{cm}^{-3}$ at the anode. The DC is 5.24 V and the magnitude of the fundamental voltage is 3.41 V. Unlike the typically short devices used for high frequency applications, this longer device produces more second harmonic power (11 mW) and has its maximum output at a larger second harmonic circuit impedance of $5.5 + j10\Omega$. Figure 6 shows the resultant third harmonic (315 GHz) power from an InP Modulated Impurity Concentration TED (MICTED). The active region is $2.125 \mu\text{m}$ in length with a 900\AA doping mesa located $0.5 \mu\text{m}$ from the cathode. The mesa is doped to $4 \times 10^{16} \text{cm}^{-3}$ on an otherwise smooth grade from $1.5 \times 10^{16} \text{cm}^{-3}$ at the cathode to $2.0 \times 10^{16} \text{cm}^{-3}$ at the anode. At a fundamental frequency of

105 GHz with $V_{DC}=5.24$ V, $V_{ac} = 4.5$ V, $Z_2^{kt} = 6.45 + j18.0\Omega$, and a mesa diameter of $30\mu\text{m}$, it is anticipated that nearly 3 mW may be obtained at 315 GHz with a third harmonic circuit embedding impedance of $Z_3^{kt} \approx 8 + j12$.

6 Conclusion

The interaction between device and circuit is critical to high frequency TED performance. With this CAD tool, efficient design of second- and third-harmonic TEDs is possible. Typical convergence time for a given operating point involves about ten harmonic balance iterations and a total wall time of under a minute on a Hewlett Packard 735 workstation. Although specific circuit embedding impedances are unavailable for Rydberg's cavity, over the range of impedances offered, simulations compare favorably for both second- and third-harmonic performance. The potential increase in output power for 200-300 GHz second harmonic InP TEDs is expected for longer, higher impedance devices. Also, increases in third-harmonic power using a modulated doping profile in the TED active region [11] are expected and are being further explored.

7 Acknowledgements

The authors wish to thank Dr. J. D. Carlstrom for stimulating discussions.

This work is supported by NSF grant ECS-9202037.

References

- [1] A. Rydberg, "High efficiency and output power from second- and third-harmonic millimeter wave InP-TED oscillators at frequencies above 170 GHz", *IEEE Electron Device Lett.*, **11**, 10 (1990), pp. 439-441.
- [2] A. R. Kerr, "A Technique for Determining the Local Oscillator Waveforms in a Microwave Mixer", *IEEE Trans. Microwave Theory and Tech.* **23** (1975), pp. 828-831.
- [3] M. F. Zybur, S. H. Jones, G. B. Tait and J. M. Duva, "Efficient CAD of GaAs and InP millimeter wave transferred electron devices including detailed thermal analysis", submitted *Solid-St. Electron.* 1994.
- [4] G. B. Tait and C. M. Krowne, "Efficient transferred electron device simulation method for microwave and millimeter wave CAD applications", *Solid-St. Electron.* **30**, 10 (1987), pp. 1025-1036.
- [5] G. U. Jensen, B. Lund, T. A. Fjeldly and M. Shur, "Monte Carlo simulation of semiconductor devices", *Comp. Phys. Comm.* **6** (1991), pp. 1-61.
- [6] J. S. Blakemore, "Semiconducting and other major properties of GaAs", *J. Appl. Phys.* **53** (1982), pp. R123-R181.
- [7] O. Madelung (Ed.) *Semiconductors, Group IV Elements and III-V Compounds*, Springer-Verlag, Heidelberg, Germany, 1991.
- [8] M. Shur *Physics of Semiconductor Devices*, Prentice-Hall, Englewood Cliffs, NJ, 1990.
- [9] S. A. Maas *Nonlinear Microwave Circuits*, Artech House, Norwood, MA, 1988, Ch. 2, pp. 49-51.
- [10] J. Ortega and W. Rheinboldt *Iterative Solution of Nonlinear Equations in Several Variables*. Academic Press, New York, 1970.
- [11] S. H. Jones, G. B. Tait and M. Shur, "Modulated-impurity- concentration transferred electron devices exhibiting large harmonic frequency content", *Microwave and Opt. Tech. Lett.*, Vol. 5, **8**, (1992), pp. 354-359.

Unified Numerical Device/Harmonic-Balance Nonlinear Circuit Simulator

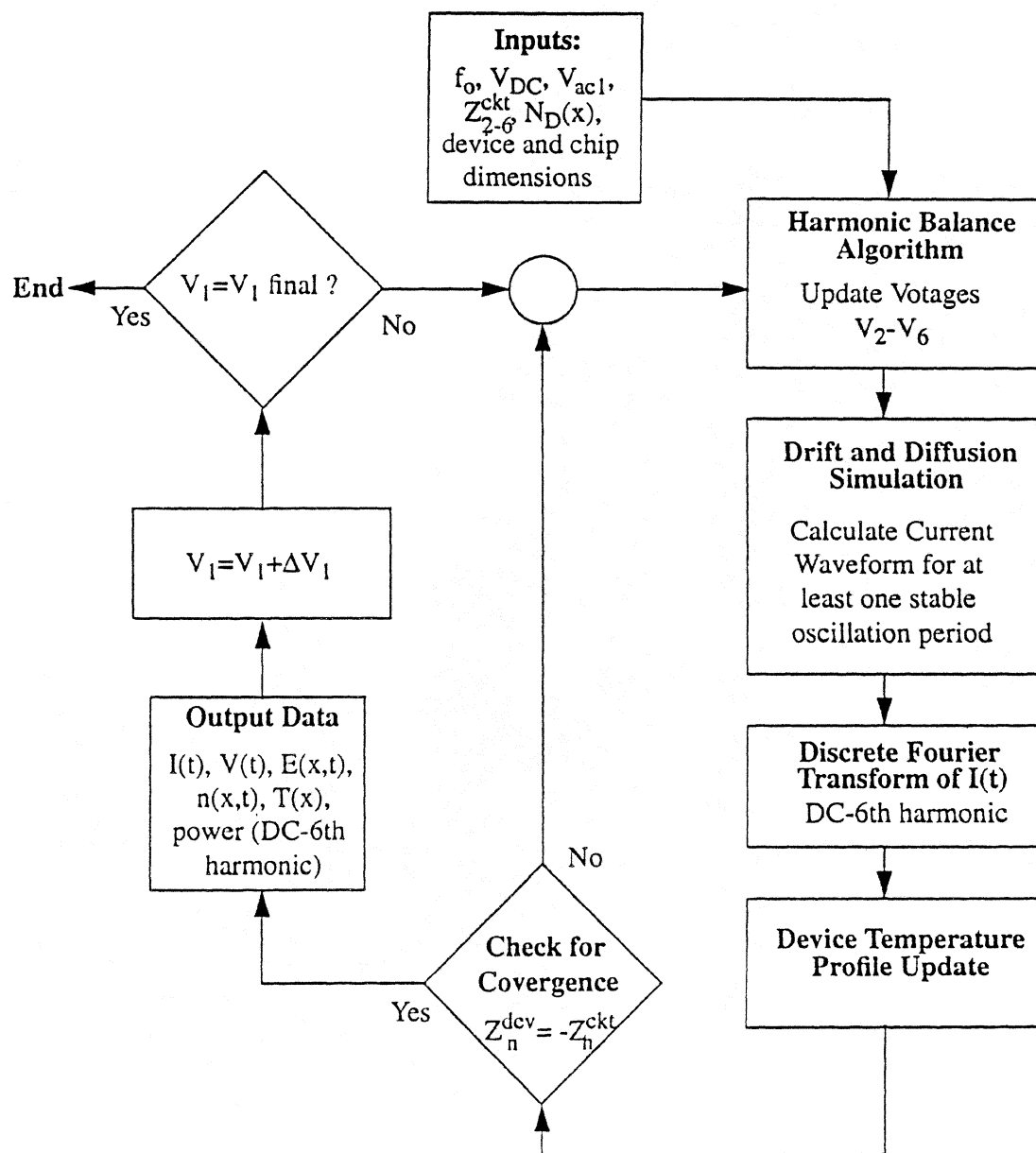
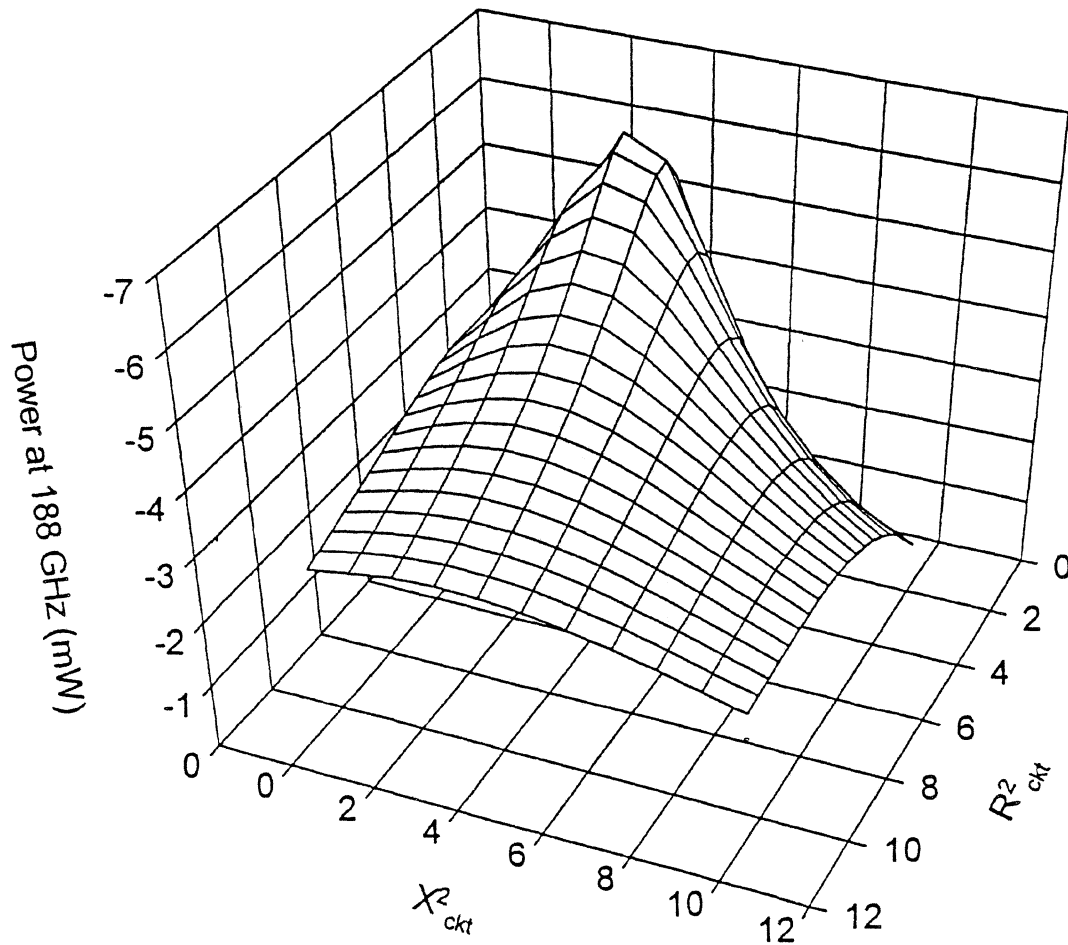


Figure 1: Computer algorithm for the linked nonlinear circuit-hydrodynamic device simulator.

Simulated 2nd harmonic Power vs. Embedding Impedance
 $f_0=94$ GHz, $V_{DC}=4.0$ V, $V_{ac}=2.0$ V

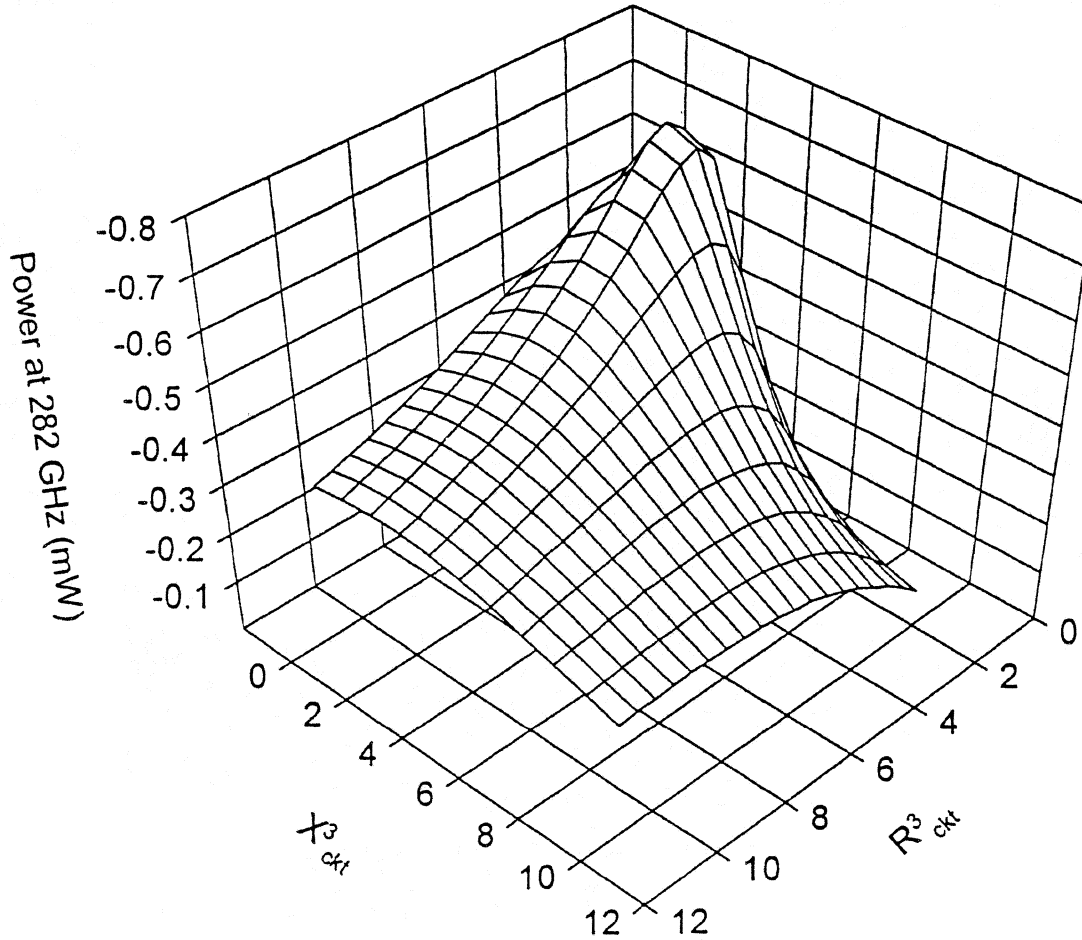


Rydberg: InP TED $I_{active}=1.1\mu\text{m}$, $N_D=1.5\text{-}2.0\text{e}^{16}\text{ cm}^{-3}$
Experimentally: Power at 188 GHz=5 mW

Figure 2: Second harmonic (188 GHz) power versus second harmonic circuit impedances for the device of reference [1] with $V_{DC} = 4.0\text{V}$, $V_{ac} = 2.0\text{V}$ and $Z_1^{ckt} = 0.8 + j6.6\Omega$. Higher harmonic ($n \geq 3$) resistive and reactive components are set to 0.001Ω .

Simulated 3rd harmonic Power vs. Embedding Impedance

$$f_0 = 94 \text{ GHz}, V_{\text{DC}} = 4.0 \text{ V}, V_{\text{ac}} = 2.0 \text{ V}, Z_{\text{ckt}}^2 = 2.0 + j3.5 \Omega$$



Rydberg: InP TED $I_{\text{active}} = 1.1 \mu\text{m}$, $N_{\text{D}} = 1.5\text{-}2.0 \times 10^{16} \text{ cm}^{-3}$
 Experimentally: Power at 282 GHz = 0.2 mW

Figure 3: Third harmonic (282 GHz) power versus third harmonic circuit impedances for the device of reference [1] with $Z_1^{\text{ckt}} = 0.8 + j6.6 \Omega$, and $Z_2^{\text{ckt}} = 2.0 + j3.5 \Omega$. Higher harmonic ($n \geq 4$) resistive and reactive components are set to 0.001Ω .

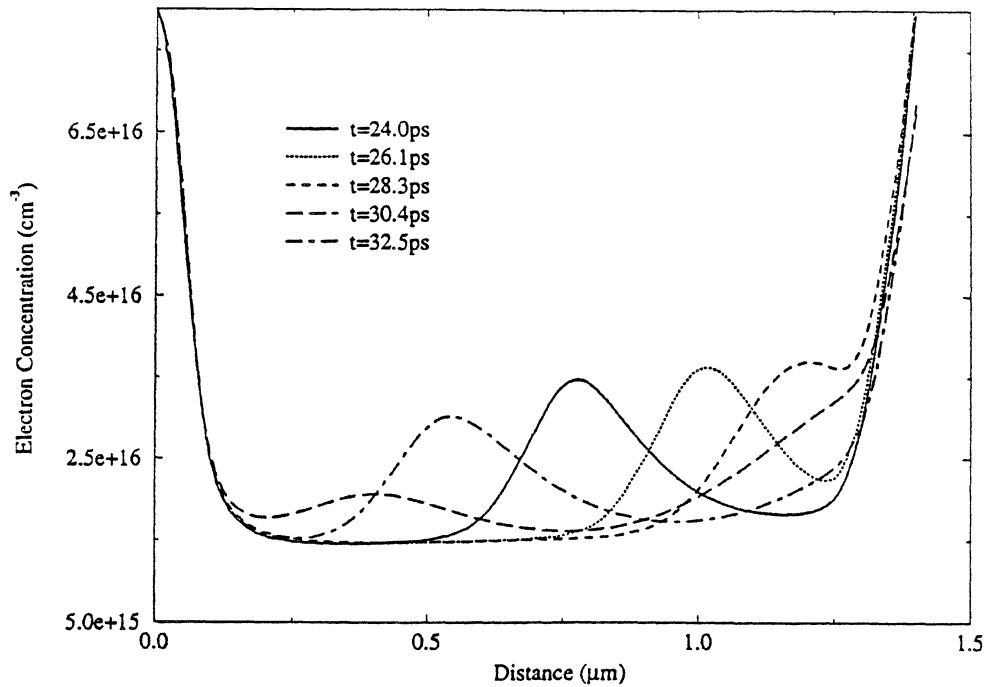


Figure 4: Simulated third harmonic (282 GHz) TED electron concentration versus time and distance for the device of reference [1]. Operating conditions are: $V_{DC} = 4.0V$, $V_{ac} = 2.0V$, $Z_3^{ckt} = 2.0 + j2.5$, and a $50\mu m$ mesa diameter.

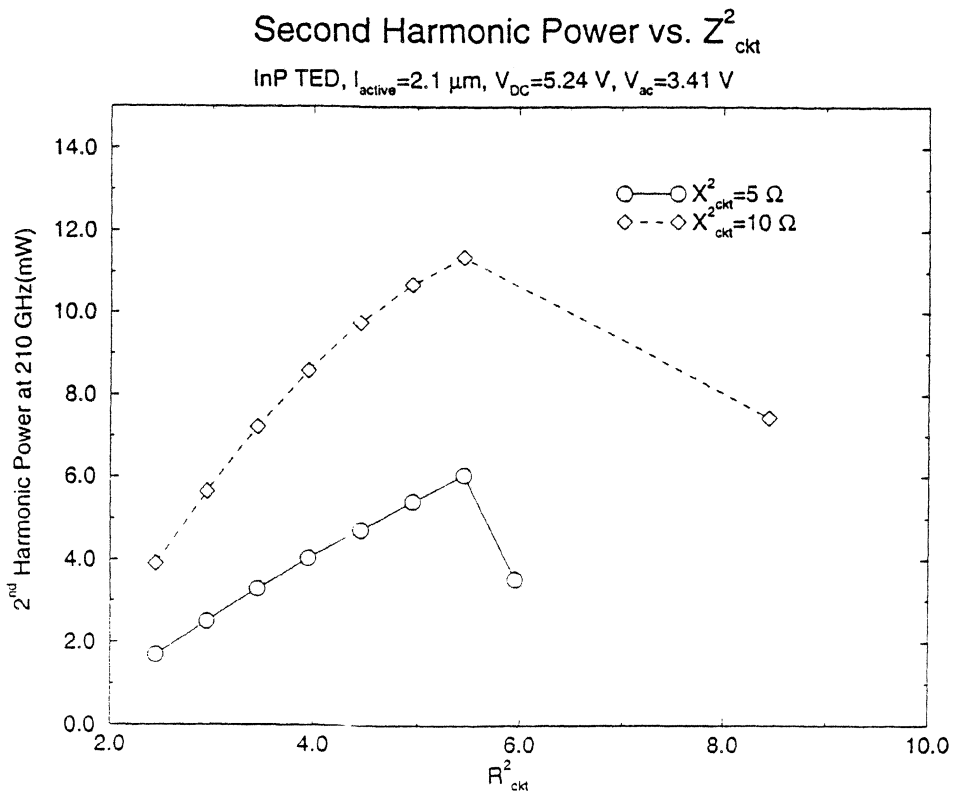


Figure 5: Simulated second harmonic (210 GHz) power versus second harmonic circuit impedances for a longer InP TED ($2.1 \mu m$). Operating conditions include $V_{DC} = 5.24 V$ and $V_{ac} = 3.41 V$.

Simulated 3rd harmonic Power vs. Embedding Impedance for InP MICTED structure, $f_0=105$ GHz

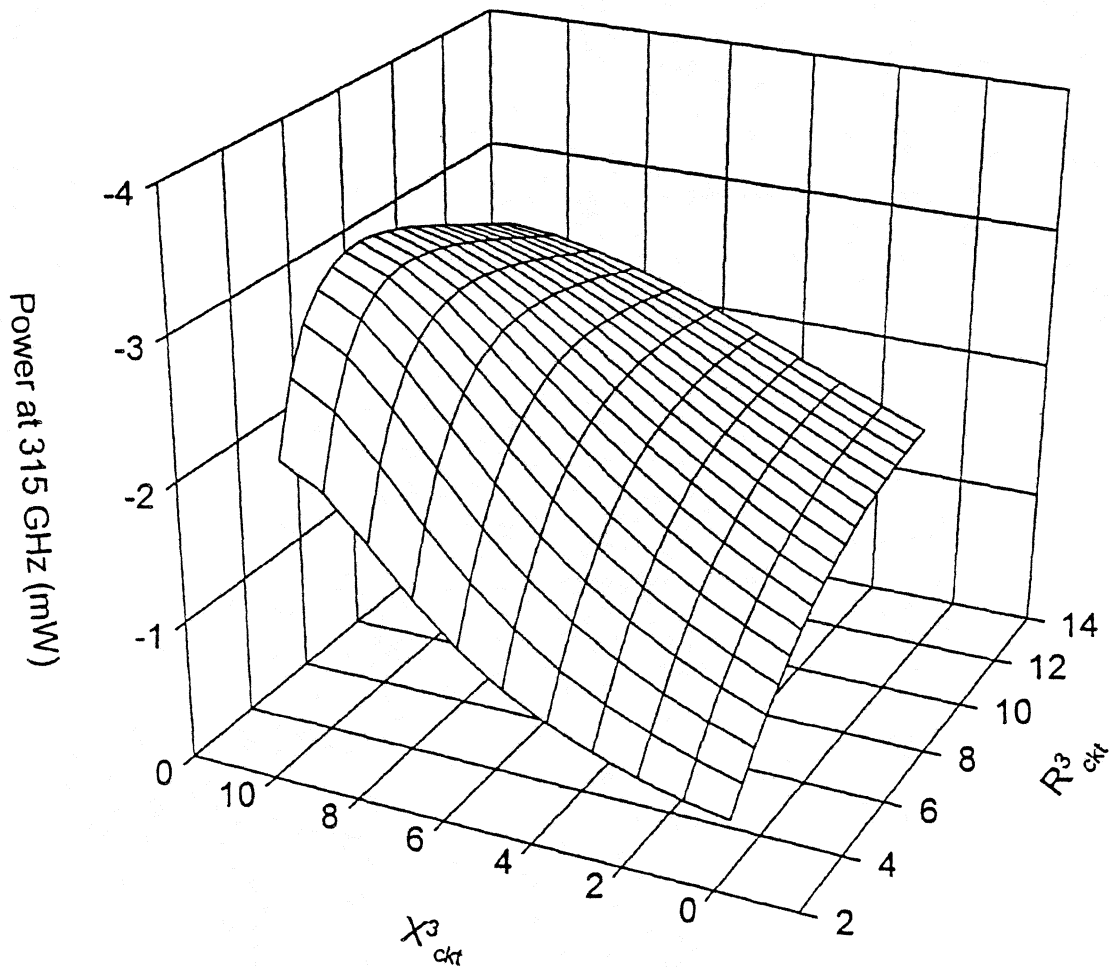


Figure 6: Simulated third harmonic (315 GHz) power versus third harmonic circuit impedances for a MICTED with $V_{DC} = 5.24$ V, $Z_1^{ckt} = 5.0 + j29.4\Omega$, and $Z_2^{ckt} = 5.45 + j18.0\Omega$. Higher harmonic ($n \geq 4$) resistive and reactive components are set to 0.001Ω .

High-Efficiency InP IMPATT Diodes for High-Frequency Power Generation[†]

Chien-Chung Chen, Richard K. Mains, George I. Haddad and Heribert Eisele

Department of EECS, The University of Michigan, Ann Arbor, Michigan 48109-2122

Abstract

Numerical simulation based on the average-energy transport model shows that InP IMPATT diodes in general have higher DC-to-RF conversion efficiency and higher negative resistance than GaAs diodes at high frequencies, which implies that InP is a better material than GaAs for building two-terminal transit-time devices. Reasons for the superiority of InP diodes over GaAs diodes are:

- InP has higher drift velocities than GaAs.
- The decrease of electron velocity at increased electric field is faster in InP. When the space-charge effect is strong, electrons are more localized in InP diodes.
- InP diodes are much more IMPATT-like (i.e. tunneling is less significant) than GaAs ones and therefore have higher efficiency.
- The impact ionization of InP is smaller than GaAs at low electric fields while higher at high fields. Because of this, the generated charge pulse is sharper in InP diodes, which also leads to higher efficiency.
- InP has better thermal conductivity than GaAs.

Simulation results for InP diodes intended for power generation for W-band and above are presented in this paper. Comparison of RF performance with GaAs diodes are also presented.

[†]This work was supported by NASA under contract NAGW-1334.

1 Introduction

Since the proposal by Read[1] in 1958 and the first report of experimental observation of RF oscillations from a Si diode by Johnston *et al.* in 1965[2], IMPATT diodes have been extensively studied and used as high-power and high-efficiency solid-state microwave power sources. GaAs IMPATT diodes, due to negative differential electron mobility of GaAs, usually achieve higher DC-to-RF conversion efficiency than Si diodes at low frequencies, e.g. 35.5% at 8.15 GHz from a GaAs diode reported by Kim and Matthei[3] vs. 11.8% at 8.5 GHz from a Si diode reported by Seidel and coworkers[4]. At high frequencies such as 94 GHz, the interband tunneling current severely degrades the conversion efficiency of the hi-lo structure, while in the flat-doped structure the positive differential electron mobility of Si is preferred to the negative differential electron mobility of GaAs. Therefore, GaAs diodes do not have significant advantage over Si diodes at high frequencies.

According to the InP impact ionization rates measured at various temperatures by Taguchi *et al.*[5], InP has higher impact ionization rates at high electric fields but lower impact ionization rates at low electric fields than GaAs. The interband tunneling rate calculation based on Kane's theory[6] indicates that, although the interband tunneling generation rates of InP are higher than those of GaAs, the difference is not as significant as that for impact ionization generation rates. It is therefore expected that the tunneling current is smaller in an InP diode than in a GaAs diode. Other advantages of InP are higher electron saturation velocity, higher thermal conductivity and higher differential electron mobility. For these reasons, InP diodes have the potential of achieving better RF performance than GaAs diodes at high frequencies.

This paper presents the numerical simulation model, material parameters and simulation results of GaAs and InP diodes. Simulation results for GaAs and InP diodes will be compared to show the superiority of InP diodes over GaAs ones.

2 Simulation Model and Material Parameters

The simulation programs in addition to Poisson's equation solve the following equations to obtain the diode states:

$$J_p = qp\mu_p(E)E - \frac{\partial [qD_p(E)p]}{\partial x} \quad (1)$$

$$J_{n1} = qn_1\mu_{n1}(w_1)E + \frac{\partial [qD_{n1}(w_1)n_1]}{\partial x} \quad (2)$$

$$J_{n2} = qn_2\mu_{n2}(w_2)E + \frac{\partial [qD_{n2}(w_2)n_2]}{\partial x} \quad (3)$$

$$\frac{\partial w_1}{\partial t} = \frac{J_{n1}}{qn_1} \frac{\partial w_1}{\partial x} + \frac{J_{n1}E}{n_1} - \frac{w_1 - w_{th}}{\tau_{w1}(w_1)} \quad (4)$$

$$\frac{\partial w_2}{\partial t} = \frac{J_{n2}}{qn_2} \frac{\partial w_2}{\partial x} + \frac{J_{n2}E}{n_2} - \frac{w_2 - w_{th}}{\tau_{w2}(w_2)} \quad (5)$$

$$\frac{\partial p}{\partial t} = -\frac{1}{q} \frac{\partial J_p}{\partial x} + G_p \quad (6)$$

$$\frac{\partial n_1}{\partial t} = \frac{1}{q} \frac{\partial J_{n1}}{\partial x} + G_{n1} \quad (7)$$

$$\frac{\partial n_2}{\partial t} = \frac{1}{q} \frac{\partial J_{n2}}{\partial x} + G_{n2} \quad (8)$$

where $w_{th} = \frac{3}{2}k_B T$ is the thermal equilibrium energy for electrons, and the carrier generation rates G_p , G_{n1} and G_{n2} are given by

$$G_p = G_{II} + G_T + G_{th} - R_{th} \quad (9)$$

$$G_{n1} = G_{II} + G_T + G_{th} - R_{th} + \frac{n_2}{\tau_{n2-1}(w_2)} - \frac{n_1}{\tau_{n1-2}(w_1)} \quad (10)$$

$$G_{n2} = \frac{n_1}{\tau_{n1-2}(w_1)} - \frac{n_2}{\tau_{n2-1}(w_2)} \quad (11)$$

In the simulation programs, holes follow the drift-diffusion equation, while electrons are described by a variation of the two-valley drift-diffusion equation with the mobilities and diffusion coefficients being functions of electron energies instead of the electric field. The electron energies are governed by the two energy equations.

Close examination of the above equations reveals that the momentum relaxation times for electrons are actually neglected in the program. This is justified as long as the momentum relaxation times are much smaller than the period of the RF voltage.

The materials used for devices in this work are GaAs and InP. Since these devices are intended for RF power generation, the material lattice temperature is usually very high. 500°K is assumed throughout this work. The majority of the material parameters used by the simulation programs are generated by a Monte Carlo (MC) program. This MC program provides the values of electron velocities, diffusion coefficients, relaxation times and electron energies as functions of the electric field up to 3000 kV/cm. The methods used to evaluate the relaxation times are similar to those proposed by Stewart *et al.*[7], while the electron (longitudinal) diffusion coefficients are calculated in the MC program using the method mentioned by Fawcett[8]. Other electron parameters such as the material intrinsic concentration and electron-hole recombination lifetime and all the hole parameters are set according to empirical expressions or assumed values.

Two important material parameters used by the simulation programs are the impact ionization and tunneling rates. They have very profound effects on the device operation, but still lack adequate determination in the electric field range where the devices are operated (up to 3000 kV/cm). The impact ionization generation rate is expressed as

$$G_{II} = (\alpha_n J_n + \alpha_p J_p)/q \quad (12)$$

For GaAs, α_n and α_p are given by

$$\alpha_n = A_n \exp \left[-(B_n/E)^2 \right] \quad (13)$$

$$\alpha_p = A_p \exp \left[-(B_p/E)^2 \right] \quad (14)$$

with the following values being used for GaAs at 500°K

$$A_n = A_p = 2.1205 \times 10^5 \text{ cm}^{-1}$$

$$B_n = B_p = 6.71 \times 10^5 \text{ V/cm}$$

For α_n and α_p in InP, we adopt the expressions given by Okuto and Crowell[9] as follows

$$\alpha_n, \alpha_p = \frac{qE}{E_{th}} \exp \left(0.217 (E_{th}/E_R)^{1.14} - \left\{ \left[0.217 (E_{th}/E_R)^{1.14} \right]^2 + \left(\frac{E_{th}}{qE\lambda} \right)^2 \right\}^{1/2} \right) \quad (15)$$

with the parameters E_{th} , E_R and λ fitted by Taguchi *et. al.*[5], which leads to

$$\alpha_n = \frac{E}{1.78} \exp \left\{ 31.75 - \left[31.75^2 + \left(\frac{8.75 \cdot 10^6}{E} \right)^2 \right]^{1/2} \right\}$$

$$\alpha_p = \frac{E}{1.59} \exp \left\{ 47.0 - \left[47.0^2 + \left(\frac{9.75 \cdot 10^6}{E} \right)^2 \right]^{1/2} \right\}$$

for InP at 500°K, where the unit of electric field E is V/cm, and the unit of α_n and α_p is 1/cm.

As to the interband tunneling rate, we adopt the expression which complies with the highly idealized form proposed by Kane[6] as shown below

$$G_T = A_T E^2 \exp(-B_T/E) \quad (16)$$

For GaAs at 500°K, we use

$$A_T = 1 \times 10^{20} \text{ cm}^{-1}\text{s}^{-1}\text{V}^{-2}$$

$$B_T = 1.2 \times 10^7 \text{ V/cm}$$

And for InP at 500°K

$$A_T = 1.37 \times 10^{20} \text{ cm}^{-1}\text{s}^{-1}\text{V}^{-2}$$

$$B_T = 1.178 \times 10^7 \text{ V/cm}$$

The dead space for impact ionization and interband tunneling is considered in the simulation program. For impact ionization, the energy relaxation effect automatically includes the dead space in the model. As to interband tunneling, we use the bandgap to determine the dead space as illustrated in Figure 1. The principle is that tunneling only occurs where there are empty states in the conduction band and filled states in the valance band.

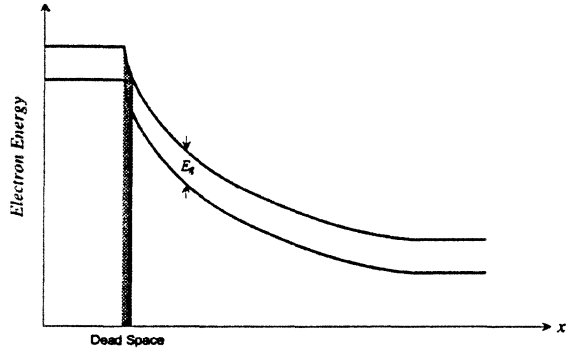


Figure 1: Dead space for interband tunneling.

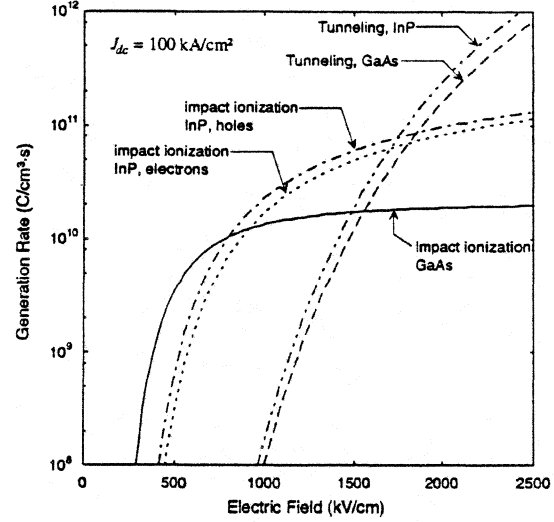


Figure 2: The impact ionization and tunneling generation rates for GaAs and InP at 500°K.

In the simulation programs, all material parameters for electrons except the tunneling rate are tabulated according to the electron energy. In other words, they are treated as functions of the electron energy instead of the electric field. The tunneling rate is considered as a function of the electric field since it is related more to the electric field that electrons in the valence band experience than to the energy of electrons in the conduction band. Figure 2 shows the impact ionization and tunneling generation rates for 500°K GaAs that are used in the simulation programs. Inside the simulation program, the impact ionization rate is transformed into a function of electron energy.

The metal-semiconductor contact resistances are estimated by solving the Schrödinger's equation. The p-type Ohmic contact resistance for InP is very high due to the high barrier height for holes. This high p-type contact resistance can be greatly reduced by using lattice-matched InGaAs cap layers or Schottky collectors[10]. Thermal resistance of a diode is calculated using the approximate thermal model discussed in [11]. Devices with high thermal resistance should be biased at low current densities or operate in the pulsed mode in order to keep the p-n junction temperature below 500°K.

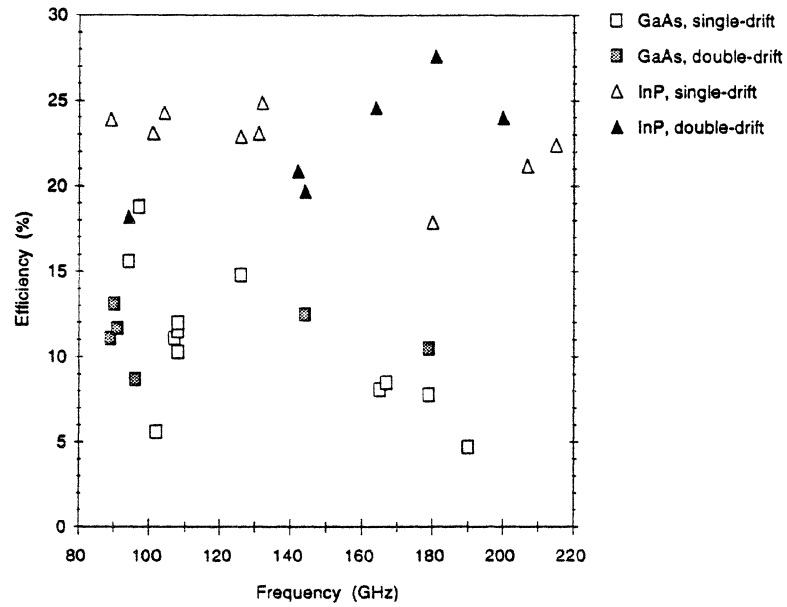


Figure 3: The efficiency for GaAs and InP diodes at various frequencies.

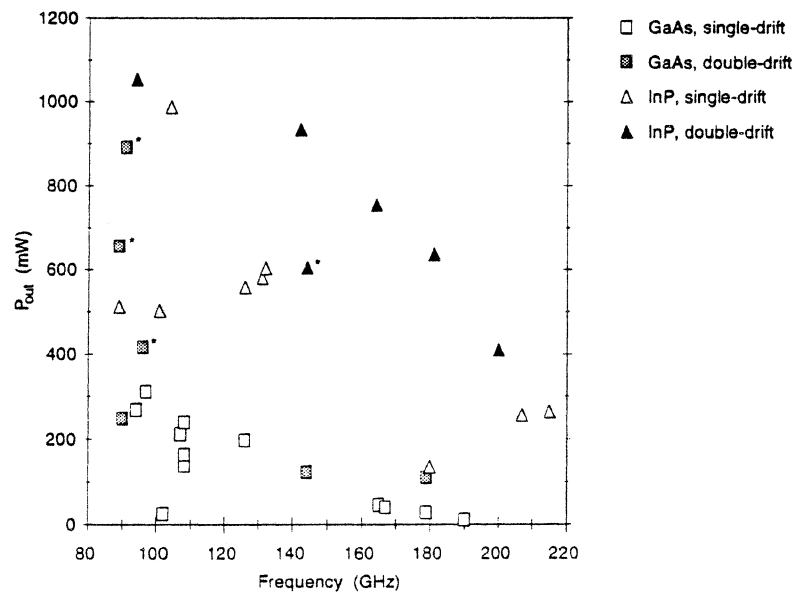


Figure 4: The 1- Ω RF output power for GaAs and InP diodes at various frequencies. Points marked with * represent average power from pulsed diodes.

3 Simulation Results and Discussion

Sixteen GaAs diodes and sixteen InP diodes designed to operate at 94 GHz and above were simulated in this work. Figures 3 and 4 present the DC-to-RF conversion efficiency η and 1- Ω RF output power $P_{1\Omega}$ calculated for all the structures simulated in this work. It can be clearly seen that InP diodes have significantly higher conversion efficiency than GaAs diodes. Part of the reason why InP diodes have higher conversion efficiency can be explained by Figure 5, which displays typical injected and induced current waveforms of GaAs and InP diodes obtained from simulation. First, the carrier injection angle in the InP diode is larger than that in the GaAs diode, indicating lower contribution of interband tunneling to the generation current in the InP diode. Second, the InP diode has sharper turn-on and turn-off characteristics in the injected current due to the steeper slopes of the impact ionization generation rates in InP shown in Figure 2. The higher breakdown field of InP shown in Figure 2 allows higher electric field in the drift region, which also leads to a higher conversion efficiency. Third, higher induced current peak near 270° in the InP diode, which results from electrons' high-speed surfing through the drift region at low fields. Fourth, the higher negative electron differential mobility in InP causes the electron pulse to get sharper as it travels through the drift region. Less electrons are left in the drift region at the end of an RF cycle, resulting in a lower induced current in the first half of the next RF cycle.

As the simulation results indicate, the device negative resistance, in many occasions, is more important than the conversion efficiency since the matching condition requires a diode with low negative resistance to have small cross-sectional area, while the negative resistance of a device is proportional to its RF output power. The double-drift structures have longer device lengths and therefore lower capacitance effects than the single-drift structures, making the RF output power of the double-drift diode significantly higher than that of the single-drift one. The higher carrier drift velocity of InP also leads to higher negative resistances of InP diodes, which explains the reason why InP diodes have much higher RF output power than GaAs ones as shown in Figure 4.

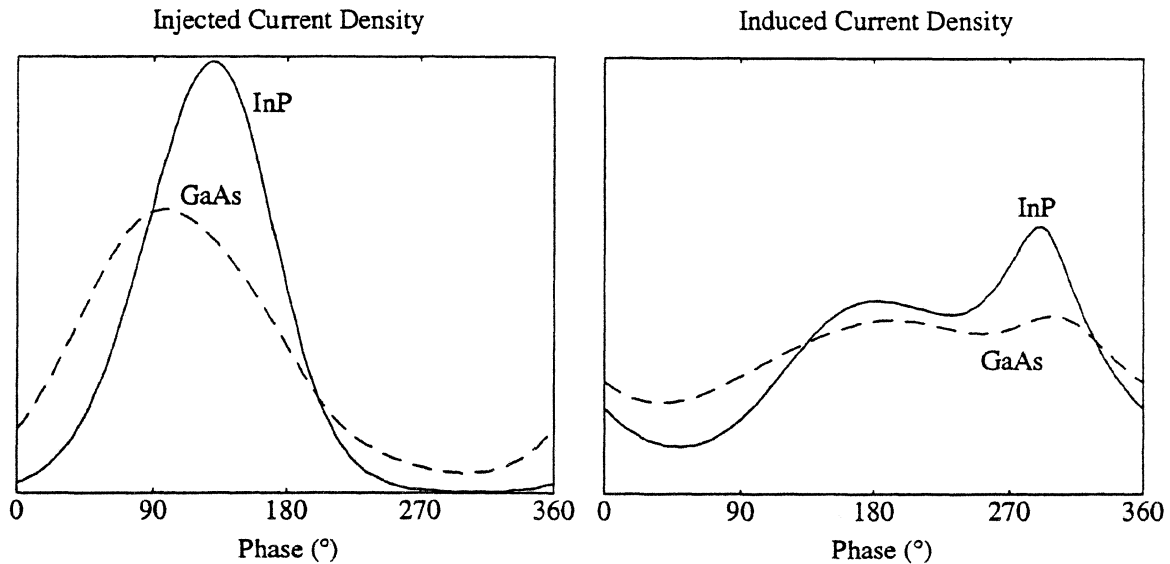


Figure 5: Typical injected and induced currents of the GaAs and InP diodes at high frequencies.

Devices having Schottky contacts in place of Ohmic contacts suffer less from the parasitic contact resistance, and therefore have higher conversion efficiency and overall negative resistance. Besides, the absence of the buffer layer required by the conventional Ohmic-contacted diode makes the thermal resistance of the Schottky-contacted diode much smaller.

Note that since the thermal conductivity of InP is about 25% higher than that of GaAs, InP diodes can be biased at higher current densities to achieve higher negative resistance and higher RF output power.

4 Conclusion

Numerical programs capable of simulating high-frequency transit-time diodes have been developed, for which the transport model and material parameters have been briefly discussed. Several GaAs and InP diodes are simulated. InP diodes, due to higher carrier drift velocities, higher thermal conductivity, higher negative differential electron mobility and higher impact ionization rates,

have better RF performance than GaAs.

References

- [1] W. J. Read, "A Proposed High Frequency Negative Resistance Diode," *Bell System Tech. J.*, **33**, pp. 401-446, March 1958.
- [2] R. L. Johnston, B. C. DeLoach, Jr. and B. G. Cohen, "A Silicon Diode Oscillator," *Bell System Tech. J.*, **44**, pp. 369-372, February 1965.
- [3] C. K. Kim and W. G. Matthei, "GaAs Read IMPATT Diode Oscillators," *Proc. Fourth Biennial Electrical Engineering Conf.*, Ithaca, NY, pp. 299-305, August 1973.
- [4] T. E. Seidel, W. C. Niehaus and D. E. Iglesias, "Double-Drift Silicon IMPATT's at X-band," *IEEE Trans. Electron Dev.*, **ED-21**, pp. 523-531, August 1974.
- [5] K. Taguchi, T. Torikai, Y. Sugimoto, K. Makita and H. Ishihara, "Temperature Dependence of Impact Ionization Coefficients in InP," *J. Appl. Phys.*, **59**, January 1986.
- [6] E. O. Kane, "Theory of Tunneling," *J. Appl. Phys.*, **32**, pp. 83-91, 1961.
- [7] R. A. Stewart, L. Ye and J. N. Churchill, "Improved Relaxation-Time Formulation of Collision Terms for Two-Band Hydrodynamic Models," *Solid-State Electronics*, **32**, No. 6, pp. 497-502, 1989.
- [8] W. Fawcett, "Non-ohmic transport in semiconductors," *Electrons in Crystalline Solids*, International Atomic Energy Agency, Vienna, pp. 531-618, 1973.
- [9] Y. Okuto and C. R. Crowell, "Energy-Conservation Considerations in the Characterization of Impact Ionization in Semiconductors," *Phys. Rev. B*, **6**, pp. 3076-3081, 1972.

- [10] C.-C. Chen, "Non-Equilibrium Modeling of Mixed Tunneling and Avalanche Breakdown Effects in Transit-Time Diodes," Ph.D. Dissertation, 1994, The University of Michigan, Ann Arbor.
- [11] R. K. Mains and G. I. Haddad, "Properties and Capabilities of Millimeter-Wave IMPATT Diodes," *Infrared and Millimeter Waves*, **10**, pp. 111-231, 1983.

A Quasi-Optical Power Combiner with a Metallic Grating

K. Mizuno^{*,}, J. Bae^{*}, Y. Aburakawa^{*}, and T. Fujii^{*}**

A Fabry-Perot resonator with a metallic grating is used as a circuit for coherent power combining of active devices (oscillators). Solid state devices such as Gunn diodes and FET's are mounted at grooves of the grating to form an oscillator array. The metallic grating is used to obtain impedance matching between the device and the circuit, and also acts as a heat-sink for the devices. The capability of heat sink is essential for high power active device arrays, because normal efficiency of FET's is less than 50% and that of Gunn diodes is at most 10%.

This paper describes an equivalent circuit for the resonator with Gunn diodes as well as the circuit for FET's.

^{*}K. Mizuno, J. Bae, Y. Aburakawa, and T. Fujii are with the Research Institute of Electrical Communication, Tohoku University, Sendai, 980 Japan.

^{**} K. Mizuno is also with Photodynamics Research Center, RIKEN, Sendai, 981 Japan.

Near-Field Characterization of 2-D Beam Patterns of Submillimeter Superconducting Receivers

Cheuk-yu Edward TONG, Scott PAINE and Raymond BLUNDELL

Harvard-Smithsonian Center for Astrophysics,
60 Garden St., Cambridge, MA 02138, USA

Abstract

In order to reap the maximum benefit from the low noise temperature of submillimeter superconducting receivers in submillimeter systems, it is important to optimize the illumination of the primary reflector by the receiver feed antennas. Therefore, we have developed a two-dimensional near-field measurement system which probes the beam pattern of submillimeter receiver feed antennas *in situ*, in both amplitude and phase. This system is basically an extension of well-established near-field techniques employed at microwave frequencies and is appropriate for probing paraxial beams where probe correction is not very important. The system has been used to about 500 GHz. The measured near-field data agree well with theoretical models. This system is currently used to characterize feed antennas developed for the Sub-Millimeter Array and is used as a tool in developing an SIS receiver with an integrated planar feed antenna.

I. Introduction

There is increasing interest in measuring the radiation patterns of antennas at submillimeter wavelengths [1,2], particularly for optimizing the illumination of primary reflectors of submillimeter systems. The incentive is particularly strong for the development of planar feed antennas [3-5] because, unlike the more popular waveguide horn antennas, their radiation patterns are not well documented and their open structure nature renders them more susceptible to influence from surrounding mounting structures.

Far field measurements are traditionally used to characterize antenna patterns. At millimeter and submillimeter wavelengths, this is the preferred method because only amplitude measurement is required. However, far field techniques suffer from two main disadvantages:

- (1) For measurement of a feed antenna with its associated receiver optics, the far field criterion of $2R^2/\lambda_0$ may impose an unreasonably long range for measurement [1].
- (2) Far field techniques require that the antenna under test be rotated. This proves to be difficult for measuring cryogenic receivers *in situ*. In most cases, the measurement is only convenient in a single plane.

In most submillimeter radio-telescopes, the receivers and the primary and secondary reflectors are coupled through a beam waveguide designed using Gaussian beam modes [6,7]. Consequently, the far field patterns of the feed antennas are not very relevant because the overall efficiency of the feed is dictated by the coupling of the beam emerging from the receiver to the beam waveguide, and this coupling takes place in the near-field [8].

We have developed a near-field scanning system that measures the 2-D beam profile of submillimeter Superconductor-Insulator-Superconductor (SIS) receivers *in situ*. The system is basically an extension of well established near field techniques employed at microwave frequencies [9]. Both amplitude and phase patterns are measured in our system. We believe that this is the first full vectorial near field measurement performed at submillimeter wavelengths.

II. Measurement Set Up

A block diagram of our set-up is given in Fig. 1. For convenience and in order not to saturate the sensitive SIS receiver, we use a harmonic mixer pumped by an HP83620A frequency synthesizer running in the Ku band as the transmitting source. Typical harmonic output power is less than 1 nW above 200 GHz. The probe is an open waveguide with its front wall chamfered to reduce cross-sectional area. The smallest probe available is in WR-3 waveguide. Consequently some over-moding is inevitable above 350 GHz.

The probe and the harmonic generator are mounted on a stepper motor controlled XY scanner that has a resolution of $5\mu\text{m}$ and covers a span of 150 mm in each axis. A low phase distortion flexible cable bent in a loop connects the synthesizer to the harmonic generator. A wide dynamic range is obtained by down converting the IF output of the SIS mixer to 21.7 MHz where it is passed through a narrow band filter before its amplitude and phase are measured by a vector voltmeter against a reference signal.

The master reference of the entire system is the 10 MHz internal reference of the synthesizer. An RF frequency multiplier unit is locked to this reference signal and delivers the frequency reference to the phase lock loop of the Local Oscillator (LO) pumping the SIS mixer. It also provides intermediate LO drives for multiple down conversions in the IF chain and phase lock circuitry, and supplies the reference signal to the vector voltmeter used for the vector measurement.

The measurement set-up is automated by a PC equipped with a GPIB interface controller. The measurement speed is limited at high Signal-to-Noise Ratios (SNR) by the speed of the stepping stages. At low SNR (< 20 dB), integration time is the limiting factor. The total scan time is usually kept to below 1 hour to avoid system drift and temperature fluctuation effects.

III. System Performance and Limitations

One of the major concerns in near-field measurement is the presence of phase errors due to flexible cables and probe positioning [10]. Amplitude error is negligible in this set-up because the harmonic generator is driven to saturation by the 50 mW of available pumping power.

In our measurement set-up, the only moving cable is a 90 cm low distortion flexible cable linking the synthesizer and the harmonic generator. By maintaining this cable in a loop form, phase errors are minimized because the curvature of the loop stays quite constant except at the corners of the scan plane. In order to quantify the phase error, we have performed a dummy scan in which the moving end of the cable was shorted and the phase of the cable was measured by a network analyzer at 15 GHz. The measured RMS phase fluctuation is about 0.2° . This corresponds to an RMS fluctuation of 4° at 300 GHz. However, it should be noted that the largest phase excursion occurs at the corners of the scan plane and the phase variation over a wide region near the center of the scan plane is significantly less. Therefore, we expect that the impact of phase error introduced by the cable is limited in particular near the center of the scan.

The maximum cumulative positioning error of the XY stages is specified by the manufacturer to be $40\mu\text{m}$ over a 100 mm linear scan. While this positioning accuracy is generally adequate for measurement around $\lambda_0 = 1\text{ mm}$, higher accuracy is desirable at higher frequencies. Nevertheless, the system works well at least up to 500 GHz for paraxial beams in which transverse phase variation is slow.

Unlike microwave ranges, the waveguide probes used have very thick walls. In fact, the smallest probe is made from a piece of electroformed waveguide section with walls much thicker than the dimensions of the waveguide itself. Chamfering of the open end helps to reduce probe scatter and improves the probe pattern. Absorbers are also carefully placed so as to out metal structures that might give rise to spurious reflections. Probe correction may be introduced using a generalized electromagnetic solver to enhance the measured data [11]. In our measurements so far, we have limited ourselves to paraxial beams where probe correction is less important.

As an initial test of the system, we probed the beam emerging from a plano-convex lens illuminated by a W-band 25 dB standard gain pyramidal horn. The experiment was carried out at room temperature using a commercial Schottky diode mixer receiver operating at 85 GHz. The measured amplitude pattern is given in Fig. 2. The two-dimensional complex data set was then Fourier transformed to derive the far-field beam pattern. This is compared to experimentally measured far-field data in Fig. 3. Clearly a reasonable match exists between the two data sets to the -20 dB level. This indicates that the near field data is reliable to about the -25 dB level and the total RMS phase

error is less than a few degrees. Some of the amplitude and phase deviations are due to insufficient electromagnetic shielding as the measurements were performed on an optical bench and not in an anechoic chamber.

IV. Measured Patterns

The system has been used to measure a number of feed antennas developed for the Smithsonian Astrophysical Observatory Sub-Millimeter Array (SMA). Fig. 4 displays the measured amplitude and phase profiles at 240 GHz of the corrugated feed horn developed for the lowest frequency band of the array [13]. Also shown in the figure are the theoretical profiles derived from a scalar model that assumes axial symmetry. Excellent agreement between the theoretical and measured data is obtained for the H-Plane cut. The E-plane cut differs slightly from the H-plane but the overall beam eccentricity is small.

The horn measured above was then used to illuminate a lens of focal length 55 mm. The lens was positioned 50 mm in front of the aperture of the feed horn. The measured 2-D amplitude and phase patterns at 211 GHz are given in Fig. 5. An SNR in excess of 50 dB was attained during the measurement. In Fig. 6, we compare the measured profile of Fig. 5 to the theoretical model for both the E and H plane cuts. While an excellent match exists around the center of the beam, the match to the theoretical data is poorer at lower power levels. This is attributed to insufficient electromagnetic shielding. This is reflected in the fact that the -25 dB contour in Fig. 5a shows some irregularity in contrast to other contours. We expect a higher beam symmetry if the LO injector and mounting structure of the dewar have larger clear apertures and improved shielding.

The system works well up to 500 GHz. Fig. 7 shows the 2-D amplitude pattern measured at 465 GHz of a corrugated feed horn designed to operate in the band 400 - 520 GHz. In this experiment, the SNR achieved was about 25 dB and the SIS receiver noise temperature was around 150 K. Once again the measured pattern and the theoretical model are seen to be in good agreement, particularly for the phase profile (see Fig. 8). This indicates that systematic phase errors are sufficiently small to allow measurement to frequencies probably in excess of 500 GHz.

The near-field range was also used to characterize an SIS receiver with integrated feed antenna. Fig. 9 shows the 2-D amplitude pattern of a twin dipole antenna on an

ellipsoidal immersion lens measured at 255 GHz. The pattern shows a beam with an elliptical cross-section. This is probably due to undesirable radiation from the coplanar strip feed lines feeding the dipoles.

V. Conclusion

A near-field probing system has successfully been implemented to characterize the 2-D complex beam profile of SIS receivers. This system performs well up to about 500 GHz. We believe that this is the first near-field range operating in the sub-millimeter frequency band. The system is currently used to characterize feed antennas developed for the Sub-Millimeter Array to allow optimization of the illumination of the telescope. It has also been used as a tool in developing an SIS receiver with an integrated planar feed antenna.

References

- [1] J. Tuovinen, "Testing reflector antennas in the THz frequency range," in, *Proc. 4th Intl. Symp. Space THz Tech., Los Angeles*, pp. 249-262, March 1993.
- [2] J. Tuovinen, T.M. Hirvonen and A.V. Raisanen, "Near-field analysis of a thick lens and horn combination: theory and measurements," *IEEE Trans. Antenna Propagat.*, vol. 40, pp. 613-619, June 1992.
- [3] R. Blundell and C.E. Tong, "Submillimeter receivers for radio astronomy," *Proc. IEEE*, vol. 80, pp. 1702-1720, Nov. 1992.
- [4] G.M. Rebeiz, "Millimeter-wave and terahertz integrated circuit antenna," *Proc. IEEE*, vol. 80, pp. 1748-1770, Nov. 1992.
- [5] D.F. Filipovic, S.S. Gearhart and G.M. Rebeiz, "Double-slot antennas on extended hemisphere and elliptical silicon dielectric lens," *IEEE Trans. Microwave Theory Tech.*, vol. 41, pp. 1738-1749, Oct. 1993.
- [6] S. Paine, D.C. Papa, R.L. Leombruno, X. Zhang and R. Blundell, "Beam waveguide and receiver optics for the SMA," *these proceedings*, , .
- [7] A.J. Murphy, A. Egan and S. Withington, "Truncation in millimeter and sub-millimeter optical systems," *IEEE Trans. Antenna Propagat.*, vol. 41, pp. 1408-1413,

Oct. 1993.

- [8] J. Lesurf, *Millimeter-wave optics, devices and systems*, Adam Hilgar, New York, 1990.
- [9] A.D. Yaghjian, "An overview of near-field antenna measurements," *IEEE Trans. Antenna Propagat.*, vol. 34, pp. 30-45, Jan. 1986.
- [10] G.E. Evans, *Antenna measurement techniques*, Artech House, Boston, 1990.
- [11] Y. Fujino and C.E. Tong, "Analysis of an open-ended waveguide as a probe for near field antenna measurements by using TLM method," To appear in, *Proc. IEICE*, Japan, 1994.
- [12] A.C. Newell, "Error analysis techniques for planar near-field measurements," *IEEE Trans. Antenna Propagat.*, vol. 36, pp. 754-768, June 1988.
- [13] X. Zhang, "Design of conical corrugated feed horns for wide-band high-frequency applications," *IEEE Trans. Microwave Theory Tech.*, vol. 41, pp. 1263-1274, Aug. 1993.

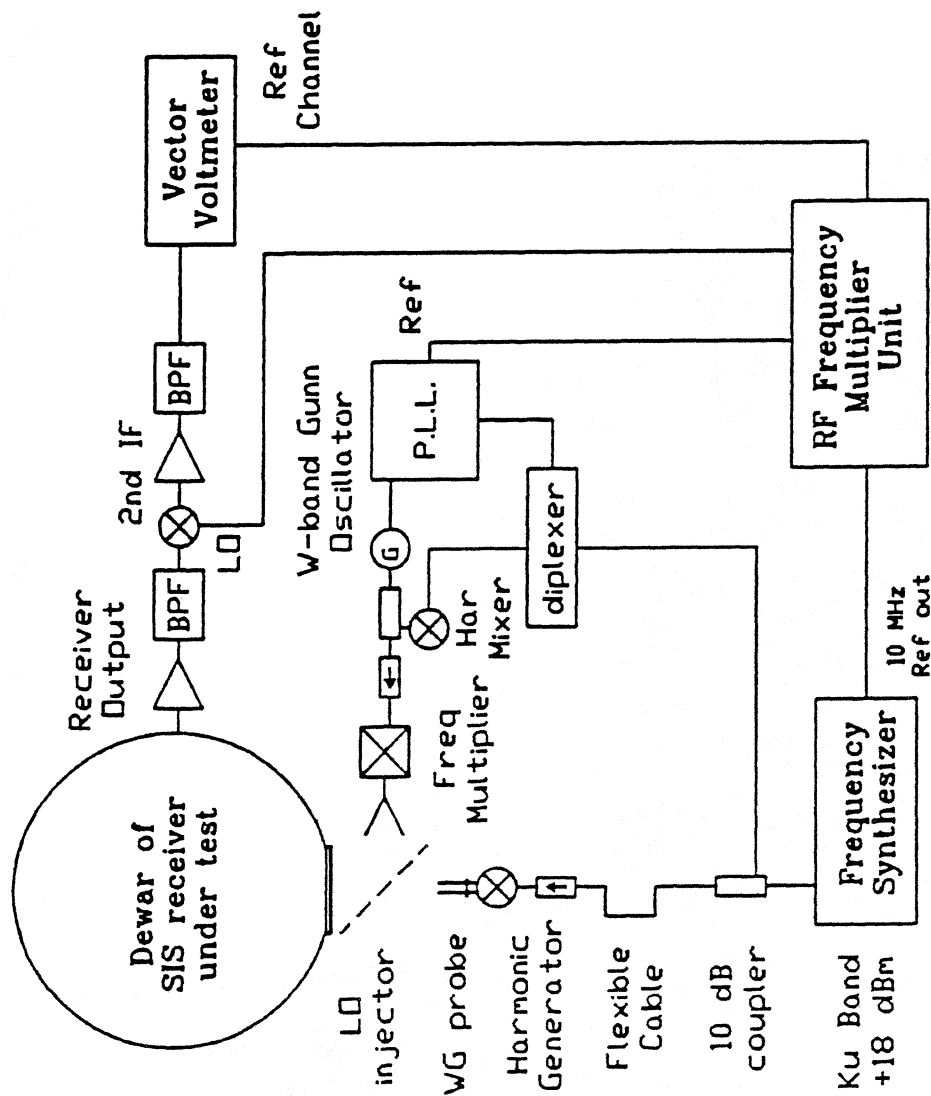


Fig. 1 Block Diagram of Near Field System

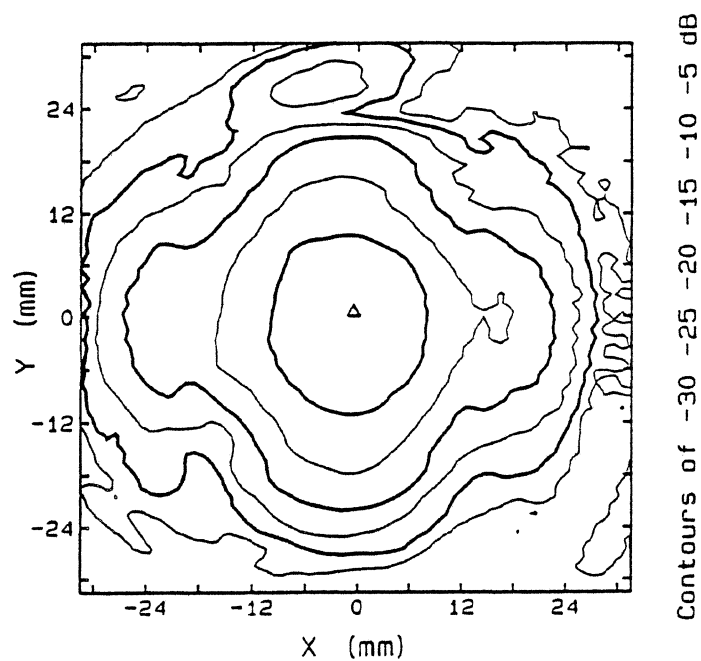


Fig. 2 Near Field Amplitude Data at 85 GHz
of a Horn-Lens Combination

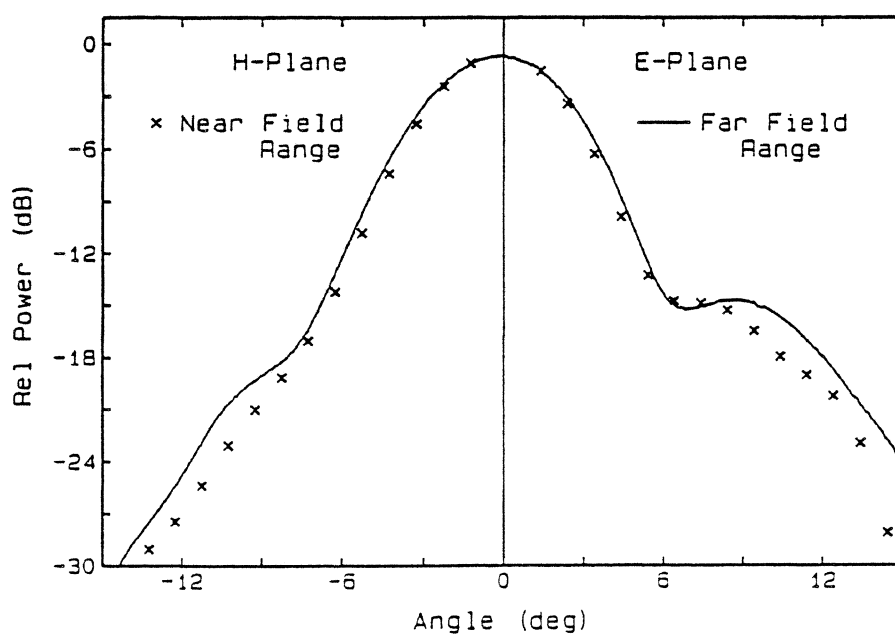


Fig. 3 Comparison of Transformed Near Field Data
and Measured Far Field Pattern

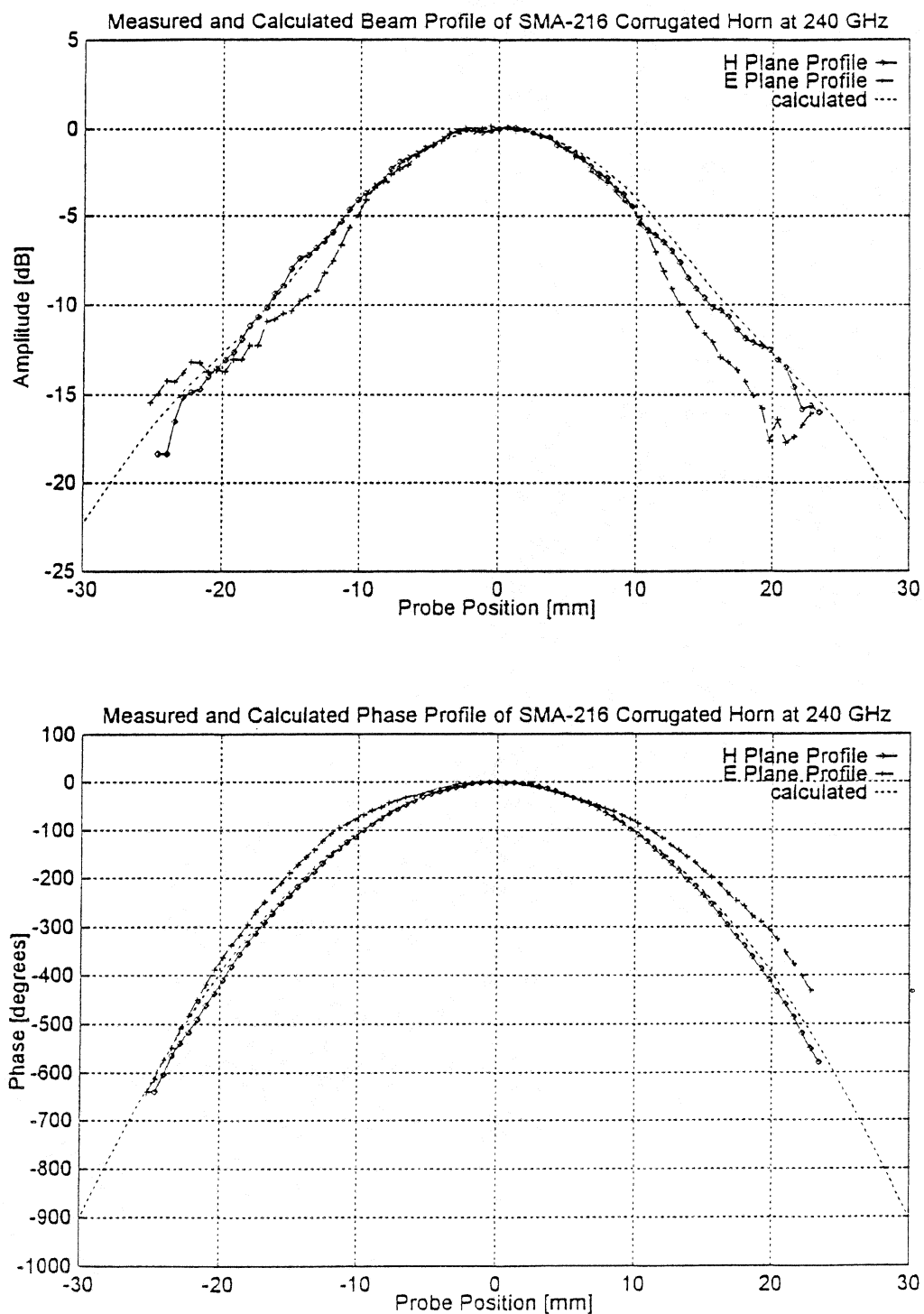


Fig. 4

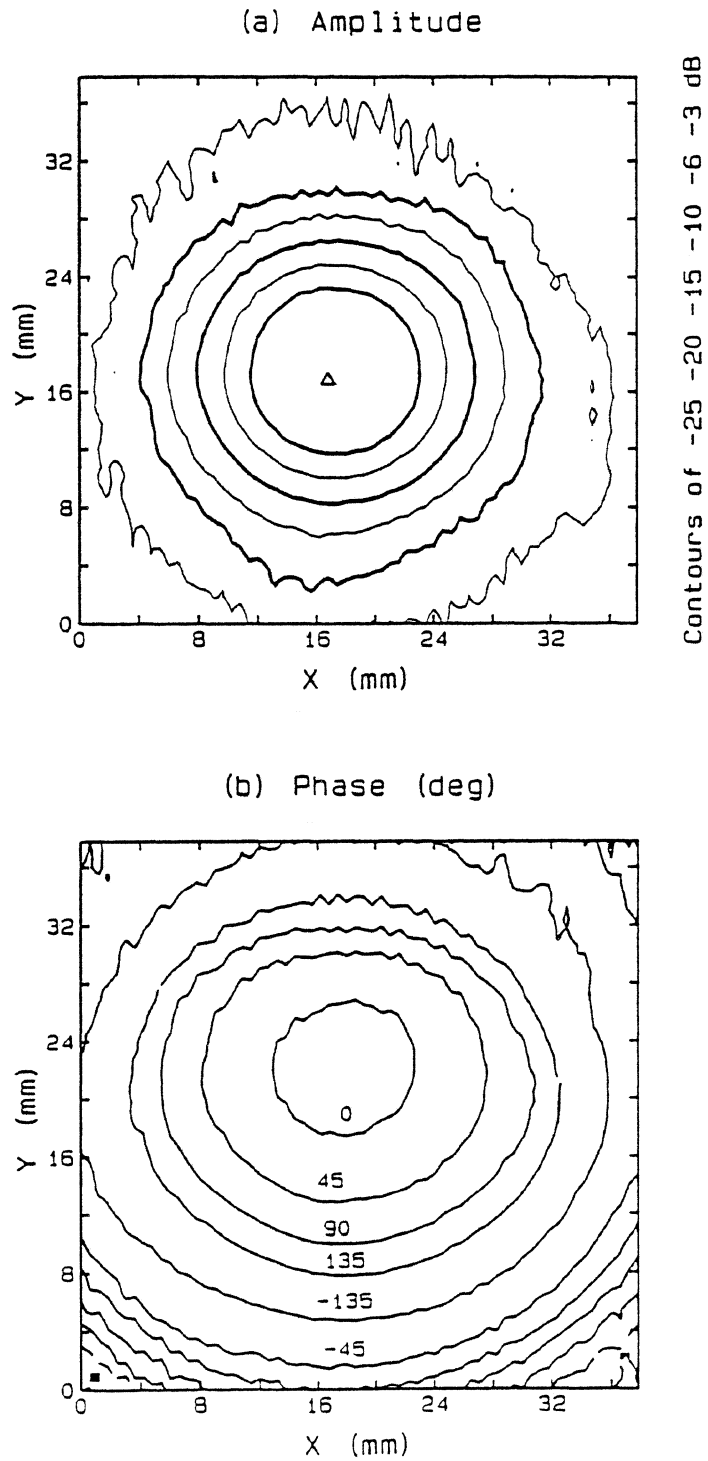


Fig. 5 Near-Field Beam Pattern at 211 GHz
of SMA-216 Horn - Lens Combination

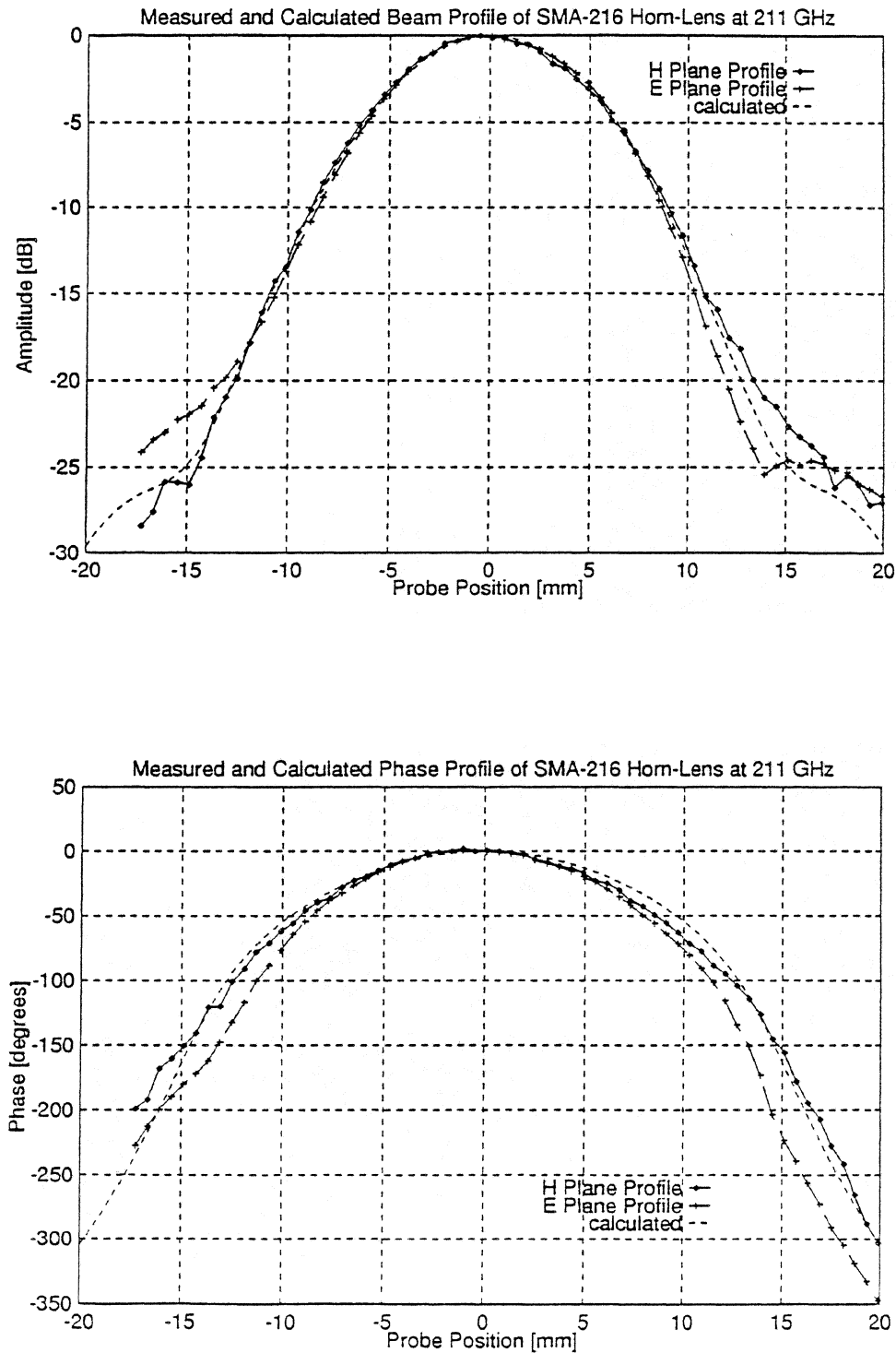


Fig. 6

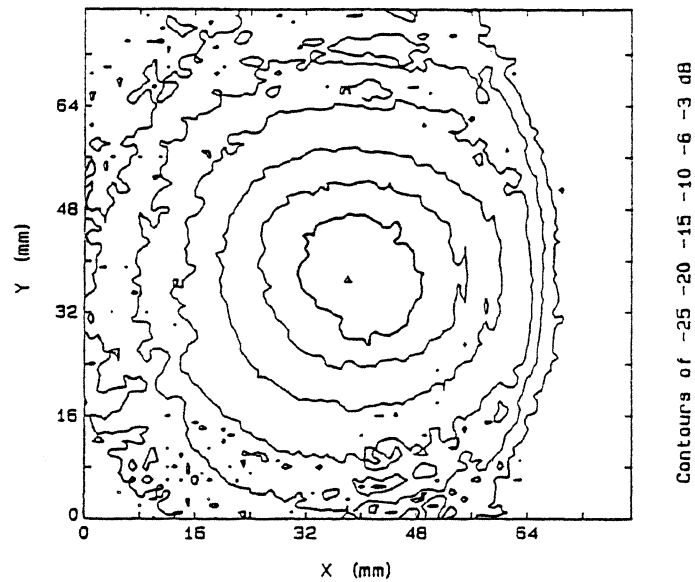


Fig. 7 Near Field Amplitude Data at 465 GHz
of SMA-460 Horn-Lens Combination

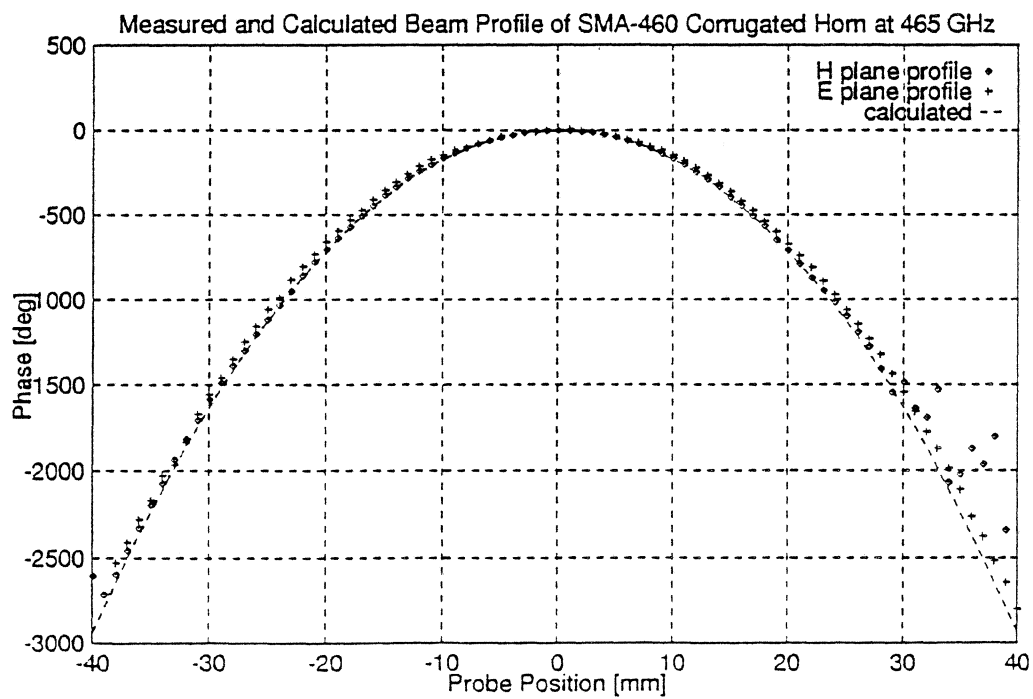


Fig. 8

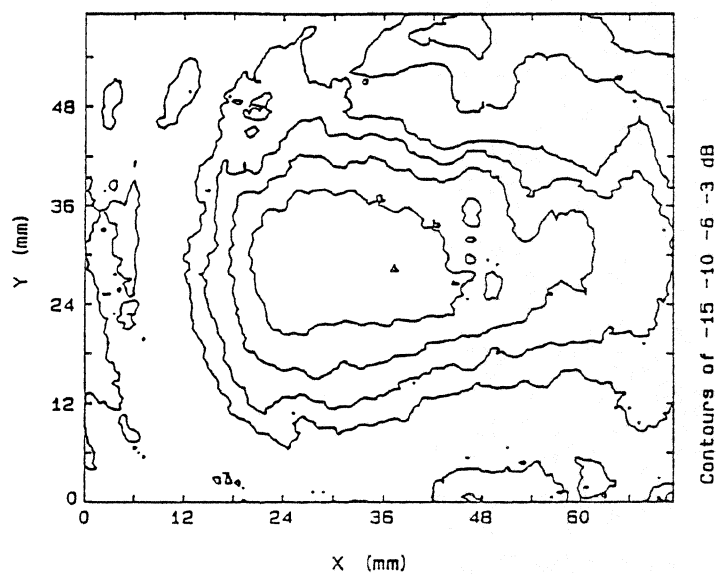


Fig. 9 Near Field Amplitude Data at 254 GHz
of Twin Dipole Receiver on Ellipsoidal Lens

A SUBMILLIMETER WAVE PLATELET HORN ARRAY: FABRICATION AND PERFORMANCE

Robert W. Haas: Aerojet Electronic Systems
Sanjay Raman, Gabriel Rebeiz: NASA Center for Space Terahertz
Technology
William R. McGrath: Jet Propulsion Laboratory
Gordon Chin: Goddard Space Flight Center
Hemant Dave: Applied Research Corp.

Abstract

A technique has been developed for the economical construction of arrays of efficient corrugated conical feedhorns for use in multiple beam antenna systems. These horns, called "platelet horns", are constructed from platelets, thin metallic plates in which holes are photoetched and which are then stacked and diffusion bonded together to form a monolithic structure with internal features. This technique was first demonstrated by the fabrication and test of a nine element array for W-Band [1]. Since that demonstration, this technique has been further advanced with the fabrication and test of a 16-element array of profiled corrugated horns for W-Band as well as an array for 550 - 750 GHz operation.

This paper presents the results of performance measurements of these arrays at W-band and at 527 GHz and 762 GHz.

Introduction

Millimeter wave and submillimeter wave remote sensing systems such as those used for radio astronomy and earth observations from space require highly efficient antenna systems. This high efficiency translates directly into reduced observation time and more accurate calibration. Platelet horn arrays were developed in response for a need for a method to fabricate relatively large arrays of highly efficient feed horns for focal plane array remote sensing systems.

It is well known that the corrugated horn is an excellent feed because of its symmetrical Gaussian beam, low side lobes and low cross polarization. However, with conventional methods, the manufacture of arrays of such horns for millimeter wave frequencies and higher is very expensive since the horns must be individually fabricated using non-reusable mandrels. Also, it is extremely difficult to make them for frequencies above 400 GHz.

Platelet Horn Arrays

As shown in Figure 1, the platelet horn array is fabricated using platelet technology. Platelets are thin sheets of metal containing patterns of holes. These sheets are sandwiched together in a stack of many layers, and then diffusion bonded together to make a single monolithic construction, having within it, holes, channels, cavities, etc., or arbitrary shapes. These hole patterns are defined and etched in the platelets using standard photolithographic or laser machining techniques. Thus, once a design is completed, and the photolithographic masks or machine programs are created, many platelets can be reproduced accurately and economically. It is estimated that arrays for up to 1200 GHz can be fabricated with this technique.

Besides etching out holes in the platelets to form the horns, additional cavities can also be created to lighten the structure. Also channels through which a coolant can be circulated can be incorporated for thermal control of the attached electronics.

In the original work on platelet horn arrays [1], the fabrication and test of an array of nine W-band conical corrugated horns was reported. It was shown, that for this array, which was made out of zirconium copper, the horns performed just as well as an identical electroformed horn, which demonstrated that there was no deterioration in performance due to this new manufacturing technique. However, that array was quite heavy, as it was mostly solid copper. Accordingly, a second array was fabricated with the goal of making a much lighter array, suitable for eventual space applications. This was accomplished by using shorter "profiled" horns, substituting aluminum for copper, and etching out much of the unnecessary material between the horns. The resulting W-band sixteen-horn array is shown in Figure 2. Again, measurements demonstrated that these array horns also performed just as well as an identical electroformed version. Typical patterns are shown in Figure 3. This figure also shows that this particular profiled horn design [2], does not produce the Gaussian patterns expected from a conical horn; note the shoulders at -8 dB. It is possible to get a much better pattern [3], but it takes a computer intensive optimization routine which is usually very slow [4].

Submillimeter Wave Horn Array

Having demonstrated the suitability of platelet technology for producing horn arrays at W-band, it was next attempted to extend this technology to the submillimeter regime. The above sixteen horn design was scaled up to 626 GHz to be compatible with an SIS receiver at this frequency

at JPL and is shown in Figure 4. The same horn design was used to save platelet design time. The resulting horns were 0.296 inches long with aperture diameters of 0.1232 inches. The design called for platelets of only 0.002 inches thick and they were made of #347 stainless steel, copper plated, both as a bond aid and to reduce the surface electrical resistance.

In order to make the pattern measurements, a matching detector array was fabricated at the University of Michigan. This array consisted of dipole fed bolometers suspended on membranes in etched silicon pyramidal cavities. The geometries of these integrated horn antennas are shown in Figures 5 and 6. It has previously been demonstrated that such integrated horn antennas can be used to drive metallic horn extensions [5]. In this case, the "extensions" were the platelet horns. The array of integrated horn antennas was mounted behind the SMMW platelet horn array and aligned by looking down the boresight of the platelet horn with a microscope. The aperture of the integrated horn was brought into firm contact with the feed side of the platelet horn array using x-y-z micrometers and kept flush by mechanical pressure. Pattern measurements were made at 527 GHz and 762 GHz and the results are shown in Figure 7. The groove depths are such that the horn should work reasonably well from 550 GHz to 750 GHz.

527 GHz Measurements

These measurements were made at the University of Michigan using a RPG-Radiometer 450-520 GHz sextupler fed by a Carlstrom tunable Gunn oscillator operating at 87.8 GHz. The specified output power was 460 μ W. However, the power was coupled out using a 345 GHz standard gain horn which probably lost a significant fraction of the power to higher order modes. This resulted in a low dynamic range of about 18 dB. The measured patterns show excellent rotational symmetry. No cross-polarization measurements could be made due to the low signal-to-noise ratio, but no cross-polarization could be detected above the noise floor. The directivity of the horn, calculated from the E-plane measured data and assuming perfect rotational symmetry, is 21.75 dB. Since the physical aperture is 7.7 mm², this directivity translates into an aperture efficiency of 50% at 527 GHz.

762 GHz Measurements

These measurements were performed at the NASA Goddard Space Flight Center using a CO₂-laser-pumped FIR gas laser. The 762 GHz radiation was produced from the 393.6 μ m line of Formic acid. The output of the laser was estimated to be 500 μ W and it was chopped at 100 Hz with a mechanical chopper. The resulting dynamic range was about 20 dB. The pattern showed good rotational symmetry and the shoulders expected from

the W-band measurements were clearly observed. In fact, the 3- and 10- dB beamwidths were almost exactly the same as those measured on the W-band array at 106 GHz and the shoulders were at the same power level (762 GHz scales to 110 GHz). The directivity of the horn at this frequency, calculated from the E-plane measured data and again assuming perfect rotational symmetry, is 23.2 dB, which translates into an aperture efficiency of 34%.

Conclusion

A technique has been demonstrated for the production of arrays of submillimeter wave corrugated horns and it is estimated that the technique can be used for horns up to 1200 GHz. Measurements have been made up to 762 GHz and show the radiation patterns to be similar to those measured from a W-band version. While measurements have shown no added losses due to this manufacturing technique at W-band, loss measurements have not yet been performed at submillimeter wave frequencies. but are planned for the near future.

References

- [1] R.W. Haas, et. al., "Fabrication and Performance of MMW and SMMW Platelet Horn Arrays", *International Journal of Infrared and Millimeter Waves*, Vol. 14, No. 11, , Nov. 1993, pp 2289-2293
- [2] Olver, A.D. & Xiang, J., "Design of Profiled Corrugated Horns", *IEEE Trans. on Antennas and Propagation*, Vol. 36, No. 7, July, 1988, pp 936-940
- [3] Clarricoats, P.J.B., & Olver, A.D., "Corrugated Horns for Microwave Antennas", Published by Peter Peregrinus Ltd., London, UK, 1984, p 82
- [4] Olver, A.D., Private communication, Aug. 1993
- [5] G.V. Eleftheriades, W.Y. Ali-Ahmad, & G.M. Rebeiz, "A 20-dB Quasi-integrated horn antenna", *IEEE Microwave and Guided Wave Letters*, vol. 2, Feb. 1992, pp 73-75

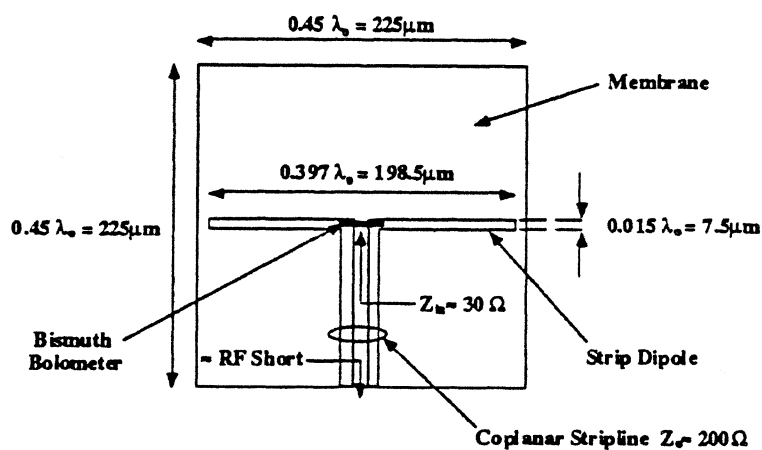
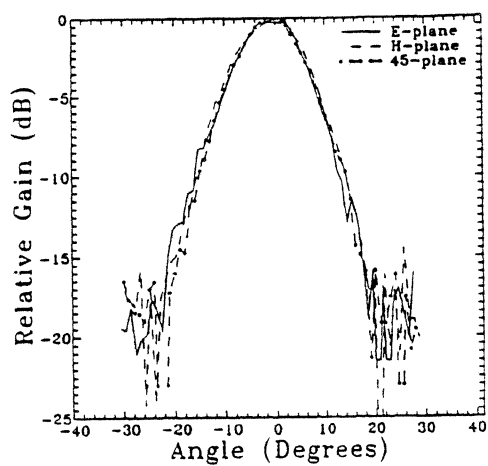
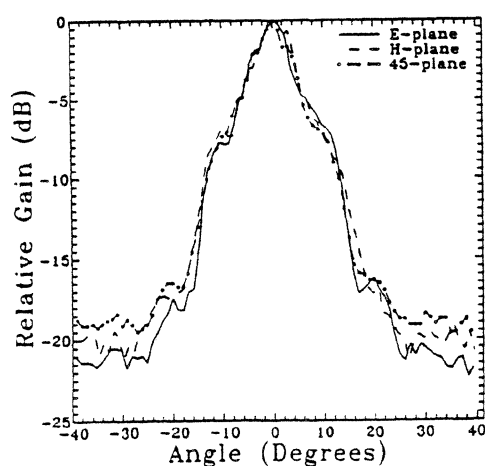


Figure 6. Antenna and Feed Structure



527 GHz



762 GHz

Figure 7. Submillimeter Wave Array Radiation Patterns

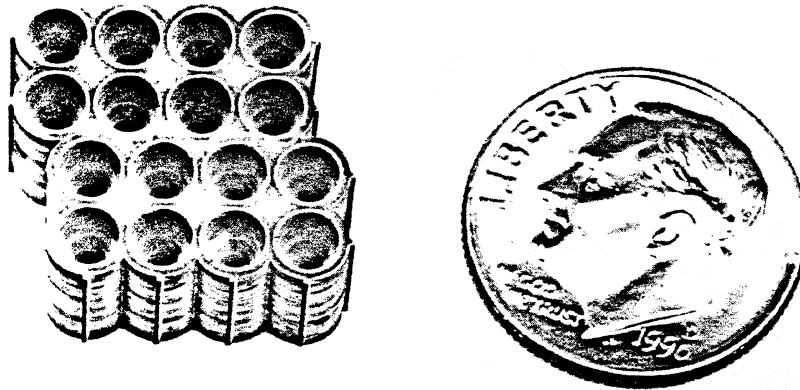


Figure 4. Submillimeter Wave Platelet Horn Array

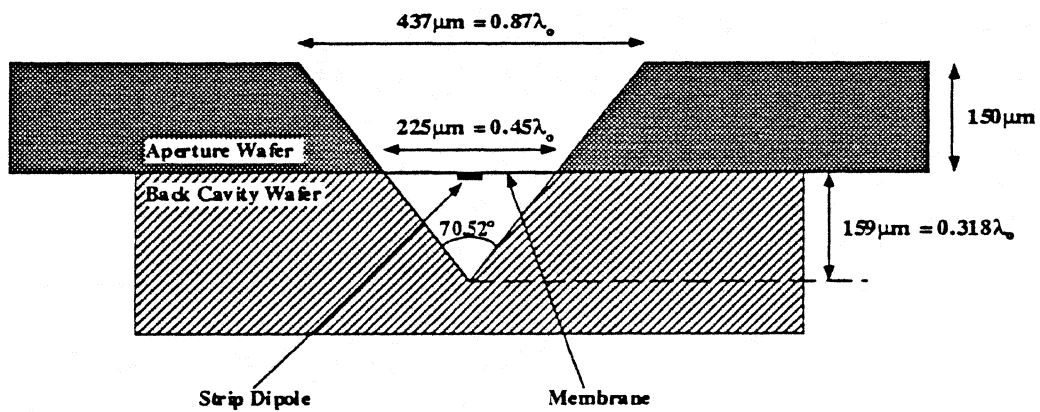


Figure 5. Integrated Pyramidal Horn Structure

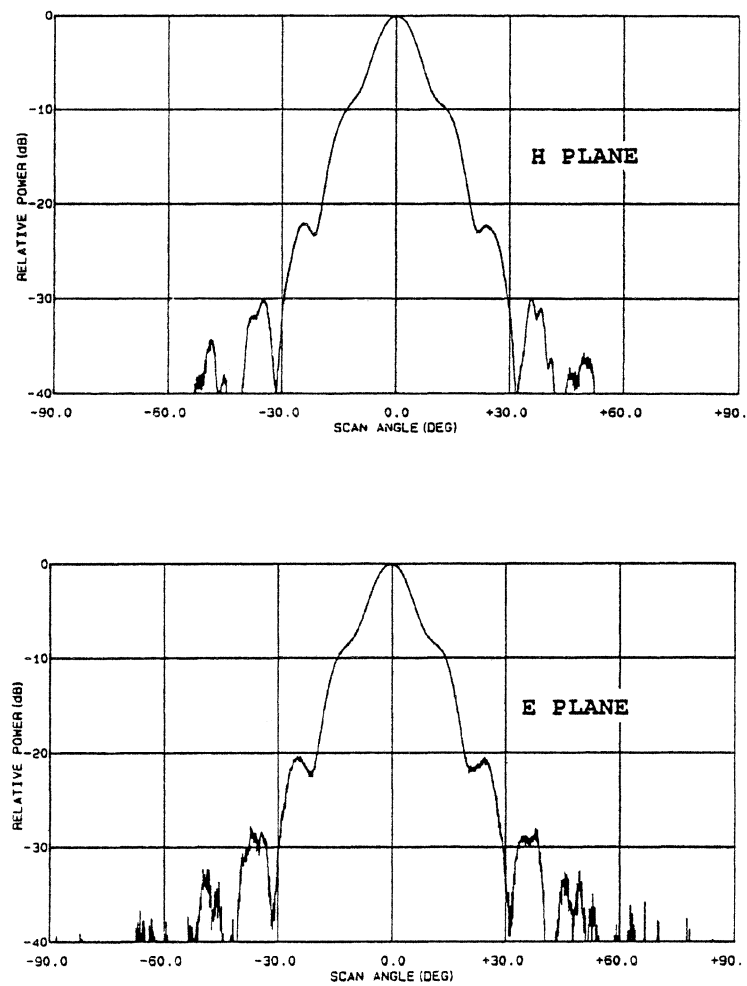
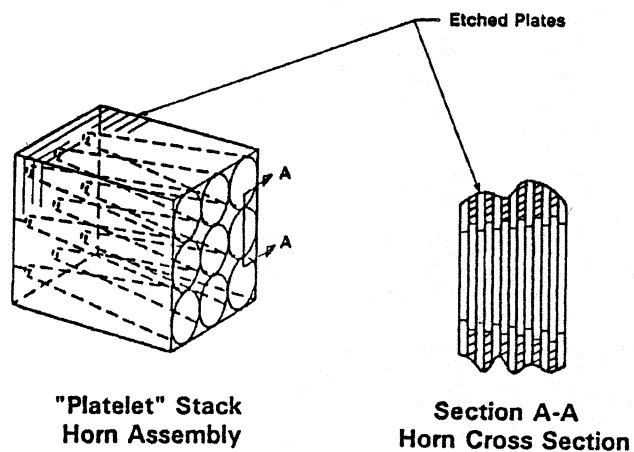
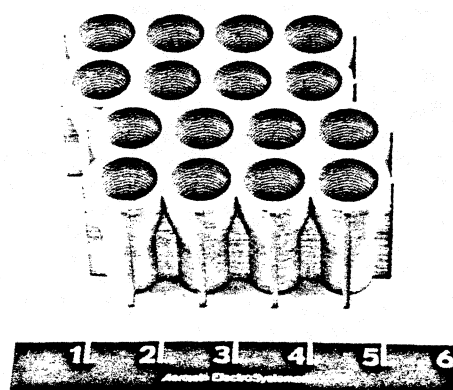


Figure 3. 94 GHz Radiation Patterns of Profiled Platelet Horns



**Figure 1. Principle of the
Platelet Horn Array**



**Figure 2. W-Band Array of
Profiled Platelet
Horns**

Quasi-Optical Optimization and Modal Analysis of Cornercube Schottky-Diode Mixers

J. Brune, P. Bierschneider

Laboratories for High Frequency Technology

University Erlangen-Nürnberg

Cauerstr.9

D-90518 Erlangen. Federal Republic of Germany

Abstract

An optimization of the system cornercube mixer – Gaussian beam requires a calculation of the power coupling coefficient. First, the cornercube field is determined by the use of image theory. Then the field of a Gaussian beam is transformed into the cornercube coordinate system. The transformation used here allows both: a tilt of the mixer relative to the beam and also longitudinal and lateral shifts. Now the evaluation of the coupling integral will be performed numerically.

The optimization of the beam parameters for the standard cornercube mixer ($L = 4\lambda$, $s = 1.2\lambda$) and for a commercially available mixer ($L = 4\lambda$, $s = 0.93\lambda$) resulted in maximum power coupling coefficients of 59 % and 77 % respectively. If the antenna dimensions are also involved in the optimization process a coupling of 88 % can be reached for an antenna configuration with $L = 0.92\lambda$ and $s = 0.83\lambda$. Finally the frequency response is shown and a modal analysis is performed for all three mixer types. It can be concluded that the standard configuration used in many quasi-optical systems all over the world is far away from the optimum.

1 Introduction

Schottky-diode mixers of the cornercube-type are still widely used in quasi-optical submillimeterwave systems for radioastronomy [1], plasma diagnostics [2] and environmental monitoring [3]. While waveguide Schottky mixers [5] and SIS mixers are limited to about 700 GHz. Cornercube mixers are currently employed in radiometer systems for frequencies up to 2.5 THz and higher [4]. However, waveguide mixers provide a better coupling to Gaussian beams if equipped with suitable horn antennas. The intention of this paper is to provide an insight in the coupling calculations and the parameters which influence the coupling of a cornercube and a Gaussian beam. Suggestions will be given how the performance of existing cornercube mixers can easily be improved.

After the invention of the whisker antenna in 1970 by MATARRESE et.al. [6], in 1977 KRÄUTLE et.al. [7],[8] started to improve the coupling between the field

of a Gaussian beam and the whisker antenna field by placing rooftop-reflectors behind the antenna. The spacing between the antenna and the rooftop reflector and the opening angle of the rooftop was experimentally optimized in order to get a round main lobe which was believed to give the best coupling to a Gaussian beam. The optimisation resulted in a 4λ whisker antenna spaced 1.2λ from a 90° -rooftop reflector. This design is still used as a “cookbook recipe” all around the world and will be referred to as the “standard configuration” in this paper. In 1984 HERRMANN [9] calculated the coupling between a Gaussian beam and a Schottky diode mixer in rooftop configuration for the first time. He found that the coupling is about 50 %. However, the calculations only involved the amplitudes of the two fields. In the analysis of KELLY et.al. [10] in 1985 the rooftop mixer was analyzed and practical suggestions for the mixer design and fixture were given. GROSSMAN [11] performed in 1989 an evaluation of the coupling integral for a 90° -rooftop reflector. He could show that the standard configuration is in no sense optimal and gave recommendations for improved antenna dimensions in a 90° -rooftop reflector.

However, most of the open structure Schottky diode mixers are rather in a cornercube than in a rooftop configuration, this means that an additional ground reflector is employed which influence has been neglected in the former studies. Additionally the radiation attenuation and shifts of the input coupling Gaussian beam along the cartesian coordinate axes were not taken into account up to now. These factors will be included in our cornercube model we present in the following.

2 Field calculations

Fig. 1 shows the geometry of a typical cornercube configuration. The whisker antenna with length L stands vertically on the ground reflector and is spaced at a distance s from the apex of the 90° rooftop reflector. On the bottom of the antenna the diode chip is placed on a choke structure (for design optimization of the choke structure see [12]). A Gaussian beam is focused onto the cornercube, the variable beam parameters are the waist position in space, the waist radius and the direction of propagation.

The calculation of the coupling between the incoming Gaussian beam and the antenna structure will be performed in different steps: First, the electric fields of the cornercube and the Gaussian beam are required. The antenna field will be determined according to the reciprocity principle [13] for the case of a load-independent current wave with amplitude I_0 . The electrical field of the Gaussian beam will then be transformed into the same spherical polar coordinate system as the cornercube. Now, the coupling integral [14] can be evaluated numerically.

2.1 Cornercube mixer

Before the corner reflector is taken into account, the electrical field \vec{E}_W of a free standing single longwire whisker-antenna of length L is required. It can be shown

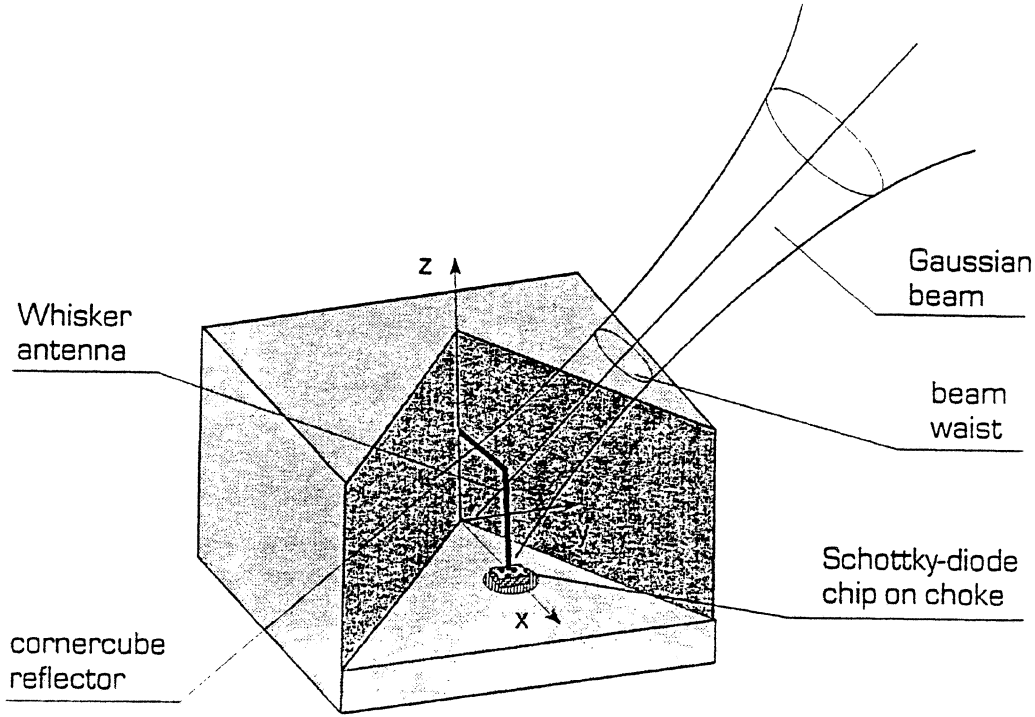


Figure 1: Quasi-optical cornercube Schottky-diode mixer

that only the z -component exists [9]:

$$E_z w(r, \vartheta, \varphi) = -\frac{\mu_0 I_0 L}{4\pi r} \cdot \exp\{-jkr\} \cdot j\omega \cdot \frac{\exp\{jkL(\cos(\vartheta) - 1) - \alpha L\} - 1}{jkL(\cos(\vartheta) - 1) - \alpha L} \cdot \exp\{j\omega t\} \quad (1)$$

Eq.(1) is given in a mixed representation of cylindrical and spherical polar coordinates. The dependence on spherical polar coordinates is useful because the evaluation of the coupling integral will be performed over a spherical surface, while the scalar product between the fields of the cornercube and the Gaussian beam is easier to perform with the z -component instead of a superposition of the r - and ϑ -components. The ϑ -component of the whisker field alone is not sufficient for the coupling calculations because translational shifts of the Gaussian beam will also be allowed during mixer optimization. From Eq.(1) one sees that the electric field is independent of φ , it is therefore axially symmetric to the z -axis. In Fig. 2 the antenna pattern of a 4λ longwire whisker-antenna is displayed.

This axially symmetric beam pattern can be shaped by introducing plane reflectors around the antenna in order to give a main lobe and therefore to improve the coupling to a Gaussian beam. While in the beginning of the development of the standard configuration only one rooftop-mirror was employed, nowadays most of the open-structure mixers have an additional ground reflector for mechanical and optical reasons. The influence of this ground reflector must not be neglected.

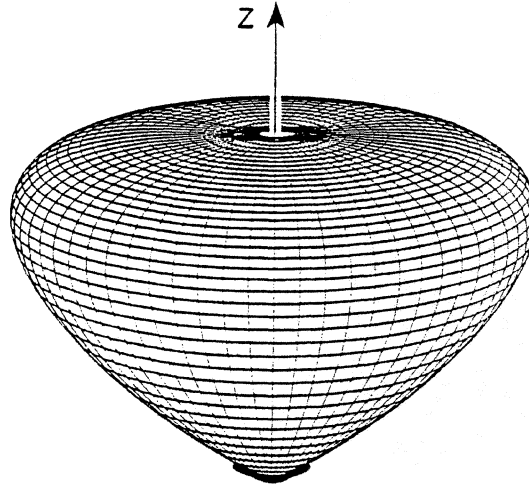


Figure 2: Linear antenna pattern of a 4λ whisker-longwire-antenna

With the theory of images the influence of the reflectors can be determined: the whisker antenna and its images will be considered as an antenna group [15] and the electric field can be calculated by a proper superposition of the single antenna fields. However, the current wave will have a different sign depending on whether the antenna is parallel or perpendicular to the reflector plane. In Fig. 3 the relevant cases for a reflection of the whisker antenna on a plane reflector are displayed: corresponding to the static case the current wave on the image antennas will be of opposite sign. The case of the whisker being parallel to the reflector plane can therefore be replaced by a real whisker antenna with positive sign of its current wave and the image antenna with negative sign. Both waves are travelling in the same direction (Fig. 3a)). If the whisker is standing perpendicular on the reflector as in the case of the ground reflector, the image current wave is of opposite sign and travels into opposite direction (Fig. 3b)). In the case of a rooftop reflector also a second reflection of the two negative image antennas occurs which finally results in a positive current wave on the resulting image antenna (Fig. 3c)).

Fig. 4 shows the case of the cornercube mixer configuration. The influence of the whisker and its seven images have to be superimposed with proper sign and phase. Advantage can be taken out of Fig. 3 b): with Eq. (1) the influence of the four image antennas below the ground reflector can be taken into account as follows, where $E_{z\ CC}$ represents the field of the cornercube and $E_{z\ RT}$ the field of the rooftop configuration, i.e. the four antennas above the ground reflector:

$$E_{z\ CC}(r, \vartheta, \varphi) = E_{z\ RT}(r, \vartheta, \varphi) + E_{z\ RT}(r, (\pi - \vartheta), \varphi) \quad (2)$$

To determine the field $E_{z\ RT}$ the fields of the real whisker antenna and its three images will be superimposed. By using the far field approximation only the different phases of the antennas in a distant point P will be considered. This can be done by multiplying the field $E_{z\ W}$ of the whisker antenna with the additional phase shifts

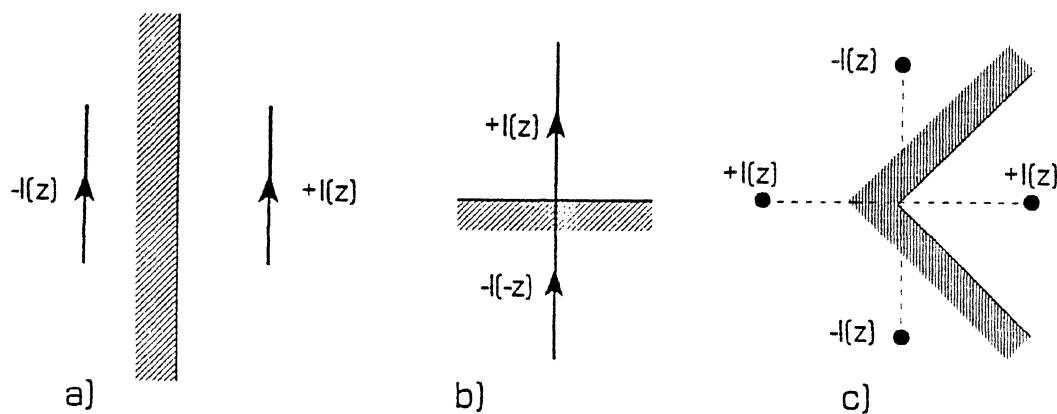


Figure 3: Reflection of the whisker-antenna at plane reflectors
 a) whisker antenna parallel to the reflector plane
 b) whisker antenna perpendicular to the reflector plane
 c) Rooftop-reflector (from above)

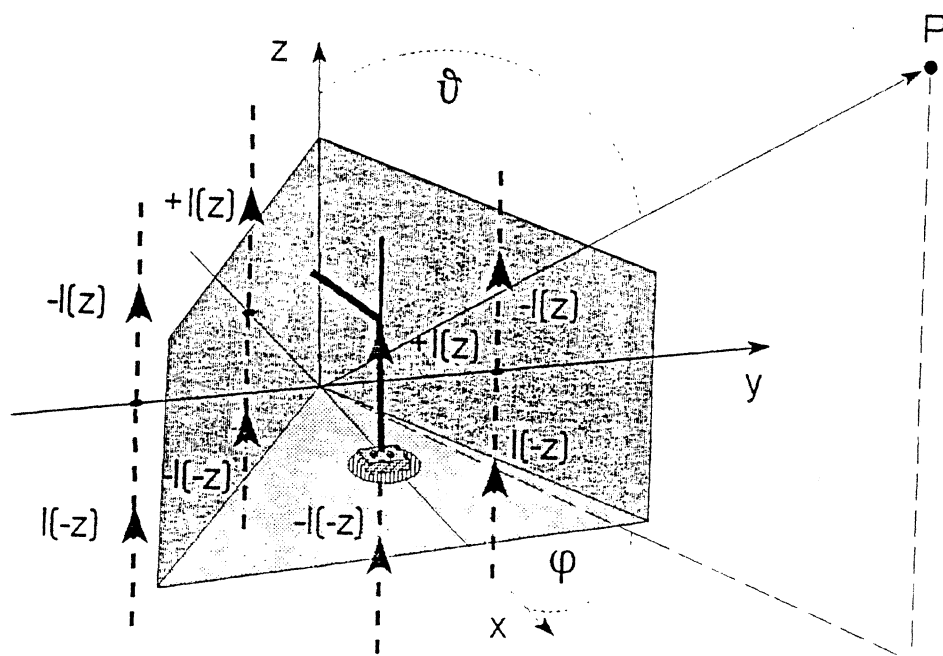


Figure 4: Whisker antenna and its images in a cornercube mixer configuration

Φ^n of each single antenna in the distant point P . The amplitude differences in P will be neglected because the distance from the antennas to P is much larger than the distances of the antennas from each other.

$$E_{zRT}(r, \vartheta, \varphi) = \sum_{n=1}^4 E_{zw}^n(r, \vartheta, \varphi) \approx E_{zw}(r, \vartheta, \varphi) \sum_{n=1}^4 \Phi^n \quad (3)$$

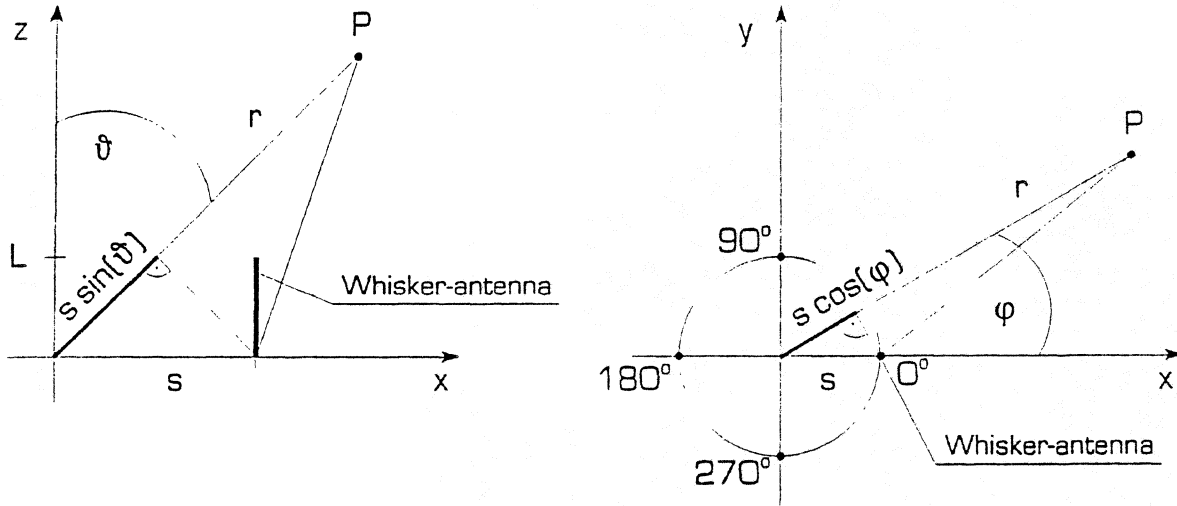


Figure 5: Phase differences of the four single antennas in a distant point P with respect to the origin

Fig. 5 explains, where the phase differences of the four antenna fields in a distant point P come from. The origin of the coordinate system from Fig. 4 will be used as reference point. Under consideration of the current signs corresponding to Fig. 3 one obtains for the four phases:

$$\Phi^1 = + \exp \{ + j k s \sin(\vartheta) \cos(\varphi) \} \quad (4)$$

$$\Phi^2 = - \exp \{ + j k s \sin(\vartheta) \cos(\varphi - 90^\circ) \} \quad (5)$$

$$\Phi^3 = + \exp \{ + j k s \sin(\vartheta) \cos(\varphi - 180^\circ) \} \quad (6)$$

$$\Phi^4 = - \exp \{ + j k s \sin(\vartheta) \cos(\varphi - 270^\circ) \} \quad (7)$$

With these four additional phase shifts the electrical field $E_{zRT}(r, \vartheta, \varphi)$ of the rooftop-configuration, i.e. the four upper antennas will now be determined according to Eq. 3.

$$\begin{aligned} E_{zRT}(r, \vartheta, \varphi) &= \\ &= E_{zw}(r, \vartheta, \varphi) \cdot \sum_{n=1}^4 \Phi^n \\ &= 2E_{zw}(r, \vartheta, \varphi) \{ \cos(k s \sin(\vartheta) \cos(\varphi)) - \cos(k s \sin(\vartheta) \sin(\varphi)) \} \end{aligned} \quad (8)$$

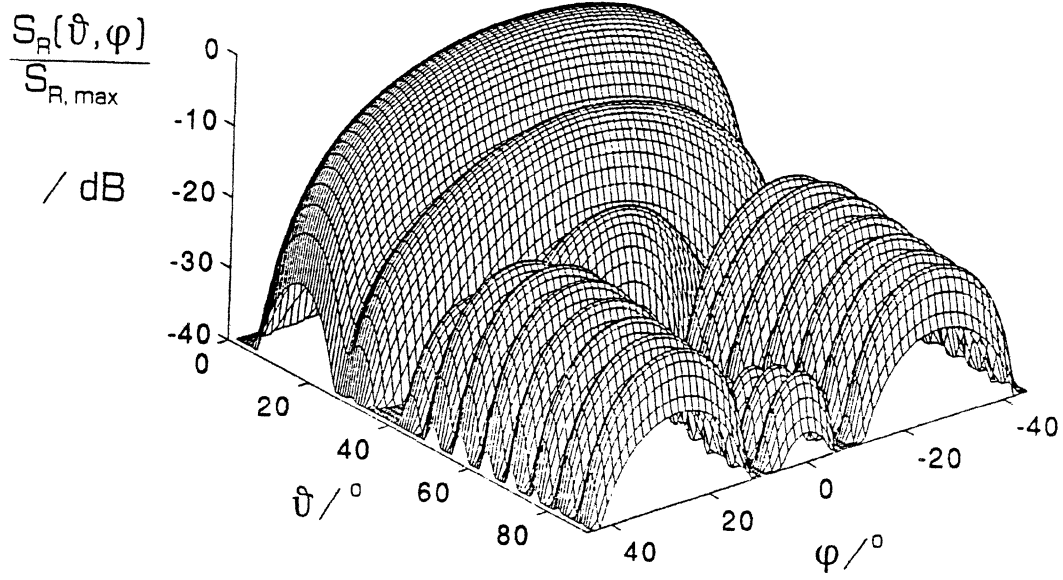


Figure 6: Calculated antenna pattern for a cornercube mixer in standard configuration ($L = 4\lambda$; $s = 1, 2\lambda$)

With Eq.(2) and $\omega = kc$ one finally gets the electric field of the rooftop mixer configuration.

$$\begin{aligned}
 E_{z\,CC}(r, \vartheta, \varphi) = & \\
 = & \frac{\mu_0 I_0 c}{2\pi r} \cdot j \cdot \exp\{-jkr\} \cdot \exp\{j\omega t\} \\
 & \cdot \{\cos(ks \sin(\vartheta) \cos(\varphi)) - \cos(ks \sin(\vartheta) \sin(\varphi))\} \\
 & \cdot \left[\frac{\exp\{-jkL(\cos(\vartheta) + 1) - \alpha L\} - 1}{j(\cos(\vartheta) + 1) + \alpha/k} - \frac{\exp\{jkL(\cos(\vartheta) - 1) - \alpha L\} - 1}{j(\cos(\vartheta) - 1) - \alpha/k} \right]
 \end{aligned} \tag{9}$$

In Fig. 6 the calculated antenna pattern of a cornercube mixer in standard configuration ($L = 4\lambda$; $s = 1, 2\lambda$) is shown. Note that a distorted representation of the two angles ϑ and φ is given instead of a depiction in polar coordinates.

2.2 Gaussian beam

The electrical field for a linearly polarized fundamental Gaussian beam mode will be extracted from the literature (e.g. [16]). For the transversal field component of a fundamental mode which travels along the $+z'$ -axis and which is polarized in x' -direction one gets:

$$E_{00_{x'}} = u_{00} \cdot e^{-jkz'} \cdot e^{j\omega t} \tag{10}$$

with

$$u_{00}(x', y', z') = \sqrt{\frac{2}{\pi}} \cdot \frac{1}{w} \cdot \exp \left[\frac{-(x'^2 + y'^2)}{w^2} \right] \cdot \exp \left[-j \frac{k(x'^2 + y'^2)}{2R} \right] \cdot \exp [i(\varphi + \varphi_0)] \quad (11)$$

and

$$w^2 = w_0^2 \cdot \left[1 + \left(\frac{2(z' - z'_0)}{kw_0^2} \right)^2 \right] \quad (12)$$

$$R = \frac{k^2 w_0^4}{4(z' - z'_0)} + (z' - z'_0) \quad (13)$$

$$\varphi = \arctan \left\{ \frac{2(z' - z'_0)}{kw_0^2} \right\} \quad (14)$$

For the modal analysis performed later, also higher order beam modes are required. In this paper Hermite-Gaussian (HG) beam modes will be used, although the generalized Laguerre-Gaussian (LG) modes are fully equivalent (the transformation relations between HG and LG modes can be found in [17]). With Eq.(11) one gets for the HG-Modes:

$$u_{mn}(x', y', z') = \left\{ \frac{1}{2^{n+m} n! m!} \right\}^{\frac{1}{2}} \cdot H_m \left[\sqrt{2} \frac{x'}{w} \right] \cdot H_n \left[\sqrt{2} \frac{y'}{w} \right] \cdot \exp \{j(m+n)\varphi\} \cdot u_{00}(x', y', z') \quad (15)$$

2.3 Coordinate transformation

In Fig. 7 the location of the coordinate system (x, y, z) of the cornercube mixer relative to the coordinate system (x', y', z') of the Gaussian beam is shown. For the determination of the coupling integral the (x', y', z') system has to be transformed into the system (x, y, z) of the cornercube mixer. The origins of the (x, y, z) - and the (x', y', z') -systems are coincident, however they are tilted by the angles ϑ_G and φ_G which represent the incoming angle of the Gaussian beam. Finally, the position of the beam waist is determined by the point $P_0(x'_0, y'_0, z'_0)$. With these definitions the transformation relations can be given:

$$\begin{aligned} x' &= -x \cos(\vartheta_G) \cos(\varphi_G) - y \cos(\vartheta_G) \sin(\varphi_G) + z \sin(\vartheta_G) - x'_0 \\ y' &= -x \sin(\varphi_G) + y \cos(\varphi_G) - y'_0 \\ z' &= -x \sin(\vartheta_G) \cos(\varphi_G) - y \sin(\vartheta_G) \sin(\varphi_G) - z \cos(\varphi_G) - z'_0 \end{aligned} \quad (16)$$

2.4 Evaluation of the coupling integral

The coupling integral Eq.(17) gives the amount of power coupled from one antenna field (transmitter) into the other (receiver) [14]. In our case the electrical field \vec{E}_{mn}

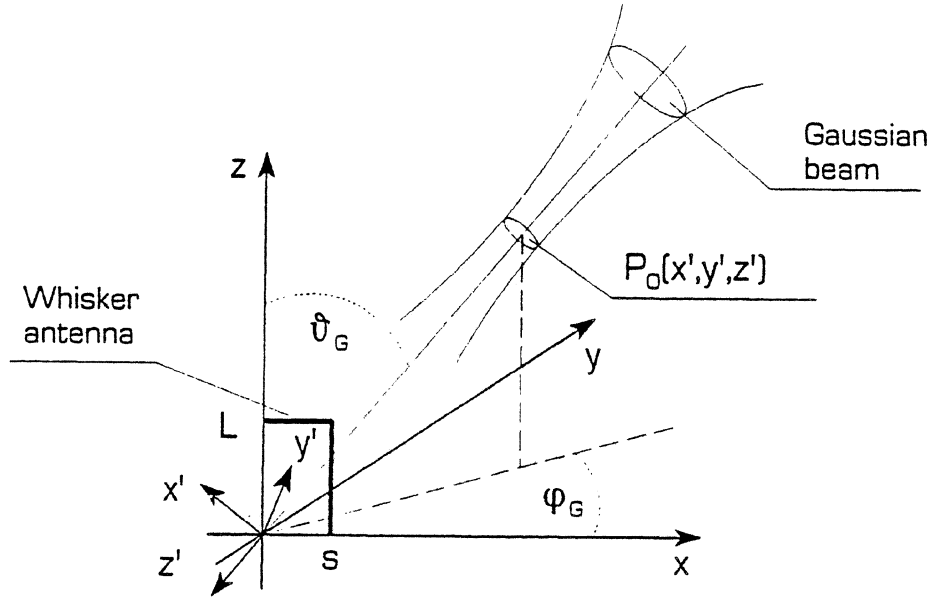


Figure 7: Location of the coordinate system (x, y, z) of the cornercube antenna relative to the coordinate system (x', y', z') of the Gaussian beam

of the Gaussian beam mode of order m, n can be considered as the transmitter field while the cornercube antenna field E_{CC} is the receiver field:

$$K_{mn} = \frac{\left| \int \int_A \vec{E}_{CC} \cdot \vec{E}_{mn}^* dA \right|^2}{\left[\int \int_A |\vec{E}_{CC}|^2 dA \right] \left[\int \int_A |\vec{E}_{mn}|^2 dA \right]} \quad (17)$$

The integration will be evaluated over an octant $-\pi/4 < \phi < \pi/4$ and $0 < \vartheta < \pi/2$ of a sphere with radius r_i because the cornercube field disappears outside this area. By numerical investigations it was found that the integration radius r_i should be chosen between 32λ and 128λ . If the value of r_i is too big the paraxial approximation is no longer valid. Too small values of r_i cause the far field approximation to be hurt. For the coupling calculations we finally chose $r_i = 100\lambda$ and 2500 integration points.

3 Optimization of the beam coupling to Cornercube mixers

During the quasi-optical optimization of the cornercube mixer the beam parameters and the antenna dimensions will be affected. The beam parameters are the waist radius w_0 , the beam waist position in space and the direction of beam propaga-

tion. The latter are described by the angles ϑ_G , φ_G and the beam waist position $P_0(x', y', z')$ as given in Fig. 7. This representation was chosen because it represents the situation in practical mixer adjustment: in most cases the mixer itself instead of the incoming Gaussian beam will be adjusted. First the mixer mount will be tilted by the angles ϑ_G and φ_G relative to the Gaussian beam in order to increase video response or to decrease the noise temperature respectively. Then, the tilted mixer will be translationally shifted in order to maximize the mixer performance, i.e. a fine adjustment along the cartesian coordinate axes (x', y', z') of the coordinate system of the Gaussian beam will be performed.

From the range of possible mixer parameters only the antenna length L and the spacing s between the antenna and the apex of the corner reflector will be involved in the optimization process because only the whisker has to be changed for improving the mixer while the mixer housing can be reused. Therefore the opening angle of the apex will be kept constant at an angle of 90° . According to experimentally obtained values [9] the radiation attenuation will be set to 200 m^{-1} . With Eq. (11) the power coupling factor K_{00} of the cornercube field and the fundamental Gaussian beam mode can now be calculated.

The optimizations were performed on a standard PC in TURBO PASCAL. In our program all the mixer and beam parameters can be changed. However due to long computing times not more than two parameters have been varied at once in practical operation. After an optimum has been found, two other parameters have been chosen. This procedure will be performed until the optimum is reached. A problem is the presence of local maxima: an optimization towards those relative maxima can be avoided by performing several optimizations with different starting values and by repeating the optimization procedure several times.

First the radiation resistance R_S was determined for different antenna dimensions L and s . Its value is important for the coupling between the antenna and the Schottky diode and strongly influences the performance of the mixer. With the Poynting vector \vec{S}_r , the integration surface A around the antenna, the free-space wave resistance Z_0 and the impressed current I_0 , R_S is defined by

$$R_S = \frac{\iint_A \vec{S}_r \cdot d\vec{A}}{|I_0|} = \frac{\iint_A |E_z|^2 \sin^2(\vartheta) dA}{Z_0 |I_0|^2} \quad (18)$$

In Fig. 8 the radiation resistance is depicted depending on L and s . The significant difference in comparison to the diagram of GROSSMAN [11] is caused by the influence of the radiation attenuation and the ground reflector and shows the importance of considering them.

After these calculations the optimum beam parameters for two given mixer configurations were determined: for the standard configuration ($l = 4\lambda$: $s = 1,2\lambda$) and for a commercially available cornercube mixer [18] ($l = 4\lambda$: $s = 0,93\lambda$). Starting with these given antenna parameters the beam parameters were gradually changed in order to maximize K_{00} . In a third case also the antenna dimensions were changed during the optimization process. This procedure finally results in an optimum mixer configuration. The results are given in Tab. 1

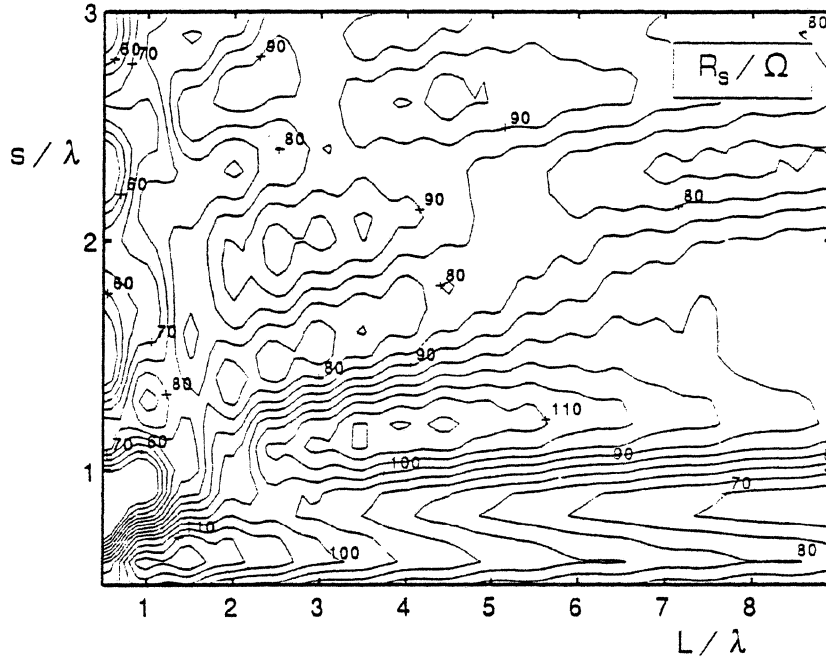


Figure 8: Radiation resistance R_S depending on the relative whisker length l/λ and the relative whisker spacing s/λ

From Tab. 1 we can easily extract that the optical coupling efficiency of the standard mixer configuration can be highly exceeded by the commercial and the optimum configurations. The coupling of the whisker-antenna to the Schottky diodes however, will decrease if a mismatch between the radiation resistance R_S and the diode impedance R_D occurs. To account for this effect, we define the overall coupling efficiency $K_{\text{tot.}}$:

$$K_{\text{tot.}} = K_{\text{DA}} \cdot K_{00} \quad (19)$$

with the coupling efficiency due to diode-antenna mismatch [9] K_{DA} :

$$K_{\text{DA}} = 1 - \left| \frac{R_D - R_S}{R_D + R_S} \right|^2 \quad (20)$$

The diode impedance R_D is dependent on many parameters including LO power and bias current. For most submillimeterwave mixers with Schottky diodes R_D can be estimated to lie between 100Ω and 200Ω [9]. For our calculations the more optimistic value $R_D = 100\Omega$ was used. The resulting coupling efficiencies are given in the last column of Tab. 1. The difference between the optimum and the commercial mixer is only about 5 %. It can however be expected that beam distortion occurs due to $w_0/\lambda < 1$. We therefore recommend the use of the commercial configuration.

The differences between the different mixer configurations can even more clearly be seen if we look at the frequency dependence of the quasi-optical power coupling coefficient. In Fig. 9 the three mixer types are compared for the case of a design for the center frequency $f = 600$ GHz. The beam parameters have been optimized for maximum optical coupling at the design frequency and have been kept constant over

	design parameter	Mixer type		
		standard	commercial	optimum
antenna parameters	L/λ	4.0	4.0	0.92
	s/λ	1.2	0.93	0.83
	$\alpha[\text{m}^{-1}]$	200	200	200
beam parameters	w_0/λ	1.66	1.46	1.01
	$\vartheta[^\circ]$	24	26.5	44.5
	$\varphi[^\circ]$	0	0	0
	x'_0/λ	-0.7	-0.6	-0.25
	y'_0/λ	0	0	0
	z'_0/λ	2	1.6	4.12
optimization results	R_S/Ω	115	91	59
	Quasi-optical Coupling Efficiency K_{00}	59.5 %	77.2 %	88.0 %
	Overall Coupling Efficiency $K_{\text{tot.}}$	59.2 %	77.0 %	82.1 %

Table 1: Optimization of the quasi-optical coupling to cornercube mixers

the varied frequency. This is typical for frequency independent quasioptical setups where no adjustments during operation will be performed (e.g. [19]). It can clearly be seen that the standard configuration is not at all an optimum one: it reaches its maximum coupling at lower frequencies, where the relative antenna length L/λ is shorter. The performance of the commercially available mixer is again closer to the optimum.

From Tab. 1 it can also be seen that it is worth not only to allow rotational but also translational adjustment in mixer fixtures. The 3-dB adjustment tolerances lie within some tenths of the wavelength and a few degrees respectively for all given parameters. Therefore care should be taken when designing the mixer fixture.

At last a modal analysis of the three mixer types was performed by evaluating the coupling integral Eq. 17 for the higher order modes instead of the fundamental mode. The beam parameters have been extracted from Tab. 1. In the following modal tables Tab. 2 to Tab. 4 power distribution on the first 100 Gauß-Hermite modes is given. In the caption the amount of power P_{sum} contained in these first 100 modes is given relative to the total radiated power by the cornercube mixer P_{CC} . One can see that a significant amount of beam power is contained outside the Gaussian (paraxial) regime for the standard mixer while for the optimum mixer the field can be better represented by Gaussian beams.

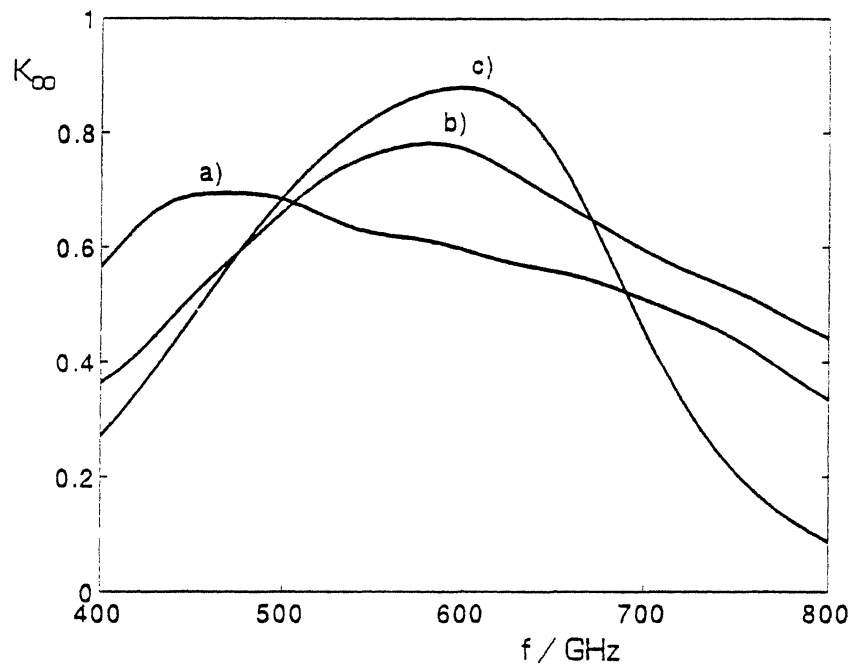


Figure 9: Frequency dependence of the quasi-optical coupling to cornercube mixers for the case of optimum coupling
 a) standard configuration ($L = 4\lambda$, $s = 1.2\lambda$)
 b) commercial configuration ($L = 4\lambda$, $s = 0.93\lambda$)
 c) optimum configuration ($L = 0.92\lambda$, $s = 0.83\lambda$)

$m \ n$	0	1	2	3	4	5	6	7	8	9
0	0.5952	0	0.0037	0	0.0014	0	0.0002	0	0.0001	0
1	0.0001	0	0	0	0	0	0.0001	0	0.0001	0
2	0.0030	0	0.0042	0	0.0005	0	0.0004	0	0.0001	0
3	0.0008	0	0.0001	0	0.0007	0	0.0004	0	0.0004	0
4	0.0005	0	0.0001	0	0.0003	0	0.0002	0	0.0003	0
5	0.0001	0	0.0006	0	0.0006	0	0.0008	0	0.0005	0
6	0.0003	0	0.0005	0	0.0005	0	0.0007	0	0.0006	0
7	0.0001	0	0.0006	0	0.0009	0	0.0007	0	0.0006	0
8	0	0	0.0005	0	0.0009	0	0.0008	0	0.0009	0
9	0	0	0.0006	0	0.0008	0	0.0007	0	0.0007	0

Table 2: Table of the power coupling coefficients for a cornercube mixer in standard configuration (see Tab. 1)
 Relative mode power $P_{sum}/P_{CC} = 63 \%$

$m \ n$	0	1	2	3	4	5	6	7	8	9
0	0.7720	0	0.0107	0	0.0034	0	0.0005	0	0.0001	0
1	0.0005	0	0.0011	0	0.0006	0	0.0003	0	0.0001	0
2	0.0100	0	0.0007	0	0.0001	0	0.0001	0	0.0001	0
3	0.0090	0	0.0012	0	0.0003	0	0.0001	0	0	0
4	0.0079	0	0.0015	0	0.0003	0	0.0003	0	0.0001	0
5	0.0103	0	0.0013	0	0.0002	0	0.0001	0	0	0
6	0.0047	0	0.0012	0	0.0005	0	0.0002	0	0.0001	0
7	0.0053	0	0.0009	0	0.0003	0	0	0	0	0
8	0.0045	0	0.0008	0	0.0004	0	0.0001	0	0.0001	0
9	0.0031	0	0.0006	0	0.0002	0	0	0	0	0

Table 3: Table of the power coupling coefficients for a cornercube mixer in commercial configuration (see Tab. 1)
Relative mode power $P_{sum}/P_{CC} = 86 \%$

$m \ n$	0	1	2	3	4	5	6	7	8	9
0	0.8797	0	0.0002	0	0.0095	0	0.0047	0	0.0010	0
1	0	0	0.0007	0	0.0002	0	0	0	0	0
2	0.0011	0	0.0074	0	0.0034	0	0.0008	0	0.0002	0
3	0	0	0	0	0	0	0	0	0	0
4	0.0179	0	0.0032	0	0.0006	0	0.0002	0	0.0001	0
5	0.0001	0	0	0	0	0	0	0	0	0
6	0.0076	0	0.0007	0	0.0002	0	0.0001	0	0.0001	0
7	0.0001	0	0	0	0	0	0	0	0	0
8	0.0019	0	0.0003	0	0.0002	0	0.0001	0	0.0001	0
9	0	0	0	0	0	0	0	0	0	0

Table 4: Table of the power coupling coefficients for a cornercube mixer in optimum configuration (see Tab. 1)
Relative mode power $P_{sum}/P_{CC} = 95 \%$

4 Conclusions

The performance of the standard cornercube Schottky-diode mixer could be highly improved by relatively simple changes in the antenna and beam parameters. In an optimum configuration its optical coupling efficiency reaches the performance of horn antennas. Especially for frequencies higher than 600 GHz it is expected that the cornercube configuration performs better than waveguide Schottky-diode mixers because no waveguide losses occur.

Acknowledgement

This work was proposed by Prof. Dr.-Ing. H.Brand and has been supported by the Deutsche Forschungsgemeinschaft (DFG) under project number Br 522/14.

References

- [1] Titz, R.U., Auel, B.; Esch, W.; Röser, H.P.; Schwaab, G.W.: *Antenna Measurements of Open Structure Schottky Mixers and Determination of Optical Elements for a Heterodyne System*, Infrared Physics, November 1989
- [2] Kelly, W.M.; Vizard, D.R.; Donné, A.J.H.; Kim, S.K.: *Thermonuclear Plasma Diagnostics using Corner Cube Mixer Arrays*, Mikrowellen & HF Magazin, Vol. 15, No. 3, 1989
- [3] Hartmann, G.K.; Künzi, K.F.; Schwartz, P.R.: *Millimeterwellen-Atmosphären-Sondierer (MAS) für den Einsatz auf Space Shuttle*, Mikrowellen Magazin, Vol. 11, No. 3, 1985
- [4] Titz, R.U., Röser, H.P.; Schwaab, G.W.; Neilson, H.J.; Wood, P.A.; Crowe, T.W.; Peatman, W.C.B.; Prince, J.; Deaver, B.S.; Alius, H.; Dodel, G.: *Investigation of GaAs Schottky Barrier Diodes in the THz Range*, International Journal of Infrared and Millimeter Waves, Vol. 11, No. 6, 1990
- [5] Keen, N.; Ediss, G.: *Measurements of a Waveguide Schottky-Barrier Mixer at 690 GHz*, Proceedings of the 21st European Microwave Conference, Stuttgart, Germany, 1991, pp. 243-246
- [6] Matarrese, L.M.; Evenson, K.M.: *Improved Coupling to Infrared Whisker Diodes by Use of Antenna Theory*, Applied Physics Letters, Vol. 17, No. 1, July 1970
- [7] Kräutle, H.; Sauter, E.; Schultz, G.V.: *Antenna Characteristics of Whisker Diodes used as Submillimeter Receivers*, Infrared Physics, Vol. 17, 1977, pp. 477-483
- [8] Kräutle, H.; Sauter, E.; Schultz, G.V.: *Properties of a Submillimeter Mixer in an Open Structure Configuration*, Infrared Physics, Vol. 18, 1978, pp. 705-712

- [9] Herrmann, Karl: *Untersuchungen zum Submillimeterwellen-Empfang bei 600 GHz mit dem System Wisker-Antenne/Schottky-Diode*, Dissertation, Universität Erlangen-Nürnberg, Erlangen, 1984
- [10] Kelly, W.M.; Gans, M.J.; Eivers, J.G.: *Modelling the Response of Quasi-Optical Corner Cube Mixers*, SPIE Vol. 598, Instrumentation for Submillimeter Spectroscopy (1985), pp. 72-77
- [11] Grossman, E.N.: *The coupling of Submillimeter Corner-Cube Antennas to Gaussian Beams*, Infrared Physics, Vol. 29, No. 5, pp. 875-885, 1989
- [12] Brune, J.: *An Open Structure 600 GHz Mixer with Broadband IF Output Coupling*, Proceedings of the 21st European Microwave Conference, Stuttgart, Germany, 1991, pp. 247-252
- [13] Simonyi, K.: *Theoretische Elektrotechnik*, VEB Deutscher Verlag der Wissenschaften, Berlin 1989
- [14] Schwarz, S.E.: *Efficiency of Quasi-Optical Couplers*, International Journal of Infrared and Millimeter Waves, Vol. 5, No. 12, 1984
- [15] Voges, E.: *Hochfrequenztechnik*, Band 2, Hüthig Verlag, Heidelberg, 1987
- [16] Marcuse, D.: *Light Transmission Optics*, Van Nostrand Reinhold, New York 1972
- [17] Kimel, I.; Elias, L.R.: *Relations between Hermite and Laguerre Gaussian Modes*, IEEE Journal of Quantum Electronics, Vol. 29, No. 9, September 1993
- [18] N.N.: *Farran Technology Product Catalogue*, Edition 1990
- [19] Brune, J.: *A Flexible Quasi-Optical System for Polarimetric Submillimeter-Wave Reflectometry*, IEEE Transactions on Microwave Theory and Techniques, Vol. 40, No. 12, December 1992, pp. 2321-2324

Terahertz-Bandwidth Transmission Lines on Low-Permittivity Substrates

H. Cheng and J.F. Whitaker

Center for Ultrafast Optical Science, University of Michigan, 2200 Bonisteel Blvd., Room 1006, Ann Arbor, MI 48109-2099

T.M. Weller and L.P.B. Katehi

NASA Center for Space Terahertz Technology, Department of Electrical Engineering and Computer Science, University of Michigan, Ann Arbor, MI 48109-2122

Coplanar waveguides and coplanar striplines fabricated on different substrates—including GaAs, quartz, and a 1.4 μm -thick dielectric membrane [1] were characterized up to terahertz using a novel technique. This technique utilizes an *in situ*, laser-driven photoconductive switch to generate a subpicosecond electrical test pulse with a 3-dB bandwidth of over 500 GHz on the transmission line. The photoconductive switch is formed by first lifting-off a 1- μm -thick low-temperature-grown GaAs epi-layer from its original substrate. This thin film, while supported by the wax, is then bonded to the new substrate using a van der Waals force bond [2]. By monitoring the pulse propagation along the transmission line with a non-contacting electro-optic sampling probe [3], the attenuation coefficients have been determined through the Fourier transform of the time-domain waveforms. For the transmission lines fabricated on the dielectric membrane, there is virtually no dispersion

observed in pulses after 3 mm propagation (Fig.1), and only a small loss can be seen. In contrast, the pulses on the transmission line with the GaAs substrate suffered huge losses and severe phase distortion after the same propagation distance. The attenuation coefficient shown in figure 2 is calculated from the time-domain waveforms. For the transmission lines on membrane, it can support signal bandwidth over 1 THz, while the lines on GaAs substrate can only support signals bandwidth less than 150 GHz. For quartz substrates, which provide enhanced mechanical support for devices, a moderate 300 GHz bandwidth has been observed. The even and odd modes of the CPW has also been resolved from the experimental time domain waveforms (Fig.3). The results shown that the difference between the phase velocity of even and odd mode is only 5% . Therefore, the circuit on membrane would be less sensitive to circuit asymmetries of

comparable size to those typically found on GaAs substrates.

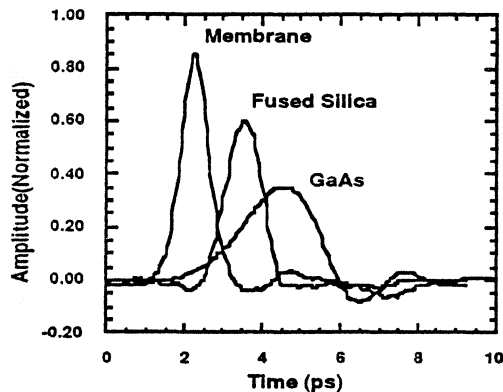


Figure 1. Time domain waveforms of pulses after 3 mm propagation on different substrates. The input pulse has magnitude of 1 and 720 fs FWHM.

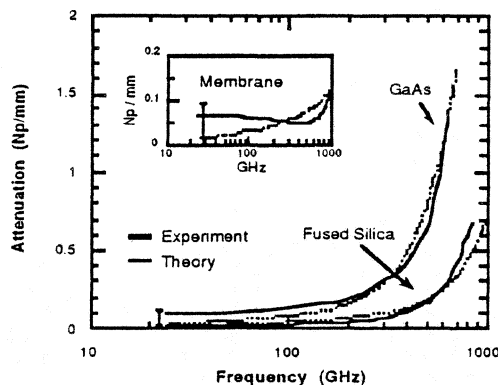


Figure 2. Attenuation coefficients for coplanar stripline on different substrates. The CPS on membrane substrate shows significant lower loss than that of GaAs substrate. At 1 THz, the CPS on membrane only has loss for about 0.1 Np/mm.

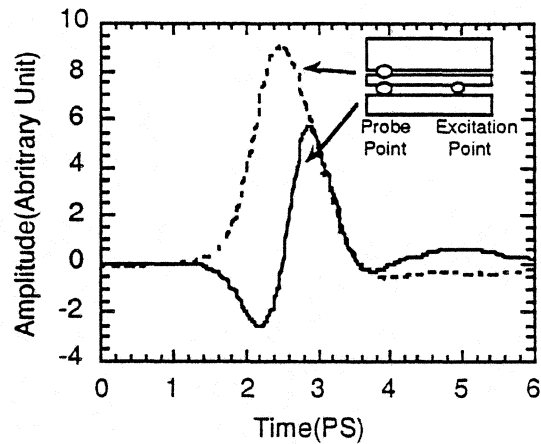


Figure 3. Asymmetrical excitation of Coplanar waveguide to generate both the even and odd modes. The bipolar waveform measured in lower slot shows the opposite direction of electric field of two modes in that slot.

- [1] N.I.Dib, W.P. Harokopus, L.P.B. Katehi, C.C.Ling and G.M. Rebeiz, "Study of a novel planar transmission line," 1991 IEEE MTT-S International Symposium Digest.
- [2] E. Yablonovitch, D.D. Hwang, T.J. Gmitter, L.T. Flores, and J.P. Harbison, "Van der Waals bonding of GaAs epitaxial liftoff films onto arbitrary substrates," *Appl. Phys. Lett.*, vol. 56, pp. 2419-2421, 1989.
- [3] J.A. Valdmanis and G.A. Mourou, "Subpicosecond electrooptic sampling: Principles and applications," *IEEE J. Quantum Electronics.*, vol. 22, pp. 69-78, 1986.

FINITE DIFFERENCE TIME DOMAIN ANALYSIS OF COPLANAR TRANSMISSION LINE CIRCUITS AND A POST- GAP WAVEGUIDE MOUNTING STRUCTURE

John E. Oswald[†], Peter H. Siegel[†], Sami M. Ali[‡]

[†]Jet Propulsion Laboratory
California Institute of Technology
Pasadena, CA 91109

[‡]Ministry of PTT Telecom. College of Jeddah
Jeddah 21461
Saudi Arabia

The finite difference time domain (FDTD) method is used to calculate the S-parameters for two coplanar line filters intended for use at submillimeter wavelengths. The analysis is compared with experimental measurements made on microwave models of the two filter structures. In addition, the FDTD method is used to determine the embedding impedances of a simple post-gap waveguide mounting structure with a single backshort tuning element. The analysis results are presented as a function of backshort setting and are compared both with experimental measurements and with the results of an established theoretical model [1] of such a mounting structure.

1 Introduction

Although the finite difference time domain (FDTD) method was introduced in 1966 by K. S. Yee [2], it was not until the more recent advent of faster, more powerful computing environments that this technique has found a wide range of applicability. One of the first problems Yee considered with the FDTD method was the scattering of fields caused by conducting cylinders in free space. Now the method is being applied to the analysis of many problems including, but not limited to, microstrip filters [*e.g.*, 3] and antennas [*e.g.*, 4, 5], waveguide discontinuities [*e.g.*, 6, 7], and dielectric resonators [*e.g.*, 8].

In this paper, we demonstrate the applicability of the FDTD method to several types of problems of interest in the submillimeter wave region. First, a coplanar strip

filter designed for use at 2.5 THz is considered, and FDTD analysis is compared with scale model measurements as well as with data from Hewlett Packard's commercial program, Microwave Design System (MDS). Next, the FDTD method is used to examine a coplanar waveguide filter designed for the same purpose, and the computations are compared with the MDS calculations. Finally, a simple waveguide post-gap mounting structure with a single backshort is examined. The input impedances measured on a microwave scale model are compared to the computed values for various backshort settings.

2 Coplanar Transmission Line Circuits

Coplanar strip transmission line (twin-lead fabricated on a dielectric half space) and coplanar waveguide are ideal media for feeding a wide range of planar integrated antennas. For applications where more than one frequency will be present at the antenna terminals or where resistive or reactive matching is important it may be necessary to incorporate distributed filter elements with the feed line. Unfortunately, the limited realizable impedance range associated with twin lead makes standard high-low impedance filters difficult to implement. In cases where the size of the feed line may be an issue [*e.g.*, 9] it is helpful to have a filter design with minimal projected area. Using the FDTD analysis in conjunction with scale model measurements we have designed distributed line band-reject filters in both coplanar stripline and coplanar waveguide. Both filters exhibit extremely narrow cross section and can be used at frequencies where the realizable thickness of the deposited metallic conductors contributes significantly to the filter characteristics.

2.1 Coplanar Strip Filter

The basic coplanar strip filter is detailed in Figure 2.1 and consists of quarter-wave high and low impedance sections which are contained within the confines of the 200Ω coplanar strips fabricated on a thick fused quartz substrate. The smallest proposed dimension is the 1 μm gap of the low impedance sections which, when combined with the 3 μm gap of the 200Ω line, gives approximately 2:1 impedance change. The filter is intended to reject the signal band centered at 2.5 THz and to pass the intermediate frequencies from 8-12 GHz in a 2.5 THz mixer. The thickness of the conducting lines ($t = 1.0$ μm) is a significant portion of their width so as to minimize skin effect losses for the IF. The FDTD technique was used to analyze the effects of the metal line thickness, width and air-gap as well as to determine the radiative losses, the characteristic line impedance, the effective dielectric constant, the open-circuit reference plane and the transmission properties of the coplanar strip filter. The

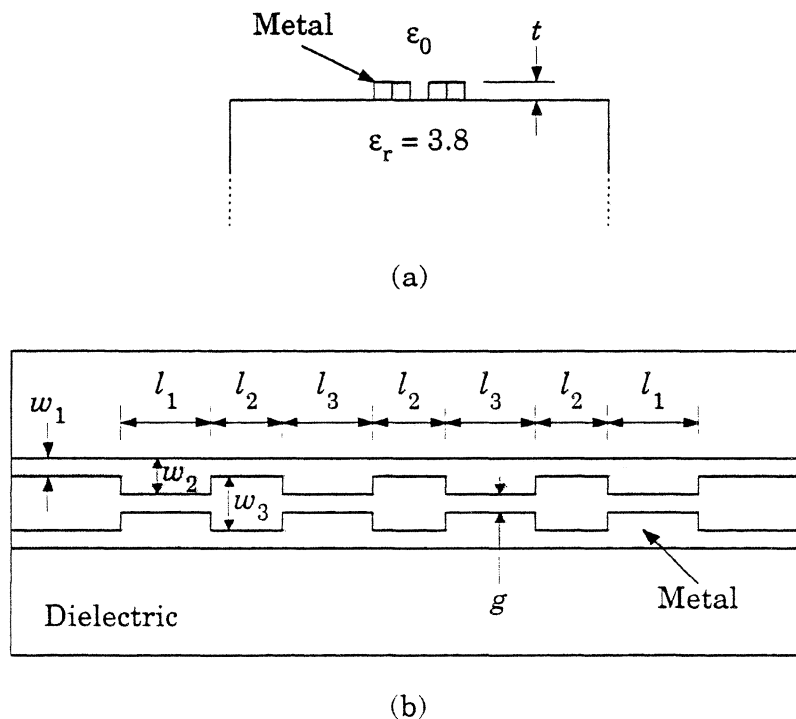


Figure 2.1 Coplanar strip filter (not to scale): (a) Cross section showing filter metal thickness on a dielectric half space; (b) Top view showing metal pattern. Dimensions (in μm) are: $t = 1.0$, $w_1 = 1.0$, $w_2 = 2.0$, $w_3 = 3.0$, $l_1 = 22.113$, $l_2 = 18.711$, $l_3 = 23.814$, $g = 1.0$.

analysis was verified using a 1680 \times scale model of the proposed 2.5 THz filter with a thick brass sheet to form the metallic lines and stycast $\epsilon_r = 3.8$ to model the quartz substrate. In Figure 2.2 the FDTD calculations of the S_{21} magnitude are compared with the available scale model measurements made on an HP8510 vector network analyzer. The large standing waves present in the measurements are primarily due to a mismatch between the HP8510 50 Ω test cable and the $\sim 200\Omega$ coplanar strip line, and no correction for this has been made. Although the agreement with the measurements is not perfect, the computations accurately predict the pass band ripple pattern and the cutoff frequency as well as the radiation loss in this structure.

The filter structure of Figure 2.1 is also analyzed with the FDTD method for the case where the thickness of the metallization is $t = 0.5 \mu\text{m}$. In Figure 2.3 the S_{21} magnitude responses for filters with metal thicknesses of 0.5 and 1.0 μm are compared. Although the effect of the metal is not enormous, the figure clearly shows

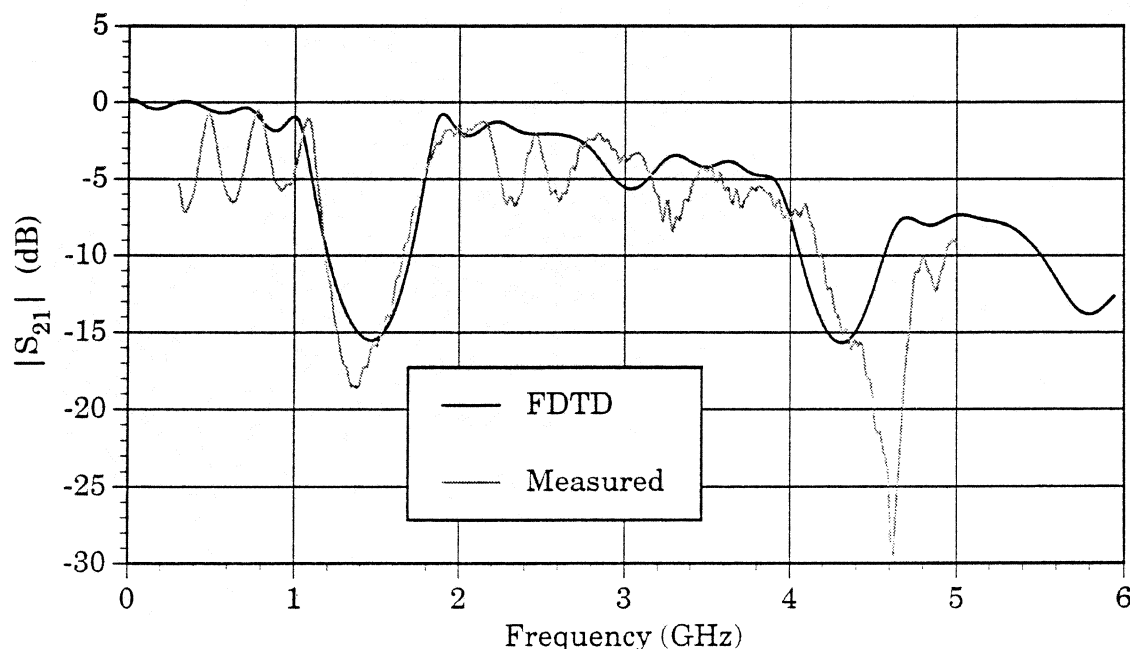


Figure 2.2 S_{21} response of the coplanar strip filter of Figure 2.1. Measurements were performed on a 1680 \times scale model. Scaled signal reject band is centered at 1.49 GHz and IF passband is from 4.7-7.2 MHz.

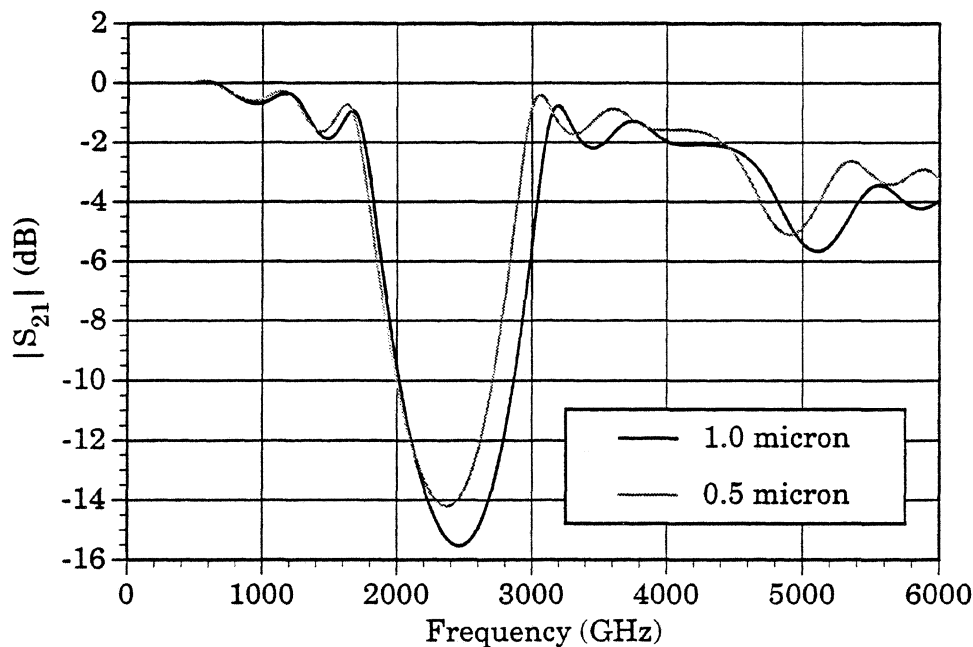


Figure 2.3 FDTD analysis of filter of Figure 2.1 with metal thicknesses of 1.0 and 0.5 μm .

that the reject bandwidth is reduced by about 10% when the metal thickness is reduced by 0.5 μm .

The coplanar strip filter was also simulated using MDS for the case where the metal thickness is 1.0 μm . In Figure 2.4, the FDTD and MDS calculations are compared. With only a small shift in the frequency response and a small difference in the magnitude, they both predict the same ripple pattern in the pass regions as well as the same cutoff frequency. The growing discrepancy in magnitude in the region beyond 4 THz is largely due to radiation loss present in the FDTD calculations but not present in the MDS simulation. This example shows that, at least for this simple filter, both the FDTD method and MDS can be used to provide useful design information about the coplanar strip filter; however, the FDTD method is able to provide more quantitatively accurate results.

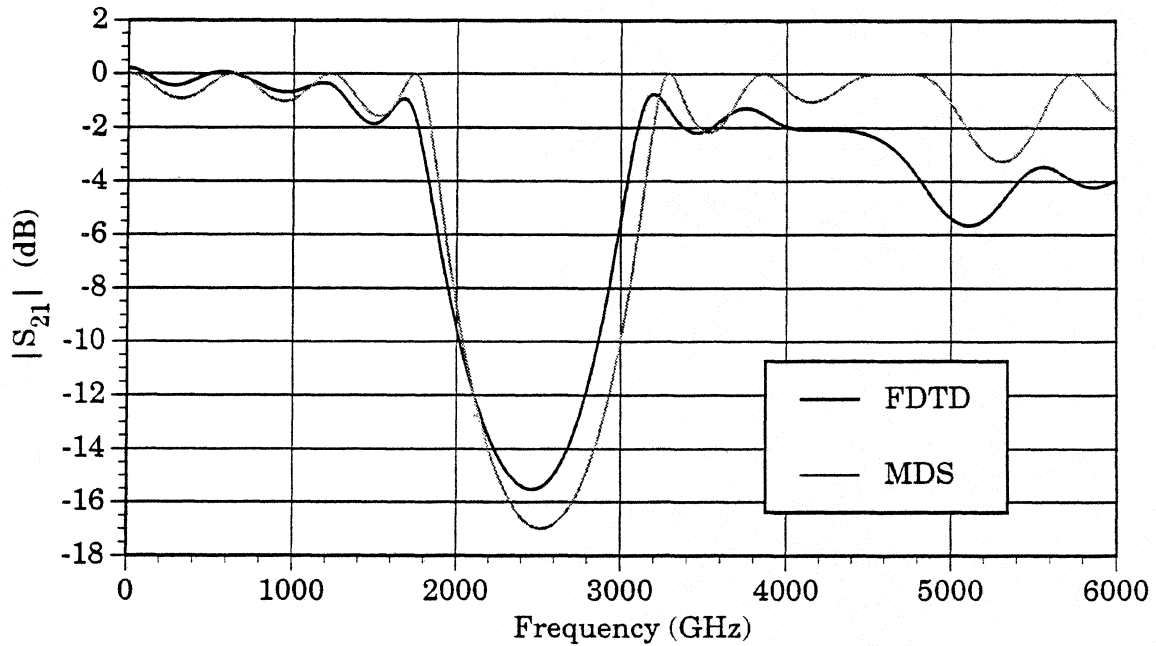
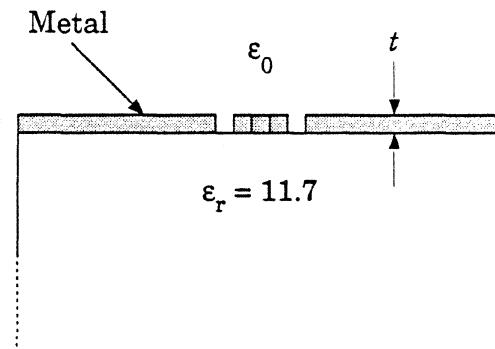


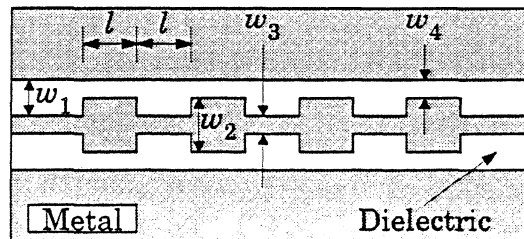
Figure 2.4 Comparison of FDTD and MDS analyses of filter of Figure 2.1

2.2 Coplanar Waveguide Filter

The good agreement obtained with the FDTD analysis and measurements on the coplanar strip filter gave us confidence to apply the FDTD method to the design of the coplanar waveguide filter shown in Figure 2.5. The function of the filter remains the same; that is, it rejects the signal band and passes the intermediate frequencies for the 2.5 THz mixer. The filter is fabricated on a GaAs ($\epsilon_r = 11.7$) substrate rather than on quartz and is meant to be used with a dual slot antenna mixer design [10] similar to that described in [11]. The final filter section lengths and widths are given in Figure 2.5. In Figure 2.6, the FDTD and MDS results are compared with fair agreement for the case of zero metal thickness. The MDS simulation does not include the radiation loss or the effect of the capacitive discontinuity between adjacent filter elements and these factors are the most likely causes of the discrepancies between the two analyses.



(a)



(b)

Figure 2.5 Coplanar waveguide filter (not to scale): (a) Cross section showing coplanar waveguide metal on a dielectric halfspace; (b) Top view showing metal filter pattern. Dimensions (in μm) are: $t = 0.0$, $l = 12.0$, $w_1 = 3.25$, $w_2 = 6.0$, $w_3 = 0.5$, $w_4 = 0.5$.

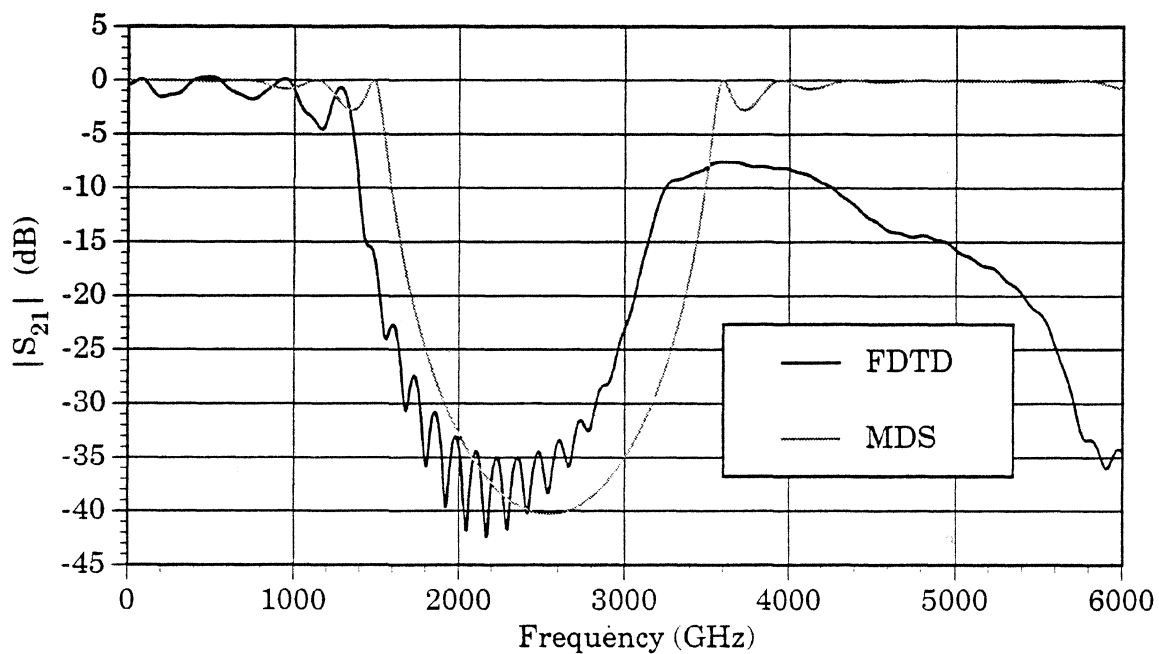


Figure 2.6 Comparison of FDTD and MDS analyses of filter of Figure 2.5.

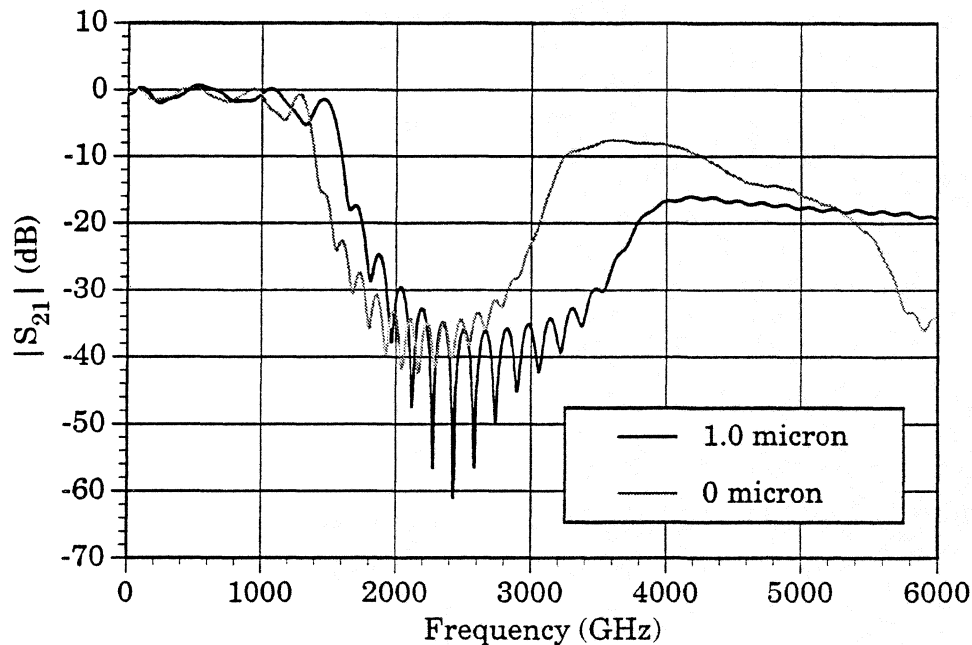


Figure 2.7 FDTD analysis of filter of Figure 2.5 with metal thicknesses of 1.0 and 0.0 μm .

The coplanar waveguide filter is also considered for the case where the metal thickness is 1.0 μm . In Figure 2.7, the FDTD calculations for the same filter with different metal thickness are compared. The effect of increasing the metal thickness is to shift the cutoff up in frequency by 10% as well as to increase the width of the stop band by about 20%.

3 Post-Gap Mounting Structure

Typical millimeter wave mixer (or multiplier) mounting structures combine waveguide and microstrip circuits for coupling energy into and out of a nonlinear device. The design and characterization of these structures is complicated by the often complex geometries and by the multimodal nature of the structure. Often, low frequency scale model measurements are employed to derive the impedances which the mount can present to the nonlinear element (such as a Schottky diode) over the

frequency range of interest. These impedances must be known at the LO and RF frequencies as well as at all relevant higher harmonic sidebands. Analytical methods [1, 12, 13] can be used to calculate the driving point impedance and derive equivalent circuits for simple waveguide mounts; however, the accuracy of the results is limited by the simplifying assumptions underlying the methods.

The FDTD method is an ideal technique for analyzing such structures. A single simulation can provide impedance information over the entire frequency range of interest, and the flexibility of this method allows for easy modeling of a wide range of mount designs. As a first step in applying the FDTD analysis to a complex waveguide mount, the simple mount of Figure 3.1, composed of a set of shorted square posts protruding towards the center of the E-plane wall of a full height rectangular waveguide, is analyzed. One end of the waveguide is terminated with a backshort

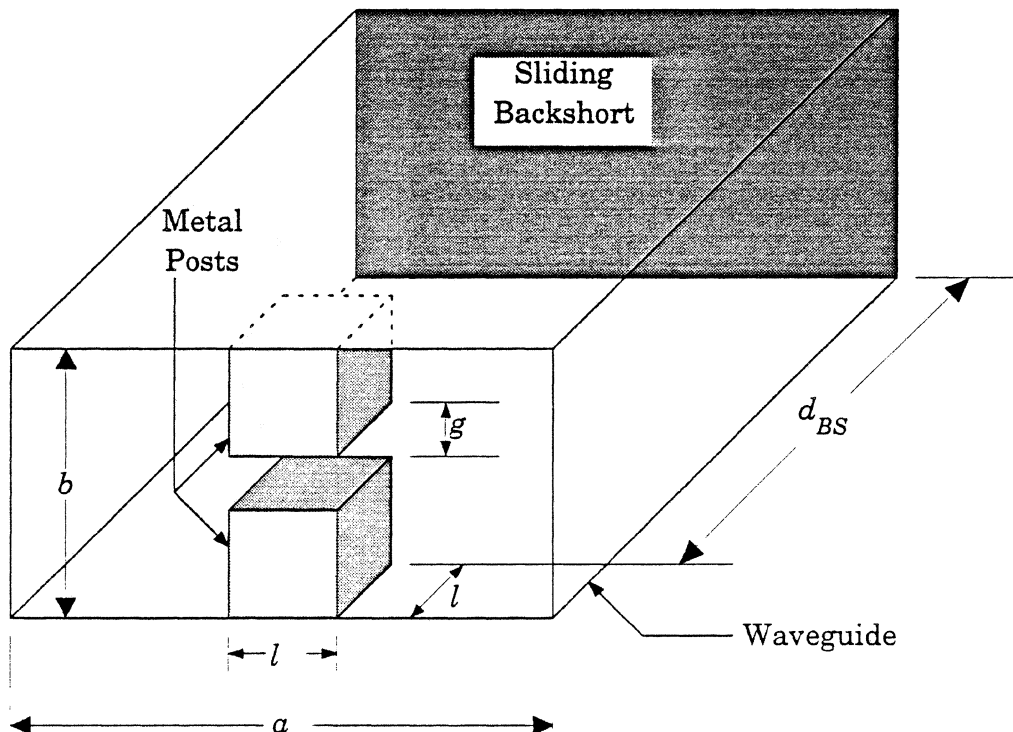


Figure 3.1 Post-gap waveguide mounting structure. Dimensions (in cm) for the 8 GHz scale model are: $a = 2.54$, $b = 1.27$, $l = 0.762$, $g = 0.381$; d_{BS} has settings of 0.4, 0.8, 1.2, 1.6, 2.0 and 2.4 cm.

tuning element while the other end is considered to be matched to free space. The impedance is calculated at the centered gap in the posts where a non-linear device might be located. The analysis is supported by experimental measurements on an 8 GHz mount model. In addition to the measurements and FDTD modeling, the mount is also characterized by the method developed by Eisenhart and Khan [1].

3.1 Measurement Technique

The embedding impedance of the post-gap mount of Figure 3.1 is measured on a an 8 GHz scale model using the buried coaxial probe technique of Eisenhart and Khan [1]. A small UT85 (0.085" outer diameter) coaxial cable extends through a small hole in one of the protruding posts with the outer conductor and dielectric cut so they are flush with the face of the post. The inner conductor of the coax extends across the gap and is electrically connected to the second post. The opposite end of the cable is then connected to an HP8510 network analyzer for measurement. During the calibration of the HP8510, the reference plane is moved to the face of the first post. On one side of the post-gap mount, the waveguide is terminated with a contacting sliding backshort. On the other side the waveguide is terminated with a tapered absorber to simulate a matched condition. Measurements are taken in the frequency range 8-13 GHz for six different backshort settings: $d_{BS} = 0.4, 0.8, 1.2, 1.6, 2.0$ and 2.4 cm where d_{BS} is as shown in Figure 3.1.

3.2 FDTD Analysis

The structure is numerically modeled using space step sizes $\Delta x = \Delta z = 0.9525$ mm and $\Delta y = 0.5080$ mm. The waveguide cross section is $26\Delta x \times 25\Delta y$, while the posts are $8\Delta x \times 8\Delta z$ and centered in the x direction of the waveguide. The six backshort settings of 0.4, 0.8, 1.2, 1.6, 2.0 and 2.4 cm are modeled, respectively, as $4\Delta z, 8\Delta z, 13\Delta z, 17\Delta z, 21\Delta z$ and $26\Delta z$. The gap size of $g = 0.254$ cm is modeled as $5\Delta y$.

The waveguide walls and the backshort are modeled as perfect conductors so the electric fields tangential to these surfaces are forced to be zero. The remaining boundary, representing the open ended waveguide, is located far from the posts so that no reflections from this boundary can reach the points of interest during the computation, thus simulating a matched waveguide condition. This step was necessary to avoid the small amount of reflections caused by first order absorbing boundaries which can adversely affect the frequency domain results.

Fields are excited between the centers of the faces of the two posts by using a matched source condition [14]. Since the post faces are separated by five nodes, a source conductance of $\sigma = 56.0 (\Omega\text{m})^{-1}$ is chosen to simulate a 50Ω source. The fields are excited as Gaussian pulses in time with $T = 1/2f_{\text{max}} = 35.71$ ps chosen to cover up to 14 GHz. The time step is chosen to be $\Delta t = 1.02$ ps and the simulation is performed for 4300 time steps. At each time step the voltage and current between the two posts is calculated and after the simulation the impedance is found by taking the ratio of the Fourier transform of the voltage to the Fourier transform of the current.

The input impedance of the post-gap mount is calculated as a function of frequency in the range 8-13 GHz for each of the six backshort positions. Figures 3.2a and 3.2b compare the computed and measured real and imaginary parts of the input impedance for backshort settings of 1.6 and 2.4 cm, respectively. In Figure 3.3, the measured and computed input impedance as a function of backshort position at $f = 8.5$ GHz are compared.

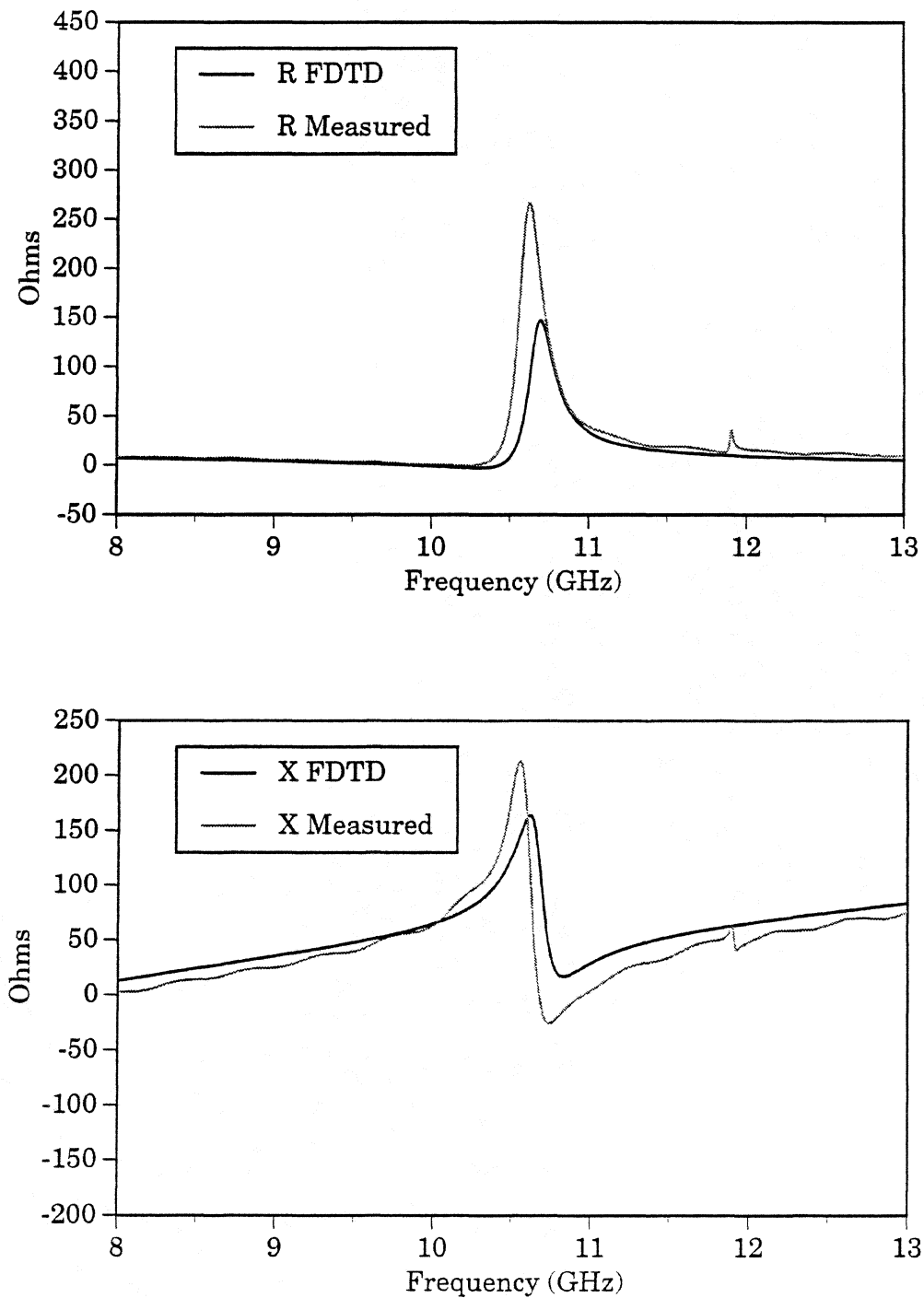


Figure 3.2a FDTD and measured real (R) and imaginary (X) parts of the input impedance for the mount of Figure 3.1 with $d_{BS} = 1.6$ cm.

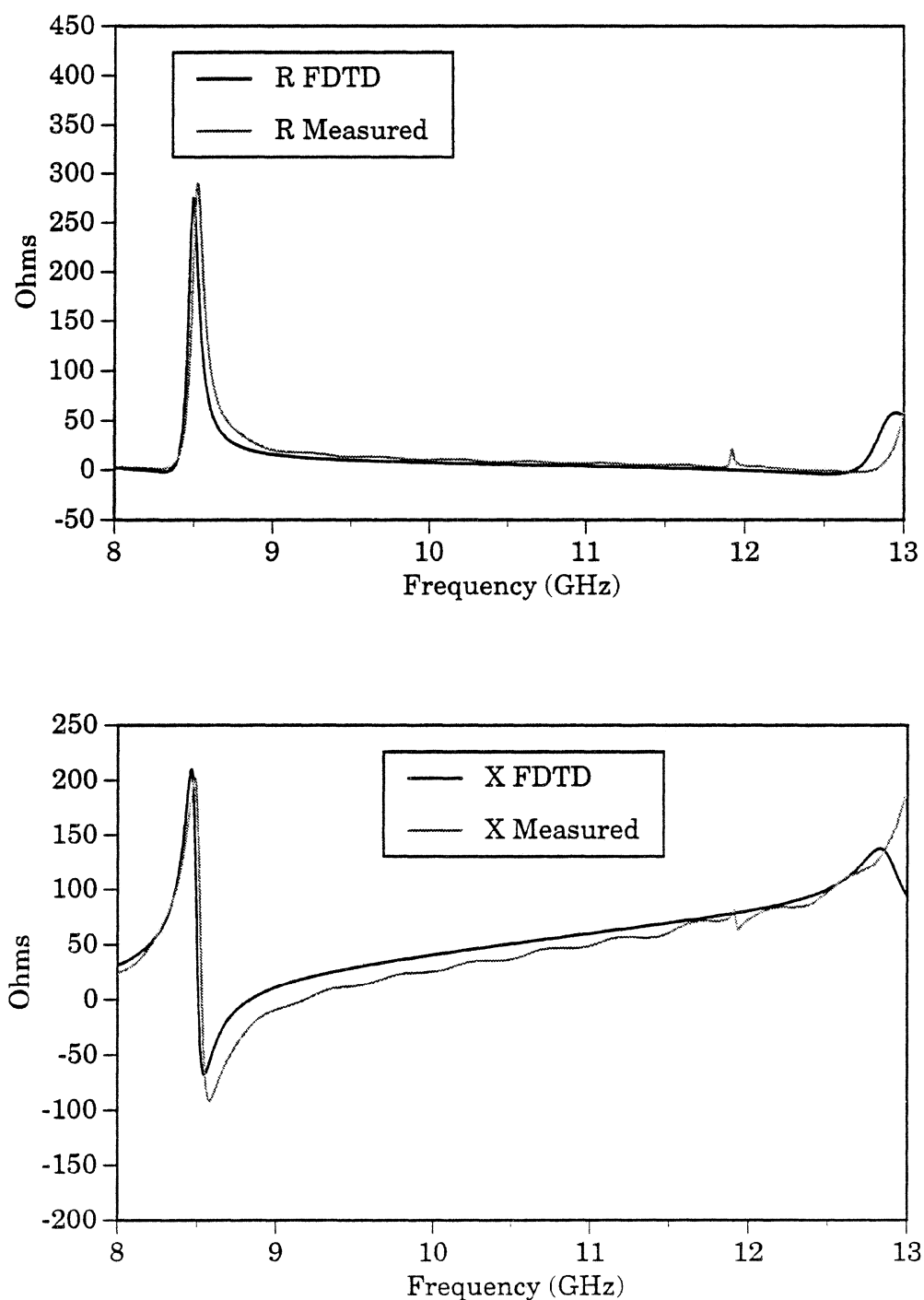


Figure 3.2b FDTD and measured real (R) and imaginary (X) parts of the input impedance for the mount of Figure 3.1 with $d_{BS} = 2.4$ cm.

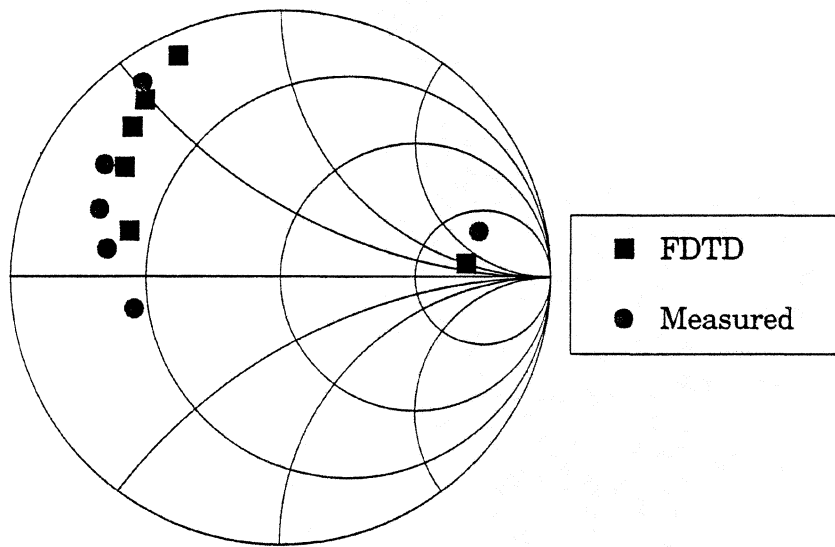


Figure 3.3 FDTD and measured post-gap mount input impedance as a function of backshort setting at $f = 8.5$ GHz.

Figures 3.2 and 3.3 show good agreement between the computed and measured input impedances for this mount. The slight difference between the measured and computational values of the impedance at resonance is attributed to an uncertainty in the exact position of the shorting plane of the sliding backshort in the model. The phase difference in Figure 3.3 is attributed to the effects of fringing capacitance at the end of the probe cable, which is not present in the calculations, and to the fact that the experimental and computational reference planes are slightly different.

3.3 Theoretical Analysis

A theoretical expression for the embedding impedance of a post-gap mounting structure has been derived by Eisenhart and Khan [1]. The analysis is strictly valid only for flat strips. As such, the three-dimensional posts are approximated by equivalent flat strips of zero thickness. Also, this method imposes restrictions on the normalized gap size ($g' = g/b < 0.25$, where g is the gap size and b is the waveguide height) and the normalized strip width ($w' = w/a < 0.25$, where w is the strip width and a is the waveguide width). The derivation of the impedance expression involves the

dyadic Green's function for a waveguide and the expansion of the electric field and current density into sets of orthogonal functions.

In testing their theoretical expression for the mount impedance, Eisenhart and Khan considered posts which are circular with a diameter, d . These posts are subsequently replaced by equivalent flat strips of effective width, $w = 1.8d$. In this same vein the square posts of the mount in Figure 3.1 are substituted with circular posts of the same cross sectional area, or of diameter, $d = 2l/\sqrt{\pi}$. Then, the strip width is approximated as $w = 1.8d = 1.548$ cm.

This Eisenhart and Khan analysis is applied to the post-gap mount for each of the six backshort settings over the frequency range 8-13 GHz. In Figures 3.4a and 3.4b the theoretical and measured mount impedances are compared as a function of frequency for the backshort settings of $d_{BS} = 1.6$ and 2.4 cm, respectively. Figure 3.5 compares the theoretical input impedance with the FDTD calculations and the measurements as a function of backshort position at $f = 8.5$ GHz.

Figures 3.4 and 3.5 indicate a considerable amount of error in the theoretical impedance. However, this is not unexpected as the posts are rather large and, in fact, the normalized strip width used to approximate the posts is larger than what is allowed by the analysis ($w' = w/a = 0.61 > 0.25$). Nevertheless, this method still does a decent job of predicting the resonant frequency of the structure if the uncertainty of the experimental backshort setting is taken into account. However, this example points out that although the FDTD method requires more computer time and memory to run, it does an excellent job of properly calculating the impedances and at the same time offers much greater flexibility in the structures which can be analyzed.

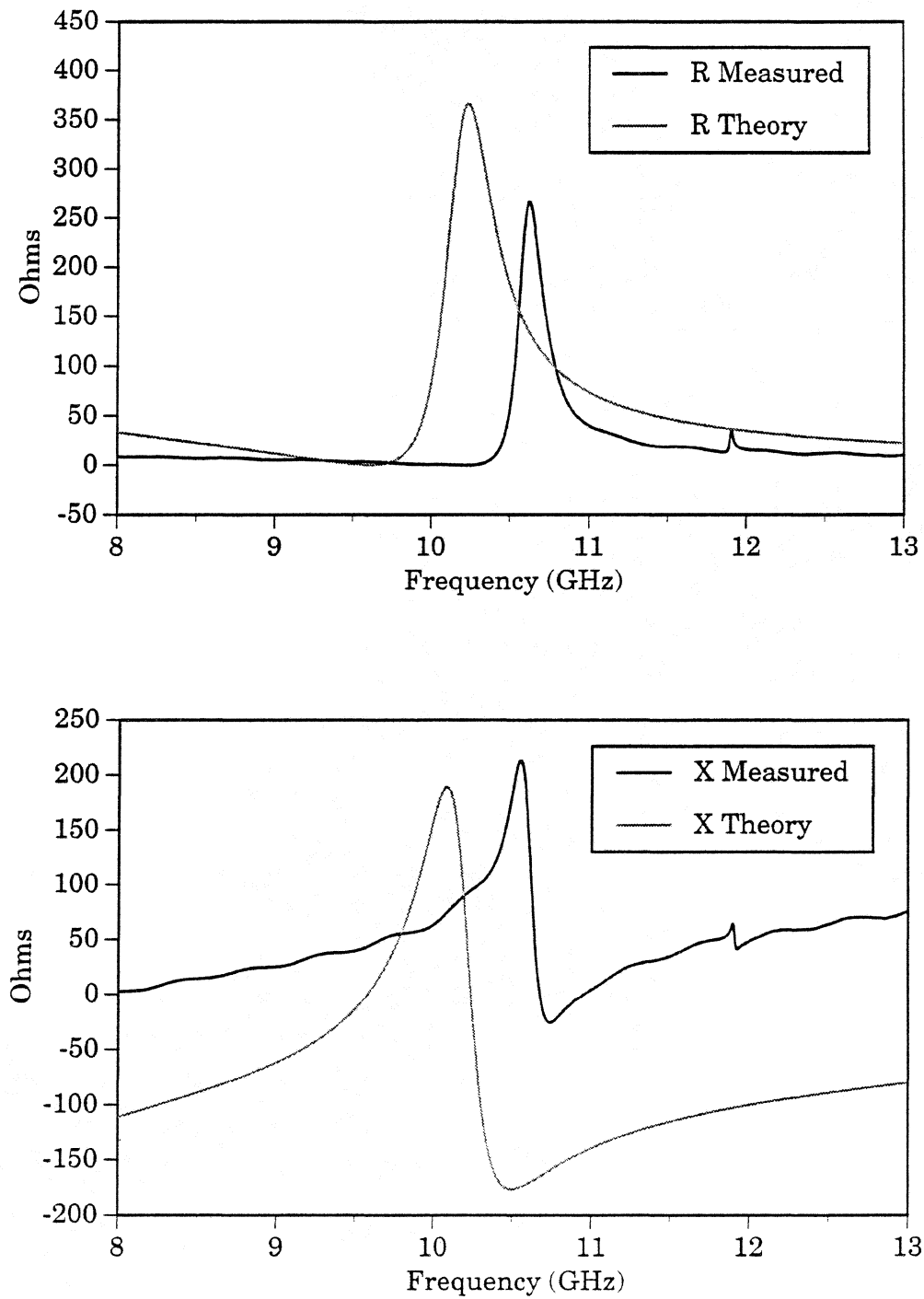


Figure 3.4a Theoretical [1] and measured real (R) and imaginary (X) parts of the input impedance for the mount of Figure 3.1 with $d_{BS} = 1.6$ cm.

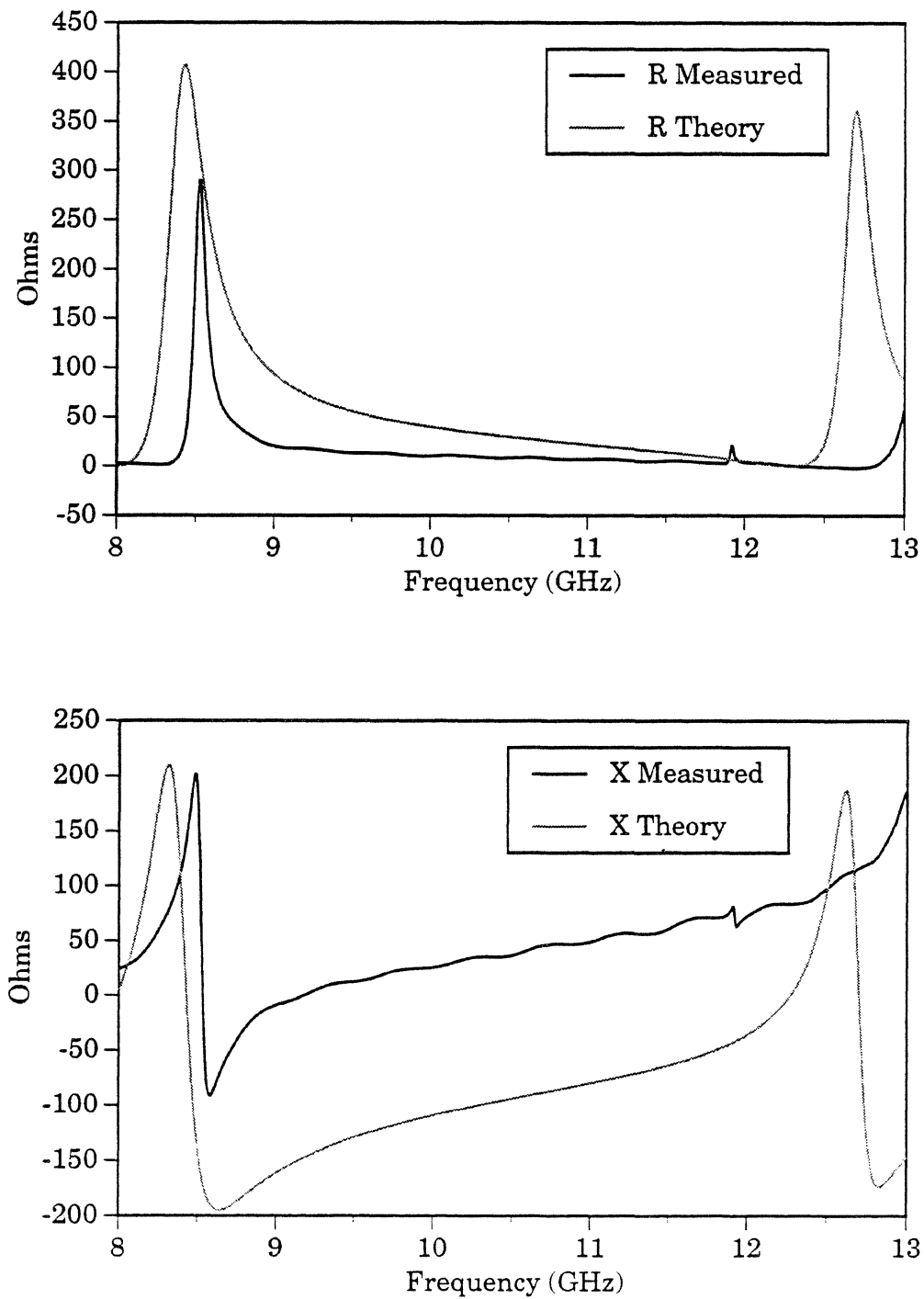


Figure 3.4b Theoretical [1] and measured real (R) and imaginary (X) parts of the input impedance for the mount of Figure 3.1 with $d_{BS} = 2.4$ cm.

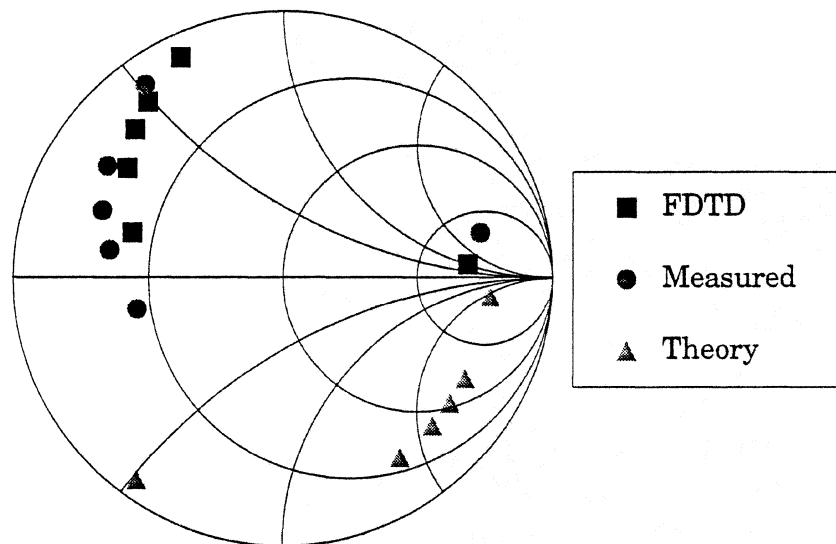


Figure 3.5 FDTD, measured and theoretical [1] post-gap mount input impedance as a function of backshort setting at $f = 8.5$ GHz.

4 Conclusions

We have demonstrated the utility of the FDTD method for problems in the millimeter and submillimeter wave bands. Good agreement between the FDTD calculations and scale model measurements and/or MDS simulations has been achieved in the analysis of the coplanar filter structures and the simple post-gap waveguide mounting structure. We are currently employing the FDTD method to analyze a coplanar waveguide fed twin-slot antenna, and preliminary results are encouraging.

Although the ability to accurately simulate the above mentioned structures is in and of itself a useful and important capability, more often these structures are only a part of a larger system whose characterization is desired. For example, the coplanar waveguide filter studied in this paper must be carefully designed to perform the proper signal separation; however, it must also interface properly with the antenna and active device structure it is meant to feed. The memory and speed available in modern computing environments allow us to begin to consider extending the FDTD

method to the analysis of much larger problems. An example which would be of interest to many researchers working with millimeter-wave mixers and frequency multipliers would combine waveguide tuning and coupling circuits with microstrip filter circuits to analyze the complete mounting structure. In addition, some researchers are also considering active device characterization [15, 16] as part of the FDTD analysis which would allow not only passive mount parameters to be determined, but also the complete nonlinear system to be characterized. Over the next several years, the FDTD method will continue to increase in importance as a unique tool for the characterization of millimeter and submillimeter wave structures.

Bibliography

- [1] R. L. Eisenhart and P. J. Khan, "Theoretical and Experimental Analysis of a Waveguide Mounting Structure," *IEEE Trans. Microwave Theory Tech.*, Vol. MTT-19, No. 8, pp. 706-719, August 1971.
- [2] K. S. Yee, "Numerical Solution of Initial Boundary Value Problems Involving Maxwell's Equations in Isotropic Media," *IEEE Trans. Antennas Prop.*, Vol. AP-14, No. 3, pp. 302-307, May 1966.
- [3] P. H. Siegel, J. E. Oswald, R. J. Dengler, D. M. Sheen and S. M. Ali, "Measured and Computed Performance of a Microstrip Filter Composed of Semi-insulating GaAs on Fused Quartz Substrate," *IEEE Microwave and Guided Wave Letters*, Vol. 1, No. 4, pp. 78-80, April 1991.
- [4] A. Reineix and B. Jecko, "Analysis of Microstrip Patch Antennas Using Finite Difference Time Domain Method," *IEEE Trans. Antennas Prop.*, Vol. 37, No. 11, pp. 1361-1369, November 1989.
- [5] D. M. Sheen, S. M. Ali, M. D. Abouzahra and J. A. Kong, "Application of the Three-Dimensional Finite-Difference Time-Domain Method to the Analysis of Planar Microstrip Circuits," *IEEE Trans. Microwave Theory Tech.*, Vol. 38, No. 7, pp. 849-857, July 1990.
- [6] P. Alinikula and K. S. Kunz, "Analysis of Waveguide Aperture Coupling Using the Finite-Difference Time-Domain Method," *IEEE Microwave and Guided Wave Letters*, Vol. 1, No. 8, pp. 189-191, August 1991.

- [7] N. I. Dib and L. P. B. Katehi, "Analysis of the Transition from Rectangular Waveguide to Shielded Dielectric Image Guide Using the Finite-Difference Time-Domain Method," *IEEE Microwave and Guided Wave Letters*, Vol. 3, No. 9, pp. 327-329, September 1993.
- [8] Z. Bi, Y. Shen, K. Wu and J. Litva, "Fast Finite-Difference Time-Domain Analysis of Resonators Using Digital Filtering and Spectrum Estimation Techniques," *IEEE Trans. Microwave Theory Tech.*, Vol. 40, No. 8, pp. 1611-1619, August 1992.
- [9] P. H. Siegel, "A Submillimeter-wave Heterodyne Array Receiver Using a Dielectric-filled Parabola: Concept and Design," First International Symposium on Space Terahertz Technology, Ann Arbor, Michigan, pp. 218-234, March 1990.
- [10] P. H. Siegel, "An Open-Structure Mixer Using an All-GaAs Integrated Diode/Antenna Wafer for Millimeter and Submillimeter Wavelengths," Jet Propulsion Laboratory New Technology report #8972, 7 pgs., January 1994.
- [11] G. Gauthier, T. P. Budka, W. Y. Ali-Ahmad, D. F. Filipovic and G. M. Rebeiz, "A Low Noise 86-90 GHz Uniplanar Schottky-Receiver," IEEE International Symposium on Microwave Theory and Techniques, Atlanta, GA, pp. 325-328, June 1993.
- [12] R. L. Eisenhart, "Discussion of a 2-Gap Waveguide Mount," *IEEE Trans. Microwave Theory Tech.*, Vol. MTT-24, No. 12, pp. 987-990, December 1976.
- [13] J. S. Joshi and J. A. F. Cornick, "Analysis of Waveguide Post Configurations," *IEEE Trans. Microwave Theory Tech.*, Vol. MTT-25, No. 3, pp. 169-181, March 1977.
- [14] D. M. Sheen, "Numerical Modeling of Microstrip Circuits and Antennas," Ph.D. Dissertation, Department of Electrical Engineering and Computer Science, Massachusetts Institute of Technology, Cambridge, MA, June 1991.
- [15] W. Sui, D. A. Christensen and C. H. Durney, "Extending the Two-Dimensional FDTD Method to Hybrid Electromagnetic Systems with Active and Passive Lumped Elements," *IEEE Trans. Microwave Theory Tech.*, Vol. 40, No. 4, pp. 724-730, April 1992.
- [16] B. Toland, B. Houshmand and T. Itoh, "Modeling of Active Regions with the FDTD Method," *IEEE Microwave and Guided Wave Letters*, Vol. 3, No. 9, pp. 333-335, September 1993.

TIME-DOMAIN CHARACTERIZATION OF DIODE MOUNTING STRUCTURES

E. Tentzeris, N. Dib, L. Katehi
University of Michigan, Ann Arbor

J. Oswald and P. Siegel
JPL

Abstract

The application of the FDTD technique in the calculation of the S-parameters of specific diode mounting and waveguide probe structures is discussed in this paper. Comparative results are given and the FDTD technique is evaluated as an optimized CAD tool.

Introduction

The finite difference time domain method is used in the RF characterization of diode mounting and waveguide probe structures. A variety of excitation functions are considered and their effect on numerical convergence is studied. One of these functions, the Gabor function, offers a wavelet-like behavior. This function is localized both in time and frequency domain and its characteristics can be chosen such that its spectral content is centered around a desired frequency. As a first step, a number of simple geometries are analyzed and the FDTD results are compared to data derived through the integral equation and finite element methods for validation purposes. The same technique has been applied to waveguide-probe structures and the S-parameters as a function of frequency have been evaluated.

Theory

The FDTD method is formulated by discretizing Maxwell's curl equations

$$\mu \frac{\partial \bar{H}}{\partial t} = -\nabla \times \bar{E} \quad (1)$$

$$\epsilon \frac{\partial \bar{E}}{\partial t} = \nabla \times \bar{H} \quad (2)$$

over a finite volume and approximating the derivatives with centered difference approximations [1] .

To obtain discrete approximations to the curl Maxwell's equations, the centered difference approximation is used on both the time and space first-order partial derivatives. For convenience, the six field locations are considered to be interleaved in space as shown in Fig.1, which is a drawing of the FDTD unit cell. The entire computational domain is obtained by stacking these rectangular cubes into a larger rectangular volume. The x, y and z dimensions of the unit cell are Δx , Δy and Δz , respectively. The advantages of this field arrangement are that centered differences are utilized in the calculation of each field component and that continuity of tangential field components is automatically satisfied. Because there are only six unique field components within the unit cell, the six field components touching the shaded upper eighth of the unit cell in Fig.1 are considered to be a unit node with subscript indices i, j and k corresponding to the node numbers in the \hat{x} , \hat{y} and \hat{z} directions. This notation implicitly assumes the 1/2 space indices and thus simplifies the notation, rendering the formulas directly implementable on the computer. The time steps are indicated with the superscript n.

Due to the use of centered differences in these approximations, the error is second order in both the space and time steps; i.e., if Δx , Δy , Δz and Δt are proportional to Δl , then the global error is $O(\Delta l^2)$. The maximum time step that may be used is limited by the stability criterion of the finite difference equations,

$$\Delta t \leq \frac{1}{v_{max}} \cdot \left(\frac{1}{\Delta x^2} + \frac{1}{\Delta y^2} + \frac{1}{\Delta z^2} \right)^{-1/2} \quad (3)$$

where v_{max} is the maximum velocity of light in the computational volume. Typically, v_{max} will be the velocity of light in free space unless the entire volume is filled with dielectric. These equations will allow the approximate solution of $\vec{E}(r,t)$ and $\vec{H}(r,t)$ in the volume of the computational domain ; however, special consideration is required for the conductors, the mesh boundaries and the excitation.

The electric conductors are assumed to be perfectly conducting with zero thickness and are treated by setting the electric field components that lie on the conductors to zero.

Due to the finite capabilities of the computers used to implement the finite-difference equations, the mesh must be limited in the x, y and z directions. The difference equations cannot be used to evaluate the field components tangential to the outer boundaries since they would require the values of field components outside of the mesh. The tangential electric field components must be specified in such a way that outgoing waves are not reflected using absorbing boundary conditions. For TEM structures (e.g. coaxial) the pulses will be normally incident to the mesh walls. This leads to a simple approximate continuous absorbing boundary condition, which is that the tangential fields on the outer boundaries will obey the one-dimensional wave equation in the direction normal to the mesh wall. For the \hat{y} normal wall the one-dimensional wave equation may be written in the following form:

$$\left(\frac{\partial}{\partial y} - \frac{1}{v} \cdot \frac{\partial}{\partial t} \right) E_{tan} = 0 \quad (4)$$

This equation is Mur's first approximate absorbing boundary condition [2] and it may be easily discretized using only field components on or just inside the mesh wall yielding an explicit finite difference equation

$$E_0^{n+1} = E_1^n + \frac{v\Delta t - \Delta y}{v\Delta t + \Delta y} \cdot (E_1^{n+1} - E_0^n) \quad (5)$$

where E_0 represents the tangential electric field components on the mesh wall and E_1 represents the tangential electric field components one node inside of the mesh wall. Similar expressions are immediately obtained for the other absorbing boundaries by using the corresponding normal directions for each wall. The normal incidence assumption is not valid for the fringing fields which are propagating tangential to the walls. For this reason for non-TEM structures, the superabsorbance boundary condition is used in conjunction with the Mur's first ABC. The superabsorbance is a 2nd order ABC which takes into consideration both electric and magnetic fields [3].

The finite difference equations are used with the above boundary conditions to simulate the propagation of a preselected excitation function on the simulated structure. The essential aspects of the time-domain algorithm are as follows:

Three different functions have been used as excitations: First choice was the Gaussian pulse

$$f_0(t) = e^{-((t-t_0)/(pw))^2} \quad (6)$$

This is the most widely used excitation function, since it has the same shape in both time and frequency domains. Nevertheless, it contains a very strong D.C. component, which can be a possible cause for oscillations and slow convergence in structures that do not propagate the low frequencies (e.g. waveguides).

One excitation function that does not contain D.C. component is the Gaussian pulse derivative

$$f_1(t) = \frac{t - t_0}{pw^2} \cdot e^{-((t-t_0)/(pw))^2} \quad (7)$$

This function presents a better concentration around a specific central frequency than the gaussian pulse, but is still characterized by a significant low-frequency content.

Our final choice was the Gabor function

$$f_2(t) = e^{-((t-t_0)/(pw))^2} \sin(wt) \quad (8)$$

where

$$\begin{aligned} pw &= 2 \cdot \frac{\sqrt{6}}{\pi(f_{max} - f_{min})} \\ t_0 &= 2pw \\ w &= \pi(f_{min} + f_{max}) \end{aligned}$$

It can be easily observed that by modifying appropriately the parameters pw and w , we can restrict the frequency spectrum of the above function in a specific region $[f_{min}, f_{max}]$ (wavelet-like behavior). As a result, we can avoid all problems associated with D.C. or low frequency components without losing the time-bounded behaviour of the excitation function.

The above points can be easily observed from the time and frequency domain plots for all three excitation choices, which are presented in Fig. 1a (Gaussian pulse), 1b (Gaussian pulse derivative) and 1c (Gabor function).

Numerical Results

Numerical results have been computed for three configurations, an iris geometry and two waveguide probes. The first two configurations were used for the validation of the FDTD technique.

a. Rectangular iris geometry

The actual dimensions of this geometry are shown in Fig. 2a. There is a p.e.c. at the one end of the waveguide and the Gaussian pulse excitation impinges on the other end. We have calculated the S_{11} parameter using the FDTD technique at a position close to the iris. Input impedance for this configuration may be calculated from the $S_{11}(\omega)$ by transforming the reference plane for the S_{11} calculation to the reference plane of the input impedance calculation, through the formula

$$Z_{in} = Z_o \frac{1 + S_{11}e^{j2kL}}{1 - S_{11}e^{j2kL}} \quad (9)$$

where k is the wavenumber in the waveguide, L is the distance between the two reference planes and Z_o is the dominant mode wave impedance of the waveguide. Results for the input admittance and S_{11} at a plane parallel to the pec and at a distance $2a$ from it are shown in Fig. 2a. These results are compared with results obtained using the lumped-element technique and the agreement is very good (Fig. 2b).

b. Waveguide Probe

The waveguide-probe configuration of Fig. 3a was analyzed using the FDTD technique. The two probes are embedded on a dielectric slab with $\epsilon_r = 3.8$. The one end of the waveguide is short-circuited and the Gaussian pulse excitation is applied at the other end. We calculated the input impedance Z_{in} between the two probes, by using the relationship

$$Z_{in} = \frac{V}{I} \quad (10)$$

$$V = \oint \vec{E} \cdot \vec{dl} \quad (11)$$

$$I = \int \vec{H} \cdot \vec{dl} \quad (12)$$

The voltage V was calculated by integrating along a vertical path connecting the two probes and the current I by integrating along a horizontal closed loop at the plane located in the

middle of the distance between the two probes. Though V was independent on the choice of the paths, I was slightly sensitive to the closed-loop size. This sensitivity lessened as the dielectric was thinner, since it was due to the displacement current inside the dielectric. The results for the real part of the input impedance are compared with those obtained from Moment method technique and the agreement is again very good.(Fig. 3b)

c. Coaxial-fed probe

The geometry of Fig. 4a is similar to the geometry of the probe discussed above. Again, we had two probes embedded on a dielectric slab inside a waveguide. One end of the waveguide was short-circuited and we calculated the input impedance between the two probes. Nevertheless, there is a major difference between (B) and (C). Now the probes are coaxial (center) fed, however in (B) the excitation was applied at the input of the waveguide. That means that in (C) we have a near-field excitation, though in (B) we had a far-field.

As a first step of our simulation, the excitation pulse was impressed in the region between the two probes and we tried to calculate the input impedance by use of the formulas (10) - (12). This effort was unsuccessful, since the value of the current I became very sensitive on the size of the horizontal closed loop. This was due mainly to two factors, the displacement current and the fact that the edge conditions could not be perfectly satisfied.

To avoid the above problems the whole structure with the coaxial feed was analyzed. The feed was simulated with a rectangular 50Ω coaxial with $\epsilon_r=2.2$. The excitation pulse was applied at the input of the feed-line. In this way the problems coming from the near-field excitation vanished and the input impedance was calculated by use of the formula

$$Z_{in} = Z_o \frac{1 + S_{11}}{1 - S_{11}} \quad (13)$$

The results for the S_{11} are presented in Fig.4b. There is total reflection below the waveguide dominant mode cutoff frequency (2.89GHz). Above this frequency, propagation inside the waveguide magnifies and S_{11} starts decreasing.

We have to emphasize on the fact that around resonance, the calculation of Z_{in} from S_{11} by use of the above formula is characterized by very high numerical errors. For example, 1% error in S_{11} (0.993 instead of 0.983) due to computer round-off errors causes 145% error in Z_{in} (14236 instead of 5832 Ohm). As a result, the values of Z_{in} around resonance have no significant practical meaning.

Autoregressive predictors have been used to extrapolate accurately the calculated field values. As a result, the execution time has been reduced drastically by one order.

Conclusion

The finite-difference time-domain method has been used to perform time-domain simulations of pulse propagation in several waveguide probe and diode mounting structures. The frequency-dependent scattering parameters and the input impedance have been calculated by a Fourier transform of the time-domain results. These results have been verified successfully by comparison with other numerical techniques and with measured data. The versatility of

the FDTD method allows easy calculation for complicated structures. As the computational power of computers is rapidly increasing, this technique is very promising for the CAD of many types of waveguide probe and diode mounting structures.

Acknowledgement

This work was supported by the NASA Center for Space and Terahertz technology, University of Michigan, Ann Arbor.

References

- [1] K. S. Yee, "Numerical solution of initial boundary value problems involving Maxwell's equations in isotropic media," *IEEE Trans. Antennas Propagation*, pp. 302-307, May 1966.
- [2] G. Mur, "Absorbing boundary conditions for the finite-difference approximation of the time-domain electromagnetic-field equations," *IEEE Trans. Electromagnetic Compatibility*, pp. 377-382, Nov. 1981.
- [3] K. Mei and J. Fang, "Superabsorption-A method to improve absorbing boundary conditions," *IEEE Trans. Antennas Propagation*, pp. 1001-1010, Sep. 1992.

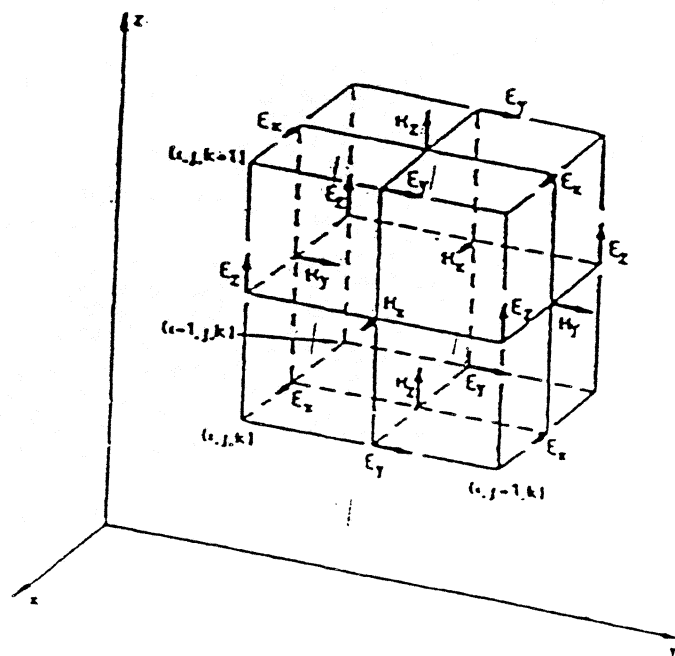


Fig. 1

$p_w=0.1\text{nsec}$, $t_o=0.3\text{nsec}$

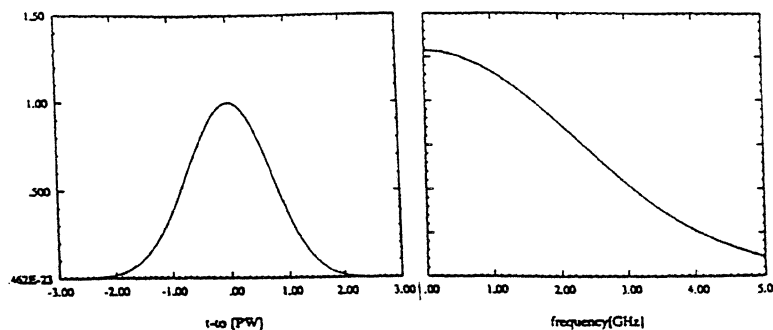


Fig. 1a

$p_w=0.1\text{nsec}$, $t_o=0.3\text{nsec}$

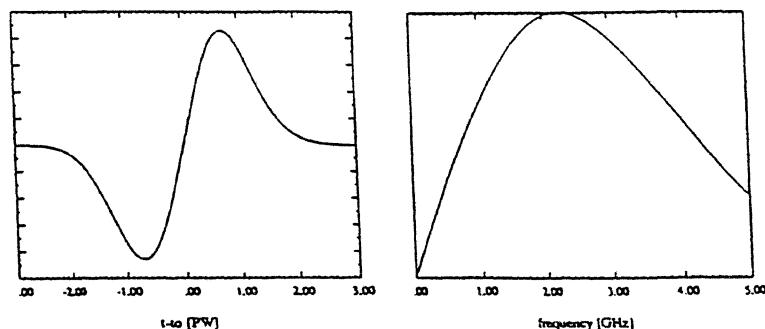


Fig. 1b

$p_w=0.52\text{nsec}$, $t_o=1.04\text{nsec}$

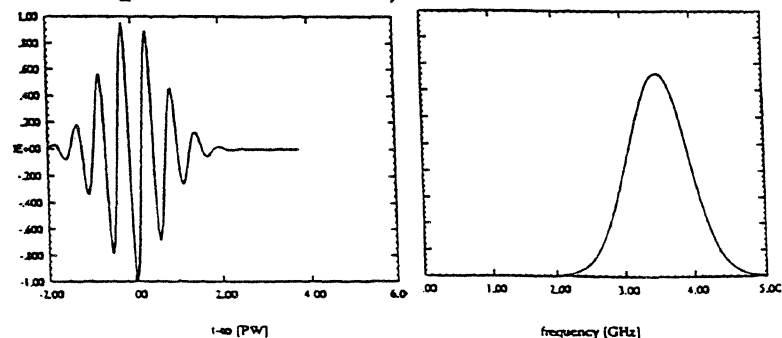


Fig. 1c

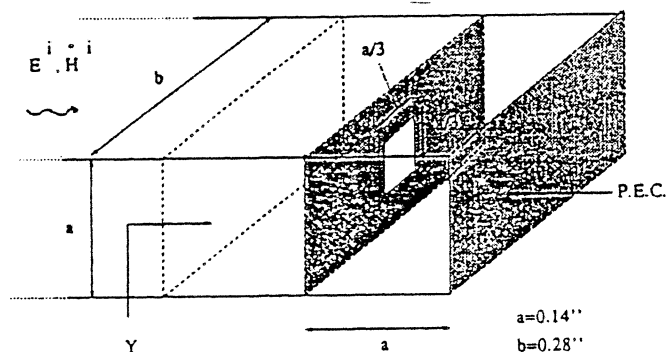


Fig. 2a

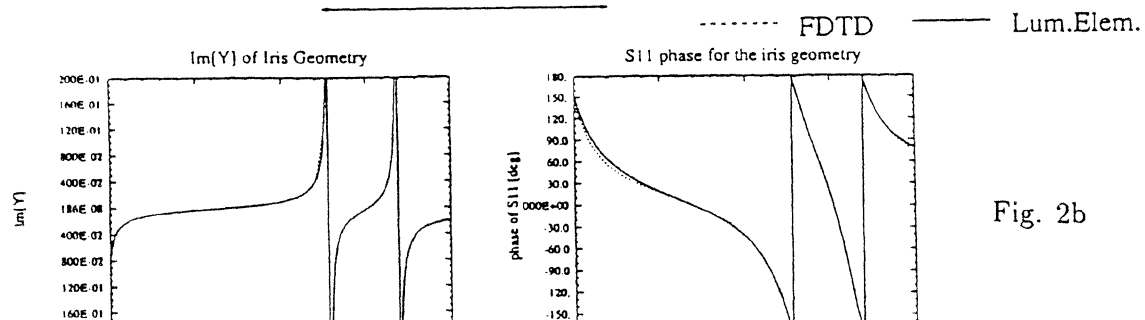


Fig. 2b

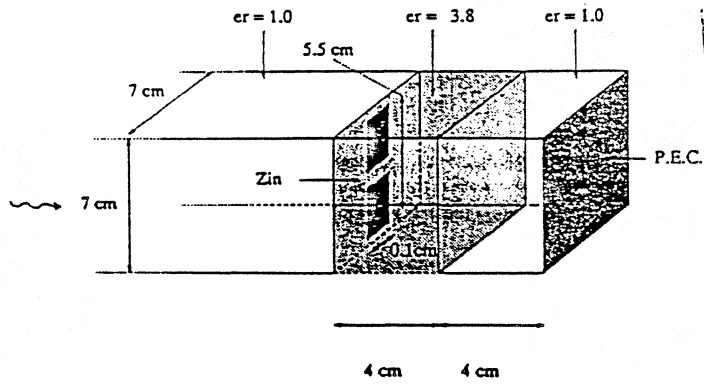


Fig. 3a

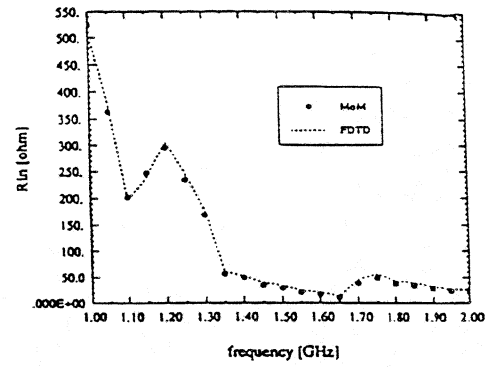


Fig. 3b

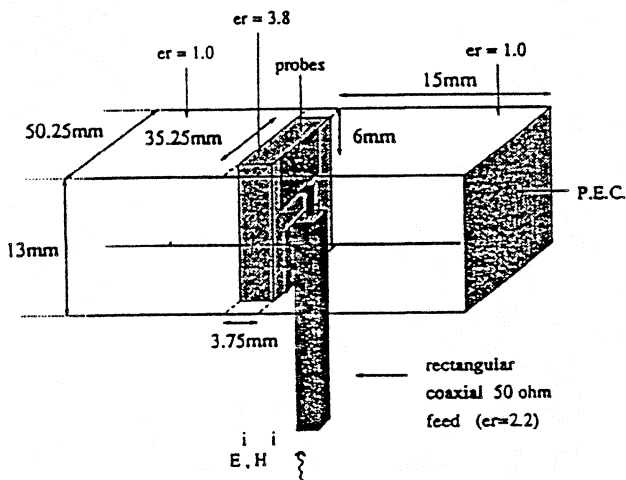


Fig. 4a

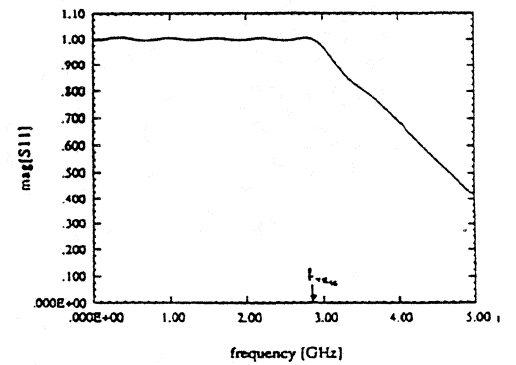


Fig. 4b

Large Signal Impedance of Resonant Tunneling Diodes

J. F. Lampin*, O. Vanbésien*, O. Tanguy* and D. Lippens*

Abstract: The large signal impedance of resonant tunneling diodes has been evaluated using reflection coefficient measurements and power measurements for self-oscillating devices. To this aim, small area devices were fabricated with necessary coplanar lines for microwave wafer probing in a low parasitic planar technology. For large applied or self-sustained rf voltages, marked differences between the slope of the $I(V)$ curve at the bias point (small signal conditions) and the large signal conductance have been found. These measurements have been interpreted satisfactorily on the basis of self-consistent treatment of the power delivered (generated) to (by) the diodes and of Fourier transforms of the current components.

Introduction: In recent years, there has been an intensive effort in the development of high frequency nonlinear applications on the basis of double barrier Resonant Tunneling Diodes (RTD's) used as oscillators, harmonics multipliers, detectors and mixers. Beyond the benefit that the resonant tunnelling effect can be very fast, interest in these devices is motivated by pronounced room temperature Negative Differential Conductance effect (NDC). While the small signal impedance is now well understood with frequency measurements at microwave and millimeter wavelengths, relatively little attention has been paid to impedance under large signal conditions. Recently O. Boric-Lubecke et al.^[1] have analyzed large signal negative conductance for predicting the output power and conversion efficiency of a quantum well oscillator. Other results were published by S.M. Nilsen and L. Lundgren^[2] for describing the maximum available output versus oscillation frequency. Since our first measurements we carried out in negative differential resistance by cooling a GaAs/AlGaAs sample down to 77K^[3], we have reported extensive measurements at room temperature^[4] and up to 40 GHz recently^[5]. In this work we take advantage of this know-how to study in what extent the large signal impedance can be measured directly and related to the physical device.

Measurement conditions: Figure 1 shows the essential features to understand the conditions for successfully measuring the large signal impedance. In brief, we can distinguish three parts in the $I-V$ curve which correspond to various conduction regimes. The first one, close to equilibrium, is achieved when the tunneling current components between emitter and collector and reciprocally are unbalanced. It can be shown that the current grows exponentially against voltage as demonstrated by measuring the first and the second derivatives of current with respect to V . The second part corresponds to the NDC regime when the resonant enhancement of the overall transmission is lost. The subsequent drop in the current values depends on device structure and notably on spacer layers which acts as "lever arms" and thus amplify the voltage values. Nevertheless as a general rule, an abrupt transition can be noticed for bias close to V_p whereas, in the vicinity of the valley voltage V_v the change in current is more gradual. In passing, let us note that, in this last range of the characteristics, accurate measurements of the small signal impedance can be made provided the stability criteria are satisfied. In the third part, the current exhibits again an exponential dependence versus voltage. This was recently demonstrated and used to quickly determine the series resistance^[6].

The voltages involved in the various processes are typically of a few hundreds millivolts. This means that the large signal admittance (impedance) can be measured simply if we succeed in optimizing the power transfers between the device under test and the analysis tool. For a given heterostructure and hence current density and voltage, a common method is

to vary the device area in the range of a few square microns so that the conductance level fits the source. In the following, we will see that jointly the imaginary part vanishes.

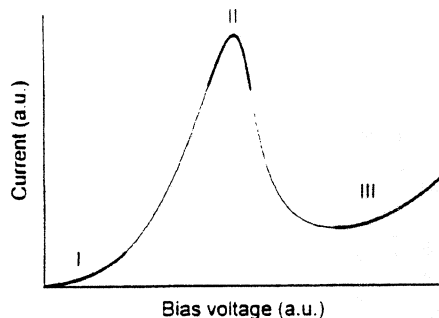


Fig. 1 Schematic of RTD's I-V characteristics

GaAs	$3 \cdot 10^{18} \text{ cm}^{-3}$	500 nm
GaAs	$1 \cdot 10^{17} \text{ cm}^{-3}$	10 nm
GaAs	Undoped (UD)	5 nm
In _{0.1} Ga _{0.9} As	UD	5 nm
GaAs	UD	0.5 nm
AlAs	UD	1.7 nm
GaAs	UD	0.5 nm
In _{0.1} Ga _{0.9} As	UD	4 nm
GaAs	UD	0.5 nm
AlAs	UD	1.7 nm
GaAs	UD	0.5 nm
In _{0.1} Ga _{0.9} As	UD	5 nm
GaAs	UD	5 nm
GaAs	$1 \cdot 10^{17} \text{ cm}^{-3}$	10 nm
GaAs	$3 \cdot 10^{18} \text{ cm}^{-3}$	500 nm
Si Substrate		

Fig. 2 Growth sequence

Fabrication: Resonant tunneling diodes were fabricated from pseudomorphic epitaxies in the InGaAs/AlAs/GaAs material system. The fact to introduce InGaAs strained layers permits one to decrease the peak voltage while maintaining spacer layers which guarantee epitaxial quality. Fig. 2 describes the various layers of growth sequence starting from a semi-insulating substrate. Barriers with thickness of 1.4 nm were here chosen in order to achieve relatively high current density, a key feature for a high frequency operation. In return, we will see that the diodes cannot be stabilized over the overall NDC bias range. These considerations are the primary motivations for developing a two-step mesa technology using air-bridge techniques which permit to integrate small area devices and to maintain the parasitic element at an extremely low level.

Figure 3 gives a scanning electron micrograph of an air-bridged representative device. For the present case the lateral dimensions were about $2 \mu\text{m}$ by $10 \mu\text{m}$. Detailed of technological processes can be found elsewhere[7]. In brief, top contacts were formed by defining AuGeNi ohmic contacts by lift off techniques and by chemically etching down to the n^+ buffer layer to implement the side contacts. A secondary mesa isolation was then formed leaving the semi-insulating substrate exposed where coplanar transmission lines were deposited. Top contacts and central lines were interconnected by means of air-bridges formed by evaporation or electroplating. Figure 4 gives the I-V curve of a representative device in forward and reverse bias directions measured at room temperature with dc probes and a curve tracer. The devices exhibit a high degree of symmetry in the I-V which is a good indicator of epitaxial quality. As expected, instabilities in NDC bias distort the characteristics which otherwise verify the general considerations aforementioned. Peak current densities are typically 50 kA cm^{-2} . Peak-to-valley current ratios vary between 5:1 to 7:1. The peak voltage is 600 mV for a voltage excursion for NDC effects of about 400 mV.



Fig. 3 SEM of an air-bridged device

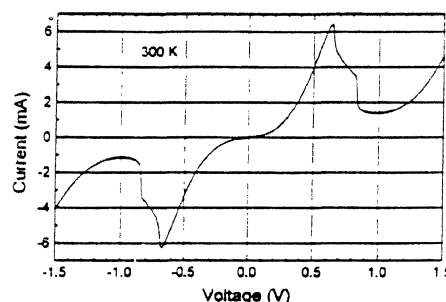


Fig. 4 Typical I(V) at 300K

Small signal impedance: At this stage, a first idea of the voltage dependence conductance can be achieved by dc characterizing the devices by means of low inductance microwave probes and by taking the derivative of the I-V characteristics. A typical plot of the small signal conductance corresponding to the slope of the I-V curve at each bias point is given in Figure 5 over the whole range of interest. Close to equilibrium, conductance varies quasi-exponentially. In the NDC region, spikes in the conductance are apparent due to the well-known shoulder-like I-V variations resulting from self-biasing effects. Close to V_v and hence at high impedance level, devices are unconditionally stable. In that case, impedance measurements can be conducted and the device reflection coefficient exceeds unity. This voltage range over which the characterization in NDC makes sense is however very narrow. This implies that, under large signal conditions, the rf swing superimposed on the bias voltage exceeds very rapidly this voltage range for stability. One way to overcome this drawback is to further decrease the device area. This requires to use more advanced technological resources notably direct writing of anode (cathode) patterns by electron beam lithography at submicron scale.

Turning now to the voltage dependence of G close to $V=0V$ we obtained the results depicted in Figure 6. Pronounced variations can be evidenced over a voltage range of a few tens of millivolts. It is worth mentioning the role played by the series resistance due to contact and epitaxial layers. Indeed, for high current drivability samples the rise in current versus voltage can be affected by the voltage drop across the access resistance. As a consequence, the intrinsic nonlinearity of the tunneling process can be seriously attenuated and even completely vanishes in case of poor contact resistivity.

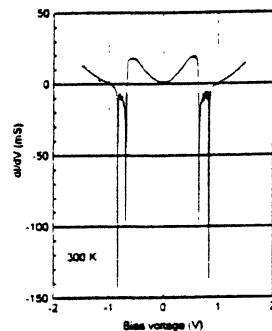


Fig. 5 Conductance versus voltage
(Area=20 μm^2)

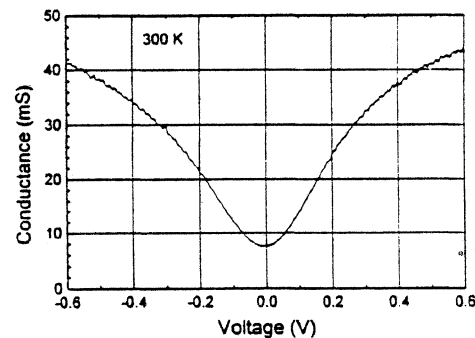


Fig. 6 $G(V)$ in PDC region
(Area=100 μm^2)

The frequency dependence of the small signal impedance, used for comparison in the following, is exemplified in Figure 7. Here, measurements were made by means of rf probes up from 0.5 to 40 GHz, when the device is biased in NDC region. The figure gives a Smith chart plot of S_{11} scattering parameter at diode terminals. The magnitude of outer circle is 2.5. At 40 GHz, impedance Z is $-30-j52 \Omega$. No oscillating behavior was detected in this case. At higher frequencies the negative resistance rolls off and goes positive by intersecting the inner circle of unitary magnitude. Such a characterization over a broad frequency band can also be used to accurately derive an equivalent circuit for the dipole which is of importance for evaluating the ratio between available and delivered powers and subsequently the rf voltage swing across the diode. To this aim we used the lumped-element circuit, reported in figure 8, very similar to that of the Esaki tunnel diode. It consists of a single capacitor C_d with a parallel negative resistance R_d . These intrinsic elements are completed by the parasitic capacitance C_p and inductance L_p due to interconnects and R_s the overall series resistance. "A priori", one should expect also a variation of the capacitance against voltage. Indeed, the capacitance of the

diode measured at lower frequency was found almost constant because the diode is rapidly under punch-through conditions. Here again attention has to be paid to the series resistance which can lead to an apparent variation of C_d versus V when the relation $R_d/R_s \gg 1$ is not satisfied. In practice, the determination of the lumped elements can be made very accurately by measuring samples with different areas, shifting by this way the resonance frequencies introduced by L_p and by varying the bias conditions. The parasitic capacitance contribution was determined with open circuited devices. Finally, we found for the S_{11} plot of Figure 7 $R_d = -180\Omega$, $C_d = 37\text{fF}$, $R_s = 9\Omega$, $L_p = 60\text{pH}$, $C_p = 13\text{fF}$ values which gives the best fit with experimental data.

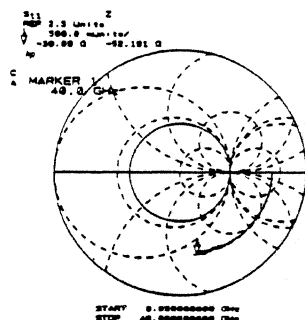


Fig. 7 Frequency dependence of S_{11}
Small signal conditions

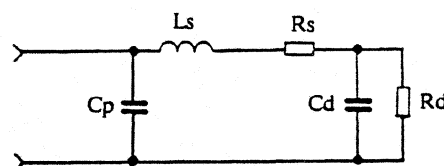


Fig. 8 Equivalent circuit

Large signal conditions: Increasing the power delivered by the generator of network analyzer (HP 8510) leads to drastic changes in the measured values of impedance. Figure 9 gives typical variations we obtained up to 26 GHz when the device is unbiased for two values of attenuation and hence of incident power P_{in} . Here device area is $100\mu\text{m}^2$. An attenuation value of 20 dB corresponds to a measure under small signal conditions because decreasing further P_{in} does not affect the results. At low frequencies the differences are particularly important whereas at high frequencies they are progressively attenuated. This can be explained by the fact that in the present case the power delivered by the generator is not constant. This can be checked in Figure 10 which gives the incident power at port 1 measured with a bolometer. Measurements at constant power can be conducted however by narrowing the analysis window. Therefore, the highest incident power which was possible to apply was $800\mu\text{W}$ without distortion in the detection. This level was kept constant up to 6 GHz. The results achieved for this case are plotted in Figure 11 along the variations of the small signal impedance. With an increase of the power absorbed at diode terminals the real part becomes progressively insensitive to frequency and the imaginary part tends to vanish. These results have been obtained for a $20\mu\text{m}^2$ area sample.

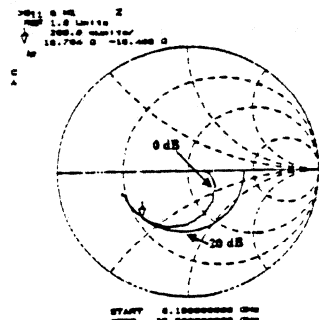


Fig 9 S_{11} versus frequency for two attenuations

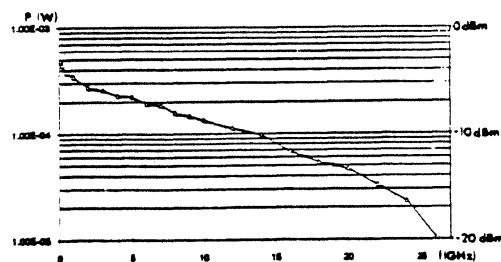


Fig. 10 P_{in} versus frequency

Further insight into this natural matching between source and device can be obtained by plotting the frequency dependence of the real and imaginary part of impedance respectively taking R_d as a parameter. The results of these calculations by varying R_d between 10 and 100Ω with a step of 10Ω are reported in Figure 12 for the following circuit elements $C_d=42\text{fF}$, $L_s=65\text{pH}$ and $C_p=15\text{fF}$. For $R_d = 20\Omega$ one can note that $\text{Re}(Z)$ in the input plane is very close to 50Ω between 0 and 50 GHz and $\text{Im}(Z)$ practically vanishes.

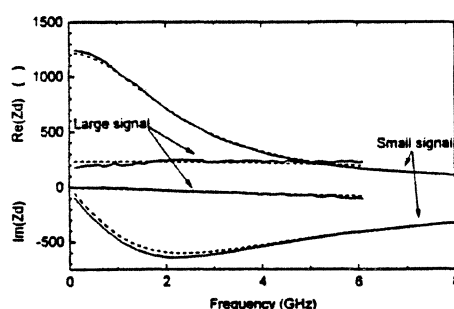


Fig 11 Comparison of large and small signal impedances

This effective matching can be experimentally verified notably when the device is biased at voltages close to V_p . At this bias point, for a $20\mu\text{m}^2$ device the diode resistance is typically 20Ω as it was required previously. The variations of Z as a function of frequency we measured for a 20dB attenuation are displayed in Figure 13. At the marker frequency $\text{Re}(z)$ is 51.3Ω and $\text{Im}(Z)$ is -2Ω . In this Figure, it can also be seen that large signal measurements (0dB) lose their meaning (presence of strong instabilities) because the large rf signal reaches the zone of high NDC.

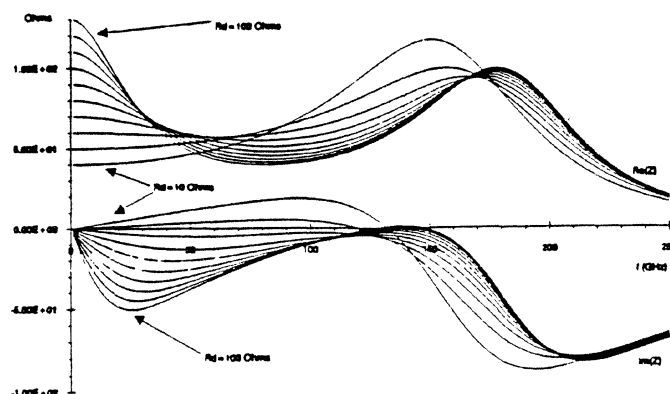


Fig. 12 $Z(f)$ calculated for various resistance values

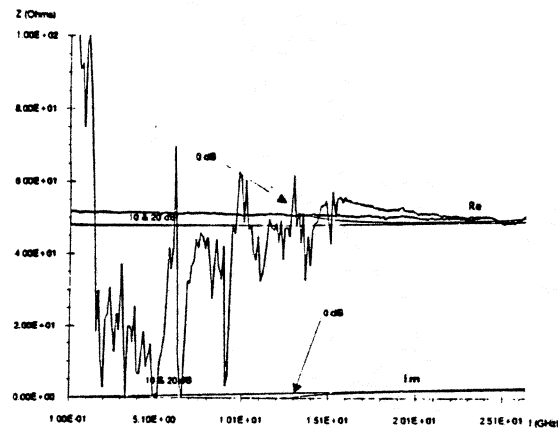


Fig. 13 Variations of impedance for bias close to V_{peak} under small and large signal conditions

In order to analyze the experiment reported above, a simulation program was written to calculate the large signal impedance. For sake of simplicity, only the fundamental frequency component of the rf voltage was assumed while the current harmonics were taken into account. For calculating the voltage swing across the resistance, we have self consistently evaluated the power transfer between the source and the resonant tunneling diode. Starting from small signal impedance values the conductance level was iteratively updated as a function of the transfer efficiency. For this calculation of G , the current waveform $I(t)$ is derived from the dc I-V curve. From a Fourier series expansion of $I(t)$, the large signal conductance is then found as $G = I_1/V_{rf}$ where I_1 is the current amplitude at the fundamental frequency. The procedure is repeated until convergence on G is obtained. Using this procedure, agreement between measured and calculated values is excellent as noted in figure 11 which gives a comparison between theory and experiment.

The large signal conductance cannot be measured directly when the devices exhibit strong NDC effect as noted before. However it is possible to extract this information when the diodes are used as oscillators. To this end devices were mounted in a rf test fixture in order to achieve a free running sinusoidal oscillation. From a $9\mu\text{m}^2$ area device, oscillations in the frequency range 18-23GHz were thus obtained. In figure 14 a typical oscillation spectrum is displayed at a frequency of 19.7GHz. The highest output power we achieved was $83\mu\text{W}$. For the derivation of G the measured part of the I-V curve was fitted in the NDC region by a \tan^{-1} function which is connected to the stable region of the characteristic. In Figure 15 the validity of the fit can be verified. On the basis of this approximation the rf voltage dependence of G can be calculated at various bias voltages and notably at the bias for oscillation. For the later the large signal G exhibits a maximum at $V_{rf} = 200\text{mV}$.

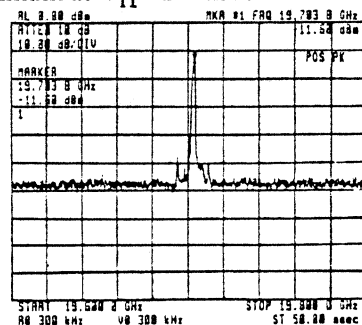


Fig. 14 Oscillation spectrum for the device mounted in a rf test-fixture

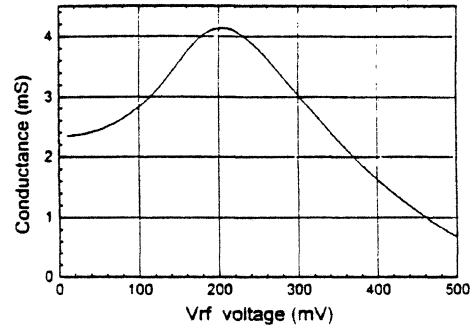
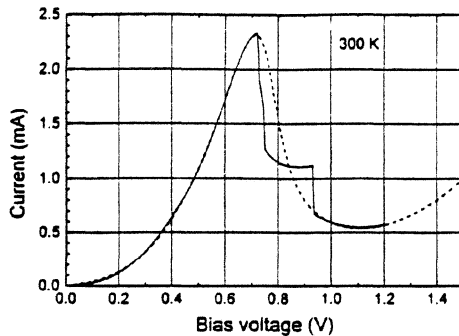


Fig. 15 Measured and fitted I-V curves

Fig. 16 Calculated large signal conductance

Conclusion: The impedance of Resonant Tunneling diodes have been characterized under small and large signal conditions by direct measurement of reflection coefficients using a network analyzer and by analysis of the output power for devices used as oscillators. Using a Fourier transform of $I(t)$, after evaluation of the rf voltage at diode terminals the large signal conductance have been calculated and compared satisfactorily with experiment.

This work was supported by the D.R.E.T.(Contract 91.099)

Acknowledgements: We would like acknowledge the technical assistance of E. Delos

*J.F. Lampin, O. Vanbésien, O. Tanguy and D. Lippens are with
Institut d'Electronique et de Microélectronique du Nord
Avenue Poincaré, BP 69, 59652 Villeneuve d'Ascq, France

- [1] O. Boric-Lubecke, et al., Conference proceedings EuMC, Sept 1993, pp817-818
- [2] S. M. Nilsen, et al., Microwave and Optical Technology Letters, Vol. 6, No. 11, Sept. 1993, pp621-623
- [3] D. Lippens, et al., Electronics Letters, Vol. 24, No. 18, Sept. 1988, pp1180-1181
- [4] O. Vanbésien, et al., Microwave and Optical Technology Letters, Vol. 5, No. 8, July 1992, pp351-354
- [5] P. Mounaix, et al., Electronics Letters, Vol. 27, No. 15, July 1991, pp1358-1359
- [6] M. J. Deen, Electronics Letters, Vol. 28, No 13, June 1992, pp1195-1197
- [7] E. Lheurette, et al., Electronics Letters, Vol. 28, No. 10, May 1992, pp937-938

EXCITATION OF AN OSCILLATOR WITH SEVERAL RESONANT TUNNELING DEVICES INTEGRATED IN SERIES USING RF SOURCE

Olga Boric-Lubecke, Runhua Sun, Dee-Son Pan and Tatsuo Itoh

Department of Electrical Engineering, University of California at Los Angeles

405 Hilgard Avenue, Los Angeles, CA 90024, USA

ABSTRACT

An oscillator using several tunneling devices in series has a difficult excitation condition due to the difference in the I-V characteristics of the individual devices and to the DC instability triggered by the noise. Due to the DC instability, a bias voltage tends to be distributed so that all the devices are biased in the positive differential resistance (PDR) region. A fast electrical pulse, optical illumination or RF source may be used to overcome this problem. The RF source is used only to redistribute the total bias voltage applied to the devices, so that they would all be biased in the negative differential resistance (NDR) region, and is applied for the short amount of time. Simulation results for the RF source excitation will be presented, as well as one experimental example.

INTRODUCTION

Series integration of resonant tunneling diodes has been proposed in order to increase the oscillator output power [1]. Due to the difference in the I-V characteristics of the individual devices and to the DC instability triggered by noise, an oscillator using such a device has several distinct features. Such an oscillator requires a minimum amplitude below which oscillation cannot be maintained, it exhibits a low frequency cut-off, and it has a difficult excitation condition. If the DC bias is applied gradually, the DC instability will divide such a bias among the diodes so that they are all biased in the PDR region. An external RF source may be used to switch the devices from the PDR region to the NDR region [2], so that the oscillation will occur if the circuit is properly designed. The RF excitation frequency may be close to the oscillation frequency of the circuit, or much lower. This paper will treat the excitation with the RF source that has a frequency very close to the

oscillation frequency of the circuit. The lower frequency excitation will be presented elsewhere [3].

Excitation with the RF source close to the frequency of oscillation may be useful in a multiplier circuit. To have a stable oscillation in a circuit with several tunneling devices in series, a large amplitude of oscillation is necessary. If a resonant-tunneling diode is biased in the middle of the NDR region, and large signal oscillation occurs, the diode will behave as a highly nonlinear device, and strong higher harmonics will be generated. A device that has a heating problem, such as pulsed IMPATT diode, may be used as a RF excitation source [2].

If the RF source frequency is close to the oscillating frequency of the circuit, RF power comparable to the oscillator output power is necessary for the switch. Similar to the injection-locking technique, there is a certain frequency band for which excitation is possible for a given RF power. The higher the quality factor of the circuit, the smaller the frequency band will be. There is a cut-off value for the amplitude of the injected signal, below which the diodes cannot be switched from the positive resistance region (PDR) to the negative resistance region (NDR), no matter how close the frequency is to the oscillation frequency of the circuit. Turn-off time of the RF source is not critical, because the circuit is only switching from the amplifier mode to the oscillator mode. This type of excitation is easy to implement experimentally.

THEORY

If the DC bias is applied gradually to the circuit, it will be distributed among the diodes so that they are all biased in the PDR region due to the DC instability. For example, if there were two diodes connected in series, one of them would be biased on the first raising branch of the I-V curve (Fig. 1 (a), (b).), while the other would be biased on the second raising branch of the I-V curve. Current through both devices has to be the same at any instant of time.

When the RF signal is applied, resistive currents will change due to the averaging affect. For the low DC bias point, V_1 (the first diode), resistive current will decrease, whereas for the high DC bias point, V_2 (the second diode), resistive current will increase. Capacitive currents have to compensate for this change. For the first diode capacitive current has to be positive, which means that V_1 will start to increase. For the second diode capacitive current

has to be negative and V_2 will start to decrease. There has to be sufficient change in the resistive currents to start this process, and hence there is a cutoff value for the amplitude of the RF signal below which switching cannot happen.

SIMULATION RESULTS

Several oscillators with two tunnel diodes in series have been designed in a microstrip configuration. The large signal impedance of the diode has been calculated using the procedure described in [4], and the oscillator design was made for several different oscillation amplitudes. EEsof's MWSpace program was used for the simulation. The 5th order polynomial was used to model the tunnel diode I-V curve, and the diodes were assumed to be identical. The DC bias was applied sufficiently slow so that both diodes would be biased in the PDR region at first. After a while, the RF signal was applied, and if its amplitude was large enough diodes would switch to the NDR region. After the RF signal was turned-off, if the circuit was designed for a large enough oscillation amplitude, stable oscillation was maintained.

For the RF frequency close to the oscillation frequency of the circuit, very little RF power was necessary for the switch. With the larger RF source power, the switching happens faster. A turn-off time of the RF signal was not critical at all. Fig. 2. shows the voltage on each diode as a function of time, for the RF source frequency of 2 GHz, which is equal to the oscillation frequency of the circuit. For the RF amplitude of 0.15 V (Fig. 2 (a).), the diodes cannot switch to the NDR region. For the RF amplitude of 0.19 V (Fig. 2 (b).), which is the cut-off amplitude, the diodes switch into the NDR region after fifteen oscillation periods, and oscillation is maintained even after RF signal is turned-off. For the RF amplitude of 0.30 V (Fig. 2 (c).), the diodes switch into the NDR region much faster, after only four periods.

EXPERIMENT

The RF excitation of an oscillator with two tunnel diodes in series with the RF frequency close to the oscillation frequency of the circuit has recently been demonstrated. The oscillator was made in the microstrip configuration. The tunnel diodes were fabricated by Metelics Co., with a peak current of about 0.5 mA. The excitation signal and the oscillator output were separated by a circulator. DC bias was applied using bias T network. A DC current was monitored during the experiment, to check if the diodes were biased in the PDR region or in the NDR region.

The circuit oscillation frequency was 1.861 GHz, with an output power of -29 dBm (Fig. 3.). An RF signal in the frequency range from 1.8 GHz to 1.885 GHz was used for excitation, with input power of -25 dBm. There was 3 dB loss in the measurement system, and hence the oscillator output power was about -26 dBm, whereas the RF input power was about -28 dBm, which is about 2dB lower than the output power. Using an injection-locking technique the quality factor of the oscillator was determined to be about 100.

CONCLUSIONS

The RF source excitation of an oscillator with several tunneling devices in series has been presented. Simulation results for the RF frequency close to the oscillation frequency were obtained. RF excitation with the frequency close to the oscillation frequency was demonstrated experimentally for the oscillator with two tunnel diodes in series.

ACKNOWLEDGMENT

We would like to thank Prof. M. Rodwell of UC Santa Barbara for helpful discussions. This work is supported by Joint Services Electronics Program, through AFOSR F49620-92-C-0055.

REFERENCES

- [1] C.C. Yang and D.S. Pan, "Theoretical Investigations of a Proposed Series Integration of Resonant Tunneling Diodes for Millimeter-Wave Power Generation", *IEEE Trans. Microwave Theory and Tech.*, vol. 40, pp. 434-441, March 1992.
- [2] C. C. Yang and D.S. Pan, "A Theoretical Study of an Integrated Quantum-Well Resonant Tunneling Oscillator Initiated by an IMPATT Diode", accepted for publication in *IEEE Trans. Microwave Theory and Tech.*
- [3] R. Sun, O. Boric-Lubecke, D.S. Pan and T. Itoh, "Simulation of a Subharmonic Excitation of Series Integrated Resonant Tunneling Diodes", submitted for publication in *IEEE Electron Device Letters*.
- [4] O. Boric-Lubecke, D.S. Pan and T. Itoh, "Large Signal Quantum-Well Oscillator Design", *Proc. of 23rd European Microwave Conf.*, Madrid, Spain, Sept. 1993, pp. 817-818.

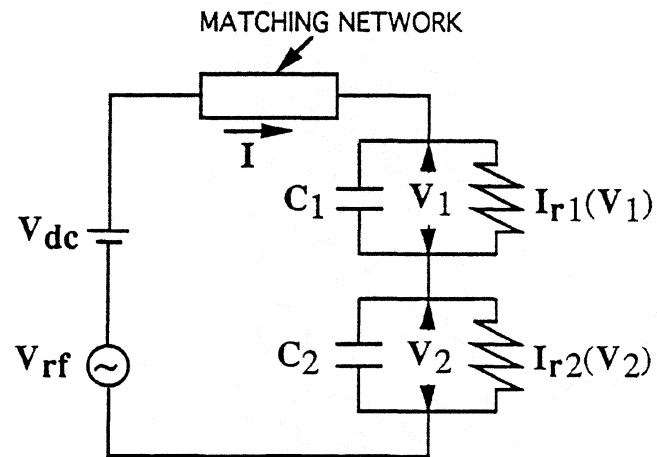


Fig. 1 (a). Equivalent circuit of an oscillator with two tunnel diodes in series

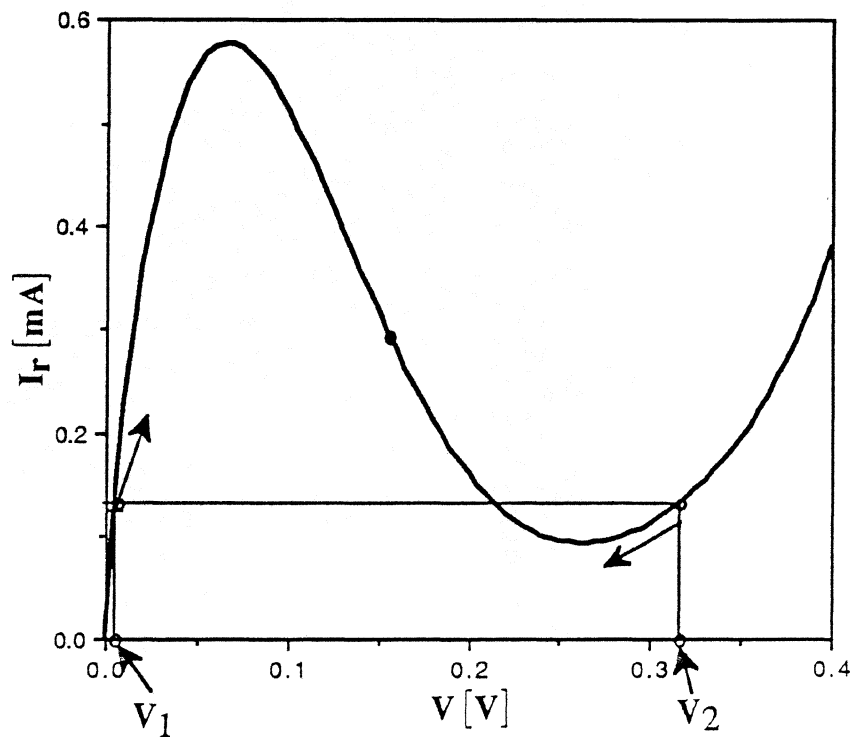
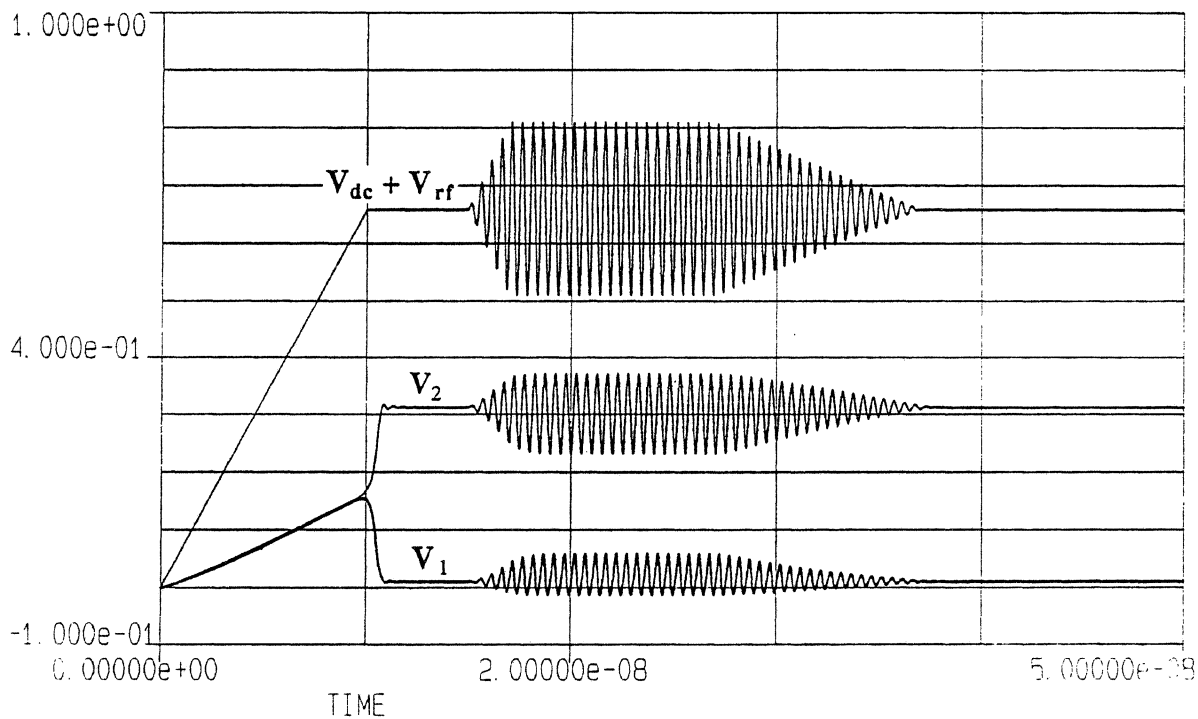
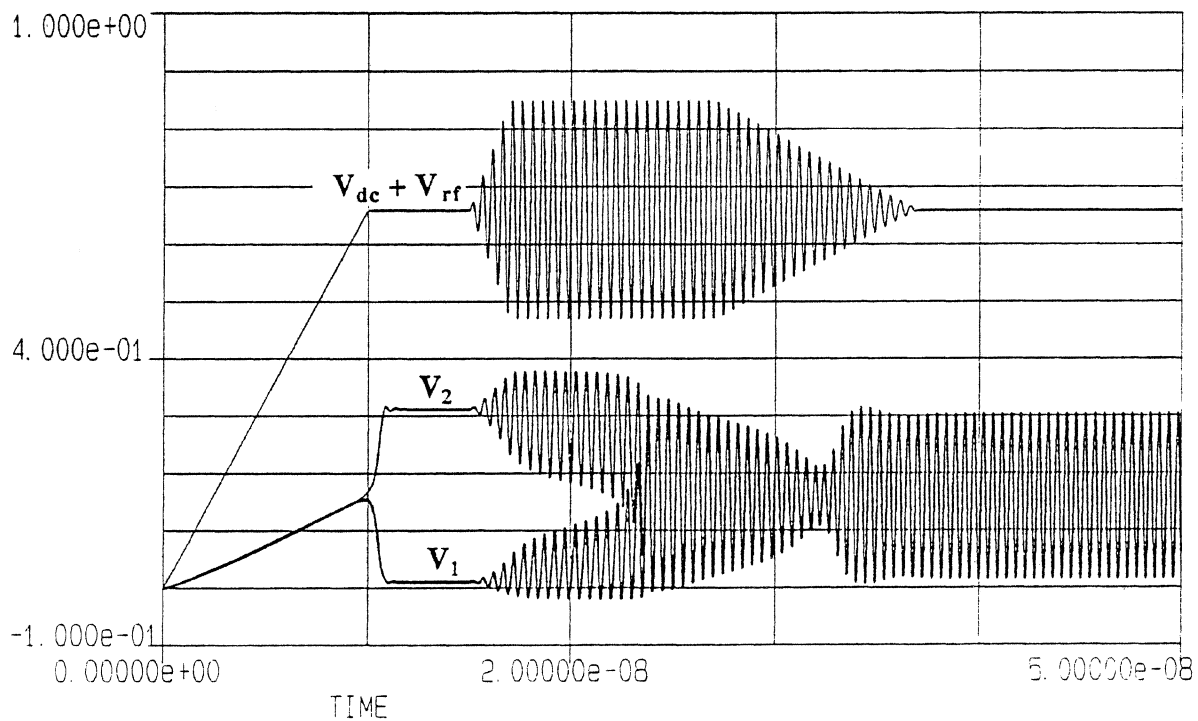


Fig. 1 (b). DC I-V curve of a tunnel diode: initial DC bias voltage distribution

Fig. 2 (a). RF source excitation: $|V_{rf}| = 0.15$ VFig 2 (b). RF source excitation: $|V_{rf}| = 0.19$ V

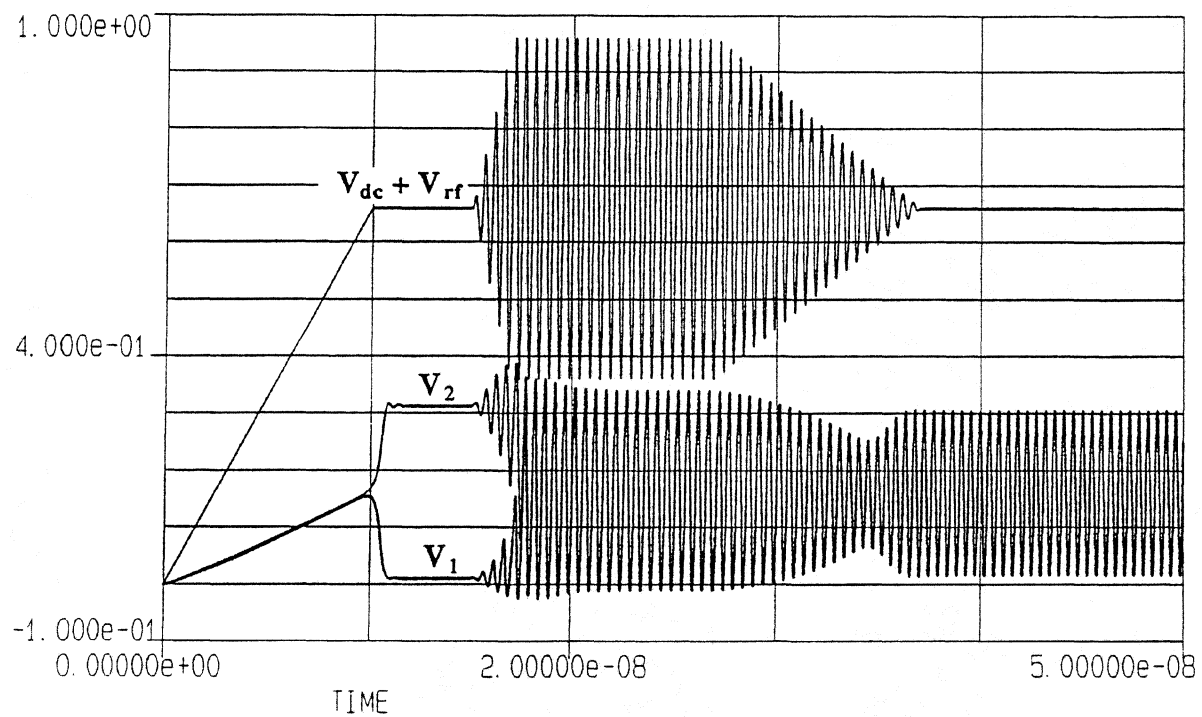


Fig. 2 (c). RF source excitation: $|V_{rf}| = 0.30$ V

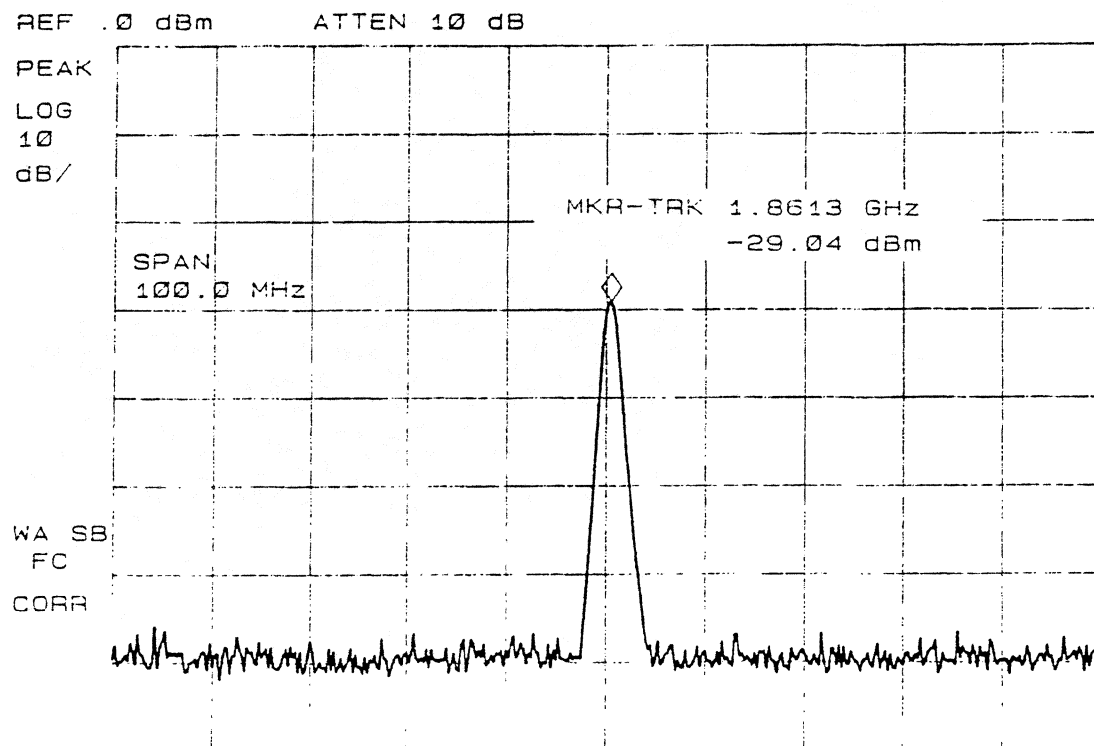


Fig. 3. Oscillation spectrum

An Heterojunction Schottky Barrier Diode with RTD Emitter

X.J. Lu*, T.E. Kosica and B.S. Perlman

U.S. Army Research Laboratory, Fort Monmouth, New Jersey 07703

(May 3, 1994)

Abstract

The possible application of Schottky diodes as detector elements in receivers and image sensing systems operating in the THz frequency range has been demonstrated in the literature. In addition to metal-semiconductor (M-S) Schottky diodes, the use of heterojunction Schottky barrier diodes for detection and mixing applications has also been explored. Such diodes require lower d.c. bias voltages, which is important for certain types of detector and mixer designs which strive to achieve higher signal-to-noise ratios.

A new detector design is proposed which utilizes a heterojunction Schottky barrier and a double barrier structure jointly for high sensitivity detection. The diode is designed so that the resonant energy level of the double barrier structure is lower than the Schottky barrier at low bias and becomes higher than the barrier as bias increases. In this regime, the thermo distribution of emitted electrons is altered by the presence of double barrier structure, leading to a sharp knee point and a significant improvement in sensitivity.

As compared with a "plain" heterojunction Schottky diode, high frequency response will be affected by the tunneling time through the RTD in addition to the capacitance from junction itself. Such high frequency influences are discussed.

I. INTRODUCTION

The potential application of heterojunction Schottky barrier diodes as mixer and detector elements for the THz frequency range has stimulated interest because of lower possible turn-on voltage, which in turn leads to a lower LO power requirement [1]. In much of the recent literature, the heterojunction Schottky barrier has been treated as an extension of a metal-semiconductor (M-S) Schottky junction. In this case, a generalized model of carrier transport through the heterojunction is used which considers drift-diffusion as well as thermionic emission. In the analysis of Wu and Yang [2] and also Bhapkar [3], quantum mechanical tunneling is considered which includes the current contribution from electrons with energy lower than the barrier height. Applying quantum mechanical modeling to heterojunction Schottky barrier diodes becomes attractive because it not only allows better understanding and modeling of the transport process across the heterojunction (which is important for HEMT and HBT devices), but also allows exploration of more complicated MBE grown heterostructures.

While the I-V curve of a heterojunction Schottky barrier diode is very similar to its M-S counterpart, an intrinsic complexity stems from the non-degenerate character of electron gases on both sides of the interface. In general, the solution of Poisson equation is needed to first obtain the potential profile in the heterojunction region under various bias voltages. Once these potential profiles are determined, the current density can then be calculated using the transmission coefficient method as shown in [3].

In this paper, the current through the heterojunction is computed using the transmission coefficient method of Wu and Yang for such parameters as bias voltage, barrier height, electron density, etc. This method is then applied to the new diode structure proposed here, namely a design utilizing a double barrier quantum filter adjacent to the heterojunction. Since the double barrier structure blocks electrons from tunneling through except at selected energies, the I-V character of the diode is altered dramatically. This novel I-V characteristic will be computed and then compared to a diode without the double barrier structure.

II. CURRENT COMPUTATION

The boundary condition for electron current across a M-S interface as given by Crowell and Sze [4] is:

$$J = q(n_s - n_0)v_{rn} \quad (1)$$

where n_s is the electron density present at the potential maximum and n_0 is the electron concentration at the same point at equilibrium. In Eq. (1) n_s can also be defined as the density in the bulk region if we notice that:

$$n_s = N_0 \exp\left(\frac{E_f - V}{kT}\right) = n_{s,bulk} \exp\left(\frac{-V}{kT}\right) \quad (2)$$

applies under the Boltzman distribution assumption. Also it is straightforward to think of $qv_{rn}n_0$ as the current injection from the metal to the semiconductor side, due to the fact that at equilibrium the net current flow is zero. Thus, the current can be written as $J = J_{sm} - J_{ms}$ where J_{sm} is the current flux from semiconductor to metal side, while J_{ms} is the current flux from metal to semiconductor side.

For a heterojunction Schottky barrier, a similar result has been given in Ref. [2] based on the transmission coefficient approach:

$$J = q\eta(n_1v_1 - \theta n_2v_2 \exp(-\frac{E_B}{kT})) \quad (3)$$

where n_1 and n_2 are the electron densities on side-1 and side-2 of the interface, E_B is the energy difference between bottoms of conduction bands on the two sides, and θ accounts for the ratio of the effective masses, that is $\theta = m_1/m_2$. Furthermore, the effective recombination velocities for each side are given as $v_1 = A_1^*/qN_{c1}$ and $v_2 = A_2^*/qN_{c2}$, where $A_1^* = (qm_1^*k^2/2\pi^2\hbar^3)$ and $A_2^* = (qm_2^*k^2/2\pi^2\hbar^3)$ are the Richardson constants for each side. Also in Eq. (3), η is a term which comes from the integration over the transmission coefficient and the distribution functions. Specifically, it is computed as:

$$\eta = \int_{\max(E_B, 0)}^{\infty} dE_{||} \exp\left(-\frac{E_{||}}{kT}\right) \int_0^{(E_B - E_{||})/(1/\theta - 1)} dE_{\perp} T(E_{||}, E_{\perp}) \exp\left(-\frac{E_{\perp}}{kT}\right) \text{ if } \theta < 1 \quad (4)$$

$$= \int_0^{\infty} dE_{||} \exp\left(-\frac{E_{||}}{kT}\right) \int_{\max((E_B - E_{||})/(1 - 1/\theta), 0)}^{\infty} dE_{\perp} T(E_{||}, E_{\perp}) \exp\left(-\frac{E_{\perp}}{kT}\right) \text{ if } \theta > 1 \quad (5)$$

where E_{\parallel} , E_{\perp} are the energy components corresponding to electron motion parallel to and perpendicular to the heterojunction interface, respectively. As shown by Horio [6], the classical thermionic emission situation (no tunneling) can be described by assuming that the transmission coefficient takes the form:

$$T(E_{\parallel}, E_{\perp}) = \Theta(E_{\perp} - \Delta\phi) \quad (6)$$

where Θ is the Heavyside step function. Eq. (6) shows that only those electrons with E_{\perp} greater than the barrier height can cross the interface without being blocked and thereby contribute to the current. A substitution of T from Eq. (6) into Eq. (5) will lead to an analytic η in the simple form of:

$$\eta = T^2 \exp\left(-\frac{\Delta\phi}{kT}\right) \quad (7)$$

Without loss of generality, this calculation assumes that side-1 is GaAlAs, and that side-2 is GaAs. Thus θ (from Eq. (5)) is always greater than 1. Also, consistently with this notation, $E_B < 0$ for forward bias.

Using the η given in Eq. (7), the current density in Eq. (3) can be readily identified with M-S Schottky barrier results. However, unlike the M-S Schottky barrier, $\Delta\phi$ in heterojunction-based diodes generally does not have a linear dependence on bias voltage even at low bias due to the non-degenerate character of material on either side. This leads to less ideal I-V curves as compared with what given by M-S Schottky diodes.

III. HETEROJUNCTION DIODE MODELING

In order to calculate the barrier height variation as a function of the applied bias voltage, first we solve the Poisson equation to obtain the band profile near the heterojunction region. Only one species of carrier, namely the electron, is considered and thus the Poisson equation becomes:

$$\frac{d^2\phi}{dx^2} = -\frac{q}{\epsilon}(-n + N_d) \quad (8)$$

where N_d is the donor density in the device bulk region, $n = n_i \exp(-\frac{E_f - E_c - \phi(x)}{kT}) = N_c \exp(-\frac{\phi(x)}{kT})$ is the electron density in the conduction band, E_f is the electron Fermi energy, E_c is the position of conduction band, and N_c is the density of state in the conduction band. This computation was applied to the device shown in Fig. 1 and the resulting conduction band profiles for three different biases are plotted in Fig. 2. The barrier height bias voltage dependence, $\Delta\phi - V$, extracted from this calculated band structure is plotted in Fig. 3. As can be seen in the figure, this dependence is approximately linear but it does exhibit a slight non-linear dependence due to the non-degenerate character mentioned previously. Moreover, note that the $\Delta\phi - V$ term is less than one, due to an applied voltage drop over series resistances in the other parts of the device. However, as can be observed from the plot, the change of the depth of the well on the GaAs side (refer to Fig. 2, where it is noted as $\Delta\phi_{GaAs}$), is relatively small, as a result of the relatively heavy doping on the GaAs side as compared with the GaAlAs side.

Knowing the potential profile around the heterojunction region, the quantum mechanical transmission coefficient can be calculated. In this paper, the transmission line technique of Khondker et al [5] is used to calculate the transmission coefficient. The first step in the method is to approximate the conduction band profile within the entire region under consideration by a series of voltage steps, named $V_i(x_i, x_{i+1})$, ($i = 1 \dots N$). Next the corresponding "load impedance" Z_{iN} and the "characteristic impedance" Z_0 is iteratively computed through each step. The reflection coefficients and transmission coefficients are obtained from these impedances using the forms:

$$\rho = \frac{Z_{iN} - Z_{0N}}{Z_{iN} + Z_{0N}} \quad (9)$$

$$T = 1 - |\rho|^2 \quad (10)$$

where Z_{iN} is the load impedance and Z_{0N} is the characteristic impedance for step N . Since the transmission coefficient calculation depends only on the energy in the perpendicular direction, the integration in Eq. (5) degenerates to one dimension, and thus becomes:

$$\eta_Q = kT \int_0^\infty dE_\perp T(E_\perp) \exp(-\frac{E_\perp}{kT}) \text{ if } \theta > 1 \quad (11)$$

As compared to Eq. (6), this quantum mechanical transmission coefficient will be somewhat larger than zero for energy lower than the barrier height because of the inclusion of a tunneling contribution in the overall transport current. It also leads to a less than one transmission probability for an electron with energy larger than the barrier height due to the scattering by the barrier. The η_Q calculated from Eq. (11) is plotted in Fig. 4, and also included in this plot is the η_C which is the same value calculated from the classical approximation discussed earlier. This plot clearly shows quantum effects characteristic of the problem. For example, at low bias η_Q is little larger than η_C since the tunneling portion of the current is, of course, neglected in the classical approximation. At higher bias, η_C is larger than η_Q since the quantum model takes scattering into account.

IV. EXAMPLE CALCULATION

In the sample device used for computations (Fig. 1), the barrier width at $E = 0$ is about 1000Å (Fig. 2), thus the tunneling effect is not very important. However, if the GaAlAs side were more heavily doped, then the barrier would become thinner and the tunneling effect would be more significant.

The GaAlAs/GaAs heterojunction structure modeled here is intended to be used as THz detector, thus current density (e.g. power handling) is not a stringent device performance requirement. For the Schottky barrier heterostructure under consideration, it is possible to further modify the I-V characteristics by adding a superlattice structure next to the heterojunction interface as shown in Fig. 1. A similar approach has been used in the RTD design to reduce the series resistance coming from the ohmic contact by replacing it with a Schottky barrier ⁷. At low bias, the resonant energy is lower than the Schottky barrier, and the current is small due to the blocking of barrier. As the voltage increases, the resonant energy gradually approaches the top of Schottky barrier and eventually becomes higher than the barrier height. At this turning point, there is a sharp, steep increase in the current

as compared with the ideal/classical diode I-V curve. Note that the potential profile as obtained from the solution of Poisson equation is used in this computation.

The calculated η_Q for this structure is plotted in Fig. 5, and the curve indeed shows a sharp knee point around 40meV. As the bias voltage increases, the current response sharply turns on and then sustains a rapid increases, implying much higher possible detector gains for small signals. The original result also shows several small "bumps", especially in the mid-bias region, which come from resonances between the Schottky barrier and the double barrier structure. Although these are indeed accounted for in the modeling, their amplitudes are invariably very weak, and therefore there is virtually no practical implication and is smoothed out. Now, as the voltage increases further, the major part of voltage drop is over the double barrier structure region, which finally leads the diode to negative differential conduction behavior.

One key "circuit-level" parameter which characterizes the detector performance is the open circuit sensitivity, described by:

$$\beta = (1/2) \frac{f''(v_0)}{f'(v_0)^2} \quad (12)$$

where $f(v)$ is the I-V relation of the device. For the device parameters under discussion including an assumed device area of $10\mu\text{m}^2$, β is estimated to be 63888 (mV/mW) for an applied bias of 0.04V. This compares with $\beta = 2500\text{mV/mW}$ (based on the thermionic theory calculation) for an conventional same size diode biased at same voltage. The current density is estimated to be $1.5 \times 10^{-2}\text{mA}\mu\text{m}^{-2}$, which is only fractionally smaller than the current density in an ideal Schottky barrier diode. The series resistance from the bulk regions and the ohmic contacts were not considered in this calculation, thus the results shown here are somewhat optimistic. However, using the methods presented here the series resistance is estimated to be about 60Ω , which would not greatly degrade the device performance.

V. OTHER CONSIDERATIONS AND CONCLUSIONS

The overall detection efficiency is also greatly affected by the reactive behavior of the diode. For the Schottky barrier portion (i.e., contacts) of the overall structure, the major reactive contribution is capacitive, while in the double barrier device portion the situation is more complicated. For a double barrier region it has been shown that the reactance could be either capacitive or inductive depending on the frequency of operation and device parameters. Although such reactive behavior is not yet fully characterized via current research [8], it is known generally that when the resonant level electron charge density variation is large and the signal frequency is comparable with the inverse of tunneling time (e.g. $1/\tau$), then the diode's behavior becomes inductive. This observation explains why the inductance increases with barrier thickness and why inductive effects are more pronounced when the diode is biased in the NDC region. For the device structure under consideration, the barrier is relatively thin and the device is operated at low bias, therefore the inductance is expected to be small. However, since the intended operation is at very high frequencies (i.e. approaching 1 THz), this inductance still has a finite influence. Since it is of importance, this inductance was estimated to be less than 10^{-2} nH. The capacitance of the heterojunction is also of importance as well, of course, and it is given by $C_j = A\epsilon_s/w$ where A is the device area and w is the width of the depletion layer. A 0.04V bias voltage and $w = 0.11\mu\text{m}$ leads to $C_j \approx 10^{-2}$ pF.

From the junction capacitance and the series resistance, the time constant for the overall device is estimated to be $\tau = R_s C_j = 4\text{pS}$. Here the inductances from double barrier region and Schottky contacts were not considered. Since the impedance stemming from these inductances is comparable to that from the junction capacitance at the frequency of 1 THz, this would present a formidable simulation task.

REFERENCES

- * X.J. Lu is a postdoc fellow from National Research Council, Washington, D.C.
- ¹ Y. Anand and W.J. Moroney, *Microwave mixer and detector diodes* Proc. of IEEE **59** pp1182-1190 (1971).
- ² C.M. Wu and E.S. Yang, *Carrier transport across heterojunction interfaces*, Solid State Electron. **22** pp.241-248 (1979).
- ³ Udayan V. Bhapkar and R.J. Mattuach, *Numerical simulation of the current-voltage characteristics of heteroepitaxial Schottky-barrier diodes*, IEEE Tran on Elec. Devices, **ED40** pp. 1038-1046 (1993).
- ⁴ C.R. Crowell and S.M. Sze, *Current transport in metal-semiconductor barriers* Solid State Electron. **9** pp1035-1048 (1966).
- ⁵ A.N. Khondker, M.R. Khan and A.F.M. Anwar, *Transmission line analogy of resonance tunneling phenomena; The generalized impedance concept*, J. Appl. Phys. **63** pp5191-5193(1988).
- ⁶ K. Horio and H. Yanai, *Numerical modeling of heterojunctions including the thermionic emission mechanism at the heterojunction interface*, IEEE Trans. Electron Devices, **ED37** pp1093-1098 (1990).
- ⁷ Y. Konishi, S.T. Allen, M. Reddy, M.J.W. Rodwell, R.P. Smith and J. Liu, *AlGa/GaAs Schottky-collector resonant-tunneling-diodes*, Solid State Electronics, **36** pp 1673-1676 (1993).
- ⁸ J.M. Gering, D.A. Crim, D.G. Morgan, P.D. Coleman, W. Kopp and H. Morkoc, *A small-signal equivalent-circuit model for GaAs-AlGaAs resonant tunneling hetrostructures at microwave frequencies*, J. Appl. Phys. **61** pp 271-276(1987).

$n^+ \text{Al}_{0.2}\text{Ga}_{0.8}\text{As} (7 \times 10^{18})$ 1000Å
$n \text{Al}_{0.2}\text{Ga}_{0.8}\text{As} (2 \times 10^{16})$ 500Å
AlAs 7Å
$n \text{Al}_{0.2}\text{Ga}_{0.8}\text{As} (2 \times 10^{16})$ 60Å
AlAs 7Å
$n \text{Al}_{0.2}\text{Ga}_{0.8}\text{As} (2 \times 10^{16})$ 250Å
$n \text{GaAs} (1 \times 10^{17})$ 400Å
$n^+ \text{GaAs} (5 \times 10^{18})$ 1000Å

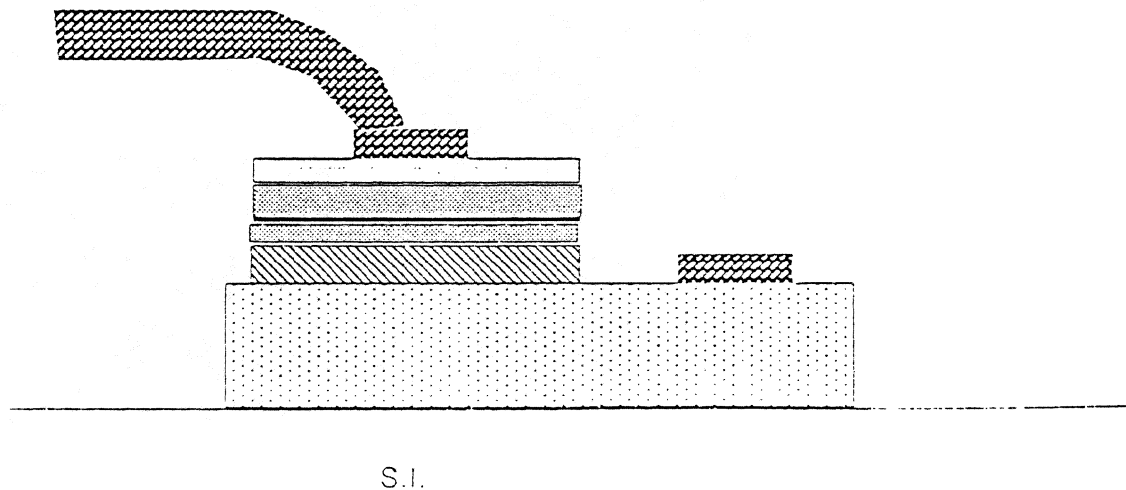


Fig. 1 Cross-section of the heterojunction Schottky barrier diode, and schematic drawing of the detector

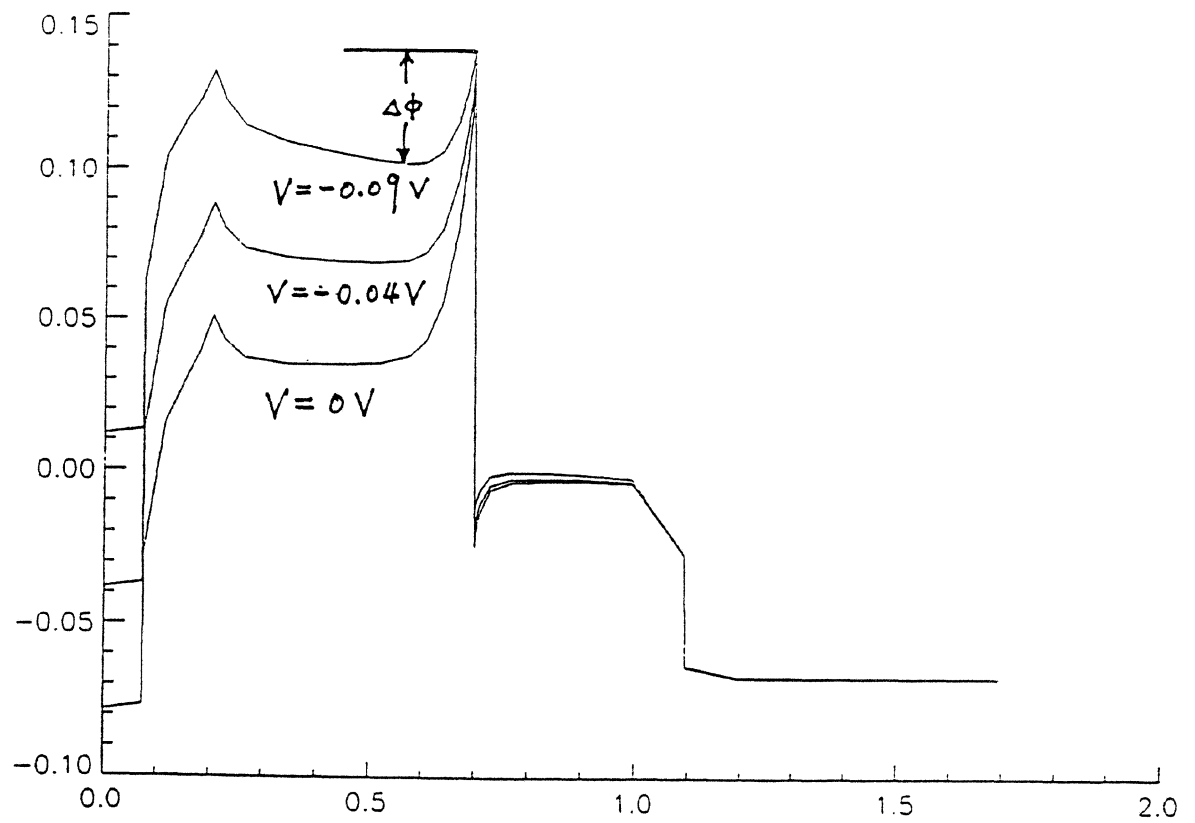


Fig. 2 The band profiles of Schottky heterojunction under various bias voltages.

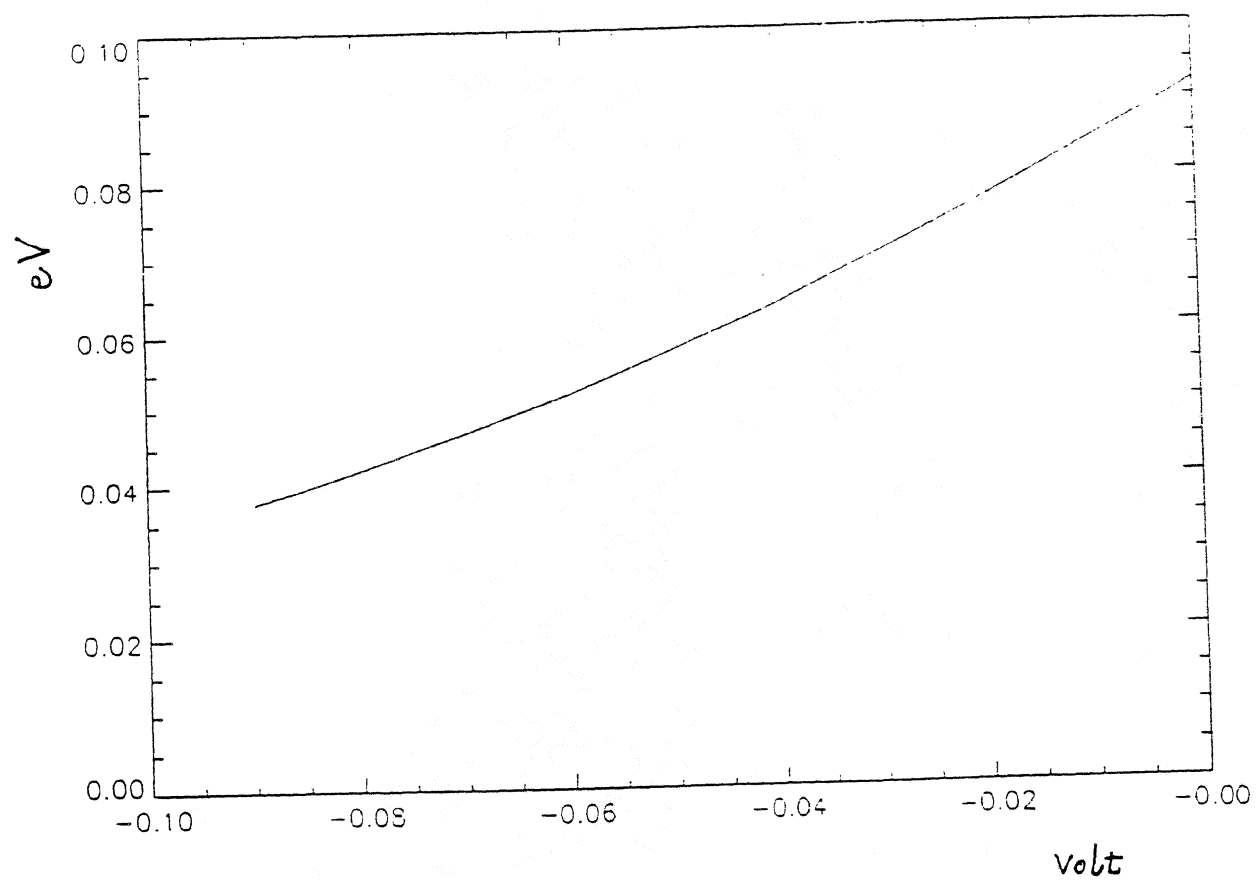


Fig. 3 The variation of Schottky barrier height vs. the bias voltage increase.

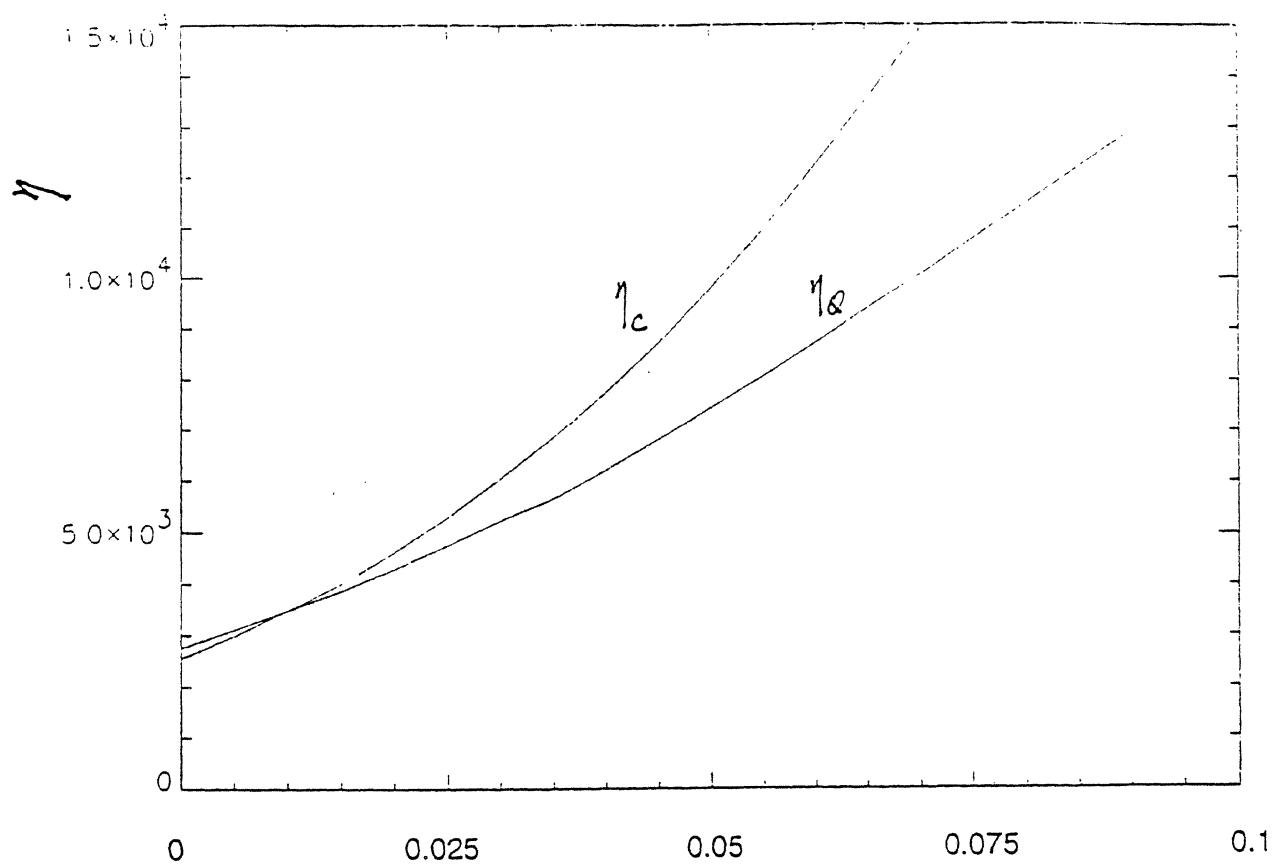


Fig. 4 Modification factor calculated using quantum mechanical transmission coefficient method η_Q and from thermionic theory η_c .

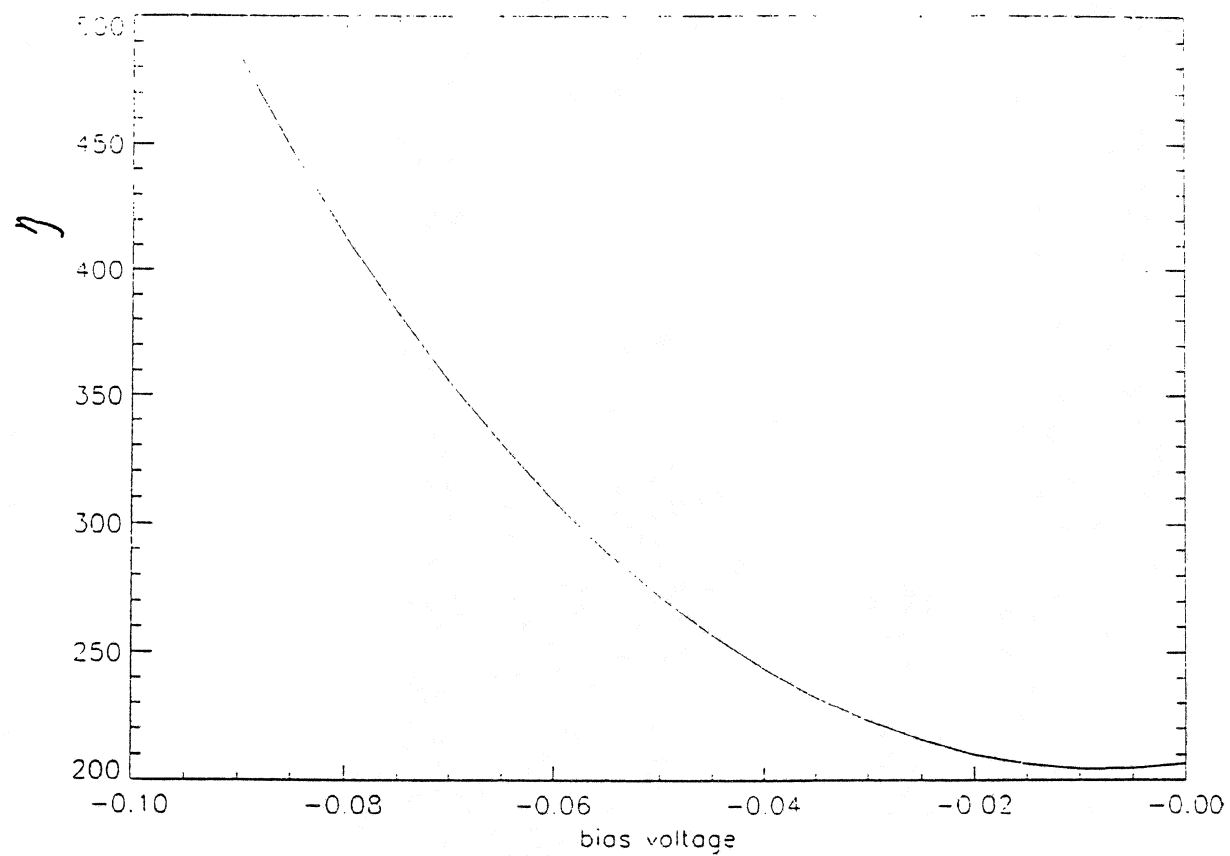


Fig. 5 The modification factor for the Schottky barrier diode with RTD on the emitter side.

DEMONSTRATION OF POWER COMBINING AT W-BAND FROM GaAs/AlAs RESONANT TUNNELLING DIODES

D.P. Steenson*, R.E. Miles*, R.D. Pollard*,
J.M. Chamberlain*, M. Henini*.

* Microwave and Terahertz Technology Group, Department of Electronic
and Electrical Engineering, University of Leeds, LS2 9JT, UK.

* Department of Physics, University of Nottingham, NG7 2RD, UK.

Abstract

Double barrier resonant tunnelling diodes (DBRTDs) have been fabricated from GaAs/AlAs structures. Oscillation is noted at 75GHz for whisker contacted devices. A modified Kurokawa-Magalhaes combiner circuit has been constructed and with two devices a quadrupling of output power (in comparison with a single device) has been achieved at W-band.

Introduction.

The Double Barrier Resonant Tunnelling Diode (DBRTD) has been claimed as the fastest purely electronic device in existence. In defence of these claims fundamental oscillations at 712GHz have been noted [1] from a DBRTD and although the available power was modest, this result indicates the potential of this device for generating terahertz power.

The DBRTD has been the subject of extensive study over the past ten years [2] Negative differential resistance in the device arises from the resonant enhancement of

the tunnelling current through a quantum-confined region between two atomic-scale barriers. Various material systems have been chosen to realize DBRTD structures: the 712 GHz oscillation result [1] was achieved using an InAs/AlSb structure; at 2GHz, 20mW output power, and 50% dc to rf conversion efficiency, has been measured from AlAs/InGaAs DBRTDs. The proven materials system GaAs/AlAs [3] offers many advantages for the production of DBRTDs which include high interface quality, good uniformity across the wafer and predictable current-voltage characteristics; oscillations from GaAs/AlAs DBRTD devices have been reported up to 412GHz [3]. These advantages accrue from the mature state of GaAs/AlAs molecular beam epitaxy (MBE) growth technology and the resulting layers are compatible with other existing GaAs devices such as monolithic microwave integrated circuits (MMIC).

For DBRTD devices to make any technological impact, it is essential that the power levels generated at high frequencies by these diodes be increased. However, the relatively high efficiency obtained at 2GHz [4] illustrates the potential of these devices when the match between the device and the cavity is optimized; this optimization problem represents the main difficulty with the practical application of these devices at 100GHz and above. At these frequencies the requirements on mechanical tolerances of the cavity and any matching circuits are extreme and approaching the limits of conventional machining capabilities. Electro Discharge Machining (EDM) and the techniques of micro-machining can provide alternatives for realizing these millimetre-wave cavities.

Although the maximum frequency of oscillation of the DBRTD device has been set at several THz [5], in practice this upper limit is reduced by device parasitics such as capacitance and contact resistance. To overcome the limitation of the DBRTD capacitance it is essential to use small ($<10\mu\text{m}$) mesa structures. The combination of small device size, necessary for high frequency operation, and the inherent low power of existing DBRTD oscillators is currently a limiting factor in their practical application. One approach for increasing the output power available is to combine the power produced from a number of individual devices; a technique that has been successfully used for IMPATTs and Gunn devices at microwave frequencies [6]. This paper provides the first evidence of successful power combining using DBRTDs at

millimeter wave frequencies.

Device Details

Figure 1 shows a GaAs/AlAs DBRTD structure grown by MBE which has been produced specifically for whisker contacting. Figure 2 shows the current-voltage characteristic for this structure; the asymmetry of the characteristic is evident and is a result of the inclusion of a low-doped collector region adjacent to one of the barriers which results in an asymmetric voltage distribution across the device.

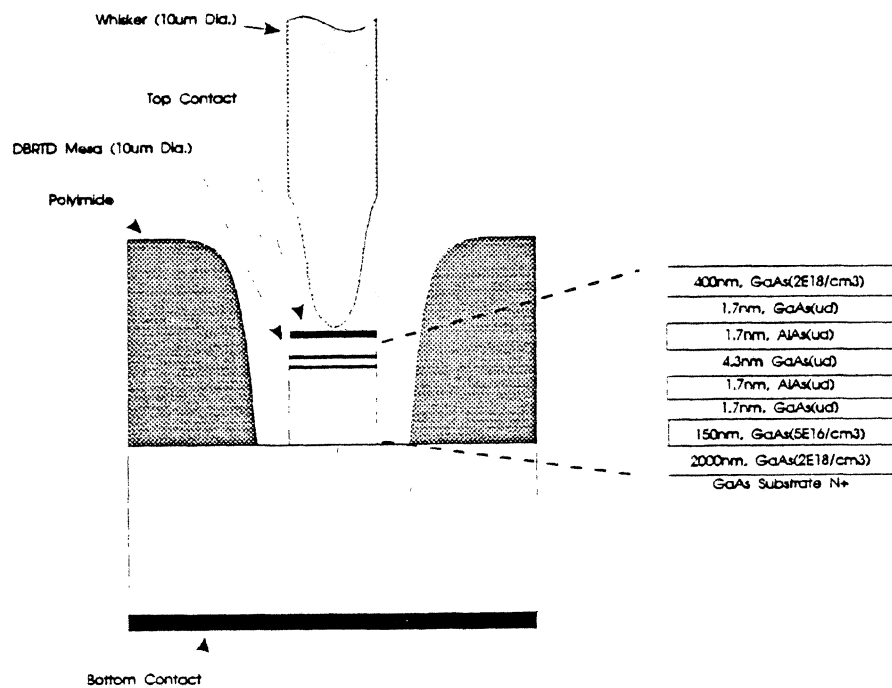


Figure 1 Layer structure and schematic of a DBRTD

Sum diameter device from NU-366

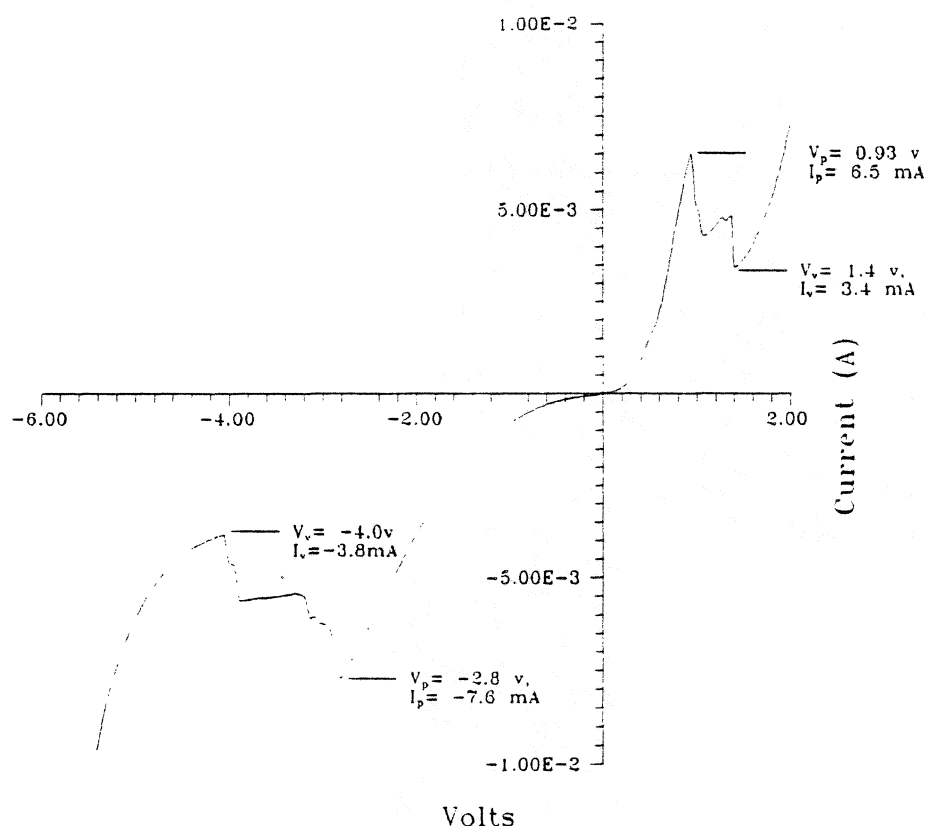


Figure 2 Current versus Voltage for a 5 μm diameter device

The purpose of the low-doped region is threefold: it increases the voltage range over which negative differential resistance (NDR) is observed; increases the magnitude of the NDR and also reduces the capacitance per unit area. The first effect results in an increase in the power available; the second improves the ability to extract the power available through improved matching capabilities and the third consideration allows a higher operating frequency. The high capacitance per unit area associated with the older Esaki tunnel diodes [7] was one of their main limitations. The restriction on device size with increasing frequency, noted previously, implies the further difficulty of providing low resistance contacts. At present, contact behaviour can only be optimised through a reduction in the specific contact resistance ($\sim 1 \times 10^{-7} \Omega \text{cm}^2$) by using especially highly-doped or indium based layers at the contacts, or by using techniques which separate the contact area from the junction area [8].

Because of their simplicity, whiskers were used to achieve contact between the small area ($<20\mu\text{m}^2$) devices and the millimetre-wave circuit. Also, the whisker is thought to act as an antenna for coupling the millimetre-wave power produced in the DBRTD device to an external circuit. A significant drawback of the present whisker contacting process is that it necessitates the use of N^+ substrates and it is suspected that the resulting separation between the device top-contact and the ground plane introduces skin-effect losses which become significant at high millimetre-wave frequencies.

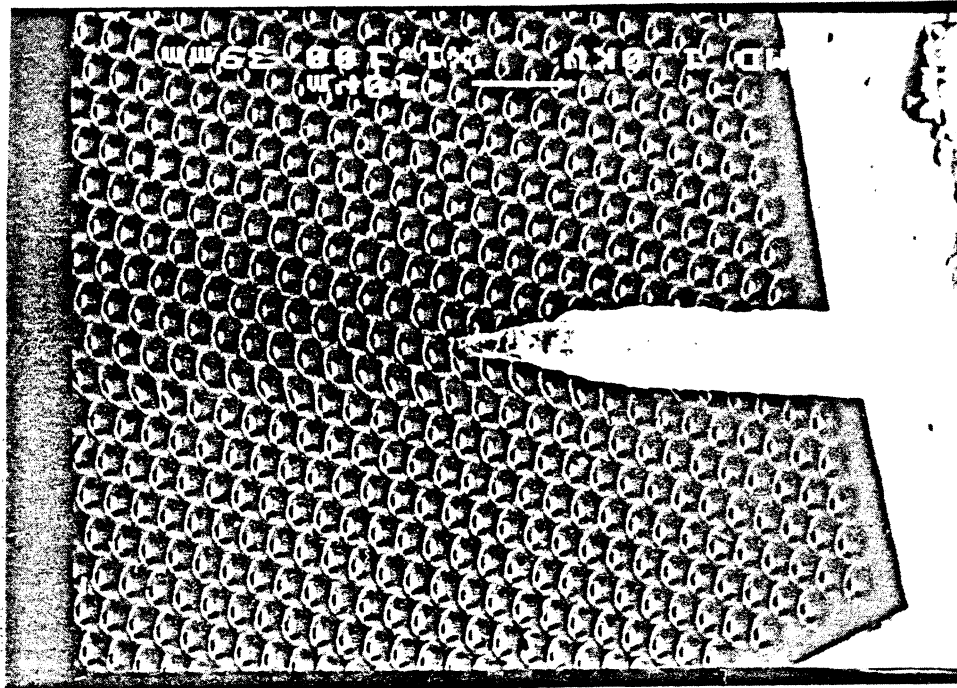


Figure 3 Micrograph of DBRTD during whisker contacting

Figure 3 shows a device in the process of being contacted and Figure 4 shows a typical output spectrum obtained from a whisker-contacted device in a quarter-height waveguide cavity. Reduced height waveguide was chosen to help improve the match with the DBRTD because it has a lower characteristic impedance (approx. 70Ω versus 310Ω for a full height waveguide at 75GHz).

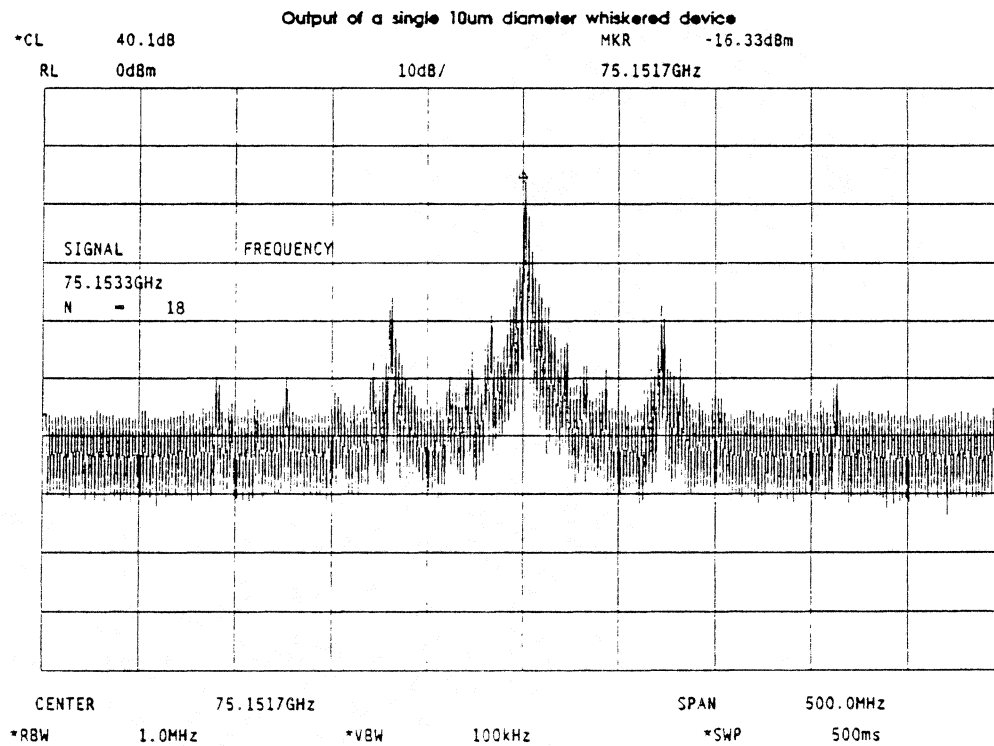


Figure 4 Output spectrum of a 10 μm diameter DBRTD

Figure 4 shows a power of $23\mu\text{W}$ from a $10\mu\text{m}$ diameter device at 75GHz for a whisker contacted DBRTD. This result was achieved after careful positioning of the device in the cavity and after tuning using a backshort. It is notable that this result compares favourably with the maximum power reported at W-band from a DBRTD device [9].

Power Combining

To compensate for the modest output power of individual DBRTDs various power combining strategies have been investigated. The approach reported on here is a modification of the Kurokawa-Magalhaes combiner [10]. The important modifications are that the devices are mounted in Sharpless-style packages [11] (Figure 5) and the necessary phase separation between devices is achieved by using appropriate length spacers which are themselves simply sections of waveguide. The separation is half the wavelength in the guide at the oscillation frequency.

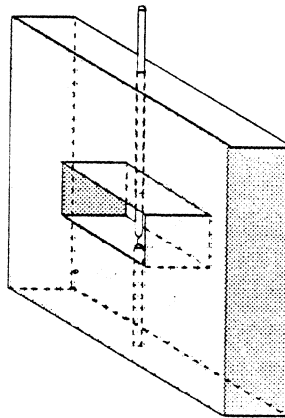


Figure 5 Schematic of a W-band package

The device cavity consists of a section of quarter height W-band waveguide with an array of $10\mu\text{m}$ dia. DBRTDs on a chip mounted on a pin protruding through the bottom wall of the guide. The whisker consists of a $10\mu\text{m}$ diameter phosphor-bronze wire $250\mu\text{m}$ long mounted on an insulated pin protruding through the top wall of the guide. The DBRTDs are placed centrally at the bottom of the waveguide sections which ensures stronger coupling between neighbouring devices compared to the original Kurokawa design. Coherent combining results from the injection locking of two strongly coupled devices oscillating at the same frequencies. Investigation of the electromagnetic environment in the immediate vicinity of the device has been undertaken using the High Frequency Structure Simulator (HFSS) software package from Hewlett Packard. These investigations reveal that the electromagnetic field disturbance is restricted to a region of $500\mu\text{m}$ around the device which equates to approximately 10% of the wavelength in the guide at this frequency.

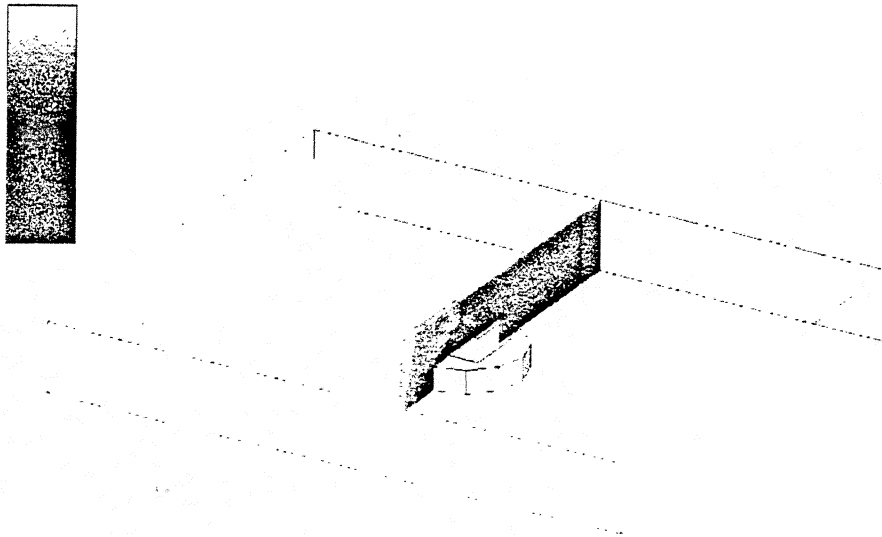


Figure 6 Electric field distribution near DBRTD in reduced height waveguide. lighter areas denote higher fields.

Figure 6 illustrates the results of this simulation. The electromagnetic field modelling reveals the sensitivity of the electric field at the device to its position with respect to the top wall of the waveguide; as a result care was taken to position each device accurately in its cavity to achieve an operating frequency similar to its neighbours.

In the example of the combiner pictured in Figure 7, the oscillation frequencies of adjacent DBRTDs are adjusted by slight variations to the bias of each device. This is possible due to the relatively low "Q" of the cavity afforded by the Sharpless package (as used in the above example). This typically permits the frequency of either DBRTD to be varied by about $\pm 300\text{MHz}$ for a 200mV variation in bias.

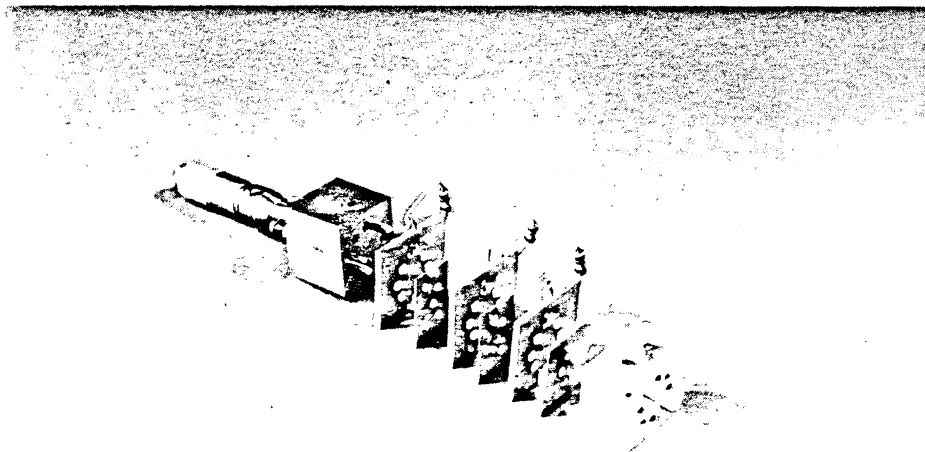


Figure 7 W-band power combiner with devices ready for assembly

Figure 8 shows the output spectra of two DBRTD's before and after combining and shows that the combined output power is quadrupled over that produced by a single device (the unmarked peaks represent alias of the real signals and are artifacts of the process used to acquire the spectra). The extra power produced over and above that of the straightforward addition of the individual device powers is thought to arise from the more favourable impedance seen by either device as a result of the shunting effect of its neighbours.

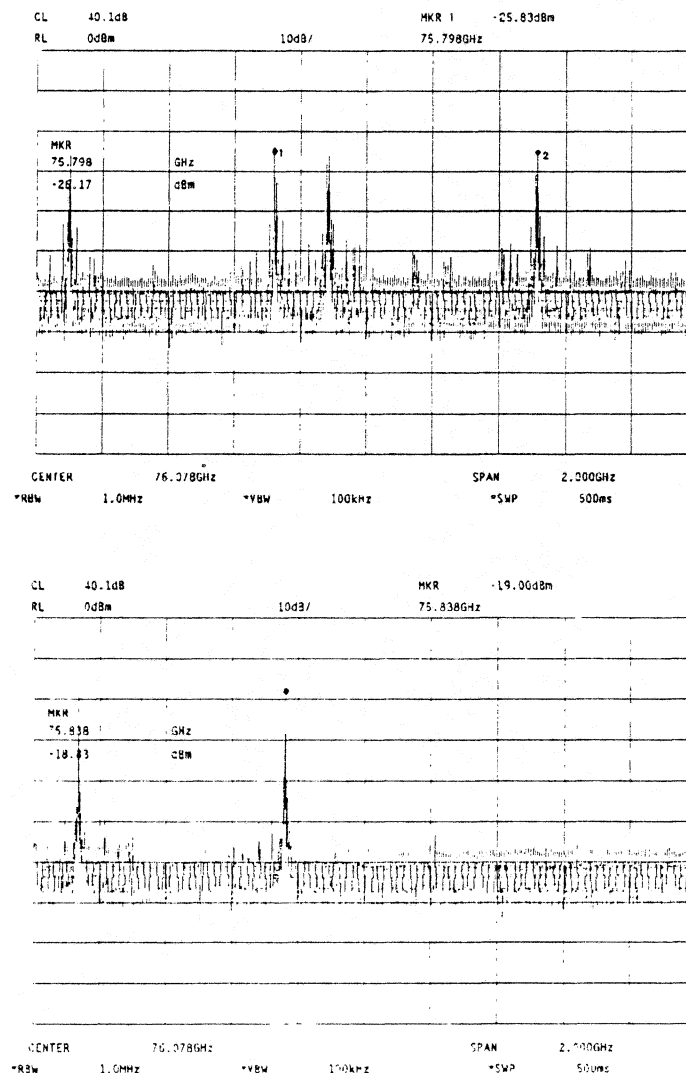


Figure 8 Output spectrum of two DBRTD's before (top) and after combining (bottom).

It is worth noting that the two devices shown in Figure 8 do not produce nearly as much power as the device shown in Figure 4 and this is due to later refinements in the match for this device-cavity combination. Efforts are underway to improve this match still further, and then to combine these improved devices in a similar way to those of Figure 8.

Conclusions

Power combining has been achieved using two DBRTDs and has quadrupled the output power available from a single device. A power of $23\mu\text{W}$ has been measured for a single device and attempts are being made to combine the output of these improved devices.

In the future, the development of planar devices and circuits should increase the control over matching conditions and further improve the output power of individual devices. This is especially important at higher frequencies such as G-band (140-220GHz) and will involve the integration of devices on stripline and other circuits.

Acknowledgements:

The Science and Engineering Research Council for the financial support to enable the work reported here to be carried out under the grants; GR/H-59497, GR/H-59503 and GR/H-96997.

The mechanical workshop at the University of Leeds, Department of Electronic and Electrical Engineering and especially Mr T Moseley for the fine machining of the reduced height W-band cavities.

The SERC III-V Semiconductor processing facility at the University of Sheffield, Department of Electrical and Electronic Engineering and especially Dr G Hill and Mr M Pate for carrying out various processing stages in the fabrication of the DBRTDs mentioned here.

References:

- [1] Brown, E.R. Söderström, J.R. Parker, C.D. Mahoney, L.J. Molvar, K.M. McGill, T.C. (1991). Oscillations up to 712GHz in InAs/AlSb resonant tunneling diodes. *Appl. Phys. Lett.* **58**(20), 2291-2293.
- [2] Sollner, T.C.L.G., Brown, E.R., Goodhue, W.D. & Le, H.Q. (1987). Observation of Millimeter wave oscillators from resonant tunneling diodes and some theoretical considerations of ultimate frequency limits. *Appl. Phys. Lett.* **50**(6), 322-334.
- [3] Brown, E.R., Sollner, T.C.L.G., Parker, C.D., Goodhue, W.D. & Chen, C.L. (1989). Oscillations up to 420 GHz in GaAs/AlAs resonant tunneling diodes E. R. Brown. *Appl. Phys. Lett.* **55**(17), 1777-1779.
- [4] Javalagi, S. Reddy, V. Gullapalli, K. and Neikirk, D. (1992). High Efficiency Microwave Diode Oscillators. *Electronics Letters.* **28**(18), 1699-1701
- [5] Sollner, T.C.L.G., Goodhue, W. D., Tannenwald, P.E., Parker, C.D. & Peck, D.D. (1983). Resonant tunnelling through quantum wells at frequencies up to 2.5 Thz. *Appl. Phys. Lett.* **43**(6), 588-590.
- [6] Chang, K. and Sun, C. (1983). Millimetre-wave power combining. *IEEE Trans. Microwave Theory Tech.* **31**(2). 91-107.
- [7] Esaki., L. (1958). New phenomena in narrow germanium p-n junctions. *Phys. Rev.* **109**, 603.
- [8] Steenson, D. P. (1993). The High-Frequency Application of Double-Barrier Resonant Tunnelling Diodes. *PhD Thesis. University of Nottingham.*
- [9] Rydberg, A., Grönqvist, H. & Kollberg, E. (1988). A theoretical and experimental investigation on millimeter-wave quantum well oscillators. *Microwave & Optical Technol. Lett.* **1**(9), 333-336.
- [10] Kurokawa, K. and Magalhaes, F.M. (1971). An X-band 10-Watt multiple-IMPATT Oscillator. *Proc. IEEE* **59**(1), 102-103.
- [11] Sharpless, W.M. (1956). Wafer-type Millimetre wave rectifiers. *Bell Syst. Tech. J.* **35**, 1385-1402.

AN ELECTRO-OPTIC ATTENUATOR FOR TERAHERTZ FREQUENCIES

Guillermo F. Delgado[†], Stellan W. Jacobsson[‡], Joakim F. Johansson[†]

[†] Department of Radio and Space Science
with Onsala Space Observatory

[‡] Department of Microwave Technology

Chalmers University of Technology
S-412 96 Gothenburg
Sweden

ABSTRACT

At Gigahertz and Terahertz frequencies the signals are commonly handled quasi-optically. Thus, a large number of devices have been developed to perform various manipulations of the signals. However, simple devices for fast and continuous power attenuation of a Gaussian beam are still lacking.

We have previously shown that a 100 GHz quasi-optical beam can effectively be attenuated by means of generation of excess carrier densities under photonic excitation of a semiconductor material at room temperature. The particular material used was a molecular beam epitaxy (MBE) engineered III-V semiconductor. The photonic excitation was achieved by illuminating the MBE material with an infrared LED.

Here, we present a further investigation of the same material into the THz region. A polarising Michelson Fourier transform spectrometer was used to characterise the material between 0.5 and 8 THz. The material was found to modulate over the region between 0.5 and 5 THz and have a modulation depth, in transmission mode, of more than 3 dB between 0.5 and 2.5 THz.

1. INTRODUCTION

Presently the technology of sub-millimeter waves has been pushed towards the *last frontier*, i.e. the Terahertz range. This development has been partly supported by natural extensions of the mature techniques developed and improved for the sub-millimeter wave range.

Due to the short wavelengths at the THz frequencies, and high losses in conventional guided wave systems, there has been a need to use extensively quasi-optical techniques, and this has been done with a lot of success. In fact almost all the signal processing at these frequencies is done quasi-optically.

One particular area of the quasi-optical handling that lacks a good and simple solution (at these frequencies as well as at lower frequencies), is continuous attenuation of a Gaussian beam. There are some solutions to this problem, but they involve the use of interferometric devices with moving grids or reflecting planes, and while they might work quite well at lower frequencies, the sizes involved become so small at higher frequencies that a practical mechanical device becomes too difficult or expensive to manufacture.

Of course there are more crude approaches like the use of graduated filters, more or less in the same way as in the optical regime, but these solutions are not applicable if the desire is to have a continuous power control.

Recently there have been some reports of a completely quasi-optical electro-optic control of a Gaussian beam [1, 2] at millimeter wavelengths (70 and 100 GHz). The material used in both cases is a molecular beam epitaxy (MBE) engineered III-V semiconductor [3]. Since the physical principle involved in these modulators has no theoretical limit towards the THz region we initiated a deeper study of the potential of this material as a modulator for this region of the spectrum.

2. THEORY

The MBE grown structure consists of 44 $\text{In}_{0.2}\text{Ga}_{0.8}\text{As}$ quantum wells (QW), each 6.5 nm thick, separated by 78 nm thick GaAs barriers. In the centre of each GaAs barrier, a Be-doped plane (p-type) with a sheet density of $9 \cdot 10^{16} \text{ m}^{-2}$ is inserted. On both sides of the QWs, using 10 nm thick spacer layers, Si-doping planes (n-type) with sheet densities of $3 \cdot 10^{16} \text{ m}^{-2}$ are inserted. The excess hole concentration locates the Fermi level sufficiently far below the electron ground state in the QWs to ensure that the QWs are essentially free from electrons under thermal equilibrium.

During electron-hole pair generation, electrons will be attracted to the QWs and the holes to the barrier region midway between the wells, resulting in their spatial separation. This spatial separation of the carriers reduces the recombination rate and thus large densities of electrons can be established in the QWs using low excitation densities.

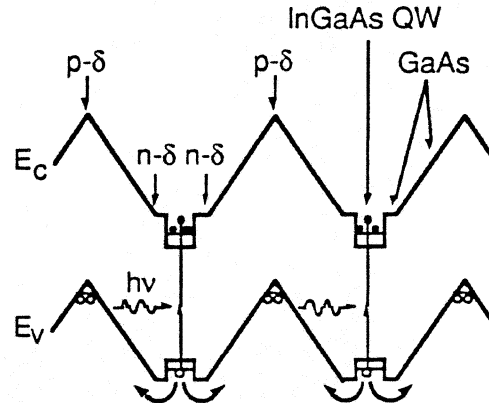


Figure 1. Energy band diagram for the periodically doped InGaAs/GaAs MQW sample showing the spatial separation (figure kindly provided by Professor Anders Larsson).

The structure has been described elsewhere, as well as its main properties at near IR wavelengths [3, 4, 5].

For a TEM wave propagating through a two dielectric layered medium, the ratio for the reflected and transmitted field to the incident field is given by

$$\frac{E_R}{E_0} = \frac{\Gamma_{01} + \Gamma_{12} \left(e^{-j2\kappa_1 t_1} + \Gamma_{01} \Gamma_{20} e^{-j2\kappa_2 t_2} \right) + \Gamma_{20} e^{-j2(\kappa_1 t_1 + \kappa_2 t_2)}}{1 + \Gamma_{12} \left(\Gamma_{01} e^{-j2\kappa_1 t_1} + \Gamma_{20} e^{-j2\kappa_2 t_2} \right) + \Gamma_{01} \Gamma_{20} e^{-j2(\kappa_1 t_1 + \kappa_2 t_2)}} e^{j2\kappa_0 t_1} \quad (1)$$

$$\frac{E_T}{E_0} = \frac{(1 + \Gamma_{01})(1 + \Gamma_{12})(1 + \Gamma_{20})}{1 + \Gamma_{12}(\Gamma_{01} e^{-j2\kappa_1 t_1} + \Gamma_{20} e^{-j2\kappa_2 t_2}) + \Gamma_{01} \Gamma_{20} e^{-j2(\kappa_1 t_1 + \kappa_2 t_2)}} e^{-j(\kappa_1 - \kappa_0)t_1} e^{-j(\kappa_2 - \kappa_0)t_2} \quad (2)$$

where Γ_{01} , Γ_{12} and Γ_{20} refer to the reflection coefficients at the boundaries between air (subscript 0), first dielectric (subscript 1), and second dielectric (subscript 2).

$$\Gamma_{01} = \frac{\kappa_0 - \kappa_1}{\kappa_0 + \kappa_1} = \frac{1 - \sqrt{\epsilon_1}}{1 + \sqrt{\epsilon_1}} \quad (3)$$

$$\Gamma_{12} = \frac{\kappa_1 - \kappa_2}{\kappa_1 + \kappa_2} = \frac{\sqrt{\epsilon_1} - \sqrt{\epsilon_2}}{\sqrt{\epsilon_1} + \sqrt{\epsilon_2}} \quad (4)$$

$$\Gamma_{20} = \frac{\kappa_2 - \kappa_0}{\kappa_2 + \kappa_0} = \frac{\sqrt{\epsilon_2} - 1}{\sqrt{\epsilon_2} + 1} \quad (5)$$

Here, the magnitude of the wave vector is dependent of the relative dielectric constant of the material:

$$\kappa_i = \kappa_0 \sqrt{\epsilon_i} = \kappa_0 n_i \quad (6)$$

where n_i is the complex refractive index of the material.

The geometry of the problem is shown in Figure 2, together with the relevant parameters.

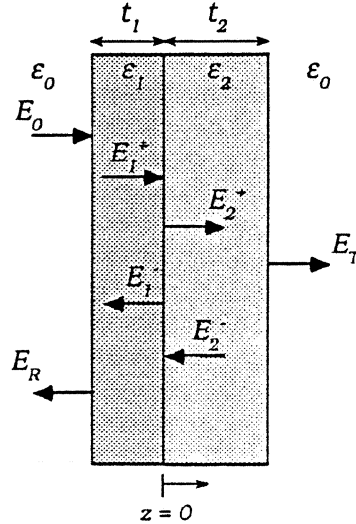


Figure 2. Geometry of the problem with the associated electric fields and relevant parameters

In a semiconductor material the conductivity is given as a function of the carrier density N_e , the electron charge e , the average relaxation time T_m , and the effective mass of the carriers m_e^* (effective electron mass in GaAs):

$$\sigma = \frac{N_e e^2 \langle T_m \rangle}{m_e^*} \quad (7)$$

Relation (7) is valid provided that we assume that only electrons contribute to the charge transport (current). This holds since the mobility of holes in GaAs is nearly 20 times lower than the one for electrons.

In the active region of the semiconductor the average relaxation time, T_m , is a complex function of the frequency of the incident radiation, ω , and the effective relaxation time, τ_m .

$$\langle T_m \rangle = \frac{1}{\frac{1}{\tau_m} + j\omega} = \frac{\tau_m}{1 + (\omega \tau_m)^2} - j \frac{\omega \tau_m^2}{1 + (\omega \tau_m)^2} \quad (8)$$

The former is just an alternative formulation of the classic Drude model for free electrons that can be applied to the doped semiconductor case, and where τ_m is defined as

$$\frac{1}{\tau_m} = \frac{1}{\tau_{life}} + \frac{1}{\tau_{coll}} \quad (9)$$

with τ_{life} the carrier lifetime (which is of the order of milliseconds in this material [1, 6]), and τ_{coll} is the collision time for the carriers (of the order of femtoseconds in GaAs [7]). We see that since the carrier lifetime is so long in the material used, the relaxation time will be dominated by the collision time.

Combining (7) and (9), we have that the complex conductivity can be expressed as

$$\sigma(N_e, \omega) = \frac{N_e e^2}{\frac{m_e^*}{\tau_{coll}} + j\omega m_e^*} = \frac{N_e e^2 \tau_{coll}}{m_e^* [1 + (\omega \tau_{coll})^2]} - j \frac{N_e e^2 \omega \tau_{coll}^2}{m_e^* [1 + (\omega \tau_{coll})^2]} \quad (10)$$

In a lossy dielectric the relative permittivity is given by

$$\tilde{\epsilon}_r = \epsilon_r - j \frac{\sigma}{\epsilon_0 \omega} \quad (11)$$

Using (10) in (11) we can summarise our results in

$$\tilde{\epsilon}_r(N_e, \omega) = \epsilon_r - \frac{N_e e^2 \tau_{coll}^2}{m_e^* \epsilon_0 [1 + (\omega \tau_{coll})^2]} - j \frac{N_e e^2 \tau_{coll}}{m_e^* \epsilon_0 \omega [1 + (\omega \tau_{coll})^2]} \quad (12)$$

In order to get simpler approximations of (12), we should check the value of the product $\omega \tau_{coll}$. Using $\tau_{coll} = 200$ fs, we have that the turn-over point is close to 800 GHz, so in the low Terahertz range we have to use the complete expression.

From equations (1) to (5) and the value of the complex relative permittivity obtained in (12), it is clear that the reflection and transmission properties of the *nipi* MQW material will be functions of the semiconductor properties like scattering time, effective mass of the carriers, and relative dielectric constant of the base material. But, most important for our work, they will also be functions of the frequency and of the free carrier density. Now, assuming that we work at a fixed frequency — or rather a narrow frequency range —, we find that the optical properties of the material can be effectively changed by modulating the carrier density and this is in turn done by modulating the IR optical power incident on the *nipi* MQW structure.

3. MEASUREMENT TECHNIQUE

Fourier transform spectroscopy (FTS) is a well known general spectrometric method. The spectrum is obtained via a numerical Fourier transformation of a recorded interferogram obtained by a two-beam interferometer (e.g. Michelson) [8, 9]. The FTS concept is applicable in any part of the electromagnetic spectrum, although the majority of the spectrometers work at the longer wavelength side of the visible part of the spectrum.

The signal source is a mercury lamp, known to emit an excess of power in the millimeter and submillimeter part of the spectrum. The beam from the mercury lamp is collimated and equally divided, by wire grid polarizers, between the two arms of the interferometer. The interferogram is obtained by step-wise moving one of the mirrors in the interferometer to a large number of equidistant positions. In each position the power impinging on the detector is sampled. By numerical Fourier transformation of the interferogram the power spectrum is obtained. The total optical path length the mirror has travelled during the measurement determines the spectral resolution, whereas the distance between the sampling positions determines the maximum frequency. In order to improve the signal-to-noise ratio and to separate the signal from the background, phase modulation is used. This is accomplished by vibrating (≈ 30 Hz) the mirror (in the fixed arm of the interferometer) in order to introduce a small path length modulation. The phase modulation is wavelength dependent and creates nulls in the calculated spectra at frequencies corresponding to vibration amplitudes equal to half a wavelength (in the measurements done for this paper, the nulls are located outside the frequency range of interest). The interference signal is detected and later demodulated by a lock-in amplifier.

The particular spectrometer (Graseby SPECAC Ltd.) used in this study is of the polarising Michelson type and can be used between (approximately) 100 GHz and 30 THz. The useful spectral range is determined by the power emitted by the mercury lamp, but also on the particular detector and window materials being used. The spectrometer has a maximum obtainable resolution of 0.75 GHz (corresponding to a 0.2 m maximum travelling range of the movable interferometer arm). The sample chamber can be evacuated to avoid water vapour absorption.

The *nipi* MQW sample under test and the IR illuminator for the structure were mounted in the evacuated test compartment. By flipping a mirror, either the transmission or reflection could be measured. A Golay cell was used as a detector. A filter arrangement was used to protect the *nipi* structure from being illuminated by the UV, visible and IR emission from the mercury lamp. The measurements are differential in the sense that the transmission (or reflection) is obtained by normalizing the sample spectrum to a reference spectrum.

The reference spectra were taken without the sample, but keeping the rest of the set-up, including the protection filters in front of the sample. For the reflection reference we used a polished copper mirror (10 μm RMS).

Each one of the measured spectra comprised two independent ones; one of 20 minutes and a second one of 60 minutes, thus giving a total integration time of 80 minutes for each spectrum. The "short" spectrum was used as a reference to check any possible deviation of the "long" one. In every case the agreement between them was excellent.

The sample was measured twice: a *dark* measurement, i.e. the sample without any light excitation, and a *illuminated* measurement, i.e. the sample illuminated with an IR power density of the order of 200 Wm^{-2} (100 mA forward current on a commercial IR LED: Texas Instruments TIL 31B)

4. RESULTS

4.1 Transmission

In Figure 3 we have the result of the series of measurements done in transmission mode. We can see that the modulator ceases to respond at a frequency around 5.5 THz, defining the absolute limit for this device.

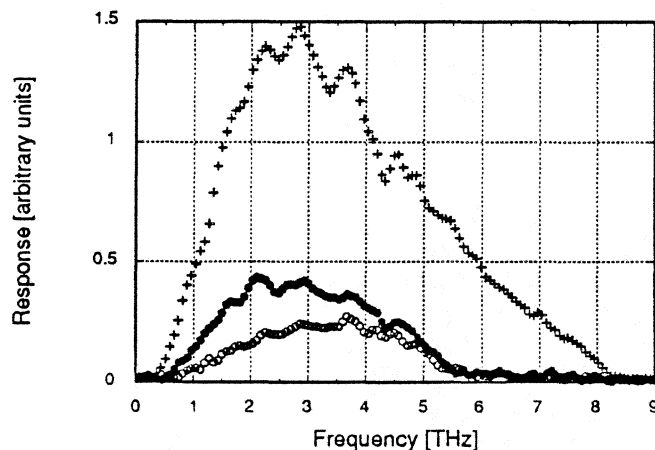


Figure 3. Response of a nipi MQW structure to different illumination levels in transmission mode. The upper curve (crosses) represents the reference, the second one (filled circles) the dark response, and the last one (open circles) the illuminated response.

The modulation depth for this mode is shown in Figure 4. We can see that for frequencies between 0.5 and 5 THz the device modulates more than 1 dB and for frequencies between 0.5 and 2.5 THz the modulation depth is better than 3 dB, reaching a maximum modulation depth between 5 and 6 dB in the lower frequency range.

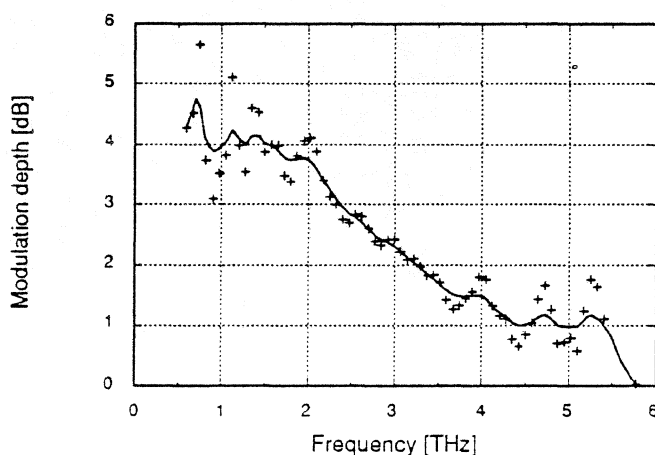


Figure 4. Modulation depth in transmission mode for a nipi MQW structure.

The insertion loss is shown in Figure 5 where it is possible to see that in the range where the device gives better performance (0.5 to 2.5 THz), the losses are of the order of 4-5 dB, being rather flat around the frequency range between 1 and 5 THz.

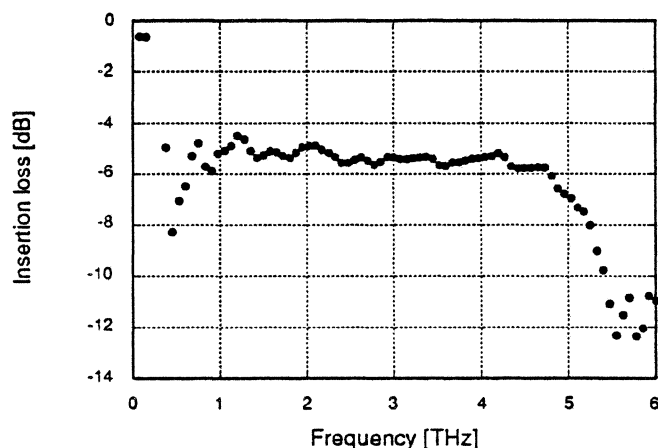


Figure 5. Insertion loss in transmission mode for a nipi MQW structure.

4.2 Reflection

Figure 6 gives the result of the series of measurements done in reflection mode. This time we cannot see a cut-off for the modulator response before the cut-off of the sensitivity of the Golay cell in the FTS. Note that in this case we have less attenuation when the sample is illuminated.

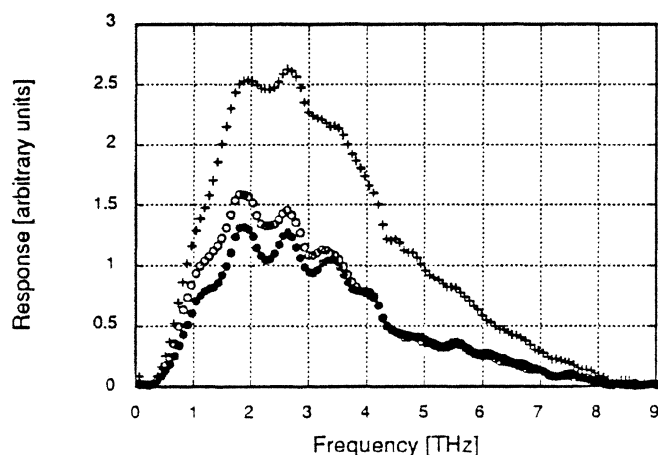


Figure 6. Response of a nipi MQW structure to different illumination levels in reflection mode. The upper curve (crosses) represents the reference, the second one (open circles) the illuminated response, and the last one (filled circles) the dark response.

The modulation depth observed for this mode is shown in Figure 7. It can be seen that this device does not offer that much of modulation working in reflection mode, hardly reaching 2 dB at the lower frequency side and going below 1 dB of modulation at around 1.5 THz.

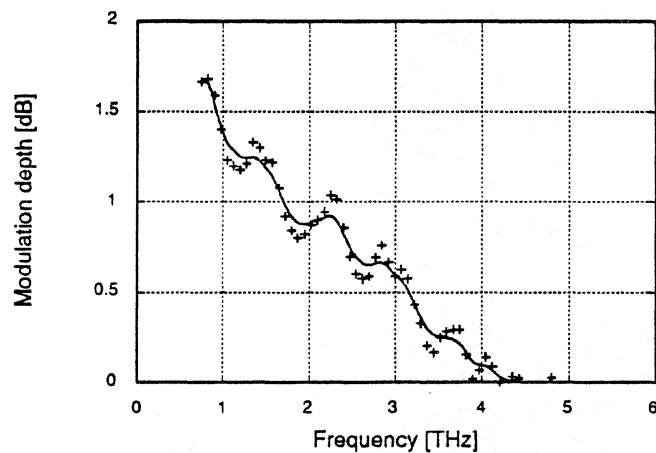


Figure 7. Modulation depth in reflection mode for a nipi MQW structure

Finally, the reflection loss is shown in Figure 8 where we can see that, for this mode of operation, the device offer a small advantage compared with the transmission mode since the losses are of the order of 3-4 dB.

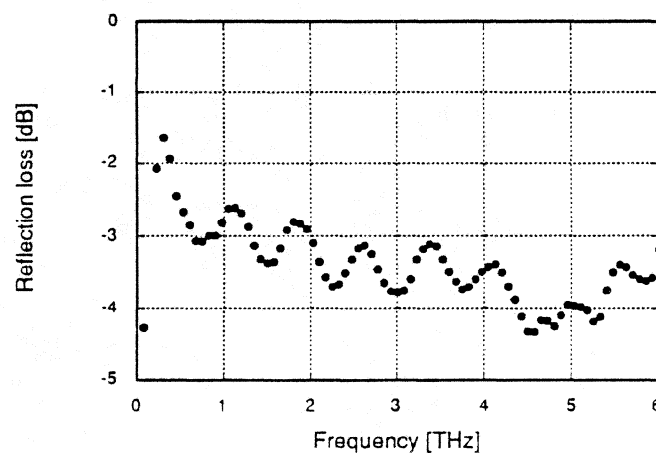


Figure 8. Reflection loss in reflection mode for a nipi MQW structure

5. DISCUSSION AND CONCLUSIONS

We have investigated the possibilities of using a *nipi* MQW engineered material as a continuously adjustable quasi-optical attenuator at Terahertz frequencies. The device achieves electro-optic modulation from 0.5 up to 5 THz and this modulation is better than 3 dB over the range of 0.5 to 2.5 THz in transmission mode.

The losses found in the material are moderately large (of the order of 4 dB) and is something that can be improved by, for example, reducing the thickness of the GaAs substrate [2].

The use of this type of material, provided that the losses can be afforded, fills a gap in the range of quasi-optical devices used for signal handling at Terahertz frequencies. The power control is achieved by the use of a commercial IR LED (TIL 31B) and very low optical power levels (6 mW @ 100 mA of forward current through the IR LED) are needed due to the long carrier lifetime inherent to this *nipi* MQW material

Possibly, the modulation depth can be improved by increasing the IR optical power density on the *nipi* MQW structure, but due to mechanical constraints in the sample holder, the distance between the sample and the IR LED was too large in our case, yielding an IR optical power density about half of the one required to generate all the free carriers available.

6. ACKNOWLEDGEMENTS

The authors want to thank Professor Anders G. Larsson at the Dept. of Optoelectronics and Electrical Measurements, Chalmers University of Technology (CTH), for designing the material and being a very helpful discussion partner. Dr. Thorvald Andersson at the MBE Group, Physics Dept., CTH is gratefully acknowledged for providing the MBE engineered sample.

7. REFERENCES

- [1] G. Delgado and J. Johansson, "Electro-optic power control of a millimeter wave Gaussian beam," to be published in *Proc. Intl. Conf. on mm and sub-mm Waves and Appl.*, SPIE, San Diego, January 1994.
- [2] A. Kost, L. West, T. Hasenberg, J. White, and M. Matloubian, "Optical control of microwaves with semiconductor *n-i-p-i* structures," *Appl. Phys. Lett.*, Vol. 63, No. 25, pp. 3494-3496, December 1993.
- [3] A.G. Larsson and J. Maserjian, "Molecular beam epitaxy engineered III-V semiconductor structures for low-power optically addressed spatial light modulators," *Opt. Eng.*, Vol. 31, No. 7, pp. 1576-1582, July 1992.
- [4] J. Maserjian, P. Andersson, B. Hancock, J. Iannelli, S. Eng, F. Grunthaner, K. Law, P. Holtz, R. Simes, L. Coldren, A. Gossard, and J. Merz, "Optically addressed spatial light modulators by MBE-grown *nipi* MQW structures," *Appl. Opt.*, Vol. 28, No. 22, pp. 4801-4807, November 1989.
- [5] A. Larsson, and J. Maserjian, "Optically Induced Absorption Modulation in a periodically δ -doped InGaAs/GaAs Multiple Quantum Well Structure," *Appl. Phys. Lett.*, Vol. 58, No. 10, pp. 1946-1948, 1991.

- [6] B. Jonsson, A. Larsson, O. Sjölund, S. Wang, T. Andersson, and J. Maserjian, "Carrier Recombination in a Periodically δ -doped Multiple Quantum Well Structure," *Technical Report No. TR 92308*, Department of Optoelectronics and Electrical Measurements, Chalmers University of Technology, Gothenburg, Sweden, 1992.
- [7] S. Sze, **Physics of Semiconductors Devices**, 2nd Ed., Wiley-Interscience Publication, 1981.
- [8] D. Martin, "Polarising (Martin-Puplett) interferometric spectrometers for the near- and submillimeter spectra", in **Infrared and millimeter waves: Systems and components**, Vol. 6, Ed. K.J. Button, Academic Press, 1982.
- [9] J. Chamberlain, **The principles of interferometric spectroscopy**, Wiley, 1979.

Off-Axis Imaging Properties of Substrate Lens Antennas

Daniel F. Filipovic, George V. Eleftheriades and Gabriel M. Rebeiz

NASA/Center for Space Terahertz Technology
Electrical Engineering and Computer Science Department
University of Michigan
Ann Arbor, MI 48109-2122

ABSTRACT

In this paper, the theoretical far-field patterns and Gaussian-beam coupling efficiencies are investigated for a double-slot antenna placed off-axis on extended hemispherical silicon and quartz lenses. Measured off-axis radiation patterns at 258GHz agree well with the theory. Results are presented which show all important parameters versus off-axis displacement: scan angle, directivity, Gaussicity, and reflection loss. Directivity contour plots are also presented which show that near diffraction-limited performance can be achieved at off-axis positions at non-elliptical extension lengths.

I. INTRODUCTION

A convenient method to eliminate substrate modes with integrated antennas is to place the antenna on a substrate lens. If the substrate lens has the same dielectric constant as the planar antenna wafer, then substrate modes will not exist. In addition, antennas placed on substrate lenses tend to radiate most of their power into the lens side, making the pattern unidirectional on high dielectric constant lenses. The ratio of powers between the dielectric and air is approximately $\epsilon_r^{3/2}$ for slot and dipole-type antennas, where ϵ_r is the relative dielectric constant of the lens. The substrate lens is an attractive solution for millimeter-wave antennas, since it also provides mechanical rigidity and thermal stability.

Previous investigations [1,2,3,4] have shown that the directivity of the substrate lens can be controlled by increasing or decreasing the extension length. In particular, as the extension length increases from the hyperhemispherical length (R/n , where R is the radius and

n is the index of refraction of the lens), the directivity increases until it reaches a maximum diffraction-limited value. At the extension length which realizes maximum directivity, the extended hemispherical lens has a surface which approximates an elliptical lens, with the planar antenna at the more distant focus.

While the directivity increases at higher extension lengths, the pattern-to-pattern coupling value to a fundamental Gaussian-beam (Gaussicity) decreases [1]. Since the double-slot feed antenna used in these studies launches a nearly perfect fundamental Gaussian-beam into the substrate lens, the Gaussicity can also be thought of as a measure of the aberrations introduced by the lens. For extension lengths up to the hyperhemispherical position the Gaussicity is close to 100%. This is expected since the hyperhemispherical lens is aplanatic, implying the absence of spherical aberrations, and satisfies the sine condition, which guarantees the absence of circular coma [5]. As the extension length increases past R/n , the Gaussicity continuously decreases, which implies the introduction of more and more aberrations. In addition, the reflection loss typically increases after the hyperhemispherical extension length (depending on the beamwidth of the feed antenna). The total power coupling into the antenna, termed the Gaussian-coupling efficiency, is the product of the Gaussicity and all losses (reflection loss, dielectric loss, backside loss, etc.). This implies that the Gaussian-coupling efficiency decreases after the hyperhemispherical extension length (R/n). Calculations in [1] and [3] indicate that for an intermediate position between the hyperhemispherical and diffraction-limited extension lengths, the Gaussian-coupling efficiency decreases by a small amount ($< 10\%$), while the directivity is close to that of the diffraction-limited case.

If the substrate lens is to be used with an imaging array, it is necessary to characterize its off-axis performance (Fig. 1). A ray-optics/field-integration formulation similar to that described in [2] is used to solve for the radiation patterns and Gaussian-coupling efficiencies.

II. THEORETICAL CALCULATIONS

The resulting scan angle for a displacement off-axis (D/R , where D is the distance off-axis and R is the radius of the lens) is shown in Figure 2 at three different extension lengths

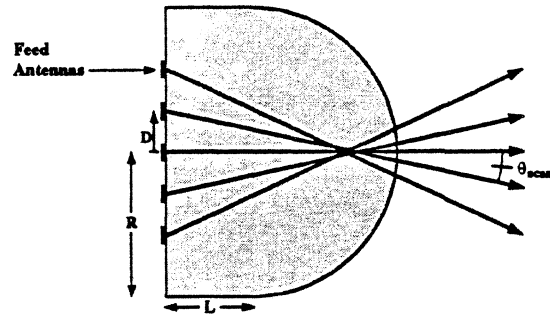


Figure 1: Imaging Array on Extended Hemispherical Lens

(L/R , where L is the extension length): hyperhemispherical, intermediate, and synth. ellipse (diffraction-limited position), and for both silicon ($\epsilon_r=11.7$) and quartz ($\epsilon_r=3.8$) dielectric lenses. As expected, for a given D/R off-axis, a silicon dielectric lens will have a larger scan angle than the quartz lens due to its higher dielectric constant. Also, note that the off-axis positions are not dependent on the wavelengths away from the center, but on the percentage of the lens radius.

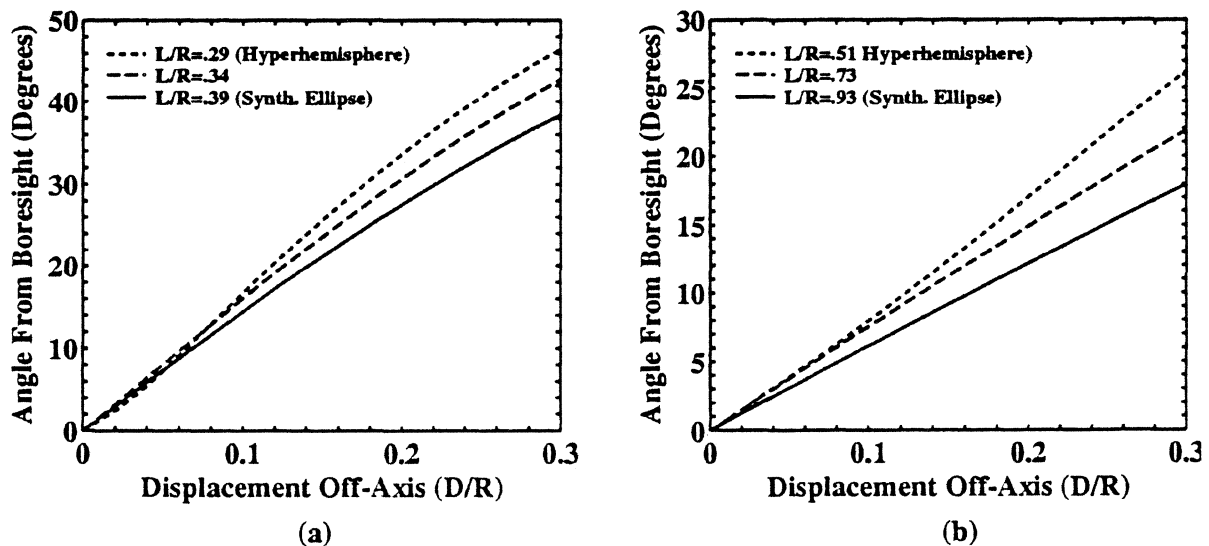


Figure 2: Scan angle versus off-axis displacement at fixed extension lengths for a silicon (a) and a quartz (b) lens.

The effect of an off-axis displacement in the H-plane at the hyperhemispherical po-

sition ($L/R=0.29$) for a 12λ -diameter silicon lens is shown in Figure 3. It is interesting to see that the patterns become sharper, and achieve a maximum directivity of 29.6dB at $D/R=0.24$, after which the directivity begins to slowly decrease. Therefore diffraction-limited performance can be nearly achieved by either increasing the extension length on-axis past the hyperhemispherical position, or by moving the feed antenna position off-axis in the hyperhemispherical plane. This can best be seen by the directivity contour plots for silicon and quartz in Figure 4. Note that moving off-axis does not achieve the full diffraction limited performance possible, and in the case of the silicon lens in the hyperhemispherical plane, it is 1.2dB lower than the maximum possible on-axis directivity of 30.8dB at $L/R=0.38$.

Figure 5 shows the maximum Gaussicity plots for a 12λ -diameter silicon and quartz lens. To calculate the maximum Gaussicity, the Gaussian-beam waist and radius of curvature are optimized for each displacement off-axis. In addition, the phase center (the point through which the axis of the Gaussian-beam lies) is also changed to optimize the beam, however nearly the same result will be achieved if the phase center is assumed to be about $0.4R$ behind the tip of the lens (see Fig. 1). Note for off-axis displacements, that the Gaussicity drops the most in the hyperhemispherical plane and the least for the synthesized elliptical plane. In fact, for a 12λ -diameter quartz lens, the Gaussicity is a nearly constant 85% for off-axis displacements in the synthesized elliptical plane. Similar characteristics are observed in a 24λ -diameter silicon and quartz lens, and is shown in Figure 6. However, for the larger lens the decreases in Gaussicity are magnified (for the same reasons as explained in [1]).

To calculate the Gaussian-coupling efficiency it is necessary to know the reflection loss in addition to the Gaussicity. The reflection loss for silicon and quartz lenses (independent of frequency or physical lens radius) is shown in Figure 7 for off-axis displacements. Note that the reflection losses rapidly increase for a silicon lens after $D/R=0.1$, while quartz lenses can be used to $D/R=0.25$ with less than a 1dB increase in reflection loss. These curves are expected to be about 1.5dB lower for a silicon lens and 0.65dB lower for a quartz lens with a matching-cap layer.

III. EXPERIMENTAL RESULTS: PATTERNS

A three element linear array of double-slot antennas was fabricated and measured on a silicon substrate lens at 258GHz [6]. The lens radius is 6.858mm and the extension length is chosen to be $L=2.20\text{mm}$. The double-slot antenna design is similar to that in [1], but with integrated Schottky diodes replacing the bolometers. The slot antennas are chosen to be $0.30\lambda_0$ -long ($354\mu\text{m}$) with a separation of $0.16\lambda_0$ ($190\mu\text{m}$) where λ_0 is the free-space wavelength at 258GHz. The central antenna element is aligned to the center of the substrate lens, while the other two elements are $800\mu\text{m}$ and $1600\mu\text{m}$ off-axis in the H-Plane, respectively. The measured and theoretical H-plane patterns are shown in Figure 8. The agreement is quite good, predicting the scanned angle and even the -17dB sidelobe of the $800\mu\text{m}$ off-axis pattern. The deviation between experimental and theoretical patterns at the $1600\mu\text{m}$ off-axis position is most likely due to lens blockage and/or mount reflections at extreme angles.

IV. CONCLUSION

The well-known hyperhemispherical position (R/n) has the least aberrations and the best Gaussian-coupling efficiency. However, we have demonstrated that the hyperhemispherical plane is not the best extension length for imaging applications, since the directivity increases (and beamwidth decreases) by large values (9dB for a 12λ -diameter silicon lens) for off-axis displacements. For high off-axis Gaussian-coupling efficiencies, this would necessitate the use of narrower Gaussian-beams off-axis, an impossible consideration since most optical systems utilize nearly fixed beam parameters. It was found for different types of lenses, that an extension length just before the synthesized elliptical position maintains the directivity and the Gaussian-beam parameters the most constant.

REFERENCES

- [1] D.F. Filipovic, S.S. Gearhart and G.M. Rebeiz, "Double slot antennas on extended hemispherical and elliptical silicon dielectric lenses," *IEEE Trans. on Microwave Theory Tech.*, vol. 41, pp. 1738-1749, October 1991.
- [2] T.H. Büttgenbach, "An improved solution for integrated array optics in quasi-optical millimeter and submillimeter waves receivers: the hybrid antenna," *IEEE Trans. on Microwave Theory Tech.*, vol. 41, pp. 1750-1761, October 1991.
- [3] D.F. Filipovic and G.M. Rebeiz, "Double slot antennas on extended hemispherical and elliptical quartz dielectric lenses," *Int. J. Infrared Millimeter Waves*, vol. 14, pp. 1905-1924, October 1991.
- [4] G.V. Eleftheriades, "Double slot antennas on extended silicon lenses-general treatment," *University of Michigan Radiation Laboratory Report RL903*, February 1994.
- [5] M. Born and E. Wolf, *Principles of Optics*. New York: Permagon Press, pp. 252-252, 1959.
- [6] S.S. Gearhart and G.M. Rebeiz, "A monolithic 250GHz Shottky-diode receiver," to appear in the 1994 IEEE-MTT Symposium Issue, December 1994.

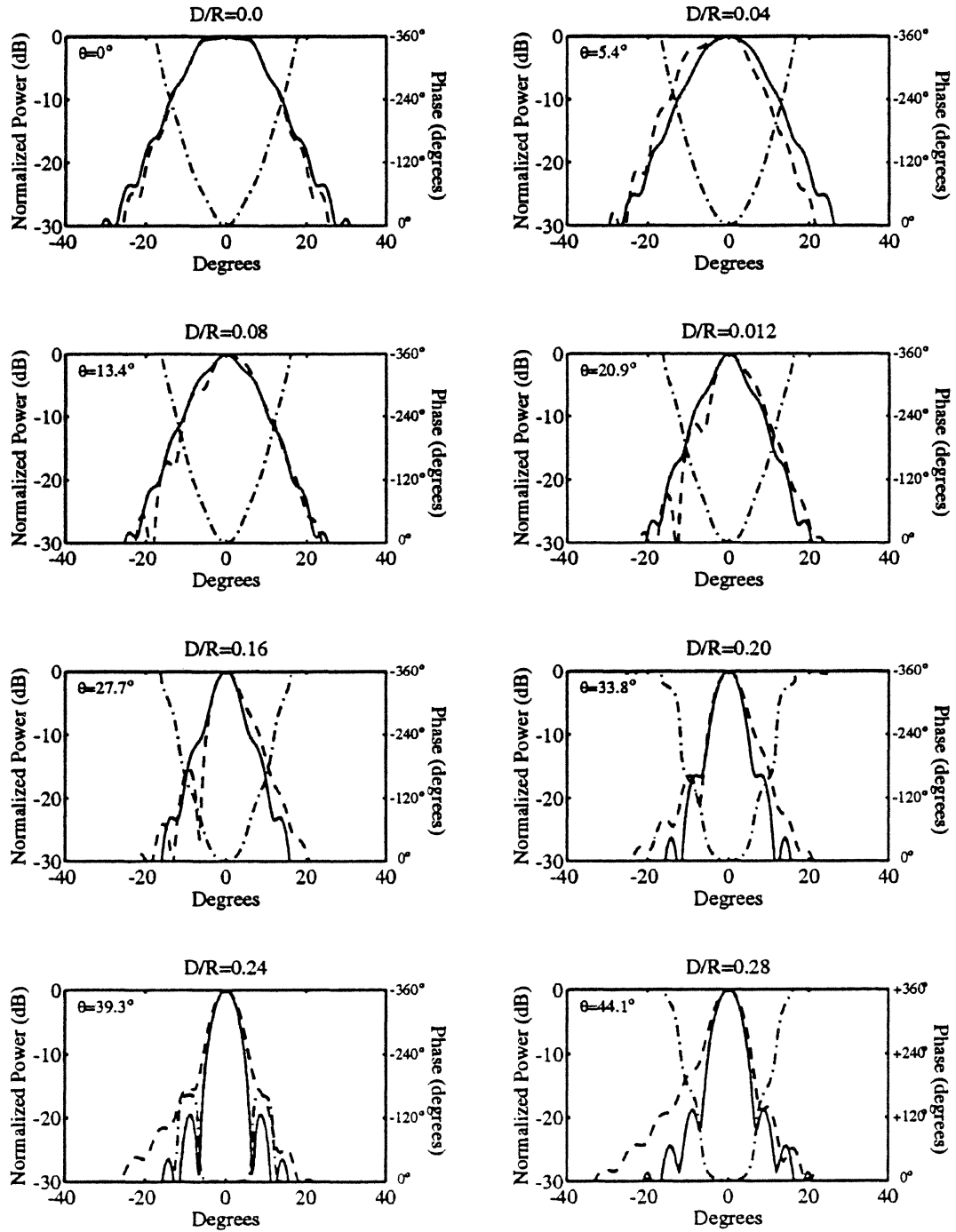


Figure 3: E and H-plane power patterns and H-plane phase for off-axis displacements in the H-plane at the hyperhemispherical extension length ($L/R=0.29$) for a 12λ -diameter silicon lens. The dashed/dotted line corresponds to the phase.

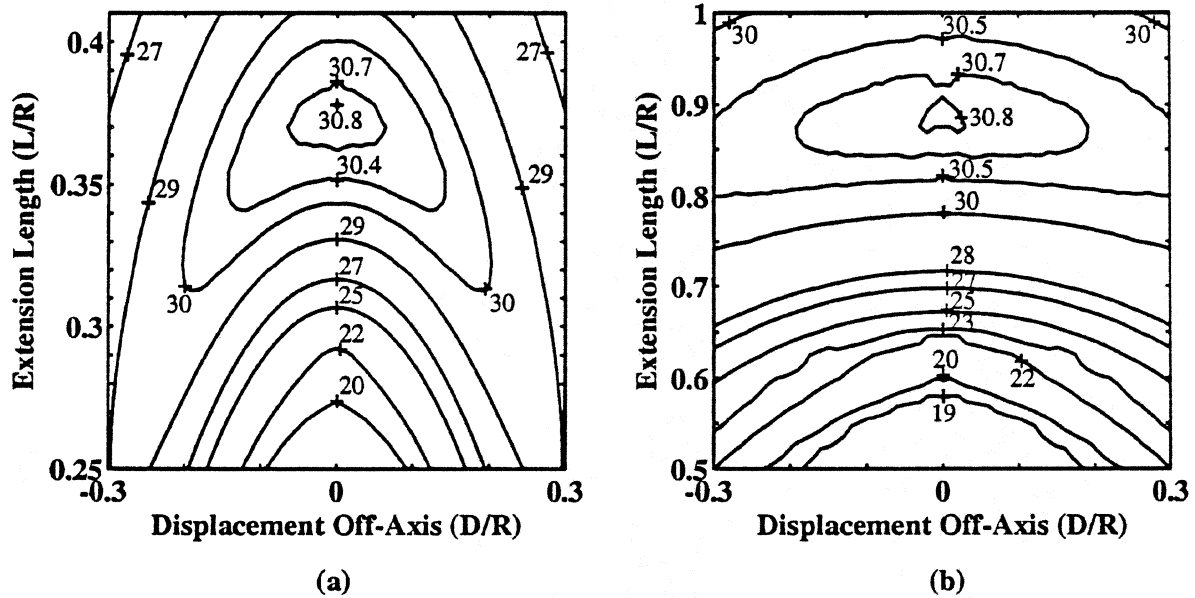


Figure 4: Directivity contour plots of silicon (a) and quartz (b) versus extension length and off-axis displacement.

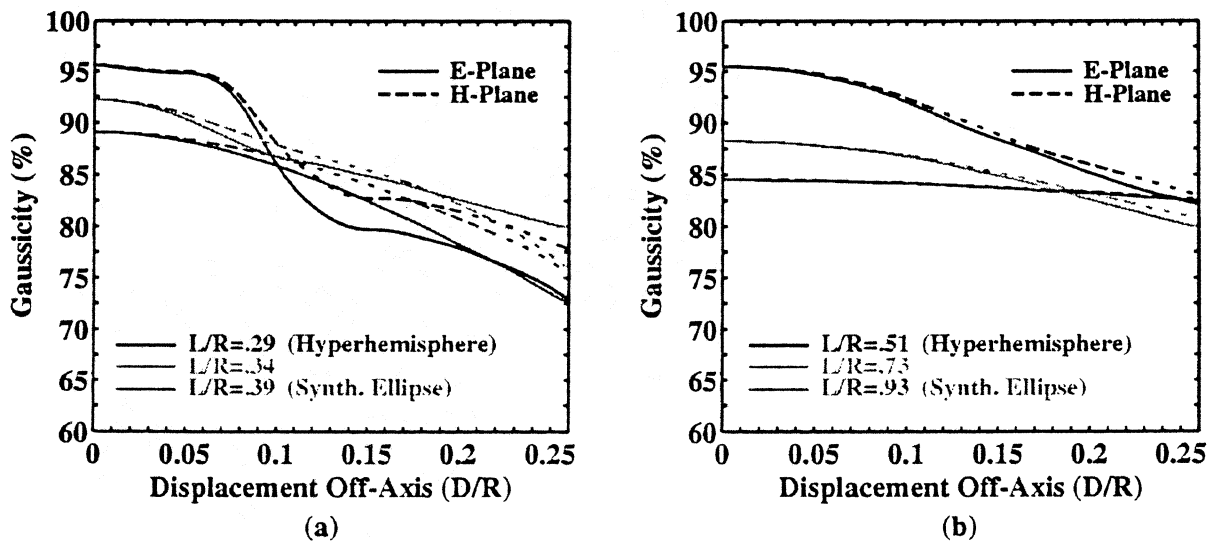


Figure 5: Gaussicity versus off-axis displacement at fixed extension lengths for a 12λ -diameter silicon (a) and quartz (b) lens.

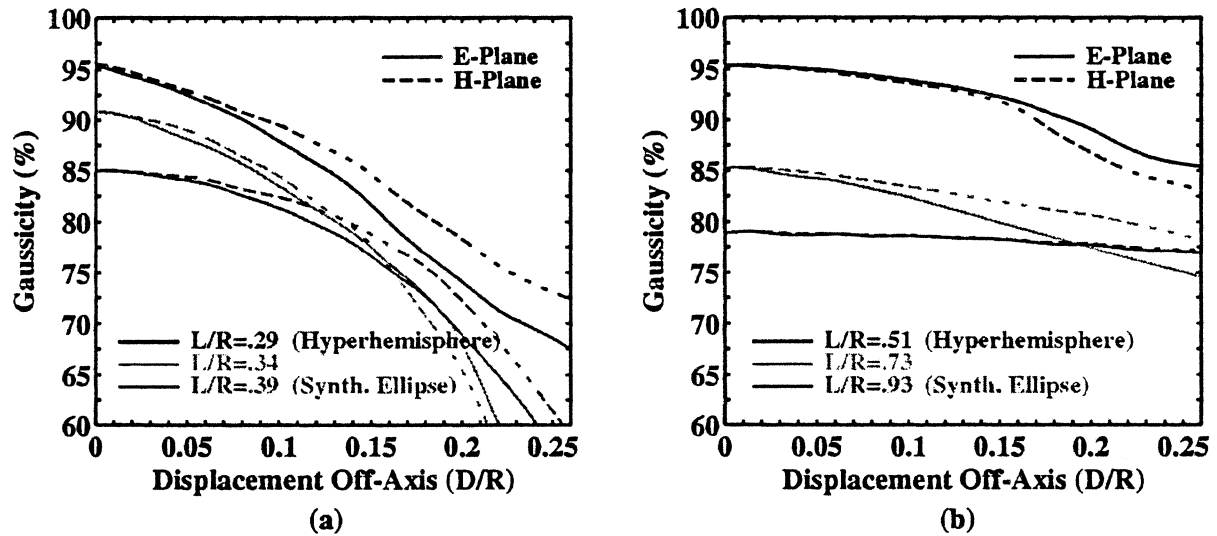


Figure 6: Gaussicity versus off-axis displacement at fixed extension lengths for a 24λ -diameter silicon (a) and quartz (b) lens.

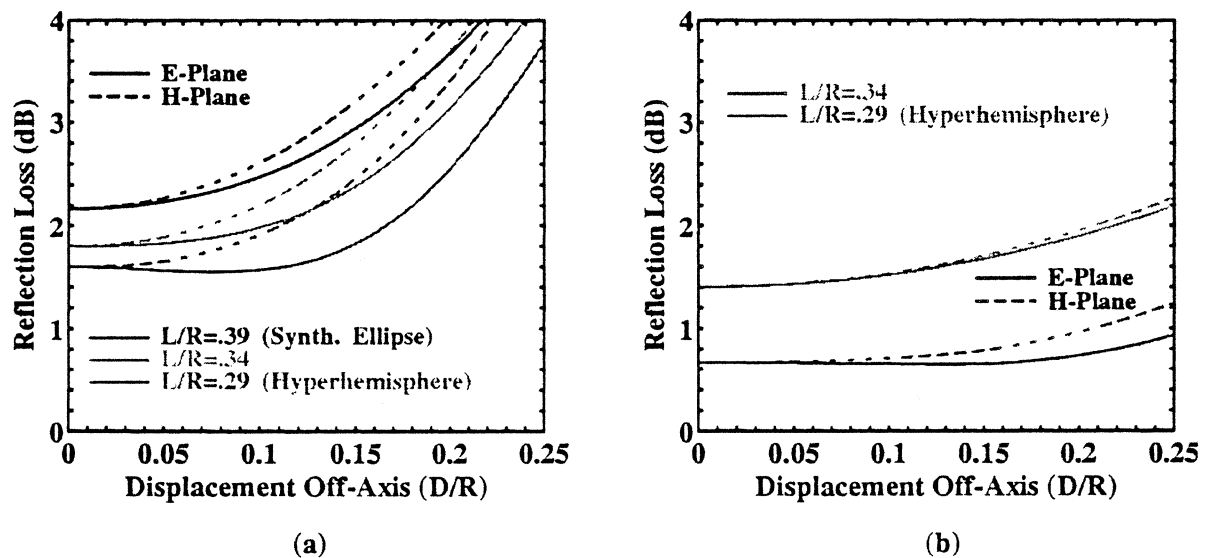


Figure 7: Reflection loss versus off-axis displacement at fixed extension lengths for a silicon (a) and quartz (b) lens.

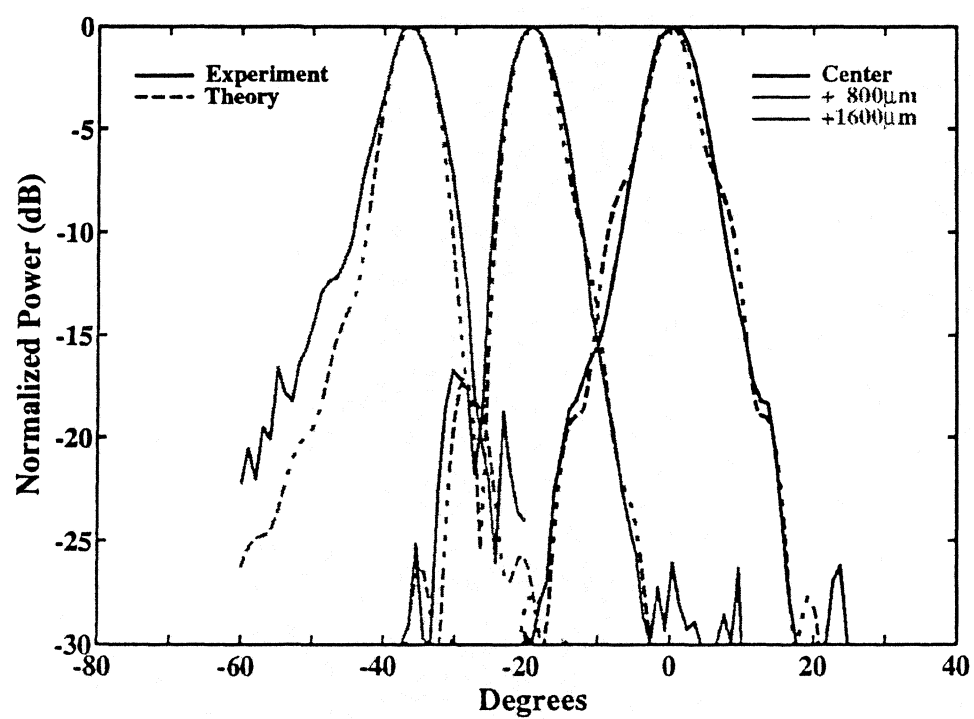


Figure 8: Comparison of theoretical and measured H-plane patterns at 258GHz.

230 GHz Beam Pattern Measurements of a Dipole Array-Fed Dielectric Filled Parabola

S. Raman, D.F. Filipovic, P.A. Stimson[†],
R.J. Dengler[†], P.H. Siegel[†], and G.M. Rebeiz

NASA/Center for Space Terahertz Technology
Electrical Engineering and Computer Science Department
University of Michigan, Ann Arbor, MI 48109-2122 USA

[†] Jet Propulsion Laboratory, Pasadena, CA 91109 USA

Abstract

The Dielectric Filled Parabola (DFP) has been proposed as an efficient feeding structure for high f -number quasi-optical systems, combining the advantages of a parabolic reflector and a substrate lens. A DFP has been designed and constructed for operation at 230 GHz, and integrated with a 2x5 dipole array for imaging applications. We report here the measurement of antenna beam patterns for the elements of the array at 230 GHz.

1. Introduction

The Dielectric Filled Parabola (DFP) has been proposed as an efficient feeding structure for high f -number quasi-optical systems [1, 2]. It is well known that an antenna on a dielectric half-space does not lose power into substrate modes, and radiates preferentially into the dielectric, making the pattern of a normally bi-directional antenna nearly unidirectional [3]. The ratio of power radiated into the dielectric to that radiated into the air is $\epsilon_r^{3/2}$ for slot and dipole antennas at normal incidence. The broad beamwidths associated with planar antenna elements can be matched to high gain quasi-optical systems by placing a low- f -number prime-focus parabola in front of the antenna. The DFP design combines the advantages of the dielectric substrate lens with those of a high-gain parabolic reflector in a single structure.

The main component of the DFP is a plano-convex dielectric lens with the convex surface in the shape of a parabola with an f/D ratio of 0.25. The parabola face is metalized and planar antenna elements are integrated at the center of the flat surface of the dielectric lens. Intermediate frequency (IF) removal and DC biasing is accomplished by means of coplanar stripline feeds. Incident RF radiation enters the dielectric, reflects off the parabolic surface, and is focused onto the planar antennas/detectors. Off-axis rays enter the dielectric substrate inclined from normal incidence and are refracted, focusing off-center. Thus, the elements of an array arranged about the focus will each “look” in a different direction providing an imaging capability. There is a reflection loss at the dielectric-air interface, which

can be eliminated by using a quarter-wavelength matching layer. The major features of the DFP are summarized below:

1. The parabola has an f/D ratio of 0.25 and can thus accommodate planar antennas with beamwidths approaching 180° .
2. The parabolic reflector is in the far-field of the planar antenna elements, and paraxial rays travel an equal distance in the dielectric to the focal point.
3. For heterodyne receiver operation the local oscillator (LO) can be injected from the back through a hole in the center of the reflector, eliminating the need for quasi-optical diplexing.
4. Antenna elements/detectors can be readily heat-sunk through the dielectric paraboloid to the backing metal, which is especially important for SIS mixers.
5. For array use, off-axis elements produce beams inclined from the optical boresight; the presence of the dielectric increases the extent of the off-axis beam tilt for a given lateral displacement of the antenna in the focal plane.

2. Construction of the 230 GHz Dielectric Filled Parabola

A photograph of a 230 GHz DFP (without cover plate installed) is shown in Fig. 1(a). An exploded schematic detailing the DFP assembly is shown in Fig. 1(b).

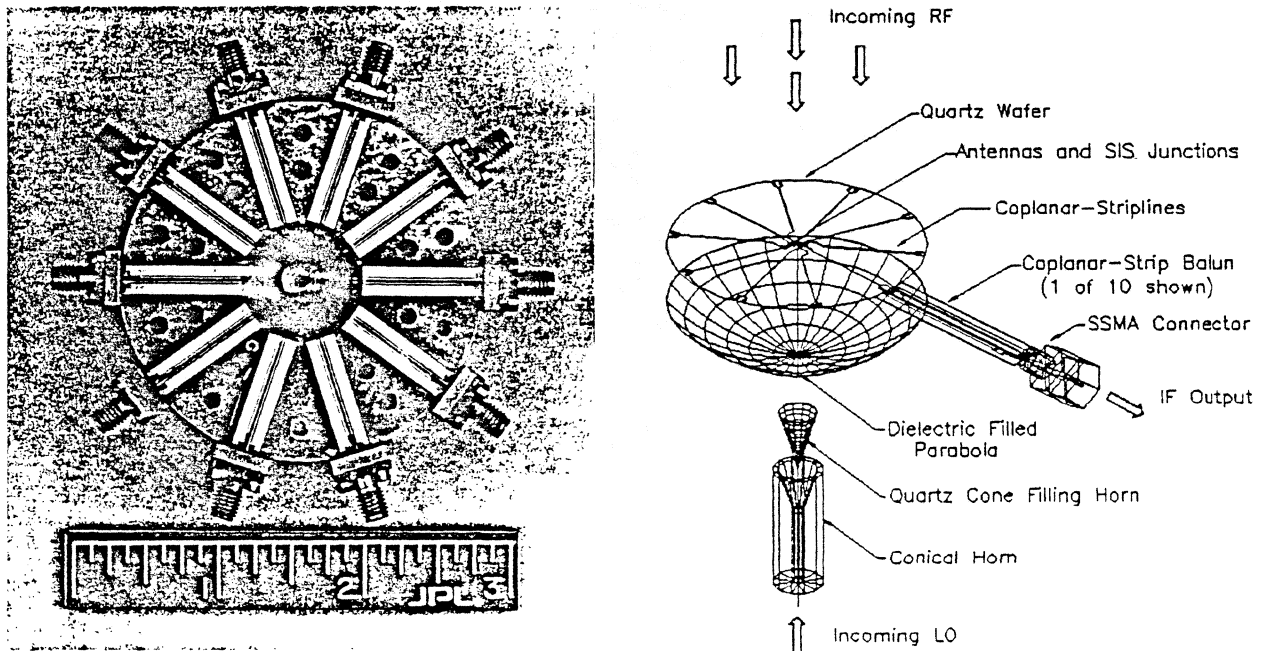


FIGURE 1. (a) Photograph of 230 GHz DFP without cover plate installed. (b) Exploded schematic of the DFP assembly.

The structure is composed of four basic parts: (1) the quartz wafer containing the antennas and feedlines; (2) the dielectric paraboloid; (3) the LO feed horn; and (4) the IF output, balun transformer, and DC bias lines. The 2x5 dipole array was fabricated on a 254 μm (10 mil) thick quartz wafer 19.5 mm (0.768") in diameter. The array layout and numbering convention is shown in Fig. 2.

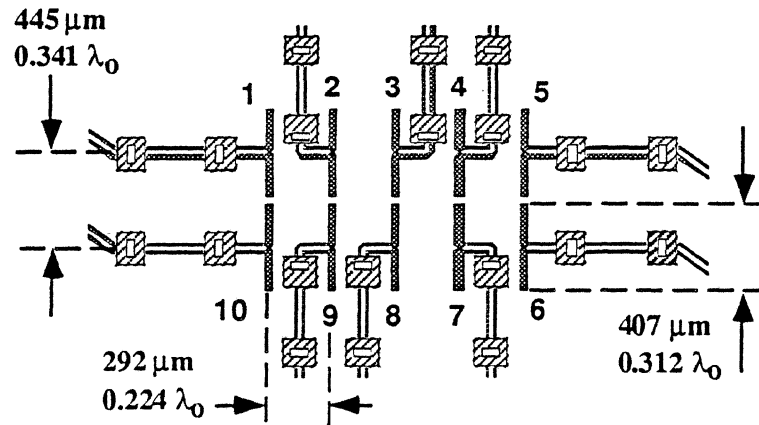


FIGURE 2. 2x5 dipole array layout and numbering convention.

Dipoles 3 and 8 are referred to as center elements, dipoles 2, 4, 7, and 9 are intermediate elements, and dipoles 1, 5, 6, and 10 are edge elements (Note: the "center" elements are not centered in the E-plane). The antenna and feed line pattern was formed by evaporation and liftoff of 4000 Å Cr/Au. The dipoles are 407 μm long which corresponds to the resonant length on a quartz substrate. The element spacing in the horizontal direction (292 μm) was chosen to achieve a 3 dB overlap in the individual element H-plane patterns, and the element spacing in the vertical direction (445 μm) was made as close as practical. The spacings were optimized using 20 GHz model pattern measurements. These feed antennas provide an effective optical system f -number of 0.4 due to under-illumination of the parabola aperture. RF blocking capacitors are located $\lambda_g/4$ and $3\lambda_g/4$ from the dipoles, ensuring RF open circuits at the detectors. SIS mixers were fabricated in this configuration and mixer results were reported in [4]. For the 230 GHz pattern measurements, bismuth bolometers were used as detectors. A photograph of the bismuth bolometer dipole array is shown in Fig. 3.

The thickness of the DC feed lines is 2.0 μm of Cr/Au/Ti/Al/Ti/Au to just before the first set of capacitors in order to reduce the series resistance of the thin coplanar strips. The rest of the pattern is 4000 Å Cr/Au to allow for step coverage of the capacitor dielectrics and bismuth bolometers. The capacitor dielectrics are SiN_x deposited at a thickness of 2000 Å by PECVD and defined by CF_4 plasma etching; the upper plate metallization was 3500 Å of evaporated Cr/Au. A 1500 Å thick bismuth bolometer is evaporated at each antenna apex in order to achieve good sensitivity while keeping a reasonable match with the dipole impedances.

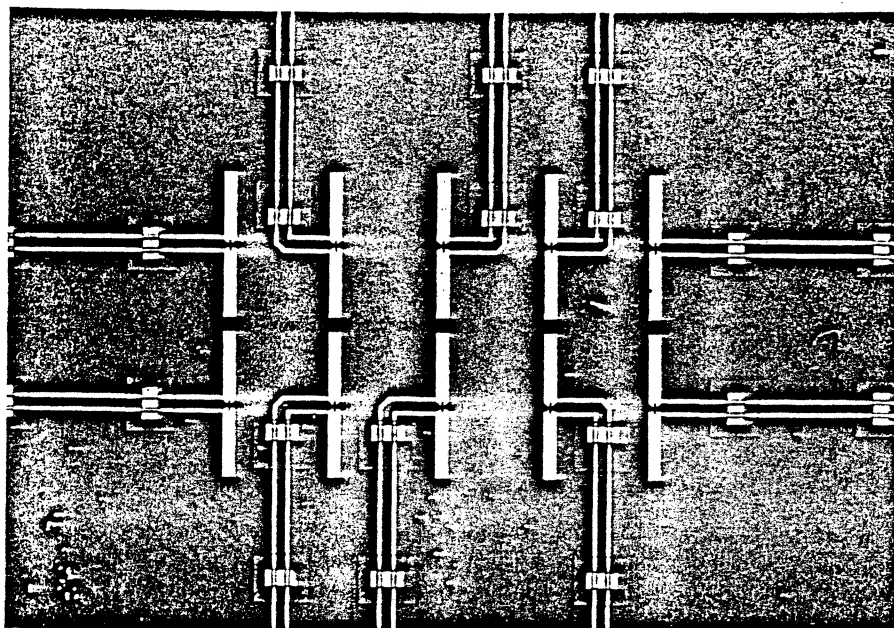


FIGURE 3. Photograph of the 230 GHz bismuth bolometer dipole array.

The dielectric parabola was ground from fused quartz to have a diameter of 19.5 mm (0.768") and an f/D ratio of 0.25. Once ground and polished, the parabolic substrate lens was vacuum coated with several skin depths of gold. A small rectangle sized to match the LO feed horn aperture was masked off at the center of the parabola before depositing the metal. The holder for the parabola was fabricated from brass and contains a parabolic depression for accurately mating to the quartz lens. The center of the housing contains a pyramidal feed horn for injection of the LO. The feed horn tapers to the face of a standard WR-3 waveguide flange on the rear of the holder. A quartz insert fits into the horn in order to minimize the mismatch presented to the LO.

The ends of the coplanar lines on the wafer flare out to form bonding pads where they are wire bonded to the planar balun transformers. The IF baluns are designed to work from 1-2 GHz and convert the balanced 200 Ω coplanar strip line impedance on the quartz wafer to 50 Ω unbalanced coaxial line impedance. The quarter wavelength delay is achieved through the use of chip capacitors, which behave as open circuits to the bolometer DC bias.

A brass cover plate bolts down to clamp the whole assembly together.

3. 230 GHz Antenna Pattern Measurements

Antenna pattern measurements at 230 GHz for the 2x5 bolometer array were made at the University of Michigan. The DFP was illuminated using a 77 GHz Gunn diode oscillator feeding a tripler with a conical horn output. An automated 2D mount was used to scan the DFP boresight through θ and ϕ . The axis definitions are shown in Fig. 4. The x-axis is the boresight of the DFP. Since the elements of the array are not located exactly at the focus of the parabola, the main beams of their antenna patterns are scanned away from the x-axis.

Two-dimensional patterns are centered on the boresight of the DFP; elevation scans in the theta direction and azimuth scans in the phi direction about this origin. The pattern planes of interest are cuts taken through the main beam of a given element. Hence, the "E"-plane of an element is that plane parallel to the E-field of the dipole intersecting the peak of the given element's main beam ($\phi = \phi_{\max}$). The true "H"-plane of an element does not occur at constant θ , but since the elements were displaced by relatively small amounts in the vertical direction, "H"-plane cuts taken with $\theta = \theta_{\max}$ are considered to be accurate.

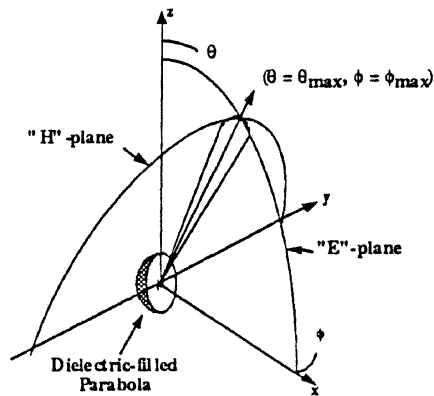


FIGURE 4. Axis definitions of the measurement system.

Measured 230 GHz two-dimensional patterns for typical center, intermediate, and edge elements are shown in Fig. 5.

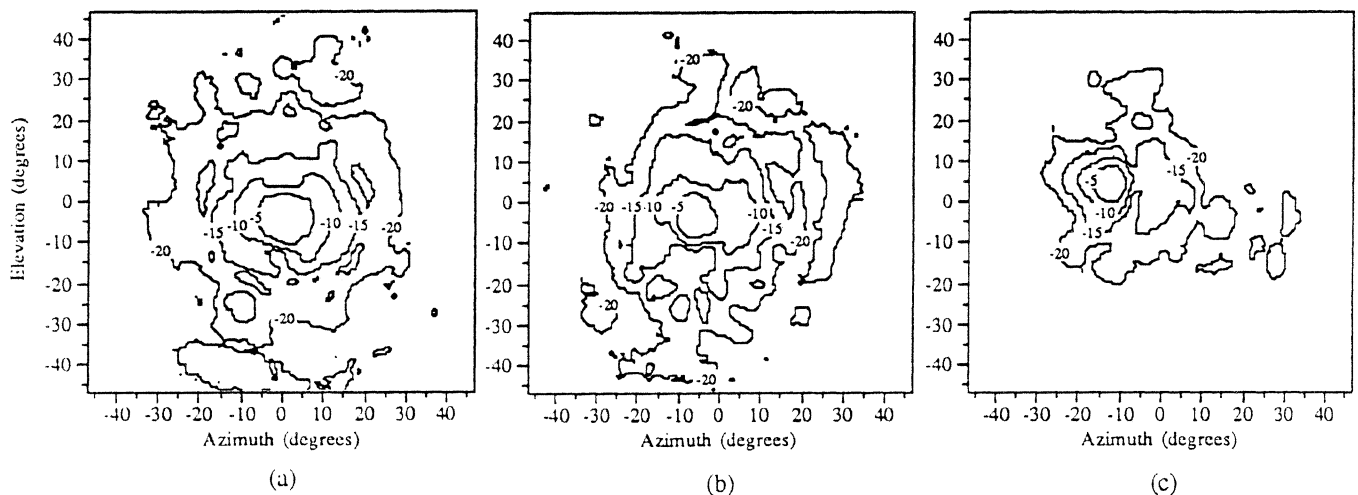


FIGURE 5. 2D patterns for typical elements: (a) Center (#3); (b) Intermediate (#4); (c) Edge (#6).

The center element (#3) has its main beam scanned to -4.6° in elevation and -0.9° in azimuth. The beam should ideally be at 0° in azimuth, indicating a slight misalignment between the 2×5 array and the dielectric parabola. The directivity is calculated from the 2D-pattern data at 21.4 dB. The intermediate element (#4) has its main beam scanned to -3.6° in elevation and -7.4° in azimuth, and a directivity of 22.1 dB. The edge element (#6) has its main beam scanned to $+4.6^\circ$ in elevation and -12.0° in azimuth, and a directivity of 23.4 dB. The trend in directivities does not represent an increase in gain as the element position moves away from the boresight since each pattern was normalized to its respective peak and no absolute power calibration was done for the detectors. However, there is a definite sharpening of the main beam as off-axis position is increased. This is similar to the behavior noted in [5] for off-axis elements on extended dielectric substrate lenses. It is felt that more uniform directivities could be achieved for the off-axis DFP elements through a change in extension length as has been proposed for the substrate lenses. Actual gain is expected to decrease as the element is moved off axis due to increased reflection and dielectric losses, as was seen in the 20 GHz model measurements.

“E”-plane scans for a typical upper row/lower row pair of antennas, and “H”-plane scans for typical center, intermediate, and edge elements are shown in Fig. 6.

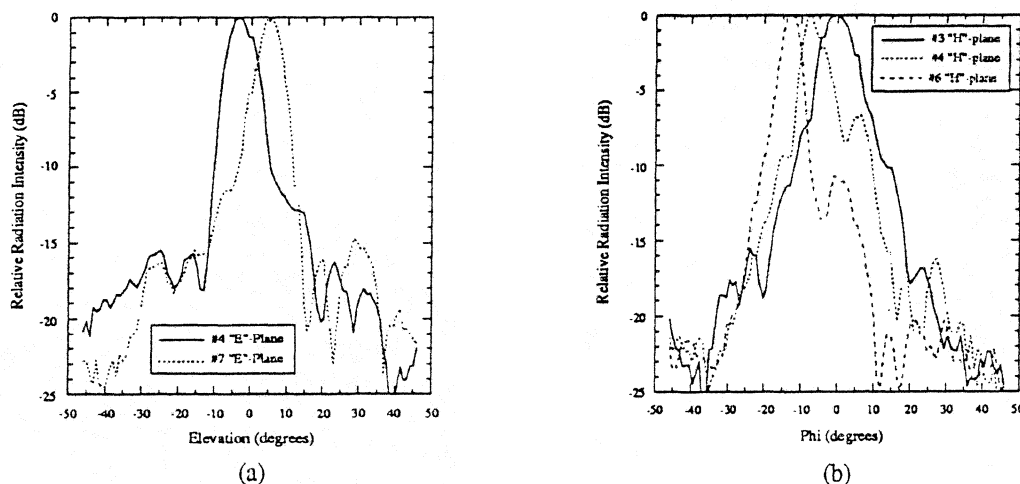


FIGURE 6. (a) “E”-plane scans (elements #4 and #7). (b) “H”-plane scans (elements #3, #4, #6).

The “E”-plane scans show that the lower and upper row elements scan in elevation by approximately $\pm 4^\circ$. The increased sidelobe levels are due to a combination of dipole air radiation and aperture blockage. Some comatic aberration can be seen emerging from each main lobe on the side towards the DFP boresight at about -12 dB. The “H”-plane scans show that the center, intermediate, and edge elements scan in azimuth by approximately 0° , 7° , and 12° respectively. The narrowing of the main lobe with off axis position can be clearly seen. The most significant feature, however, is the behavior of the coma lobe. Both

theoretical work [6] and 20 GHz model measurements show that the primary coma lobe should increase monotonically with off axis position. However, the 230 GHz measurements have a higher intermediate element coma lobe level (-7 dB) than edge element coma lobe level (-11 dB). All element scan angles, and the center and edge element coma lobe levels show good agreement between the 20 GHz model and the 230 GHz version (see Table 1). The only physical difference between the two is the presence of the LO feed horn in the back of the 230 GHz DFP. It is possible that this discontinuity in the reflector may be contributing differing amounts of aperture blockage for the intermediate and edge elements, raising the intermediate element coma lobe level, but this has not yet been confirmed. The effect of the LO feed could be eliminated by coating the gap in the reflector with metal.

TABLE 1. Comparison of 20 GHz model and 230 GHz DFP pattern measurements.

Element	“H”-plane Scan Angle (degrees)		Coma Lobe Level (dB)	
	20 GHz	230 GHz	20 GHz	230 GHz
Center	0.0	0.9	- 18	- 16
Intermediate	5.8	7.4	- 16	- 7
Edge	12.4	12.0	- 12	- 11

4. Conclusions and Future Work

Beam pattern measurements at 230 GHz have been performed for a 2x5 dipole/bolometer array on a Dielectric Filled Parabola (DFP). The measured patterns agreed well with those obtained from a 20 GHz model with the exception of the intermediate element coma lobe level which was significantly higher. The only physical difference between the two versions is the presence of the LO feed horn in the back of the 230 GHz DFP, but this has not been confirmed to be the cause. Further measurements with the gap in the reflector metalized will be performed to determine the effect of the LO feed. Also, software is currently under development to model the off-axis properties of the DFP and will be used to help diagnose the cause of the high coma lobe levels.

5. References

- [1] P.H. Siegel, "A Submillimeter-wave Heterodyne Array Receiver Using a Dielectric-filled Parabola: Concept and Design", *Proc. of the First International Symposium on Space Terahertz Technology*, Ann Arbor, MI, Mar. 5-6, 1990, pp. 218-235.
- [2] P.H. Siegel and R.J. Dengler, "The Dielectric-filled Parabola: A New Millimeter/Sub-millimeter Wavelength Receiver/Transmitter Front End", *IEEE Trans. on Antennas and Propagation*, Vol. 39, No. 1, pp. 40-47, Jan. 1991.
- [3] D.B. Rutledge, D.P. Neikirk, and D.P. Kasilingam, "Integrated-circuit Antennas", in *Infrared and Millimeter-Waves*, Vol. 10, K.J. Button, ed., Academic Press, Orlando, 1983.
- [4] P.A. Stimson, R.J. Dengler, H.G. LeDuc, and P.H. Siegel, "A Prototype Quasi-optical SIS Array Receiver", *1994 IEEE MTT-S International Microwave Symposium Digest*, San Diego, CA, May 23-27, 1994, pp. 1337-1339.
- [5] D.F. Filipovic, G.V. Eleftheriades, and G.M. Rebeiz, "Off-axis Imaging Properties of Substrate Lens Antennas", published in these proceedings.
- [6] J. Ruze, "Lateral-feed Displacement in a Paraboloid", *IEEE Trans. on Antennas and Propagation*, Vol. 13, pp. 660-665, Sep. 1965.

MICROMACHINED DETECTOR MOUNTS FOR MILLIMETER WAVE APPLICATIONS

R. F. Drayton, C. Kidner, J. East and L. P. B. Katehi
NASA Center for Space Terahertz Technology
University of Michigan
Ann Arbor, MI 48109-2122

Abstract

High frequency circuit development requires that circuits are miniature in size with good electrical performance. These types of circuits can be achieved by utilizing micromachining techniques that allow individual planar geometries and shielding environment to be fabricated monolithically. This paper will present the development of such circuits including a detector mount where the advantage of this configuration is a lowcost circuit system with small weight and volume. Since the shield is integrated with the planar geometries, characterization is simplified and the resulting circuit performance is comparable to conventional planar lines. At the higher frequencies this is particularly useful since various geometries can be easily fabricated using silicon micromachining techniques.

1.0 Introduction

Micromachined circuits have been studied at the University of Michigan for development of passive circuit components [1] where the individual planar geometries and shielding environment are fabricated monolithically resulting in miniaturization of conventional circuit components. The advantage of this configuration is a lightweight circuit system with small weight and volume. In addition, characterization of such systems is simplified since the shield is integrated with the planar components resulting in circuit performance that is comparable to conventional planar lines. For higher frequency applications, this is particularly useful since various geometries can be easily fabricated to desired dimensional requirements using silicon micromachining techniques.

This paper presents the development of a variety of micromachined circuits including a detector mount that utilizes the advantages of micromachining to create the circuit components and a

mounting structure for planar diodes. A description of the development of the system and the sub-components required along with a discussion of circuit performance is presented.

2.0 Fabrication Issues

The mounting structure is a two silicon <100> wafer system which relies primarily on standard fabrication processes and etching techniques. The semiconductor processing steps include standard photolithography techniques for wafer patterning along with lift-off and evaporation techniques for metallization of the patterned areas. Ethylene diamine pyrocatechol (EDP), an anisotropic etchant, is used to etch silicon where it selectively stops on the <111> crystal plane resulting in sidewall angles of 54.7° as shown in Figure 1.

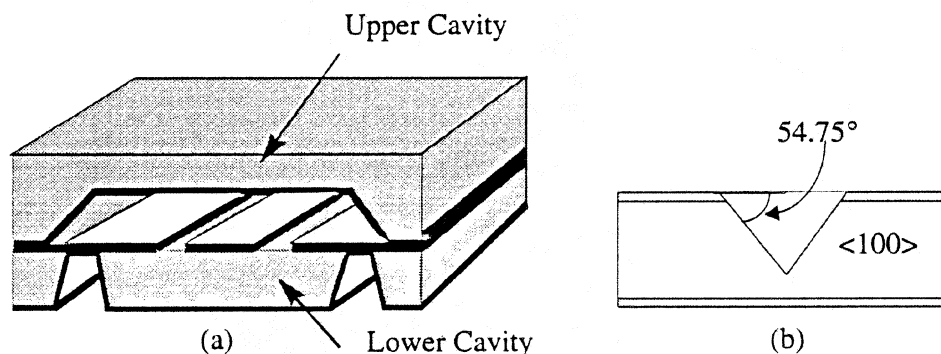


FIGURE 1. Two wafer silicon system of the transmission line with integrated shielding environment.

In Figure 1, the top wafer shows the air-filled upper cavity, having a width of $1200\ \mu\text{m}$ and height of $280\ \mu\text{m}$, that is metallized after etching low resistivity silicon. On the bottom wafer coplanar waveguide transmission lines are printed on the polished side of high resistivity silicon using photolithography with lift-off and evaporation techniques for metallization. Since the etched grooves on the bottom side of this wafer define the lower substrate-filled cavity, they are metallized last to provide the lower shielded region having a height of $350\ \mu\text{m}$ and width of $950\ \mu\text{m}$. Once the indi-

vidual wafers are fabricated, they are secured using adhesion techniques while alignment is done via alignment windows.

3.0 Circuit Design and Results

Since micromachining techniques allow the integration of the shield with the transmission line components, circuit parameters are needed to establish a feedline that matches to 50 ohm systems. For the configuration shown in Figure 1, the transmission lines are coplanar waveguides having a conductor width of $180\text{ }\mu\text{m}$ and a slot width of $130\text{ }\mu\text{m}$ with above shielding dimensions.

For very high frequency circuits, initial circuit performance can be determined using on-wafer measurement techniques in the Ka-band. The results provide good indicators of the expected circuit response when scaled to terahertz frequencies excluding loss performance. In order to accurately measure the circuits, however, the measurement test wafer contains various circuit components having identical upper and lower shielded regions in addition to individual calibration lines, needed for the performance of a Thru-Reflect-Line (TRL) de-embedding [2,3]. Resulting experimental measurements of the micromachined circuits are thus obtained using on-wafer probing techniques [4] via a measurement system which consists of an HP 8510B Network Analyzer, Alessi Probe Station, and Cascade Microtech ground-signal-ground (GSG) probes with $150\text{ }\mu\text{m}$ pitch.

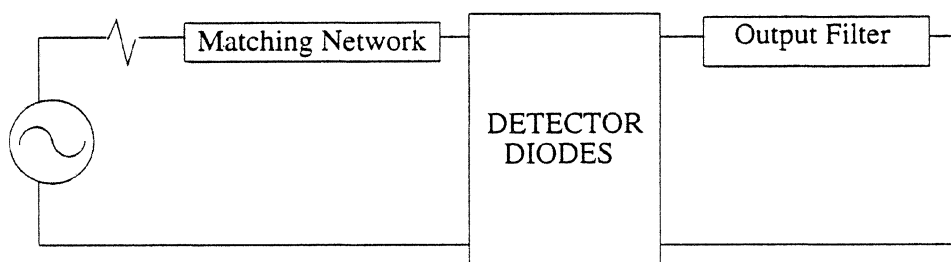


FIGURE 2. Detector Mounting Structure Design Scheme

Specific design issues are addressed in order to develop a micromachined detector which requires the use of the circuit shown in Figure 1 [5]. The design procedure begins by determining [6] and evaluating the range of realizable impedances available to implement a lowpass filter with a requirement of -20 dB insertion loss and the open circuit input impedance at the design frequency. Using the cross-sectional dimensions of the shielded regions given above, the high and low impedances are determined where the low impedance sections have a conductor width of $380\text{ }\mu\text{m}$ and slot width of $30\text{ }\mu\text{m}$ and high impedance section has conductor width of $20\text{ }\mu\text{m}$ and slot width of $210\text{ }\mu\text{m}$. The filter response shown below in Figure 2 for a 5 section stepped impedance filter is compared to results obtained from a finite difference time-domain model [7].

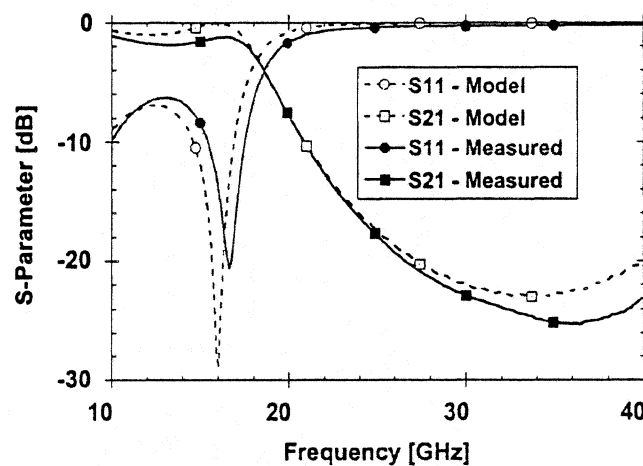


FIGURE 3. 5-section Stepped Impedance Lowpass Filter

The above response is needed in order to match the output of the filter design. Since the transmission lines are coplanar waveguides, this detector scheme uses the diodes in an anti-parallel configuration across the slots. In order to determine an appropriate input matching network the dc parameters of the diodes must be determined to minimize the power reflected from the diode input.

4.0 Conclusion

Subsystem components have been developed for a detector mounting scheme. In order to complete the detector system, in-house or commercially available diodes may be used which determine the type of appropriate input matching network. From a circuit perspective, micromachining can be used to develop detector mounting structures quite easily, where the problem is addressed from a component level prior to cascading these elements into the overall system.

5.0 Acknowledgments

This work has been supported by the Office of Naval Research under contract No.N00014-92-J-1070 and the NASA Center for Space Terahertz Technology. The authors would like to thank Dr. Nihad Dib for his contribution of theoretical models and Mr. Chen-Yu Chi and Mr. Steve Mollenkopf for technical discussions.

6.0 References

- [1] R. F. Drayton and L. P. B. Katehi, "Micromachined Circuits for Mm-Wave Application", *23rd European Microwave Conference*, Madrid, Spain, pp. 587-588, September 1993.
- [2] G. Engen and C. Hoer, "Thru-Reflect-Line: An improved Technique for Calibrating the Six-Port Automatic Network Analyzer", *IEEE Trans. Microwave Theory Tech.*, Vol. MTT-27, No 12, Dec. 1979, pp. 987-993.
- [3] M. Maury, S. March, and G. Simpson, "LRL Calibration of Vector Automatic Network Analyzers", *Microwave Journal*, May 1987, pp.387-391.
- [4] E.W. Strid and K.R. Gleason, "Calibration Methods for Microwave Wafer Testing", *1984 IEEE MTT-S Digest*, pp. 93-97.

- [5] Bhartia-Bahl, *Microwave Solid State Circuit Design*, John Wiley & Sons, Inc., New York, 1988, Chap. 11.
- [6] N.I. Dib and L.P.B. Katehi, "Impedance Calculation for the Microshield Line", *IEEE Microwave and Guided Wave Letters*, Vol.2, No. 10, pp. 406-408, October 1992.
- [7] N.I. Dib, personal communication.

Millimeter and Submillimeter Wave Microshield Line Components

Thomas M. Weller, Stephen V. Robertson, Linda P. B. Katehi, and Gabriel M. Rebeiz

NASA Center for Space Terahertz Technology
The University of Michigan
Ann Arbor, MI 48109

Abstract

Recent efforts at the University of Michigan have resulted in the successful development of high-performance planar components which operate in Ka- and W-Bands. These circuits are fabricated using silicon micromachining techniques, and they are placed on a thin dielectric membrane which is shielded by a metallized cavity on one side (see Fig. 1). This type of line, called microshield line, has exhibited very low radiation and ohmic losses for frequencies as high as 1 THz.

A variety of microshield components have been fabricated and their performance has been measured at the facilities of the Radiation Laboratory at the University of Michigan and NASA Lewis Research Center. These circuit components exhibit superior performance compared to planar components made with conventional microstrip or coplanar technology. In this paper, basic transmission line properties such as dispersion and attenuation are first examined. This is followed by a sample of the measured results obtained at Ka-Band for right angle bends, low-pass filters, and band-pass filters. Furthermore, extension of this technology to higher frequencies is explored.

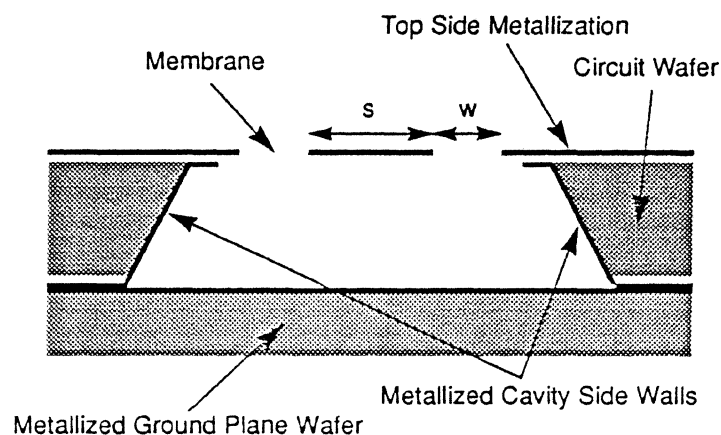


Figure 1. Microshield line uses micromachining techniques to suspend components in air on a thin dielectric membrane.

1. Introduction

The need for high performance microwave circuit components which could operate in the THz frequency range led to the development of the microshield line in 1991 [1]. Microshield line uses silicon micromachining and membrane technology to locally remove the substrate underneath a conventional CPW type transmission line. The resulting configuration propagates a pure TEM wave in a homogeneous air dielectric with very low loss and virtually no dispersion over an extremely wide bandwidth [2].

In this work we present results showing the high performance characteristics of microshield line. Measurements of loss and effective dielectric constant show the low loss and low dispersion as expected. Microshield line components are compared to conventional planar components. In particular, right angle bends show better return loss performance when fabricated with microshield line instead of CPW. Also, planar filters for high frequency applications which normally suffer due to the presence of a dielectric substrate are shown to operate effectively when implemented using microshield line.

2. Fabrication

Microshield circuits are fabricated on high-resistivity ($> 2,000 \Omega\text{-cm}$) silicon wafers with a $1.5 \mu\text{m}$ -thick $\text{SiO}_2/\text{Si}_3\text{N}_4/\text{SiO}_2$ composite deposited on both sides [3]. After the circuit metallization is patterned on the top side of the wafer using evaporation and lift-off, infrared alignment is used to pattern the backside membrane. The membrane layers are then etched to expose the silicon, at which point ethylenediamine pyro-catechol (EDP) anisotropic silicon etchant is used to define cavities underneath the circuit metallization. Once the silicon has been etched away, the top side membrane remains in tension to support the circuits. Next, the cavity side walls are metallized using a shadow mask evaporation which prevents an RF short from occurring between the signal line and the upper ground planes. Finally, the wafers are placed on a metallized ground plane wafer to completely shield the cavity (2-D geometry shown in Fig. 1).

3. Microshield Line Characteristics

A. Effective Dielectric Constant

Due to the air substrate of the microshield line, the effective dielectric constant, $\epsilon_{r,\text{eff}}$, is very close to 1. The presence of the membrane, however, causes a slight increase in $\epsilon_{r,\text{eff}}$ since a fraction of the fields will be contained within the thin dielectric layers which have

relative dielectric constants of 3.9 (SiO_2) and 7.5 (Si_3N_4). As shown in Figure 2, the measured $\epsilon_{r,\text{eff}}$ changes from around 1.09 to 1.15 as the slot width is reduced from 55 μm to 25 μm . This increase is a result of greater field confinement in the slot and thus in the membrane, and represents a decrease of nearly 3% in the guided wavelength. This dependence on the slot width is similar to the characteristics of CPW lines on a substrate such as GaAs or quartz [4]. As the line geometry approaches single micrometer dimensions which are comparable to the membrane thickness, $\epsilon_{r,\text{eff}}$ could increase to around 2.0.

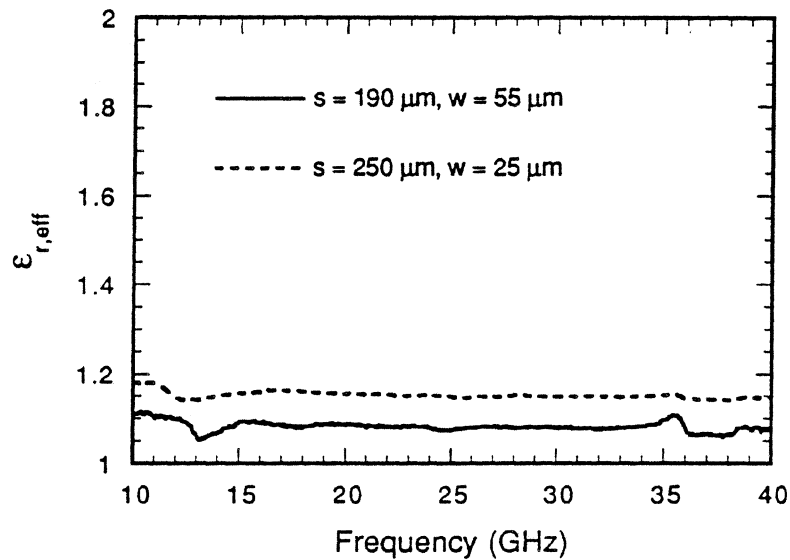


Figure 2. Effective dielectric constant at Ka-Band for two geometries of microshield line.

B. Attenuation

The attenuation characteristics of the microshield line have been investigated by comparing measured data on different microshield geometries against experimental and theoretical results for coplanar waveguide which are found in the literature. At low frequencies, the two types of lines are expected to perform equally well, since dielectric and radiative losses are relatively small and attenuation is dominated by conductor loss, which should be about the same in microshield and CPW due to the similar geometry of the metallization. At higher frequencies, however, the microshield line gains an increasing advantage since it has essentially zero dielectric loss and does not radiate energy into the substrate, as with a substrate-supported CPW line. This characteristic has been verified by recent electro-optic sampling experiments, which have provided attenuation data on membrane lines up to 1000 GHz [2].

The comparison between the microshield and CPW attenuation is shown in Figure 3. The curves shown for comparison were chosen either because the CPW dimensions are similar to the microshield dimensions (curves C,F,G) or to illustrate the effects of reducing the line geometry (curves D,E). All pertinent geometrical parameters for the CPW and microshield examples are given in Table 1 beneath the figure, and it is noted that the conductor thickness is only about 2 skin depths at 25 GHz for all but two cases (note: the technique used in [5] assumes zero conductor thickness).

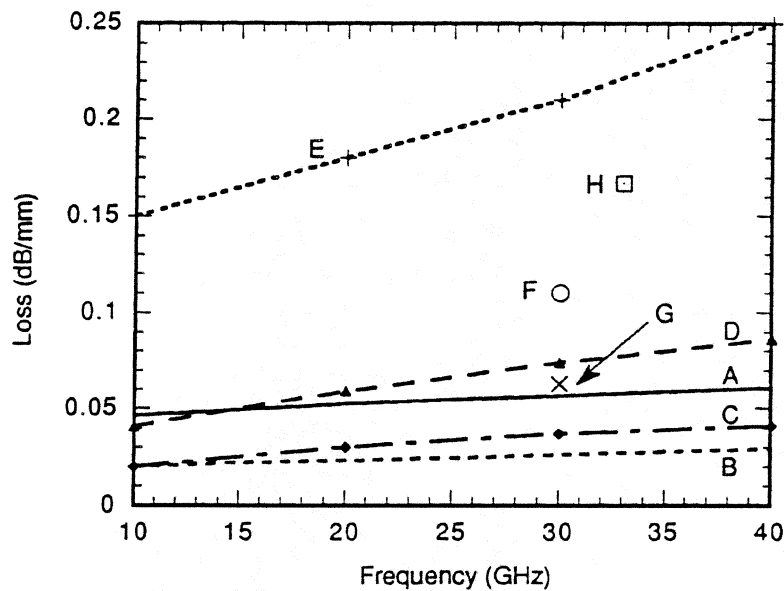


Figure 3. Comparison of microshield and CPW attenuation.

Table 1. Attenuation for microshield and coplanar waveguide lines. S is the center conductor width, W the slot width, H the substrate height, and t the metal thickness (in μm). The width of the lower shielding cavity for the microshield lines is $1800\ \mu\text{m}$.

Curve	Line	ϵ_r	Substr.	S	W	H	t	$Z_0 (\Omega)$	Data	Ref
A	μ shield	1.0	Air	250	25	355	1.2	75	Meas	—
B	μ shield	1.0	Air	190	55	355	1.2	100	Meas	—
C	CPW	12.8	GaAs	232	84	100	—	50	Calc	[5]
D	CPW	12.8	GaAs	69	28	100	—	50	Calc	[5]
E	CPW	12.9	GaAs	88	16	500	1.0	30	Meas	[6]
F	CPW	12.9	GaAs	250	25	500	1.0	30	Calc	[4]
G	CPW	4.0	Quartz	250	25	250	1.0	50	Calc	[4]
H	GCPW	11.7	Si	50	125	355	1.2	73	Meas	—

The results presented here confirm that the microshield line is free from unexpected or excessive conductor-loss mechanisms, and has performance which is comparable to conventional substrate-supported coplanar waveguide at lower frequencies. Furthermore, the absence of dielectric-related loss and the ability to maintain non-dispersive, single-mode propagation over a very broad bandwidth lead to low attenuation well into the millimeter-wave frequencies.

4. Microshield Line Components

A. Right Angle Bends

A very common circuit 'element' in millimeter-wave systems is the right-angle bend. This structure gains significance with increasing frequency due to the parasitic capacitance and inductance which are associated with the abrupt change in the field orientation. These problems, combined with mode-conversion, result in a high reflection of the incident power (large S_{11}). In coplanar waveguide designs, the typical means of improving the return loss is to utilize air-bridges or dielectric overlays [7]. Both of these techniques are meant to offset the effects of different electrical path lengths along the two slots. Without this type of compensation, the asymmetry of the CPW right-angle bend will lead to excitation of the unwanted slot-line mode.

Many of the problems inherent to bends which are printed on conventional CPW can be minimized with the microshield geometry. The absence of the high dielectric constant material has two important effects: it leads to a reduction in the parasitic capacitance and, for a fixed physical size, it reduces the difference in electrical path lengths through the two slots. The shielding cavity, furthermore, provides continuous ground plane equalization without introducing additional discontinuities, thus improving upon conventional air-bridges. A comparison between the measured performance of a microshield-line bend and a typical CPW bend on GaAs [8] is shown in Figure 4; the microshield bend has an S_{11} which is at least 8 dB lower over the 10-40 GHz band. The noise in the data below 18 GHz is due to calibration error.

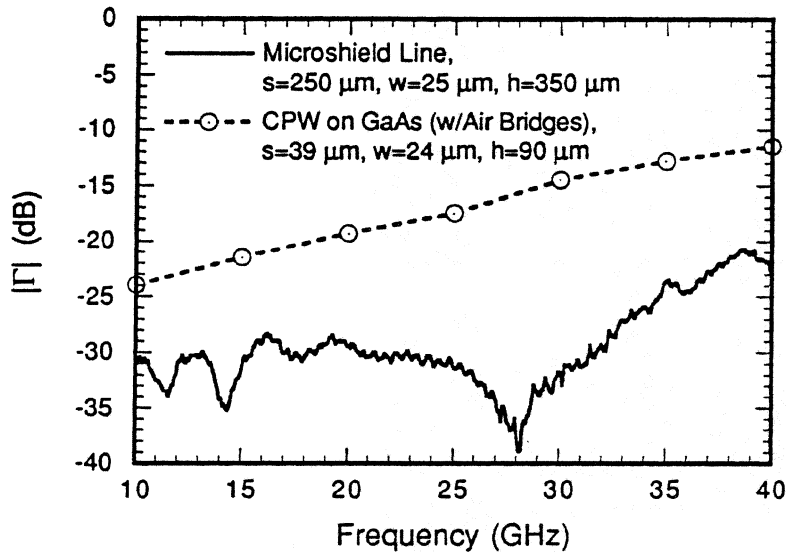


Figure 4. Performance of microshield and CPW right-angle bends.

B. Low-Pass Filters

The stepped-impedance approach to low-pass filter design is a relatively easy technique to use, and it is well suited for applications which do not require a sharp roll-off in the insertion loss. Often, however, the filter specifications call for high rejection over multiple-octave bandwidths, a requirement which may be difficult to meet using conventional substrate-supported lines due to the propagation of higher order modes. Thus, the very broad, single-mode bandwidth of the microshield line can provide superior filter performance in this respect. In addition, the absence of dielectric-related loss reduces both attenuation and parasitic radiation, resulting in very low passband insertion loss.

Stepped-impedance filters using 5-, 7-, and 9-sections have been designed and tested. Some of the results were previously presented in [9], where it was shown that the measured performance compared very well with ideal transmission line theory, as a result of the pure TEM nature of the microshield propagating mode. In Figure 5, measured data for a 5-section filter is compared with results from a full-wave moment-method analysis. The rejection is greater than 20 dB up to 75 GHz, which is about 1.5 octaves above the 3-dB point at 26 GHz. The measured passband insertion loss of this filter is between 0.2 and 0.5 dB from 20-23 GHz.

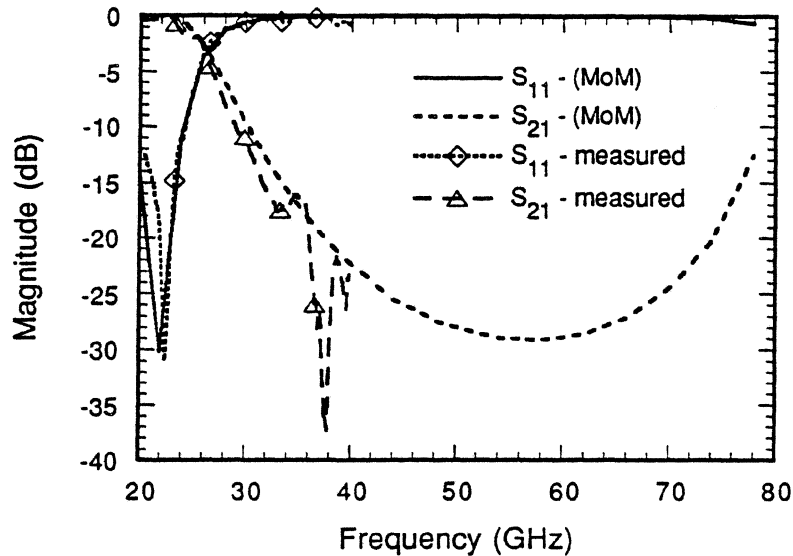


Figure 5. Performance of a 5-section stepped-impedance low-pass filter.

C. Band-Pass Filters

By cascading multiple open-end tuning stubs in series, it is quite simple to realize a bandpass response with high out-of-band rejection and low insertion loss. The geometry of a three-stage design is shown in Figure 6, in which each section is separated by $150\text{ }\mu\text{m}$. The measured response, shown in Figure 7, has an insertion loss of only 1.0 dB from 22-32 GHz, which is competitive with the best shielded bandpass filters using suspended stripline [10]. The performance of this microshield filter could be further improved using thicker metallization (since the one micron thickness is equivalent to just over two skin-depths) or larger slot widths to minimize the conductor loss. The calculated data included in the plot is generated by using the scattering parameters found from the full-wave analysis of a single stub section and treating the filter as three non-coupled elements in series. The agreement between the measured and calculated performance is quite good and indicates that there is very little electromagnetic coupling between the stubs, even though the stub separation is only $150\text{ }\mu\text{m}$. The response of the filter can also be modeled almost exactly by cascading the *measured* results for a single stub, and this approach accurately predicts the 1.0 dB insertion loss.

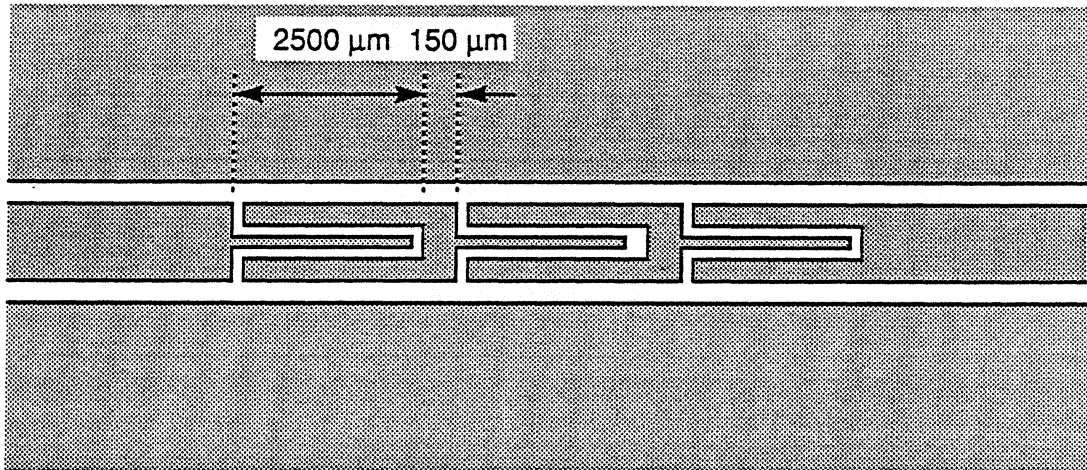


Figure 6. Geometry of a microshield line bandpass filter.

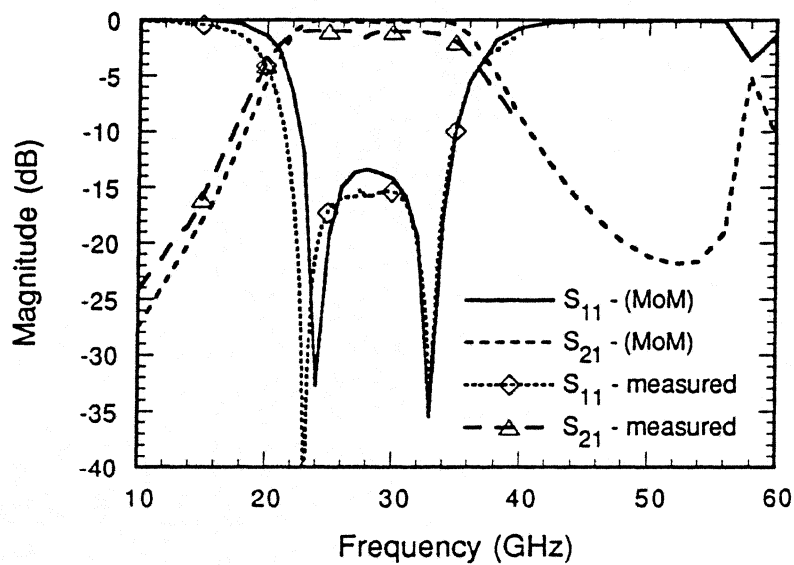


Figure 7. Performance of a microshield line bandpass filter.

5. Conclusions

Microshield line has been shown to be a very low loss, low dispersion transmission line well into the sub-millimeter wave frequency range. This work has demonstrated microshield circuit components with excellent performance at frequencies as high as 40 GHz, and continuing work at the University of Michigan has realized a 90 GHz low-pass filter and a 250 GHz band-pass filter. This recent work will be presented in detail in forthcoming publications.

6. Acknowledgments

This work was supported by the NASA Center for Space Terahertz Technology and the Office of Naval Research.

References

- [1] N.I. Dib, W.P. Harokopus Jr., L.P.B. Katehi, C.C. Ling, and G.M. Rebeiz, "Study of a Novel Planar Transmission Line," *1991 IEEE MTT-S Digest*, pp. 623-626.
- [2] H. J. Cheng, J. F. Whitaker, T. M. Weller, and L. P. Katehi, "Terahertz-Bandwidth Characterization of Coplanar Waveguide on Dielectric Membrane via Time-Domain Electro-Optic Sampling," *Presented at the 1994 MTT-S International Microwave Symposium*.
- [3] G.M. Rebeiz, D.P. Kasilingam, Y. Guo, P.A. Stimson, D.P. Rutledge, "Monolithic Millimeter-Wave Two-Dimensional Horn Imaging Arrays," *IEEE Trans. Antennas and Propagation*, Vol. 38, pp. 1473-1482, September 1990.
- [4] W. H. Haydl, W. Heinrich, R. Bosch, M. Schlechtweg, P. Tasker, and J. Braunstein, "Design data for millimeter wave coplanar circuits," *1993 European Microwave Conference Proceedings*, pp. 223-228.
- [5] M. Zhang, C. Wu, K. Wu, and J. Litva, "Losses in GaAs Microstrip and Coplanar Waveguide," *1992 IEEE MTT-S Digest*, pp. 971-974.
- [6] W. H. Haydl, J. Braunstein, T. Kitazawa, M. Schlechtweg, P. Tasker, and L. F. Eastman, "Attenuation of Millimeterwave Coplanar Lines on Gallium Arsenide and Indium Phosphide Over the Range 1-60 GHz," *1992 IEEE MTT-S Digest*, pp. 349-352.
- [7] R. N. Simons and G. E. Ponchak, "Modeling of Some Coplanar Waveguide Discontinuities," *IEEE Trans. Microwave Theory Tech.*, Vol. 36, December, 1988, pp. 1796-1803.
- [8] Amjad A. Q. Omar, "An Accurate Solution of 3-D Coplanar Waveguide Circuits," Ph.D. Thesis, University of Waterloo, Waterloo, Ontario, Canada, 1993.
- [9] T. M. Weller, G. M. Rebeiz, and L. P. Katehi, "Experimental Results on Microshield Line Circuits," *1993 IEEE MTT-S Digest*, pp. 827-830.
- [10] W. Menzel, "Broadband Filter Circuits Using an Extended Suspended Substrate Transmission Line Configuration," *Proceedings of the 22nd European Microwave Conference*, Aug. 24-27, 1992, pp. 459-463.

Beam Waveguide and Receiver Optics for the SMA

Scott Paine, D. Cosmo Papa, R. Louie Leombruno, Xiaolei Zhang, and Raymond Blundell

Harvard-Smithsonian Center for Astrophysics,
60 Garden Street, Cambridge, MA 02138, USA

Abstract

This paper gives an outline of the optics design for the Submillimeter Array. It emphasizes the natural frequency-independence and simplicity of Fresnel imaging principles as the starting point for the optics design, with multi-mode Gaussian beam methods used as a computational tool for working out the detailed behavior. A calculation of the coupling loss at the beam waveguide mirrors is presented as an example of the design method.

Introduction

The Submillimeter Array (SMA), currently under construction by the Smithsonian Astrophysical Observatory, will be a submillimeter interferometer initially comprising six 6-meter antennas configurable on baselines ranging from 9 meters to 465 meters. The completed array will ultimately be outfitted with up to eight receivers housed in a single cryostat for each antenna covering all atmospheric windows from 176 GHz to 900 GHz. This paper presents an overview of the SMA optics, with emphasis on the Fresnel imaging approach used for the optics design.

The body of the paper is divided into three sections. The first describes the physical layout of the receiver and beam waveguide optics. This is followed by a section on the principles of the optics design. The main point of this section is to illustrate the use of an approach to the design of broadband systems which takes Fresnel imaging as a starting point, as opposed to approaches which focus on the propagation of a particular Gaussian mode or mode set. From this viewpoint, multi-mode Gaussian beam methods

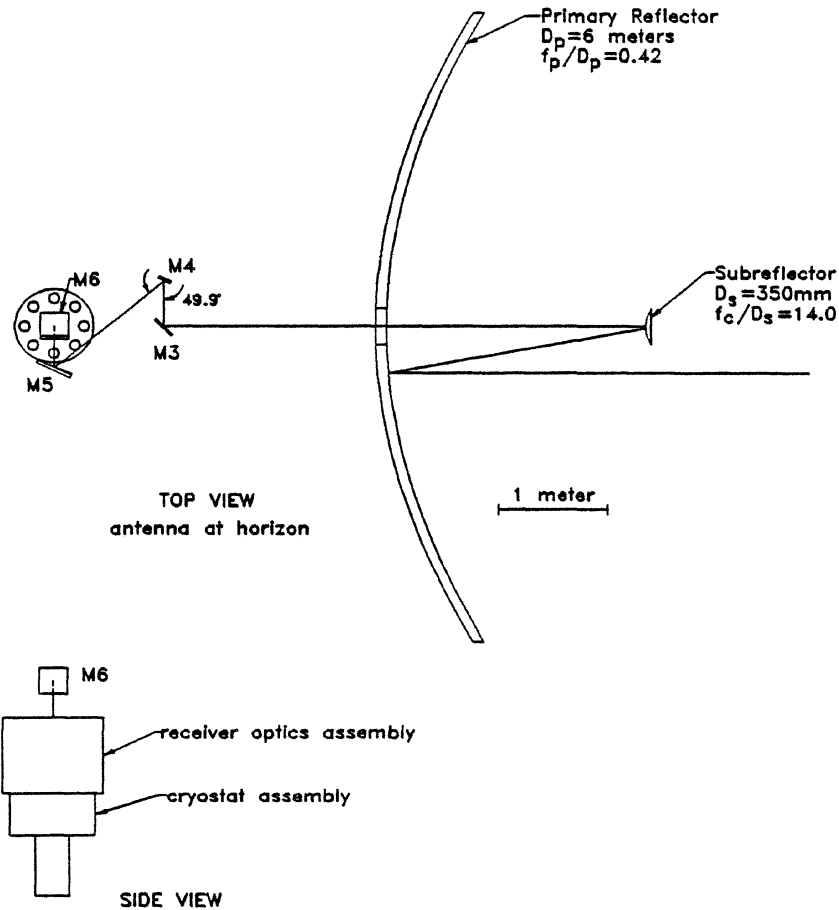


Figure 1 - SMA antenna optics layout

are a tool for handling propagation between image planes, with a particular mode set chosen to optimize computational efficiency for the design problem at hand. A final section will illustrate the application of this method to the detailed design of the optics, using a calculation of the coupling loss at one of the beam waveguide focusing mirrors as an example.

Optics Layout

The overall layout of the SMA antenna optics is illustrated schematically in Fig. 1. A 6-meter diameter paraboloidal primary reflector with focal ratio $f/D=0.42$ is combined with a 350 mm diameter hyperboloidal secondary with an effective focal ratio at the Cassegrain focus of 14.0. Mirrors M3 through M6 form a beam waveguide (Fig. 2) which

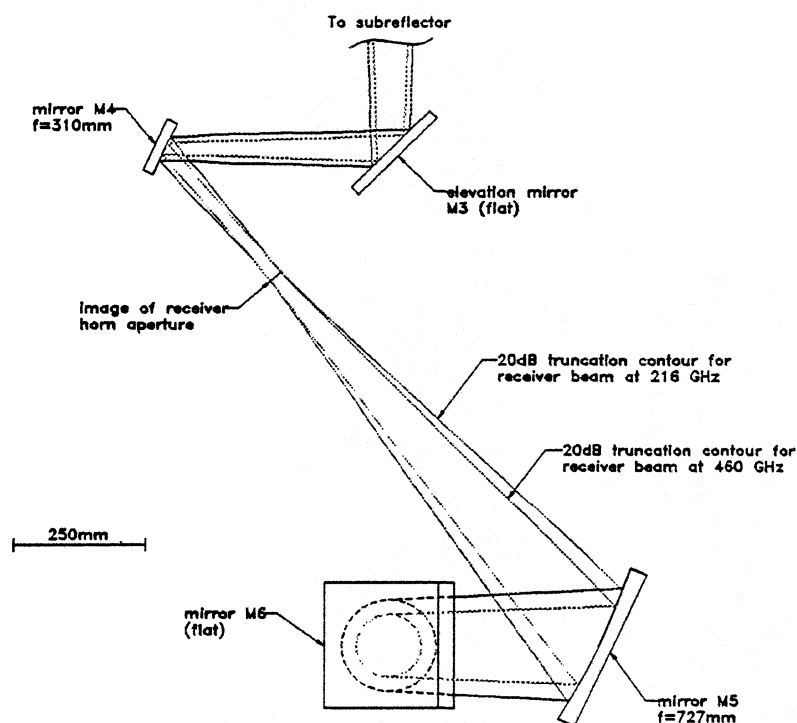


Figure 2 - Beam waveguide mirrors

directs the beam from the antenna vertically downward into the receiver optics assembly. The folded Naysmith configuration of the beam waveguide was adopted for two primary reasons. First, it allows the receivers to operate in a fixed orientation relative to gravity, avoiding mechanical disturbance of the receivers when the antenna is moved. Second, it fits within the compact receiver cabin design required for the SMA antennas.

A schematic showing the receiver optics layout and the arrangement of receivers in the cryostat is shown in Fig. 3. The beam from mirror M6 is split into two orthogonally polarized beams by a diplexer consisting of a polarizing wire grid and mirror which rotate independently about the axis of the incoming beam. The two orthogonally polarized beams are directed by the diplexer to a pair of receivers oriented 90° apart in the cryostat assembly. The eight receiver positions in the cryostat are divided into two groups: four low-frequency ($\nu < 360$ GHz) positions and four high-frequency ($\nu > 330$ GHz) positions, arranged so that every right angle pair of receivers consists of one receiver from each

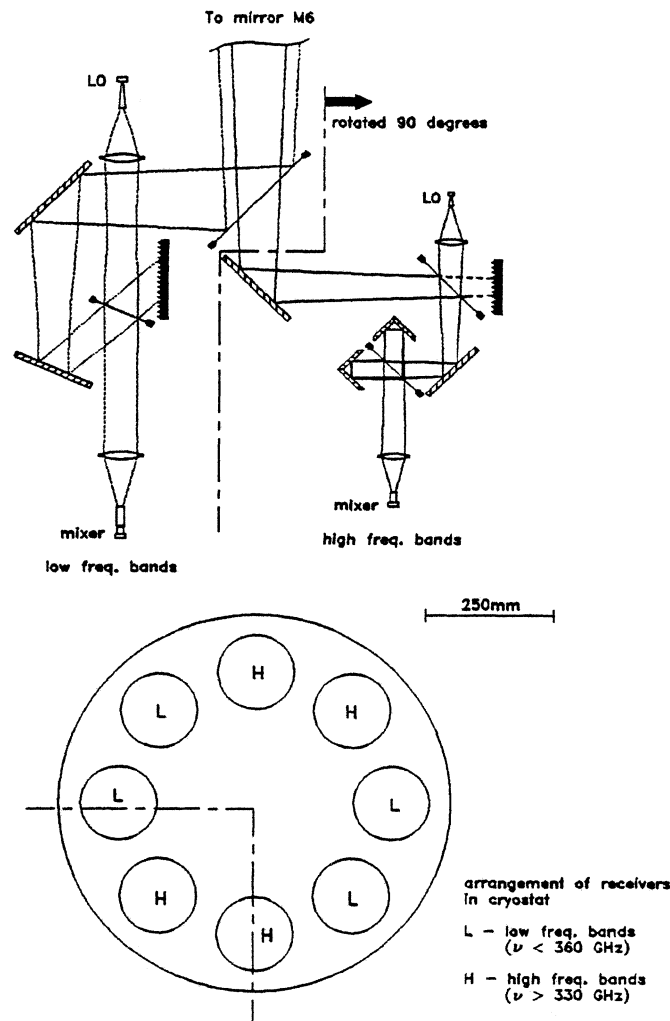


Figure 3 - Receiver optics layout. 20 dB truncation contours for the receiver beam are shown at 216 GHz for the low-frequency optics and at 460 GHz for the high-frequency optics.

group. An overlapping pair of high- and low-frequency receiver bands will permit dual-polarization operation from 330 GHz to 360 GHz.

Because a large number of receivers will eventually be installed in the SMA, the receiver optics design has been kept as simple as possible. For example, apart from the horn-lens combinations, which are unique to each receiver band, the optics for all four receivers in each group are identical. No focusing mirrors are used between the feed lens and the central diplexer, which simplifies the optical alignment of each individual receiver as well as the mutual co-alignment of all the receiver beams. The local-oscillator (LO)

injection scheme for the low-frequency receivers is a simple rotatable wire-grid polarizer adjusted to transmit a small fraction of the LO power and reflect nearly all of the signal power, with the reflected LO power diverted to an absorbing load. It is anticipated that sufficient LO power will be available at these frequencies to limit the signal loss using this scheme to 1% or less. Since available LO power for the high-frequency bands will be more limited, the LO for these bands will be coupled to the mixer via a Martin-Puplett diplexer. No sideband filtering is planned for the receiver optics at present. This results in a considerable simplification of the optics at the expense of somewhat increased system temperature for single-sideband operation. When the array is operating as an interferometer, phase switching techniques will be used to separate the upper and lower sidebands.

The mixer block, feed horn, and lens for each receiver are mounted in the cryostat on a removable cylindrical insert. It is anticipated that scalar feeds will be used for frequency bands up to at least 720 GHz. So far, prototype scalar horns have been produced for the SMA up to 520 GHz, using the design described in reference [1]. The lenses have been designed using the procedure described by Lee in Ref. [2] to provide a quadratic phase transformation free from amplitude distortion. The horn-lens combinations are designed to produce a virtual image of the horn aperture located behind the horn which is standardized for all receiver inserts, as will be described in the next section.

Optics Design

Traditionally, quasioptical feed systems for reflector antennas have been designed using fundamental-mode Gaussian beam analysis [3]. More recently, the importance of including higher-order modes in the analysis has been demonstrated [4],[5]. Nevertheless, the emphasis has been on propagation of a particular mode set and its associated phase slippage through the entire optical system. We have adopted a somewhat different approach which emphasizes the simplicity and natural frequency-independence of Fresnel imaging relations as a starting point for design. Multi-mode Gaussian beam techniques are

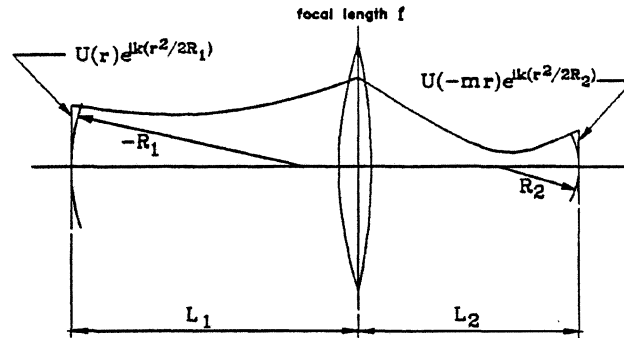


Figure 4 - Fresnel imaging by a focusing element.

then used as a computational tool for working out the propagation of the beam between images, with the choice of an appropriate mode set for a given calculation motivated chiefly by consideration of minimum computational effort to achieve the desired numerical accuracy [6]. The use of Fresnel imaging principles in beam waveguide design is not new. Previous work has discussed Fresnel imaging in the context of single-mode [7] and multi-mode [5] beam waveguide design. Here, our purpose is to stress the usefulness of a global application of imaging principles to broadband system design.

The basic Fresnel imaging relations for a single focusing element are illustrated in Fig. 4. For the parameters shown in the figure, the following relations hold for the fields at the images on either side of the focusing element:

$$\frac{1}{L_1} + \frac{1}{L_2} = \frac{1}{f} \quad \text{Eq. 1}$$

$$\frac{1}{R_2} = \frac{1}{L_2} \cdot \left[1 + \frac{L_1}{L_2} \cdot \left(1 + \frac{L_1}{R_1} \right) \right] \quad \text{Eq. 2}$$

$$m = \frac{L_1}{L_2} \quad \text{Eq. 3}$$

Eqs. 1-3 are derived using Gaussian beam propagation formulas in Ref. [7]; a more general derivation is given in Ref. [8]. The wavefront radii R_1 and R_2 at the two image planes represent quadratic phase curvatures which, when factored out of the fields in their respective image planes, yield two fields which are simply scaled and inverted images of one another. Note that this imaging property is independent of frequency.

The Fresnel imaging equations form the basis for the design of a broadband imaging beam waveguide which functions to image a plane at the receiver feed where the form and phase curvature of the field is independent (or nearly-independent) of frequency onto the subreflector. The phase curvature radius of the image at the subreflector is set equal to the Cassegrain focal length. The size of the image at the subreflector depends on the application— for a radio interferometer the goal is to maximize the antenna gain; in other applications considerations such as reduced sidelobes may be important. The choice of the image plane at the receiver depends on the nature of the feed. For horns, the form and phase curvature of the aperture field can be made nearly independent of frequency over a broad bandwidth. For other types of feeds such as quasioptical antennas, the choice of the optimum frequency-independent image plane has not been investigated thoroughly.

The design of the SMA optics presents a typical case for application of Fresnel imaging principles. The main constraints on the design were the size of the secondary mirror, the permissible range of locations for the beam waveguide mirrors within the allotted receiver cabin space, and the optical path length through the rotating diplexer and the receiver optics. The desire to avoid focusing mirrors in the individual receiver optics led to a requirement that all of the feed-lens combinations for the various receivers present the same image to the beam waveguide in order that any pair of receivers could simultaneously illuminate the antenna. A maximum size of 75 mm for the windows in the cryostat was established based on considerations of heat load and overall space available.

As a starting point for establishing the common image plane for all of the feed-lens combinations, the beam at the lowest frequency was assumed to have flat phase at the cryostat window in order to minimize the size of the low-frequency receiver optics and of mirrors M5 and M6. Since it was both undesirable and unnecessary for the lenses and windows at higher frequencies to be as large, the image plane was chosen to be located behind the feeds with negative phase curvature, producing a “virtual feed” located behind the real feeds as shown in Fig. 5. Choosing this location for the virtual feed allows the lenses to be smaller and hence thinner with increasing frequency, easing the problem of increasing absorption loss in the lens materials as well as reducing the heat load on the

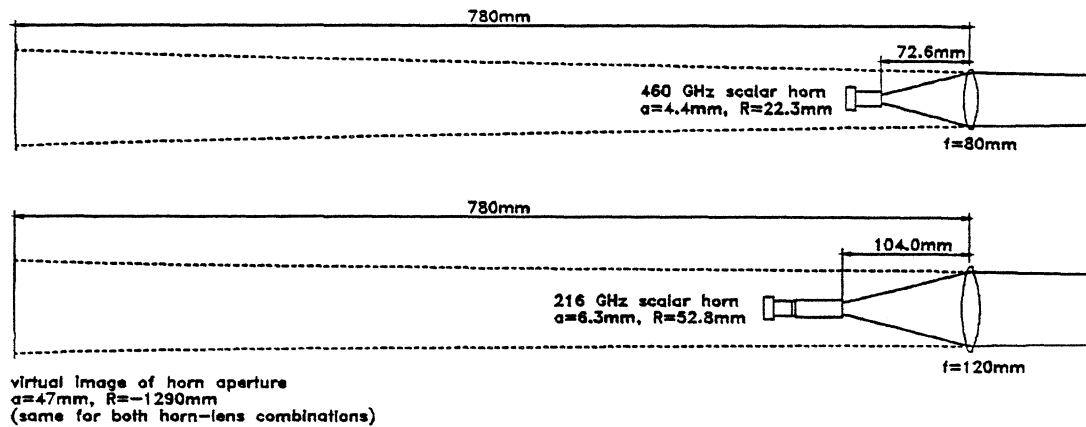


Figure 5 - Scalar horn-lens combinations for two receiver bands covering 176-256 GHz and 400-520 GHz. Both produce identical “virtual feeds” located behind the lens.

cryostat. Once the location of the virtual feed was established, the receiver optics were sized to reduce truncation effects to an acceptable level at the lowest frequency used in each receiver group (176 GHz for low-frequency receivers, 330 GHz for high-frequency receivers.) The truncation calculations were performed using multi-mode Gaussian beam methods described by Murphy *et al.* [9]. Lens diameters were chosen to minimize the product of truncation loss at the lens aperture and absorption loss through the center of the lens.

The virtual feed is imaged onto the subreflector by the beam waveguide consisting of mirrors M3 through M6. For scalar horns, an image of the truncated Bessel field at the feed aperture with 10.0 dB edge taper maximizes the antenna gain. The mechanical layout of the SMA antenna prevented the imaging from being accomplished with a single focusing mirror so two mirrors, M4 and M5, are used. For these mirrors, two design options were possible— two ellipsoidal mirrors, with an additional real image produced between M4 and M5, or an ellipsoidal M5 and hyperboloidal M4, with a virtual image behind M4. While the latter option would have resulted in a design with slower beams and hence more attractive from the standpoint of minimizing coupling loss and cross-polarization, the former option was chosen since the real image is a particularly good location for the receiver calibration loads and for the quarter-wave plate which will be used for circular polarization measurements near 345 GHz. Motivated by coupling loss

calculations of the kind described in the next section, the Z-shaped configuration shown in Fig. 2 for the beam waveguide mirrors was adopted to reduce the incidence angle, and hence the coupling loss, at the beam waveguide mirrors to an acceptable level.

Beam Waveguide Mirror Loss

Several mechanisms lead to beam coupling loss at focusing mirrors employed in beam waveguides [10]-[13]. For mirrors intended to couple two axially-symmetric beams, the change in beam divergence on either side of the mirror produces a geometric mismatch of the two beams across the mirror surface, with resulting coupling loss. For broadband mirrors, phase errors result in additional loss when the mirror is operated away from its design frequency. Finally, at points on the mirror away from the plane of incidence, the electric field of the incoming beam undergoes a rotation about the axis of propagation which produces a cross-polarization loss. With two similar mirrors located near images of one another, these losses can be minimized by using one mirror to partially cancel the effects of the other. For the SMA beam waveguide, this option was not feasible. Instead, the mirror losses have been held to a minimum by keeping the incidence angles small at M4 and M5 as mentioned above.

Mirror M5, which operates at a smaller effective focal ratio than M4 at all frequencies, contributes the greatest coupling loss— approximately four times that at M4. To estimate the coupling loss at M5, a method based on evaluating the aperture efficiency coupling integral across the mirror surface is used. Neglecting blockage and the smaller beam distortion caused by M4, a distant point source illuminating the antenna produces a uniform top-hat field distribution at the image of the subreflector between M4 and M5. This image is taken as the source plane for the beam on the sky side of M5. The source plane for the beam on the receiver side is the virtual feed, where the field is taken to be the truncated Bessel distribution produced by a scalar feed. (For the highest frequency bands, a different type of feed may actually be used.) The coupling between these two beams is then evaluated by direct numerical integration over the mirror surface. Based on the local conservation of the area-intensity product at the mirror surface [14], the coupling integral may be written as

$$C = \int_M (d\vec{a} \cdot \vec{S}_1)^{1/2} (d\vec{a} \cdot \vec{S}_2)^{1/2} E_1 E_2^*, \quad \text{Eq. 4}$$

where E_1 and E_2 are the incident and reflected fields, normalized to unit power in each beam, and

$$\vec{S}_1 = \frac{\nabla[\arg(E_1)]}{|\nabla[\arg(E_1)]|} \quad \text{Eq. 5}$$

$$\vec{S}_2 = \frac{\nabla[\arg(E_2)]}{|\nabla[\arg(E_2)]|} \quad \text{Eq. 6}$$

are the local normals to the incident and reflected wavefronts.

Fig. 6 shows the power coupling CC^* evaluated from Eq. 4 over the range of SMA operating frequencies and for four different ellipsoids with the same effective focal length, but designed to match the on-axis wavefront curvatures of the beams on either side of the mirror at four different frequencies. The theoretical aperture efficiency in the absence of mirror distortion is 86.9%. Bearing in mind the approximation introduced by ignoring the effects of M4, the difference between this figure and the calculated coupling integral gives a measure of the loss at M5. The overall trend exhibited by all of the curves in Fig. 6 is primarily due to the geometric loss, which increases as the effective focal ratios at the mirror decrease towards low frequencies. The differences between the curves indicate the effects of phase loss due to operation away from the design frequency. For the SMA, a design frequency of 345 GHz has been chosen as a suitable compromise between the low-frequency loss (~3.8%) and the high-frequency loss (~1.8%). It is worth noting that the loss estimated this way is considerably higher than what would be expected based on the method in Ref. [11], which considers the loss for a fundamental-mode Gaussian beam. This point should be borne in mind when attempting to design high-efficiency feed systems. Increasing the angle of incidence at M5 from its present value of 25° up to 45° nearly doubles the loss at all frequencies, which was the reason for adding the additional flat mirror M6 to effect the 90° turn in the optical path.

In performing the above calculation, two different Gauss-Laguerre mode sets are used to represent the beams on either side of the mirror. To achieve convergence of the

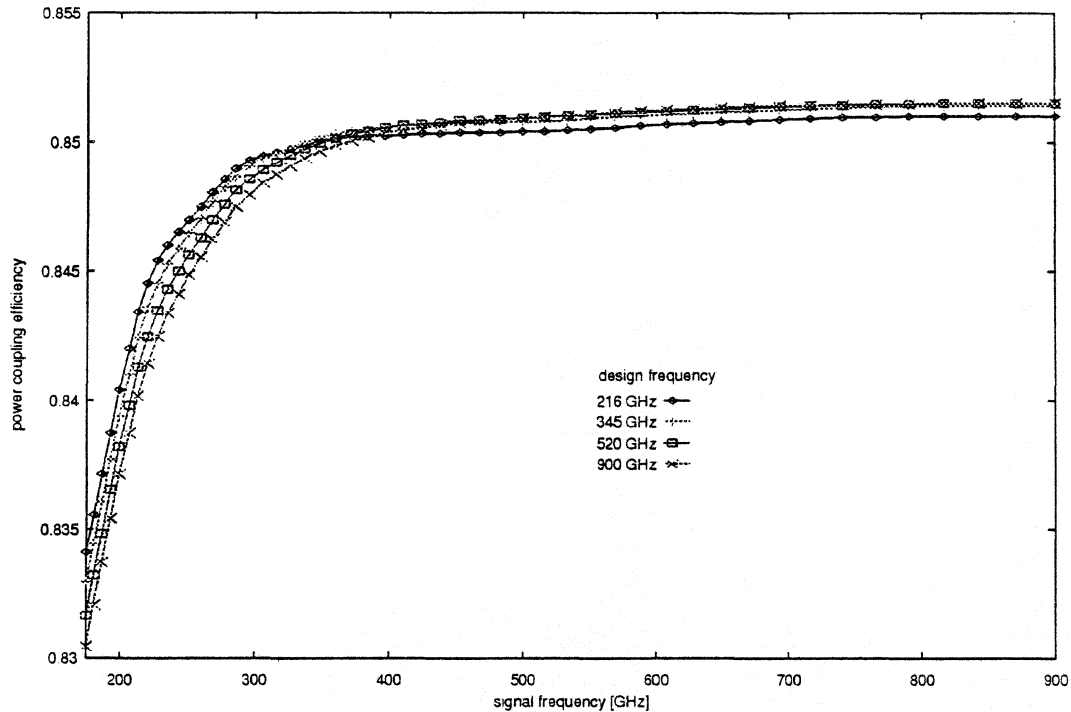


Figure 6 - Aperture efficiency coupling integral evaluated at the surface of mirror M5. In the absence of the mirror loss mechanisms discussed in the text, the theoretical efficiency would be 0.869.

integral to a few parts in 10^4 , a set of 10 modes with beam radius $w = 0.28 \cdot a_f$, where a_f is the radius of the horn aperture image, is used for the beam on the receiver side of the mirror, and a set of 20 modes with beam radius $w = 0.22 \cdot a_s$, where a_s is the radius of the subreflector image, is used for the beam on the sky side. The expansion coefficients for the scalar feed beam are calculated by numerical integration; those for the uniform top-hat are calculated using the recursion formulas given in Ref. [9]. To calculate the field at a point on the mirror surface, these two beams are each propagated to the surface point from their respective source planes using the usual multi-mode beam propagation methods.

Conclusions

This paper has presented an outline of the optics for the Submillimeter Array telescopes as an example of a Fresnel imaging approach to broadband millimeter- and submillimeter-

wave optical system design. Using the calculation of the beam waveguide mirror coupling loss as an example, it has shown how this point of view leads naturally to the identification of appropriate source planes and mode sets for calculations related to the detailed analysis of system performance.

References

- [1] X. Zhang, "Design of Conical Corrugated Feed Horns for Wide-Band High-Frequency Applications," *IEEE Trans. Microwave Theory Tech.*, **MTT-41** 1263 (August 1993.)
- [2] J. J. Lee, "Dielectric Lens Shaping and Coma-Correction Zoning, Part I: Analysis," *IEEE Trans. Antennas Propagat.*, **AP-31** 211 (January 1983.)
- [3] P. Goldsmith, "Quasi-Optical Techniques at Millimeter and Submillimeter Wavelengths," Chapter 5 in Infrared and Millimeter Waves, Vol. 6, K. Button, ed. Academic Press (1982.)
- [4] J. W. Lamb, "Quasioptical Coupling of Gaussian Beam Systems to Large Cassegrain Antennas," *International Journal of Infrared and Millimeter Waves* **7** 1511 (July 1986.)
- [5] R. Padman, J. A. Murphy, and R. E. Hills, "Gaussian Mode Analysis of Cassegrain Antenna Efficiency," *IEEE Trans. Antennas Propagat.* **AP-35** 1093 (October 1987.)
- [6] See J. W. Lamb, "Beam-mode expansion applied to focal-region fields," *IEE Proceedings-H* **139** 513 (December 1992) for an example of basis optimization as well as a demonstration of the relationship between Gaussian beam-modes and Fourier optics.
- [7] Ta-Shing Chu, "An Imaging Beam Waveguide Feed," *IEEE Trans. Antennas Propagat.* **AP-31** 614 (July 1983.)
- [8] J. W. Goodman, Introduction to Fourier Optics, McGraw-Hill (1968.)
- [9] J. A. Murphy, Aidan Egan, and S. Withington, "Truncation in Millimeter and Submillimeter-Wave Optical Systems," *IEEE Trans. Antennas Propagat.* **AP-41** 1408 (October 1993.) Also see J. A. Murphy, S. Withington, and A. Egan, "Mode Conversion at Diffracting Apertures in Millimeter and Submillimeter Wave Optical Systems," *IEEE Trans. Microwave Theory Tech.* **MTT-41** 1700 (October 1993.)

- [10] M. J. Gans, "Cross-Polarization in Reflector-Type Beam Waveguides and Antennas," *Bell System Technical Journal* **55** 289 (March 1976.)
- [11] J. A. Murphy, "Distortion of a Simple Gaussian Beam on Reflection from Off-Axis Ellipsoidal Mirrors," *International Journal of Infrared and Millimeter Waves* **8** 1165 (September 1987.)
- [12] J. C. G. Lesurf, Millimetre-wave Optics, Devices, and Systems, Adam Hilger (1990.)
- [13] S. Withington and J. A. Murphy, "Gaussian-mode Analysis of 'Thin' Mirrors," *Fourth Int. Symp. on Space Terahertz Technology* pp.211-222 (1993.)
- [14] M. Born and E. Wolf, Principles of Optics, 6th ed. Pergamon (1980) (section 3.1.2)

Alignment for the PRONAOS Submillimeter segmented telescope.

I.Ristorcelli¹, G.Recouvreur², M.Giard¹, B.Leriche², M.Gheudin³, G.Beaudin³, P.Encrenaz³, F.Buisson⁴, J.M.Lamarre², G.Serra¹.

1- Centre d'Etudes Spatiales des Rayonnements, BP 4346, F-31055 Toulouse Cedex

2- Institut d'Astrophysique Spatiale, Université Paris XI, Bâtiment 121, F-91405 Orsay Cedex.

3- DEMIRM-Observatoire de Meudon, 5 Place Jules Janssen, 92195 Meudon Cedex.

4- Centre National d'Etudes Spatiales, 18 av. Edouard Belin, F-31055 Toulouse Cedex.

Abstract

PRONAOS, a french balloon borne experiment devoted to Submillimeter Astronomy, consisting of a stabilized gondola, a telescope, a multiband photometer and a heterodyne spectrometer, is developed in collaboration between CNRS and the french space agency, CNES, to prepare the future space programs in astrophysics. Observations in this part of the spectrum requires low atmospheric water vapor and oxygen molecule emission, so that the telescope fly under a 1 000 000m³ balloon at an altitude of ≈ 37 km. First flight should occur in September 1994 from the USA, using a multiband photometer; the second flight is scheduled in 1995 with an heterodyne spectrometer. The telescope is a Cassegrain type, of a weight less than 250kg, with a 2m diameter primary mirror divided into 6 panels made of carbon fiber (core with a honeycomb structure and skin) and covered by a gold coating. The whole primary mirror has a surface accuracy of 12 μ m rms (all defects included). The global WFE for the telescope is assessed to be lower than 43 μ m.

The PRONAOS telescope has raised new technological problems: how to control the image quality and how to mark out the optical axis of a wide diameter segmented telescope, when it is integrated with its focal instrument. The difficulties induced by submillimeter measurements had pushed for a solution by mean of a visible wavelength method. We have summed up in this paper the method for the panels tilts control, based on an autocollimation procedure, by mean of a visible laser which produces a real image at the telescope focus.

However, on the contrary, the piston control along the optical axis can only be realized in the submillimeter wavelength. The method developed in that purpose is summarized in the paper. The precision reached for the final alignments of the primary mirror has been estimated to 8 arcsecond for the tilts and 7 μ m for the piston.

The reference for the optical axis of the payload (telescope + focal instrument) has been obtained by an original way. With the direct detection focal instrument, the method we have developed consisted into mapping the image given by a collimated beam whose axis had been referred to the star sensor in the visible range.

A similar method will be developed with the heterodyne focal instrument using another submillimetric source and a collimator with a larger diameter.

I - INTRODUCTION

The submillimeter band is one of the few regions of the electromagnetic spectrum which is still unexplored in Astronomy, because of the attenuation of the Earth's atmosphere. This spectral range is of great importance because the gas and dust of our galaxy and other galaxies, which is in processes of forming new stars, emits most of the energy precisely at these wavelengths.

Observations from a stratospheric balloon are unobstructed by the atmosphere which is opaque at submillimeter and far-infrared wavelengths, from the ground (Fig. 1). For this reason, a submillimeter balloon-borne observatory (PRONAOS) is being developed. It is scheduled to flight in 1994 and 1995 using a 1 000 000 m³ balloon at an altitude of 37 km (Fig. 2).

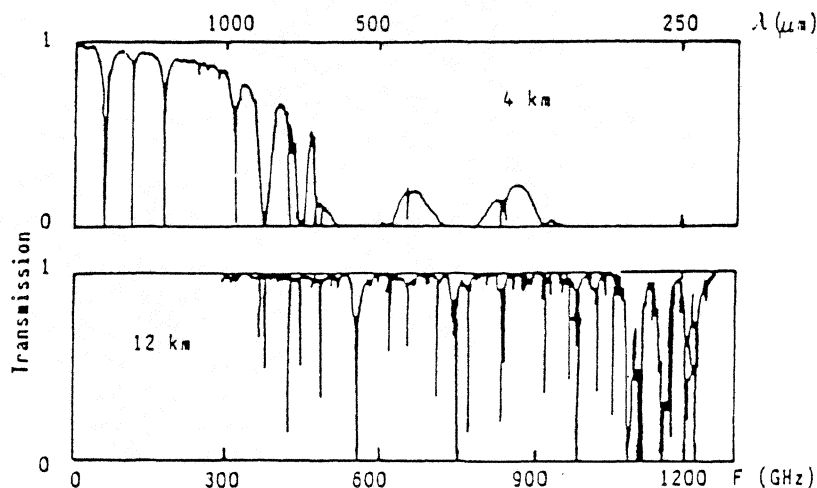


Figure 1 : Atmospheric transmission from mountain site (Hawaii) or airplane (KAO).

PRONAOS is intended to provide a facility for long duration flights (20 - 30h) for photometry and spectroscopy in the spectral region : $\approx 180 \mu\text{m}$ to 1.2 mm. The first flight will start from Fort Sumner (USA) next september ; long missions are also foreseen in the southern hemisphere.

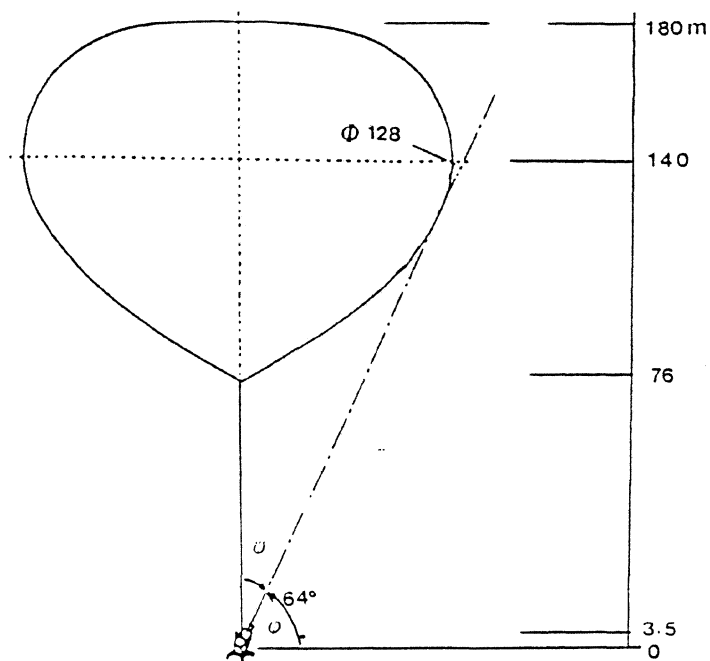
PRONAOS should also be considered as a preparatory programme for the next generation of space-borne Submm satellite contemplated by European and US agencies for the next century.

Funded mainly by the French space agency, CNES, PRONAOS is developed in close cooperation with French scientific institutes from CNRS and "Ministère de l'Enseignement Supérieur" in France, acting in this domain.

PRONAOS consists of a stabilised gondola supporting a 2 m diameter segmented telescope, associated alternately with an infrared Multiband SpectroMeter (SPM) or a high resolution submillimeter Heterodyne SpectroMeter (SMH).

- SPM will measure the Sunyaev-Zeldovitch effect in the clusters of galaxies, which permits to know their distance and their radial speed (and so the direct Hubble constant measurement) ; SPM is also dedicated to measure the thermal emission of cold dusts in the nearby galaxies which permits to know mass and space distribution of these dusts.
- SMH will be used to simultaneously detect the O₂ line and the H₂O line in the interstellar medium which permits the progress in the knowledge of the chemical processes and of the temperature and density in star formation regions.

The system Balloon-Gondola is working in a very specific environment, with the following characteristics :



- A balloon considered as fix with regard to the earth (considerable inertia for the dimensions $\varnothing \approx 60\text{m}$, $M \approx 2800\text{ kg}$).
- Long period "pendulations" of the gondola with regard to point A, $T \approx 18\text{ sec.}$ and amplitude $\approx 5\text{ arcminutes}$ on roll and yaw axis.
- Oscillations around the center of gravity of the gondola, due to the internal disturbances, $T \approx 1.5\text{ sec.}$ and amplitude about 5 arcminutes.
- Rotation around point B, due to the rotation of the balloon, and of the earth, on pitch axis.
- Wind disturbances due to the differential speed of the wind between balloon and gondola (about 5 km/h of differential wind applied to the gondola in the worst cas) on all axis.

Figure 2 : Flight configuration at ceiling.

II - PRONAOS GENERAL DESIGN

The PRONAOS on board instrumentation architecture consists of three parts :

- a carry away vehicle : the stabilised gondola.

The gondola vertical size is typically 7 m and its horizontal area is around 50 m² (Fig. 3). The on-board energy will permits a capacity of 30 kWh by a set of lithium batteries. The dry mass is 2400 kg for a total launching mass of 2800 kg, the mass of the pointed payload including the telescope, one focal-plane instrument and various equipments is approximately 500 kg.

- a common facility : a submillimeter telescope.

The two meters segmented telescope with a light weight primary mirror is a Cassegrain telescope with a focal ratio F/10. The telescope is pointed (accuracy of 5 arc seconds) with a three axis system : an azimuth axis providing decoupling in rotation between the balloon and the gondola, and an elevation/cross-elevation gimbal.

- a multiband scientific payload : 2 focal plane instruments :

. A SpectroPhotoMeter (SPM) using He3 cooled bolometers, dichroïcs filters, on the field 180 μ m - 1.2 mm over four bands. This focal instrument is described in Lamarre et al., 1994.

. An Heterodyne SpectroMeter receiver (SMH) with high resolution $\nu/\Delta\nu \approx 2.10^6$ will operate, in the first generation, to detect simultaneously the 368 GHz and the 380 GHz lines (Beaudin et al 1993), with a next goal of operating at 557 GHz.

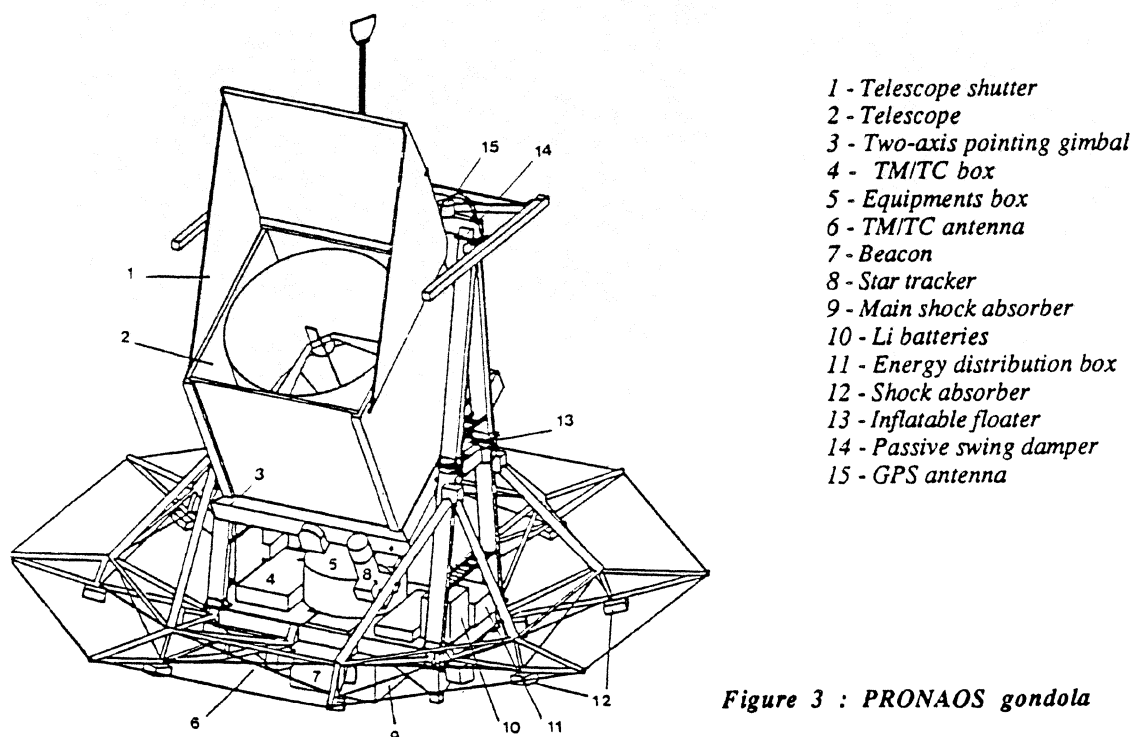


Figure 3 : PRONAOS gondola

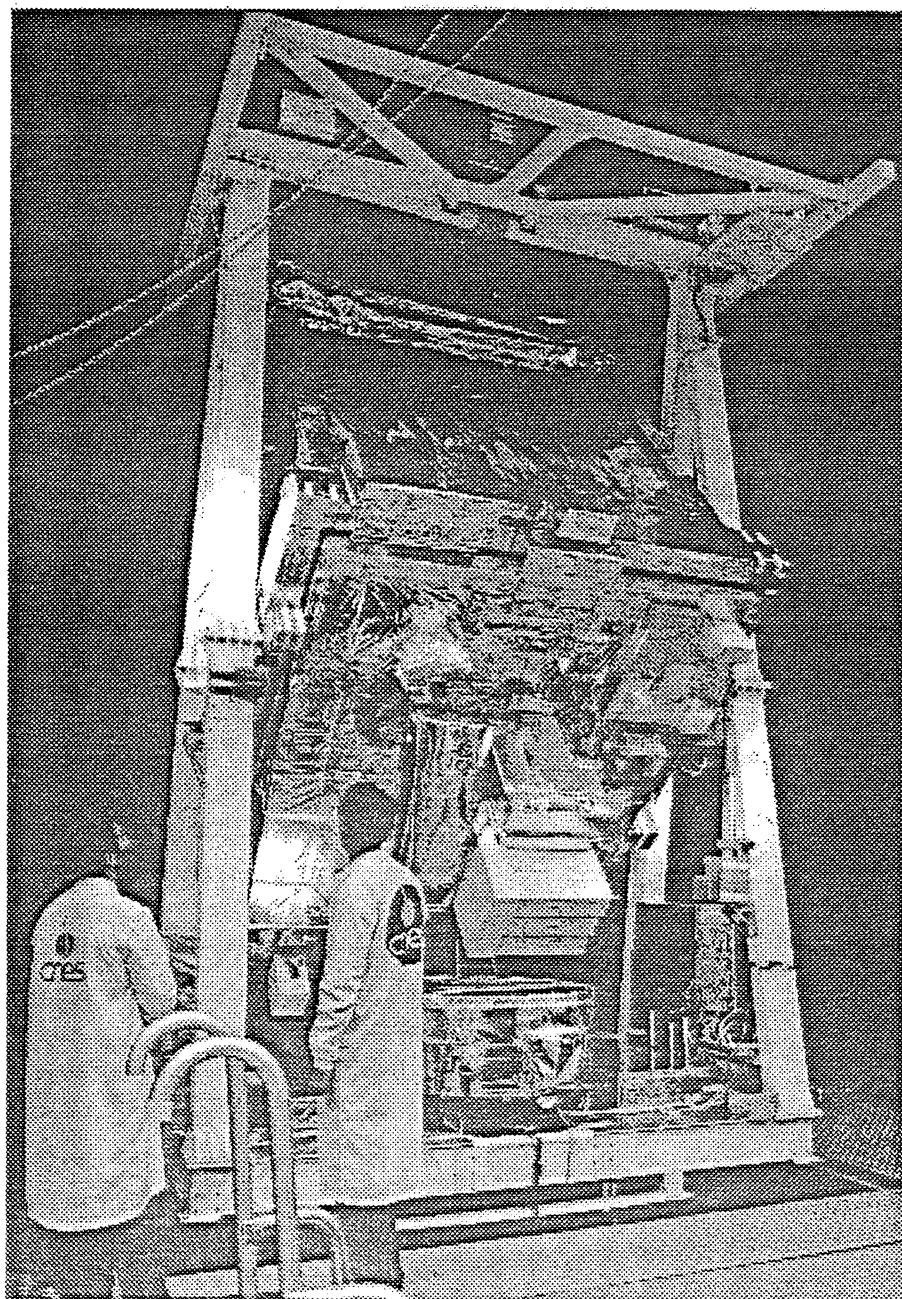


Figure 3' : PRONAOS - gondola, Telescope, SPM

III - PRONAOS TELESCOPE DESCRIPTION

In the frame of that project, CNES gave to MATRA-SPACE in Toulouse, the responsibility for the design, the development and the fabrication of the telescope ; its is pointed with an accuracy and a stability of 5 arcsecond RMS by the gondola stabilisation equipment and by a stellar sensor. It will collect the energy towards the focal instrument. A detailed description of the telescope is given in Buisson and Duran, 1990. In the following, we intend to summarize the main specifications of the telescope its design and innovative aspects and to describe its measurement procedures.

III.1. General specifications

Optical Design

The telescope design results from a compromise between on one hand the scientific requirements asking for a collecting area as large as possible and for a high spatial resolution and on the other hand the constraints concerning the height granted by the launching system and the total weight which can be launched.

The resulting optical specifications are summarized in the following table :

Type	Axi-symmetric Cassegrain
Focal length	20 m
Aperture ratio	F/10
Secondary focal length	2818.2 mm
Primary Secondary distance	1528.2 mm
Primary mirror	
- focal length	1778.8 mm
- diameter	2045 mm
- central hole diameter	255 ± 5 mm
Secondary mirror	
- focal length	275.1 mm
- diameter	273 mm
- reflecting central cone	ϕ 50 mm, h = 4 mm
Reflectivity efficiency	> 0.97

Telescope optical characteristics

Requirements concerning image quality are issued from the value wished for radiometric energy concentration in the focal plane of the integrated telescope considering various points of the field and the spectral domain of work. It is translated into :

- requirements concerning the r.m.s. wave front error which must be better than $43\mu\text{m}$.
- requirement concerning geometrical concentration of light beams that is i) 80 % of energy in a circle of diameter smaller than 17mm, ii) 90 % of energy in a circle of diameter smaller than 19 mm.

The image quality requirements and its relations with the main specified characteristics will be discussed later in this paper.

Mechanical design

The mechanical design must optimize the following constraints : i) stability under gravity and thermal variations, ii) rigidity (no global eigen mode lower than 20 Hz), iii) resistance to shock at landing (10g), iv) interface with two different focal instruments, v) mounting of several equipments (star tracker, inertial block, electronics) necessary to the pointing system. The total mass is 250 kg.

Thermo-emissive characteristics

Because all the instrumental variations of the emitting flux induce parasitic signals, the part of the telescope such as the mirrors, the inner sides of the baffle or the structure supporting the secondary mirror (which are either in the beam of the main lobe or close to that beam and so could intercept the secondary lobes created by diffraction) must have very faint sub-millimetre emissivity. For the same reason, their temperature must remain as stable as possible.

III.2. Main features of the telescope design

The telescope is made up of the following main parts (see Fig. 4)

- a basic box manufactured in CFRP honeycomb, supporting the reference plate, the secondary structure, the quadripod and assuring the interface firstly with the gondola pointing system and secondly with the focal instrument,
- the secondary structure made from carbon lattice which provides the frame for the Sun baffle as well as for the thermal protection. This structure is ended by an active cover whose functions are : i) to protect the mirrors from dust and light during integration and launching, when it is closed and ii) to protect the internal part of the telescope from solar light when it is open (during most of the day part of the flight),

- the jack mechanism for opening/closing the cover,
- the active primary mirror and its 6 panels,
- the fixed secondary mirror,
- the structure carrying the secondary mirror, in carbon fibre,
- the electronics boxes and harness required for the command of the primary mirror, the thermal control, and the command of the cover.

An inner sub-mm baffle manufactured with aluminised mylar (in reverse side) minimize the emitted submm radiation and maximize the thermal infrared coupling allowing to optimize the thermal homogeneity inside the telescope.

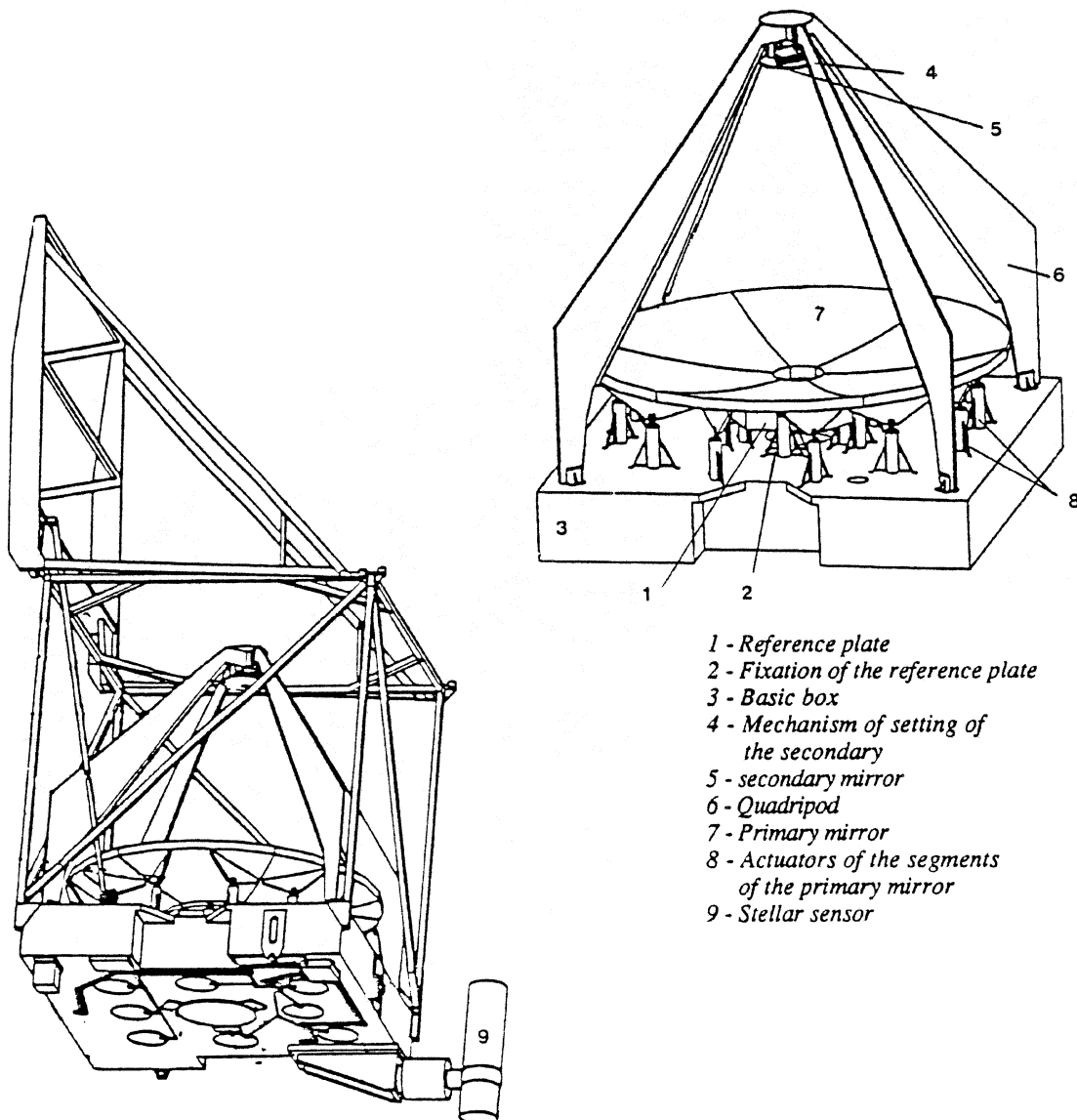


Figure 4-5 : Main PRONAOS telescope features

III.3. The semi-active primary mirror

Main reflector configuration

The primary mirror (Fig. 5) consists of six identical panels each being positioned in respect with a central reference plate by means of a servo-controlled loop using capacitive sensors. This configuration has been selected because a single mould was sufficient to manufacture all the identical panels. The central reference plate was produced in the same composite material as the panels that is two skins in carbon fibre of M40 type separated by a core in the same material. It is fixed on the main box.

The positioning of each segment versus the reference plate is controlled using 30 capacitive distance sensors and 18 electrical screwjacks actuators.

This servo-loop mechanism and its associated electronics represent the main contribution (23 μ m rms) to the global w.f.e. ("wave front error").

Panels

Their realisation was under MAN (Germany) responsibility. Eight panels (6 flight models, 1 qualification and 1 spare) were manufactured by a replica-thermique technique from one mould in zerodur glass, on a structure of honeycomb and skins in carbon fibre.

The process includes an injection of epoxy resin and a vacuum gold deposit (coating) of 0.15 μ m. The measured surface profile on one panel has been made using a 3D machine, for a set of points spaced by a few centimeters.

Mould

It has been manufactured by REOSC (France), in zerodur glass-ceramic. The final surface quality was reached through polishing with a computer-controlled polishing machine.

Servo-control system

- Sensors

They comprise :

- 6 intersegments sensors measuring the relative displacement of two adjacent panels
- 24 sensors (4 by panel) giving information about the panel positioning in respect to the reference plate

The system has 18 degrees of freedom; one sensor by panel is then in redundancy; it is used to improve the performance of the system and to be used as a spare model if any failure appears in one sensor.

The resolution of the sensors is 50 nm, reached by using differential capacitive sensors.

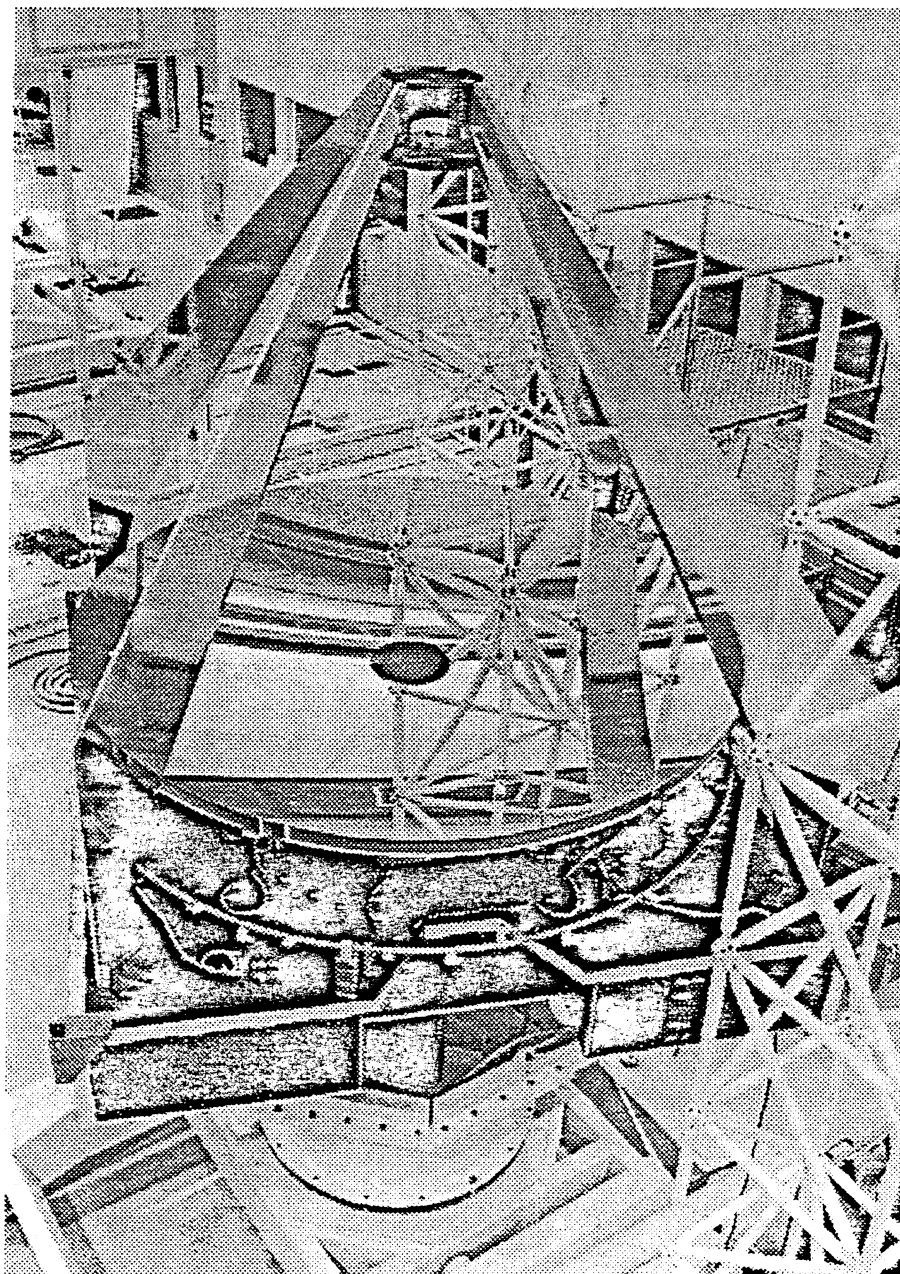


Figure 5' : PRONAOS Telescope without the baffle

- Actuators

Three actuators are dedicated to the maintaining of each panel in position according to 6 degrees of freedom. They are constituted by electrical screwjacks whose resolution is 0.1 μ m.

- Electronic

It realizes the control loop at a rate of 150 Hz. It is composed of 3 parts :

- an analogic electronic which generates pulses towards the leads and acquires the signal issued by the sensors,
- a numeric electronic which processes those data and converts them into commands. That electronic is based on a 80C86. The implementation of the algorithm of process of the necessary matrix (18.30) is made by software. That same computer assures other functions such exchanges with the gondola data processing system including TM/TC communications through a high speed serial data line,
- a power electronics which realizes the command of the screwjacks.

IV - TELESCOPE CONTROL ALIGNMENT PROCEDURES

The segmented primary mirror has been tuned by MATRA using a specific procedure derived from Hartman method combined by a rotation of the whole mirror respectively to its symmetry axis. Made in the visible range, these operations control, with a sufficient accuracy, the positioning of each panel in rotation. But the positioning in translation along the telescope optical axis has been made in the first stage by means of direct metrology.

After the delivery of the whole telescope by MATRA-MARCONI SPACE to the scientific team, the main problem to resolve was to control : i) the positioning of each panel belonging to the main reflector, ii) the relative positioning of the two telescope mirrors, each respectively to the other, and in respect to the nominal focal plane location. This positioning had to be controlled regarding the image quality specification.

IV-1. Specifications and spectral range for alignment

Each panel of the primary mirror presents 3 degrees of freedom:

- β , about the Y axis,
- 2 tilts:
 - ϕ , about the Z axis,
- 1 translation, called "piston": Tx, along the optical axis.

The specifications for the image quality of the Pronaos telescope have been described as the following. The ratios of 80% and 90% of the encircled energy must be contained respectively into 17 and 19mm diameter values in the focal plane. These values are coherent with a requirement on the root mean square of the wave front error value (WFE_{rms}) equal to $43\mu m$ (all telescope). An allocation of a $WFE_{rms} = 9\mu m$ has been given to the primary mirror.

Using a ray-tracing modelling and the Strehl criterion, Safa (1991) has shown that such specifications were equivalent to the following panel alignment tolerances:

- $\beta_{max} = 5.2$ arcsecond
- $\phi_{max} = 2.2$ arcsecond
- $T_x = 7\mu m$.

Moreover, those modellings have pointed out a drastic dependance of the image quality on the wavelength range of the incident radiation field. This is due to the spatial frequency of the surface defaults: it corresponds to $\lambda/15$ in the submillimeter and 24λ in the visible. In consequence, the visible image energy distribution is limited by the diffusion, while it is diffraction limited in the submillimeter range.

In particular, this implies that a misalignment of a panel will induce different aberration effects in the visible and in the Submm range. Using its modelling, Safa (1992) has shown that the diffusion image (visible) is not modified within a wide range of translation misalignment; on the contrary, this can degrade considerably the diffraction image quality, because of interference effects.

In consequence, the panels piston alignment must be achieved in the Submm range. It has been necessary to develop a new method for the piston control, able to satisfy both the image quality specifications and feasibility criterions with a view to operate the defined procedures on the launching site.

On the contrary, the modelling for the alignment of the panels tilts shows that it can be obtained in the visible wavelength. Since the development of an experiment in the visible is much less constrained in the visible than in the Submm we have decided to proceed in two stages: first, we have achieved the tilts alignments in the visible range, and then completed with the piston alignment.

The following two sections summarize this method which has been described in detail by Ristorcelli et al. 1994.

IV-2 Tilts alignment

Principle: we use an autocollimation process in the visible range. The objectives are to analyse the diffusion image associated with each panel in the focal plane and to get it centered on the focus position by mean of its tilts movement (β , ϕ).

- Mounting description: a schematic view of the autocollimation mounting is given in fig.6. We use an helium-neon laser source operating at $\lambda=632\text{nm}$. The source hole ($\varnothing=200\mu\text{m}$), placed at the focus distance, is enlightened by the laser beam passed through an objective. The beam is then partially separated ($\sim 50\%$) by a beam splitter. The collimated beam, reflected by a plan mirror ($\varnothing=800\text{mm}$), gives a diffusing image in the focal plane of the telescope, which is visualised by mean of a frosted glass. The image acquisition is made using a CCD camera. We can then analyse the image associated with a given panel. A special software allows to determine the barycenter position, from which we deduce the deviation from the nominal focus point. Each panel is then tilted in consequence, by mean of its actuators and in respect to the nominal optical axis.

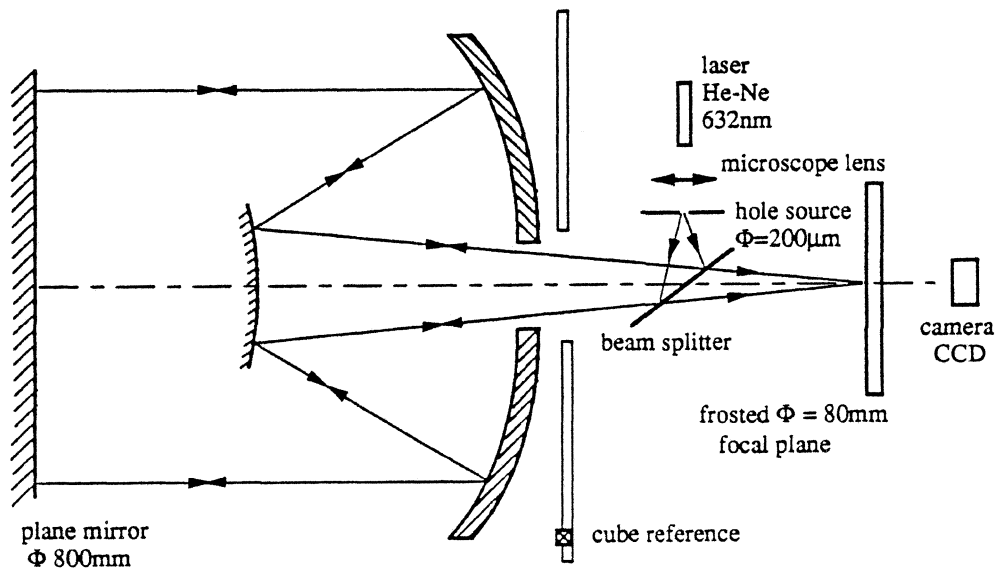


Figure 6: Autocollimation schema

The nominal optical axis of the telescope has been defined by Matra-Marconi-Space and is given by a mirror cube fixed on the basic box of the telescope (see figure 6).

- Precision of the tilts alignment: with the method described above, we have obtained a tilt control within a precision of 10 arcsecond.

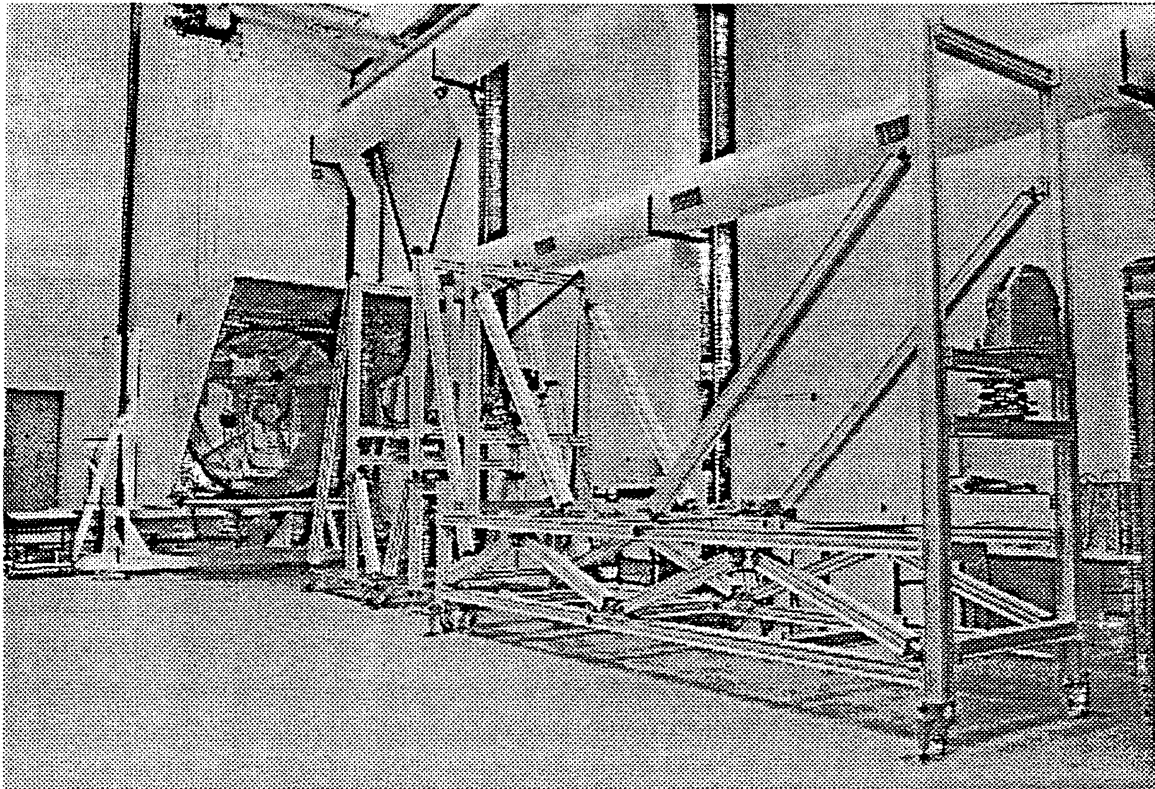


Figure 6' : PRONAOS telescope under alignment procedure

IV-3. Translation alignments:

- Principle: the objective is to analyse the distortion of the diffraction image associated with a point source when the panel piston varies.

Let's consider a monochromatic (λ) parallel incident beam centred on an intersegment of the primary mirror. If there is a translation misalignment $\delta \neq 0$ between the two panels, then the diffraction image at the focus is altered by interferences which are function of the ratio δ/λ .

This distortion is maximum for $\delta=\lambda/4$ and periodic with a $\Delta\delta=\lambda/2$ period. On the contrary, if we use a large wavelength passband incident beam, then the periodicity is broken by the superposition of the different wavelengths and the distortion variations decrease when the width of the wavelength band increases. A unique piston value which gives a nominal diffraction image ($\delta=0$) is obtained when using an intermediate value of the bandwidth, located around $\lambda/\Delta\lambda \approx 1$.

The locating of this particular position for each intersegment allows the alignment translation of the whole primary mirror.

In addition, the incident beam lights up in practice only a small surface sub-pupil of the primary mirror. An analyse of the diffraction image obtained for different radial positions of the sub-pupil on the intersegment leads to further information on the tilts alignment of the two panels.

- Mounting description

The Submm mounting that we have developed is shown in figure 7.

- Source system: we have used a high pressure mercury vapor arc lamp, which radiates both in the visible and the Submm, as a blackbody at a temperature $T \approx 1800\text{K}$. Its emission beam is then refocused by a parabolic mirror onto a hole source ($\varnothing=1.3\text{mm}$) and is modulated by mean of a chopper.

The hole source has been placed at the focus point of a collimator ($\varnothing=200\text{mm}$), in order to obtain an output parallel beam.

- The focal system: A diaphragm ($\varnothing=10\text{mm}$) is centred at the nominal focus point, in order to sample the diffraction image. The detector we have used is a silicium bolometer cooled at liquid helium temperature ($T \approx 4\text{K}$). It is located inside a dewar containing high passband wavelength filters and a quartz lens to focus the sampled image on the detector. The

electrical signal delivered by the bolometer is then analysed by a lock-in amplifier connected to the chopper.

- **Measurement process:** in order to obtain a cartography of the diffraction image in the focal plane, the easiest way is to move the hole source in its focal plane so that the collimated beam axis varies. For that purpose, the system source (arc lamp + mirrors + chopper + hole source) has been rigidly mounted on a motorized micro-control movement. The amplitude of the motion, the value and number of steps and the integration time have been optimized in order to cover the whole diffraction image, with a sufficient signal to noise ratio and within a reasonable time. A processor connected both with the micro-control movement and the lock-in amplifier allows a simultaneous acquisition of the signal and the source position. This leads to a cartography of the diffraction image which can then be analysed through different criteria such as its barycenter position or the energy distribution. We repeat this image analysis for a sample of piston values applied by mean of the three actuators.

- **Accuracy of the method:** the image distortion is detectable by this method within $\pm 7\mu\text{m}$ around the nominal translation position. An analyse of the diffraction images obtained for different positions of the sub-pupil along the intersegment has also allowed to improve the tilts control accuracy to ± 8 arcsecond.

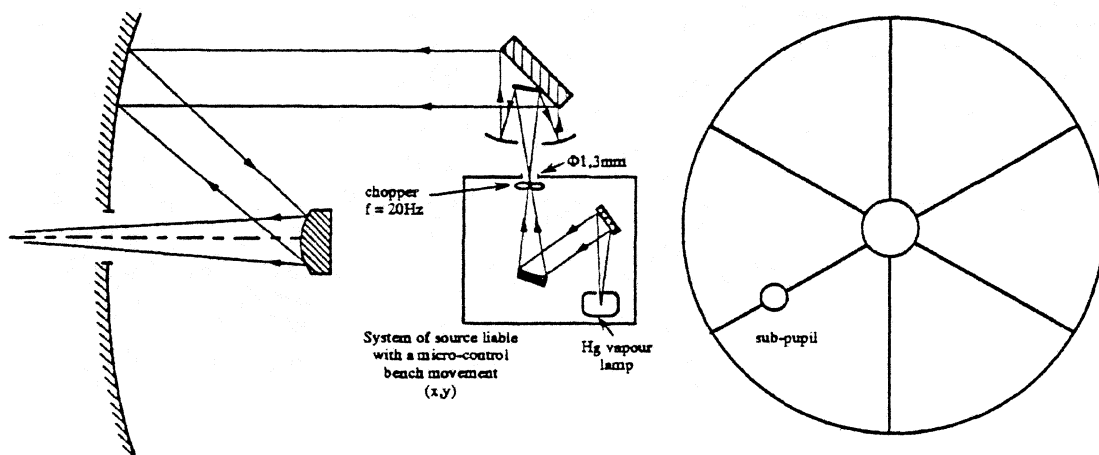


Figure 7: Mounting of the collimated beam

V- Payload alignment control

We call "payload" the integrated PRONAOS sub-system containing the telescope and one of the two focal instruments.

The payload axis may deviate from the nominal telescope axis mainly because of the optics alignment inside the focal instrument and a slight structure deformation due to the different mass configuration of this integrated system. It is important to locate the real axis of the payload nearby the nominal telescope axis, in order to avoid geometrical aberrations damaging the image quality.

The method developed and applied for SPM has been described by Ristorcelli. et al 1994. It consists in using the multiband photometer with a view to map the illumination in the focal plane when a collimated beam scans incident directions around the nominal telescope axis. The incident direction is controlled using a high accuracy theodolite (± 2 arcsecond).

The technological difficulty is increased with the heterodyne focal instrument SMH because the wavelength passband of the heterodyne instrument is reduced and the use of a continuum incoherent source would lead to an insufficient signal to noise ratio. In addition, the requirement on the focal positioning in translation along the optical axis is more constrained.

The development of a modified method derived from the one described above is now in progress. The source used will be a line source increasing the radiated energy inside the instrumental bandwidth but the principle of the alignment procedures will remain the same. Another need will be a collimator with a larger diameter, lightening a sub-pupil with a much more larger area.

VI Conclusion

PRONAOS constitutes a new step in the french ballooning. Devoted to get astrophysical results and to support new technological developments with a view to prepare future satellite Submm astronomical experiments, PRONAOS gives the opportunity to develop new subsystems methods. In particular, the alignment procedures and control, involving the telescope and the payload, need to operate using non-conventional methods.

Combining measurements respectively in the visible and in the submillimeter ranges, we reach to control the positioning of each panel of the segmented main reflector, within ± 8 arcsecond in rotation (two axis) and $\pm 7\mu\text{m}$ in translation along the nominal telescope axis. The procedures used allows to measure the angular off-axis existing between the payload and the star-sensor, with an accuracy of ± 10 arcsecond. This measure will be confirmed during the first PRONAOS flight, scheduled in September 1994, with the multiband photometer SPM.

References and bibliography:

- Buisson F. and Duran M., 1994, Proc. 29th Liege International Astrophysical Colloquium From Ground-Based to Space-Borne Submillimeter Astronomy, Liège, Belgium, 3-4 July 1990, ESA SP 314 (December 1990).
- Lamarre J.M. et al. 1994, IR Phys. Tecno., Vol. 35, N0. 2/3, pp.277-289.
- Ristorcelli I., Lamarre J.M., Giard M., Recouvreur G., Leriche B., Serra G., submitted to "Experimental Astronomy", 1994.
- Safa H., Applied Optics, Vol. 31, No. 13, 1992.
- Safa H., Ph. D. Thesis, 1991, CESR Toulouse, France.
- Beaudin G., Deschamps A., Encrenaz P., Feautrier P., Febvre P., Gheudin M., Léridon B., Maoli R., Pernot J.C., Robert C., Ruffié : "PRONAOS" a balloon borne experiment for submillimeter radioastronomy whith a 380 GHz SIS heterodyne receiver , SPIE LASE Astronomy Instrumentation, L.A., USA, january 1993 ; 18th International conference on Infrared and Millimeter waves, University of Essex, U.K., sept. 1993.

'Towards the Realisation of Space Borne Terahertz Waveguide Devices'

C M Mann, B J Maddison, D N Matheson, *M L Oldfield, B N Ellison

Rutherford Appleton Laboratory, Chilton, Didcot, Oxon, OX11 0QX, UK

* University of Kent, Canterbury, Kent, UK

Abstract

A new method for assembling dot matrix Schottky diode mixing structures in a single moded terahertz waveguide is described. A novel integrated 'whisker-filter' has been developed which allows very low inductance whiskers to be implemented. The quasi-planar whisker/diode structure is extremely rugged and has obvious applications for space borne devices. In addition, the simple lithographic technique used to fabricate the whisker makes it ideal for applications in place of the more traditional wire whisker.

Introduction

Although open structure terahertz mixers have been reported with excellent sensitivity [1] there are good reasons for pursuing the development of terahertz waveguide devices. Waveguide devices can be built with near perfect antenna coupling, and this may be important in atmospheric sounder applications. It is easy to incorporate tuning elements into waveguide cavities, and a wide range of circuit embedding impedances can be implemented: this may allow greater flexibility in the choice of diode design than in current open structure devices. The frequency dependent nature of waveguide allows harmonic frequencies to be easily separated; this is an advantage when building harmonic mixers and multipliers. Finally, there is a vast heritage of waveguide design and fabrication techniques.

For these and other reasons waveguide devices are invariably chosen for low noise radiometers in preference to open structure devices at wavelengths longer than ~500 microns. However, the feasibility of terahertz waveguide devices depends crucially on the answers to three questions, and these will be considered in turn.

- Can mechanical cavities of suitable tolerance be manufactured?
- Are associated waveguide losses acceptable?
- Can a low inductance whisker contacting scheme be realised?

Firstly, it is clear that structures with suitable mechanical tolerance can be manufactured. Preliminary results reported elsewhere [2] show that corrugated feedhorns with good beam efficiencies can be manufactured at frequencies at least as high as 2.5 THz.

Waveguide and feedhorn loss, however, remains a concern and is currently being investigated. But there are good grounds for optimism. A simple estimate suggests that waveguide loss remains small compared with intrinsic mixer loss even at 3 THz, and we are encouraged by mixer conversion loss measurements which demonstrate that waveguide loss remains low at frequencies at least as high as 700 GHz. Of course, loss may be a strong function of waveguide surface finish and conventional machining techniques may not be adequate at terahertz frequencies: but in this case it should be possible to fabricate waveguide with mirror finish surfaces using standard lithographic techniques [3].

We therefore expect that it is realistic to scale the mechanical cavity. It is doubtful, however, whether a traditional wire whisker can be made sufficiently short to operate at terahertz frequencies because of excessive circuit inductance. For example, a simple calculation suggests that even a $\sim 50\mu\text{m}$ long whisker will have a high inductance, and this will make it difficult to couple power efficiently to the diode. Furthermore, excessively short wire whiskers are often mechanically unstable, a problem exacerbated by the small area diodes which are inevitable at terahertz frequencies. In order to circumvent this problem we have developed and prototyped a new 'quasi-planar' whisker which is fabricated photolithographically.

The 'quasi-planar' whisker structure

The 'quasi-planar' whisker [4], a schematic diagram of which is illustrated in figure 1, has a number of potential advantages. For example, it can be made very short, is easy to fabricate and all dimensions can be specified to a very high tolerance ($< 1\mu\text{m}$). Finally, the natural spring of the thin strip obviates the need for a bend in the whisker.

The Planar Whisker

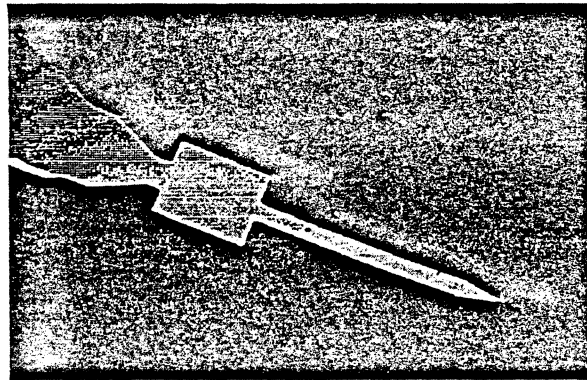
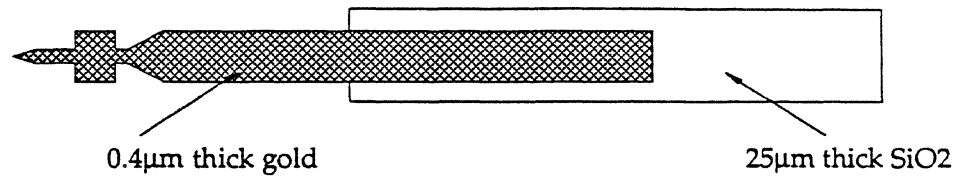


Figure 1

The fabrication process involves only straightforward lithographic techniques used in conjunction with some micro-machining carried out on a precision dicing saw, and is described as follows. The whisker is formed from a pure gold film which is deposited onto a quartz substrate using either evaporation or sputtering. The thickness of the film (and hence the whisker) determines the smallest diode that can be contacted: the whisker discussed here was made from an 0.4μm thick film. Thicker films have been tried successfully and we do not expect problems to arise from the use of even thinner films.

The basic form of the whisker is patterned into the gold using standard wet etch lithography. Wet etching has an unexpected advantage over dry etching in that it is not necessary to accurately reproduce the exact dimensions of the whisker tip in the photoresist used. This is due to the undercutting action of the gold etch resulting in a natural sharpening of the whisker tip.

Next, the whole substrate is mounted face down onto a carrier substrate using a proprietary wax. The back side of the quartz substrate is back lapped to the required thickness and a trench is cut directly behind the array of whiskers (figure 2).

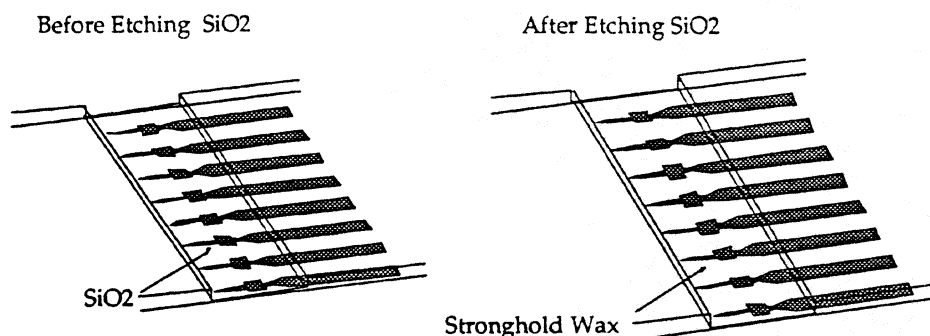


Figure 2

A few microns is left directly above the whiskers, and this is then completely removed using a standard quartz etch. The whisker array is then diced and all of the individual whiskers are then washed off the carrier substrate using acetone. By leaving the whisker attached to a quartz substrate, handling problems are greatly alleviated because by comparison the substrate is very large.

Large numbers of identical whiskers can be produced in a few hours, typically 100-200 in each run and this dramatically reduces the time required to assemble an RF device when compared with the traditional whisker.

The integrated whisker/RF filter

Whilst the whiskers described in the last section are useful for incorporating into standard millimetric or sub-millimetric devices it is a very simple step to integrate the whisker with another element of the circuit, in particular the RF/IF filter circuit upon which normally a diode chip or whisker is mounted. This simplifies the device construction procedure considerably (compared with using a normal wire whisker) and the size to which the components can be made is dependent only upon the photolithographic process used. Thus, it becomes relatively straightforward to fabricate RF circuits that have the low parasitics required for terahertz operation. A schematic diagram of such an integrated whisker/RF filter is shown in figure 3 and the prototype component fabricated using the technique previously described is shown in figure 4. In this example the dimensions of the whisker structure have been designed for operation at 2.5 THz.

For these novel whisker structures the substrate has been removed from underneath the four section RF/IF filter so as to avoid the presence of a

dielectric in the microstrip filter channel where it breaks through into the waveguide. In order to demonstrate the electrical feasibility of this arrangement scale model measurements have been carried out. These show that this is a valid electrical structure, and that a good range of diode embedding impedances can be accessed by varying the 'whisker' length and/or the length of the first filter section.

The Integrated Whisker/ Filter

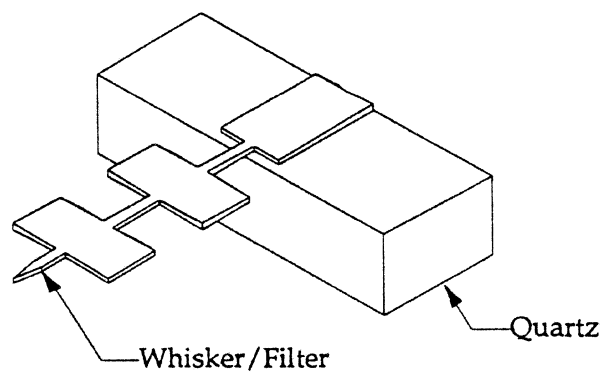


Figure 3

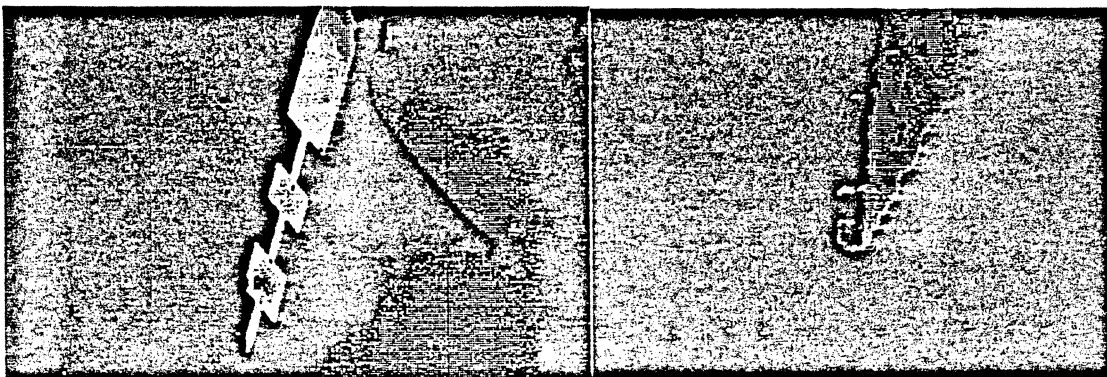


Figure 4

Diode contact tests

The mechanical feasibility of the whisker arrangement has been assessed by repeatedly contacting a dot-matrix diode in a simple test jig which allows diode and whisker to be positioned and contacted with sub-micron precision under an optical microscope, whilst monitoring the IV characteristic. A number of interesting and perhaps surprising features have been noted. Firstly, once a contact has been achieved it is possible to continue to move the diode and whisker together by many microns without changing the diode characteristic: rather, the whisker is observed to bend in a smooth arc along its length, and spring back flat once the pressure is removed. Secondly, even after repeated contacts the whisker tip remains essentially undamaged. The whisker/filter in figure 4 has made twenty diode contacts prior to this SEM photograph being taken. This behaviour is attributed to the 'two dimensional' nature of the structure: because it bends more readily than a wire whisker, the force on the diode tip and anode is dramatically reduced, thereby allowing it to be recontacted again and again. This behaviour has been observed with whiskers which are as thin as $0.4\text{ }\mu\text{m}$. In similar circumstances the tip of a wire whisker (even when thinned to a few microns) rapidly blunts, shears, or punctures through the diode anode.

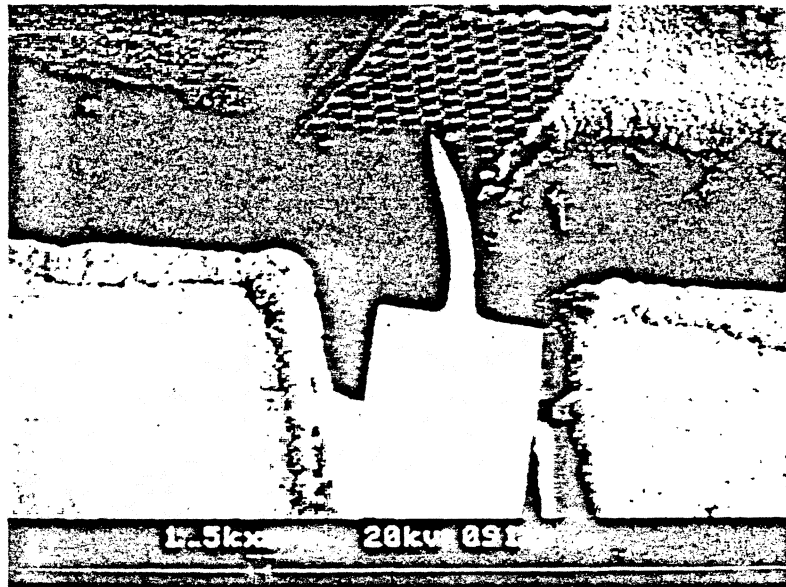


Figure 5

Once a contact has been established a small bend is left in the whisker to hold it in place, the quartz IF substrate is glued into the block and the final IF

connection is made. Figure 5 shows a finished 'mixer circuit' fabricated in this way. In this example, which uses a whisker-filter similar to that in figure 4, the whisker is 25 μ m long. The mixer diode is a UVA 1H24, a type used in the UARS MLS space instrument, and was chosen for this test to demonstrate known contact reliability.

In order to be a realistic arrangement it is important that the whisker diode contact is rugged. We have therefore subjected the test structure to a series of rigorous environmental tests. These included a thermal test (described in figure 6).

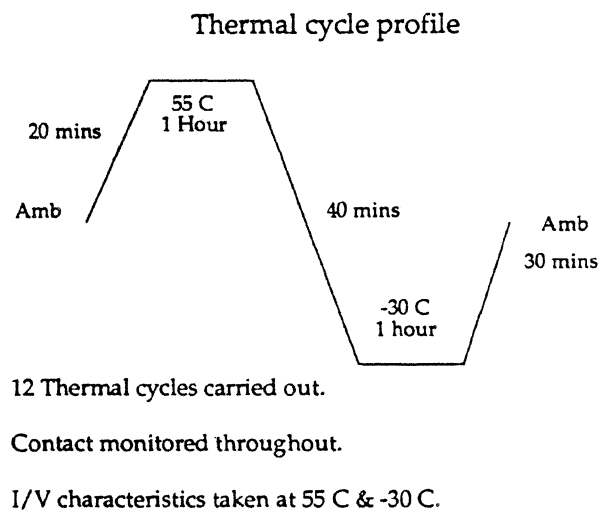


Figure 6

No change was noted to the ambient IV characteristic. In addition to the thermal cycle the test structure was also put through a three axis vibration test. The vibration test specification is shown in tables I and II, and is believed to be representative of a 'typical' space application.

Vibration Test Levels

Table I

Sine	Frequency (Hz)	Level	Duration
All models	5 - 20.35	18 mm pk pk	1 sweep
	20.35 - 100	15 g	
	2 oct/min sweep		

As was the case with the thermal test, no change was observed to the IV. This was a very encouraging result and it is believed that this is the first time that a whisker contact suitable for terahertz operation has survived this level of testing.

Table II

Random	Frequency (Hz)	Level	Duration
Qualification level	20 - 50	+ 3 dB/Oct	3 Minutes
	50 - 300	0.3 g ² /hz	
	300 - 2000	- 3 db/Oct	
		15.7 GRMS	

Conclusion

In the course of investigating waveguide technology for terahertz applications we have developed a new type of 'quasi-planar' whisker technology which may permit the use of dot-matrix diodes in single moded waveguide at wavelengths as short as 100 μm . A representative whisker and RF/IF filter structure designed for use at 2.5 THz has been prototyped and used to contact various diode types in a mechanically realistic terahertz mixer test block. The whisker diode structure has been shown to be encouragingly rugged.

The new whisker technology has a number of other benefits. It is simple to make, does not require prior bending and can be handled with ease. Diode contact tests show that both anodes and whisker tip are extremely difficult to damage. If, as in the example described here, it is integrated with the RF/IF filter, circuit design and assembly is simplified and mechanically (and therefore electrically) similar circuit structures can be more easily repeated than is the case with wire whiskers.

We expect that the new whisker technology may find applications at lower frequencies. The tolerant mechanical behaviour, circuit simplicity and potential for making electrically similar structures are all attractive features.

Acknowledgements

We would like to thank members of the Precision workshop at RAL, Mr J J Spencer, Mr M J Culver and Mr D S Wilsher for their enthusiastic approach and invaluable input, and Mr A Jones who was responsible for much of the design of the mixer test block and contacting jigs. We would also like to thank Dr E Armandillo and Dr U Kraft for their helpful advice and encouragement.

This work was supported by the European Space Agency, and the prime contractor was Deutsche Aerospace AG.

References

- [1] H. P. Roeser and R. Wattenbach, "A sub-millimetre heterodyne receiver with Schottky diode mixer and its application for radio astronomy physics," *IX. Int. Conf. on IR and MM Waves, Osaka, 1994*
- [2] B. N. Ellision, M. L. Oldfield, D. N. Matheson, B. J. Maddison, C. M. Mann and A. F. Smith, "Corrugated Feedhorns at Terahertz Frequencies - Preliminary Results," *The Fifth Space Terahertz Conference, Ann Arbor, 1994*
- [3] A. S. Treen, N. J. Cronin, "Terahertz Metal Pipe Waveguides," *XVIII Int. Conf. on Inf. and MM. Waves, , Colchester, UK, September, 1993.*
- [4] C. M. Mann, "A Novel 183GHz Subharmonic Schottky Diode Mixer," *PhD Thesis, Queen Mary and Westfield College, University of London, May, 1992.*

Corrugated Feedhorns at Terahertz Frequencies — Preliminary Results

B.N. Ellison, M.L. Oldfield*, D.N. Matheson, B.J. Maddison, C.M. Mann and
A.F. Smith

Rutherford Appleton Laboratory, Chilton, Didcot, OX11 0QX, UK.

* University of Kent at Canterbury, Canterbury, Kent, CT2 7NT, UK.

Abstract

Corrugated feedhorns radiate a near perfect Gaussian beam and are often used as feeds for receiver systems at millimetre and, increasingly, sub-millimetre wavelengths. Perceived constructional difficulties of such feedhorns have tended to limit their use to frequencies below 1 THz. We demonstrate that corrugated feedhorns can be constructed that will allow operation at frequencies well in excess of 2.5 THz and that the resulting antenna patterns are of excellent quality.

Introduction

There is increasing interest in using heterodyne receiver systems at frequencies in excess of 1 THz. This interest has originated primarily from the astronomical and atmospheric science community who wish to study the emission of molecular species from space or the Earth's atmosphere respectively.

Although heterodyne systems operating at frequencies above 1 THz have been demonstrated previously [1], the structure in which the detecting element (normally a Schottky diode) is embedded is not necessarily optimum. For example, it is known that the radiation pattern from a corner cube is not ideal with the best calculated coupling efficiencies being < 80% [2]. Further, due to the relatively long diode contact whisker used which also forms part of the antenna structure, these devices can be unreliable when cooled to low temperatures and may not lend themselves readily to space flight qualification.

Waveguide structures, on the other hand, have shown excellent performance when used with Schottky and superconducting tunnel junction (SIS) detectors

at frequencies up to 700 GHz [3], [4] and waveguide/feedhorn combinations provide efficient coupling to the radiation field at microwave and millimetre wavelengths.

Of the various feedhorn types available the corrugated, or scalar, feed is generally considered to be superior due to its relatively large operational bandwidth, symmetric (Gaussian) power distribution and low sidelobe and cross-polarisation levels. To date, the highest frequency at which corrugated feedhorns have been used is ~ 700 GHz [3], the primary disadvantage being the perceived difficulty of construction. Although it is clear that using corrugated feeds in the terahertz frequency range necessitates the machining of structures with dimensions on the scale of microns and to sub-micron accuracy, we demonstrate that such feedhorns can be produced by a combination of conventional machining and novel coating techniques. A corrugated feedhorn has been fabricated and tested at 2.5 and 3.1 THz using a far-infrared laser as a source. The preliminary beam patterns measured are of high quality, exhibiting low sidelobe levels and Gaussian power distribution.

Feedhorn Design and Manufacture

The corrugated feedhorn described here has been scaled from an existing and successful 490 GHz design; the feedhorn mandrel, which is a 'negative' of the actual feedhorn, is shown in Figure 1. The aperture size is 0.84 mm diameter and the slant angle and length are 5.98° and 4.04 mm respectively. Along the slant length of the mandrel 64 corrugations are machined with a width, pitch and average depth of 26, 52 and $32\text{ }\mu\text{m}$ respectively. The last 10 corrugations in the throat region vary in depth to a maximum of $52\text{ }\mu\text{m}$ in order to provide a good impedance match between the feedhorn and the circular waveguide output. The corrugation structure selected allows a typical operational bandwidth of $\pm 20\%$ about the centre frequency of 2.5 THz. The design methods used are based on those described by Thomas [5] and Clarricoats [6].

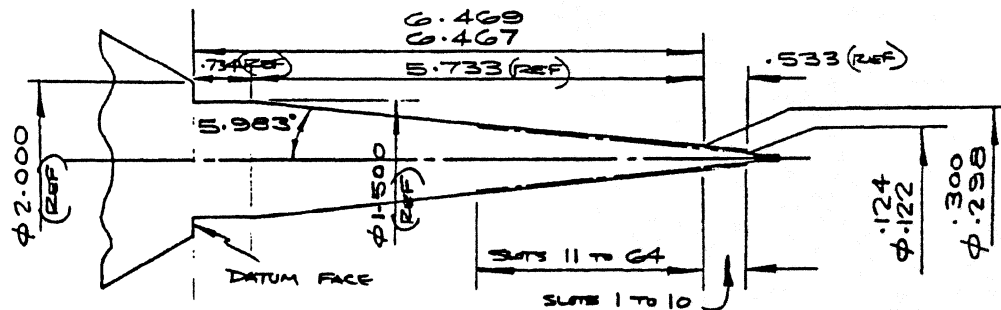


Figure 1: Drawing of aluminium mandrel

The aluminium mandrel was manufactured by using a high precision lathe and conventional machining techniques. Figure 2a shows a machined mandrel with a circular waveguide output; this type was used during the current measurements. Figure 2b shows a similar mandrel, but in this case with step sections added to allow an interface to a reduced height rectangular waveguide of dimensions 96 by 24 μm .

Once the mandrel is machined it must be coated with gold and copper and the aluminium etched away to produce the feedhorn. Normally the mandrel is coated using an electroforming process. A difficulty often encountered with this is that copper grows preferentially around the top of the corrugations leaving voids filled with the electrolyte solution which can leach out and damage the interior of the feedhorn. This problem is exacerbated as the structure size decreases. In addition, aluminium is difficult to gold or copper plate directly and a pre-etch, which tends to degrade the mandrel surface finish, is required.

Although techniques have been developed to try to control these problems, e.g. by filling the voids with solder or epoxy, we have avoided these difficulties by developing a novel form of coating procedure that uses RF sputtering which, as a consequence, does not require the mandrel to be pre-etched and effectively closes the corrugations in a low pressure argon atmosphere. Using this process means that at worst harmless low pressure argon may be trapped in any residual voids and at best the corrugations are completely filled with copper. This may prove a considerable advantage for devices required for space flight.

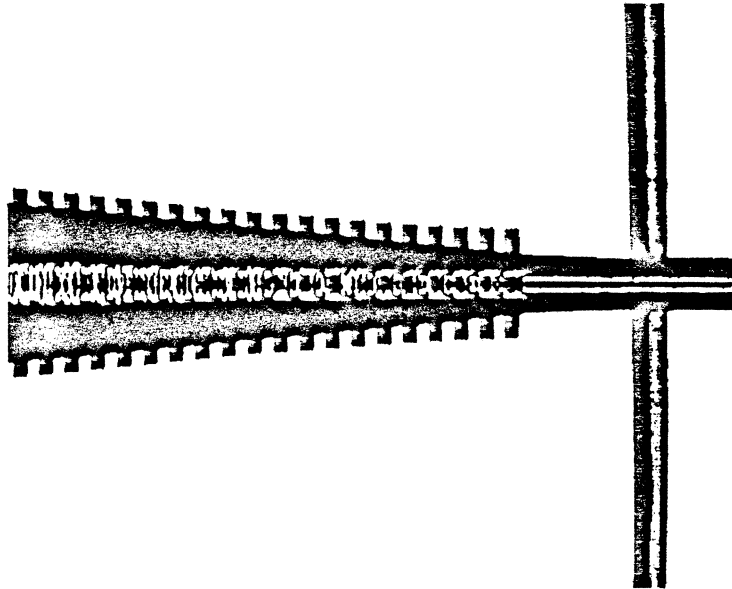


Figure 2a: Machined mandrel with circular waveguide output (shown with a human hair).

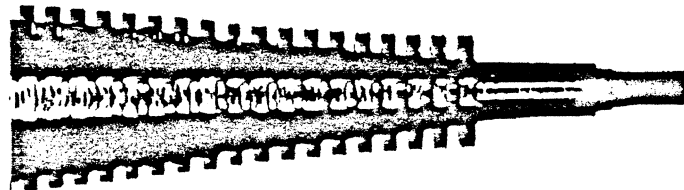


Figure 2b: Machined mandrel with integrated circular to rectangular waveguide transition.



Figure 3: Sectioned test piece with partially filled corrugations.

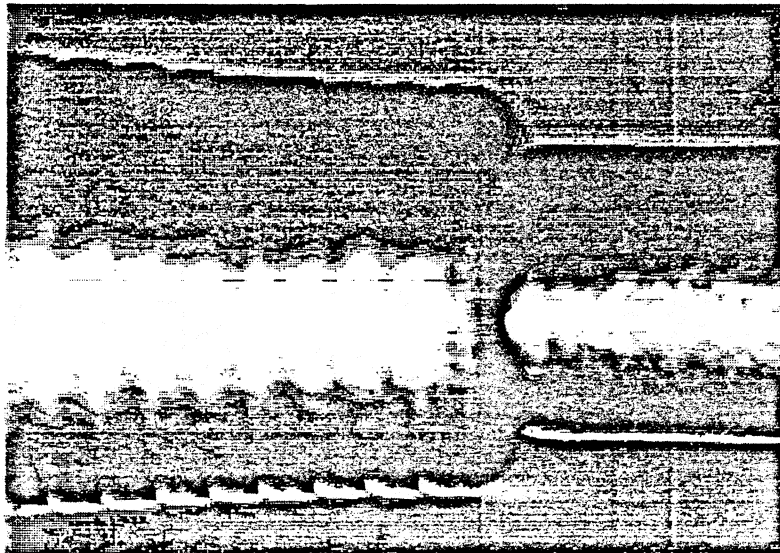


Figure 4: Sputter coated mandrel

During the coating process the mandrel is chemically cleaned and placed on a 'rotating spit' inside the sputtering system [7]. An initial thin ($\sim 2 \mu\text{m}$) layer of gold is deposited onto the surface. Copper is next deposited until the corrugations are filled or a substantial thickness is achieved. The copper provides a support layer for the corrugation and is protected by the gold layer during the aluminium etching process. The sputtering parameters, e.g. rate of deposition time etc., that provide coating of the top, base and vertical walls of the corrugations were established by a series of trials on test pieces. A sectioned test piece with partially filled corrugations is shown in Figure 3 and a coated mandrel is shown in Figure 4.

After deposition of the copper is complete a further thin layer of gold is deposited to prevent oxidation of the copper and the whole mandrel is finally electroformed with copper to provide a bulk structure which can be machined and inserted into a suitable holder. The final process step is to etch the aluminium in a bath of sodium hydroxide which leaves the finished feedhorn. Figure 5 shows an example of a finished feedhorn mounted in a holder.

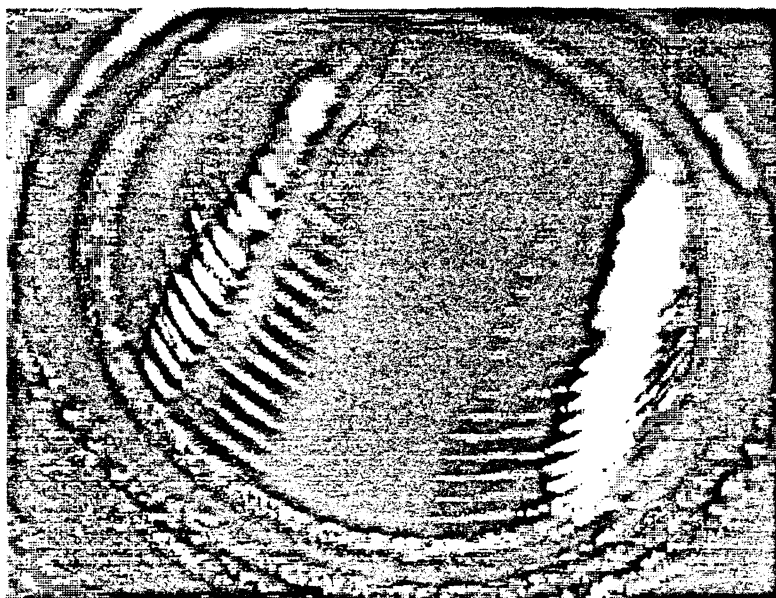


Figure 5: Finished feedhorn mounted in holder.

Measurement Technique

Figure 6 illustrates the measurement scheme which consisted of a far infrared (FIR) CO_2 pumped laser used as a source, a polyethylene coupling lens and a Golay cell detector. The coupling lens coupled the FIR laser beam into one of

two feedhorns that were mounted back to back and the emergent beam from the second feedhorn was scanned by a Golay cell, the aperture of which was stopped down by a small (~ 0.4 mm diameter) hole cut into paper (paper is a good block, though not necessarily an absorptive one, to $120\text{ }\mu\text{m}$ radiation). The output of the Golay cell was amplified and integrated by a phase sensitive detector and the voltage output digitised and stored in a computer. A second Golay cell was used to monitor the laser output power and to correct for level variations during a scan. With this set-up it was possible to perform linear scans across the feedhorn in both E and H planes and to generate a 2D raster image of the complete pattern. In addition, the scanning mechanism could be moved along the axis of propagation in order to investigate the beam expansion and standing wave effects. Finally, a Fabry-Pérot interferometer was used to check the frequency of the source.

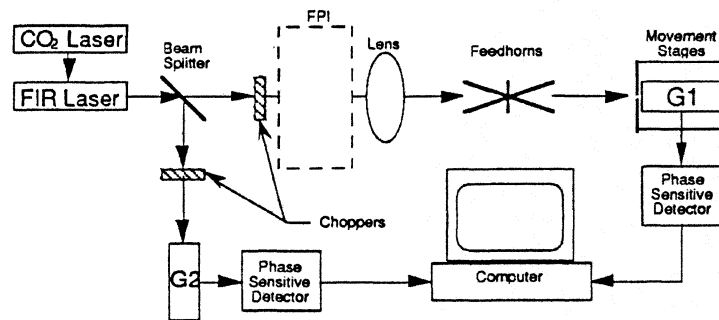


Figure 6: Measurement set-up using FIR laser as source.

Ideally, the radiation patterns would be measured by moving the detector in an arc about the phase centre of the feed. However, it proved difficult to configure our system to allow both E and H plane measurements to be made and to keep the detector close to the feedhorn in order to give the best signal to noise ratio. The half angle divergence of the beam from the feedhorn is typically 15° at 25 dB below the on axis value and truncation effects due to the aperture being moved off-axis are small.

Results

The radiation patterns produced by the feedhorn have so far been measured in the far field at 2.5 THz (the design frequency) and 3.1 THz and the data presented here are not corrected for the effects of the measurement aperture. In Figure 7 we show the measured intensity distributions for both the E and H planes at 2.5 THz and include a fitted Gaussian profile. Figure 8 presents similar measurements performed at 3.1 THz. From these data it appears that

at the design frequency the E and H plane patterns have a high degree of symmetry. At 3.1 THz the E and H patterns are slightly asymmetric, but this frequency was beyond the nominal feedhorn bandwidth due to a restriction in the FIR laser lines available. At both frequencies the sidelobes are below -18 dB, implying a beam efficiency for the feedhorn of > 90%.

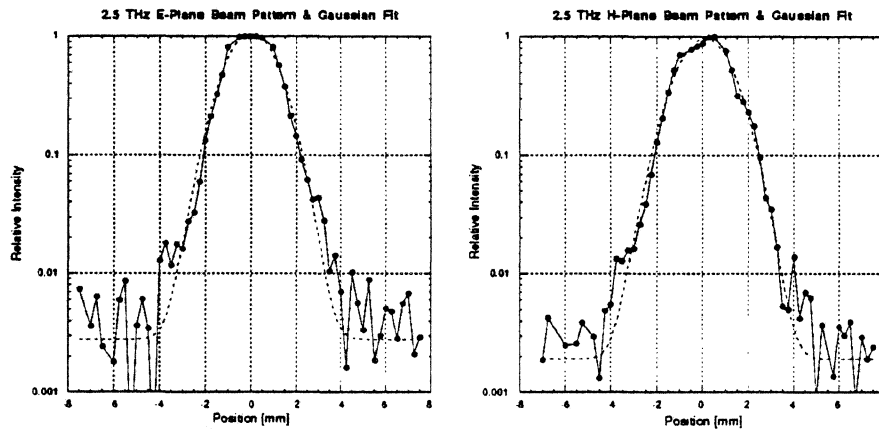


Figure 7: 2.5 THz E- & H-plane intensity distributions.

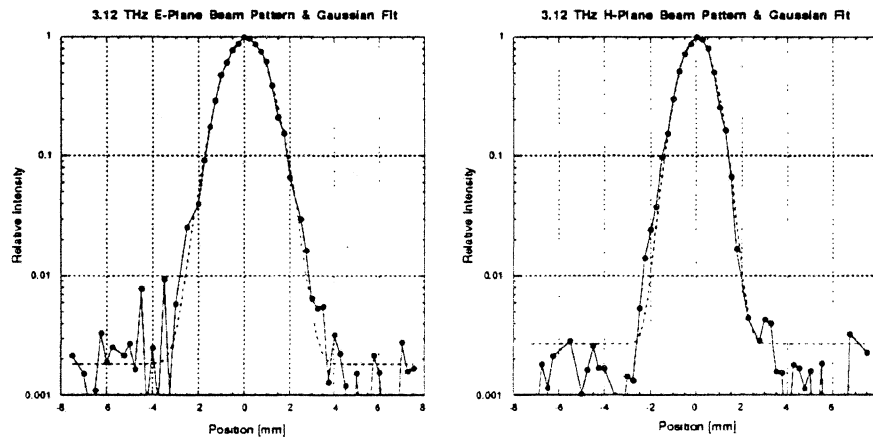


Figure 8: 3.1 THz E- & H-plane intensity distributions.

A curve fit to data obtained at different points along the axis of propagation gives an estimate of the feedhorn minimum beam waist size of ~ 0.33 mm at

2.5 and 3.1 THz. This compares reasonably well with the predicted value of ~ 0.25 mm [8].

Finally, Figure 9 shows a full 2D raster scan of the feedhorn at 2.5 THz with contour lines plotted at 3 dB intervals. This plot emphasises the symmetry of the beam pattern.

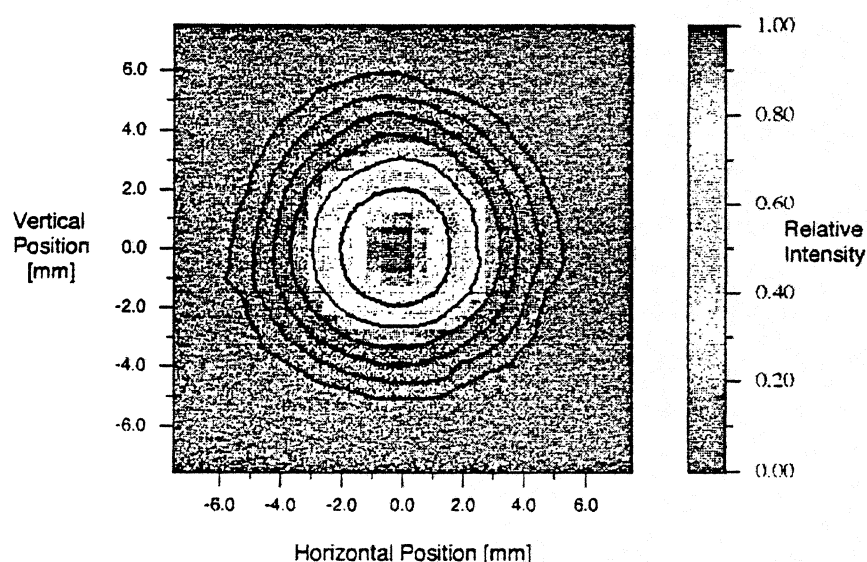


Figure 9: 2D raster scan of feedhorn radiation pattern at 2.5 THz.

Conclusion

A corrugated feedhorn has been fabricated and tested at 2.5 and 3.1 THz. Conventional mandrel machining techniques have been used and a novel method of mandrel coating has been developed.

The data presented are of a preliminary nature: for example we have not rigorously examined the effect of the measurement aperture on the measured patterns, but expect this to be small. Also there are outstanding measurements yet to be made, including additional frequencies, cross-polarisation and insertion loss. However, it would appear that the beam profiles in both E and H planes exhibit excellent symmetry at the design centre frequency, a Gaussian distribution to < -15 dB and have sidelobe levels < -18 dB, the latter implying a beam efficiency $> 90\%$.

Finally, use of these feedhorns need not be confined solely to heterodyne systems. For example, applications may exist with bolometric detectors in which the use of fundamental mode waveguide coupled with high quality

beam patterns could yield improvements in sensitivity for devices operated at terahertz frequencies.

Acknowledgements

We gratefully acknowledge J. Culver, J. Spencer and D. Wilsher of the RAL precision workshop whose machining skill made this work possible . We would also like to thank Dr E. Armandillo and Dr U. Kraft for their helpful advice and encouragement and Prof. G. Rebeiz for allowing the late inclusion of this paper in the Space Terahertz conference.

This work was supported by the European Space Agency and the prime contractor was Deutsche Aerospace AG.

References

- [1] H.P. Roeser and R. Wattenbach, "A sub-millimeter heterodyne receiver with Schottky diode mixer and its application for radio astronomy and atmospheric physics," *IX. Inf. Conf. on IR and MM Waves*, Osaka, 1994.
- [2] E.N. Grossman, "The coupling of sub-millimeter corner cube antennas to Gaussian beams," *Infrared Phys.*, Vol. 29, No. 5, 1989.
- [3] J.W. Kooi, C.K. Walker, H.G. LeDuc, T.R. Hunter, D.J. Benford and T.G. Phillips, "A low noise 665 GHz SIS quasi-particle waveguide receiver," *Int. J. of IR and MM Waves* Vol. 15, No. 3, March 1994.
- [4] G. de Lange, "Quantum limited heterodyne detection of 400–840 GHz radiation with superconducting Nb tunnel junctions," PhD Thesis, 1994.
- [5] MacA. B. Thomas, "Design of corrugated conical horns," *IEEE Trans. Antennas Propagat.*, Vol. AP-26, No. 2, March 1978.
- [6] P.J.B Clarricoats and A.D. Olver, "Corrugated horns for microwave antennas," *IEE Electromagnetic Wave Series 18*, (Peter Peregrinus 1984).
- [7] A450 sputtering system manufactured by Alcatel, Annecy, France.
- [8] R.J. Wylde, "Millimetre-wave Gaussian beam-mode optics and corrugated feedhorns," *IEE Proc.*, Vol. 131, Pt. H, No. 4, August 1984.